Pankaj Saha
P. M. V. Subbarao
Basant Singh Sikarwar   *Editors*

# Advances in Fluid and Thermal Engineering

## Select Proceedings of FLAME 2018

Springer

# Lecture Notes in Mechanical Engineering

**Lecture Notes in Mechanical Engineering (LNME)** publishes the latest developments in Mechanical Engineering - quickly, informally and with high quality. Original research reported in proceedings and post-proceedings represents the core of LNME. Volumes published in LNME embrace all aspects, subfields and new challenges of mechanical engineering. Topics in the series include:

- Engineering Design
- Machinery and Machine Elements
- Mechanical Structures and Stress Analysis
- Automotive Engineering
- Engine Technology
- Aerospace Technology and Astronautics
- Nanotechnology and Microengineering
- Control, Robotics, Mechatronics
- MEMS
- Theoretical and Applied Mechanics
- Dynamical Systems, Control
- Fluid Mechanics
- Engineering Thermodynamics, Heat and Mass Transfer
- Manufacturing
- Precision Engineering, Instrumentation, Measurement
- Materials Engineering
- Tribology and Surface Technology

To submit a proposal or request further information, please contact the Springer Editor in your country:

**China:** Li Shen at li.shen@springer.com

**India:** Dr. Akash Chakraborty at akash.chakraborty@springernature.com

**Rest of Asia, Australia, New Zealand:** Swati Meherishi at swati.meherishi@springer.com

**All other countries:** Dr. Leontina Di Cecco at Leontina.dicecco@springer.com

To submit a proposal for a monograph, please check our Springer Tracts in Mechanical Engineering at http://www.springer.com/series/11693 or contact Leontina.dicecco@springer.com

**Indexed by SCOPUS. The books of the series are submitted for indexing to Web of Science.**

More information about this series at http://www.springer.com/series/11236

Pankaj Saha · P. M. V. Subbarao ·
Basant Singh Sikarwar

Editors

# Advances in Fluid and Thermal Engineering

Select Proceedings of FLAME 2018

Springer

*Editors*
Pankaj Saha
Oak Ridge Institute for Science
and Education
Oak Ridge, TN, USA

U.S. Department of Energy
National Energy Technology Laboratory
Morgantown, WV, USA

Basant Singh Sikarwar
Department of Mechanical Engineering
Amity School of Engineering and
Technology, Amity University Uttar Pradesh
NOIDA, Uttar Pradesh, India

P. M. V. Subbarao
Department of Mechanical Engineering
Indian Institute of Technology Delhi
New Delhi, Delhi, India

# Preface

We are pleased to introduce the proceedings of cutting-edge research articles on fluid and thermal engineering from the First International Conference on Future Learning Aspects for Mechanical Engineering (FLAME 2018) organized by the Department of Mechanical Engineering, Amity University, Uttar Pradesh, Noida, India, from 3 to 5 October 2018.

The primary mission of this conference was to lay a platform that brings together academicians, scientists, researchers and industry experts across the globe to share their scientific ideas and vision in the areas of thermal, design, industrial, production and interdisciplinary areas of mechanical engineering. FLAME 2018 played a significant role to set up a bridge between academician and industry.

The conference hosted almost 550 participants to exchange scientific ideas. During 3 days of the conference, researchers from academic institutes and industries presented the most recent cutting-edge discoveries, went through various scientific brainstorm sessions and exchanged ideas on practical socio-economic problems. This conference also provided a scope to establish a network for joint collaboration between academician and industry. Major emphasis was focused on the recent developments and innovations in various fields of mechanical engineering through plenary lectures.

This book covers the thermal and fluid engineering topics such as heat transfer enhancement and heat transfer equipment; heat transfer in nuclear applications; microscale and nanoscale transport; multi-phase transport and phase change; multi-mode heat transfer; numerical methods in fluid mechanics and heat transfer; refrigeration and air conditioning; thermodynamics; space heat transfer; transport phenomena in porous media; turbulent transport; theoretical fluid dynamics: fundamental issues and perspectives; experimental fluid dynamics: flow measurement techniques and instrumentation; computational fluid dynamics: theory and applications; fluid machinery; turbomachinery; and fluid power.

This book indulges the fluid and thermal science engineering aspects, mainly will serve as the reference guide for researchers and practitioners and is expected to foster better communication and closer cooperation between academia and industry partners.

We would like to acknowledge all the participants who have contributed to this volume. We also deeply express our gratitude for the generous and constant support provided by Amity University, Noida; Science and Engineering Research Board (SERB), an enterprise of Department of Science and Technology (DST), Government of India; Siemens; ISME; and Begell House. We express our gratitude to the publishers and every staff of the department and institute who have dedicated their countless time and support to bring these manuscripts into a book. We would like to thank all the reviewers for their time and effort in reviewing the document. Finally, we would also like to express our gratitude to Respected Founder President, Amity University, Dr. Ashok K. Chauhan, for providing all kinds of support, and this book is not complete without his blessings.

We welcome your suggestions for useful reviews and compelling and creative ideas for further improvement for the continuing success of this book.

NOIDA, India                                          Prof. (Dr.) Basant Singh Sikarwar
New Delhi, India                                         Prof. (Dr.) P. M. V. Subbarao
Oak Ridge/Morgantown, USA                                         Dr. Pankaj Saha
January 2019

# Contents

# About the Editors

**Dr. Pankaj Saha** holds a PhD in Mechanical Engineering from IIT Kanpur, India. Currently, he is an ORISE-ORAU research fellow in the Multiphase Flow team at DOE-NETL, Morgantown, WV, USA. He has developed complete in-house 3D NS solver implementing finite-difference-method in both serial and parallel architecture. His present work at NETL deals with the modeling of turbulent oil jet discharged into water.

**Dr. P. M. V. Subbarao** received his PhD from the department of Mechanical Engineering, IIT Kanpur, India. Currently, he is Associate Dean and Professor in the department of Mechanical Engineering, IIT Delhi. His research interest includes analysis of supercritical vapour power cycles, steam generators and turbines, experimental and computational analysis of heat transfer enhancement, flame tomography, thermodynamic analysis of organic power generation cycles, design and development of pico-hydel power plants for rural applications, and development of bio-fuel systems. He has published more than hundred papers in international journals and conferences as well as several book chapters.

**Dr. Basant Singh Sikarwar** obtained his PhD from IIT Kanpur, India followed by a postdoc at the Iowa State University, USA. Currently, he is Professor and Head of the Department of Mechanical Engineering, Amity University, Noida, India. He has published about 80 journal and conference papers. Dr. Sikarwar is a member of the Indian Society of Mechanical Engineering. He is a co-holder of four national and international patents, and also a recipient of DST and MSME funding for research.

# Simple Analytical Method for Performance of an Absorber Plate in Flat-Plate Solar Collectors for Two-Dimensional Heat Flow

**Jayanarayan Mahakud and Balaram Kundu**

**Abstract** In this paper, two-dimensional temperature distributions in the absorber plate of a flat-plate solar collector have been determined by an approximate analytical technique. In case of two-dimensional heat flow in the absorber plate under actual boundary conditions, the determination of temperature field using an exact analytical method might not be possible. Alternatively, this temperature field can be evaluated using numerical methods. In the present study, finite difference method has been employed as a numerical tool. However, it is well known that the numerical calculations increase the computational cost. For the ease of calculations, an approximate analytical model has been proposed in the present study and the accuracy of the present analytical method has been checked with the comparison of results obtained between the present analytical and numerical techniques. It can be demonstrated that there is an excellent agreement between two results and the deviation between these two have never exceeded by 5%. Therefore, the present analytical method might have a significant importance for analyzing the performance of an absorber plate in order to avoid difficulties of the numerical solution.

**Keywords** Solar collector · Approximate analytical solution · 2-D heat transfer · Absorber plate

## Nomenclature

| | |
|---|---|
| $A$ | Dimensionless variable defined in Eq. (5b) |
| $D$ | Deviation of temperature, $(\theta_{analytical} - \theta_{numerical})/\theta_{analytical}$ |
| $k$ | Thermal conductivity of an absorber plate material (W m$^{-1}$ K$^{-1}$) |
| $L$ | Half-pitch distance between flow tubes as shown in Fig. 1 (m) |
| $M$ | Dimensionless thermogeometric parameter of absorber plate, see Eq. (3) |
| $N$ | Dimensionless absorbed solar flux, see Eq. (3) |
| $S$ | Absorbed solar flux (W m$^{-2}$) |
| $t$ | Thickness of the absorber plate (m) |

J. Mahakud · B. Kundu (✉)
Department of Mechanical Engineering, Jadavpur University, Kolkata 700032, India
e-mail: bkundu@mech.net.in

$T$     Local absorber plate temperature (°C)
$T_\infty$     Ambient temperature (°C)
$U_L$     Overall heat loss coefficient (W m$^{-2}$ K$^{-1}$)
$x$     $X$-coordinate shown in Fig. 1 (m)
$X$     Dimensionless coordinate, $x/L$
$y$     $Y$-coordinate shown in Fig. 1 (m)
$Y$     Dimensionless $y$-coordinate, $y/W$
$W$     Length of the symmetric heat transfer module (m)

**Greek letters**

$\alpha$     Temperature variable along $x$-direction, used in Eq. (6)
$\beta$     Temperature variable along $y$-direction, see Eq. (6)
$\delta$     Aspect ration defined in Eq. (3)
$\theta$     Dimensionless temperature expressed in Eq. (3)

# 1   Introduction

Among the non-conventional energy sources, utilization of solar energy in practical applications like domestic hot water and space heating, in industrial drying processes, absorption refrigeration system is grown up exponentially. The solar energy absorbed in the absorber plate in flat-plate collectors transforms it to collector fluid for usable energy to be used in different practical applications. The flat-plate collector is suitable for creating a moderate temperature heat transfer field, and therefore, it is applicable to the places where there is available strong solar radiation intensity throughout the year. Among various types of collectors, flat-plate solar collector is a special type of heat exchanger and it has been preferred in myriad applications due to its simple design and ease of fabrication. The main part of the flat-plate solar collector is the absorber plate, through which the solar incident energy is absorbed and converted it into thermal energy. This thermal energy transfers to a fluid flowing in the tubes, which is an integral part of the plate. As a result, the energy of the collector fluid increases. Therefore, the performance of the solar collector is mainly dependent on the performance of the absorber plate.

A large number of research activities have been devoted to various collector system performances using several theoretical, experimental, and analytical analyses. The first analytical study on flat-plate solar collector was carried out by Hottel and Woertz [1]. They had taken one-dimensional heat conduction equation with lumped model for their analysis. Later on with consideration of constant heat loss coefficient, Hottel and Whillier [2], and Bliss [3] separately exhibited a model to regulate the useful thermal energy through an absorber plate from solar radiation. Duffie and Beckman [4] sighted a thorough work on the thermal analysis of

absorber plates with a constant thickness. Seeing that a suitable shape of the plate geometry is quite important from the design point of view, different innovative shapes of absorber plates have been suggested by Hollands and Stedman [5], Kundu [6–8], Kundu and Lee [9] for the enhancement of the thermal performance based on the objective optimization point of view. On the other hand, a constant thickness absorber plate is extensively used in practical applications because of simplicity of its design Kundu [10].

In all the above studies, thermal analysis was carried out based on the one-dimensional heat conduction in the plate. However, a two-dimensional temperature distribution may exist over the absorber plate of the flat-plate collector due to typical shape and principle of operation. Therefore, it is obvious that the two-dimensional analysis gives always a more accurate evaluation on the performance of the absorber plate. Consequently, less number of works have been done in two-dimensional heat flow aspects with different boundary conditions. Rao et al. [11] proposed a two-dimensional model for the thermal analysis of absorber plates to compute the fluid temperature. Lund [12] used approximate analytical technique in terms of perturbation infinite series to solve the governing partial differential equations for two-dimensional heat transfer model on the flat-plate solar collector with adiabatic boundary conditions at the upper and lower edges of the collector. Kazeminejad [13] solved the one- and two-dimensional conduction equations of the absorber plate with different boundary conditions using an efficient finite volume method.

From the literature survey summarized above, it can be pointed out that a few of studies have been found with the consideration of two-dimensional heat flow in the absorber plate. However, to analyze the absorber plate under an actual design aspect, two-dimensional effects are always present for the absorber plate as it is made of thin thickness and highly conductive material. Almost all the analyses for absorber plates for conducting heat in two directions were done numerically. There is inherent problem to establish an exact analytical model for the two-dimensional temperature field in the absorber plate with adopting practicable boundary conditions to solve the energy equation. For the above reasons, an approximate analytical method has been proposed in this study to determine the thermal behavior of the absorber plate to have a simplified model to establish for the thermal analysis. The results obtained from the present approximate model have been compared with the data generated by the finite difference method. There is a well match between the two results.

## 2 Mathematical Formulations

The flat-plate solar collector mainly consists of an absorber plate and fluid-carrying tubes as shown in Fig. 1. Due to the absorption of solar flux in the plate, both the plate and fluid temperatures increase as well. For the thermal analysis of absorber plate, a symmetric heat transfer module of length $W$ and width $L$ repeats between
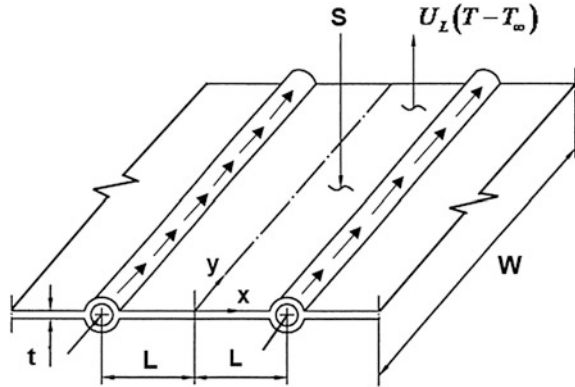
two fluid-carrying tubes can be considered. As the temperature of the plate is higher than the ambient, there is heat loss occurred between the absorber plate and the surrounding by convection and radiation. These heat losses are incorporated by the calculation of the overall heat loss coefficient. The energy equation for an absorber plate considering two-dimensional heat conduction equation under steady state can be written in differential form as

$$\frac{\partial}{\partial x}\left(k\frac{\partial T}{\partial x}\right) + \frac{\partial}{\partial y}\left(k\frac{\partial T}{\partial y}\right) + \frac{S}{t} - \frac{U_L(T-T_\infty)}{t} = 0 \tag{1}$$

Since there existed a low temperature variation for the flat-plate collector due to direct absorption of solar energy, the thermophysical properties of an absorber plate can be assumed to be constant. Therefore, Eq. (1) can be written in dimensionless form as follows:

$$\frac{\partial^2\theta}{\partial X^2} + \delta^2\frac{\partial^2\theta}{\partial Y^2} + N - M^2\theta = 0 \tag{2}$$

where

$$\theta = \frac{T-T_\infty}{T_{\text{in}}-T_\infty};\; X = \frac{x}{L};\; Y = \frac{y}{W};\; \delta = \frac{L}{W};$$
$$N = \frac{SL^2}{kt(T_{\text{in}}-T_\infty)};\; M^2 = \frac{U_L L^2}{kt} \tag{3}$$

For the solution of Eq. (2), two boundary conditions in the x-direction and two boundary conditions in the y-direction are necessary for it is a closed-form solution. There is no net heat transfer along the x-direction at the midsection of the plate between two tubes due to zero value of net heat transfer across that section for the symmetric geometry. At the tube section, an energy balance can be made between conduction and convection. In the y-direction, negligible heat exchange at the edge

of the plate can be assumed for the small surface area exposed to the surrounding. Mathematically, the boundary conditions taken in the present study are expressed as follows:

$$\text{at } x = 0 \ (0 \le y \le W), \partial T/\partial x = 0 \tag{4a}$$

$$\text{at } x = L \ (0 \le y \le W), -kt\frac{\partial T}{\partial x}\mathrm{d}y = \dot{m}c_p\mathrm{d}T_f \tag{4b}$$

$$\text{at } y = 0 \ (0 \le x \le L), \partial T/\partial y = 0 \tag{4c}$$

$$\text{at } y = W(0 \le x \le L), \partial T/\partial y = 0 \tag{4d}$$

The dimensionless boundary conditions can be written as

$$\text{at } X = 0 \ (0 \le Y \le 1), \partial\theta/\partial X = 0 \tag{5a}$$

$$\text{at } X = 1 \ (0 \le Y \le 1), \partial\theta/\partial X = -A = -\frac{\dot{m}c_pL}{kt(T_{\text{in}} - T_\infty)}\frac{\mathrm{d}T_f}{\mathrm{d}y} \tag{5b}$$

$$\text{at } Y = 0 \ (0 \le X \le 1), \partial\theta/\partial Y = 0 \tag{5c}$$

$$\text{at } Y = 1 \ (0 \le X \le 1), \partial\theta/\partial Y = 0 \tag{5d}$$

Here it may be noted that the exact analytical solution of Eq. (2) is not possible due to the boundary conditions taken above (Eq. 5a, 5b, 5c, 5d). However, from the actual analysis point of view, the above expressed boundary conditions are required to consider in the analysis. Therefore, a continuous effort might be there to establish an analytical model from academic as well as practical aspects. This development not only considers the appropriate boundary conditions but also avoids rigorous mathematical calculations in numerical analysis.

For the approximate closed-form solution of Eq. (2), the following variables can be chosen on the basis of the nature of governing equation.

$$\theta(X, Y) = \alpha(X) + \beta(Y) + \mathrm{e}^{-MX} + \mathrm{e}^{-\left(\frac{M}{\delta}\right)Y} \tag{6}$$

Combining Eqs. (2) and (6), the following equations are obtained:

$$\frac{\mathrm{d}^2\alpha(X)}{\mathrm{d}X^2} - M^2\alpha(X) + N = 0 \tag{7}$$

and

$$\frac{\mathrm{d}^2\beta(Y)}{\mathrm{d}Y^2} - \frac{M^2}{\delta^2}\beta(Y) = 0 \tag{8}$$

Equations (7) and (8) are solved separately along with the boundary conditions expressed in Eq. (5a, 5b, 5c, 5d), and the following unknown temperature dependent variables are determined:

$$\alpha(X) = C_1 \cosh(MX) + C_2 \sinh(MX) + \frac{N}{M^2} \tag{9}$$

and

$$\beta(Y) = C_3 \cosh\left[\left(\frac{M}{\delta}\right)Y\right] + C_4 \sinh\left[\left(\frac{M}{\delta}\right)Y\right] \tag{10}$$

where

$$C_1 = \frac{M[e^{-M} - \cosh(M)] - A}{M \sinh(M)}; C_2 = 1; C_3 = \frac{e^{-\frac{M}{\delta}} - \cosh\left(\frac{M}{\delta}\right)}{\sinh\left(\frac{M}{\delta}\right)}; C_4 = 1 \tag{11}$$

Combining Eqs. (6), (9), (10), and (11), the final expression for the non-dimensional temperature distribution of an absorber plate can be written as

$$\theta(X, Y) = \left[\frac{M[e^{-M} - \cosh(M)] - A}{M \sinh(M)}\right] \cosh(MX) + \sinh(MX)$$

$$+ \frac{N}{M^2} + e^{-MX} + \left[\frac{e^{-\frac{M}{\delta}} - \cosh\left(\frac{M}{\delta}\right)}{\sinh\left(\frac{M}{\delta}\right)}\right] \cosh\left[\left(\frac{M}{\delta}\right)Y\right] + \sinh\left[\left(\frac{M}{\delta}\right)Y\right] + e^{-\left(\frac{M}{\delta}\right)Y}$$

$$\tag{12}$$

Equation (12) is an approximate temperature distribution of an absorber plate in flat-plate solar collector for conducting heat in the plate in two directions. From this mathematical expression, it can be highlighted that one-dimensional temperature field can be possible to obtain by omitting the other directional heat flow.

## 3  Results and Discussion

The main concern for establishing any approximate model is to obtain a high accuracy level with respect to the actual value. It has already been mentioned in the previous sections that the classical analytical solution of the present governing equation with the boundary conditions is not feasible in order to achieve 100% accurate results. Alternatively, the present governing equation has been solved numerically to have data to validate the present approximate model. Using Taylor series central difference scheme with the second order of accuracy, the governing and boundary equations have been discretized [14]. The difference equations obtained from the discretization are then solved by Gauss–Seidel iteration, and results are

taken with satisfying necessary and sufficient criteria of convergence. In the present study, the necessary convergence criterion was taken as $10^{-6}$. The grid independence test has also been done to take the numerical results.

For comparisons of results between the present approximate analytical and numerical values, Fig. 2 has been plotted. Figure 2 shows the temperature distribution in an absorber plate in the $x$-direction for a set of design constants. In the absorber plate, solar energy is absorbed and is conducted toward the fluid-carrying tubes. Therefore, the temperature at the middle of the plate between two successive tubes is always a maximum, and the temperature of that section increases in the direction of fluid flow in tubes as the absorbed energy is carried out by the collector fluid. In the plate, heat transfer takes place toward the collector fluid. The temperature is plotted in Fig. 2a as function of $X$ for a thermogeometric parameter $M = 0.5$, a constant solar incident rate of $N = 0.2$, and collector fluid temperature gradient, and aspect ratio both taken as 0.1. The proposed approximate analytical results and the numerical values are in good agreement with each other, which confirms the validity of the approximate analytical method. Figure 2b depicts the trend of the percentage of deviation between the analytical and numerical determinations as a function of $X$ for the same design variables taken in Fig. 2a. It is interesting to note that the deviation depends on the spatial coordinates and a peculiar variation of the deviation of temperature has been found. There is a position where the deviation becomes a minimum. Overall, the deviation of temperature predictions reaches a maximum at the plate attached to the fluid-carrying tube. However, the maximum deviation value is around 1% which indicates a negligible variation from the engineering accuracy point of view.



(a) Temperature distribution          (b) Percentage of deviation
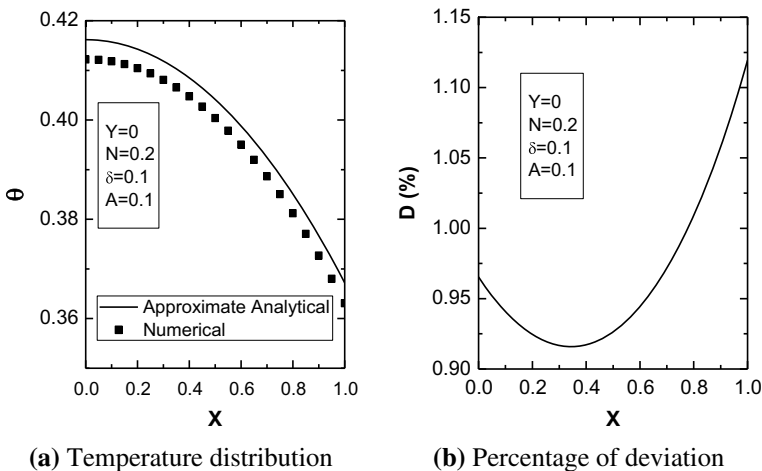
**Fig. 2** Comparison of temperature distribution in an absorber plate as a function of $X$ predicted by approximate analytical and numerical methods for $M = 0.5$

The same observation can be made by plotting Fig. 3 for $M = 0.4$ to understand the accuracy level of the proposed approximate analytical model. For this observation, it is noted that the accuracy of the analytical model is also function of $M$. However, the trend of deviation is obtained same as shown in Fig. 2. Moreover, a little high difference is found in this figure and the maximum percentage of relative deviation is below 4.6%. Therefore, it can be concluded that the accuracy level of proposed approximate model enhances with an increase in $M$ value. On the other hand, as the thermogeometric parameter $M$ increases, the overall loss coefficient increases and as a result, the temperature of the plate decreases due to more heat loss from the plate to the surrounding. This effect can clearly be understood from the plotted Figs. 2 and 3.

Next an effort has been devoted to obtain the temperature in the absorber plate predicted by the present analytical and numerical methods to show the effect of the absorbed solar flux and the collector fluid temperature gradient by plotting Fig. 4. Increasing the parameter $N$ causes to absorb more solar flux in the absorber plate, and thus, the plate temperature enhances. This effect can be verified by comparing the results shown in Figs. 2 and 4a. The deviation of percentage of temperature $D$ at $N = 0.3$ as a function $X$ has been displayed in Fig. 4b. From this figure, it is clearly understood that the relative difference in temperature prediction is an incremented function with $N$. Figure 4c shows the temperature distribution in the absorber plate determined at a collector fluid temperature gradient parameter $A = 0.15$. The influence of this gradient parameter on the absorber plate temperature can be envisaged by comparing the temperature shown in Fig. 4a, c. A correct trend has been displayed as the temperature diminishes with $A$ due to more amount of energy carried out by the collector fluid. The deviation results have also been plotted in Fig. 4d. By comparing the data from Fig. 4b, d, it is obvious that the relative



(a) Temperature distribution          (b) Percentage of deviation
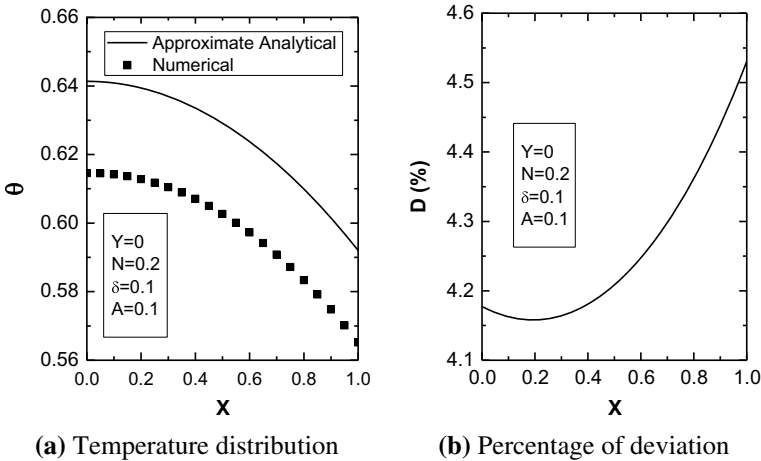
**Fig. 3** Comparison of temperature distribution in an absorber plate as a function of $X$ predicted by approximate analytical and numerical methods for $M = 0.4$

deviation of temperature from approximate analytical and numerical methods amplifies with an increase in temperature gradient of collector fluid.

Finally, the exact values of the dimensionless temperature at various locations in the absorber plate for different values of solar insolation and collector fluid temperature gradient are shown in Tables 1 and 2. The relative deviation of temperature of the approximate analytical analysis from the numerical value does not exceed 5% in a range of design input values taken in the present study. Thus from the results, it can be highlighted that the proposed analytical model has been correctly established
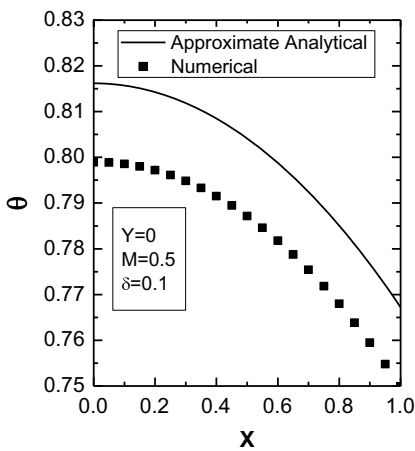


(a) Temperature vs. X at N=0.3, A=0.1
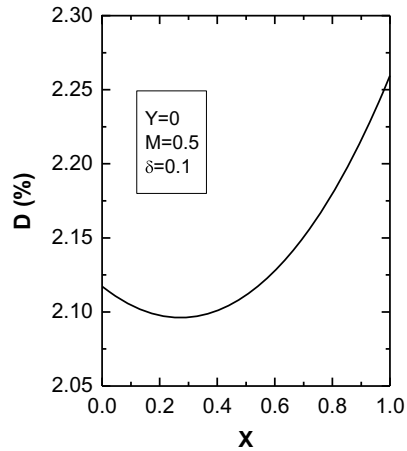
(b) Deviation vs. X at N=0.3, A=0.1
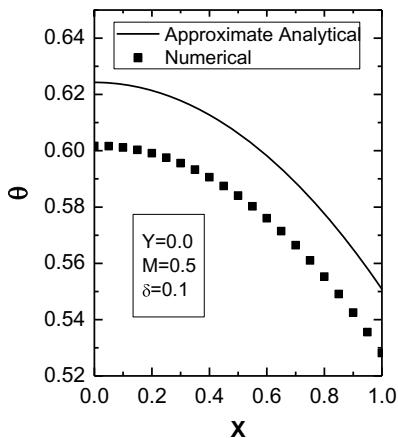
(c) Temperature vs. X at N=0.3, A=0.15
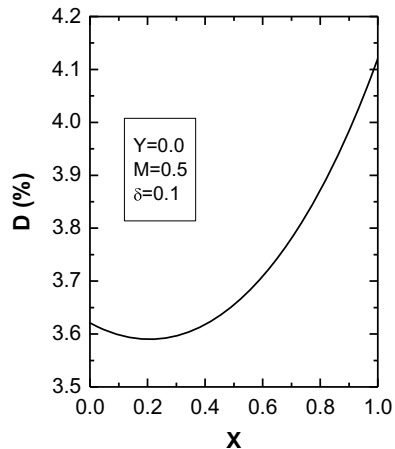
(d) Deviation vs. X at N=0.3, A=0.15

**Fig. 4** Accuracy analysis for approximate analytical model depending on collector fluid temperature gradient parameter

**Table 1** Absorber plate temperature determined by the present approximate analytical and numerical methods for $N = 0.2$, $M = 0.5$, $\delta = 0.1$, and $A = 0.1$

| Coordinates X, Y | Temperature $\left(\theta_{\text{analytical}}\right)$ | Temperature $\left(\theta_{\text{numerical}}\right)$ | % of $D = \left(\frac{\theta_{\text{analytical}} - \theta_{\text{numerical}}}{\theta_{\text{analytical}}}\right) \times 100$ |
|---|---|---|---|
| 0.0, 0.0 | 0.41619 | 0.41218 | 0.96538 |
| 0.1, 0.0 | 0.41571 | 0.41180 | 0.94072 |
| 0.2, 0.0 | 0.41427 | 0.41044 | 0.92463 |
| 0.3, 0.0 | 0.41187 | 0.40809 | 0.91679 |
| 0.4, 0.0 | 0.40849 | 0.40474 | 0.91728 |
| 0.5, 0.0 | 0.40414 | 0.40039 | 0.92632 |
| 0.6, 0.0 | 0.39879 | 0.39503 | 0.94426 |
| 0.7, 0.0 | 0.39244 | 0.38863 | 0.97166 |
| 0.8, 0.0 | 0.38508 | 0.38119 | 1.00927 |
| 0.9, 0.0 | 0.37667 | 0.37269 | 1.05809 |
| 1.0, 0.0 | 0.36721 | 0.3631 | 1.11943 |

**Table 2** Temperature determined by the present approximate analytical and numerical methods for $N = 0.3$, $M = 0.5$, $\delta = 0.1$, and $A = 0.15$

| Coordinates X, Y | Temperature $\left(\theta_{\text{analytical}}\right)$ | Temperature $\left(\theta_{\text{numerical}}\right)$ | % of $D = \left(\frac{\theta_{\text{analytical}} - \theta_{\text{numerical}}}{\theta_{\text{analytical}}}\right) \times 100$ |
|---|---|---|---|
| 0.0, 0.0 | 0.62429 | 0.60168 | 3.62100 |
| 0.1, 0.0 | 0.62357 | 0.60113 | 3.59826 |
| 0.2, 0.0 | 0.62141 | 0.59910 | 3.59003 |
| 0.3, 0.0 | 0.6178 | 0.59558 | 3.59654 |
| 0.4, 0.0 | 0.61274 | 0.59057 | 3.61811 |
| 0.5, 0.0 | 0.6062 | 0.58405 | 3.65534 |
| 0.6, 0.0 | 0.59819 | 0.5760 | 3.70911 |
| 0.7, 0.0 | 0.58867 | 0.56641 | 3.78064 |
| 0.8, 0.0 | 0.57761 | 0.55525 | 3.87157 |
| 0.9, 0.0 | 0.56501 | 0.54250 | 3.98401 |
| 1.0, 0.0 | 0.55081 | 0.52812 | 4.12068 |

and has a high accuracy to predict temperature field of the absorber plate in a wide range of design aspects using its simple mathematical expressions.

In this section, it can be highlighted that the proposed analytical model has ability to determine the temperature field accurately for two-dimensional heat transfer in absorber plates. This mathematical approach is very simple for understanding and implementation. Using the present analysis, collector performance parameters can easily be determined. So this study may help to a designer to determine the unknown designed information easily without any rigorous mathematical calculations. Therefore, from the industrial point of view, the present study will provide a positive aspect in calculating unknown variables to be required in thermal designs.

# 4　Conclusions

The main objective of the present paper is to establish an analytical model for the thermal analysis of an absorber plate in flat-plate solar collectors for two-dimensional heat conduction in the plate. Due to typical shape of the symmetric sector of the plate for the thermal analysis, a closed-form solution might not be possible exactly. Alternatively, an approximate analytical analysis is developed in the present work to obtain the thermal design information easily. The accuracy of the present model has been checked from the results produced by a numerical analysis based on the finite difference method. The percentage of relative deviation of temperature is a function of spatial coordinates as well as system design variables. From the results, it has been established that the maximum temperature deviation is within 5% and therefore, the model presented in this paper might be considered to analyze absorber plate under two-dimensional and steady-state energy transfer. As the present analysis is very simple, no computational step is required to design the plate. Thus, the present closed-form analysis may help to designers for determination of unknown thermal design information by using ordinary calculators.

# References

1. Hottel H, Woertz B (1942) Performance of flat plate solar heat collectors. Trans Am Soc Mech Eng 64:91–104
2. Hottel HC, Whillier A (1958) Evaluation of flat-plate collector performance. In: Transactions of the conference on the use of solar energy, vol 2, Pt. 1. University of Arizona Press, Tuscan, Ariz, p 74
3. Bliss RW (1959) The derivations of several plate-efficiency factors useful in the design of flat-plate solar heat collectors. Sol Energy 3:55–69
4. Duffie JA, Beckman WA (1974) Solar energy thermal processe. Wiley, New York
5. Hollands KGT, Stedman BA (1992) Optimization of an absorber pate fin having a step change in local thickness. Sol Energy 49:493–495
6. Kundu B (2002) Performance analysis and optimization of absorber plates of different geometry for a flat-plate solar collector: a comparative study. Appl Therm Eng 22:999–1012
7. Kundu B (2007) The influence of collector fluid inlet temperature on the performance of a solar-assisted absorption system using step-finned flat-plate collector. Heat Transf Eng 28(5):496–505
8. Kundu B (2008) Performance and optimum design analysis of an absorber plate fin using recto-trapezoidal profile. Sol Energy 82:22–32
9. Kundu B, Lee K-S (2012) Fourier and non-Fourier heat conduction analysis in the absorber plates of a flat-plate solar collector. Sol Energy 86(10):3030–3039
10. Kundu B (2010) Analytic method for thermal performance and optimization of an absorber plate fin having variable thermal conductivity and overall loss coefficient. Appl Energy 87:2243–2255
11. Rao PP, Francis JE, Love TJ Jr (1977) Two-dimensional analysis of a flat-plate solar collector. J Energy 1(5):324–328

12. Lund KO (1986) General thermal analysis of parallel-flow flat-plate solar collector absorbers. Sol Energy 36(5):443–450
13. Kazeminejad H (2002) Numerical analysis of two-dimensional parallel flow flat-plate solar collector. Renew Energy 26(2):309–323
14. Patankar SV (1980) Numerical heat transfer and fluid flow. Hemisphere Publishing, Taylor and Francis Group, New York

# Energetic and Exergetic Analyses of a Solid Oxide Fuel Cell (SOFC) Module Coupled with an Organic Rankine Cycle

**Dibyendu Roy, Samiran Samanta and Sudip Ghosh**

**Abstract** In this article, energetic and exergetic analyses of a natural gas-fueled solid oxide fuel cell (SOFC) and organic Rankine cycle (ORC)-integrated power generation system are presented. In the topping, SOFC cycle of the proposed power generation system, anode channel as well as cathode channel recirculation has been done. Toluene has been used as a working fluid in the ORC. Influence of major operating and design parameters, viz. current density of SOFC, cell temperature on the performance of the proposed system has been examined. Results show that maximum energetic and exergetic efficiencies of the proposed power generation are found to be 67.06 and 58.17%, respectively.

**Keywords** SOFC · ORC · Power plant · Energy · Exergy · Efficiency · Waste heat

## 1 Introduction

Conventional fossil-fired power plant yields lower efficiency and emits a huge amount of greenhouse gases. Nowadays, focus has been given on developing new and renewable power plants having higher energy efficiency with lower environmental impact. In that context, high-temperature fuel cells, viz. solid oxide fuel cell (SOFC)

D. Roy
Department of Mechanical Engineering, Indian Institute of Engineering Science and Technology, Shibpur, Howrah 711103, West Bengal, India

S. Samanta (✉)
School of Mechanical Engineering, Kalinga Institute of Industrial Technology, Deemed to Be University, Bhubaneswar 751024, Orissa, India
e-mail: samirankgec@gmail.com

S. Ghosh
Indian Institute of Engineering Science and Technology, Shibpur, India

and molten carbonate fuel cell (MCFC) can be considered to be a suitable alternative to conventional coal-fired power plants specifically in small-scale distributed power generation systems. These fuel cells emit lesser carbon dioxide and exhibit higher electrical efficiency. Organic Rankine cycle (ORC) is suitable for generating power by utilizing low-temperature waste heat. The ORCs are similar to the conventional Rankine cycles having organic fluids as a working fluid. In previous years, several SOFC-integrated thermodynamic models have been developed and analyzed. Akkaya et al. [1] modeled and analyzed methane-fed tubular SOFC module exergetically. Mahmoudi and Khani [2] proposed an indirect incorporation of methane-fueled SOFC with a gas turbine cycle and a pressurized warm water generation system. Meratizaman et al. [3] proposed a methane-driven SOFC-GT power plant in the range of 11–42.9 kW for household application. Akikur et al. [4] modeled a solar powered SOFC-integrated cogeneration system. Al-Sulaiman et al. [5] studied the performance analysis of a tri-generation system driven by methane-fueled SOFC. In this paper, an attempt has been made to integrate SOFC with ORC. Methane-fueled SOFC-based power generation system with bottoming ORC has been proposed. As SOFC is the major power production component of the system, the influence of its major designing and operating parameters on thermodynamic performance of the designed power generation system have been conducted.

## 2   System Description

Schematic representation of the proposed system is shown in Fig. 1. It is comprised of a topping SOFC module with a bottoming ORC. In the topping SOFC cycle of the proposed system, anode channel as well as cathode channel recirculation have been done. Compressed natural gas is first heated by a heat exchanger (HEX1) and mixed with the recirculated stream before feeding to the SOFC anode channel. On the other hand, heated compressed air is supplied to the SOFC cathode channel. Due to the chemical and electrochemical reactions, chemical energy stored at the natural gas is transformed into electrical energy at the SOFC unit. After recirculation, unutilized methane from the SOFC unit is completely burned at the after burner (AB) unit. Heat exchangers, viz. HEX1 and HEX2 are used to preheat the compressed methane and air, respectively, by using the flue gas from the AB exhaust. Waste heat from the heat recovery vapor generator (HRVG) unit is utilized to operate ORC. Toluene has been selected as working fluid at the ORC.
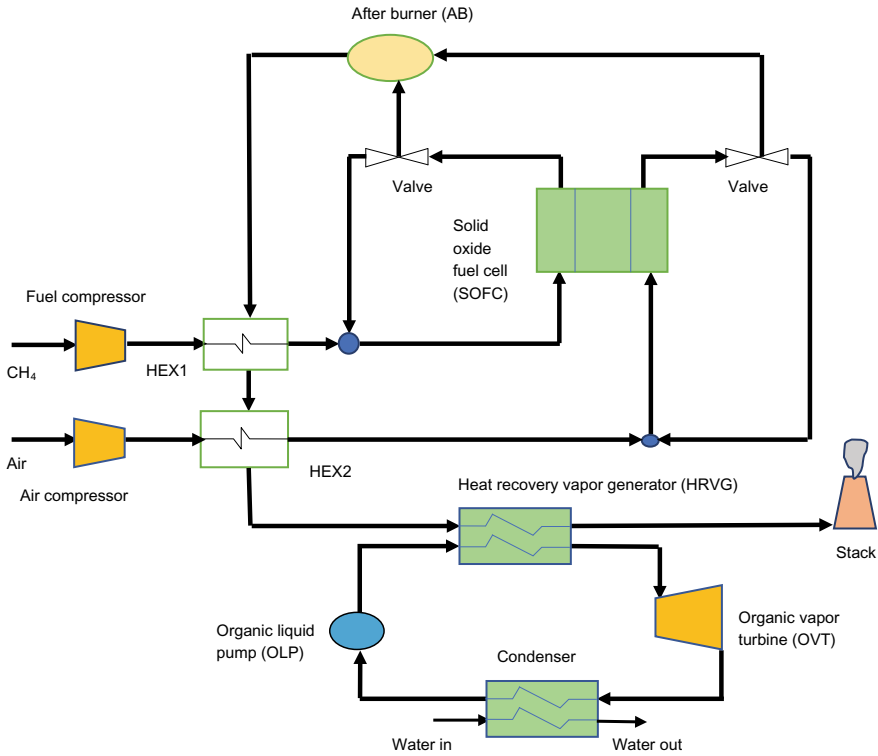
**Fig. 1** Schematic of proposed system

## 3 Thermodynamic Modeling

SOFC considered for the system analysis is of internal reforming type. Three simultaneous reactions are supposed to be taken place, viz. steam reforming, water gas shift, and electrochemical reaction. These reactions are shown below.

$$CH_4 + H_2O \leftrightarrow CO + 3H_2 \tag{1}$$

$$CO + H_2O \leftrightarrow H_2 + CO_2 \tag{2}$$

$$H_2 + 0.5O_2 \leftrightarrow H_2O \tag{3}$$
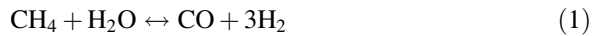
Reversible cell voltage is obtained by considering Nernst equation [1]

$$V_N = -\frac{\Delta g^\circ}{2F} - \frac{RT_{cell}}{2F} \ln\left(\frac{p_{H_2O}}{p_{H_2} p_{O_2}^{0.5}}\right) \tag{4}$$

Cell voltage ($V_c$) is determined by deducting the total voltage losses from the Nernst voltage as follows

$$V_c = V_N - V_{Loss} \tag{5}$$

Three major voltage losses developed in the SOFC cell are ohmic loss ($V_{OHM}$), activation loss ($V_{ACT}$), and concentration loss ($V_{CONC}$). Total voltage losses developed in the cell are the summation of these three losses.

$$V_{Loss} = V_{OHM} + V_{ACT} + V_{CONC} \tag{6}$$

Ohmic loss is determined as follows [6]

$$V_{OHM} = (\rho_A L_A + \rho_C L_C + \rho_E L_E + \rho_{INT} L_{INT})j \tag{7}$$

where

$$\rho_A = 0.00298 \exp\left(\frac{1392}{T_{cell}}\right) \tag{8}$$

$$\rho_C = 0.00814 \exp\left(\frac{-600}{T_{cell}}\right) \tag{9}$$

$$\rho_E = 0.00294 \exp\left(\frac{-10,350}{T_{cell}}\right) \tag{10}$$

$$\rho_{INT} = 0.1256 \exp\left(\frac{-4690}{T_{cell}}\right) \tag{11}$$

Activation over-potential is calculated as follows [7, 8]

$$V_{ACT} = V_{ACT,a} + V_{ACT,c} \tag{12}$$

$$V_{ACT,a,c} = \frac{RT_{cell}}{F} \ln\left[\frac{1}{2j_{oa,oc}} + \left\{\left(\frac{1}{2j_{oa,oc}}\right)^2 + 1\right\}^{0.5}\right] \tag{13}$$

$$j_{oa} = \gamma_a \frac{p_{H_2}}{p_o} \frac{p_{H_2O}}{p_o} \exp\left(\frac{-E_{act,a}}{RT_{cell}}\right) \tag{14}$$

$$j_{oc} = \gamma_c \left(\frac{p_{O_2}}{p_o}\right)^{0.25} \exp\left(\frac{-E_{act,c}}{RT_{cell}}\right) \tag{15}$$

Concentration loss is determined as follows [9, 10]

$$V_{\text{CONC}} = V_{\text{CONC,Anode}} + V_{\text{CONC,Cathode}} \tag{16}$$

$$V_{\text{CONC,Anode}} = -\frac{RT_{\text{cell}}}{2F} \ln \left[ \frac{\left(1 - \frac{j}{j_{L,H_2}}\right)}{\left(1 + \frac{j}{j_{L,H_2O}}\right)} \right] \tag{17}$$

$$V_{\text{CONC,Cathode}} = \frac{RT_{\text{cell}}}{2F} \ln \left[ \frac{1}{1 - \frac{j}{j_{L,O_2}}} \right] \tag{18}$$

$$j_{L,\text{gas}} = \frac{2FD_{\text{eff,gas}}p_{\text{gas}}}{100,000 RT_{\text{cell}}L_a} \tag{19}$$

Current flow during an individual cell is estimated as

$$i_{\text{cell}} = j.A_{\text{cell}} \tag{20}$$

where $A_{\text{cell}}$ represents cell area.

Power developed in a single SOFC stack is calculated as follows

$$W_{\text{Stack}} = N_{\text{cell}}V_c i_{\text{cell}} \tag{21}$$

where $N_{\text{cell}}$ is the quantity of cells in a SOFC stack

Power achieved by the SOFC module is estimated as follows

$$W_{\text{SOFC}} = N_{\text{SOFC}}W_{\text{Stack}} \tag{22}$$

Where $N_{\text{SOFC}}$ is the total number of stacks in the SOFC module

Power consumed by compressors is determined as follows

$$W_{\text{C1/C2}} = N_{\text{fuel/air}}(h_{\text{out}} - h_{\text{in}}) \tag{23}$$

Power consumed by organic liquid pump (OLP) is calculated as follows

$$W_{\text{OLP}} = n_{\text{ORC}}(h_{\text{out}} - h_{\text{in}}) \tag{24}$$

The power output of organic vapor turbine (OVT) is given by:

$$W_{\text{OVT}} = n_{\text{ORC}}(h_{\text{in}} - h_{\text{out}}) \tag{25}$$

## 4    Exergy Analysis

Exergy associated with any stream consists of physical exergy ($Ex_{phy}$) and chemical exergy ($Ex_{che}$). It is written as follows

$$Ex = Ex_{phy} + Ex_{che} \tag{26}$$

$$Ex_{phy} = \sum_j N_j \left( \left( \bar{h}_j - \bar{h}_o \right) - T_o \left( s_j - s_o \right) \right) \tag{27}$$

$$Ex_{che} = N_J \left( \sum_J y_J \overline{ex}^0_{che} - RT_o \sum_j y_j \ln y_j \right) \tag{28}$$

Exergy destruction ($Ex_D$) taking place in any system component, during a process, can be calculated as [11]

$$Ex_D = \sum_k \left( 1 - \frac{T_o}{T_k} \right) Q_k - W_{cv} + \sum_{in} Ex_{in} - \sum_{ex} Ex_{ex} \tag{29}$$

Exergy destruction of any component of the proposed system is calculated as a function of incoming fuel exergy. It is represented as follows

$$x_D = \frac{Ex_D}{Ex_{IN}} \tag{30}$$

Exergy loss is determined as a function of incoming fuel exergy. It is shown as follows

$$x_{Loss} = \frac{Ex_{Lost}}{Ex_{IN}} \tag{31}$$

## 5    Performance Parameters

The total power developed from the system is estimated as

$$W_{sys} = W_{SOFC} + W_{OVT} - W_{Aux} \tag{32}$$

where $W_{Aux}$ denotes auxiliary power consumption and is estimated as follows

$$W_{Aux} = W_{C1} + W_{C2} + W_{OLP} \tag{33}$$

The net energetic efficiency of the designed power plant can be written as

$$\eta_{\text{sys}} = \frac{W_{\text{sys}}}{n_{\text{fuel}} LHV_{\text{fuel}}} \tag{34}$$

Exergetic efficiency of the proposed system is determined as

$$\phi_{\text{sys}} = 1 - \sum x_{\text{D}} - \sum x_{\text{Loss}} \tag{35}$$

# 6   Results and Discussions

Base case input parameters are shown in Table 1. System performance at base case is given in Table 2. In this section, the effect of major operating and designing plant parameters, viz. SOFC current density and cell temperature ($T_{\text{cell}}$) on major plant performance parameters has been examined.

Figure 2 depicts the effect of SOFC current density from 1000 to 9000 A/m$^2$ on $W_{\text{SOFC}}$, $W_{\text{OVT,}}$ and $W_{\text{NET}}$. It is seen from Fig. 3 that with the increase of current density, $W_{\text{SOFC}}$ first increases, then reaches an optimal point, then decreases. Optimum power of SOFC found to be 280 kW at a current density of 6000 A/m$^2$. With the increase of current density, fuel consumption at the SOFC unit increases. Thus, $W_{\text{SOFC}}$ increases with the increase of current density. It is also found that, $W_{\text{OVT}}$ increases with the increase of current density. Increase of fuel and air

| Table 1   Input parameter for base case performance analysis of the system | Parameters | Values |
|---|---|---|
| | SOFC operating temperature | 850 °C |
| | SOFC current density | 2000 A/m$^2$ |
| | Cell area | 0.01 m$^2$ |
| | Number of cell | 500 |
| | Number of stack | 20 |
| | SOFC fuel utilization factor | 0.52 |
| | SOFC oxygen utilization factor | 0.20 |
| | Cathode pre-exponential factor | 1.3 × 10$^9$ A/m$^2$ |
| | Anode pre-exponential factor | 1.4 × 10$^9$ A/m$^2$ |
| | Activation energy for cathode | 120 × 10$^3$ kJ/kmol |
| | Activation energy for anode | 110 × 10$^3$ kJ/kmol |
| | Electrolyte thickness | 4 × 10$^{-5}$ m |
| | Anode thickness | 1 × 10$^{-4}$ m |
| | Cathode thickness | 0.0019 m |
| | Interconnect thickness | 8.5 × 10$^{-5}$ m |
| | OVT inlet temperature | 280 °C |
| | OVT inlet pressure | 30 bar |

**Table 2** Base case performance parameters of the proposed system

| Parameters | Value |
|---|---|
| SOFC stack power ($W_{stack}$) | 7.5 kW |
| SOFC module power output ($W_{SOFC}$) | 150 kW |
| OVT power ($W_{OVT}$) | 14.51 |
| Auxiliary power demand ($W_{Aux}$) | 6.10 kW |
| Net power developed ($W_{NET}$) | 158.41 kW |
| Net energy efficiency ($\eta_{sys}$) | 61.87% |
| Net exergy efficiency ($\phi_{sys}$) | 53.8% |
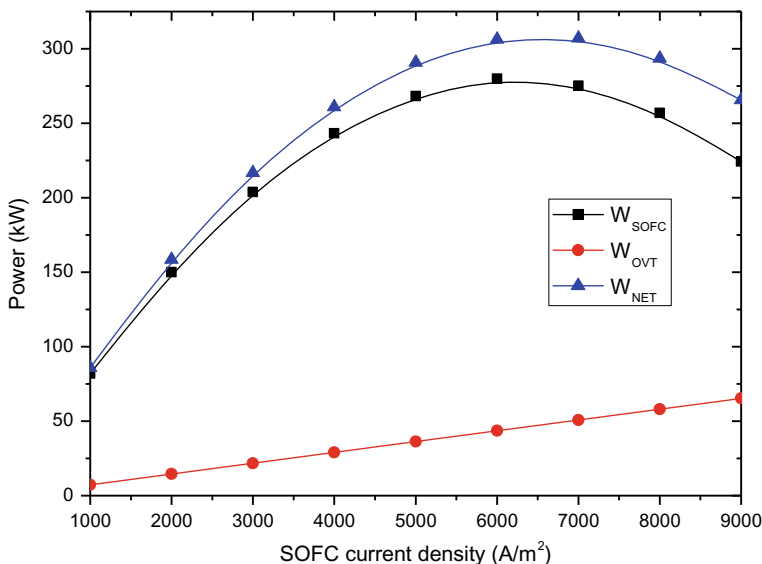


**Fig. 2** Effect of current density of power

consumption at the SOFC unit results in higher molar flow rate of flue gas. It results in higher amount of heat recovery in the HRGH unit. Thus, $W_{OVT}$ also increases. It is observed that $W_{NET}$ first increases, then reaches an optimal point, then decreases. Optimum $W_{net}$ is found to be 307 kW at a current density of 6000 A/m$^2$.

Figure 3 illustrates the effect of SOFC current density in the operating range of 1000–9000 A/m$^2$ on energetic and exergetic efficiency of the power plant. It is observed that as the SOFC current density rises, energetic as well as exergetic efficiency decreases. As the current density increases, energetic efficiency as well as exergetic efficiency of the power plant decreases due to drop in cell voltage. Highest energetic and exergetic efficiencies of the power plant are estimated to be 67.05 and 58.17%, respectively.

Figure 4 depicts the effect of $T_{cell}$ on $W_{SOFC}$, $W_{OVT,}$ and $W_{NET}$. It is found that $W_{SOFC}$ and $W_{NET}$ reduce with the rise of $T_{cell}$. As the voltage decreases with the rise
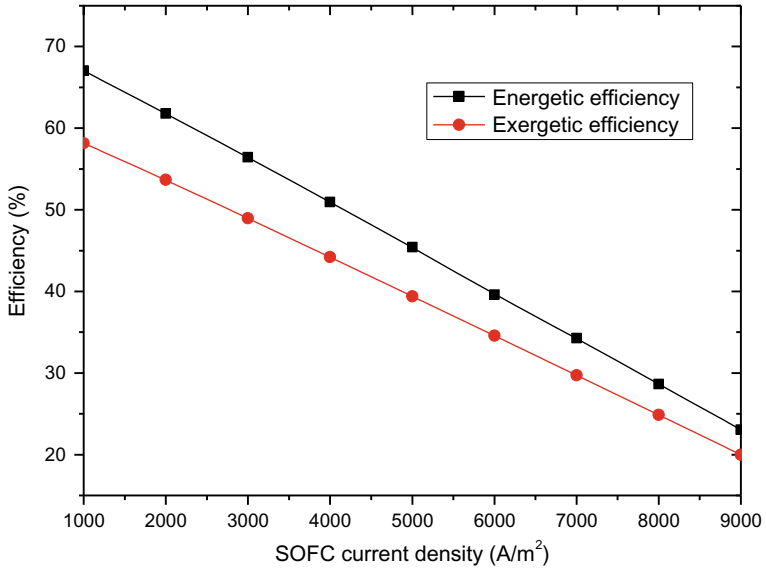
**Fig. 3** Effect of current density of efficiency
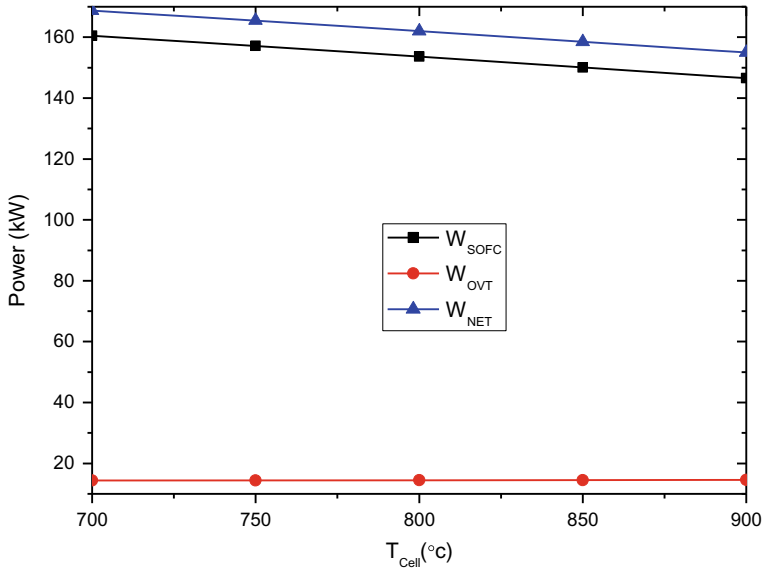


**Fig. 4** Effect of cell temperature on power
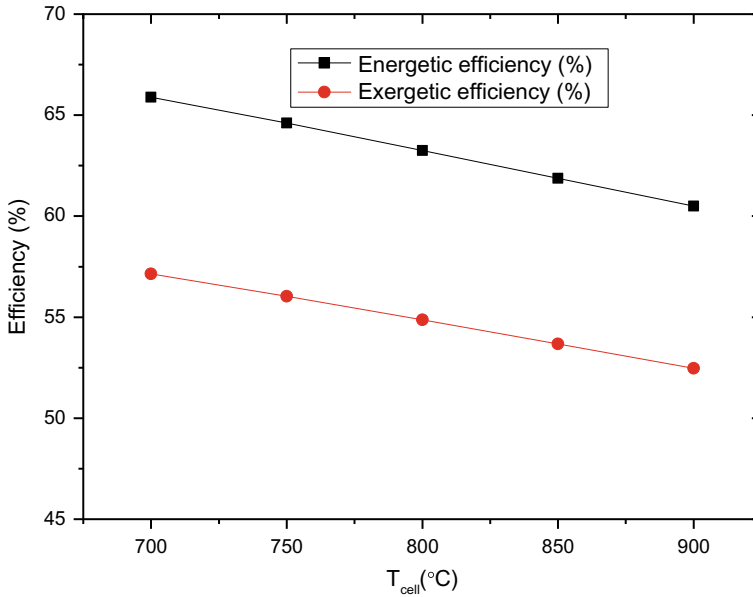
**Fig. 5** Effect of cell temperature on efficiency

of $T_{cell}$, $W_{SOFC}$ and $W_{NET}$ also decreases. Maximum $W_{NET}$ is obtained to be 168.76 kW at $T_{cell} = 700$ °C. Effect of $T_{cell}$ does not have much effect of the performance of $W_{OVT}$.

Figure 5 illustrates the influence of $T_{cell}$ on energetic and exergetic efficiency of the power plant. Performance of the system has been observed for the cell temperature in the range of 700–900 °C. It is found that as the $T_{cell}$ increases, energetic



**Fig. 6** Stack loss, useful exergy, and exergy destruction of system
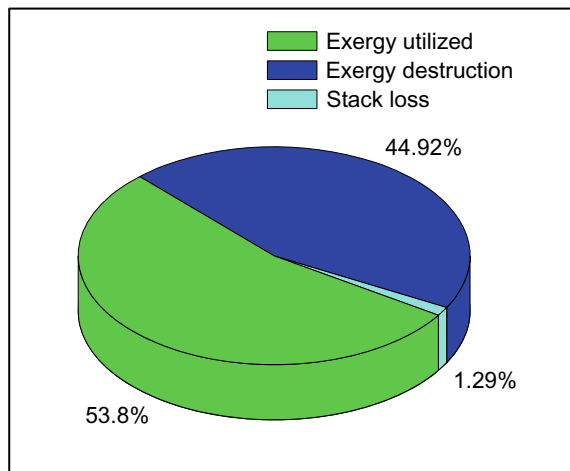
as well as exergetic efficiency decreases. Drop of efficiency of the system is highly attributed to the decrease of $W_{\text{NET}}$. Thus, as the cell temperature increases, both energetic efficiency and exergetic efficiency of the system decreases.

Useful exergy, total exergy destruction, and stack loss of the integrated system with respect to total fuel exergy input have been depicted in the pie chart as shown in Fig. 6. The useful exergy, total exergetic destruction, and stack loss of the proposed power plant are found to be 53.8, 44.92, and 1.29%, respectively.

# 7  Conclusion

In this paper, a methane-fueled SOFC and ORC incorporated power plant is modeled and analyzed. Performances of the proposed system are found to be influenced by the major operating and design parameters, viz. current density of SOFC and cell temperature. The main conclusions are as follows:

- As the current density of SOFC increases, $W_{\text{NET}}$ first increases, then reaches an optimal point, then decreases. Optimum $W_{\text{NET}}$ is found to be 307 kW at a current density of 6000 A/m$^2$.
- Highest energetic and exergetic efficiency of the power plant are found to be 67.05 and 58.17%, respectively.
- Increase in cell temperature results in decrease of both energetic efficiency as well as exergetic efficiency of the system.
- The useful exergy, total exergetic destruction, and stack loss of the proposed power plant are found to be 53.8, 44.92, and 1.29%, respectively.

# References

1. Akkaya AV, Sahin B, Erdem HH (2008) An analysis of SOFC/GT CHP system based on exergetic performance criteria. Int J Hydrogen Energy 33:2566–2577
2. Mahmoudi SMS, Khani L (2016) Thermodynamic and exergoeconomic assessments of a new solid oxide fuel cell-gas turbine cogeneration system. Energy Convers Manag 123:324–337
3. Meratizaman M, Monadizadeh S, Amidpour M (2014) Techno-economic assessment of high efficient energy production (SOFC-GT) for residential application from natural gas. J Nat Gas Sci Eng 21:118–133
4. Akikur RK, Saidur R, Ping HW, Ullah KR (2014) Performance analysis of a co-generation system using solar energy and SOFC technology. Energy Convers Manag 79:415–430
5. Al-Sulaiman FA, Dincer I, Hamdullahpur F (2010) Energy analysis of a trigeneration plant based on solid oxide fuel cell and organic Rankine cycle. Int J Hydrogen Energy 35:5104–5113
6. Bossel UG (1992) Final report on SOFC data facts and figures. Swiss Federal Office of Energy
7. Calise F, Palombo A, Vanoli L (2006) Design and partial load exergy analysis of hybrid SOFC-GT power plant. J Power Sour 158(1):225–244

8.  Roy D, Ghosh S (2017) Energy and exergy analyses of an integrated biomass gasification combined cycle employing solid oxide fuel cell and organic Rankine cycle. Clean Technol Environ Policy 19(6):1693–1709
9.  Chan SH, Khor KA, Xia ZT (2001) A complete polarization model of a solid oxide fuel cell and its sensitivity to the change of cell component thickness. J Power Sourc 93(1–2):130–140
10. Pirkandi J, Ghassemi M, Hamedi MH, Mohammadi R (2012) Electrochemical and thermodynamic modeling of a CHP system using tubular solid oxide fuel cell (SOFC-CHP). J Clean Prod 29–30:151–162
11. Kotas TJ (1985) The exergy method of thermal plant analysis. Butterworths, London

# Numerical Investigation of Single Gas Bubble Rising in Liquid Column

**Arjun Pradeep, Anil Kumar Sharma, D. Ponraju, B. K. Nashine and P. Selvaraj**

**Abstract** Analysis of bubble fluid dynamics forms the primary step to evaluate heat/mass transport phenomena encountered from rising bubble in liquid pool. Bubble rise in pools of fast reactor (FR) finds important applications in source term evaluation, purification of cover gas, and air cleaning efficiency of submerged wet scrubbers. In this study, interFoam module available in OpenFOAM numerically investigates bubble rise in liquid pool. The FVM solver solves transient conservation equations, and phase interface is bounded using MULES. Verification of interFoam module is done for 2- and 3-D benchmarks available in the literature. Bubble behavior has been simulated for 5 mm bubble rise in sodium for both 2- and 3-D cases. The 3-D bubble case is validated with data available from the literature for velocity. The study shows that terminal velocity changes with domain dimension and 3-D case predicts realistic velocity values. The bubble rise investigation is useful for safety studies related to FRs.

**Keywords** Bubble rise velocity · Sodium · OpenFOAM

## 1 Introduction

In fast reactor (FR), bubble results from entrainment of gas within the sodium from cover gas/fuel pin failure [1]. The areas of reactor safety concerned with FR source term due to gas bubble rising in pool depend on rise velocity, shape, and path. The rise velocity limits heat/mass transfer phenomena from bubble in pool of FR.

A study has to be done to understand bubble fluid dynamics in sodium pool. Bubble fluid dynamics depends on characteristics, gas–liquid properties, and operating conditions. The bubble fluid dynamics knowledge is an intermediate step to the heat/mass transport phenomena associated with FR safety. Until now, bubble velocity in sodium was evaluated from correlations [2] or equation of motion [3].

A. Pradeep (✉) · A. K. Sharma · D. Ponraju · B. K. Nashine · P. Selvaraj
Indira Gandhi Centre for Atomic Research, HBNI, Kalpakkam, Tamil Nadu, India
e-mail: arjun@igcar.gov.in

InterFoam solver of OpenFOAM was used in the study. Verification of interFoam module with the discretization schemes is done with numerical benchmark results available in the literature. Effect of dimension of domain on bubble velocity is simulated using 5 mm bubble rise case. Validation of interFoam solver is done with available terminal velocity data. The study is an intermediate step to set up a framework for bubble rise with heat/mass transfer required for fast reactors.

## 2 Computational Method

Gas bubble rise in 2- and 3-D domains is studied using OpenFOAM [4]. The 4 GB RAM, Ubuntu14.04 OS machine used for computation is Intel Core2Duo@2.4 GHz. Initially, the spherical bubble of diameter $d_B$ was positioned at an elevation of 0.5 $d_B$ from the bottom wall, along the central vertical axis. The dimension in horizontal direction is 4 $d_B$ to avoid wall effect and in vertical direction is 16 $d_B$ for bubble to reach terminal velocity. The Present study considers atmospheric pressure above liquid and phase thermal equilibrium.

### 2.1 Governing Equations

Governing conservation equations:

$$\nabla \cdot \vec{u} = 0 \tag{1}$$

$$\frac{\partial(\rho\vec{u})}{\partial t} + \nabla \cdot (\rho\vec{u}\vec{u}) = -\nabla p_{rgh} + \nabla \cdot \left[\mu\left(\nabla\vec{u} + (\nabla\vec{u})^T\right)\right] - \vec{g} \cdot \vec{x}\nabla\rho + \sigma\kappa\nabla\alpha_1 \tag{2}$$

$$\frac{\partial\alpha_1}{\partial t} + \nabla \cdot (\vec{u}\alpha_1) + \nabla \cdot [\vec{u}_r\alpha_1(1-\alpha_1)] = 0 \tag{3}$$

where the phase/volume fraction of fluid

$$\alpha_1 = \begin{cases} 1 & \text{in fluid 1} \\ 0 & \text{in fluid 2} \\ 0 < \alpha_1 < 1 & \text{at the interface} \end{cases} \tag{4}$$

interface curvature is given as

$$\kappa = -\nabla \cdot \hat{n} = -\nabla \cdot \left(\frac{\nabla\alpha_1}{|\nabla\alpha_1|}\right) \tag{5}$$

$\hat{n}$ is normal vector, $\vec{x}$ is position vector, $\vec{g}$ is gravitational acceleration, $\sigma$ is surface tension, $\vec{u}_r = \vec{u}_1 - \vec{u}_2$ is the relative velocity of phases, $\vec{u} = \alpha_1 \vec{u}_1 + (1 - a_1)\vec{u}_2$ is the mixed velocity, $\rho = \alpha_1 \rho_1 + (1 - \alpha_1)\rho_2$ is the mixed fluid density, $\mu = \alpha_1 \mu_1 + (1 - \alpha_1)\mu_2$ is the mixed fluid viscosity, and $p_{rgh} = p - \rho \vec{g} \cdot \vec{x}$ is the pseudo-hydrostatic (dynamic) pressure.

## 2.2 Boundary Conditions

The bottom and side boundaries are considered to be walls, and top boundary is atmosphere. The software-specific boundary conditions of '$\alpha$', '$p_{rgh}$', and velocity are accordingly chosen. Boundary condition of '$\alpha$' and velocity are zero gradient at walls. Pseudo-hydrostatic (dynamic) pressure at wall boundaries is *fixedFluxPressure*. *PressureInletOutletVelocity is the top boundary velocity condition*. Dynamic pressure at top boundary is *totalPressure*. The '$\alpha$' at top boundary is *inletOutlet*.

## 2.3 Solver

The interFoam solver solves governing conservation equations. Description of interFoam solver algorithm is available in the literature [5]. Spatial discretization is done using finite volume. MULES method is used for limiting phase interface [4]. The PIMPLE method couples velocity and pressure. PBiCG solver is used for velocity, and pressure solver is CG [4].

# 3 Results and Discussion

## 3.1 Verification

Verification of interFoam module is done for 2- and 3-D benchmarks available in the literature [6–8]. Three-dimensional domain considered for verification is a cuboid of 1 m length, 1 m breadth, and 2 m height. Two-dimensional domain is a rectangular space of 2 m height and 1 m width. A bubble containing fluid 2 is positioned in both domains filled with fluid 1 at 0.5 m above bottom along axis. Verification was done for $d_B = 0.5$ m using the fluid properties of Table 1. The benchmark cases were studied using a mesh size of $h = 1/40$.

**Table 1** Fluid properties for two benchmark verification cases

| Case | $\rho_1$ (kg/m³) | $\rho_2$ (kg/m³) | $\mu_1$ (Pa s) | $\mu_2$ (Pa s) | $\sigma$ (N/m) | $g$ (m/s²) |
|------|------------------|------------------|----------------|----------------|----------------|------------|
| 1 | 1000 | 100 | 10 | 1 | 24.5 | 0.98 |
| 2 | 1000 | 1 | 10 | 0.1 | 1.96 | 0.98 |

**Table 2** Grid refinement $1/h$, number of elements, and computation time used in the present study for benchmark verification cases

| Domain | $1/h$ | $n_{elements}$ | Computation time case 1 | Computation time case 2 |
|--------|-------|----------------|-------------------------|-------------------------|
| 2-D    | 40    | 3200           | 3.5 min                 | 3.7 min                 |
| 3-D    | 40    | 128,000        | 1.8 days                | 1.5 days                |

The final time of 3 s and corresponding computing times for both test cases are presented in Table 2 for understanding of computing performance. Boundary conditions for top and bottom were *no slip,* and sides were *slip*. The bubble vertical velocity and center of gravity of bubbles were verified quantitatively with benchmark solution [6–8].

Figure 1 shows the verification of rise velocity and center of mass position for benchmark cases 1 and 2 in 3-D domain for a mesh size, $h = 1/40$. The simulation results are compared with corresponding benchmark results available in the literature [6]. Adelsberger et al. [6] carried out 3-D numerical simulation for benchmark cases 1 and 2 using VOF approach implemented in OpenFOAM version 2.2.2. The vertical position of the bubble in the present study is higher than for DROPS and
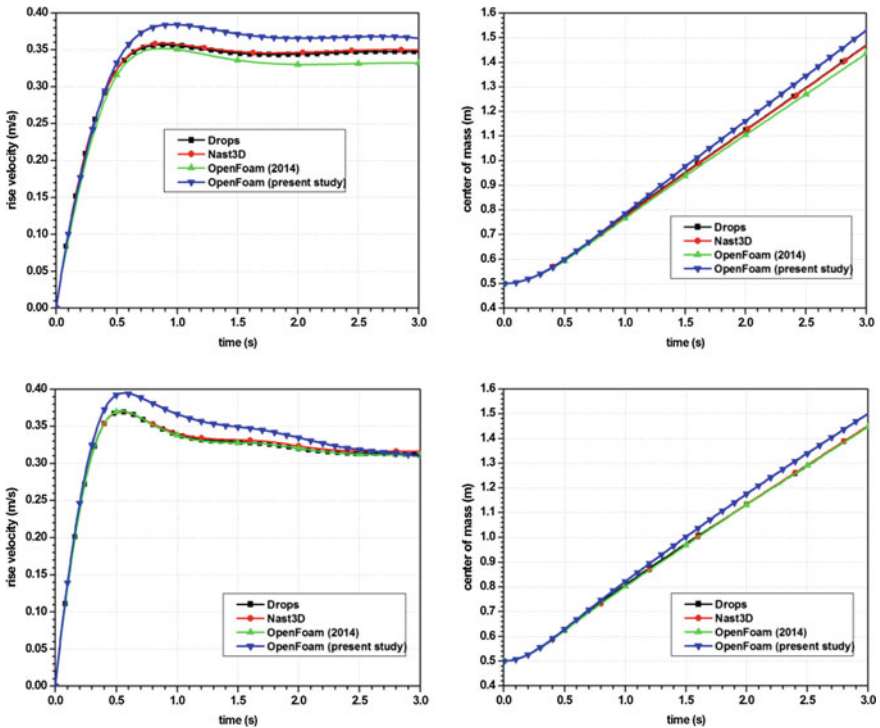


**Fig. 1** Quantitative parameters (**top**) case 1 and (**bottom**) case 2 for 3-D domain

NaSt3D as indicated in Fig. 1. For benchmark case 1 with high surface tension, the bubble rise velocity is visualized in Fig. 1. In the early stage of simulation, the vertical velocity increases from its initial value zero up to a maximum value of 0.384 m/s at about 0.95 s. The maximum velocity is roughly 0.357 m/s in DROPS, 0.358 m/s in NaSt3D, and 0.352 m/s in OpenFOAM V. 2.2.2 [6]. The rise velocity in the present study then decreases to 0.365 m/s at 3 s. Rise velocity decreases to 0.347 m/s in DROPS, 0.35 m/s in NaSt3D, and 0.33 m/s in OpenFOAM V. 2.2.2 [6]. Due to differences in rise velocity during final stage of simulation, center of mass position is higher in Fig. 1 for the present study. For benchmark case 2 with low surface tension, the rise velocity plot of bubble in Fig. 1 is also in high agreement for all considered flow solvers. All solvers obtain maximum velocities in the order of 0.37 m/s at 0.54 s, whereas the present study achieves a maximum rise velocity of 0.395 m/s at 0.56 s. The bubble velocity decreases with ongoing time so that a final velocity of 0.31 m/s is obtained at 3 s.

Figure 2 gives verification of quantitative parameters for benchmark cases 1 and 2 in 2-D domain. The simulation results for mesh size, $h = 1/40$, are compared with benchmarks [7]. For benchmark case 1 with high surface tension, predictions were in close range of the benchmark results. For benchmark case 2, predictions were close to result of FreeLIFE code as given in Fig. 2. The verification studies showed
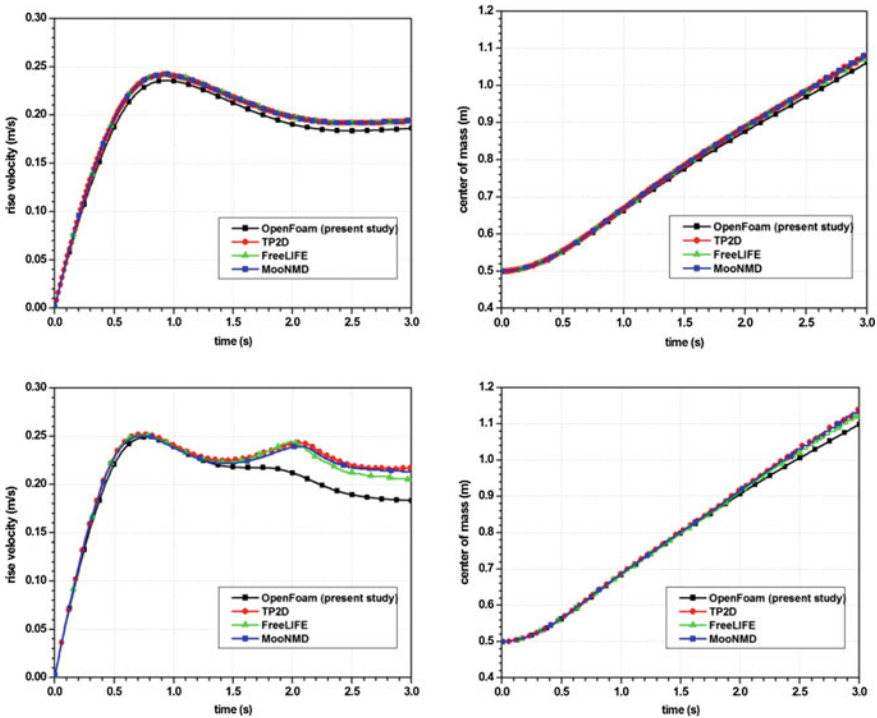


**Fig. 2** Quantitative parameters (**top**) case 1 and (**bottom**) case 2 for 2-D domain

**Table 3** Fluid properties for argon–sodium system at 473 K

| $\rho_1$ (kg/m³) | $\rho_2$ (kg/m³) | $\mu_1$ (Pa s) | $\mu_2$ (Pa s) | $\sigma$ (N/m) | $g$ (m/s²) |
|---|---|---|---|---|---|
| 904 | 1.04 | $4.5 \times 10^{-4}$ | $3.2 \times 10^{-5}$ | 0.189 | 9.8 |

that interFoam solver used in the study predicted 2- and 3-D benchmark results for bubble dynamics.

## 3.2 Bubble Dynamics in Sodium System

Effect of dimension of domain on bubble velocity is simulated using 5 mm bubble rise case. Table 3 gives the argon–sodium system considered for analysis at 473 K.

Figure 3 gives the bubble's evolution with time. Figure 4 gives bubble quantitative parameters variation with domain dimension.

Figure 4 shows that 2- and 3-D simulations evaluate terminal velocities of 0.224 and 0.331 m/s, respectively. The computing times for 2- and 3-D are given in Table 4 to understand computing efficiency. 3-D case predicts realistic velocity value of 0.338 m/s, which is in close agreement with Mendelson's correlation [9].



**Fig. 3** Bubble results. **a** 2-D and **b** 3-D
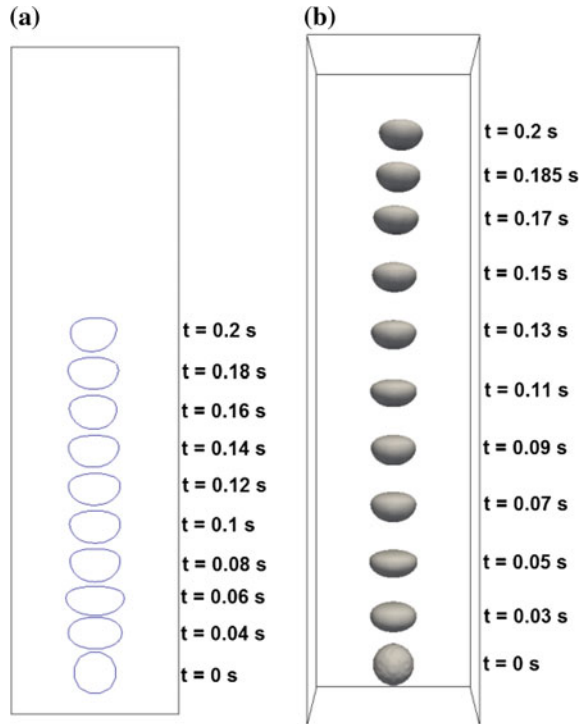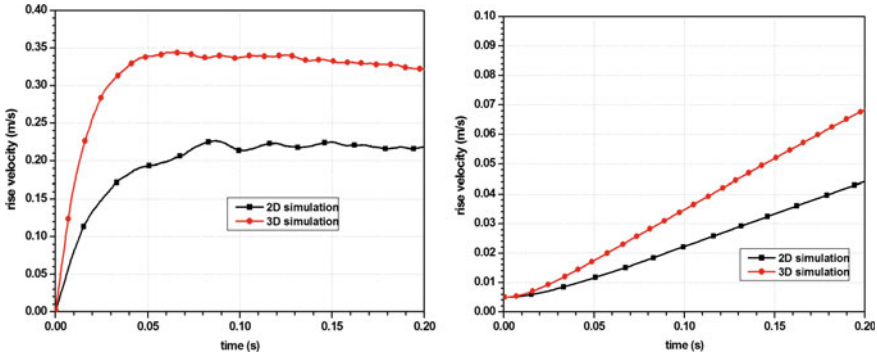
**Fig. 4** Quantitative parameters for 5-mm bubble

**Table 4** Grid refinement $1/h$, number of elements, and computation time used in the present study for 5 mm argon bubble rise in sodium pool

| Domain | $1/h$ | $n_{elements}$ | Computation time |
|--------|-------|----------------|------------------|
| 2-D    | 4     | 28,000         | 11.3 min         |
| 3-D    | 4     | 2,048,000      | 6 days           |

## 4 Conclusions

The interFoam module available in OpenFOAM numerically investigates bubble rise in liquid pool. Verification of interFoam module is done for 2- and 3-D benchmarks available in the literature. Bubble behavior has been simulated for 5 mm bubble rise in sodium for both 2- and 3-D cases. The 3-D bubble case is validated with data available from the literature for velocity. The study shows that terminal velocity changes with domain dimension and 3-D case predicts realistic velocity values. The study is an intermediate step to set up a framework for bubble rise with heat/mass transfer required for fast reactors.

## References

1. Henry RE, Grolmes MA, Fauske HK (1971) Pressure-pulse propagation in two-phase one- and two- component mixtures, No ANL-7792. Argonne National Laboratory Illinois, Lemont
2. Umbel M (2011) Containment source terms for sodium-cooled fast reactor accidents. Master's thesis, The Ohio State University (2011)
3. Miyahara S, Sagawa N (1996) Iodine mass transfer from xenon-iodine mixed gas bubble to liquid sodium pool, (II) development of analytical model. J Nucl Sci Technol 33:220
4. Greenshields CJ (2016) OpenFOAM user guide
5. Klostermann J, Schaake K, Schwarze R (2013) Numerical simulation of a single rising bubble by VOF with surface compression. Int J Numer Meth Fluids 71:960

6. Adelsberger J et al (2014) 3D incompressible two-phase flow benchmark computations for rising droplets. In: Proceedings of the 11th world congress on computational mechanics (WCCM XI), vol 179. Barcelona, Spain
7. http://www.featflow.de/en/benchmarks/cfdbenchmarking/bubble/bubble_reference.html
8. Hysing S et al (2009) Quantitative benchmark computations of two-dimensional bubble dynamics. Int J Numer Meth Fluids 60:1259
9. Mendelson HD (1967) The prediction of bubble terminal velocities from wave theory. AIChE J 13(2):250–253

# Natural Convection Heat Transfer Enhancement Using Cooling Pipes in the Heat Generating Debris Bed

**Vidhyasagar Jhade, Anil Kumar Sharma, D. Ponraju, B. K. Nashine and P. Selvaraj**

**Abstract** The whole core meltdown scenario is considered as a beyond design basis accident with a probability of occurrence less than $10^{-6}$ per reactor year. To prevent and mitigate such a hypothetical severe accident, in fast breeder reactors, research has been focused on accommodating the destroyed core debris within the primary containment boundary. An in-vessel core catcher is provided to receive the fuel debris arising out of core meltdown and disperses it uniformly, thus enabling safe and adequate heat transfer by natural convection. The present study is focused on the thermal hydraulic analysis of in-vessel core catcher. A 3-D numerical analysis has been carried out in the lower plenum of the fast reactor. Turbulence is modeled using the standard k-ε turbulent model. The Boussinesq approximation is assumed for liquid sodium. The heat source is assumed to have spread on the heat shield plate and has a total volume of 5.12 m$^3$ with inbuilt decay heat source. The mathematical model is validated with the available benchmark experimental results in the literature. The existing design of core catcher plate is modified by providing cooling pipes in the top collection plate with different configurations to assess the cooling capability of the debris by natural convection. The temperature and velocity contour are obtained to observe the flow field established above the heat source in the sodium pool. It has been found that new design of core catcher improves the natural circulation of sodium toward the center of CC and more than 50 °C temperature decrement is observed in upper heat shield plate.

**Keywords** Natural convection · Boussinesq approximation · Core catcher · Severe accident

## Nomenclature

| | |
|---|---|
| $g$ | Gravitational acceleration (m/s$^2$) |
| $T$ | Temperature, k |
| $u$, $v$, $w$ | Velocity along $r$, $\theta$ and $z$ direction in m/s |

V. Jhade · A. K. Sharma (✉) · D. Ponraju · B. K. Nashine · P. Selvaraj
Indira Gandhi Centre for Atomic Research, HBNI, Kalpakkam, Tamil Nadu, India
e-mail: aksharma@igcar.gov.in

**Greek Symbol**

$\beta$          Isobaric cubical expansion coefficient of fluid, $K^{-1}$
$\rho$ and $\rho_0$   Density ($kg/m^3$) at T and $T_0$ temperature

# 1   Introduction

Whole core meltdown scenario in nuclear reactors is considered as a beyond design basis event (BDBE) with a probability of occurrence less than $10^{-6}$/reactor year. After the Fukushima Dai-Ichi accident, it has gained more interest from researchers and scientists around the world. Melting of core occurs due to failure of cooling system to remove heat generated in the core. The excess temperature in core is essentially due to loss of coolant flow, i.e., unprotected loss of flow accident (ULOFA) or increase in the core power, i.e., unprotected transient overpower accident (UTOPA) [1]. UTOPA or ULOFA initiates the melting of subassembly (SA). The molten fuel along with the liquid sodium will fragment and is expected to settle at the bottom of the main vessel in the absence of any melt retention arrangement. This fragmented core debris constantly generates heat because of decay of fission products. The core debris will damage the integrity [2] when it comes in contact with the main vessel. To avoid such event, a core retention assembly called core catcher (CC) is placed below the grid plate. A chimney along with top heat shield plate (HSP) and core catcher plate all together is named as core catcher. It retains the core debris and enhances the decay heat removal by natural convection. The CC can be in-vessel or ex-vessel. Ex-vessel CC, where debris is collected and transfers outside the main vessel but within the containment building. A separate cooling system is provided for ex-vessel type CC [3, 4] which is extensively used in water-cooled nuclear reactors. In-vessel CCs are used in liquid metal cooled fast breeder reactors (LMFBR). In a sodium-cooled fast reactor (SFR), in-vessel CC is a favorable choice because sodium has a tendency to react violently with water and air. The CC for Indian Prototype Fast Breeder Reactor (PFBR) which has a total 500 MWe capacity is designed to take care of the mechanical load of all 181 SA and thermal load of 7 SA.

Hung [5] carried out the comprehensive numerical study to examine the decay heat removal capacity without any active heat removal mechanism. They have concluded that a passive air cooling system is capable to remove the decay heat by conduction, convection, and radiation. They have implemented the extended liner in the inner vessel. It prevents the downward flow from partition to the core area and improved the convective heat transfer. However, modification in pool geometry will change the entire reactor vessel design and economically it is not beneficial. Alternatively, the modification in CC would be a more favorable approach such as two different design of chimney of CC used by Sharma et al. [6] or multi-layer CC plate concept for SFRs suggested by Sudha et al. [7]. It is essential to note that

material compatibility with liquid sodium has to be evaluated along with the manufacturing feasibility for the entire life of the reactor.

To ensure the sufficient cooling during operation and shutdown condition, multiple sources of the power supply are incorporated in SFR. However, inherent passive safety during core meltdown situation has been studied by Verma et al. [8], under varying number of decay heat exchangers. They have proposed that relocation of core debris at the gap between the core-periphery and inner vessel reduces the thermal load on the CC plate. Also, concluded that integrity of inner vessel will not be hampered even when half of the core debris settled in the gap. This thermal load can also be reduced when, rather than distributing the entire core debris on a single plate, use of multiple plates could be advantageous. Sharma et al. [9] show that using multiple plates increases the thermal load carrying capacity of core catcher. It was assumed in their study that the heat load is distributed uniformly in all plates. Essentially, it is not possible for the debris to settle equally on all plates. The passage needs to be provided so that the debris can flow down the plate as proposed in a numerical study of Rakhi et al. [10]. Also, it has been concluded in their study that multiple trays improve the natural circulation in lower plenum. However, providing such opening will make the upper heat shield plate (HSP) annular. Additional support is needed for each annular plate and that increases the complexity in the lower plenum. To overcome such complexity and provide more realistic design, a new concept of core catcher is presented in the current study as shown in Fig. 1. Hollow pipes have been protruded at the top of HSP, which are closed from the top, and liquid sodium flows inside this pipes. Three-dimensional simulations have been carried out for the lower plenum of a reactor to evaluate the change in the coolabilty of core catcher under core disruptive accident. The results obtained from the present analysis have been compared with existing design.
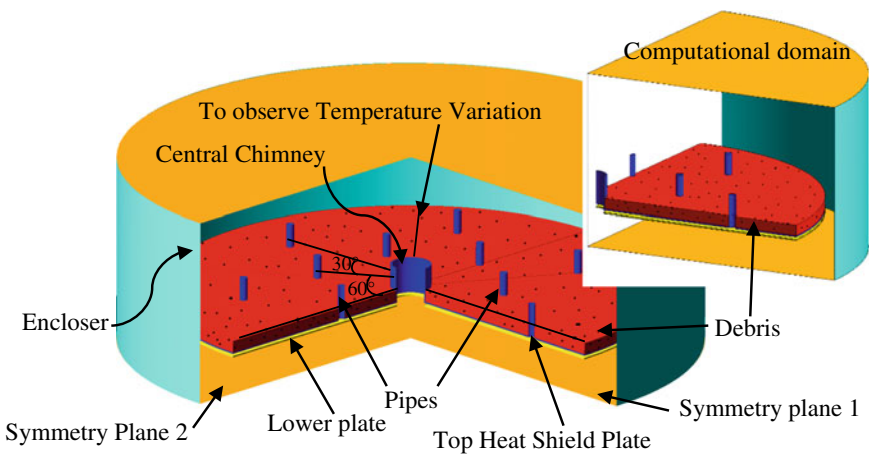


**Fig. 1** Physical model of CC assembly

## 2 Mathematical Modeling

For the present numerical analysis, the 1/4th sector of complete lower plenum has been considered as the computational domain of interest. The domain has taken all the important components of the lower plenum of reactor viz. HSP, chimney, lower tray, etc. The material used for core catcher assembly is SS316LN. Important properties of SS316LN, debris and liquid sodium are shown in Table 1.

Following are the assumptions considered during the analysis-

1. Boussinesq's approximation is assumed to hold good for liquid sodium and variation in density with temperature is solely important for producing buoyancy effect.
2. All other physical properties, except density, are assumed to be invariant.
3. Liquid sodium is considered as viscous, Newtonian, and incompressible.

### 2.1 Physical Mode

The physical model is shown in Fig. 1, comprises an encloser whose diameter is 7.7 m and height 2.5 m. Pipes are extruded on a top HSP at the radial distance of 1.263 m for inner, and 2.256 m for the outer row from the center. Each row has six pipes, whose internal diameter is 100 mm, at an angle of 60° while the angle between inner and outer rows pipe is 30°. The thickness of upper HSP and the lower plate is 20 mm, and they are separated by a distance 30 mm. The height of pipes is considered equal to chimney height, i.e., 480 mm.

### 2.2 Governing Equations

A three-dimensional mass, momentum, and energy equation [11] along with equation for turbulence kinetic energy ($k$) and dissipation rate ($\varepsilon$) [12]

Boussinesq equation for calculating density

$$(\rho - \rho_0) \cong -\rho_0 \beta g (T - T_0)$$

**Table 1** Properties of material used in the model

| Material | $\rho$ (kg/m$^3$) | $C_p$ (J/kg K) | K (W/m K) | $\mu$ (kg/m s) | $\beta$ (K$^{-1}$) |
|---|---|---|---|---|---|
| SS316LN | 7749.5 | 576.5 | 21.15 | – | – |
| Debris | 6158.3 | 743.23 | 33.735 | – | – |
| Liquid sodium | 766.76 | 1259.4 | 65.1 | $2.35 \times 10^{-4}$ | $2.9183 \times 10^{-4}$ |

## 2.3  Boundary Conditions

1. Adiabatic wall with no-slip boundary condition for the top and bottom of encloser

$$Q = 0; u = v = w = 0$$

2. Isothermal along with no-slip boundary condition was imposed at the peripheral wall of encloser

$$T_{\text{wall}} = 673\,\text{K}; u = v = w = 0$$

3. Constant heat generation per unit volume of debris.

$$\dddot{q} = 5\,\text{MW/5.12}\,\text{m}^3$$

Initial condition $u = v = w = 0$ and $T_0 = 673$ K.

## 3  Methodology

For the present numerical simulation, a commercial CFD code FLUENT is used to solve transient governing equations. Finite volume method is used for the discretization of governing equations. The SIMPLE algorithm for pressure-velocity coupling has been considered. The second-order upwind method is used for pressure term while the first order is used for convection term. The solution is assumed to converge when the residual of continuity and momentum fall down to 10–4 whereas for energy it is 10–6. The Boussinesq approximation is used to consider the change in density of liquid sodium.

## 3.1  Grid Independence Test

To have a solution, which is independent of grid size, a grid independence test was performed. The three different types of grids 1,00,745, 1,36,578, and 1,48,404 have been exercised for the test and variation of velocity was plotted at the vertical center axis of a chimney as depicted in Fig. 2. From the plot, it can be seen that variation of velocity is insignificant after 1,36,578 nodes grid. Therefore, 1,36,578 size grid has been chosen for further analysis.
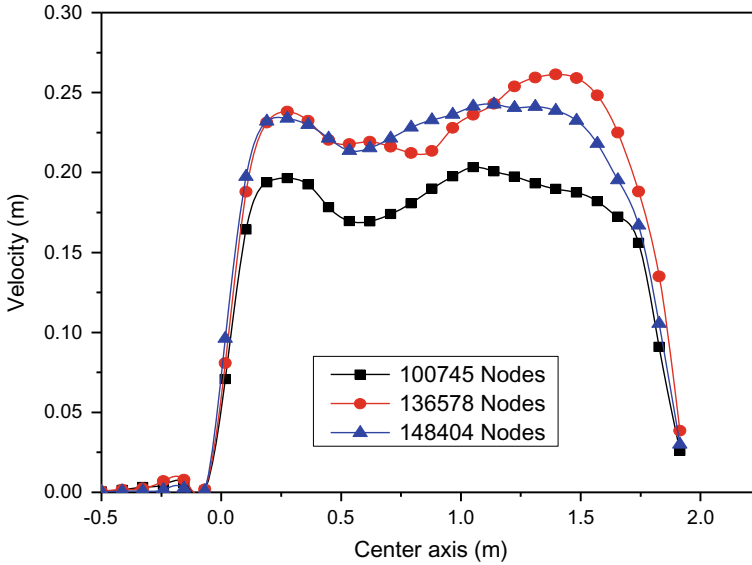
**Fig. 2** Grid independence test

## 3.2 *Validation*

The numerical model used for the present study has been validated with experimental result of PATH experimental facility [13]. PATH facility is a 1:4 scale water model of the PFBR and is exclusively dedicated to post-accident thermal-hydraulic experiment. An 18 kW heat load is imposed on the top heat shield plate and variation of temperature along the symmetry axis was plotted after 2 h as shown in Fig. 3. From the graph it can be seen that the numerical results provide good agreement with the experimental data.

## 4  Results and Discussion

The present work is focused on the three-dimensional (3D) numerical analysis of turbulent natural convection in the lower plenum of the PFBR. The objective of the present numerical study is to provide more realistic fluid flow characteristic and heat transfer phenomena in a modified design of core catcher. Results and plots are taken when the steady state attained and temperature of CC plate reached the maximum. The temperature contour and velocity vectors for the existing CC design have been presented in Fig. 4. It has been found through the analysis that when there are no pipes protruded in the top plate, liquid sodium gets heated and a large anti-clockwise vortex was formed above the debris bed. It has also revealed from
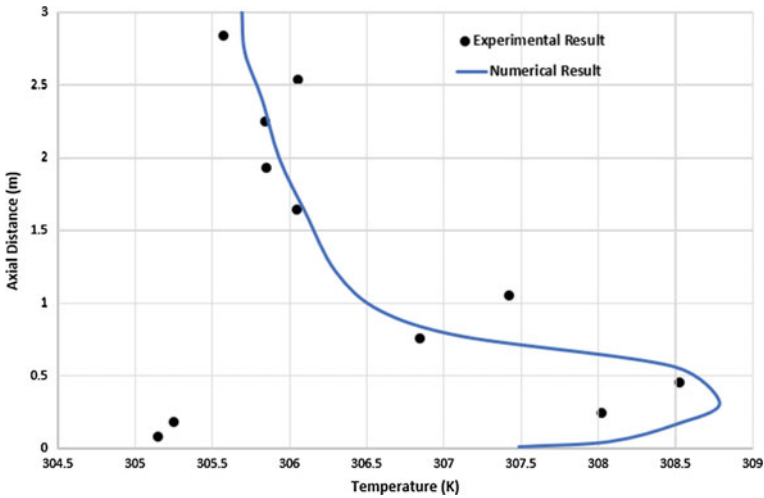
**Fig. 3** Validation of numerical result

temperature contour that region below the lower tray has not observed any significant changes in the temperature. The fluid is stagnated in this region and the change in temperature is very marginal.

Providing the pipes at regular interval on the upper plate improves the heat transfer by natural convection around the pipes. This can be seen in the temperature contour as depicted in Fig. 5. A change in temperature contour around the pipes can easily be noticed along with the change in temperature at a lower region below the plate. A velocity vector at the symmetry plane shows the enhanced natural circulation and increase in velocity of liquid sodium to 0.459 m/s as depicted in Fig. 6. Circulation of sodium inside the pipes can also be seen in this figure, in which both the pipes have similar zone inside them. The sodium enters from the bottom of pipe, gets heated, and rises to upward. This sodium transfers the heat to the upper pool sodium through conduction from pipes. The authors have also observed that due to



**(a)** Velocity vectors                    **(b)** Temperature Contour
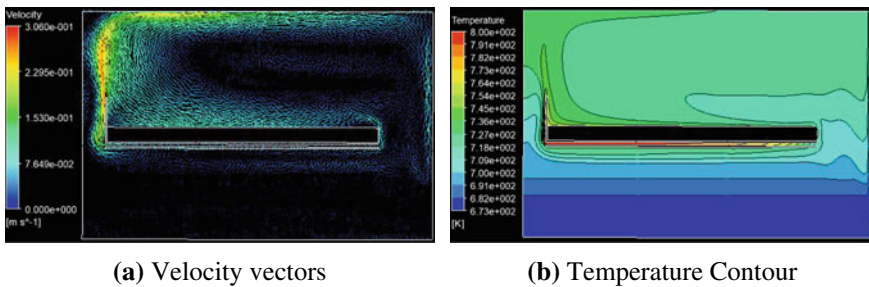
**Fig. 4** Velocityvectors and temperature contour for existing CC

**(a)** Temperature contour at symmetry plane

**(b)** Temperature contour at different radial plane
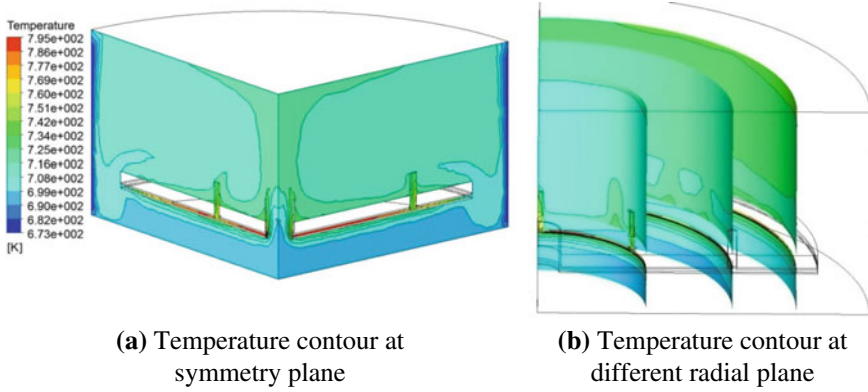
**Fig. 5** Temperature contour for present analysis



Inner row pipe

Velocity vectors at symmetry plane 1
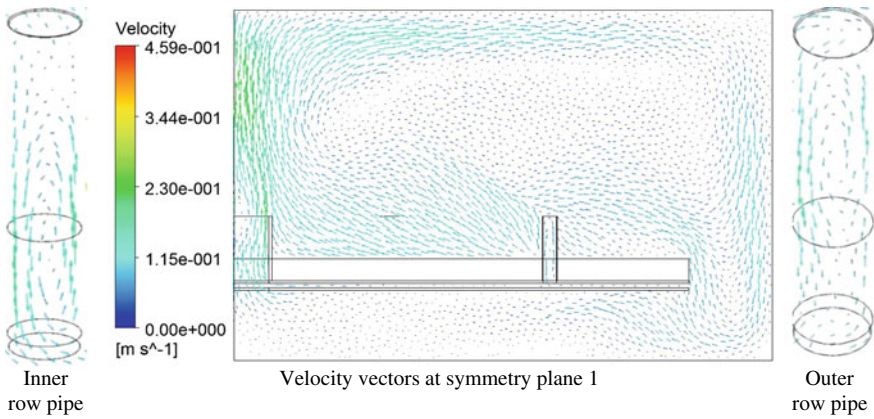
Outer row pipe

**Fig. 6** Velocity vectors with pipe

the chimney and inner row pipes, the temperature on top HSP is less toward a center of chimney compared to the peripheral side. This can be seen by plotting temperature variation on the top HSP. Figure 7 shows the temperature variation on top HSP for both designs of CC assembly. It has been also found that the area weighted average temperature of upper plate decreases to 786.2 K, compared to existing design where it was 843 K. The present study shows the improvement over existing design in terms of coolabilty.

Temperature variation on upper HSP with pipes          Temperature variation on upper HSP without pipes
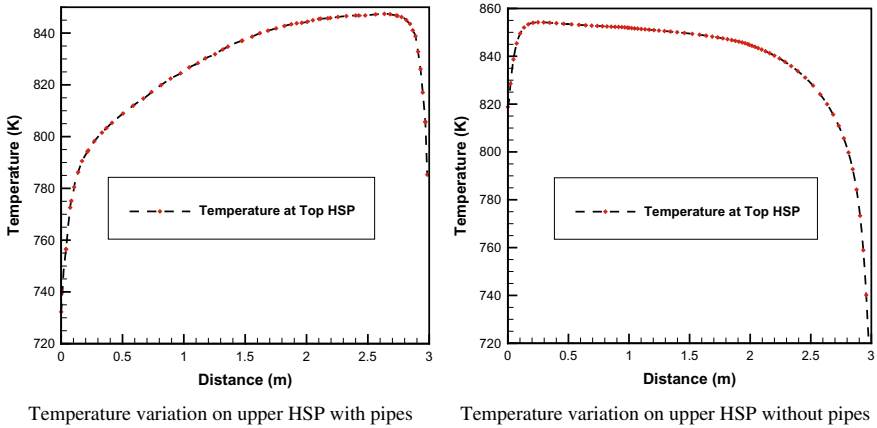
**Fig. 7** Variation of temperature on upper HSP for both the cases

## 5    Conclusion

A transient numerical analysis was carried out on a 3D model of core catcher with pipes at the top of HSP. Natural convection in lower plenum of LMFBR has been analyzed to assess the coolabilty of the new design of CCP under whole core meltdown scenario. The k-ε turbulence model has been used for the simulation, and the governing equations are discretized using finite volume scheme. The current study has revealed that using pipe at the top plate will enhance the natural circulation of liquid sodium. The results obtained from the study have been compared with existing design. The area weighted average temperature at the upper plate is found out to be 786.1 K. The present study shows decrease in temperature in HSP of more than 50 °C over existing CCP design. A variation of temperature shows improved natural convection toward chimney side than the periphery of the plate. The circulation of sodium inside the pipes increases the heat transfer from debris to upper pool sodium. The present numerical analysis provides the basis to further extend present work toward optimum core catcher plate design for future SFR.

## References

1. Srinivasan GS, Chetal SC, Chellapandi P (2013) Primary containment capacity of Prototype Fast Breeder Reactor against core disruptive accident loadings. Nucl Eng Des 256:178–187
2. Louis Baker J (1977) Core debris behavior and interactions with concrete. Nucl Eng Des 42(1):137–150
3. Fischer M (2004) The severe accident mitigation concept and the design measures for core melt retention of the European Pressurized Reactor (EPR). Nucl Eng Des 230(1–3):168–180
4. Suh ND, Songa JH (2009) An evolution of molten core cooling strategies. Nucl Eng Des 239(7):1338–1344

5. Dhir V, Chang J, Wang S, Hung TC (2011) CFD modeling and thermal-hydraulic analysis for the passive decay heat removal of a sodium-cooled fast reactor. Nucl Eng Des 241(1):425–432
6. Das SK, Harvey J, Sharma AK (2009) Experimental and numerical analysis of natural convection in geometrically modeled core catcher of the liquid-metal-cooled fast reactor. Nucl Technol 165(1):43–52
7. Velusamy K, Chellapandi P, Sudha AJ (2014) A multi layer core catcher concept for future sodium cooled fast reactors. Ann Nucl Energy 65:253–261
8. Sharma, AK, Velusamy K, Verma L (2017) Thermal hydraulic parametric investigation of decay heat removal from degraded core of a sodium cooled fast Breeder reactor. Nucl Eng Des 313:285–295
9. Velusamy K, Balaji C, Sharma AK (2009) Turbulent natural convection of sodium in a cylindrical enclosure with multiple internal heat sources: A conjugate heat transfer study. Int J Heat Mass Transfer 52(11–12):2858–2870
10. Sharma AK, Velusamy K, Rakthi (2017) Integrated CFD investigation of heat transfer enhancement using multi-tray core catcher in SFR. Ann Nuc Energy 104:256–266
11. Verstee, WMH (2007) An introduction to computational fluid dynamics: the finite volume method, 2nd edn. Pearson
12. Eswaran V, Biswas G (2002) Turbulent flows: fundamental, experiments and modeling. CRC Press
13. Sharma AK, Malarvizhi B, Murthy SS, Rao EH, Kumaresan M, Ramesh SS, Harvey J, Nashine BK, Chellapandi P, Chetal SC, Gnanadhasa L (2011) PATH—an experimental facility for natural circulation heat transfer studies related to Post Accident Thermal Hydraulics. Nucl Eng Des 9:3839–3850

# Effect of Flow Maldistribution on Thermal Performance of Water-Cooled Minichannel Heat Sink

**Sanjeev Kumar, Ritesh Dwivedi and Pawan Kumar Singh**

**Abstract** Flow maldistribution affects the cooling capacity of a water-cooled minichannel heat sink and cooling capacity of heat sink can be improved by minimizing flow maldistribution. Flow maldistribution depends upon the number of parameters such as flow rate, inlet/outlet position, and number of channels. This computational study has been performed using ANSYS Fluent 16.0 to investigate the effect of inlet/outlet positions and flow rate to delineate the flow maldistribution in minichannel heat sink. In this study, a minichannel heat sink with 28 numbers of rectangular parallel minichannels having hydraulic diameter 1.5 mm has been considered. Water and aluminum have been selected as a working fluid and heat sink material, respectively. In order to see the effect of inlet/outlet positions on flow maldistribution, four different types of inlet/outlet flow arrangements such as I-Type, Z-Type, C-Type, and U-Type have been considered. Effect of flow rate on flow maldistribution has been observed for the flow rate ranged from 0.5 to 1 LPM. Based on the results, it is found that flow maldistribution is strongly dependent on inlet/outlet positions and flow rate. Among all the arrangement, U-Type arrangement has small flow maldistribution which implies more uniformity in flow distribution in parallel minichannels and Z-Type arrangement has non-uniform flow distribution in parallel minichannels. It is also found that flow maldistribution affects the thermal performance of minichannel heat sink. A heat sink with U-Type flow arrangement has better thermal performance as compared to others arrangement.

**Keywords** Heat sink · Maldistribution · ANSYS · CFD

## Nomenclature

$c_\mathrm{p}$   Fluid-specific heat (J kg$^{-1}$ K$^{-1}$)
$k_\mathrm{f}$   Fluid thermal conductivity (W m$^{-1}$ K$^{-1}$)
$k_\mathrm{s}$   Solid thermal conductivity (W m$^{-1}$ K$^{-1}$)

S. Kumar (✉) · R. Dwivedi · P. K. Singh
Indian Institute of Technology (ISM), Dhanbad 826004, Jharkhand, India
e-mail: sanjeev.kumar8696@gmail.com

$d_h$        Hydraulic diameter of minichannel (mm)
$p$          Pressure (Pa)
$q_w$        Heat flux (W m$^{-2}$)
$R_{th}$     Heat sink thermal resistance (K/W)
$Re$         Reynolds number (-)
$T_{in}$     Fluid inlet temperature (K)
$u$          Channel average velocity (m/s)
$V_{in}$     Fluid inlet velocity (m/s)
$m$          Mass flow rate in channel (kg/sec)
$m_{avg}$    Average mass flow rate (kg/sec)
$T_{bmax}$   Maximum heat sink base temperature (K)

**Greek symbols**

$\rho$   Fluid density (kg m$^{-3}$)
$v$      Kinematic viscosity (m$^2$ s)

# 1   Introduction

One common factor that most firmly affects the heat transfer performance of the mini-microchannel heat sink is the uneven distribution of flow in the different parallel channels. This uneven distribution of flow is called maldistribution. It is extremely important to distribute flow equally among the channels because the uneven distribution of flow in the mini-microchannel is a cause of the lowering in both thermal and hydraulic performances. Recently, plenty of research has been carried out by scientific community to explicate the underlying mechanism of flow maldistribution for single-phase flow in the mini-microchannel heat sink both experimentally and numerically. Bajura and Jones [1] investigated the flow distribution in parallel branches for different headers, analytically as well as experimentally, using pressure flow equation and flow distribution equation and found that uniform flow was achieved when header considered as infinite reservoirs. Kim et al. [2] concluded that the flow distribution inside parallel channels of heat sink also depends on header shape and Reynolds number. Cho et al. [3] imposed a non-uniform heat flux condition and elucidate the mass flow distribution with a comprehensible modelling and simulation in a microchannel heat sink. Results showed that for low viscosity and high flow rate, maldistribution increases because of inertial phenomena. Kumaraguruparan et al. [4] studied flow maldistribution numerically and experimentally, and results show that manufacturing tolerances can produce small variations in the channel dimensions which affect the flow distribution in channels. Nielsen et al. [5] found that flow maldistribution can curb the performance of microchannel heat exchangers. Pistoresi et al. [6] numerically

analyzed that flow maldistribution can be minimized by changing the angle of a triangular header and decreasing the number of channels. They found that with the help of greater inclined angle or less number of channels, uniform flow is achieved in parallel minichannels. Jajja et al. [7] investigated the systematic effect of heat sink geometry (by reducing fin spacing) with water as fluid on the microprocessor base temperature and found that the fin spacing has a significant effect on heat transfer and maximum base temperature can be reduced. Liu and Yu [8] performed a numerical study and found that by using non-uniform inlet baffles, flow distribution inside the minichannel can be improved and become more uniform. Anbumeenakshi and Thansekhar [9] performed an experimental investigation to determine the effect of various inlet configurations and header shapes on maldistribution in the microchannel, and significant affects can be noticed for different flow rates. It shows that for low flow rate, less flow maldistribution can be achieved with triangular and trapezoidal headers and for high flow rate, less flow maldistribution can be achieved with rectangular header. Saeed and Kim [10] concluded that flow maldistribution in parallel minichannel heat sink can be minimized by proper designing of the distributor and collector headers for minichannel heat sink. Siva et al. [11] carried out experimental study on flow maldistribution and its effect on thermal performance of parallel microchannel cooling systems. Experimental results show that flow distribution among the channel improves with decrease in hydraulic diameter due to higher pressure drop. Mohammadi et al. [12] performed a numerical study with low Reynolds number using the CFD tool COMSOL. They found that a short vertical spacing at the corner of manifolds is critical to achieving a high level of flow uniformity.

Literature review suggests that plenty of research has been carried out on flow maldistribution, but there are very few studies which provide the proper solution of flow maldistribution in minichannel heat sink using full domain simulation; thus, a detailed investigation is required to minimize flow maldistribution. The aim of the present study is to explore the effect of inlet/outlet flow arrangements and volumetric flow rate on the flow maldistribution to enhance the heat sink performance.

## 2 Geometric Configuration of Minichannel Heat Sink

The minichannel heat sink has been tested in this study contained 28 minichannels having hydraulic diameter 1.5 mm. Four types of flow arrangements such as I-Type, Z-Type, C-Type, and U-Type have been considered as shown in Fig. 1b–e, respectively. Rectangular header has been used for all the arrangements.

Fluid has been distributed to all the minichannels through distributor header and collected by collector header. The length of distributor and collector header is same as heat sink width. The depth of header has been considered same as of depth of
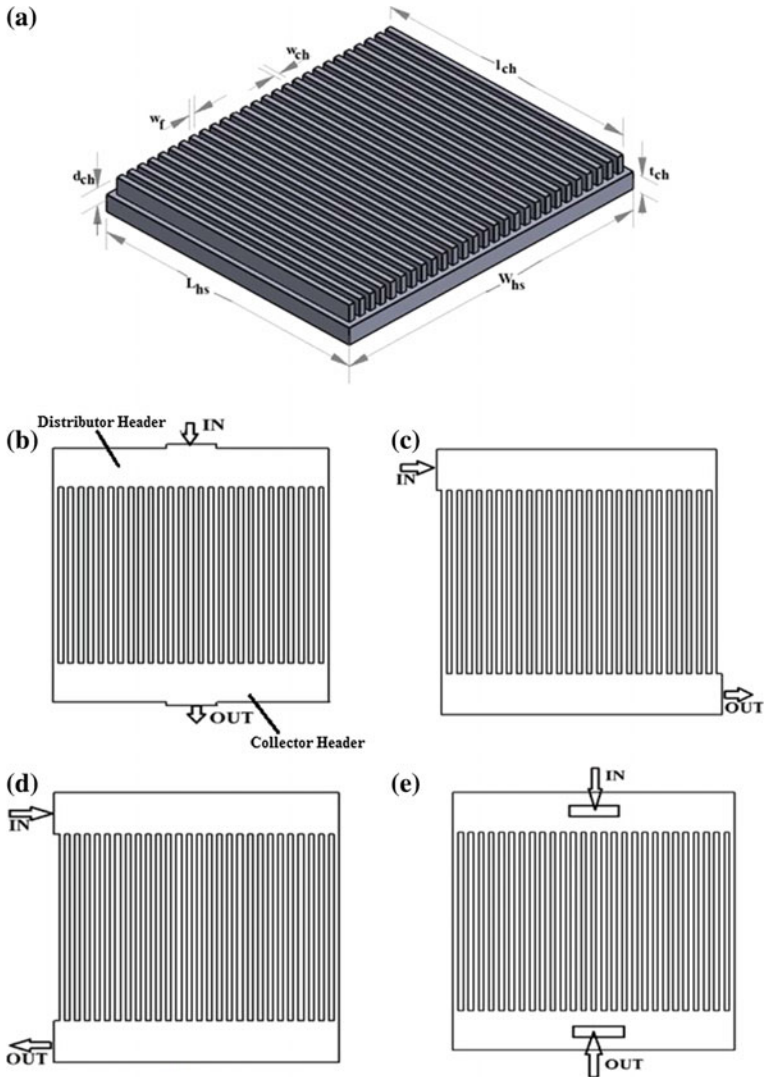
**Fig. 1 a** Minichannel heat sink. **b** I-Type flow arrangement. **c** Z-Type flow arrangement. **d** C-Type flow arrangement. **e** U-Type flow arrangement

minichannels. In case of I-Type, Z-Type, and C-Type arrangements, water entered in distributor header horizontally, but in case of U-Type arrangement, water entered in distributor header vertically upward as shown in Fig. 1. All dimensions of minichannel heat sink and header are given in Table 1.

**Table 1** Dimensions of minichannel heat sink

| Parameter | Value |
|---|---|
| Heat sink length ($L_{hs}$) | 47 mm |
| Heat sink width ($W_{hs}$) | 55 mm |
| Minichannel length ($l_{ch}$) | 45 mm |
| Minichannel width ($w_{ch}$) | 1 mm |
| Minichannel depth ($d_{ch}$) | 3 mm |
| Width of fin ($w_f$) | 1 mm |
| Number of channels ($N$) | 28 |
| Header length ($l_h$) | 55 mm |
| Header depth ($d_h$) | 3 mm |
| Header width ($w_h$) | mm |

## 3  Governing Equations and Boundary Conditions

Based on the problem, governing equations (continuity equation, momentum equation, and energy equation) has been applied for the fluid domain as given in Eqs. (1), (2), and (3), respectively.

$$\nabla \cdot \vec{V} = 0 \tag{1}$$

$$\rho(\vec{V} \cdot \nabla \vec{V}) = -\nabla p + \mu \nabla^2 \vec{V} \tag{2}$$

$$p c_p(\vec{V} \cdot \nabla T) = k_f \nabla^2 T \tag{3}$$

Energy equation for solid domain is given in Eq. (4)

$$k_s \nabla^2 T = 0 \tag{4}$$

In this present numerical study, the aluminum was considered as the heat sink material. The properties of working fluid (water) are $\rho = 998.2$ kg m − 3, $c_p = 4182$ J kg − 1 K–1, $k_f = 0.6$ W m − 1 K − 1, $v = 1.0 \times 10 – 6$ m² s, and thermal conductivity of aluminum is $k_s = 202.4$ W m − 1 K −1. Inlet temperature of working fluid is set at 298 K. The simulation has been conducted for different inlet velocity from 0.2777 to 0.5555ms −1. At outlet, the pressure outlet condition is applied. In this study, the Reynolds number is varying from 300 to 1000 and hence the flow can be assumed as laminar flow. Constant heat flux (20 Wcm$^{-2}$) condition has been applied to the base of the heat sink because most of the electronic components generate heat flux between 10 to 50 Wcm$^{-2}$.
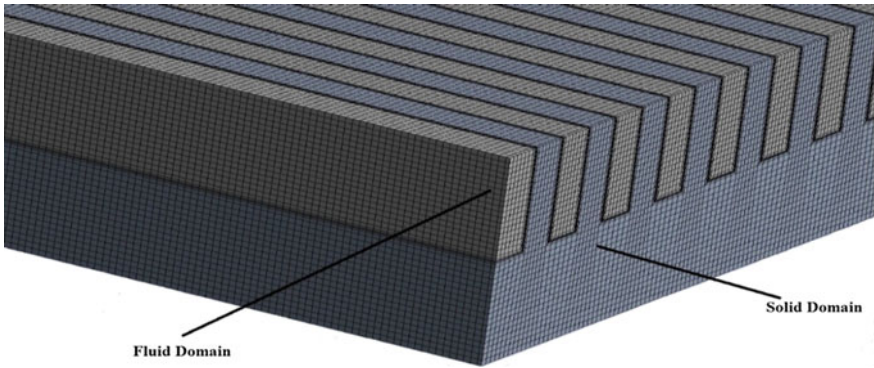
**Fig. 2** Meshing of fluid and solid domain

## 4 Grid Independence and Validation

Both solid domain and fluid domain were discretized using ANSYS Fluent 16. Hexahedral elements with $14 \times 10^5$, $44 \times 10^5$, $70 \times 10^5$, and $100 \times 10^5$ nodes have been considered to test the grid independence of the solution as shown in Fig. 2. The velocity variations along 28 channels in Z-Type arrangement are shown in Fig. 3. It is found that $70 \times 10^5$ and $100 \times 10^5$ nodes have almost same velocity in minichannels as shown in Fig. 3.

Numerical results have been validated by Jajja et al. [7]. They used copper as a heat sink material, but in this study, aluminum has been taken as a heat sink material; therefore, higher value of thermal resistance has been obtained for present study because of lower thermal conductivity of aluminum.
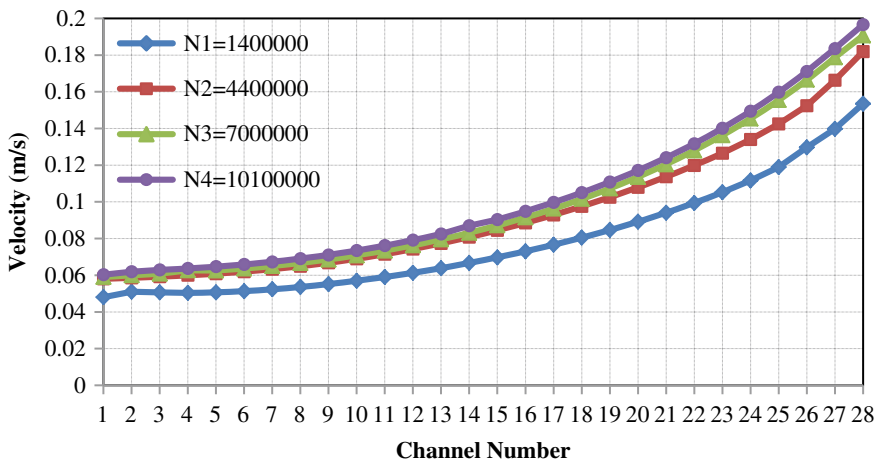


**Fig. 3** Grid independence for Z-Type arrangement at 0.5 LPM

## 5 Results and Discussions

Flow uniformity in parallel minichannel is calculated with the help of maldistribution factor (MF) given in Eq. (5).

$$MF = \sqrt{\frac{1}{N} \sum_{k=1}^{N} \left( \frac{m^k - m_{avg}}{m_{avg}} \right)^2} \tag{5}$$

$$m_{avg} = \frac{\sum_{k=1}^{N} m^k}{N} \tag{6}$$

The thermal performance of minichannel heat sink is evaluated with the help of Eq. (7)

$$R_{th} = \frac{T_{b\max} - T_{in}}{q_w W_{hs} L_{hs}} \tag{7}$$

where $R_{th}$ is known as thermal resistance.

### 5.1 Effect of Inlet/Outlet Arrangement on Flow Distribution

Flow maldistribution can be minimized by making proper inlet/outlet arrangement. There are total 28 numbers of channels, the first channel is on left side, and last channel is on right side for all inlet/outlet arrangements as shown in Fig. 1. Water entered distributor header horizontally in the case of I-Type, Z-Type, and C-Type while in case of U-Type, water entered distributor header vertically upward. In I-Type arrangement, due to the inlet velocity effect, velocity is more in middle (10–18) channels as compared to left side channels (1–9) and right side channel (19–28). In Z-Type arrangement, velocity is more in channels those are away from the inlet as compared to the channels those are near the inlet due to inertia of incoming water. In C-Type arrangement, velocity was high in the channels, those are near the inlet and outlet as compared to those are away from inlet and outlet.

This was due to the pressure difference between distributor header and collector header. The channels which were near the inlet and outlet, pressure difference was more due to zero gauge pressure at outlet as compared those were away from inlet and outlet. In U-Type arrangement, water entered in distributor header vertically upward via inlet due to that velocity effect has been minimized. When water entered in distributor header, water strikes the upper wall of header and get bounce back and spread out in the header due to that flow distribution was more uniform in this arrangement as compared to others arrangements shown in Fig. 4.
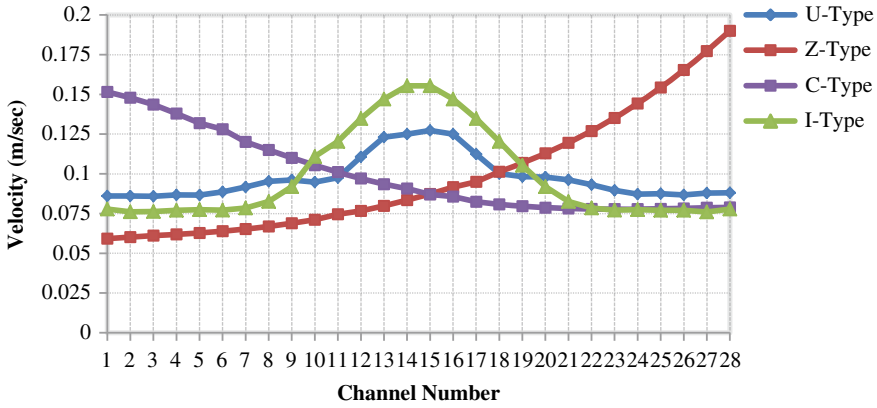
**Fig. 4** Velocity in minichannels for different type inlet/outlet arrangements for 0.5 LPM

## 5.2 Effect of Volumetric Flow Rate on Flow Maldistribution

Flow maldistribution in parallel minichannels is dependent on volumetric flow rate, as volumetric flow rate increases maldistribution factor also increases as shown in Fig. 5.

## 5.3 Effect of Flow Maldistribution on Thermal Resistance of Heat Sink

For same volumetric flow rate, it is observed that U-Type heat sink has more uniform cooling among all other arrangements due to uniform flow distribution.
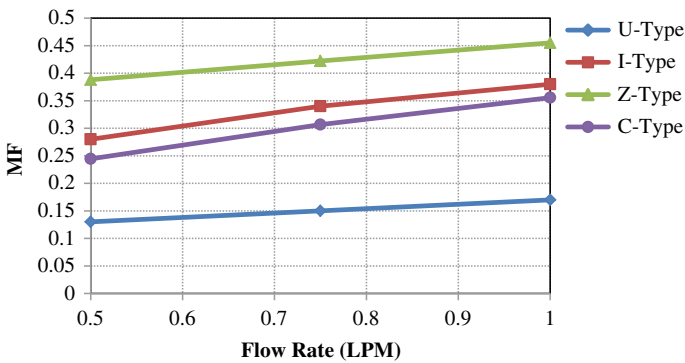


**Fig. 5** Maldistribution factor as function of volumetric flow rate
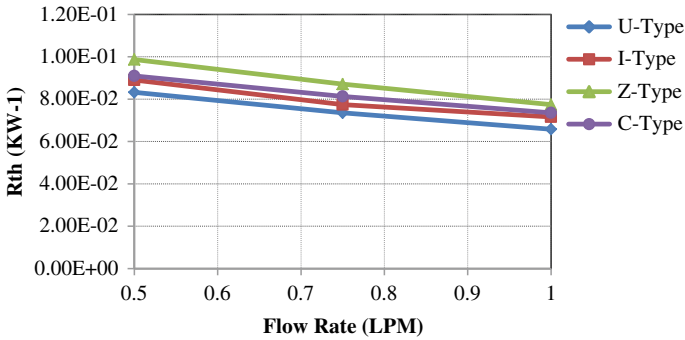
**Fig. 6** Thermal resistance as function of volumetric flow rate

U-Type arrangement has minimum thermal resistance, and Z-Type has maximum thermal resistance. Thermal resistance decreases with increase in volumetric flow rate as shown in Fig. 6.

## 6    Conclusions

All the inlet/outlet flow arrangements have been studied carefully, and it is found that U-Type arrangement has small flow maldistribution which implies more uniformity of flow distribution in parallel minichannels due to reducing the inertial effect and Z-Type arrangement has highest non-uniform flow distribution in parallel minichannels due to inertia of incoming fluid. It is also found that lowest maldistribution factor has been found for U-Type arrangement and highest for Z-Type arrangement. The value of maldistribution factor should be close to zero for better hydraulic performance of heat sink. Maldistribution factor increases with volumetric flow rate. For better thermal performance, the value of thermal resistance should be small which is found in U-Type arrangement. Thermal resistance decreases with increase in volumetric flow rate for all the arrangements.

## References

1. Bajura RA, Jones EH Jr (1976) Flow distribution manifolds. J Fluids Eng 654–666
2. Kim S, Choi E, Cho YI (1995) The effect of header shapes on the flow distribution in a manifold for electronic packaging applications. Int Commun Heat Mass Transf 22(3):329–341
3. Cho ES, Choi JW, Yoon JS, Kim MS (2010) Modeling and simulation on the mass flow distribution in microchannel heat sinks with non-uniform heat flux conditions. Int J Heat Mass Transf 53(7):1341–1348

4. Kumaraguruparan G, Kumaran RM, Sornakumar T, Sundararajan T (2011) A numerical and experimental investigation of flow maldistribution in a micro-channel heat sink. Int Commun Heat Mass Transf 38(10):1349–1353
5. Nielsen KK et al (2012) Degradation of the performance of microchannel heat exchangers due to flow maldistribution. Appl Therm Eng 40:236–247
6. Pistoresi C, Fan Y, Luo L (2015) Numerical study on the improvement of flow distribution uniformity among parallel mini-channels. Chem Eng Process Process Intensif 95:63–71
7. Jajja SA, Ali W, Ali HM, Ali AM (2014) Water cooled minichannel heat sinks for microprocessor cooling: effect of fin spacing. Appl Therm Eng 64:76–82
8. Liu X, Yu J (2016) Numerical study on performances of mini-channel heat sinks with non-uniform inlets. Appl Therm Eng 93:856–864
9. Anbumeenakshi C, Thansekhar MR (2016) Experimental investigation of header shape and inlet configuration on flow maldistribution in microchannel. Exp Thermal Fluid Sci 75:156–161
10. Saeed M, Kim M-H (2017) Header design approaches for mini-channel heatsinks using analytical and numerical methods. Appl Therm Eng 110:1500–1510
11. Siva VM, Pattamatta A, Das SK (2014) Effect of flow maldistribution on the thermal performance of parallel microchannel cooling systems. Int J Heat Mass Transf 73:424–428
12. Mohammadi M, Goran NJ, Kendra VS (2013) Numerical study of flow uniformity and pressure characteristics within a microchannel array with triangular manifolds. Comput Chem Eng 52, 134–144

# Mixed Convection Heat Transfer in a Cavity with Rotating Cylinder Under the Influence of Magnetic Field

**Ranjit J. Singh and Trushar B. Gohil**

**Abstract** The present study investigates the influence of magnetic field on the heat transfer phenomena of rotating cylinder kept in the center of the square cavity. The numerical code for mixed convective flow with Magnetohydrodynamics is developed on the open-source CFD platform OpenFOAM. The developed solver is capable of simulating steady and unsteady flows on any arbitrary geometry. The center of the cylinder is fixed at the center of the cavity with varying blockage ratio ($L/d = 2$ and 4). The surface of the cylinder is kept as hot, and the two opposite vertical sides are kept cold, while the top and bottom surface are maintained as thermally insulated. The cylinder is rotated clockwise ($\omega = 50$) and anticlockwise ($\omega = -50$) about its center. The fluid is assumed to be incompressible and electric conducting in nature and the all walls of the cavity is also maintained as electrically insulated. The intensity of magnetic field is varied in terms of Hartmann number ($Ha$) in the range of $Ha = 0$ and 100 for the fixed Rayleigh number of $Ra = 10^5$. The flow and thermal field are analyzed through streamlines, isotherm contours for various $Ha$ and $\omega$ (angular rotation). Furthermore, pertinent transport quantities as the Nusselt number is also determined to analyze the influence of magnetic field and angular rotation of the cylinder on the heat transfer. It is observed that the heat transfer and fluid flow behavior is significantly affected by the magnetic field and rotation of the cylinder.

**Keywords** OpenFOAM · MHD · Mixed convection · Rotating cylinder

## Nomenclature

| | |
|---|---|
| $U$ | Velocity of fluid (m s$^{-1}$) |
| $p$ | Pressure (N m$^{-2}$) |
| $T$ | Temperature (K) |
| $T_{ref}$ | Ambient temperature (K) |

R. J. Singh · T. B. Gohil (✉)
Department of Mechanical Engineering, Visvesvaraya National Institute of Technology, Nagpur 440010, India
e-mail: trushar.gohil@gmail.com

$j$      Electric current density (A m$^{-2}$)
$B$      Applied magnetic field (kg s$^{-2}$ A$^{-1}$)
$g$      Acceleration due to gravity (m s$^{-2}$)
$\phi$      Electric potential (m$^2$ kg s$^{-3}$ A$^{-1}$)
$L$      Side length of cube (m)
$Gr$     Grashof number
$Ha$    Hartmann number
$Ra$    Rayleigh number
$F$      Lorentz force ($j \times B$) (N m$^{-3}$)
$Pr$     Prandtl number
$Nu$    Nusselt number
$d$      Diameter of cylinder (m)
$\omega$      Angular velocity (rad/s)
$x, y$   Cartesian coordinates (m)

**Greek symbols**

$\alpha$   Thermal diffusivity (m$^2$ s$^{-1}$)
$\beta$   Coefficient of thermal expansion (K$^{-1}$)
$\rho$   Fluid density (kg m$^{-3}$)
$\sigma$   Fluid electrical conductivity (s$^3$ A$^2$ m$^{-3}$ kg$^{-1}$)
$\mu$   Dynamic viscosity (kg m$^{-1}$ s$^{-1}$)
$v$   Kinematic viscosity (m$^2$ s$^{-1}$)

# 1 Introduction

Since few decades, the numerical analysis of convectional heat transfer and fluid flow has come to be one of the essential engineering applications in industrial or commercial fields. The active or passive regulation of heat and fluid flow are enormously vital in the designing of nuclear reactors, heat exchanger, cooling of electronic components, etc. It has been observed that the most of the researches are concentrated on the natural convection flow with the existence of bodies bounded within enclosures. Various exploration have dealt with the presence of the object with different thermal circumstances on natural convection within the square domain with either horizontal [1, 2] and vertical [3, 4] temperature difference or heat flux. Asan [5] numerically analyzed the free convection flow in the two-dimensional concentric isothermal square annulus for the Rayleigh number of $Ra$ up to $10^6$. The obtained results showed that the Rayleigh number ($Ra$) and aspect ratio have a substantial effect on the heat transfer and flow fields. Ghaddar [6] presented the numerical outcomes for the heated horizontal cylinder located inside the big rectangular enclosure. It was observed that the thermal and flow

performance be contingent on the heat flux applied to the inner cylinder and got the correlation between the Nusselt number and Rayleigh number. Kim et al. [7] observed the numerical assessment of the natural convection arise by the temperature variation by the heated inner cylinder and the cold outer surface of different $Ra$ ranges vary from $10^3$ to $10^7$.

The size, quantity, and development of convection rolls depend on the location of the cylinder altered in the centerline of the outer domain and the Rayleigh number. Reymond et al. [8] had executed the experimentation on the free convection heat and fluid flow from a couple of vertically attached horizontal cylinders at various Rayleigh numbers and cylinder positioning. It is revealed that the presence of lower cold cylinder does not disturb the heat dissipation and fluid flow for the heated upper cylinder. Conversely, when the top and bottom cylinders are kept hot, then the heat dissipation and fluid flow close to the hot upper cylinder is intensely influenced because the plume emerging from heated lower cylinder intermingles with heated upper cylinder. Kareem et al. [9] numerically inspected the turbulent heat dissipation and fluid flow in the three-dimensional lid-driven enclosure with rotating cylinders. The large eddy simulation (LES) and unsteady Reynolds-averaged Navier–Stokes (URANS) approaches are assumed to analyze the fluid flow and heat transfer; it is shown that LES can predict the structure details of secondary vortices that have strong upshot on heat transfer. Chatterjee et al. [10, 11] considered the heat and fluid flow under the lid-driven square enclosure, and static enclosure for the rotating cylinder positioned at the center of the cavity. It has been perceived that the heat transfer is highly affected by the angular rotation of the cylinder. Park et al. [12] numerically observed the free convection heat and fluid flow in the square domain with static cylinder kept at the different position. The result revealed that the increase in the gap between the center of cylinder to the square cavity and Rayleigh number the heat transfer upsurges.

In this present numerical observation, The MHD-based free convection heat and fluid flow solver are established in the OpenFOAM to carry out the numerical investigation of the fluid flow and heat transfer rate under the impact of the magnetic field. The comparison of streamlines, isotherms, and Nusselt number over the heated cylinder under the influence of magnetic field with the angular rotation of cylinder at $\omega = 50$ (clockwise (CW) and counter-clockwise (CCW) and stationary conditions are reported. The streamlines, isotherms, and the Nusselt number show the significant variation in the presence of magnetic field.

## 2   Mathematical Formulations and Numerical Scheme

Let us consider the steady buoyancy-driven natural convection flow in the cubic cavity heated from inner cylinder within the square enclosure. The physical transport properties fluid is supposed to be independent of temperature. The working fluid is assumed to be viscous, incompressible, and electrically conducting. The thermal and electrical conductivity of outer wall is expected to be uniform.

Therefore, the governing equation for present numerical analysis can be written as follows:

Continuity equation:

$$\nabla \cdot \vec{U} = 0 \tag{1}$$

Momentum equation with Lorentz force and Boussinesq approximation:

$$\frac{\partial \vec{U}}{\partial t} + (\vec{U} \cdot \nabla)\vec{U} = -\frac{\nabla p}{\rho} + v \cdot \nabla^2 \vec{U} + \frac{\vec{j} \times \vec{B}}{\rho} - \beta(T - T_{\text{ref}})\vec{g} \tag{2}$$

Ohm's law current density for fluid:

$$\vec{j} = \sigma(-\nabla \phi + \vec{U} \times \vec{B}) \tag{3}$$

Conservation of charge:

$$\nabla \cdot \vec{j} = 0 \tag{4}$$

Conservation of thermal energy of fluid:

$$\frac{\partial T}{\partial t} + (\vec{U} \cdot \nabla)T = \nabla \cdot (\alpha . \nabla T) \tag{5}$$

The Poison's electric potential equation is completed by correlating the Ohm's law of current density (Eq. 3) and conservation of charge (Eq. 4) is mentioned as follow:

$$\nabla^2 \phi = \nabla \cdot (\vec{U} \times \vec{B}) \tag{6}$$

The three non-dimensional parameters included in this investigation to observe the fluid behavior under the effect of magnetic field are as follows:

$$Ha = BL\sqrt{\frac{\sigma}{\rho v}} Ra = \frac{g\beta(T - T_{ref})L^3}{v\alpha} = Gr \cdot Pr = \frac{v}{\alpha}$$

where the *Ha* is the Hartmann number, which is used to estimate the intensity of magnetic field. It is defined as the ratio of Lorentz force to viscous force. The *Ra* is the Rayleigh number, expresses the range of stability of fluid (laminar or unsteady). Grashof number narrates the association between the buoyancy and viscosity of the fluid and the Prandtl number expresses the association between momentum diffusivity and thermal diffusivity. Here, *L* stands for the characteristic length taken as the side length of cube. The present solver computes the Eqs. 1–6 using PIMPLE algorithm. The Boussinesq approximation is included in the solver to get buoyancy effect in the fluid. The Rhie and Chow [13] interpolation scheme is available in the

**Table 1** Boundary conditions and non-dimensional parameters

| Parameters | Cylinder | Right and left side walls | Top/bottom |
|---|---|---|---|
| $U$ | $\omega = 0$ and 50 (CW and CCW) | No slip | No slip |
| $p$ | $\partial p / \partial n = 0$ | | |
| $T$ | 1 | 0 | $\partial T / \partial n = 0$ |
| $\phi$ | $\partial \phi / \partial n = 0$ | | |
| $Ra$ | $10^5$ ($Ha = 0$ and 100) | | |
| $Pr$ | 0.71 | | |
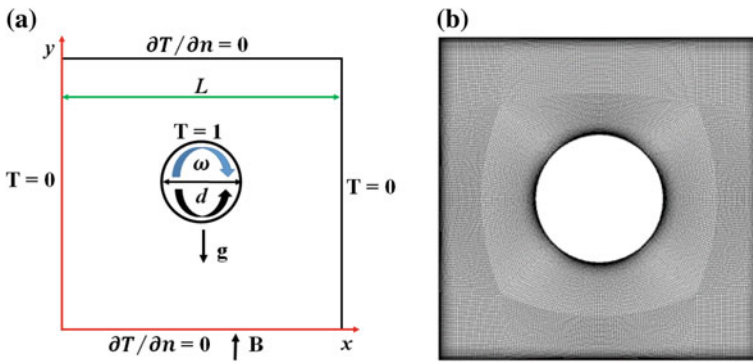


**Fig. 1** **a** Schematic view of square enclosure with cylinder and **b** mesh distribution at the plane $z = 0.5$

solver to compute the Navier–Stokes equation, where velocity is attained from momentum equation and pressure is obtained from continuity equation. Henceforth, the velocity is employed to obtain the electric potential, electric current, and hence Lorentz force. The Lorentz force behaves as source term along with Boussinesq approximation in the momentum equation. The Euler and second-order central difference scheme are used to discretize the time derivate and convection as well as diffusion term, respectively. Table 1 illustrates the boundary condition and non-dimensional parameters utilized in the present study to perform numerical simulations (Fig. 1).

## 3 Validation and Grid Independence Test

The results produced from the present solver have been validated with the results revealed in the published literature by Chatterjee et al. [14]. The physical boundary condition and geometrical information are retained same as mentioned in the reference [14]. Figure 2a confirmed the velocity profile comparison attained in the vertical y-direction with reference [14]. The grid independence test is performed on
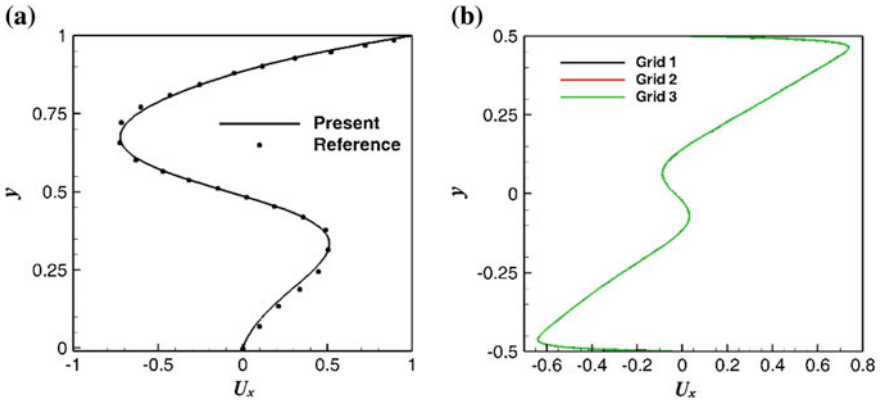
**Fig. 2** **a** Comparison of the horizontal velocity along the vertical y-direction at $x = 0.25$, $\omega = 50$ with Ref. [14]. **b** Grid independence

three different grid sizes for $Ra = 10^5$ and $Ha = 100$ and $\omega = 50$ (CW) as follows; grid 1 = 20,000 elements, grid 2 = 30,000 elements, and grid 3 = 40,000 elements. Figure 2b expresses the grid independence comparison and hence the grid 2 can be decided for further computation, as it has enough mesh quality to accommodate all the boundary layer physics.

## 4 Results and Discussion

The present study is focused to investigate the mutual effect of buoyancy-driven flow with the angular rotation of cylinder in the free convection flow. The Rayleigh number and angular rotation of cylinder for the present analysis is fixed as $Ra = 10^5$; $\omega = 0$ and 50 rad/s (CW and CCW). The intensity of magnetic field is fixed at $Ha = 0$ and 100, which has the substantial outcome on the heat transfer and fluid flow structures. Figure 3 shows the streamlines for the stationary as well as rotating cylinder at $Ha = 0$ and 100 for $L/d = 2$ and 4, expresses the uniform distribution of flow on both sides for $Ha = 0$. As soon as the rotation is given to the cylinder, it has been observed that the flow pattern is shifted in the direction of rotation and the angular rotation of the cylinder results into the uneven distribution of the flow. The magnetic field is applied in the vertical direction against the gravity. The non-uniform distribution of the flow (Fig. 3b, c, h, and i) at an angular rotation of $\omega = 50$ (CW and CCW) brought to the uniform pattern at low intensity of magnetic field ($Ha = 50$) imposed on system as shown in Fig. 3e, f, k, and l. Similarly, Fig. 4 reveals the temperature contours and isotherms pattern at different magnetic field intensity and angular rotation. It has been observed from the isotherms that the plume generated by the ordinary convection flow has dissipation pattern as per the buoyancy force and centrifugal force offered by the rotation of the
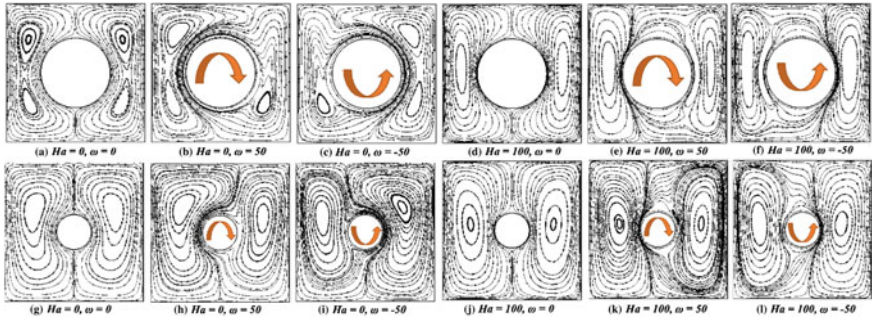
**Fig. 3** Streamline variations for $L/d = 2$ (top) and $L/d = 4$ (bottom)

cylinder. The application of magnetic field produces the electric current, which further interacts with the magnetic field to produce Lorentz force. The Lorentz force has the direction of flow opposite to the flow of the fluid. Hence, it opposes the flow of fluid in the cavity and hence the plume. Therefore, isotherms are distributed independently of rotation of cylinder as the Lorentz force is balancing the centrifugal force offered by the cylinder. Figure 4e, f, k, and l shows the isotherms which are against the rotation of cylinder and Fig. 5 shows the local Nusselt number variation over the hot cylindrical surface at different Hartmann number and angular rotation. It has been observed from Fig. 5a and b that the peak value of local Nusselt number increases with rotation. In the case of $L/d = 4$, there is a decrement in the peak local Nusselt number is observed with the application of magnetic field and angular rotation. The centrifugal forces in the domain offered by the angular rotation of smaller cylinder do not overcome the buoyancy forces compared to larger cylinder. Hence, the heat dissipation is constricted by the magnetic field even at the angular rotation of the smaller cylinder. Figure 6a and b shows the variation of horizontal component of velocity ($U_x$) along the vertical $y$-direction at the plane $x = 0.25$. It is understood from Fig. 6a that the larger diameter
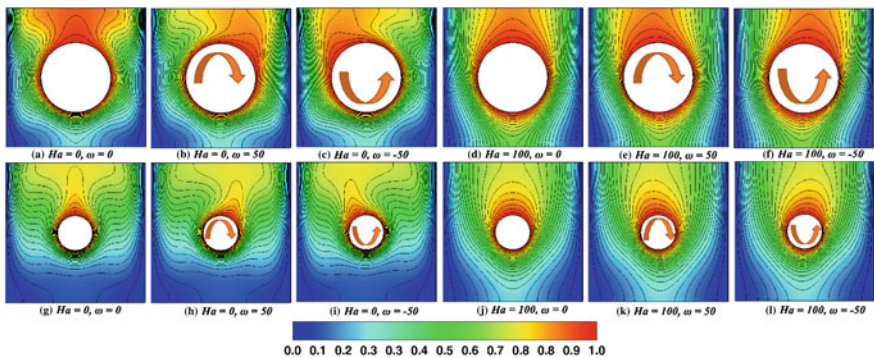


**Fig. 4** Temperature Isotherms variation for $L/d = 2$ (top) and $L/d = 4$ (bottom)
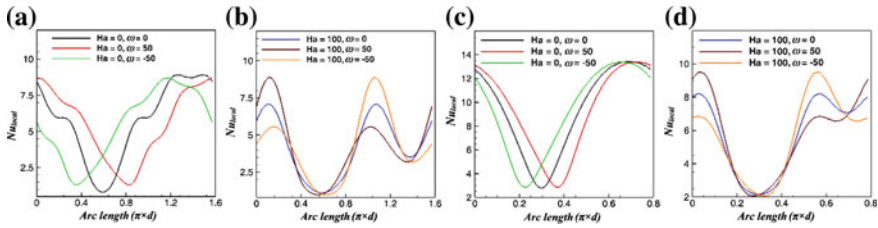
**Fig. 5** Local Nusselt number variation over the surface of cylinder for $L/d = 2$ (**a** and **b**) and $L/d = 4$ (**c** and **d**)
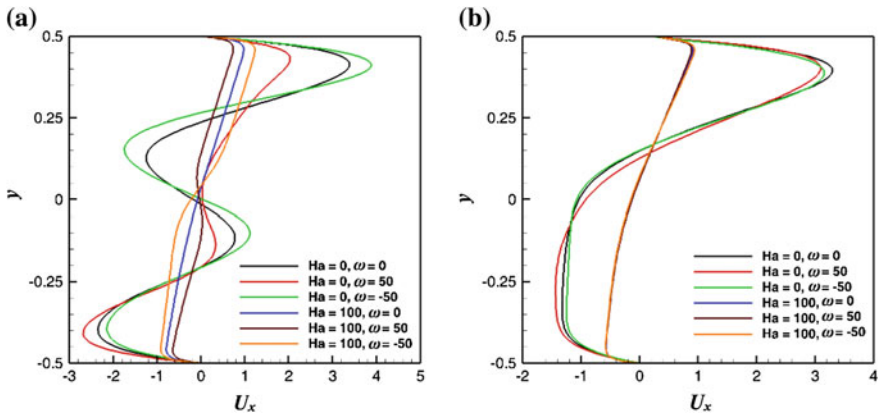


**Fig. 6** Comparison of horizontal component pof velocity ($U_x$) along the vertical $y$-direction at different $Ha$ and $\omega$ at the plane $x = 0.25$, **a** $L/d = 4$ and **b** $L/d = 4$

of the cylinder has a substantial effect on the flow distribution in the domain even at the higher magnetic field. The velocity variation in the case of the smaller cylinder (Fig. 6b) does not have any significant change in the flow behavior even at the angular motion, this is happening because of the high magnetic field opposing the flow motion and low centrifugal force offered by the smaller cylinder.

## 5  Conclusion

The present examination is focused on the transformation in the flow and heat dissipation structure within a square enclosure with hot rotating cylinder under the impact of magnetic strength. The angular rotation of the cylinder is kept uniform at $\omega = 50$ (CW and CCW) with the variable magnetic field strength of $Ha = 0$ and 100. The Rayleigh number of the system is kept at $Ra = 10^5$ with Prandtl number of $Pr = 0.71$. It is understood from the results when the cylinder is stationary the flow

and heat transfer follow the steady nature, as soon as the cylinder started the angular rotation the shift in the heat transfer and flow pattern begins. This shifting in the flow pattern shows the effect of centrifugal force in the domain. Furthermore, the application of magnetic field assists to bring the shifted nature of the flow structure and Nusselt number in a symmetrical form which can be seen in Figs. 5 and 6. However, the magnetic intensity reduced the heat transfer rate and regulated the flow pattern in the regular sequences, which can be seen in Fig. 4. The Nusselt number at stationary cylinder without magnetic field is higher compared with the system imposed with the magnetic field. This is so because the intensity of the magnetic field ($Ha = 50$) consequently suppresses the flow affecting the drop in the heat transfer. Figure 6 shows the decrease in the peak velocity when the magnetic field of $Ha = 50$ is applied to the system.

# References

1. Ha MY, Kim IK, Yoon HS, Lee SS (2002) Unsteady fluid flow and temperature fields in a horizontal enclosure with an adiabatic body. Phys Fluids 14:3189–3202
2. Lee JR, Ha MY (2015) A numerical study of natural convection in a horizontal enclosure with a conducting body. Int J Heat Mass Transfer 48:3308–3318
3. Misra D, Sarkar A (1997) Finite element analysis of conjugate natural convection in a square enclosure with a conducting vertical wall. Comput Methods Appl Mech Eng 141:205–219
4. Jami M, Mezrhab A, Bouzidi M, Lallemand P (2007) Lattice Boltzmann method applied to the laminar natural convection in an enclosure with a heat-generating cylinder conducting body. Int J Thermal Sci 46:38–47
5. Asan H (2000) Natural convection in an annulus between two isothermal concentric square ducts. Int Comm Heat Mass Transfer 27:367–376
6. Ghaddar NK (1992) Natural convection heat transfer between a uniformly heated cylindrical element and its rectangular enclosure. Int J Heat Mass Transfer 35:2327–2334
7. Kim BS, Lee DS, Ha MY, Yoon HS (2008) A numerical study of natural convection in a square enclosure with a circular cylinder at different vertical locations. Int J Heat Mass Transfer 51:1888–1906
8. Reymond O, Murray DB, O'Donovan TS (2008) Natural convection heat transfer from two horizontal cylinders. Exp Thermal Fluid Sci 32:1702–1709
9. Kareem AK, Gao S (2017) Mixed convection heat transfer of turbulent flow in a three-dimensional lid-driven cavity with a rotating cylinder. Int J Heat Mass Transf 112:185–200
10. Chatterjee D, Mondal B, Halder P (2014) Hydromagnetic mixed convective transport in a vertical lid-driven cavity including a Heat conducting rotating circular cylinder. Numer Heat Transfer, Part A 65:48–65
11. Chatterjee D, Halder P (2014) MHD mixed convective transport in square Enclosure with two rotating circular cylinders. Numer Heat Transfer Part A 65:802–824
12. Park YG, Yoon HS, Yeong Ha M (2012) Natural convection in square enclosure with hot and cold cylinders at different vertical locations. Int J Heat Mass Transf 55:7911–7925

13. Ferziger JH, Peric M (2002) Computational Methods for Fluid Dynamics, 3rd edn. Springer, Verlag Berlin Heidelberg, pp 247–251
14. Chatterjee D, Gupta SK, Mondal B (2014) Mixed convective transport in a lid-driven cavity containing a nanofluid and a rotating circular cylinder at the center. Int. Commun. Heat Mass Transf 56:71–78

# Numerical Simulation of Fluid Flow Inside Nozzle Check Valve

**Anshul Bhardwaj** and **Basant Singh Sikarwar**

**Abstract** The check valve and non-return valve are specially designed valves for permitting only unidirectional fluid flow and are employed as a measure of safety for the protection of expensive equipment such as compressor, rotating parts, feed pump, and discharge reservoir. This crucial significance of nozzle check valve gives rise to its exhaustive and thorough study to meet safety standards and ISA valve specifications. The valve design primarily comprises of generating a converging and diverging fluid flow across the valve's inner geometrical surface by keeping least surface area around the valve disc at fully opened position. To better predict the valve's performance, this paper manifests the numerical simulation of fluid flow in a twelve-inch nozzle check valve and calculates its flow coefficient ($C_q$). The steady-state 3D Navier-Stokes equations with appropriate boundary conditions are numerically solved using FVM method. The computational domain consists of a 10-D and 7-D length of pipe attached to the inlet and outlet section of the valve, respectively, to capture flow development where D is the diameter of pipe. The simulation is carried for incompressible fluid (water) at numerous Reynolds numbers (3.1E4–9.3E5). Consequently, the velocity and pressure contours are plotted at corresponding Reynolds numbers, and the analysis of flow through the valve for estimating flow coefficient of the valve ($C_q$) is 2863 $\pm$ 5%. It is found that the flow coefficient remained constant for various Reynolds numbers. Hence, the flow coefficient is only a strong function of the shape of valve.

**Keywords** Check valve $\cdot$ Flow coefficient $\cdot$ 3D numerical simulation $\cdot$ Incompressible flow $\cdot$ CFD

A. Bhardwaj (✉)
Department of Mechanical and Industrial Engineering, UIC, Chicago, IL, USA
e-mail: abhard22@uic.edu

B. S. Sikarwar
Department of Mechanical Engineering, Amity University Uttar Pradesh, Noida, Uttar Pradesh, India
e-mail: bssikarwar@amity.edu

**Nomenclature**

| | |
|---|---|
| $A_c$ | Cross-sectional area at valve seat |
| $C_q$ | Flow coefficient of valve |
| $d$ | Diameter of inlet section of valve (m) |
| $D$ | Diameter of pipe (m) |
| $f$ | Darcy–Weisbach friction factor |
| $F_p$ | Piping geometry factor |
| $g$ | Acceleration due to gravity (9.8 m/s$^2$) |
| $G_f$ | Liquid specific gravity at upstream |
| $k$ | Borda–Carnot constant |
| $K_N$ | Resistance coefficient of inlet and outlet fittings, respectively |
| $K_B$ | Bernoulli's coefficient for inlet and outlet fittings, respectively |
| $l$ | Length of pipe (m) |
| $N_n$ | Numerical constants for units of measurement used |
| $q$ | Volumetric flow rate (m$^3$/hr) |
| $t$ | Time (second) |
| $u$ | $x$-velocity of fluid flow (m/s) |
| $v$ | $y$-velocity of fluid flow (m/s) |
| $v_{avg}$ | Average velocity of fluid flow (m/s) |
| 3D | Three dimension |
| $\rho$ | Density of fluid (kg/m$^3$) |
| $\Sigma K$ | Algebraic sum of effective velocity head coefficients of all fitting attached in the piping system (not including valves) |
| $\Delta P$ | Pressure differential or pressure loss |

## 1  Introduction

The surge in energy deficiency and power crisis has raised concern for optimization in industrial piping system. One such crucial part of piping system is a device called valve. The valves are used to control, maintain and regulate the flow of fluid. Valve requires great attention during its designing phase as improper selection and sizing of valve can deteriorate whole piping equipment and cause heavy energy losses. This problem attracts fluid mechanics engineers to work on and fabricate valve as per the requirement of industrial process.

Various valves have found huge application in industries. However, check valves have found extensive industrial as well as domestic application by automatically permitting fluid flow in only one direction without needing to be controlled by any operator. It incorporates the use of moving valve disc (can be plug, plate or wedge) which opens when fluid from inlet flows beyond the critical velocity and closes due to the backflow pressure and helical spring(s) force as shown in Fig. 1. Different types of check valves are characterized accordingly to
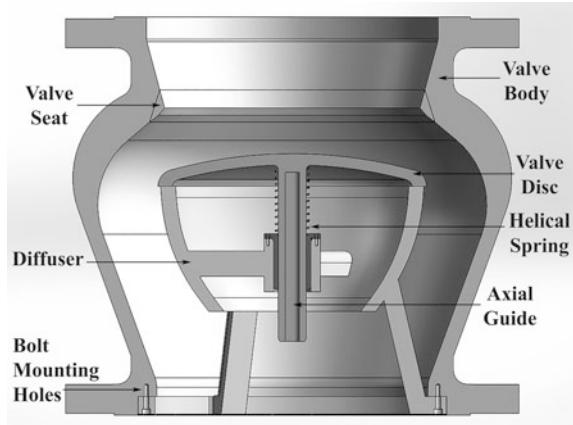
their application and geometry of valve disc. Generally, there are three types of check valves known as lift check valves, swing check valve and pump control valves [1].

Nozzle check valve is a type of lift check valve widely known and used for its zero-seat leakage with minimal pressure loss. The body of the nozzle check valve mainly houses the disc, spring and diffuser. The flow near the valve is segregated by valve disc into smaller channels whose cross-sectional area increases as the flow proceeds downstream direction. This study of the valve performance is focused on optimizing the valve disc's and diffuser's geometrical profile; valve interior surface and disc diffuser outline shape greatly influence the flow characteristics. Various fluid processes in industries require appropriate piping systems and so do the profile of disc and diffuser to enable optimum fluid flow and improve valve's flow coefficient ($C_q$).

Several numerical simulation studies [2–9] have been carried out to understand the flow development inside the valve. Majority of the fluid flow found inside the valves and pipes are turbulent and require appropriate turbulent model to be employed; also, selection of right turbulence model is necessary as Sibilla et al. [2] concluded that even with intense mesh refinement, the results are greatly dependent on the flow domain model used in solver. The check valve exhibits huge application in industries such as pumping station, nuclear plants and boiler units, but the pressure surge or disc fluttering usually generated in valve calls forth the attention towards its experimentation and numerical modelling [3].

Thorley [4] has worked on transient flow in check valve and demonstrated the usage of non-dimensional valve performance curves for valve selection which simplifies the work of design engineer. Kruisbrink in 1988 [5] has performed experimentation on dynamic characteristics of check valves and deduced a model that can be implemented for flow development in check valves; also, in his water hammer analysis, he concluded that results of ideal check valve over real model are far too optimistic and cannot be used for high-risk system.

Davis and Stewart [6, 7] took up this challenge and portrayed a numerical study which accurately predicted valve $C_v$ and inherent valve characteristics using axisymmetric flow models, and the results obtained in part 1 of CFD modelling was collaborated with part 2 of experimentation verification with better accuracy. Xue and Young utilized the same approach and studied the hydrodynamic flow and torque coefficient, respectively, of the butterfly valve of diameter 1.8 m at different opening angles [8]. Also, study was not limited to the usage of water as a fluid in valves as Fu and Ger [9] published a method for determining valve flow coefficient of diaphragm valve under compressible gas flow and also showed that the $C_v$ flow equation conventionally being used is no longer valid. This paper is distinctive in itself as the valve disc and diffuser's geometrical profile are unique with respect to other nozzle check valve designs; also, 3D numerical simulation is carried out rather than 2D axis-symmetric simulation. Furthermore, the valve disc is supported only by a single helical spring.

We adopted valve capacity calculations and test procedures described by International Society of Automation (ISA) [10] for the designing of nozzle check valve. The ISA-S75.01 [11] thoroughly enumerates the globally accepted standards for check valves and flow equations required to predict the valve performance. The ANSYS ICEM CFD® meshing tool is used for grid generation, followed by grid independence test to arrest appropriate grid size for 3D volumetric meshing. In Amity CFD solver, $K$-epsilon turbulence model is implemented to numerically simulate the flow characteristics inside the nozzle check valve. The numerically simulated data thus obtained are tabulated, and calculations are done to predict the valve flow coefficient. This study of the valve fluid flow pattern allowed various transformations and optimizations, committed to the valve profile to amplify the mass flow rate by maintaining the low-pressure drop leading to maximum flow coefficient ($C_q$).

## 2  Valve Description and Mathematical Modelling

Various types of check valves are available in the market based on the suitability of the required non-return flow applications. Among which nozzle check valve's excellent and precise throttling ability even for a low-flow rate system, featuring with non-slamming disc and orientation free mounting are prominent and readily available. The crucial decision for correct nozzle check valve sizing is to appropriately select right mechanical spring(s) for a given inlet velocity of fluid flow [12]. It is used not only to restrict or allow the fluid flow but is highly suited for protection from failure in pipe system such as abrupt pump downtime or sudden reduction in flow rate. Also, its self-acting nature and unidirectional operation enable it to be efficiently used where prevention of back flooding is required by means of a non-slam and fasting closing valve disc contributed by its short stroke.

Generally, nozzle check valve is operated in fully opened condition and installed where the inlet velocity of fluid flow is greater than critical velocity, required to overcome valve disc's inertia and spring force. Therefore, the analysis and simulation of fluid flow are carried out by keeping the valve at fully opened position.

The 3D Navier–Stokes equations with appropriate boundary condition are solved using finite volume method (FVM). Equation (1) describes the Navier–Stokes equation in modern notation. Primarily, the set of continuity and momentum equations are solved by utilizing computational techniques.

$$\frac{\partial u}{\partial t} + u \cdot \nabla u = -\frac{\nabla P}{\rho} + v \nabla^2 u \tag{1}$$

While evaluating variable component at grid points in the fluid flow, assumptions are made initially and 'semi-implicit method for pressure linked equations' algorithm is used to derive the corresponding velocity and pressure components to form a matrix which is then cross-verified by satisfying the continuity Eq. (2).

$$\frac{\partial \rho}{\partial t} + \nabla \cdot \rho \vec{V} = 0 \tag{2}$$

If the matrix elements do satisfy the mass conservation equation, then the values are marked as correct and used as base for calculation of successive neighbouring cells. This numerical solving process goes on till each and every variable component of the grid point throughout the flow domain is determined. Thus, all the simulated values obtained are then assigned to the respective grid points, and analysis of the control volume is accomplished.

## 3 The Equation of Flow Coefficient and Valve Sizing

Researchers have worked on determining the flow coefficient of the valves and have adopted various procedures to govern diverse flow phenomena such as cavitation, torque and transient flow through valves [8, 13, 14]. The testing procedures and expressions regarding the flow coefficient equations for check valve are adopted from ISA-75.01 [11].

The coefficient of flow is the index of flow capacity. In a fluid system, it equalizes to the flow in gallons per minute at a temperature of 60 °K across a valve or fitting with a pressure drop of 1-psi. It is defined as per US imperial system of measurement and by below expression:

$$C_q = \frac{q}{N_1 F_p} \sqrt{\frac{G_f}{\Delta P}} \tag{3}$$

Moreover, $F_p$ is additional variable added in the above equation to account for the losses generated inside the piping system due to fitting and attachments. The piping geometry factor ($F_p$) is calculated as:

$$F_p = \left( \frac{\Sigma K C_q^2}{N_2 d^4} + 1 \right)^{\frac{-1}{2}} \tag{4}$$

where $\Sigma K$ is algebraic sum of effective velocity head coefficients of all fitting attached in the piping system (not including valves) and is expressed by:

$$\Sigma K = K_1 + K_2 + K_{B_1} - K_{B_2} \tag{5}$$

For same diameter of inlet and outlet fittings, both $K_B$ terms are dropped out of the equation and $K_1 + K_2$ is considered as:

$$K_1 + K_2 = 1.5 \left( 1 - \frac{d^2}{D^2} \right)^2 \tag{6}$$

In our problem set-up, the diameter of valve ($d$) is equivalent to the diameter of pipe ($D$), which implies the value of above Eq. (6) to be zero. Hence, the magnitude of piping geometry factor ($F_p$) is found to be 1, when no reducer and fittings are used in the experimental system. Thus, the flow coefficient of valve becomes a dimensional quantity, and its modified equation for SI units of variables is given by:

$$C_q = \frac{q}{0.0865} \sqrt{\frac{G_f}{\Delta P}} \tag{7}$$

The valve sizing of the nozzle check valve denotes the outer diameter of the valve. The selection of valve outer diameter is demystified by incorporating the flow quantity rate also known as volume flow rate ($q$). The correct valve size and its outer diameter or the cross-sectional area at valve's disc are defined by Eq. (8) as

$$C_q = A_c \sqrt{\frac{2}{k}} \tag{8}$$

The calculation of flow coefficient of valve ($C_q$) provides accurate data for determining the flow condition inside the valve, thus allowing design engineers to better understand about the cross-sectional area and just the right size of restriction to be introduced by the valve so as to achieve smooth flow streamlines.

# 4 Numerical Simulation

The geometry of the valve is designed in the CAD software 'SOLIDWORKS' and then imported in the ICEM CFD® to generate mesh. To optimize the simulation process, the complex geometry surface of the valve is altered. The filleted and bent edges are replaced with sharp and steep edges providing much simpler surface. Such modification in geometry benefits heavily in doing computation by reducing the unnecessary resources and time required to complete the simulation. Although these changes may affect analysis and cause it to deviate from the actual values, it will not affect the final simulation significantly.

In the valve geometry, two pipes of 10D and 7D length are attached at the inlet and outlet sections of the valve, respectively, to create a fully developed flow where D is the diameter of the pipe as shown in Fig. 2a. The valve is meshed as fine with more seed elements, whereas the pipes are meshed as coarse with less seed elements as shown in Fig. 2b, c, allowing the mesh to be optimized without incurring heavy computational resources and provided enough node points to conduct detailed analysis and resolve even the smallest eddies.

The mesh is generated using ANSYS ICEM CFD® grid generation codes. It is a versatile and powerful meshing software with capabilities to generate both structured and unstructured meshes. While generating initial mesh of the 3D modelled valve, we encountered creating structured mesh as highly resource demanding and time-consuming even for coarse mesh, let alone fine mesh. Also, smaller fillet radius, shorter edges and complex geometries of the check valve inhibit generating



Fig. 2 Nozzle check valve geometry and mesh visualization along with 10D and 7D length of pipe attached at inlet and outlet sections of the valve, respectively, where D is the diameter of pipe, are shown by **a** the computational set-up and boundary conditions, **b** extent view and **c** close-up view of valve 3D volumetric mesh
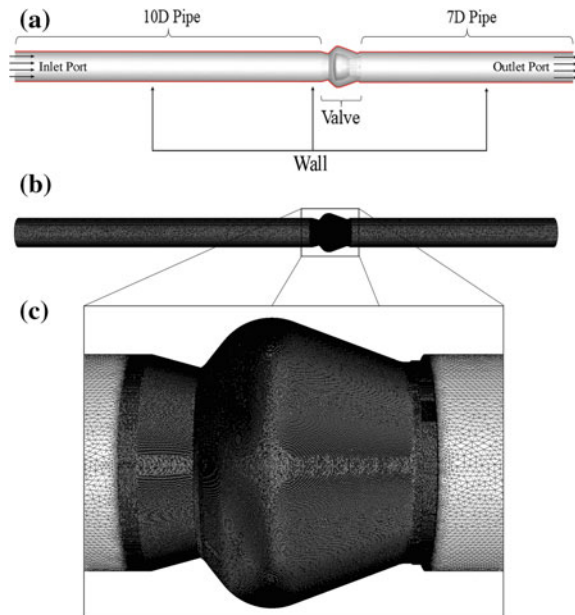
**Fig. 3** Grid independence
test of twelve-inch nozzle
check valve at valve's outlet
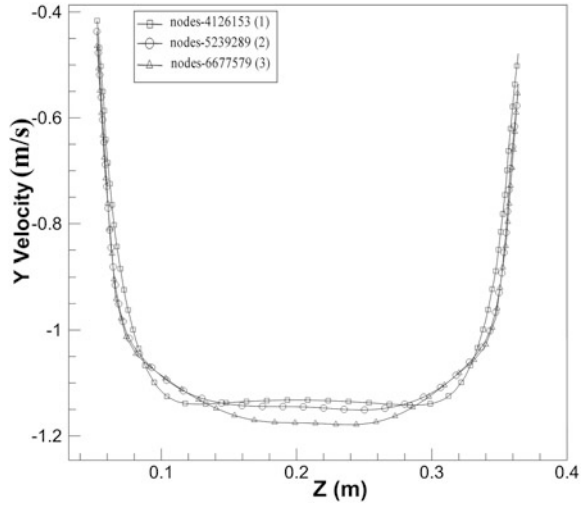


structured mesh. Thus, we generated fine unstructured tetragonal mesh elements
with Octree mesh method. The global mesh size is 20, and the curvature size is kept
1.0 throughout the mesh.

Moreover, part mesh set-up is used to enhance the mesh element of the valve and
its surrounding walls. The grid independence test is conducted to ensure the final
mesh used in simulation is free from any divergence with respect to further mesh
refinement. Three meshes of different sizes are generated and simulated with same
parameters (3 m/s inlet flow velocity). As per the grid independence test shown in
Fig. 3, we choose mesh (2) having 5239289—number of nodes for our final sim-
ulation study because further refinement in mesh size showed no uncertainty with
plot between velocity (V) and distance (Z) at valve's outlet.

In-house Amity CFD solver is used for conducting simulations. The mesh file is
imported in the solver, and the computational problem is prepped up for the sim-
ulation to be run at variable inlet flow velocities. The incompressible fluid material,
water, is considered for the simulation. The fluid flow is kept at steady-state case,
and due to turbulence nature of the flow, a K-epsilon RNG turbulent model was
implemented. Neither any phase change nor any heat transfer phenomenon is
invoked in the problem; therefore, energy equation is not applied in the solver.
Boundary conditions of the problem set-up can be visualized in Fig. 2a as:

- Inlet and outlet were assigned 'velocity inlet' and 'pressure outlet' respectively.
- In between inlet and outlet ports, the walls are set at 'no-slip' boundary
  condition.
- The valve profile at the centre is also allotted 'no-slip' wall condition.
- With successive simulation, inlet flow velocities are increased from 0.1 to 3 m/s.

# 5   Results

The numerical simulation results of the nozzle check valve are shown in Figs. 4 and 5; furthermore, the velocity and pressure contour were plotted against variable inlet flow velocity of fluid ranging from 0.1 to 3 m/s. All the contours plotted are drawn on *YZ*-plane. The pressure contours preserved their homogeneity and mirrored pressure gradient throughout the valve when revolved around the central axis.

   The simulations carried out at different Reynolds numbers are used to calculate volumetric flow rate and pressure differential values at valve's inlet and outlet section. The information obtained is then tabulated and shown in Table 1. Furthermore, these datasets are employed in Eq. (8) to calculate flow coefficient of the valve at variable Reynolds number. It was observed that the magnitude of flow coefficient ($C_q$) remained identical for different inlet flow velocities.
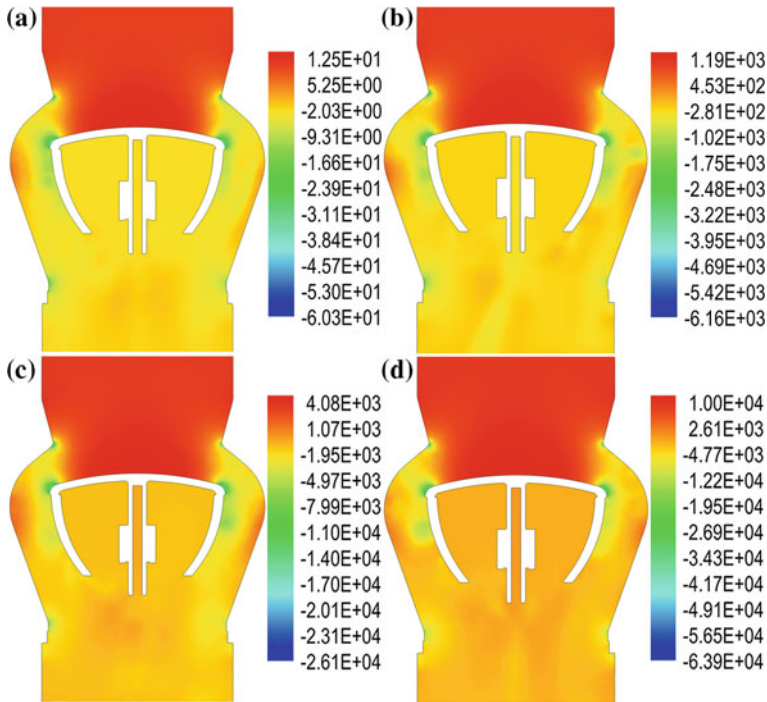


**Fig. 4**   Static pressure contour (Pascal) of nozzle check valve at **a** 0.1 m/s, **b** 1 m/s, **c** 2 m/s and **d** 3 m/s inlet flow velocities plotted on *YZ*-plane
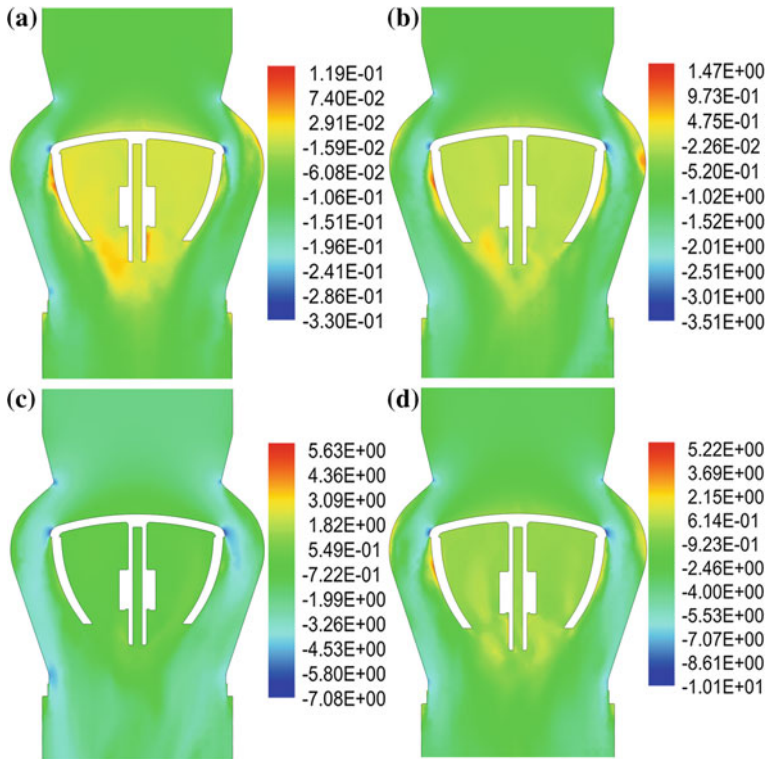
**Fig. 5** *Y*-velocity (m/s) contour of nozzle check valve at **a** 0.1 m/s, **b** 1 m/s, **c** 2 m/s and **d** 3 m/s inlet flow velocities plotted on *YZ*-plane

**Table 1** Numerical data obtained from calculations and simulation of nozzle check valve

| S. no. | Inlet velocity ($v$) | Volumetric flow rate ($q$) | | Pressure differential at valve ($\Delta P$) | Flow coefficient ($C_q$) | | Reynolds number |
|---|---|---|---|---|---|---|---|
| | m/s | m³/h | gallons/min | KPa | $\frac{m^3/h}{(KPa)^{1/2}}$ | $\frac{g/m}{(psi)^{1/2}}$ | |
| 1 | 0.1 | 27.52 | 121.18 | 0.012 | 2857.42 | 2857.47 | 3.10E4 |
| 2 | 0.5 | 137.62 | 605.91 | 0.3 | 2900.47 | 2900.55 | 1.55E5 |
| 3 | 1 | 275.23 | 1211.82 | 1.33 | 2756.49 | 2756.56 | 3.10E5 |
| 4 | 2 | 550.47 | 2423.65 | 4.86 | 2886.31 | 2886.39 | 6.21E5 |
| 5 | 3 | 825.70 | 3635.45 | 10.70 | 2918.08 | 2918.15 | 9.31E5 |

# 6 Conclusion

Among valve manufacturers, the quest to attain maximum flow coefficient out of same sizing of valve is highly competitive. Thus, it is very crucial to arrest the flow characteristics responsible for change in flow coefficient of the valve. The velocity contour visualized the stagnation points formed at the centre of the valve's disc as the local velocities reach zero. Therefore, at high Reynolds number, the disc would be subjected to huge hydrodynamic forces, and hence, it should be made robust enough to withhold the impact of incoming fluid flow; however, at the same time, it should be kept lightweight enough to close quickly before the development of backward flow. In this way, the main function of nozzle check valve for protection of equipment from reverse flow or water hammering is accomplished.

It is interpreted from the simulated data and calculations that the valve's flow coefficient is strongly the function of valve's geometry and not dependent upon the volumetric flow rate or pressure differential of the flow. Therefore, in order to maximize the flow coefficient, the design engineers must utilize the simulated data to address and rectify the irregularities in valve's inner geometry. In our study, we achieved maximum magnitude of mean flow coefficient for NCV as 2863.76 m$^3$/h (KPa)$^{1/2}$.

The flow coefficient ($C_q$), a dimensional quantity, is globally accepted by all valve industries as a measure of valve performance. Furthermore, the numerically calculated flow coefficient's value can effectively be used by valve design engineers to enumerate the cross-sectional area at the valve seat by using Eq. (8). This study can be further enhanced by implementing fluid–structure interaction at the valve disc and simultaneously by simulating the effect of spring forces on its flow characteristics.

# References

1. Val-matic valve and manufacturing corp: design and selection criteria of check valves, Illinois, USA (2011)
2. Sibilla S, Gallati M (2008) Hydrodynamic characterization of a nozzle check valve by numerical simulation. J Fluids Eng 130:121101. https://doi.org/10.1115/1.3001065
3. Pandula Z, Halász G (2002) Dynamic model for simulation of check valves in pipe systems. Period Polytech Mech Eng 46:91–100
4. Thorley ARD (1989) Check valve behavior under transient flow conditions: a state-of-the-art review. J Fluids Eng 111:1–6
5. Kruisbrink ACH (1988) Check valve closure behaviour; experimental investigation and simulation in waterhammer computer programs. In: Developments in valves and actuators for fluid control. Manchester, UK, pp 281–300

6. Davis JA, Stewart M (2002) Predicting globe control valve performance—part I: CFD modeling. J Fluids Eng 124:778. https://doi.org/10.1115/1.1490126
7. Davis JA, Stewart M (2002) Predicting globe control valve performance—part II: experimental verification. J Fluids Eng 124:778. https://doi.org/10.1115/1.1490126
8. Song XG, Park YC (2007) Numerical analysis of butterfly valve-prediction of flow coefficient and hydrodynamic torque coefficient. Proc World Congr Eng Comput Sci 2007:2–6
9. Fu W-S, Ger J-S (1998) A concise method for determining a valve flow coefficient of a valve under compressible gas flow. Exp Therm Fluid Sci 18:307–313. https://doi.org/10.1016/S0894-1777(98)10045-6
10. Standards I (1996) Control valve capacity test procedures. ISA (October 1, 1996), North Carolina
11. Standards I (1985) Flow equations for sizing control valves. North Carolina
12. Botros KK (2011) Spring stiffness selection criteria for nozzle check valves employed in compressor stations. J Eng Gas Turbines Power 133:122401. https://doi.org/10.1115/1.4004113
13. Rahmeyer W, Driskell L (1985) Control valve flow coefficient. J Transp Eng 111:358–364
14. Praveen JVS, Pathan M (2017) Flow coefficient analysis for a globe valve by using CFD. Int J Sci Res 6:756–763. https://doi.org/10.21275/ART20178896

# Design and Simulation of Isolation Room for a Hospital

**Simeon Jacob, Siddharth Singh Yadav and Basant Singh Sikarwar**

**Abstract** Heating, ventilation and air conditioning (HVAC) of hospitals is a highly specialized field and critical care units like isolation rooms and operation theatres deserve special attention, as infected patients must be isolated from ambient environment in order to prevent the infection from spreading and to save the life of the patient. This manuscript aims to optimize the ventilation strategy towards contaminant suppression in the isolation room. 3D Navier-Stokes and energy equation using finite volume method (FVM) with a domain of isolation room is solved for appropriate boundary conditions. The patient's body is approximated as a semi-cylindrical shape resting on a bed and is treated as a constant heat source. Velocity and temperature profile inside the isolation room for various configurations are simulated. Our results suggest that immune-suppressed patients should be kept near the air supply and infectious patients near the exhaust.

**Keywords** Nosocomial · Infection · Isolation · Ventilation · Air conditioning · CFD · Simulation

## 1 Introduction

The later stage of twentieth century witnessed an alarming spread of Tuberculosis (TB) across the European nations, and this sparked an extensive research in the field of infection control techniques [1]. This led to development in the field of infection suppression in order to reduce the spread of disease. A logical solution to the problem was isolation of the infected patient. Deadlier threats like AIDS, bioterrorism (anthrax attacks, Tokyo Metro Sarin Gas attack etc.) and SARS have triggered many concerns about the control of the indoor environment and unveiled the role of ventilation system design in isolating an infected or vulnerable patient [2].

S. Jacob (✉) · S. S. Yadav · B. S. Sikarwar
Department of Mechanical Engineering, Amity University Uttar Pradesh,
Noida, India
e-mail: simeonjacob24@gmail.com

More recent global outbreaks like swine flu, bird flu and Ebola virus have shown that even though we have advanced technologically, there is still a lot left to be done in the field of contaminant suppression [3].

Medical facilities are places where relatively high levels of pathogenic (disease-causing) micro-organisms are generated and concentrated by an infected patient population or by procedures that handle infected human tissues and bodily fluids. These pathogens are spread by a number of contact and noncontact (airborne) causes. Hospital-acquired infections (HAIs, also referred to as nosocomial infections) have a significant impact on patient care. Mortality rates from HAIs are significant and affect the overall cost of healthcare delivery. It is agreed that 80–90% of HAIs are transmitted by direct contact, with 10–20% resulting from an airborne transmission (representing 0.4–1% of admitted patients) [4]. It is, therefore, imperative that we take a closer look at the design of healthcare facilities with respect to suppression of contaminants while at the same time providing patient comfort to ensure that the patient does not get worse after admission and leaves the facility healthy. For achieving this goal, the design of the heating, ventilation and cooling (herein referred to as HVAC) system of a healthcare facility is important and has to be economically viable. The term is often used interchangeably with the more common 'air conditioning'. The term air conditioning refers to a system that controls temperature, moisture in the air (humidity), supply of outside air for ventilation, filtration of airborne particles, and air movement in the occupied space. HVAC systems in healthcare facilities provide a broad range of services in support of populations who are uniquely vulnerable to an elevated risk of health, fire and safety hazard. The role of the HVAC system in life safety and infection control becomes more important with increasing complexity of the medical services provided and the acuity of illness of the patient population [5].

Isolation refers to the separation of a seriously ill patient to stop the spread of infection or protect the patient from irritating factors. A patient known or suspected to harbour transmissible micro-organisms should be placed in a single room. A single room with appropriate air handling and ventilation is particularly important for reducing the risk of airborne transmission of micro-organisms from a source patient to susceptible patients and other persons in hospitals. Airborne transmission is just one of the means by which nosocomial infection spreads. Other modes of infection include contact, droplet, common vehicle and vector-borne. An isolation room is designed and provided with all the facilities that are required to ensure protection from all the above-mentioned modes of transmission of infectious microbes. Standard isolation rooms have a pan sanitizer near the room, a staff hand-wash basin within the room, an en suite bathroom, a self-closing door, a label as a standard isolation room. The most predominant mode of infection communication, i.e. airborne transmission is taken care of by an appropriate HVAC system. Broadly speaking, there are two classes of isolation rooms: Class N—negative pressure room and Class P—positive pressure room [6]. Negative pressure rooms are for patients who are suffering from infectious or contagious diseases like TB and SARS. The aim of placing infected persons in negative pressure rooms is to reduce transmission of disease via the airborne route. Conroy et al. [7] came up with a list

of features, which should exist in a negative pressure room to effectively isolate the patient. Positive pressure rooms are installed in certain facilities to isolate profoundly immune-compromised patients, such as those suffering from AIDS. A lot of research has hence been focussed towards the design of isolation wards with respect to ventilation strategy for contaminant suppression and patient comfort.

A patient in an uncomfortable environment is exposed to thermal stress that may hinder the body's ability to properly regulate body heat, interfere with rest and be psychologically harmful. As per healthcare guidelines [8, 9], ventilation strategy in an isolation room should be such that there are no stagnant and under-ventilated areas where infectious particles might be accumulated. In addition, healthcare providers subjected to an uncomfortable environment may not function at peak performance levels [5]. A study [8] of isolated patients concluded that healthcare workers visited patients in contact isolation less often than they visited regular patients, which might compromise patient safety and healthcare quality. Keeping this in mind, a proper ventilation strategy must be devised which provides for infection control and mitigation, comfort of both patients and healthcare providers, and efficient power consumption.

As such, there are many challenges to overcome in the design of an efficient HVAC system for contaminant suppression. The initial design problem of an isolation room is to fix a location of the supply and exhaust vents inside the isolation room. Cheong and Phua [10] proposed a ventilation strategy for effective removal of pollutant from hospital isolation wards and inferred that a low-lying exhaust together with a ceiling supply duct delivering laminar air was the best combination. The role of air changes per hour (ACH) in order to reduce the effective residence time of contaminant was also of prime research interest. Memarzadeh and Xu [11] investigated the role of air changes per hour in possible transmission of airborne infections by simulating various ventilation system configurations and concluded that the dominant factor that affects the transmission and control of contaminants is the path between the contaminant source and exhaust, and not the airflow ventilation rate as was expected. This observation was also corroborated experimentally by Mousavi and Grosskopf [12] and Walker et al. [13]. More in-depth studies on the path of a contaminant inside an isolation ward and its response to various strategies have been carried out. Tung et al. [14] carried out a study on contaminant (sulphur hexafluoride, SF6) dispersion inside isolation room by varying the room negative pressure (from $-2.5$ to $-15.0$ Pa), the ventilation rates (12 and 24 $h^{-1}$), by factoring in the local air quality index, and the exposure index of hospital workers. Derakshan and Shaker [15], in an attempt to reduce energy consumption by increasing the efficiency of natural ventilation, investigated volumetric flow rate in a building for various aspect ratios of the windows and their locations for various wind directions. Wan et al. [16] proposed a new method for selecting optimum indoor temperature and relative humidity to achieve minimum energy consumption for a required indoor thermal comfort level, which is evaluated with effective temperature. The research into contaminant suppression can be further extended to general hospital wards in order to reduce HAIs. Beggs et al. [17] conducted research into the need of ventilation system inside general multi-bed hospital wards.

They found that bio-aerosol concentration was least when the supply and exhaust were ceiling mounted as opposed to other strategies.

Chung et al. [18] studied the different ventilation patterns arranged by two outlet and two inlet diffusers at various locations. A three-dimensional k-ε turbulence model using a finite difference code (UNIC), which was developed by Engineering Science Inc., USA, was adopted in this work. The numerical simulation was first adopted to predict the airflow patterns and ventilation performance and later, a laboratory experiment at room air and contaminant distribution in a full-scale test chamber was conducted to validate the simulation results. The results indicated that the location of inlet and outlet diffusers severely affected the ventilation efficiency. The arrangement of inlet/outlet diffusers can cause different flow recirculation patterns, and this may change the mean age of indoor contaminant, thus deciding how quickly the indoor contaminant can be removed. Yu et al. [19] conducted a study on ventilation strategies for hospitals to mitigate the risk of infections. They studied the effects of location of infected patients and air change per hour to minimize deposition and floating time of airborne virus particles while maximizing energy efficiency. Although there is a plethora of research [7–15, 17, 18, 20–23] on making contaminant removal systems efficient and optimizing power consumption in buildings, a comprehensive research that amalgamates effective ventilation systems with infection control in isolation wards of hospitals has a long way to go.

In this background, the manuscript is to be used as a basis to set up a more advanced study on the subject of contaminant suppression and HVAC design. Here, we intend to understand the effect of placement of air supply and exhaust vents on the fluid flow and temperature profile inside the isolation ward. Our research intends to develop the existing theories and put forward an inclusive solution to the problem of HVAC design of an isolation ward keeping all the above factors in mind. The model for various orientation of air supply and exhaust vents of the isolated room was developed and simulation was carried out using in-house CFD solver. Details of CFD solver were reported elsewhere [24].

## 2 Computational Model and Solution Methodology

The physical domains in this work are for an isolation room of a hospital. It can be any ordinary room in a hospital, which is spacious enough for a patient, care provider/s, various equipment, etc. Figure 1 shows the complete flow diagram of our study. In unidirectional flow, the air supply and exhaust vent are on opposite walls. However, the position of patient bed is varied. In multi-directional flow, air supply inlets are placed on the ceiling, and exhaust on the sidewall close to the patient bed. Figure 2 shows the schematic diagram of various ventilation schemes, which are to be analysed. The isolation room studied in this work has the dimensions 4.88 m × 3.60 m × 3.05 m. The ventilation rate is taken as twelve air change per hour (ACH) which is equivalent to 0.1812 $m^3$ $s^{-1}$ as recommended in literature [25–29]. For the case of simplicity, the infiltration of air through the door

and windows and the radiation effects have not been taken into consideration, and as such it is considered logical to hypothesize the room as one without any door or window.

For the unidirectional flow cases, high sidewall supply opening is provided on one wall and the exhaust is positioned 0.3048 m above the floor on the opposite sidewall. The dimensions of inlet and exhaust vents for the unidirectional flow case are 1.0668 m × 0.4572 m. This ensures an inlet velocity of 0.3716 m s$^{-1}$ [29]. The patient's body is approximated as a cylinder 0.3048 m in diameter. The bed is placed at a height of 0.4572 m from the ground. In case-1, the bed is 0.9144 m away from the air supply sidewall, whereas in case-2, the bed is near the exhaust sidewall as shown in Fig. 2a, b, respectively. Furthermore, the location of the air supply duct in cases 1 and 2 is lowered along the wall and the changes in flow pattern and temperature profile across the room are analysed. In this manner, two sub-cases for two locations of the air supply duct are studied in both the bed configurations of the isolation room. In all the cases, the temperature of the supply air is held constant at 300 K; the inlet velocities are constant for the cases 1 and 2.

The third case is that of a mixed-ventilation system—multi-directional flow. It consists of multiple inlet vents strategically located on the ceiling and an exhaust vent near the patient's bed as shown in Fig. 2c. The inlet vents are of size 0.6096 m × 0.2286 m. The ACH rating is maintained at 12 air changes. However, to ensure proper mixing of air inside the domain, high momentum air is to be supplied. That is, the inlet velocity is 0.46 m s$^{-1}$. The patient's body is directly under one of the supply openings, but it is ensured that the face/head of the patient does not receive the impinging jet of the supply air. The other two vents are located symmetrically on two sides of the central air supply vent.
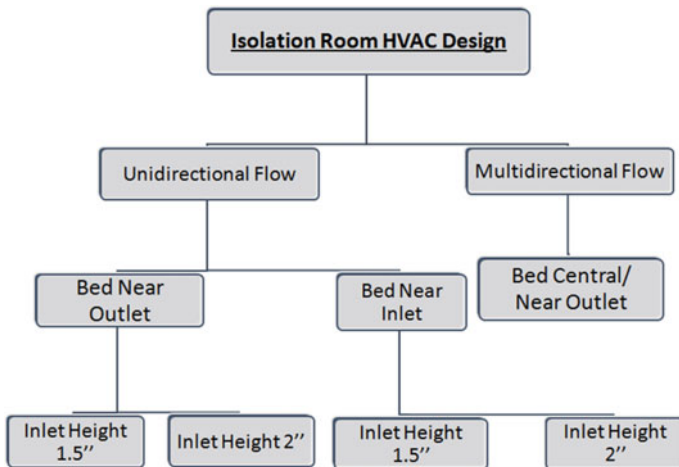


**Fig. 1** Flow diagram of study carried in present work
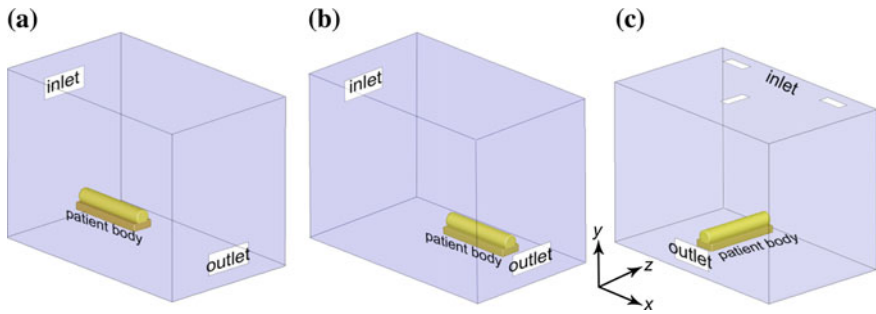
**Fig. 2** Schematic diagram of isolation room with bed and body of the patient. **a** Case-1: unidirectional flow and bed close to air supply inlet. **b** Case-2: unidirectional flow and bed close to air outlet and **c** Case-3: multi-directional flow bed position close to the outlet

**Table 1** Thermo-physical properties of the computational domain

| Domain | Material | Density Kg m$^{-3}$ | C$_P$ J Kg$^{-1}$ K$^{-1}$ | Thermal conductivity W m$^{-1}$ K$^{-1}$ | Viscosity Kg m$^{-1}$ s$^{-1}$ |
|--------|----------|---------|---------|---------------------|-----------|
| Fluid | Air | 1.225 | 1006.43 | 0.0242 | 1.789E−5 |
| Walls | Calcium carbonate | 2800 | 856 | 2.25 | – |
| Bed | Wood | 700 | 2310 | 0.173 | – |
| Body | Approximate to human bones | 1800 | 3470 | 0.45 | – |

Approximations for Patient's Body: The patient's body is a constant source of sensible heat at roughly 70 watts of strength. This amounts to around 590 W m$^{-3}$. It has been simulated as a cylinder 1.76 m in length and 0.3048 m in diameter. The density is taken as 1800 kg m$^{-3}$, specific heat as 3470 J Kg$^{-1}$ K$^{-1}$ and thermal conductivity as 0.34 W m$^{-1}$ K$^{-1}$ to simulate a material close enough to human flesh. The source of this data is the website of School of physics, University of Sydney [30]. For the sake of simplicity, no other heat source has been considered in the present work. The present study aims to simulate the human body in the presence of externally supplied conditioned air at 300 K and 50% relative humidity [31]. The problem is rendered transient and as such is solved until steady state is attained in terms of net heat exchange across the entire domain (Table 1).

## 2.1 Mathematical Model

The k-ε model is amongst the most widely used turbulence models. The standard k-ε model is the simplest 'complete model' of turbulence in which the solution of

two separate transport equations allows the turbulent velocity and length scales to be independently determined and it has become the workhorse of practical engineering flow calculations in the time since Launder and Spalding [32] proposed it. Robustness, economy and reasonable accuracy for a wide range of turbulent flows explain its popularity in industrial flow and heat transfer simulations.

The various conservation equations used in standard k-ε model are given hereunder:

$$\frac{\partial u_i}{\partial x_i} = 0 \tag{1}$$

$$\frac{\partial u_i}{\partial t} + \frac{\partial u_i u_j}{\partial x_j} = -\frac{\partial}{\partial x_i}\left(\frac{P}{\rho} + \frac{2}{3}k\right) + \frac{\partial}{\partial x_j}\left[v_t + \left(\frac{\partial u_i}{\partial x_j} + \frac{\partial u_j}{\partial x_i}\right)\right] \tag{2}$$

$$\frac{\partial k}{\partial t} + \frac{\partial k u_j}{\partial x_j} = \frac{\partial}{\partial x_j}\left(\frac{v_t}{\sigma_1}\frac{\partial k}{\partial x_j}\right) + v_t S - \varepsilon \tag{3}$$

$$\frac{\partial \varepsilon}{\partial t} + \frac{\partial \varepsilon u_j}{\partial x_j} = \frac{\partial}{\partial x_j}\left(\frac{v_t}{\sigma_2}\frac{\partial \varepsilon}{\partial x_j}\right) + C_1\frac{\varepsilon}{k}v_t S - C_2\frac{\varepsilon^2}{k} \tag{4}$$

$$v_t = C_\mu \frac{k^2}{\varepsilon} \tag{5}$$

$$S = \left(\frac{\partial u_i}{\partial x_j} + \frac{\partial u_j}{\partial x_i}\right)\frac{\partial u_i}{\partial x_j}; \tag{6}$$

where $\sigma_1 = 1.0, \sigma_2 = 1.3, \sigma_3 = 1.0, C_\mu = 0.09, C_1 = 1.44, C_2 = 1.92$.

This family of equations is generally known as the k-ε model. In the present work, k-ε turbulence (two-equation) model is used for 3D simulation.

The standard k-ε is a semi-empirical model based on model transport equations for the turbulence kinetic energy ($k$) and its dissipation rate ($\varepsilon$). In this technique, the Reynolds stress is modelled in terms of two turbulence parameters, the turbulent kinetic energy, $k$ and the turbulent energy dissipation rate, $\varepsilon$ are defined below:

$$k = \frac{1}{2}\left(\overline{u'^2} + \overline{v'^2} + \overline{w'^2}\right) \tag{7}$$

$$\varepsilon = v\left[\left(\frac{\partial u'}{\partial x}\right)^2 + \left(\frac{\partial u'}{\partial y}\right)^2 + \left(\frac{\partial u'}{\partial z}\right)^2 + \left(\frac{\partial v'}{\partial x}\right)^2 + \left(\frac{\partial v'}{\partial y}\right)^2 \right.$$
$$\left. + \left(\frac{\partial v'}{\partial z}\right)^2 + \left(\frac{\partial w'}{\partial x}\right)^2 + \left(\frac{\partial v'}{\partial y}\right)^2 + \left(\frac{\partial w'}{\partial z}\right)^2\right] \tag{8}$$
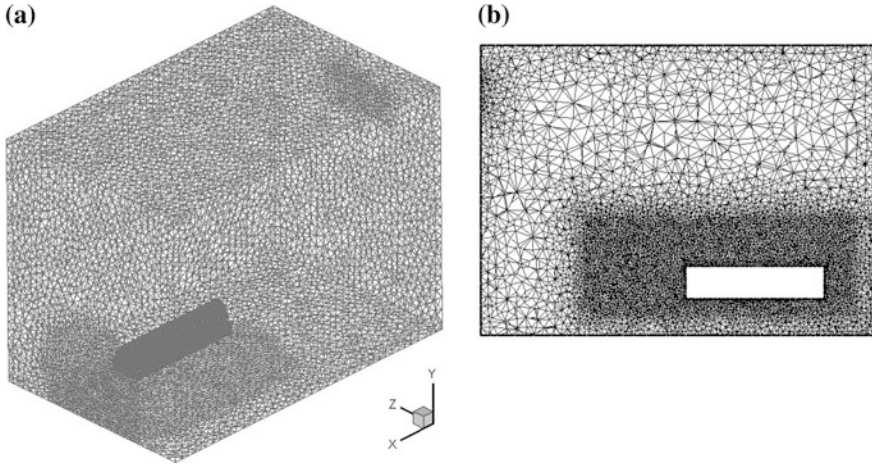
**Fig. 3** Mesh on computational domain **a** isometric view **b** sectional view at $z = 1.525$ m

where $(u', v', w')$ is the fluctuating velocity vector. $k$, the turbulent kinetic energy, is defined as the variance of the fluctuations in velocity. It has dimensions of (L2 T-2). $\varepsilon$, the turbulence eddy dissipation rate, is the rate at which the velocity fluctuations dissipate in a turbulent flow. It has dimensions of turbulent kinetic energy per unit time (L2 T-3). The kinetic energy is zero for laminar flow and can be as large as 5% of the kinetic energy of the mean flow in a highly turbulent case.

The finite volume method (FVM) is adopted to solve the aforementioned Eqs. (1–8). The details of this method were reported by authors elsewhere [24]. In this method, the physical domain is subdivided into a number of contiguous control volumes on an unstructured tetrahedral grid, as shown in Fig. 3. Unstructured tetrahedral grids are constructed by dividing the computational domain into small cells that have a tetrahedral shape. The strength of this type of grid lies in its flexibility for handling very complex geometries. A commercial software package (ICEMCFD) was used to generate meshes. The generated mesh was made very fine near the patient body (0.01 m) and coarse towards the isolation room walls (0.2 m). A refined mesh was also generated at the air supply inlet and the exhaust. To effectively capture the air flow around the patient body, a mesh density box was generated with elements of size 0.025 m as can be seen from Fig. 3b. Equations (1–8) were discretized using FVM Techniques. Convective term is discretized using hybrid upwind scheme. The diffusion terms are discretized using second-order central difference. Weighted average of surrounding cell-centred properties is used for determining nodal quantities. SIMPLE like algorithm is used for handling pressure velocity decoupling. Collocated grid arrangement is applied, and movement interpolation is used to determine the face flux of each cells. System of algebraic equation is solved using BICGStab.

**Fig. 4** Velocity distribution at various locations inside chamber (4 m × 3 m × 2.5 m) for inlet supply velocity 1.36 m s$^{-1}$
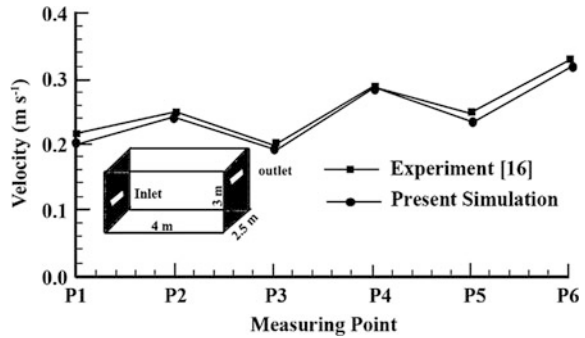
## 3    Result and Discussion

Before analysing the flow pattern of aforementioned configuration of inlet and outlet of isolated room, the present numerical methodology is validated against data available in the literature [18]. Figure 4 shows the velocity at various location of room, and it has good agreement against the experiment.

Post-validation, simulations were carried out for different cases of the isolation room. Each case has a fixed location of patient's bed in the room. In the first two cases, air supply inlet and exhaust were placed on opposite walls of the isolation room as shown earlier in Fig. 2a, b and the position of the patient bed was moved from the air supply sidewall to the exhaust sidewall. The third case had multiple air supply inlets on the ceiling of the isolation room with the exhaust on the sidewall, as shown in Fig. 2c. Further, two more cases were studied, which were sub-cases of the first two cases. In these sub-cases, the height of the air supply inlet was varied and its effect on the ventilation inside the isolation room was studied. The two inlet heights studied were 0.4572 m from the ceiling and 0.6096 m from the ceiling. In all cases, the height of the exhaust vent was 0.3048 m from the floor of the room.

The results of the isolation room were plotted at various planes such as $x$-$y$ plane ($z = 1.225$ m) and $z$-$y$ plane ($x = 1.4$ and 2.44 m) for knowing the temperature and velocity distribution close and away to the patient. The patient body was modelled as a semi-cylindrical heat source.

Figure 5 shows the velocity and temperature contours in $x$-$y$ plane and $z$-$y$ plane of the first case study. The air supply inlet is lowered to 0.4572 m below the ceiling. The position of the bed of patient was near the air supply sidewall. Figure 6 shows the flow pattern in the form of velocity vectors in the in the $x$-$y$ plane and in the $z$-$y$ plane.

It can be observed that the zone between the patient's bed and the air jet is stagnant. However, below the bed there is comparatively better airflow due to the recirculation of the air jet that hits the exhaust sidewall, as shown in Fig. 6. Such a location of bed would be hazardous for an infectious patient because the stagnant air above the patient's bed would permit the bacteria to proliferate. However, this situation is favourable for the immune-suppressed patient since he needs to be
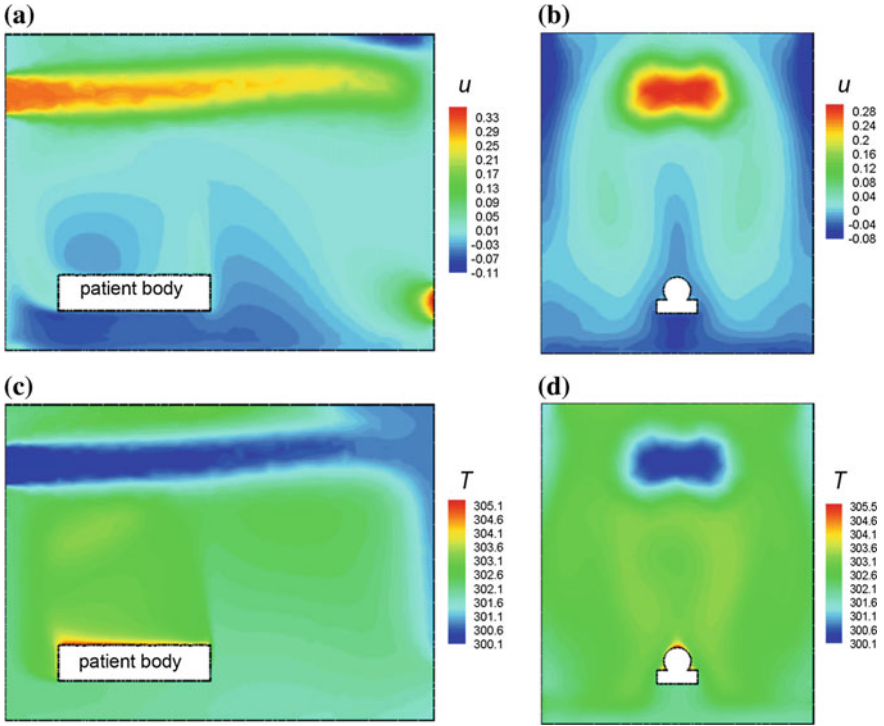
**Fig. 5** X-velocity and temperature contour of isolation room in the *x-y* plane (*z* = 1.525 m) and the *z-y* plane (*x* = 1.4 m). The height of air supply inlet is 0.4572 m from the ceiling and the patient is close to the air supply sidewall. **a**, **c** show *u* velocity and temperature contour in *x-y* plane and **b**, **d** *u* velocity and temperature contour in the *z-y* plane
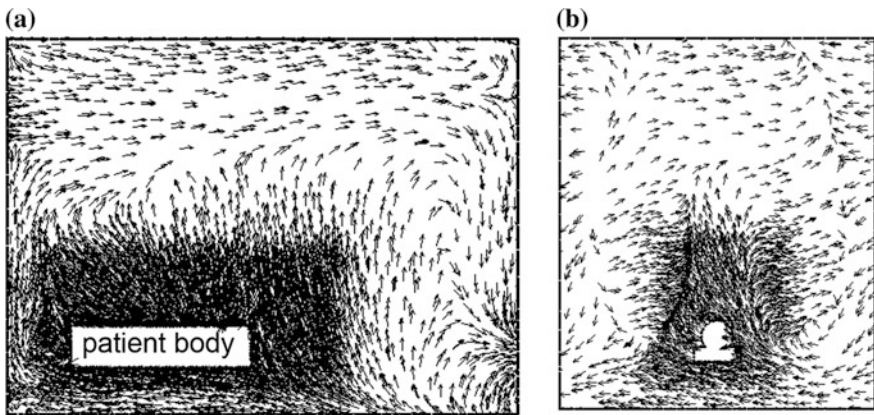


**Fig. 6** Flow pattern (*u* and *v* velocity vectors) of air in **a** *x-y* plane (*z* = 1.525) and **b** *z-y* plane (*x* = 1.4 m): inlet at 0.4572 m from the ceiling

protected from the supply air directly hitting his body. Such an airflow field serves as a defence shield for an immune-suppressed patient. As far as the rest of the room is concerned, it is under the sole effect of supply air having a temperature of 300 K. The air in the vicinity of the patient's body is slightly warmer than that in the rest of the space in room, as shown in Fig. 5c, d.

Figure 7 shows the velocity and temperature contour in the $x$-$y$ plane and the $z$-$y$ plane. The air supply inlet is lowered to 0.6096 m below the ceiling. The position of the bed of patient was near the air supply sidewall. Figure 8 shows the flow pattern in the $x$-$y$ plane and the $z$-$y$ plane for this case. It can be observed that the recirculation zones above and below the bed have decreased and stagnation zones have formed. This ventilation strategy as such is not recommended for an immune-suppressed patient because he might start complaining about draught sensation. Placing an infectious patient in the room is not recommended as well due to significant stagnation zones that exist inside the room. Another recirculation zone is formed above the jet, as can be seen from Fig. 8a, and this could possibly lead to a stagnation zone above the jet further deteriorating the ventilation of the room.
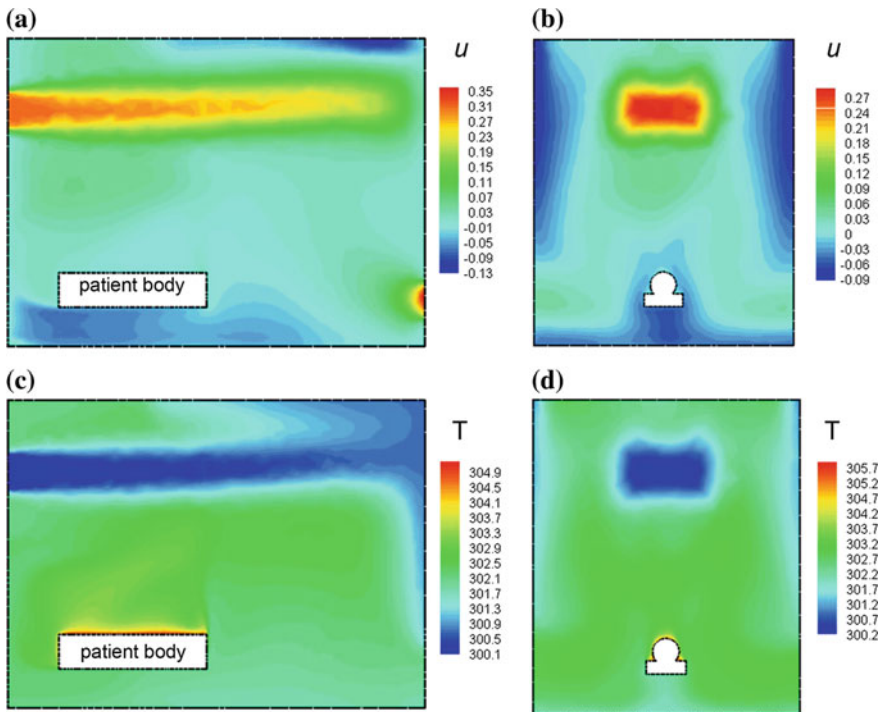


**Fig. 7** X-velocity and temperature contour of isolation room in the $x$-$y$ plane ($z$ = 1.525 m) and the $z$-$y$ plane ($x$ = 1.4 m). The height of air supply inlet is 0.6096 m from the ceiling and the patient is close to the air supply sidewall. **a, c** show $u$ velocity and temperature contour in the $x$-$y$ plane and **b, d** $u$ velocity and temperature contour in the $z$-$y$ plane
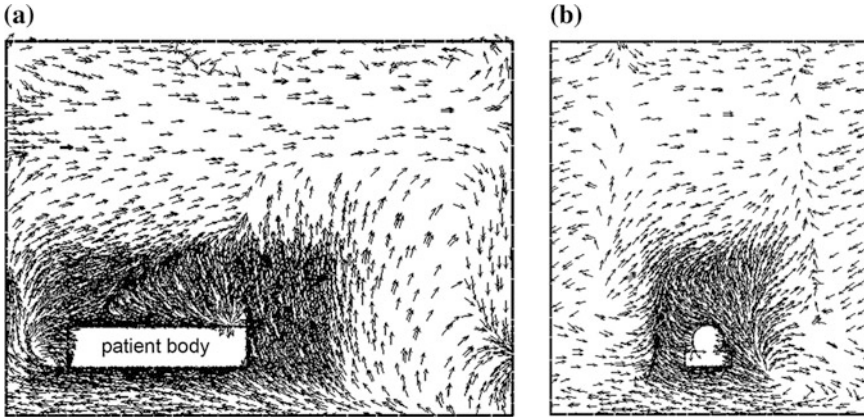
**Fig. 8** Flow pattern (*u* and *v* velocity vectors) of air in **a** *x-y* plane (*z* = 1.525) and **b** *z-y* plane (*x* = 1.4 m): inlet at 0.6096 m from ceiling

These effects can be linked to the short-circuiting of the airflow due to reduced vent height. The temperature inside the room is more evenly distributed than in the previous case.

Figure 9 shows the velocity and temperature contours in the *x-y* plane and *z-y* plane of the third case. The air supply inlet is located 0.4572 m below the ceiling. The position of the bed of patient was near the exhaust sidewall. Figure 10 shows the flow pattern in the form of velocity vectors in the *x-y* plane and the *z-y* plane.

The height of the air supply inlet is 0.6096 m from the ceiling and the patient is close to the exhaust sidewall. Figure 11a, c shows *u* velocity and temperature contour in the *x-y* plane and Fig. 11b, d *u* velocity and temperature contour in the *z-y* plane.

The patient's body starts receiving direct air jet, which deflects down from the exhaust sidewall. However, the feet continue to be in slightly stagnant zone. There is appreciable recirculation in both the upper and lower zones of the isolation room leading to better overall ventilation. This configuration is ideal for immune-suppressed patients as the patients would typically be in a region of stagnation as shown in Fig. 9b, which would protect them from any possible infections. The draught rating would also not be very high leading to optimal configuration for the immune-suppressed patient.

Figure 12 shows the velocity and temperature contour in the *x-y* and the *z-y* plane of the fourth case. The air supply inlet was lowered to 0.6096 m below the ceiling. The position of the bed of patient was near the exhaust sidewall. Figure 13 shows the velocity vectors in the in the *x-y* plane and the *z-y* plane.

As the inlet height is lowered with the patient near exhaust sidewall, the room becomes very poorly ventilated. Although the space near the patient is agitated, there is a considerable fraction of the whole space that is experiencing stagnation in this strategy. Short-circuiting of flow would also be noticed in this case.
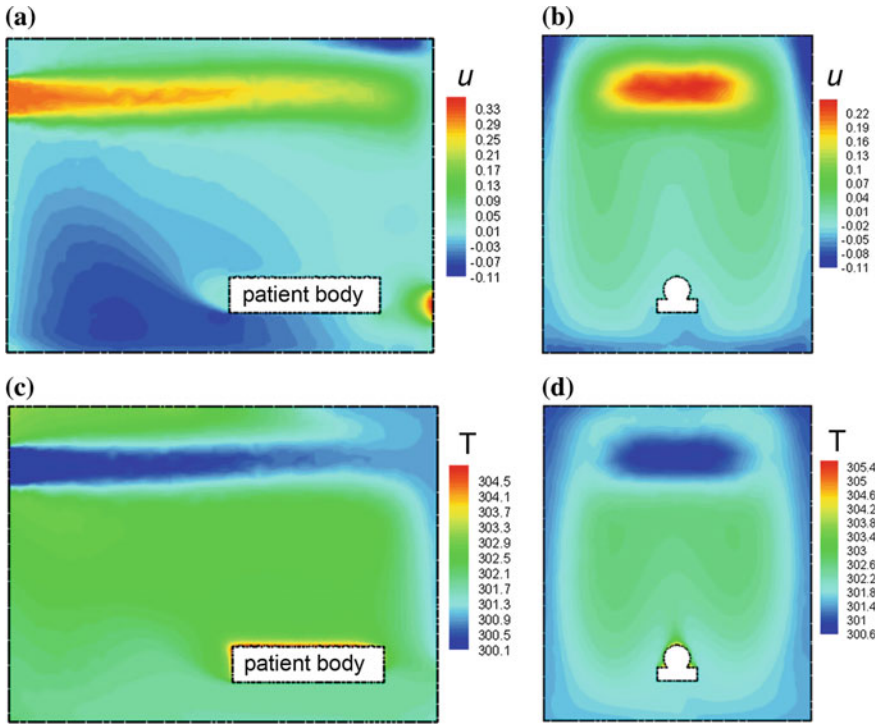
**Fig. 9** X-velocity and temperature contour of the isolation room in the *x-y* plane (*z* = 1.525 m) and the *z-y* plane (*x* = 1.4 m). The height of air supply inlet is 0.4572 m from the ceiling, and the patient is close to exhaust sidewall. **a, c** show *u* velocity and temperature contour in the *x-y* plane and **b, d** *u* velocity and temperature contour in the *z-y* plane
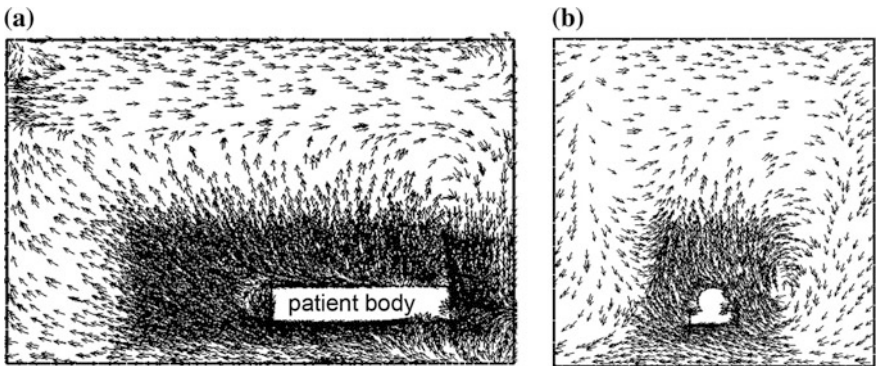


**Fig. 10** Flow pattern (*u* and *v* velocity vectors) of air in **a** *x-y* plane (*z* = 1.525) and **b** *z-y* plane (*x* = 1.4 m): inlet at 0.4572 m from the ceiling
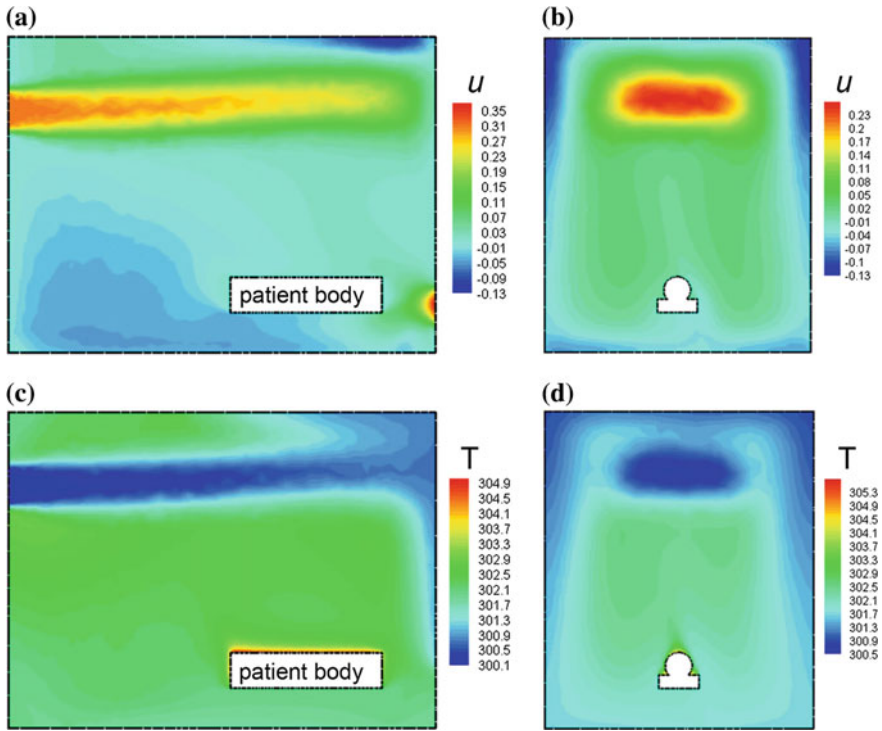
**Fig. 11** *x*-velocity and temperature contour of the isolation room in the *x-y* plane (*z* = 1.525 m) and the *z-y* plane (*x* = 1.4 m)
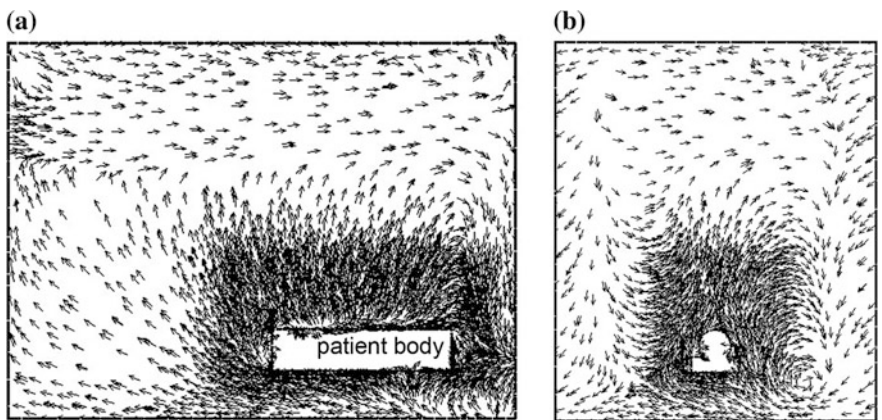


**Fig. 12** Flow pattern (*u* and *v* velocity vectors) of air in **a** *x-y* plane (*z* = 1.525) and **b** *z-y* plane (*x* = 1.4 m): inlet at 0.6096 m from ceiling
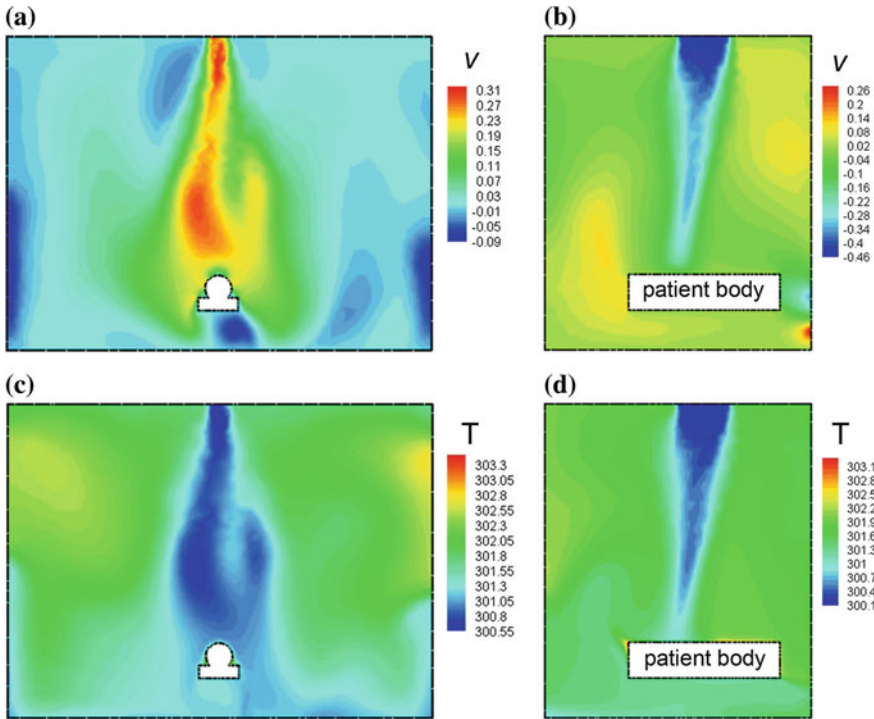
**Fig. 13** y-velocity and temperature contour of the isolation room in the *x-y* plane (*z* = 1.525 m) and the *z-y* plane (*x* = 2.44 m). Three air supply inlets are located on the ceiling and the patient is close to exhaust sidewall. **a**, **c** show *v* velocity and temperature contour in the *x-y* plane and **b**, **d** *v* velocity and temperature contour in the *z-y* plane

Figure 14 shows the velocity and temperature contour in *x-y* and *z-y* plane for the fifth case. Multiple air supply inlets are located on the ceiling of the isolation room. The position of the bed of patient was near the exhaust sidewall. Figure 15 shows the flow pattern in the *x-y* and the *y-z* plane with the air supply mounted on the ceiling.

Figure 15 shows the y-velocity profile as it develops across different levels in the *z-x* plane. An infectious patient is advised to be kept in an isolation room provided with a mixed-ventilation system. It has multiple laminar diffusers on the ceiling, and the patient's bed is strategically located with respect to the diffusers so that the bacteria concentration is diluted effectively. The upper zone between the two symmetrically located inlet vents shows some stagnation but in the occupied zone, the air is well mixed due to the presence of two supply openings in the farther corners of the room. With multiple inlet vents, a mixed-ventilation system offers improved control over the whole airflow field inside the domain. The upper zone between the two symmetrically located inlet vents shows some stagnation but in the occupied zone, the air is well mixed due to the presence of two supply openings

(a)                                                          (b)
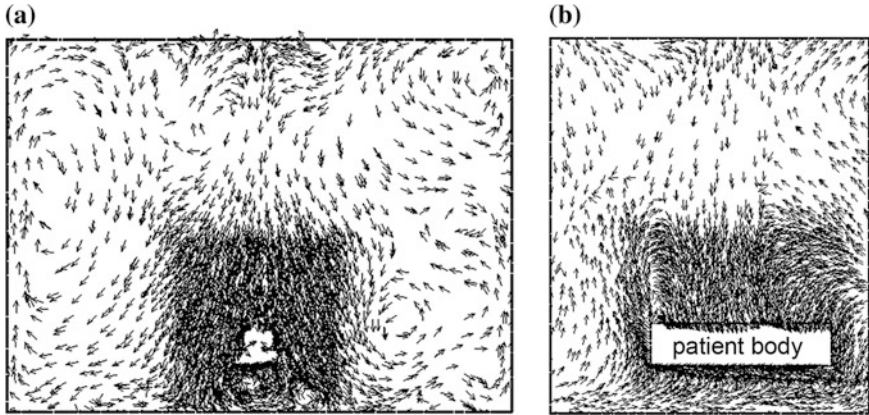


**Fig. 14** Flow pattern (*u* and *v* velocity vectors) of air in **a** *x-y* plane (*z* = 1.525) and **b** *z-y* plane (*x* = 2.44 m)
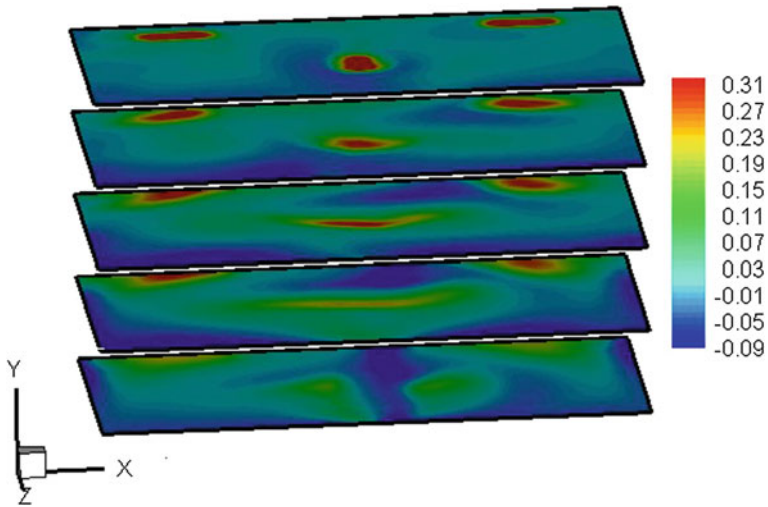


**Fig. 15** y-velocity profile across the across the isolation room (*y* = 0.3 m to *y* = 3.3 m)

towards the corners of the room. This arrangement makes the whole room well ventilated. However, higher draught ratings must be expected in such a ventilation system.

## 4   Conclusion

The position of the patient bed and air supply inlet of isolation room for two kinds of patients: infectious and immune-suppressed were simulated using in-house CFD solver. An immune-suppressed patient is one who is vulnerable to infection from any contaminant that accompanies the supply air. The location of the bed and the ventilation system for such a system should be designed to provide the patient maximum protection against the possible contamination in the supply air by ensuring that contaminant resident time inside the room is minimum.

The infectious patient on the other hand is one who produces infectious micro-organisms by means of breathing, coughing and sneezing. A TB or a SARS patient would be the suitable example. The ventilation system for such a patient should perform the function of flushing out the infectious bacteria as soon as they are generated. This is possible when the air flows from the less contaminated zone to the most contaminated zone.

Against this background, a mathematical model of hospital isolation room was developed and simulated. Based on the simulation results, the following conclusions can be made:

- The locations for the immune-suppressed patient inside the isolation room should be near the supply sidewall.
- An infectious patient's bed should be located near the ventilation exhaust.
- To get rid of the stagnation zones, it would be reasonable to have some constant heat sources like lamps and medical equipment inside the room so that the temperature difference causes the incoming cool air to settle down and displace the warmer air upwards via convection. In this fashion, stagnation observed in the velocity profiles for immune-suppressed patient would not be as severe.
- Mixed ventilation is a good solution for the infectious patients. It offers better control over the HVAC and ventilation parameters due to the multiple inlet vents.
- In this study, many simplifications/assumptions were taken that render our results only approximate. For our research to aide in the practical design of a hospital isolation ward or operation theatre, these approximations must be reduced and a model as exact as computationally possible, must be developed.

## References

1. Phillips DA, Sinclair RJ, Schuyler GD (2004) Isolation room ventilation. Design case studies. In: Proceedings of IAQ conference, ASHRAE
2. Health Canada, Guidelines for preventing the transmission of tuberculosis in Canadian health care facilities and other institutional settings. Engineering controls to minimize TB transmission. Canada Communicable Disease Report 1996; 22S1

3. http://www.vox.com/2016/5/31/11638796/why-there-are-more-infectious-disease-outbreaks
4. Memarzadeh F (2011) Literature review of the effect of temperature and humidity on viruses that cause epidemics & pandemics. ASHRAE Trans 117(2):24–37
5. ASHRAE, HVAC Design Manual for Hospitals and Clinics 2013. American Society of Heating, Refrigerating and Air-Conditioning Engineers, Atlanta
6. Department of Human Services (1999) Guidelines for the classification and design of isolation rooms in health care facilities. Standing Committee on Infection Control, Victoria, Australia
7. Conroy LM, Franke JE, Dimos J, Vittallo JA, Lee SC (1997) Ventilation survey of tuberculosis isolation rooms in five hospitals. In: Ventilation '97, Proceedings of the 5th international symposium on ventilation for contaminant control, vol 9, issue 1
8. Guidelines for the classification and design of isolation rooms in health care facilities, 2007
9. CDC (2005) Guidelines for preventing the transmission of mycobacterium tuberculosis in health-care settings. Morb Mortal Wkly Rep (MMWR) 54(17):1–141
10. Cheong KWD, Phua SY (2006) Development of ventilation design strategy for effective removal of pollutant in the isolation room of a hospital. Build Environ 41:1161–1170
11. Memarzadeh F, Xu W (2012) Role of air changes per hour (ACH) in possible transmission of airborne infections. Build Simul 5(1):15–28
12. Mousavi ES, Grosskopf KR (2015) Ventilation rates and airflow pathways in patient rooms: a case study of bioaerosol containment and removal. Ann Occup Hyg 5(9):1190–1199
13. Walker JT, Hoffman P, Bennett AM (2007) Hospital and community acquired infection and the built environment—design and testing of infection control rooms. J Hosp Infect 65:43–49
14. Tung Y-C, Hu S-C, Tsai T-I, Chang I-L (2009) An experimental study on ventilation efficiency of isolation room. Build Environ 44(2):271–279
15. Derakhshan S, Shaker A (2016) Numerical study of the cross-ventilation of an isolated building with different opening aspect ratios and locations for various wind directions. Int J Vent
16. Wan JW, Yang K, Zhang WJ, Zhang J (2009) A new method of determination of indoor temperature and relative humidity with consideration of human thermal comfort. Build Environ 44(2):411–417
17. Beggs CB, Kerr KG, Noakes CJ, Hathway EA, Sleigh PA (2016) The ventilation of multiple-bed hospital wards: review and analysis. Am J Infect Control 36(4):250–259
18. Chung K-C, Hsu S-P (2001) Effect of ventilation pattern on room air and contaminant distribution. Build Environ 36(9):989–998
19. Yu HC, Mui KW, Wong LT, Chu HS (2016) Indoor and built ventilation of general hospital wards for mitigating infection risks of three kinds of viruses including Middle East respiratory syndrome coronavirus. Indoor Built Environ 1–14
20. Xu Z, Zhou B (2016) Dynamic isolation technologies in negative pressure isolation wards. Springer, Beijing
21. Bivolarova MP, Melikov AK, Mizutani C, Kajiwara K, Bolashikov ZD (2016) Bed-integrated local exhaust ventilation system combined with local air cleaning for improved IAQ in hospital patient rooms. Build Environ 100:10–18
22. Cao G, Awbi H, Yao R, Fan Y, Sirén K, Kosonen R, Zhang J (2014) "SC," Build Environ
23. Peren JI, Van Hooff T, Leite BCC, Blocken B (2014) CFD analysis of cross-ventilation of a generic isolated building with asymmetric opening positions: impact of roof angle and opening location. 31:1–21
24. Sikarwar BS, Khandekar S, Muralidhar K (2013) Simulation of flow and heat transfer inside a liquid drop sliding underneath a hydrophobic surface. Int J Heat Mass Transf 57(2):786–811
25. AIA (2006) Guidelines for design and construction of health care facilities, 2nd edn. The American Institute of Architects, Washington, DC
26. Siegel JD, Rhinehart E, Jackson M (2007) 2007 guideline for isolation precautions: preventing transmission of infectious agents in healthcare settings. Am J Infect Control 35:S65–S124
27. ASHRAE (2008) Standard, 170–2008 Ventilation of health care facilities. ASHRAE, Atlanta, GA
28. Atkinson J, Chartier Y, Pessoa-Silva CL (2009) Natural ventilation for infection control in health-care settings. World Health Organization. ISBN 978 92 4 154785 7

29. ASHRAE. Handbook of Fundamentals 1997. American Society of Heating, Refrigeration and Air Conditioning Engineers, Inc., Atlanta
30. http://www.physics.usyd.edu.au/teach_res/db/d005c.htm
31. McDowall R (1987) Fundamentals of HVAC systems. American Society of Heating, Refrigerating and Air-Conditioning Engineers Inc., Atlanta
32. Launder BE, Spalding DB (1972) Lectures in mathematical models of turbulence. Academic Press, London; New York

# CFD Analysis of GM Pulse Tube with Functional Gradient Regenerator

**Pankaj Kumar, Manoj Kumar and Ranjit Kumar Sahoo**

**Abstract** The present research aims to establish a stable and reliable simulation of GM pulse tube using commercially available CFD software. In line with aforementioned objective, three major tasks have been addressed in detail. First, a GM pulse tube has been taken from the literature for analysis. Unlike the present state of the art, the present analysis has been carried out using multi-component models in 3D environment. Various components involved in a pulse tube have been modelled, and the corresponding assembly model has been analysed. The proposed approach introduces tremendous amount of numerical complexities which have been addressed in detail. The numerical result agrees to lowest temperature achieved experimentally with 95% accuracy. In second, the thermoacoustic phenomena have been analysed regarding work done at various locations, which re-establishes the fact and phenomena which takes place in a double inlet GM pulse tube. At last, functionally gradient regenerator (FGR) has been proposed to enhance the performance of pulse tube. This particular task has two major sections. The first section enlightens the modelling of functionally gradient porous material (FGPM) for analysis, and the second section focuses on the realistic modelling from manufacturing point of view. Summarizing, the contribution establishes a practice to investigate a GM pulse tube in 3D component level together with an approach to the model functionally gradient regenerator.

**Keywords** Computational fluid dynamics (CFD) · GM pulse tube · Functionally gradient porous material (FGPM) · Functionally gradient regenerator (FGR)

P. Kumar (✉) · M. Kumar · R. K. Sahoo
Department of Mechanical Engineering, National Institute of Technology Rourkela, Rourkela 769008, Odisha, India
e-mail: pankajcryo@gmail.com

## 1   Introduction

The argument, need of analysing a pulse tube is still a question or requirement, is still debatable. Some important factor which is considered during pulse tube refrigerator analysis, first one is to understand the thermoacoustic phenomena and other one is establishing the technique to design a pulse tube for the desired requirement. Such intentions provoke us to concentrate the research on establishing a methodology to analyse a GM pulse tube using commercially available CFD software. The fact, "Why", is acknowledged by the audience, however, how with trustworthiness is still a prerequisite. CFD analysis of GM tube pulse tube refrigerator (GMPTR) has been investigated which demonstrates the potential of FLUENT$^{©}$ a CFD (commercially available) software [1]. Later on, researchers have investigated pulse tube using CFD and have addressed various challenges. Out of them, estimating response of various components in pulse tube attracts our attention, which is quite promising from an industrial design point of view [2–4].

From the literature review, it can be noticed that 3D analysis of pulse tube is a basic requirement which has not been addressed in detail till now. The component, regenerator, which is the heart of pulse tube, has been modified experimentally and observed effective in enhancing the capacity of pulse tube has not been modelled in CFD for design point of view. The reliability analysis of thermoacoustic phenomena is still a challenge and incomprehensible. The present work aims to address aforesaid observation in detail, moreover, with an adequate effort from prospective industrial design.

## 2   Underlying Theory

The governing equation of CFD and turbulent model can be found in the literature [5, 6].

The after cooler (AFT), regenerator, cold heat exchanger (CHX) and hot heat exchanger (HHX) are modelled using porous media. The aforementioned porous zones consist of packed stacked steel mesh screens. In order to model the porous media in FLUENT, three parameters are required such as porosity, viscous resistance and inertial resistance. The equivalent porosity can be calculated by [7]

$$\text{Porosity} = 1 - \frac{\pi m d_{\text{w}}}{4 \times 0.0254}, \tag{1}$$

where $m$ is the mesh number and $d_{\text{w}}$ is the wire diameter. The equivalent viscous resistance (VR) and inertial resistance (IR) values are estimates using hydraulic dia. $d_{\text{h}}$ and Reynolds number ($Re$).

$$d_h = \frac{p}{1-p} d_w \tag{2}$$

$$\begin{cases} VR = \dfrac{1}{\text{Permeability}(\alpha)}, \alpha = \dfrac{d_h^2}{64.5} \\ \quad IR = \dfrac{2.91}{d_h} Re^{-0.103} \end{cases} \tag{3}$$

## 3 GM Pulse Tube Modelling

From literature, it can be noticed that pulse tube has been modelled from numerical analysis perspective [8]. Nevertheless, present modelling tries to mimic the experimental model design and assembly. Referring literature, the acoustic cavity of pulse tube has been modelled using SolidWorks$^{©}$ platform. Total nine no. of components have been modelled from manufacturing assembly perspective. The assembled model (see Fig. 1) has been imported to ANSYS$^{©}$/FLUENT$^{©}$ platform for further analysis. The detailed dimension of pulse tube is tabulated in Table 1. Such design technique provides the flexibility for controlling meshing in terms of reducing elements, however, increases ample amount of complexity in analysis (Fig. 2).

Initially, default tetrahedron elements are used to generate the mesh, which is observed to be 98 thousand, where, only the transfer line contributes 35 thousand elements. In order to reduce the number of elements, the component level models have been proposed and introduced following aforementioned method, total number of elements in transfer line including orifice and double inlet has been observed to be 4678 and total number of elements of GM pulse tube has been observed to be 36,072, which is quite promising compared to literature [9]. The reduced number of



1. Transfer line
2. After cooler
3. Regenerator
4. CT
5. Cold heat exchanger
6. Pulse tube
7. Hot heat exchanger
8. Double inlet Valve
9. Orifice
10. Reservoir
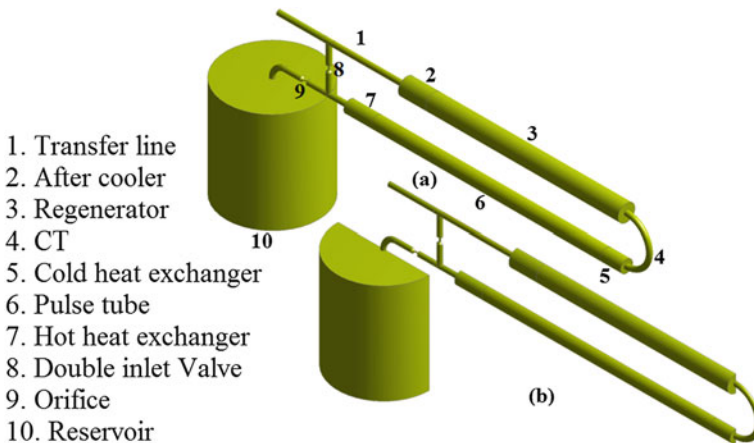
**Fig. 1** Schematic geometry of the GM Pulse tube under investigation; **a** 3D geometry, and **b** sectional geometry

**Table 1** Detailed dimensions of GM pulse tube

| AFT | Regenerator | Pulse tube | CHX |
|---|---|---|---|
| $R = 22.00E{-}03$ | $R = 20.00E{-}03$ | $R = 15.00E{-}03$ | $R = 15.00E{-}03$ |
| $L = 20.00E{-}03$ | $L = 21.00E{-}02$ | $L = 25.00E{-}02$ | $18.0E{-}02$ |
| Isothermal | Adiabatic | Adiabatic | Adiabatic |
| Orifice/DI | Reservoir | Transfer line | HHX |
| $D$ OR $= 2$ | $R = 10.0E{-}02$ | $R = 5.30E{-}03$ | $R = 22.00E{-}03$ |
| $D$ DI $= 3$ | $L = 30.00E{-}02$ | $L = 11.50E{-}02$ | $L = 20.00E{-}03$ |
| Isothermal | Isothermal | Isothermal | Isothermal |

All components are circular, $D$ Diameter, $R$ Radius, $L$ Length, in mm. $W$ Wall thickness is 3 mm for all components

**Table 2** Component and number of elements and number of nodes

| S. No. | Component | No. of elements | No. of nodes |
|---|---|---|---|
| (a) | Transfer line | 4032 | 2289 |
| (b) | After cooler (AFT) | 1810 | 1166 |
| (c) | Regenerator | 8050 | 4896 |
| (d) | Cold heat exchanger (CHX) | 2879 | 684 |
| (e) | Pulse tube | 5180 | 3479 |
| (f) | Hot heat exchanger (HHX) | 3651 | 862 |
| (g) | Surge volume | 9824 | 2092 |
| (h) | Orifice | 323 | 486 |
| (i) | Double inlet | 323 | 486 |

elements not only reduces the computational overhead, moreover, increases the productivity in analysis. Further increasing in number of elements does not contribute in achieving enhanced result at CHX. The reduced number of elements not only reduces the enhanced result at CHX. The reduced number of elements not only reduces the computational overhead, moreover, increases the productivity in analysis. Further increasing in number of elements does not contribute in achieving enhanced result at CHX. Table 2 shows the No. of Element as well as No. of Nodes of each component of GMPTR .

## 4 Analysis Technique

The CFD analyses were carried out using pressure-based solver and standard turbulent k-epsilon model with standard wall function. The AFT, Regenerator, CHX and HHX have been modelled using porous media [7]. The turbulence model is used to simulate the wave propagation in porous media. The turbulence parameters at inlet have been decided with 5% intensity and 10% viscosity ratio. The
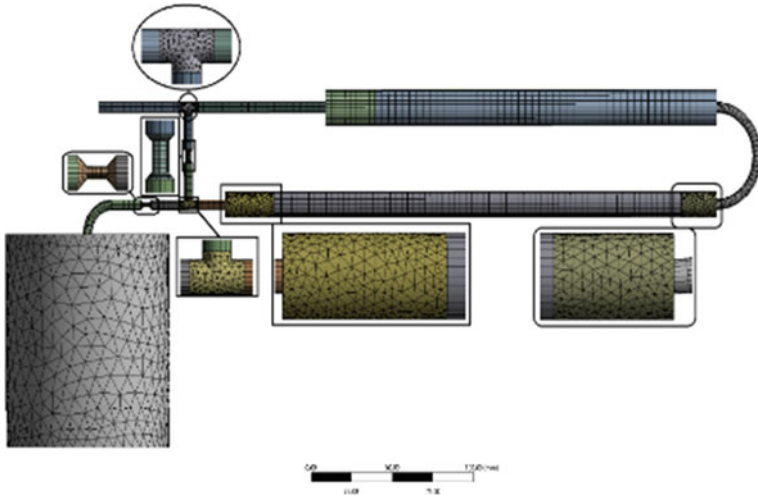
**Fig. 2** 3D model and meshing of GM pulse tube

**Table 3** Porous material modelling parameters of regenerator

| Regenerator | Viscous resistance | Inertial resistance | Porosity |
|---|---|---|---|
| $Regenerator_0$ | 4.150e+09 | 12,140 | 0.679 |
| $Regenerator_1$ | 2.083e+10 | 34,189 | 0.686 |
| $Regenerator_2$ | 4.167e+10 | 51,707 | 0.607 |
| $Regenerator_3$ | 6.667e+10 | 67,758 | 0.607 |

configuration of first-order implicit unsteady pressure-based segregated solver with pressure-velocity coupling using SIMPLE scheme was opted in CFD for analysis. The converging value was set to for continuity and velocity and for energy equations. A time step of 1 ms and 30 maximum iterations per time step has been observed optimal and used for all analysis. The compressor has been replaced with a user-defined function (UDF) and applied in pressure inlet. The charging pressure of pulse tube has been maintained at 16 bar and a sine wave of 2 Hz frequency, amplitude of 5 bar has been applied to simulate the compressor. Table 3 shows the porous material property which is used in GMPTR.

## 5   Results and Discussion

The benchmark GM pulse tube refrigerator (GMPTR) taken from the literature [9] has been modelled in 3D for subsequent analysis. The dimension of corresponding GMPTR has been mentioned in Table 1. For save the computational time, the symmetric sectional geometry has been simulated. Figure 1 represents the geometry
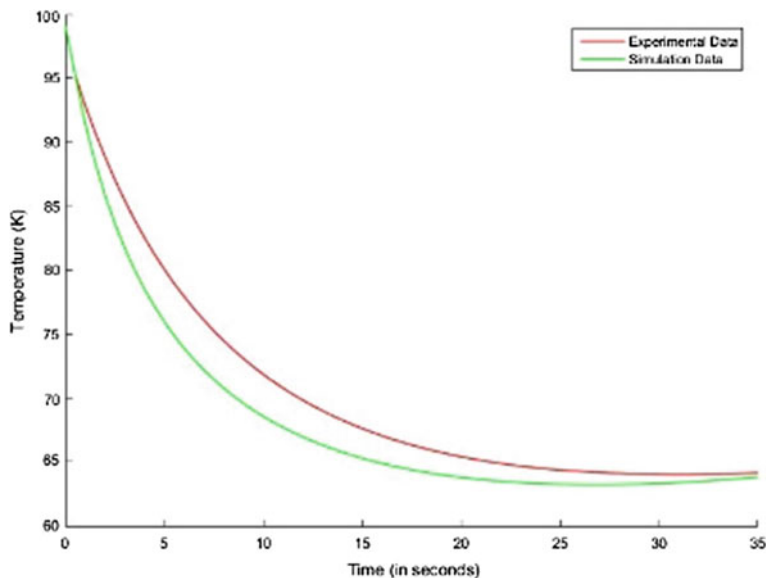
**Fig. 3** Cooling curve or average temperature profile at CHX

of the GMPTR under investigation. The simulation converges very fast, due to applied pressure UDF at inlet of transfer line and also applied temperature profile for reducing computational time. The observed average temperature at CHX has been observed to be 64.2 K. At steady state, the temperature distribution over the domain has similar nature like Prof. Subhash Jacob model result [10], shown in Fig. 3. It can be inferred from above analysis that the executed benchmarking simulation is adequate and efficient to explain the heat transfer phenomena with respect to pressure wave. The cooling effect at CHX, moreover, on the axis also agrees adequately with reported literature.

A detailed comparative study of temperature along the axis of GMPTR has been carried out and shown in Fig. 4.

The present analysis is also prompted to investigate the Functional Gradient Regenerator (FGR) behaviour in ANSYS/Fluent for achieving possible lowest temperature. In order to aforesaid effect of FGR which is play an important role in GM pulse tube refrigerator. After using FGR in similar geometry of GMPTR, the aforementioned observations indicate that with functional gradient regenerator the efficiency of the GMPTR has been increased by 10.83% ($\approx$11%) in achieving the lowest temperature.

From Fig. 5, it can be inferred that the nature of cooling curves remains equivalent, however, with apply the FGR the lowest temperature, observed at CHX and varies significantly at steady state, i.e. 53.2 K. Afterwards, various parameters
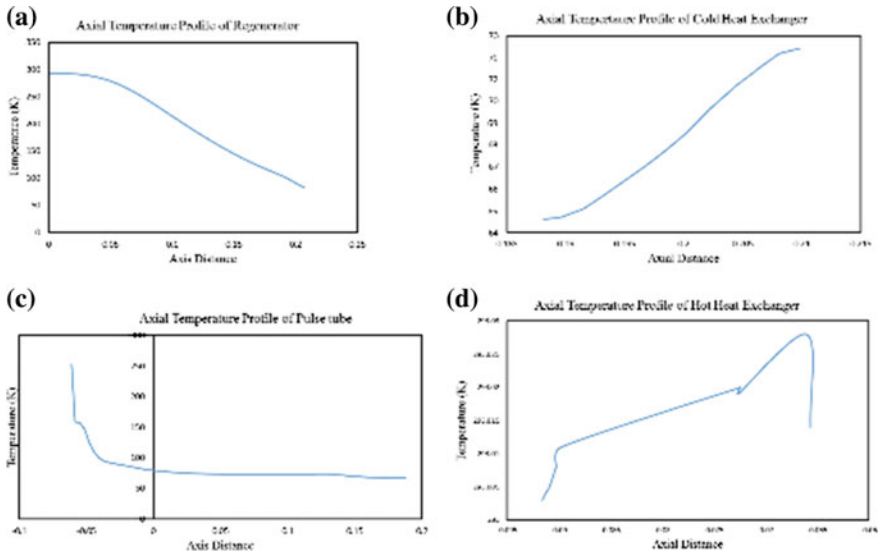
**Fig. 4** Steady-state temperature at axis of the GM pulse tube
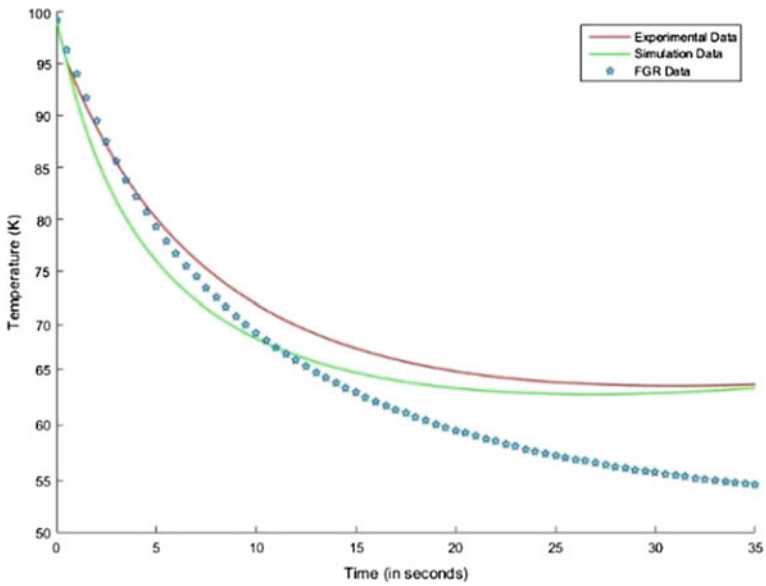


**Fig. 5** Cooling curve temperature profile at CHX with FGR
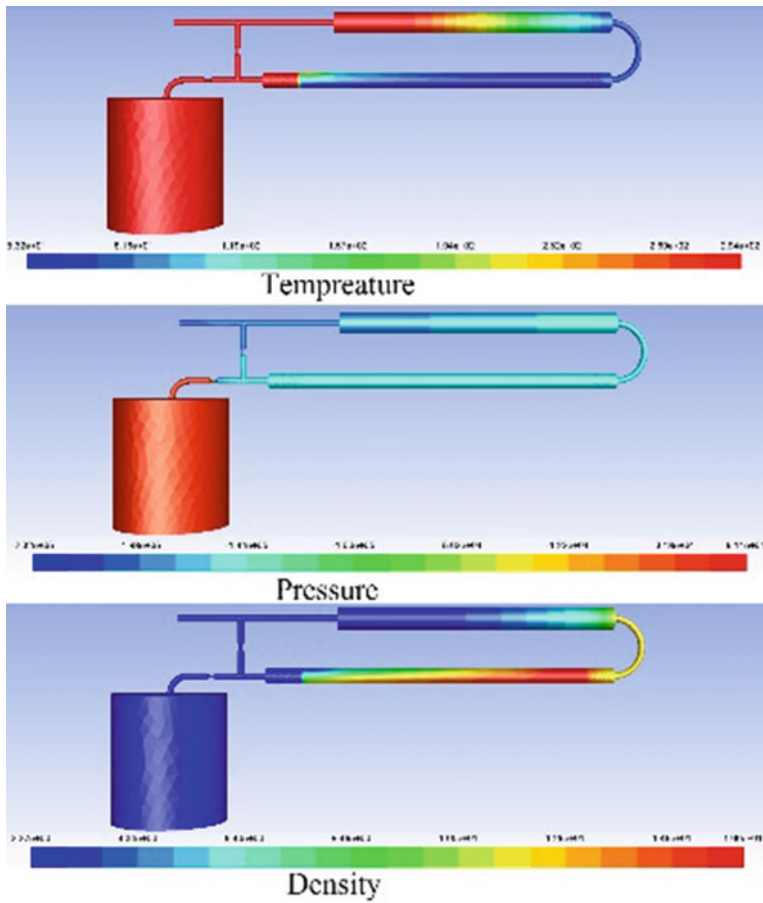
**Fig. 6** contour plot of temperature, pressure, and density of FGR model

over GMPTR, the contour plot of temperature, pressure and density have been extracted and shown in Fig. 6.

Next, for detailed understanding the contour of pressure, temperature and density distribution have been extracted and have been shown in Fig. 6. From contour, it has been observed that the temperature distribution gradually decreases in regenerator where ever in pulse tube it is not that gradual.

# 6 Conclusion

The present numerical investigations re-establish the robust numerical analysis of a GMPTR; however, using proposed methodology the computational overhead is significantly reduced. The proposed method enables us to optimize the GMPTR to next level. From Function Gradient Regenerator, it has been observed that the porosity factor in porous component is critical parameters in designing an GMPTR with higher performance. However, the FGR has been demonstrated effective in achieving further lowest temperature at CHX, i.e. 53.2 K which is lower than the reported literature. The proposed analysis has been shown adequate in optimizing any GMPTR from industrial design prospective.

# References

1. Zhang XB, Qiu LM, Gan ZH, He YL (2007) CFD study of a simple orifice pulse tube cooler. Cryogenics 47:315–321
2. Badgujar AD, Atrey MD (2011) Theoretical and experimental investigation of flow straighteners in U-type pulse tube cryocoolers. Cryogenics-16
3. Beck JV, Blackwell BC, Clair R (1985) Inverse heat conduction—ill-posed problems. Wiley, London
4. Dang H, Zhao Y (2016) CFD modeling and experimental verification of a single-stage coaxial Stirling-type pulse tube cryocooler without either double-inlet or multi-bypass operating at 30–35 K using mixed stainless steel mesh regenerator matrices. Cryogenics 78:40–50
5. Krishnappa GB, Madhu D, Kasthurirengan S (2012) Comparison of 1D and 2D flow numerical analysis applied to two stage pulse tube cryocooler. In AIP conference proceedings, vol 1434
6. Hindasageri V, Vedula RP, Prabhu SV (2014) A novel method of estimation of adiabatic wall temperature for impinging premixed flame jets. Int J Heat Mass Transfer 77:185–193
7. Banjare YP, Sahoo RK, Sarangi SK (2009) CFD simulation of a Gifford–McMahon type pulse tube refrigerator. Cryogenics 48:2280–2287
8. Zhu S, Matsubara Y (2004) A numerical method of regenerator. Cryogenics 44(2):131–140
9. Kasthurirengan S, Jacob S, Karunanithi R (2000) Development and studies on convection free single stage pulse tube cooler operating at 77 K. Final Technical Report, April 2000, Centre for cryogenic Technology IISC, Bangalore
10. http://www.iuac.res.in/reres/cryo/icc/SJacob.pdf

# Thermodynamic Analysis of Biomass Gasification-Based Power Generation System Through Indirectly Heated GT and S–CO$_2$ Cycle

**Samiran Samanta and Pradip Mondal**

**Abstract** The study emphasizes on the modeling and thermodynamic performance prediction of a novel biomass gasification-based combined cycle plant. It consists of a topping indirectly heated topping gas turbine (GT) cycle and a bottoming supercritical CO$_2$ (S–CO$_2$) cycle for combined power generation. Sawdust is considered as the driving fuel of the plant, which is gasified in a downdraft gasifier and thus the derived producer gas is further burnt in a combustor-heat exchanger combined (CHX) unit. The CHX unit indirectly heat-up the working medium (air) of the topping GT cycle and the CHX exhaust is further utilized in the bottoming S–CO$_2$ cycle to produce electricity in a combined manner. Simulated performance of the plant is judged over wide ranges of considered pressure ratio ($r_p$) and the gas turbine inlet temperature (TIT). The $r_p$ value is varied between 4–16 and the TIT is varied between 900 and 1100 °C. Overall electrical efficiency of the plant is about 46% at $r_p$ = 4 and TIT = 1000 °C. At the same thermodynamic state points, calculated value of required biomass input is 0.017 kg/s and also the combined net output from the plant is about 140 kW. Overall electrical efficiency value increases with increase in $r_p$ value, for all GT TITs as well as hot end temperature difference (HETD) of the CHX unit.

**Keywords** Biomass gasification · Power generation · Gas turbine · S–CO$_2$ · Electrical efficiency

S. Samanta
School of Mechanical Engineering, Kalinga Institute of Industrial Technology, KIIT University, Deemed to be University, Bhubaneswar 751024, India

P. Mondal (✉)
Department of Mechanical Engineering, National Institute of Technology Sikkim, Ravangla 737139, Sikkim, India
e-mail: mondal.pradip87@gmail.com

# 1  Introduction

Biomass is defined as any decomposable organic matter, derived from plants or animals available on a renewable basis [1]. Biomass gasification is a process in which solid biomass is converted into producer gas. The producer gas contains $H_2$, CO, $CO_2$, $N_2$, and $CH_4$ as its primary constituents while some other species are also found in traces [2]. Significant varieties of biomass gasifier–producer gas engines are commercially available since past two decades. However, they suffer from extensive gas cleaning problems, lower overall efficiency, and higher maintenance cost [3]. Usage of bio-producer gas in combined cycle power plant has also been investigated, both theoretically and experimentally [4]. Although the improvement in overall efficiency is found for such plants but as the GT blades are directly exposed to the products of combustion; corrosion, erosion and particulate matter deposition related problems occurs of the blades [5].

Bio-producer gas can furthermore be used by employing the indirect/external technique of heating of the GT cycle working fluid through a heat exchanger. This method helps to get rid of the gas cleaning requirement, as the working fluid of the GT cycle (very commonly air) gets heated through that heat exchanger. Therefore, the GT blades are safe from the corrosion and erosion-related problems [6]. Then the exhaust from the heat exchanger as well as the GT unit can be further used in a bottoming cycle either for power or heat generation. This type of thermodynamic cycle is commonly called as biomass gasification-based indirectly heated/ externally fired combined cycle plant [5–9]. However, efficiency of such plants is comparatively lower than conventional BIGCC plant. Different bottoming cycle configurations have also been suggested by different group of researchers for overall efficiency improvement [7–9]. Techno-economic analyses of them are also attempted to check the economic viability of such plants [10].

Research works carried out by different groups as conferred above, have advanced the knowledge of the biomass gasification-based indirectly heated combined cycle plant and some of the analysis dealt with thermodynamic, environmental, and economical aspects. Present study focuses on the thermodynamic analysis of such plant employing supercritical $CO_2$ cycle as bottoming cycle. The plant is designed for community scale application ($\sim 200$ kW generations). Effects of compressor pressure ratio ($r_p$), gas turbine inlet temperature (TIT), and hot end temperature difference (HETD) on the thermodynamic performance of the plant have been studied and reported here.

# 2  Proposed Plant Configuration

Diagram of the proposed plant is schematically shown in Fig. 1. Initially solid biomass is gasified in the downdraft gasifier (G) under sub-stoichiometric condition. Then the generated producer gas after passing through the filters (F) enters the
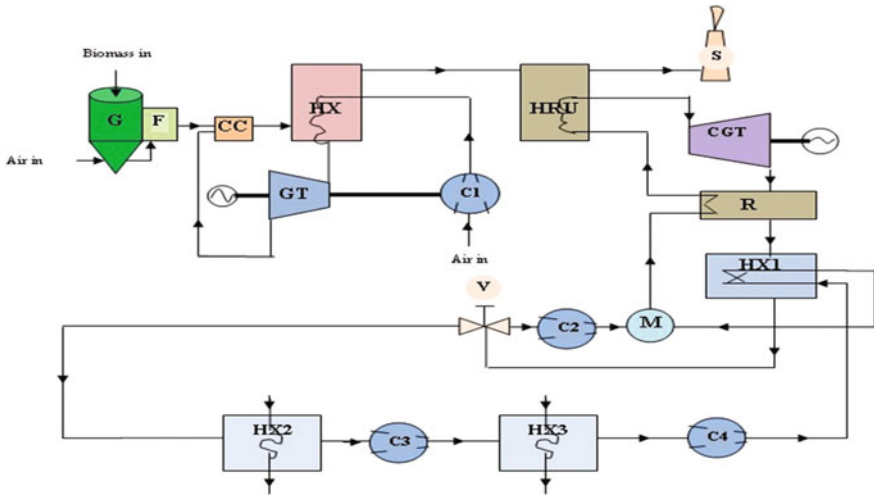
**Fig. 1** Schematic representation of the proposed plant

combustion chamber (CC) of the topping cycle and gets burnt in the presence of topping GT exhaust air. The combustion products enter the shell side of the heat exchanger (HX) to heat-up the topping cycle working fluid, coming out from the compressor (C1). Together the topping combustion chamber and heat exchanger is often called as combustor-heat exchanger (CHX) duplex unit. Furthermore, the CHX exhaust is utilized to run a bottoming supercritical $CO_2$ cycle. Exhaust of CHX unit passes through the heat recovery unit (HRU) and finally exhausted through the stack (S). $CO_2$ gas after expanding in the turbine (CGT) enters the recuperator (R), which transfers heat to the feed stream of $CO_2$ gas to the HRU, where it gets heated again and then enters the CGT. Now, exhaust from the R enters the heat exchanger 1(HX1) and then enters the control valve (V). Fraction of valve exhaust enters the two dual heat exchanger compressor loop (HX2-C3 and HX3-C4) and then heated at the HX 1 and enters the gas mixture (M). Remaining fraction of the valve exhaust enters another compressor (C2) and enters the gas mixture. Finally, the mixed gas is fed to the R unit and thus the bottoming cycle continues. Thus, together topping indirectly heated GT cycle and bottoming supercritical $CO_2$ cycle together constitute a combined cycle which run via biomass-derived producer gas.

## 3   Thermodynamic Model Development

Energetic performance evaluation of the plant, viz. overall electrical efficiency, work output from the turbines, electrical specific biomass consumption, etc. are carried out using standard thermodynamic relations and are represented as follows:

### 3.1 Assumptions

The following assumptions are made while analyzing the performance:

1. Chemical equilibrium model of downdraft gasifier is considered here.
2. Raw sawdust contains C-52.28%, H-5.2%, N-0.47%, O-40.85%, and Ash-1.2% [1].
3. Moisture content of biomass is 16%. Equivalence ratio is 0.35 and the temperature of the gasifier bed is 700 °C [2, 6].
4. Only $SiO_2$ is assumed to be present in the ash [7].
5. Heat loss and pressure loss are considered as per the available literatures [5–7].
6. The main compressor of $CO_2$ cycle is considered to be a two-stage compressor with a single intercooling. Inlet temperature of the gas turbine of $CO_2$ cycle is about 200 °C
7. Efficiencies of turbine and compressor of $CO_2$ cycle are assumed to be 90 and 85%, respectively. $CO_2$ cycle pressure ratio is 1.3.
8. A recompression type S–$CO_2$ cycle is considered here, 50% of the total mass flow rate through the $CO_2$ cycle is considered to be recompressed.

### 3.2 Gasifier Unit

Generalized global gasification reaction of biomass feed is represented as follows:

$$CH_aO_bN_c + pH_2O + n_0(O_2 + 3.76N_2) \rightarrow n_1H_2 + n_2CO$$
$$+ n_3CO_2 + n_4H_2O + n_5CH_4 + n_6N_2 \tag{1}$$
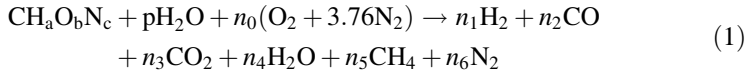
where $n_1$–$n_6$ are the number of moles of the respective gas species. $n_0$ is the mol of $O_2$ present in gasification air, feed to the gasifier and $p$ is the mol moisture feed with each mol of the biomass. Constituents in producer gas along with gas outlet temperature are estimated from the mass balance as well as overall energy balance, considering reaction equilibrium for methanation and shift reactions are as follows:

$$h_{fB} + p.h_{fH_2O} + .\sum_j n_j(h_{fj}^0 + \Delta\overline{h})_{Air} = \sum_j n_j(h_{fj}^0 + \Delta\overline{h})_{producergas} \tag{2}$$

Enthalpy of formation of biomass is taken from its heating value. Gas composition and gas outlet temperature are also dependent on the equivalence ratio of the gasifier.

## 3.3 Combustor-Heat Exchanger Duplex (CHX) Unit

Combustion equation across the combustor is given as follows:

$$
\begin{aligned}
& n_1\mathrm{H}_2 + n_2\mathrm{CO} + n_3\mathrm{CO}_2 + n_4\mathrm{H}_2\mathrm{O} + n_5\mathrm{CH}_4 + n_6\mathrm{N}_2 \\
& + n_0'(\mathrm{O}_2 + 3.76\mathrm{N}_2) \rightarrow n_7\mathrm{CO}_2 + n_8\mathrm{H}_2\mathrm{O} + n_9\mathrm{O}_2 + n_{10}\mathrm{N}_2
\end{aligned}
\tag{3}
$$
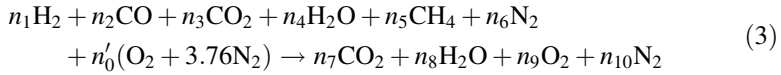
where $n_0'$ represents the number of air mol available at the compressor outlet. Post-combustion temperature is calculated using energy balance equation of the streams and considering the adiabatic condition as:

$$
\sum_j n_j\left(h_{fj}^0 + \Delta\bar{h}\right)_B + \sum_j n_j'\left(h_{fj}^0 + \Delta\bar{h}\right)_{GTexhaust} = \sum_j n_j\left(h_{fj}^0 + \Delta\bar{h}\right)_{fluegas}
\tag{4}
$$

Total mol of flue gas generated during the combustion process is calculated as:

$$
n_{fg} = n_7 + n_8 + n_9 + n_{10}
\tag{5}
$$

Flue gas temperature at the gasifier outlet is calculated as:

$$
n_{fg}.c_{p,fg}.(\Delta T_{fg}) = n_a.c_{p,a}.(\Delta T_{fg})
\tag{6}
$$

For a counter flow heat exchanger, the temperature difference of the hot flue gas at its inlet and the turbine inlet temperature is known as HETD.

## 3.4 Topping Compressor and GT Unit

Compressor's and the gas turbine's power inputs and outputs are calculated using standard thermodynamic relations and isentropic efficiencies. Work input and output equations for the GT block, per unit mass flow rate basis, are given as follows:

$$
\begin{aligned}
w_{C1} &= c_{p,air}\left(T_{c.o} - T_{c,i}\right) \\
w_{GT} &= c_{p,air}\left(T_{GT,i} - T_{GT,o}\right)
\end{aligned}
\tag{7}
$$

### 3.5  Bottoming S–CO₂ Unit

Specific power output from GT is given by:

$$w_{CGT} = c_{p,CO_2} \Delta T_{CGT} \tag{8}$$

Specific power requirement of the bottoming compressors are calculated as:

$$w_{C2/C3/C4} = c_{p,CO_2} \Delta T_{C2/C3/C4} \tag{9}$$

Specific net power output from the $CO_2$ cycle is estimated as follows:

$$(w_{Net})_{CO_2} = w_{CGT} - w_{C2} - w_{C3} - w_{C4} \tag{10}$$

### 3.6  Performance Parameters

Net electrical output from the plant is calculated as:

$$W_{CC} = (W_{GT} - W_{C1}) \cdot \eta_g - (W_{Net})_{CO_2} \cdot \eta_{g1} \tag{11}$$

Overall electrical efficiency of the plant can be defined as:

$$\eta_e = {W_{CC}}/{m_B \cdot LHV_B} \tag{12}$$

$m_B$ stands for the mass flow of solid biomass (kg/s). Hence, specific biomass consumption is presented as:

$$SBC = {3600 \cdot m_B}/{W_{CC}} \tag{13}$$

## 4   Results and Discussions

Constituents of waste-derived producer gas on dry basis are as $H_2$—22.22%, $CH_4$—0.54%, CO—23.94%, $N_2$—45.25%, and $CO_2$—9.05%. The gasification efficiency is 76% and LHV of the producer gas is 4.75 MJ/kg. Model predicted gasifier data matches very well with the experimental results, as reported in the literature [2].

Base case performance ($r_p$ = 4, TIT = 1000 °C, and HETD = 100 °C) of the plant at is shown in Table 1. It is observed from the table that the plant delivers a combined GT-CGT electrical output of about 130 kW. The plant efficiency is about 46% at this thermodynamic state of operation.

**Table 1** Base case performance of the plant

| Parameter | Unit | Value |
|---|---|---|
| Air flow rate through topping cycle | kg/s | 0.375 |
| GT output | kW | 77.01 |
| $CO_2$ flow rate | kg/s | 0.694 |
| CGT output | kW | 51.25 |
| Specific biomass consumption | $kg/kW_eh$ | 0.462 |
| Overall electrical efficiency | % | 45.98 |

**Fig. 2** Variation in efficiency with $r_p$
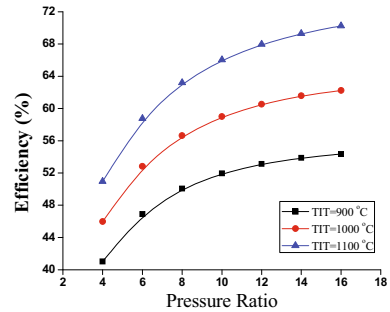


**Fig. 3** Variation in ESBC with $r_p$
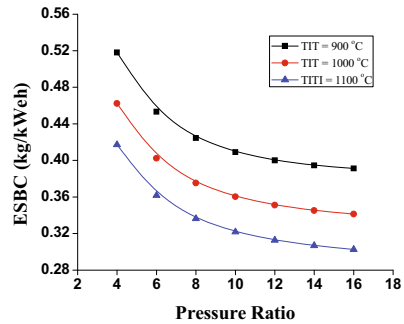


Variation in overall efficiency with $r_p$ is shown in Fig. 2. It is seen from the plot that the efficiency value monotonously increases with increase in $r_p$ value. Also high TIT of the topping GT yields more efficient performance of the plant. Biomass feed rate to the plant is considered to be fixed in this study. As the $r_p$ value increases, required heat input to the plant decreases which ultimately helps to improve the efficiency.

It is observed from Fig. 3 that ESBC decreases with increase in $r_p$. Although the topping GT output value decreases after certain value of $r_p$ (ref to Fig. 4), the CGT output monotonously increases with increase in $r_p$ (ref to Fig. 5). Thus, combined work output of the plant, however, increases with increase in $r_p$. As the biomass input to the plant is considered to be fixed in this study, the ESBC decreases with

**Fig. 4** Variation in GT work
with $r_{\mathrm{p}}$
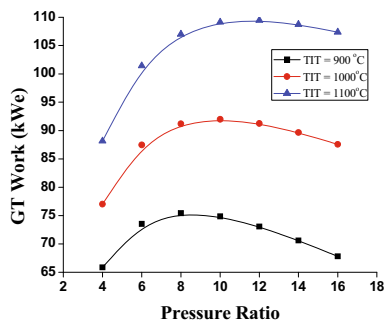


**Fig. 5** Variation in CGT
work with $r_{\mathrm{p}}$
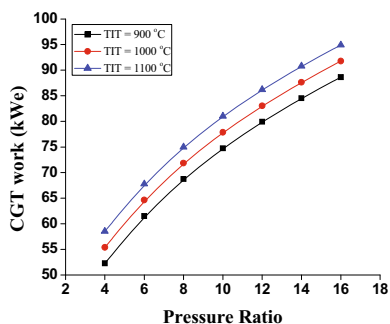


increase in $r_{\mathrm{p}}$. It is also observed from the figure that an increase in topping GT TIT
helps to lower the ESBC value.

Figure 4 shows the variation in topping GT work output with changes in $r_{\mathrm{p}}$
values. It shows that work output from the GT gets maximized at certain $r_{\mathrm{p}}$ value,
depending on the TIT. This $r_{\mathrm{p}}$ values shifts toward the right side of the plot as the
TIT value increases. Also higher values of TIT help to improve the GT output.

Figure 5 shows the variation of bottoming $CO_2$ gas turbine (CGT) work output
with variation $r_{\mathrm{p}}$. CGT work output monotonously increases with increase in $r_{\mathrm{p}}$.
Higher values of $r_{\mathrm{p}}$ result in more bottoming $CO_2$ (cyclic) generation, ultimately
leading toward higher CGT output. Required heat input to the bottoming cycle gets
lower at higher TITs. Now, this is recovered through the bottoming cycle, leading
toward more $CO_2$ generation (and therefore CGT output) at higher TITs.

Variation in net efficiency with HETD of the topping cycle heat exchanger (of
the CHX unit) is shown in Fig. 6. HETD value indirectly indicates the size of the
CHX unit. Higher HETD value indicates lower size of the topping cycle heat
exchanger. It is observed from Fig. 6 that efficiency value linearly increases with
increase in HETD. As seen from Fig. 9 that with increase in HETD, the CGT work
output increases. This helps to increase in efficiency of the plant (as GT work output

**Fig. 6** Variation in efficiency with HETD
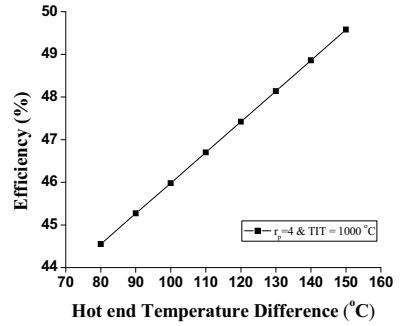


**Fig. 7** Variation in ESBC with HETD
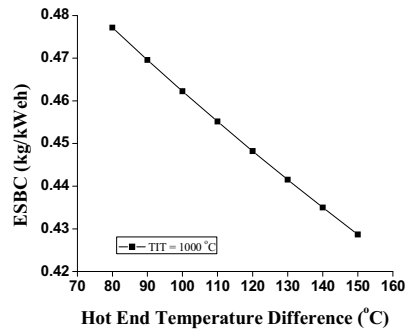


**Fig. 8** Variation in GT work with HETD
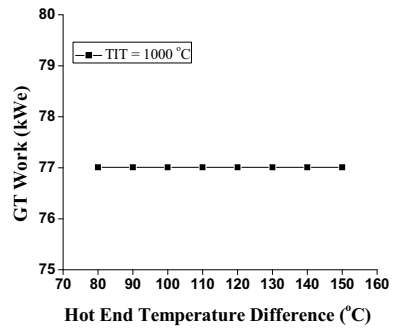


does not vary with HETD). Variation in ESBC with change in HETD of the CHX is plotted in Fig. 7. As the CGT work output increases with increase in HETD, ESBC decreases.

Topping GT work output does not gets influenced by the variation in HETD, as seen from Fig. 8. However, CGT work output monotonously increases with increase in HETD (Fig. 9).

**Fig. 9** Variation in CGT work with HETD
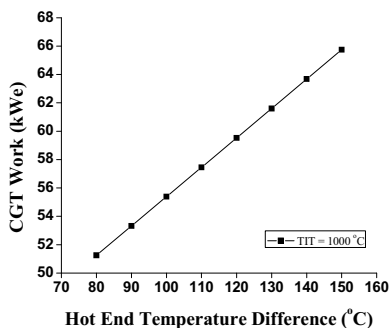


# 5  Conclusions

Thermodynamic model development and analysis of an efficient combined cycle plant, employing topping indirectly heated GT cycle and a bottoming supercritical $CO_2$ plant is carried out and reported here. The plant runs via solid biomass as fuel. It is observed that the plant can deliver electricity of about 200 kW, depending on the thermodynamic conditions. Overall plant efficiency increases with increase in $r_p$ as well as HETD of the heat exchanger. However, further increase in $r_p$ value beyond the considered range linearizes the efficiency value. Also higher TIT and HETD of the heat exchanger offer better plant performance, however metallurgical consideration limits their increase. Overall plant efficiency value is much higher compared to other developed BIGCC plant configurations, reported in the literature. So, the modeled plant configuration can be used practically by evaluating its exergetic, economic, and environmental performances.

# References

1. Buragohain B, Mahanta P, Moholkar VS (2010) Biomass gasification for decentralized power generation: the Indian perspective. Renew Sustain Energy Rev 14(1):73–92
2. Barman NS, Ghosh S, De S (2012) Gasification of biomass in a fixed bed downdraft gasifier —a realistic model including tar. Biores Technol 107:505–511
3. Nouni MR., Mullick SC, Kandpal TC (2007) Biomass gasifier projects for decentralized power supply in India: a financial evaluation. Energy Policy 35:1373–1385
4. Rodrigues M, Faaij APC, Walter A (2003) Techno-economic analysis of co-fired biomass integrated gasification/combined cycle systems with inclusion of economies of scale. Energy 28:1229–1258 (2003)
5. Soltani S, Mahamoudi SMS, Yari M, Rosen MA (2013) Thermodynamic analyses of an externally fired gas turbine combined cycle integrated with biomass gasification plant. Energy Convers Manage 70:107–115
6. Datta A, Ganguli R, Sarkar L (2010) Energy and exergy analyses of an externally fired air turbine (egft), cycle integrated with biomass gasifier for distributed power generation. Energy 35:341–350

7. Mondal P, Mondal K, Ghosh S (2015) Bio- gasification based distributed power generation system employing indirectly heated GT and supercritical ORC: Energetic and exergetic performance assessment. Int J Renew Energy Res 5(3):773–781
8. Soltani S, Mahamoudi SMS, Yari M, Morosuk T, Rosen MA, Zare V (2013) A comparative exergoeconomic analysis of two biomass and co-firing combined power plants. Energy Convers Manage 76:83–91
9. Vera D, Jurado F, de Mena B, Schories G (2011) Comparison between externally fired air turbine and gasifier-air turbine system for the olive oil industry. Energy 36:6720–6730
10. Mondal P, Ghosh S (2016) Bio- gasification based externally fired combined cogeneration plant: thermo-economic and exergo-economic analyses. Int J Exergy 20(4):496–516

# Experimental Investigation of Forced Convection on Square Micro-Pin Fins

**Ramendra Singh Niranjan, Onkar Singh and J. Ramkumar**

**Abstract** An investigation is to be conducted to determine whether micro-pin fin can increase heat transfer under forced convection or not. This would be accomplished by performing an experimental investigation. In the present analysis, thermal effectiveness of square micro-pin fin arrays under forced convection conditions in air was studied. Square micro-pin fins of different sizes are tested for three different heat loads, and it was observed that heat transfer performance of stainless steel micro-pin fins was enhanced 5–15% compared with flat plate fins. Further, increase in the overall Nusselt number of the surface was found due to boundary layer regeneration and enhanced flow mixing. In addition, heat transfer effectivity and thermal resistance were decreases with the increase of Reynolds numbers.

**Keywords** Plate fin · Micro-pin-fin · Forced convection · Heat transfer coefficient (HTC)

## Nomenclature

| | |
|---|---|
| $A_f$ | Cross-sectional area of micro-pin fin |
| $A_p$ | Cross-sectional area of plate fin |
| $H$ | Height of the plate fin sample |
| $H_f$ | Fin height ($H - t_b$) |
| $h$ | Heat transfer coefficient |
| $h_p$ | Convective heat transfer coefficient of plate fin |
| $h_f$ | Convective heat transfer coefficient of micro-pin fin array |
| $L$ | Length of the micro-pin fin array |
| $Nu$ | Nusslet number |

R. S. Niranjan (✉)
Department of Mechanical Engineering, UIET CSJMU, Kanpur, India
e-mail: ramendrasingh@rediffmail.com

O. Singh
Department of Mechanical Engineering, HBTU, Kanpur, India

J. Ramkumar
Department of Mechanical Engineering, IIT Kanpur, Kanpur, India

$Q_c$     Heat dissipated in convection mode from micro-pin fin array
$Q_{in}$    Power in input
$Q_{loss}$   Heat loss in different mode through the insulating case
$Q_p$     Heat transferred by convection from plate fin
$Q_f$     Heat transferred by convection from micro-pin fin array
$Q_r$     Heat dissipated in radiation mode from micro-pin fin array
$Re$     Reynolds number
$R_p$     Thermal resistance of plate fin sample
$R_f$     Thermal resistance of micro-pin fin array
$S$       Micro-pin fin spacing
$T$       Temperature
$T_{amb}$   Ambient temperature
$T_f$     Temperature of micro-pin fin array surface
$T_p$     Temperature of plate fin surface
$T$       Micro-pin fin thickness
$t_b$     Base thickness
$W$      Width of the micro-pin fin array sample
$\varepsilon_f$      Overall fin effectiveness

# 1  Introduction

The heat is generated in various engineering devices during their operation. This may cause rise in temperature of the system or device which may cause problems in the system performance and may even lead to its failure. This generated heat must be rejected to its surrounding to maintain the device at preferable temperature for its optimal working. Hence, the enhancements of heat transfer play an important role in controlling the working temperature. For enhancement of heat transfer between heat exchanging devices to the surrounding atmosphere, extended surface techniques are commonly used in conventional macro-system. Similar configurations are used for thermal enhancement in micro-scale system. They find applications in electronic equipment and other important areas like electrical transformers, heat exchanger and chemical processing system.

In literature on heat transfer mechanism, we find strong inclination towards pin fins against plate fins owing to higher heat transfer coefficient observed in pin fins. Usage of pin fin in place of plate fins result is increase of 3–7% in overall fin effectiveness [1]. Researchers have found increase in heat transfer rate with use of horizontal micro-fins under natural convection [2]. Further perforating fins increase contact surface causing enhanced convective heat transfer [3]. The fin spacing, fin thickness and fin height also influence the heat transfer rate; with the increase in fin spacing and thickness the heat transfer coefficient increase and it decreases with increase in fin height [4]. The parameters used to judge the effectiveness of heat

transfer are heat transfer, drag force and total entropy generation rate. It has been found among various sections for fins, the square geometry gives worst performance on the above parameters and the circular geometry gives best results. The circular geometry results in lower dimensionless total entropy generation rate for smaller perimeters, larger aspect ratios and lower Reynolds number [5]. As far as fin diameter is concerned, its thermal performance has a weak dependence for a given fin spacing of pin fin. Thermal performance improves with increase in fin length. It is also noticed that there exists a point of dimensioning return depending on fin length [6]. By optimizing dimension of pin fin, one can obtain the mass-specific heat transfer that can increase mass-specific power up to 50% compared to flat surface [7]. The overall conclusion based on the literature on heat sink geometries is that rounded geometries outperformed sharp edge fin shapes. In electrical devices heat sink phenomena, it is better to work at lower values of pressure drop and pumping power [8]. Among the sharp edge sections, triangular cross sections show the maximum blocking effects for the coolant flowing and hence better convective heat transfer [9]. Micro-scale cylindrical pin fin array shows better thermo-hydraulic performance compared to plane micro-channel-based cooling [11].

The current research in domain of heat transfer is more involved in micro-pin fins to study convective/radiative heat transfer compared to plate fins with the same area. This work is also involved in investigating the forced convection heat transfer taking into account different micro-pin fins geometry. The work is thus extension into the domain of forced convection. Experimental investigation is done on both plate fin and square micro-pin fin, and the results are further analysed.

## 2    Experimental Set-up

In this study, forty-eight square micro-pin-fin samples have been experimentally investigated, and one of the samples is shown in Fig. 1. Stainless steel rectangular flat plates of dimensions 147 mm ($\pm1$ mm) $\times$ 23.5 mm ($\pm0.5$ mm) wide, 1.4 mm-thick were used. On the flat surface, micro-pin fin has been created through laser machining which contains 13,432–14,208 number of micro-pin fins. The dimensions of square micro-pin fins for 48 samples are reported in Table 1. In each geometry, different fin thickness and fin spacing were found due to variation in laser machining parameters.

The experimental set-up shown in Fig. 2 was used for the current investigation. The square micro-pin fin sample was placed in an insulating case made of steel whose three sides were covered with thick glass wool. Further, it was wrapped by thick polystyrene layer. The square micro-pin fin sample was heated indirectly through 65 W electrical heater operated via an AC power supply. Two digital multi-meters of make MTC and Yokins, respectively, have been used to measure voltage and current input for calculation of heat produced. The sample was placed inside the middle of rectangular duct of dimension 45 cm $\times$ 15 cm $\times$ 10 cm, the other end of the duct connected to the suction side of a blower and the flows past
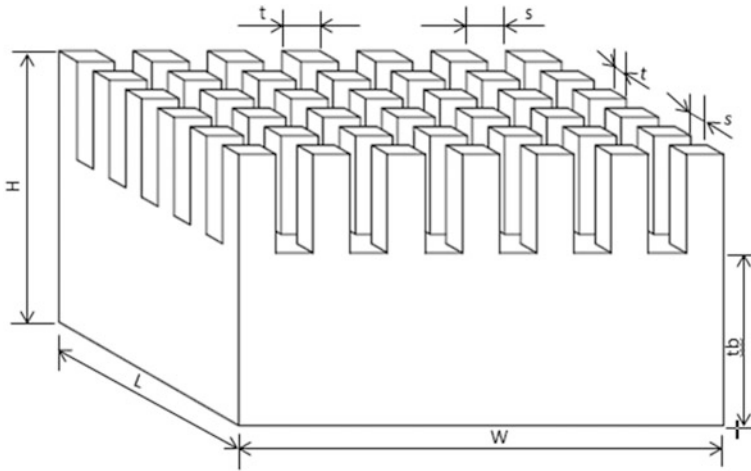
**Fig. 1** Geometry of the micro-pin fin arrays. Here: $s$ is fin spacing, $t$ is fin thickness, $t_b$ is base thickness, $W$ is width and $L$ is Length

**Table 1** Fin dimensions of each square geometry [10]

| Sample no. | Fin spacing, $s$ (μm) | Fin height, $H_f$ (μm) | Fin thickness, $t$ (μm) | Sample no. | Fin spacing, $s$ (μm) | Fin height, $H_f$ (μm) | Fin thickness, $t$ (μm) |
|---|---|---|---|---|---|---|---|
| 1 | 35 | 7.402 | 465 | 25 | 38 | 6.432 | 462 |
| 2 | 30 | 7.054 | 470 | 26 | 39 | 4.01 | 461 |
| 3 | 38 | 6.675 | 462 | 27 | 45 | 3.45 | 455 |
| 4 | 28 | 3.867 | 472 | 28 | 34 | 3.123 | 466 |
| 5 | 60 | 8.86 | 440 | 29 | 48 | 7.32 | 452 |
| 6 | 60 | 7.86 | 440 | 30 | 48 | 6.89 | 452 |
| 7 | 43 | 7.78 | 457 | 31 | 51 | 5.56 | 449 |
| 8 | 43 | 7.213 | 457 | 32 | 42 | 5.345 | 458 |
| 9 | 65 | 9.894 | 435 | 33 | 70 | 9.986 | 430 |
| 10 | 72 | 8.832 | 428 | 34 | 58 | 9.894 | 442 |
| 11 | 62 | 8.325 | 438 | 35 | 57 | 8.523 | 443 |
| 12 | 60 | 7.901 | 440 | 36 | 57 | 7.86 | 443 |
| 13 | 41 | 7.33 | 459 | 37 | 31 | 7.356 | 469 |
| 14 | 37 | 7.81 | 463 | 38 | 34 | 7.032 | 466 |
| 15 | 26 | 5.19 | 474 | 39 | 20 | 6.867 | 480 |
| 16 | 37 | 3.712 | 463 | 40 | 18 | 5.899 | 482 |
| 17 | 53 | 8.901 | 447 | 41 | 56 | 8.245 | 444 |
| 18 | 58 | 7.12 | 442 | 42 | 45 | 9.42 | 455 |
| 19 | 57 | 8.321 | 443 | 43 | 48 | 7.986 | 452 |
| 20 | 50 | 5.013 | 450 | 44 | 49 | 6.896 | 451 |
| 21 | 63 | 11.98 | 437 | 45 | 66 | 11.045 | 434 |
| 22 | 56 | 11.69 | 444 | 46 | 58 | 10.891 | 442 |
| 23 | 57 | 10.58 | 443 | 47 | 56 | 10.59 | 444 |
| 24 | 60 | 9.865 | 440 | 48 | 53 | 9.874 | 447 |
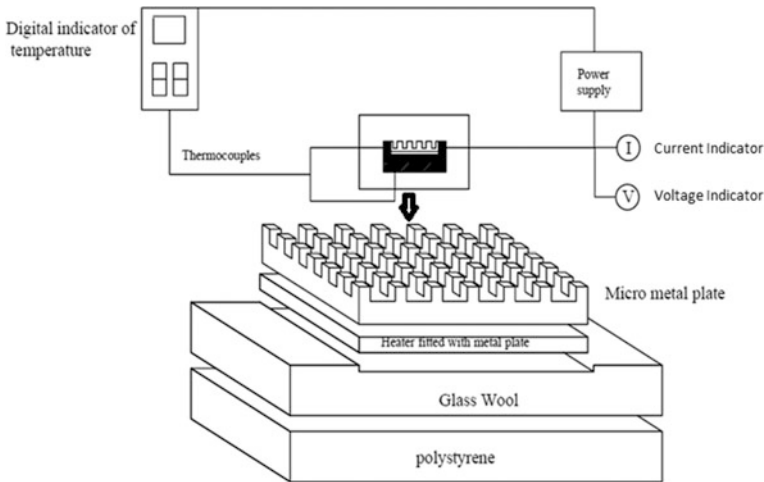
**Fig. 2** Schematic of the experimental set-up and of the exploded structure of the micro-pin fin sample

the fins. When blower is on, air is being forced against the fins. The temperature of the plate and micro-pin-fins has been measured by the two measuring devices K-type thermocouple and HTC infrared thermometer (MT-6). In the sample, we have assumed that temperature across the fin array and the fin height are constant. The ambient temperature was measured by the K-type thermocouple and maintained at 25 °C. The fin array temperature was also measured by the K-type thermocouples at three different locations. All the experimental data were reported at steady-state condition and measured three times for each investigation. Power inputs of 40, 60 and 80 V were applied to the heater, which resembled to heating power densities of 1.1, 2.2 and 3.6 kW/m$^2$.

## 3 Results and Discussions

### 3.1 Thermal Resistance

In the present investigation, dependency of thermal resistance of the pin fins on the power in input is shown in Fig. 3 and thermal resistance was calculated from the following equation.

$$R_{th} = \frac{1}{h \cdot A} \tag{1}$$

It is clearly seen from Fig. 3 that the thermal resistance of square micro-pin fins is consistently lower than that of plate fins under forced convection in air. This reveals that the micro-pin fins are competent to transfer a larger amount of heat by
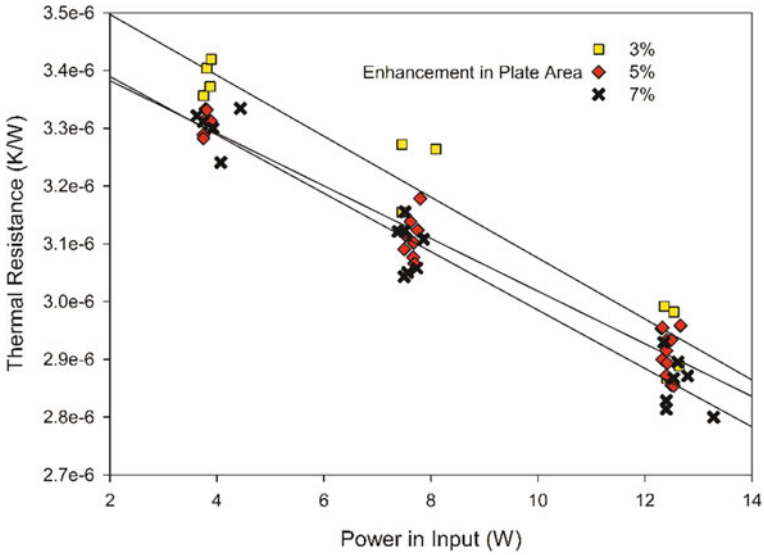
**Fig. 3** Thermal resistance of square micro-pin-fins under forced convection

forced convection compared to the plate fins for the same input parameters. This is possible due to significant volume is available in between the micro-pin fins to facilitate air for heat dissipation. Further, it was observed that thermal resistance is a function of percentage enhancement in surface area and found 3–6% reduction compare to plate fins.
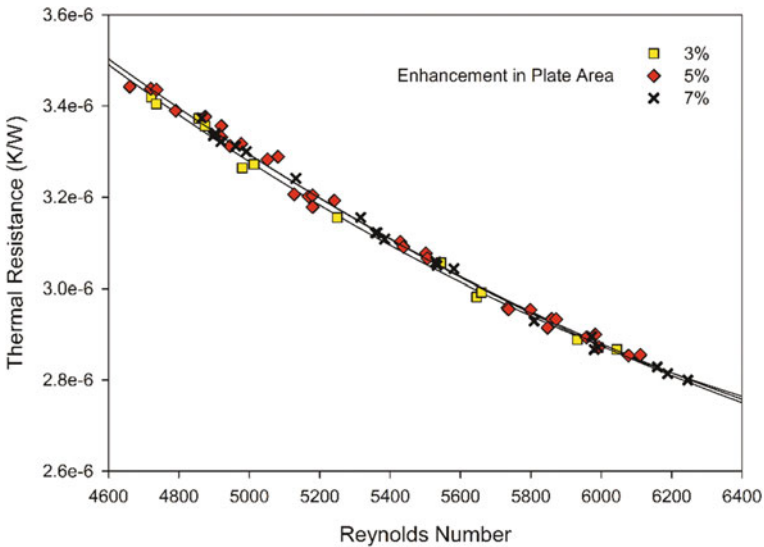


**Fig. 4** Effects of Reynolds number on thermal resistance

The effects of Reynolds number on thermal resistance are illustrated in Fig. 4 for enhanced plate area. It is clearly seen from figure that the thermal resistance is inversely proportional to Reynolds number for constant inlet air temperature and constant heat flux. This is due to enhancement in heat transfer rate as air flow rate increases. Further, it is clearly seen from figure that the thermal resistance of 7% enhanced plate surface are slightly lower compared to 3% enhanced plate surface due to square micro-pin-fins.

## 3.2 Nusselt Number

The effect of Reynolds number on the average Nusselt number is shown in Fig. 5 for 3–7% enhancement in plate area. For each sample, four experiments were performed for different power in input (heat flux). The results obtained from the experiments are best fitted by the straight line as shown in figure. Further, it was found that the square micro-pin-fins having 3% enhanced plate area yield minutely higher Nusselt number for the range of Reynolds numbers considered here. The Nusselt number for 7% enhanced plate area is lower compared to others. This because of air confined in between four micro-pin-fins creates stagnation zones where air acts as an insulating layer due to low thermal conductivity. In addition, high viscous forces come in pictures due to narrow path between the micro-pin fins. Therefore, lower value of convective heat transfer coefficient (Nusselt Number) was found.

## 3.3 Fin Effectiveness

The overall fin effectiveness ($\varepsilon_f$) has been used to determine the enhancement in thermal performance of square micro-pin-fins. This measures the impact of the fins on the heat transfer rate. The overall fin effectiveness is defined as the ratio of the heat transferred through the square micro-pin-fins to the flat surface of the same area as follow:

$$\varepsilon_f = \frac{Q_f}{Q_p} \tag{2}$$

The effect of Reynolds number on overall fin effectiveness of square micro-pin-fins has been plotted in Fig. 6 and compared to the flat surface. The effectiveness of pin fins is always higher than unity for all type fin arrays.

It means that the use of fin arrays leads to an advantage on heat transfer enhancement. Further, it was observed that Reynolds number inversely affects the fin effectivity; however, in the present investigations, we have found small changes. From Fig. 6, one can also find that for 7% enhancement in plate area due to square
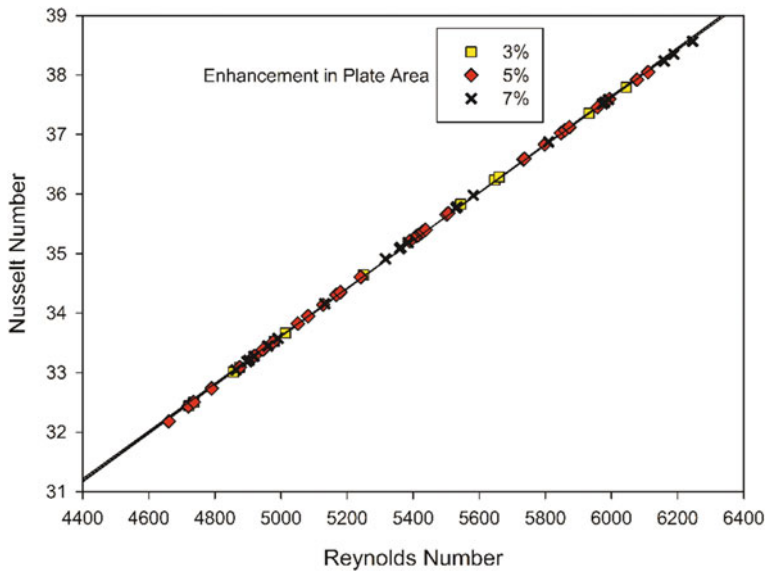
**Fig. 5** Nusselt number variation at different Reynolds number
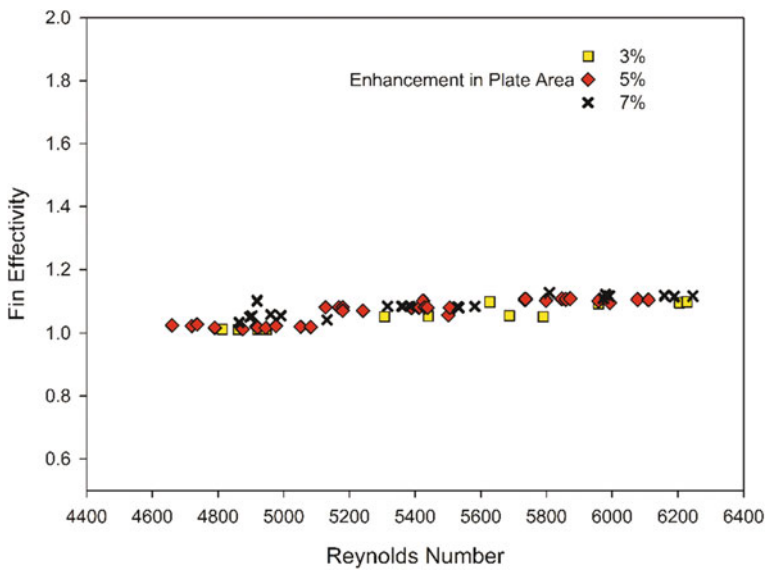


**Fig. 6** Performance of micro-pin-fin effectiveness with Reynolds number

micro-pin-fins have minutely higher heat transfer performance compared to 3%. This because of minutely large area is available to exchange heat between surfaces to ambient.

# 4 Conclusion

In the present experimental study, thermal performance of square micro-fins array under forced convection was analysed and compared with flat surface and found good heat transfer performance. Micro-pin fins have 5–15% higher overall fin effectiveness compared to flat surface since fins optimizing the material usage. Further, the heat transfer rate in square micro-pin fins was found minutely higher compared to flat plate under forced convection because fins create obstruction in the flow thus more circulation and irregularity in flow this leads to increase Reynolds and Nusselt numbers.

The use of square micro-pin fins should be encouraged to enhance heat transfer in micro-scale, likewise to macro-pin fins. Future studies are recommended in this scenario to refine this technique and to extend the investigation for radiation heat transfer. The effects of fins materials, orientation and shape will be considered and presented in future works.

# References

1. Micheli L, Reddy KS, Malliick TK (2016) Experimental comparison of micro-scaled plate-fins and pin-fins under natural convection. Int Commun Heat Mass Transfer 75:59–66
2. Micheli L, Reddy KS, Malliick TK (2016) Thermal effectiveness and mass usage of horizontal micro-fins under natural convection. Appl Therm Eng 97:39–47
3. Ismail MF, Reza MO, Zobaer MA, Ali M (2013) Numerical investigation of turbulent heat convection from solid and longitudinally perforated rectangular fins. Procedia Eng 56:497–502 (2013)
4. Micheli L, Reddy KS, Malliick TK (2015) General correlations among geometry, orientation and thermal performance of natural convective micro-finned heat sinks. Int J Heat Mass Transf 91:711–724
5. Khan WA, Culham JR, Yovanovich MM (2006) The role of fin geometry in heat sink performance. Trans ASME 128:324
6. Kobus CJ, Oshio T (2005) Development of a theoretical model for predicting the thermal performance characteristics of a vertical pin-fin array heat sink under combined forced and natural convection with impinging flow. Int J Heat Mass Transf 48:1053–1063
7. Micheli L, Reddy KS, Malliick TK (2015) Plate micro fins in natural convection: an opportunity for passive concentrating photovoltaic cooling. Energy Procedia 82:301–308
8. Soodphakdee D, Behnia M, Copeland DW (2001) A comparision of fin geometries for heatsinks in laminar forced convection: part I—round, elliptical, and plate fins in staggered and in-line configurations. Int J Microcircuits Electron Packaging 24(1). ISSN 1063-1674

9. Yang D, Wang Y, Ding G, Jin Z, Zhao J, Wang G (2016) Numerical and experimental analysis of cooling performance of single-phase array microchannel heat sinks with different pin-fin configurations. Appl Therm Eng. http://dx.doi.org/10.1016/j.applthermaleng.2016.08.211

10. Niranjan RS, Singh O, Ramkumar J (2017) Optimization of process parameters for laser fiber micromachining of micro-channels on stainless steel. Int J Eng Res Gen Sci 5(6):15–23

11. Peles Y, Kosar A, Mishra C, Jung C, Schneida KB (2005) Forced convection heat transfer across a pin-fin micro heat sink. Int J Heat Mass Transf 48:3615–3627

# Highly Confined Flow Past a Stationary Square Cylinder

**Shravan Kumar Mishra, Deepak Kumar, Kumar Sourav, Pavan Kumar Yadav and Subhankar Sen**

**Abstract** Present work explores a numerical study based on Finite-Element Method for fluid flow past a stationary square cylinder placed symmetrically in the channel with high Blockage, $B = 0.9$. Reynolds Number ($Re$) progressively varied from 5 to 150 in the laminar region. An attention has been paid to capture the exact point of laminar flow separation on the surface of the cylinder and the separation $Re$ for high blockage flow. The steady to unsteady flow transition is observed at a $Re$ ($Re_c$) of 62. A very high drag coefficient, order of magnitude $= 10^3$ is reported for the computation. Inconsistency with unbounded flow solutions, the wake bubble for 90% blockage cylinder shows nonlinear variation with $Re$ in the steady flow regime. In a very narrow regime near the beginning of unsteadiness, the flow is found to be quasi-periodic whereas, for all remaining Reynolds number values considered for the present study, periodic flow is observed.

**Keywords** Stabilized finite-element · Confined flow · High blockage

## 1 Introduction

Bluff body flow had been a widely explored research area for several decades. While a majority of earlier works used a circular cylinder to study the flow characteristics in both steady and unsteady conditions, knowledge of flow around other cross-sections lacked. The researchers have been trying to study the physics of the flow behind other cross-sections like a square, rectangle, ellipse, etc. Confining the flow significantly affect the flow characteristics around a bluff body. Owing to vast applications of confined flow (viz., flow in journal bearing, in the arteries of the

S. K. Mishra (✉) · D. Kumar · K. Sourav · P. K. Yadav · S. Sen
Department of Mechanical Engineering, Indian Institute of Technology
(Indian School of Mines) Dhanbad, Dhanbad 826004, Jharkhand, India
e-mail: shravan.1992.mishra@gmail.com

human body, etc.), a number of studies had been and are being performed to study the effect of blockage on flow. Blockage ($B$), being an influential parameter, is the ratio of the characteristic dimension of an object across the flow to the width of the computational domain.

Unconfined and moderately confined flow had been studied vastly by researchers [1–5]. An interesting outcome from the above studies makes the platform for the need of study of highly blocked flow around an obstacle. For a square cylinder, [6] presented drag coefficients and Strouhal number for different cases in $Re$ = [37.5, 150] and $B$ = [0.05, 0.5] range. For a circular cylinder, [7] investigated wall effect up to high blockage $(0.1 \leq B \leq 0.9)$ on two-dimensional (2D) flow $(0 < Re \leq 280)$. They focused on hydrodynamic force range in the wake structure behind the cylinder. They reported pitchfork and supercritical Hopf bifurcation. In addition, the presence of co-dimension point on the neutral stability curve had also been reported. The existence of the steady asymmetric state and its transition due to pitchfork bifurcation was obtained by employing linear stability study. [8], for laminar flow ($Re$ = [6–40]) and $B$ = [0.00125, 0.80], around a stationary circular cylinder, reported the separation $Re$ ($Re_s$) to be 6.29 (approximately) for 0.5% blocked flow. They also observed that the effect of blockage had negligible influence on the flow parameters for $B \leq 0.01$. The bubble length, separation angle, and $Re_s$ exhibit monotonic variation with blockage. They were the first to present the variation of separation angle with $Re$. For a square cylinder at zero incidence, [9] performed direct numerical simulations (DNS) at different $Re$ over a wide range of $B$ between 10 and 90%. They noted that critical $Re$ ($Re_c$) display a non-monotonic variation with increasing blockage as earlier reported by [3] for a square and [4] for a circular cylinder.

It is quite clear that there are not plenty of works available to wrap the physics of high blockage flow. Thus, in the present work, an attempt has been made to study the effect of high blockage on flow characteristics and fluid forces for flow around a square cylinder.

## 2 Governing Equations and Finite-Element Formulation

The momentum and mass conservation equations (Eqs. 1 and 2) govern the movement of an incompressible viscous fluid. The equations, in their vector form, using primitive variables are:

$$\rho(\partial \mathbf{u}/\partial t + \mathbf{u} \cdot \nabla \mathbf{u}) - \nabla \cdot \boldsymbol{\sigma} = 0 \tag{1}$$

$$\nabla \cdot \mathbf{u} = 0. \tag{2}$$

Here $\rho$, **u**, $t$ and $\boldsymbol{\sigma}$ are the fluid density, velocity field, time and the Cauchy stress tensor, respectively. The stress can further be described as the sum of its isotropic ($p\mathbf{I}$) and deviatoric parts (**T**). Mathematically,

$$\sigma = p\mathbf{I} + \mathbf{T}; \quad \mathbf{T} = 2\mu\varepsilon(u); \quad \varepsilon(u) = \frac{1}{2}\left((\nabla u) + (\nabla u)^{\mathrm{T}}\right) \tag{3}$$

where $p$, **I**, $\mu$ and $\varepsilon$ are the pressure, identity tensor, dynamic viscosity of the fluid and strain rate tensor, respectively.

A stabilized finite-element method is employed to discretize the fluid flow equations (Eqs. 1 and 2). The discretized equations are solved iteratively over the co-allocated mesh. The use of co-allocated mesh violates the Babuska-Brezzi condition and hence involves the addition of extra stabilizing terms for velocity (SUPG: Streamline-Upwind/Petrov Galerkin) and pressure (PSPG: Pressure-Stabilized/Petrov Galerkin), respectively. Further details of the finite-element formulation can be found in [10, 11].

## 3 Problem Description

### 3.1 Computational Domain and Boundary Conditions

A square cylinder of dimension $D$ is placed symmetrically between in a rectangular computational domain *PQRS*. The lateral walls are separated by a distance $H$; the width of the computational domain (here, $H = 1.1111D$). In Fig. 1, the set-up is shown for $B = 0.9$. The inlet is at a distance of $L_\mathrm{u} = 32D$ behind the cylinder center while the exit is $L_\mathrm{d} = 63D$ past the cylinder center. The origin of the Cartesian coordinate system coincides with the cylinder center.

A fully developed flow enters the channel and exits without stress. The lateral walls and cylinder surface are governed by the no-slip condition.
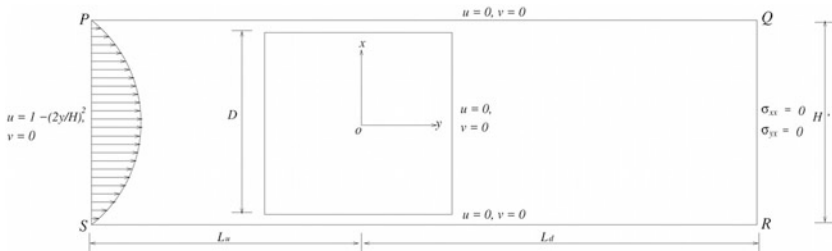


**Fig. 1** Problem set-up for flow past a stationary square cylinder at high blockage ($B/H = 0.9$)
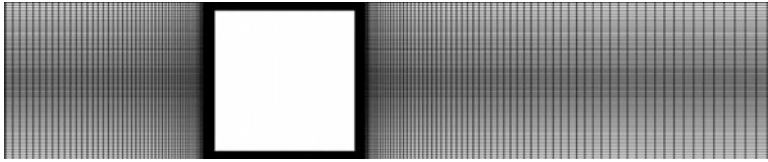
**Fig. 2** Finite-element mesh with 90,460 nodes and 89,472 bilinear quadrilateral elements

## 3.2   The Finite-Element Mesh

Truncated finite-element mesh for the problem is shown in Fig. 2. The mesh consisting of 90,460 nodes and 89,472 bilinear quadrilateral elements is structured, non-uniform and has three blocks. The cylinder is placed in the central block. A total of 384 nodes are used to define the cylinder surface which makes an extremely fine mesh in the central block.

# 4   Validation and Mesh Convergence Study

## 4.1   Validation with Earlier Studies

A successful validation study in terms of drag coefficient ($C_d$) and normalized bubble length ($L/D$) has been performed for flow around a square cylinder at $Re = 40$ and $B = 0.067$. Validation with [11] has been tabulated in Table 1 with a maximum deviation of 2.24% obtained for $C_d$.

## 4.2   Mesh Convergence Test

To finalize the size of the mesh to be used for the optimized solution, a mesh convergence study has also been performed on several meshes. Table 2 lists two meshes M1 and M2 where M2 has approximately twice as many nodes and elements as M1. The convergence study has been studied at $Re = 100$ and $B = 0.9$. It is noticeable that the results for both the meshes do not vary significantly. Thus, mesh M1 is adequate to be used for the present computations.

**Table 1** Validation study for flow past a square cylinder at zero incidence

| Studies | $C_d$ | $L/D$ |
|---|---|---|
| [11] | 1.8990 | 2.7000 |
| Present | 1.8565 | 2.7348 |
| Deviation (%) | 2.24 | 1.3 |

**Table 2** Mesh convergence study for flow past a highly confined square cylinder at $Re = 100$

| Mesh | Nodes | Elements | Equations | $N_t$ | $C_d$ |
|---|---|---|---|---|---|
| M1 | 90,460 | 89,472 | 267,618 | 96 | 661.012573 |
| M2 | 173,776 | 172,368 | 516,013 | 162 | 661.163879 |

## 5   Results

### 5.1   *Development of Steady Separation Bubble with* Re

Development of the steady separation bubble is determined by streamline contour plots. For $B = 0.9$, Fig. 3a–e presents the streamline contours at $Re = 15, 20, 30, 40$ and 62, respectively. It is noteworthy that at highly blocked flow ($B = 0.9$), wake formation initiates directly from the sharp trailing edges of the square cylinder unlike from base ($\theta = 180°$) at low blockage ($B = 0.01$) [12]. For the present case, wake formation with two counterclockwise eddies initiates at $Re = 15$ (Fig. 3a). With an increase in $Re$, the wake bubbles expand and elongate (Fig. 3b–d) and then sheds at $Re = 62$ (Fig. 3e). Thus, $Re = 62$ marks the onset of unsteadiness in the highly blocked flow around a square cylinder.
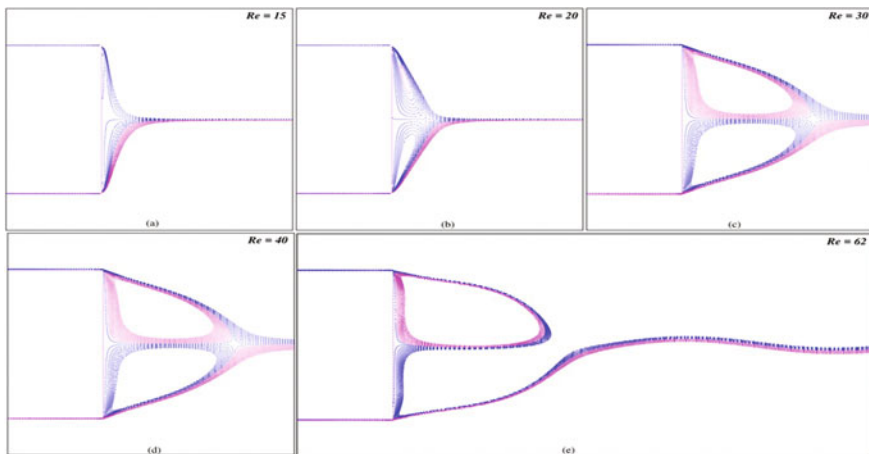


**Fig. 3** Bubble separation and its development with Reynolds number for $15 \leq Re \leq 62$

**Fig. 4** Variation of eddy
length with Re
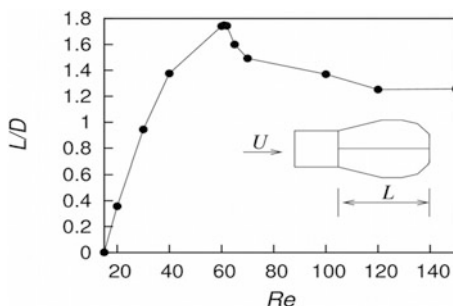


## 5.2 Variation of Eddy Length with **Re**

Eddy length is the stream-wise distance of wake stagnation (saddle) point from the
backward stagnation point on the cylinder. *L/D–Re* curve (Fig. 4) shows a variation
of wake length with *Re*. In accordance with the result obtained in Sect. 5.1, *L/D*
increases in the steady regime ($15 \leq Re \leq 61$) and decreases in the unsteady flow
regime ($Re \geq 62$). The onset of unsteadiness is accompanied by the sudden drop in
the eddy length.

## 5.3 The Onset of Steady Flow Separation

The vorticity distribution on the cylinder surface is used to determine critical *Re* and
exact point of flow separation on the surface of the cylinder. Figure 5 shows $\omega$–$\theta$
plot for *Re* = 7–11. Only one crossover point at $\theta = 180°$ in the $\omega$–$\theta$ plot (Fig. 5) is
an evidence of attached flow for *Re* < 8. Flow separation initiates at *Re* $\approx$ 8;
$\theta = 136.8°$, where the plot cuts the zero vorticity line even number of times (re-
gions A, B). These bubbles are very small and reattaches with the surface of
cylinder mush ahead of the base point.

## 5.4 Variation of Drag Width **Re**

The dependence of drag coefficient on *Re* is shown in Fig. 6. As expected, drag
continues to fall in the entire regime. In the present study, the drag values are quite
high (of the order of magnitude $10^3$) unlike 1 for unconfined flow [12]. The
decrease in $C_d$ is attributed to the increasing pressure recovery at the cylinder base
(Fig. 7). The variation of $C_{dp}$ and $C_{dv}$ are nearly identical while the pressure drag is
more significant.
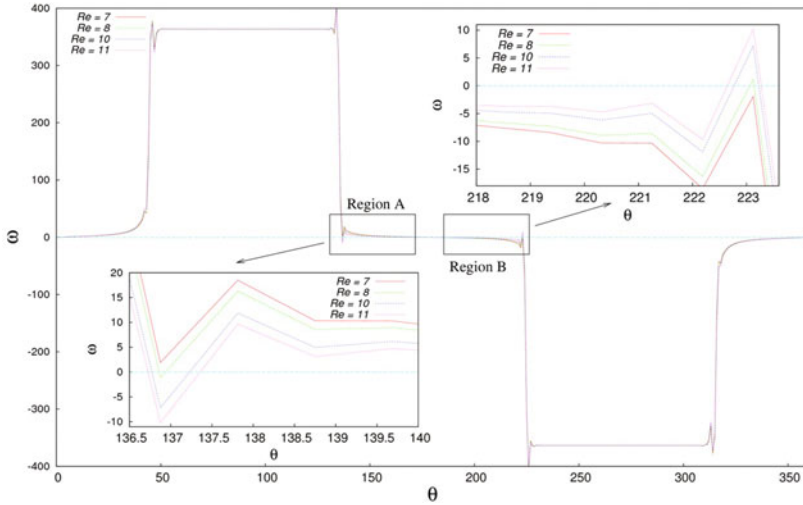
**Fig. 5** Flow past a stationary square cylinder at $B = 0.9$: variation of surface vorticity distribution for $7 \leq Re \leq 11$. The insets are the close-up of regions A, B. The circumferential angle ($\theta$) is measured counter-clockwise from forward stagnation point
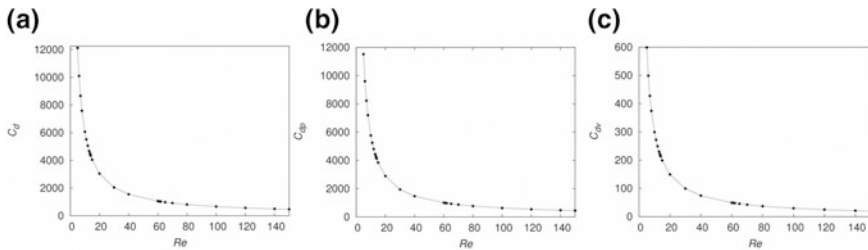


**Fig. 6** Variation of $C_d$ with $Re$: **a** total drag, **b** pressure drag and **c** viscous drag

## 5.5 Surface Pressure Distribution

Surface pressure ($C_p$) distribution for the lower half of the cylinder is shown in Fig. 7 at different $Re$ between 5 and 150. A very large value of $C_p$ is observed at low $Re$. $C_p$ remains almost constant on front and the rear edge of the cylinder while decreases gradually on the lateral edge. A very narrow negative pressure region is observed near $\theta = 135°$ for all $Re$.
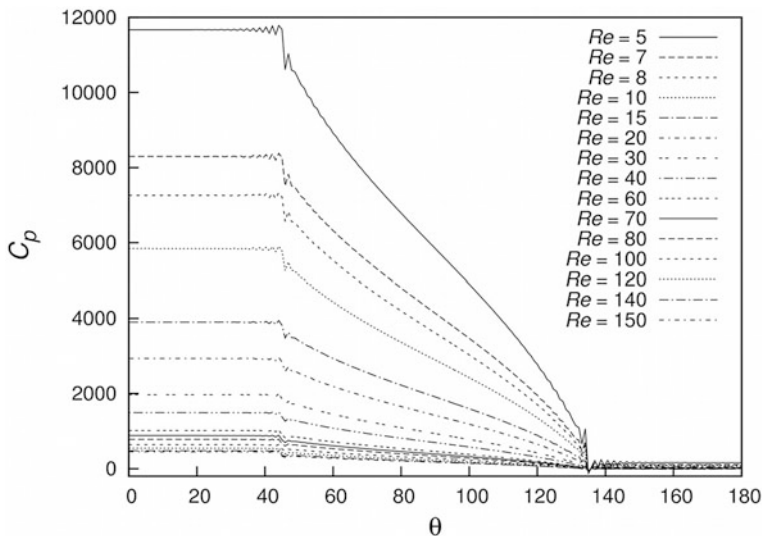
**Fig. 7** Variation of $C_p$ along the lower half the cylinder with $\theta$

## 5.6 The Flow

The onset of unsteadiness obtained at $Re = 62$ is reconfirmed with the help of vorticity contours (Fig. 8). At $Re = 61$, the flow is steady as there is no undulation in the downstream flow. While at another representative $Re$ of 62, 70, 100, 120 and 150, the disturbance in the flow is clearly observed and alternate vortex shedding from top and bottom of the cylinder starts. The existence of additional vortices on the lateral walls is also observed. The flow is periodic in the unsteady regime (suggested by figure '8' in $C_d$–$C_l$ phase plots).
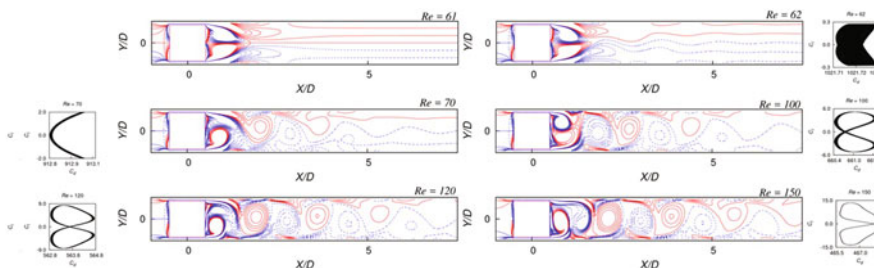


**Fig. 8** Flow past a stationary square cylinder at $B = 0.9$: vorticity contours for $62 \leq Re \leq 150$. The respective $C_d$–$C_l$ phase plots are shown alongside each contour

# 6 Conclusions

Results have been presented for flow past a stationary square cylinder for $5 \leq Re \leq 150$ at $B = 0.9$. It is found that flow remains steady for $Re < 62$. The wake formation starts at Re = 15. *L/D–Re* curve depicts a non-linear variation of wake length in steady flow regime. This is in contrast with the linear profile of *L/D–Re* for low and moderate blockage flow problems in the steady flow regime. Drag is significantly higher in confined flow (Order of $10^3$) as compared to unconfined flow. Drag decreases continuously due to pressure recovery at the rear end of the cylinder. Flow becomes unsteady at $Re = 62$. It is seen that vortices generate at the cylinder surface get diffuse into the vortices on both walls due to confinement and 2S mode of vortex shedding is observed in the downstream region. Phase plots show the quasi-periodic nature of flow at $Re = 62$ and periodic for $Re = 70, 100, 120$ and $150$.

# References

1. Davis RW, Moore EF, Purtell LP (1984) A numerical-experimental study of confined flow around rectangular cylinders. Phys Fluids 27(1):46–59
2. Sohankar A, Norberg C, Davidson A (1996) Low-Reynolds-number flow around a square cylinder at incidence: study of blockage, onset of vortex shedding and outlet boundary condition. Int J Numer Method Fluids 26(1):39–56
3. Sharma A, Eswaran V (2004) Effect of channel confinement on the two-dimensional laminar flow and heat transfer across a square cylinder. J Numer Heat Transf 47(1):79–107
4. Kumar B, Mittal S (2006) Effect of blockage on critical parameter for flow past a circular cylinder. Int J Numer Meth Fluids 50(8):987–1001
5. Patil P, Tiwari S (2008) Effect of blockage ratio on wake transition for flow past a square cylinder. Fluid Dyn Res 40(11–12):753–778
6. Suzuki H, Inoue Y, Nishimura T, Fukutani K, Suzuki K (1993) Unsteady flow in a channel obstructed by square rod (criss-cross motion of vortex). J Heat Fluid Flow 14(1):2–9
7. Sahin M, Owens RG (2004) A numerical investigation of wall effects up to high blockage ratios on two-dimensional flow past a confined circular cylinder. Phys Fluid 16(5):1305–1320
8. Sen S, Mittal S, Biswas G (2009) Steady separated flow past a circular cylinder at low Reynolds numbers. J Fluid Mech 620:89–119
9. Verma A, Saha AK, Behra S (2017) Characteristics of two-dimensional flow past a square cylinder placed in a channel with high blockage. Fluid Mech Fluid Power Contemp Res 115–123
10. Tezduyar TE, Behr M, Mittal S, Liou J (1992) A new strategy for finite-element computations involving moving boundaries and interfaces—the DSD/ST procedure: II. Computation of free-surface flows, two-liquid flows, and lows with drifting cylinders. Comput Methods Appl Mech Eng 94:353–371
11. Paliwal B, Sharma A, Chhabra RP, Eshwaran V (2003) Power law fluid flow past a square cylinder: momentum and heat transfer characteristics. Chem Eng Sci 58:5315–5329
12. Sen S, Mittal S, Biswas G (2011) Flow past a square cylinder at low Reynolds numbers. Int J Numer Meth Fluids 67(9):1160–1174

# Transport Phenomenon Improvement Using Induce Draught in Cold Storage

**Pankaj Mishra** and **K. R. Aharwal**

**Abstract**  Air is heat transport medium in cold storage operation and its distribution plays a vital role in preservation of agricultural products like fruits and vegetables with desired quality. Thermal behaviours of cold storage system are based on air transport arrangements. Convective heat transfer from stored perishable stuff to cooling system within the chamber is subjected to airflow and its distribution. Transport characteristics can handle with axillary arrangements such as induce draught system. Experimental investigation for impact of induce draught on air transportation is carried out in a 1/4th reduced scaled model of the cold storage [size 6 m (l) × 4 m (w) × 4 m (h)] at HT Laboratory, MANIT, Bhopal. Air transport velocity was measured at 96 stations in the chamber with hot wire anemometer. Measurements indicate supply air approaches rear section of the chamber comparatively at higher velocity with induce draught. Markable improvement noticed with slotted duct wall which boosts airflow velocity by three times at mid-sections compare without induces draught. Overall 1.5 times to three times better supply airflow velocity observed in the chamber, as compare to general configuration, while return air velocity measured almost double during the experiment. Experimental results suggests shift of turbulence mixing of air from evaporator side to central zone of the chamber. Better mixing of air can help in a fast setting of thermodynamic equilibrium in the chamber. It will lead to homogenous thermal environment which can extend the life of perishable goods with maintaining their quality.

**Keywords**  Cold storage · Air transportation · Induce draught · Duct · Preservation

P. Mishra (✉) · K. R. Aharwal
Department of Mechanical Engineering, Maulana Azad National Institute
of Technology, Bhopal, Madhya Pradesh, India
e-mail: pankajhnmishra@yahoo.com

# 1 Introduction

Cold storages accommodate biodegradable items to preserve them at very low (frozen or chilled) temperature, with desired quality [1]. Efficient cold storage operation depends on various factors like chamber geometry, size and capacity of evaporator along with its mounting position, wall insulation, stockpiling arrangements, items stored and airflow distribution. [1, 2]. Airflow pattern or flow distribution is very crucial factor for life and quality of preserved food items in cold chamber. Heterogeneity in airflow causes various temperature zones in camber and it results in uneven cooling rate of stored products [1]. Samuel et al. exhibit in their research that effects of stacking arrangements on airflow and show various temperature zones in the chamber set-up due to airflow variation in chamber [2]. Irregularity in airflow causes loss of foodstuff because of high respiration rate at high temperature or injury due to frosting at low temperature [3]. Heterogeneous supply air distribution leads to higher relative humidity zone which is responsible for deterioration of potatoes because of moisture condensation at various parts of stacking [4]. Thermal behaviours of cold rooms can be altered with various ways like evaporator coil repositioning, fan speed variation and stacking arrangements changes.

Researchers were observed higher temperatures zones, because of the stagnant zones with poor ventilation in the rear part of the cold storage chamber [5–7]. To address stagnant zone problem in cold chamber, a reduced scale model is adopted in this research work. Experimental investigation of cold storage transport phenomenon is a costly affair thus most of the researchers adopt computational techniques like CFD for their research. Airflow in cold chamber analysed for various stacking arrangements, evaporator passions or for blower speed but use of auxiliary methods like induce duct, of baffled surface or other means were not considered for cold storage air distribution analysis.

In the operation of thermal power plants, kitchen and building exhaust system reverse or induce draught with duct well-established concept for enhance the flow velocity in stagnant zone. Reverse duct is a structure which produces induce draught, which causes airflow in the direction of duct, as chimney draught does in power plant. As large space of cold storage and close air circulation are major constrains for natural draught setup in cold room for the same artificial induce draught can serve the purpose.

Evaporator coil throws supply air axially along the length of the room but supply air is not able to cover whole length of the room because of flow resistance and obstacles in airflow path. As a result, stagnant zone or low airflow zone is created at rear part of the cold room. In stagnant zone, heat transfer rate through convection is low, and it may cause damage of stored foodstuff.

Presented work demonstrates effect of induce draught on airflow circulation in cold chamber with the help of flow velocity measurements at different sections of room for various conditions. Alvarez and Flick [8] find hot wire anemometer suitable to measure flow velocity, with the help of that they had investigate turbulence intensity in a cold storage chamber they also demonstrated turbulence

generation on sphere bed in airflow, when it penetrates media. Hot wire anemometer is used in present research work for flow velocity measurements.

## 2 Experimental Set-up

A cold storage prototype of 6 m (l) × 4 m (w) × 4 m (h) (at MANIT, Bhopal) was taken as reference to developed scale model for visualization purpose of airflow characteristic inside the cold storage. Model is prepared in ratio of 1:4, i.e. 1.5 m (l) × 1 m (w) × 1 m (h) with transparent acrylic sheets of 3 mm thickness. Tapsoba et al. successfully used reduced scale model for cold storage chamber mounted on truck for airflow investigation. The model was used to demonstrate and analyse of effects of various factors on airflow velocity pattern inside a cold store [9].

Geometrical and kinematic similarity is desirable between model and prototype. Model is geometrical similar with 1/4 reduction ratio as compare to prototype. For kinematic similarity, common range of Reynolds number for model and prototype is desirable. To calculate Reynolds number for prototype cross-sectional area for evaporator is 0.6 m × 2 m (1.2 m$^2$) where flow velocity at outlet of evaporator average is 1 m/s is considered. Reynolds number for prototype is calculated at the temperature of 25 °C is $Re_p$ = 59,090.91. Likewise for model evaporator cross section is 0.5 m × 0.16 m and average flow velocity, according to flow capacity required as discussed further, is selected 3.5 m/s. Reynolds number for model at 25 °C is calculated $Re_m$ = 54,449.43.

Reynolds number calculated for both has a difference of 7.85%, while taking allowance of 10% for model, Reynolds numbers are approximately in same range.

Flow capacity required for model can calculate as by Eq. 1.

$$\frac{C(\text{flow capacity}) \, \text{m}^3/\text{h}}{V(\text{Volume of cold room}) \, \text{m}^3} \tag{1}$$

$$\frac{C_p}{V_p} = \frac{C_m}{V_m} \tag{2}$$

where $C_p$ is flow capacity of prototype evaporator and $V_p$ is volume of prototype, $C_m$ and $V_m$ are flow capacity of evaporator and volume of model, respectively.

$$\text{Volume of prototype cold room} = 96 \, \text{m}^3$$
$$\text{Volume of model} = 1.5 \, \text{m}^3$$
$$\text{Capacity of evaporator coil for prototype} = 8640 \, \text{m}^3/\text{h}.$$

Thus, flow capacity for evaporator's fan in model is calculated 2.25 m$^3$/min or 135 m$^3$/h. Four axial blower fans with 0.57 m$^3$/min rated capacity each were chosen for the model with overall capacity of 2.28 m$^3$/min.

Airflow velocity measurement within cold storage chamber is a difficult work as there is turbulence present in flow because of this flow direction is not fixed, along with this reason, there is no robust and accurate device is available for flow measurement [10]. In this research work, HTC AVM 08 hot wire anemometer (shown Fig. 3b) used. It can measure air velocity in the range from 0.1 to 25 m/s with 0.01 m/s resolution. The line diagram of the experimental set-up and its photographic view is shown in Figs. 1 and 2, respectively. Line diagram represents basic arrangement of set-up and airflow direction in the chamber. Evaporator with axial blower fan is fitted such that its midpoint is 86 cm above the base of the chamber, 14 cm from back side wall and 50 cm from both side walls as shown in Fig. 1. Front face of evaporator is 22 cm from back wall.

Test is conducted on scaled model for the following three conditions:

- General configuration (without duct arrangement)
- With induce duct arrangement
- With induce duct wall having equally spaced slots cut on it.

General configuration deals with only closed chamber equipped with evaporator and measuring arrangements, no other auxiliary arrangements are placed inside the chamber. It is similar to empty cold storage plant. In this case, flow velocity in chamber was measured along the vertical central plane at different locations which were marked along the length and height of vertical planes as shown in Fig. 3a. Total ninety-six (96) stations were selected for velocity measurement.

Velocity of airflow also measured in reverse direction as well to map pattern of return air. In closed chamber, air circulation is established, i.e. supply cold air thrust
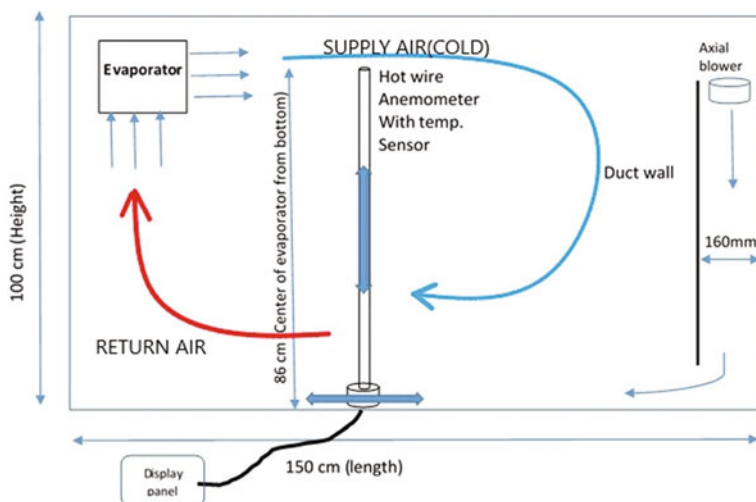


**Fig. 1** Line diagram and actual photograph of experimental set-up
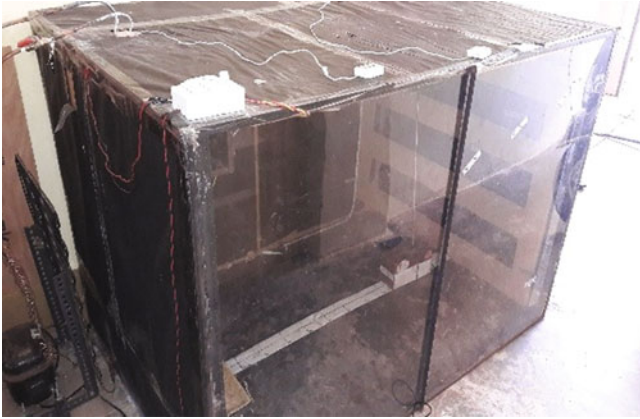
**Fig. 2** Actual photograph of experimental set-up

from evaporator is return back to it as shown in Fig. 1. Air circulation insures convective heat transfer from products to refrigerant.

For second configuration testing, induce draught system is placed at rear section of chamber, where reverse duct with two axial blowers, of flow capacity 0.57 m³/min per blower, were mounted. Duct wall is placed 16 cm away from rear wall of chamber (Fig. 1) with a gap of 11 cm from top plane and 10 cm at bottom plane. Two axial blower fans are placed in gap to force air in downward direction. These fans have mass flow rate is 1.14 CMM in combination. These fans create pressure drop as a result induce airflow through duct section.

Third experimental configuration consists of two equally spaced horizontal slots of 12 cm × 84 cm cuts on the duct wall along width of it. Fans in evaporator section run at their full combine rated capacity, i.e. 2.28 m³/min.

## 3    Result and Discussion

Airflow velocity measurements were conducted inside the model cold storage chamber for all three above-stated configurations. Velocity profile plotted between airflow velocity and length of room. Figure 4 represents velocity profile for general configuration. Evaporator fans run at their full capacity without any additional flow affecting medium in the chamber. Supply airflow velocity 10 cm in front of evaporator is almost same as that of the fan's air thrust velocity, i.e. 3 m/s. Flow velocity continuously drops from evaporator end to rear part of the chamber, as supply air move away from the evaporator section. Initially, rate of velocity drop is quite high as just 50 cm away from evaporator flow velocity remain half of the initial velocity. At 90 cm away from evaporator coil and 86 cm above ground, velocity became almost 83% less that of the initial value. Supply air velocity at
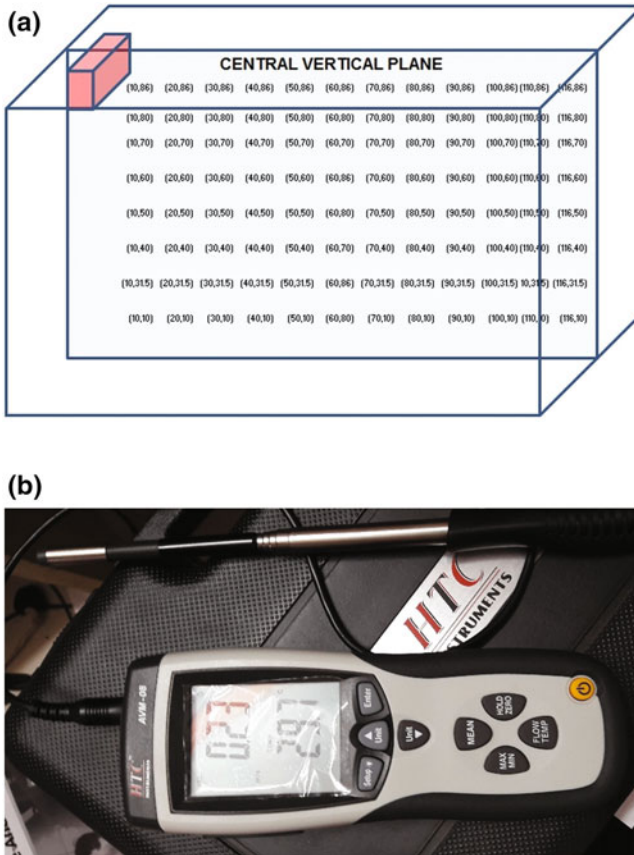
**Fig. 3** Measurement location map and instrument used. **a** Location map for observation. **b** HTC AVM -08 hot wire anemometer

50 cm above the ground recorded 1.3 m/s near evaporator and 0.25 m/s at rear section of the chamber. The results indicate that supply airflow velocity is very low at the farthest part of the chamber, because of that poor mixing conditions are prevailing. Results indicate that airflow near the evaporator coils is highly turbulent and because of this good convective heat transfer rate is likely in this part of chamber. Lowest supply air velocity was observed near rear wall of the chamber at 10 cm above ground was 0.27 m/s. Return air move through evaporator's bottom section as shown in Fig. 1. Close air circulation is setup in side the chamber as, there is no leak of air neither outward nor inward to cold storage.

In Fig. 4, airflow velocity in reverse direction plots with legends having negative signs. Plots show that return airflow velocity pickup just below evaporator section, as evaporator draw maximum airflow from its bottom and throw it axially in positive X distraction. Return air velocity at 10 cm in front of evaporator,
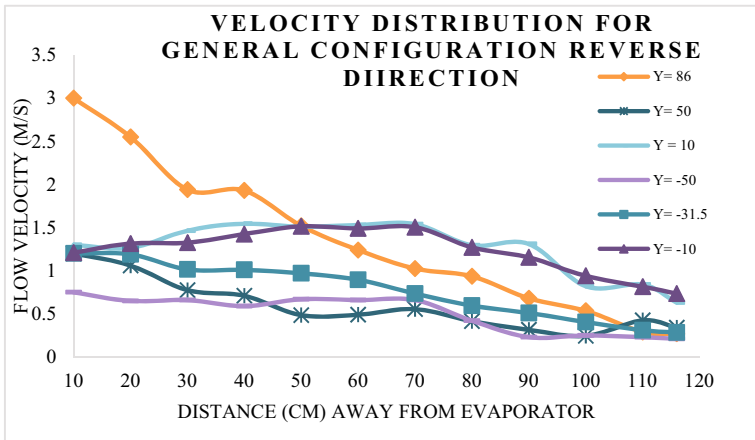
**Fig. 4** Flow velocity versus distance form evaporator graph; flow away from evaporator and flow towards evaporator (value with (−) sign shows flow towards evaporator) for cold chamber in general configuration

31.5 cm above base is 1.2 m/s and it is 1.3 m/s at 40 cm above the base. Measurements for general configuration clearly illustrate that there are certain areas in the chamber where airflow is not properly reached because of that heat transfer suffer in those sections.

It is clear from the above discussion that there is a need to build such arrangements which would be able to improve flow distribution in such a manner so that supply air can reach farthest parts of the chamber. On the basis of above discussion, the concept of induce duct is introduced here as a solution. In Figs. 4 and 5, results were plotted which indicated the impact of induce draught on cold storage chamber in terms of velocity profile.

An induce duct arrangement is placed opposite to evaporator section or in rear section of chamber. Figure 5 represents effect of duct on airflow pattern in chamber, and it indicated that there is a significant rise in flow velocity inside the chamber because of induce draught arrangements.

On comparing Figs. 4 and 5, it is observed that airflow inside the chamber is improved when reverse duct system is in action. Graph plotted for velocity profile represents that at 86 cm above ground and 110 cm in front of evaporator, the flow velocity is improved from 0.5 to 1.4 m/s. It reflects that because of induce duct the reach of supply airflow improved in farthest parts of the chamber. The flow velocity was almost fifty present at mid-way if induce draught was not used.

On the observation of velocity profile (Fig. 5) for return airflow when induce drought is in operation, it is found that return airflow velocity is 35–44% more as compared to general configuration. Induce draught clearly improves flow at top and bottom section as flow velocities were higher as compare to general configuration, but central region is merely affected. Flow velocity in central zone, i.e. at 40 cm in
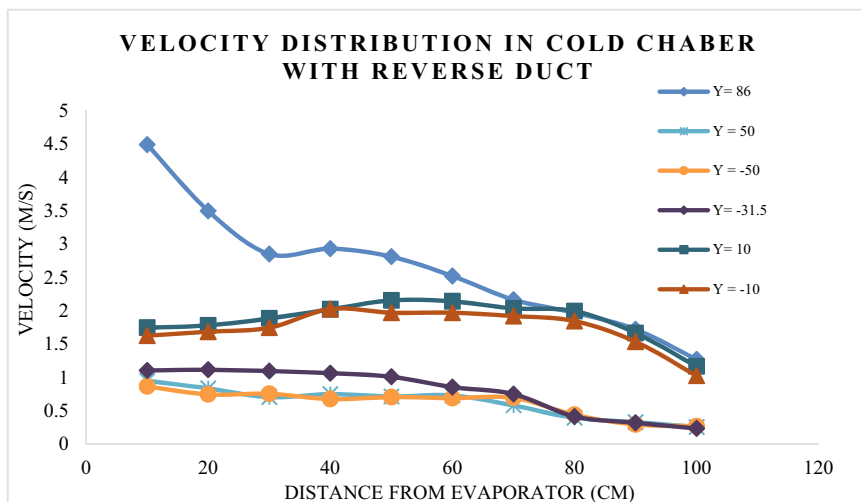
**Fig. 5** Flow velocity versus distance form evaporator graph; flow away from evaporator and flow towards evaporator (value with (−) sign shows flow towards evaporator) for cold chamber with reverse duct

front of duct and 40 mm above base is marginally affected by reverse duct and values of velocity similar as in the first condition. To overcome this situation, slots were cuts on duct wall as discussed in experimental set-up section and measurements were taken for the same, results are as indicates in Fig. 6.

Observations made for the third configuration indicted that flow velocity is slightly drop at top level of the room, but overall flow velocity was improved in remaining parts of the chamber. Even though return airflow is also improved as compared to first two cases. Velocities were recorded for third configuration, 9–16% higher as compared to the second configuration at mid-parts of the chamber. More ducting arrangements may be tested for better solution.

Experimental results as discussed above indicate that induce duct system can improve the airflow distribution in cold chamber. Slots cut on induce duct in the last case further improve velocity, especially in mid-section of cold chamber. Experimental results conclude that use of induce duct is advantageous in cold storage operation as because of this uniform flow distribution reduce the load on cooling system. More convective heat transfer could be possible because of proper mixing of air. Results suggest that with reverse draught air movements in the chamber is cover all parts that insure even temperature distribution. Uniform temperature distribution ensures reduction in frosting chance inside the chamber.
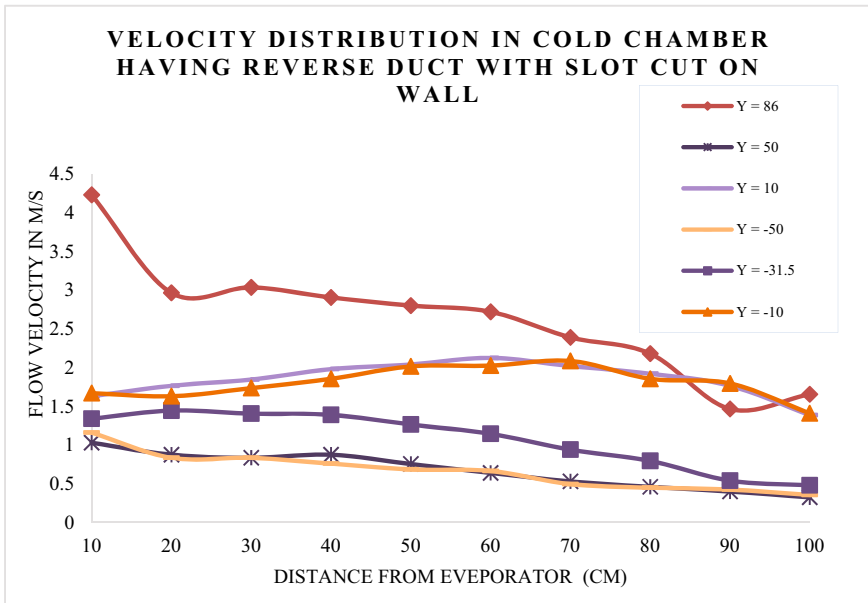
**Fig. 6** Flow velocity versus distance form evaporator graph; flow away from evaporator and flow towards evaporator (value with (−) sign shows flow towards evaporator) for cold chamber with reverse duct and slot cuts on duct wall

## 4    Conclusion

In the present study, the velocity distribution and instantaneous temperature of flow air inside the cold chamber for three different conditions have been investigated. Results show that there is significant improvement in airflow velocity with induce duct arrangement. The use of induce duct is advantageous in cold storage operation as it will be able to maintain uniform flow distribution inside the chamber which reduces cooling load on refrigerating system. The proper air circulation will also ensure reduction in frosting chance inside the chamber and increase the life of food articles. More reverse ducting arrangements with various position and size of slots and blower fans can be investigated for future research work. In this investigation, empty cold storage was used, for better picture same investigation can repeat with live load of agricultural products.

## References

1.  Getahun S, Ambaw A, Delele M, Meyer CJ, Opara UL (2017) Analysis of airflow and heat transfer inside fruit packed refrigerated shipping container: part I—model development and validation. J Food Eng 203(June):58–68

2. Getahun S, Ambaw A, Delele M, Meyer CJ, Opara UL (2017) Analysis of airflow and heat transfer inside fruit packed refrigerated shipping container: part II—evaluation of apple packaging design and vertical flow resistance. J Food Eng 203(June):83–94

3. Nahor HB, Hoang ML, Verboven P, Baelmans M, Nicolai BM (2005) CFD model of the airflow, heat and mass transfer in cool stores. Int J Refrig 28:368–380

4. Chourasia MK, Goswami TK (2001) Losses of potatoes in cold storage vis-à-vis types, mechanism and influential factors. J Food Sci Technol 38:301–313

5. Meffert HFT, Nieuwenhuizen GV (1973) Temperature distribution in refrigerated vehicles. In: Proceedings of I.I.F.-I.I.R., Commissions D1, D2 and D3, Barcelona, Spain

6. Gogus AY, Yavuzkurt S (1974) Temperature pull-down and distribution in refrigerated trailers. In: Proceedings of I.I.F.-I.I.R. Commissions D2, 2, Wageningen, Netherlands

7. Lenker DH, Wooddruff DW, Kindya WG, Carson EA, Kasmire RF, Hinsch RT (1985) Design criteria for the air distribution systems of refrigerated vans. ASAE Paper 28(6):2089–2097

8. Alvarez G, Flick D (1999) Analysis of heterogeneous cooling of agricultural products inside bins. Part I: aerodynamic study. J Food Eng 39:227–237

9. Tapsoba M, Moureh J, Flick D (2006) Airflow patterns in an enclosure loaded with slotted pallets. Int J Refrig 29:899–910

10. Hoang ML, Verboven P, De Baerdemaeker J, Nicolai BM (2000) Analysis of the airflow in a cold store by means of computational fluid dynamics. Int J Refrig 23:127–140

# Thermal Performance of Solar Air Heater Having Triangular-Shaped Hollow Bodies Inside

**Ambreesh Prasad Shukla, Bhupendra Gupta, Rakesh Kushwaha and P. K. Jhinge**

**Abstract** Today, solar energy has emerged as an alternate to the conventional source of energy. Solar air heater (SAH) is one of the significant devices to convert solar energy into heat energy of fluid. Lower efficiency of SAHs is one of the major drawbacks. Hence, researcher in the recent past tried to increase efficiency of SAHs by putting different shapes and arrangement of roughness and baffles on the absorber plate. In this work, triangular-shaped hollow bodies are putted inside the solar air heater to improve its efficiency. Turbulence is produced locally due to existence of these bodies. Here, these bodies will act as fins also. This results in increase of heat transfer area and heat transfer coefficient between absorber and air. Loss of pressure is also less. Maximum enhancement obtained in efficiency is 8.34% for the mass flow rate at 0.012 kg/s. Maximum rise in temperature for Case-I (without triangular bodies) was recorded as 10.2 °C, whereas for Case-II (with triangular bodies) 13.1 °C achieved. CFD simulation results and experimental results obtained have good agreement.

**Keywords** Solar air heater · Triangular hollow bodies · Efficiency

## 1 Introduction

Solar energy is easily, freely, and abundantly available in nature. It is a clean and cheap energy to be exploited for various applications in India. Flat plate solar collectors are commonly used to harness solar thermal energy [1]. Solar air heater (SAH) significantly converts solar energy into thermal/heat energy. It acts as a type of heat exchanger. It has various applications like room heating, crop drying, banana drying, and rubber drying. [2]. Standard components of solar air heater are: a rectangular box structure insulated from three sides, a top glass cover, and air passage/duct. Sometimes, an air blower is used to force flow of air. The bottom of the

A. P. Shukla · B. Gupta (✉) · R. Kushwaha · P. K. Jhinge
Jabalpur Engineering College, Jabalpur 482011, India
e-mail: bhupendra243@yahoo.com

rectangular box consists of metallic absorber plate. The box is thermally insulated from all the sides and bottom surface. On the top of the box, a glass or plastic cover is used to trap the solar radiations and transfer heat to the absorber plate and inside air [3]. The efficiency of SAH is low due to low convective heat transfer coefficient between flowing air and absorber [4]. Enhancement of the efficiency of solar air heater can be done by either increasing heat transfer coefficient, or by increasing the heat transfer area. In order to increase heat transfer coefficient the laminar sub layer formed adjacent to absorber plate within the turbulence zone must be destroyed. It can be achieved by providing roughness element on the absorber plate which will dissolve the laminar sublayer from adjacent to absorber plate. Various configurations of SAHs and various roughness geometries studied by the investigators and also experimentally tested [5–8].

Saxena et al. [9] designed and evaluated thermal performance of a novel solar air heater. Chabane et al. [10] have experimentally studied the effect of placing longitudinal fin on absorber plate. Gawande et al. [11] have performed an experimental and analytical study of thermos-hydraulic performance of roughened solar air heater roughened with angled square rib. Singh et al. [12] experimented investigation and developed correlation for Nusselt number and friction factor for solar air heater, artificially roughened with multiple arc shapes. Thakur et al. [13] have experimentally investigated the effect of placing hyperbolic rib on the absorber plate of solar air heater. Gabhane et al. [14] have planned to investigate the effect of placing multiple C-shape rib on absorber plate of solar air heater. Sawhney et al. [15] have been experimentally studied artificially roughened solar air heater with wavy-up delta winglet vortex generators.

In continuation with the line of research going on, experiments have been conducted on self-constructed solar air heater placed at Mechanical Engineering Department building of JEC, Jabalpur, India (latitude 23.1815°N, longitude 79.9864°E, altitude 412 m above the Sea level). In this work, efficiency comparison has been carried out between two SAHs with and without triangular-shaped hollow bodies provided on the absorber plate. Two different absorbing plates (with and without hollow bodies) are used in this study. The efficiencies of both the SAHs are determined from the experimental data.

## 2 Experimental Setup and Methodology

Figure 1a, b shows actual Photographs of experimental setup for solar air heater fabricated on site at Jabalpur, India. A schematic diagram of single flow SAH with absorber plates is shown in Fig. 2a, b.

In this study, two types of absorber plates were constructed and used, i.e., with and triangular-shaped hollow bodies. Aluminum is used to make absorber plate which is coated with normal black paint. Plate thickness, length, and width for both types of absorber plates are 1 mm $\times$ 1 m $\times$ 0.5 m, respectively. Single top glass having 5 mm thickness is used as glaze surface. Thermal radiation losses and wind
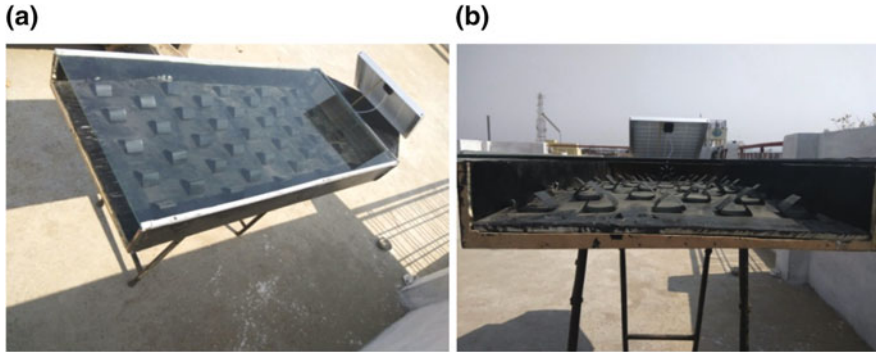
**Fig. 1** Various images of experimental setup



**(a) Top view of Case-II**

**(b) Front view of Case-II**
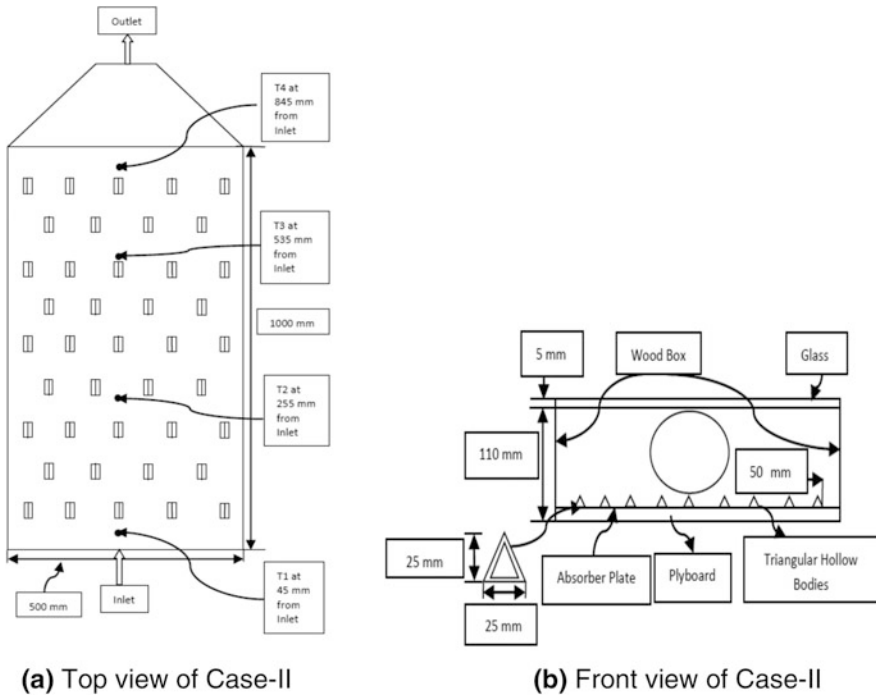
**Fig. 2** Schematic top and front view of solar air heaters

losses are presumed negligible. Case-I refers to the simple absorber plate with no bodies, whereas Case-II refers to the absorber plate with triangular-shaped hollow bodies. All these bodies are also coated with normal black paint. These bodies are arranged in zigzag configuration, and 45 numbers of bodies have been used in this setup. Surface cleaning of these bodies is done using water. For weathering

processes, both SAHs were left operational few days before starting readings. Overall dimensions of the setup are $1350 \times 500 \times 110$ mm$^3$. Air has a rectangular inlet and circular outlet.

Inlet area is $500 \times 80$ mm$^2$ and circular outlet has 80 mm diameter. At outlet pipe of 80 mm diameter is provided so that outside air does not influence the properties of air coming out from the solar air heater. Digital thermometer is used to measure inlet and outlet air temperatures. Total solar radiations (direct plus diffused) instance on the top glass is measured using Solar Power Meter (in W/m$^2$) in the same plane. The velocity of air flowing through the setup is measured using anemometer in m/s. The anemometer is placed at outlet. All these measurements were recorded manually. The measurements were recorded after every hour. Various measured parameters are: inlet and outlet temperatures of air flowing through the setup, absorber plate temperatures at specified locations and air velocity, incident solar radiation. Experiments were started from 9 am and ended up around sunset 6 pm.

## 3   Thermal Performance Analysis of SAHs

The mathematical model is presented to study the thermal performance of both Case-I and Case-II solar air heater. Useful heat gain by the air and overall heat loss coefficient is calculated. First of all heat balance equation is applied on the SAH,

$$[Q_{\text{acu}}] + [Q_{\text{gain}}] = [Q_{\text{abs}}] - [Q_{\text{L}}] \tag{1}$$

Here,

Accumulated energy = Energy absorbed by the absorber plate and mathematically given by

$$Q_{\text{acu}} = M_{\text{p}} C_{\text{p}} (\mathrm{d}T_{\text{p,ave}}/\mathrm{d}t) \tag{2}$$

Energy gain = Energy gain by air during flow from inlet to outlet and given by

$$Q_{\text{g}} = m_{\text{a}} C_{\text{pa}} (T_{\text{in}} - T_{\text{out}}) = h_{\text{pa}} A_{\text{ht}} (T_{\text{fm}} - T_{\text{mp}}) \tag{3}$$

Absorbed energy = Solar Energy transmitted to the absorber plate and is given by

$$Q_{\text{abs}} = I A_c \tag{4}$$

Lost energy $Q_{\text{L}}$ = Top Loss $(Q_{\text{T}})$ and bottom surface Loss $(Q_{\text{B}})$

$$Q_{\text{L}} = Q_{\text{T}} + Q_{\text{B}} \tag{5}$$

From Eqs. (1)–(5), the thermal energy balance equation for the solar collector becomes

$$M_{\text{p}}C_{\text{p}}\big(\mathrm{d}T_{\text{p,ave}}/\mathrm{d}t\big) + m_{\text{a}}C_{\text{pa}}(T_{\text{in}} - T_{\text{out}}) = IA_{\text{c}} - Q_{\text{L}} \tag{6}$$

SAH thermal efficiency is the ratio of energy gain by air flowing from inlet to outlet to the total solar radiations instance on the top glass,

$$\eta = \big[m_{\text{a}}C_{\text{pa}}(T_{\text{in}} - T_{\text{out}})\big]/(IA_{\text{c}}) \tag{7}$$

Air flow rate can be given by,

$$m_{\text{a}} = \rho A v \tag{8}$$

To calculate SAH efficiency, different parameters like $T_{\text{in}}$, $T_{\text{out}}$, $I$, $v$, $m_{\text{a}}$, have been measured.

## 4 Numerical Solution

To study the performance of SAHs with given changes, three-dimensional fluid domain model was created using ANSYS design software for Case-I (without hollow bodies) and Case-II (with rectangular hollow bodies) as indicated in Fig. 3a, b. For Case-I, simple cuboidal shape fluid domain with dimension $1000 \times 500$ $80 \text{ mm}^3$ has been created. For Case-II, fluid domain along with triangular-shaped hollow bodies is prepared. Outer dimension of type-II fluid domain is same as of type-I. After preparing fluid domain for both the cases, meshing is done. ANSYS FLUENT 16.0 is used to solve the fluid domain with given boundary conditions. Boundary conditions are: outlet is considered as pressure outlet and inlet is defined as mass flow inlet. The top surface is considered as glazing and made of glass and exposed to mixed heat transfer, i.e., convection along with radiation heat transfer. The bottom absorber plate is considered as an opaque surface made of aluminum. Constant heat flux condition is applied to bottom surface. Side surface is also considered as an opaque, made of wood material. Side surface considered to be subjected to convection. $K$-$\varepsilon$ turbulence model is used to solve fluid domains. The sun's direction vector is defined by inbuilt solar calculator. Results have been evaluated using standard solution approach.

**(a)** Case-I                                               **(b)** Case-II
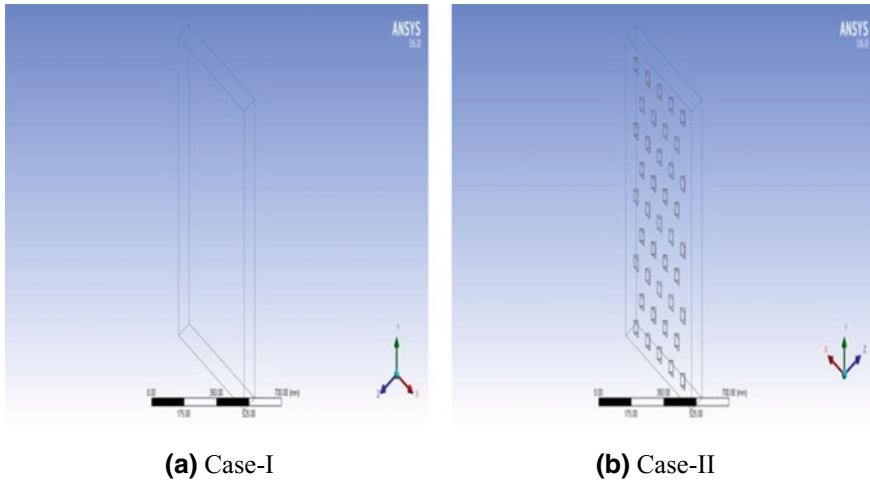
**Fig. 3** Fluid domains

## 5    Results and Discussion

### 5.1    *Experimental Results*

Tests have been conducted on two consecutive days in September 2017 under almost similar weather conditions. Both the SAHs were kept in horizontal position facing south direction. All parameters were recorded at a regular interval of 1 h. All experiments were performed from 9:00 am to 6:00 pm.

(i) *Fig.* 4*a, b shows* variation of inlet and outlet air temperature with respect to time. Figure also shows that how outlet air temperature varies with inlet temperatures. Maximum air temperature raise of 10 and 13.1 °C have been recorded for Case-I and for Case-II, respectively.

(ii) *Fig.* 5 *shows* the variation of efficiency of solar air heater with respect to time. Maximum efficiency for Case-I is 36.18% at 2:00 pm and for Case-II is 39.20% at 1:00 pm recorded. It can also be seen from graphs that efficiency for Case-II increases at faster rate than for Case-I. The maximum enhancement for efficiency of Case-II is 8.34% higher than Case-I.

### 5.2    *Results from CFD Simulation*

CFD analysis has also been carried out for Case-I and Case-II to validate experimental results trend. Results obtained are discussed below.

**(a)** Case-I          **(b)** Case-II
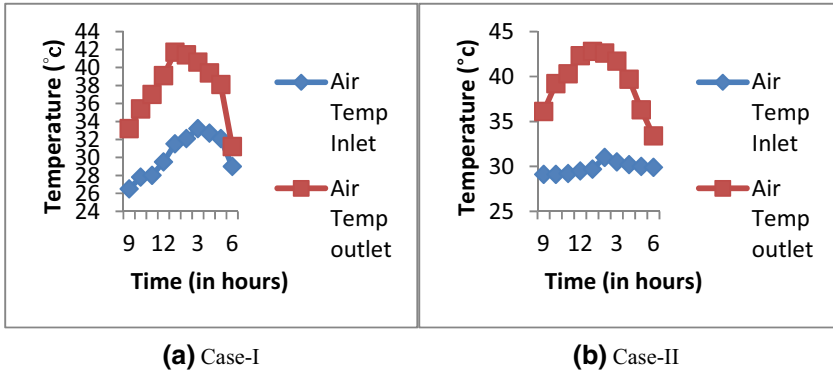
**Fig. 4** Comparison between inlet and outlet temperatures with time

**Fig. 5** Comparison of thermal efficiency for Case-I and Case-II
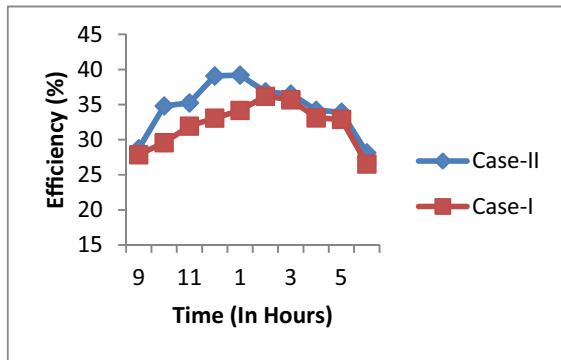


(i) *Case-I (SAH without hollow bodies)*

Figure 6a shows temperature profile of SAH for Case-I. It shows that the temperature of air is maximum near the absorber plate, this is due to the layer of air near absorber plate achieves thermal equilibrium with plate but in transverse plane near the entry section, effect of heat transfer has not breached in the center lamina. But, as the distance from inlet increases, wall temperature effect penetrates into the center lamina, but still near outlet heat transfer effect has not breached into entire stream of air. Figure 7a shows temperature distribution of absorber plate for Case-I.

(ii) *Case-II (SAH with triangular hollow bodies)*

Temperature profile of SAH for Case-II is shown in Fig. 6b. As we go away from inlet, the wall temperature effect, i.e., heat transfer effect has penetrated into the free stream of air earlier then in Case-I, this is due to the presence of triangular hollow bodies due to which heat transfer area is increased and at the same time turbulence

**(a)** Case-I  **(b)** Case-II
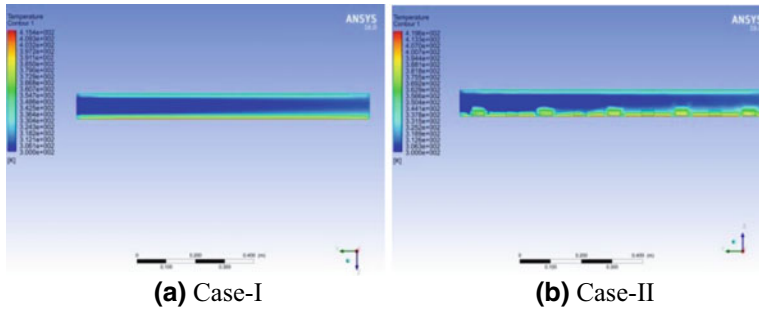
**Fig. 6** Temperature contour of SAH



**(a)** Case-I  **(b)** Case-II
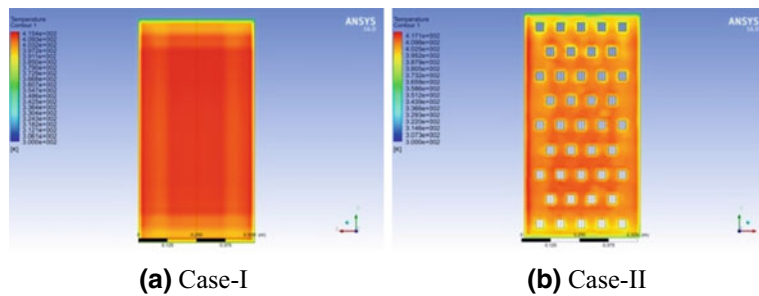
**Fig. 7** Temperature contour of absorber plate

is also produced locally due to which breaking of laminar sublayer takes place and heat is transferred more efficiently to the stream of air. It has also been seen that near outlet heat transfer effect has breached into entire air stream, resulted in enhancement of outlet air temperature. For Case-II, temperature distribution profile of absorber plate is shown in Fig. 7b.

## 6 Conclusions

Following conclusion can be made from experimental and CFD simulation results:

- The efficiency of solar air heater without hollow bodies and with hollow bodies were 36.18 and 39.20%, respectively. So, an increase of 8.34% in efficiency has been recorded with hollow bodies.
- Air temperature rise for solar air heater without hollow bodies and with hollow bodies were 10.2 and 13.1 °C, respectively. So, air temperature raised by 2.9 °C more.

- CFD simulation results obtained for Case-I and Case-II also show good agreement with the experimental results.
- Finally, we can conclude enhancement in performance of SAH has been recorded by putting such triangular hollow bodies.

## References

1. Kumar K, Prajapati DR, Samir S (2017) Heat transfer and friction factor correlations development for solar air heater duct artificially roughened with 'S' shape ribs. Exp Therm Fluid Sci 82:249–261
2. Sharma SK, Kalamkar VR (2017) Experimental and numerical investigation of forced convective heat transfer in solar air heater with thin ribs. Sol Energy 147:277–291
3. Omojaro AP, Aldabbagh LBY (2010) Experimental performance of single and double pass solar air heater with fins and steel wire mesh as absorber. Appl Energy 87:3759–3765
4. Esen H (2008) Experimental energy and energy analysis of a double-flow solar air heater having different obstacles on absorber plates. Build Environ 43:1046–1054
5. Gupta AD, Varshney L (2017) Performance prediction for solar air heater having rectangular sectioned tapered rib roughness using CFD. Therm Sci Eng Prog 4:122–132
6. Alam T, Kim M-H (2016) Numerical study on thermal hydraulic performance improvement in solar air heater duct with semi ellipse shaped obstacles. Energy 112:588–598
7. Li S, Meng X, Wei X (2015) Heat transfer and friction factor correlations for solar air collectors with hemispherical protrusion artificial roughness on the absorber plate. Solar Energy 118:460–468
8. Priyam A, Chand P (2016) Thermal and thermohydraulic performance of wavy finned absorber solar air heater. Sol Energy 130:250–259
9. Saxena A, Srivastava G, Tirth V (2015) Design and thermal performance evaluation of a novel solar air heater. Renew Energy 77:501–511
10. Chabane F, Moummi N, Benramache S (2014) Experimental study of heat transfer and thermal performance with longitudinal fins of solar air heater. J Adv Res 5:183–192
11. Gawande VB, Dhoble AS, Zodpe DB, Chamoli S (2016) Analytical approach for evaluation of thermo hydraulic performance of roughened solar air heater. Case Stud Therm Eng 8:19–31
12. Singh AP, Varun, Siddhartha (2014) Heat transfer and friction factor correlations for multiple arc shape roughness elements on the absorber plate used in solar air heaters. Exp Therm Fluid Sci 54:117–126
13. Thakur DS, Khan MK, Pathak M (2017) Solar air heater with hyperbolic ribs: 3D simulation with experimental validation. Renew Energy 113:357–368
14. Gabhane MG, Kanase-Patil AB (2017) Experimental analysis of double flow solar air heater with multiple C shape roughness. Solar Energy 155:1411–1416
15. Sawhney JS, Maithani R, Chamoli S (2017) Experimental investigation of heat transfer and friction factor characteristics of solar air heater using wavy delta winglets. Appl Therm Eng 117:740–751

# Heat Transfer Enhancement in Oblique Finned Channel

**Badyanath Tiwary, Ritesh Kumar and Pawan Kumar Singh**

**Abstract** In the modernistic day, cooling is one of the predominant challenges of electronic and automobile industry. The demand for faster and smaller devices increases the thermal load, and at the same time, conventional cooling techniques that use extended surfaces (fins, microchannel, heat sink, heat pipe, etc.) reached their limits. Recently, oblique fin heat sink has been found as an alternative to conventional heat sink because of their improved heat transfer performance and a marginal increase in pressure drop. The reason behind this improved heat transfer is the breakage of the continuous fin into oblique fin which keeps the flow in developing condition. Also, the secondary flow through oblique channel diverts a small fraction of flow and enhances mixing. The present paper tries to capitalize the advantage of the oblique fin with the benefits of nanofluid by carrying out a detailed numerical simulation. Alumina–water nanofluid has been used for numerical analysis using single-phase and discrete phase modeling approaches through oblique fin microchannel. Conjugate heat transfer between the oblique fin heat sink and nanofluid is computed numerically. Approximately, 115 and 145% heat transfer enhancement has been observed in oblique channel compared to rectangular microchannel in single-phase modeling and discrete phase modeling, respectively.

**Keywords** Nanofluid · Enhanced microchannel · Oblique fin · DPM

## Nomenclature

| | |
|---|---|
| $P$ | Pressure (Pa) |
| $C_p$ | Specific heat capacity (J/kg K) |
| $T$ | Temperature (°C or K) |

B. Tiwary (✉) · R. Kumar · P. K. Singh
Department of Mechanical Engineering, Indian Institute of Technology (ISM),
Dhanbad 826004, Jharkhand, India
e-mail: tiwary21@gmail.com

R. Kumar
e-mail: ritesh.kumar.mec11@gmail.com

P. K. Singh
e-mail: pawan@iitism.ac.in

| $k$ | Thermal conductivity (W/m K) |
|---|---|
| $t$ | Time (S) |
| $F_D$ | Drag force (N) |
| $g$ | Gravitational acceleration (m/s$^2$) |
| $F$ | Force term |
| $h$ | Heat transfer coefficient (W/m$^2$ K) |
| $D_h$ | Hydraulic diameter (mm) |
| $\Delta P$ | Pressure drop (Pa) |
| $Re$ | Reynolds number |
| $f$ | Friction factor |
| DPM | Discrete phase model |

**Greek Symbols**

| $\nabla$ | Del (operator) |
|---|---|
| $\rho$ | Density (kg m$^{-3}$) |
| $\mu$ | Dynamic viscosity (Pa s) |
| $\phi$ | Nanoparticle volumetric fraction |

**Subscripts**

| eff | Effective |
|---|---|
| f | Pressure drop penalty factor |
| NF | Nanofluid |
| BF | Base fluid |
| P | Particle |
| l | Liquid |
| avg | Average |

# 1  Introduction

The continuous growth in the direction of miniaturization and advancement in electronics and automobile industries have been pushed to boost the system performance which often comes up with high heat generation which needs to be dissipated within limited space. International Technology Roadmap for Semiconductors (ITRS) forecast in 2012 that the integrated circuits demand high power density up to 100 W/cm$^2$ in 2020 [1]. Moreover, power density in microscale with elevated packing density in the field such as weapon, laser, and radar could generate 1000 W/cm$^2$ of heat flux [2]. The conventional cooling methods are not enough to fulfill the present-day cooling requirement. The cooling achieved by microchannel has been pushed to its limit, and there is a need for novel microchannels which can enhance heat dissipation with marginal or no increase in

the pressure drop compared to the conventional microchannel. One of the microchannels is oblique fin channel. The reason behind this is the breakage of the continuous fin into oblique fin keeps the flow in developing condition and also the secondary channel diverts flow in a small fraction and enhances mixing. The efficiency of these microchannels can be further increased by using a better cooling liquid having higher thermal conductivity compared to a conventional cooling fluid, which is a colloidal suspension of nanoparticle in a base fluid having magnificent thermo-physical properties named as nanofluid. The nanoparticle is made up of metal, oxides, carbide, carbon nanotube (CNT), etc [3–5].

As early, Tuckerman and Pease [6] suggested the concept of liquid cooling with the microchannel to enhance the heat transfer performance by accomplishing greater heat transfer rate up to 800 W/cm$^2$ with microchannels in single-phase and discrete phase flows. This landmark work paved the door for further research in the field of microchannel heat transfer.

Wang and Peng [7] investigated experimentally the single-phase forced convective heat transfer characteristics of water/methanol flowing through the rectangular microchannel. The results show considerable insight and significant data into the nature of forced-flow convection in microchannels.

Lee et al. [8] made oblique fin in a microchannel heat sink in order to modulate the flow. This results in the local and global heat transfer enhancement. Numerical analysis of laminar flow and heat transfer showed that heat transfer enhanced significantly with negligible pressure drop. The mixing of primary and secondary flow effect gives much improved heat transfer performance by 80%. Also, there is a decrement of maximum wall temperature and temperature gradient.

Lee et al. [9] investigated the outcome of heat transfer performance on the secondary channel in the oblique fin microchannel. The secondary flow was introduced by parting a small channel in the straight channel at a certain angle. Simulation results are validated by conducting an experiment. The width of 100 and 200 µm is used in this study for a different flow range of 100 to 500 mL/min. It was found that heat dissolution potential in the oblique fin is much improved than the straight channel. However, edge effect caused a large fluctuation in the distribution of temperature and decreased the thermal performance. The present study has been validated with this research paper for water before taking alumina–water nanofluid as working fluid.

From the detailed literature survey, it has been noticed that very few studies have been conducted on the novel oblique fin micro-/minichannel heat sink with nanofluid as cooling fluid may result in good heat transfer performance. Thus, in the present study numerical simulation on heat transfer performance using an oblique finned channel with the use of nanofluid is to be performed using both single-phase and discrete phase modeling.

## 2   Mathematical Modeling

The two main approaches which are to be considered for numerical simulation of nanofluid are mixture rule or single-phase modeling and discrete phase modeling (DPM). In mixture rule, nanofluid is assumed to be single-phase homogeneous fluids, whereas in DPM the fluids are assumed to have continuous phase and for this continuous phase, flow and heat transfer are governed by general Navier–Stokes equation and energy balance equation. It is also called Eulerian–Lagrangian approach. The particles are injected in this flow field, and the motion of these particles is governed by Newton's second law which depends on various forces acting on the particles.

For the purpose of the numerical study, a single row of the rectangular and oblique channel has been designed in SOLIDWORKS and meshed in ANSYS 15 [10]. Meshing for both fluid and solid domains is done separately. The simulation domain has been meshed using face sizing, body sizing, and sweep method in ANSYS mesh (Figs. 1, 2, and 3; Table 1).

To simplify the analysis, certain assumptions are considered in the analysis of flow such as steady state, laminar, negligible radiative heat transfer, negligible convective heat transfer, negligible viscous dissipation from the oblique fin heat sink, and constant fluid properties.

**Solution Method**

The governing differential equations for alumina nanofluid using mixture rule are

1. Continuity equation

$$\nabla \cdot (\rho \vec{v}) = 0 \tag{1}$$
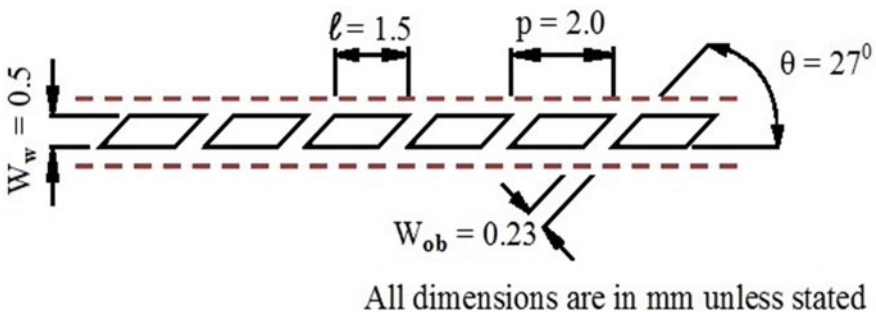


**Fig. 1** Schematic diagram of oblique fins
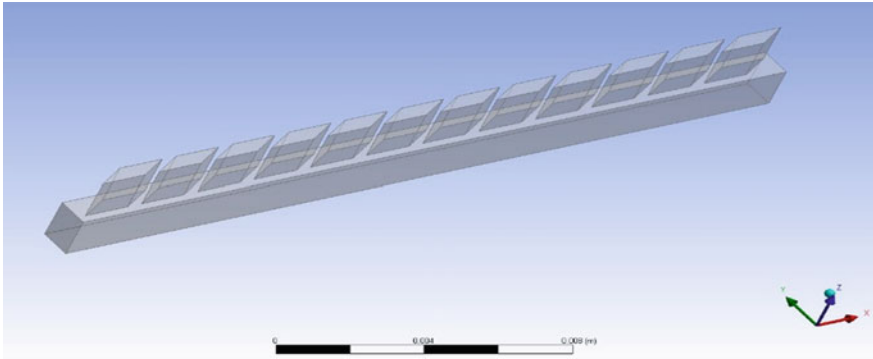
**Fig. 2** Geometry of oblique fin channel
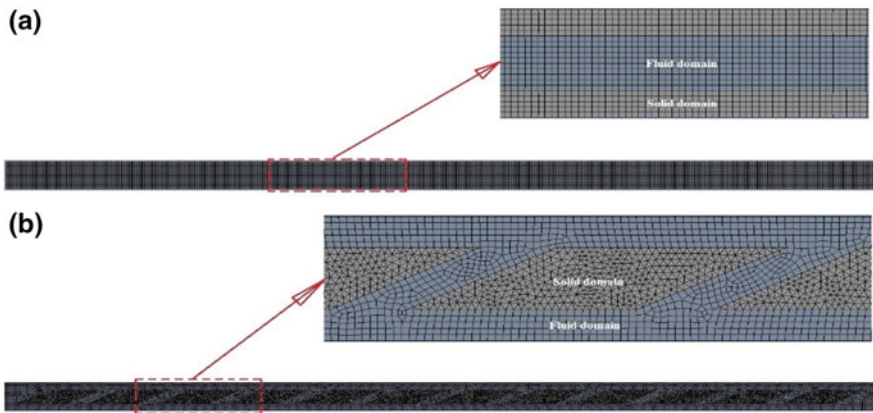


**Fig. 3** Meshing of **a** straight channel and **b** oblique finned channel

| | Characteristics | Dimensions |
|---|---|---|
| **Table 1** Dimension of oblique finned channel | Material | Aluminum |
| | Channel width, $W_{ch}$ (μm) | 500 |
| | Fin width, $W_w$ (μm) | 500 |
| | Channel depth (μm) | 1500 |
| | Fin length, $l$ (μm) | 1500 |
| | Fin pitch, $p$ (μm) | 2000 |
| | Oblique angle, $\theta$ (°) | 27 |
| | No. of fins | 12 |

2. Momentum equation

$$\nabla \cdot (\rho \vec{v}\vec{v}) = -\nabla P + \nabla \cdot (\mu \nabla \vec{v}) \tag{2}$$

3. Energy equation

$$\nabla \cdot (\rho \vec{v} C_p T) = \nabla \cdot (k \nabla T) \tag{3}$$

The thermo-physical properties of alumina-based nanofluid at 1, 2, and 4% volumetric concentration in this analysis, for mixture rule, have been calculated by the following equation.

The thermal conductivity of the alumina nanofluid is given by Hamilton–Crosser model [11],

$$k_{\text{eff}} = k_f (1 + C_k \varnothing) \tag{4}$$

where $C_k$ is taken as 4.

The viscosity of the suspension is given by:

$$\mu_{\text{NF}} = \mu_{\text{BF}} (1 + C_\mu \varnothing) \tag{5}$$

where $C_\mu$ is viscosity coefficient. The value of $C_\mu$ is taken as 5 for alumina–water nanofluids.

The effective density of nanofluids is given by:

$$\rho_{\text{NF}} = \rho_{\text{BF}} (1 - \varnothing) + \rho_P \varnothing \tag{6}$$

The specific heat of nanofluids is defined as (Tables 2 and 3):

Table 2 Thermo-physical property of nanofluid using mixture rule

| $\phi$ (%) | $\rho$ (kg/m$^3$) | $C_p$ (J/kg K) | $K$ (W/m K) | $\mu$ (Pa s) × e-03 |
|---|---|---|---|---|
| 1 | 1027.01 | 4147.94 | 0.632 | 0.933 |
| 2 | 1055.83 | 3938.73 | 0.656 | 0.978 |
| 4 | 1113.47 | 3720.73 | 0.705 | 1.067 |

Table 3 Thermo-physical property of alumina

| Properties | Value |
|---|---|
| Density (Kg/m$^3$) | 3890 |
| Specific heat capacity (J/Kg K) | 776.42 |
| Thermal conductivity (W/m K) | 37.717 |

$$C_{\text{pNF}} = \frac{\rho_{\text{f}} C_{\text{pf}}(1 - \varnothing) + \rho_{\text{P}} C_{\text{Pp}\varnothing}}{\rho_{\text{f}}(1 - \varnothing) + \rho_{\text{P}}\varnothing} \tag{7}$$

For discrete phase modeling, differential equations are as follows [12]
Continuity equation

$$\nabla \cdot (\rho \vec{v}) = 0 \tag{8}$$

Momentum equation for base fluid

$$\nabla \cdot (\rho \vec{v}\vec{v}) = -\nabla P + \nabla \cdot (\mu \nabla \vec{v}) + S_{\text{m}} \tag{9}$$

Momentum equation for nanoparticle

$$\frac{\mathrm{d}\vec{v_{\text{P}}}}{\mathrm{d}t} = F_{\text{D}}(\vec{v} - \vec{v_{\text{P}}}) + \frac{g(\rho_{\text{P}} - \rho_{\text{l}})}{\rho_{\text{P}}} + \vec{F} \tag{10}$$

F term represents the additional thermophoretic force, Saffman lift force, Brownian motion, etc.

## 3   Results and Discussion

Figure 4 shows pressure drop in flow through the rectangular channel and oblique finned channel. Both are nearly same at lower Reynolds number, but at higher Reynolds number, a significant change in pressure drop has been observed in the oblique finned channel due to irregular flow.
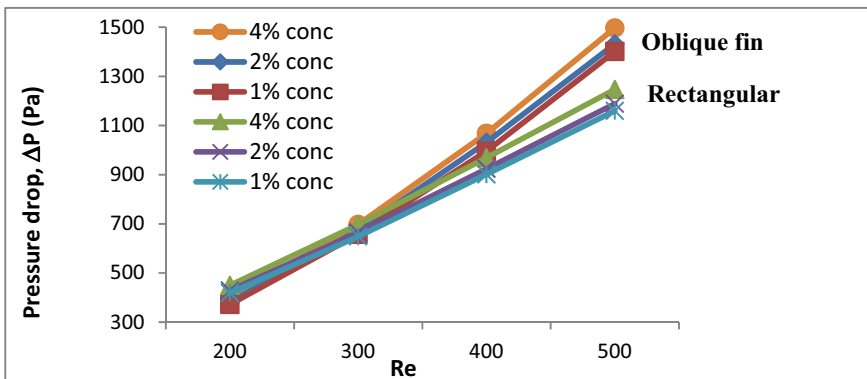


**Fig. 4** Pressure drop versus *Re* in oblique fin and rectangular channel using mixture rule
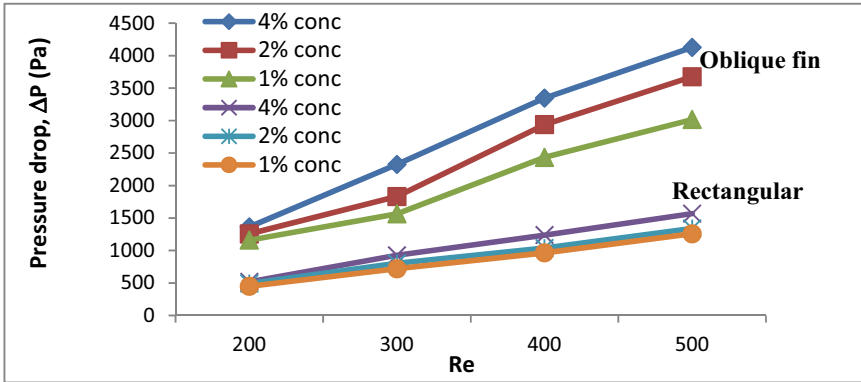
**Fig. 5** Pressure drop versus *Re* in oblique fin and rectangular channel using DPM
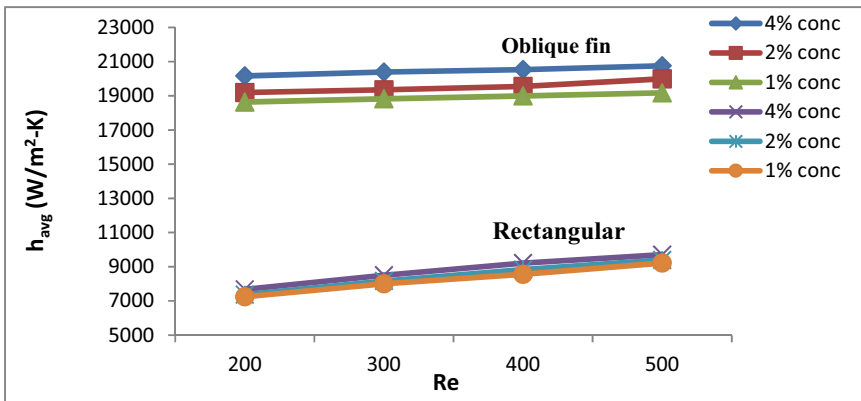


**Fig. 6** Heat transfer coefficient versus *Re* in oblique fin and rectangular channel using mixture rule

Figure 5 shows the variation in pressure drop with Reynolds number in discrete phase modeling. Oblique finned microchannel shows more pressure drop at higher concentration due to more number of particles and individual particle behavior considered in DPM.

Figure 6 shows the variation of $h_{avg}$ with Reynolds number in the rectangular and oblique channel. There is high heat transfer enhancement observed in oblique finned microchannel compared to rectangular channel as there is continuous breakage of the thermal boundary layer at the end of every oblique fin.
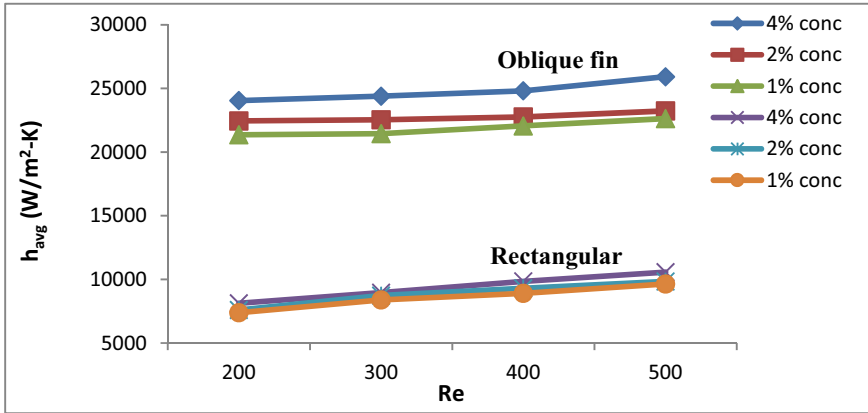
**Fig. 7** Heat transfer coefficient versus *Re* in oblique fin and rectangular channel using DPM
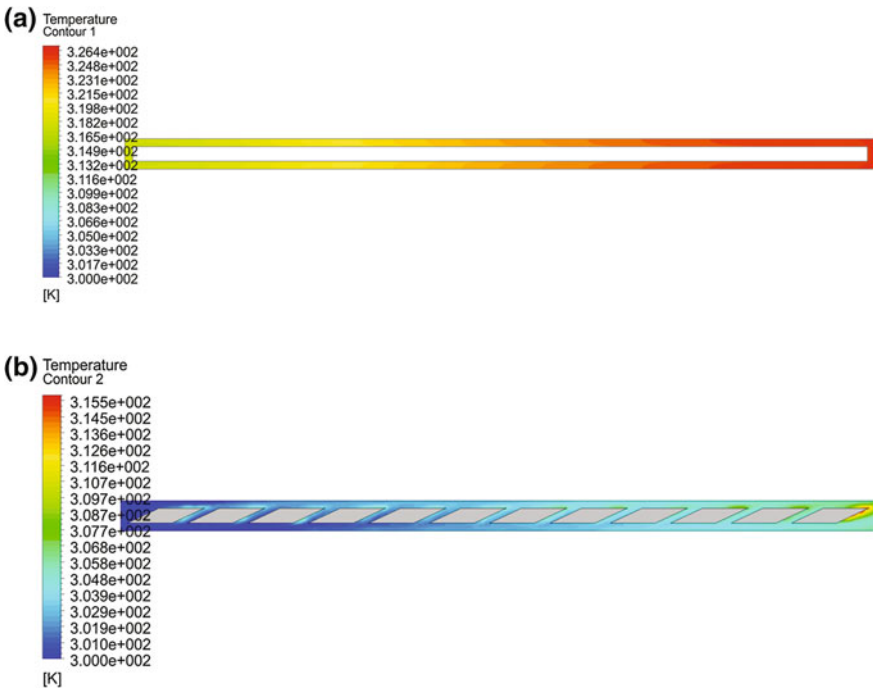


**Fig. 8** Temperature contour at the base of **a** rectangular channel and **b** oblique fin channel

Figure 7 shows less variation in the $h_{avg}$ value at lower Reynolds number. In oblique finned microchannel, there is 145% enhancement in heat transfer coefficient compared to rectangular microchannel due to more mixing of nanofluid particles at 500 Reynolds number.

**Temperature Contour**

Figure 8 shows the temperature variation at the base in the rectangular and oblique finned channels. In oblique geometry, there is more uniform temperature distribution compared to that of a rectangular channel. Also, the temperature near the end of the rectangular channel is 10 °C more than the oblique channel. Thus, it acts as a better alternative to rectangular microchannel for cooling purpose.

# 4 Conclusion

In the present study, hydrodynamic and heat transfer behaviors of Al2O3-water-based nanofluid are studied in an oblique finned channel. The result is obtained for laminar flow Reynolds numbers 200, 300, 400, and 500 and nanoparticle volume fraction of 1, 2, and 4%. At 4% volumetric concentration and $Re = 500$, there is an enhancement of 115% heat transfer coefficient that has been observed in oblique channel compared to rectangular microchannel in mixture rule, whereas 145% enhancement has been observed in discrete phase modeling. Therefore, oblique finned channel can be a potential alternative to microchannel heat sink application.

# References

1. Gong L, Zhao J, Huang S (2015) Numerical study on layout of microchannel heat sink for thermal management of electronic devices. Appl Therm Eng 88:480–490
2. Khan JA, Morshed AKMMM, Fang R (2014) Towards ultra-compact high heat flux microchannel heat sink. Procedia Eng 90:11–24
3. Choi SU, Eastman JA (2016) Enhancing thermal conductivity of fluids with nanoparticles (No. ANL/MSD/CP–84938; CONF-951135–29). Argonne National Lab, IL (United States)
4. Buongiorno J (2016) Convective transport in nanofluids. J Heat Transf 128(3):240–250
5. Yu W, France DM, Routbort JL, Choi SU (2008) Review and comparison of nanofluid thermal conductivity and heat transfer enhancements. Heat Transf Eng 29(5):432–460
6. Tuckerman DB, Pease RFW (1981) High-performance heat sinking for VLSI. IEEE Electron Device Lett 2:126–129
7. Peng XF, Wang BX (1995) Experimental investigation of heat transfer in flat plates with rectangular microchannel. Int J Heat Mass Transf 38(1):127–137
8. Lee YJ, Lee PS, Chou SK (2009) Inter PACK 2009-89059. In: International conference on energy sustainability, Proceedings 2009, San Francisco, California, USA, 19–23 July
9. Lee YJ, Singh PK, Lee PS (2015) Fluid flow and heat transfer investigations on enhanced microchannel heat sink using oblique fins with parametric study. Int J Heat Mass Transf 81:325–336
10. Fluent ANSYS (2016) Fluent 15 users guide. Lebanon, USA

11. Hamilton RL, Crosser OK (1962) Thermal conductivity of heterogeneous two component systems. Ind Eng Chem Fundam 1(3):187–191
12. Goutam S, Paul MC (2014) International conference on advances in civil, structural and mechanical engineering—CSM 2014, Birmingham, UK, 16–17 Nov

# Augmenting Distillate Output of Single-Basin Solar Still Using Cement Blocks as Sensible Heat Energy Storage

Jyoti Bhalavi, Bhupendra Gupta, P. K. Jhinge and Mukesh Pandey

**Abstract** Solar still is a green energy product. It uses heat energy of the sun to purify muddy or salty water. Single-basin passive solar still is the best choice for drinking water-prone remote areas. Investigations show its limitation because of its lower performance in terms of distillate output. Several attempts were made by different researchers for improving the performance of conventional solar still. One of the proven methods to improve the output of solar still is to incorporate sensible heat energy storage material. In this experimental work, prime focus is to enhance the output of the single-basin conventional solar still by putting cylindrical cement blocks as a heat storage material in basin water. A comparative study between the modified still (with cement blocks) and conventional still (without cement blocks) of the same size was carried out for the same experimental condition of Jabalpur, India (23° 10′ N, 79° 59′E), with different depth of water ranging from 2 to 5 cm. Result recorded indicates that the output depends on the water depth and mass of sensible energy storage material. The maximum yield was obtained for least water depth of 2 cm. The daylight yield was found enhanced up to 67% in the modified still as compared to conventional still, while decreased performance is observed in overnight productivity. The overall yield increased by 17% considering 24 h. of output. Uncertainty and error analysis have also been carried out.

**Keywords** Distillate output · Cement blocks · Water depth · Sensible energy storage material · Passive solar still · Daylight and overnight productivity · Uncertainty and error analysis

J. Bhalavi · B. Gupta (✉) · P. K. Jhinge
Jabalpur Engineering College, Jabalpur 482011, India
e-mail: bhupendra243@yahoo.com

M. Pandey
School of Energy and Environment Management, UIT, RGPV, Bhopal 462033, India

**Nomenclature**

| | |
|---|---|
| $T_a$ | Ambient temperature (°C) |
| $T_w$ | Basin water temperature (°C) |
| $T_v$ | Vapor temperature (°C) |
| $T_{gi}$ | Inside surface temperature of glass (°C) |
| $T_{go}$ | Outside surface temperature of glass (°C) |
| $I_g$ | Solar radiation (W/m$^2$) |
| $D_w$ | Water depth (cm) |
| PCM | Phase change material |

# 1    Introduction

Pure and drinkable water is primitive to life and sustainable development. Today, most of the health problems are because of non-availability of hygienic drinking water. Water availability, as well as clean drinking water on earth, has reduced drastically in recent years due to, climate change, industrialization, increased population drought, etc. According to the survey, about 79% of the water on the earth is saltwater, 20% is brackish, and rest 1% of all the water on earth is freshwater [1] hence to resolve the problem of freshwater, solar desalination is proven technique. It is an environment-friendly method used to convert salty water into drinkable water. Extensive research work has been carried out to find out ways to improving the efficiency of solar still. Velmurugan and Srithar [2] reviewed the performance analysis on the factors affecting the productivity of solar still and concluded that productivity enhancement can be done by changing the various operational parameters with modification in the solar still. Abdallah et al. [3] used black rocks and black (coated and uncoated) metallic wiry sponges as a heat absorbing material and found yield increment around 60, 43, 28%, respectively. Srivastava and Agrawal [4] modified a single slope solar still with twin reflector booster and blackened jute cloth as floating absorbers. It recognized that the modification in the solar still enhanced the yield by 68%. Panchal and Mohan [5] have studied and reviewed the numerous methods used to increase solar still output. It is fin attachment, energy storage materials, and multi-basin solar still for improvement in distillate output. They concluded that all the three approaches contribute significantly to increment in distillate production. Gupta et al. [6] evaluated and compared the performance of two solar stills. He modified the conventional solar still by painting it white at inside walls and attached a water sprinkler on the glass cover. They concluded that the overall efficiency is increased by 21%. Gupta et al. [7] in his another work used nanoparticles to improve thermal characteristics of the fluid and found that the yields increase from 2351 to 2814 ml/m$^2$-day in the modified solar still. Sellamia et al. [8] used layers of blackened sponge on absorber surface and premeditated the sponge thickness effect on the efficiency of

the solar stills. It was found that distillate output is increased by 57.77 and 23.03%, with sponge thicknesses of 0.5 and 1.0 cm compared with a conventional solar still. Akash [9] conducted experiments using different absorption materials. They achieved increment of daily still yield around 35, 45, and 60% with use of black rubber mat, black dye, and black ink, respectively. Bassam et al. [10] anticipated an alteration to increase the distillate production by using sponge cubes on the water surface. They concluded that the evaporation surface area of water increased, hence, caused the augment of yield by 18%. Murugavel et al. [11] experimented with cement concrete pieces, washed stones quartzite rock, red brick pieces in the solar still basin at least water depth and found 19 mm quartzite rock as the best option. Velmurugan et al. [12] used sand, gravel, pebbles sponges, and black rubber as storage material in modified still and found 14% yield increment with sand as compared to the conventional still. Kabeel and Abdelgaied [13] experimentally investigated the effect of paraffin wax as PCM on the behavior of the solar still he concluded 67.18% yield improvement as compared to the conventional solar still.

Literature review shows a research gape of work with natural heat absorbing materials with different shape and weight configurations. So, in this work, the effect of cement blocks as heat storage material in conventional solar still has been analyzed. The experiment is performed at water depth of 2, 3, and 5 cm at the same ambient conditions and results of modified solar still are compared with the results of conventional solar still.

## 2  Experimental Setup

Figure 1a, b shows actual photographs and schematic of solar still fabricated on-site at Jabalpur, India. Two identical solar still were designed, fabricated, and installed at Jabalpur Engineering College, Jabalpur, India. The solar stills are kept facing South–North direction to get utmost solar energy. Basin of solar still is made by 1 mm thick galvanized iron sheet having the basin area of 1 m$^2$ (1 m $\times$ 1 m). Front wall height of solar still is 21 cm and rear wall height is 63 cm. Basin of solar still is painted black color to absorb maximum radiation. Thermocol sheets are used as insulation material to prevent heat losses from the sidewalls and bottom of the solar still. 10 mm thick plywood is used for outside support of both solar still, and 5 mm thick plain glass inclined at 23° to the horizontal is used to cover the top of both the solar stills. An arrangement of inlet and outlet valve is provided to supply saline water into basin and distillate output from the basin. Setup is well equipped with instruments such as K-type thermocouple is used to measure the temperatures of various sections of solar still. Solar radiation is measured with the help of solar radiation meter. A measuring flask was used to measure distillate yield from modified and conventional solar stills.

**(a)** Various Images
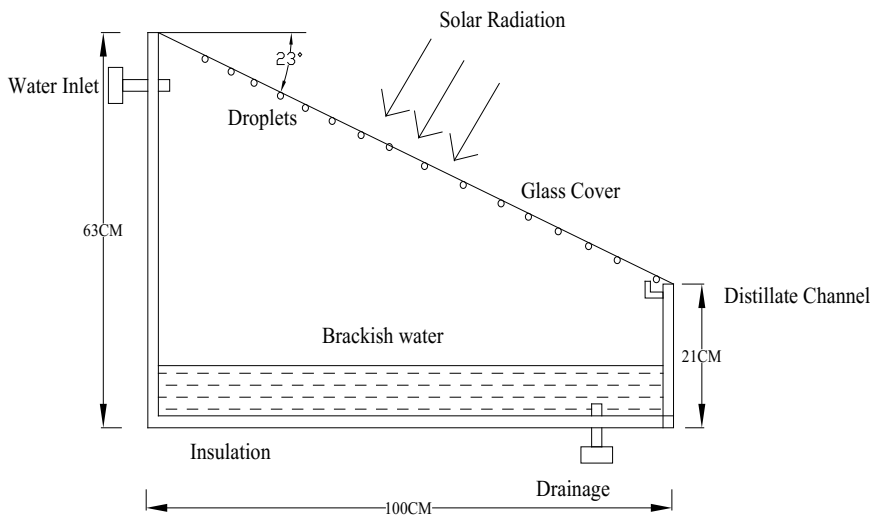


**(b)** Schematic diagram

**Fig. 1** Experimental setup of solar still

## 3 Experimental Procedure

The experimental procedure was carried out in January and February 2018 at Jabalpur city, Madhya Pradesh, India. Thirteen cement blocks of weighing 300 g each were tapped in the basin. Experiments were executed to compare output of modified solar still at three different water depths by maintaining the equal number of cement block. The results are compared with conventional solar still set aside at the same ambient condition. At the beginning of the experiment, the water depth of 5 cm was maintained inside both the basins. Hourly measurements were taken from 9 am to 6 pm. Variables measured in the present experiments were ambient

temperature, water temperature, inside and outside glass temperature, vapor temperature, and distillate output. The distillate is measured at every hour in daytime and collectively for the night at next morning. The days with clear sky conditions were considered for experimentation and assessment. Similar tests were repeated with the water depth of 3 cm 2 cm and again distillate output is compared. All these measurements were recorded manually.

## 4    Error Analysis

Several parameters were measured throughout the experiments, in order to assess the performance of solar still. Owing to the limited precision of the instrument and uncertainty of the method of measurement, some inaccuracies are present in measured parameters that are recognized as percentage of uncertainty. The accuracies and ranges of instruments used are presented in Table 1. The uncertainty percentage of experimental measurement has been measured by adopting the method proposed by Holman [14] based on the precision of measuring equipment the maximum uncertainty was found about 2%.

## 5    Results and Discussion

### 5.1    Variation of Ambient Temperature with Solar Radiation

Figure 2 shows a typical hourly variation of solar radiation and ambient temperature at Jabalpur on February 28, 2018. It is observed that both solar radiation intensity and ambient temperature increases to the extreme level around mid-day and steadily decrease after that. Solar variation is parabolic and reached up to 750, 740, and 860 W/m$^2$ at around 2 pm, 12 noon, and 1 pm, respectively, on January 25, 2018, February 23, 2018, and February 28, 2018 and goes to zero at 6 pm on respective days. Peak ambient temperatures are observed 30, 36, and 35 °C at 3 pm and 12 noon, respectively.

**Table 1** Ranges and accuracies of instruments used

| S. no. | Device | Range | Accuracy |
|---|---|---|---|
| 1. | Thermocouple | −100 to 200 °C | ±1 °C |
| 2. | Solar power meter | 0–2000 W/m$^2$ | ±1 W/m$^2$ |
| 3. | Measuring beaker | 0–100 ml | ±5 ml |
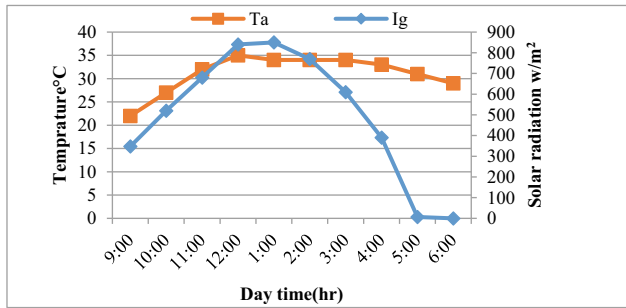
**Fig. 2** Hourly variation of solar insolation, ambient temperature for February 28, 2018

## 5.2 Solar Still Temperatures Variation with Solar Radiation

Figure 3a, b shows solar still temperatures variation with daytime at the water depth of 2 cm. In case of modified solar still having cement blocks, the highest water temperature attended in basin is 64 °C, glass temperature at inside and outside are in the ranges of 28–63 and 30–56 °C, respectively. The maximum basin water temperature is 62 °C in conventional solar still, and inside and outside glass temperature are in the ranges of 26–56 and 28–54 °C, respectively. The basin water temperature in modified still is higher than the conventional solar still by about 0–10 °C. This is primarily because the high heat energy storage capacity of cement block, and it continuously dissipating heat to the basin water as a heat source. The maximum water temperature occurs at 3–4 pm.



**(a)** Modified Solar Still                    **(b)** Conventional Solar Still
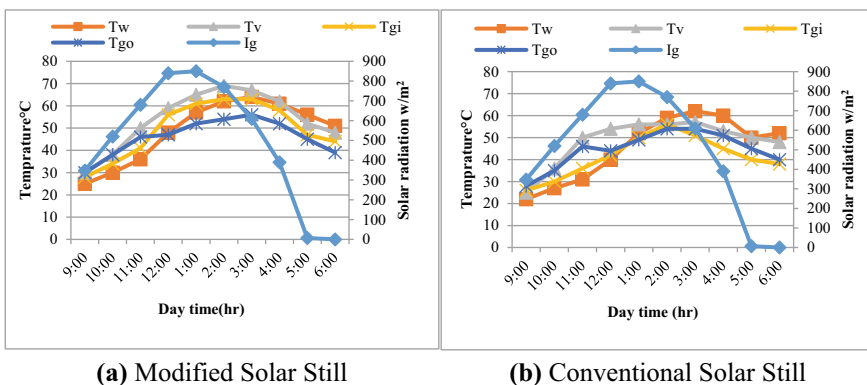
**Fig. 3** Variation of temperatures at different locations with 2 cm water depth on February 28, 2018

## 5.3 Hourly Output Variation During Daylight Hours

Figure 4a–c shows hourly distillate variation for both solar stills with 5, 3, and 2 cm basin water depth. The underneath area of the curve shows the daylight output of modified and conventional stills. It is observed that daylight yield reduces with increasing water depth. Maximum daily distillate is obtained for the least water depth of 2 cm. Maximum hourly output is observed at 4 pm, i.e., 155 ml for 5 cm depth, 265 ml for 3 cm depth, 340 ml for 2 cm depth.

**(a)** At 5 cm water depth

**(b)** At 3 cm water depth

**(c)** Hourly variation of yield for both solar still for 2 cm water depth
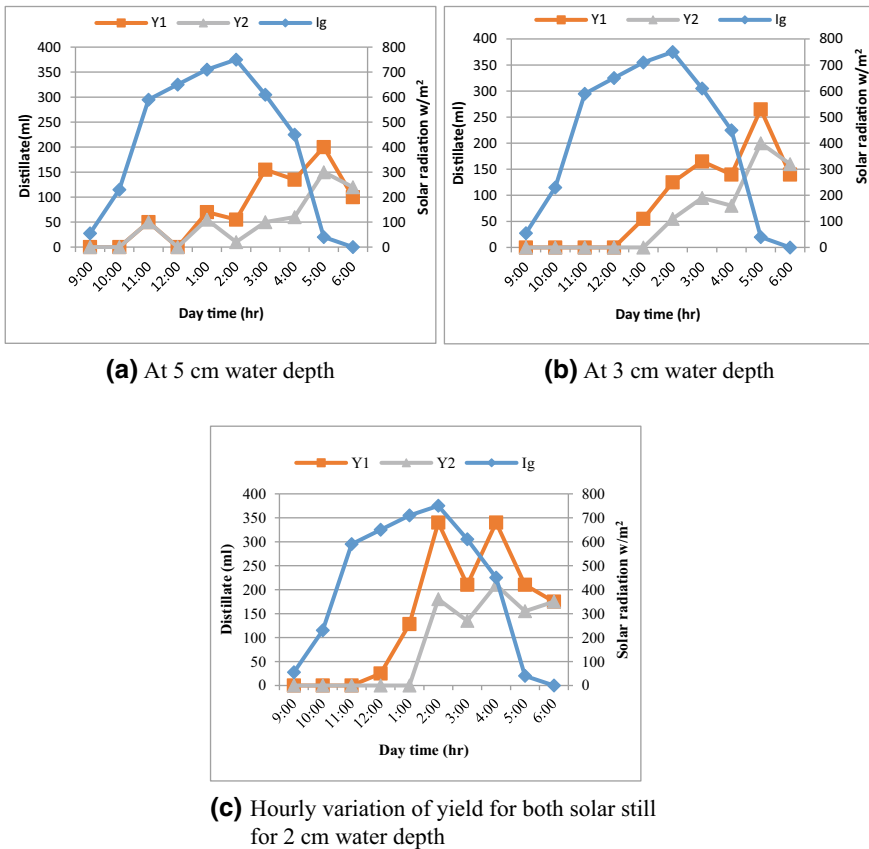
**Fig. 4** Hourly variation of yield for both solar stills

**Fig. 5** Productivity variation
with water depth
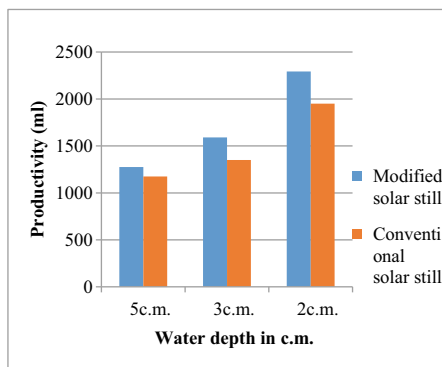


## 5.4 Daily Productivity

Figure 5 shows accumulated freshwater productivity variation with different water depths. At 5 cm water depth, distillate yield of 1275 and 1175 ml/m$^2$-day was obtained for modified and conventional solar stills respectively. At 3 cm water depth, distillate yield of 1590 and 1350 ml/m$^2$-day was obtained for modified and conventional solar stills respectively. At 2 cm water depth, distillate yield of 2293 and 1955 ml/m$^2$-day was obtained for modified and conventional solar stills, respectively.

## 6 Cost Analysis

The project must be economically viable for its success. Table 2 indicates apparatus/utilities and associated cost. Life span of the setup is implicit to be 10 years. In a year, sunlight is available roughly around 300 days. At 3 cm of water

**Table 2** Cost of modified and conventional solar still

| Material units | Modified solar still cost (INR) | Conventional solar still cost (INR) |
|---|---|---|
| Galvanized iron sheet | 1200 | 1200 |
| Plain glass | 540 | 540 |
| Black paint | 300 | 300 |
| Plyboard | 750 | 750 |
| Padding | 150 | 150 |
| Stand | 780 | 780 |
| Manufacturing cost | 800 | 800 |
| Cement blocks | 600 | – |
| Total fixed costs | 5120 | 4520 |

depth in the basin, the approximate cost of water was obtained INR 1.13/L and INR 1.07/L for conventional and modified still. While at 2 cm water depth in the basin, it was INR 0.77/L for conventional still and INR 0.74/L for modified still respectively. Higher total fixed cost for modified still with cement blocks is compensated by positive increment in freshwater productivity.

## 7 Conclusions

Experiments were conducted with cement blocks as sensible heat storage material in a conventional solar still. The distillate productivity is compared with the conventional solar still (without cement blocks). Following points are drawn:

- Cement blocks in basin water increase evaporation rate. They act as heat storage material and liberate energy to water thereby increasing the overall productivity.
- Daytime output of modified still is 67% more than conventional solar still while off-daytime productivity was 27% lowered.
- Output trend reverses after sunset, and yield gradually starts increasing in the conventional still as compared to modified.
- Overall productivity (yield) increases by 17% in modified still. This implies that cement blocks satisfactory working as heat storage material.

## References

1. Tiwari GN (2008) Solar energy; fundamentals, design, modelling, and applications. Narosa Publishing House, New Delhi
2. Velmurugan V, Srithar K (2011) Performance analysis of solar stills based on various factors affecting the productivity—a review. Renew Sustain Energy Rev 15:1294–1304. https://doi.org/10.1016/j.rser.2010.10.012
3. Abdallaha S, Abu-Khaderb MM, Badranc O (2009) Effect of various absorbing materials on the thermal performance of solar stills. Desalination 242:128–137
4. Srivastava PK, Agrawal SK (2013) Experimental and theoretical analysis of single sloped basin type solar still consisting of multiple low thermal inertia floating porous absorbers. Desalination 311:198–205
5. Panchal H, Mohan I (2017) Various methods applied to solar still for enhancement of distillate output. Desalination 415:76–89
6. Gupta B, Sharma R, Shankara P, Baredar P (2016) Performance enhancement of modified solar still using water sprinkler: an experimental approach. Perspect Sci 8:191–194
7. Gupta B, Shankara P, Sharmaa R, Baredar P (2016) Performance enhancement using nano-particles in modified passive solar still. Procedia Technol 25:1209–1216
8. Sellamia MH, Belkis T, Ali Ouar ML, Meddour SD, Bouguettaiab H, Loudiyi K (2010) Improvement of solar still performance by covering absorber with blackened layers of sponge. Desalination 264:24–31
9. Akash BA (1998) Experimental evaluation of a single basin solar still using different absorbing materials. Renew Energy 14:307–314

10. Bassam A, Abu-Hijleh K, Rababah HM (2003) Experimental study of a solar still with sponge cubes in basin. Energy Convers Manage 44:1411–1418
11. Murugavel KK, Sivakumar S, Ahamed JR, Chockalingam KK, Srithar K (2010) Single basin double slope solar still with minimum basin depth and energy storing materials. Appl Energy 87:514–523
12. Velmurugan V, Deenadayalan CK, Vinod H, Srithar K (2008) Desalination of effluent using fin type solar still. Energy 33:1719–1727
13. Kabeel AE, Abdelgaied M (2016) Improving the performance of solar still by using PCM as a thermal storage medium under Egyptian conditions. Desalination 383:22–28
14. Holman JP (1994) Experimental method for engineering, 6th ed. McGraw-Hill, Singapore

# Design and Numerical Analysis to Visualize the Fluid Flow Pattern Inside Cryogenic Radial Turbine

**Manoj Kumar, Pankaj Kumar and Ranjit Kumar Sahoo**

**Abstract** In this paper, the mean-line design and numerical analysis to visualize the flow field characteristics of the cryogenic radial turbine for the liquefaction of nitrogen are reported. The three-dimensional design of blade profile and a fluid passage is created using Blade-Gen©. The meridional plane, hub, and shroud layers are optimized to increase the efficiency, minimize the vortex formation, and losses in the fluid passage. Turbo Grid has been used to create the computational grid. Numerical simulations are carried out using shear stress transport turbulence model using CFX© to visualize the fluid flow behavior, high-pressure zone, heat transfer characteristics, vortex formation, pressure, velocity, Mach number, temperature, entropy generation, etc., using nitrogen as a working fluid. The blade-loading characteristics, blade thickness, and blade angle variation at leading and trailing edge are also being discussed.

**Keywords** Radial turbine · Nitrogen · Flow pattern · Turboexpander · CFD

## 1 Introduction

Cryogenic turboexpander required high-energy input, so turbine efficiency plays a major parameter to minimize the operating cost of the plant. Liquid nitrogen has wide applications in modern physics like nuclear fusion reactors and particle accelerators which demands efficient nitrogen liquefaction plant. In the modern era, to achieve cryogenic temperature, maintain superconductivity, and produce superconducting magnets, liquid nitrogen has very much demand. Cryogenic fluids such as liquid helium, nitrogen, oxygen, and hydrogen are used due to its variety of applications in the fields such as rocket propulsion and aerospace appliances, superconducting equipment, and industrial applications. The advent of modern

M. Kumar (✉) · P. Kumar · R. K. Sahoo
Department of Mechanical Engineering, National Institute of Technology Rourkela, Rourkela 769008, Odisha, India
e-mail: manojbeg526@gmail.com

superconductors which will achieve superconductivity at or above liquid nitrogen temperature will increase the importance of liquid nitrogen as a refrigerant [1].

Ghosh et al. [2] performed the CFD analysis of helium and nitrogen turboexpander. Hasselgruber's approach was used to design the blade profile. The CFD analysis was carried on to the flow variation and concluded that entropy generation in the helium turboexpander was higher as compared to that of the nitrogen due to the difference in specific heat capacity ratio [3]. Wang et al. [4] conducted the unsteady state analysis for a turbine stage to visualize the effect of total pressure on the flow pattern, heat transfer characteristics, velocity vector, etc., during the flow between the blade passages.

The numerical analysis of flow field behavior is essential to reduce the various losses like rotor passage loss, leading and trailing edge loss, friction loss in vaneless space, and tip clearance loss. To minimize these losses, refining different layers should optimize the blade profile. The advent of modern superconductors which will achieve superconductivity at or above liquid nitrogen temperature will increase the importance of liquid nitrogen as a refrigerant [3, 5].

This work reports to design and numerical analysis to predict the flow pattern of the nitrogen inside radial turbine using commercial software ANSYS CFX® 18.1. The study visualizes the flow field characteristics, flow separation, vortex formation, etc., of fluid in the flow passage. The blade profile is optimized to reduce these losses by refining the initial geometry obtained by the Blade-Gen. The variation of pressure, relative and meridional velocity, blade-loading characteristics, inlet and outlet angle variation at leading and trailing edge, temperature, Mach number, etc., inside the flow passage is also discussed. Shear stress turbulence model is used to predict the flow field inside the domain.

## 2 Design of Radial Turbine and Mesh Generation

The design parameters such as stagnation temperature, stagnation pressure, mass flow rate, rotational speed, blade speed ratio, the geometry of the blade, and number of blades are the inputs for the design of radial turbine in Blade-Gen©. The aerodynamic (blade to blade and thickness variation) and geometrical specifications of radial turbine obtained from Blade-Gen are presented in Table 1 and Fig. 1.

The geometry obtained from Blade-Gen and its different dimensions are mentioned in Fig. 1b and Table 2, respectively.

The accuracy and computational time of numerical solution depend upon discretization of the computational domain. ANSYS Turbo Grid is used to generate the mesh in the domain. ATM-optimized mesh topology was selected due to its potential to generate a high-quality mesh. The $Y^+$ method is used for near wall element size specification for refining the mesh. H-grid type is used to mesh the inlet and outlet domains. The grid is refined near the blade leading and trailing edges which is in contact with the hub and shroud surfaces to predict the fluid flow behaviour accurately. The mesh generation in between the passage of two

**Table 1** Design parameters of radial turbine

| Parameters | Unit | Value |
|---|---|---|
| Inlet stagnation pressure | bar | 2.50 |
| Inlet stagnation temperature | K | 100.00 |
| Inlet angle | Degree | 75.00 |
| Outlet angle | Degree | −2.80 |
| Rotational speed | rpm | 90,000 |
| Tip clearance/vane height | | 0.40 |
| Tip clearance | mm | 1.00 |
| Number of blades | | 10 |
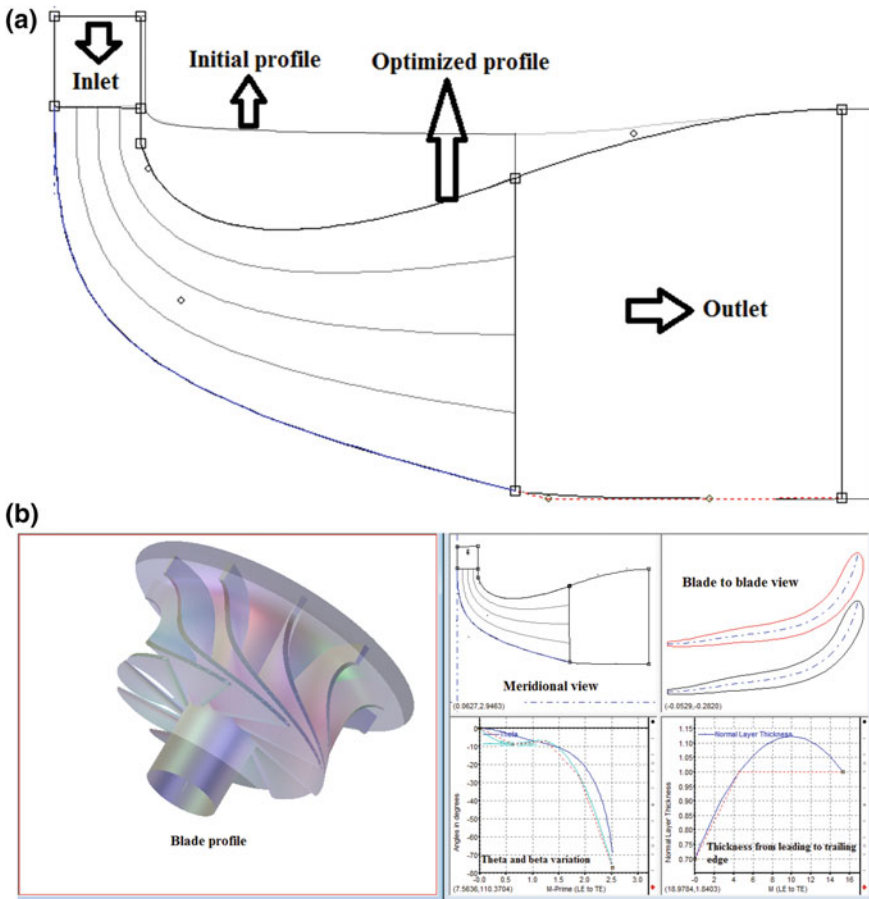


**Fig. 1** **a** Initial and optimized meridional profile, **b** rotor specifications obtained from Blade-Gen

**Table 2** Specification of designed radial turbine

| Parameters | Unit | Value |
|---|---|---|
| Impeller diameter | mm | 25.01 |
| Tip width | mm | 2.07 |
| Impeller hub diameter | mm | 7.51 |
| Impeller eye tip diameter | mm | 14.30 |
| Blade thickness at inlet | mm | 0.50 |
| Blade thickness at outlet | mm | 0.30 |
| Shroud clearance | mm | 1.00 |
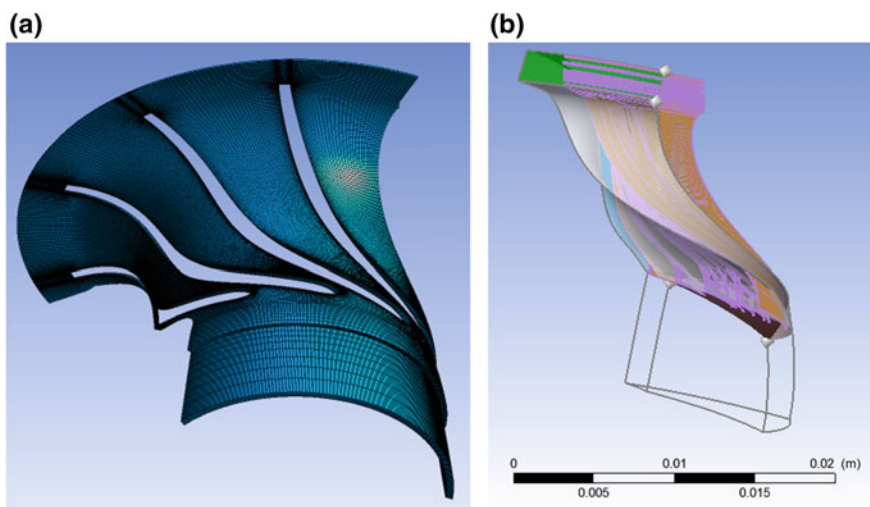


**Fig. 2 a** Mesh at 50% span, **b** single blade passage

consecutive blades used for numerical simulation is shown in Fig. 2. The computational domain is represented by 587,365 nodes.

## 3 Governing Equations and Boundary Conditions

In the current analysis, governing equations which is used to solve the computational domain in CFX are as follows.

Continuity Equation:

$$\frac{\partial \rho}{\partial t} + \nabla \cdot (\rho U) = 0 \tag{3.1}$$

Momentum Equation:

$$\frac{\partial(\rho U)}{\partial t} + \nabla \cdot (\rho U \otimes U) = -\nabla p + \nabla \cdot \tau + S_{\mathrm{M}} \tag{3.2}$$

Total Energy Equation:

$$\frac{\partial(\rho h_{\mathrm{tot}})}{\partial t} - \frac{\partial p}{\partial t} + \nabla \cdot (\rho U h_{\mathrm{tot}}) = \nabla \cdot (\lambda \nabla T) \\ + \nabla \cdot (U \cdot \tau) + U \cdot S_{\mathrm{M}} + S_{\mathrm{E}} \tag{3.3}$$

Shear stress transport turbulence model is used to obtain an efficient prediction of pressure, relative and meridional velocity, blade loading, pressure, temperature, Mach number, etc. Nitrogen is taken as working fluid. Non-slip and adiabatic boundary conditions are imposed on the solid walls, and zero relative velocity with rotating reference frame is assumed for the moving walls. Total pressure and total temperature (2.5 bar and 100 K) are set as an inlet boundary condition, whereas averaged static pressure (1.4 bar) with pressure blend of 0.05 is set as an outlet boundary condition. Turbulence intensity is set to be 5% at the inlet. Convergence criteria are taken as the maximum residuals for mass, and momentum equations are less than 10–6 as recommended in the ANSYS CFX® User Manual.

## 4 Results and Discussion

Blade-loading profile is an important parameter which shows the pressure and velocity variation on the pressure and suction side as shown in Fig. 3. The pressure is decreased from inlet to outlet due to reaction-type turbine.
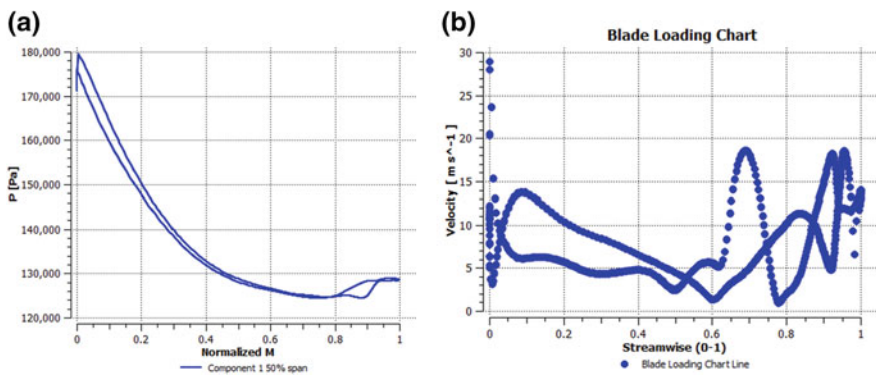


**Fig. 3** **a** Pressure at 50% span, **b** velocity along streamwise direction
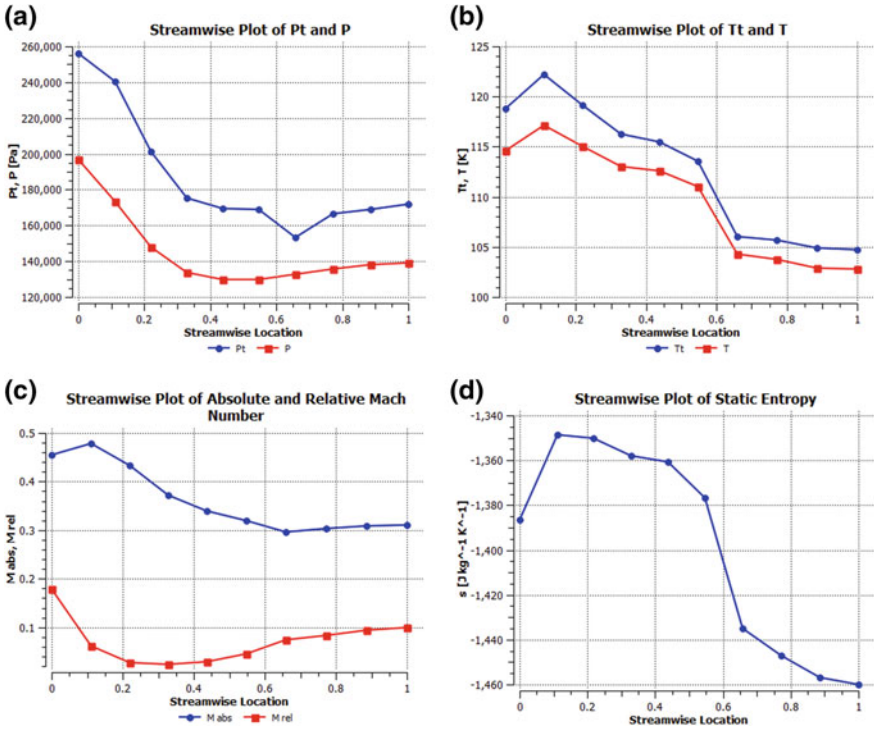
**Fig. 4**  **a** Pressure, **b** temperature, **c** Mach number, **d** entropy along streamwise location

The pressure on both the sides of the blade cut each other at 0.65, 0.85, and 0.94, whereas it cuts the velocity at 0.16, 0.53, 0.74, 0.88, and 0.94, respectively.

Figure 4 represents the static and total pressure, temperature, absolute and relative Mach number, and entropy along the streamwise location. The total pressure drop is approximately 1.78 due to which 15 K temperature is reduced which is quite important at the ultra-low temperature which is also shown at the meridional plane (Fig. 8). The absolute and relative Mach number is 0.45 and 0.19 at the inlet.

Figure 5 represents the variation of Alpha (absolute flow angle) and Beta (relative flow angle) along streamwise location and at leading and trailing edges (LE and TE) along the normalized span.

Figure 6 represents the velocity vector, relative Mach number, and entropy contours at 50% span. The high-pressure fluid enters inside the rotor due to which the maximum velocity 40 m/s is obtained. It is also noticed that the flow circulation is obtained at the pressure side which diminishes as one moves toward the trailing edge. The velocity vector shows the secondary flows in the turbine blade passage. The secondary flow occurs near the blade leading and trailing edges due to rotation of the turbine. It happens due to Coriolis acceleration of the fluid is higher as compared to the radial pressure gradient. The similar effect is observed by
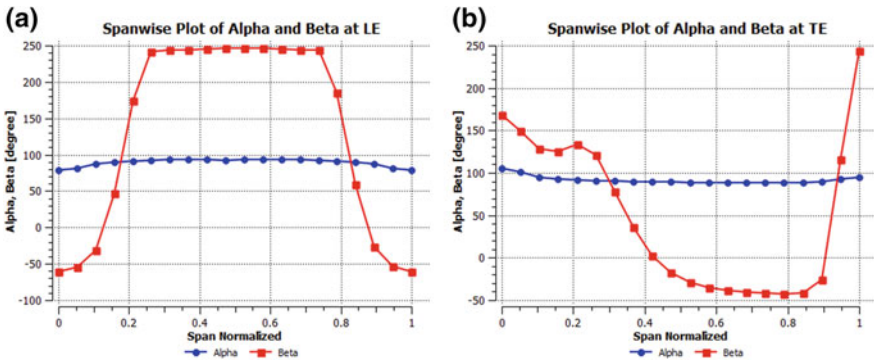
Fig. 5 Variation of alpha and beta angles. a Leading edge, b trailing edge
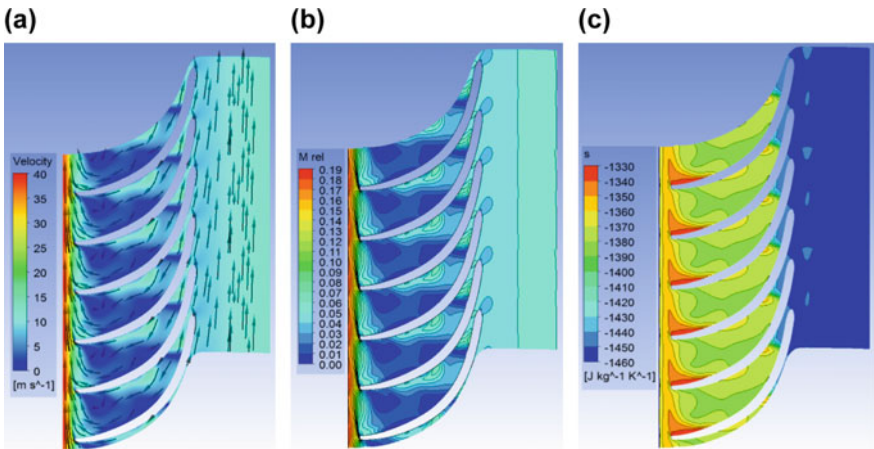


Fig. 6 a Velocity vector, b relative Mach number, c entropy at 50% span

Zangeneh et al. [6] for centrifugal impeller case. The secondary flow occurs from the pressure side to suction side due to the curvature of the blade profile as well as induced pressure gradient.

The kinetic energy of the fluid increases at the cost of the pressure drop of the fluid due to which relative Mach number at the inlet is 0.19. The fluid velocity decreases continuously, and minimum velocity is obtained at the outlet which is approximately 10 m/s. It is found from the initial profile that vortex is formed near the leading edge which is reduced by optimizing the blade profile as shown in Fig. 1a. The entropy is maximum at the leading edge because pressure energy is converted into the rotational energy. It reduces toward the outlet, and the fluid has less entropy.
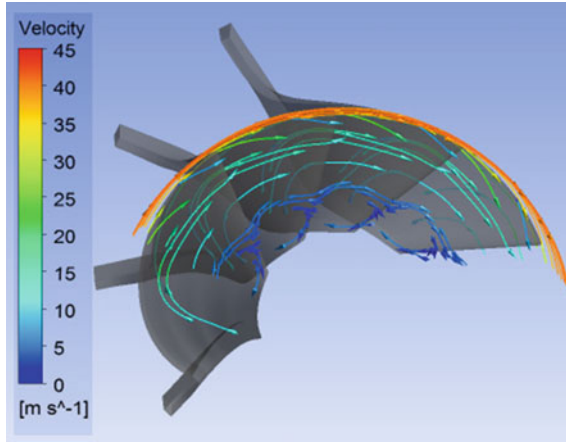
**Fig. 7** Velocity streamline between the blades
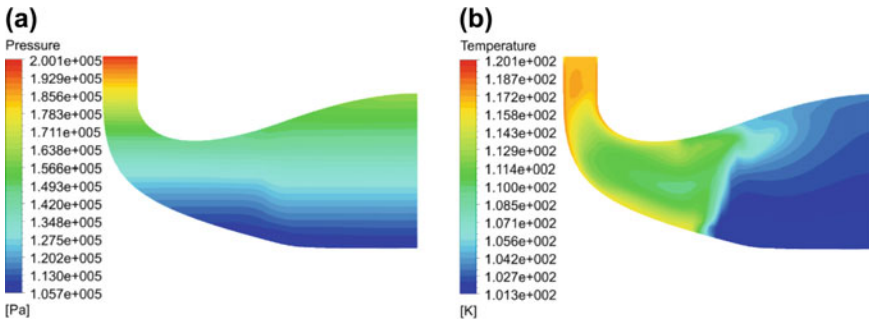


**Fig. 8** Meridional contour of **a** pressure, **b** temperature variation

The velocity streamlines between the two blades are shown in Fig. 7. It is observed that the scrapping flow is obtained near the trailing edge. It occurs due to boundary layer separation corresponding to the rotation of the rotor.

The contour of pressure and temperature distribution at the meridional plane is shown in Fig. 8. The maximum pressure occurred at the inlet, whereas it is continuously decreasing toward the outlet. The pressure at the outlet is maximum at the top side as compared to that of at the bottom side due to relatively higher kinetic energy of the fluid in this zone. The temperature is reduced due to enthalpy drop which is caused by the change in pressure. The pressure energy of the fluid is converted into kinetic energy for which static enthalpy and temperature of the fluid have been decreased. The temperature is to be reduced (approximately 19 K) due to pressure drop; thereafter, kinetic energy of the fluid decreases which affects the rise in pressure energy up to 1.2 bar at the outlet.

# 5 Conclusions

The present work describes the mean-line design approach and numerical analysis of a high-speed cryogenic turbine for the development of an efficient turboexpander. The results of this study can be used for the mean-line design of nitrogen turbine. Based on the above methodology, the blade profile has been refined at the hub and tip surfaces, blade thickness, etc., to reduce the flow blockage and vortex formation. The optimized blade profile reduces the tip leakage flow which is responsible for losses and vortex formation. The absolute Mach number at the inlet and temperature drop in this study is approximately 0.45 and 15 K. The blade-loading characteristics of velocity and pressure define the effectiveness of the designed turbine under these operating conditions.

# References

1. Kumar M, Sahoo RK (2017) Development and numerical analysis to visualize the flow pattern of cryogenic radial turbine for helium gas. In: Proceedings of the 24th national and 2nd international ISHMT-ASTFE heat and mass transfer conference 2017, BITS-Pilani, Hyderabad, India
2. Ghosh SK, Sahoo RK, Sarangi SK (2009) A computational approach to the design of a cryogenic turbine blade profile. Int J Eng Sci Technol 1:43–60
3. Kumar M, Behera SK, Kumar A (2016) A numerical analysis of predicting flow pattern inside a turbo-expander. In: Proceedings of the 6th international and 43rd national conference on fluid mechanics and fluid power, MNNITA, Allahabad, U.P., India
4. Wang Z, Wang D, Liu Z, Feng Z (2017) Numerical analysis on the effects of inlet pressure and temperature non-uniformities on aero-thermal performance of a hp turbine. Int J Heat Mass Transf 104:83–97
5. Ohira K, Nakayama T, Nagai T (2012) Cavitation flow instability of subcooled liquid nitrogen in converging-diverging nozzle. Cryogenics 52:35–44
6. Zangeneh M, Goto A, Harada H (1998) On the design criteria for suppression of secondary flows in centrifugal and mixed flow impellers. J Turbomach 120(4):723–735

# Evaluation of Heat Recovery Steam Generator for Gas/Steam Combined Cycle Power Plants

**Achintya Sharma, Meeta Sharma ⓘ, Anoop Kumar Shukla ⓘ and Nitin Negi**

**Abstract** The combined cycle power plant consists of topping cycle, bottoming cycles and heat recovery steam generators (HRSGs) as the integral systems. The main focus of this work is to predict and analyse fluid flow behaviour in HRSG. The heat transfer and pressure drop analysis are performed by using computational fluid dynamics (CFD) model. The CFD model capability for predicting heat transfer and pressure drop performance of finned tube in cross-flow is analysed. The HRSGs having serrated tube and steady-state approach, with a two-equation turbulence model, is employed to examine fluid flow having Reynolds numbers variation from 5000 to 30,000. The external flow Nusselt number and overall pressure drop predicted by the CFD model are compared with those predicted by published empirical correlations.

**Keywords** Heat recovery steam generator · Serrated tubes · Heat transfer · Pressure drop · Combined cycle power plants

## Nomenclature

| | |
|---|---|
| $A$ | Area ($m^2$) |
| CFD 27 | CFD model results for 27 fins |
| CFD 30 | CFD model results for 30 fins |
| $d_f$ | Outer diameter of the fin (m) |
| $d_i$ | Inner diameter of the fin (m) |
| $d_o$ | Outer diameter of the tube (m) |
| $G_{max}$ | Average mass flux at the minimum flow cross-sectional area within the tube bundle ($kg/sm^2$) |
| $h$ | Specific enthalpy (J/kg) |
| $h_f$ | Total fin height (m) |
| $h_{total}$ | Total specific enthalpy (J/kg) |

A. Sharma (✉) · M. Sharma · A. K. Shukla · N. Negi
ASET, Amity University Uttar Pradesh, Noida, India
e-mail: Achintyasharma19@gmail.com

M. Sharma
e-mail: contactmeeta@yahoo.com

189

| | |
|---|---|
| $k$ | Specific kinetic turbulent energy (m$^2$/s$^2$) |
| $L$ | Total length of the tube (m) |
| $p$ | Pressure in (Pa) |
| $Pr$ | Prandtl number |
| $Pr_\text{t}$ | Turbulent Prandtl number |
| $Re$ | Reynolds number |
| $t$ | Time (s) |
| $T$ | Temperature (K, °C) |
| $T^+$ | Dimensionless temperature |
| $t_\text{f}$ | Fin thickness |
| $t_\text{w}$ | Tube wall thickness (m) |
| $U$ | Overall heat transfer coefficient (W/m$^2$K) |
| $\varepsilon$ | Rate of dissipation of turbulent kinetic energy (m$^2$/s$^3$) |
| $\varepsilon_\text{H}$ | Thermal eddy diffusivity (m$^2$/s) |
| $\lambda$ | Thermal conductivity (W/mK) |
| $\mu$ | Dynamic viscosity |
| $\mu_\text{t}$ | Turbulent viscosity |
| $\rho$ | Fluid density (kg/m$^3$) |
| $\tau_{ij}$ | Viscous shear stress tensor (Pa) |
| $a_\text{o}$ | Outside tube surface area available per unit length (m$^2$/m) |
| $A_\text{o}$ | Total outside tube surface area available per unit length (m$^2$/m) |

# 1   Introduction

The combined cycle power plants are popular as they are better in power generation and less polluting. The combined cycle power plant (CCPP) basically comprises three main systems such as gas turbine cycle, HRSG and steam turbine cycle. The heat recovery steam generator (HRSG) is an essential component of CCPP as it is an energy recuperation device. It has a very high impact on thermal efficiency for power production as it utilizes the usable heat from the exhaust gases and converts it into mechanical work through the steam turbine. The gas turbines produce high-temperature exhaust gases typically varying between 400 and 550 °C. The waste heat potential can be enhanced by the optimal design of HRSG which can improve overall plant performance. The HRSG has three major parts such as the economizer, evaporator and the superheater. The economizer is the component in which sensible heat is absorbed by the water from exhaust gases before passing them through the stack. In the evaporator, the saturated water absorbs latent heat

and the saturated steam will allow to pass through superheater to get superheated steam as per the designed conditions.

This work emphasizes upon the economizer section of heat recovery steam generator to preheat water and reduce energy consumption. The simulation approaches used to analyse the economizer performance are computational fluid dynamics (CFD) technique or by using semi-empirical models. The CFD tool is an efficient and economical method to design thermal and fluid flow systems.

The design of HRSG section requires appropriate geometry, proper knowledge of heat transfer and fluid flow phenomenon. A computational fluid dynamics model is more capable of predicting pressure drop and heat transfer phenomenon in the tubes of the HRSG which can improve the energy recovery from the exhaust gases. Therefore, optimal design of the HRSG always justified and requires high-quality modelling and gas side information for both the heat transfer and pressure drop calculations.

The few correlations for heat transfer and pressure drop are discussed by various authors—Weierman [1] gave the correlation for heat transfer and friction factor for different tube bundles with solid and segmented fins. The ESCOA (Extended Surface Corporation of America) analysed the Weierman correlation and obtain better results. Ganapathy [2] and Nir [3] analysed and developed the correlation for heat transfer and pressure drop for helically finned tube bundles and validate it with experimental data and predicted 10% of maximum deviation. Weierman [1], ESCOA [4] and Nir [3] models were validated experimentally by Hofmann et al. [5] and carried out the comparative analysis by considering Weierman and Leveque for heat transfer and pressure drop Hofmann [5]. Naess [6] analysed the academic equipment of Weierman and Nir [6]. Later Martinez [7] analysed the model of Weierman, ESCOA and experimentally validated it. Sharma and Singh [8–10] studied and investigated various energy and exergy aspects of HRSG for gas and steam combined cycle power plants.

In this work, the simulation of the economizer tube section through CFD model is analysed and predicted the heat transfer and pressure drop in solid finned tube and segmented finned tube. The solid finned tube refers to solid fins helically wrapped around the economizer tubes. Similarly, the segmented/serrated finned tube refers to fins having segments and helically wrapped around the economizer tube. At different Reynolds numbers, the behaviour of fluid interaction is noticed and compared with the result obtained through empirical models for different tubes (Figs. 1 and 2).
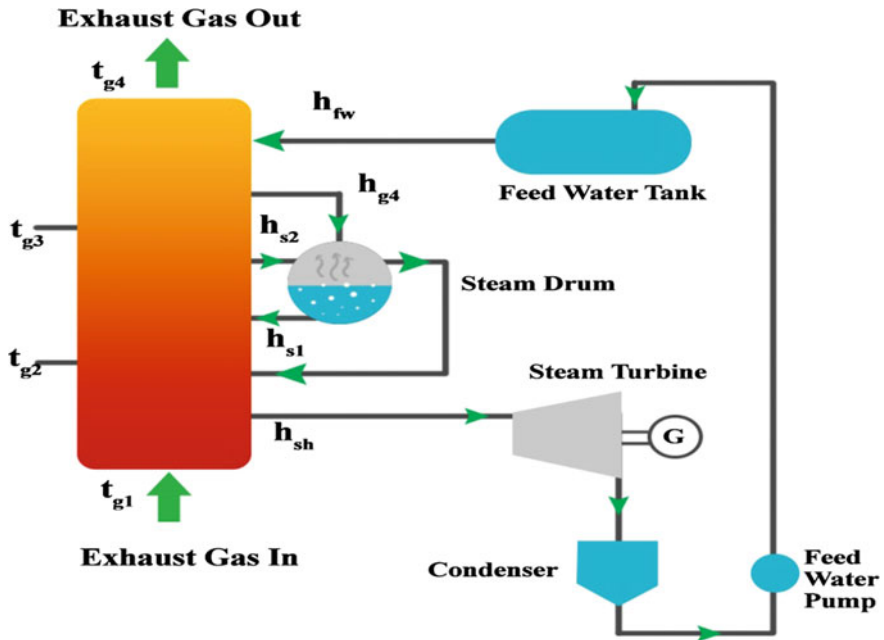
**Fig. 1** Detailed layout of heat recovery steam generator (HRSG)
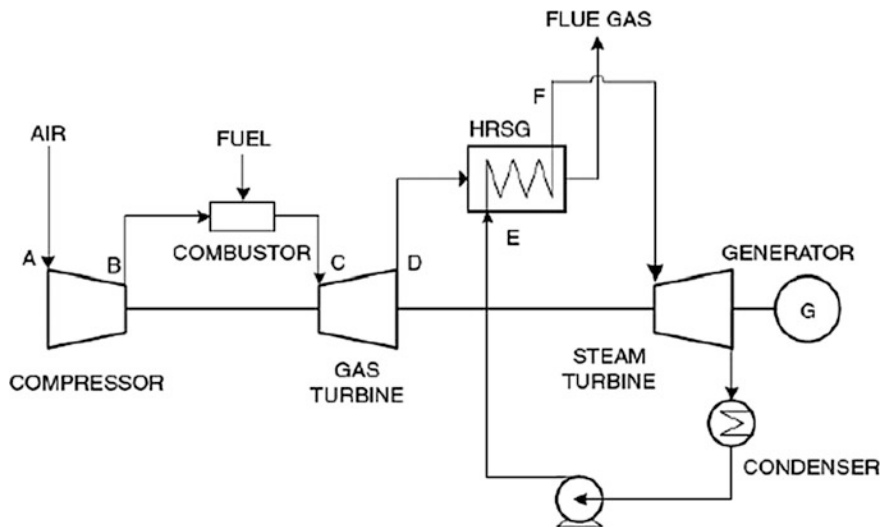


**Fig. 2** Schematic layout of combined cycle power plant

## 2    Model Description

This work presents the comparative analysis for helically segmented finned tubes by using heat transfer and pressure drop model by using CFD tool for the economizer. Three tubes are compared with each other based on Nusselt number, pressure drop, temperature difference and overall heat transfer coefficient for the interaction of fluid. The water flows inside the tubes and the gas flows outside the tubes. The tubes are arranged in a shell in the horizontal direction, while the flue gases are allowed to flow vertically. The interaction of flue gases and feed water is noticed and how the serrated tube disrupts the boundary layer of flue gases thickened near the tubes. The thermal evaluation was analysed using properties of fluid, tube and fin materials, tube geometry and operating conditions. The theoretical model was compared with the simulated model. The different tube geometry is analysed with different configurations such as solid tube, 27-segmented tube and 30-segmented tube. These evaluations are based on different Reynolds numbers from 5000 to 30,000 of flue gases. To study and compare the performance based on existing plant, the material used for HRSG (Economizer) has been considered similar to the one being currently used in the existing HRSG at combined cycle power plant of Delhi, India [8]. The tube material considered in economizer section of the HRSG is detailed in Table 1. The fluid properties (exhaust gases and water) and the material properties are taken from Sharma and Singh [8].

The CFD model used in this simulation is $k$-$\varepsilon$ realizable, scalable viscous heating turbulence model.

**Table 1**   Physical parameters of tubes [8, 11, 12]

| Physical parameters | Solid fin | 30-segment fin | 27-segment fin |
|---|---|---|---|
| Tube dia., $d_o$ (mm) | 42 | 42 | 42 |
| Fin height, $h_f$ (mm) | – | 15 | 20 |
| Fin thickness, $t_f$ (mm) | 1.5 | 1 | 0.8 |
| Segment width, $W_s$ (mm) | – | 5 | 5 |
| Tube wall thickness, $t_w$ (mm) | 4 | 4 | 4 |
| Length of the tube, $L_{tube}$ (mm) | 1000 | 1000 | 1000 |
| Fin density, (fins/m) | 70 | 100 | 100 |
| Tube bundles | Staggered | Staggered | Staggered |
| Design temperature (°C) | 510 | 510 | 510 |
| Tube material | SA210GrA1 | | |

# 3   Governing Equations

The mathematical model chosen for the present study for the CFD analysis of the economizer section is given ahead and considered from Cléirigh and Smith [13]. The basic fundamental energy equation for the HRSG are taken from [14] and [15].

The continuity and Reynolds-Averaged Navier-Stokes (RANS) equations as used for the model are given as:

$$\frac{\partial p}{\partial t} + \frac{\partial(\rho U_i)}{\partial X_i} = 0 \tag{1}$$

$$\frac{\partial(\rho U_i)}{\partial t} + \frac{\partial(\rho U_i U_j)}{\partial X_i} = -\frac{\partial p}{\partial X_i} + \frac{\partial\left(\tau_{ij} - \overline{\rho \grave{U}_i \grave{U} j}\right)}{\partial X_i} \tag{2}$$

Viscous stress tensor ($\tau_{ij}$) given by:

$$\tau_{ij} = \mu\left(\frac{\partial U_i}{\partial X_j} + \frac{\partial U_j}{\partial X_i} - \frac{2}{3}\delta_{ij}\frac{\partial U_k}{\partial X_k}\right) \tag{3}$$

$$\frac{\partial(\rho h_{\text{total}})}{\partial t} - \frac{\partial p}{\partial t} + \frac{\partial(\rho U_j h_{\text{total}})}{\partial X_j} = \frac{\partial}{\partial X_j}\left(\lambda\frac{\partial T}{\partial X_j} - \rho h\overline{U_j}\right) + \frac{\partial}{\partial X_j}\left(U_i\left(\tau_{ij} - \overline{\rho \grave{U}_i \grave{U}_j}\right)\right) \tag{4}$$

The specific total enthalpy is given by $h_{\text{total}}$:

$$h_{\text{total}} = h + \frac{1}{2}U_i^2 + k, \quad \text{where } k = \frac{1}{2}\overline{U_i^2}. \tag{5}$$

# 4   Turbulence Modelling

Reynolds stresses are evaluated by (Fig. 3):

$$-\overline{\rho \grave{U}_i \grave{U}_j} = \mu_{\text{t}}\left(\frac{\partial U_i}{\partial X_j} + \frac{\partial U_j}{\partial X_i}\right) - \frac{2}{3}\delta_{ij}\left(\rho k + \mu_{\text{t}}\frac{\partial U_k}{\partial X_k}\right) \tag{6}$$

The eddy viscosity ($\mu_{\text{t}}$) was calculated using the $k$-$\varepsilon$ model. The Reynolds flux term in the energy equation is

$$-\overline{\rho \grave{U}_i h} = \rho\varepsilon_{\text{H}}\frac{\partial h}{\partial X_i} \tag{7}$$
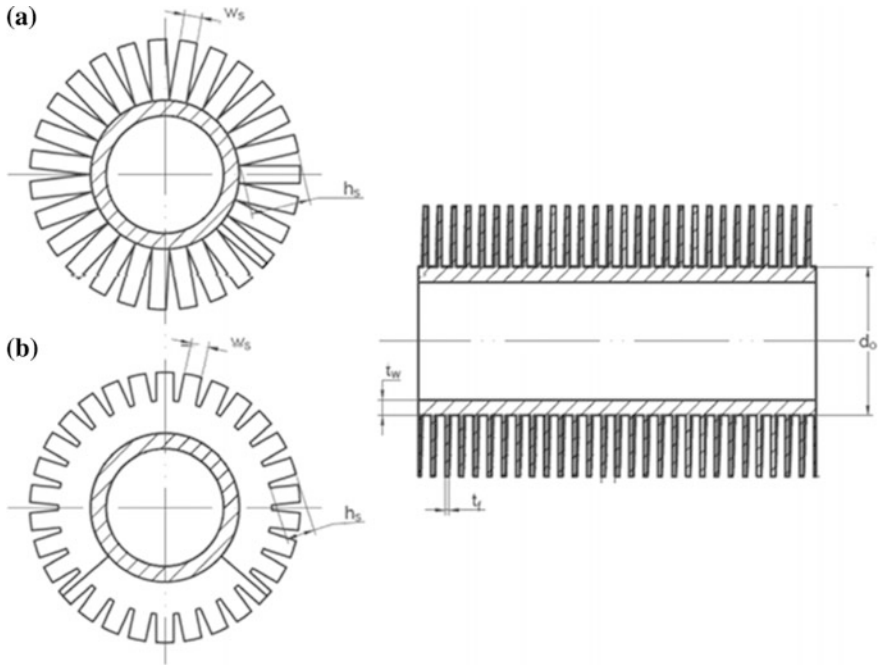
**Fig. 3** Detailed geometry of segmented finned tubes **a** 27-segmented finned tube **b** 30-segmented finned tube

$$Pr_t = \frac{\mu_t}{\rho \varepsilon_H}. \tag{8}$$

## 5 Near-Wall Modelling and Computational Mesh

The heat flux at the fin/tube wall ($q_w$), wall temperature ($T_w$) and near-wall fluid temperature ($T_f$), dimensionless temperature, $T^+$:

$$T^+ = \frac{\rho C_p U_\tau (T_w - T_f)}{q_w} \tag{9}$$

$$T^+ = Pr.y^+.e^{-\Gamma} + (2.12 \ln(y^+) + \beta)e^{\left(-\frac{1}{\Gamma}\right)} \quad y^+ = \frac{\rho \Delta y U_\tau}{\mu} \tag{10}$$

## 6 Results and Discussion

The CFD model results for solid and serrated tubes are analysed and compared/validated with empirical correlations results from the literature.

The results for solid tubes are shown in Fig. 4 with different empirical correlation models. The graphical result is plotted between the Nusselt number and Reynolds number, and different correlations are compared with CFD model for solid finned tubes. It is observed that the dotted curved line lies within the parameters obtained from the literature models [1, 3, 5]. The Hofmann and Weierman model has more accurate result than Nir and Zukauskas. The variations in the Nusselt number as the Reynolds number increases in the CFD solid fin model is 27% more than the model predicted by Nir and Zukauskas. The values predicted for solid fins by Hofmann and Weierman has higher values for the Nusselt number. As the Reynolds number increases, the variations in Nusselt number for CFD solid model are more in comparison with Nir and Zukauskas, and these variations are less in comparison with Hofmann and Weierman. At the Reynolds number equal to 5000, the variation in the Nusselt number is not very much as it lies close to the Nir and Zukauskas correlation. By increasing the Reynolds number to 10,000, the curve moves more towards the Hofmann and Weierman model. At the Reynolds number equal to 15,000, graphical trend becomes more uniform and near to Hofmann and Weierman predictions. By increasing the Reynolds number further both Zukauskas and CFD solid model come close to each other and moves towards the Hofmann and Weierman model.

The result for CFD 30 and CFD 27 are compared with other correlations for segmented fins as shown in Fig. 5. This result shows that the graphical variation is more towards the Hofmann and Naess, as the model predicted by Hoffman and Naess for segmented fins is more accurate than the other correlations. Nir model is also based on both 30- and 27-segmented fins but CFD 30 and CFD 27 has more variations in the Nusselt number as compared with Nir model for both segmented fins. Segmented fins have better accuracy than the solid fins and the higher Nusselt
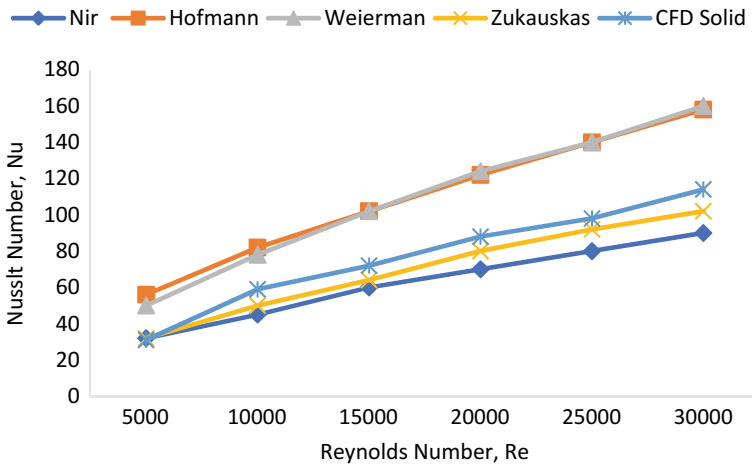


**Fig. 4** Nusselt number versus Reynolds number for solid fin tubes CFD and empirical correlations
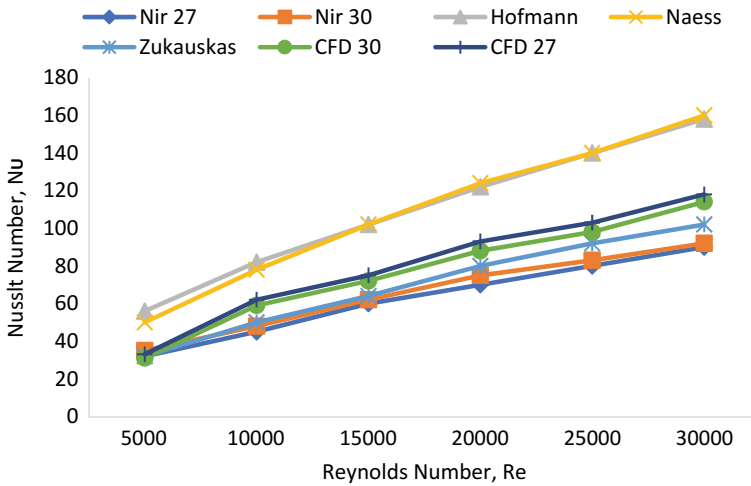
**Fig. 5** Nusselt number versus Reynolds number for CFD 30, CFD 27 and other correlations

number. CFD 30 model has 22% more accurate than the model predicted by Nir and Zukauskas.

In comparison with solid fins, CFD 30 and CFD 27 have high Nusselt number, and the graphical trend is more towards the Hoffman correlation. CFD 27 is more efficient than CFD 30 as the fin thickness is less which reduces the surface area of serration. The serration with CFD 27 creates better gas to liquid interaction at the surfaces in comparison with CFD 30 and solid fins as verified with the published results [3, 5]. The values predicted by CFD 27 are 15% more than the values predicted by CFD 30. The CFD 30 curve is more towards the Nir model than the CFD 27 and CFD 27 is more towards the Hoffman model which has high accuracy. By comparing solid fins, CFD 30 segmented fins and CFD 27 segmented fins with each other, CFD 27 segmented fins have high Nusselt number with the increase in the Reynolds number. The Nusselt number varies from 31 to 114 for 30-segmented fins and from 33 to 118 for 27-segmented fins. For solid fins, variation in the Nusselt number is from 28 to 108 (Figs. 6 and 7).

Pressure drop in CFD 30 segmented fins, CFD 27-segmented fins, and solid fins are compared with each other. CFD 27-segmented fins have higher pressure drop on increasing Reynolds number for flue gases. It has higher pressure drop than the CFD 27-segmented and solid fins as it is observed in the previous results Figs. 4 and 5 that CFD 27 has high thermal accuracy and characteristics but also have high pressure drop among the three cases. Pressure drop curve for solid fins is more towards CFD 27 as it lies between CFD 27- and 30-segmented fins. CFD 30 has least pressure drop values among three of them for greater Reynolds number. It is observed that for Reynolds number 5000, CFD 30-segmented fins has higher pressure drop values among the three but as the Reynolds number increases the pressure drop in CFD 30 become the least and CFD 27 has higher pressure drop and
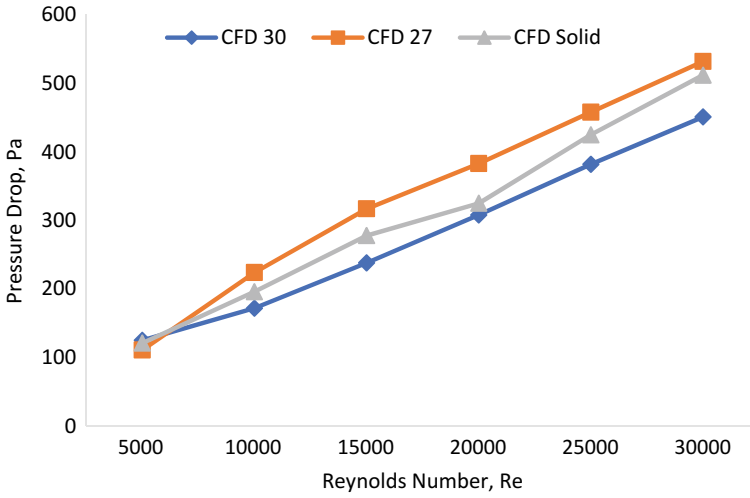
**Fig. 6** Pressure drop versus Reynolds number
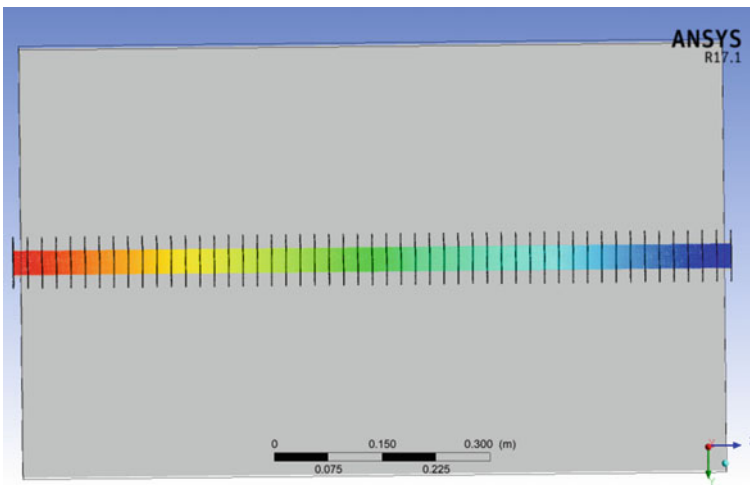


**Fig. 7** Pressure drop versus length of the tube

Solid fins lie between them. Pressure drop variation in 30-segmented fins is from 125 to 451 Pa according to the variation in Reynolds number while pressure drop values for 27-segmented varies from 111 to 532 Pa. In case of solid fins, it varies from 121 to 512 Pa.

# 7 Conclusions

The CFD simulation of segmented and solid fins for economizer has been done. The analysis based on the empirical/experimental values obtained from the literature is compared with CFD results. The following conclusions are obtained from the analysis done on the solid finned tube and segmented finned tube for economizer of an HRSG.

1. Economizer having segmented fins shows higher values for the Nusselt number as compared to solid fins. The results are more accurate in case of segmented fins than the solid fins.
2. Two different segmented fins are obtained 30-segmented and 27-segmented fins as these two are considered more accurate and optimum in design considerations.
3. The 30-segmented fins have a more accurate result for the increase in the Nusselt number than 27-segmented fins.
4. Pressure drop variation in 30-segmented fins is from 125 to 451 Pa according to the variation in Reynolds number while pressure drop values for 27-segmented varies from 111 to 532 Pa. In case of solid fins, it varies from 121 to 512 Pa.
5. The most accurate values are for 27-segmented fins but it has more pressure drop with increase in Reynolds number as compared to 30-segmented and solid fins.

# References

1. Weierman C (1976) Correlations ease the selection of finned tubes. Oil Gas J 74(36):94–110
2. Ganapathy V (2003) Industrial boilers and heat recovery steam generators
3. Nir A (1991) Heat transfer and friction factor correlations for crossflow over staggered finned tube banks. Heat Transf Eng 12(1):43–58
4. Weierman C (1979) Escoa engineering manual. ESCOACorp, Pryor, OK
5. Hofmann R, Frasz F, Ponweiser K (2007) Heat transfer and pressure drop performance comparison of finned-tube bundles in forced convection. WSEAS Trans Heat Mass Transf 2(4):72–88
6. Naess E (2010) Experimental investigation of heat transfer and pressure drop in serrated-fin tube bundles with staggered tube layouts. Appl Therm Eng 30(13):1531–1537
7. Martinez E, Vicente W, Soto G, Salinas M (2010) Comparative analysis of heat transfer and pressure drop in helically segmented finned tube heat exchangers. Appl Therm Eng 30(11–12):1470–1476
8. Sharma M, Singh O (2014) Parametric evaluation of heat recovery steam generator (HRSG). Heat Transf Asian Res 43(8):691–705
9. Sharma M, Singh O (2017) Exergy analysis of the dual pressure HRSG for varying physical parameters. Appl Therm Eng 114:993–1001
10. Sharma M, Singh O (2018) Exergo-economic study of dual pressure HRSG in gas/steam combined cycle plants. Int J Ambient Energy 1–27

11. Martínez E, Vicente W, Soto G, Campo A, Salinas M (2011) Methodology for determining the optimal fin dimensions in helically segmented finned tubes. Appl Therm Eng 31(10):1744–1750
12. Gnielinski V, Zukauskas A, Skrinska A (1983) Banks of plain and finned tubes. In: Heat exchanger design handbook, vol 2
13. Cléirigh CTÓ, Smith WJ (2014) Can CFD accurately predict the heat-transfer and pressure-drop performance of finned-tube bundles? Appl Therm Eng 73(1):681–690
14. Horlock JH (1995) Combined power plants—past, present, and future. J Eng Gas Turbines Power 117(4):608–616
15. Bergman TL, Incropera FP, DeWitt DP, Lavine AS (2011) Fundamentals of heat and mass transfer. Wiley

# Two-Phase Spray Impingement Density Determination in Microchannel Cooling: Measurement and Optimization Results

**Sasmita Bal, Purna Chandra Mishra and Ashok Kumar Satapathy**

**Abstract** Within the past few years, electronic industry has developed vastly. Emerging technologies tend to increase demand for higher power densities in small dimensions. Hence, performance of the equipments used for military or electronic industry needs high heat removal from small areas which directly increase its performance. Hybrid cooling which takes advantage of both microchannel and spray impingement cooling is considered as one of the best technologies for critical heat removal so far. Among all controlling parameters of spray, mass impingement density (MID) is considered as the most influencing parameter for high heat removal. This paper describes an experimental study to evaluate and optimize MID for different values of air and water pressure and nozzle-to-surface height during spray-on microchannel. A mechanical patternator was used for collecting water during spray of base dimension 27 mm × 25 mm which was like the microchannel for which MID was calculated. The air and water pressures were varied from 1 bar to 3 bar for nozzle-to-surface height 10–20 mm. Optimal solution was found through response surface methodology (RSM) which concludes at air pressure 1 bar, water pressure 2.87 bar and nozzle tip to surface distance 17.52 mm maximum MID is achieved.

S. Bal (✉) · P. C. Mishra
KIIT Deemed to be University, Bhubaneswar, Odisha, India
e-mail: sasmitabal@gmail.com

P. C. Mishra
e-mail: pcmishrafme@kiit.ac.in

A. K. Satapathy
NIT, Rourkela, Odisha, India
e-mail: aksatapathy2010@gmail.com

201

# 1   Introduction

Due to rapid growth in electronic industry, mini- and micro-chips are in high demand. Small size and high-power requirement lead to high heat generation in micro-level for which performance and efficiency both are matter of concern. Critical issues related to high heat flux removal in microelectronics beyond 100 W/cm$^2$ was mostly addressed [1]. To deal with this problem an exhaustive comparison of all possible cooling processes for micro-level cooling was made [2, 3]. Spray is one of the most promising among all direct cooling techniques applied in laser technique, steel quenching, casting cooling, microprocessor, and chip cooling. Spray cooling has been successfully implemented in thermal management of microelectronics [4]. Though single jet and multi-jet cooling was proposed by many researchers [5, 6], parametric investigation was done by very few researchers where they reported that pressure of the coolant, nozzle-to-surface height and mass flux impingement has a vital role to play [7, 8]. Current investigation reveals a method to find mass impingement density during spray on microchannel and optimize it for different level of parameters.

# 2   Air–Water Spray Impingement Setup

The following experiment was conducted with the assist of proper experimental setup fabricated and arranged at KIIT University, Bhubaneswar, Odisha, India. The various components that were used in the setup were spray setup, air–water supply, test stand, and patternator. The whole setup was designed to obtain optimized results for every run and to investigate the optimized mass flux impingement for air–water spray cooling. Figure 1 depicts the schematic arrangement of the air–water spray arrangement.

## 2.1   Spray Generator

The spray nozzles used in this experiment are made by the spraying system co. industrial spray nozzles (1/4 J pressure spray setup internal mix). These are air atomizing nozzles. This setup of spray cooling was specially designed for measurement of heat transfer coefficient (HTC). The spray generator again consists of three different parts, namely (a) pumping system (b) control panel (c) spray cooling test stand.

**Fig. 1** Experimental setup for spray impingement
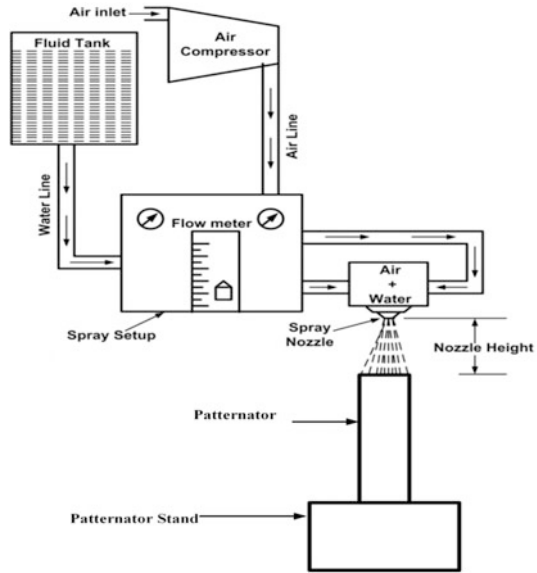


The spray nozzle consists of two steam chambers, namely

(a) Pressurized fluid water chamber
(b) Pressurized air chamber

The pressurized air influences the water or the fluid coming out of the hole and along these lines it also atomizes the fluid film. In this current experiment, the air atomizing nozzle (1/4 J pressure spray setup internal mix) is used. The increase in pressure difference between the fluid and air results in an increase in the relative speed between them.

## 2.2  Test Stand

The test bed was designed and fabricated to conduct the test for average and local value of mass flux impingement for spray cooling system. The test bed was designed in such a way that the height of the nozzle, the distance of the patternator from the nozzle and its positioning can be adjusted according to the needs. The test is kept gently on a stand that consists of an area of 250 mm × 200 mm.

## 2.3   Patternator

The mass flux in a given period is measured by collecting the water sprayed in a patternator. It is a device that is used to measure the amount of spray emitted and visualize its pattern at the same time. The distribution of fluid particles from the spray nozzle is called patternation. A nozzle spray which shows good patternation concludes that the spray has a preferable degree of symmetry and spray distribution.

## 2.4   Methodology and Procedure

The pumping system through which the compressed air and water shall flow was turned on and set according to the required adjustments. The pipes were checked for any kind of leakages. The control panel was turned on. Using the rotameter, the pressure of air and water were set. The experiment was conducted at three various pressures for air, i.e., 1, 2, and 3 bars. The water was also set at three different pressures during the various runs at 1, 2, and 3 bars. The spray nozzle was moved with the help of the pulley and fixed at the required height. The test bed was then measured from the nozzle tip and kept at distance of 10, 15, and 20 mm. The test was conducted at three different heights to find out the height where the optimized value for mass flux impingement will be achieved. The test bed was fixed at its position by the help of rubber stoppers. Then the experiment was conducted at various pressures and heights. To find more optimized value of the mass flux impingement, five test runs were made. The water collected in the patternator was measured after each run and the experiment proceeds.

## 3   Result and Analysis

### 3.1   Measurement of Average Mass Impingement Density

A graduated square glass compartment having measurements (25 mm × 27 mm 20 mm) was utilized to gather and measure the amount of water at various pressures of water and air. The different air and water pressures taken into consideration were 1, 2, and 3 bars. The length of splash is 4 s for accumulation of water in the rectangular patternator for count of normal impingement density at a specific mix of air–water. In the wake of setting the spray, the patternator was put under the spray and the distance between the nozzle tip and the patternator was maintained as 10, 12, and 15 mm for various test runs. The gathered water ($m_w$) was utilized to find mass impingement density using Eq. 1.

$$\dot{m} = \frac{m_{\mathrm{w}}}{A \times \Delta\tau \times 3600} \tag{1}$$

where $\dot{m}$ = mass impingement density, L/m²-h, $A$ = cross-sectional area of the patternator = $(0.025 \times 0.027)$ m², $\Delta\tau$ = duration of spray = 4 s, $m_{\mathrm{w}}$ = mass of water collected in liter.

## 3.2 Response Surface Optimization of Spray Parameters

The response surface methodology (RSM) was applied to develop optimization models for the influencing spray parameters. Before performing the cooling experiments, the optimal values of the MID were determined with the help of design of experiments and test data.

**Design of Experiments (MID)**

Water pressure, air pressure, and nozzle-to-target distance are the three levels of input variables are used. Twenty runs were produced by this procedure to perform the MID determination experiments. Table 1 shows the input variables with their levels and the coded model matrix along with the experimental outcome.

**Table 1** CCF RSM formed coded experimental model matrix (MID)

| Std | Run | Factor 1 | Factor 2 | Factor 3 | Response 1 |
|---|---|---|---|---|---|
| | | $A$: water pressure ($p_{\mathrm{w}}$) | $B$: air pressure ($p_{\mathrm{a}}$) | $C$: nozzle height ($H$) | MID |
| | | bar | bar | mm | L/h m² |
| 1 | 1 | 1 | 1 | 10 | 113,927 |
| 2 | 2 | 3 | 1 | 10 | 260,103 |
| 3 | 3 | 1 | 3 | 10 | 98,477 |
| 4 | 4 | 3 | 3 | 10 | 239,037 |
| 5 | 5 | 1 | 1 | 20 | 201,515 |
| 6 | 6 | 3 | 1 | 20 | 299,691 |
| 7 | 7 | 1 | 3 | 20 | 178,148 |
| 8 | 8 | 3 | 3 | 20 | 282,747 |
| 9 | 9 | 1 | 2 | 15 | 201,515 |
| 10 | 10 | 3 | 2 | 15 | 310,155 |
| 11 | 11 | 2 | 1 | 15 | 266,827 |
| 12 | 12 | 2 | 3 | 15 | 257,387 |
| 13 | 13 | 2 | 2 | 10 | 173,672 |
| 14 | 14 | 2 | 2 | 20 | 242,293 |
| 15 | 15 | 2 | 2 | 15 | 259,259 |
| 16 | 16 | 2 | 2 | 15 | 257,159 |
| 17 | 17 | 2 | 2 | 15 | 259,259 |
| 18 | 18 | 2 | 2 | 15 | 259,556 |
| 19 | 19 | 2 | 2 | 15 | 258,963 |
| 20 | 20 | 2 | 2 | 15 | 259,325 |

## Experimental Model Obtained Using RSM (MID)

The regression analysis was accomplished, and a quadratic model was obtained for determining the MID from experimental values, which is represented in Eq. 2:

$$\begin{aligned} MID = & -12.392 + 2.767 \times p_{\mathrm{w}} - 21783.87045 \times p_{\mathrm{a}} \\ & + 71407.196H + 100.875 \times p_{\mathrm{a}} \times p_{\mathrm{w}} - 2099.025 \times p_{\mathrm{a}} \\ & \times H - 94.875 \times p_{\mathrm{a}} \times H - 2677.36364 \times p_{\mathrm{w}}^2 + 3594.63 \\ & \times p_{\mathrm{a}}^2 - 2021.194 \times H^2 \end{aligned} \tag{2}$$

## Response Surface Analysis

The response surface investigation of the experimental values was conducted by design expert 8 software. The variation of MID is shown in Fig. 2 corresponding to air and water pressures. The peak value of MID was obtained at high value of water pressure and low value of air pressure. This is because the atomization of the water particle is more potent at greater values of air pressure, which allows maximum blownup of the water droplets and thus MID decreases. Figures 3 and 4 show variation of MID with water pressure and nozzle height and with air pressure and nozzle height, respectively. As water pressure increases MID increases, and as nozzle height increases, MID increases for a certain height and after that it decreases. Figure 4 shows significant effect of air pressure and nozzle height on MID.

## Adequacy Test for Model

In this case, $A$, $B$, $C$, along with $AC$ and $C^2$ are significant model terms. Values greater than 0.1 indicate the model terms are not significant. Table 2 shows adequacy test for the model.
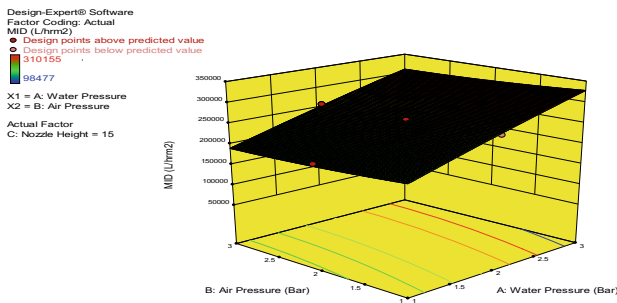


**Fig. 2** Variation of MID with respect to $p_{\mathrm{w}}$ and $p_{\mathrm{a}}$ at $H = 15$ mm
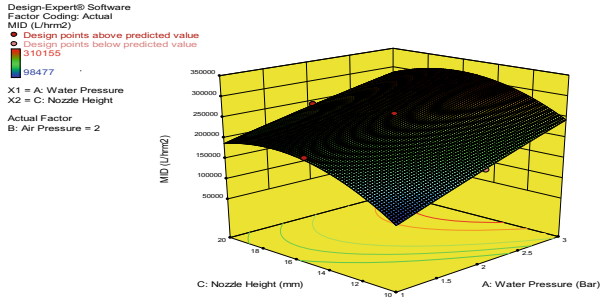
**Fig. 3** Variation of MID with respect to $p_w$ and $H$ at $p_a = 2$ bar
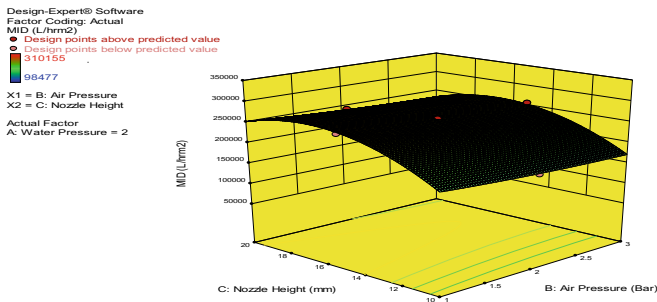


**Fig. 4** Variation of MID with respect $p_a$ and $H$ at $p_w = 2$ bar

### Response Surface Optimization

The response surface optimization was conducted to find the favorable condition in which the optimal MID was achieved. The condition is mentioned in Table 3.

### Experimental Validation

Test was performed at the predicted maximum parametric conditions, i.e., for $p_w = 2.87$(bar) and $p_a = 1$(bar), nozzle height $= 17.52$ mm. The same procedure was followed to find MID in those conditions [9]. In the trial of experiment at the optimal conditions, the MID was obtained to be 318,448.14 (L/m$^2$-h). Comparing this value of MID with the key data, the experimental validity was verified with a minimum deviation. This may be due to the reason that due to experimental set up limitations.

**Table 2** Adequacy test for the model

| Source | Sum of squares | Mean square | $F$ value | $p$-value Prob > $F$ | |
|---|---|---|---|---|---|
| Model | 6.012E+010 | 6.680E+009 | 443.81 | <0.0001 | Significant |
| $A$-water pressure | 3.578E+010 | 3.578E+010 | 2376.90 | <0.0001 | |
| $B$-air pressure | 7.442E+008 | 7.442E+008 | 49.44 | <0.0001 | |
| $C$-nozzle height | 1.019E+010 | 1.019E+010 | 676.79 | <0.0001 | |
| $AB$ | 81406.13 | 81406.13 | 5.408E-003 | 0.9428 | |
| $AC$ | 8.812E+008 | 8.812E+008 | 58.54 | <0.0001 | |
| $BC$ | 1.800E+006 | 1.800E+006 | 0.12 | 0.7366 | |
| $A^2$ | 1.971E+007 | 1.971E+007 | 1.31 | 0.2791 | |
| $B^2$ | 3.553E+007 | 3.553E+007 | 2.36 | 0.1554 | |
| $C^2$ | 7.021E+009 | 7.021E+009 | 466.46 | <0.0001 | |
| Residual | 1.505E+008 | 1.505E+007 | | | |
| Lack of fit | 1.466E+008 | 2.932E+007 | 37.58 | 0.0623 | Insignificant |
| Pure error | 3.901E+006 | 7.803E+005 | | | |
| Cor total | 6.027E+010 | | | | |
| Std. dev. | 3879.77 | $R$-squared | 0.9975 | AICc | 417.88 |
| Mean | 2.340E+005 | | | | |

**Table 3** Optimized predicted MID value

| $p_w$ (bar) | $p_a$ (bar) | Nozzle height (mm) | MID (L/h m$^2$) | Desirability |
|---|---|---|---|---|
| 2.87 | 1 | 17.52 | 318456.82 | 1 |

## 4   Conclusion

Mass impingement density during spray plays an important role as it is directly associated with heat transfer rate. Increase in water pressure results in increase in spray density. On the other hand, at fixed water pressure, decrease in air pressure tends to increase mass flux. The reason may be because of increment of air pressure, intensity of atomization increases. The effect of nozzle-to-surface distance on mass impingement density (MID) was experimentally investigated. It was observed that, as the impingement height is increased from 10 to 15 mm, the nozzle cone angle increases and MID also increases. However, further increase of height from 15 to 20 mm causes lesser number of liquid droplets impinged on the target area.

The current research includes the optimization of controlling parameters like air–water pressure, nozzle-to-target distance on MID, etc., using RSM. Test was carried out at the estimated maximum parametric conditions, i.e., for $p_w$ = 2.87 bar, $p_a$ = 1 bar and nozzle height = 17.52 mm. The same method was followed to find the maximum MID in those conditions. In the trial of experiment at the maximum conditions, the MID was obtained to be 318,448.14 L/m$^2$-h. Comparisons of this data of MID with the key data confirmed the experimental validity with a minimum deviation.

# References

1. Kandlikar SG (2005) High flux heat removal with microchannels—a road map of challenges and opportunities. Heat Transf Eng 26(8):5–14
2. Smakulski P, Pietrowicz S (2016) A review of the capabilities of high heat flux removal by porous materials, microchannels and spray cooling techniques. Appl Therm Eng 104:636–646
3. Kandlikar SG, Bapat AV (2007) Evaluation of jet impingement, spray and microchannel chip cooling options for high heat flux removal. Heat Transf Eng 28(11):911–923
4. Hsieh SS, Luo SY (2016) Droplet impact dynamics and transient heat transfer of a micro spray system for power electronics devices. Int J Heat Mass Transf 92:190–205
5. Fabbri M, Dhir VK (2005) Optimized heat transfer for high power electronic cooling using arrays of microjets. J Heat Transf 127(7):760–769
6. Labergue A, Gradeck M, Lemoine F (2015) Comparative study of the cooling of a hot temperature surface using sprays and liquid jets. Int J Heat Mass Transf 81:889–900
7. Mohapatra SS, Ravikumar SV, Pal SK, Chakraborty S (2013) Ultra-fast cooling of a hot steel plate by using high mass flux air atomized spray. Steel Res Int 84(3):229–236
8. Mohapatra SS, Chakraborty S, Pal SK (2012) Experimental studies on different cooling processes to achieve ultra-fast cooling rate for hot steel plate. Exp Heat Transf 25(2):111–126
9. Nayak SK (2016) Heat transfer enhancement of spray cooling with water and nanofluids. Doctoral dissertation, KIIT deemed to be university, Patia, Bhubaneswar

# Experimental Investigations into Performance Evaluation of Thermosyphon Solar Heating System Using Modified PCM Modules

**T. K. Naveen and T. Jagadesh**

**Abstract** The demand for effective and efficient use of solar heating arrangement is increasing in domestic and industrial applications. The existing renewable energy resources are intermittent and fluctuate depending upon the meteorological conditions. So, the main aim of this present work is to develop thermosyphon solar heating system for improving the performance using modified phase change material (PCM) modules. Paraffin wax material is used as PCM for holding the heat energy to attain an effective solar fraction. A detailed stratification experimental analysis for heat energy accumulation tank has been carried out on without PCM, PCM without fins, PCM with ring type fins and spiral fins. An hourly based charging and discharging efficiency are also calculated for the above cases and compared. All the experiments are carried out three times and average values are taken for the analysis. From the results measured experimentally, it is inferred that the discharging time of solar water heating system with cylindrical PCM ring type fins is 3 h more than without PCM. The discharging time of solar water heating system with cylindrical PCM took 7 h more than without PCM. The charging energy efficiency of heat energy accumulation tank with cylindrical PCM ring type and PCM in spiral module fins confers better results than cylindrical PCM and without PCM. This shows that the PCM get better stratification time and increases the overall performance of solar water heating system.

**Keywords** Solar · Paraffin wax · Stratification number · Charging efficiency

T. K. Naveen
Department of Mechanical Engineering, Sri Krishna College of Technology,
Coimbatore 641042, India

T. Jagadesh (✉)
Department of Mechanical Engineering, Amrita Vishwa Vidyapeetham,
Amritapuri, India
e-mail: jagadeshvel@gmail.com

# 1 Introduction

Energy conversation plays a vital role for manufacturing of products in industries and on our daily lives. The demand for generating renewable energy more efficiently is increasing and thereby there is a challenge in many industries. Solar energy already exists in nature and considered as one type of renewable energy for the future. During summer season, solar systems accumulate extensive energy than required for straight utilization. In the direction of satisfying an energy requirement in the dark time, a sporadic natural thermal supply entails heat energy accumulation space.

PCM modules are widely used in industries for heat energy storage because of substantial energy storage space density for small difference in the temperature. PCM was effective to store and release heat during phase change [1]. Generally, the phase change materials are used to improve the heat transfer in crucial environmental management applications like temperature controlled, drying, air conditioning, solar energy storage space, passive cooling, heat exchangers and thermal barrier applications. The purpose of using PCM in heat energy storage system is to accumulate and release latent heat energy. Researchers developed different phase change materials for creating PCM modules for thermal storage system, i.e. myristic acid, sodium acetate trihydrate and paraffin wax. A few researchers established heat transfer convection coefficient intended for the cylindrical geometry provided with vertical fins. Results revealed that the temperature variation needed to accomplish a certain value of convection coefficient is reduced [2]. Jesumathy et al. reported that heat transfer distinctiveness in latent heat accumulation space by means of paraffin wax [3]. Several researchers used myristic acid and water as PCM and heat transfer liquid to study the thermal characteristics of solar system. The packing bed used in this system has spherical capsules which enhances the effectiveness of the system [4]. Garnier et al. developed model for the analysis of stratification in an integrated collector storage solar system using different solar water heaters for same aspect ratio [5]. Murali et al. investigated performance of PCM added solar system and validated experimental results with CFD simulations [6].

Mondol et al. developed a heat exchanger named as solasyphon for solar hot water system and compared with conventional heat exchanger. Results suggested that proposed system is more effective compared with conventional heat exchanger for two coil arrangement [7]. Ait Hammou et al. suggested a new system called hybrid heat energy storage system (HTESS) to store thermal and electric energy simultaneously. HTESS retains heat in day time and discharges heat during night time in coldness season. This system is to store energy during off hours and liberate heat energy through peak hours. Results revealed that the energy consumption in HTESS reduced by 32% in the time period of four months [8]. Khalifa et al. integrated PCM material in solar domestic hot water system. It is clearly found that by integration of PCM we can get more amount of hot water after sunset [9].

Sharma et al. suggested latent heat accumulation system by PCM is a best method of retaining heat energy because of above average energy storage compactness. They also reported that various PCM having different temperatures designed for melting and solidifying state [10]. Felix Regin et al. examined thermal performance of paraffin wax for different orientations of spherical capsules. It consists of spherical capsule filled with PCM integrated in solar water heating system [11]. Knudsen et al. investigated the performance of stratification at different positions of mantle [12].

There are several researchers worked on waste heat recovery during manufacturing process. In manufacturing of cast components, most of the heat lost to moulding sand. In view of this [13] studied detailed analysis on waste heat recovery system in casting process by keeping aluminium shots over moulded sand. The aluminium shots absorb the heat when they pour the molten metal into sand mould during moulding process. After absorbing the waste heat by using aluminium shots, it transfers the heat to scraps by conduction. Results proved that they could achieve 6.4% of waste heat recovery. Parthasarathy et al. analysed a porous insert of different size and orientations in a 3D square duct insert to improve the efficiency in high-temperature thermal equipment [14]. Selvaraj et al. developed solar parabolic collector for utilization of the maximum solar energy to preheat the scrap for casting industries. Results revealed that a preheating temperature of 100 °C when the scrap is placed in the receiver and 110 °C when they use copper shots and transfer heat by conduction. This yields an energy conservation of 6%. Solar flat plate collector is one of the cheapest methods of utilizing the solar energy for commercial purpose as well as industrial applications in tropical climatic conditions [15]. Gopi Krishnan et al. analysed temperature distribution and thermal fluxes within the profile using ANSYS 14 to improve solar flat plate collector by replacing the conventional solar absorbing plate with rigid conclave plate [16].

A very few investigations have been carried out to enhance the thermosyphon solar heating system using PCM modules. So, in this present work an attempt has been made to enhance the charging efficiency and stratification number by varying PCM modules. Charging and discharging time was evaluated for without cylindrical PCM, with cylindrical PCM heat exchanger and cylindrical PCM with ring type and spiral fins in clear days. The phase change material used in the present work is paraffin wax. The thermal conductivity, melting range, heat of fusion and density in solid and liquid range are given in Table 1.

**Table 1** Properties of paraffin wax

| Parameter | Value |
|---|---|
| Melting range (°C) | 56 |
| Heat of fusion (kJ/kg) | 142.7 |
| Density (g/mL$^3$) | 670 (24 °C)—solid |
|  | 640 (56 °C)—liquid |
| Thermal conductivity (W/mK) | 0.2 |

## 2 Experimental Details

The experimental setup consists of insulated water storage tank, aluminium heat exchanger with fins, phase change material, flat plate collector and data logger. Figures 1 and 2 show the photograph and schematic representation of experimental setup used in the present work. Figure 3a–c shows the PCM module without fin, ring type fin and spiral fin, respectively. The diameter of spiral type PCM module is 20 mm. The insulated water storage tank has three layers and thickness of thermocoal, sheet made of coconut coir and polyurethane foam sheet are 20, 10 and 10 mm, respectively.

The insulated water storage tank used in the present work has a storage space of 78 L. The vertical height and diameter of the tank are 460 and 470 mm, respectively. The PCM is put in a nutshell having cylindrical geometry made of aluminium. The diameter, wall thickness and height of geometry are 121, 3 and 300 mm, respectively. The heat transfer fluid (HTF) considered in the present work is water. The HTF is distributed from the beginning of the insulated tank to the solar collector plate by gravity feeding system and also by density difference of cold and hot water. The HTF take up thermal energy sagaciously, and interactions with the PCM in cylindrical tank, which is primarily at normal temperature.
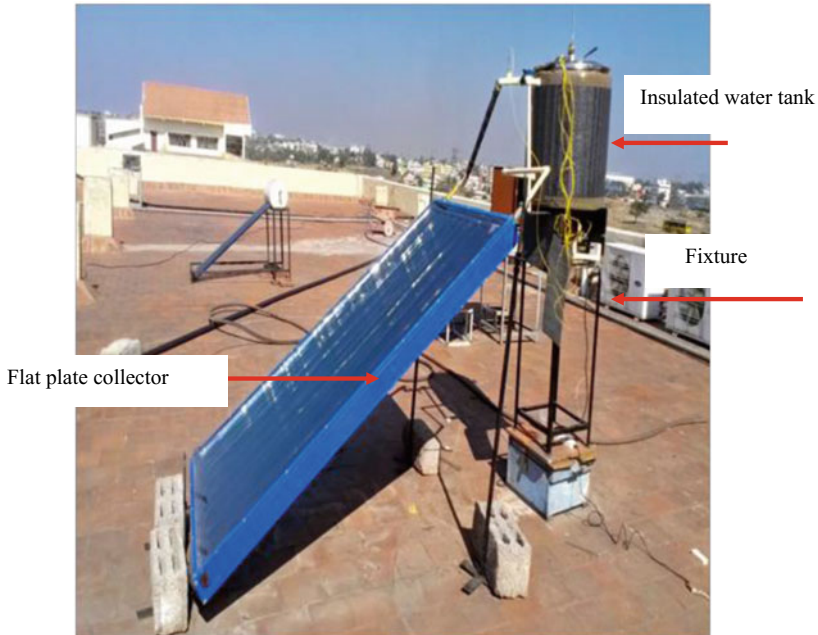


**Fig. 1** Experimental setup
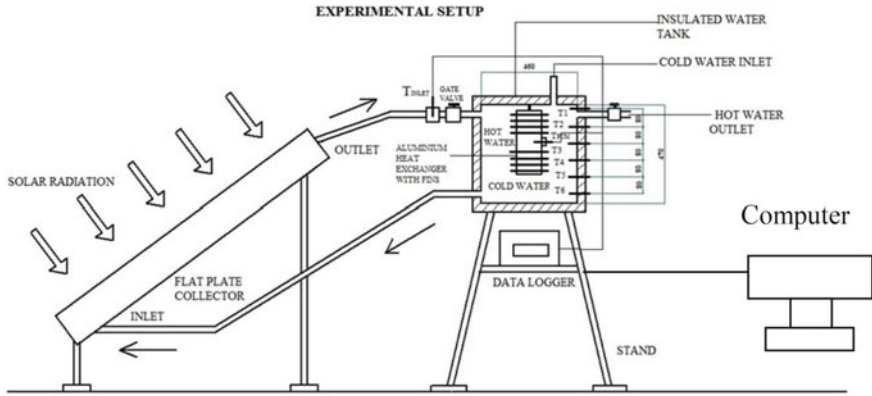
**Fig. 2** Schematic representation of setup
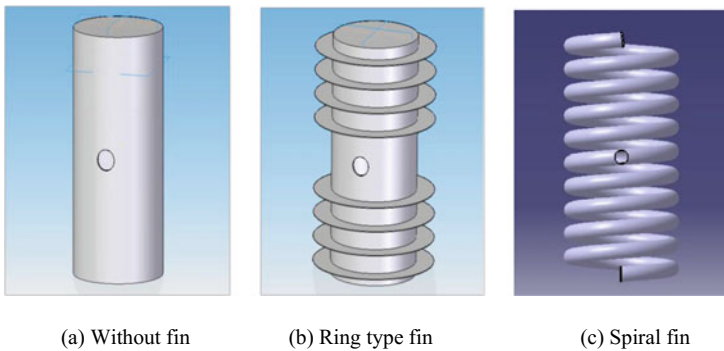


(a) Without fin              (b) Ring type fin              (c) Spiral fin

**Fig. 3** PCM module

The PCM gradually acquire sensible heat at first, and finally, it increased to melting temperature. When the charging proceeds, latent heat is attained by the PCM and reaches melting temperature of $56 \pm 2$ °C. With further addition of heat, paraffin wax reaches superheat, thus again accumulating sensible heat. The charging process prolongs until it reaches 65 °C. Data logger is used to record the temperature at time intervals of ½ hour. The discharging process is started after the charging process and the reading is taken and it is repeated for intervals of 30 min, in which time transfer of energy from the PCM to the HTF would occur. Thermocouples are provided at six locations of the storage tank and inside one thermocouple for PCM tank to measure the paraffin wax temperature. The temperature of the PCM and the HTF are continuously recorded at different locations (eight data logger inputs). This procedure is continued till an average temperature of 45 °C is attained. The PCM tank is assembled with the main tank by means of the adjustable screw with nut. The heat transfer is carried out till the thermal

**Table 2** Specifications of data logger

| Parameters | Range | Temperature | Humidity | Accuracy | Type of thermocouple |
|---|---|---|---|---|---|
| Values | 0–1200 °C | 25 °C ± 5% | 30–65% RH | ±1 °C | K type |

**Table 3** Specifications of solarimeter

| Parameters | Measuring range | Resolution | Spectral response | Accuracy | Sampling rate | Operating temperature |
|---|---|---|---|---|---|---|
| Values | 0–2000 W/m² | 0.1 W/m² | 400–1000 Nm | ±10 W/m² (or) ±5% | 4 times/ second | 0–50 °C |

equilibrium obtains between the PCM tank and the water. The trial experiments have been conducted at three different collector angles of 30°, 45° and 60°. The maximum intensity of solar radiation is observed at 45°. So tilt angle for further experiments are kept at 45°. Table 2 shows the specification of the data logger. The solar energy is measured using solarimeter. The specifications of solarimeter are given in Table 3. The experiments were conducted for three clear sky days and repeated for 3 months in summer season at Hosur (12.7409°N, 77.8253°E).

### 2.1 Charging Energy Efficiency

It is defined as the ratio of difference between average and initial temperature to the difference between inlet and initial temperature. The ratio of output to input for charging efficiency is given in Eq. 1.

$$\eta = \frac{T_{\text{avg}} - T_{\text{initial}}}{T_{\text{inlet}} - T_{\text{initial}}} \tag{1}$$

where,

$T_{\text{avg}}$     Average charging temperature (°C)
$T_{\text{initial}}$     Average initial temperature (°C)
$T_{\text{inlet}}$     Inlet temperature of water (°C).

### 2.2 Stratification Number

Fernández-Seara et al. proposed expression for evaluating the stratification number of the fluid in heat energy accumulation tank [17]. The equation for stratification number is given in Eqs. 2 and 3.

$$\text{Stratification number} = \frac{(\partial T/\partial z)_{t=j}}{(\partial T/\partial z)_{t=0}} \tag{2}$$

$$\frac{\partial T}{\partial Z} = \frac{1}{j-1}\left[\sum_{j=1}^{j-1}\frac{T_j - T_{j+1}}{\Delta Z}\right] \tag{3}$$

where,

$\Delta Z$   Distance between two thermocouples
$J$    Number of thermocouples.

## 3   Results and Discussion

The variation of charging efficiency with time for PCM in spiral module, cylindrical PCM module, cylindrical PCM with fins and without PCM are shown in Fig. 4. The total time duration considered for the evaluation of charging efficiency is 4 h. For the initial time period of 60 min, the charging efficiency varies linearly for all the four conditions. The efficiency curve gradually increases from 10 to 50% after the time duration of 180 min. In case of without PCM modules, the charging efficiency is comparatively low up to 120 min because of less heat transfer area which in turn lead to less heat transfer rate. The maximum charging efficiency achieved in PCM in spiral module, cylindrical PCM module, without PCM and cylindrical PCM with fins are 71, 66, 58 and 53, respectively. The highest efficiency is achieved for PCM
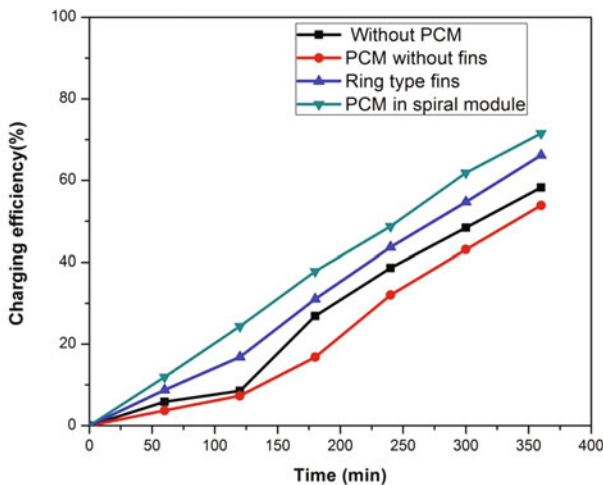


**Fig. 4** Variation of charging efficiency with time
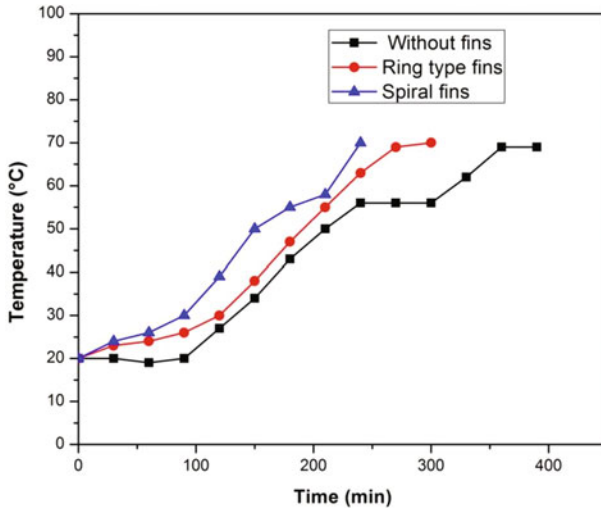
**Fig. 5** Temperature versus time for charging of PCM

in spiral module and cylindrical PCM with ring type cross-section fins. This is because of increase in the area of heat transfer which in turn increase the rate of heat transfer.

In the charging process, the water is circulated from solar plate collector to heat energy accumulation tank by natural convection and density difference. The charging efficiency is evaluated for 6 h to change the phase mode of paraffin wax from solid to liquid. The variation of temperature with time for charging of cylindrical PCM, cylindrical PCM with ring type fins and PCM in spiral module condition is shown in Fig. 5. The time taken for solidification of phase change material in cylindrical PCM without fins is 390 min and with ring type fins is 270 min. Whereas in case of PCM in spiral module, surface to volume ratio is high which results in less time, i.e. 240 min for charging.

Figure 6 shows the variation of time taken for solidification of phase change material for cylindrical PCM and cylindrical PCM with fins. In the discharging process, the paraffin wax phase mode changes from liquid to solid thereby releases latent and sensible heat. Cylindrical PCM with fins reaches solidification at faster rate than cylindrical PCM. To become less hot of PCM material with ring type cross-section fins from 70 to 55 °C the time required is 21.5 min and PCM material without fins took 25.5 min. The discharging time of spiral fins in PCM modules is less when compared with ring type and without fins.

The variation of stratification number with time for without PCM, PCM without fins, ring type fins and spiral fins is shown in Fig. 7. At initial condition, the stratification number is same and close to 1 with the PCM module. This is because
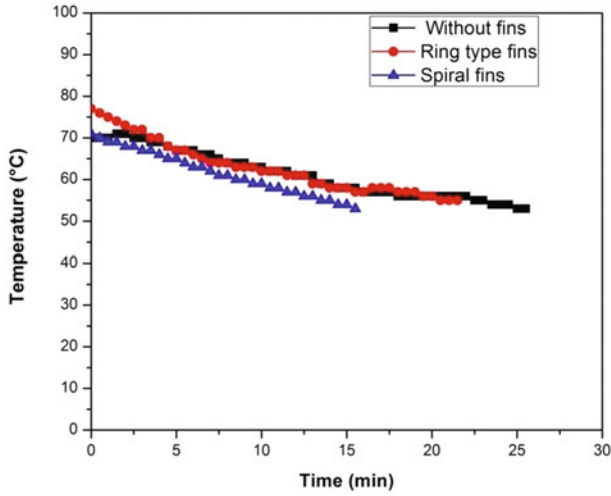
**Fig. 6** Temperature versus time for discharging of PCM
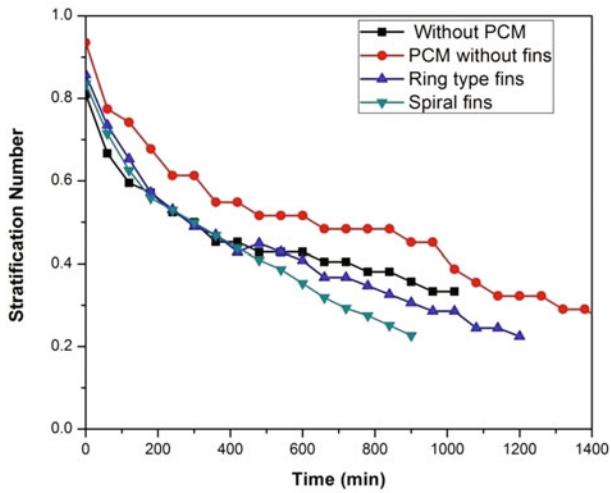


**Fig. 7** Stratification number versus time

of high temperature gradient between hot and cold water. When the time duration increases the stratification, the number decreases exponentially. The effective stratification number is attained for PCM without fins and least stratification number for spiral fins.

# 4   Conclusion

In this paper, a detailed experimental investigation has been done on the stratification number, charging efficiency, charging and discharging time on heat energy accumulation tank without fins, ring type fins and spiral fins.

The stratification for the heat energy accumulation tank for cylindrical PCM gave better performance compared to the thermal energy storage tank without fins and ring type fins. The discharging time of solar water heating system without PCM took 18 h 30 min, only cylindrical PCM took 25 h 30 min and cylindrical PCM with ring type fins took 21 h 30 min.
However, in the charging energy efficiency comparison, heat energy accumulation tank for cylindrical PCM tank with ring type fins and spiral fin module gave better results than the thermal energy storage tank with cylindrical PCM tank and without PCM. This is because the heat transfer rate is increased which improves the charging energy efficiency. The discharging time of solar water heating system for cylindrical PCM with ring type fins took 3 h more than solar water heating system without PCM.

# References

1. Huang MJ, Eames PC, McCormack S, Griffiths P, Hewitt NJ (2011) Microencapsulated phase change slurries for thermal energy storage in a residential solar energy system. Renew Energy 36:2932–2939
2. Castell A, Solé C, Medrano M, Roca J, Cabeza LF, García D (2008) Natural convection heat transfer coefficients in phase change material (PCM) modules with external vertical fins. Appl Therm Eng 28:1676–1686
3. Jesumathy SP, Udayakumar M, Suresh S (2012) Heat transfer characteristics in latent heat storage system using paraffin wax. J Mech Sci Technol 26:959–965
4. Wu S, Fang G (2011) Dynamic performances of solar heat storage system with packed bed using myristic acid as phase change material. Energy Build 43:1091–1096
5. Garnier C, Currie J, Muneer T (2009) Integrated collector storage solar water heater: temperature stratification. Appl Energy 86:1465–1469
6. Murali G, Mayilsamy K, Arjunan TV (2015) An experimental study of PCM-incorporated thermosyphon solar water heating system. Int J Green Energy 12:978–986
7. Mondol JD, Smyth M, Zacharopoulos A (2011) Experimental characterisation of a novel heat exchanger for a solar hot water application under indoor and outdoor conditions. Renew Energy 36:1766–1779
8. Ait Hammou Z, Lacroix M (2006) A new PCM storage system for managing simultaneously solar and electric energy. Energy Build 38:258–265
9. Khalifa AJN, Suffer KH, Mahmoud MS (2013) A storage domestic solar hot water system with a back layer of phase change material. Exp Thermal Fluid Sci 44:174–181
10. Sharma A, Tyagi VV, Chen CR, Buddhi D (2009) Review on thermal energy storage with phase change materials and applications. Renew Sustain Energy Rev 13:318–345

11. Felix Regin A, Solanki SC, Saini JS (2009) An analysis of a packed bed latent heat thermal energy storage system using PCM capsules: numerical investigation. Renew Energy 34:1765–1773
12. Knudsen S, Furbo S (2004) Thermal stratification in vertical mantle heat-exchangers with application to solar domestic hot-water systems. Appl Energy 78:257–272
13. Selvaraj J, Thenarasu M, Aravind S, Ashok P (2015) Waste heat recovery from castings and scrap preheating by recovered heat using an intermediate heat transfer medium. Appl Mech Mater 813–814:776–781
14. Parthasarathy P, Talukdar P, Kishore VR (2009) Enhancement of heat transfer with porous/solid insert for laminar flow of a participating gas in a 3-D square duct. Num Heat Transf Part A Appl 56:764–784
15. Selvaraj J, Jawahar CC, Bhatija KA, Thenagan S (2015) Preheating metal scrap in foundries using solar thermal energy. Appl Mech Mater 813–814:760–767
16. Gopi Krishnan R, Venkatesan V, Nayak P, Yadav AK, Rajesh VR (2015) Performance analysis and thermal modeling of a solar flat plate collector with concave ridged profile
17. Fernández-Seara J, Uhia FJ, Sieres J (2007) Experimental analysis of a domestic electric hot water storage tank. Part II: dynamic mode of operation. Appl Therm Eng 27:137–144

# Performance Analysis of an IC Engine Using Methanol, Ethanol, and Its Blend with Gasoline and Diesel as a Fuel

**Nitin Dabas, Vinay Dubey, Mayank Chhabra and Gaurav Dwivedi**

**Abstract** Lot of research work is being carried out to find a suitable alternate fuel so as to decrease the exhaust emission level and to enhance the power output of an engine. The main objective of this paper is to analyze the performance of an IC engine using alcohol and its blends as a fuel. The alcohols which are reviewed in this paper are methanol and ethanol. It has been observed that as the percentage of alcohol increases with gasoline, exhaust emission level of CO, HC decreases. Due to high octane number of alcohols they can be used at high compression ratio. The low density and low viscosity of alcohols help in improving the spray characteristics and enhance the air–fuel mixing process in a CI engine. Also, oxygen present in alcohol is favorable for complete combustion and increases the thermal efficiency. The study in this paper is based on technical as well as quantitative data available from different research and finds out what is the effect of alcohols and its blend on exhaust emission level and effect on various engine performance parameters and the future aspect of alcohol as a fuel.

**Keywords** Methanol · Ethanol · Blends · Diesel · Gasoline · Diesel engine

## 1 Introduction

Gasoline and diesel are widely used over the past century in automotive industries. In spark ignition (SI) engine, the combustion of gasoline fuel undergoes flame propagation after an initial spark event igniting the homogeneous air–fuel mixture, while in CI engines the fuel is auto-ignited as the fuel exposed to high-temperature gas, heated by compression [1] but gasoline and diesel have lots of negative impact

N. Dabas (✉) · V. Dubey · M. Chhabra
Department of Mechanical and Automation Engineering, Amity University, Noida 201301, India
e-mail: nitindabas95@gmail.com

G. Dwivedi
School of Mechanical Engineering, Vellore Institute of Technology, Vellore, India

on environment as well as on the health of living organism as they produce lots of harmful emission [1]. The main aim of the study of this review paper is to enhance the performance of running engine using different percentage of the methanol/gasoline, methanol/diesel, ethanol/gasoline and ethanol/diesel, and other alcohol derivative with gasoline and diesel. The various subsequent alternative fuels by considering the different aspects like compression ratio, ignition time, air-fuel ratio, and other parameters which are related to engine performance, after the comparison of ignition temperature of methanol, ethanol, and gasoline, we get the methanol that has higher ignition temperature followed by ethanol then gasoline at the same compression ratio. Ethanol provides higher overall efficiency and shaft power to the SI engine, because the heat of vaporization of ethanol is higher than gasoline [2–18]. The burning of ethanol fuel is cleaner than gasoline; therefore, it reduces the inside peak temperature of engine cylinder and hence it increases the power of the engine.

## 1.1 Fuel Requirements for SI Engines

Spark ignition engine is an IC engine, also known as petrol and gasoline engine, where the combustion process of air–fuel mixture is ignited by spark from the spark plug. The following are the requirements for alternative fuel for SI engines as shown in Table 1.

## 1.2 Fuel Requirement for CI Engine

The difference between CI and SI engine is that in CI engines, fuel is injected directly into the cylinder and it works on the principle of diesel cycle. The following are the requirements of alternative fuel for CI engines as shown in Table 2.

**Table 1** Alternative fuel requirements for spark ignition engine [16, 17]

| Properties | Description |
|---|---|
| Octane number | It is used to determine the knock resistance of any fuel. Cooperative fuel research (CFR) engine is used to determine the octane number of any unknown fuel |
| Flammability related to lean limit | Flammability of fuel itself determine the air-fuel mixture's lean limit; fuels with wider flammability of fuels help in increasing tolerance of EGR which leads to further emission reduction of $NO_x$ |
| LHV (of air–fuel mixture) | It is determined by subtracting heat of vaporization of the water from the higher heating value |
| Volatility | Ability of liquid fuel to change into vapor is known as volatility. Volatility of fuel affects the starting of the engine |

**Table 2** Alternative fuel requirements for CI engine [16, 18]

| Properties | Description |
| --- | --- |
| Cetane number | It determines ignition quality of fuel |
| Boiling point | Point at which there should be change of state occurs from liquid to gas throughout bulk of fuel |
| Narrow density and viscosity spread | Higher viscosity causes poor fuel atomization during spray, increases the carbon deposition on fuel filter and also wears the fuel pumps and injectors. The variation of density affects power and fuel spray characteristics during fuel injection and combustion in cylinder |
| Low aromatic compounds contents | The emission of exhaust smoke and $NO_x$ are highly correlated with fuel mono-aromatic content, when a set of 14 diesel was used having low aromatic contents between 0 and 27%. And further increase in exhaust smoke but no change in $NO_x$ when some mono-aromatic content was replaced by di-aromatic compounds |

## 2 Literature Review

Various authors have worked on methanol, ethanol, and their blends with diesel and gasoline as a fuel. The properties of methanol and ethanol in comparison with diesel and gasoline are described in Table 3.

## 2.1 *Methanol*

Methanol as an alcohol is neutral, polar, colorless, and flammable fluid. It is not miscible with alcohols, esters, water, and other organic solvents. In fat and oil, methanol is little soluble [2]. Reasons for which methanol is considered as most favorable fuel for engine is it can be used in (a) a inlet port injection SI engine; (b) a high-compression direct-injection stratified charge SI engine; (c) a direct-injection SI engine; and (d) a turbocharged, port-fuel-injected, high-compression ratio medium-duty engine.

### 2.1.1 Using Methanol–Diesel Blends

Methanol is highly oxygenated as well as a renewable fuel. so, it receives increasing attention nowadays. Several blends can be prepared by methanol and diesel, like D85M15 or other percentages [2]. Advantages and disadvantages of methanol as compared to gasoline are discussed below.

**Table 3** Properties of fuel

| Fuel property | Unit | Gasoline | Methanol | Ethanol | Diesel | Reference |
|---|---|---|---|---|---|---|
| Formula | | C5–12 | CH$_3$OH | C$_2$H$_6$O | C10–26 | [2] |
| Molecular weight | gm | 95–120 | 32 | 46.07 | 180–200 | [2] |
| Oxygen percentage | | 0 | 50 | 34.73 | 0 | [2] |
| Stoichiometric air/fuel ratio | | 14.3–14.8 | 6.45 | 8.87 | 14.5 | [2, 4, 6–8] |
| Boiling point | °C | 20–300 | 64.8 | 78.3 | 175–360 | [2, 8] |
| Flash point | °C | −45 | 11 | 17 | 52–55 | [2, 4] |
| Auto-ignition | °C | 228–470 | 465 | 420 | 220–260 | [2] |
| Temperature | °C | | | | | |
| Cetane number | | 0–10 | 3–5 | 8 | 40–55 | [2, 5] |
| R.O.N | | 80–98 | 108.7 | 120–135 | – | [2] |
| M.O.N | | 81–84 | 88.6 | 100–106 | – | [2] |
| Density (20 °C) | kg/L | 0.74 | 0.792 | 789.4 | 0.83–0.84 | [4, 5] |
| Viscosity (20 °C) | cP | 0.29 | 0.6 | 1.13 | 3.9 | [2] |
| Latent heat | kJ/kg | 310 | 1109 | 918.42 | 270 | [2] |
| High calorific value | MJ/kg | 46.6 | 22.3 | 29.845 | 45.8 | [2, 10] |
| Lower calorific value | MJ/kg | 44.5 | 19.66 | 26.96 | 42.5 | [2, 10] |

Advantages of methanol as compared to diesel fuel are [3]:

1. Methanol has high-fuel–air stoichiometric ratio.
2. It has high-percentage content of oxygen as compared to diesel.
3. It has greater value of latent heat as compared to diesel and gasoline.
4. Due to greater percentage of oxygen, it improves the combustion and reduces the soot and smoke.

The disadvantages are [3]:

1. It shows bad ignition behavior and high ignition temperature due to low cetane number. Therefore, it may show longer ignition delay.
2. It shows corrosive nature with copper, rubber, aluminum, brass, and many plastics.
3. As compared to diesel, it has low flash point as well as low energy content.

### 2.1.2 Use of Methanol–Gasoline Blend as a Fuel

There are many properties of methanol that make it cleaner burning in gasoline engines. It enhances fuel combustion as it contains oxygen. It also has smooth burning due to high-blending octane value, better fuel vaporization in cold engines due to lower boiling point, the highest hydrogen-to-carbon ratio for a lower carbon intensity fuel, and no any contamination of sulfur which poisons catalytic converter operation [1]. Because of high octane number of methanol, engines can be used under a high-compression ratio [15]. Methanol has a higher flame propagation speed and higher percentage content of oxygen which help in improving the engine thermal efficiency as well as helps in complete combustion of fuel which helps in reduction of HC and CO emissions [6, 7]. Methanol has corrosive nature with some materials like rubber and some aluminum alloys [1].

## 2.2 Ethanol

Ethanol ($C_2H_5OH$) is a transparent, colorless, neutral, volatile, flammable, and natural fuel, which is obtained from renewable energy source [18].

### 2.2.1 Reason for Advocating Ethanol

Ethanol has regenerative and ecological characteristics. In SI engine, ethanol permits higher detonation-free compression ratio which ensure higher overall efficiency and shaft power. At the same compression ratio, ethanol has higher self-ignition temperature then gasoline. Ethanol has a pungent odor. Due to high heat of vaporization, it improves volumetric efficiency. As the octane number of ethanol is higher than gasoline, the engine power abruptly rises. Ethanol has better Anti-knocking character, due to high heat of vaporization of ethanol, and it reduces the peak temperature inside the cylinder and also increases the power of the engine [11].

### 2.2.2 Octane Prediction Model

It is not always possible to measure the octane rating, due to limited access to CFR engines. In this octane prediction model we discussed below, there are three RON and MON prediction models for the prediction of the ethanol blends [12].

1. LMC described as,

$$RON\ blend = ((1 - Xmole) \times RON\ base + X\ mole \times RON\ ethanol)$$

2. NMC described as,

$$\text{RON blend} = (1 - \text{Xmole}) \times \text{RON base} + \text{X mole} \times \text{RON ethanol}$$
$$+ \text{Pg} \times (1 - \text{Xmole}) \times (\text{RON ethanol} - \text{RON base})$$

3. Linear volumetric weighted model (LVC) described as,

$$\text{RON blend} = (1 - \text{Xmole}) \times (\text{RON base} + \text{X vol} \times \text{RON ethanol})$$

where, RON blend = Research octane number of ethanol blend,
X vol and X mol = volume fraction and mole fraction of ethanol in ethanol–gasoline blends.

## 3 Result and Discussion

Various studies have been done on using methanol, ethanol, and their blends with diesel and gasoline as a fuel. Some of the results are shown in the below Sects. 3.1 and 3.2.

### 3.1 Methanol with Conventional Diesel Blends Result

See Table 4.

**Table 4** Finding of different methanol–diesel blends as compared to conventional diesel fuel

| Fuel | Engine specifications | Findings | Reference |
|---|---|---|---|
| $D_{100}$ $M_0$<br>$D_{95}$ $M_5$<br>$D_{90}$ $M_{10}$<br>$D_{85}$ $M_{15}$ | 4-cylinder, 4-S, direct injection, water-cooled, turbocharged and compression ratio of 17:1 | CO emission decreases and $NO_x$ emission increases as methanol quantity in diesel–methanol blend increases. HC emission decreases | [3] |
| Diesel–methanol blends up to 15% blending | Single cylinder, 4-stroke, direct-injection compression-ignition, water-cooled, variable compression ratio engine | Fuel–air equivalence ratio decreases as methanol content increases and as well as rpm of engine increases M (10%) + D (90%) have more effective power as compared to other methanol–diesel blends | |

**Table 4** (continued)

| Fuel | Engine specifications | Findings | Reference |
|------|----------------------|----------|-----------|
| Diesel–methanol blends up to 80% methanol in blend | Four-stroke, four-cylinder diesel engine | Higher torque in all ratio of methanol–diesel blends than diesel fuel alone. The BSFC decreases with increase of methanol concentration but with all ratios, BSFC is higher than pure diesel. When speed is higher, $D_{70}M_{30}$ produces more break thermal efficiency as compared to pure diesel, $D_{90}M_{10}$ or D80M20 | [4] |

## 3.2 Methanol with Gasoline Blends Result

See Table 5.

**Table 5** Finding of using methanol–gasoline blends as fuel

| Fuel | Engine specifications | Findings | Reference |
|------|----------------------|----------|-----------|
| Gasoline and methanol blends | 3-cylinder, bore 68.5 mm, displacement 0.8 L S.I engine | The increase of methanol increases the formaldehyde emissions and methanol emission increases with the increase of engine load under different speeds. When the engine is fueled with $M_{20}$, the maximum pressure is higher than that of pure gasoline operation. When methanol is added into gasoline, the fuel blend contains more oxygen, which reduces CO and HC emissions $NO_x$ emission increases as methanol content increases | [6] |
| Various gasoline–methanol blends | 3-cylinder, 4-S, electronic control fuel injection S.I engine | The brake thermal efficiencies of M10, M20, and M85 are 6.67, 8.88, and 10.85% higher than that of the gasoline based operation, respectively | [7] |

## 3.3 Ethanol–Gasoline and Ethanol–Diesel Blends Result

### 3.3.1 Effects of E0, E10, and E85 on Spark Ignition Engine (SI)

a. E10 and E85 fuels improved energy conversion efficiency but when engine run on E85, specific fuel consumption (SFC) increased.
b. E10 and E85 slightly improved CO emission at stoichiometric air-to-fuel ratio.
c. When engine run on E85, the specific hydrocarbon emission (HC) increased and (E10) also increased (HC) emission in smaller amount.
d. Relative to E0, the E10 and E85 fuels run at OEM spark timing produced lower specific emission level of NO. E85 is the best fuel for lower specific emission of nitric oxide (NO).
e. In the fuel system, when IR fuel-conditioning device is used, it improved energy conversion efficiency of the engine but had adverse effects on HC and NO emission at the near rated speed.
f. IR fuel-conditioning device does not much affect the CO emission.
g. E85 reduced the temperature of the mixture before it entered the cylinder, when the heat of vaporization of E85 is higher [13, 14].

### 3.3.2 Effects of D50E40 on Engine Performance

a. Brake thermal efficiency of diesel engine increases and brake specific fuel consumption decreases, when the use of D50E40 blend.
b. CO emission is increased when using the blended fuel (D50E40) as compared to diesel engine.
c. The smoke density emission of the blended fuel is lower than diesel fuel.
d. $CO_2$ emission is increased when the blended fuel (D50E40) is used as compared to diesel engine.
e. In CI engine, the cylinder pressure and heat release rate of D50E40 emulsified fuel is higher than other blended fuel and diesel fuel at full load [15].

## 4 Conclusion

a. By blending methanol with diesel or gasoline, the BSFC increases as the percentage of methanol and ethanol increases, and the emission of CO and HC deceases but there is no significant effect on the emission of $NO_x$. The emission of $NO_x$ also increases as the concentration of methanol increases in the blend.

b. Ethanol blend with gasoline in lower proportion that improves the torque and B. P of the engine. Using the different blends like E5, E10, and E20, an increment of engine break power in significant amount as 2.32, 2.78, and 4.17%, respectively, and also increment of engine torque as 0.29, 0.58, and 4.78%, respectively.

c. BSFC of engine increases when the volume of ethanol content is higher.

d. BTE of the SI engine varied significantly when using these blends, maximum BTE of 3.5% for E20, 2.5% for E10, and 6% for E40.

# References

1. Dwivedi G, Kumar P, Sharma MP (2014) Impact of biodiesel on combustion, performance and exhaust emissions of diesel engines. J Integr Sci Technol 2(2):57–63
2. Zhen X, Wang Y. An overview of methanol as an internal combustion engine fuel. Renew Sustain Energy Rev. https://www.researchgate.net/publication/282744095
3. Solmaz O, Ciniviz M, Kose H, Canli E. An experimental investigation on effect of methanol blended diesel fuels to engine performance and emission of a diesel engine. Sci Res Essay 69 (15):3189–3199
4. Yusaf T, Hamawand I, Baker P, Najafi G. The effet of methanol-diesel blended ratio on CI engine performance. Int J Automot Mech Eng 1385–1395
5. Bayraktar H. Experimental study on the performance parameters of an experimental CI engine fueled with diesel-methanol-dodecanol blends. https://doi.org/10.1016/j.fuel.2007.04.021
6. Clemente ERC, Liu S, Hu T, Wei Y (2007) Study of spark ignition engine fueled with methanol-gasoline fuel blends. Appl Therm Eng 27:1904–1910
7. Ying W, Yanju W, Shenghua L, Hongsong L, Rui Y, Jie L (2008) Effect of methanol-gasoline blend on a SI engine performance and emission. Energy Fuel 22:1254–1259
8. Taha AA, Abdel-Salam TM, Vellakal M. Alternative fuels for internal combustion engines: an overview of the current research. Int Energy Environ Found. https://www.researchgate.net/publication/272167333
9. Dwivedi G, Verma P, Sharma MP. Operational and environmental impact of biodiesel on engine performance. Int J Renew Energy Res-IJRER 5(4):961–970
10. Thakur A, Mehra R, Mer KKS (2017) Progress in performance analysis of ethanol-gasoline blends on SI engine. Renew Sustain Energy Rev 69:324–340
11. Lenger T, Von Meine OF, Yamamoto CI (2005) A predictive thermodynamic model for the Brazilian gasoline. Fuel 84:1099–1104
12. Wang C, Xiang L, Xu H (2017) Ethanol blends in SI engine: RON, octane-added value, cooling effect, compression ratio and potential engine efficiency gain. Appl Energy 191:603–619
13. Kahraman N, Tangoz S (2017) Experimental study of gasoline-ethanol-hydrogen blends combustion in an SI engine. Int J Hydrog Energy 1–10
14. Elfasakhany A (2016) Engine performance evaluation and pollutant emission analysis using ternary bio-ethanol-iso-butanol-gasoline blends in gasoline engine. J Clean Prod 139:1057–1067
15. Ogut H, Aydin F. Effects of using ethanol-biodiesel-diesel fuel in single cylinder diesel engine to engine performance and emissions. Selcuk University, Faculty of Agriculture 42130 Konya/Turkey
16. Kim J, Bae C (2016) Alternative fuels for IC engines. In: Proceedings of combustion institute, 5 Sept 2016

17. Pitsch H, Beeckmann J, Cai L (2013) Experimental investigation of laminar burning velocities of methanol/ethanol/n-propanol and n-butanol at high pressure. Fuel
18. Ladommatos N, Xiao Z, Zhao H (2000) Effects of the fuels with a low aromatic content on diesel engine exhaust emission. J Automob Eng

# Ultra-Fast Cooling of Flat Metal Pate in a Modified Runout Table

Check for updates

## Sudhansu Mohan Padhy, Purna Chandra Mishra, Ruby Mishra and Achintya Kambli

**Abstract** Cooling of metal components at the end of the steel production process is a highly critical step in production. The cooling process rate is time critical, and it helps determine various crucial steel properties. There is continuing research which is being done to help improve the process to boost the quality of steel produced as well as reduce the overall cost of production. Ultra-fast cooling involves the use of varied water and air pressures as the cooling media. Surface heat flux at each experimental condition was computed from the transient temperature history measured by K-type thermocouples embedded at the bottom surface of the plate. Peak heat flux on the surface of 2.954 MW/m$^2$ was obtained using an inlet pressure of water 5 bar, pressure of air 3 bar, strip velocity of 5 cm/s, and nozzle to plate height of 100 mm for a starting temperature of 1123 K of the 4-mm-thick steel plate.

**Keywords** Runout table · Spray cooling · Ultra-fast cooling · Metal plate · Pressure

## 1 Introduction

The rising requirements for high-strength but low-cost metal products have led the industry to pursue advancements in material-processing technology suitable for attaining lower production costs, higher levels of productivity, and superior-quality products while simultaneously reducing the production time. Traditionally utilized thermo-mechanical-controlled processes are used to perfect the microstructure and yield two- or poly-phase microstructure and offer a good blend of high-strength and low-temperature impact toughness [1]. Experimentally, it has been found that the rate of cooling plays a critical role in the formation of specific microstructures. One of the most sought-after microstructures in formed metal products is martensite. Martensite formation requires the specimen to be cooled from recrystallization

S. M. Padhy · P. C. Mishra (✉) · R. Mishra · A. Kambli
KIIT, Deemed to be University, Patia, Bhubaneshwar 751024, Odisha, India
e-mail: pcmishrafme@kiit.ac.in

temperature to room temperature at a very high rate of cooling [2, 3]. As improved microstructure is obtained by accelerated cooling, laminar single-phase jet cooling currently used has been proven to be an inefficient method. Thus, two-phase (water and air) spray cooling is the superior method in the manufacturing of steel of superior quality accompanied with all the essential characteristics [4].

The change of thermo-metallurgical properties in steel occurs while cooling on the runout table (ROT), and this method invariably alters the mechanical properties of the material. Typically, on the runout table, the steel strips and the temperature are elevated to an excess of approximately 1173 K and moved through roughing and completing plants. The strips are cooled down to 873 K [4] thereafter. From experimentation, an increase of 100 K in the temperature during finishing results in an increase in the temperature of transition by nearly 5 K in tear tests and nearly 4 K for Charpy test [5]. Overall, a boost in yield strength (YS) of the manufactured rolled strips is an outcome of lower temperature while finishing. It must be noted that ultimate strength or lengthening remains mostly unaffected. Recently, the enhanced cooling concept that has been developed to bring down the product temperature on the ROT is being denoted to as 'controlled cooling' or 'thermo-mechanical processing' (TMP). It eliminates the variance of strength in different areas of a coil while the resistance to fracture and strength of the steel has been shown to increase. Steel so produced has properties that corresponding or exceed properties of regularly heat-treated strips. It additionally allows for a decrease in materials required for alloying vital to reach an essential property value; thereby, ease of welding is enhanced. All things considered, TMP allows for a substantial reduction of cost of production of steel strips in addition to lowering the cost of products that would subsequently employ the steel [5]. The relationship of structure and property in low carbon steel, micro-alloyed with titanium (Ti) and niobium (Nb), was investigated by V. S. A. Challa et al. at diverse temperatures while coiling. It was observed that the microstructure chiefly contained lath bainite as well as polygonal ferrite.

Zhao et al. investigated the effect of temperature of coiling on the microstructure of hot-rolled enamel steel [6]. Results showed a substantial amount of interphase precipitates of nanosized TiC were attained at coiling temperatures of 923 and 973 K. But smaller amount of precipitates was detected in steel when the temperature was 873 K. The UTS and the YS deteriorated with rising coiling temperature and showed increased elongation.

A continuous cooling diagram is given in Fig. 1. The enhanced cooling process is defined by $\gamma \rightarrow \alpha$ conversion. Steel increases strength by subduing the static recovery process and deformed $\alpha$ by recrystallization. Consequently, both variants of $\alpha$ (non-deformed and deformed) grow atop bainite's microstructure.

As improved microstructure is obtained by accelerated cooling, laminar single-phase jet cooling currently used has been proven to be an inefficient method. Thus, two-phase (water and air) spray cooling (SC) or spray impingement cooling (SIC) is the superior method in the manufacturing of steel of superior quality accompanied with all the essential characteristics [4]. An assessment of coefficients of heat transfer (HTC) measured during several cooling methods is shown in Fig. 2.

**Fig. 1** Schematic of controlled rolling without and with accelerated cooling [5]
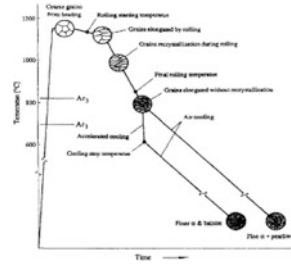


**Fig. 2** Heat transfer coefficient (W/cm$^2$ °C) [7]
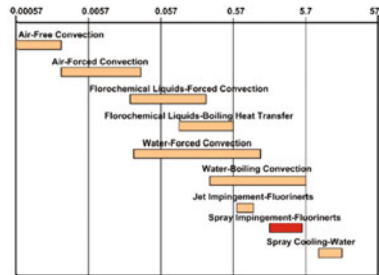


There exist many experimental and theoretical works which are elementary in attaining a general elementary understanding and possible use cases of SIC in diverse engineering utilization [7, 8]. The literature available in the public domain divulges no major data arising from experimentation in the vastly inter-connected fields of bubble dynamics, droplet impingement, mass impingement density (MID), pool-boiling, and plate thickness at elevated temperatures through a transient heat transfer process [9, 10], environments regularly seen in the metal molding trade.

Rate of cooling grows with a rise in the rate of impingement. Impact of velocity was recognized predominantly during film boiling, which is known to happen when the temperature exceeds 573 K. The tendency was also observed by Choi and Yao [11]. Pereira et al. [12] and Aamir et al. [13] methodically looked into the impact of the characteristics of the spray on duration of cooling and the rate under influence of various pressures at inlet with water being employed as coolant. Mohapatra et al. [14] looked into transfer of heat from a steel plate (12 mm thick) held in stationary position at various starting temperatures utilizing an atomized spray of water with added surfactant. Somasundaram and Tay [15] performed experiments by utilizing commercially obtainable nozzle fitted to solenoid actuated valves and an insulated block of copper. Nayak et al. [4] studied heat flux and its relation to SIC characteristics. The studies were done using varying plate thicknesses with spray impingement cooling as the cooling medium. For a 4-mm plate, the maximum heat flux obtained was 4.895 MW/m$^2$ with parameters $P_w$ = 0.4 MPa, $P_a$ = 0.3 MPa, and $h$ = 120 mm.

The complex interactions among the phases (vapor and liquid phases) as well as impact of liquid and change of phases during SIC are an obstacle in the way of grasping the detail workings of the process of heat removal; thereby,

comprehension of SIC is still in its nascent periods [16, 17]. Significant experimental and computational work is vital for the development of an in-depth comprehension of SIC's process of removal of heat.

## 2  Experimental Setup

A representation of the setup used is given in Fig. 2. The primary components used were a spray system, a moving bed setup, a plate heating system, and a wireless controller. The spray delivery system is made up of an overhead tank, an air compressor, a positive displacement pump, a pressure gauge and regulator, flow meter, an internally mixing nozzle. The setup can be used to generate sprays with varying air and water pressures. The moving bed setup consists of a moving bed which is wirelessly controlled using LabVIEW via a MyRIO microcontroller (Fig. 3).

The nozzle with which the spray was generated was placed above the moving bed, and the spray height could also be adjusted. The motion itself was provided by a stepper motor. The plate heating system consisted of a flat coil heater which could heat the plate to 1100 °C. The heated plate had to manually be placed onto the moving bed. A similar heating setup was used by Nayak et al. [4] and Mishra et al. [18] for their work. The workpiece was simulated using a plate of dimension 120 mm by 120 mm and thickness of 4 mm. The plates themselves had K-type thermocouples embedded into them as shown in Fig. 4. Because of its dependability and precision, K-type thermocouples were utilized broadly at temperatures

**Fig. 3** Schematic of the setup
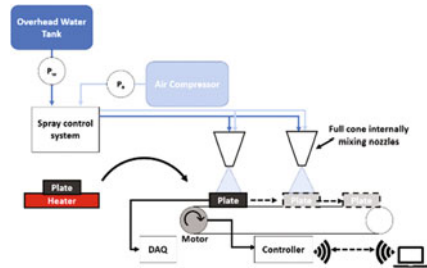


**Fig. 4** Schematic of plate
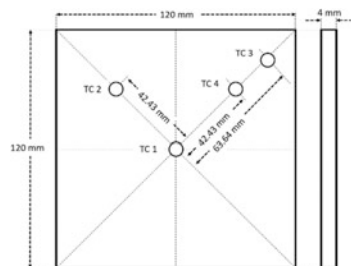
up to 1260 °C. Data were recorded using a CHINO Graphic Recorder KR2000 data acquisition system. The data were stored on a compact flash memory card and could be downloaded onto a PC for further analysis.

## 3 Experimental Procedure and Design of Experiments

The general experimental procedure was as follows. The plate with the embedded thermocouples was plated onto the flat coil heater and heated till 1100 °C. While plate heating, a temperature clearance of +100 °C was maintained to compensate for the drop in initial temperature due to higher rates of convective cooling at elevated temperatures while moving the plate from the heater onto the bed. The heated plate was then placed onto the moving bed, and the spray cooling system was turned on. The moving bed was then passed through the spray repeatedly till its temperature dropped down to room temperature. The spray settings along with the moving bed speed as well as the nozzle height were predetermined using Taguchi method for optimization. Taguchi method suggests, for optimization of a process or product, a three-step approach should be carried out which includes system design, parameter design, and tolerance design. Taguchi method involves factors selection, design of experiments, conducting experiments, data analysis, determining the optimal combination of factor levels, and verification [19].

Water pressure, air pressure, nozzle height, and speed were the input parameters for experimenting with spray cooling. Orthogonal array obtained from Minitab software for water–air spray experiment is given in Table 1. Here, the parameters

**Table 1** Orthogonal array obtained by Taguchi's method

| $P_w$ | $P_a$ | $h$ | $v$ |
|-------|-------|-----|-----|
| 1 | 1 | 1 | 1 |
| 1 | 2 | 2 | 2 |
| 1 | 3 | 3 | 3 |
| 1 | 4 | 4 | 4 |
| 2 | 1 | 2 | 3 |
| 2 | 2 | 1 | 4 |
| 2 | 3 | 4 | 1 |
| 2 | 4 | 3 | 2 |
| 3 | 1 | 3 | 4 |
| 3 | 2 | 4 | 3 |
| 3 | 3 | 1 | 2 |
| 3 | 4 | 2 | 1 |
| 4 | 1 | 4 | 2 |
| 4 | 2 | 3 | 1 |
| 4 | 3 | 2 | 4 |
| 4 | 4 | 1 | 3 |

**Table 2** Spray, nozzle distance, and speed parameters and their ranges

| Parameters | | Ranges | Levels |
|---|---|---|---|
| Water pressure | (bar) | 2–5 | 2, 3, 4, 5 |
| Air pressure | (bar) | 2–5 | 2, 3, 4, 5 |
| Nozzle distance | (mm) | 100–250 | 100,150, 200, 250 |
| Speed | (cm/s) | 5–20 | 5, 10, 15, 20 |

are water pressure, air pressure, nozzle height, and speed, respectively. The levels used are given in Table 2.

# 4   Results and Discussion

## 4.1   Cooling Curves

Figure 5 shows the cooling for a combination of water pressure (4 bar), air pressure (4 bar), nozzle distance (100 mm), and plate speed (10 cm/s) at four locations on the plate.

The initial temperature for the initiation of spray cooling was approximately 850 °C. As can be observed, there was a variation of temperature between thermocouples of approximately $\pm 50$ °C at the end of the heating phase of the experimentation. This can be attributed to the uneven heating of the plate due to constraints of heater size.

A maximum cooling rate of 187.75 °C/s was achieved for a combination of water pressure (5 bar), air pressure (3 bar), nozzle distance (200 mm), and plate speed (5 cm/s).

**Fig. 5** Cooling curve (experimental conditions: $P_w = 4$ bar, $P_a = 4$ bar, $V = 10$ cm/s, $h = 100$ mm)
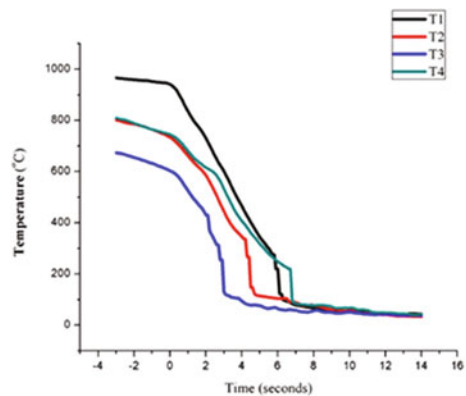
## 4.2 Calculation of Surface Heat Flux ($\dot{q}$)

This method utilized for computation of surface heat flux was employed by Nayak et al. for their research [4]. Heat flux was computed using Eq. 1:

$$\dot{q} = h_c \times (T_s - T_c) = \rho \times C_P \times t \times \text{CR} \tag{1}$$

where

$$h_c = \left(\frac{\rho \times C_P \times t \times \text{CR}}{T_s - T_c}\right) \tag{2}$$

$$\text{CR} = \left(\frac{T_i - T_f}{\tau_i - \tau_f}\right) \tag{3}$$

$T_i$     Temperature of the plate at start of cooling in °C
$T_f$     Temperature of the plate at end of cooling in °C
$\tau_i$     Start time of cooling in s
$\tau_f$     End time of cooling in s
$t$     Plate thickness in m
$\rho$     Material density of plate in kg/m$^3$
$C_P$     Specific heat capacity of plate material in J/kg °C

Using the above formula, the maximum heat flux observed is 2953.7 kW/m$^2$.

## 4.3 Effect of Parameters on Heat Flux

Taguchi-based grey relational analysis was used for optimization of the parameters ($P_w$, $P_a$, $h$, and $v$) for performance characteristics (i.e., $\dot{q}$) of the steel plate during SIC environment. Plot for $S{:}N$ ratios is given in Fig. 6. Response table for means is given in Fig. 7. Using the $S{:}N$ ratios, an optimized set of parameters can be determined which are as follows: $P_w$ = 5 bar, $P_a$ = 3 bar, $v$ = 5 cm/s, and $h$ = 100 mm. These parameters are used for validation studies.

**Fig. 6** $S{:}N$ plot for means (larger is better)

**Fig. 7** Response table for means

| Level | $P_w$ | $P_a$ | v | h |
|-------|-------|-------|------|------|
| 1 | 58.99 | 60.96 | 64.67 | 63.61 |
| 2 | 59.69 | 62.9 | 63.45 | 60.32 |
| 3 | 63.1 | 60.32 | 59.99 | 61.55 |
| 4 | 64.01 | 61.62 | 57.68 | 60.31 |
| Delta | 5.02 | 2.58 | 6.99 | 3.3 |
| Rank | 2 | 4 | 1 | 3 |

## 4.4 Regression Analysis

Using the experimental data, regression analysis was performed, and a quadratic model was developed for heat flux (Eq. 4).

$$\dot{q} = -8701 + 3058P_w - 342P_a + 134h - 830v - 551P_w^2 + 71P_a^2 - 0.138h^2 \atop + 23.9v^2 + 447P_wP_a - 4.75P_wh - 59.9P_wv - 18P_ah + 118P_av \tag{4}$$

## 4.5 Validation Studies

Using the optimized parameters obtained from Taguchi analysis ($P_w$ = 5 bar, $P_a$ = 3 bar, $v$ = 5 cm/s, $h$ = 100 mm), validation studies were performed. The heat flux obtained for the optimized parameters was 2982 kW/m$^2$ which is higher than the maximum heat flux obtained using unoptimized parameters.

## 5 Conclusion

As from the results, we can arrive at the following conclusions:

1. The strip velocity was found to be the dominant factor on heat flux. Lower strip velocity results in higher heat flux. This can be attributed to the increased time spent by the plate under the influence of SIC.
2. Water pressure had the second greatest impact. It can be deduced that increase in $P_w$ increased the quantity of water available for cooling.
3. Validation studies showed that the optimized parameters gave the highest heat flux (2982 kW/m$^2$).
4. Maximum heat flux obtained is lower than that obtained in previous studies conducted in static condition. This indicates that effect of strip velocity is significant.

# References

1. Challa VSA, Zhou WH, Misra RDK, O'Malley R, Jansto SG (2014) The effect of coiling temperature on the microstructure and mechanical properties of a niobium-titanium microalloyed steel processed via thin slab casting. Mater Sci Eng, A 595:143–153
2. Biss V, Cryderman RL (1971) Martensite and retained austenite in hot-rolled, low-carbon bainitic steels. Metall Mater Trans B 2(8):2267–2276
3. Elmay W et al (2013) Effects of thermomechanical process on the microstructure and mechanical properties of a fully martensitic titanium-based biomedical alloy. J Mech Behav Biomed Mater 18:47–56
4. Nayak SK, Mishra PC, Parashar SKS (2016) Influence of spray characteristics on heat flux in dual phase spray impingement cooling of hot surface. Alexandria Eng J 55(3):1995–2004
5. Chen SJ, Tseng AA (1992) Spray and jet cooling in steel rolling. Int J Heat Fluid Flow 13 (4):358–369
6. Zhao Y, Huang X, Yu B, Yuan X, Liu X (2017) Effect of coiling temperature on microstructure, properties and resistance to fish-scaling of hot rolled enamel steel. Materials (Basel) 10(9)
7. Zhang Z, Jiang P-X, Hu Y-T, Li J (2013) Experimental investigation of continual- and intermittent-spray cooling. Exp Heat Transf 26(5):453–469
8. Lucas A et al (2004) Metallurgical aspects of ultra fast cooling in front of the down-coiler. Steel Res Int 75(2):139–146
9. Sussman M, Smereka P, Osher S (1994) A level set approach for computing solutions to incompressible two-phase flow. J Comput Phys 114(1):146–159
10. Amon CH, Murthy J, Yao SC, Narumanchi S, Wu CF, Hsieh CC (2001) MEMS-enabled thermal management of high-heat-flux devices EDIFICE: embedded droplet impingement for integrated cooling of electronics. Exp Therm Fluid Sci 25(5):231–242
11. Choi KJ, Yao SC (1987) Mechanisms of film boiling heat transfer of normally impacting spray. Int J Heat Mass Transf 30(2):311–318
12. Pereira RH, Filho EPB, Braga SL, Parise JAR (2013) Nucleate boiling in large arrays of impinging water sprays. Heat Transf Eng 34(5–6):479–491
13. Aamir M, Qiang L, Xun Z, Hong W, Zubair M (2014) Ultra fast spray cooling and critical droplet diameter estimation from cooling rate. J Power Energy Eng 2:259–270
14. Mohapatra SS, Ravikumar SV, Ranjan R, Pal SK, Brat Singh S, Chakraborty S (2013) Ultra fast cooling and its effect on the mechanical properties of steel. J Heat Transf 136(3):32101
15. Somasundaram S, Tay AAO (2013) Comparative study of intermittent spray cooling in single and two phase regimes. Int J Therm Sci 74(C):174–182
16. Bhattacharya P, Samanta AN, Chakraborty S (2009) Spray evaporative cooling to achieve ultra fast cooling in runout table. Int J Therm Sci 48(9):1741–1747
17. Selvam RP, Lin L, Ponnappan R (2006) Direct simulation of spray cooling: effect of vapor bubble growth and liquid droplet impact on heat transfer. Int J Heat Mass Transf 49(23–24):4265–4278
18. Mishra PC, Mukhopadhyay A, Sen S (2014) Experimental investigation of heat transfer characteristics in water shower cooling of steel plate. J Enhanc Heat Transf 21(1)
19. Taguchi RP (1988) Techniques for quality engineering. McGraw Hill

# A Novel System for Exhaust Emission Reduction of Diesel Engine by Using Electrochemical Technique

**Priyanka Sharma, Prem Pal, Ashutosh Mishra, Mohit Bhandwal and Ajay Sharma**

**Abstract** In this research, an experimental setup was fabricated, and the new device was designed in conjugation with the catalytic converter. This paper is concerned to enhance the efficiency of the exhaust control system by using electrochemical principle. It relates to the use of a solid electrolyte to convert the $NO_x$ into $N_2O$ and $O_2$. A freezer gel pack along with the thermocouple is used on the exhaust pipe to maintain the temperature of the reaction. At a temperature range of 200–300 °C, $N_2O$ is further reduced to $N_2$ and $O_2$ while the oxidation of HC, CO, and elemental carbon is done in the catalytic converter. Carbon dioxide ($CO_2$) produced is allowed to pass through normal water in an aluminum alloy chamber. Also, particulate matter is treated in a meshed filter downstream to the aluminum chamber. The result shows a significant reduction in $NO_x$ emission.

**Keywords** Freezer gel pack · Catalytic converter · Particulate matter · Exhaust

## 1 Introduction

In today's world, the rapid development and advancement of the technologies have led to the increase in the degradation of the environment. One of the main threats to the environment is the air pollution. It is of major concern to the humans as well as to the other creatures on the earth. According to the US Embassy, the level of particulate matter (PM 2.5) in the ambient air reached to more than 1200 μg/m$^3$ in New Delhi [1]. The indicated value of PM 2.5 was 48 times the guideline value prescribed by World Health Organization (WHO) [2]. So, it has become a matter of concern and there is an immediate need to reduce the air pollution as it is severely affecting the health of individuals both in cities and rural areas.

P. Sharma · P. Pal · M. Bhandwal (✉) · A. Sharma
Department of Mechanical Engineering, Amity University, Noida, Uttar Pradesh, India
e-mail: mbhandwal@amity.edu

A. Mishra
Motilal Nehru National Institute of Technology, Allahabad, India

**Table 1** Emission gases from diesel engine exhaust

| Emission gases | Amount |
|---|---|
| CO | 300–1200 ppm |
| HC | 50–350 ppm |
| $NO_x$ | 350–1000 ppm |
| $SO_x$ | 10–100 ppm |
| $H_2O$ | 1.4–7% |
| $CO_2$ | 7% |
| $O_2$ | 10–15% |
| PM | 65 mg/m$^3$ |

Burning fossil fuels, and smoke from various power plants and transportation are some of the primary causes of air pollution. The transport system is the second largest section responsible for increasing air pollution. Gasoline engines and diesel engines are the prime selection for nearly all automobile companies due to the easy availability of the fuel. The drawback of these engines is that they release a considerable amount of harmful gases ($NO_x$, HC, CO, PM, $SO_x$) to the environment and is widely responsible for causing air pollution globally. Among internal combustion engines, diesel engines are widely employed in the automobiles especially in commercial vehicles due to reliability, durability, and energy efficiency, and the most dominant factor is low operating cost. However, besides numerous positive factors, diesel engines adversely affect the environment as the exhaust gases emitted by diesel engine are more harmful than those from a petrol engine. The harmful emission of diesel engine contains the gases shown in Table 1.

In the literature [3–14], various procedures were reported to reduce the pollutants in the emission. Biodiesel mixed with the diesel reduces harmful emission. Also biodiesel–diesel and ethanol–biodiesel–diesel blends produce less carbon dioxide (main constituents of the greenhouse effect), CO, HC, and particulate matter [3–6], but increase the NO level and had a minor effect on the transient performance [7]. The metal-based additive added with biodiesel reduces NO, CO, and HC [8]. Multistage fuel injection is another method to reduce the emission from automobiles. A small amount of fuel injection before main fuel injection reduces the emission such as two pilot injections prior to the main injection reduces HC, $NO_x$, and particulate matter [9, 10].

In the secondary method, catalytic filters coated with cordierite monoliths with alumina-based suspensions containing Cu, Co, or V and K were prepared to remove particulate matter and nitrogen oxides [11]. Treatments of exhaust gasses that use the alkali solution reduce $CO_2$ [12]. The efficiency of catalytic converter also increases when turbulence-induced devices are fitted before it [13–15].

The engine exhaust system is developed in such a way that it will emit a small number of pollutants. It is done by affixing catalytic converter to the exhaust system of the engine, by doing so the emissions had reduced to some extent. According to the emission norms, the limit of some of the pollutants is given in Table 2.

**Table 2** Emission standards

|  | CO (vol.%) | HC (ppm) | NO (ppm) | $H_2$ (vol.%) | $H_2O$ (vol.%) | $CO_2$ (vol.%) | $O_2$ (vol.%) |
|---|---|---|---|---|---|---|---|
| BS III | 0.5 | 350 | 900 | 0.17 | 10 | 10 | 0.5 |

The catalytic converter is the device used in an automobile to reduce the various emissions from the diesel engine. It minimizes the formation of $NO_x$, HC, and CO by reduction and oxidation process shown in Eqs. 1–3.

$$\text{Reduction: } 2NO_x \rightarrow XO_2 + N_2 \tag{1}$$

$$\text{Oxidation: } 2CO + O_2 \rightarrow 2CO_2 \tag{2}$$

$$CXH_{2X+2} + [(3x+1)/2] O_2 \rightarrow XCO_2 + (X+1) H_2O \tag{3}$$
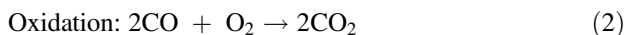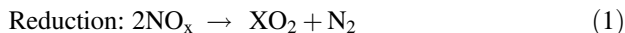
Although catalytic converter minimizes the formation of $NO_x$, HC, and CO, $CO_2$ formation after the oxidation of CO and HC remains unreacted and released to the environment. In this research, $NO_x$ is getting eliminated by using an electrochemical method and $CO_2$ is removed by passing it through the water. The particulate matter is allowed to trap in a mesh filter having the geometry of 0.5–0.7-μ lattice.

## 2 Experimental Setup

The experimental setup consists of a diesel engine whose technical specification is given in Table 3.

When the temperature into the combustion chamber reaches to the range of 1200–1400 °C, the formation of $NO_x$ takes place due to the reaction between $O_2$ and $N_2$ from the air in the chamber. But, when this emission reaches the exhaust pipe, the temperature becomes 750 °C approximately and at this temperature, the

**Table 3** Engine specifications

| Type | BS3, 16 valves, DOHC |
|---|---|
| Engine capacity | 1405 cc |
| Max. power (PS@RPM) | 48.9 PS @ 5000 RPM |
| Max. torque (NM @ RPM) | 85 NM @ 2500 RPM |
| Fuel type | Diesel |
| Emission norms | BS3 |
| Manufacturer | TATA Company, India |
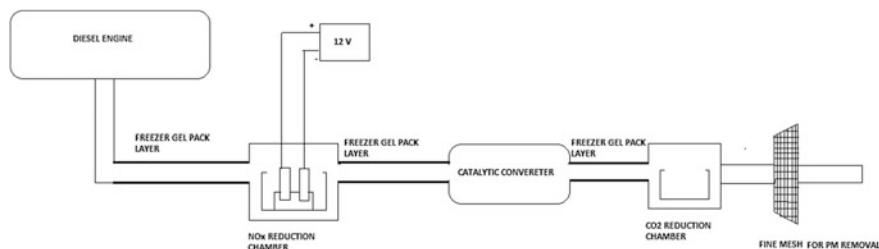
**Fig. 1** Line diagram of the experimental setup

exhaust enters the catalytic converter in most of the present exhaust systems. To lower down the temperature of the exhaust gases about 350–500 °C for the electrochemical reaction to take place, three layers of the cool pack were enfolded on the exhaust pipe as shown in Fig. 1. The gel pack is of carboxymethyl cellulose and propylene glycol. This material was useful in absorbing heat from the surface and hence decreases the temperature for the further operation.

Now, after minimizing the temperature of the gases from the converter, the exhaust was allowed to pass through the section made up of an aluminum container accommodating solid electrolyte and two electrodes of the material of platinum for electrochemical reaction. The solid electrolyte used was the proton conductor preferably made of $Sr\, Zr_{0.9}\, Yb_{0.1}\, O_{3-\alpha}$ (zeolite), and the platinum electrodes which were used in the system comprise of platinum sponge and $Sr/Al_2O_3$ catalyst on the platinum cathode and pure platinum anode. The exhaust was passed through the chamber where NO gas was reduced to nitrogen ($N_2$) and nitrous oxide ($N_2O$) at cathode, whereas at anode oxygen gas was liberated at low current density. The amount of gases at the cathode depend upon the rate of reaction, and the low current density at anode was attained by the regular supply of current from the car battery (6–12 V) to the proton conductor.

For further reduction of the $N_2O$ gas to nitrogen ($N_2$) and oxygen ($O_2$) gases, the exhaust pipe was again surrounded by two layers of cool pack to reduce the temperature of the gases about 200–250 °C. Further, this $O_2$ will react with carbon monoxide (CO), hydrocarbon (HC), and elemental carbon (C). This will form carbon dioxide ($CO_2$) as in case of catalytic converter. To overcome the problem of unreacted HC, CO, and elemental carbon, two-way catalytic converter is used in the system.

To remove $CO_2$ from the exhaust, a separate section is designed which is fitted after the catalytic converter. This separate section comprises a closed aluminum container having normal water in it. The operating temperature for the section is around 20–35 °C, which is attained by using two layers of cool pack on the exhaust pipe from the catalytic converter. The exhaust at this temperature was passed through the section, it reduced the concentration of $CO_2$ gas, and the concentration

of other gases like nitrous oxide and oxygen will also get reduced by the same. The reaction at this section is given in Eq. 4

$$CO_2(g) + H_2O(l) = dil.\ H_2CO_3 \tag{4}$$

In this process, carbon dioxide ($CO_2$) when absorbed by normal water was converted to carbonic acid ($H_2CO_3$).

The quantity of the electrolyte solution will depend on the amount of exhaust entering the containers. Now, to reduce the emission of particulate matter a fine mesh having a lattice of approximately 1 micron was used to trap the particles that are having almost same size as that of the lattice of mesh.

## 3 Results

Nitrogen Oxide: Fig. 2 shows the reduction of nitrogen oxide from the catalytic converter. A significant reduction of $NO_x$ is seen when a novel device is used in conjugation with the catalytic converter.

Carbon Dioxide: Fig. 3 shows the decrease in the $CO_2$ level when we use the novel device which uses the normal water. The exhaust gas is passed through the normal water which absorbs the $CO_2$ and converts it into $H_2CO_3$.



**Fig. 2** $NO_x$ emission with the device and without the device
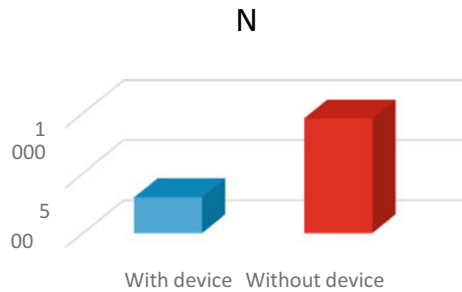


**Fig. 3** $CO_2$ emission with the device and without the device
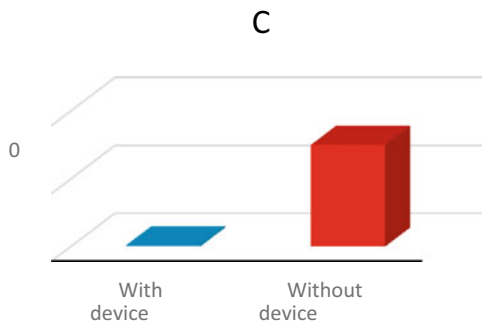
**Fig. 4** PM 2.5 emission with the device and without the device
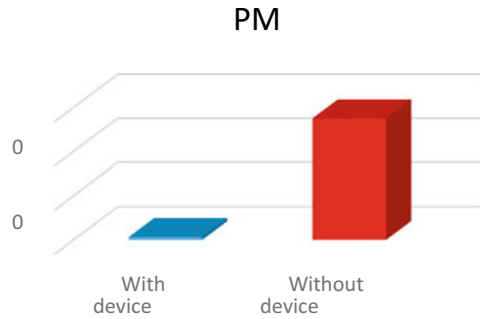
Particulate matter 2.5: The PM 2.5 is removed, and only 2% of it is passed through the mesh filter. A very significant amount of reduction in the PM 2.5 is seen which is shown in Fig. 4.

## 4 Conclusion

The design was fabricated and patented. The experimental study was done to reduce the chemical effects of $NO_x$, $CO_2$, and PM 2.5, and the results demonstrate the effectiveness of the developed device. NOx reduction is 70% when this device is used in conjugation with the two-way catalytic converter. $CO_2$ and PM 2.5 level is decreased to a negligible value. Furthermore, experiments will be performed with different combinations of this device with catalytic converter and other devices. This device can be very useful if fitted with the automobiles. Miniaturized model will be fabricated in the future.

## References

1. US Embassy, Air Quality Data: U.S. Embassy and Consulates (2018)
2. BBC, Anu Anand, Breathing poison in the world's most polluted city. http://www.bbc.com/news/magazine-32352722
3. Pelkmans L, Lenaers G, Bruyninx J, Scheepers K, De Vlieger I (2011) Impact of biofuels blends on the emission of modern vehicles. IMechE 225:1204–1220
4. Giakoumis EG (2012) A statistical investigation of biodiesel effects on regulated exhaust emissions during transient cycles. Appl Energy 98:273–291
5. Mofijur M, Rasul MG, Hyde J, Azad AK, Mamat R, Bhuiya MMK (2016) Role of biofuel and their binary (diesel–biodiesel) and ternary (ethanol–biodiesel diesel) blend on internal combustion engines emission reduction. Renew Sustain Energy Rev 53:265–278
6. Hulwan DB, Joshi SV (2011) Performance, emission and combustion characteristic of a multi-cylinder DI diesel engine running on diesel–ethanol–biodiesel blends of high ethanol content. Appl Energy 88:5042–5055

7. Rakopoulos CD, Dimaratos AM, Giakoumis EG, Rakopoulus DC (2011) Study of turbocharged diesel engine operation, pollutant emissions and combustion noise radiation during starting with bio-diesel or n-butanol diesel fuel blends. Appl Energy 88:3905–3916

8. Kannan GR, Karvembu R, Anand R (2011) Effect of metal-based additive on performance emission and combustion characteristics of a diesel engine fuelled with biodiesel. Appl Energy 88:3694–3703

9. Ryu K (2013) Effects of pilot injection timing on the combustion and emissions characteristics in a diesel engine using biodiesel–CNG dual fuel. Appl Energy 111:721–730

10. Suh HK (2011) Investigations of multiple injection strategies for the improvement of combustion and exhaust emissions characteristics in a low compression ratio (CR) engine. Appl Energy 88:5013–5019

11. Schejbal M, Stepanek J, Koci P, Marek M, Kubicek M (2010) Sequence of monolithic converters DOC–CDPF–NSRC for lean exhaust gas detoxification: A simulation study. Chem Eng Sci 49:943–952

12. Bhandwal M, et al. A novel exhaust system for reducing the gases and particulate matter emitted from vehicles, 3010/DEL/2015 (filed)

13. Sharma SK, Goyal P, Tyagi RK (2015) The Conversion efficiency of the catalytic converter. Int J Ambient Energy 37:507–512

14. Bhandwal M, Sikarwar BS, Tyagi RK (2018) Estimate the performance of catalytic converter using turbulence induce devices. IJE Trans. B 31:696–705

15. Bhandwal M et al (2018) The effect of using the turbulence enhancement unit before the catalytic converter in diesel engine emissions. Int J Ambient Energy 39:73–77

# Effect of Shallow Dimple on Cylindrical Surface for Heat Transfer and Pressure Penalty

**Mayank Shah and Rupesh Shah**

**Abstract** Effect of shallow dimples on convective heat transfer from cylinder surface is investigated numerically. Relative assessment of circular cylinder and cylinder with shallow dimple on full surface of the cylinder and shallow dimple only on downstream surface of the cylinder are done for heat transfer and pressure penalty. Two-dimensional numerical investigations are performed for air with velocity in the range of 1–5 m/s. Turbulence is modeled using RSTM closer model. The comparison of heat transfer rate for all the reported cases reveals that inclusion of shallow dimple on circular cylinder enhances heat transfer rate. Heat transfer rate augments by 20% in case of full shallow dimple surface compared to plain cylindrical surface. In case of dimple on downstream surface of the cylinder, heat transfer is 10% more than plain surface. Cylinder with shallow dimple downstream outperforms in terms of heat transfer rate and pressure penalty.

**Keywords** Heat transfer · Pressure penalty · Turbulence

## 1 Introduction

One of the important processes in the field of thermal engineering is the heat transfer between flowing fluid, and various types of heat transfer equipment are designed to satisfy the requirements of higher heat transfer rate for different purposes. Design of heat exchanger involves various important considerations which include thermal performance, pressure drop, flow capacity, volume of device, and requirement of heat transfer rate [1]. Among all these factors, determination of pressure drops across the tube bank is vital for many applications because the fluid needs to be pumped through the heat exchanger and its value depends upon the flow pattern of fluid.

When the heat transfer process is associated with air, the main thermal resistance is on air side due to low thermal conductivity and heat transfer coefficient. There are various methods proposed by Bergles et al. [2] for enhancing the heat transfer rate in a heat exchanger. In general, an increment in conventional heat transfer can be achieved by increasing the heat transfer coefficient or the turbulence in fluid. In case of reducing the thermal resistance on air side, one frequently used method for heat transfer enhancement is to employ fins on the surface of tubes. Despite the fact that fins can improve the rate of heat transfer, the associated drawback of pressure drop is also enormous. So, there is a need to have some alternative in which the turbulent flow can be developed with negligible pressure penalty.

The dimple surface is one of the effective methods to enhance the heat transfer rate without the significant pressure drop [1–5]. Many researchers had carried out investigations to examine the heat transfer augmentation with dimpled surface. Chyu et al. [3] studied the flow behavior over the hemispherical and teardrop shaped concavities. The local heat transfer coefficient of air over a dimpled surface was calculated numerically and experimentally for Reynolds number range of $10^4$ to $5 \times 10^4$. The heat transfer augmentation on a dimpled surface was reported by 25% as compared to that of a smooth surface.

Katkhaw et al. [4] experimentally investigated the flow characteristics over an ellipsoidal dimpled surface for a velocity range of 1–5 m/s. The rate of heat transfer and drag was calculated for the different angular arrangements of dimples on a rectangular plate. The augmentation in heat transfer rate was reported in the range of 15–20%. Voroyos et al. [5] carried out the heat transfer analysis of dimpled surface. The pitch length and arrangement of dimples were changed during the investigation. An augmentation in heat transfer rate in staggered arrangement was around 26 and 25% in in-line arrangement as compared to that of a smooth surface. In 2016, Li et al. [6] conducted experiments to study the flow physics inside the dimpled surface tube. The rate of heat transfer drag coefficient and pressure drop was calculated for different shapes of dimples during the study.

The influence on surrounded fluid structure due to dimple arrangement on circular cylinder had not been investigated thoroughly. The objective of this study is to observe the thermal characteristics of airflow across the cylinder having dimpled surface.

## 2 Numerical Formulation and Modeling

### 2.1 Physical Description

A 2-D numerical study is carried out with 0.0426 m diameter circular tube. Three different surface geometries on a circular tube are investigated numerically for the Reynolds number in the range of 2500 to 13,250. In the first case, the numerical investigation is conducted on a smooth surface circular tube used to carry hot flue
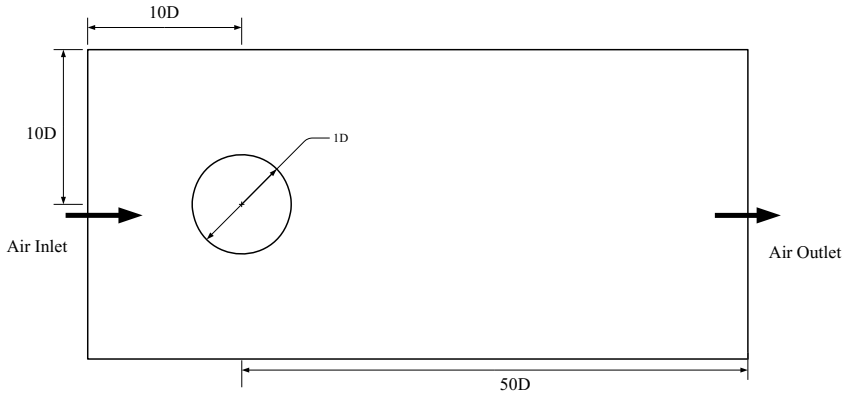
**Fig. 1** Computational domain

**Fig. 2** Arrangement of
dimple on cylindrical surface
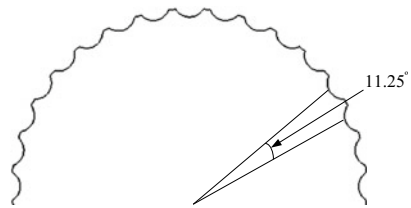


gases at 798 K and surrounded by atmospheric air. In the second case, 0.001 m
deep and 0.0035 m wide shallow dimples are used on a surface of a circular tube to
create turbulence in the airflow. The angular distance between two dimple centers is
11.25°. The arrangement of dimple is shown in Fig. 2. In the third case, the shallow
dimples are imprinted only on downstream of the cylindrical surface. The
enhancement in heat transfer by increasing the turbulence intensity with negligible
pressure penalty is the main motive of this numerical study. The dry air is
considered as a surrounding fluid with no attempts for condensation effects.
Physical properties of dry air are taken at 300 K (Fig. 1).

In order to examine the heat and momentum transfer of various geometrical
cases, some preliminary conditions of the physical model have to be defined
appropriately. Four different boundary conditions are used for the evaluation of this
problem. Table 1 shows the values of these boundary conditions.

## 2.2 Governing Equation

The two-dimensional governing equations for steady, incompressible fluid are
utilized and mentioned here.

**Table 1** Boundary conditions

| Zone name | Boundary type | Specification |
|---|---|---|
| Air inlet | Velocity inlet | Velocity in x-direction varies from 1– 5 m/s, Temp = 300 K, Turbulence intensity ($I$) = 5% |
| Air outlet | Pressure-outlet | Zero pascal (gauge) $I$ = 5% |
| Cylinder surface | Wall | $T$ = 798 K |
| Top and bottom surfaces of domain | Symmetry | – |

The concept of mass conservation is stated numerically by continuity equation. The mass conservation equation (equation of continuity) is represented as:

$$\frac{\partial V_x}{\partial x} + \frac{\partial V_y}{\partial y} = 0 \tag{1}$$

The momentum variation rate of a fluid particle is determined by calculating the total applied force on that particle. Resulting momentum equations for 2-D are:

X—momentum equation,

$$V_x \frac{\partial V_x}{\partial x} + V_y \frac{\partial V_x}{\partial y} = -\frac{1}{\rho}\left(\frac{\partial p}{\partial x}\right) + \vartheta\left(\frac{\partial^2 V_x}{\partial x^2} + \frac{\partial^2 V_y}{\partial y^2}\right) \tag{2}$$

and Y—momentum equation,

$$V_x \frac{\partial V_y}{\partial x} + V_y \frac{\partial V_y}{\partial y} = -\frac{1}{\rho}\left(\frac{\partial p}{\partial x}\right) + \vartheta\left(\frac{\partial^2 V_x}{\partial x^2} + \frac{\partial^2 V_y}{\partial y^2}\right) + g\beta\theta \tag{3}$$

where

$V_x$   Velocity in x-direction,
$V_y$   Velocity in y-direction,
$\rho$   Density of fluid,
$\vartheta$   Kinematic viscosity,
$p$   Pressure,
$\theta$   Temperature difference and
$\beta$   Thermal expansion coefficient.

The temperature variation in the flow field is captured by solving energy equation, and the energy equation represents the first law of thermodynamics.

$$\rho C_p \left( V_x \frac{\partial T}{\partial x} + V_y \frac{\partial T}{\partial y} \right) = k_f \left( \frac{\partial^2 T}{\partial x^2} + \frac{\partial^2 T}{\partial y^2} \right) + q_f \tag{1}$$

where

$C_p$  Specific heat,
$T$   Temperature of fluid,
$k_f$  Thermal conductivity of fluid and
$q_f$  is the heat generation term.

## 2.3  Parametric Study of Computational Domain

Actual flow physics of current domain involves solution of mass, momentum, and energy transfer. Fluent is used as a solver to investigate the flow structure over a cylinder. In present numerical analysis, RSTM model is used to determine turbulence kinetic energy and dissipation rate. For the aspect of pressure-velocity coupling, SIMPLE algorithm is adopted. For discretization of governing equations, the second-ordered upwind scheme is used. Turbulence level at inlet and outlet faces is specified by calculating hydraulic diameter and turbulence intensity is assigned as 5%. The convergence criteria for mass and momentum conservation equation are set to $10^{-4}$ and for energy equation it is set to $10^{-6}$.

## 3  Results and Discussions

## 3.1  Validation of Results

The analysis is done by changing geometrical parameters and velocity of air. Grid generation is the important stage of the investigation. Grid independence study is carried out to achieve the finest grid for the domain that does not allow solution to change largely. In the present study, three different grid sizes are taken for grid independency study.

The heat transfer rate is calculated at Reynolds number 13,250. In Fig. 3, it is observed that total heat transfer rate is comparable for 3.57E+05 and 7.6E+05 numbers of elements, which is more than the value for coarse mesh. It is cleared that the results are not affected beyond the limit of 3.57E+05 number of elements.

Three different geometrical cases are investigated for the velocity range of 1–5 m/s. The average Nusselt number is calculated for smooth cylindrical surface from computational results and validated with analytical results.

**Fig. 3** Grid independence
study
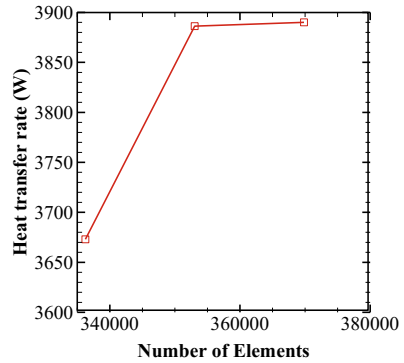


**Fig. 4** Validation of
numerical results
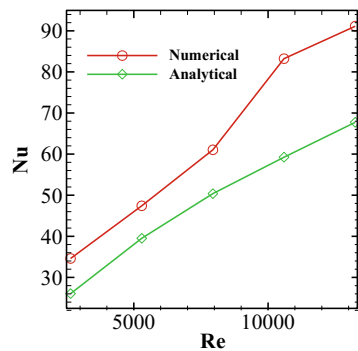


Analytically, the Nusselt number is calculated by the following relation [7],

$$Nu = 0.26 \times Re^{0.6} \times Pr^{0.37} \tag{5}$$

Figure 4 represents the comparison of relation is quite accurate, and the results
obtained from it can be off by twenty percent [7].

## 3.2   Flow Physics Over the Cylindrical Surface

Flow behavior over a various shape of circular cylinder is studied for the inlet
velocity range of 1–5 m/s. In Fig. 5, velocity contours represent the weak zone and
flow behavior near the surface of the cylinder. As shown in Fig. 5b, the stagnant
region of air is expanding in upstream due to the arrangement of dimples on a
circular tube surface. The arrangement of dimples at normal to the direction of flow
increases the pressure force and when the arrangement is in the flow direction, it

**(a)**

**(b)**

**(c)**

Velocity = 1m/s                    Velocity = 3m/s                    Velocity = 5m/s

0.000  0.345  0.690  1.034  1.379  1.724  2.069  2.414  2.759  3.103  3.448  3.793  4.138  4.483  4.828
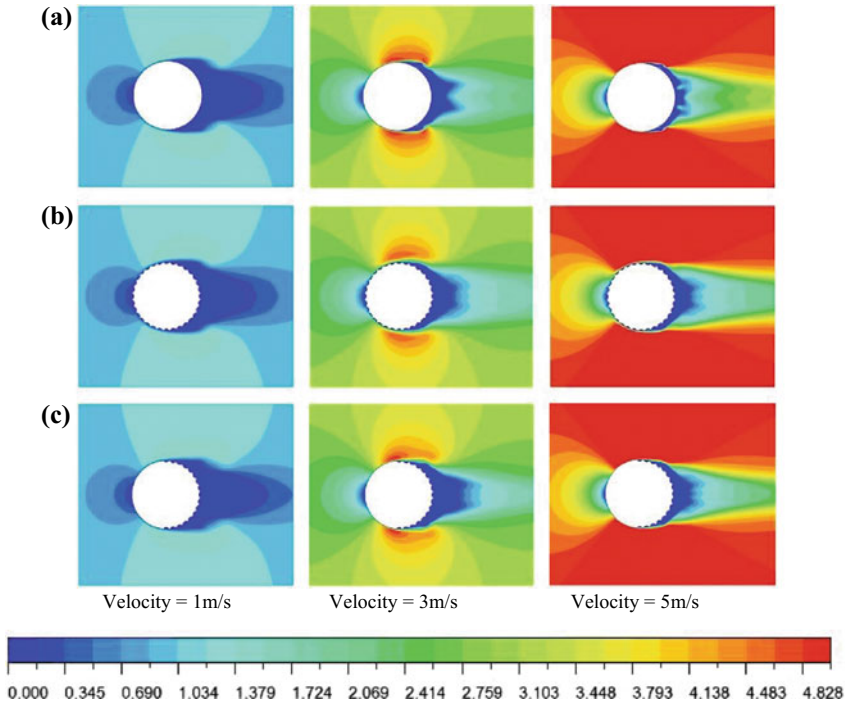
**Fig. 5** Velocity contours for **a** Smooth surface cylinder, **b** Fully dimpled surface and **c** Dimples at downstream of the cylinder surface

increases the viscous force. So in the third case, dimples are arranged only at a downstream of the cylinder surface. The flow separation point and the region of turbulence can be easily identified from Fig. 5.

## 3.3 Calculation of Heat Transfer and Pressure Drop

To demonstrate the effect of dimples on a cylinder surface, numerical investigations are carried out for Reynolds number range of 2500–13,250. Figure 6 represents variation in of ratio of heat transfer rate with respect to Reynolds number. For all geometrical cases considered here, heat transfer increases with increase in Reynolds number. At all Reynolds number, smooth surface cylinder has the lowest heat transfer rate and fully dimpled surface cylinder has the highest rate of heat transfer. At Reynolds number 13,250, fully dimpled surface has 20% higher rate of heat transfer and semi-dimpled surface has 10% higher rate of heat transfer compared to smooth surface.

**Fig. 6** Effect of dimple on
heat transfer rate
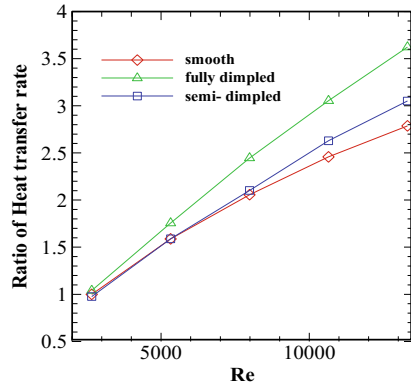


**Fig. 7** Effect of dimple on
operating pressure
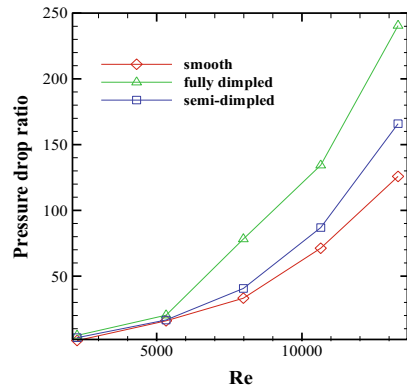


Figure 7 represents variation of pressure drop ratio of dimpled surface to smooth surface with respect to Reynolds number. The comparative study for all three cases has been done to evaluate the optimum design. At Reynolds number 13,250, fully dimpled surface has 25% higher pressure penalty and semi-dimpled surface has 10% higher pressure penalty compared to that for smooth surface.

## 4   Conclusion

Two-dimensional numerical analysis of flow over cylinder with and without dimple surface is performed. Major conclusions of the present study are;

- Total heat transfer rate increases by 10 and 20% in fully dimpled circular surface tube and circular tube with dimples at downstream of the surface, respectively.
- Fully dimpled surface has 25% higher pressure penalty and semi-dimpled surface has 10% higher pressure penalty compared to smooth surface.

# References

1. Kamel MS (2012) Heat transfer enhancement and fluid flow across tube banks heat exchanger with passive control techniques by using vortex generator. Int J Sci Res 3:363–367
2. Bergles AE, Nirmalan V, Junkhan GH (1983) Bibliography on augmentation of convective heat and mass transfer-II. Iowa State University ISU-ERI-84221
3. Chyu M, Yu Y, Ding H, Downs J, Soechting F (1997) Concavity enhanced heat transfer in an internal cooling passage. In: The 1997 international gas turbine & aeroengine congress & exposition
4. Kathaw N, Vorayos N, Kiatsiriroat T, Khunatorn Y, Bunturat D, Nunthphan A (2014) Heat transfer behaviour of flat plate having $45°$ ellipsoidal dimpled surface. Case Stud Therm Eng 2:67–74
5. Vorayos N, Katkhaw N, Kiatsiriroat T, Nuntaphan A (2016) Heat transfer behavior of flat plate having spherical dimpled surfaces. Case Study Therm Eng 8:370–377
6. Li M, Khan TS, Hajri EA, Ayub ZH (2016) Geometric optimization for thermal-hydraulic performance of dimpled enhanced tubes for single phase flow 103:639–650
7. Cengel Y (2002) Heat transfer—a practical approach, 2nd edn. McGraw-Hill Education, USA

# Numerical Investigation
# of Two-Dimensional Laminar Flow Past
# Various Oscillating Cylinder

**Ankit Dekhatawala and Rupesh Shah**

**Abstract** Two-dimensional laminar flow over oscillating cylinder is analyzed numerically. Three different cylinder shapes namely circular, square, and ellipse are considered for analysis. Cylinder shapes are set to oscillate at frequency ranged such that frequency ratio (oscillating frequency/natural vortex shedding frequency, $f_r$) varies between 0.8 and 1.2. The oscillation amplitude is varied between 30 and 50% of the cylinder diameter at fixed Reynolds number of 185. Numerical study is carried out using dynamic mesh features of commercial code FLUENT. Simple harmonic motion to the cylinder is applied using user-defined function (UDF) facility of FLUENT. The formation of anticlockwise or clockwise motion vortices from surface of cylinder depends upon geometrical shape of the cylinder as well as frequency ratio of oscillation at extreme positive displacement of the cylinder. Wake pattern mode behind the surface of the cylinder is 2S mode or 2P mode. Elliptical cylinder outperforms square and circular cylinder in terms of drag and lift characteristics. The range of time-averaged drag coefficient is lowest. Drag and lift increase linearly for all amplitude and frequency ratio in elliptical cylinder compared to square and circular cylinder.

**Keywords** Frequency ratio · Lift coefficient · Drag coefficient

## 1 Introduction

The major concern in design of an offshore structure is calculation of fluid forces. These forces are exerted on offshore structure due to the interaction of waves with structure. Due to this study of cylindrical body, oscillation laterally in a free stream is one of the important problems of fluid mechanics. Separation, vortex shedding pattern and turbulence in a wake at relatively low flow speed are the primary

A. Dekhatawala · R. Shah (✉)
Sardar Vallabhbhai National Institute of Technology, Surat 395002, Gujarat, India
e-mail: rds@med.svnit.ac.com

physical phenomenon flow past oscillating cylinder. When circular cylinder oscillation frequency equal to vortex formation frequency, the fundamental lock-in regions occurred which is found by Williamson and Roshko [1]. They also classified the wake pattern in accordance with wavelength. Guilmineau and Queutey [2] numerically examined vortex shedding in-line oscillation and cross-flow oscillation from circular cylinder. As the frequency of oscillation cylinder increases relative to natural vortex formation frequency, the primarily formed concentration of vorticity moves nearer to the cylinder until a minimum position is reached.

Okajima et al. [3] experimentally studied flow induced in-line oscillations for circle and rectangular-shaped cylinder of various side ratios. From flow visualization images, they determined that the shape of body has major impact in in-line oscillation. Dutta [4] extensively examined stationary as well as oscillating square cylinder wake pattern in the range of Reynolds number 100–600. As the oscillation frequency increases, the recirculation zone length behind the cylinder reduces significantly which directly contracts the time-averaged drag force acting on cylinder.

A very few researchers numerically studied flow over stationary elliptical cylinder as well as rotationally oscillating elliptical cylinder by varying Reynolds number and aspect ratio. As the steady secondary vortex shedding formed behind the elliptical cylinder, the variation of drag and Strouhal number is noted by Joshan et al. [5]. The local minimum RMS value of lift coefficient and local maximum value of drag coefficient for rotationally oscillating cylinder are found at natural vortex shedding frequency of elliptical cylinder [6].

In the present research, two-dimensional laminar flow over oscillating circular-, square- and elliptical-shaped cylinders is examined using commercial code FLUENT with special feature of dynamic mesh. User-defined function (UDF) facility of Fluent is used to give simple harmonic motion to cylinder. The purpose of the present numerical study is to identify major changes in wake pattern and the hydrodynamic forces on the cylinder due to the change in geometrical shape, variation of frequency, and amplitude ratio.

## 2 Computational Approach

In current investigation, the Navier–Stokes equations describing unsteady incompressible viscous flow field for two dimensions of space are solved numerically. Governing equations of flow physics are,

Continuity Equation:

$$\frac{\partial \rho}{\partial t} + \frac{\partial u}{\partial x} + \frac{\partial v}{\partial y} = 0 \tag{1}$$

and momentum Equation:

$$\frac{\partial u}{\partial t} + \frac{\partial u^2}{\partial x} + \frac{\partial(uv)}{\partial y} = -\frac{\partial p}{\partial x} + \frac{1}{Re}\left[\frac{\partial^2 u}{\partial x^2} + \frac{\partial^2 u}{\partial y^2}\right] \tag{2}$$

$$\frac{\partial v}{\partial t} + \frac{\partial(uv)}{\partial x} + \frac{\partial v^2}{\partial y} = -\frac{\partial p}{\partial y} + \frac{1}{Re}\left[\frac{\partial^2 v}{\partial x^2} + \frac{\partial^2 v}{\partial y^2}\right] \tag{3}$$

where $u$ and $v$ are velocity components, respectively, in $x$- and $y$-directions, $p$ is the pressure, Reynolds number $Re$ is defined as $Re = \frac{\rho VD}{\mu}$ in which $V$ is free stream velocity of water, $D$ is equivalent hydraulic diameter of cylinder, $\rho$ is density of water and $\mu$ is dynamic viscosity of water. In the present research $\rho = 998.2\text{kg m}^{-3}$ and $\mu = 0.001003$ kg/m-s are consider for all cases. The oscillating motion of cylinder is defined using UDF. The equation used to give harmonic motion in UDF is as follows:

$$V(y) = A\omega\cos(\omega t) \tag{4}$$

where $V(y)$ is velocity of cylinder in $y$-direction. $A$ is amplitude of oscillation. Amplitude of oscillation is determined from amplitude ratio which is defined by $A_r = A/D$. $\omega$ is angular frequency of oscillation which defined by $\omega = 2\pi f_e$, $f_e$ is frequency of oscillation derived from frequency ratio $(f_r = f_e/f_o)$. $f_o$ is vortex shading frequency. Drag and lift are major hydrodynamic forces, which act on cylinder surface during oscillation, respectively, in $x$- and $y$-direction. The non-dimensional form of lift and drag forces are defined as given below

$$C_{\text{L}} = \frac{F_j}{1/2\rho V^2 D} \tag{5}$$

$$C_{\text{D}} = \frac{F_i}{1/2\rho V^2 D} \tag{6}$$

where $C_{\text{L}}$ and $C_{\text{D}}$ are lift coefficient and drag coefficient. $F_i$ and $F_j$ are drag and lift forces in $x$- and $y$-direction, respectively.

The schematic computational flow domain for oscillating cylinder is shown in Fig. 1. Circular-, square- and elliptical-shaped cylinders are considered in the present investigation. The equivalent hydraulic diameter $D$ for various geometrical shape cylinders is 0.01 m. The computational flow domain is divided into two parts. The $6D \times 6D$ square domain surrounding the cylinder is the first part. The first part is meshed with dynamic mesh, which will oscillate with the cylinder. The remaining region is the second part. Length and width of computational domain in terms of equivalent hydraulic diameter $D$ as well as boundary conditions used for present analysis are shown in Fig. 1. Computational flow domain modeling and meshing are done in GAMBIT software. FLUENT software is used for the current numerical study.
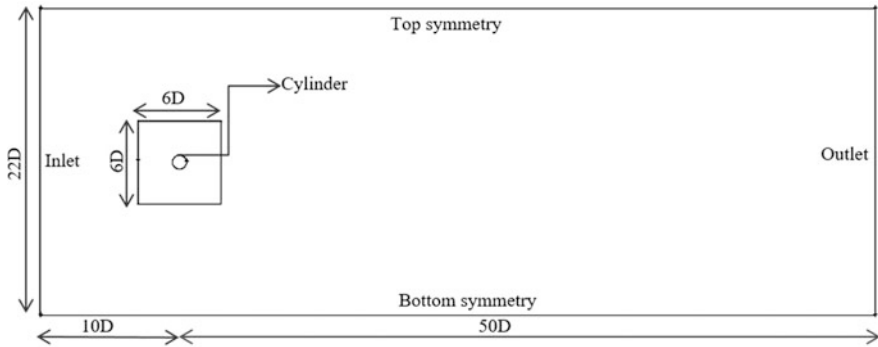
**Fig. 1** Schematic of computational flow domain

Unstructured mesh is generated in the first part of computational domain using tri-elements, and the second part of computational domain is meshed using quadrilateral elements. At inlet, velocity boundary type is assigned. Cylinder surface is considered as wall, whereas oscillating motion is given to cylinder using Eq. [4] via UDF. Pressure outlet boundary condition is set at outlet of domain in which the gauge pressure $p = 0$ is adopted. Reynolds number is fixed for all geometrical shape of cylinder, which is 185. For this, laminar viscous model is selected. The segregated first-order implicit unsteady solver approach is selected together with the PISO algorithm for pressure-velocity coupling. PISO algorithm is more suitable for quick convergence and with larger time step size.

## 3 Numerical Validation

One of the important stages in numerical investigation is meshing. Mesh density affects the solution. The grid independence test of oscillating cylinder is carried out at $Re = 185$ and $f_r = 0.8$, $A_r = 0.2$ for all geometrical shape of the cylinder. The variation of mesh density is carried out by changing the grid points along the cylinder surface and $6D \times 6D$ square domain side and evaluating the result of mesh density on $\overline{C}_D$ and $C_{Lrms}$. The number of grid points along the different geometrical cylinder surface and square domain side are indicated by Nc and Nsl, respectively. Tri-elements mesh (Nc $\times$ Nsl = 250 $\times$ 100) in $6D \times 6D$ square domain is considered for further analysis of all cases.

The current numerical study involves three geometrical shape cylinders undergoing transversally oscillating motion at various frequency ratios with various amplitude ratio; hence, the numerical method followed here needs to be validated. The numerical results of oscillating circular cylinder are compared with published results of Guilmineau and Queutey [2] for $Re = 185$ and $f_r = 0.8$–1.2, $A_r = 0.2$. The numerical results of the current analysis are validated with the values of

**Fig. 2** Comparisons of $\overline{C}_D$ and $C_{Lrms}$ for oscillating circular cylinder with Guilmineau and Queutey [2] for $Re = 185$, $A_r = 0.2$
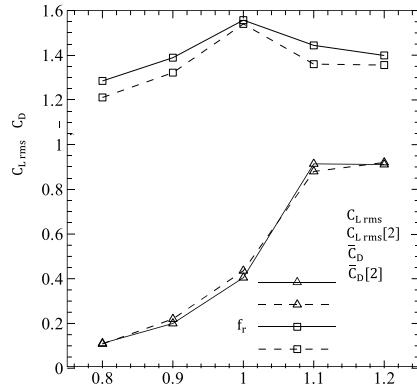


time-averaged drag coefficient ($\overline{C}_D$) and root means square lift coefficient ($C_{Lrms}$) values. Figure 2 shows good quantitative agreement for the values $\overline{C}_D$ and $C_{Lrms}$ between present investigation with those obtained by Guilmineau and Queutey [2].

## 4    Numerical Results and Discussion

The detail quantitative information about derived variables which are the $\overline{C}_D$, $C_{Lrms}$ and vorticity of various geometrical shape cylinders undergoing transversally oscillating motion at different frequency ratio with amplitude ratio are presented in this section. The range of frequency ratio for cylinder is 0.8–1.2, while the oscillation amplitude is between 30 and 50% of the cylinder equivalent hydraulic diameter. The vortex shedding frequency ($f_o$) of different geometrical shapes of stationary cylinder is obtained from non-dimensional Strouhal number which is defined as

$$St = \frac{f_o D}{V} \qquad (7)$$

Strouhal number of various geometrical shapes of stationary cylinder is obtained from the literature. Every simulation is extended up to 100 s where periodic flow condition is achieved.

### 4.1    Circular Cylinder

The full periodicity in the flow has been established when the cylinder reached to maximum displacement so vorticity isolines contour of all cases has been taken $t = 2\tau/4$ (when cylinder reaches at maximum positive displacement). Clockwise

**(a)**



**(b)**



**(c)**
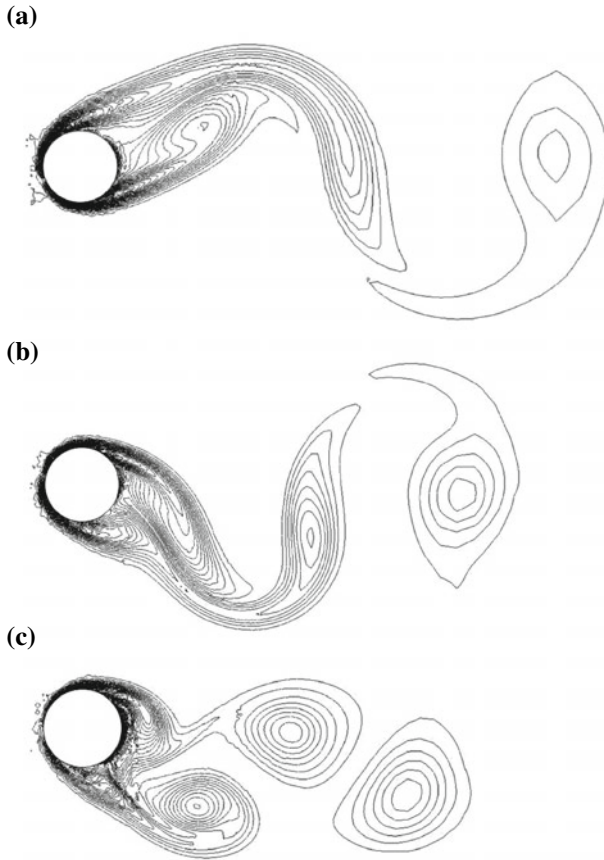


**Fig. 3** Vorticity isolines contour for circular cylinder at $Re = 185$, $A_r = 0.5$ at $t = 2\tau/4$. **a** $f_r = 0.8$, **b** $f_r = 1$ and **c** $f_r = 1.2$

vortices formed from top side of all geometrical shape cylinders. Anticlockwise vortices formed from bottom side of all geometrical shape cylinders. At $f_r = 0.8$, the vortex has enough time to stretch in longitudinal direction before detachment from cylinder surface which can be observed from Fig. 3a. The resulting wake formation mode behind cylinder is 2S mode or karman street-type wake. This flow behavior shows good agreement with experimental studies of Williamson and Roshko [1]. When circular cylinder oscillating frequency is equal to vortex shedding frequency, the well-known lock-in occurs. In this fundamental lock-in region, there are four vortices are shaded during complete cycle of oscillation. Figure 3b shows that vortex is less stretched in longitudinal direction compare to $f_r = 0.8$ and resulting wake formation is still 2S mode. When circular cylinder is oscillated higher than natural vortex shedding frequency, vortex is detached from cylinder surface without stretching in longitudinal direction which is found from Fig. 3c. The resulting wake
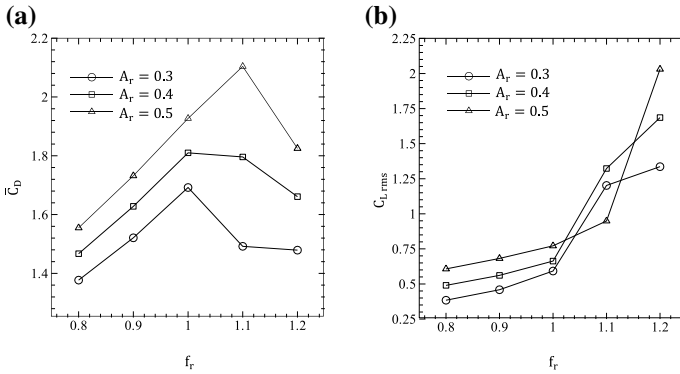
**Fig. 4** **a** $\overline{C}_D$ of circular cylinder, **b** $C_{Lrms}$ of circular cylinder

behind the cylinder is 2P mode in which vortex pair is shaded from the wake centerline. The similar wake pattern is obtained by Williamson and Roshko [1] for the same conditions.

The plots of $\overline{C}_D$ and $C_{Lrms}$ for circular cylinder as a function of frequency ratio with various amplitude ratios are shown, respectively, in Fig. 4a, b. The linear increment in $\overline{C}_D$ is found up to $f_r = 1$ for $A_r = 0.3$ and 0.4, while for $A_r = 0.5$, it is up to $f_r = 1.1$. At $f_r > 1$, the value of $\overline{C}_D$ is decreased. This is due to vortex detachment from cylinder surface quickly without stretching in longitudinal direction. There is small linear rise in the value of $C_{Lrms}$ up to $f_r = 1$ and after that sudden rise in value of $C_{Lrms}$ for all $A_r$. The maximum value of $C_{Lrms}$ is observed at $f_r = 1.2$.

## 4.2 Square Cylinder

Figure 5 shows vorticity isolines contour of transversally oscillating square cylinder for $Re = 185$, $A_r = 0.5$ at $t = 2\tau/4$ with frequency ratio 0.8–1.2. In square shape cylinder, clockwise vortex is formed from top left corner of square. Anticlockwise vortex is generated from bottom left corner of square. After developing vortex from top or bottom side of square, vortex reattached with rear vertical side of square then elongated in longitudinal direction before detachment from square cylinder surface. Therefore, the elongation length of vortex in longitudinal direction before separation from square cylinder surface is higher compared to circular cylinder. As the frequency ratio increases from 0.8 to 1.2, the elongation of vortex in longitudinal direction before detachment from square cylinder surface decreases. When square cylinder oscillation frequency synchronized with natural vortex shedding frequency of square cylinder, fundamental lock-in region occurred similar to circular cylinder and two vortices are shaded during complete cycle of oscillation. The wake

**(a)**

**(b)**

**(c)**
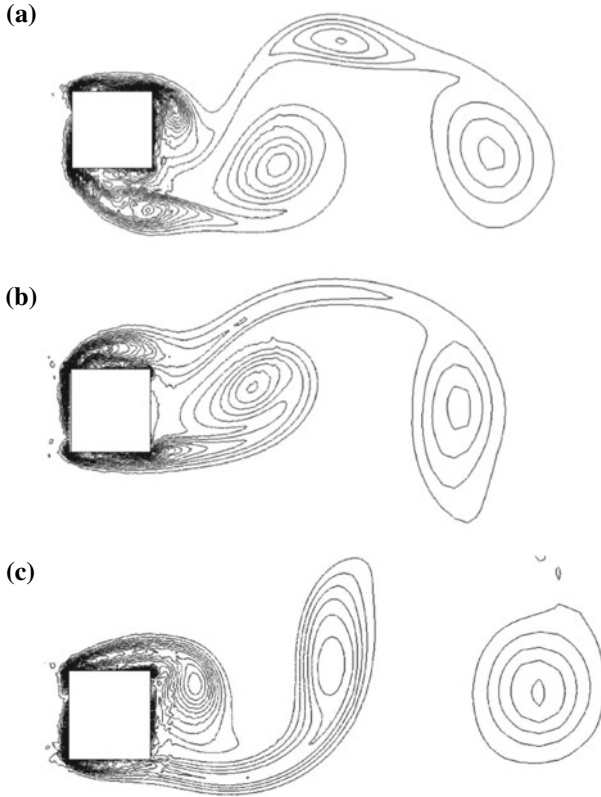


**Fig. 5** Vorticity isolines contour for square cylinder at $Re = 185$, $A_r = 0.5$ at $t = 2\tau/4$. **a** $f_r = 0.8$, **b** $f_r = 1$ and **c** $f_r = 1.2$

structure formation due to oscillation behind square cylinder is in 2S mode for all frequency ratio while in circular cylinder, 2S mode wake structure up to $f_r = 1$ and at $f_r > 1$, 2P mode wake structure is observed.

Figure 6a, b shows the plot of $\overline{C}_D$ and $C_{Lrms}$ for square cylinder as a function of frequency ratio with various amplitude ratios. The value of $\overline{C}_D$ for square cylinder is higher compared to circular cylinder for all cases. The lowest value of $\overline{C}_D$ is observed at $f_r = 1$ in square cylinder while maximum value of $\overline{C}_D$ is found in circular cylinder at the same frequency ratio. In case of circular cylinder, the value of $C_{Lrms}$ rises continuously with increasing frequency ratio and amplitude ratio while the $C_{Lrms}$ value is increasing in between $f_r < 1$ and $f_r > 1$ for square cylinder.
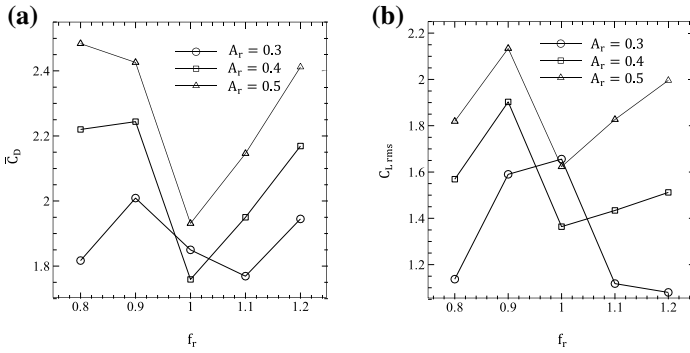
**Fig. 6** **a** $\overline{C}_D$ of square cylinder, **b** $C_{Lrms}$ of square cylinder

## 4.3 Elliptical Cylinder

The vorticity isolines contour of oscillating elliptical cylinder shows the effect on the flow field in Fig. 7 for various frequency ratio, $Re = 185$ and $A_r = 0.5$ at $t = 2\tau/4$. Ellipse is streamlined object so vortices formation started at the beginning of horizontal centerline of ellipse. When elliptical cylinder oscillates transversally at

**Fig. 7** Vorticity isolines contour for elliptical cylinder at $Re = 185$, $A_r = 0.5$ at $t = 2\tau/4$. **a** $f_r = 0.8$, **b** $f_r = 1$ and **c** $f_r = 1.2$
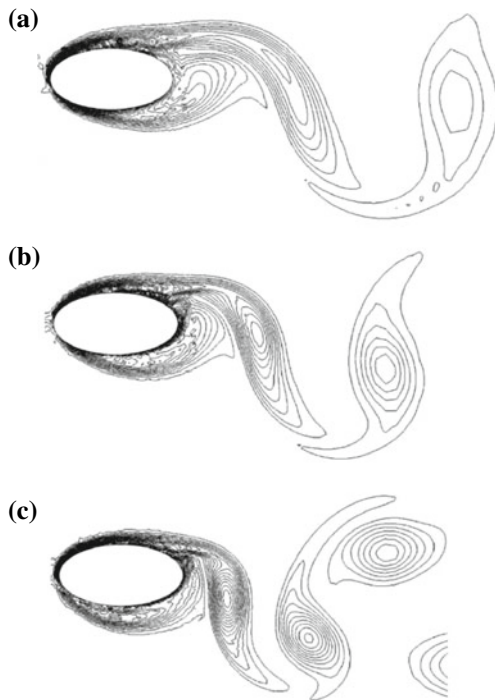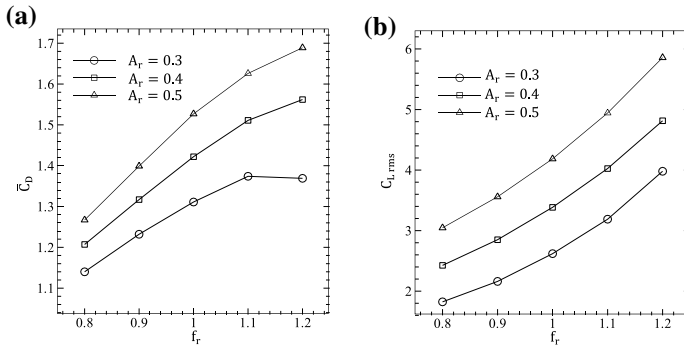
**Fig. 8** **a** $\overline{C}_D$ of elliptical cylinder, **b** $C_{Lrms}$ of elliptical cylinder

lower than natural vortex shedding frequency, vortices are stretched in longitudinal direction up to surface of elliptical cylinder then elongated in lateral direction. As the oscillation, frequency is equal to natural vortex shedding frequency or higher than, vortices are stretched in lateral direction and detached vortices are concentrated near the rear surface of ellipse. The vortex shedding formation mode is 2S mode for all frequency ratio.

The plots of $\overline{C}_D$ and $C_{Lrms}$ for elliptical cylinder as a function of frequency ratio with various amplitude ratios are presented in Fig. 8a, b. $\overline{C}_D$ and $C_{Lrms}$ rise linearly for all cases of elliptical cylinder. The maximum value of $\overline{C}_D$ of and $C_{Lrms}$ elliptical cylinder found at $f_r = 1.2$ for all $A_r$.

# 5 Conclusions

Numerical study of two-dimensional flow past oscillating cylinder with different geometrical shapes is carried out using CFD code in this work. The major outcome of current research is following

(1) Geometrical shape of the cylinder and frequency ratio of oscillation influence anticlockwise motion or clockwise motion vortices of shedding process at maximum positive displacement of cylinder.
(2) The vortex shedding formation mode for circular cylinder is 2S mode up to $f_r \leq 1$ and 2P mode is found at $f_r > 1$, while 2S mode wake structure found for all $f_r$ in square and elliptical shape cylinder.
(3) The time-averaged drag coefficient value of elliptical is lowest as well as linearly increases with increment in amplitude and frequency ratio compared to circular and square cylinder.
(4) Highest value of $C_{Lrms}$ is observed in elliptical cylinder for all cases compared to circular and square cylinder.

# References

1. Williamson CHK, Roshko A (1988) Vortex formation in the wake of an oscillating cylinder. J Fluid Struct 2:355–381
2. Guilmineau E, Queutey P (2002) A numerical simulation of vortex shedding from an oscillating circular cylinder. J Fluid Struct 16(6):773–794
3. Okajima A, Yasuda T, Iwasaki T (2000) Flow visualization of in-line oscillation of a cylinder with circular or rectangular section. In: 6th triennial international symposium on flow control, measurement and flow visualization, F1048, Sherbrooke (Qc)
4. Dutta S (2006) Sensitivity of a square cylinder wake to orientation and oscillation in the intermediate Reynold number regime, Ph.D. Thesis, Kanpur
5. Johnson SA, Thompson MC, Hourigan K (2001) Flow past elliptical cylinders at low Reynolds numbers. In: 14th Australasian fluid mechanics conference, pp 343–350. Adelaide
6. Alawadhi EM (2015) Numerical simulation of flow past an elliptical cylinder undergoing rotationally oscillating motion. J Fluid Eng 137:031106-1–031106-9

# Compact Solar Air Heater: A Review

**Vijay Singh Bisht, Anil Kumar Patil and Anirudh Gupta**

**Abstract** In this review work, a theoretical study of solar air heater is carried out by considering compact heat exchanger criteria into account. The present investigation comprises different performance parameters for a compact solar air heater. In this review work, Reynolds number is the only variable parameter which varies from 4000 to 18000. Stanton number ($St$), Stanton number ratio ($St/St_0$), Colburn factor ($j$), and area goodness factor ($j/f$) are considered as performance parameters. Stanton number ratio ($St/St_0$) is maximum for multi-V-shaped ribs with gaps. Colburn factor ($j$) value is highest for multi-V-shaped ribs with gaps. In the present investigation, goodness factor ($j/f$) is highest for circular protrusions organized in angular arc form. This study is beneficial for the researchers to conduct the experimental and theoretical investigation in order to search out the new roughness geometries to design compact solar air heater.

**Keywords** Stanton number ($St$) · Colburn factor ($j$) · Area goodness factor ($j/f$) · Artificial roughness · Reynolds number ($Re$)

## Nomenclature

| | |
|---|---|
| $C_p$ | Specific heat (J/kg-K) |
| $D_h$ or $D$ | Equivalent hydraulic diameter of duct (m) |
| $e$ | Rib height (m) |
| $e/D_h$ or $e/D$ | Relative roughness height |
| $f$ | Friction factor |
| $St_r$ | Stanton number of roughened duct |
| $St_s$ | Stanton number of smooth duct |

V. S. Bisht (✉)
Department of Thermal Engineering, Faculty of Technology, UTU, Dehradun, India
e-mail: vsinghbisht5@gmail.com

A. K. Patil
Department of Mechanical Engineering, DIT University, Dehradun, India

A. Gupta
Department of Mechanical Engineering, BTKIT, Dwarahat, India

| $J$ | Colburn factor (kg/s-m$^2$) |
| $h$ | Convective heat transfer coefficient (W/m$^2$-K) |
| $Nu$ | Nusselt number |
| $P$ | Pitch of rib |
| $P/e$ | Relative roughness pitch |
| $Re$ | Reynolds number |
| $W$ | Width of absorber plate |
| $W/w$ | Relative roughness width (W/m$^2$-K) |
| $W/H$ | Duct aspect ratio |
| $G_d/L_v$ | Relative gap distance |
| $k$ | Thermal conductivity of air W/m$^2$-K |
| $j/f$ | Area goodness factor |
| $g/p$ | Gap to pitch ratio |
| $\alpha$ | Flow angle of attack (°) |
| $\phi$ | Chamfer angle (°) |
| $Pr$ | Prandtl number |
| $g/e$ | Relative gap width |

# 1   Introduction

Rapid industrialization, urbanization, and globalization deplete maximum resources of energy which is accessible on our planet. Every day, modernistic generation demands enormous energy consumption, and for this, they mostly depend upon non-renewable resources of energy like fossil fuels. Fossil fuels are not everlasting resources, and eventually, they will dissipate. Other major concerns with fossil fuels are environmental pollution and global warming of the earth. So there is need of source energy that is clean and longlasting. Solar energy is a clean and lifelong source of energy as life exists on our planet is all due to Sun. Solar energy could play a significant role in eco-friendly development and economic growth of a nation. Solar air heater is basic device that harnesses solar energy in a very simple way. Solar air heater has plenty of utilization in agriculture industries also. But the heat transfer potential of the solar heater is very low. Artificial roughness is used as turbulent promoters to intensify the heat transfer rate. Prasad and Saini [1] used wire transverse roughness. They had concluded that up to 12,000 value of Reynolds number, Stanton number increases, and after that, there is a decrease in value of Stanton number with further increase in Reynolds number. Taslim et al. [2] studied the effect of V-shaping of the ribs roughness on the intensification of heat transfer rate in solar air heater. Numbers of roughness elements were used as turbulent promoters by a lot of researchers. The various roughness geometries (turbulent promoters) are displayed in Table 1.

**Table 1** Mathematical formulation of Nusselt number and Friction factor

| Roughness geometry | Range of parameters | Correlations |
|---|---|---|
| V-shaped ribs [3] | $e/D_h$: 0.02–0.034<br>$p/e$: 10<br>$\alpha$: 30°–90° | $Nu = 0.067(Re)^{0.888}\left(\dfrac{e}{D_h}\right)^{0.424}\left(\dfrac{\alpha}{60}\right)^{-0.077}$<br><br>$\exp\left\{-0.782\left(\ln\dfrac{\alpha}{60}\right)^2\right\}$<br><br>$f = 6.266(Re)^{-0.425}\left(\dfrac{e}{D_h}\right)^{0.565}\left(\dfrac{\alpha}{60}\right)^{-0.093}$<br><br>$\exp\left\{-0.719\left(\ln\dfrac{\alpha}{60}\right)^2\right\}$ |
| Wedge-shaped ribs [4] | $e/D_h$: 0.015–0.033<br>$p/e$:<br>$60.17\emptyset^{-1.0264} < p/e < 12.12$<br>$\emptyset$: 8°,10°, 12°,15°<br>$Re$: 3000–18000 | $Nu = 0.000189\left(\dfrac{e}{D_h}\right)^{0.426}\left(\dfrac{p}{e}\right)^{2.94}(Re)^{1.21}\left(\dfrac{\emptyset}{10}\right)^{-0.018}$<br><br>$\exp\left[-0.71\left(\ln\dfrac{p}{e}\right)^2\right]\exp\left[-1.5\left(\ln\dfrac{\emptyset}{10}\right)^2\right]$<br><br>$f = 12.44\left(\dfrac{e}{D_h}\right)^{0.99}\left(\dfrac{p}{e}\right)^{-0.52}(Re)^{-0.18}\left(\dfrac{\emptyset}{10}\right)^{0.49}$ |
| Rib–groove combination [5] | $e/D_h$: 0.0181–0.0363<br>$p/e$: 4.5–10<br>$Re$: 3000–21,000<br>$g/p$: 0.3–0.7 | $Nu = 0.002062\left(\dfrac{e}{D_h}\right)^{0.349}\left(\dfrac{p}{e}\right)^{3.318}(Re)^{0.936}$<br><br>$\exp\left[-0.868\left(\ln\dfrac{p}{e}\right)^2\right]\left(\dfrac{g}{p}\right)^{1.108}$<br><br>$\exp\left[2.486\left(\ln\dfrac{g}{p}\right)^2 + 1.406\left(\ln\dfrac{g}{p}\right)^3\right]$<br><br>$f = 0.001227\left(\dfrac{e}{D_h}\right)^{0.585}\left(\dfrac{p}{e}\right)^{7.19}(Re)^{-0.199}$<br><br>$\exp\left[-1.854\left(\ln\dfrac{p}{e}\right)^2\right]\left(\dfrac{g}{p}\right)^{0.645}$<br><br>$\exp\left[1.513\left(\ln\dfrac{g}{p}\right)^2 + 0.8662\left(\ln\dfrac{g}{p}\right)^3\right]$ |
| Arc-shaped wire ribs [6] | $e/D_h$: 0.02–0.042<br>$p/e$: 10<br>$W/H$: 12<br>$\alpha/90$: 0.333–0.666<br>$Re$: 2000–17,000 | $Nu = 0.001047\left(\dfrac{e}{D_h}\right)^{0.3772}\left(\dfrac{\alpha}{90}\right)^{-0.1198}(Re)^{1.3186}$<br><br>$f = 0.14408\left(\dfrac{e}{D_h}\right)^{0.1765}\left(\dfrac{\alpha}{90}\right)^{0.1185}(Re)^{-0.17103}$ |
| Multi-V-shaped ribs [7] | $e/D_h$: 0.019–0.043<br>$p/e$: 3–8<br>$\alpha$: 30°–75°<br>$W/w$: 1–10<br>$Re$: 2000–20,000 | $Nu = 0.0000335(Re)^{0.92}\left(\dfrac{e}{D_h}\right)^{0.77}\left(\dfrac{W}{w}\right)^{0.43}$<br><br>$\exp\left\{-0.61\left(\ln\dfrac{\alpha}{90}\right)^2\right\}$<br><br>$\alpha\,90 - 0.49\exp - 0.1177\ln Ww2pe8.54\exp - 2.0407\ln pe2$<br><br>$f = 0.000447(Re)^{-0.3188}\left(\dfrac{e}{D_h}\right)^{0.73}\left(\dfrac{W}{w}\right)^{0.22}$<br><br>$\exp\left\{-0.52\left(\ln\dfrac{\alpha}{90}\right)^2\right\}a\left(\dfrac{\alpha}{90}\right)^{-0.39}\left(\dfrac{p}{e}\right)^{8.9}$<br><br>$\exp\left\{-2.133\left(\ln\dfrac{p}{e}\right)^2\right\}$ |
| W-shaped rib roughness [8] | $e/D_h$: 0.018–0.03375<br>$p/e$: 10<br>$\alpha$: 30°–75°<br>$Re$: 2000–20,000 | $Nu = 0.0613(Re)^{0.9079}\left(\dfrac{e}{D_h}\right)^{0.4487}\left(\dfrac{\alpha}{60}\right)^{-0.1331}\exp\left\{-0.5307\left(\ln\dfrac{\alpha}{60}\right)^2\right\}$<br><br>$f = 0.6182(Re)^{-0.2254}\left(\dfrac{e}{D_h}\right)^{0.4622}\left(\dfrac{\alpha}{60}\right)^{0.0817}$<br><br>$\exp\left\{-0.28\left(\ln\dfrac{\alpha}{60}\right)^2\right\}$ |

**Table 1** (continued)

| Roughness geometry | Range of parameters | Correlations |
|---|---|---|
| Dimple-shaped roughness [9] | $e/D_h$: 0.021–0.036<br>$p/e$: 10–20<br>$W/H$: 11<br>$\alpha$: 45°–75°<br>$Re$: 3600–18,000 | $Nu = 7.1 \times 10^{-3} Re^{1.1386} (e/D_h)^{0.3629} (P/e)^{-0.047} (\alpha/60)^{-0.0048}$<br><br>$\qquad \exp\left(-0.7792 \ln(\alpha/60)^2\right)$<br><br>$f = 4.869 \times 10^{-3} Re^{0.223} (e/D_h)^{0.2663} (P/e)^{-0.059} (\alpha/60)^{0.0042}$<br><br>$\qquad \exp\left(-0.4801 \ln(\alpha/60)^2\right)$ |
| Circular protrusions arranged in circular arc manner roughness [10] | $e/D_h$: 0.015–0.03<br>$p/e$: 12–24<br>$\alpha$: 45°–75°<br>$Re$: 3600–18,100 | $Nu = 0.154 Re^{1.017} (P/e)^{-0.38} (e/D)^{0.521} (\alpha/60)^{-0.213}$<br><br>$\qquad \exp\left(-2.023(\ln(\alpha/60))^2\right)$<br><br>$f = 7.207 Re^{-0.56} (P/e)^{-0.18} (e/D)^{0.176} (\alpha/60)^{0.38}$<br><br>$\qquad \exp\left(-1.412(\ln(\alpha/60))^2\right)$ |
| Multi-V-shaped ribs with gap roughness [11] | $e/D_h$: 0.022–0.043<br>$p/e$: 6–12<br>$W/H$: 1–10<br>$\alpha$: 30°–75°<br>$g/e$: 0.5–1.5<br>$G_d/L_v$: 0.24–0.80<br>$Re$: 2000–20,000 | $Nu = 8.532 \times 10^{-3} Re^{0.932} (e/D)^{0.175} (w/W)^{0.506}$<br><br>$\qquad \exp\left(-0.0753 \left(\ln \frac{W}{w}\right)^2\right) (G_d/L_v)^{-0.0348}$<br><br>$\qquad \exp\left(0.0653 \left(\ln \frac{G_d}{L_v}\right)^2\right) (g/e)^{-0.0708}$<br><br>$\qquad \exp\left(-0.223 \left(\ln \frac{g}{e}\right)^2\right) (\alpha/60)^{-0.0239}$<br><br>$\qquad \exp\left(0.1253\ln \left(\ln \frac{\alpha}{60}\right)^2\right) (P/e)^{1.196}$<br><br>$\qquad \exp\left(-0.2805 \left(\ln \frac{P}{e}\right)^2\right)$<br><br>$f = 3.1934 Re^{-0.31513} (e/D)^{0.268} (w/W)^{0.1132}$<br><br>$\qquad \exp\left(0.0974 \left(\ln \frac{W}{w}\right)^2\right) (G_d/L_v)^{0.0610}$<br><br>$\qquad \exp\left(-0.1065 \left(\ln \frac{G_d}{L_v}\right)^2\right) (g/e)^{-0.1769}$<br><br>$\qquad \exp\left(0.6349 \left(\ln \frac{g}{e}\right)^2\right) (\alpha/60)^{0.1553}$<br><br>$\qquad \exp\left(0.1527 \left(\ln \frac{\alpha}{60}\right)^2\right) (P/e)^{-0.7941}$<br><br>$\qquad \exp\left(0.1486 \left(\ln \frac{P}{e}\right)^2\right)$ |
| Multi-arc-shaped rib roughness [12] | $e/D_h$: 0.018–0.045<br>$p/e$: 4–16<br>$W/w$: 1–7<br>$\alpha$: 30°–75°<br>$Re$: 2200–22,000 | $Nu = 1.564 * 10^{-4} (e/D)^{0.048} Re^{1.343} (W/w)^{0.407}$<br><br>$\qquad \exp\left(-0.099(\ln(W/w))^2\right) (p/e)^{0.572}$<br><br>$\qquad \exp\left(-0.148(\ln(p/e))^2\right) Z^{-0.355}$<br><br>$\qquad \exp\left(-0.272(\ln(\alpha/90))^2\right)$<br><br>$f = 0.063(e/D)^{0.102} Re^{-0.16} (W/w)^{0.277}$<br><br>$\qquad \exp\left(-0.099(\ln(W/w))^2\right) (p/e)^{0.562}$<br><br>$\qquad \exp\left(-0.140(\ln(p/e))^2\right) (\alpha/90)^{0.023}$<br><br>$\qquad \exp\left(-0.013(\ln(\alpha/90))^2\right)$ |
| Reverse L-shaped rib roughness [13] | $e/D_h$: 0.042<br>$p/e$: 7.14–17.86<br>$Re$: 3800–18,000 | $Nu = 0.032 Re^{0.8332} (P/e)^{0.3479} \exp\left(-0.1004\ln(P/e)^2\right)$<br><br>$f = 0.2805 Re^{-0.2617} (P/e)^{0.0815} \exp\left(-0.0319 \ln(P/e)^2\right)$ |

## 2  Performance of Solar Air Heater

Stanton number ($St$) [14]: Stanton number is given in Eq. 1. Stanton number ratio ($St/St_0$) shows relative performance of rough surface over the smooth duct.

$$St = \frac{Nu}{Re.Pr} = \frac{h}{\rho \mu c_p} \qquad (1)$$

The frictional factor ($f$) [14] shows the pressure drop occurred in the fluid flow by the incorporation of turbulent promoters in the duct. The friction factor is defined as:

$$f = \frac{2\left[\frac{\Delta p}{l}\right]D}{\rho V^2} \qquad (2)$$

Colburn factor ($j$) [15]: Colburn factor is product of Stanton number and two-thirds power of Prandtl number; it is defined by Eq. 3. Colburn factor is very helpful in comparative study of different heat transfer surfaces.
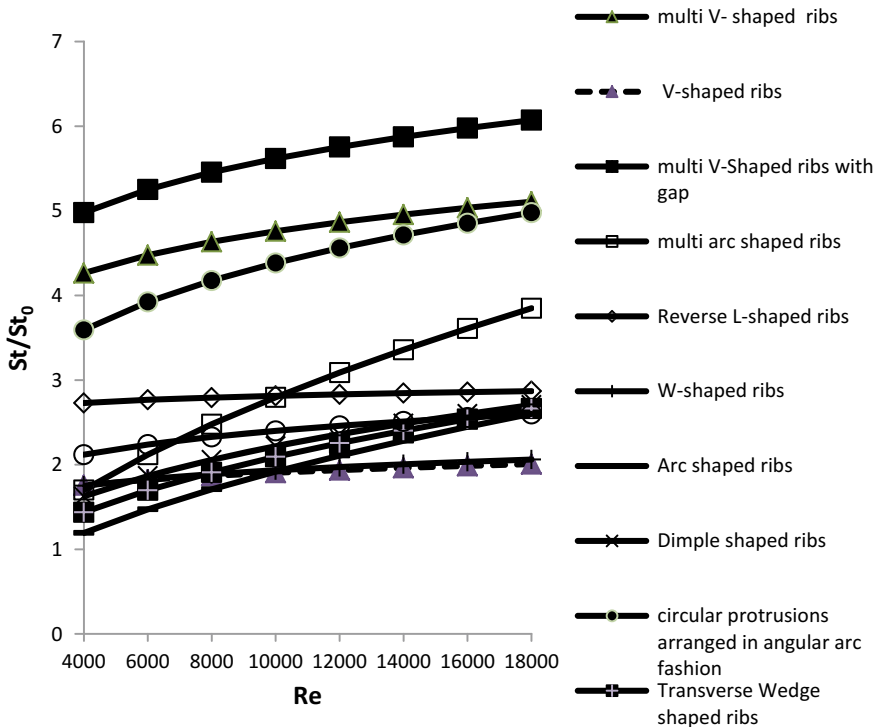


**Fig. 1** Effect of Reynolds number on Stanton number ratio

$$j = \frac{Nu}{RePr^{\frac{1}{3}}} = StPr^{\frac{2'}{3}} \tag{3}$$

Flow area goodness factor ($j$/$f$) [15]: It is the ratio of Colburn factor ($j$) to the friction factor ($f$). This factor shows the maximum heat transfer capability from smallest surface area.

The heat transfer intensification relative to smooth surface is signified by Stanton number ratio. The change in Stanton number ratio depends on heat transfer intensification in rough and smooth surface. Figure 1 displays the effect of Reynolds number on Stanton number ratio for different turbulent promoters. For all the roughness geometries, Stanton number ratio increases with increase in Reynolds number. Reynolds number is varied from 4000 to 18,000. Figure 2 projects the effect of Reynolds number on Colburn factor ($j$) for different turbulent promoters. For some roughness geometries, Colburn factor is increasing function of Reynolds number, and for others, Colburn factor is decreasing function of Reynolds number. Figure 2 defines that multi-V-shaped ribs with gap outperformed all the different
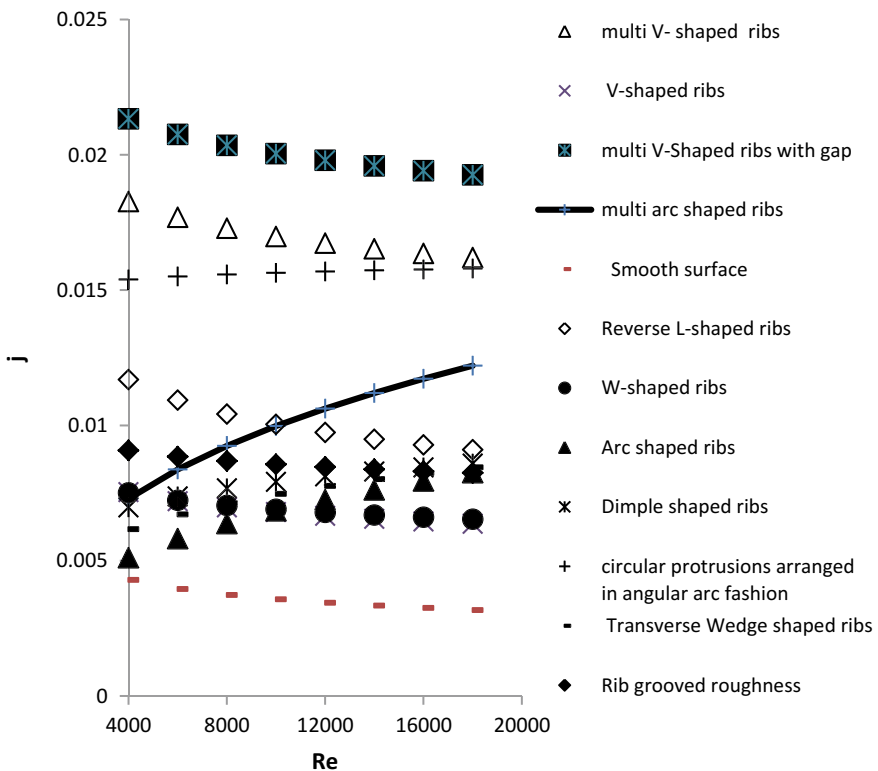


**Fig. 2** Effect of Reynolds number on Colburn factor ($j$)
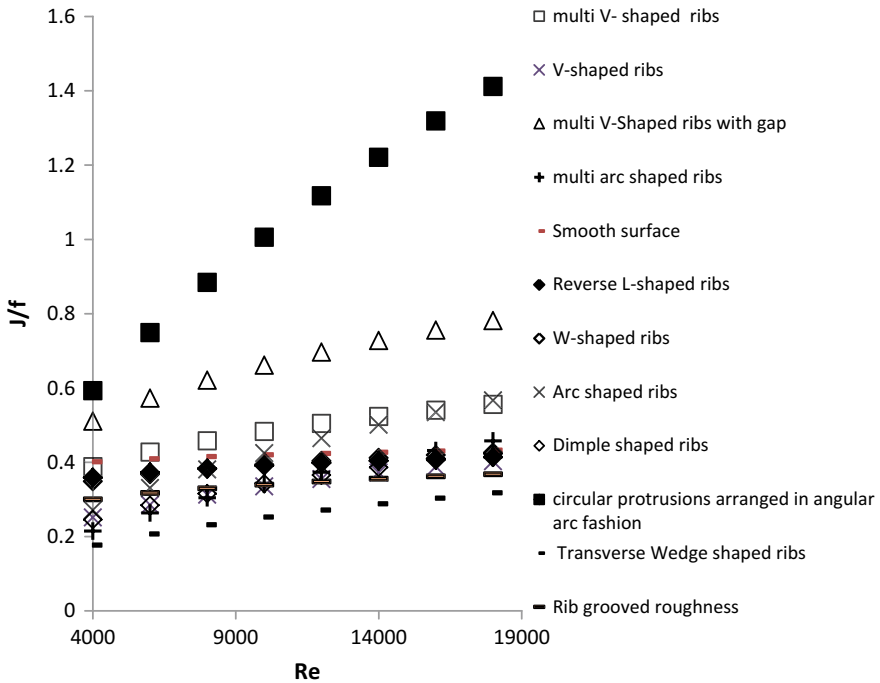
**Fig. 3** Effect of Reynolds number on area goodness factor (*j/f*)

turbulent promoters. The highest percentage increased in Colburn factor for Reynolds number from 4000 to 18,000 is 113.09% for multi-arc-shaped roughness geometry.

Figure 3 gives the effect of Reynolds number on area goodness factor (*j/f*) for distinct turbulent promoters. For all turbulent promoters, area goodness factor (*j/f*) is increasing function of Reynolds number. Circular protrusions are organized in a circular arc form geometry showing the highest value of area goodness factor (*j/f*). The highest percentage increase in area goodness factor (*j/f*) is for circular protrusions organized in circular arc form and has value of 138.18%. The circular protrusions organized in circular arc form have the maximum heat transfer capability from smallest surface area among the all turbulent promoters considered in this review work.

# 3   Conclusions

The following conclusions are drawn from this review work

- Stanton number ratio increases for all geometries with increase in Reynolds number from 4000 to 18,000. Multi-V-shaped ribs with gap have better values of Stanton number ratio than all other turbulent promoters.
- The highest percentage increased in Stanton number ratio for Reynolds number from 4000 to 18,000 is 126.34% for multi-arc-shaped ribs. For some turbulent promoters, Colburn factor increases with Reynolds number, and for others, Colburn factor decreases with Reynolds number.
- The highest percentage increased in Colburn factor for Reynolds number from 4000 to 18,000 is 113.09% for multi-arc-shaped turbulent promoter. At higher Reynolds number, multi-arc-shaped turbulent promoter could perform better.
- *j/f* value is highest for circular protrusions organized in circular arc form. The highest percentage increase in value of *j/f* is for circular protrusions organized in circular arc form and has value of 138.18%.

This review work stated that V-shaping of turbulent promoters intensifies the heat transfer rate at a high level, but simultaneously it brings plenty of frictional pressure drop. It is cleared from the present review work that there should be new roughness geometry having high heat transfer intensification with low frictional pressure drop. As mentioned in Bisht et al. [16], turbulent promoters in the form of circular protrusions organized in V-shaped manner could be considered for economic compact solar heater design.

# References

1. Prasad BN, Saini JS (1988) Effect of artificial roughness on heat transfer and friction factor in a solar air heater. Sol Energy 41:555–560
2. Taslim ME, Li T, Kercher DM (1996) Experimental heat transfer and friction in channels roughened with angled, V-shaped and discrete ribs on two opposite walls. ASME Journal of Turbomachinery 118:20–28
3. Momin AME, Saini JS, Solanki SC (2002) Heat transfer and friction in solar air heater duct with V-shaped rib roughness on absorber plate. Int J Heat Mass Transf 45:3383–3396
4. Bhagoria JL, Saini JS, Solanki SC (2002) Heat transfer coefficient and friction factor correlations for rectangular solar air heater duct having transverse wedge shaped rib roughness on the absorber plate. Renew Energy 25:341–369
5. Jaurker AR, Saini JS, Gandhi BK (2006) Heat transfer and friction characteristics of rectangular solar air heater duct using rib-grooved artificial roughness. Sol Energy 280:895–907
6. Saini SK, Saini RP (2008) Development of correlations for Nusselt number and friction factor for solar air heater with roughened duct having arc-shaped wire as artificial roughness. Sol Energy 82:1118–1130
7. Hans VS, Saini RP, Saini JS (2010) Heat transfer and friction factor correlations for a solar air heater duct roughened artificially with multiple V-ribs. Sol Energy 84:898–911

8. Lanjewar A, Bhagoria JL, Sarviya RM (2011) Heat transfer and friction in solar air heater duct with W-shaped rib roughness on absorber plate. Energy 36:4531–4541
9. Sethi M, Varun Thakur NS (2012) Correlations for solar air heater duct with dimpled shape roughness elements on absorber plate. Solar Energy 86:2852–2861
10. Yadav S, Kaushal M (2013) Varun, Siddhartha, Nusselt number and friction factor correlationsfor solar air heater duct having protrusions as roughness elements on absorber plate. Exp Thermal Fluid Sci 44:34–41
11. Kumar A, Saini RP, Saini JS (2013) Development of correlations for Nusselt number and friction factor for solar air heater with roughened duct having multi v-shaped with gap rib as artificial roughness. Renew Energy 58:151–163
12. Singh AP, Varun, Siddhartha (2014) Heat transfer and friction factor correlations for multiple arc shape roughness elements on the absorber plate used in solar air heaters. Exp Thermal Fluid Sci 54: 117–126
13. Gawande VB, Dhoble AS, Zodpe DB, Chamoli S (2016) Experimental and CFD investigation of convection heat transfer in solar air heater with reverse L shaped ribs. Sol Energy 131:275–295
14. Bejan A, Kraus AD (2003) Heat transfer handbook, 3rd edn. Wiley & Sons, New York
15. Kays WM, London AL (1984) Compact heat exchangers, 3rd edn. McGraw-Hill, New York
16. Bisht VS, Patil AK, Gupta A (2018) Review and performance evaluation of roughened solar air heaters. Renew Sustain Energy Rev 81(1):954–977

# Conventional and Advanced Exergy Analysis of Air-Film Blade Cooled Gas Turbine Cycle

**Shivam Mishra, Yasin Sohret, Sanjay and Anoop Kumar Shukla**

**Abstract** Air-film blade cooling is widely used gas turbine blade cooling technique. The present paper carries out conventional as well as advanced exergy analysis of air-film blade cooled gas turbine cycle based on a film cooling model which takes into account the effect of radiative heat transfer from hot combustion gases to gas turbine blade surface. From the basic concept of thermodynamics, it is well known that the rise in temperature at which heat is added in a cycle results in an increase in thermal efficiency. This could be possible by increasing turbine inlet temperature (TIT) for a fixed maximum allowable blade temperature. The study further analyses air-film blade cooled gas turbine cycle thermodynamically and further carries out conventional and advanced exergy analysis. The study shows that component-wise exergetic efficiency has been observed as 97.5, 80.2, and 91.4% for AC, CC, and GT, respectively, while exergy efficiency for gas turbine cycle is observed to be 37.43%. The maximum exergy destruction has been observed for CC $\sim$ 251.5 kW. The results of advanced exergy analysis show that most of the exergy destruction within cycle components is endogenous. This is indicative of weak mutual interactions between cycle components. The study further shows that $\sim$81.2% of exergy destruction for cycle is unavoidable which indicates the least improvement potential for cycle.

S. Mishra (✉)
G L Bajaj Institute of Technology & Management, Greater Noida, India
e-mail: shivamnml07@gmail.com

Y. Sohret
Suleyman Demirel University, Isparta, Turkey

Sanjay
National Institute of Technology, Jamshedpur, India

A. K. Shukla
Amity School of Engineering and Technology, Noida, India

# 1 Introduction

The lack of energy resources has forced the researchers to come up some efficient solution to improve the thermal performance of energy conversion cycle, and hence, thermal investigation of gas turbine-based power plants is suggested for improvement in thermal efficiency. The first law and second law of thermodynamics play a major role in carrying out this analysis [1]. The first law of thermodynamics has few limitations as it just quantifies the energy and energy efficiency of any thermal system. The exergy analysis or second law analysis of any thermal system can overcome this problem as it provides insight into entropy changes, exergy destruction, and exergy degradation in an individual component of a thermal system [2].

Exergy analysis plays a vital role in the analysis of any thermal system as it determines the amount of exergy and quantifies inefficiency in any individual component of a thermal system. However, conventional exergy analysis merely gives any information about the mutual dependency of system components, their improvement potential and avoidable part of the destruction [3]. Also, exergy destruction occurring within any component might be affected by its surrounding components also. Hence, it is better to analyze and improve other components also rather than just improving the system component with the highest exergy destruction. For carrying out this analysis, a detailed and innovative approach of exergy analysis has been adopted and discussed. This new approach to analyze any thermal system splits exergy destruction into parts namely endogenous and exogenous as well as avoidable and unavoidable exergy destruction and is known as advanced exergy analysis [4, 5]. This approach is expected to facilitate improvement in any energy conversion system from thermodynamics, economics, and environmental point of view [6]. The splitting of exergy destruction into parts gives an upper hand to reanalyze outcome of conventional exergy analysis and then leads to improve accuracy of the exercise. The advanced exergy analysis approach has emerged in the last decade. It splits exergy destruction of any individual components of any energy conversion cycle into parts namely endogenous and exogenous parts of the exergy destruction along with avoidable and unavoidable exergy destruction. The literature shows advanced exergy analysis has been used to analyze various energy systems.

Morosuk and Tsatsaronis [3] discussed methodologies and approach of advanced exergy analysis and applied it for analysis of absorption refrigeration machine. Five different approaches to carry out advanced exergy analysis had been mentioned and discussed in detail by Kelly et al. [4]. The papers further explained the procedure to carry out advanced exergy analysis of an absorption refrigeration machine and a gas turbine cycle. Morosuk et al. [7] discussed the concept of analyzing any chemically reacting system based on advanced exergy analysis. The advanced exergy analysis of a combined cycle power plants was carried out by Petrakopoulou et al. [8].

**Fig. 1** Schematic diagram of air-film blade cooled gas turbine cycle
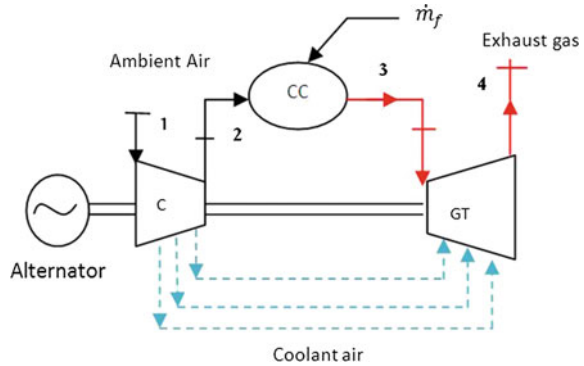


Morosuk and Tsatsaronis [9] discussed the importance of advanced exergy analysis and also carried out this exercise over refrigeration machines using different working fluids. Tsatsaronis et al. [10] carried out advanced exergy analysis and also discussed how thermodynamic inefficiencies in a combustion process can be minimized. Soltani et al. [11] analyzed an externally fired combined cycle power plant based on advanced exergy analysis. Sohret et al. [12] investigated an aircraft gas turbine engine by carrying out advanced exergy analysis and concluded that the system has low improvement potential as a greater fraction of exergy destruction is unavoidable. Mishra et al. [2] carried out advanced exergy analysis of LM-2500+ a marine gas turbine cycle and concluded that system components have weak mutual interactions.

The present study carries out conventional and advanced exergy analysis of air-film blade cooled gas turbine cycle. Figure 1 shows schematics of air-film blade cooled gas turbine cycle.

## 1.1 Assumptions of Advanced Exergy Analysis

1. Air and exhaust gases are assumed to be ideal.
2. The dead-state temperature and pressure have been adopted as 273.15 K and 101.325 kPa, respectively.
3. The thermodynamic process in compressor and turbine is assumed to be polytropic.
4. The kinetic and potential exergies are neglected.
5. The chemical exergy has been neglected except combustor.

## 2 Modeling and Governing Equations

### 2.1 Air/Gas Property Model

The present analysis has taken specific heat of air/gas to be a function of temperature only, and polynomials have been adopted from the work of Touloukain and Tadash [13] and are represented as follows:

For the temperature range of 250–599 K:

$$C_{p,a} = 1.023204 - 1.76021 \times 10^{-4}T + 4.0205 \times 10^{-7}T^2 - 4.87272 \times 10^{-11}T^3 \tag{1}$$

For the temperature range of 600–800 K:

$$C_{p,a} = 0.874334 - 3.22814 \times 10^{-4}T + 3.58694 \times 10^{-8}T^2 - 1.99196 \times 10^{-11}T^3 \tag{2}$$

The specific heat of flue gas has been modeled based on polynomial given by:

$$C_{p,g} = \left[15.276826 + 0.01005T - 3.19216 * 10^{-6}T^2 + 3.48619 * 10^{-10}T^3 \right. $$
$$\left. + x_0\left(0.104826 + 5.54150 \times 10^{-5}T - 1.67585 \times 10^{-8}T^2 + 1.18266 \times 10^{-12}T^3\right)\right]/V \tag{3}$$

Thus, enthalpy of the air and gas is expressed as follows:

$$h = \int_{T_o}^{T} C_p(T)\mathrm{d}T \tag{4}$$

### 2.2 Energy and Exergy Balance

The basic thermodynamics equations, i.e., energy and exergy analyses, have been adopted from the literature [14, 15] and are as under:

$$\sum \dot{m}_i = \sum \dot{m}_e \tag{5}$$

$$\dot{Q} - \dot{W} = \sum \dot{m}_e h_e - \sum \dot{m}_i h_i \tag{6}$$

Total exergy of a system is the assumed to a sum of its kinetic, potential, chemical, and physical exergy.

$$\dot{E} = \dot{E}_{ke} + \dot{E}_p + \dot{E}_{ph} + \dot{E}_{ch} \tag{7}$$

Also, for the present analysis kinetic and potential exergies have been neglected, and hence,

$$\dot{E} = \dot{E}_{ph} + \dot{E}_{ch} \tag{8}$$

The physical exergy, in specific form, can be expressed as:

$$e_{ph} = [(T - T_o) - T_o[\ln(T/T_o) - R.\ln(P/P_o)]] \tag{9}$$

Similarly, specific chemical exergy can be defined as [15]:

$$e_f^{ch} = \text{LHV}[1.0403] \tag{10}$$

The exergy destruction ($\dot{E}_D$) from conventional exergy point of view, for a system, is expressed as the difference of total inlet exergy ($\dot{E}_F$) and total output exergy ($\dot{E}_P$), i.e.,

$$\sum \dot{E}_D = \sum \dot{E}_F - \sum \dot{E}_P \tag{11}$$

## 2.3　Compressor

The temperature at any section of the compressor can be calculated by using formula:

$$\frac{dT}{T} = \left(\frac{R}{\eta_{p,c}C_{p,a}}\right)\frac{dp}{p} \tag{12}$$

The enthalpy within the compressor at any point can be calculated determined with the help of Eqs. (1, 2, 4, and 12).

The work of compressor is evaluated by employing mass and energy balance across control volume of compressor

$$\dot{m}_{ac,i} = \dot{m}_{ac,e} + \sum \dot{m}_{cl,j} \tag{13}$$

$$W_{ac} = \dot{m}_e h_e + \sum \dot{m}_{cl,j} h_j \tag{14}$$

## 2.4 Combustion Chamber

Modeling of combustion chamber (CC) takes into account the losses within CC while determining fuel requirement for achieving a specific combustor exit temperature.

The mass balance of the combustor is given as follows:

$$\dot{m}_3 = \dot{m}_2 + \dot{m}_f \tag{15}$$

while energy balance of combustor is mentioned below:

$$\dot{m}_f \cdot \text{LHV} \cdot \eta_{\text{comb}} = \dot{m}_3 \cdot h_3 - \dot{m}_2 \cdot h_2 \tag{16}$$

The mass fuel requirement has been determined by using mass and energy balance across the combustion chamber.

$$\dot{m}_f = \left[ \frac{\dot{m}_3 h_3 - \dot{m}_2 . h_2}{\text{LHV} \cdot \eta_{\text{comb}} - h_3} \right] \tag{17}$$

## 2.5 Cooled Gas Turbine Model

Figure 2 represents the schematic diagram of gas turbine blade row subjected to air-film cooling with radiative heat transfer taken into account. The proposed blade cooling model is expected to predict blade coolant mass fraction which might be close to real engine requirements. The amount of blade coolant mass fraction is expressed as follows [2, 16]:



$$Q_{net} = \overline{h_g} \cdot A_{sg} \cdot (T_{g,i} - T_{bl})$$
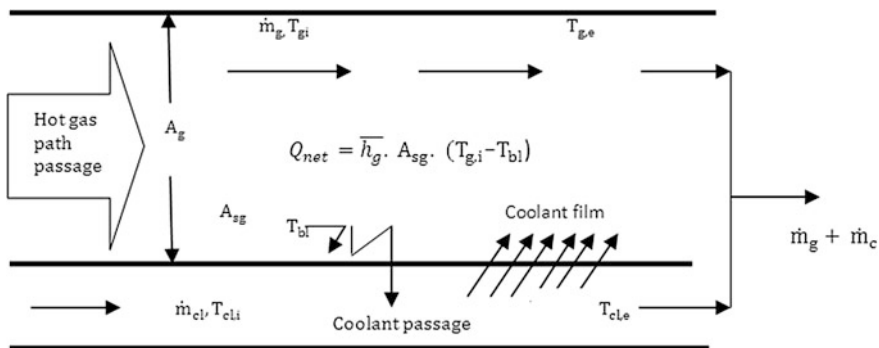
**Fig. 2** Schematics of air-film blade cooled gas turbine cycle

$$\frac{\dot{m}_{cl}}{\dot{m}_g} = \frac{\lambda \cdot (c_{pg}/c_{pcl}) \cdot St_g.F_{ec}}{\eta_{cl} \cdot (T_{bl} - T_{cl,i})} \left[ (T_{g,i} - T_{bl}) - \varepsilon_{aw} \cdot \left(T_{g,i} - \left\{\eta_{cl} \cdot (T_{bl} - T_{cl,i}) + T_{cl,i}\right\}\right) \right. $$
$$\left. + \frac{\sigma\left(\alpha_g \cdot T_{g,i}^4 - \varepsilon_g \cdot T_{bl}^4\right)}{\overline{h}_g} \right] \tag{18}$$

## 3 Methodology

### 3.1 Conventional Exergy Analysis

The conventional exergy analysis has been carried out by following fuel–product–loss (F-P-L) exergy analysis approach. The components with the highest exergy destruction have been identified by flowing this F-P-L approach; i.e., exergy of product $\dot{E}_{P,k}$, and exergy of fuel, $\dot{E}_{F,k}$, have been determined. Also, exergy destruction as well as exergy efficiency for a component '$k$' has been calculated by:

$$\dot{E}_{D,k} = \dot{E}_{F,k} - \dot{E}_{P,k} \tag{19}$$

$$\varepsilon = \dot{E}_{P,k}/\dot{E}_{F,k} \tag{20}$$

### 3.2 Advanced Exergy Analysis

Advanced exergy analysis is a new methodology to calculate the amount of exergy destruction that can be minimized. The advanced exergy analysis splits exergy destruction into parts to have an understanding of the cause of irreversibility within system components.

– endogenous and exogenous exergy destruction,
– avoidable and unavoidable exergy destruction.

#### 3.2.1 Endogenous–Exogenous (EN-EX) Exergy Destruction

The rate of endogenous exergy destruction ($\dot{E}_{D,k}^{EN}$) in $k$th component is the indicative of a component's exergy destruction when it is operated at its real operating condition while rest of the cycle components are assumed to operate theoretically [17].

$$\dot{E}_{D,k} = \dot{E}_{D,k}^{EN} + \dot{E}_{D,k}^{EX} \qquad (21)$$

### 3.2.2 Avoidable–Unavoidable (AV-UN) Exergy Destruction

The unavoidable exergy destruction $(\dot{E}_{D,k}^{UN})$ is that part of exergy destruction which is almost impossible to eliminate from a component even if the best possible technologies are available.

Also,

$$\dot{E}_{D,k} = \dot{E}_{D,k}^{UN} + \dot{E}_{D,k}^{EN} \qquad (22)$$

Here, unavoidable exergy destruction (UN) can be calculated as:
And hence, avoidable exergy destruction (AV) can be evaluated as:

$$\dot{E}_{D,k}^{AV} = \dot{E}_{D,k} - \dot{E}_{D,k}^{UN} \qquad (23)$$

## 4  Results and Discussions

### 4.1  Conventional Energy and Exergy Analysis

Based on mathematical models detailed in the previous sections, C++ code has been developed to analyze the gas turbine cycle for its thermodynamic performance.

The input data for analysis of the proposed gas turbine cycle is detailed in 'Table 1.'

Table 2 represents the F-P-L approach for calculation of exergy destruction.

**Table 1** Input parameters for the present analysis [20–25]

| Parameters | Symbol | Units |
|---|---|---|
| Compressor | Polytropic efficiency ($\eta_{pc}$) = 90 | % |
| | Mechanical efficiency ($\eta_m$) = 98.5 | % |
| Combustor | Combustor efficiency ($\eta_{comb}$) = 99.5 | % |
| | Pressure loss ($p_{loss}$) = 2.0% of entry pr. | % |
| Gas turbine | Polytropic efficiency ($\eta_{pt}$) = 90.0 | % |
| | Exhaust pressure = 1.08 | Bar |
| | Turbine blade temperature = 1123 | K |
| Air-film blade cooling | Film cooling efficiency ($\eta_{cl}$) = 70 | % |
| | Adiabatic wall effectiveness ($\varepsilon_{aw}$) = 40<br>Prandtl no. ($Pr_g$) = 0.7<br>Reynolds no. ($Re_g$) = $1 \times 10^6$ | % |

**Table 2** Definition of F-P-L approach for air-film blade cooled gas turbine cycle

| Components | Fuel (MW) | Product (MW) |
|---|---|---|
| AC | $W_{AC}$ | $\dot{E}_2 + \dot{E}_6 + \dot{E}_7 + \dot{E}_8 + \dot{E}_9 - \dot{E}_1$ |
| CC | $\dot{E}_3 + \dot{E}_2$ | $\dot{E}_4$ |
| GT | $\dot{E}_4 + \dot{E}_6 + \dot{E}_7 + \dot{E}_8 + \dot{E}_9 - \dot{E}_5$ | $W_{GT}$ |
| Overall cycle | $\dot{E}_3$ | $W_{GT,net}$ |

Figure 3 shows the variation of blade coolant mass fraction with a change in different values of compressor pressure ratio and turbine inlet temperature for air-film blade cooled gas turbine cycle. Figure 3 shows that blade coolant mass fraction increases with an increase in TIT for a fixed value of $r_{pc}$. This is attributed to the fact that as TIT is increased keeping $r_{pc}$ constant, the blade coolant exit temperature increases, and this in turn increases the adiabatic wall effectiveness and this increases the blade coolant mass fraction. The result obtained from the current analysis shows good consent from available literature [18, 19].

Figure 4 represents component-wise exergy destruction and exergy loss for air-film blade cooled gas turbine cycle. Figure 4 shows that maximum exergy destruction has been observed for combustion chamber (CC) $\sim$ 251.58 kW, followed by expansion turbine (GT) $\sim$ 75.88 kW. The combustor is the main source of exergy destruction because of incomplete combustion, thermal degradation
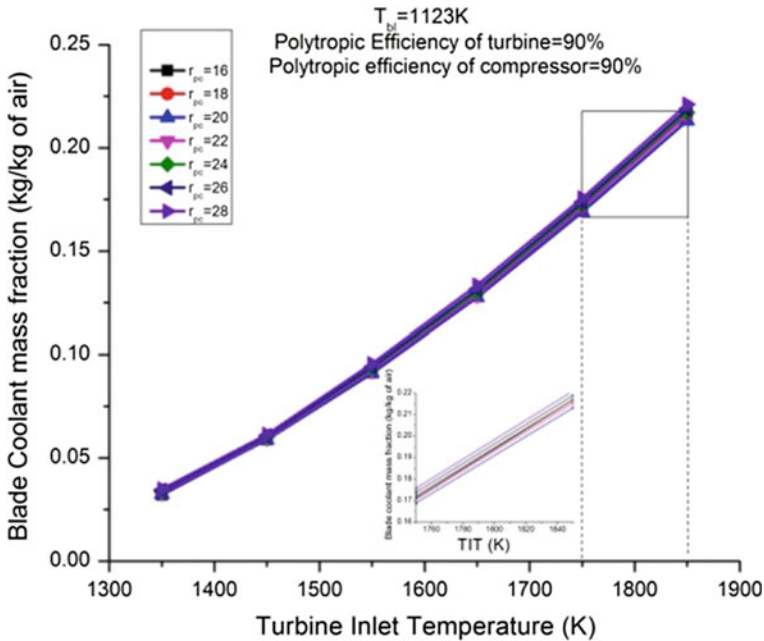


**Fig. 3** Variation of blade coolant mass fraction with a change in TIT and $r_{pc}$
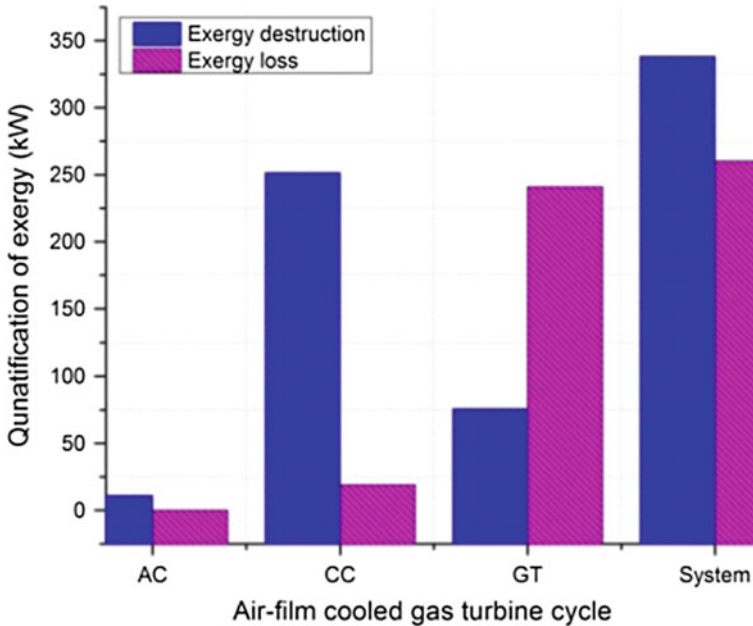
**Fig. 4** Quantification of exergy destruction and exergy loss for air-film blade cooled gas turbine cycle

(because of heat released during combustion), and pressure drop within CC. This represents that CC needs to be redesign in order to improve overall system. Maximum exergy loss has been found observed for GT.

Figure 5 shows component-wise and overall system exergetic efficiency for air-film blade cooled gas turbine cycle. Figure 5 shows that maximum efficiency has been observed for AC, followed by GT, followed by CC. The exergy efficiency for AC has been observed as 97.5%, while for GT, it is 91.48%. The CC has least exergetic efficiency $\sim$80%, which is the indicative of exergy destruction within CC. The exergy efficiency for overall cycle has been observed as $\sim$37.43%.

## 4.2 Advanced Exergy Analysis

Figure 6 depicts a picture of component-wise exergy destruction for following advanced exergy analysis approach, i.e., endogenous and exogenous exergy destruction. Figure 6 shows that all the components of air-film blade cooled gas turbine cycle show endogenous exergy destruction which exceeds exogenous exergy destruction. This shows that since most part of exergy destruction within system components is endogenous ($\sim$85.17%) because of inefficiency within component itself, this indicates weak mutual interactions between system
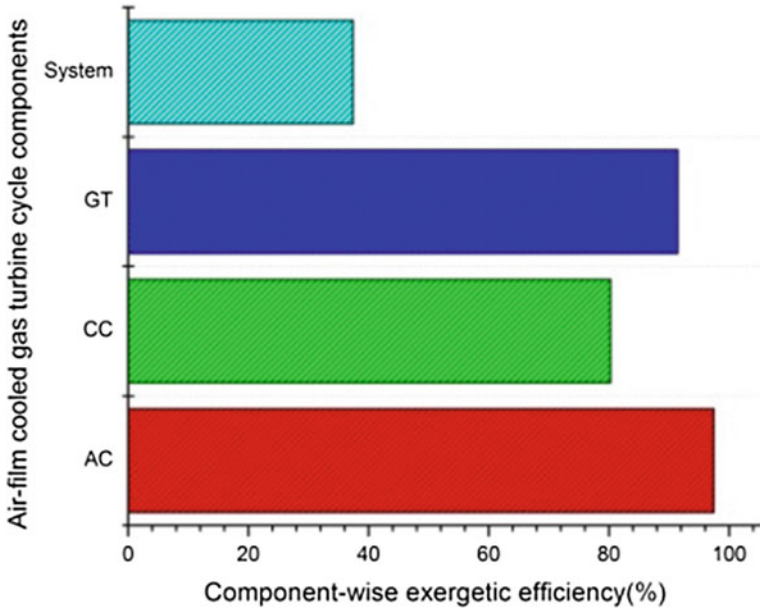
**Fig. 5** Component-wise exergetic efficiency for air-film blade cooled gas turbine cycle
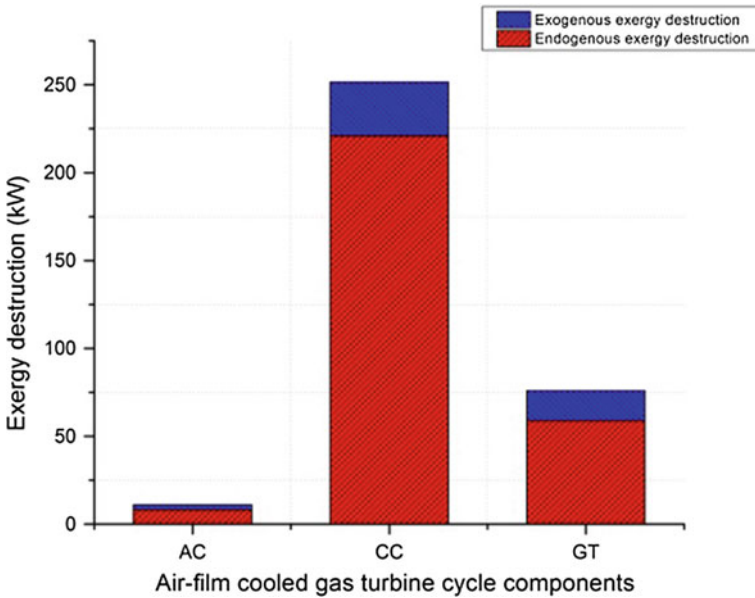


**Fig. 6** Component-wise endogenous/exogenous exergy destruction for air-film blade cooled gas turbine cycle
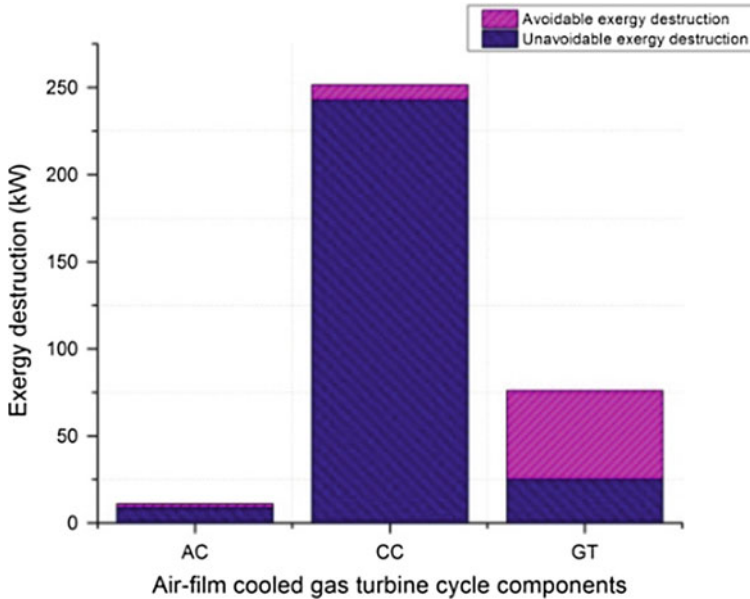
**Fig. 7** Component-wise avoidable/unavoidable exergy destruction for air-film blade cooled gas turbine cycle

components. The CC has highest endogenous exergy destruction $\sim$220.9 kW ($\sim$87.8%) of overall exergy destruction within CC which amounts to be 251.58 kW.

Figure 7 depicts that CC and AC show higher unavoidable exergy destruction as compared to avoidable exergy destruction. This indicates that these components have low improvement potential depending on aforesaid thermodynamic limitations even if they operate at their best possible technological development and improvement in the recent future. The maximum unavoidable exergy destruction has been observed for CC ($\sim$242.7%) which is $\sim$96.4 of exergy destruction within CC [12]. The graph also shows that for expansion turbine (GT), the avoidable exergy destruction is higher to unavoidable exergy destruction. This is indicative of that preference should be given to expansion turbine (GT) for improvement, and this will result in improvement in overall cycle.

## 5 Conclusion

In the present paper, advanced exergy analysis of air-film blade cooled gas turbine has been performed. Based on the analysis, the following points can be concluded:

- The blade coolant mass fraction requirement generally increases with an increase in TIT ad $r_{pc}$.
- The conventional exergy analysis shows that exergetic efficiency has been observed as 97.5, 80.2, and 91.4% for AC, CC, and GT, respectively, while exergy efficiency for overall system is observed as 37.43%.
- The maximum exergy destruction has been observed for CC $\sim$ 251.5 kW.
- Majority of exergy destruction (85.7%) within cycle is endogenous which shows that interactions between system components are weak.
- Majority of exergy destruction (81.8%) of overall system is unavoidable showing very low improvement potential of system.
- The result recommends that for maximum improvement of overall cycle, designer should focus on GT, followed by CC for minimization of exergy destruction.

# References

1. Balli O (2017) Advanced exergy analyses of an aircraft turboprop engine (TPE). Energy. https://doi.org/10.1016/j.energy.2017.02.121
2. Mishra S, Sohret Y, Sanjay R (2018) Advanced exergy analysis of air-film blade cooled marine gas turbine cycle (LM-2500+). SAE Technical Paper, 2018-01-1372. https://doi.org/10.4271/2018-01-1372
3. Morosuk T, Tsatsaronis G (2008) A new approach to the exergy analysis of absorption refrigeration machines. Energy 33:890–907
4. Kelly S, Tsatsaronis G, Morosuk T (2009) Advanced exergetic analysis: approaches for splitting the exergy destruction into endogenous and exogenous parts. Energy 34:384–391
5. Morosuk T, Tsatsaronis G, Schult M (2013) Conventional and advanced exergetic analyses: theory and application. Arab J Sci Eng 38:395–404
6. Şöhret Y, Ekici S, Altuntaş O, Hepbasli A et al Exergy as a useful tool for the performance assessment of aircraft gas turbine engines: a key review. Prog Aerosp Sci. http://dx.doi.org/10.1016/j.paerosci.2016.03.001
7. Morosuk T, Tsatsaronis G (2009) Advanced exergy analysis for chemically reacting systems-application to a simple open gas-turbine system. Int J Thermodyn 12:105–111
8. Petrakopoulou F, Tsatsaronis G, Morosuk T, Carassai A (2012) Conventional and advanced exergetic analyses applied to a combined cycle power plant. Energy 41:146–152
9. Morosuk T, Tsatsaronis G (2009) Advanced exergetic evaluation of refrigeration machines using different working fluids. Energy 34:2248–2258
10. Tsatsaronis G, Morosuk T, Koch D, Sorgenfrei M (2013) Understanding the thermodynamic inefficiencies in combustion processes. Energy 62:3–11
11. Soltani S, Yari M, Mahmoudi SMS, Morosuk T, Rosen MA (2013) Advanced exergy analysis applied to an externally-fired combined-cycle power plant integrated with a biomass gasification unit. Energy 59:775–780
12. Sohret Y, Açıkkalp E, Hepbasli A, Karakoc TH (2015) Advanced exergy analysis of an aircraft gas turbine engine: splitting exergy destructions into parts. Energy 90:1219–1228
13. Touloukain YS, Tadash M (1970) Thermo-physical properties of matter. In: The TPRC Data Series, vol 6. New York, Washington: IFI/PLENUNM. https://doi.org/10.1007/s13369-012-0441-9

14. Ekici S, Sohret Y, Coban K, Altuntas O, Karakoc TH Performance evaluation of an experimental turbojet engine. Int J Turbo Jet Eng. https://doi.org/10.1515/tjj-2016-0016
15. Aydin H (2013) Exergetic sustainability analysis of LM6000 gas turbine power plant with steam cycle. Energy 57:766–774
16. Sanjay MS (2018) Energy and exergy analysis of air-film cooled gas turbine cycle: effect of radiative heat transfer on blade coolant requirement. Appl Therm Eng 129:1403–1413
17. Vučković GD, Stojiljković MM, Mića, VV (2015) First and second level of exergy destruction splitting in advanced exergy analysis for an existing boiler. Energy Convers Manage 104:8–16
18. Sanjay Y, Singh O, Prasad BN (2008) Influence of different means of turbine blade cooling on the thermodynamic performance of combined cycle. Appl Therm Eng 28:2315–2326
19. Mishra S and Sanjay Y (2017) Parametric analysis of aero-derivative gas turbine: effect of radiative heat transfer on blade coolant requirement. SAE Technical Paper 2017-01-2045. https://doi.org/10.4271/2017-01-2045
20. Sanjay Y, Singh O, Prasad BN (2009) Comparative performance analysis of cogeneration gas turbine cycle for different blade cooling means. Int J Therm Sci 48:1432–1440
21. Mishra S, Sahu M (2016) Comparative thermodynamic performance evaluation of cooled gas turbine plant. IJATES 4:496–505
22. Sahu M, Mishra S (2016) Performance analysis of reheated gas turbine based power plant cycle. IJATES X 4:490–497
23. Mishra S, Sanjay R (2018) Thermodynamic performance prediction of air-film blade cooled gas turbine based cogeneration cycle for marine propulsion applications. SAE Technical Paper, 2018-01-1364. https://doi.org/10.4271/2018-01-1364
24. Shukla AK, Singh O (2016) Performance evaluation of steam injected gas turbine based power plant with inlet evaporative cooling. Appl Therm Eng 102:454–464
25. Shukla AK, Singh O Thermodynamic investigation of parameters affecting the execution of steam injected cooled gas turbine based combined cycle power plant with vapor absorption inlet air cooling. Appl Therm Eng. http://dx.doi.org/10.1016/j.applthermaleng.2017.05.034

# Effect of Area Ratio on Flow Separation in Annular Diffuser

**Hardial Singh and B. B. Arora**

**Abstract** Annular diffusers are integral component of the axial flow compressor, combustion chambers and inlet portion of jet engine. In present study flow behavior inside the parallel hub and diverging casing annular diffuser having area ratio 2 to 4 with help of FLUENT has been predicted. The effect of different inlet swirl angles 0°, 7.5°, 12°, 17° and 25° has been studied to predict the reversal of flow and separation of flow from the wall. The result analysis shows that swirl enhances the pressure recovery up to a particular swirl angle and falls thereafter. It also helps in suppressing the flow separation. The effect of inlet swirl on the pressure recovery coefficient has also been figured out.

## Nomenclature

| | |
|---|---|
| $\eta$ | Diffuser effectiveness |
| $\theta$ | Divergence angle |
| AR | Area ratio |
| $C_p$ | Pressure recovery coefficient |
| $C_{pi}$ | Ideal pressure recovery |
| $L$ | Length of diffuser |
| $V_{av1}$ | Average velocity |
| $X/L$ | Non-dimensional axial length |

H. Singh (✉)
Department of Mechanical Engineering, Amity University, Gurgaon, India
e-mail: Hardialsingh3@gmail.com

B. B. Arora
Department of Mechanical Engineering, Delhi Technical University, Delhi, India

# 1    Introduction

A diffuser is an expanding duct. The objective of diffuser to recover the fluid static pressure in the fluid stream while reducing the flow velocity. The fluid is slow as pass through a diffuser, and portion of kinetic energy of flow is converted into the potential energy of pressure. An efficient diffuser is one which converts the highest possible percentage of kinetic energy into pressure within given diffuser length or expansion ratio. Diffuser performance is a strong function of many flow variable as well as geometric variable.

Most investigators to take advantage of the simple cascade design geometry to generate swirled in a radial inflow plane. Others preferred to use axial cascade having the advantage of closely simulating specific turbo machinery flow condition and permitting control of the spacing between the diffuser and the vanes in a form that may be more typical for actual turbo machinery. Inlet swirl, there may be changes in inlet turbulence intensity, velocity or total pressure gradients, vorticity or wake shading, and inlet aerodynamic blockage may change indirectly as a function of the swirl angle as it is varied. Agrawal et al. [1] have shown the improved flow structure with hub rotation in annular diffuser. Adkins et al. [2]; Adkins [3] performance of diffuser much more depends on geometrical and dynamic parameter. Arora [4, 7]; Arora and Pathak [5, 6] worked on the effect of geometry on the performance of annular diffuser. The behaviour of flowing fluid and pressure recovery coefficient has been analysed. Coladipietro et al. [9] found the effect of wall layer thickness and inlet swirl on the performance of equiangular annular diffuser. The performance of annular diffuser increased as diffuser length increased also improved by increasing inlet swirl angle. Mohan et al. [13] found that pressure recovery improved with particular level of swirl in the annular diffuser at the area ratio 3 and equivalent half cone angle 12.5°, 15° and 17°. Dovzhik and Kartavenko [10]; Kumar et al. [14] worked on the separation of flow from the wall at various swirl angles and to predict the behaviour of flow. Singh et al. [15] worked on flow development in diffuser passage with inlet swirl angle. Sovran and Klomp [17] tested over the hundreds of different geometries all of which had conically centre bodies. The tests were carried out with thin inlet boundary layer, and diffusers have free discharge. The contours of pressure recovery against area ratio have been analysed. Srinath [18] considered an axial flow equiangular diffuser with swirl between 0° and 15°. Peak pressure recovery was found at approximately 10º and then decreased rapidly. Hoadley [11] tested an annular diffuser with a cylindrical inner body and reported that best recovery was achieved at approximately 10° of swirl. Kumar and Kumar [12] studied experimentally the effect of inlet swirl in equiangular and unequal angle diverging annular diffusers. Swirl angle gives much better result for such diffuser.

In the fluid dynamic process, viscosity is an important parameter that is appeared in the form of a Reynolds number. Crockrell and Markland [8] state that a variation of the inlet Reynolds number has no significant effect on the diffuser performance if this variation is uncoupled from its effects on the inlet boundary layer parameters.

Sharan [16] reported that for thick boundary layers, there is no change in pressure recovery as the Reynolds number increases. Stevens [19] showed that efficiency of annular diffuser with wall angle 2.5° is deteriorated with the increase in outer wall momentum thickness.

## 2 Problem Description

Present problem involves the analysis of annular diffuser with hub angle kept constant. Casing angle are changed in accordance with AR. Where the area ratio varied as 2, 3, 4 and swirl angle varied as 0°, 7.5°, 12°, 17°, 25°. Outlet flow exhaust to atmosphere at atmospheric pressure. Figure 1 shows the annular diffuser geometrical parameters of the half section as the diffuser has been taken as axially symmetrical.

## 3 Performance Parameters

Performance parameters are very helpful in designing and predicting the performance of diffusers. These parameters reveal that diffuser geometry will give the desire output or not. The following parameters are important to find out diffuser performance.

### 3.1 Static Pressure Recovery Coefficient

The pressure recovery coefficient of a diffuser is most frequently defined as the static pressure rise through the diffuser divided by the inlet dynamic head.
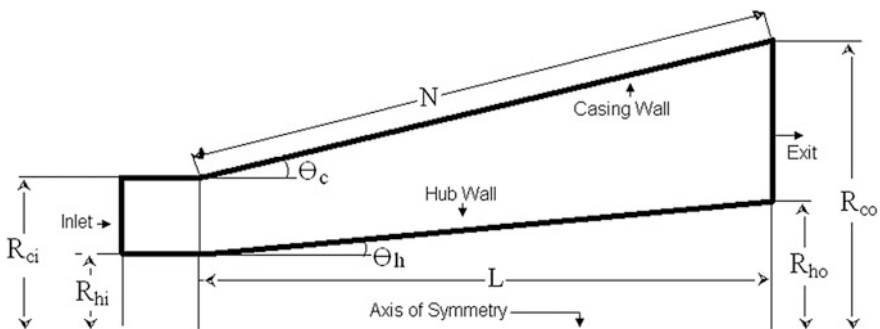


**Fig. 1** Annular diffuser geometrical parameters

$$C_{\mathrm{p}} = \frac{p_2 - p_1}{\frac{1}{2}\rho v_{\mathrm{av1}}^2}$$

where subscripts 1 and 2 refer to diffuser inlet and outlet conditions, respectively. $v_{\mathrm{av1}}$ represents the average velocity at the inlet. An ideal pressure recovery can be defined if the flow is assumed to be isentropic. Then, by employing the conservation of mass, this relation can be converted to an area ratio for incompressible flow.

$$C_{\mathrm{pi}} = 1 - \frac{1}{\mathrm{AR}^2}$$

## 3.2  Diffuser Effectiveness

The diffuser effectiveness is simply the relation between the actual recovery and the ideal pressure recovery.

$$\eta = \frac{C_{\mathrm{p}}}{C_{\mathrm{pi}}}$$

This is an excellent parameter for judging the probable level of performance when it is necessary to estimate the expected performance under unknown conditions, relative to available data.

## 4  Mathematical Formulation

k-ε turbulence model-based analysis revealed that swirling flow in diffuser helps in relocation of turbulent profile into laminar profile of axial velocity component resulting in reduced hydraulic loss. It was also observed that the swirling flow is highly influenced by geometric properties as well as flow parameters. The mathematical formulation was simulated with the help of FLUENT. Here, meshing of the physical geometry was performed in GAMBIT, and computational fluid dynamics (CFD) analysis was done in FLUENT. In the pre-study, k-ε turbulence models such as standard, RNG and realizable were attempted for the physical geometry to validate the results obtained experimentally. It was noted that the two-dimensional double precision axisymmetric RNG, k-ε turbulence model approached more closely to the experimental results. Therefore, the same model was used for predicting the performance at various inlet swirls for different area ratios. The same model was used for predicting the performance at various inlet swirls. The governing equations for 2D axisymmetric geometries have been discussed Arora and Pathak [5, 6].

# 5   Results and Discussion

## 5.1   Pressures Recovery Coefficient Graphs

Figure 2 indicates pressure recovery coefficient graph at casing and hub wall ($C_p$) for diffuser for area ratios 2 as function of non-dimensional diffuser passage X/L for various inlet swirl angle 0°, 7.5°, 12°, 17° and 25°. $C_p$ increases with the diffuser passage in each case. The marginal increase in $C_p$ is sharp in the beginning of the diffuser passage and later on it decreases with the diffuser passage. In diffuser with
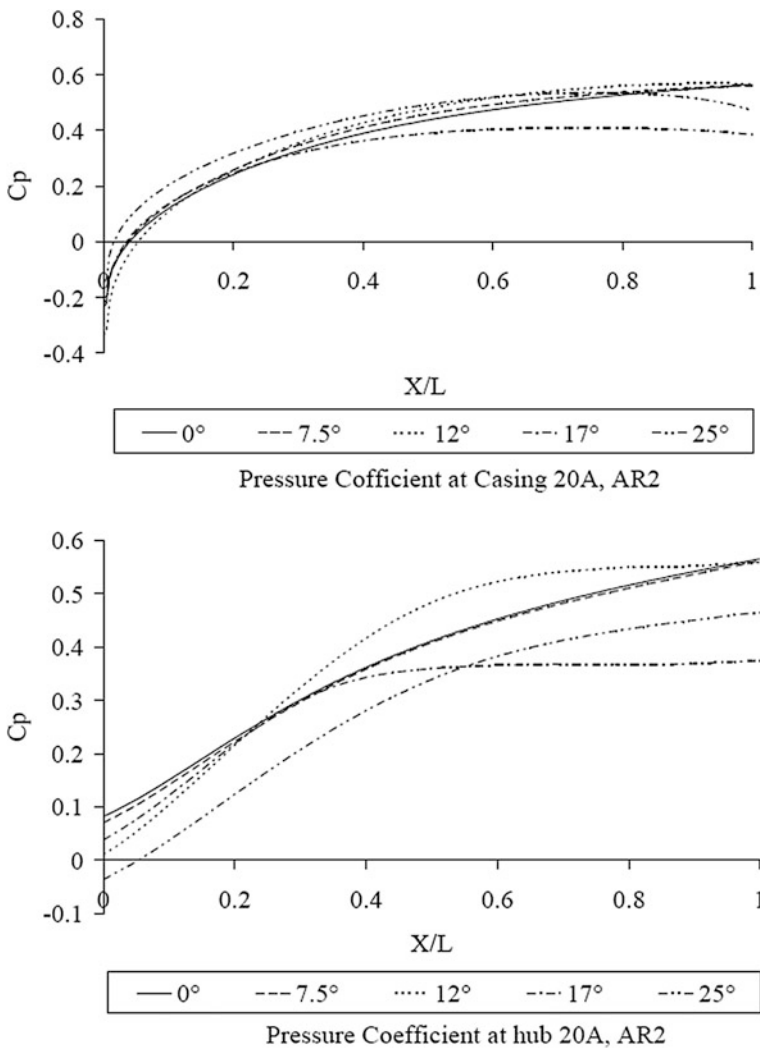


**Fig. 2** Pressure coefficient (AR 2) at casing and hub with inlet swirl angles (0° to 25°) at various transverses at *X/L* = 0.1 to 0.9

area ratio 2 for inlet swirl angle 7.5°, 12°, 17° and 25°. Inlet $C_p$ is lower than the flow without swirl beyond $X/L$ = 0.81, 0.94, 0.76, 0.48 in casing position, respectively. $C_p$ is highest up to diffuser passage length of 0.35 for 25° inlet swirl. From $X/L$ = 0.35 to 0.56 for 25° inlet swirl then from 0.56 to 0.94, it is for 12° inlet swirl on the end flow without swirl. In the case of hub for area ratio 2–4, the lower value of swirl, i.e. 7.5° and 12° gain in $C_p$ is observed up to X/L = 0.60 where as there is decrease in magnitude of $C_p$ for inlet angle of 17° and 25° to the flow without swirl. The nature and the order of magnitude of pressure recovery coefficient is reasonably well for swirl flow as well as non swirl flow Arora [4].

Figure 3 shows annular diffuser with area ratio 3, the $C_p$ increases as compared to no swirl condition with increasing swirl in beginning of diffuser passage length.
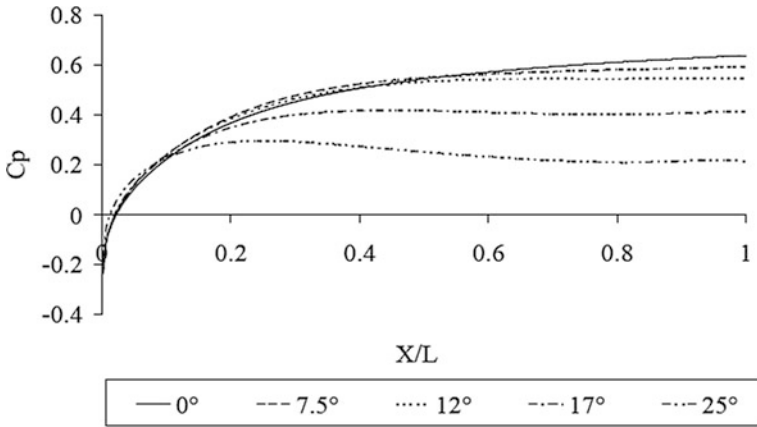


Pressure coefficient at Casing 20A, AR3
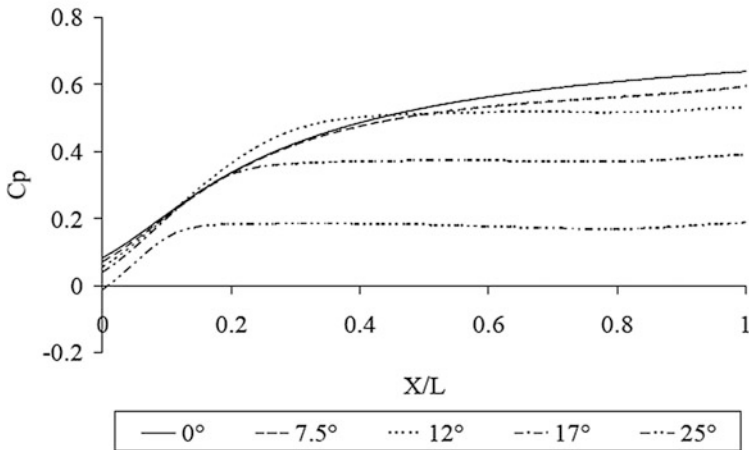


Pressure Coefficient at Hub 20A, AR3

**Fig. 3** Pressure coefficient (AR 3) at casing and hub with inlet swirl angles (0° to 25°) at various transverses at $X/L$ = 0.1 to 0.9

However for 7.5°, 12°, 17° and 25°, inlet swirl $C_p$ is lower than the flow without swirl beyond $X/L = 0.66$, 0.96, 0.58 and 0.24 casing position, respectively. $C_p$ is highest to diffuser passage length 0.18 for 25° inlet swirl. From $X/L = 0.18$ to 0.38, it is maximum for 17° inlet swirl, then from 0.3 to 0.98, it is for 12° inlet swirl.

Figure 4 represents variation of pressure recovery coefficient with axial length at an area ratio of 4 for different inlet swirl angles i.e. 7.5°, 12°, 17° and 25°. $C_p$ is lower than the flow without swirl beyond $X/L = 0.46$, 0.85, 0.38 and 0.19 casing position, respectively. $C_p$ is highest up to diffuser passage length of 1 for 25° inlet swirl. From $X/L$ 0.14 to 0.16, it is maximum for 17° inlet swirl, then from 0.15 to 0.85, it is for 12° inlet swirl, from 0.85 till end, it is for flow without swirl.
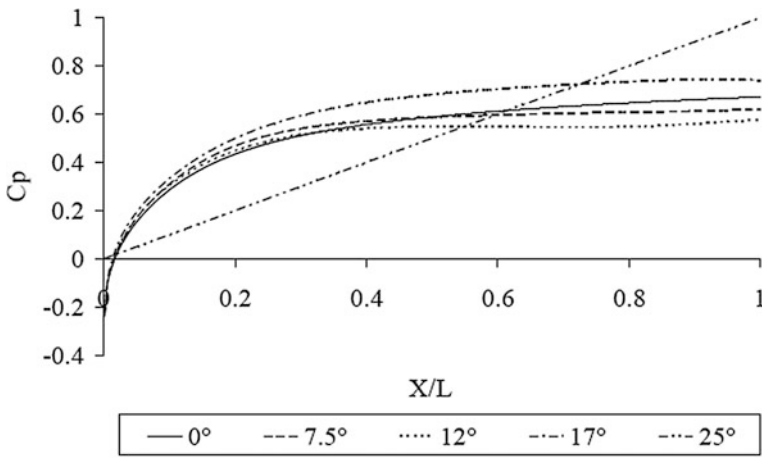


Pressure Coefficient at Casing 20A, AR4
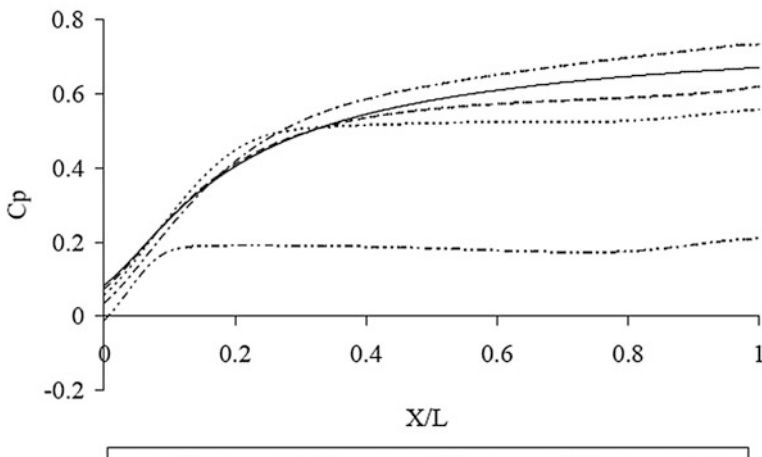


Pressure Coefficient at Hub 20A, AR4

**Fig. 4** Pressure coefficient (AR 4) at casing and hub with inlet swirl angles (0° to 25°) at various transverses at $X/L$ = 0.1 to 0.9

# 6    Conclusions

The analysis is basically performed with an advanced k-ε RNG model for swirling flows. Higher order discretization schemes and better turbulence models can be used for better results in case of swirling flows. It was noted that swirl pushed the flow towards casing wall thus making the flow stronger towards casing than hub wall. The introduction of swirl also resulted in faster recovery towards the casing wall. The effect of swirl appears to gradually decay as the flow proceeds downstream, and the recovery is negligible towards the diffuser exit. Pressure recovery coefficient increases with the diffuser passage for all value of inlet swirl. However, at higher values of swirl, the marginal recovery decreases with the diffuser passage.

# References

1. Agrawal DP, Singh SN, Sapre RN, Malhotra RC (1989) Effect of hub rotation on the mean flow of wide angle annular diffusers. HydroTurbo 1989, Czechoslovakia
2. Adkins RC, Jacobsen OH, Chevalier P (1983) A premilary study of annular diffuser with constant diameter outer wall. ASIVIE paper no. 83-GT-218
3. Adkins RC (1983) A simple method for design optimum annular diffusers. ASTVE Paper No. 83-GT-42
4. Arora BB (2007) Aerodynamic analysis of diffuser. PhD thesis, DU, Delhi
5. Arora BB, Pathak BD (2005) Flow characteristics of parallel hub diverging casing axial annular diffusers. ISME publication, pp 794–798
6. Arora BB, Pathak BD (2009) Effect of geometry on the performance of annular diffuser. Int J Appl Eng Res 14(12)
7. Arora BB (2014) Performance analysis of parallel hub diverging casing axial annular diffuser with 20° equivalent cone angle. Aust J Mech Eng 12(2)
8. Cockrell DJ, Markland E (1963) A review of incompressible diffuser flow. Aircr Eng 35:286
9. Coladipietro R, Schneider JM, Sridhar K (1974) Effects of inlet flow conditions on the performance of equiangular annular diffusers. Trans CSME 3(2):75–82
10. Dovzhik SA, Kartavenko VM (1975) Measurement of the effect of flow swirl on the efficiency of annular ducts and exhaust nozzles of axial turbo-machines. Fluid Mech/Sov Res 4(4): 156–172
11. Hoadley D (1970) Three-dimensional turbulent boundary layers in an annular diffuser. Ph.D. thesis, Department of Engineering, University of Cambridge, London
12. Kumar DS, Kumar KL (1978) Effect of swirling flow through annular diffusers. In: Ist International conference on centrifugal compressors technology, pp D1-1 to D1-10
13. Kumar M, Arora BB, Maji S (2010) Analysis of flow separation in wide angle annular diffusers. Int J Appl Eng Res 5(20):3419–3428. ISSN 0973-4562
14. Mohan R, Singh SN, Agrawal DP (1998) Optimum inlet swirl for annular diffuser performance using CFD. Indian J Eng Mater Sci 5:15–21
15. Singh SN, Agarwal DP, Sapre RN, Malhotra RC (1994) Effect of inlet swirl on the performance of wide angled diffusers. Indian J Eng Mater Sci 1:63–69
16. Sharan VK (1972) Diffuser performance correlation. J Aeronaut Soc India 24:415–419
17. Sovran G, Klomp ED (1967) Experimentally determined optimum geometries for rectilinear diffusers with rectangular, conical or annular cross section. In: Sovran G (ed) Fluid mechanics of internal flow. Elsevier, Amsterdam, pp 270–319

18. Srinath T (1968) An investigation of the effects of swirl on fl ow regimes and performances of annular diffuser with inner and outer cone angles. MASc thesis, University of Waterloo, Canada
19. Stevens SJ (1968) The performance of annular diffusers. Proc Inst Mech Eng 182, Part 3D:58–70

# Identification and Inquisition of Thermoelectric Generator Unit for Efficient Waste Heat Recovery

**Abhishek Khanchi, Harkirat Sandhu, Mani Kanwar Singh, Satbir S. Sehgal and Bharat Bajaj**

**Abstract** A Peltier device or thermoelectric generator is a solid-state semiconductor device which works on the principle of thermoelectric effect or Seebeck effect and has an inherent capability to convert heat flux directly into an EMF. Thermoelectric effect which is a result of having a physical contact between two dissimilar conductors with the presence of temperature difference across its ends is further enhanced by effective use of semiconductor materials for its fabrication. Its potential to harness low-grade waste has attracted a lot of attention of various researchers worldwide. Thermoelectric effect is difficult to maintain for longer period of time because of its continuous and consistent dependence on temperature difference across its surfaces. Early experiments indicated possibility of heat leakages within the module itself, which could have been causing drop in temperature difference along with working efficiency. The objective of this experimentation is to identify possibility of heat leakages and its possible effects (if any) on its efficiency. Two different positions were used, for the first one heat input surface was upside (hot side up) and second with heat input from below (Hot side down). This change in position will affect the convective motion of trapped air molecules and effect (if any) could be noticed. Results showed that heat transfer rate was more for hot side down with 0.22% more voltage output, 0.44% more power output, and 0.521% increment in Seebeck coefficient.

**Keywords** Waste heat recovery · Thermoelectric generator module · Internal heat losses · Heat flux · Temperature difference

A. Khanchi (✉) · H. Sandhu · M. K. Singh · S. S. Sehgal
Department of Chemical Engineering, Chandigarh University, Gharuan, Mohali, India
e-mail: abhishek110793@gmail.com

B. Bajaj
Department of Applied Physics, Delhi Technological University, New Delhi, India

**Nomenclature**

| | |
|---|---|
| CPVC | Chlorinated polyvinyl chloride |
| dt | Temperature difference |
| $I$ | Output current of TEG |
| PVC | Polyvinyl chloride |
| $R$ | Internal resistance of TEG |
| TEG | Thermoelectric generator |
| $T_C$ | Temperature cold side of TEG |
| $T_H$ | Temperature hot side of TEG |
| $V_{OC}$ | Open circuit voltage |
| $Z$ | Figure of merit |

# 1 Introduction

For twenty-first century and beyond, 'Sustainability' is that term which is fabricating our present and will shape our coming future. Every process, machine and activity that is performed either needs heat as raw form of energy or emits heat as waste. In most of the cases, waste heat released is low-grade and cannot be harnessed with conventional means leading to its disposal in atmosphere. So, to increase the efficiency of the device along with making it more sustainable, it is important to harness it. This is where thermoelectric devices can play a very significant role in harnessing of low-grade waste. They are highly compact, slim solid-state device which converts heat flux directly into DC output. Its only prime requirement for proper functioning which is also its biggest drawback is the continuous requirement of temperature difference across its surfaces. So, to maintain it consistently requires a cooling system to remove heat. Early experiments without cooling system showed almost instantaneous drop in temperature difference indicating heat leakages from hot side and not internal heat generation. This experimental study is focused to identify bottlenecks which are reducing final output efficiencies.

Thermoelectric generators are being constantly and consistently being studied by researchers worldwide for efficient low-grade waste heat recovery employing various designs and setups. Ding et al. [1] fabricated a power unit comprised of 60 TEG units to harness waste heat from a domestic water heater run by natural gas. Remeli et al. [2] created a conceptual model to harness waste heat of TEG too along with waste heat from primary source. For this, he used Finns for addition and removal of heat, which are placed inside of a heat pipe with TEG sandwiched in between Finns. Theoretically, the system showed capacity to generate 10.39 watts of energy with 1.345 kW of primary waste heat. Liu et al. [3] fashioned a power generating unit to harness the low-grade heat from geothermal energy which was comprised of 600 units of TEG and was capable of generating 1 kW.

Experiments were also performed with different modules commercially available, to find out power generation to cost ratios. Next, Singh et al. [4] designed TEG power generation unit to harness low-grade heat from solar ponds. Organic Rankine Cycle usually cannot harness energy efficiently with low-temperature difference of 40–600 °C. So, instead TEGs were employed to harness this energy from upper convective zone and lower convective zones of solar pond. Singh et al. [5] performed an experimental investigation to validate the efficiency of TEGs working in a salinity gradient solar pond against the organic rankine cycle engine. Experimentation results indicated towards very positive prospects for such a system.

Shu et al. [6] theoretically analyzed efficiency of Organic Rankine Cycle combined with TEG power unit. This system was supposed to harness waste heat of IC engine using R123 refrigerant. Parameters like max temperature, temperature of condensation, internal heat exchanger efficiency, etc. Tan et al. [7] created a conceptual model for utilizing sun rays as a source of heat and cooling was done with the help of PCM. It was enhanced by further utilizing thermosiphon for extraction of waste heat. Mathematically, this system was capable of maintaining temperature difference of 1500 °C for a longer period of time.

The primary focus of this work is to indicate flaws with the present system and if possible to finding a viable solution too. Usually for a TEG final efficiency is result of type of material, working temperature, no of P-N junctions and various other parameters. But, it's possible that gaps between P-N cells and heat leakages through it could also be affecting final proficiency of the device and could these heat leakages also be affecting power output of the device as well. This study will try to answer some of these questions.

## 2    Experimental Setup

For this experiment, heat addition and removal from the TEG module were performed with the help of heat exchangers and regular tap water was employed as working fluid. Figure 1 shows photographic view of the setup. Fabrication of heat exchangers was done with the help of quarter inch diameter copper pipes placed in PVC and CPVC pipes as shown in Fig. 2. Further, a 42-gauge copper sheet was used to enclose heat exchanger pipe for providing uniform surface for heat addition and removal from TEG module. Thermal paste was used for efficient heat transfer. For hot water, CPVC pipes were employed and as for cold water, PVC pipes were used. Reason for their selection is inherent properties of their fabrication material to minimize heat loss during transmission to and from fluid reservoir. Temperatures reading were taken down with the help of K-type thermocouple of Model: 50338 manufactured by Cooper Atkins. Its response time is 1 s and accuracy of ±0.20 °C with temperature range of 00–4800 °C.

**Fig. 1** Photographic view of experimental setup
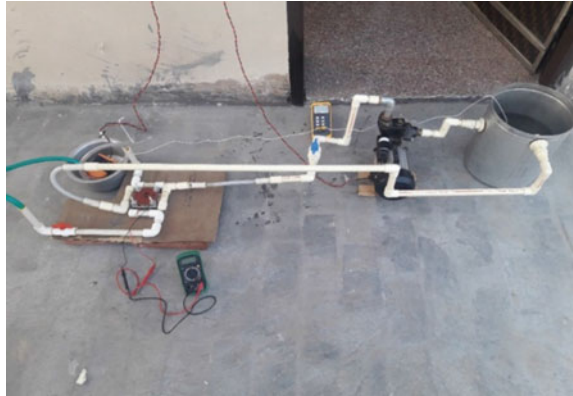


**Fig. 2** Heat exchanger with hot side up
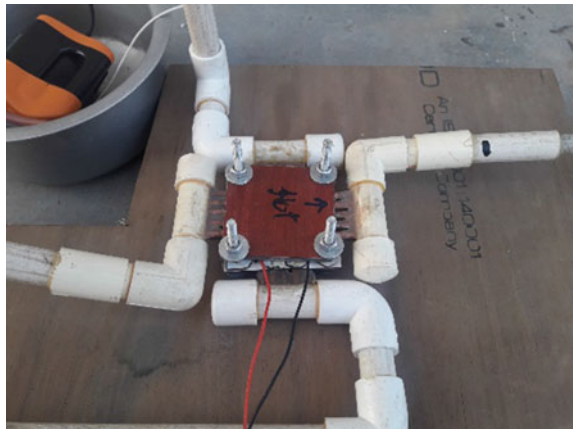


## 3 Experimental Results

Primary objective for this experimental investigation was to look for science backed evidence for heat leakages in a TEG and its ill effect on power output in terms of voltage and current. Quantitative aspect of TEG was evaluated using the following mathematical correlations:

$$\text{Seebeck Coefficient} = (V_{\text{OC}}/\text{dt}) \tag{1}$$

$$\text{Conversion Unit}, M = \left\{ 1 + \left[ \left( \frac{Z}{2} \right) * (T_{\text{H}} - T_{\text{C}}) \right] \right\}^{(1/2)} \tag{2}$$

$$\text{Power Output}, P = \left( I^2 * R \right) \tag{3}$$

where

$V_{OC}$  Open Circuit Voltage, (in Volts)
dt    Temperature Difference, (in degree Celsius)
Z     Figure of Merit, value calculated to be = 2119 K$^{-1}$,
$T_H$   Temperature of hot side of TEG,
$T_C$   Temperature of cold side of TEG,
I     Output current of TEG, (in Amps)
R     Internal resistance of TEG, (in ohms).

## 3.1 Rate of Heat Transfer

In this context, rate of heat transfer is seen as the rise in temperature of cold working fluid, which in this case is cold water at 180 °C. Graphs show that for setup with down position, rate of heat transfer is very uniform and more as compared to the second setup with up position of TEG which followed a non-uniform, abrupt transfer of energy at certain points almost in the form of pulses. Figures 3 and 4 show the graph for hot water temperature versus rise in temperature of cold water.
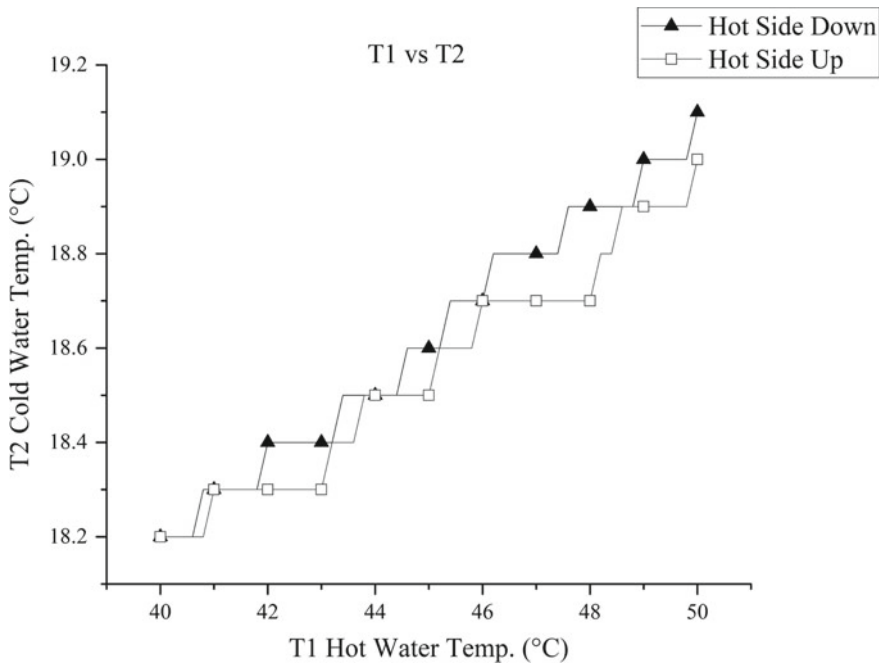


**Fig. 3** Hot water temperature ($T_1$) versus cold water temperature ($T_2$)
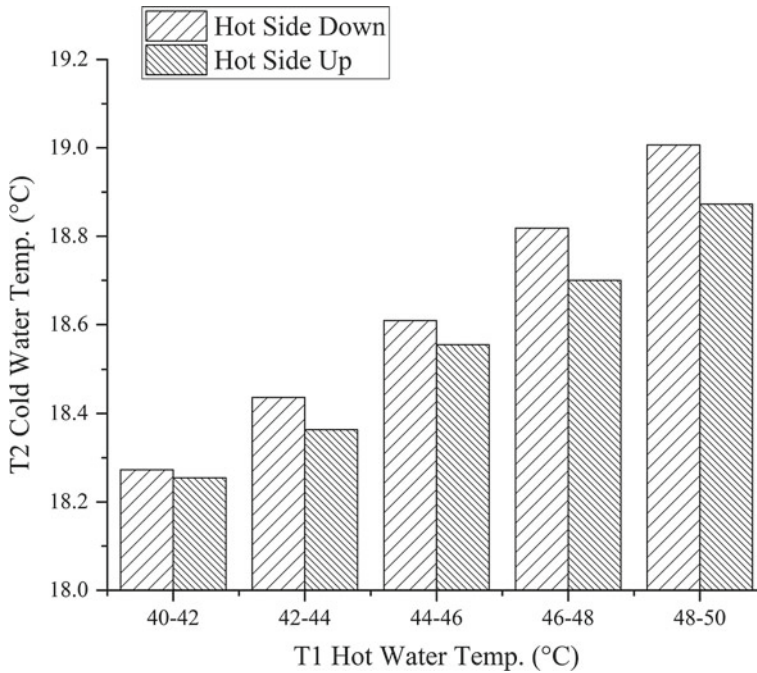
**Fig. 4** Hot water temperature versus cold water temperature

## 3.2 Seebeck Effect

Seebeck coefficient provides us with the quantitative aspect for voltage magnitude of TEG when there's a maintained temperature difference across its surfaces. It is directly proportional to voltage magnitude of TEG and this relation is shown in Fig. 5. Throughout the complete length of experiment, Seebeck coefficient was maximum for setup with hot side down and with quite high margin too indicating its advantage over another setup.

## 3.3 Effect of Heat Leakages on Power and Voltage Output

Mathematically and even practically the power, voltage output for a TEG are directly proportional to the temperature difference maintained across its surfaces. So, more the temperature difference more will be the magnitude of voltage and power output of TEG. But, the results indicate a slight variation. Throughout the experiment, temperature difference for down setup was lower than the up position,
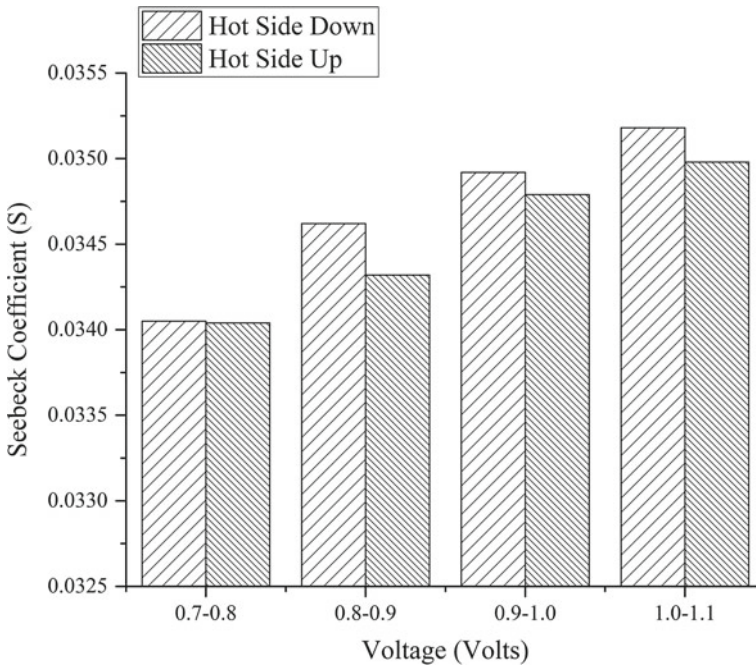
**Fig. 5** Voltage output versus Seebeck coefficient

but the voltage and power output of down position turned out to be more than the up position. Figure 6 depicts temperature difference versus voltage and Fig. 7 depicts temperature difference versus power output for TEG.

Reason: For Down position, trapped air molecules get heated up from bottom surface, then rise up and transfer it to the other one providing uniform heat transfer rate. But, in case of up position heated molecules are unable to transfer heat to another side until all of them are at same level of energy and while being there they heat up upper conductor layer connecting P-N cell of module. This over-heating leads to reduction in power output of TEG.

From all of the above results obtained from this experimental investigation, it is evident that practical results are quite the opposite of the theory regarding TEG. Analysis of the results shows that when used in down position a TEG gives 0.22% more voltage, 0.44% more power output, and 0.521% increment in Seebeck coefficient. This increment may be insignificant for a single unit, but for a power generation unit comprised of 600 unit which was fabricated by Liu et al. [3] the final effect would be extremely significant. Analysis shows that for power generation unit with 600 TEG in down position a 132% increment in voltage and 264%
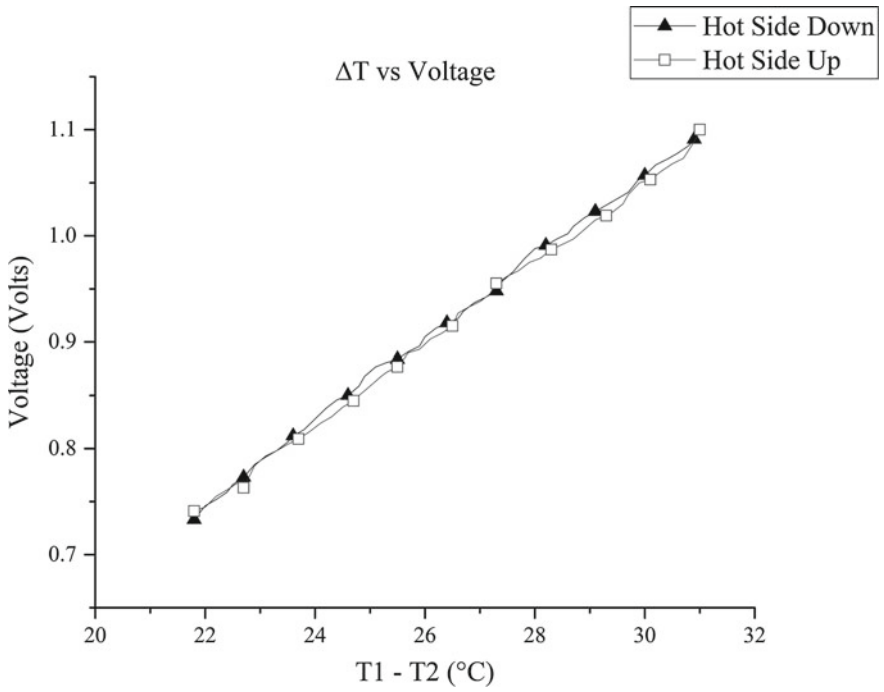
**Fig. 6** Temperature difference versus voltage
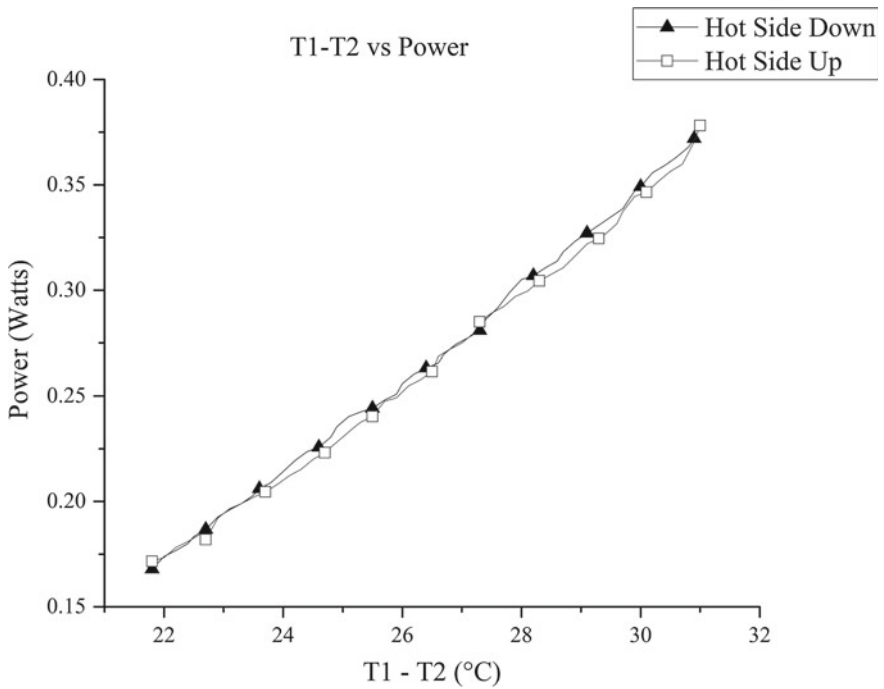


**Fig. 7** Temperature difference versus power

increment in power output can be obtained. Moreover, P-N cells of TEG are physically soldered to the conducting plates and over-heating which is caused in up position could lead to faster degradation of TEG while functioning too. So, down position will not only increase power output but will also ensure better work life of the device.

## 4 Conclusions

Hypothesis, on which this experimental study was performed, turned out to be positive in terms of flaw identification and its inquisition. The following conclusion can be drawn from this study:

1. Heat leakages do occur from hot side of TEG and are instantaneous. Heat transfer rate turned out to be more for down position of TEG.
2. Trapped air molecules act as carriers of heat within the module. Change in position causes a change in direction of convection currents and hence change in heat transfer rate.
3. Power output of TEG does get affected by heat leakages. But, overall primary effect cannot be calculated because of the absence of TEG module without heat leakage effect. Moreover, internal heat generation was neglected as voltmeter was the only connected load.
4. For the setup with hot side down heat transfer rate was more with 0.22% more voltage generation, 0.44% more power output and 0.521% better magnitude of Seebeck coefficient.

## References

1. Ding LC, Meyerheinrich N, Tan L (2017) Thermoelectric power generation from waste heat of natural gas water heater. Energy Procedia 1:1032–1037
2. Remeli MF, Tan L, Date A (2015) Simultaneous power generation and heat recovery using a heat pipe assisted thermoelectric generator system. Energy Convers Manage. https://doi.org/10.1016/j.enconman.2014.12.001
3. Liu C, Chen P, Li K (2014) A 1 kW thermoelectric generator for low-temperature geothermal resources. In: Thirty-ninth workshop on geothermal reservoir engineering, Stanford University, Stanford, California, 24–26 February 2014 SGP-TR-202
4. Singh B, Remeli F, Oberoi A (2014) Electrical power generation from low grade heat of salinity gradient solar pond using thermoelectric generators. In: Proceedings of the 52nd annual conference, Australian Solar Energy Society (Australian Solar Council), Melbourne. ISBN: 948-0-646-92219-5
5. Singh B, Varthani J, Remeli MF (2013) Experimental investigation of power generation from salinity gradient solar pond using thermoelectric generators for renewable energy application. Appl Mech Mater 393:809–814

6.  Shu G, Zhao J, Tian H (2012) Parametric and exergetic analysis of waste heat recovery system based on thermoelectric generator and organic Rankine cycle utilizing R123. Energy. https://doi.org/10.1016/j.energy.2012.07.010
7.  Tan L, Singh R, Date A (2011) Thermal performance of two-phase closed thermosyphon in application of concentrated thermoelectric power generator using phase change material thermal storage. Front Heat Pipes. https://doi.org/10.5098/fhp. v2.4.3001

# Performance Evaluation of Thermoelectric Refrigerator Based on Natural and Forced Mode of Cooling Processes

**Jatin Batra, Vishal Dabra, Pardeep Sharma and Vijay Saini**

**Abstract** The aim of this work is to evaluate the performance of portable thermoelectric refrigerator for vehicles (cars, trucks and buses). Thermoelectric refrigerator is based on the principle of a Peltier effect. TES-12704 thermoelectric module has been used in fabrication and tested. The cooling temperature of fin attached with thermoelectric module inside the refrigerator is measured and compared in natural and forced mode. The thermoelectric refrigerator is advantageous to keep perishable items at low temperature during travelling of the people. The results show that forced mode of producing cooling effect inside the thermoelectric refrigerator gave better performance as compared to natural mode-based thermoelectric refrigerator.

**Keywords** Cooling · Module · Thermoelectric · Temperature · Refrigerator

## 1 Introduction

Refrigeration is a process of producing sustainable surrounding conditions (temperature and humidity) for perishable foodstuff [1, 2]. During the twentieth century, refrigerator is one of the leading industries all around the world. But due to technology development, new refrigeration methods and techniques have been developed and eliminated the drawbacks of older technologies. Presently, three kinds of refrigeration systems are widely used in various domestic and industrial activities. They are vapour compression refrigeration system (VCR), vapour absorption refrigeration system (VAR) and thermoelectric refrigeration system (TER) [3]. Bansal and Martin [3] investigated the performance of VCR, VAR and TER systems. Out of these three refrigeration systems, VAR and TER systems are eco-friendly, i.e. never damage the ozone layer. The working of VAR and TER systems is noise-free as compared to VCR system. Entezam et al. [4] compared the

J. Batra · V. Dabra (✉) · P. Sharma · V. Saini
Mechanical Engineering Department, PIET, Samalkha, India
e-mail: vishaldabra.mech@piet.co.in

317

TER and VCR systems and concluded that TER and VCR systems give similar performance outputs if running cost is not a concern for the systems. TER has many advantages over VCR, but COP of the TER system is less as compared to VCR system [5, 6]. TER system has many advantages such as compact in size, less noise or vibrations, no refrigerant and less maintenance. TER system requires DC supply to run the system which could be provided by photovoltaic cells [7, 8]. These days, thermoelectric cooling systems are used in thermoelectric refrigeration, electronic cooling, automobile cooing, thermoelectric air-conditioning, photovoltaic–thermo-electric hybrid systems, freshwater production and many more. From design point of view, cooling power and COP are calculated to predict the feasibility of the system [7]. Martinez et al. [9] suggested that 32% electricity consumption is reduced and COP is increased 64%. Portable thermoelectric vaccine refrigeration system is designed for 0.083 L capacity and observed that 3.4 °C temperature is achieved when ambient temperature is 21 °C with 1 h 10 min of system operation [10]. Jani et al. [11] studied the solid desiccant vapour compression hybrid air-conditioning system and found 61.7% reduction in process air humidity ratio at the outlet of desiccant wheel. Jani et al. [12] suggested that psychometric properties like humidity ratio, dry-bulb temperature, wet-bulb temperature, relative humidity and specific heat at each state point of the system must be calculated and observed that performance of the system is significantly affected by the variations in ambient temperature and humidity ratio.

In this paper, a new approach is proposed to optimize the cooling inside the refrigeration box. Natural mode and forced mode of cooling are incorporated to enhance the performance of the thermoelectric refrigerator. In this approach, the inside conditions of the refrigeration box under with or without fan arrangement have been tested and analysed.

## 2   Description of Experimental Set-up

Figure 1 shows the design of the prototype of thermoelectric-based refrigeration system working on DC voltage. A box of MS sheet of dimensions 0.36 m 0.28 m × 0.24 m has been fabricated, and thermal insulation of a polyurethane sheet is provided on the wall of the box to prevent the heat flow from the inside of the box to the outside. Refrigeration set-up consists of six numbers of thermo-electric modules to maintain the temperature of the box below its surroundings. A DC power supply device is used to supply DC voltage to the TEM. The red wire of the thermoelectric model is connected with positive, and black wire of the module is connected to negative power supply. Due to this method of wire con-nection, the one surface of the thermoelectric module became cold and the other became hot. The amount of heat absorbed at the cold side is transferred to the hot side of the thermoelectric module.

**Fig. 1** Photograph of the experimental set-up

**Table 1** Detail specification of thermoelectric module

| Product | TES-12704 |
|---|---|
| Operational voltage | 12 V DC |
| Current max | 4 A |
| Voltage max | 15.4 V |
| Amax. @ delta $T = 0$ | 33.4 W |
| Delta $T$ max | 68 °C |
| P-N junction | 127 |
| Material | $Al_2O_3$ |
| Max temperature | 138 °C |
| Dimensions | $30 \times 30 \times 3.5$ mm |

Cold side of the thermoelectric module is placed on the fin inside the box, and hot side of the modules is fixed outside the box. Hot side of the module is connected with heat sink fan arrangement to dissipate more and more heat from system. The detail specification of the TEM is presented in Table 1.

Figure 2a shows a schematic diagram of a thermoelectric cooling module. It is made up of p-type thermoelement and an n-type thermoelement. Thermoelements are connected electrically in series and thermally in parallel. For p-type thermoelement, the heat due to the Peltier effect flows in the direction of electric current, but the heat flows in the opposite direction of electric current for an n-type thermoelement. The heat flow from the cold side to the hot side is defined to be positive. $T_c$ and $T_h$ are the cold side and hot side temperature of the thermocouple, respectively. Figure 2b shows the cross-sectional view of thermoelectric module in the experimental set-up, and Fig. 3 shows the isometric and top view of the refrigeration box.
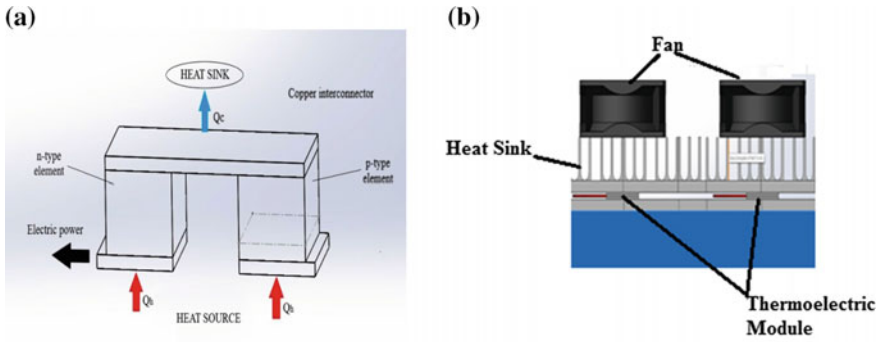
**Fig. 2** Schematic diagram of **a** thermoelectric cooling module and **b** cross-sectional view
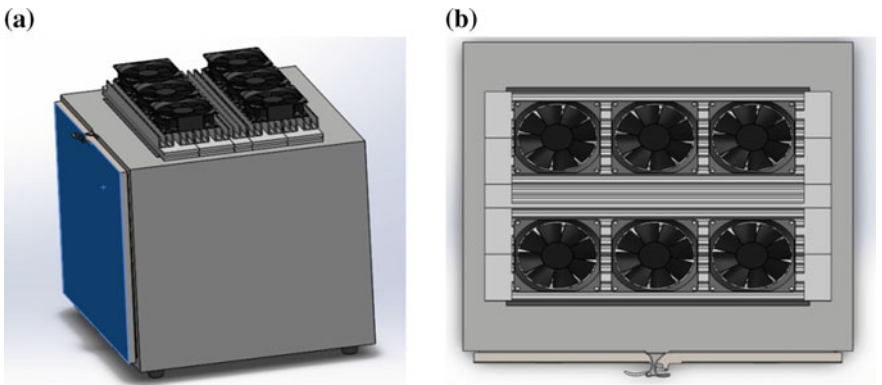


**Fig. 3** Schematic diagram of experimental set-up **a** isometric view and **b** top view

## 3  Methodology of Experimental Analysis

The objective of the thermoelectric refrigerator study is to investigate the effect of natural and forced mode of cooling process. Inner temperature of the refrigeration box is adopted as performance parameter [13]. For evaluating the cooling performance of the refrigerator, effect of mode of circulation inside the refrigeration box and heat taken place on the hot side of the thermoelectric module are observed.

## 4   Measuring Instruments

RTD PT100 thermocouples are used to measure the temperatures of refrigeration box and ambient temperature. The thermocouples are connected with a digital temperature indicator that gives the temperature with a resolution of 0.1 °C. Infrared thermometer of resolution of 0.1 °C is used to measure the heat-sink temperature.

## 5   Results and Discussion

The experiments are carried out at Panipat Institute of Engineering and Technology, Samalkha, India. The experimental data have been recorded at an interval of 10 min. In this research work, effect of mode of circulation inside the refrigeration box is observed and shown in the following two cases.

### 5.1   Case 1. Natural Mode of Cooling with Thermoelectric Module

See Figs. 4 and 5.

### 5.2   Case 2. Forced Mode of Cooling with Thermoelectric Module

Figure 4 shows the variation of refrigeration box temperature with time. In this case, the thermoelectric modules are placed on the top of the box, and cooling effect

**Fig. 4** Variation of refrigeration box temperature under natural mode condition
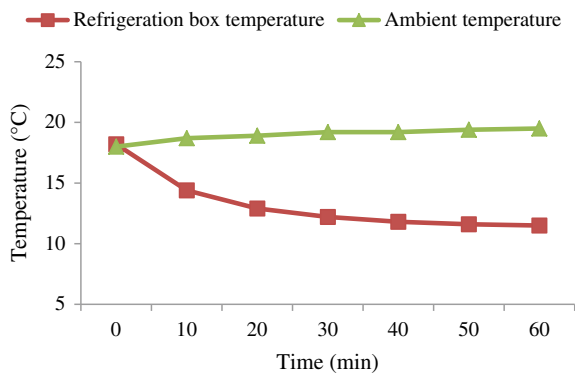
**Fig. 5** Variation of heat-sink temperature under natural mode condition
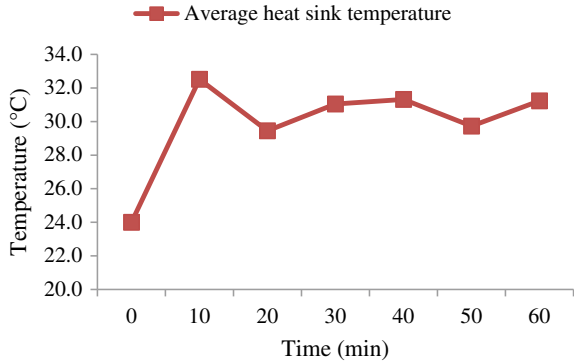


**Fig. 6** Variation of refrigeration box temperature under forced mode condition
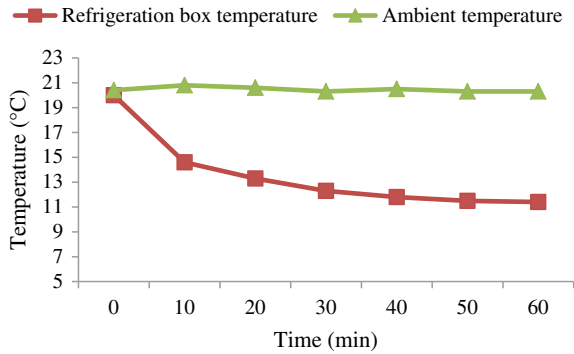
is analysed under natural circulation mode condition. Results found that temperature of the refrigeration box decreases from 18.2 to 11.5 °C after 60 min of interval of time when the ambient temperature varies from 18 to 19.5 °C during the experimental observation.

Figure 6 shows the variation of refrigeration box temperature with time. In this case, the thermoelectric modules are placed on the top of the box, and cooling effect is analysed under forced circulation mode condition. Results found that temperature of the refrigeration box decreases from 20 to 11.4 °C after 60 min of interval of time when the ambient temperature varies from 20.3 to 20.8 °C during the experimental observation.

Figures 5 and 7 show the variation of average heat-sink temperature with time in natural and forced mode conditions, respectively. This indicates that the continuous heat dissipates from the hot side of the thermoelectric module to the ambient and indicates the same amount of heat is absorbed at the cold side. Due to the mechanism of heat transfer, cooling effect takes place inside the refrigeration box.

**Fig. 7** Variation of heat-sink temperature under forced mode condition
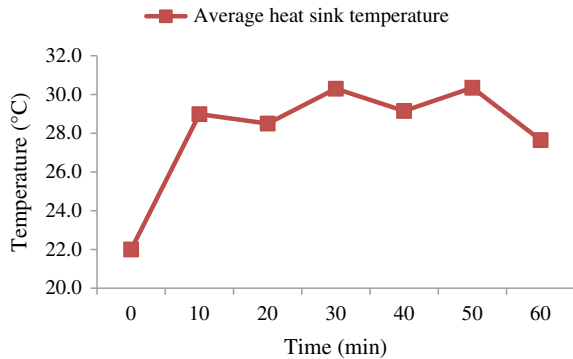


## 6 Conclusion

In this research work, a portable thermoelectric refrigerator was fabricated and tested for the cooling purpose. The thermoelectric refrigerator is based on the principle of a Peltier effect, and to perform this research work, the TES-12704 (thermoelectric module) is used. Thermoelectric module having the cooling temperature of fins inside the refrigerator is measured and compared in natural and forced mode. The refrigerator is advantageous to keep perishable items at low temperature during travelling of the people. The results found that the temperature of the refrigeration box decreases by 6.7 °C in case of natural mode and 8.6 °C in case of forced mode of cooling. The result concludes that forced mode of producing cooling effect inside the refrigerator provides better performance as compared to natural mode-based thermoelectric refrigerator.

## References

1. Riffat SB, Omer SA, Ma X (2001) A novel thermoelectric refrigeration system employing heat pipes and a phase change material: an experimental investigation. Renew Energy 23:313–323. https://doi.org/10.1016/S0960-1481(00)00170-1
2. Cengel Y, Ghajar A (2015) Heat and mass transfer: fundamentals and applications, 5th edn. McGraw-Hill Education, New York
3. Bansal PK, Martin A (2000) Comparative study of vapour compression, thermoelectric and absorption refrigerators. Int J Energy Res 24:93–107. https://doi.org/10.1002/(SICI)1099-114X(200002)24:2
4. Entezam B, Gwilliam S, Tatton S (1992) Comparison of thermoelectric and direct expansion cooling systems. Jetway Systems, pp 485–490

5. Astrain D, Martinez A, Rodriguez A (2012) Improvement of a thermoelectric and vapour compression hybrid refrigerator. Appl Therm Eng 39:140–150. https://doi.org/10.1016/j.applthermaleng.2012.01.054

6. Chen L, Meng F, Sun F (2012) Effect of heat transfer on the performance of thermoelectric generator-driven thermoelectric refrigerator system. Cryogenics 52(2012):58–65. https://doi.org/10.1016/j.cryogenics.2011.10.007

7. Zhao D, Tan G (2014) A review of thermoelectric cooling: materials, modeling and applications. Appl Therm Eng 66:15–24. https://doi.org/10.1016/j.applthermaleng.2014.01.074

8. Zhao D, Tan G (2014) Experimental evaluation of a prototype thermoelectric system integrated with PCM (phase change material) for space cooling. Energy 68:658–666. https://doi.org/10.1016/j.energy.2014.01.090

9. Martinez A, Astrain D, Rodriguez A, Perez G (2013) Reduction in the electric power consumption of a thermoelectric refrigerator by experimental optimization of the temperature controller. J Electron Mater 42:1499–1503. https://doi.org/10.1007/s11664-012-2298-9

10. Ohara B, Sitar R, Soares J, Novisoff P, Nunez-Perez A, Lee A (2015) Optimization strategies for a portable thermoelectric vaccine refrigeration system in developing communities. J Electron Mater 44:1614–1626. https://doi.org/10.1007/s11664-014-3491-9

11. Jani DB, Mishra M, Sahoo PK (2016) Experimental investigation on solid desiccant—vapor compression hybrid air-conditioning system in hot and humid weather. Appl Therm Eng 104:556–564

12. Jani DB, Mishra M, Sahoo PK (2016) Performance analysis of hybrid solid desiccant—vapor compression air-conditioning system in hot and humid weather of India. Buil Serv Eng Res Technol 37:523–538

13. Chen WH, Liao CY, Wang CC, Hung CI (2015) Evaluation of power generation from thermoelectric cooler at normal and low temperature cooling conditions. Energy Sustain Dev 25:8–15. https://doi.org/10.1016/j.esd.2014.12.004

# Pool Boiling Using Nanofluids: A Review

**Sumit Krishn, Mukund Goyal, Gopal Nandan, Satish Kumar, P. Kumar and Anoop Kumar Shukla**

**Abstract** Nanofluids have found their applications in various fields of heat transfer and their demand in various industries in ever growing. Pool boiling of nanofluids has always been a topic of great interest and research. In past years, a lot of experimental works have been done on various nanofluids and base fluid solutions to study about the influence of nanofluids on critical heat flux and heat transfer coefficient. Through these works, various factors such as surface roughness, wettability, contact angle, and particle deposition have also been studied as how these factors influence CHF. This paper also focuses on the past work and studies done on nanofluid pool boiling comprising of the very existing data.

**Keywords** Nanofluids · Pool boiling · Critical heat flux

## 1 Introduction

The cooling requirement is ever increasing due to industrial technologies from smaller-level computer chips to macro-level. In convection heat transfer, there is a limitation of hear transfer in convectional fluids such as air, water, ethylene glycol, and oil due to low thermal conductivity. The thermal conductivity of liquid–solid suspensions (nanofluids) is increased, and heat transfer is increased in convective cooling applications. Nanofluids are colloidal solutions of suspended nanoparticles in different base fluids. The name nanofluids got its name from the order of the size of the particles used to make the nanofluid, i.e., nanometers ($10^{-9}$ m). It is quite difficult to visualize such small sizes. The base fluids used in its preparation can be

S. Krishn · M. Goyal · G. Nandan (✉) · A. K. Shukla
ASET, Amity University, Noida, Uttar Pradesh, India
e-mail: gnandan@amity.edu

S. Kumar
ME Department, Thapar University, Patiala, Punjab, India

P. Kumar
NIT Jamshedpur, Jamshedpur, Jharkhand, India

water, ethylene glycol, kerosene, etc. A very high heat flux is required in many engineering applications like nuclear reactors, boilers, evaporators, recent electronics equipment, etc. The boiling heat transfer is a function of heater surface geometry, heater size, and concentration of nanoparticles, surfactants, and pressure [1–3].

Pool Boiling is a heating process in which the heater surface is completely submerged in the fluid. Researchers' community considered the possibility of further enhancement in boiling heat transfer in nanofluids. The experimental study helps in understanding the heat transfer characteristics better. The results help tackle the increasing demand of cooling applications of miniaturised high heat flux components such as LASER diagnostics, and most importantly superfast computing, etc. by utilizing higher heat flux and increase of thermal conductivity than air-based cooling systems. Still, there are problems such as sedimentation, clogging, erosion, fouling, and increase of pressure drop which occur in mostly in macro-particle suspended fluids. The varied heat transfer characteristics of nanofluids are utilized in many fields like air conditioning systems, superfast electronic devices or computers, lubricants and coolants in automobiles, aero crafts, etc. Thus, it can be said that nanofluids have great future aspects and applications. In this study, main focus is to systematically present the experimental observation of pool boiling of metallic nanofluids like $Al_2O_3$, $CuO$, $SiO_2$, and $ZnO$ with base fluids like water, ethanol, etc. Pool boiling depends on nanoparticle concentration, heater surface characteristics, size and type of heater, thermal properties of nanoparticles and base fluids, etc.

## 2 Experimental Studies on Pool Boiling Heat Transfer on Various Nanofluids

Most of the work of pool boiling is based on experimental study using various nanofluids, type of heater, and different concentration of nanofluids in the base fluids. This section covers observation of various researchers.

### 2.1 $Al_2O_3$

$Al_2O_3$ has been experimented with base fluids like water, ethanol, and carbon methyl cellulose by the researchers. It is also called emery and is one the most commonly used compounds in the preparation of nanofluids. The works done in pool boiling experiment using this nanoparticle as nanofluid are given below.

### 2.1.1 With Water as Base Fluids

Bang and Chang [4] used horizontal flat surface heater having roughness of a few tens nanometer for experimentation. They found poor heat transfer performance as compare to water with increasing concentrations of the nanoparticles. The range of the concentrations was taken to be 0.5–4% by volume. But they found an increase in the critical heat flux (CHF) of 32% with horizontal section and 13% increase in the vertical section of the heating surface. The heat transfer coefficient (HTC) to be deteriorated due to the sedimentation of the nanoparticles creating a layer over the heating surface and increase in the CHF of maximum of 47% at the volumetric concentration of the nanoparticles of 0.1% [5]. When it is used in conjunction with $TiO_2$/water, the maximum decrease in HTC was noted to be 50% at 0.0003–0.01% by volume [6]. But, a change was noted with increase in the HTC at higher concentrations of nanoparticles. The HTC is increased by $\sim$40% at 1.25% concentration by weight [7]. The nanoparticle size was kept between 10 and 50 nm for the experiment but accumulation resulted in bigger size of the particles. Despite the accumulation, the increase in HTC was found which indicated that the effects of sedimentation were over powered by other parameters [7]. Fang et al. reported a maximum increase in the HTC of about 200% using an $\alpha$-$Al_2O_3$/water nanofluid under the volumetric concentration range of 0.001–0.1% with similar trends as seen previously [6]. With pure water as base fluid, it was observed that the CHF was low, at about 540 kW/m$^2$. By adding small amount of $Al_2O_3$ (0.001 g/L), an increase in CHF up to 670 kW/m$^2$ (24% increase) was recorded. By increasing the concentration of nanoparticle ten times (0.01 g/L), there was a large change found in CHF which increased to 1460 kW/m$^2$ (170.3% increase). The graph depicts the same increase at different concentrations [8]. The effect of nanofluids is depicted in the figure given below which clearly shows the boiling regimes of pure water and nanofluids. At low heat flux (i.e., 500 kW/m$^2$), both are in the nucleate boiling regime. But, at higher heat flux (i.e., 1000 kW/m$^2$) the wire submerged in pure water has surpassed the CHF and a stable layer of bubble is engulfing the wire. This makes heat transfer possible only through radiation through the vapor layer over the surface. This hinders the heat transfer and makes the wire hot and glow red. Whereas, the nanofluid is still very much in the nucleate boiling regime and thus enabling heat transfer through conduction and convection. This is how nanofluids increase the heat transfer characteristics and its rate [9]. The use of nanofluids in heat transfer enhancement has been reported by several authors in different areas [10–16].

### 2.1.2 With Other Base Fluids

There was no notable change in the heat transfer characteristics using $Al_2O_3$ nanoparticle with the ethanol as base fluid [17]. The HTC is enhanced with the increase in concentration of the nanoparticle by using the alumina nanoparticle with

**Table 1** Pool boiling using alumina-based nanofluids

| Ref. no. | Nanofluid | Base fluid | Shape of heater | Increase in CHF/HTC |
|---|---|---|---|---|
| [4] | $Al_2O_3$ | Water | Horizontal flat Vertical flat (Ti-plate) | CHF enhanced to $\sim$32% enhanced to $\sim$13% enhanced to $\sim$64% |
| [6] | $\alpha$-$Al_2O_3$ | Water | – | HTC enhancement 200% in 0.001–0.1 vol.% |
| [19] | $Al_2O_3$ | Water | Stainless steel wire | HTC increases up to 68% |
| [6] | $Al_2O_3$ | Water | – | HTC deterioration 50% (0.0003–0.01 vol.%) |
| [20] | $Al_2O_3$ | Ethanol | Cu and CuO plates | No change in HTC |
| [21] | $Al_2O_3$ | Water | Ni–Cr wire | CHF increases 17.3% (0.01 g/L) 32.6% (0.1 g/L) 56.27% (1 g/L) |
| [22] | $\gamma$-$Al_2O_3$ | Water | – | 56% HTC enhancement (0.03 wt%) |
| [7] | $Al_2O_3$ | Water | Particle size was taken 10–50 nm | $\sim$40% increase in HTC in 1.25% by weight |
| [18] | $\gamma$-$Al_2O_3$ | Carbon methyl cellulose | – | HTC enhanced 25% in 1.4% weight concentration |

carbon methyl cellulose (CMC) as the base fluid. At 1.4% concentration by weight, the increase was noted to be 25% more than that of CMC [18]. Results of Alumina-based nanofluids are summarized in Table 1.

## 2.2 SiO₂

### 2.2.1 With Water as Base Fluids

The study was done by Kim et al. using a wire heater and at atmospheric pressure. A stainless steel wire of grade 316 and diameter of 0.381 mm was used. It was found that the CHF was increased remarkably. This generally occurred for concentration of the nanoparticles less than 0.1% by volume. During the experiments, the nanoparticles concentrated on the heater surface and formed a porous layer on it. As a result of which the contact angle between the nanofluid and the heated surface got reduced which enhanced the surface wettability. The HTC was also reduced during the experiments [23]. Truong used a stainless steel wire as the heater for

**Table 2** Boiling of silicon dioxide nanofluids

| Ref. no. | Base fluid | Heater type | Effect on CHF or/and HTC |
|---|---|---|---|
| [26] | Water | Cylindrical vessel $\phi = 10$ cm | HTC decreased |
| [26] | Ethylene glycol | Cylindrical vessel $\phi = 10$ cm | HTC decreased |
| [26] | Water | Ni–Cr wire, $\phi = 0.4$ mm | CHF increased |
| [2] | Water | Stainless steel wire | HTC increased up to 68% |
| [2] | Water | Ni–Cr wire, $\phi = 0.32$ mm | HTC decreased |
| [23] | Water | SS wire, $\phi = 0.381$ mm and $L = 12$ mm | CHF increased up to 80% |
| [27] | Water | Ni–Cr wire $\phi 0.2$ mm | CHF increased |
| [27] | Alcohol | – | CHF increased and HTC decreased |
| [28] | Water | Ni–Cr wire | CHF increased up to 270% (max) |

$SiO_2$ nanofluids and found that the HTC significantly increased up to 68%. He further showed that the increase in HTC was affected by the rate at which deposition of the particles took place [19]. A reduction in the CHF and boiling heat flux (BHF) was observed when the area of the surface of the heater is increased. But, as the nanoparticles got concentrated on the test wire there was an increment in the BHF because of great heat transfer. It was found that the CHF increased up to 270% [24]. The results are summarized in Table 2.

### 2.2.2 With Other Nanofluids

Similar results were observed with various studies on the use of other fluids as base fluids like alcohol, ethylene glycol, etc. Liu and Liao did experimental work on $SiO_2$/alcohol-based nanofluid with surface wetting agent. Major finding of their work was that HTC reduced whereas the CHF enhanced. One reason that they cited for reduction in HTC was operative nucleate cavities which reduced during the experimentation process. As a result of concentration of nanoparticles on the surface, the resistance to heat was enhanced. The contact angle got reduced because of the above reason which ultimately led to the improvement of the CHF [25]. Witharana used $SiO_2$/ethylene glycol to find a deterioration in HTC as compared to the no use of nanofluid [26].

## 2.3  $Fe_3O_4$

### 2.3.1  With Water as Base Fluids

The nanofluid made with nanoparticle $Fe_3O_4$ and water as base fluid is known as magnetite water nanofluid (MWNF). This is usually made with the two-step method of nanofluid preparation by suspending the oxide nanoparticle in pure water. Lee et al. used Ni–Cr wire for experimentation firstly with the use of pure water and then with $Fe_3O_4$ nanofluid. For one ppm, increase in CHF was 140–170% relative to water. The experiment was carried out over the pressure range of 101 kPa (atmospheric) to 1100 kPa (absolute). Also, the bubble frequency was found to be two times that of pure water with lesser contact angle at all tested pressure range [29]. The effect of magnetic field has been experimentally studied 0.1% volume concentration using distilled water as base fluids. It was found that boiling heat transfer coefficient increased about 43%. The presence of positive magnetic field decreased the boiling heat transfer. While results were opposite in case of negative magnetic field [30].

Lee et al. described the experiment using MWNF (distilled water) using a Ni–Cr wire and found the CHF enhanced approximately 160–240% of pure water as nanoparticle concentration increased. At lower concentrations of about 1–3 ppm, the CHF enhancement was around 160–190%; however, at higher concentrations up to 100 ppm the enhancement in CHF was seen to be reaching about 240% than pure water [31]. Thus, it can be easily seen that with increase in the concentration of nanoparticles the increase in CHF increases gradually but consistently.

### 2.3.2  With Ethylene Glycol–Water

Sheikhbahai et al. investigated pool boiling experiment with $Fe_3O_4$/ethylene glycol–water at atmospheric pressure on a horizontal thin Ni–Cr wire. The base fluid was kept 50% by volume of each EG and water. The particle concentration of the nanofluid in the experiment was optimum at 0.1% by volume which yielded a maximum enhancement in CHF up to 100%. The experiment was carried out under the influence of electric fields by two different electrodes, and the particles were studied using a scanning electron microscope. The study indicates enhancement due to electric field [32]. Although there is lack of studies of pool boiling in electric field.

Yu et al. used kerosene-based nanofluid grafted with oleic acid on the surface by chemical absorption method. The sizes of the nanoparticles were kept to be 15 nm, but they noticed particles formed clusters of diameter nearly 155 nm. The experiment was carried out through a temperature range of 283–333 K which showed a result as enhancement in thermal conductivity of nearly 34% at a concentration level of 0.1% by volume [33]. Refer Table 3 for results of ferric oxide.

**Table 3** Ferric oxide ($Fe_3O_4$)

| Ref. no. | Base fluid | Shape of heater | Increase in CHF or/and HTC | Other parameters |
|---|---|---|---|---|
| [30] | Water | Ni Wire | Increases BHTC more than 43% | Roughness 10% |
| [32] | Ethylene glycol-water | Ni Cr Wire | Maximum CHF enhancement of 100% | 0.1% (by volume) Atmospheric pressure |
| [34] | Water | – | Approximately 140–170% increase in CHF | At 1 ppm |
| [31] | Water | – | Up to 160–190% increase in CHF relative to distilled water As conc. increased the % increased up to 240% | Particle size range 1–100 nm |

## *2.4 CuO*

Hedge et al. [35] contemplated the qualities of the boiling heat transfer by utilizing nanoparticle with water as a base fluid. As shown in his result, as the concentration of particle increases from 0 to 0.2 vol.%, the CHF enhanced by 130%, and at concentrations more than 0.2 vol.%, the CHF was almost consistent. Liu et al. contemplated the qualities of the boiling heat transfer by utilizing water as base fluid [36]. As indicated by their result, as the concentration of nanoparticle increases CHF is also increases gradually and it became constant after 1% concentration of nanoparticle. Fifty percent enhancement in CHF was observed at atmospheric pressure, and 200% enhancement of CHF at 7.4 kPa was seen. Das et al. experimented that while taking Cu nanoparticles with base fluid water, there was a 2–4 times enhancement in the thermal conductivity when the temperature ranged from 21 to 52 °C [37].

Liu and Liao used water and alcohol as base fluids to study the boiling heat transfer coefficient [25]. They used a vertical copper bar of dimensions of diameter 80 mm and height 120 mm. The heat transfer coefficient deteriorated in their experiment. Kwark et al. used four nanofluids, i.e., $Al_2O_3$, CuO, diamond, and $TiO_2$, with base fluid being water for all the nanofluids to study the heat transfer coefficient [38]. He used a square copper plate for this experiment. The heat transfer coefficient was different in all the cases. Sundar et al. [23] studied that the dispersed nanoparticles with base fluid being the mixture with ethylene glycol and water in the ratio 50:50, respectively, show maximum enhancement of heat transfer coefficient at 24.56% (Table 4).

**Table 4** Experimental results of CuO nanofluids

| S. no | Nanofluid | Base fluid | Enhancement | Other parameter |
|---|---|---|---|---|
| [26, 39] | CuO | Water, HE-200 oil | 60% improvement | 5% volume CuO particles in water |
| [37] | CuO | Water | 2–4-fold increases | Range of 21–52 °C |
| [40] | CuO | Ethyl glycol | HTC increases | 1–4% concentration |
| [41] | CuO | R134a/oil | HTC increases | 1–4% concentration |
| [4] | CuO | Water | CHF increases: 50% at atmospheric pressure 200% at 7.4 kPa | CHF constant after 1% concentration |
| [25] | CuO, SiO$_2$ | Water, alcohol | HTC deteriorated | |
| [42] | Al$_2$O$_3$, CuO, Diamond, TiO$_2$ | Water | HTC is different in all the cases | Square cu plate |

## 2.5 ZnO

### 2.5.1 With Water

Hiswankar et al. worked on ZnO/water-based nanofluids [43]. The concentration of this mixture ranged from 0.01 volume percent to 0.0001 volume percent. For the heater surface, they used a Ni–Cr wire having a diameter of about 0.4 mm at atmospheric pressure. When their experimental work was complete, they got an increase in CHF of about 80%. They also noticed that on the heater surface a layer of nanoparticles was present and this very same thing was understood as the reason for the increase in CHF. Sharma et al. [27] conducted study with ZnO/water-based nanofluids. They used a quartz vessel which was cylindrical in shape. Inside it, he placed a grade-316 stainless steel plate heater. This complete unit was used as the test setup unit. Through this work, he found that there was a 70% increase in the CHF. The reason cited by the authors for such results was the increase in the wettability of the surface due to the accumulation of nanoparticles on the surface. Kumar et al. conducted a study with pool boiling setup and used water as a base fluid at atmospheric pressure with electrically heated Ni–Cr wire. He found 70–80% enhancement in CHF [44].

### 2.5.2 With Ethylene

Kole and Dey had performed an experimental study with ZnO particle and ethylene glycol as a base with a cylindrical stainless heater [45]. Their experimental result showed that the HTC increased 22% at 0.16% volume concentration of nanoparticle

**Table 5** Zinc oxide results

| Ref. no | Base fluid | Heater type | Enhancement | Other parameter |
|---|---|---|---|---|
| [43] | Water | Ni–Cr wire [$\phi$0.4 mm] | CHF increases up to 80% (max) | 0.01 vol.% to 0.0001 vol.% |
| [44] | Water | Ni–Cr wire | CHF increases 70% | Atmospheric pressure |
| [27] | Ethylene glycol | Stainless steel | HTC increased up to 22% | Volume fraction 0.016 |
| [27] | Ethylene glycol | Stainless steel | CHF increases to 117% | Volume fraction 2.6 |

in nanofluid. In the same study, CHF is increased 117% at 2.6% volume concentration. Roughness of the surface of the wire was the reason for such results (Table 5).

## 2.6 TiO$_2$

Kim et al. conducted study on a pool boiling apparatus with TiO$_2$-water-based nanofluid and observed that CHF has increased at different volumetric concentration of nanofluid [8]. But they postulated that the CHF was not increased due to the effect of nanofluid, but it increased due to the deposition of nanoparticle on heater surface. However, they also conducted an experiment with pure water with nanoparticles deposited heater. They concluded that the enhancement is not less than the bare heater surface. With the increase in heat flux superheat temperature (difference between surface temperature and bulk temperature), heat transfer coefficient also increases, but their increase is nonlinear [46]. The boiling pressure has a considerable effect on a bubble size. It decreases with increases in concentration of nanofluid. It occurs because of decline in heat transfer of refrigerant with increases in concentration. Moreover, heat flux also has a high influence on a rate of bubble formation [46, 47] (Table 6).

**Table 6** Results of TiO$_2$

| Ref. no | Base fluid | Heater type | Enhancement | Result |
|---|---|---|---|---|
| [47] | Refrigerant R141b and ethyl alcohol | Cylindrical brass heater | Boiling temperature decreases as particle concentration increases | Boiling heat transfer coefficient on the cylindrical brass surface and the boiling bubble characteristics are considered |
| [46] | Water | Disc shape copper heater | HTC of TiO$_2$ is higher than base fluid | Disc copper plate Sub-cooling is studied |
| [8] | Water | Auxiliary heater | CHF increases | Increases due to deposition on heater surface |

# 3 Conclusion

Boiling heat transfer characteristics of different nanofluids (different nanoparticles and base fluid combinations) were studied using various parameters like volume concentration, size of nanoparticle, shape and orientation of heating surface, etc. Nanofluids show different performance and phenomena compared to pure water in terms of natural convection and nucleate boiling. In the case of alumina nanofluid, the HTC and CHF invariably increase with the increase in concentrations of the nanoparticle in pool boiling experiments with some exception when the sedimentation of nanoparticles hinders proper heat transfer by forming a layer over the heating surface and thus deteriorating the heat transfer properties. The type of nanofluid along with their concentration had a great effect on the CHF. Various studies depicted that concentration of nanoparticles improved the wettability and the roughness of the surface. In the process of improving CHF, these factors had a significant impact.

# References

1. Vassallo P, Kumar R, D'Amico S (2004) Int J Heat Mass Transf 47(2):407. https://doi.org/10.1016/s0017-9310(03)00361-2
2. Taylor RA, Phelan PE (2009) Int J Heat Mass Transf 52(23–24):5339. https://doi.org/10.1016/j.ijheatmasstransfer.2009.06.040
3. Kim H (2011) Nanoscale Res Lett 6(1):415. https://doi.org/10.1186/1556-276x-6-415
4. Bang IC, Chang SH (2005) Int J Heat Mass Transf 48(12):2407. https://doi.org/10.1016/j.ijheatmasstransfer.2004.12.047
5. Shahmoradi Z, Etesami N, Esfahany MN (2013) Int Commun Heat Mass Transf 47:113. https://doi.org/10.1016/j.icheatmasstransfer.2013.06.006
6. Fang X, Wang R, Chen W, Zhang H, Ma C (2015) Appl Therm Eng 91:1003. https://doi.org/10.1016/j.applthermaleng.2015.08.100
7. Wen D, Ding Y (2005) J Nanopart Res 7(2–3):265. https://doi.org/10.1007/s11051-005-3478-9
8. Sapre G, Kumarappa S (2017) Int J Innovative Res Sci Eng Technol 6(3):3489
9. Kim S, Bang I, Buongiorno J, Hu L (2007) Int J Heat Mass Transf 50(19–20):4105. https://doi.org/10.1016/j.ijheatmasstransfer.2007.02.002
10. Sekhar TVR, Nandan G, Prakash R, Muthuraman M (2018) Mater Today Proc 5(2):4563. https://doi.org/10.1016/j.matpr.2017.12.026
11. Sekhar TVR, Nandan G, Prakash R, Muthuraman M (2018) Mater Today Proc 5(2):6176. https://doi.org/10.1016/j.matpr.2017.12.224
12. Vadhera J, Sura A, Nandan G, Dwivedi G (2018) Mater Today Proc 5(2):3411. https://doi.org/10.1016/j.matpr.2017.11.586
13. Sekhar TVR, Prakash R, Nandan G, Muthuraman M (2017) Prog Ind Ecol Int J 11(3):227. https://doi.org/10.1504/pie.2017.091296
14. Sekhar TVR, Prakash R, Nandan G, Muthuraman M (2018) Micro Nano Lett 13(2):248. https://doi.org/10.1049/mnl.2017.0410
15. Sekhar TVR, Prakash R, Nandan G, Muthuraman M (2018) Pressure drop characteristics & efficiency enhancement by using $TiO_2$-$H_2O$ nanofluid in a sustainable solar thermal energy collector. Int J Environ Sustain Dev 17(2/3):273. https://doi.org/10.1504/IJESD.2018.094039

16. Lalpurwala G, Jani DB (2017) Int J Res Mech Eng 2(2):25
17. Coursey JS, Kim J (2008) Int J Heat Fluid Flow 29(6):1577. https://doi.org/10.1016/j.ijheatfluidflow.2008.07.004
18. Soltani S, Etemad SG, Thibault J (2010) Int Commun Heat Mass Transf 37(1):29. https://doi.org/10.1016/j.icheatmasstransfer.2009.08.005
19. Truong BH (2007) Determination of pool boiling critical heat flux enhancement in nanofluids, undergraduate thesis. Master's thesis, MIT
20. You SM, Kim JH, Kim KH (2003) Appl Phys Lett 83(16):3374. https://doi.org/10.1063/1.1619206
21. Sunil LJ, Kumarappa S, Hegde RK (2016) Int Res J Eng Technol 3(1):674
22. Fang X, Chen Y, Zhang H, Chen W, Dong A, Wang R (2016) Renew Sustain Energy Rev 62:924. https://doi.org/10.1016/j.rser.2016.05.047
23. Kim SJ, Bang IC, Buongiorno J, Hu LW (2007) Bull Pol Acad Sci Tech Sci 55(2):211
24. Vazquez DM, Kumar R (2013) Int Commun Heat Mass Transf 41:1. https://doi.org/10.1016/j.icheatmasstransfer.2012.11.008
25. Liu Z, Liao L (2008) Int J Heat Mass Transf 51(9–10):2593. https://doi.org/10.1016/j.ijheatmasstransfer.2006.11.050
26. Wang XQ, Mujumdar AS (2007) Int J Therm Sci 46(1):1. https://doi.org/10.1016/j.ijthermalsci.2006.06.010
27. Ciloglu D, Bolukbasi A (2015) Appl Therm Eng 84:45. https://doi.org/10.1016/j.applthermaleng.2015.03.063
28. Kumar R, Vazquez DM (2010) In: International conference in heat transfer and fluid mechanics and thermodynamics (2010)
29. Ahn HS, Kim MH (2012) J Heat Transf 134(2):024001. https://doi.org/10.1115/1.4005065
30. Abdollahi A, Salimpour MR, Etesami N (2017) Appl Therm Eng 111:1101. https://doi.org/10.1016/j.applthermaleng.2016.10.019
31. Lee JH, Lee T, Jeong YH (2012) Int J Heat Mass Transf 55(9–10):2656. https://doi.org/10.1016/j.ijheatmasstransfer.2011.12.027
32. Sheikhbahai M, Esfahany MN, Etesami N (2012) Int J Therm Sci 62:149. https://doi.org/10.1016/j.ijthermalsci.2011.10.004
33. Yu W, Xie H, Chen L, Li Y (2010) Colloids Surf A 355(1–3):109. https://doi.org/10.1016/j.colsurfa.2009.11.044
34. Lee JH, Lee T, Jeong YH (2013) Int J Heat Mass Transf 61:432. https://doi.org/10.1016/j.ijheatmasstransfer.2013.02.018
35. Ham J, Kim H, Shin Y, Cho H (2017) Int J Therm Sci 114:86. https://doi.org/10.1016/j.ijthermalsci.2016.12.009
36. Liu Z, Xiong J, Bao R (2007) Int J Multiph Flow 33(12):1284. https://doi.org/10.1016/j.ijmultiphaseflow.2007.06.009
37. Wang XQ, Mujumdar AS (2008) Braz J Chem Eng 25(44):631
38. Chopkar M, Das AK, Manna I, Das PK (2007) Heat Mass Transf 44(8):999. https://doi.org/10.1007/s00231-007-0345-5
39. Trisaksri V, Wongwises S (2009) Int J Heat Mass Transf 52(5–6):1582. https://doi.org/10.1016/j.ijheatmasstransfer.2008.07.041
40. Wang XQ, Mujumdar AS (2008) Braz J Chem Eng 25(4):613
41. Peng H, Ding G, Hu H, Jiang W, Zhuang D, Wang K (2010) Int J Refrig 33(2):347. https://doi.org/10.1016/j.ijrefrig.2009.11.007
42. Kwark SM, Kumar R, Moreno G, Yoo J, You SM (2010) Int J Heat Mass Transf 53(5–6):972. https://doi.org/10.1016/j.ijheatmasstransfer.2009.11.018
43. Hiswankar SC, Kshirsagar JM (2016) Int J Eng Res Technol 2(7):2091
44. Kumar M, Bhutani V, Khatak P (2015) J Mech Eng Sci 9:1538. https://doi.org/10.15282/jmes.9.2015.2.0150

45. Kole M, Dey T (2012) Int J Therm Sci 62:61. https://doi.org/10.1016/j.ijthermalsci.2012.02.002
46. Salari E, Peyghambarzadeh SM, Sarafraz MM, Hormozi F (2015) Periodica Polytech Chem Eng. https://doi.org/10.3311/ppch.8262
47. Naphon P, Thongjing C (2014) Int Commun Heat Mass Transf 52:84. https://doi.org/10.1016/j.icheatmasstransfer.2014.01.014

# CFD Modelling and Experimental Investigation of Bimodal Slurry Flow in Horizontal Pipeline and Bends

**Kanwar Pal Singh, Arvind Kumar and Deo Raj Kaushal**

**Abstract** The effect of flow velocity in straight pipelines with horizontal bends having a pipe diameter 53 mm was experimentally investigated over silica sand and fly ash comprised bimodal slurry. Silica sand and fly ash at 80:20 ratios with solid concentration 8.82% by volume were taken for extensive experiments at flow velocity up to 3.56 m/s. Concentration samples are collected from mid-vertical plane at different cross sections in the downstream side of slurry pipe bend. The effect of the presence of fine particles in narrow sized coarse silica slurry through a 90° horizontal bend has been investigated. It is also observed that with increase in flow velocity, the pressure drop decreases. Uniform distribution of solid particles is observed just at the downstream flow of the bend except at bend outlet in case of higher flow velocity. CFD modelling is done using Eulerian two-phase model with realizable standard k–epsilon approach in ANSYS FLUENT 15 software. The predicted results for pressure drop and concentration distribution using CFD modelling have fairly correct resemblance with experimental data collected from pilot plant test loop.

**Keywords** CFD modelling · Eulerian model · Bimodal slurry · Fine particles · Flow velocity · Pressure drop

K. P. Singh (✉)
Department of Mechanical Engineering, BRCMCET Bahal, Bahal, India
e-mail: kanwarpal7@gmail.com

A. Kumar
Department of Mechanical Engineering, YMCAUST Faridabad, Faridabad, India

D. R. Kaushal
Department of Civil Engineering, IIT Delhi, New Delhi, India

# 1   Introduction

The pipelines designed for long-distance transportation of slurry are dependent on various flow parameters like critical deposition velocity, static settling concentration and pressure drop along pipeline and bends. The other major design factor, i.e. operational stability and corrosion-erosion parameters are also influenced by these flow parameters. Hydraulic conveying of solid particles through pipeline is regularly utilized as a part of industries because of its few inalienable points of interest, for example, persistent conveyance, adaptable directing, ease in mechanization and long separation transport capacity. Pipeline bends cause relatively higher pressure drop compared to the straight pipelines and leads to excessive erosion. The flow in bends for hydraulic conveying of solids particles is much more complicated than pneumatic conveying of solid particles [1]. The vast majority of the trial and computational results identified with the impact of bends in slurry pipeline framework identified with the disintegration, fixation profiles and pressure drops for the stream of solid particles [2]. It is already well established that in solid–liquid flow bends need frequent replacements because of excessive erosion and wear. In order to reduce the pressure drop through the pipe bends and to increase the life of pipe bends, complete information of the flow behaviour of the slurry along pipeline and pipe bends is very important [3–5]. Researcher experimentally investigates that bends with short radius have symmetrical flow of bimodal slurry along pipeline and for long radius bend the coarser particles migrate towards the outer wall whereas finer particles move towards inner wall [6]. The pressure loss for iron ore and zinc tailings slurries with various particles ranges with in a 90° horizontal bend. Researcher found that for iron ore and zinc tailings slurries flow the additional pressure loss is reduced due to presence of the finer particles for various particles range with in a 90° horizontal bend [7]. The addition of fine particles with a range 10–30% in coarser sized slurry leads to distribution of particles homogeneously and reduces the pressure drop along pipeline [8–11]. Researcher observed that the pressure drop in bimodal slurry decreases with increased ratio of fine particles [12]. CFD modelling using Eulerian model is applied for prediction of solid concentration distribution and pressure drop in FLUENT software, and this model shows fair similarity in the experimental and computational results [13, 14]. Researcher analysed various parameters using CFD modelling that affects the rheological and flow behaviour of slurry [15–18]. However, only limited research is available in literature for understanding the flow of bimodal slurries through pipeline and bends using Eulerian two-phase model in CFD modelling.

In this current paper, the flow of bimodal slurry with a mixture of silica sand and fly ash at 80:20 ratios with solid concentration 8.82% by volume is taken for experimental investigation for the measurements of pressure drop, concentration and particle size distribution along pipeline and pipe bends with flow velocity range keeping up to 3.56 m/s. CFD modelling is done in ANSYS 15 for measurement of solid distribution profiles along pipe cross section and drop in pressure along pipeline and horizontal bends for same slurry sample, and results are correlated with experimental outcomes.

## 2 Experimental Set-up

The entire experimental work was performed in fluid mechanics lab of IIT Delhi. The pilot plant test loop as shown in Fig. 1 is having horizontal pipe bends with 53 mm inside diameter with a length of 30 m. The loop set-up is explained by Kaushal et al. [2]. Concentration profiles were estimated by testing probes were inserted at various location along pipeline for observing solid concentration in the mid-vertical plane and distinctive statures from the base of pipeline as shown in Fig. 2. The sample collection process and bend geometry are explained by Kaushal et al. [2, 12].

## 3 Modelling Results

CFD modelling is done by choosing Eulerian two-phase Realizable $k$-$\varepsilon$ turbulence model in ANSYS 15 FLUENT software. A comparative analysis is done for predicted modelling outcomes, and experimental results for bimodal slurry flow at various flow velocities.
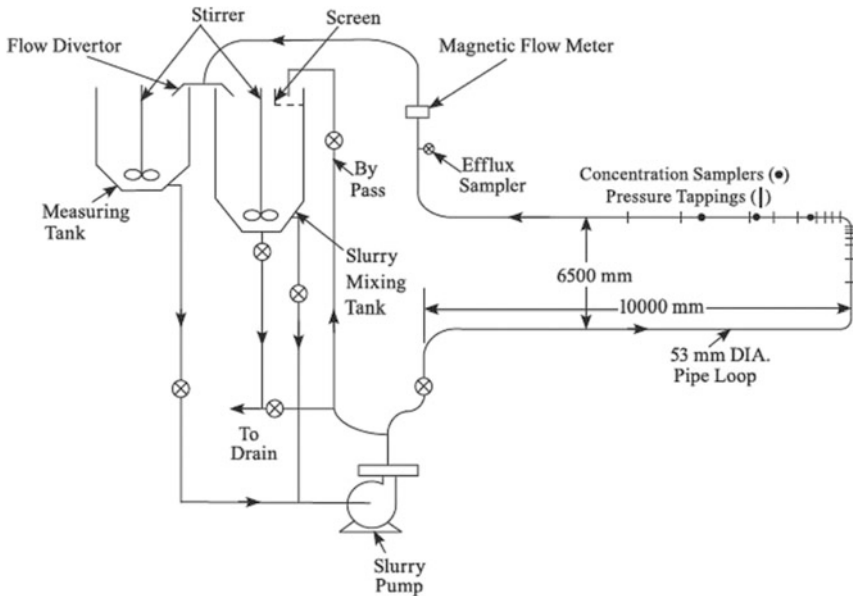


**Fig. 1** Pilot plant test loop set-up for slurry flow [2]
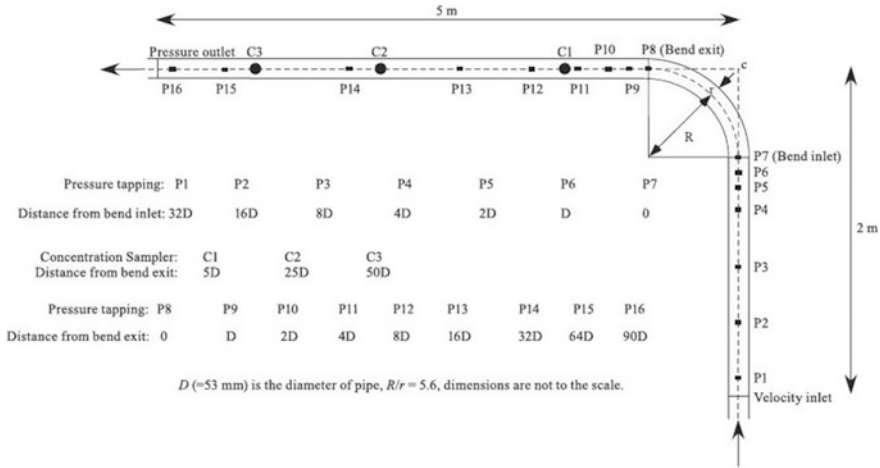
**Fig. 2** Sampling probes location and pressure tapping near to pipe bend [2]

## Pressure Drop

The predicted normalized pressure drops along pipeline are figure out for flow of bimodal slurry at solid concentration 8.82% by volume ($C_{vf}$) with 80:20 ratio of silica sand at flow velocity ($V_m$) up to 3.56 m/s. The flow pattern of the slurry is marginally bothered when it passes over the bend as shown in Fig. 3a–c. There is reduction in slop of pressure drop with slight increase in flow velocity. The mixing of finer particle of fly ash in coarser silica sand slurry uniformly scattered the solid particles along pipe cross section diminished the pressure drop.

## Concentration Distribution

Cross-sectional concentration is calculated by using FLUENT software in ANSYS 2015. The concentration distribution for silica sand and FA with ratio of 80:20 at solid concentration ($C_{vf}$) 8.82% and flow velocity ($V_m$) up to 3.56 m/s. Fly ash particles are constrained outwards alongside the silica sand particles as shown in Fig. 4a, b. The solid particles are forced to move outwards in the region of bend because of centrifugal force developed in bend and secondary flows generated by pressure. In the bend region, the effect of centrifugal force is balanced by outward increased pressure. Secondary flow appears near to the wall as the fluid velocity is very small, so the flow is driven by pressure.

From Figs. 5, 6 and 7, it clear that the predicted results for normalized concentration hold good resemblance with experimental results at $X = 5D$ from bend outlet. At velocity 3.56 m/s and $C_{vf} = 8.82\%$, the predicted concentration profile almost matches with experimental results.
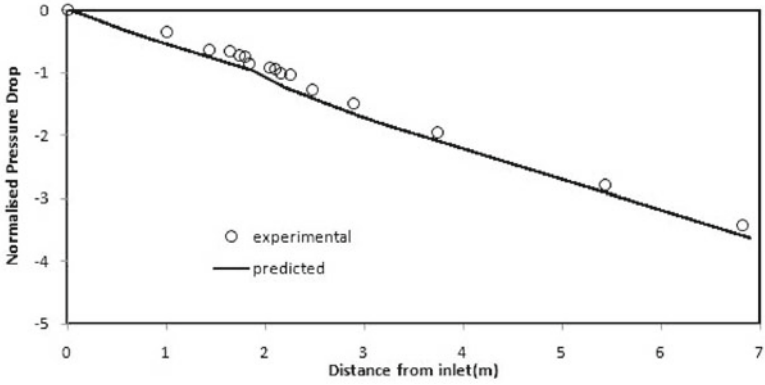
(a) $V_m=1.78 m/s$
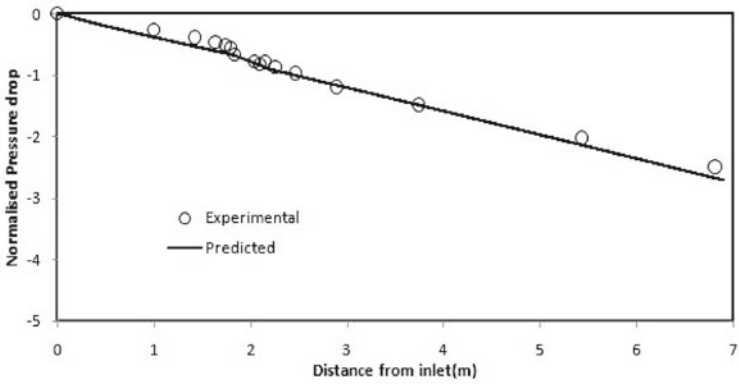


(b) $V_m=2.67$ m/s
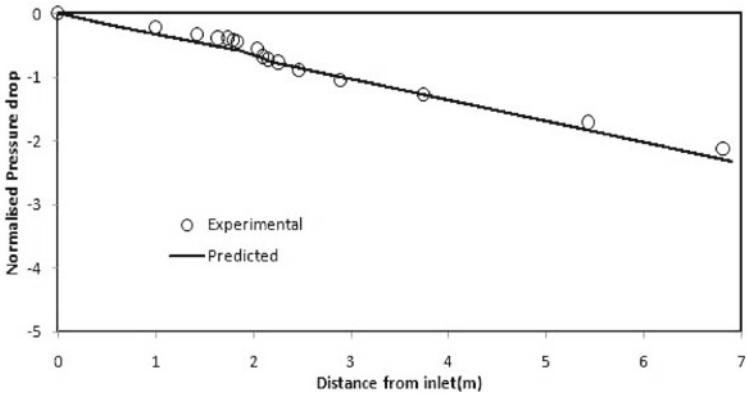


(c) $V_m=3.56$ m/s

**Fig. 3** Normalized pressure drop along pipeline at $C_{vf} = 8.82\%$ (sand: fly ash = 80:20) at various flow velocities
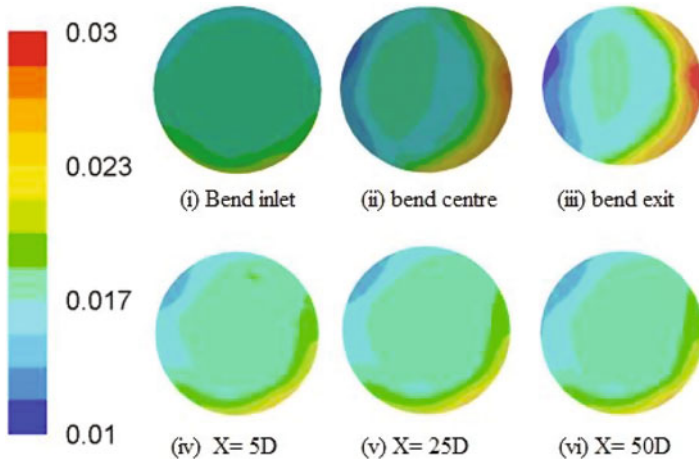
(a) Fractional concentration profile of FA at different location
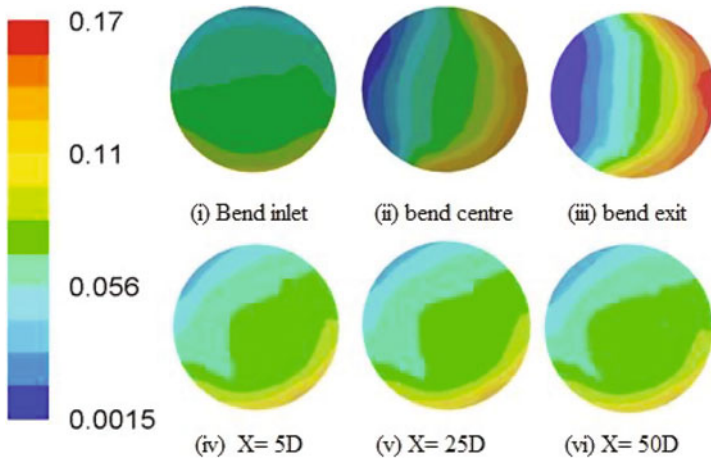


(b) Fractional concentration profile of Silica sand at different location

**Fig. 4** **a**, **b** Fractional cross-sectional concentration contour at various locations along pipeline for FA and silica sand for sand: fly ash = 80:20 at $V_m$ = 3.56 m/s and $C_{vf}$ = 8.82%
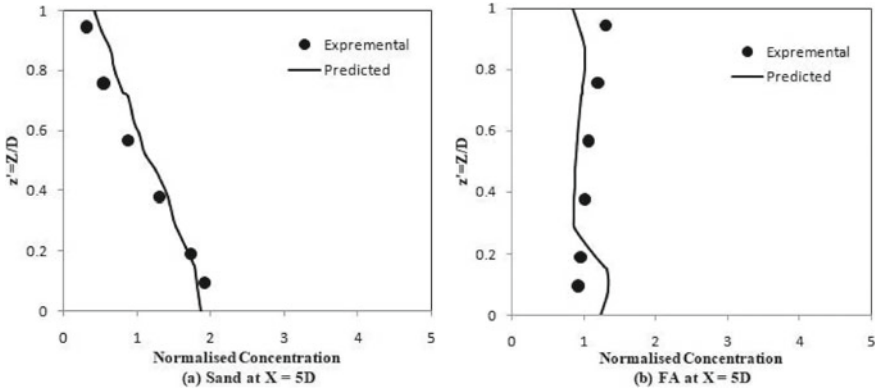
**Fig. 5** **a**, **b** Concentration distributions at $V_m = 1.78$ m/s
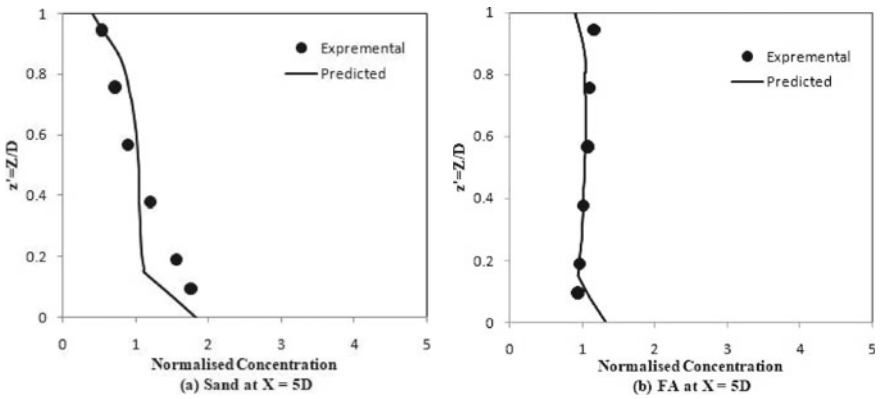


**Fig. 6** **a**, **b** Concentration distributions at $V_m = 2.67$ m/s
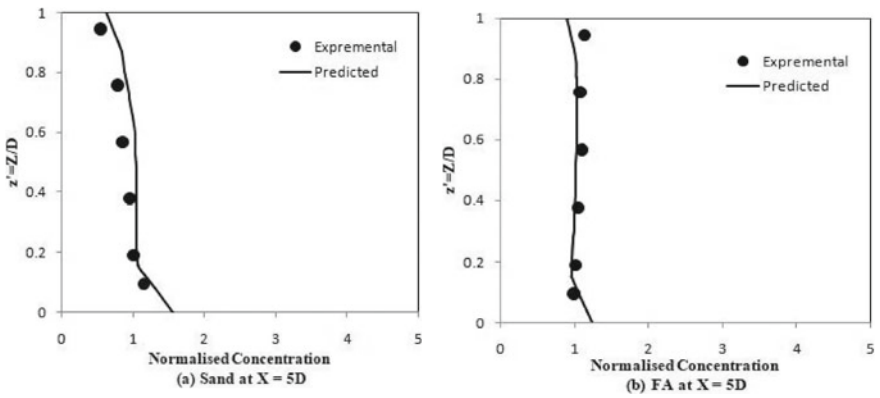


**Fig. 7** **a**, **b** Concentration distributions at $V_m = 3.56$ m/s

## 4 Conclusion

The following conclusions are made on the basis of the present study:

a. The predicted CFD modelling result for pressure drops and concentration holds reasonable exactness with the measured experimental results collected for the flow of bimodal slurry in the efflux concentration up to 8.82% for the flow velocity up to 3.56 m/s.
b. Secondary flow is observed in the pipe bend, and it causes movement of solid particles towards outer region of pipe bend and hence slightly disturbs the flow pattern of slurry in pipe bends.
c. The presence of fine particles of FA in the coarser silica sand slurry leads to uniform scattering of solid particles along pipe cross section and avoids sedimentation of coarser particles.
d. The predicted pressure drop reduces as the velocity of slurry flow increases from 1.78 to 3.56 m/s.
e. The effect of bend diminished up to $X = 5D$ downstream to the bend outlet. Solid particles are redistributed in the downstream of the bend.

## References

1. Kumar A (2010) Experimental and CFD modeling of hydraulic and pneumatic conveying through pipeline. Ph.D. thesis, Indian Institute of Technology Delhi
2. Kaushal DR, Kumar A, Tomita Y, Kuchii S, Tsukamoto H (2013) Flow of mono-dispersed particles through horizontal bend. Int J Multiphase Flow 52:71–91. http://dx.doi.org/10.1016/j.ijmultiphaseflow.2012.12.009
3. Singh KP, Singh S (2013) CFD modelling for slurry pipeline flow: a literature review. In: Proceeding of national conference on recent trends and innovation civil engineering, BRCM CET, Bahal, pp 146–150, 15–16 Nov 2013
4. Kumar N, Singh KP (2013) Numerical simulation of finer particles at higher concentration for pipeline flow. In: Proceeding of national conference on recent trends and innovation civil engineering, BRCM CET, Bahal, pp 140–145, 15–16 Nov 2013
5. Singh KP, Kumar A, Kaushal DR (2014) CFD modeling of slurry transportation in pipeline for concentration distribution using different models in national conference on recent advances in mechanical and civil engineering (RAMCE-2014), Ghaziabad, 4–5 Apr 2014
6. Nasr-El-Din H, Shook CA (1987) Effects of 90° bend on slurry velocity and concentration distribution. J Pipelines 6:239–252
7. Ahmed M, Singh SN, Seshadri V (1994) Pressure drop in a long radius 90° horizontal bend for the flow of multi-sized heterogeneous slurries. Int J Multiph Flow 21:329–334
8. Kazanskij BH, Hinsch J (1974) Influence of added fine particles on the flow structure and the pressure losses in sand-water mixture. In: Proceedings of hydrotransport. BHRA Fluid Engineering, Colorado, USA, vol 3, pp 11–21
9. Boothroyde J, Jacobs BEA, Jenkins P (1979) Coarse particle hydraulic transport. In: Proceedings hydrotransport. BHRA Fluid Engineering, Cranfield, Bedford, England, vol 6, pp 405–428

10. Hayashi H, Sampei T, Oda S, Ohtomo S (1980) Some experimental studies on iron concentrate slurry transportation in pilot plant. In: Proceedings of hydrotransport. BHRA Fluid Engineering, Cranfield, Bedford, England, vol 7, p D2

11. Verkerk CG (1982) Transport of fly ash slurries. In: Proceedings of hydrotransport. BHRA Fluid Engineering, Johannesburg, South Africa, vol 8, pp 307–316

12. Kaushal DR, Kumar A, Tomita Y, Kuchii S, Tsukamoto H (2016) Flow of bi-modal slurry through horizontal bend. Kona Powder Part J 34:258–274. https://doi.org/10.14356/kona.2017016

13. Kaushal DR, Thinglas T, Tomita Y, Kuchii S, Tsukamoto H (2012) CFD modeling for pipeline flow of fine particles at high concentration. Int J Multiphase Flow 43:85–100. http://dx.doi.org/10.1016/j.ijmultiphaseflow.2012.03.005

14. Gopaliya MK, Kaushal DR (2015) Analysis of effect of grain size on various parameters of slurry flow through pipeline using CFD. Part Sci Technol Int J 33:369–384. https://doi.org/10.1080/02726351.2014.971988

15. Gopaliya MK, Kaushal DR (2016) Modeling of sand-water slurry flow through horizontal pipe using CFD. J Hydrol Hydromech 64:261–272. https://doi.org/10.1515/johh-2016-0027

16. Singh KP, Kumar A, Assefa KM, Kaushal DR (2015) Experimental investigation on the rheological behavior of fly ash slurries without and with the addition of chemical agents IJERT. vol 4, pp 196–200. ISSN 2278-0181

17. Singh KP, Kumar A, Assefa KM, Kaushal DR (2016) Rheological analysis and CFD modelling of FA slurry at different particle size in straight pipeline using ANSYS. In: International conference on sustainable development through research in engineering and management (SDREM-16), YMCAUST, Faridabad, 26–27 Dec 2016

18. Singh KP, Kumar A, Assefa KM, Kaushal DR (2016) Experimental investigation of effects of chemical additives on the rheological properties of slurry in sustainable pipeline transportation. In: International conference cum workshop on "tools, techniques and practices for improving sustainable manufacturing", GLA University Polytechnic, 23–24 Jan 2016

# An Experimental Study On Solar Water Heater Integrated With Phase Change Material

**Pushpendra Kumar Singh Rathore**

**Abstract** This paper shows the experimental investigation of the thermal performance of solar water heater coupled with phase change material (PCM) cylinder. The cylinder contains PCM and spiral copper tubes and is properly insulated using glass wool on the outer surface. The PCM in the cylinder gets charged through hot water during the day, due to the availability of solar radiation. When there is no solar radiation (during the night or during cloudy weather), the PCM discharges and transfers its thermal energy to the cold water and hence raises its temperature. Therefore, this system ensures supply of hot water when there is no solar radiation, without using any conventional form of energy. The testing is done in the laboratory, and the thermal performance of the solar water heater integrated with PCM cylinder is determined. The thermal performance of the solar water heater at different flow rates, i.e., 0.017, 0.030, and 0.050 kg/s with PCM cylinder and without PCM cylinder was determined, and a comparative analysis is done over a period of time. It was found that heat storing capacity and thermal performance of the solar water heater will be enhanced if it is integrated with latent heat thermal energy storage PCM cylinder and hence ensures energy savings.

**Keywords** Solar · Water · Phase change material (PCM)

## 1 Introduction

The solar water heating system is one of the most popular systems of harnessing solar thermal energy and accounts for more than 94% of the energy provided by solar thermal system worldwide [1]. In the past few decades, solar water heating system has gained a rapid momentum as an environmentally friendly application which can directly reduce the fossil fuel-based energy usage and indirectly reduces the greenhouse gas emissions [2]. As per an estimate, in 2014, the final energy

P. K. S. Rathore (✉)
Department of Mechanical Engineering, GLA University, Mathura, India
e-mail: Pushpendra.rathore@gla.ac.in

savings amounted by using the solar water heating system is 36.1 million tons of oil equivalent, which corresponds to an annual $CO_2$ emissions reduction of 116.4 million tons. Indian subcontinent receives abundant solar energy throughout the year [3]; however, the biggest limitation of these systems is that the energy source is invariably time dependent which leads to the mismatch of demand and supply of hot water. This mismatch will lead to poor capacity utilization factor and low efficiency of the solar water heating system. This mismatch can effectively be minimized by using efficient thermal energy storage technique [4]. TES offers the best capability to store available heating and cooling energy in off-peak load condition to effectively match the on-peak demand period of solar water heater [5]. Broadly, thermal energy storage is classified into three categories as shown in Fig. 1. Latent heat thermal energy storage technique is more preferred than sensible and thermochemical storage because of various advantages: (1) It provides high-energy storage density, (2) it stores heat at constant temperature corresponding to the phase transition temperature of phase change material (PCM), and (3) it stores 5–14 times more energy per unit volume than sensible heat materials like water and rock.

Phase change material (PCM) is widely used for latent thermal energy storage because of the fact that they have the ability to store thermal energy, while undergoing a phase change, at room temperature. The main property which makes PCM more useful than other materials for thermal energy storage is that it stores heat energy in latent form, because of which it has a greater heat storage capacity per unit volume than other materials.

During the time when solar radiation is available, the PCM gets charged and stores thermal energy by changing its phase from solid to liquid. When there is no solar radiation during the night or at early morning, the PCM gets discharged and releases the stored thermal energy by again changing its phase from liquid to solid. This released thermal energy is then used to increase the temperature of water. This will increase the capacity utilization factor and will enhance the performance of the solar water heating system.
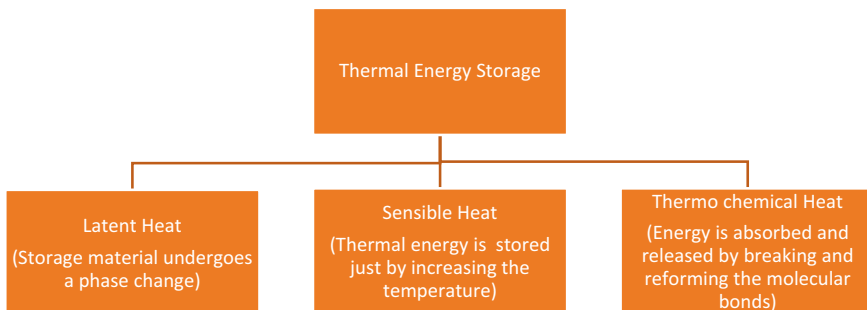


**Fig. 1** Classification of thermal energy storage [6]

The selection of PCM and the technique used to integrate the PCM in solar water heater are the critical factors and significantly affect the performance of solar water heater during the non-availability of solar radiation. In this work, a shell-and-tube PCM cylinder is developed and is then integrated with the solar water heater. A commercially available organic PCM HS29 is used in shell-and-tube cylinder to store thermal energy and then release it whenever it is required. The whole experimental setup is then tested under the natural condition for 24 h, to analyze the thermal performance of the PCM cylinder and of hot water at different flow rates.

## 2 Experimental Method

### 2.1 Material

PCM HS29 is an organic chemical-based PCM having nominal freezing and melting temperature of 29 °C. It stores thermal energy as latent heat in its crystalline form.

On changing phase, this latent heat is released or absorbed, allowing the ambient temperature within the system to be maintained. HS29 is constituted of the right mix of various additives allowing equilibrium between solid and liquid phases to be attained at the melting point. The thermophysical properties of the PCM are shown in Table 1. Differential scanning calorimetry (DSC) results were used to determine the thermal properties of the HS29 PCM. The DSC result of the HS29 PCM is shown in Fig. 2. The DSC results show that there are one endothermic and one exothermic peak for heating and cooling. The melting process starts at 28 °C and ends at 38 °C. Similarly, the cooling process starts at 27 °C and ends at 20 °C. The DSC curve also provides heat flow (mW) for each value of the temperature of the PCM. The heat flow started as soon as the melting and freezing of the PCM started. The rate of heat flow is maximum at the peak of melting cycle and at the peak of the freezing cycle.

**Table 1** Thermophysical properties of HS29 PCM

| Property | Value |
| --- | --- |
| Melting temperature (°C) | 29 |
| Latent heat (KJ/Kg) | 190 |
| Density at 35 °C (Kg/m$^3$) | 1530 |
| Density at 25 °C (Kg/m$^3$) | 1830 |
| Thermal conductivity at 35 °C (W/mK) | 0.382 |
| Thermal conductivity at 25 °C (W/mK) | 0.478 |
| Thermal stability (cycles) | $\sim 2000$ |
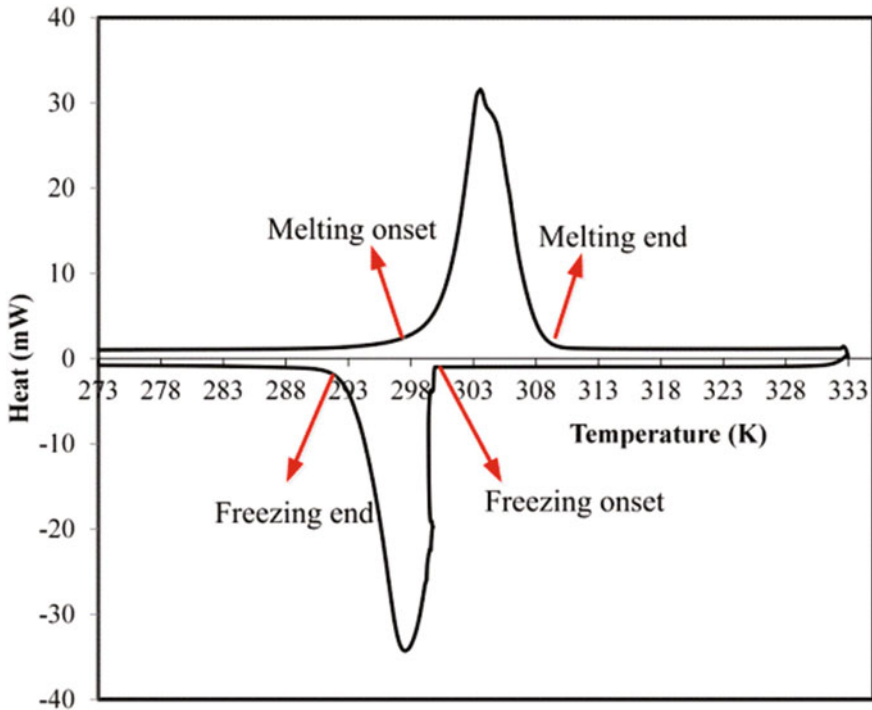
**Fig. 2** DSC result obtained for HS29 PCM [7]

## 2.2 Thermal Energy Storage Tank

Stainless steel cylinder of 10 kg PCM carrying capacity is used to contain the PCM. To charge and discharge (storage and extraction of heat) the PCM, spiral-type heat exchangers made of copper of appropriate dimensions are installed in the cylinder. Figure 3 shows the disassembled view of the PCM cylinder. The PCM and heat exchangers are meticulously arranged inside the S.S cylinders. In order to block heat loss from the PCM, the PCM cylinder is insulated with polyurethane (PUF) foam insulation having thermal conductivity of 0.033 W/mk. The detailed specification of the PCM cylinder is given in Table 2.

Water is the heat-transferring fluid (HTF) in the system. While hot water gives heat to the PCM during charging, the cold water absorbed heat from the same PCM during discharging.
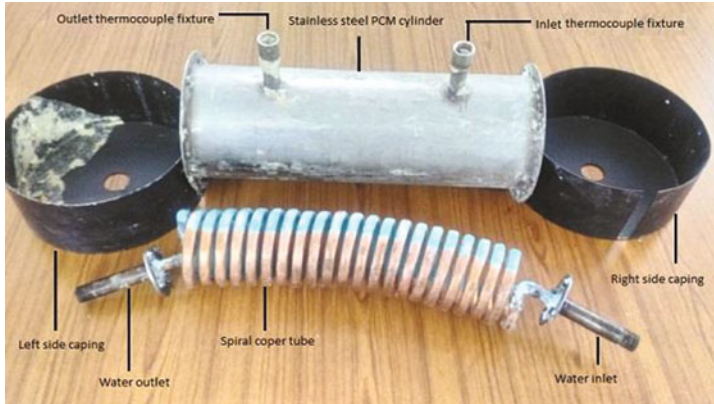
**Fig. 3** Disassembled PCM cylinder

**Table 2** Specification of PCM cylinder

| S. No. | Parameters | Value |
|---|---|---|
| 1 | Heat exchanger shell inner diameter | 140 mm |
| 2 | Heat exchanger shell thickness | 9 mm |
| 3 | Heat exchanger shell length | 200 mm |
| 4 | Heat exchanger tube (copper pipe) inner diameter | 11.5 mm |
| 5 | Heat exchanger tube (copper pipe) outer diameter | 12.7 mm |
| 6 | Heat exchanger tube (copper pipe) thickness | 0.6 mm |
| 7 | Length of heat exchanger tube (copper pipe) | 9000 mm |
| 8 | Number of spirals in the heat exchanger | 18 mm |
| 9 | Conductivity of heat exchanger tube (copper pipe) | 300 W/mk |

## 3    Experimental Setup

The experimental setup of solar water heater using thermal energy storage was shown in Fig. 4. It consists of a flat plate collector of $0.716$ m$^2$ area. To store water, it has three storage tanks of 50L capacity each. Two storage tanks are used to store cold water, and one is used to store hot water. It uses resistance temperature detector (RTD)-type thermocouple to measure inlet water temperature, outlet water temperature, and PCM temperature. The outlet pipe from the solar collector is connected to the inlet of the PCM tank, and the outlet of the PCM tank is connected to the inlet of the hot water storage tank. One thermocouple is attached at the inlet to the PCM tank, and another thermocouple is fixed at the outlet of the PCM tank to measure outlet water temperature. Two thermocouples were used to measure PCM temperature during charging and discharging. The whole apparatus is fully exposed to the solar radiation. Initially, the hot water coming out from the solar collector is
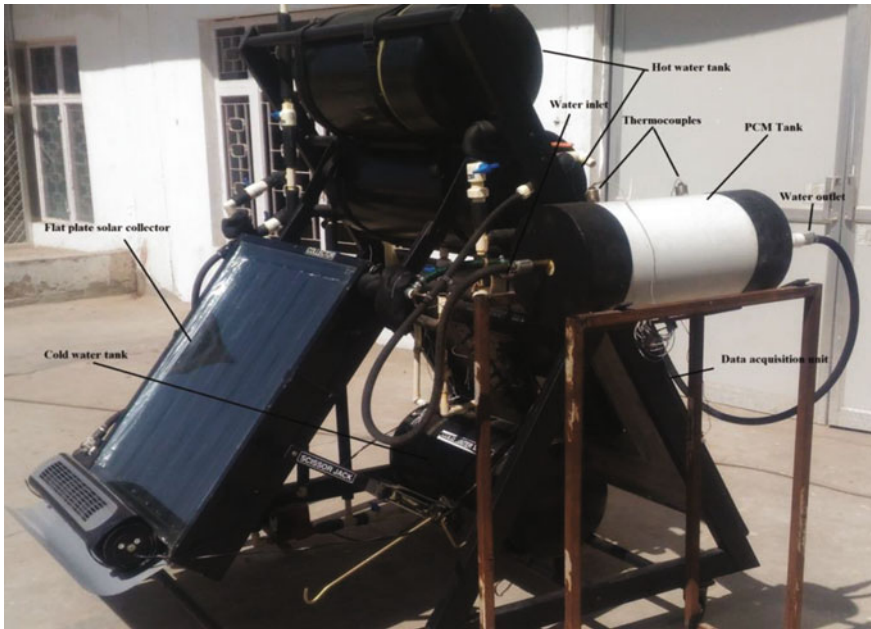
**Fig. 4** Solar water heater integrated with PCM thermal energy storage tank

used to charge the PCM. When the PCM is fully charged and reached the required temperature, the whole apparatus is then moved inside the laboratory so that testing of the solar water heater can be carried out using PCM.

# 4   Results and Discussion

The thermal performance of the solar water heater system has been analyzed at three different flow rates of water and at three different PCM temperatures. The outlet flow rate is maintained at 0.017, 0.030, and 0.050 kg/s. The PCM inside the PCM cylinder is charged at 60, 55, and 50 °C. Figure 5 shows the thermal profile of the water at a PCM temperature of 60 °C. The outlet temperature of the water is highest at 54 °C when the flow rate is maintained at 0.017 kg/s. The temperature of the water at the outlet starts falling and reaches to equilibrium for 0.017, 0.030, and 0.050 kg/s flow rates after 8, 9, and 10 h, respectively. This is because of the high latent heat energy storage capacity of the PCM. When water passes through the PCM cylinder, the PCM starts discharging and transfers its heat to the water, which leads to the rise in temperature of the water. The discharging of the PCM ended when output temperature becomes equilibrium with inlet temperature.
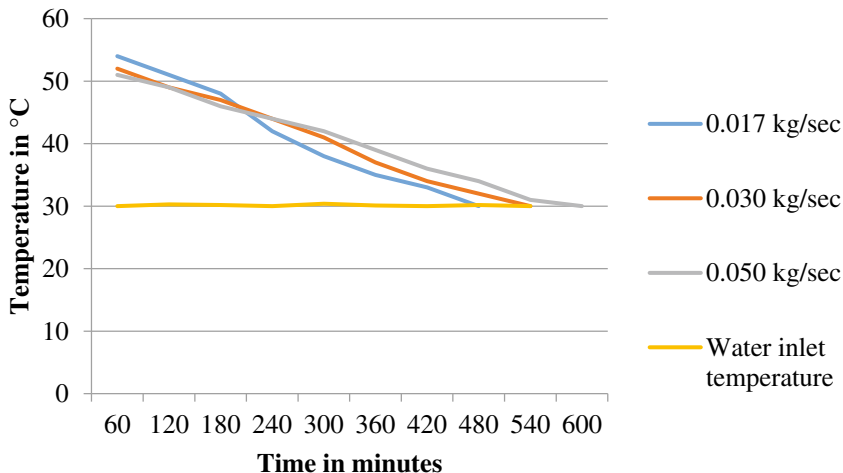
**Fig. 5** Outlet temperature of water when the PCM temperature is 60 °C
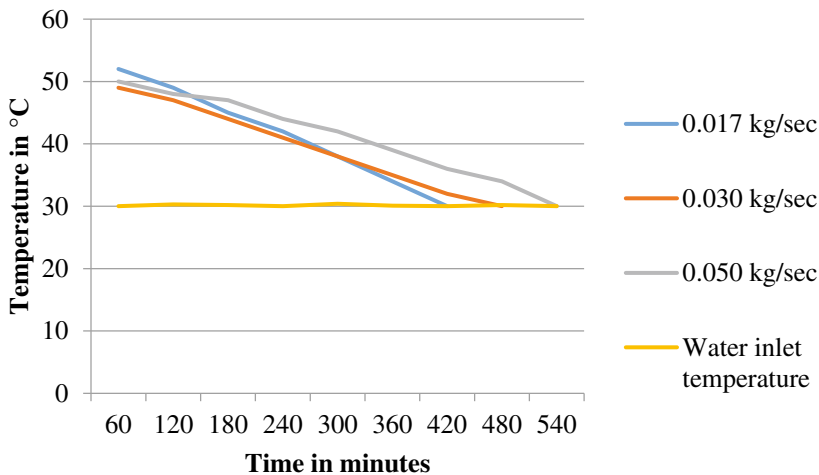


**Fig. 6** Outlet temperature of water when the PCM temperature is 55 °C

The discharging process continues till 8 h and after this, the output temperature became same as input temperature.

Figure 6 shows the outlet temperature profile of the water when PCM is charged at 55 °C. The temperature profile for all the three flow rates remains more or less same except that the flow rate of 0.017 kg/s reaches an equilibrium temperature 120 min before the time when flow rate of 0.050 kg/s reaches the input temperature of water which is 30 °C. This is because the PCM discharges faster when the flow rate of water is low and discharges slow when the flow rate is more. When the flow
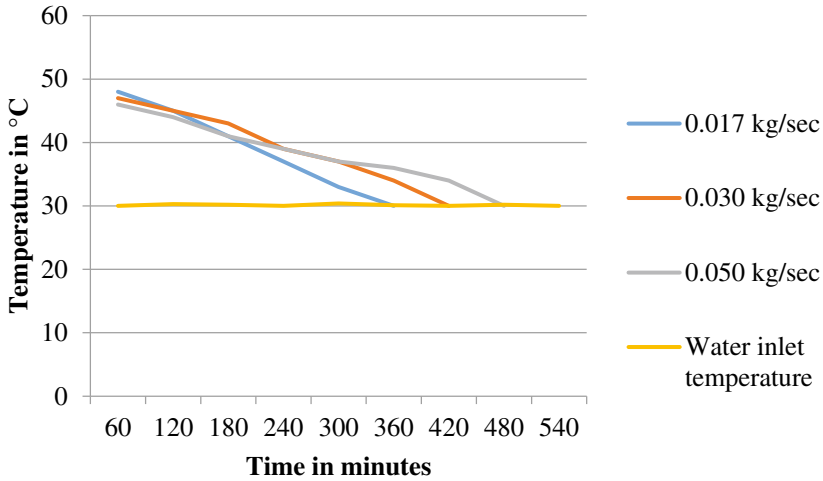
**Fig. 7** Outlet temperature of water when the PCM temperature is 50 °C

rate is slow, PCM has more time to discharge its thermal energy effectively, whereas when the flow rate is more, the duration of contact of water and PCM through the heat exchanger is decreased and hence PCM is not able to discharge its thermal energy effectively.

Figure 7 shows the outlet temperature profile of the water when PCM temperature is 50 °C. Initially, flow rate of 0.017 kg/s has the highest temperature and reaches the equilibrium temperature after 6 h, whereas flow rates of 0.030 and 0.050 kg/s reach the equilibrium after 7 and 8 h, respectively. It has been observed here that the lower flow rate reaches the equilibrium temperatures much earlier than the higher flow rate. This is because the rate of thermal energy discharge from the PCM is more at lower flow rates in comparison to energy discharge at a higher flow rate.

Figure 8 shows the thermal profile of the organic PCM when it is charged using hot water as a heat-transferring fluid (HTF) from the solar water heater. When the energy stored in the hot water is transferred to the PCM, PCM starts charging and stores the thermal energy in the form of latent heat. This leads to the change in phase (solid to liquid) of the PCM and also raises its temperature. The flow rate of 0.017 kg/s reaches the 60 °C mark much early in comparison to 0.030 and 0.050 kg/s flow rate. The time taken by 0.017 kg/s flow rate to attain the temperature of 60 °C is 360 min, whereas 0.030 and 0.050 kg/s have taken 420 and 480 min, respectively.
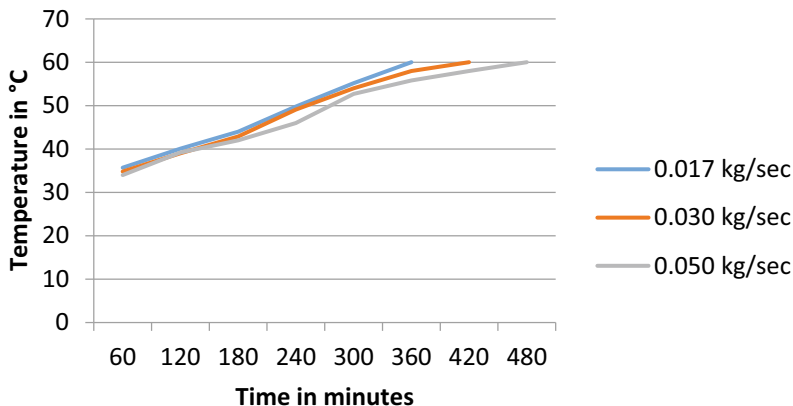
**Fig. 8** Thermal behavior of the PCM during charging to 60 °C

**Table 3** Analysis of extended utilization of solar water heater in minutes

| S. No. | Temperature Flow rate (kg/s) | 50 °C (min) | 55 °C (min) | 60 °C (min) |
|--------|------------------------------|-------------|-------------|-------------|
| 1 | 0.017 | 360 | 420 | 480 |
| 2 | 0.030 | 420 | 480 | 540 |
| 3 | 0.050 | 480 | 540 | 600 |

# 5  Conclusion

The use of organic PCM in a PCM tank, which act as a heat exchanger, represents a simple, effective, and inexpensive approach for thermal energy storage in the solar water heating system. The PCM tank can easily be integrated into the existing and the conventional solar water heater for thermal energy storage.

The PCM stores thermal energy during daytime and releases the energy during the night. This released energy is used to raise the temperature of the fluid. The experimental readings revealed that if PCM is charged to 60, 55, and 50 °C, it will increase the utilization time of solar water heater to 10, 9, and 8 h, respectively, at a flow rate of 0.050 kg/s. For the same temperature ranges and at a flow rate of 0.030 kg/s, the solar water heater will give hot water for an extended 9, 8, and 7 h, respectively. Similarly, for the flow rate of 0.017 kg/s, the utilization time will be increased to 8, 7, and 6 h, respectively. The high flow rate will increase the operational time of the solar water heater during non-availability of solar radiation while the low flow rate will reduce the utilization time but increases the output temperature. Table 3 summarizes the increase in utilization time of the solar water heater using the thermal energy storage technique. It has also been found that the time taken to charge the PCM to 60 °C marks is 6, 7, and 8 h for the flow rates of

0.017, 0.030, and 0.050 kg/s, respectively. Further, if the PCM of high latent heat storage capacity is used, then the operational time of the solar water heater would be extended to 10–15 h.

# References

1. International Energy Agency (2014) Available from: https://www.iea-shc.org/data/sites/1/publications/Solar-Heat-Worldwide-2016.pdf. Last accessed 06 Dec 2017
2. Kee SY, Munusamy Y, Ong KS (2017) Review of solar water heaters incorporating solid-liquid organic phase change materials as thermal storage. Appl Therm Eng
3. Rathore PKS, Rathore S, Singh RP, Agnihotri S (2017) Solar power utility sector in India: Challenges and opportunities. Renew Sustain Energy Rev
4. Shukla A, Buddhi D, Sawhney RL (2009) Solar water heaters with phase change material thermal energy storage medium: a review. Renew Sustain Energy Rev 13(8):2119–2125
5. Xu J, Wang RZ, Li Y (2014) A review of available technologies for seasonal thermal energy storage. Sol Energy 103:610–638
6. Sharma A, Tyagi VV, Chen CR, Buddhi D (2009) Review on thermal energy storage with phase change materials and applications. Renew Sustain Energy Rev 13(2):318–345
7. Kumarasamy K, An J, Yang J, Yang EH (2016) Numerical techniques to model conduction dominant phase change systems: a CFD approach and validation with DSC curve. Energy Build 118:240–248

# Numerical Analysis on Variations of Thermal and Hydrological Properties During Water Flow Through Unsaturated Soil

**Manjit Singh, Chanpreet Singh and D. Gangacharyulu**

**Abstract** The flow of water through unsaturated soil is based on extension of Darcy's law. The finite difference techniques are used to solve the model for evaluation of variations of hydrological and thermal variation due to flow of water into the soil. The pedotransfer function for estimating the soil properties is further used as input to simulate the problem domain. The validation of simulated result, based on transient heat conduction equation, is carried out. Further, the second-order upwind and QUICK methods are used to compare the thermal simulated results. The simulation results for variation of moisture content, the matric potential, and hydraulic conductivity with respect to rig linear dimension variation are further presented.

**Keywords** Mathematical modeling · Unsaturated soil flow · Porous media

The fluid passes through the complex channels formed by pores in the porous media. These pores may contain a variety of fluids like air, water, oil, etc. In a saturated porous media (SPM), a single fluid flows through the pores but in unsaturated porous media (USPM), two or more fluids flow simultaneously. The applications of the porous media are found in petrochemical and mechanical engineering, groundwater hydrology, agricultural and chemical engineering, environmental sciences, soil mechanics, etc.

Flow through porous media is based on generalized Darcy's law [1]. Several researchers had conducted experiments [2, 3], analytical works [4, 5] for modifying the assumptions [6, 7], validation [8], and extension of equation [9]. Unsaturated soil–water flow is derived based on nonlinear partial differential equation [10],

M. Singh (✉)
Chandigarh Engineering College, Mohali, Punjab, India
e-mail: manjit.cecme@cgc.edu.in

C. Singh
Mechanical Engineering Department, Punjabi University, Patiala, Punjab, India

D. Gangacharyulu
Thapar Institute of Engineering and Technology, Patiala, Punjab, India

Darcy's law extension [11], considering non-isotropic media [12], and unsteady flow [13, 14].

Kozney model [3] modification based on relative permeability and pore size distribution is used as Burdine model [15]. This model is utilized for the evaluation of hydraulic property relationships between pressure difference, the permeability of air with water and saturation [16, 17]. Burdine model [15] and Mualem model [18] are further used for predicting conductivity values [19]. Computer code [20] and regression approach [21] based on literature empirical relationship [18, 19] for describing the soil hydraulic properties, boundary-based value problem [22], and dynamic capillary pressure formulation [23] also supported the above approach. Constitutive relations in terms of unsaturated soil properties relationship [24], like soil–water characteristic curve [25] are water-clay interaction [26] are further used. Heat transfer analysis through porous media or in packed bed [27] using local thermal equilibrium [27–30] between the fluid and solid phase and its numerical investigation [30, 31] based on finite difference method [27–29] are presented. Based on above enormous research papers focus on theoretical and experimental aspect are covered but only few research papers covered the numerical simulation on soil hydraulic properties like permeability, capillary pressure relationship etc. In this paper study on operating parameters like pressure, temperature and flow are covered that affect unsaturated flow.

# 1 Unsaturated Soil Assumptions

The following assumptions are considered for unsaturated soil:

- Soil properties are considered as isotropic and homogeneous,
- Air presence in soil obey the perfect gas law,
- Water presence in soil is considered as incompressible fluid and there is no any water phase transfer occurs during unsaturated soil flow.

The relationship between water content and matric potential head using dimensionless water saturation is as [19]:

$$\text{Water saturation}, S_e = \frac{c - c_{\text{res}}}{c_{\text{sat}} - c_{\text{res}}} = \left[\frac{1}{1 + (\alpha h)^n}\right]^m \tag{1}$$

The relationship between relative hydraulic conductivity and matric potential head can be expressed as:

$$K_r(h) = \frac{\left\{1 - (\alpha h)^{n-1}[1 + (\alpha h)^n]^{-m}\right\}^2}{[1 + (\alpha h)^n]^{m/2}} \tag{2}$$

Based on the momentum equation in the form the modified Darcy's law as applied to flow through unsaturated soil is:

$$u = -KK_r(c)\nabla h(c) \tag{3}$$

The mass balance equation for air–water phases is given below:

$$\frac{\partial(\varepsilon s_i \rho_i)}{\partial t} + \nabla(\rho_i u_i) = 0 \quad i = \text{air, water} \tag{4}$$

$$\frac{\partial h}{\partial t} = \frac{K \frac{\partial}{\partial x}\left[K_r \frac{\partial h}{\partial x}\right]}{\frac{\partial c}{\partial h}} \tag{5}$$

where $\partial c/\partial h$ is capillary capacity [$(\text{m}^3/\text{m}^3)/\text{m}$] that can be calculated using Eq. 6 as:

$$\left(\frac{dc}{dh}\right)^{-1} = \frac{-\alpha m(\varepsilon - c_r)}{1 - m} S_e^{1/m}\left(1 - S_e^{1/m}\right)^m \tag{6}$$

## 1.1 Mathematical One-Equation Model for Heat Transfer in USPM

The mathematical thermal equilibrium or one-equation model for unsaturated soil domain considering volume averaging and the thermal properties are constant and can be rewritten as

$$(\rho c_p)_m \frac{\partial T}{\partial t} + (\rho c_p)_f u.\nabla T = \nabla.[(k_m).\nabla T] \tag{7}$$

The thermal storage capacity of unsaturated soil as:

$$(\rho c_p)_m = \varepsilon\left[(1 - s_w)\rho_a c_{pa} + s_w \rho_w c_{pw}\right] + (1 - \varepsilon)\rho_s c_{ps} \tag{8}$$

## 1.2 Numerical Solution for Flow Model

The fully implicit finite difference discretization of Eq. 5 on the basis of the matric potential head is obtained by using first-order backward differencing scheme for east and west nodes of the spatial derivative term:

$$\frac{h_i^{n+1} - h_i^n}{\Delta t} = \frac{k}{\Delta x^2}\left[K_r^e * (h_{i+1}^{n+1} - h_i^{n+1}) - K_r^w * (h_i^{n+1} - h_{i-1}^{n+1})\right] * \left(\frac{dc}{dh}\right)^{-1} \tag{9}$$

The value of relative hydraulic conductivity for east and west nodes is obtained from the harmonic mean value of upstream and downstream of the current node.

## 1.3 Numerical Solution for Heat Transfer Model

The fully implicit finite difference discretization of thermal equilibrium model equation, on the basis of implicit differencing of time domain, a backward differencing scheme for diffusion terms can be written as:

$$\frac{T_i^{n+1} - T_i^n}{\Delta t} + \frac{U_r T_r - U_l T_l}{\Delta t} = \frac{(k_m)}{(\rho c_p)_m} \left( \frac{T_{i+1}^{n+1} + T_{i-1}^{n+1} - 2T_i^{n+1}}{\Delta x^2} \right) \tag{10}$$

The term U is the velocity term, which can be numerically solved by using following approaches.

## 1.4 Second-Order Upwind Differencing Approach

Using upwind difference scheme for velocity as:

$$U_r = 0.5(U_i + U_{i+1}) \tag{11}$$

And

$$U_l = 0.5(U_i + U_{i-1}) \tag{12}$$

And $T_r$ and $T_l$ represent node position of $T$ under influence of $U_r$ and $U_l$.

If $U_r$ is greater or equal to 0, $T_r = T_i$ and if $U_r$ is lower than 0, $T_r = T_{i+1}$. Similarly, if $U_l$ is greater or equal to 0, $T_l = T_{i-1}$ and if $U_l$ is lower than 0, $T_l = T_i$.

## 1.5 Quadratic Upstream Interpolation for Convective Kinematic (QUICK) Formulation Approach

Using upwind difference scheme for velocity as:

$$U_r = 0.5(U_i + U_{i+1}) \tag{13}$$

And

$$U_l = 0.5(U_i + U_{i-1})$$ (14)

And $T_r$ and $T_l$ represent node position of $T$ under influence of $U_r$ and $U_l$. The QUICK formulation based on three-point based upstream-weighted quadratic fit interpolation on three nodes, i.e., $T_l$, $T_c$, and $T_r$. The nodes C, L, R, and FL refers to $i$th, $(i - 1)$th, $(i + 1)$th, and $(i - 2)$th node.

$$T_r = \left(\frac{3}{4}\right)T_i + \left(\frac{3}{8}\right)T_{i+1} - \left(\frac{1}{8}\right)T_{i-1}$$ (15)

$$T_l = \left(\frac{3}{8}\right)T_i + \left(\frac{3}{4}\right)T_{i-1} - \left(\frac{1}{8}\right)T_{i-2}$$ (16)

## 1.6  Initial and Boundary Conditions

The numerical simulation for fluid flow conditions along with temperature variation is carried out on the basis of initial and boundary condition. The soil is initially considered at −1 m matric potential head uniformly. As the fluid (water) enters into the bed, $h$ is set as zero at the inflow plane and having a zero derivative in the axial direction at outflow plane as followings:

$$
\begin{array}{lll}
0 \leq x \leq L \,\text{and}\, t = 0; & h = 1\,m(-ve), & T = 20°C, \\
\text{At}\, x = 0 \,\text{and}\, t > 0; & h = 0, & T = 50°C; \\
\text{At}\, x = L \,\text{and}\, t > 0; & \left(\frac{\partial h}{\partial x}\right)_{x=L} = 0, & \left(\frac{\partial T}{\partial x}\right)_{x=L} = 0;
\end{array}
$$

The boundary conditions at $x = L$, i.e., at the outlet are closed outflow conditions by considering $L$ significantly large compared to the actual distance covered by fluid in soil domain. The schematic representation of unsaturated soil is shown in Fig. 1. The grid size in the $x$-direction is 0.1% of total length of bed, and time steps



h = 0,
T=50°C,
u=0
at x = 0
for t > 0

Unsaturated

Soil

∂h/∂x = 0,
∂T/∂x = 0,
at x = L

for t >0

h = -1m, T=20°C, 0 < x < L for t = 0

x
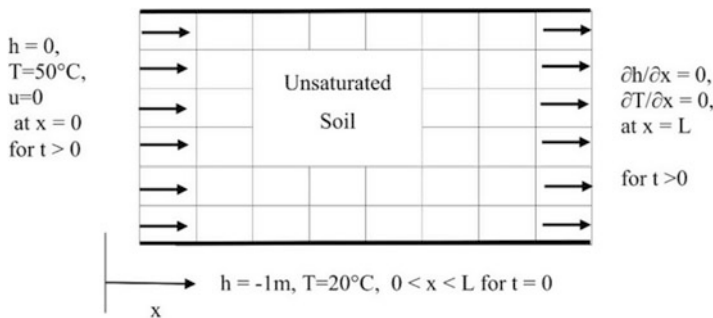
**Fig. 1**  Schematic representation of unsaturated soil

chosen are 0.05% of the total time for simulation. It is to ensure the grid independent for grid size and time steps. The numeric calculations are carried out using WINDOW 8.1-based 64-bit operating system on Intel (R) Core (TM) i5-3230 M CPU machine having 2.60 GHz processing unit and 8 GB RAM. Typical CPU time needed for a single run was of the order of 170 s.

## 1.7 Validation of Code

The validation of numerically simulated program result, based on transient heat conduction equation considering local thermal equilibrium (LTE) for the flow of fluid (water) at prescribing temperature through unsaturated soil, is compared. The simulated temperature–time profile at distinguishing spatial location from the inflow plane by considering constant Darcy's velocity is compared with work of Singh [32]. It is clearly observed that the nature of temperature–time profile at distinguishing spatial location due to heat transfer in soil is linearly agreement with the simulated results (Fig. 2).

The program is executed for water flow through unsaturated sand, i.e., loamy sand. The physical properties of loamy sand as shown in Table 1 are used as input values for the program.

The program calculates the van-Genuchten constant values, residual water content, saturated hydraulic conductivity, bubbling pressure head and pore size index before initializing through the pedotransfer functions. The typical values for physical properties of soil parameters are shown in Table 2.

Based on boundary condition, the program initializes the grid values for initial values. The typical values for initial values for matric potential head, $h$ (−ve) (m),
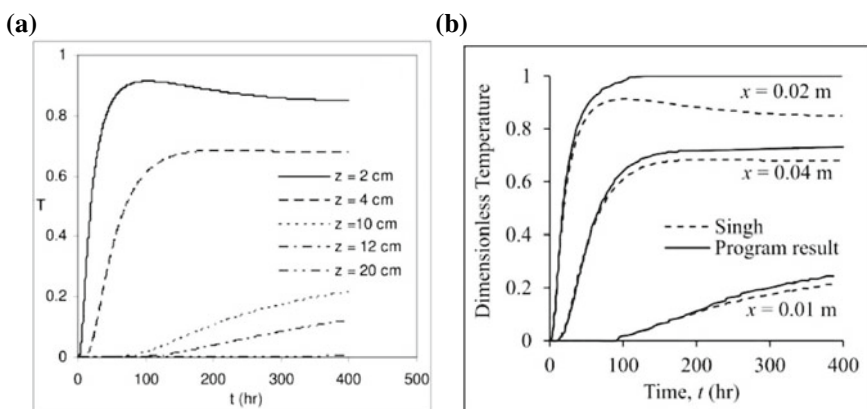


Fig. 2 Results of a unsteady temperature variation in unsaturated soil [32], and b results in comparison of temperature–time profile at distinguishing spatial location

**Table 1** Loamy sand physical properties

| Sand name | Clay percentage | Sand percentage | Porosity, $\varepsilon$ | Density |
|---|---|---|---|---|
| Loamy sand | 15% | 70% | 0.453 | 2650 kg/m$^3$ |

**Table 2** Physical properties of soil

| van-Genuchten Constant | | | Residual water content, $c_{res}$ (m$^3$/m$^3$) | Saturated hydraulic conductivity, $K$ (m/h) | Bubbling pressure head, $y_b$ (m) | Pore size distribution index, $\lambda$ |
|---|---|---|---|---|---|---|
| $n$ | $m$ | $\alpha$ (m$^{-1}$) | | | | |
| 1.3553 | 0.2621 | 1.5 | 0.0525 | 0.0964 | 0.668 | 0.3553 |

water content, $c$ (m$^3$/m$^3$), relative hydraulic conductivity, $K_r$, and slope of water content-matric potential head curve, d$c$/d$h$ are 1, 0.408963, 0.0363, and 0.069245, respectively.

## 1.8 Variation of Hydraulic Properties

The matric potential head, $h$ variations throughout the bed are shown for simulated time intervals 10, 40, 70, and 100 h in Fig. 3a. The matric potential head dimension is negative in nature to represent below atmospheric pressure. The matric potential head variation rate increases rapidly in the initial hours, but convergence gets slower in the later hours of simulations. The variation of matric potential head at the various locations is also shown in Fig. 3b. The linear horizontal locations used to plot the variation are at 0.02, 0.05, 0.1, 0.15, 0.2, and 0.75 m.

Similarly, variation of water content, water saturation, relative hydraulic conductivity, and Darcy's velocity are shown in Figs. 4, 5, 6, and 7. It is also significant to note that rate of change in variation of hydraulic properties dominates near the inflow boundary condition point. As the distance from inflow boundary condition point increases, the variation rates decrease sharply.
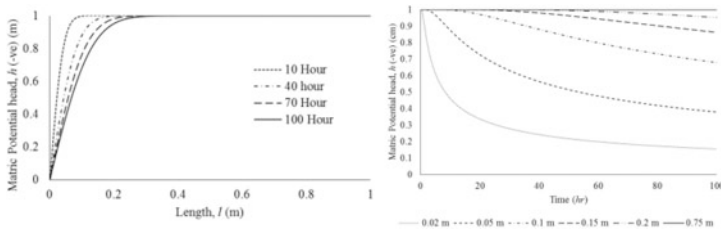


**Fig. 3** Variation of matric potential head
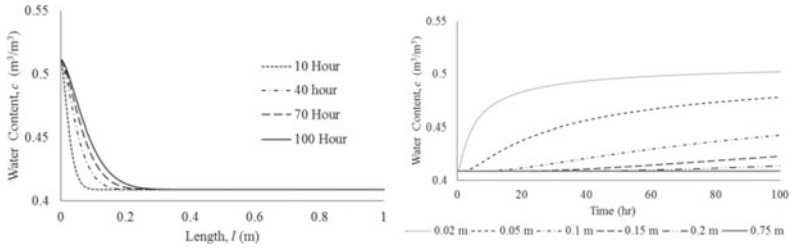
**Fig. 4** Unsteady variation of water content
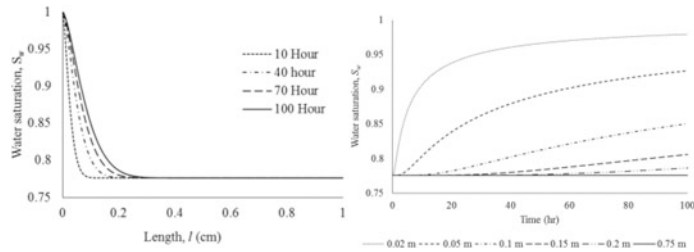


**Fig. 5** Unsteady variation of water saturation
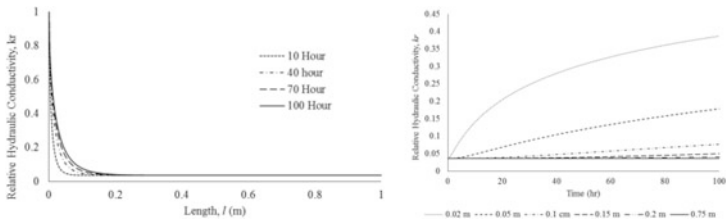


**Fig. 6** Unsteady variation of relative hydraulic conductivity
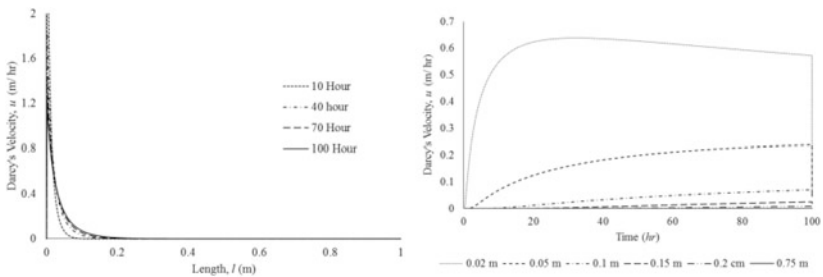


**Fig. 7** Variation of Darcy's velocity
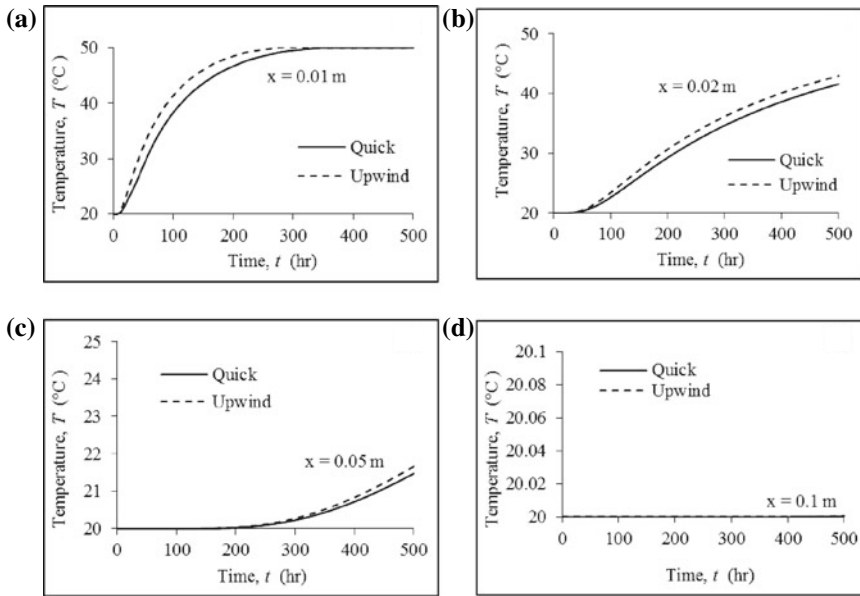
**Fig. 8** Comparison of unsteady temperature profile as function of time between QUICK and upwind methods for soil at inflow plane location, **a** 0.01 m, **b** 0.02 m, **c** 0.05 m, and **d** 0.1 m

**Comparison between second-order upwind with QUICK approach results for unsteady temperature at specific distance from inward flow**

A qualitative validation based on comparison of soil for unsteady temperature as a function of time at location 0.01, 0.02, 0.05, and 0.1 m is shown using second-order upwind and QUICK approaches in Fig. 8a–d. The simulated temperature–time profile at distinguishing spatial location from the inflow plane is compared. It is clearly observed that the variation of results is miniature or identical.

## 2    Conclusions

The present work simulated the energy transport in an unsaturated soil by using a fluid medium as domain problem. The finite difference discretization approach such as central difference scheme and a fully implicit approach for spatial deviation and time derivative, respectively, are used for above model solution. The geometric mean for considering upstream and downstream and Newton–Raphson iteration method are also used for numerical simulation. The thermal and hydraulic property variations like soil–water retention model, matric potential head, water content,

Table 3 Summaries' values of various parameters values during simulation in sand soil

| Physical properties | Inflow axial distance (m) | Simulation hour duration after | | | | | | | | | |
| --- | --- | --- | --- | --- | --- | --- | --- | --- | --- | --- | --- |
| | | After 100 h | | After 200 h | | After 300 h | | After 400 h | | After 500 h | |
| | | Value | % of variation | Value | % of variation | Value | % of variation | Value | % of variation | Value | % of variation |
| Matric Potential head (−ve), $h$, (m) | 0.01 | 0.83 | 16.84 | 0.73 | 27.46 | 0.66 | 33.93 | 0.62 | 38.48 | 0.58 | 41.93 |
| | 0.02 | 0.98 | 2.04 | 0.93 | 7.25 | 0.88 | 11.96 | 0.84 | 15.88 | 0.81 | 19.15 |
| | 0.05 | 1.00 | 0.00 | 1.00 | 0.01 | 1.00 | 0.14 | 1.00 | 0.46 | 0.99 | 0.97 |
| | 0.10 | 1.00 | 0.00 | 1.00 | 0.00 | 1.00 | 0.00 | 1.00 | 0.00 | 1.00 | 0.00 |
| | 0.15 | 1.00 | 0.00 | 1.00 | 0.00 | 1.00 | 0.00 | 1.00 | 0.00 | 1.00 | 0.00 |
| | 0.20 | 1.00 | 0.00 | 1.00 | 0.00 | 1.00 | 0.00 | 1.00 | 0.00 | 1.00 | 0.00 |
| Moisture content, $c$ (m³/m³) | 0.01 | 0.05 | 3.17 | 0.05 | 6.23 | 0.05 | 8.77 | 0.05 | 10.99 | 0.06 | 13.00 |
| | 0.02 | 0.05 | 0.31 | 0.05 | 1.18 | 0.05 | 2.08 | 0.05 | 2.94 | 0.05 | 3.74 |
| | 0.05 | 0.05 | 0.00 | 0.05 | 0.00 | 0.05 | 0.02 | 0.05 | 0.07 | 0.05 | 0.14 |
| | 0.10 | 0.05 | 0.00 | 0.05 | 0.00 | 0.05 | 0.00 | 0.05 | 0.00 | 0.05 | 0.00 |
| | 0.15 | 0.05 | 0.00 | 0.05 | 0.00 | 0.05 | 0.00 | 0.05 | 0.00 | 0.05 | 0.00 |
| | 0.20 | 0.05 | 0.00 | 0.05 | 0.00 | 0.05 | 0.00 | 0.05 | 0.00 | 0.05 | 0.00 |
| Temperature, $T$ (°C) | 0.01 | 41.33 | 106.65 | 48.40 | 142.02 | 50.00 | 150.00 | 50.00 | 150.00 | 50.00 | 150.00 |
| | 0.02 | 23.46 | 17.30 | 30.68 | 53.40 | 36.15 | 80.73 | 40.06 | 100.30 | 42.90 | 114.51 |
| | 0.05 | 20.00 | 0.00 | 20.03 | 0.16 | 20.27 | 1.37 | 20.84 | 4.19 | 21.67 | 8.35 |
| | 0.10 | 20.00 | 0.00 | 20.00 | 0.00 | 20.00 | 0.00 | 20.00 | 0.00 | 20.00 | 0.00 |
| | 0.15 | 20.00 | 0.00 | 20.00 | 0.00 | 20.00 | 0.00 | 20.00 | 0.00 | 20.00 | 0.00 |
| | 0.20 | 20.00 | 0.00 | 20.00 | 0.00 | 20.00 | 0.00 | 20.00 | 0.00 | 20.00 | 0.00 |

relative hydraulic conductivity, Darcy's velocity, and temperature are discussed in detail. A qualitative validation based on QUICK and upwind approaches is also carried out to validate the numerical simulation results. For more in-depth logical comparison, the summaries for simulation output for various parameters based on simulation time are presented in Table 3.

# References

1. Darcy H (1856) Les fontaines Publiques de la Ville de Dijon. Dalmont, Paris
2. Haxen A (1893) Some physical properties of sand and grazels with special reference to their use in filtration. Massachusetts State Broad of Health, Twenty four annual report, Massachusetts State
3. Kozeny J (1927) Ueber kapillare Leitung des Wassers im Boden. Sitzungsber Akad Wiss Wien 136(2a):271–306
4. Muskat M (1937) The flow of homogeneous fluid through porous media. Mcgraw Hill, United State of America
5. Singh M, Singh C, Gangacharyulu D, Kumar V (2013) Study on design of single pass backwash cooler. Int J Eng Sci Invention 2(7):117–122
6. Dupuit J (1863) Estudes Théoriques et Pratiques sur le mouvement des Eaux dans les canaux découverts et à travers les terrains perméables, 2nd edn. Dalmont, Paris
7. Brinkman H (1949) A calculation of viscous force exerted by a flowing fluid on a dense swarm of particles. Appl Sci Res 1:27–34
8. Stephen W (1986) Flow in porous media I: a theoretical derivation of Darcy's law. Transport in Porous Media 1, D. Reidel Publishing Company
9. Irmay S (1947) Sur le mouvement des eaux dans le sol. Rev. Universelle des Mines 3(4)
10. Richards LA (1931) Capillary conduction of liquids through porous mediums. Am Inst Phys 1 (5):318–333
11. Irmay S (1958) Extention of Darcy law to unsteady unsaturated flow through porous media. Division of hydraulic Engg, Israel Institute of Technology, Haifa, pp. 57–66
12. Irmay S (1951) Darcy law for non-isotropic soils. Int Ass Sci Hydrol I.U.G.G., Brussels 2:178
13. Irmay S (1951) On the motion of capillary moisture in soils. Sci. Publ. Hebrew Inst. Technol. Haifa 4:43
14. Singh M, Singh C, Gangacharyulu D (2016) Modeling for flow through unsaturated porous media with constant and variable density conditions using local thermal equilibrium. Int J Comput Appl 5:24–30
15. Burdine N (1953) Relative permeability calculations from pore size distribution data. J Petrol Trans, AIME 198:71–78
16. Brooks R, Corey AT (1961) Hydraulic properties of porous media. Hydrology, p. 3. Mar 1961
17. Campbell GS (1974) A simple method for determining unsaturated conductivity from moisture retention data. Soil Sci 117(6):311–314
18. Mualem Y (1986) Hydraulic conductivity of unsaturated soils: prediction and formulas. In: Methods of Soil Analysis, Part 1. Physical and Mineralogical Methods-Agronomy Monograph, 2nd edn. 677 South Segoe Road, Madison, WI 53711, USA, American Society of Agronomy-Soil Science Society of America, pp. 799–823
19. Genuchten V (1980) A closed form equation for predicting the hydraulic conductivity of unsaturated soils. Soil Sci Soc Am J 44:892–898
20. Van-Genuchten M, Leij F (1989) Indirect method for estimating the hydraulic properties of unsaturated soil. In: Proceedings of the International Workshop on Indirect Methods for Estimating the Hydraulic Properties of Unsaturated Soils Riverside, California, 11–13 Oct 1989, pp. 273–283

21. Rawls W, Brakensiek DL (1989) Estimation of soil water retention and hydraulic properties in unsaturated flow in Hydrologic Modeling. In: Morel-Seytoux HJ (ed) Proceedings of the NATO Advanced Research Workshop on Unsaturated Flow in Hydrologic Modelling Theory and Practice, Aries, Kluwer Academic Press, France, 13–17 June 1989, pp. 275–309
22. Whitaker S (1994) The closure problem for two phase flow in homogeneous porous media. Chem Eng Sci 49(5):765–780
23. Nieber JL, Dautov RZ, Egorov AG, Sheshukov AY (2005) Dynamic capillary pressure mechanism for instability in gravity-driven flows; review and extension to very dry conditions. Trans Porous Media 58(1–2):147
24. Chao L, Li R (2011) Estimation of Unsaturated Soil Hydraulic Parameters Using the Ensemble Kalman Filter. Soil Sci Soc Am 10:1205–1227
25. Fredlund DG (2006) Unsaturated soil mechanics in engineering practice. J Geotech Geoenviron Eng 132:286–321
26. Liu H-H, Li L, Birkholzer J (2012) Unsaturated properties for non-Darcian water flow in clay. J Hydrol 430:173–178
27. Vafai K, Kim SJ (1990) Analysis of surface enhancement by a porous substrate. ASME J Heat Transf 112:700–706
28. Koh YJC, Colony R (1974) Analysis of cooling effectiveness for porous material in a coolant passage. ASME J Heat Transf 96:324–330
29. Koh J, Stevens R (1975) Enhancement of cooling effectiveness by porous materials in coolant passage. ASME J Heat Transf 97:309–311
30. Sheorey T, Muralidhar K (2003) Isothermal and non-isothermal oil–water flow and viscous fingering in a porous medium. Int J Therm Sci 42:665–676
31. Nuskea P, Ronnebergerb O, Karadimitrioud NK, Helmiga R, Majid Hassanizadehc S (2015) Modeling two-phase flow in a micro-model with local thermal non-equilibrium on the Darcy scale. Int J Heat Mass Transf 88:822
32. Singh C (2009) Convective heat transfer in porous media for energy storage, VDM Verlag

# Spray Impingement Heat Transfer Using Nanofluid—Experimental Study

**Bikash Pattanayak**, **Abhishek Mund**, **J. S. Jayakumar**,
**Kajal Parashar** and **S. K. S. Parashar**

**Abstract** Spray impingement plays a vital role in the cooling process. Spray impingement acts as a cooling media for high heat flux applications. As nanofluids have enhanced thermal properties than base fluids, CuO, ZnO, and hybridized CuO and ZnO nanofluids at different volume concentrations were used in this experiment. The nanoparticles were synthesized using high-energy ball milling (HEBM) technique at 300 rpm with the ball-to-powder ratio (BPR) of 10:1. These nanoparticles were characterized by using XRD, SEM, and TEM and were found to be in the range of 30 nm. The densities, viscosity, thermal conductivity, and the specific heat of the nanofluids were calculated using different models. It was observed that increase in the volume concentration, density, and viscosity of the nanofluid increased. The heat transfer study was carried out on an electrically preheated iron plate of dimensions 100 mm × 100 mm × 8 mm at different temperatures of 200, 150, and 100 °C. The cooling rate and the effect of air pressure on cone angle were analyzed. The main sources of uncertainty in the measured data were due to the temperature fluctuations and thermocouple locations. It was observed that the time taken to reach the steady state was faster in nanofluids than normal water.

**Keywords** Nanofluid · Cooling rate · SEM · HEBM

## Nomenclature

| | |
|---|---|
| CR | Cooling rate, (°C/s) |
| $C_p$ | Specific heat (J/kgK) |
| $h$ | Heat transfer coefficient, (W/m$^2$ K) |
| $k$ | Thermal conductivity (W/mK) |

B. Pattanayak · A. Mund · J. S. Jayakumar (✉)
Department of Mechanical Engineering, Amrita Vishwa Vidyapeetham, Amritapuri, India
e-mail: jsjayan@gmail.com

K. Parashar · S. K. S. Parashar
Nano Sensor Lab, School of Applied Science, Kalinga Institute of Industrial Technology (KIIT) Deemed to Be University, Bhubaneswar, Odisha 751024, India

$NF_1$   CuO—water nanofluid
$NF_2$   ZnO—water nanofluid
$NF_3$   CuO-doped ZnO—water nanofluid
$T_1$   Impingement starting temperature of the plate, (°C)
$T_2$   Impingement ending temperature of the plate, (°C)
$t$   Time taken to cool the heated plate, (s)
$T_s$   Surface average temperature, (°C)
$T_{fl}$   Water jet temperature, (°C)

**Greek symbols**

$\varphi$   Volume concentration
$\rho$   Density (kg/m$^3$)
$\mu$   Dynamic viscosity (kg/ms)
$\varepsilon$   Effectiveness
$\tau$   Thickness of plate, (mm)

**Subscripts**

$nf$   Nanofluid
$w$   Water
$p$   Nanoparticle
1   CuO nanopowder
2   ZnO nanopowder
3   ZnO-doped CuO nanopowder

# 1   Introduction

Previously, different single-phase cooling techniques were used to enhance heat dissipation rate by increasing coolant's sensible heat. Thermal engineers further developed two-phase cooling schemes to provide enhanced cooling effectiveness by utilizing the sensible and latent heat of the coolant for rejecting heat [1]. This scheme includes jet impingements and spray cooling. The jet impingement cooling has certain shortcomings like the heat removal takes place within the central impingement zone and produces high surface temperature gradients. The interference between the neighboring jets causes flow instabilities, and coolant's flow became complicated. Spray impingement uses the liquid's momentum emerging through nozzle and break it up into droplets and impinge them singly on the hot surface [2]. It resists the separation of the liquid from the surface during boiling. The droplet's momentum makes it to get through the blanket of vapor formed by nucleating bubbles which is good for high-flux cooling. Spray requires a low

coolant flow rate but high pumping power. The effective performance of the spray is due to the boundary layer formed by unsteadiness because of the impact of droplet and cooling due to evaporation [3]. Nanofluids are dispersed stable colloidal suspension of nanoparticles in base fluids like water, oil, etc. [4]. The effective thermal conductivity of the nanofluids is higher as compared with the normal base fluids. When the volume concentration of nanofluid increases, the thickness of layer formed due to sticking of nanoparticles on the heated plate also increases, which arises a problem for spray impingement for nanofluids [5]. So in order to reduce this effect, low volume concentrations' nanofluids were used in this experiment. It has been analyzed from various research papers that the heat transfer through nanofluid in spray impingement is limited to pool boiling. The pool boiling technique shows that the critical heat flux and heat transfer coefficient are higher for nanofluids than water [6]. The experiment was compared with the research done by Teamah et al., [7] and it was observed that for the volume concentration of 10% and Reynolds number of 24,000, the heat transfer coefficient was enhanced by 62% when compared with water. It was inferred that the heat transfer by CuO nanofluid increased by 8.9% when compared with aluminum nanofluid and 12% when compared with titanium nanofluid. So the CuO water nanofluid provides optimum heat transfer [7]. So in this experiment, different volume concentrations of CuO, ZnO, and ZnO-doped CuO water-based nanofluid were used as the liquid for spray as well as water, and their comparative analysis to determine the cooling rate was conducted. This paper explained about the heat transfer and cooling rate associated with hybrid nanofluids.

## 2 Experimental Analysis

### 2.1 Synthesis of Nanoparticle and Preparation of Nanofluid

The nanometer-sized powders of copper oxide and zinc oxide were synthesized using HEBM technique at 300 rpm and BPR 10:1. Zinc oxide and copper oxide powders of the particle size approximately 25 microns and purity of 99.8% were mechanically milled using tungsten carbide jars and balls. The CuO and ZnO powders were milled for 15 h, with an hour of milling time and a half an hour gap between consecutive milling to reduce frictional overheating. The density, thermal conductivity, and viscosity of the CuO and ZnO powders are 6315 kg/m$^3$, 33 W/mK, 423 W/m K and 5610 kg/m$^3$, 17 W/mK, 514 W/mK, respectively. Nanofluids were prepared by mixing different (0.05, 0.1, 0.15, and 0.2%) volume concentrations of nanopowder in water. The nanofluids were prepared by using two-step method [8]. The mixture was magnetically stirred at 1000 rpm speed for 6 h and then was ultrasonic agitated for 2 h. The stability of the nanofluid was maintained up to 12 h by adding 3% PVA in one-tenth ratio to the mass of the nanoparticle. In the experimental practice, some nanofluid without surfactant was taken in a petri

dish and after some time cluster formation occurs and it settles down. The petri dish was then heated, and the residue was measured. The same methodology was applied with the PVA-added nanofluid, and it was observed that after 12 h cluster formation started and after 12 h it stopped. The residue was heated and measured. The mass was comparatively low so it has been concluded that the fluid is stable.

## 2.2 Characterization of Nanoparticle

The X-ray diffraction patterns (XRD) were obtained using PANalytical X'pert PRO machine for CuO and ZnO nanoparticles, analyzed for this work, and were plotted in Fig. 1a, b. All the peaks were indexed as(100), (101), (002), (102), (110), (103), (112), (201) for ZnO and (1, 1, 1), (2, 0, 0), (−1, 1, 2), (−2, 0, 2), (2, 0, 2), (−1, 1, 3), (2, 2, 0), (0, 0, 4) for CuO. The powder was of tetrahedral crystal system with a lattice constant ($A°$) $a = 3.25$, $b = 3.25$, $c = 5.2$ for ZnO and of monoclinic crystal system with a lattice constant ($A°$) $a = 4.684$, $b = 3.425$, $c = 5.129$ for CuO. SEM images were taken using JSM-6510 machine atx10000 resolution and 1 μm reference size. The particles are uniform and spherical in nature shown in Fig. 1c, d. However, in case of CuO nanoparticles are bigger than the ZnO nanoparticles. The confirmation of nanoparticles was done by FEI, Tecnai TEM. It was found that the synthesized 15-h dry ball-milled powder of CuO and ZnO was in the range of 30–40 nm shown in Fig. 1e, f. The particles are uniform and spherical in nature.

## 2.3 Experimental Setup and Procedure

In this experiment, using a heater of 2.5 KW capacity a square iron plate of dimensions 100 mm × 100 mm × 8 mm was heated (Fig. 2). The J-type thermocouples measured the temperature at four different positions on the plate. A 1.5-mm-diameter nozzle was fixed 10 cm above the plate at the different vertices of the plate, four drills of 4 mm depth were made to adjust the thermocouple, and one experiment was conducted four times and the average data was taken for final analysis. An analog pressure gauge was attached to the setup to measure the air pressure. Instead of mixing air with the nanofluid and water, air at different pressure was applied to the fluid and was then impinged. Then the final temperatures of the plate after 30 s were measured. The effect of air pressure on cone angle, cooling rate, and a cooling curve for all fluids was then analyzed.
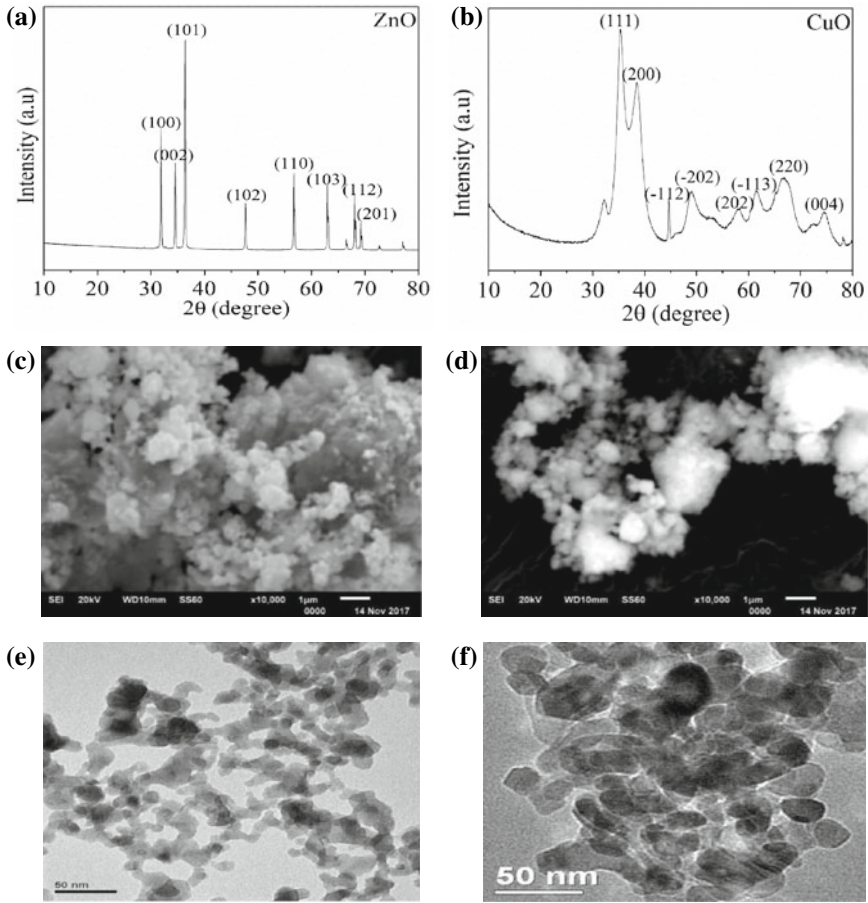
**Fig. 1** XRD (**a**, **b**), SEM (**c**, **d**), and TEM (**e**, **f**) of ZnO and CuO nanoparticles

**Fig. 2** Schematic diagram of spray impingement apparatus
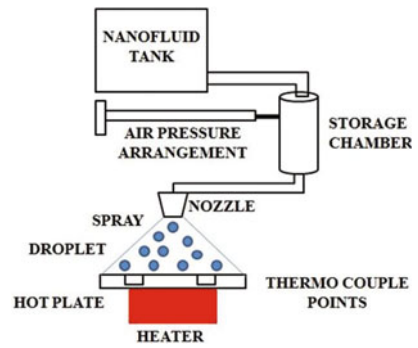
# 3 Results and Discussions

## 3.1 Calculation of Various Thermophysical Properties

Figure 3 Eqs (1)–(4) represents Pak and Choi model, WASP model, LS Sundar model, and homogeneous mixture specific heat formula which are used to determine density, thermal conductivity, viscosity, the specific heat of the nanofluids, respectively. The data obtained were shown in Table 1. It was observed that as volume concentration increases, the density, viscosity, and thermal conductivity increase but specific heat decreases. In nanofluids, thermal conductivity can be enhanced by the collision between the solid particles. By increasing the volume concentration, the number of collision between the solid particles increases, and the internal energy of the particle increases resulting in the increase in effective thermal conductivity of the nanofluid [9]. Nanofluids have dominating Brownian motions. Due to the agglomeration of nanoparticles, suspension of nanoparticles in the base fluid may decrease with time because of van der Waals forces [10]. For this reason with an increase in volume concentration, the viscosity increases.

$$\rho_{nf} = \varphi_1 \rho_1 + \varphi_2 \rho_2 + (1 - \varphi_1 - \varphi_2)\rho_w \tag{1}$$

$$\mu_{nf} = \mu_w(1 + 39.11\varphi + 533.9\varphi^2) \tag{2}$$

$$k_{nf} = k_w \frac{k_p + 2k_w - 2\varphi(k_w - k_p)}{k_p + 2k_w + \varphi(k_w - k_p)} \tag{3}$$

$$C_{pnf} = \frac{(\varphi_1 \rho C_p)P_1 + (\varphi_1 \rho C_p)P_2 + ((1 - \varphi_1 - \varphi_2)\rho C_p)_w}{\rho_{nf}} \tag{4}$$

Fig. 3 a–f represents the spray cone angle at 5, 10, and 15 psi air pressures at 200 °C plate temperature for water and NF$_3$, respectively
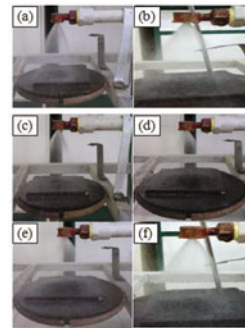
**Table 1** Thermophysical properties of the nanofluids

| Nanofluid | Volume concentration | Density | Viscosity | Thermal conductivity | Specific heat |
|---|---|---|---|---|---|
| $NF_1$ | 0.025 | 1115.2 | 0.0019 | 0.6743 | 3725.09 |
| | 0.05 | 1250.5 | 0.0035 | 0.7230 | 3296.14 |
| | 0.075 | 1345.7 | 0.0057 | 0.7743 | 3038.63 |
| | 0.1 | 1461.0 | 0.0085 | 0.8282 | 2776.62 |
| $NF_2$ | 0.025 | 1132.8 | 0.0019 | 0.6736 | 3662.47 |
| | 0.05 | 1265.7 | 0.0036 | 0.7215 | 3248.04 |
| | 0.075 | 1398.6 | 0.0058 | 0.7718 | 2912.38 |
| | 0.1 | 1531.5 | 0.0085 | 0.8248 | 2477.97 |
| $NF_3$ | 0.025 | 1248.1 | 0.0019 | 0.6727 | 3298.22 |
| | 0.05 | 1496.2 | 0.0035 | 0.7196 | 2704.21 |
| | 0.075 | 1774.3 | 0.0058 | 0.7689 | 2240.63 |
| | 0.1 | 1992.5 | 0.0085 | 0.8207 | 1959.88 |

## 3.2 Measurement of Cone Angle at Different Air Pressure for Various Volume Concentration Nanofluids

Pictures were taken during the experiment to measure the cone angle at different air pressure for different nanofluid and were shown in Table 2.

**Table 2** Cone angle at different air pressures for various volume concentration nanofluids

| Fluid | Volume concentration | Air pressure (psi) | Cone angle (°) | $T_1$ | $T_2$ | t | CR | h |
|---|---|---|---|---|---|---|---|---|
| Water | NA | 5 | 55 | 100 | 34 | 35 | 1.885 | 789.25 |
| | | 10 | 59 | 150 | 42 | 35 | 3.057 | 787.67 |
| | | 15 | 71 | 200 | 44 | 35 | 4.457 | 824.00 |
| $NF_1$ | 0.1 | 5 | 53 | 100 | 31 | 35 | 1.975 | 854.59 |
| | | 10 | 59 | 150 | 40 | 35 | 3.142 | 815.74 |
| | | 15 | 73 | 200 | 41 | 35 | 4.542 | 842.29 |
| $NF_2$ | 0.1 | 5 | 52 | 100 | 30 | 35 | 2.000 | 809.60 |
| | | 10 | 59 | 150 | 38 | 35 | 3.200 | 777.22 |
| | | 15 | 68 | 200 | 45 | 35 | 4.428 | 768.19 |
| $NF_3$ | 0.1 | 5 | 54 | 100 | 31 | 35 | 1.975 | 894.20 |
| | | 10 | 61 | 150 | 39 | 35 | 3.171 | 832.46 |
| | | 15 | 69 | 200 | 43 | 35 | 4.485 | 829.07 |

### 3.3 Cooling Curve Analysis and Calculation of Cooling Rate and Heat Transfer Coefficient

The data obtained from the experiment were analyzed, and various graphs were plotted as shown in Fig. 4. It was analyzed that the hybrid nanofluid cools faster at a higher temperature and titanium dioxide is moderate cooler at the same pressure applied. The cooling rate and heat transfer coefficient in this experiment were calculated using the equations, and all the data were shown in Table 2.

$$CR = \frac{T_1 - T_2}{t} \, ^\circ C/s \tag{5}$$

$$h = \frac{\rho * \tau * C_p * CR}{T_s - T_{fl}} W/mK \tag{6}$$

### 3.4 Uncertainty Analysis

In this experiment, the models used to measure thermophysical properties have certain limitations such as they can be used for spherically shaped nanoparticle and the volume concentration limited to 4%. The uncertainties in the measurement of voltage, current, and energy were recorded as $\pm0.5$, $\pm0.7$, and $\pm1.5$, respectively. The J-type thermocouple was used to measure temperature with $\pm0.1$ °C accuracy. The error in the measurement of mass is $\pm0.002$ g.
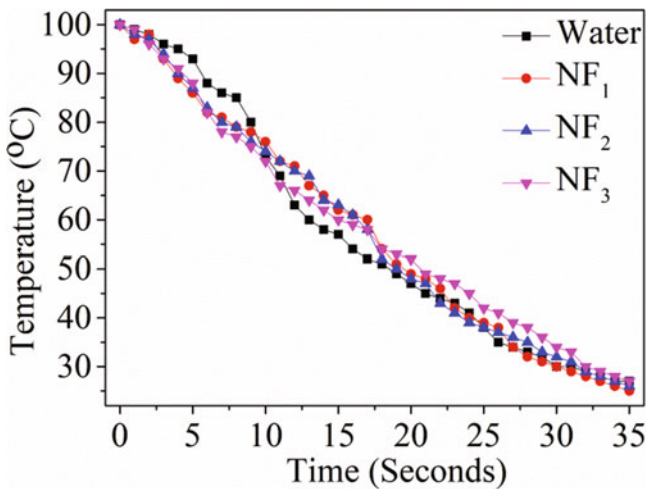


Fig. 4 Cooling curves plotted for 200 °C plate temperature at 15 psi pressure

# 4 Conclusions

Hence from the above experiment, it was concluded that nanofluids are more effective liquids to be used for cooling the iron plate than water because of their good thermophysical properties and heat capacity. It was observed that the hybrid nanofluid cools faster for a high temperature of the plate. CuO—water nanofluids have effective heat transfer characteristics at medium pressure. The heat transfer coefficient is higher at lowest volume concentration.

# References

1. Ravikumar SV, Haldar K, Jha JM et al (2015) Heat transfer enhancement using air-atomized spray cooling with water—$Al_2O_3$ nanofluid. Int J Therm Sci 96:85–93
2. Liang G, Mudawar I (2017) Review of spray cooling—part 1: single-phase and nucleate boiling regimes and critical heat flux. Int J Heat Mass Transf 115:1174–1205
3. Xu F, Gadala MS (2006) Heat transfer behavior in the impingement zone under circular water jet. Int J Heat Mass Transf 49:3785–3799
4. Taylor P, Das SK, Choi SUS, Patel HE (2007) Heat transfer in nanofluids—a review. Heat Transf Nanofluids 37–41
5. Nayak SK, Mishra PC, Parashar SKS (2016) Enhancement of heat transfer by water–$Al_2O_3$ and water–$TiO_2$ nanofluids jet impingement in cooling hot steel surface. J Exp Nanosci 11:1253–1273
6. Shojaeian M, Koşar A (2015) Pool boiling and flow boiling on micro- and nanostructured surfaces. Exp Therm Fluid Sci 63:45–73
7. Teamah MA, Khairat MM, Shehata A (2016) Numerical and experimental investigation of flow structure and behavior of nanofluids flow impingement on horizontal flat plate. Exp Therm Fluid Sci 74:235–246
8. Haddad Z, Abid C, Oztop HF, Mataoui A (2014) A review on how the researchers prepare their nanofluids. Int J Therm Sci 76:168–189
9. Tawfik MM (2017) Experimental studies of nanofluid thermal conductivity enhancement and applications: a review. Renew Sustain Energy Rev 75:1239–1253
10. Philip J, Shima PD (2012) Thermal properties of nanofluids. Adv Colloid Interf Sci 185:30–45

# Experimental Design-Based Analysis on Process Parameters for Head Loss in Pipe Bend

**Jatinder Pal Singh, Satish Kumar, S. K. Mohapatra and Gopal Nandan**

**Abstract** In the present, the parameters responsible for head loss have been optimized by using Taguchi approach. The head loss characteristics in transportation of slurry are function of various parameters like solid concentration, flow velocity and additive proportion. Present investigation is focused to recognize the most influencing parameter for the head loss in 90° pipe bend. Several influencing parameters of head loss are optimized with the help of the Taguchi method. $L_{16}$ array is used for experimental design of process parameters. The *S/N* ratio for head loss is characterized by using smaller-is-better rule. The solid concentration of slurry was varied from 30 to 60% (by weight) for flow velocity range of 2–5 m/s. Series of experiments are performed on pilot plant test loop to obtain head loss in pipe bend. Results obtained from experimental design reveal that flow velocity is found as a dominating parameter as compared to solid concentration and proportion of additive. Probability plot reveals that the experimental data follows the 95% level of confidence.

**Keywords** Head loss · Coal-water slurry · Pipe bend · Taguchi · ANOVA

## 1 Introduction

Slurry pipelines are widely used in industrial sector for transportation of solid matter. Solid particles mixed with liquid phase mainly water to form slurry [1, 2]. Transportation of solid matter through pipelines is more beneficial because it minimizes pollution as compared to traditional transportation. Moreover, this sys-

J. P. Singh (✉) · S. K. Mohapatra
Thapar Institute of Engineering and Technology, Patiala, Punjab, India
e-mail: jatinderpal.singh@thapar.edu

G. Nandan
Amity University, Noida, Uttar Pradesh, India

S. Kumar
National Institute of Technology, Jamshedpur, Jharkhand, India

tem requires minimum man power and maintenance cost. Presently, slurry conveying system is used to transport mineral ore, mineral tailings, fly and bottom ash in thermal power stations, etc. [3–6].

In previous decades, studies are carried out to investigate the head loss characteristics of solid–liquid suspension for flow through pipelines. Kumar et al. [7] studied head loss in the slurry pipeline can be improved by the addition of bottom ash for flow of fly ash water suspension. Bottom ash is act as better additive as compared to sodium sulfate and detergent. Senapati et al. [8] performed the head loss characteristics of coal ash slurry for flow through horizontal pipeline. They reported that appreciable decrease on head loss is observed with addition of bottom ash. Pavel and Zdenek [9] investigated the flow characteristics of fine and coarse sand-water slurries for flow through pipeline. They found that coarse slurry exhibits higher head loss as compared to fine slurries. The improvement in head loss behavior is noticed with addition of fine sand in coarse-water slurries. Valasak et al. [10] investigated the flow and head loss behavior of different sand slurries. They reported that sand slurries show Newtonian flow behavior at higher solid concentrations. Chen et al. [11] studied the effect of solid concentration, temperature and particle size on slip velocity of coal-water slurry suspension. They found that slip velocity is decreased by increasing solid suspension, particle size and slurry temperature. Kaushal et al. [12] conducted the study on flow behavior of glass beads through pipeline. They reported that head loss is increased by solid concentration and the rate of increase in higher at higher velocities. Literature review reveals that head loss characteristics are studied in past but limited to pipeline only, whereas very few research is reported on head loss through sharp pipe bends. So in present study, the attempt has been made to optimize the flow parameter responsible for the head loss in pipe bend for flow of fine coal-water slurry suspension. Taguchi approach along with ANOVA is used to investigate the most influencing factor responsible for head loss.

## 2  Materials and Methods

The coal sample used in study is procured from Jharia coal mine found in Jharkhand state of India. Coal sample is crushed and pulverized into the powder form. The pulverized coal sample is sieved with mechanical table-top sieve shaker. Coal sample is screened through series of sieves. Coal sample having particle size >53 μm is collected out after sieving operation and further used in experimentation. The slurry of different concentrations is prepared by mixing coal sample in water. Rheological experiments are performed to study the flow characteristics of solid–liquid suspension. It is observed that coal-water slurry shows Newtonian flow characteristics at 30% slurry concentration, whereas for concentration range of 40–60%, the slurry behaves like pseudo-plastic flow behavior. The morphological properties of coal are studied by SEM analysis. SEM image of coal sample is represented in Fig. 1. It is observed that coal particles are irregular in shape and having conical structure.

**Fig. 1** SEM micrograph of coal sample
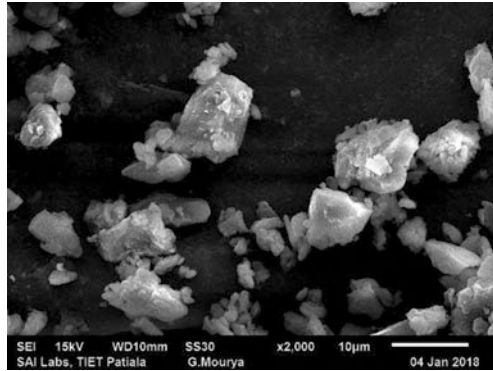
# 3 Design of Experiments

Head loss experiments are performed on pilot plant test loop developed at TIET, Patiala, Punjab, India. The schematic diagram of existing loop is presented in Fig. 2. The loop consists of slurry preparation tank in which slurry of desired concentration is prepared. The necessary driving force to solid slurry is provided by positive displacement slurry pump. The slurry after conveying through pipeline is discharged back to slurry tank so as to form a closed loop and also provide a continuous supply to pump. The flow rate and head loss in pipeline are measured with flow meter and pressure transducer installed at various locations in pipeline.
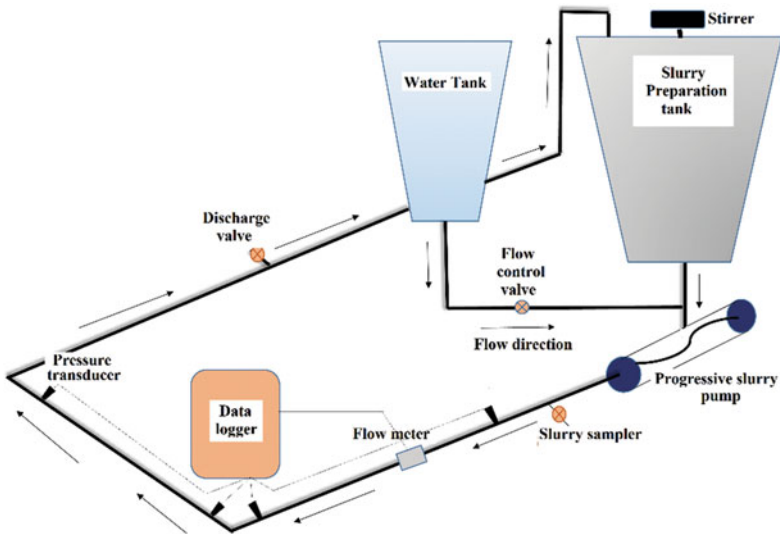


**Fig. 2** Schematic diagram of pilot plant teat loop

**Table 1** Control factors and levels

| Factors | Levels | | | |
|---|---|---|---|---|
| | I | II | III | IV |
| Solid concentration (% by weight) | 30 | 40 | 50 | 60 |
| Flow velocity (m/s) | 2 | 3 | 4 | 5 |
| Additive (% by weight) | 1 | 2 | 3 | 4 |

All the measuring devices are connected with data logger from where the readings are taken. A loop is also provided with slurry sampler to observe actual solid concentration flowing through pipeline.

The water tank is also mounted nearby slurry preparation tank. Water tank is used to provide makeup water during experimentation and to clean the pipeline after experimentation is over. The solid concentration is varied in the range of 30–60% for flow velocity range of 2–5 m/s. Sulfonic acid is used as an additive in present study. In order to reduce the number of experiments, Taguchi approach is used. L16 array is used for three input parameters having four levels as listed in Table 1. Head loss is considered as the response parameter. The input parameters are optimized by adopting smaller-is-better optimizing rule. The quality characteristics are dignified by signal-to-noise ratio through ANOVA, whereas signal represents the output characteristics and noise indicates undesirable attributes.

## 4 Results and Discussion

### 4.1 Effect of Solid Concentration and Additive on Head Loss

In present study, the effect of solid concentration and addition of additive on head loss along 90° bend is studied. The solid concentration is varied in the range of 30–60% for flow velocity range of 2–5 m/s. Figure 3a shows the variation in head loss with solid concentration at different flow velocities for flow of >53 μm fine coal-particulate slurry. It is seen that as the solid concentration of coal in slurry increases, the head loss is increased. As the flow velocity of slurry is increased, rate of increase in head loss is more as compared to lower flow velocities. The increase in head loss with solid concentration was observed due to increase in slurry viscosity of coal-water suspension. As the flow velocity of slurry is increased, the rapid increase in head loss is also observed. This increase in head loss is seen due to increase in flow separation and turbulence along the pipe bend. In present study, the attempt has been made to decrease the head loss by the addition of additive. The soap-based sulfonic acid is used as an additive. The variation in head loss with addition of additive at different flow velocities is represented in Fig. 3b. The addition of small percentage of sulfonic acid leads to decrease in head loss across bend section. It is seen that appreciable decrease in head loss is noticed irrespective
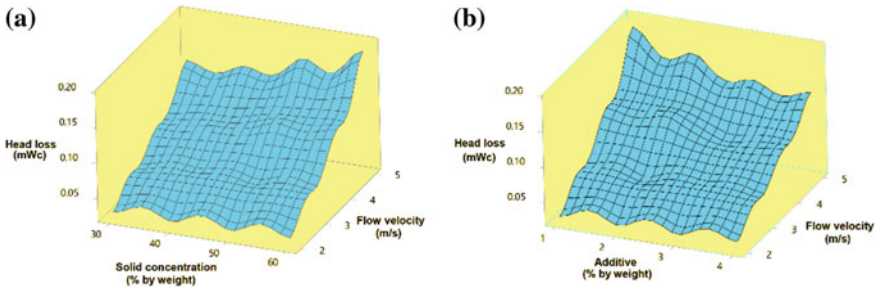
**Fig. 3** Variation in head loss with solid concentration and additive dosage

of the flow velocity. As the addition of sulfonic acid is increased from 3 to 4%, the head loss is reduced by small amount. This shows that further addition of sulfonic acid does not result in head loss. The optimum decrease in head loss is noted with 3% addition of sulfonic acid.

## 4.2 Signal-to-Noise Ratio

The *S/N* ratio for set of experiments is obtained from MINITAB 18 software. Experimental results are converted in terms of signal-to-noise ratio. The difference between in *S/N* ratio reflects the lost influencing parameter among the input parameters. The performance of experimental design is a function of *S/N* ratio. The smaller-is-better rule is adopted to determine the *S/N* ratio as given below.

$$S_{/N} = -10 \times \log\left[\frac{1}{n}\sum y_i^2\right] \tag{1}$$

where "*y*" represents the response parameter, and in present study, it is head loss and "*n*" is number of observations. The *S/N* ratio of different input parameters is determined by L16 orthogonal array as listed in Table 2. Smaller-is-better rule is used to determine the values of delta and rank. Table 3 summarized the response of *S/N* ratio of different factors. It is seen that the flow rank of flow velocity is highest among the solid concentration and additive. The delta value for the flow velocity is 0.12. The effect of *S/N* ratio on head loss is represented in Fig. 4. It is seen that minimum head loss is noticed at 30% solid concentration, 2 m/s flow velocity and 1% addition of sulfonic acid having highest value of *S/N* ratio, i.e., 31.24. However, the maximum head loss for flow of fine coal-water solid suspension is seen at 60% solid concentration, 5 m/s flow velocity and 1% addition of sulfonic acid having lowest value of *S/N* ratio, i.e., 14.49.

**Table 2** Experiment plan data $L_{16}$ and results

| S. no. | Parameter level | | | Head loss (mWc) | S/N ratio |
|---|---|---|---|---|---|
| | Solid concentration | Flow velocity | Additive | | |
| 1 | 30 | 2 | 1 | 0.02 | 31.24 |
| 2 | 30 | 3 | 2 | 0.05 | 25.24 |
| 3 | 30 | 4 | 3 | 0.08 | 21.39 |
| 4 | 30 | 5 | 4 | 0.13 | 17.36 |
| 5 | 40 | 2 | 2 | 0.03 | 30.36 |
| 6 | 40 | 3 | 1 | 0.06 | 24.12 |
| 7 | 40 | 4 | 4 | 0.09 | 20.47 |
| 8 | 40 | 5 | 3 | 0.14 | 17.05 |
| 9 | 50 | 2 | 3 | 0.03 | 30.11 |
| 10 | 50 | 3 | 4 | 0.06 | 24.58 |
| 11 | 50 | 4 | 1 | 0.11 | 18.88 |
| 12 | 50 | 5 | 2 | 0.16 | 15.66 |
| 13 | 60 | 2 | 4 | 0.03 | 30.22 |
| 14 | 60 | 3 | 3 | 0.06 | 23.89 |
| 15 | 60 | 4 | 2 | 0.12 | 18.56 |
| 16 | 60 | 5 | 1 | 0.19 | 14.49 |

**Table 3** Response table for S/N ratio

| Level | Solid concentration | Flow velocity | Additive |
|---|---|---|---|
| 1 | 0.07569 | 0.02827 | 0.09795 |
| 2 | 0.08106 | 0.05992 | 0.09079 |
| 3 | 0.09133 | 0.10259 | 0.07929 |
| 4 | 0.09993 | 0.15722 | 0.07998 |
| Delta | 0.02425 | 0.12895 | 0.01866 |
| Rank | 2 | 1 | 3 |

## 4.3 Interaction of Influencing Parameters for Head Loss

The interaction of various input parameters, i.e., flow velocity, solid concentration and additive on the response parameter, is represented in Fig. 5. The occurrence and non-occurrence of interaction between the parameters are noticed by non-parallel and parallel lines. Figure 5a–b shows that all the lines are non-parallel to each other. This shows that there is presence of interaction between additive-flow velocity and solid concentration-flow velocity. This seems that appreciable decrease in head loss can observed with change in solid concentration, flow velocity and additive percentage. Figure 5c shows that none of the lines is parallel to each other.
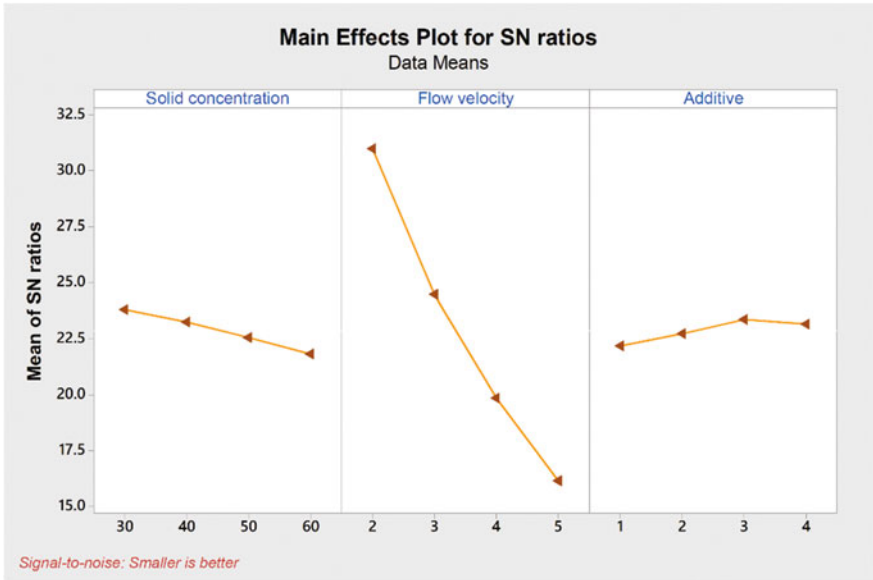
**Fig. 4** Main effect of *S/N* ratio on head loss
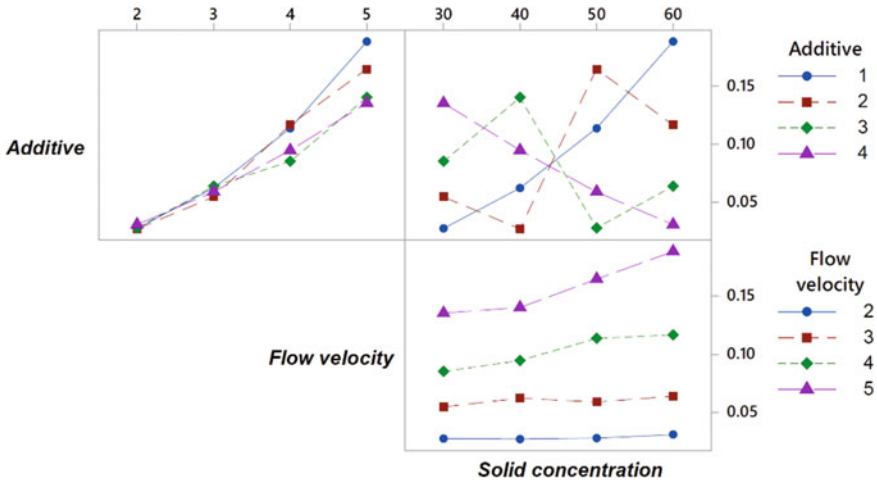


**Fig. 5** Interaction plots for head loss among various input parameters

So it is visualized that there is existence of interaction between flow velocity and solid suspension. This also implies that significant head loss is observed at higher solid concentration and flow velocities.

## 4.4 Analysis of Variance

The effect of various influencing parameters on head loss is analyzed by ANOVA technique. *S/N* ratio for head loss is determined by ANOVA and represented in Table 4. The flow velocity is found as a most influencing parameter whereas the additive is observed as a least effective. The root mean square value is found as 96.34%. Figure 6a–c represents the contour plots for head loss as a function of (a) additive versus *S/N* ratio, (b) solid concentration versus *S/N* ratio and (c) flow velocity versus *S/N* ratio. It is observed from Fig. 6a that head loss is less than 0.050 mWc for *S/N* ratio below 28.16 with addition of 4% sulfonic acid. However, the head loss is less than 0.175 mWc for *S/N* ratio below 15.2 with addition of 1% sulfonic acid. From Fig. 6b, it is seen that the head loss is less than 0.175 mWc for *S/N* ratio below 15 at solid concentration of 60%. Similar observations are observed from Fig. 6c. The normal distribution curve for the residual error was plotted and

**Table 4** Analysis of variance for S/N ratios

| Source | DF | Seq SS | Adj SS | Adj MS | F |
|---|---|---|---|---|---|
| Solid concentration | 3 | 8.901 | 8.901 | 2.967 | 288.85 |
| Flow velocity | 3 | 490.791 | 490.791 | 163.597 | 15927.11 |
| Additive | 3 | 3.279 | 3.279 | 1.093 | 106.41 |
| Residual error | 6 | 0.062 | 0.062 | 0.010 | |
| Total | 15 | 503.033 | | | |
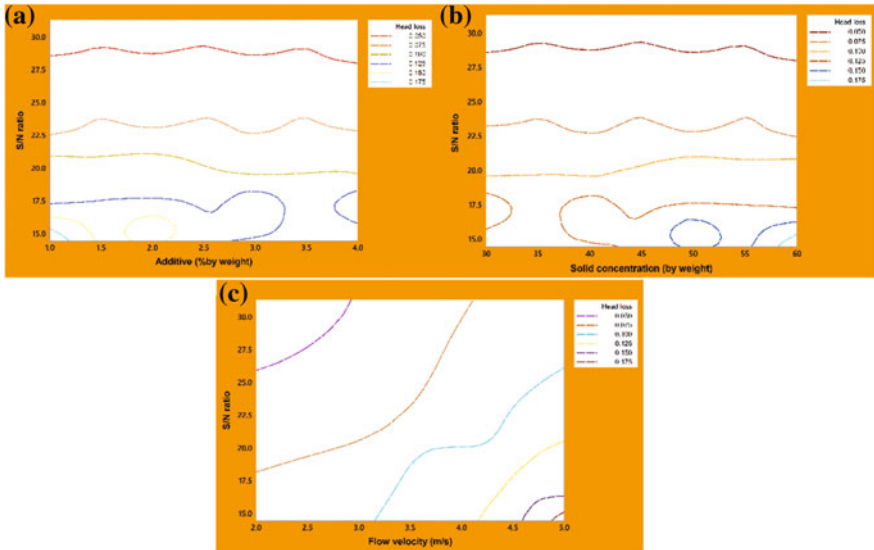


**Fig. 6** Contour plots for head loss versus *S/N* ratio for input parameters
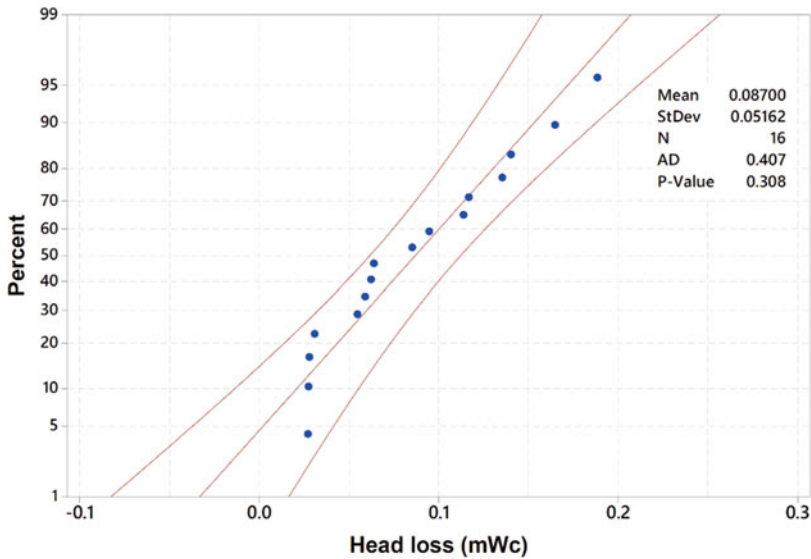
**Fig. 7** Probability plot for head loss

found to be a straight line as represented in Fig. 7. It is seen that the data points were lay within the range of $\pm 5.16\%$ and the p value is noticed as 0.31 that shows that non-liner augment of head loss.

## 5  Conclusion

Taguchi approach is used with ANOVA analysis so as to obtain the most influencing parameter responsible for head loss for flow of coal-water slurry. Solid concentration, flow velocity and additive are taken as input parameter, whereas the head loss is taken as response parameter. The following conclusions are drawn from present study.

- Increase in head loss is observed with increase in solid concentration and flow velocities. The rate of increase is higher at higher flow velocities, whereas addition of additive leads to decrease the head loss. The optimum addition of additive is found as 3%.
- There in significant interaction is found between all the input parameters from interaction graphs.
- Flow velocity is found as most dominant factor among all input parameters responsible for head loss.
- Head loss shows a normal distribution of errors that lies within the range of $\pm 5.16\%$ for confidence interval of 95%.

# References

1. Bantin RA, Streat M (1970) Dense-phase flow of solids water mixtures in pipelines. Proc Hydro Transp 1:1–24
2. Singh JP, Kumar S, Mohapatra SK (2017) Modelling of two phase solid-liquid flow in horizontal pipe using computational fluid dynamics technique. Int J Hydrogen Energy 42 (31):20133–20137
3. Duan Y, Chen L, Pu W, Zhao C (2009) CFD simulation of coal-water slurry flowing in horizontal pipelines. Korean J Chem Eng 26(4):1144–1154
4. Ganeshan G, Panda D (2017) Effect of oil viscosity on rheology of coal-oil mixtures. Int J Coal Prep Util 37(5):227–236
5. Kaushal DR, Thinglas T, Tomita Y, Kuchii S, Tsukamoto H (2012) CFD modeling for pipeline flow of fine particles at high concentration. Int J Multiph Flow 43:85–100
6. Singh J, Kumar S, Singh JP, Kumar P, Mohapatra SK (2018) CFD modeling of erosion wear in pipe bend for the flow of bottom ash suspension. Part Sci Technol https://doi.org/10.1080/02726351.2017.1364816
7. Kumar K, Kumar S, Gupta M, Garg HC (2017) Measurement of flow characteristics for multi-particulate bottom ash water suspension with additives. J Residuals Sci Technol 14 (1):11–17
8. Senapati PK, Mishra BK (2015) Bulk hydraulic disposal of highly concentrated fly ash and bottom ash-water slurries. Part Sci Technol 33(2):124–131
9. Pavel V, Zdenek C (2011) Effect of particle size distribution and concentration on flow behaviour of dense slurries. Part Sci Technol 29:53–65
10. Vlasak P, Chara Z (2009) Conveying of solid particles in newtonian and non-newtonian carriers. Part Sci Technol 27(5):428–443
11. Chen L, Duan Y, Pu W, Zhao C (2009) CFD simulation of coal-water slurry flowing in horizontal pipeline. Korean J Chem Eng 26(4):1144–1154
12. Kaushal DR, Sato K, Toyota T, Funatsu K, Tomita Y (2005) Effect of particle size distribution on pressure drop and concentration profile in pipeline flow of highly concentrated slurry. Int J Multiph Flow 31:809–823

# Novel Dryer cum Grinding Unit: A Thermal Analysis of Herbs Drying

**Avinash Kamble, Pritam Bakal and Kashinath Patil**

**Abstract** The herbs are being extensively used in Indian families as medical purpose in dried state. Many a time, it is open sun dried or control oven dried. But, open sun drying is unhygienic and inefficient process for herb drying. Further, the aroma of the herbs is get compromised at times in control oven drying. The present work discusses the herb drying process cum grinding in controlled sun drying with persevering the aroma and quality of the herb to be dried. The study shows the effect of collector area exposed to sunshine and the useful heat gain at collector end, and in the drying chamber, further the instantaneous thermal efficiency is evaluated. The various heat losses in the cabinet and their effect on the system efficiency are calculated. The area of collector is exposed to sunshine ($A_c$) (ranging from 0.6 to 1 m$^2$) for the study. The maximum thermal efficiency obtained is around 85.22%. It is observed that at lower temperature difference, i.e. at 5 °C, the instantaneous thermal efficiency is higher as compared to the 7 °C. Further, total 246 W-h is sufficient for grinding 20 kg dried herbs leaves. This study helps to find out the optimum conditions at which the drying process needs to be performed which would result in improved dryer performance.

**Keywords** Herbs · Drying · Collector area · Dryer

## 1 Introduction

Solar energy has been used for the crop drying since decades, and its importance is ever increasing. The fuel crisis raises alarm to utilize the fuel for heating and drying crops. Over a period, solar energy has been an important source of renewable energy and is also a sustainable energy resource. Different types of solar crop dryings have been practised in the agricultural drying [1]. Solar radiation in the

A. Kamble (✉) · P. Bakal · K. Patil
Department of Mechanical Engineering, K. J. Somaiya College of Engineering, Vidyanagar, Vidyavihar, Mumbai 400077, India
e-mail: avinash.ak@somaiya.edu

form of solar thermal energy is an alternative source of energy which can be used for dying vegetables, herbs, herbal leaves, agricultural grains, fruits and other products. It is well-known fact that in the developing countries a large amount of perishable goods do not reach to the consumer but get lost well before reaching to the customer. Thus, the product could be stored in dried state for longer period which retains the nutritional value of food product. Thus, to reduce the losses and increase the profitability of the agricultural product, the solar drying would be better option [2]. In the agricultural products like fruits and herbs, drying is carried out in open sun. However, it is observed that airborne particles, dust, insects, bird poop, other foreign elements get added to the food product, and it reduces the quality of the food. Sometimes, the quality degrades to the extent the food products are no longer useful for utilization. The most common type of dryer is a cabinet or chimney solar dryers [3]. In India, longer duration of sunshine is available. Roughly, 250–300 sunshine days are available which are ideal situation for the solar drying. So, India's atmosphere is the ideal place for drying crops. Totally around 3000 h of bright sunshine is available in a year [4]. A. K. Bhardwaj, Ranchan Chauhan, Raj Kumar, Muneesh Sethi and Adit Rana conducted an experimental investigation on indirect solar dryer integrated with phase change material for drying of *valeriana jatamansi* in Himalayan region of a Himachal Pradesh, and the results indicated that there was reduction in drying time by 37.54 and 64.29% compared to heat pump drying and shade drying [5]. Abhay Lingayat, Chandramohan and Raju (2016) fabricated an indirect type of banana dryer. Solar dryer consisted of solar flat plate collector of area 2 m$^2$, and the size of the drying cabinet was $1 \times 0.4 \times 1$ m. The experiments were conducted from March to June 2016, and efficiency of solar collector and drying chamber were 31.50 and 22.38% was obtained [6]. Bukola O. Bolaji and Ayoola P. Olalusi (2008) constructed and evaluated the mixed mode solar dryer for food preservation. The dryer was tested in month of September, and the material was yam chips. The cabinet was transparent at walls as well as roof so that the cabinet also absorbs solar energy through the walls and roof which resulted in increase in cabinet temperature by 74%, and the efficiency of system was around 57.5% with the drying rate of 0.62 kg/h [7]. Adelaja and Babatope developed the natural convection solar dryer for plantain drying. The performance of dryer was analysed, and experiments were conducted for drying of plantain (3 mm) samples. The results indicated that collector and instantaneous thermal system efficiencies obtained are 46.4 and 78.3%, respectively, with 0.7 m$^2$ collector area exposed to sunshine [8].

This present paper discusses the effect of collector area (exposed to sunshine) on various parameters such as useful heat energy and efficiency of a collector. Further, the effect of the temperature difference with drying material and chamber temperature is evaluated. The various losses that could arrive in the cabinet drying are discussed. The PV system is designed to power the air movement as well as grinding unit.

## 2 Experimental Analysis

The experiments were carried on herbs leaves like basil, neem and lemon grass sample of 1 g and dried under open sun, and the values of decreasing weight of sample were monitored and recorded. Further, total moisture content in the herbs are evaluated, and time taken for drying is recorded. The solar insolation available on the day is also recorded. Table 1 shows the decreasing mass of basil, neem and lemon grass sample with respect to the time of day and solar insolation at a particular day.

### 2.1 Moisture Content in Basil, Wet Basis

$$\text{moisture content} = \frac{(\text{initial mass} - \text{final mass})}{\text{initial mass}} * 100$$
$$\text{moisture content} = \frac{(1 - 0.13)}{1} * 100$$
$$\text{moisture content} = 87\%$$

### 2.2 Moisture Content in Neem, Wet Basis

$$\text{moisture content} = \frac{(\text{initial mass} - \text{final mass})}{\text{initial mass}} * 100$$
$$\text{moisture content} = \frac{(1.05 - 0.39)}{1.05} * 100$$
$$\text{moisture content} = 63\%$$

**Table 1** Mass variation of basil, neem and lemon grass

| Time | Solar radiation (W/m²-h) | Weight of sample in grams (g) | Weight of sample in grams (g) | Weight of sample in grams (g) |
|------|------|------|------|------|
| | Day 1 | Basil | Neem | Lemon grass |
| 11.30 pm | 704 | 1.00 | 1.05 | 1.05 |
| 12.30 pm | 748 | 0.19 | 0.45 | 0.50 |
| 13.30 pm | 736 | 0.13 | 0.39 | 0.47 |
| 14.30 pm | 667 | 0.13 | 0.39 | 0.43 |
| 15.30 pm | 508 | 0.13 | 0.39 | 0.42 |
| 16.30 pm | 280 | 0.13 | 0.39 | 0.42 |
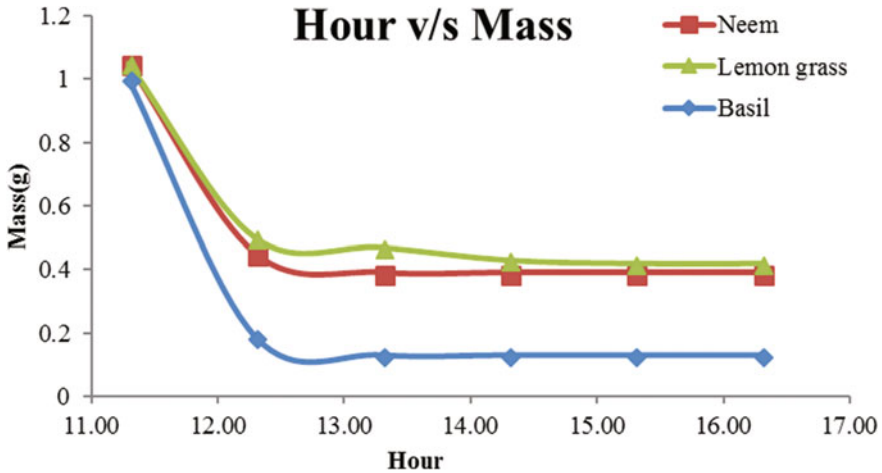
**Fig. 1** Variation of the moisture with the time of the day

## 2.3 Moisture Content in Lemon Grass, Wet Basis

$$\text{mosture content} = \frac{(\text{initial mass} - \text{final mass})}{\text{initial mass}} * 100$$

$$\text{mosture content} = \frac{(1.05 - 0.42)}{1.05} * 100$$

$$\text{mosture content} = 60\,\%$$

Figure 1 shows the mass of three samples used for drying with time of day. It is seen that the drying of basil is faster than neem and lemon grass. Initial rate of drying for all the samples is much faster, and after 2 h of drying, all samples reach the stable moisture (bonded moisture). Further, no more reduction in moisture content is observed. The final moisture content is about 0.13 g for basil, 0.39 g for neem and 0.42 g for lemon grass. The dried samples are then grinded which can be preserved for long time duration.

## 3 Design Analysis

## 3.1 Thermal Analysis

The useful heat gain and heat losses are evaluated by applying the heat balance across the collector and for the drying chamber. The fundamental starting equations used for collector analysis are given by Duffie and Beckman [9].

Grashof number, Gr

$$Gr = \frac{g * \rho^2 * \beta * \Delta T * L^3}{\mu^2} \tag{1}$$

Nusselt number, Nu

$$Nu = \frac{hxL}{k} \tag{2}$$

where Nusselt number is used to calculate the heat transfer coefficient, and it depends on the various areas of the cabinet.

- For horizontal plate: above surface

$$Nu = 0.54 Ra_L^{1/4} \quad \text{for} \quad 10^4 \leq Ra_L \leq 10^9 \tag{3}$$

$$Nu = 0.15 Ra_L^{1/3} \quad \text{for} \quad 10^7 \leq Ra_L \leq 10^{11} \tag{4}$$

- For horizontal plate: below surface

$$Nu = 0.274 Ra_L^{1/4} \quad \text{for} \quad 10^5 \leq Ra_L \leq 10^{10} \tag{5}$$

- For vertical heated plate

$$Nu = 0.68 + \frac{0.67 Ra_L^{1/4}}{\left(1 + [0.492/Pr]^{9/16}\right)^{4/9}} Ra_L \leq 10^9 \tag{6}$$

## 3.2 Collector Analysis

Radiation in the collector [10]

$$Q_{\text{rad.in}} = \alpha * A_c * I \tag{7}$$

Heat loss through the base of the collector

$$Q_u = \frac{\Delta T}{\sum R_{cb}} \tag{8}$$

$$\text{where,} \sum R_{cb} = \frac{1}{h_{cb} * A_{cb}} + \frac{X}{k_{cb}}$$

Useful heat gain of the collector

$$Q_u = mc_p(T - T_a) = Q_{rad.in} - Q_{loss} \tag{9}$$

Instantaneous thermal efficiency of collector

$$\eta_c = \frac{Q_u}{Q_{rad.in}} * 100 \tag{10}$$

## 3.3   Cabinet Analysis

Heat transfer through the wall of the collector case into the cabinet, $Q_{gc.in}$

$$Q_{gc.in} = \frac{\Delta T_{gc}}{\sum R_{gc}} \tag{11}$$

$$\text{where,} \sum R_{gc} = \frac{1}{h_{gc} * A_{gc}} + \frac{x}{k * A_{gc} * h_{gc}}$$

Heat radiated to the environment by the cabinet

$$Q_{rad.out} = \epsilon_m * \sigma * A_d * (T^4 - T_a^4) \tag{12}$$

where

$\epsilon_m$   Emissivity of metal
$\sigma$   Stefan–Boltzmann's constant

Heat lost by side wall, $Q_{vc}$

$$Q_{vc} = \frac{\Delta T}{\sum R_{vc}} \tag{13}$$

$$\text{where,} \sum R_{vc} = \frac{1}{h_{vc} * A_{vc}} + \frac{x}{k * A_{vc}}$$

Heat lost through the top wall, $Q_{tc}$

$$Q_{tc} = \frac{\Delta T}{\sum R_{tc}} \tag{14}$$

Where $\sum R_{tc} \dfrac{1}{h_{tc} * A_{tc}} + \dfrac{x}{k * A_{tc}}$

Heat lost through the bottom wall, $Q_{bc}$

$$Q_{bc} = \frac{\Delta T}{\sum R_{bc}} \qquad (15)$$

where, $\sum R_{bc} = \dfrac{1}{h_{bc} * A_{bc}} + \dfrac{x}{k * A_{bc}}$

Total heat loss through the cabinet, $Q_{loss}$

$$Q_{loss} = Q_{vc} + Q_{tc} + Q_{bc} + Q_{rad.out} \qquad (16)$$

System Efficiency, $\eta_{s}$

$$\eta_{s} = \frac{Q_{u}}{Q_{rad.out} + Q_{gc}} \qquad (17)$$

## 4  Results and Discussion

### 4.1  Collector Analysis

Figure 2 shows the outlet temperature compared to the ambient temperature; it is observed that as solar radiation increases, the outlet temperature also increases and the maximum temperature obtained is around 45 °C at 748 W/m$^2$ which is considerably good for drying.
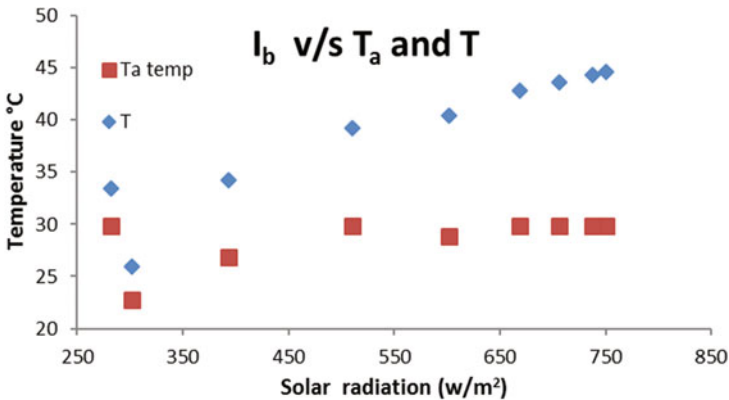


**Fig. 2** Variation of ambient temperature ($T_a$) and collector temperature ($T$) with solar radiation
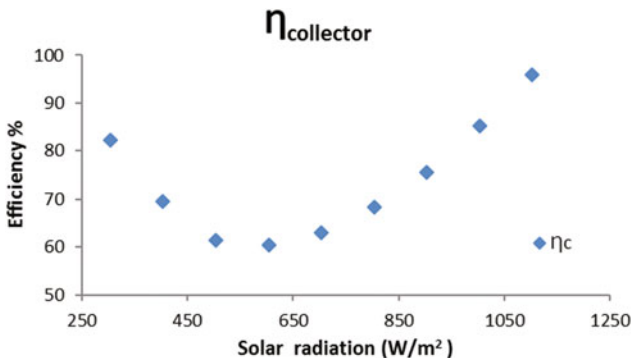
**Fig. 3** Solar radiation v/s efficiency of collector
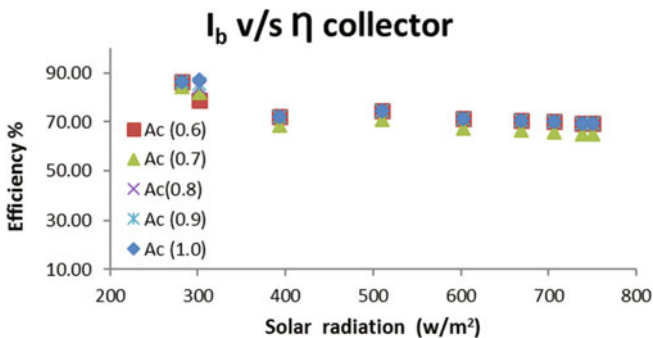


**Fig. 4** Solar radiation v/s collector efficiency at different collector surface area ($A_c$)

Figure 3 shows the efficiency of the solar box-type air collector with change in solar radiation. It is observed that the minimum thermal efficiency obtained is around 60%, while the thermal efficiency of box-type collector is 70% for lower solar radiation of 400 and 800 W/m². It is due to the fact that at lower solar radiation, the air temperature is much lower, and thus, the radiation and convection losses are very low, while at 800 W/m², the thermal efficiency is higher due to higher air temperature providing the higher useful energy, and thus, thermal efficiency is higher.

Figure 4 shows that the thermal efficiency of the box-type solar sir heater for various collector surface areas ranges from 0.5 to 1.0 m². It is observed that as area increases, the thermal efficiency increases. The increase in the thermal efficiency is not significant as compared the increase in the collector area. Further increase in the radiation the thermal efficiency decreases as the effective thermal losses increases. At higher thermal radiation, the thermal efficiency decreases from 85% at 300 W/m² to 72% at 800 W/m².

## 4.2 Cabinet Analysis

Figures 5, 6 and 7 show the useful heat energy of the collector along with the drying chamber. The maximum useful heat energy obtained at around 5–6 h after sunrise and in the morning session increases and in the afternoon session in decreases. The drying heat energy obtained is always less than 25–40 W less than the collector useful heat energy at any time of operation and with various changes in the drying temperatures with the collector temperature i.e. temperature difference form 5, 6 and 7 °C. It is observed that the maximum useful heat gain obtained is higher at 5 °C temperature difference followed by 6 and 7 °C.
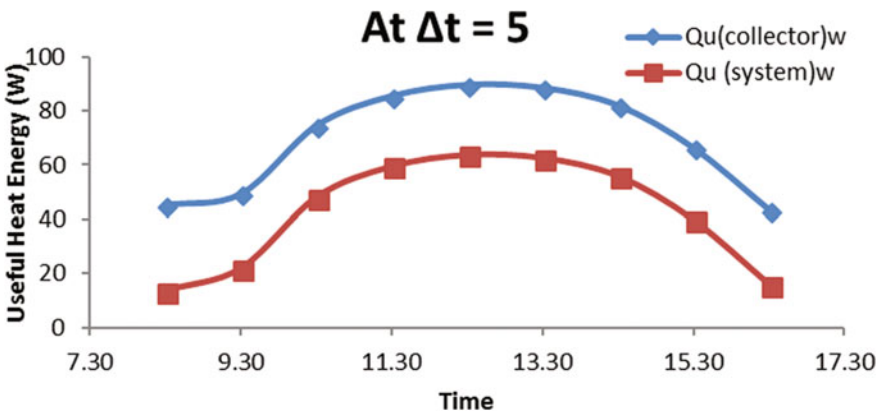


**Fig. 5** Variation of useful heat energy versus time at $\Delta t = 5$
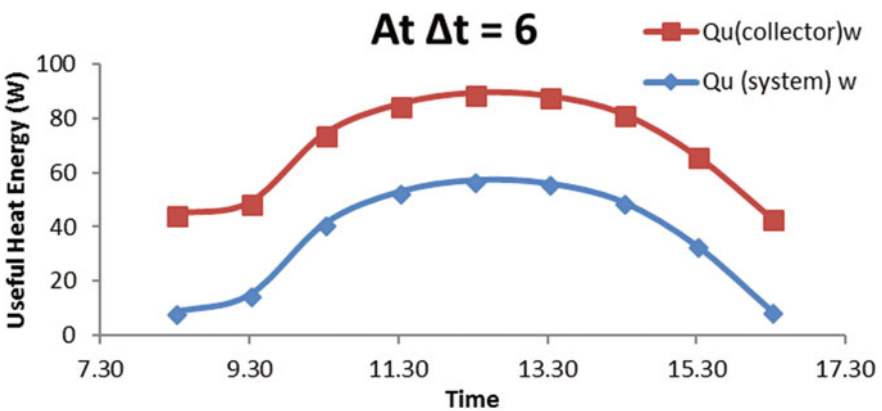


**Fig. 6** Variation of useful heat energy versus time at $\Delta t = 6$
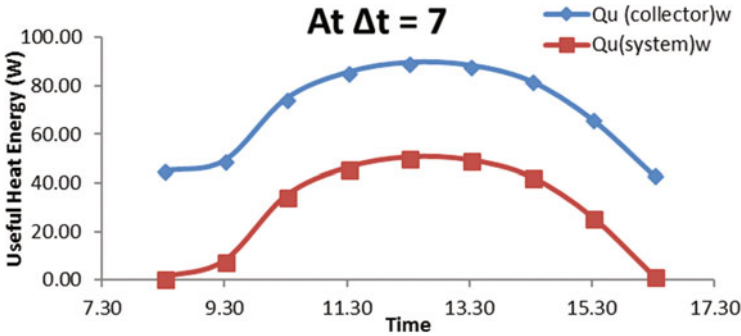
**Fig. 7** Variation of useful heat energy versus time at $\Delta t = 7$
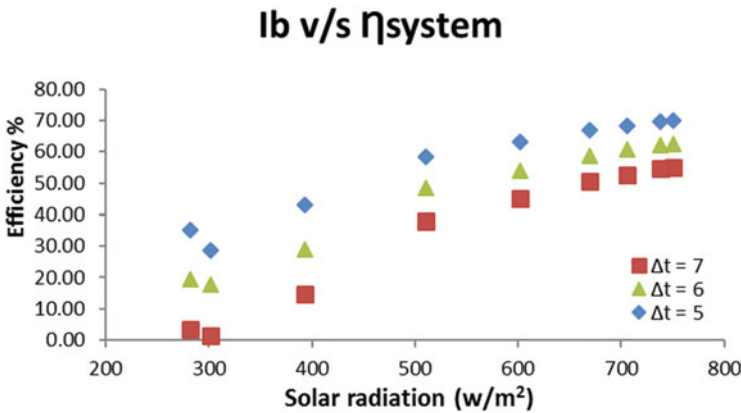


**Fig. 8** System efficiency variation with solar radiation

Figure 8 shows that change in efficiency with the change in the temperature difference with collector and the drying chamber. It is observed that at lower temperature difference at 5 °C is higher as compared to the 7 °C. It is linearly increasing with the change in radiation. The minimum thermal efficiency at 5 °C temperature difference is from 29% at 300 W/m$^2$ solar radiation to 70.6% at 800 W/m$^2$. Similarly, for 7 °C temperature difference, thermal efficiency is from 2.2% at 300 W/m$^2$ to the 55.7%, and for 6 °C the thermal efficiency, thermal efficiency is from 18.8% at 300 W/m$^2$ to 63.3% for 800 W/m$^2$.

## 4.3 Grinding Unit Analysis

Table 2 shows the number of solar PV panels required for herb grinding. Considering 1 hp motor to be operated for 20 min of operation, the minimum

**Table 2** Grinding unit calculations

| Load | Watts | Hours/day | W-h | No. of batteries | No. of modules |
|------|-------|-----------|-----|------------------|----------------|
| Motor | 746 | 0.33 | 246.18 | 1 | 1 |

energy storage is 246 Wh and the inverter of the similar rating to be selected with a single battery of the capacity 12 V with 100 Amp/h. The panel rating for the operation is 12 V with 75 WP. The single panel will be sufficient to operate the grinding mill for herb grinding.

# 5 Conclusion

The performance of solar dryer can be improved by changing dryer parameters like Ac (collector area exposed to sunshine) and cabinet design parameters. It is observed that area of collector exposed to sunshine (Ac) (ranging from 0.6 to 1 m$^2$) has a significant effect on useful heat and efficiency of collector. The maximum thermal efficiency obtained is around 85.22%. And it is observed that at lower temperature difference at 5 °C is higher efficiency as compared to the 7 °C. For grinding 20 kg of dried herbs, one PV panel of specification 75 Wp with 12 V is sufficient to generate 246 Wh in day.

# References

1. Adelaja AO, Ojolo SJ (2010) Design, analysis and experimental evaluation of photovoltaic forced convection solar dryer for the tropics. Int J Eng Res Afr 3:49–61
2. Belessiotis V, Delyannis E (2011) Solar drying. Sol Energy 85:1665–1691
3. Madhlopa A, Jones SA, Kalenga Saka JD (2002) A solar air heater with composite absorber systems for food dehydration. Renew Energy 27:27–37
4. Basu SN, Karmakar A, Bhattacharya P (2015) Growth of solar energy in India—present status and future possibilities 3(5). ISSN: 2347–2820 (Online)
5. Bhardwaj AK, Chauhan R, Kumar R, Sethi M, Rana A (2017) Experimental investigation of an indirect solar dryer integrated with phase change material for drying Valeriana jatamansi (medicinal herb). Case Stud Therm Eng 10:302–314
6. Lingayat A, Chandramohan VP, Raju VRK (2017) Design, development and performance of indirect type solar dryer for banana drying. Energy Procedia 109:409–416
7. Bolaji BO, Olalusi AP (2008) Performance evaluation of a mixed-mode solar dryer. AU J Technol 11(4):225–231
8. Adelaja AO, Babatope BI (2013) Analysis and testing of a natural convection solar dryer for the tropics. J Energy, 8, ArticleID479894
9. Duffie JA, Beckman WA (1980) Solar engineering of thermal processes, 2nd edn. Wiley, Hoboken
10. Fagbenle RO (1991) Optimum collector tilt angles and average annual global radiation for Nigerian locations. Niger J Renew Energy 2:9–17

# Investigating the Effect of Geometry on Micro-Channel Heat Exchangers Using CFD Analysis

**J. Derek, A. N. Jinoop, C. P. Paul, S. L. Nidhin, N. G. Rasu and K. S. Bindra**

**Abstract** Micro-channel heat exchangers (MCHEs) are compact and robust heat exchangers with high surface area per unit volume facilitating closer temperature of approach. MCHE is conventionally fabricated using photochemical etching followed by diffusion bonding (PCED). Though PCED allows various flow path designs for improved heat exchange, it is not deployed for MCHE with cross sections other than semi-circular. Laser additive manufacturing (LAM) can overcome this limitation. The present study is focused on thermo-hydraulic simulation of LAM built MCHE with various cross sections. A 3D steady-state computational fluid dynamics (CFD)-based analysis is performed using CFD code ANSYS CFX to estimate the temperature, pressure drop and velocity distribution across the length of channel and variation of friction factor with Reynolds number. The working fluid is supercritical helium and material of construction of MCHE is Inconel 617 (IN 617). The temperature-dependent thermo-physical properties of helium and IN 617 are taken into account for the above simulation. To validate the simulation output, the results for conventionally fabricated PCHE are compared with that of previously published results and are found to be within 5%. The study of MCHE with cross sections other than semi-circular (i.e. square and circular) is also done using the same CFD code. From this numerical analysis, it is found that the heat transfer is maximum in square geometry while pressure drop, velocity across the channel and friction factor are the least for square geometry.

**Keywords** MCHE · CFD · Supercritical helium · Heat transfer · Inconel 617 · Laser additive manufacturing

J. Derek (✉) · N. G. Rasu
Vellore Institute of Technology, Vellore 632014, Tamil Nadu, India

A. N. Jinoop · C. P. Paul (✉) · S. L. Nidhin · K. S. Bindra
Raja Ramanna Centre for Advanced Technology, Indore 452013, Madhya Pradesh, India
e-mail: paulcp@rrcat.gov.in

A. N. Jinoop · C. P. Paul · S. L. Nidhin · K. S. Bindra
BARC Training School Complex, Homi Bhabha National Institute, Anushakti Nagar,
Mumbai 400094, Maharashtra, India

# 1  Introduction

With the growing need for energy resources, high quality air, and drastic climatic changes, several multinationals all around the globe are developing nuclear reactors [1]. An important component of nuclear reactors is a midway heat exchanger that transfers heat between primary and secondary coolant system [2].

Hesselgreaves indicated that the design of heat exchanger includes learning of fluid flow and heat transfer taking place at different operating and design conditions [3]. One of the main upcoming heat exchanger candidates is micro-channel heat exchangers (MCHEs). The channels in MCHE are fabricated by photo chemically etching the plates followed by bonding to each other using diffusion bonding and forming a single block [4]. Kern explains that the strength of the heat exchanger is based on the mechanical design of channel through which the liquid is flowing [5]. UK-based company Heatric commercially fabricates straight and zigzag channel MCHE [6]. Ajinkya et al. did numerical analysis on the MCHE with S-$CO_2$ as the working fluid. It was observed that the overall heat transfer is dependent on Reynolds number and channel diameter. Further as the channel diameter reduces, the heat transfer coefficient increases, but pressure drop increase with decrease in channel diameter [7].

Kim et al. and Ishizuka et al. investigated straight and zigzag channel MCHE and found that the heat transfer performance in both of them is approximately similar [8, 9]. Aneesh et al. performed numerical analysis on straight MCHE and attributed that the overall heat transfer and pressure drop increase with mass flow rate [10]. Wu et al. studied straight micro-channel and concluded that the friction factor and Reynolds number of the liquid flowing can be quite different for different cross sections [11]. Mohammed et al. studied various channel geometries and revealed that the pressure drop and wall shear stress are minimum for straight channel [12]. Pra et al. did experimental steady-state analysis on MCHE with air as the working fluid; the maximum temperature achieved was 780 K; this proves the high-temperature applications of MCHE [13]. All the above literature is based on fabrication of MCHE using photochemical etching followed by diffusion bonding (PCED). With PCED, we can achieve different flow paths for better thermal performance, but it cannot be used to fabricate MCHEs with different cross sections. Laser additive manufacturing (LAM) can be possible solution to this deviation. LAM uses a high-power laser beam as a heat energy source to melt a layer of the substrate and powder to deposit a new layer according to the dimensions defined. Layer by layer deposition results in fabrication of 3D components. LAM has many advantages over conventional subtractive manufacturing techniques, i.e. less time for production, controlled process and potential to manufacture functionally graded entities, it gives material freedom, design freedom and logistics freedom [14]. Considering the above advantages of LAM over conventional techniques, different cross sections can be used for fabrication of MCHE. Thus, in the present work, effect of different geometries on the performance of the heat exchanger is evaluated. Inconel 617 is used as the heat exchanger material and supercritical helium is used as the liquid flowing in both the hot and cold channels.

## 2　Numerical Modelling

Figure 1 represents the geometry of semi-circular, circular and square cross sections used for current work. The top and bottom cross sections represent the cold and hot channel, respectively. As presented in Fig. 1 cross section dimensions are $6 \times 3.2$ mm while the channel diameter is 2 mm for circular and semi-circular, the side of the square channel is 2 mm. The overall channel length is 247 mm.

In this work, the Reynolds-averaged Navier–Stokes (RANS) model is used for modelling turbulence. The shear stress transport (SST) model is utilized for evaluating the Reynolds shear stress. $K$-$\omega$ based SST model records the transport of turbulent shear stress and gives accurate predictions about the flow in the beginning and the quantity of flow separated under adverse pressure conditions [15]. ANSYS CFX 18.1 is used for numerical evaluation of the MCHE [16]. The governing equations are conservation of mass, momentum and energy as presented in published literature [7]. The convection terms are solved by first-order upwind scheme. The unstructured tetrahedral meshes are created using ANSYS Meshing software by applying the multi-zone method and body sizing methodology as shown in Fig. 2.

The elements were refined until a number of elements yielded less than 1% difference in the overall temperature difference in both hot and cold channels. The boundary conditions applied to the design are shown in Table 1. The mass flow inlet and pressure outlet boundary conditions are applied at inlet and outlet of the channels. Inconel 617, a Ni-based alloy is chosen as the material for MCHE due to its high tolerance at extreme temperature and pressure conditions. The thermo-physical properties of the solid and liquid are considered as a function of temperature. The properties S-He are obtained from NIST database [17] and that of Inconel 617 are obtained from the literature [18].

**Fig. 1** Schematic of MCHE for semi-circular, circular and square channel
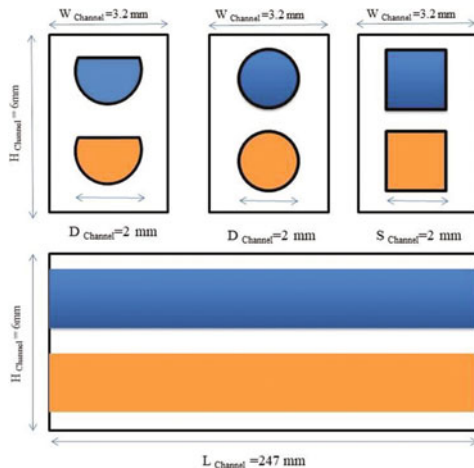
**Fig. 2** Circular MCHE
meshed face on one end
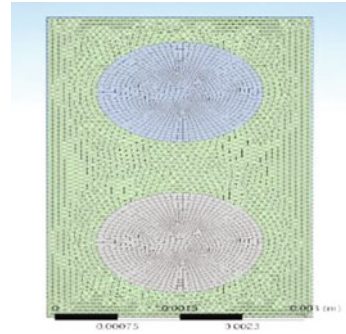


**Table 1** Boundary
conditions

| Boundary | B.C's |
|---|---|
| Fluid inlet | Mass flow inlet |
| Fluid outlet | Pressure outlet |
| Top wall | Periodic |
| Bottom wall | Periodic |
| Side walls | Adiabatic wall |
| Front wall | Adiabatic wall |
| Back wall | Adiabatic wall |

**Table 2** Size parameters

| Variable | Values (mm) |
|---|---|
| Diameter of circle/side of square (D channel/S channel) | 2 |
| Height (H channel) | 6 |
| Width (W channel) | 3.2 |
| Length (L channel) | 247 |

**Table 3** Boundary
conditions for temperature
and pressure drop along the
length

| Property | Cold-He | | Hot-He | |
|---|---|---|---|---|
| | Inlet | Outlet | Inlet | Outlet |
| T(K) | 1170 | – | 810 | – |
| P(bar) | – | 0.3 | – | 0.3 |
| ṁ (Kg/hr) | 3.04 | – | 3.04 | – |

The geometrical parameters are shown in Table 2 and the boundary conditions are shown in Table 3. Temperature, pressure and velocity distribution are evaluated at Reynolds number 15000 for all the geometry, while the variation of friction factor with Reynolds number is also obtained.
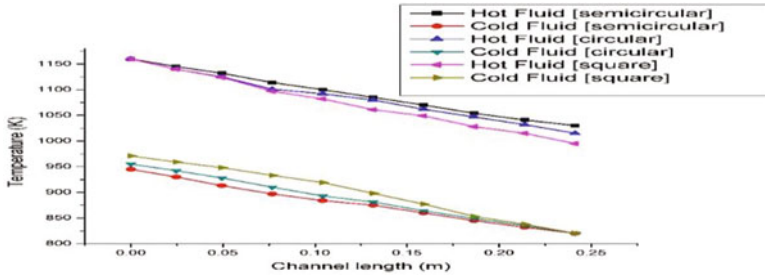
**Fig. 3** Temperature distribution of hot and cold channel along the length at Re 15000

# 3  Results and Discussion

## 3.1  Temperature Distribution Along the Channel Length

From Fig. 3, it is observed that the variation of temperature is approximately linear for all the cross sections. The slope of cold S-He is slightly lower than hot S-He. It is evident from Fig. 3 that the overall heat transfer taking place in the semi-circular channel is lowest followed by circular channel and the highest heat transfer takes place in the square channel. The heat transfer variation is due to the variation in the lateral/curved surface area where most of heat transfer takes place which is maximum for the square channel.

## 3.2  Pressure Variation Along the Channel Length

From Fig. 4, pressure drop is maximum in semi-circular channel followed by circular channel and the minimum pressure drop is in the square channel. This trend is mainly due to the inverse proportionality of pressure difference with the hydraulic diameter. As square possess maximum hydraulic diameter the pressure drop is lowest in that channel [8].
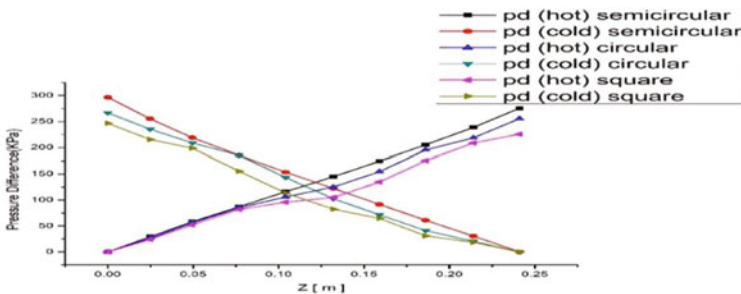


**Fig. 4** Pressure drop of hot and cold channel along the length at Re 15000
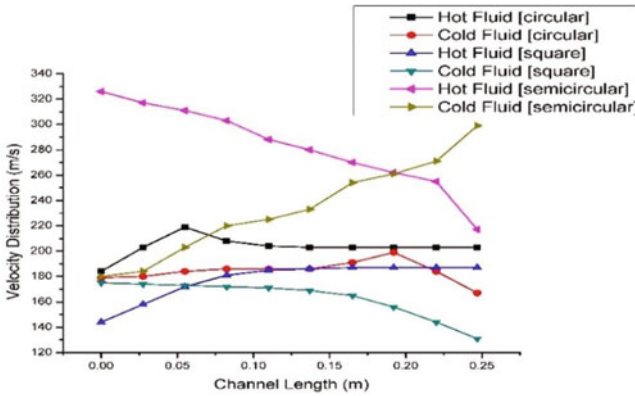
**Fig. 5** Velocity distribution of hot and cold channel along the length at Re 15000

## 3.3 Velocity Distribution Along the Channel Length

From Fig. 5, it is evident that the liquid flowing through semi-circular channel has the maximum velocity followed by circular channel and finally, the lowest velocity is in the square channel. This is due to fact that the cross-sectional area through which the fluid flows is inversely proportional to the velocity of the fluid. The velocity of the fluid in the circular channel becomes constant after a steep increase; this is due to the uniform geometry of circular channel. It is also due to this higher velocity of the fluid in the semi-circular channel and the overall heat transfer is less than the other two geometries.

## 3.4 Friction Factor with Reynolds Number

The friction factor variation in straight channel MCHE is shown in Fig. 6. It is observed that the friction factor decreases with the increase in Reynolds number. The friction factor of cold S-He is higher than hot S-He; this is due to lower density
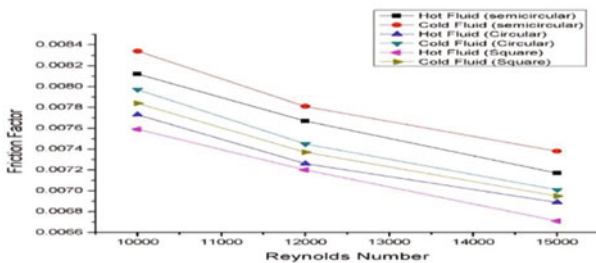


**Fig. 6** Friction factor variation with Reynolds number

values of fluid flowing in cold channel. As density decreases friction, factor increases, and friction factor decreases with the increase in Nusselt number [6]. The friction factor is maximum in semi-circular channel followed by circular channel and at least in the square channel.

# 4　Conclusions

Numerical analysis of straight MCHE with different geometries for S-He as the working fluid has been performed; this analysis leads to the following main conclusions:

- The temperature variation in the straight channel for different cross section is approximately linear. The temperature difference or the overall heat transfer is highest in the square channel and least in semi-circular, because of higher curved/lateral surface area.
- The pressure drop is maximum in semi-circular channel followed by circular channel and least in the square channel; this is due to the inverse relation of pressure drop with hydraulic diameter.
- The velocity of fluid across the channel is inversely proportional to the cross-sectional area, thus the semi-circular channel is having maximum velocity and the least in the square channel.
- Reynolds number variation with friction factor suggests that friction factor decreases with the increase in Reynolds number. Friction factor for cold S-He is higher than that of hot S-He.

# References

1. International Atomic Energy Agency. https://www.iaea.org/about/organizational-structure/department-of-nuclear-energy/division-of-planning-information-and-knowledge-management/planning-and-economic-studies-section. Last accessed on 12/03/18
2. Zhang X, Shi S, Christensen RN, Sun X (2017) Review on mechanical design of printed circuit heat exchangers, ICONE 25, Shanghai, China, 2–6 July 2017
3. Hesselgreaves JE, Law R, Reay D (2001) Compact heat exchanger: selection design and operation. Elsevier, UK, pp 35–38
4. Micro Channel Heat Exchanger [MCHE] Wikipedia. https://en.wikipedia.org/wiki/microchannelheatexchanger. Last accessed on 26/02/18
5. Kern DQ (1983) Process heat transfer. McGraw Hill book Company, Japan, pp 150–153
6. Pierres RL, Southall D, Osborne S (2011) Impact of mechanical design issues on printed circuit heat exchangers. In: Proceedings of $SCO_2$ power cycle symposium, University of Colorado, Boulder, CO, 24–25 May 2011

7. Meshram A, Jaiswal AK, Khivsara SD, Ortega JD, Ho C, Bapat R, Dutta P (2016) Modelling and analysis of a printed circuit heat exchanger for supercritical $CO_2$ power cycle applications. Appl Therm Eng 109:861–870
8. Kim SG, Lee Y, Ahn Y, Lee JI (2016) CFD aided approach to design printed circuit heat exchangers for supercritical $CO_2$ Brayton cycle application. Ann Nucl Energy 92:175–185
9. Ishizuka T, Ngo TL, Kato Y, Nikitin K (2007) Heat transfer and pressure drop correlations of micro-channel heat exchangers with S-shaped and zigzag fins for carbon dioxide cycles. Exp Therm Fluid Sci 32(2):560–570
10. Aneesh AM, Sharma A, Srivastava A, Vyas KN, Chaudhuri P (2016) Thermal-hydraulic characteristics and performance of 3D straight channel based printed circuit heat exchanger. Applied 97: 474–482
11. Wu HY, Cheng P (2003) Friction factors in smooth trapezoidal silicon micro channels with different aspect ratios. Int J Heat Mass Transfer 46:2519–2525
12. Mohammed HA, Gunnasegaran P, Shuaib NH (2011) Influence of channel shape on the thermal and hydraulic performance of micro-channel heat sink. Int Commun Heat Mass Transfer 38(4):474–480
13. Pra F et al (2008) Promising designs of compact heat exchangers for modular HTRs using the Brayton cycle. Nucl Eng Des 238(11):3160–3173
14. Paul CP, Bhargava P, Kumar A, Pathak AK, Kukreja LM (2012) Laser rapid manufacturing: technology, applications and future prospects, Laser in Manufacturing, ISTE. Ltd., pp 1–13
15. Figley J, Sun X, Mylavarapu SK, Hajek B (2013) Numerical study on thermal hydraulic performance of a printed circuit heat exchanger. Prog Nucl Energy 68:89–96
16. CFX Numerical Models. https://www.sharcnet.ca/Software/Ansys/17.0/en-us/help/ai_sinfo/cfx_intro.html. Accessed on 10/02/2018
17. NIST chemistry web book. https://webbook.nist.gov/chemistry/fluid/. Accessed on 29/03/2018
18. Inconel Properties. http://www.specialmetals.com/assets/smc/documents/alloys/inconel/inconel-alloy-617.pdf. Accessed on 29/03/2018

# Development of Air Intake Manifold Using Alternate Materials by CFD Analysis

**P. Arjunraj and M. Subramanian**

**Abstract** Vehicle with high speed is in demand these days. This results in various types of high stresses in multiple vehicular components which may ultimately lead to engine failure and loss in fuel economy. Following the demand, the main objective of the present paper is to increase the performance and volumetric efficiency of the engine by using the lightweight alternate material. However, in order to bring the advantages of alternate material into play, many issues including static burst, noise, and vibration need to be settled in its design and development phase itself. The temperature mapping is carried out for air intake manifold and air duct to ensure that they withstand the temperature. Moreover, the flow analysis with respect to the mass flow rate of exhaust gas recirculation (EGR) is done followed by vibration measurement for alternate material polyamide 6 with glass fiber of 30%. Of all the above, the greatest challenge the paper investigates vests with achieving the volumetric efficiency of the engine similar or better to that of the aluminum manifold. To maintain or improve the volumetric efficiency, the plenum and runner volume are to be considered in such a way that the actual charge of air entering the cylinder through manifold is more effective and smooth.

**Keywords** Design · Fuel · Engine · Vehicle

## 1 Introduction

Diesel engine is one of the most important components of engine where in the air–fuel (A/F) mixture ignition is done by the process of compression of fuel at high temperature, and it operates on the principle of diesel cycle [1] (Fig. 1).

A study for Ford was performed by Schuckert et al. [3] to derive the results. It evaluated aluminum air intake manifold (AIM) with the aluminum from Zytel®,

P. Arjunraj (✉) · M. Subramanian
Department of Automobile Engineering, B. S. Abdur Rahman Crescent
Institute of Science and Technology, Vandalur, Chennai, India
e-mail: panneerselvam.arjunraj@gmail.com
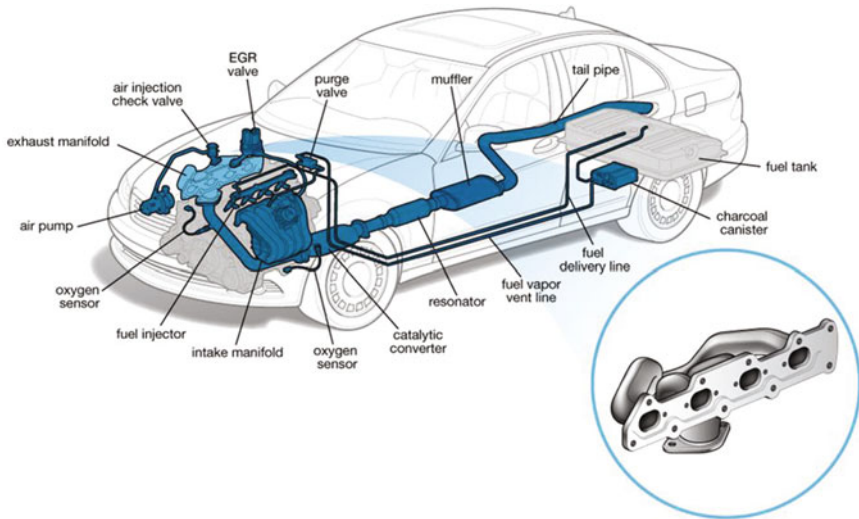
**Fig. 1** Air intake manifold of car [2]

a thermoplastic polymer with the composition of nylon 66 strengthened with 30% of fibrous glass which later got commercialized by Du Point. The end results shown by the study point are that nylon substitute has many benefits relating to environmental health, particularly in terms of greenhouse gases, material and energy consumption, and consumed landfill volume. The results show that only input connected to the acidification is near about equal to the two materials.

The study for LCA (life cycle assessment) for the 1995 Ford Contour successively compares a model sand-cast 2.0–1 aluminum AIM with a corresponding AIM composed from multi-tube-brazed aluminum to be used by the 1995 Ford Escort 1.9-L, and the outcomes derived indicate better performance of the multi-tube-brazed structure environmentally in respect of energy use, waterborne waste, and air emissions, but solid wastes are found to be lessor for the sand-cast structure.

Engine tests are done for the purpose of conducting a basic research to design a new variable length intake structure plenum. In this, the study indicates a life cycle cost (LCC) analysis of both the methods, giving almost similar results. Ceviz and Akin examine the effects of intake plenum length/volume on the performance characteristics of a spark-ignited engine with electronically controlled fuel injectors. To evaluate effects created by the variation in the length of intake plenum, characteristics of engine performance like brake power, brake torque, thermal efficiency, and precise fuel consumption were taken into account.

The results indicate that fuel consumption at higher loads and lower engine speeds moves the system ahead on metropolitan roads has a positive effect by variation in the plenum length and it improves the performance of the engine.

The test results positively indicate that plenum length is required to be extended for lower engine speeds and shortened at the higher engine speeds to make air flow

appropriate in context to the fuel to make it more combustible. The results derived were more developed to regulate the intake plenum length. In the investigation by Nour et al. [4] while injecting ethanol into the exhaust structure of a single cylinder diesel engine, the exhaust valve opened during the intake stroke, permitting vaporized ethanol to enter the cylinder where its ignition takes place by the diesel fuel injection.

Other components required to complete the AIM are throttle body gasket, runner gasket, throttle body brass inserts, and compression limiters. The investigation conducted by Melaika [5] on Formula Student car engine performance found that after applying air inlet restrictors, AV: BOOST numerical simulation model is generated in alliance with the real engine parameters.

The power loss is compensated by simulating turbocharging system for the selected engine. The experiments carried out for simulation turbocharger improved engine performance Ceviz and Akın [6] are as follows. Engine tests were carried out with the objective of doing a base study to design a new variable length intake structure plenum.

Excessive smoke is caused in diesel engines during a load increase because of poor combustion from the fuel/air mismatch which is stated by Papalambrou et al. [7].

Experiments conducted on a marine diesel engine validate the controller approach. Sarjovarra et al. [8] presented the effect of temperatures from intake air on ethanol combustion in diesel engines. This work investigated the impact of various alternative materials on air intake manifold.

## 2 Experimental Setup

The air intake manifold is shown in Fig. 2 weight of the intake manifold is reduced. The cost of the intake manifold is reduced. The cycle time to manufacture the component is reduced. As there is a weight reduction, there is always an improvement with respect to fuel economy and reduction in friction. As there is a weight reduction, there is always an improvement with respect to fuel economy and reduction in friction which lead to high thermal insulation efficiency and reduction of air pressure loss as compared to that of aluminum. Material Properties are comparable by adding glass fiber with plastic grades.

### 2.1 Material Properties

Table 1 shows the various material properties.

To predict EGR distribution and its deviation in all four cylinders. Variation of EGR in each cylinder is 0.05 negative or positive. The engine and its specification are shown in Table 2.

**Fig. 2** Air intake manifold

**Table 1** Material properties

| S. No. | Properties | Fluid |
|---|---|---|
| 1 | Density (kg/m$^3$) | Ideal gas |
| 2 | Viscosity (kg/m s) | 1.75–5 |
| 3 | Thermal conductivity (W/m K) | 0.025 |
| 4 | Specific heat (J/kg K) | 1006.43 |

**Table 2** Engine specification

| S. No. | Engine | Specification |
|---|---|---|
| 1 | Bore | 85 mm |
| 2 | Stroke | 96 mm |
| 3 | Displacement volume | 2.2 L |
| 4 | Number of cylinders | 4 Cylinder |
| 5 | Aspiration | Turbocharger |
| 6 | Compression ratio | 16.5:1 |

## 2.2 Analysis Using CAE

The various parts of air intake manifold are analyzed using CAE shown in Fig. 3. The development of Phase-Von Mises of air intake manifold is shown in Fig. 3 and (Table 3).

For the PA66 parts (air and water ducts), there are no problems concerning the mechanical behavior. As shown in Fig. 3, on the welded beads the stresses are under the allowable value. In the material, there is only one element with a value over the maximum allowable stress (53 Mpa for 50 Mpa) but is a numerical singularity due to the simplification of the mesh.
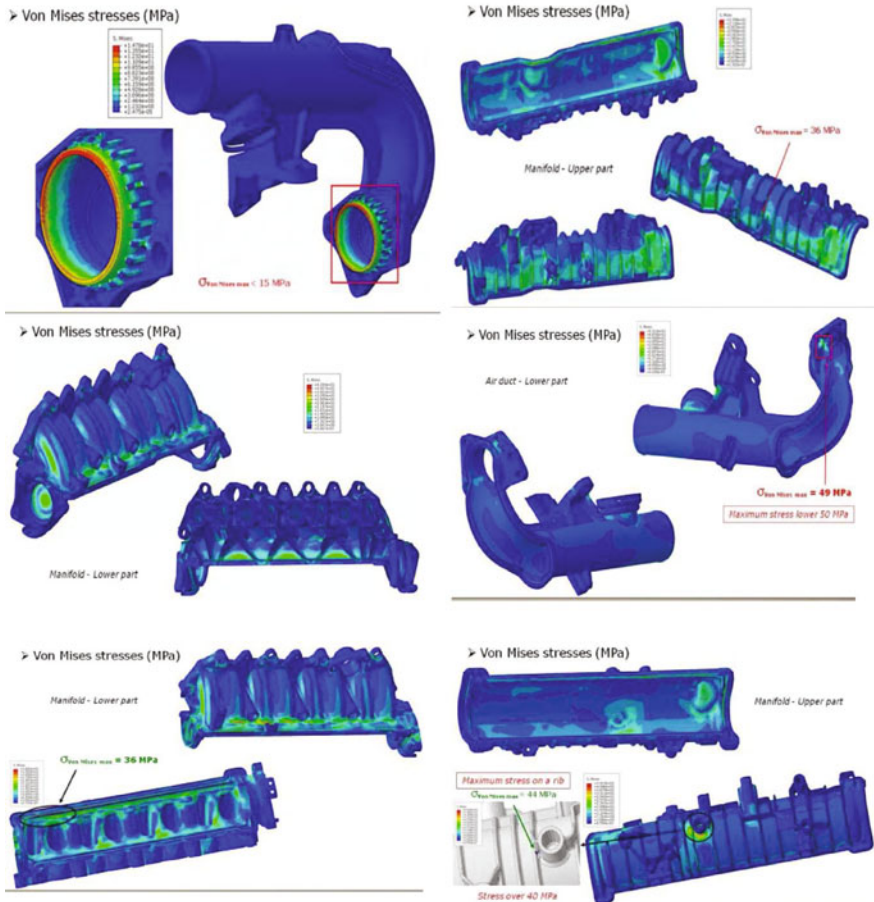
**Fig. 3** Component of air intake manifold using CAE

The quality of mesh formation depends on its quality. So the selection of grid pattern or arrangement (meshing scheme) is a very important factor in providing the result with very less error and highly accurate. Simulation for the intake manifold depends on various subclasses primitive like tetrahedral and hexahedral. Proper precaution should be done to maintain the continuity of the surface between two distinct domains to provide the complete picture in the entire design process. We use the tetrahedral mesh for this purpose which imposed on model for PA6 manifold this configuration guarantees the mechanical behavior of the system (36 Mpa for 40 allowable on the foot of the welded bead). On the welded bead, the maximum stress is 23 Mpa for 28 Mpa allowable. Hence, the design is safe. In CFD simulation, the following steps are followed:

**Table 3** Result of component of air intake manifold using CAE

| PA6 Parts | Burst pressure 4.5 bar @110 °C |
|-----------|-------------------------------|
| Umax (mm) (head cylinder sealing) | 0.16 (manifold) 0.28 (water duct) |
| Umax (mm) on the manifold | 1 |
| Umax (mm) on the air duct | 2.3 |
| σvon mises max in the material (MPa) PA6GF30 manifold | 44 (on a rib) for (60 MPa allowable) |
| σvon mises max in the material (MPa) PA6GF30 air duct | 53 (numerical singularity) for (50 MPa allowable) |
| σvon mises max on the welding joint PA6GF30 manifold | 23 for (28 MPa allowable) |
| σvon mises max on the welding joint (MPa) PA6GF30 air duct | 14 for (30 MPa allowable) |
| Umax mm in the material | 2.2 |
| Umax mm in the material | 0.36 |
| σvon mises max in the material (MPa) | 56 (for 65 Mpa allowable) |
| σvon mises max on the welding joint | <20 (for 40 Mpa allowable) |

1. Simplifying the geometry
2. Setting up the model
3. Meshing of the model which includes reduction in geometry complexity
4. Defining boundary conditions
5. CFD-Post for results
6. Computational fluid dynamics pressure drop of various parts is shown in Fig. 4.
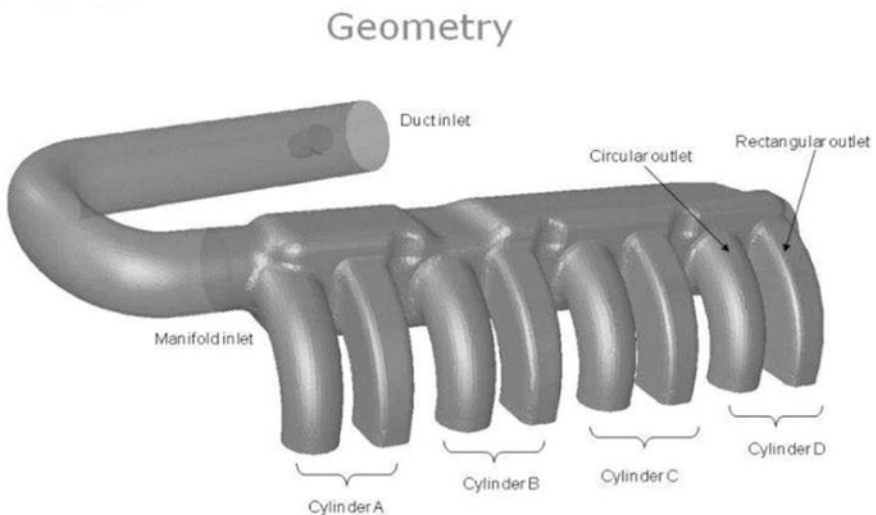


**Fig. 4** Flow analysis in air intake manifold

**Table 4** Pressure drop distributions

| Cylinder | CFD Result | | Test result | |
|---|---|---|---|---|
| | Trail 1 | Trial 2 | Trial 1 | Trial 2 |
| Cylinder 1 | 147.5 | 144.7 | 180 | 171 |
| Cylinder 2 | 138 | 134 | 163 | 155 |
| Cylinder 3 | 135.4 | 133.7 | 158 | 157 |
| Cylinder 4 | 132.3 | 131.8 | 155 | 155 |
| Average | 138.3 | 136 | 164 | 159.5 |
| % Dispersion | $<\pm 5$ | $<\pm 5$ | $<\pm 5$ | $<\pm 5$ |

It is very clear from Table 4 that the pressure drop dispersion is lesser than $\pm 5\%$ in CFD analysis and in the test results. This shows that the design of the plastic intake manifold with the plastic amide 6 with glass fiber of 30% is better design for the pressure drop across various cylinders. Transient data available for AVL Boost (pressure, temperature and mass flow rate of air) EGR flow rate 70.60 kg/hr EGR temperature 198.89 °C. EGR is assumed to be carbon dioxide. The CFD results are carried out using STAR CCM+ software. The test to find the pressure that is been acting in the individual cylinders is done with the help of adaptation. The difference between the adjacent cylinders is known as the pressure drop. The pressure drop dispersion is lesser than $\pm 5\%$ in CFD analysis and in the test results which confirms the CFD and Test requirements.

## 3 Conclusion

The experimental results show that the weight of the intake manifold is reduced by 3.48 kg and the cost of the intake manifold is reduced by INR 1000 for one component. Plastic intake manifold PA 6 with glass fiber of 30% had passed CAE, CFD, temperature analysis, and vibration test. It is very clear from the CFD and test results that the pressure drop dispersion is lesser than $\pm 5\%$. This shows that the design of the plastic intake manifold with the plastic amide 6 with glass fiber of 30% is better design for the pressure drop across various cylinders. PA6GF30 material properties are comparable with AlSi8Cu3 by adding glass fiber with plastic grades.

## References

1. Heywood JB (1988) Internal Combustion Engine Fundamentals. McGraw-Hill, New York, USA
2. RepairPal Homepage. http://repairpal.com/intake-manifold. Last accessed on 2017/09/18
3. Schuckert M, Dekorsy T, Pfleiderer I, Eyerer P (1993) Developing a comprehensive balance of an automobile air intake manifold. Kunststoffe German Plastics 83:16

4. Nour M, Kosaka H, Bady M, Sato S, Abdel-Rahman AK (2017) Combustion and emission characteristics of DI diesel engine fuelled by ethanol injected into the exhaust manifold. Fuel Process Technol 164:33–50
5. Melaika M, Rimkus A, Vipartas T (2017) Air restrictor and turbocharger influence for the formula student engine performance. Procedia Eng 187:402–407
6. Ceviz MA, Akın M (2010) Design of a new SI engine intake manifold with variable length plenum. Energy Convers Manag 51(11):2239–2244
7. Papalambrou G, Karlis E, Kyrtatos N (2015) Robust control of manifold air injection in a marine diesel engine. IFAC-Papers On Line 48(14):438–443
8. Yu J, Vuorinen V, Kaario O, Sarjovaara T, Larmi M (2013) Visualization and analysis of the characteristics of transitional underexpanded jets. Int J Heat Fluid Flow 44:140–154

# Optimization of Electrical Power of Solar Cell of Photovoltaic Module for a Given Peak Power and Photovoltaic Module Area

**Md. Meraj, M. Emran Khan, G. N. Tiwari and Osama Khan**

**Abstract** In this communication, an attempt has been made to optimize maximum electrical power (i) for a given number of solar cells by varying area of photovoltaic (PV) module and (ii) for a given PV module area by varying number of solar cell. Analytical expressions for solar cell temperature and electrical efficiency of solar cell have also been derived for opaque and semi-transparent PV module. Numerical computations have been made for New Delhi climatic conditions with the help of MATLAB R2015a. Based on numerical computation, it has been observed that (i) an electrical efficiency is maximum for higher PV module area with lower packing factor for a given peak power of PV module (75 $W_p$) and (ii) an electrical efficiency is lower with maximum packing factor for a given PV module area (2.1 m$^2$). Further, an effect of different solar cell materials (i.e., m-Si, p-Si, a-Si, CdTe, CIGS, and HIT) on electrical power has also been investigated. It is found that electrical power output for m-Si and HIT is better than other solar cell material PV module.

**Keywords** Solar cell · PV module · Peak power · Solar cell materials · Solar energy

## Nomenclature

| | |
|---|---|
| $A_m$ | Area of module (m$^2$) |
| $E_m$ | Electrical output of PV module (W) |
| $h_o$ | Heat loss coefficient from top of module to ambient (W/m$^2$) |
| $h_i$ | Heat loss coefficient from bottom of module to ambient (W/m$^2$) |
| $I(t)$ | Solar intensity (W/m$^2$) |
| $K_g$ | Thermal conductivity of glass cover of PV module (W/m K) |

Md. Meraj (✉) · M. Emran Khan · O. Khan
Mechanical Engineering Department, Faculty of Engineering & Technology,
Jamia Millia Islamia, New Delhi 110025, Delhi, India
e-mail: md.meraj1221@gmail.com

G. N. Tiwari
Bag Energy Research Society (BERS), Plot No-51, Mahamana Nagar, Karaudi,
Varanasi, Uttar Pradesh, India

417

$K_T$   Thermal conductivity of tedlar of PV module (W/m K)
$L_g$   Thickness of glass cover of PV module (m)
$L_T$   Thickness of tedlar of PV module (m)
$T_a$   Ambient temperature (°C)
$T_c$   Solar cell temperature (°C)
$T_0$   Reference cell temperature for optimum cell efficiency, i.e., 25 °C
$U_b$   Overall heat loss coefficient from bottom of solar cell to ambient (W/m$^2$ K)
$U_T$   Overall heat loss coefficient from top of solar cell to ambient (W/m$^2$ K)
$U_L$   Overall heat loss coefficient of PV module
$V$     Air velocity (m/s)
$\alpha_c$   Absorptivity of solar cell
$\alpha_T$   Absorptivity of tedlar
$\beta_0$   Temperature coefficient of materials
$\beta_c$   Packing factor of PV module
$\eta_m$   Module efficiency
$\eta_0$   Module efficiency at standard test condition
$\tau_g$   Transmissivity of glass

# 1   Introduction

In the present scenario, there is a drastic increase in energy demand due to the fast increase in the world population. Therefore, the consumption of non-renewable (fossil fuel: coal, petroleum, etc.) source of energy increases quite rapidly. Since there is a shortage of non-renewable source of energy, one needs alternate energy sources. Further, fossil fuel is also creating pollution and affecting climate change, and hence, alternate energy sources should be pollution free, and these are solar, the wind, hydro, and biomass. These energy sources are known as renewable energy sources with infinite source.

So far, solar energy has emerged a clear winner in contrast to the other renewable technologies, which is quite frequently being used to overcome the power demand in the present-day scenario. The solar energy is infinitely freely available at our disposal and can easily replace the existing non-renewable energy sources. Apart from being reliable, it is a cleaner source of energy which is complemented with being eco-friendly for the environment. Solar energy is a flexible energy source which can be effectively transformed into heat energy and further to electrical energy. With the help of collectors and photovoltaic cells, solar energy is converted into thermal and electrical energy, respectively. To effectively convert this energy into their respective forms, a system called as photovoltaic thermal (PVT) systems was developed which converts the solar energy into both heat energy and electrical energy based on requirements.

A French physicist named Alexandre-Edmond Becquerel in 1839 studied the photovoltaic effect and developed a photovoltaic cell which efficiently transforms the incident solar radiation which comprised within packets of light quanta and further changed into heat energy. The initial practical of photovoltaic cell (solar cell) was successfully tested in the year 1954 by a company named Bell Telephone Laboratories [1]. Since then, there have been a lot of developments in the performance of photovoltaic cells and technology. According to the time of evolution of photovoltaic technologies, solar cells are categorized into three generations. Crystalline silicon (c-Si)-made solar equipments are categorized in first-generation because these solar cells were manufactured in earlier days. Crystalline silicon solar cells subdivided into mono-crystalline silicon (m-Si) and polycrystalline silicon (p-Si) solar cells. In another categorization, the second- and third-generation solar equipment cells are fine thin layer-filmed solar cells, which are combined by using a variety of semiconductor materials, including amorphous silicon (a-Si), copper indium selenide (CuInSe2), cadmium sulfide (CdS), copper indium gallium diselenide (CIGS), cadmium telluride (CdTe), etc. The energy transformation capability and efficiency in the case of first-generation solar cells are comparatively higher than those of second- and third-generation solar cells [2]. It was seen in case of electrical applications, solar cells when connected in series generate a favorable amount of power and were found to be quite successful. Thereby, these cells are linked in series with each other and sandwiched between the transparent encapsulant ethylene-vinyl acetate (EVA). Later on, to enhance the design, it is merged between upper transparent (glass) layer and lowermost opaque (tedlar) layer or transparent (glass) layer and finally covered with a frame to secure it from hostile climatic conditions. The whole setup in which cells are coupled in series arrangement is called as photovoltaic (PV) modules. These modules can be coupled in series or parallel or in combination of both based on the requirement and are further named as PV array. According to the requirement of electrical power, the size of PV modules and array is designed.

Cuce et al. [3] investigated the dependency of electrical characteristic and thermodynamic performance (energy efficiency, energy conversion efficiency, and exergetic efficiency) on the solar intensity and operating module temperature of a polycrystalline PV module. Radziemska and Kucharek [4] presented an experimental evaluation to maintain the temperature of silicon PV module at an optimum level which is stabilized by use of phase change material to get maximum possible module output. Abdullahi et al. [5] analyzed the performance parameters of a system which generated a power of 85 W using m-Si PV systems undergoing various outdoor and indoor conditions. Gaur and Tiwari [6] investigated the effect of water flow on an a-Si thin layered PV module in order to understand its working and further developed a reasonable analytical expression in order to obtain the electrical capability and efficiency of the system. The conclusion stated clearly that the temperature readings of a PV module when water flowing over module are lower than those without the flow of water. Further, an increase in electrical efficiency of PV modules was found when water was kept in constant flow. Assoa and Menezo [7] performed an experiment to study the behavior of thermal- and

electrical-based readings using a polycrystalline PV module under the application of forced and natural ventilation by providing an air gap underside of PV module. It is observed that the force mode ventilation is more suitable for the thermal production than the electricity production. Dubey et al. [8] presented a review paper in which a number of references listed which shows that calculated efficiency readings of PV module decrease on the increment of temperature of the PV-based module. Vats and Tiwari [9] compared the performance of six dissimilar types of semi-transparent PV module, namely m-Si, a-Si, p-Si, CdTe, CIGS, and HIT integrated with building to provide thermal and electrical energy. Finally, it was observed that HIT- and a-Si-based PV module generates maximal electrical power and thermal power among them.

The preceding literature survey indicates that a lot of researches have been done on the performance of PV-based module and its multipurpose applications to improve its efficiency. Evan [10] has studied the dependency of electrical efficiency and temperature of PV-based module. Further, Dubey et al. [11] and Gaur and Tiwari [12] have done studies on the semi-transparent and opaque PV-based module. It was found by them that semi-transparent PV module provides enhanced electrical performance in comparison with opaque ones. However, the effect of area of PV module for a given peak power output (fixed number of solar cells) and the effect of peak power output for fixed given area of PV module have not been considered so far in case of opaque and semi-transparent PV-based module. Therefore, in this study an analysis has been done in order to optimize the following parameters:

An area of semi-transparent PV module for a given power output and
The power output for a fixed area of semi-transparent PV module.

## 2 Problem Formulation

Six configurations of semi-transparent PV module each 75 $W_p$ (36 solar cells) under study are shown in Fig. 1a–f. The different areas of PV module have been considered as 0.6–2.1 m$^2$ with packing factor of 0.89–0.2543, respectively. Further, another configuration of four semi-transparent PV modules, each 2.1 m$^2$ with varying $W_p$ from 75 to 225 as shown in Fig. 2a–d, has also been considered. Basic energy balance equations for opaque and semi-transparent PV module for each case have been written. Following Gaur and Tiwari [12] and on foundation of various energy balance formulas, a mathematical expression was developed to obtain the solar cell temperature, thereby calculating its overall electrical efficiency for various climatic conditions.

The hourly variation of solar intensity radiation throughout the day and corresponding temperature for a typical day in the month of May of New Delhi was obtained by taking radiation data from Indian Meteorological Department (IMD),
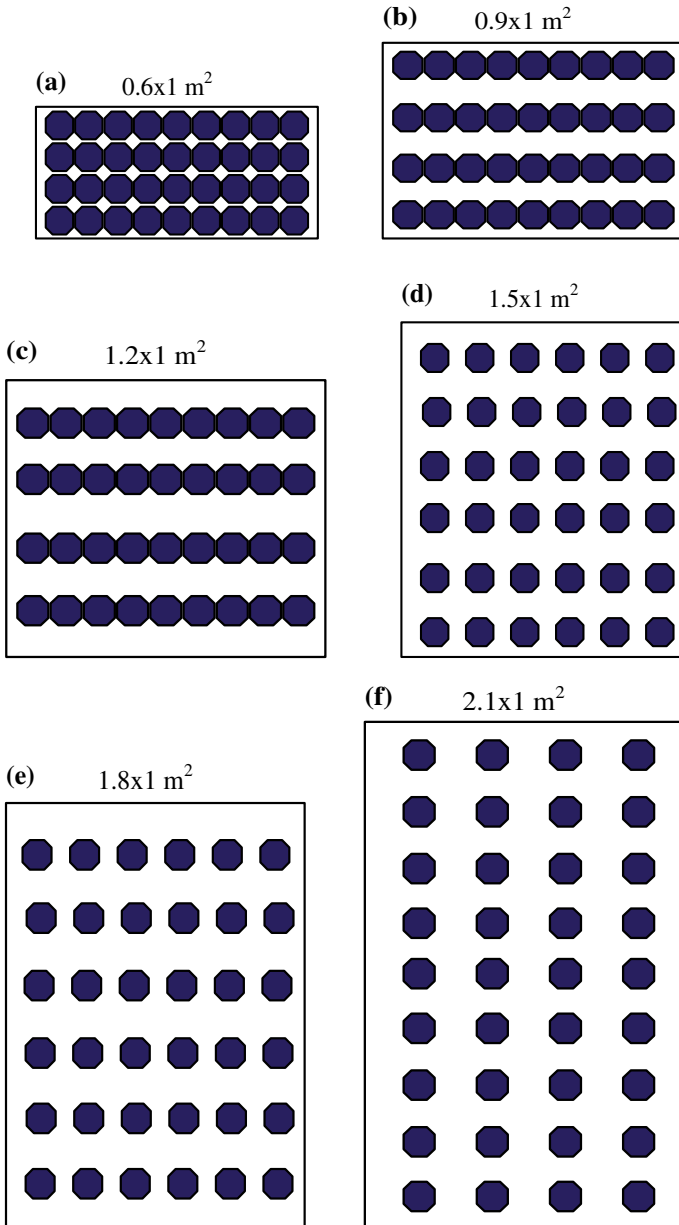
**Fig. 1** A typical representation of semi-transparent PV module, each 75 $W_p$ (36 Solar cells) with varying area of module

**(a)**  75 Wp (36 Solar Cells)



**(b)**
175 Wp (60 Solar Cells)

**(c)**
175 Wp (84 Solar Cells)

**(d)**
225 Wp (108 Solar Cells)
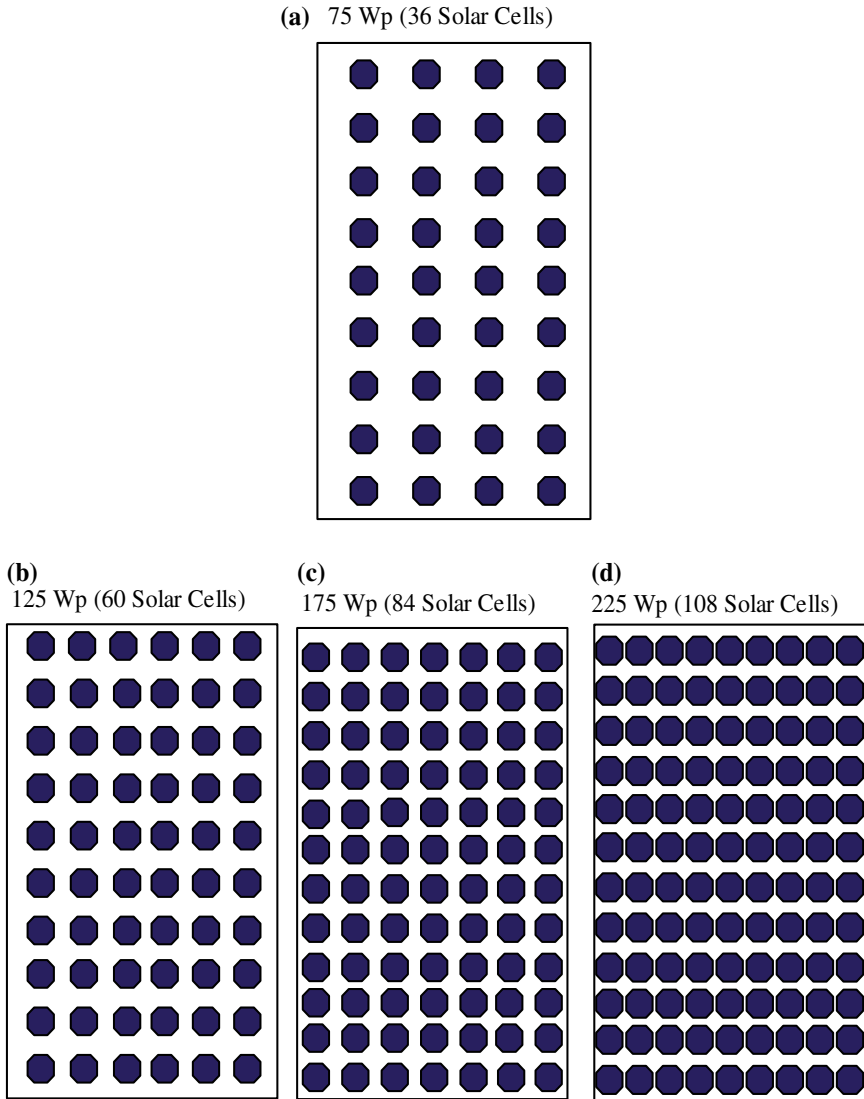


**Fig. 2** A typical representation of semi-transparent PV module, each 2.1 m$^2$ area with varying Watt peak ($W_p$) of PV module

Pune, India, which is shown in Fig. 3. The design parameters of solar cells are given in Table 1. Also, optimization for getting maximum electrical efficiency and power has also been obtained.
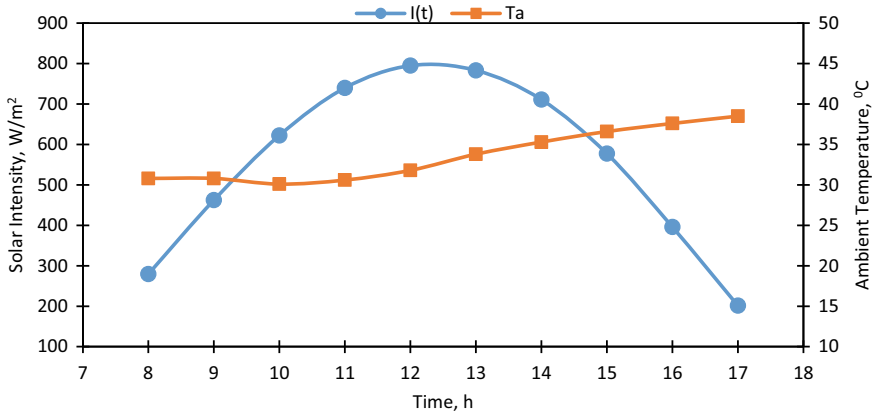
**Fig. 3** Hourly variation of solar intensity $I(t)$ and ambient air temperature $T_a$ for a typical day in the month of May

**Table 1** Design parameters of solar cells

| Parameter | Value | Type of PV module | Module efficiency STC, $\eta_0$ | Temperature coefficient, $\beta_0$ | References |
|-----------|-------|-------------------|-------------------------------|-----------------------------------|------------|
| $\alpha_c$ | 0.9 | m-Si | 0.15 | 0.0045 | [14] |
| $\tau_g$ | 0.95 | p-Si | 0.116 | 0.004 | [15] |
| $\alpha_T$ | 0.5 | a-Si | 0.063 | 0.0026 | [16] |
| $h_0$ | 5.7 + 3.8 v $v = 0.5$ m/s | CdTe | 0.069 | 0.002 | [16] |
| $h_i$ | 2.8 + 3.0 v $v = 0.2$ m/s | CIGS | 0.082 | 0.0045 | [16] |
| $L_g$ (m) | 0.003 | HIT | 0.17 | 0.0033 | [9] |
| $K_g$ (W/m K) | 1.1 | | | | |
| $L_T$ (m) | 0.0005 | | | | |
| $K_T$ (W/m K) | 0.033 | | | | |

## 3 Thermal Modeling

The solar cell temperature and electrical efficiency of PV module are derived by using energy balance equations. Following assumptions have been made to write energy balance equations:

- The PV module has been considered in a quasi-steady state.
- One-dimensional heat conduction in solar cell.
- The ohmic losses between solar cells in PV module have been neglected.

## 3.1 Energy Balance Equations for Opaque PV Module

Following Gaur and Tiwari [12], the energy balance in terms of watt (W) for opaque PV module can be written as:

[Rate of solar radiation absorbed by solar cells] + [Rate of solar radiation absorbed by tedlar through non-packing area] = [Rate of overall upward heat loss through top glass surface] + [Rate of overall backward heat loss through back glass surface] + [Rate of electrical power generation by solar cells]

$$\alpha_c \tau_g \beta_c I(t) + (1 - \beta_c) \alpha_T \tau_g I(t) = U_T(T_c - T_a) + U_b(T_c - T_a) + \eta_c \tau_g \beta_c I(t) \quad (1)$$

where an expression for $U_T$ and $U_b$ is given by

$$U_T = \left[\frac{L_g}{K_g} + \frac{1}{h_0}\right]^{-1}, \quad (2a)$$

and

$$U_b = \left[\frac{L_g}{K_g} + \frac{1}{h_i}\right]^{-1} \quad (2b)$$

From Eq. (1), one can get the solar cells temperature as:

$$T_c = \frac{\left[\tau_g \{\alpha_c \beta_c + (1 - \beta_c)\alpha_T - \eta_c \beta_c\}\right] I(t) + T_a(U_T + U_b)}{(U_T + U_b)}, \quad (3)$$

or

$$T_c = \frac{\left[\tau_g \{\alpha_c \beta_c + (1 - \beta_c)\alpha_T - \eta_c \beta_c\}\right] I(t) + T_a U_L}{U_L}, \quad (4)$$

or

$$T_c - T_0 = T_a - T_0 + \frac{\left[\tau_g \{\alpha_c \beta_c + (1 - \beta_c)\alpha_T - \eta_c \beta_c\}\right] I(t)}{U_L} \quad (5)$$

where, $U_L = (U_T + U_b)$. According to Evan [10], the temperature-dependent electrical efficiency of solar cells can be written as:

$$\eta_c = \eta_0[1 - \beta_0(T_c - T_0)]. \quad (6)$$

By using Eqs. (5) and (6), one can derive an electrical efficiency of the solar cell as follows:

$$\eta_c = \frac{\eta_0\left[1 - \beta_0\{(T_c - T_0) + (\{\alpha_c\tau_g\beta_c + (1 - \beta_c)\alpha_T\}/U_L)I(t)\}\right]}{\left[1 - (\eta_0\beta_0\tau_g\beta_c/U_L)I(t)\right]}. \tag{7}$$

## 3.2 Energy Balance Equations for Semi-Transparent PV Module

Similarly, for semi-transparent PV module as shown in Figs. 1 and 2, the energy balance equation can be written as:

[Rate of solar radiation absorbed by solar cells] = [Rate of overall upward heat loss through top glass surface] + [Rate of overall backward heat loss through back glass surface] + [Rate of electrical power generation by solar cells]

$$\alpha_c\tau_g\beta_c I(t) = U_T(T_c - T_a) + U_b(T_c - T_a) + \eta_c\tau_g\beta_c I(t) \tag{8}$$

In this case too, an expression for solar cell temperature, an electrical efficiency of the solar cell and PV module and an electrical power can be obtained as follows:

$$T_c = \frac{T_a U_L + (\alpha_c\tau_g\beta_c - \eta_c\tau_g\beta_c)I(t)}{U_L} \tag{9}$$

$$\eta_c = \frac{\eta_0\left[1 - \beta_0\{(T_c - T_0) + (\alpha_c\tau_g\beta_c/U_L)I(t)\}\right]}{\left[1 - (\eta_0\beta_0\tau_g\beta_c/U_L)I(t)\right]} \tag{10}$$

Further, the module electrical efficiency for opaque and semi-transparent PV module can be expressed as follows:

$$\eta_m = \eta_c\tau_g\beta_c. \tag{11}$$

After determining the module efficiency ($\eta_m$), the electrical output of PV module can be obtained as:

$$E_m = \eta_m A_m I(t) \tag{12}$$

or

$$E_m = \eta_c A_m \beta_c\tau_g I(t). \tag{13}$$

In the present paper, the following two cases have been considered for study:

Case (i)   In this case, for constant peak electrical power (75 $W_p$), an effect of the variation of area of PV module on solar cell temperature, electrical efficiency, and electrical power has been studied.

Case (ii)  In this case, for constant PV module area (2.1 $m^2$), an effect of the variation of the number of solar cells (area of the solar cells) on solar cell temperature, electrical efficiency, and electrical power has been studied.

## 4   Methodology

The following methodologies have been adopted:

- Climatic data from Fig. 3 and design parameters from Table 1 have been used to calculate solar cell temperature from Eqs. 4 and 9 for opaque and semi-transparent PV module.
- After getting solar cell temperature, an electrical efficiency for both cases has also been computed from Eqs. 7 and 10, respectively.
- Further electrical power in each case has also been obtained from Eq. 13 after knowing electrical efficiency.
- All equations are solved by using MATLAB R2015a.
- All results have been summarized in Figs. 4, 5, 6, 7, 8, 9, 10, and 11.

## 5   Results and Discussion

Equations 4 and 7 have been computed for case (i) for hourly variation of solar cell temperature and its electrical efficiency for climatic data of Fig. 3 and design parameters of Table 1. The results obtained for opaque PV modules are shown in Fig. 4a. The results shown in Fig. 4a indicate that with the increase of solar cell temperature, an electrical efficiency of solar cell decreases as reported by earlier researchers [13]. However, there is an increase in electrical efficiency with the increase of area of PV module. It is due to the fact that with the increase of the PV module area the temperature of solar cell decreases. In other words, the packing factor of PV module decreases with the increase of area of PV module as per our expectation. Also, the same conclusion can be inferred for semi-transparent PV module from Fig. 4b obtained from Eqs. 9 and 10. Further one can also conclude from Fig. 4a, b that the maximum electrical efficiency of semi-transparent PV module is higher by 2.71% in comparison with opaque PV modules for case (i).

**(a)**



**(b)**
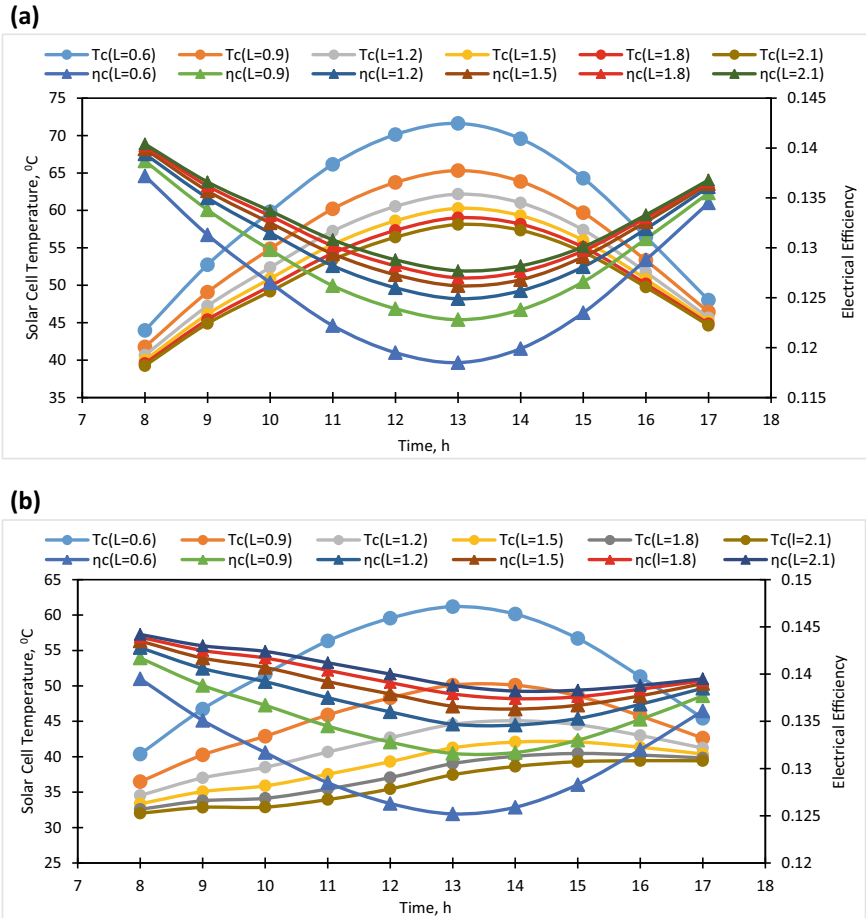


**Fig. 4** **a** Hourly variation of solar cell temperature ($T_c$) and electrical efficiency of solar cell ($\eta_c$) for opaque PV module for constant peak electrical power (75 $W_p$). **b** Hourly variation of solar cell temperature ($T_c$) and electrical efficiency of solar cell ($\eta_c$) for semi-transparent PV module for constant peak electrical power (75 $W_p$)

Equation 13 has been used for evaluating the hourly variation of electrical power for opaque and semi-transparent PV module for the same climatic condition, and the results are shown in Fig. 5. One can observe that an electrical power is also maximum for 2.1 m$^2$ (75 $W_p$) due to higher electrical efficiency as shown in Fig. 6. This gap is reduced by 0.6 m$^2$. It is due to the increase in solar cell temperature for 0.6 m$^2$ (Fig. 6). Further, a maximum daily electrical output for semi-transparent is 6.75% higher than opaque PV module for 2.1 m$^2$ (75 $W_p$) as shown in Fig. 7.

**(a)**



**(b)**
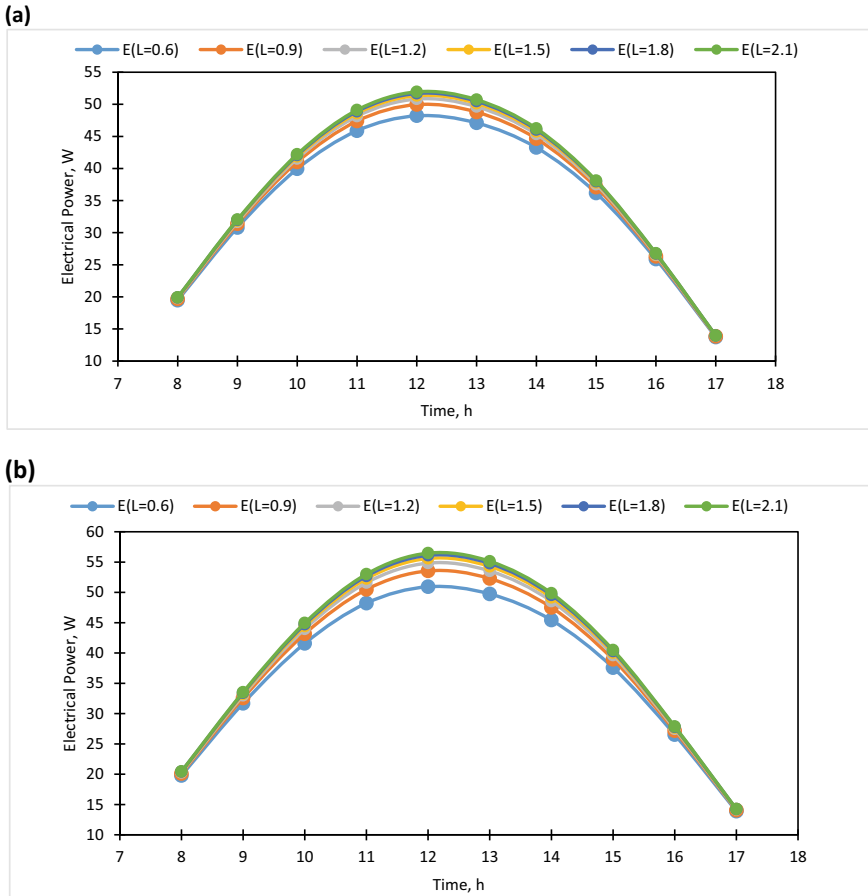


**Fig. 5** **a** Hourly variation of electrical power ($E$) for opaque PV module for constant peak electrical power (75 $W_p$) for the month of May. **b** Hourly variation of electrical power ($E$) for semi-transparent PV module for constant peak electrical power (75 $W_p$) for the month of May

For case (ii), an area of PV module (2.1 m²) is fixed and area of solar cell has been considered as a variable for semi-transparent PV module due to its higher electrical efficiency. In this case, the results for solar cell temperature (Eq. 9) and an electrical efficiency (Eq. 10) have been summarized in Fig. 8. Figure 8 shows that an electrical efficiency is maximum for a minimum number of solar cells due to lower solar cell temperature (lower packing factor) as expected. However, electrical power is maximum for higher packing factor (more solar cell areas) (Fig. 9) for
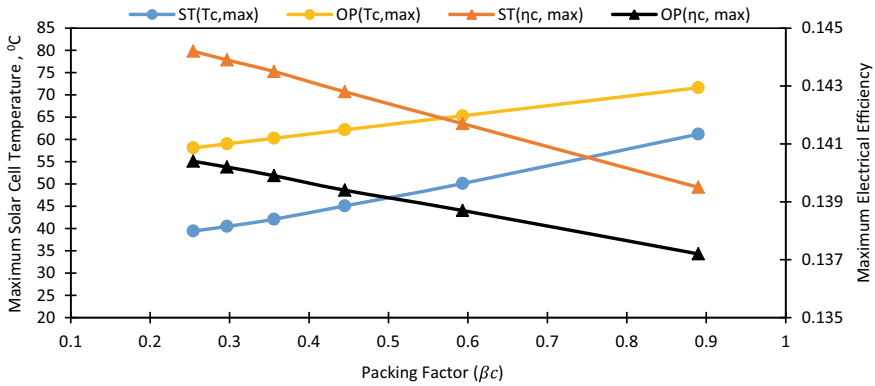
**Fig. 6** Effect of packing factor on maximum solar cell temperature ($T_{c,max}$) and electrical efficiency ($\eta_{c,max}$) for opaque and semi-transparent PV module for constant peak electrical power (75 $W_p$)
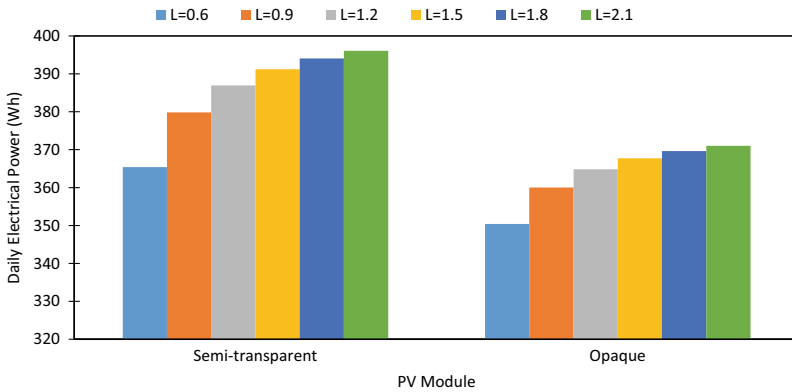


**Fig. 7** Daily variation of electrical power output in Watt-hours (Wh) of semi-transparent and opaque PV module for constant peak electrical power (75 $W_p$) for the month of May

even lower electrical efficiency (Fig. 8). These results are not in accordance with the results shown for case (i) as expected. It is important to mention that even maximum power (56.48 W) under the outdoor condition is lower than peak power condition (75 $W_p$). This finding is valid for any peak power.
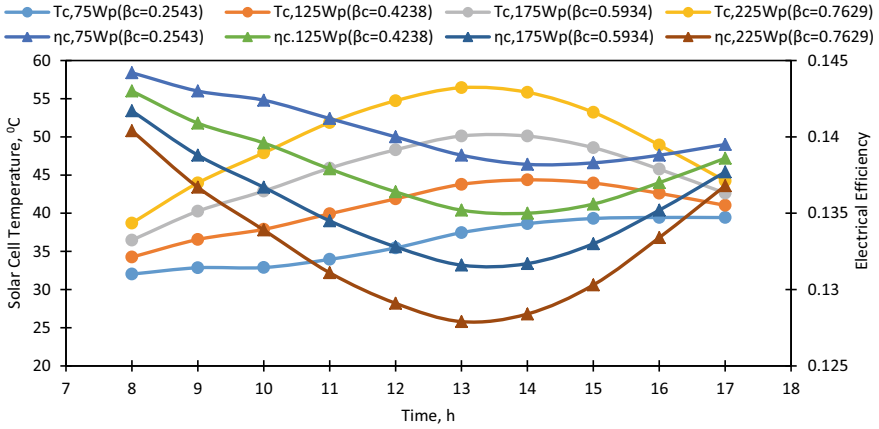
**Fig. 8** Hourly variation of solar cell temperature ($T_c$) and electrical efficiency ($\eta_c$) of solar cell for semi-transparent PV module for constant area of PV module (2.1 m$^2$)
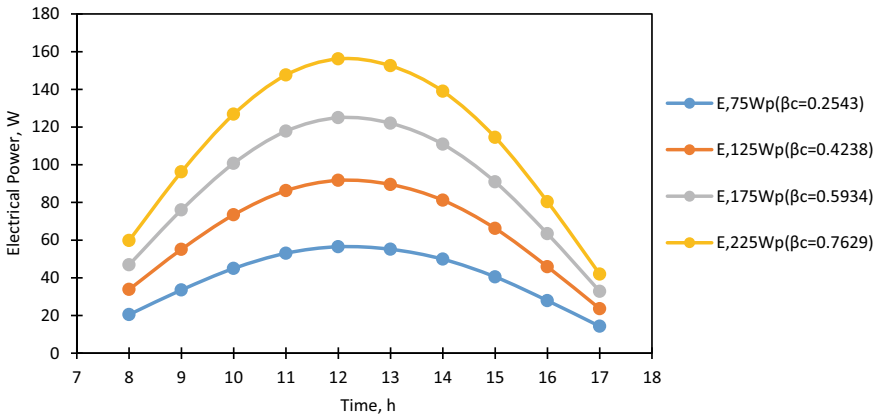


**Fig. 9** Hourly variation of electrical power ($E$) for semi-transparent PV module for constant area of PV module (2.1 m$^2$) for the month of May

Figures 10 and 11 show hourly variation of electrical power and daily variation of electrical power output for different types of semi-transparent PV module, i.e., m-Si, p-Si, a-Si, CdTe, CIGS, and HIT, for constant area of PV module (2.1 m$^2$) and Watt peak (225 $W_p$), respectively. From these figures, it is observed that electrical power output for m-Si and HIT is better than another.
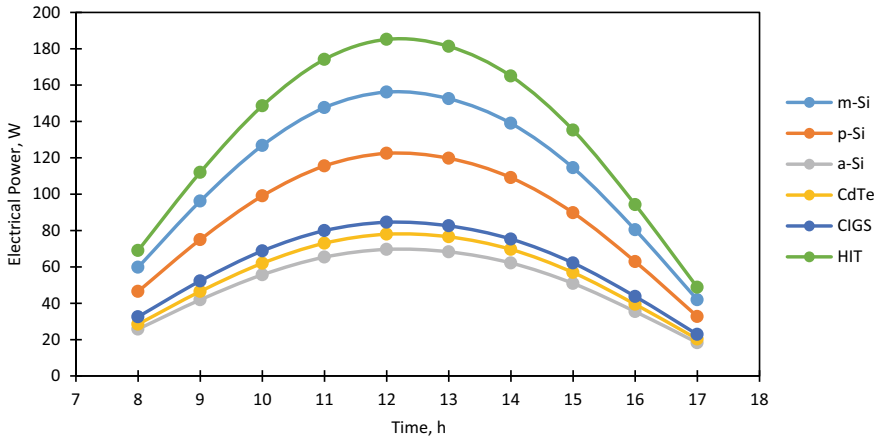
**Fig. 10** Hourly variation of electrical power ($E$) for different types of semi-transparent PV module for constant area of PV module (2.1 m$^2$) and Watt peak (225 $W_p$) for the month of May
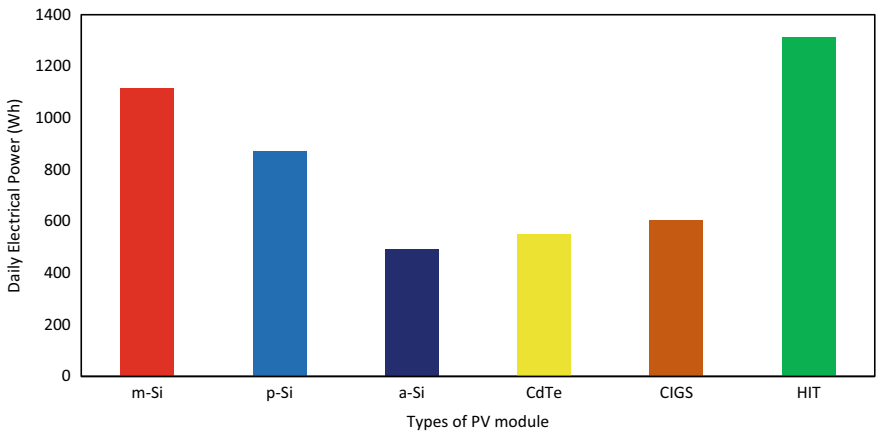


**Fig. 11** Daily variation of electrical power output in Watt-hours (Wh) for different types of semi-transparent PV module for constant area of PV module (2.1 m$^2$) and Watt peak (225 $W_p$) for the month of May

# 6 Conclusions

Based on the present study, the following conclusions have been drawn:

- Electrical efficiency and electrical power output for semi-transparent PV module are higher than opaque PV module.

- Electrical efficiency of PV module increases with increasing the packing factor of PV module.
- From solar thermal point of view, packing factor should be minimum with higher electrical efficiency (case i).
- From electrical power point of view, the packing factor of PV module should be maximum with lower electrical efficiency (case ii).

## 7  Recommendations

Based on the present studies, the following recommendations have been made:

- Fully covered semi-transparent PV module with minimum packing factor ($\beta c$) can be used for the design of PVT collectors, PVT-CPC collectors, PVT greenhouse for cultivation and drying, and building integrated PVT thermal system from thermal energy point of view with a high electrical efficiency of solar cell of PV module.
- Fully covered semi-transparent PV module with maximum packing factor ($\beta c$) can be used for the design of a rooftop and stand-alone PV system for highest electrical power to meet the electrical demand of buildings, water pumping, lighting system, and energy security to sustain a climate and environmental change.
- Either m-Si or HIT should be used for fabrication of semi-transparent PV module.

## References

1. Chapin DM, Fuller CS, Pearson GJ (1954) A new silicon p-n junction photocell for converting solar radiation into electrical power. J Appl Phys 25(5):676–677
2. Tiwari GN, Tiwari A, Shyam (2016) Handbook of solar energy: theory, analysis and applications. Springer, Singapore. https://doi.org/10.1007/978-981-10-0805-4
3. Cuce E, Cuce PM, Karakas IH, Bali T (2017) An accurate model for photovoltaic (PV) modules to determine electrical characteristics and thermodynamic performance parameters. Energy Convers Manag 146:205–217
4. Radziemska E, Kucharek P (2017) Photovoltaic module temperature stabilization with the use of phase change materials. Sol Energy 150:538–545
5. Abdullahi N, Saha C, Jinks R (2017) Modelling and performance analysis of a silicon PV module. J Renew Sust Energy 9(4):1–11. https://doi.org/10.1063/1.4982744
6. Gaur A, Tiwari GN (2014) Performance of a-Si thin film PV modules with and without water flow: an experimental validation. Appl Energy 128:184–191
7. Assoa YB, Ménézo C (2014) Dynamic study of a new concept of photovoltaic–thermal hybrid collector. Solar Energy 107:637–652
8. Dubey S, Sarvaiya JN, Seshadri B (2013) Temperature dependent photovoltaic (PV) efficiency and its effect on PV production in the world—a review. Energy Procedia 33:311–321

9. Vats K, Tiwari GN (2012) Energy and exergy analysis of a building integrated semitransparent photovoltaic thermal (BISPVT) system. Appl Energy 96:409–416
10. Evans DL (1981) Simplified method for predicting PV array output. Sol Energy 27(6):555–560
11. Dubey S, Sandhu GS, Tiwari GN (2009) Analytical expression for electrical efficiency of PV/T hybrid air collector. Appl Energy 86(5):697–705
12. Gaur A, Tiwari GN (2013) Performance of photovoltaic modules of different solar cells. J Solar Energy. http://dx.doi.org/10.1155/2013/734581
13. Skoplaki E, Palyvos JA (2009) On the temperature dependence of photovoltaic module electrical performance: A review of efficiency/power correlations. Sol Energy 83(5):614–624
14. Shyam, Tiwari GN (2016) Analysis of series connected photovoltaic thermal air collectors partially covered by semitransparent photovoltaic module. Solar Energy 137: 452–462
15. Yamawaki T, Mizukami S, Masui T, Takahashi H (2001) Experimental investigation on generated power of amorphous PV module for roof azimuth. Sol Energy Mater Sol Cells 67 (1–4):369–377
16. Nann E, Emery K (1992) Spectral effects on PV-device rating. Sol Energy Mater Sol Cells 27 (3):189–216

# Fluid–Structure Interaction Simulation: Effect of Endovascular Coiling in Cerebral Aneurysms Considering Anisotropically Deformable Walls

**Vidhya Vijayakumar and J. S. Jayakumar**

**Abstract** In the present research, we use fluid–structure interaction to study the effect of endovascular coiling in brain aneurysms. We simulate pulsatile flow of blood through a tubular hypothetical bulge filled with a homogenous porous medium; however, the wall mechanical properties of the aneurysm wall are different from that of the non-aneurysmal vascular vessel wall. The numerical simulations were carried out using Open FOAM. The FSI technique has a nonlinear material model to represent the ICA tissue. Fully implicit method of coupling employed ensured that the solid and the fluid domain attained convergence at each of the time steps. The results from the FSI simulations show that the presence of a coil in an aneurysm sac reduces fluid loading within the sac, and hence, the velocity of blood flow becomes negligible within the aneurysm. The von Mises stresses and the wall shear stress values on the wall of the aneurysm decrease to a great extent after the coil is inserted. Consequently, the displacement of the blood vessel's wall also decreases, and hence, the risk of rupture of the aneurysm reduces. In conclusion, treatment using endovascular coiling technique delays further disintegration of the blood vessel and hence proves to be an effective treatment technique for cerebral aneurysm.

**Keywords** Cerebral aneurysm · Endovascular coiling · Fully implicit coupling · ICA tissue · Fluid–structure interaction

V. Vijayakumar (✉) · J. S. Jayakumar
Department of Mechanical Engineering, Amrita Vishwa Vidyapeetham, Amritapuri, India
e-mail: vidhya94vijay@gmail.com

J. S. Jayakumar
e-mail: jsjayan@gmail.com

435

# 1 Introduction

An intracranial aneurysm, generally occurring at the base of the brain, is a condition when a local and progressive balloon-like dilation occurs in the arteries. The initiation, growth, and the rupture of an aneurysm are generally associated with hemodynamic factors including wall shear stress, wall pressure, and flow rate of blood [1]. The commonly employed treatment options for a cerebral aneurysm include endovascular coiling and surgical clipping. In endovascular coiling embolization, a coil is inserted into the aneurysm sac, which averts blood circulation in the aneurysm, and ultimately, further rupture of the aneurysm can be prevented while in case of surgical clipping blood flow to the aneurysm is averted by placing a clip at the aneurysm neck.

The effect of stents on intra-aneurysmal flow using an ideal geometry has been experimentally investigated by Canton et al. [2]. Majority of the aneurysms generally occur at the bifurcation point of the blood vessel. This can be attributed to the fact that the risk of rupture associated with these sites increases manifolds due to the high magnitude of the wall shear stress. Flow shear stress may result in the dysfunction of endothelial cells, which leads to the destruction of the vessel walls [3]. Mitsos et al. [4] have investigated the effect of endovascular treatment on a patient-specific geometry.

The numerical simulation of the blood flow can effectively predict growth and rupture of aneurysm with minimal cost [5]. The study of the interaction of blood flow and the vessel walls is essential to predict this, owing to the elastic nature of the vessel. Hence, the fluid–structure interaction (FSI) simulation method is implemented in the current work.

The use of FSI simulations to determine the stress distribution within the wall of a hypothetical ICA geometry prior to treatment as well as after treatment using coil embolization technique, considering inconsistent mechanical properties for the aneurysm wall as well as that of the unaffected vessel wall, is described in this article. The FSI technique was implemented using OpenFOAM. The aim of this work was to study the effect of endovascular coiling in the prevention of further disintegration of an aneurysm wall.

# 2 Mathematical Modeling

## 2.1 Geometry

The fluid geometry under consideration is a bent tube with a sphere-shaped aneurysm as shown in Fig. 1 [6].The dimensions of the geometry have been scaled up by a factor of 4 in comparison to a human subject [7]. The aneurysms of this model have been found in patients [8]. Dynamic similarity has been ensured by maintaining the same values of the Reynolds number and Womersley number (*Re*

**Fig. 1** Geometrical model
for aneurysm analysis
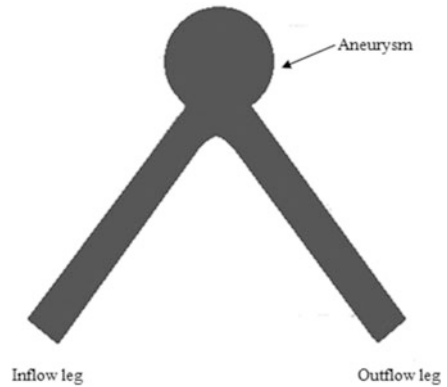


and *Wo*). The diameter of the tube (*d*) is 10 mm. The length of the legs is considered 70 mm so that fully developed flow enters the aneurysm. The angle between the two legs of the tube is 75 °C. The bulge parameter is *D/d* = 3, for the model given below.

For the solid domain, different wall thickness was considered for the tube region and the bulge region. The tube wall thickness, excluding the bulge region, was considered to be 0.3 mm [9]. The minimum thickness of an aneurysm before rupture was reported to be 0.05 mm by Abruzzo et al. [10]. So, the thickness of 0.20 mm was used for the bulge. In the second case, the aneurysm was considered to be fully filled with a porous medium to model endovascular coiling treatment in cerebral aneurysm.

## 2.2 Governing Equations and Boundary Conditions

**Fluid region**. The blood flow is laminar and pulsatile. Blood is modeled as an incompressible fluid with a density equal to 1050 kg/m³. The porous medium is present in the bulge region.

The governing equations for incompressible fluid flow through the non-porous and porous media, Nield and Bejan [11]:

$$\frac{\partial u_i}{\partial x_j} = 0 \tag{1}$$

$$\frac{\partial u_i}{\partial t} + u_j \frac{\partial u_i}{\partial x_j} = -\frac{\partial p}{\partial x_i} + \frac{1}{Re} \frac{\partial}{\partial x_j} \left( \frac{\mu}{\mu_\infty} \left[ \frac{\partial u_i}{\partial x_j} \frac{\partial u_j}{\partial x_i} \right] \right) - \frac{\phi}{ReDa} \frac{\mu_\infty}{\mu} u_i - \frac{C_f}{\sqrt{Da}} |u_i| u_i \tag{2}$$

The last three terms of Eq. (2) are referred to as the Brinkman, Darcy, and Forchheimer terms, respectively. For simulating flow through a clear medium,

**Table 1** Parameters for governing equations

| $\mu_o$, $P_{a\text{-}s}$ | $\mu_{\infty}$, $P_{a\text{-}s}$ | $M$ | $n$ | $a$ | $\rho$, kg/m$^3$ | $\varphi$ [20] | $K$, m$^2$ [20] | $Cf$ [20] |
|---|---|---|---|---|---|---|---|---|
| 0.16 | 0.0035 | 8.2 | 0.64 | 1.23 | 1050 | 0.735 | 1.55e−8 | 0.2 |

Darcy and Forchheimer terms will be zero. The non-Newtonian properties of blood are simulated using the Carreau–Yasuda model [12]:

$$\mu(\gamma) = \mu_{\infty} + \frac{\mu_0 - \mu_{\infty}}{(1 + m\gamma^n)^a} \tag{3}$$

where $\gamma = \left(0.5 e_{ij} e_{ij}\right)^{0.5}$ and, $e_{ij} = \frac{1}{2}\left(\frac{\partial u_i}{\partial x_j} + \frac{\partial u_j}{\partial x_i}\right)$

The term $m$ represents the relaxation time, and terms $\mu_{\infty}$ and $\mu_o$ represent the viscosity at infinite and zero shear rate, respectively. The values are given in Table 1.

where $\varphi$ = porosity, $K$ = permeability and $Cf$ = inertia coefficient for the porous media within the bulge. The Darcy number ($Da$) of the coil is $K/D^2 = 1.55 \times 10^{-4}$. For a Reynolds number of 480 and a frequency of $f = 1.2$ Hz, the Womersley number $Wo$ was found to be 7.8 and is consistent with flow in the brain.

$$Wo = \frac{d}{2}\sqrt{\frac{2\pi f \rho}{\mu_{\infty}}} \tag{4}$$

For the unsteady flow simulation, at each time step the Womersley profile [13] as given in Fig. 2 is specified as the inlet. Based on the inlet velocity profile, the mean Reynolds number was found to be 480. Pressure is specified as gradient outflow at the exit and has been derived from the work of Abdi et al. [14].

**Solid Region**. To the inner vascular wall of the geometry, 16 kPa (120 mm Hg) of peak systolic pressure was applied while zero external pressure was applied to
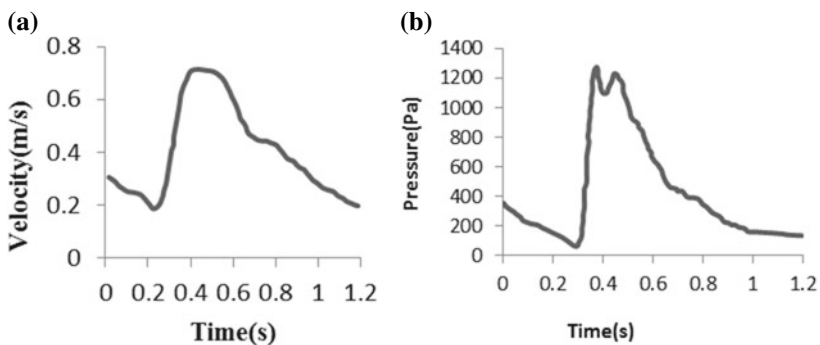


**Fig. 2** **a** Inlet velocity boundary condition. **b** Outlet pressure boundary condition

the outer vascular wall. The mechanical properties assigned to the aneurysm and the arterial wall were different. A nonlinear elastic material is modeled as described by Kelly and O'Rourke [15], wherein the following procedure was used for simulating the solid domain. Based on the relationship between stress $T$ and stretch ratio $\lambda$ for the arterial wall, provided by Raghavan and Vorp [16]

$$T_1 = \left[2\alpha + 4\beta\left(\lambda_1^2 + 2\lambda_1^{-1} - 3\right)\right]\left[\lambda_1^2 - \lambda_2^{-1}\right] \tag{5}$$

Value of $\alpha$ and $\beta$ was taken as 174000 and 1881000 Pa, respectively. Utilizing the previous relation an average stress–strain curve was calculated and is given by

$$\sigma = 2.744 \times 10^8 e^{7.275} - 2.744 \times 10^8 e^{7.272} \tag{6}$$

where $\varepsilon$ represents strain and $\sigma$ represents stress. The Young modulus of elasticity, $E$, is given by

$$E = \frac{d\sigma}{d\varepsilon} = 1996260000 e^{7.275\varepsilon} - 1995436800 e^{7.272\varepsilon} \tag{7}$$

The Young modulus of elasticity was then determined at each time step using the above equation. The material is now assumed to follow a linear elastic trend, and the corresponding values of displacement, stress, and strain are calculated. Similarly, the aneurysm was also modeled on the basis of the characteristics of intraluminal thrombus (ILT) as observed by Wang et al. [17].

$$T_1 = 2\left[c_1 + 2c_2\left(2\lambda_1 + \frac{1}{\lambda_1^2} - 3\right)\right] \tag{8}$$

The values of $c_1$ are taken as 28,000 Pa and $c_2$ as 28,600 Pa, respectively. The stress–strain relationship of ILT was calculated to be:

$$\sigma = 2.298 \times 10^7 e^{1.014\in} - 2.298 \times 10^7 e^{1.008\in} \tag{9}$$

Furthermore, the equation was differentiated to obtain a relationship for the Young modulus of elasticity, $E$

$$E = \frac{dy}{dx} = 23301720 e^{1.041\in} - 23163840 e^{1.008\in} \tag{10}$$

The momentum equation for a linear elastic material for the displacement $d$ is given by

$$\frac{\partial^2(\rho d)}{\partial t^2} = \nabla . \left[\mu\nabla d + \mu(\nabla d)^{\mathrm{T}} + \lambda Itr(\nabla d)\right] \tag{11}$$

where $\mu$ and $\lambda$ are Lame's coefficient which is related to Poisson's ratio $v$ and Young's modulus of elasticity $E$ as:

$$\mu = \frac{E}{2(1+\vartheta)} \text{ and } \lambda = \frac{\vartheta E}{(1+\vartheta)(1-2\vartheta)} \tag{12}$$

**FSI Simulation**. Iterations are separately carried out for both the fluid and solid systems to achieve convergence separately, and then, the entire system is solved for each time step, and hence, convergence is ensured. This is the general basis of various fluid–solid coupling codes which have been developed [18, 19].

## 2.3 Discretisation

The geometry was meshed in Gambit and thereafter imported into OpenFOAM. Mesh independency study was carried out considering both fluid and solid domains. The mesh independency studies produce the same results for $1.08 \times 106$ and $1.25 \times 106$ elements for the fluid region. For the solid domain, the value of maximum von Mises stress was used in order to conduct the mesh independency test and it was found that a mesh giving $1.21 \times 105$ elements, produced mesh-independent results. A grid quality of 0.9 was ensured throughout the geometry. The FSI solver was validated with the results of Kelly [15].

## 3 Results and Discussion

The quantities of interest in this study include (i) flow distribution, (ii) wall shear stress, (iii) wall pressure, (iv) von Mises stresses, and (v) wall displacement in the bulge.

## 3.1 Velocity Contour

In Fig. 3a, b, the time-averaged velocity contour has been shown in $x$-$y$ mid-plane for the case prior to and succeeding endovascular treatment. The flow in the bulge is stronger in a clear media, and the corresponding velocities are subsequently greater in the case of clear medium. However, after the placement of a coil the circulating velocities in the bulge reduce. This is because of the fact that the coil is creating a bypass, which leads to a drastic reduction of the wall loading in the aneurysm.

**Fig. 3** Time-averaged contours of (**a**, **b**) absolute velocity (at mid-plane in front view), (**c**, **d**) wall pressure, (**e**, **f**) wall shear stress, (**g**, **h**) wall displacement (systolic phase) and (**i**, **j**) maximum von-Mises stress in clear media (first column) versus porous media (second column) for *Re* = 480 and *Wo* = 7.82
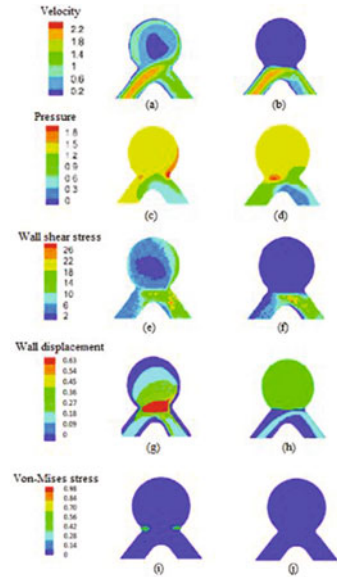


## 3.2 Pressure

The pressure levels were found to be marginally higher in the case of flow through a clear medium; however, from Fig. 3c, d it can be observed that pressure remains relatively unaffected by coil embolisation. This is because the bulge is a zone of separation even prior to the insertion of the coil, and hence, even after coil embolisation a uniform pressure exists because of low value of flow occurring within the bulge.

## 3.3 Wall Shear Stress

Time-averaged WSS contours are given for both the cases in Fig. 3e, f. The wall shear stress values were found to reduce nearly by a factor of 7 after insertion of coil, because of subsequent reduction of flow in the bulge. This can subsequently reduce the probability of rupture of the aneurysm.

## 3.4 Wall Displacement

Figure 3g, h shows the contour of solid displacement for both cases during the systolic phase. The maximum displacement is found to be 0.63 and 0.33 mm for the

case before and after coil embolisation, respectively. The value indicates that the maximum displacement for the treated aneurysm is 47% less than in case of untreated aneurysm. This clearly signifies that treatment using endovascular coiling can decrease the displacement of the blood vessel's wall and hence reduce the risk of rupture, thus proving to be an efficient treatment technique.

## 3.5   *Von Mises Stress*

Von Mises stress is a combination of the normal and shear stresses exerted on the solid wall. Hence, when compared to the material strength of the blood vessel's wall can determine the chances of rupture of the aneurysm wall. The contours of the von Mises stress that occur at the neck of the aneurysm have been given in Fig. 3i, j. The maximum stress for the cases prior to and succeeding treatment is 0.98 and 0.12 MPa, respectively. With the insertion of the coil, the relative reduction of the maximum von Mises stress is 87%.

## 4   Conclusion

In the present study, coil embolization modeling of cerebral aneurysm is reported. The coils are modeled as a porous medium. The linear elastic model is used to model the solid wall. The Womersley velocity profile is applied at the inlet of the fluid. The finite volume method is used to solve the unsteady state governing equations in 3D for both the solid and fluid solver. The results obtained show that in the presence of a coil in the bulge, the flow is bypassed, and the wall loading in the bulge drastically reduces. The wall shear stress decreases, and the displacement of the aneurysm wall is also found to decrease to a considerable extent. The von Mises stresses drastically reduce after coil embolization. However, the pressure was found to remain relatively unaffected. The percentage reduction in von Mises stress and the wall displacement was also appreciable. Thus, it is safe to conclude that coil embolization technique can be used to effectively treat cerebral aneurysms. Also, it can be concluded that FSI-based simulations can be effectively carried out to model blood flow in suitable biological models to determine the effectiveness of various treatment techniques. This solver can be applied to patient-specific models to effectively predict the response of the patient to the treatment.

## References

1. Lieber BB et al (2002) Particle image velocimetry assessment of stent design influence on intra-aneurysmal flow. Annals of Biomed Eng 30(6):768–777

2. Cantón Gádor, Levy David I, Lasheras Juan C (2005) Changes in the intraaneurysmal pressure due to HydroCoil embolization. Am J Neuroradiol 26(4):904–907

3. Boussel L et al (2008) Aneurysm growth occurs at region of low wall shear stress: patient-specific correlation of hemodynamics and growth in a longitudinal study. Stroke 39 (11):2997–3002

4. Mitsos AP et al (2008) Haemodynamic simulation of aneurysm coiling in an anatomically accurate computational fluid dynamics model. Neuroradiology 50(4):341–347

5. Wu Jiacheng, Shadden Shawn C (2015) Coupled simulation of hemodynamics and vascular growth and remodeling in a subject-specific geometry. Ann Biomed Eng 43(7):1543–1554

6. Agrawal V et al (2015) Effect of coil embolization on blood flow through a saccular cerebral aneurysm. Sadhana 40(3):875–887

7. Weir B (1987) Aneurysms affecting the nervous system. Williams & Wilkins, Philadelphia

8. Gobin YP, Counord JL, Flaud P, Duffaux J (1994) In vitro study of haemodynamics in a giant saccular aneurysm model: influence of flow dynamics in the parent vessel and effects of coil embolisation. Neuroradiology 36(7):530–536

9. Torii R et al (2010) Influence of wall thickness on fluid–structure interaction computations of cerebral aneurysms. Int J Numer Methods in Biomed Eng 26(3–4):336–347

10. Abruzzo T et al (1998) Histologic and morphologic comparison of experimental aneurysms with human intracranial aneurysms. Am J Neuroradiol 19(7):1309–1314

11. Nield DA, Bejan A and Nield-Bejan (2006) Convection in porous media Vol. 3. Springer, New York

12. Leuprecht, A, Perktold, K (2001) Computer simulation of non-Newtonian effects of blood flow in large arteries. Comput Methods Biomech Biomed Eng 4:149–163

13. Hale JF, McDonald DA, Womersley JR (1955) Velocity profiles of oscillating arterial flow, with some calculations of viscous drag and the Reynolds number. J Physiol 128(3):629–640

14. Abdi M, Navidbakhsh M, Razmkon A (2016) A lumped parameter method to calculate the effect of internal carotid artery occlusion on anterior cerebral artery pressure waveform. J Biomed Phys Eng 6(1):33

15. Kelly SC, O'rourke MJ (2010) A two-system, single-analysis, fluid—structure interaction technique for modelling abdominal aortic aneurysms. Pro Inst Mech Eng, part H: J Eng Med 224(8):955–969

16. Raghavan ML, David A (2000) Vorp: toward a biomechanical tool to evaluate rupture potential of abdominal aortic aneurysm: identification of a finite strain constitutive model and evaluation of its applicability. J Biomech 33(4):475–482

17. Wang DHJ et al (2001) Mechanical properties and microstructure of intraluminal thrombus from abdominal aortic aneurysm. J Biomech Eng 123(6):536–539

18. Ivankovic A et al (2002) Towards early diagnosis of atherosclerosis: the finite volume method for fluid–structure interaction. Biorheol 39(3–4):401–407

19. Karac A, Ivankovic A (2003) Modelling the drop impact behaviour of fluid-filled polyethylene containers. In: European structural integrity society, Elsevier, Amsterdam, vol 32, pp 253–264, 2003

20. Kakalis NMP et al (2008) The haemodynamics of endovascular aneurysm treatment: a computational modelling approach for estimating the influence of multiple coil deployment. IEEE Trans Med Imaging 27(6):814–824

# Numerical Investigation of Solar Air Heater Duct with Square Transverse and Inclined Ribs

**Gaurav Lad, Nikhil Raghuvanshi, Pranshu Mehrotra and Ankur Srivastava**

**Abstract** A numerical investigation has been carried out in order to investigate the effect of artificial roughness on heat transfer coefficient and pressure loss of air flow through an asymmetrically heated rectangular solar air heater duct with constant heat flux condition on absorber plate. Reynolds number is varied from 3000 to 15000. Artificial roughness in the form of transverse and inclined ribs is applied to the surface of the absorber plate. Heat transfer coefficient, friction factor and thermo-hydraulic performance parameter (THPP) are calculated for the range of roughness parameters; relative roughness pitch ($P/e$) from 11 to 25 at constant relative roughness height ($e/D$) of 0.8. RNG $k$-$\varepsilon$ turbulence model has been selected for CFD simulation. Artificially roughened surface increased heat transfer coefficient at the expense of increased pressure loss of air flow through the duct.

**Keywords** Solar air heater · CFD · Thermo-hydraulic performance parameter

## 1 Introduction

Solar air heater is a device which converts solar thermal energy into heat energy. The simplicity in designing, operational and maintenance costs makes solar air heaters cost-effective and is popularly used as a conversion device for the solar energy. It comprises an absorber plate, a heater, insulation, blower, and the air flows between the absorbing plate and rear plate. Because of low convective heat transfer coefficient between the absorber plate and flowing air stream yields an increased collector plate temperature, greater loss of thermal energy and poor thermo-hydraulic performance. The development of a viscous sub-layer is a possible cause for convective heat poor transfer coefficient. The resistance to heat

G. Lad · N. Raghuvanshi · P. Mehrotra (✉) · A. Srivastava
Mechanical Engineering Department, Manipal University Jaipur, Jaipur, India
e-mail: mehrotrapranshu@gmail.com

transfer arises due to this viscous sub-layer which can be eliminated by providing protrusions in the form of artificial roughness on the underside of the absorber plate. Artificial roughness in the form of repeated ribs has been found to be a convenient method to enhance the rate of heat transfer.

Prasad and Mullick [1] introduced the application of artificial roughness attached underneath the absorber plate in the form of a small diameter wire to enhance the thermo-hydraulic performance of solar air heater for drying purposes.

Saini and Verma [2] conducted an experiment on heat transfer and fluid flow characteristics of solar air heater with dimple-shaped roughness and found the maximum value of Nusselt number corresponding to the relative roughness height ($e/D$) of 0.0379 and relative roughness pitch ($p/e$) of 10. Bhushan and Singh [3] conducted an experimental investigation with chamfered repeated rib roughness on the airflow side of the absorber plates and found a considerable increase in thermal efficiency (10–40%) over smooth duct solar air heater. Heat transfer characteristic of the rectangular duct having periodic 'discrete V-down rib' was investigated by Singh et al. [4], and the maximum value of friction factor and the Nusselt number was found corresponding to relative roughness pitch ($p/e$) of 8. Aharwal et al. [5] conducted a numerical investigation on 60 ° inclined square ribs with a gap and relative roughness pitch ($p/e$) of 8; due to the gap, the secondary flow along the rib joins the main flow to accelerate it. Yadav and Bhagoria [6] conducted the numerical analysis of fluid flow and heat transfer characteristic on solar air heater having the roughness of square-sectioned transverse rib underside the absorber plate. The maximum value of thermo-hydraulic performance parameter was 1.82 corresponding to a relative roughness pitch ($p/e$) of 10.71. Table 1 shows work done by various authors.

On basis of the investigations, it is depicted that not only the rib geometry but also the geometrical arrangement plays a vital role in enhancing the heat transfer coefficient. Artificial roughness enhances the local heat transfer coefficient by creating turbulence in the flow, thus breaking the formation of viscous sub-layer. However, it also leads to an increase in friction losses, hereby leading to greater pumping power requirements for air through the duct. In order to keep the friction losses at a bare minimum, the turbulence must be created only in the region very close to the duct surface, i.e. in the vicinity of the laminar sub-layer region.

The present analysis revolves around the effect of roughness height ($H$), roughness pitch ($e$), relative roughness pitch ($p/e$) and relative roughness height ($e/D$) on fluid flow in a two-dimensional rib-roughened rectangular duct with only one wall subjected to uniform heat flux by making use of computer simulation. The ribs are provided only on the heated wall. The remaining wall is smooth and insulated.

**Table 1** Roughness geometries and their parameters

| S. no. | Investigators | Rib geometry | Optimum parameters |
|---|---|---|---|
| 1 | Prasad and Saini [7] | Transverse continuous rib | $p/e$ = 10–20,<br>$e/D$ = 0.02–0.033<br>$Re$ = 5,000–50,000 |
| 2 | Gupta et al. [8] | Inclined continuous rib | $p/e$ = 7.5–10,<br>$e/D_h$ = 0.02–0.53,<br>$Re$ = 5,000–30,000,<br>$\alpha$ = 30°–90° |
| 3 | Saini and Saini [9] | Expanded metal mesh | $e/D_h$ = 0.012–0.039<br>$Re$ = 1,900–13,000<br>$L/e$ = 25–71.87<br>$S/e$ = 15.6–46.87 |
| 4 | Momin et al. [10] | V-shaped continuous rib | $p/e$ = 10<br>$e/D_h$ = 0.02–0.034<br>$Re$ = 2,000–18,000<br>$\alpha$ = 30°–90° |
| 5 | Karwa et al. [11] | Chamfered rib | $p/e$ = 4.5–8.5<br>$e/D_h$ = 0.0141–0.0328<br>$Re$ = 3,000–20,000°<br>$W/H$ = 4.8–12<br>$\Phi$ = −15°–18° |
| 6 | Sahu and Bhagoria [12] | Transverse broken rib | $Re$ = 3,000–12,000<br>$p$ = 10–30 mm<br>$W/H$ = 8 |
| 7 | Aharwal et al. [13] | Inclined rib with gap | $p/e$ = 4–10<br>$e/D_h$ = 0.018–0.037<br>$Re$ = 3,000–18,000<br>$d/W$ = 0.16–0.5<br>$g/e$ = 0.5–2<br>$\alpha$ = 30°–90° |
| 8 | Hans et al. [14] | Multiple v-shaped ribs | $Re$ = 2,000–20,000<br>$e/D_h$ = 0.019–0.043<br>$p/e$ = 6–12°<br>$W/w$ = 1–10<br>$\alpha$ = 30°–75° |
| 9 | Kumar et al. [14] | Multiple v-shaped ribs with gap | $p/e$, $e/D$, $g/p$, $d/w$, $\alpha$ |
| 10 | Yadav and Bhagoria [6] | Square-sectioned rib | $p/e$ = 10.71, $e/D$ = 0.042 |
| 11 | Yadav and Bhagoria [15] | Equilateral triangular-sectioned rib | $p/e$ = 7.14, $e/D$ = 0.042 |

## 2 CFD Investigation

The simulations were conducted in ANSYS Fluent 14.1 which comprised of both heat transfer and fluid flow phenomenon in an artificially roughened duct. The artificial roughness having a different relative roughness pitch ($p/e$) was in the form of square transverse and inclined ribs. The following assumptions are considered for computational analysis of fluid flow and heat transfer through an artificially roughened solar air heater duct:

1. A 2-D steady, incompressible fully developed flow is considered so that the governing equation does not change by region to region and hence the analysis can be done easily.
2. The absorber plate, top and bottom walls and roughness elements are homogenous and isotropic.
3. Thermal conductivity of solution domain is independent of temperature.
4. Effects of radiation heat transfer are neglected.

The methodology, computational model and all the relevant details are explained below in the following sections.

### 2.1 Solution Domain

Figures 1 and 2 represent the experimental set-up for square-sectioned and inclined geometries, respectively. Both the domains are divided into three sections, which are the entry section ($L_1$), test section ($L_2$) and exit section ($L_3$). The dimensions of the set-up are according to ASHRAE standards (2003). A rectangular duct with height ($H$), rib height ($e$), relative roughness pitch ($p/e$) ratios varying from 25, 18, 11 for fixed relative roughness height ($e/D$) of 0.08 ratio and aspect ratio (AR) of 11 has been taken for analysis. The absorber plate is made up of 2-mm-thick aluminium sheet which contains the roughened artificial ribs of both transverse and inclined geometries. The top and bottom walls are smooth and insulated. A uniform heat flux of 1200 W/m$^2$ is provided on the absorber plate only at test section. A 2-D analysis is carried out in Fluent 14.1. Table 2 shows the geometrical parameters,
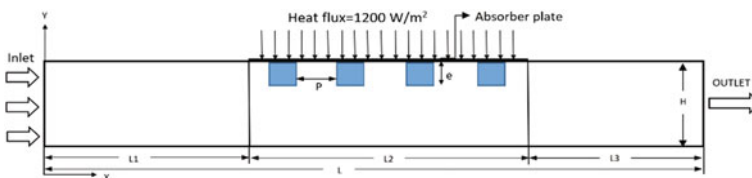


**Fig. 1** Schematic of 2-D computational domain with square transverse ribs
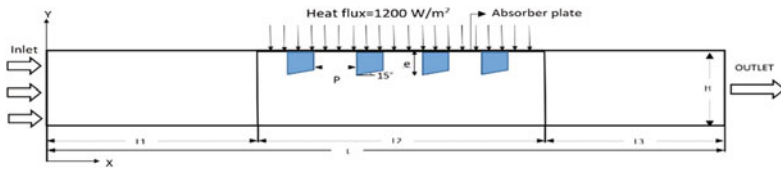
**Fig. 2** Schematic of 2-D computational domain with 15° inclined ribs

**Table 2** Geometrical parameters

| $L_1$ (mm) | $L_2$ (mm) | $L_3$ (mm) | $W$ (mm) | $H$ (mm) | $D$ (mm) | Rib height 'e' (mm) | Pitch 'P' (mm) |
|---|---|---|---|---|---|---|---|
| 490 | 1700 | 250 | 300 | 27 | 49.54 | 4 | 100,72,44 |

**Table 3** Operating parameters

| Operating parameters | Range |
|---|---|
| Uniform heat flux 'q' | 1200 W/m$^2$ |
| Reynolds number 'Re' | 3000–15000 |
| Prandtl number 'Pr' | 0.7132 |
| Relative roughness pitch 'P/e' | 25, 18, 11 |
| Relative roughness height 'e/D' | 0.08 |
| Duct aspect ratio 'W/H' | 11 |

**Table 4** Thermo-physical properties

| Properties | Working fluid (air) | Absorber plate (aluminium) |
|---|---|---|
| Density '$\rho$' (kg/m$^3$) | 1.225 | 2719 |
| Specific heat '$C_p$' (J/kg k) | 1006.2 | 871 |
| Viscosity '$\mu$' ($Ns$/m$^2$) | $1.798 \times 10^{-5}$ | – |
| Thermal conductivity '$k$' (W/mK) | 0.0261 | 202.4 |

Table 3 shows the operating parameters, and Table 4 shows the thermo-physical properties employed in our simulation.

## 2.2 Grid Generation

A 2-D non-uniform structured mesh is generated using ICEM CFD v15.0 such that mesh is fine at adjacent to the absorber plate because it resolves the laminar sub-layer formed near the absorber plate (Fig. 3). The simulations were carried out for grids with different numbers of nodes ranging from 200,000 to 800,000 cells.
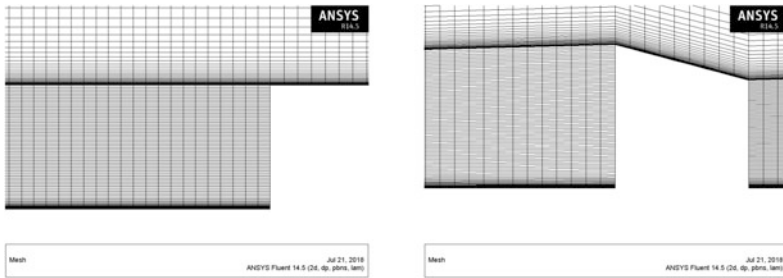
**Fig. 3** Non-uniform unstructured mesh for square and inclined geometries
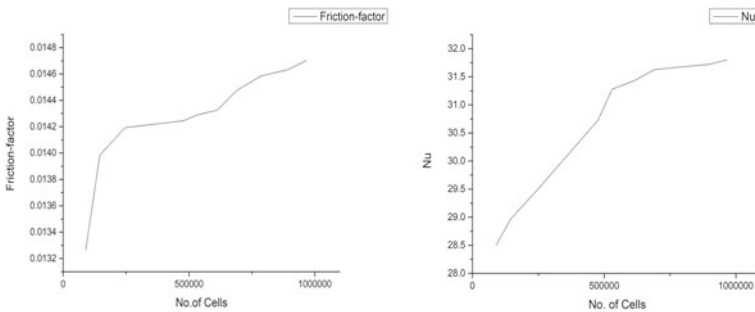


**Fig. 4** Grid independency test for case of $f_t$ and $Nu$ at $Re = 5000$

After 612,456 cells, the variation in values of Nu and friction factor holds not that much of significance. It has been observed that there is less than a 1% difference in successive values for results obtained after 612,456 cells. Hence, values above 612,456 cells are considered to be grid independent (Fig. 4).

## 2.3 Governing Equations

The following continuity, conservation of momentum and energy equation govern the fluid flow and heat transfer through artificially roughened solar air heater duct:

Continuity equation:

$$\frac{\partial u}{\partial x} + \frac{\partial u}{\partial y} = 0 \tag{1}$$

Momentum equation:

$$u\frac{\partial u}{\partial x} + v\frac{\partial v}{\partial y} = -\frac{1}{\rho}\frac{\partial p}{\partial x} + \vartheta\left(\frac{\partial^2 u}{\partial x^2} + \frac{\partial^2 u}{\partial y^2}\right) \tag{2}$$

$$u\frac{\partial v}{\partial x} + v\frac{\partial v}{\partial y} = -\frac{1}{\rho}\frac{\partial p}{\partial y} + \vartheta\left(\frac{\partial^2 v}{\partial y^2} + \frac{\partial^2 v}{\partial y^2}\right) \tag{3}$$

Energy equation:

$$u\frac{\partial T}{\partial x} + v\frac{\partial T}{\partial y} = \alpha\left(\frac{\partial^2 T}{\partial x^2} + \frac{\partial^2 T}{\partial y^2}\right) \tag{4}$$

In the interest of CFD investigation, the relevant dimensionless numbers, i.e. Reynolds number ($Re$), Nusselt number for roughened duct ($Nu$), friction factor for roughened duct ($f_r$), thermo-hydraulic performance parameter (THPP), are defined.

$$Re = \frac{\rho u D}{\mu} \tag{5}$$

$$Nu = \frac{hD}{k} \tag{6}$$

$$f_r = \frac{2\Delta PD}{\rho L u^2} \tag{7}$$

$$THPP = \frac{Nu_r/Nu_s}{\left(f_r/f_s^{1/3}\right)} \tag{8}$$

Dittus–Boelter equation predicts the value of average $Nu$ over the smooth duct and is given by the correlation

$$Nu_s = 0.023\,Re^{0.8}Pr^{0.4} \tag{9}$$

Modified Blasius result is used to predict friction factor over the smooth duct and is given by the correlation,

$$f_s = 0.0791\,Re^{-0.25} \tag{10}$$

## 2.4 Boundary Conditions

The boundary condition is applied to the computational domain which is a 2-D rectangular duct in the $X$-$Y$-plane that consists of an inlet, outlet and absorber plate, and bottom wall. The velocity at the inlet is varied from 0.884 to 4.421 m/s

corresponding to the *Re* at a fixed inlet temperature of 300 K. A fixed pressure is given at the outlet which is 100000 Pa. The absorber plate and the bottom wall are modelled adiabatic, and no-slip condition is applied to them. The absorber plate (top wall) which consists of artificial rib roughness is applied with a constant heat flux of 1200 W/m$^2$.

## 2.5   Selection of Turbulence Model

The derivation of the RNG-based *k-ε* turbulence model is derived from the instantaneous Navier–Stokes equations, using a mathematical technique called 'renormalization group' (RNG) methods. The additional terms in its *ε* equation significantly improve the accuracy for rapidly strained flows in RNG equation. Yadav and Bhagoria [6] carried out the comparison between various turbulence models; namely, standard *k-ε* model, renormalization group *k-ε* model, realizable *k-ε* model, standard *k-ω* and shear stress transport *k-ω* model are compared with the empirical correlation available for smooth duct of a solar air heater, i.e. Eq. (9), for predicting the Nusselt number.

## 3   Results, Discussion and Validation

A thorough examination of several CFD simulations concerning about the effects due to the provision of squared transverse ribs and inclined ribs having operating parameters like the relative roughness pitch (*p/e*) over a range of Reynolds number (*Re*) (3000–15000) on thermal and fluid flow characteristics of an asymmetrically heated solar air heater duct has been presented. The obtained results are then compared to those of a smooth duct which is being functioned under identical operating conditions to determine the enhancement of thermo-hydraulic performance on account of the artificial roughness.

## 3.1   Thermal Characteristics

This section involves discussions about the numerical results describing the varying effects in heat transfer characteristics such as average Nusselt number (*Nu*), turbulent kinetic energy and turbulent intensity. Figure 5 shows the varying trends in average Nusselt number (Nu) for different orientations of rib geometries at a different relative roughness pitch (*p/e* = 25, *p/e* = 18, *p/e* = 11) with a fixed relative roughness height (*e/D*) of 0.08. The simulated values of average Nusselt number for smooth duct (*Nu*$_s$) have been found in close limits to values calculated by Dittus–Boelter equation (Eq. (9)). We observed an increase in the value of average Nusselt

number ($Nu$) by a factor of 1.3–1.9 when compared to the average Nusselt number for smooth duct ($Nu_s$). The main cause of its increase is due to the introduction of artificial roughened ribs which increases turbulence within the viscous sub-layer region formed in the vicinity of wall surface. It is also a known fact that turbulent kinetic energy and turbulent dissipation rate are enhanced as there is an increment in the value of Reynolds number ($Re$). This leads to an increase in the turbulent intensity, hereby increasing the average Nusselt number ($Nu$). Reattachment of velocity layers between the inter-rib regions also contributes to this effect. This is evident from the temperature contour (Fig. 6) and velocity streamline plot (Fig. 7) obtained for Reynolds number ($Re$) 5000 for $e/D = 0.08$. Due to the provision of artificial roughness, better heat enhancement is observed which tends to increase in static temperature near the rib surface. Similar results were observed for Reynolds number ($Re$) ranging from 3000 to 15000. Figure 8 shows the comparison of the increase in average Nusselt number ($Nu$) amongst square-sectioned and inclined ribs. Inclined ribs offer better heat transfer characteristics; an increment by a factor of about 1.05–1.1 in average Nusselt number ($Nu$) is observed in the case of inclined ribs compared to square-sectioned ribs. Overall highest increase in average Nusselt number ($Nu$) is found out in 15° inclined ribs with relative roughness pitch ($p/e$) 11 for the range of Reynolds number ($Re$) 10,000–15,000. The heat transfer phenomenon is also found to increase as we reduce relative roughness pitch ($p/e$) for both square-sectioned and inclined geometries.

## 3.2   Fluid Flow Characteristics

The numerical results describing variation in friction factor obtained through CFD simulations are presented in this section. Figure 9 shows the varying trend in friction factor ($f_r$) for different orientations of rib geometries at a different relative roughness pitch ($p/e = 25$, $p/e = 18$, $p/e = 11$) with a fixed $e/D$ of 0.08. Values of



**Fig. 5** Variation of $Nu$ for transverse and inclined geometries at different $p/e$ compared with smooth duct at different $Re$
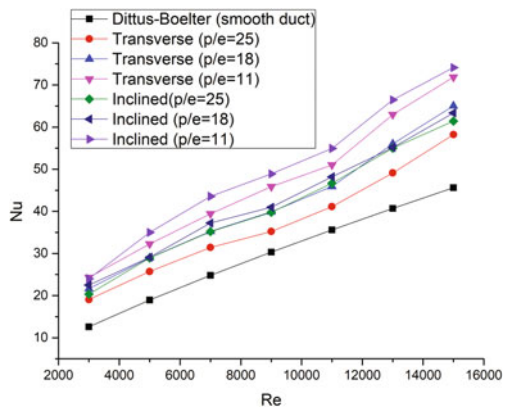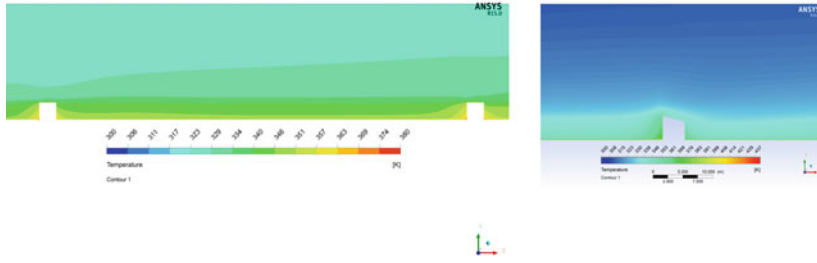
**Fig. 6** Contour plot for temperature for square transverse and inclined ribs at $Re = 5000$, $p/e = 25$, $e/D = 0.08$
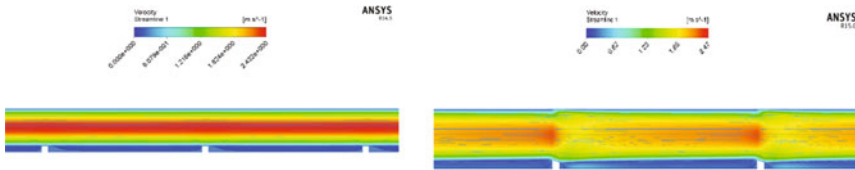


**Fig. 7** Streamline plot for velocity for square transverse and inclined ribs at $Re = 5000$, $p/e = 25$, $e/D = 0.08$

**Fig. 8** Comparison of $Nu$ for square and inclined geometries with different $p/e$ at different $Re$
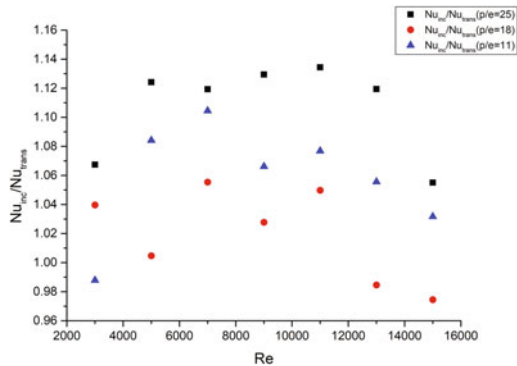


friction factor for smooth duct ($f_s$) are calculated by using modified Blasius equation (10). The friction factor is found to decrease as Reynolds number ($Re$) is increased. Upon the air's entry in the roughened region of the rectangular duct, the gradually accelerating air faces resistance due to the presence of ribs and vortex formation is seen between the inter-rib regions. This phenomenon is responsible for an increased pressure drop, and hence friction factor for the roughened duct ($f_r$) increases by a greater value compared to the friction factor of the smooth duct ($f_s$). It can be demonstrated via pressure contour across the duct in Fig. 10. Comparison of friction factors ($f_r$) of both rib geometries with friction factor of smooth ($f_s$) duct records

an increment in friction factor ($f_r$) for roughened duct by a factor of about 2.5–4 at lower values of Reynolds number ($Re$). This difference then decreases to a factor of 1.2–1.3 at Reynolds number ($Re$) 13000 and above. Highest increase is being observed at lower values of relative roughness pitch ($p/e$). Friction factor ($f_r$) increases as we decrease relative roughness pitch ($p/e$) Fig. 9. Mostly, it is evident that square-sectioned ribs under similar working parameters and dimensions offer higher pressure drop compared to inclined ribs and hence result in the greater value of average friction factor ($f_r$). When compared amongst each other, average friction factor ($f_r$) of square-sectioned ribs is found to be 1.1–1.4 times greater than average friction factor ($f_r$) of inclined ribs for an entire range of Reynolds number ($Re$), Fig. 11. This difference seems to decrease at around Reynolds number ($Re$) ranging from 8000 to 11000. By comparing all the results, it is deduced that 15° inclined ribs with relative roughness pitch ($p/e$) 11 with fixed $e/D$ of 0.08 offer most optimum values of increase in friction factor when compared to other geometries.

## 3.3 Thermo-hydraulic Performance Parameter

Thermo-hydraulic performance parameter represents the overall performance of a solar air heater; its value is evaluated by simultaneously considering thermal effects as well as the hydraulic performance using Eq. (8). In this study, thermo-hydraulic performance parameter based on constant pumping power requirement has been adopted for the optimization of roughness and flow parameters for artificially roughened solar air heater. Figure 12 shows the variation in THPP for square-sectioned and inclined geometries at different Reynolds numbers ($Re$). There is a significant difference in the value of THPP between square-sectioned and inclined geometries. After thorough analysis, it is found that inclined geometries offer slightly better THPP than square transverse geometries for corresponding $p/e$. This is due to better heat enhancement and low-pressure drop observed in inclined geometries at all $p/e$, as compared to square transverse geometry. Value of

**Fig. 9** Variation of friction factor for transverse and inclined geometries at different $p/e$ compared with smooth duct at different $Re$
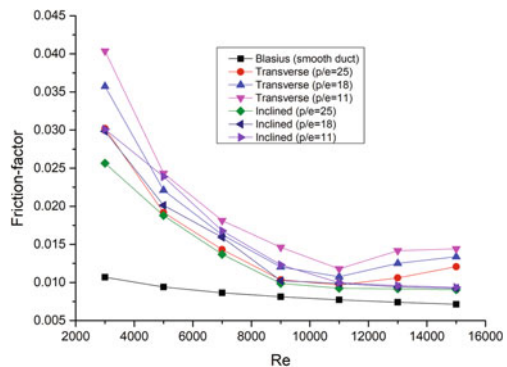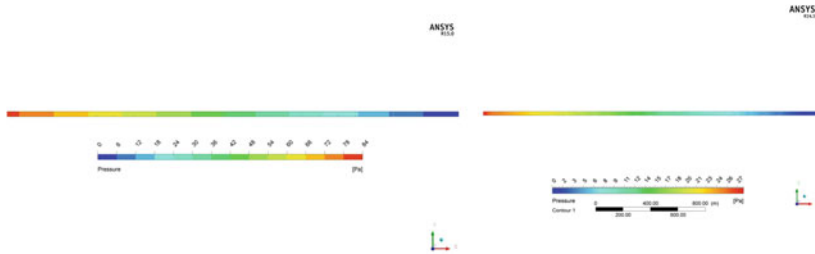
**Fig. 10** Contour plot for static pressure for square transverse ribs and inclined ribs at $Re = 5000$, $p/e = 25$, $e/D = 0.08$

**Fig. 11** Comparison of friction factor for square and inclined geometries with different $p/e$ at different $Re$
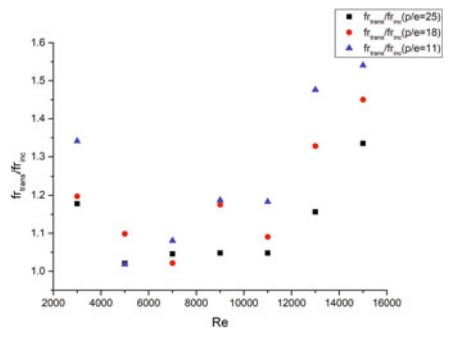


**Fig. 12** Variation in THPP for transverse and inclined geometries at different $Re$
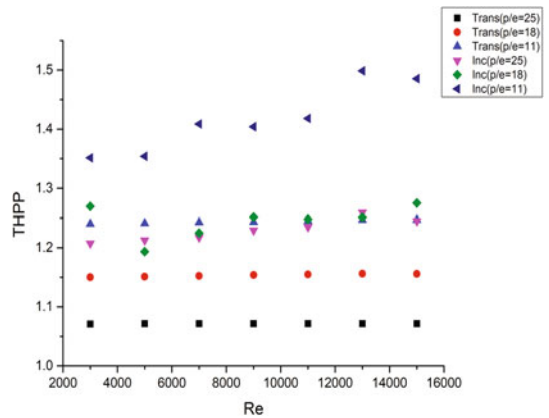


THPP is dropped down by small increment at higher Reynolds number ($Re$) for both geometries. Overall 15° inclined ribs with relative roughness pitch ($p/e$) 11 offer most optimum THPP which is around 1.35–1.49 for the complete range of Reynolds number ($Re$).

## 3.4   Validation

Computational simulations are only recognized if they are validated against experimental data or by widely accepted numerical models using similar boundary conditions. This method is used to test the accuracy of computational simulations. Validation of the results obtained is carried out as follows:

- Trends of average Nusselt number ($Nu$), average friction factor ($f_r$) and THPP of present CFD analysis are compared with the experimental results of Giovanni Tanda [16] and numerical results of Chaube et al. [17] and Yadav and Bhagoria [6] having roughly same dimensions of geometry and operating parameters used. Simulated values of Nusselt number ($Nu$) and friction factor ($f_r$) lie within an approximate 10–15% range when compared to those experimentally obtained by Tanda [16] which validates this study.
- A thorough literature review of previous studies suggests the optimum value of relative roughness pitch to lie in the range of 6–12 for the various arrays of rib roughness and geometries. On comparing those results, it is noticed that the value of relative roughness pitch ($p/e$) of this present work is found out as 11 which lies between the acceptable ranges prescribed by previous well-known results.

## 4   Conclusion

After a thorough analysis of results, the following arguments can be made.

The RNG $k$-$\varepsilon$ turbulence model yielded results which were in fair agreement with experimental results obtained by Tanda [16]. We can find maximum enhancement of average Nusselt number ($Nu$) at Reynolds number ($Re$) 3000 for square transverse ribs having relative roughness pitch ($p/e$) 11. Its value is found to be 1.93 times the Nusselt number for a smooth duct ($Nu_s$). The minimum increment in average friction factor ($f_r$) occurs at Reynolds number ($Re$) 11000 for inclined ribs having relative roughness pitch ($p/e$) 25. Its value is found to be 1.25 times friction factor for smooth duct ($f_s$). The maximum THPP obtained for inclined ribs (15°) with relative roughness pitch ($p/e$) 11 is 1.49, whereas for square transverse ribs it is 1.246, and these values occur at Reynolds number ($Re$) 13000. This study predicts the use of 15° inclined ribs with relative roughness pitch ($p/e$) of 11 in order to enhance the overall thermal performance of a solar air heater duct for given dimensions.

# References

1. Prasad K, Mullick SC (1983) Heat transfer characteristics of a solar air heater used for drying purposes. Appl Energy 13(2):83–93
2. Saini RP, Verma J (2008) Heat transfer and friction factor correlations for a duct having dimple-shaped artificial roughness for solar air heaters. Energy 33:1277–1287
3. Bhushan B, Singh R (2010) A review on methodology of artificial roughness used in duct of Solar air heaters. Energy 35:202–212
4. Singh S, Chander S, Saini JS (2011) Heat transfer and friction factor correlations of solar air heater ducts artificially roughened with discrete V-down ribs. Energy 36:5053–5064
5. Aharwal KR, Gandhi BK, Saini JS (2009) Heat transfer and friction characteristics of solar air heater ducts having integral inclined discrete ribs on absorber plate. Int J Heat Mass Transfer 52:5970–5977
6. Yadav AS, Bhagoria JL (2013) A CFD based heat transfer and fluid flow analysis of a solar air heater provided with circular transverse wire rib roughness on the absorber plate. Energy 55:1127–1142
7. Prasad BN, Saini JS (1988) Effect of artificial roughness on heat transfer and friction factor in a solar air heater. Sol Energy 41(6):555–560
8. Gupta D, Solanki SC, Saini JS (1997) Thermo-hydraulic performance of solar air heaters with roughened absorber plates. Sol Energy 61(1):33–42
9. Saini RP, Saini JS (1997) Heat transfer and friction factor correlations for artificially roughened Ducts with expanded metal mesh as roughness element. Int J Heat Mass Transfer 40(4):973–986
10. Karwa R, Solanki SC, Saini JS (1999) Heat transfer coefficient and friction factor correlation for the transitional flow regime in rib-roughened rectangular duct. Int J Heat Mass Transfer 42:1597–1615
11. Momin AME, Saini JS, Solanki SC (2002) Heat transfer and friction in solar air heater duct with V-shaped rib roughness on absorber plate. Int J Heat Mass Transfer 45:3383–3396
12. Sahu MM, Bhagoria JL (2005) Augmentation of heat transfer coefficient by using 90 broken transverse ribs on absorber plate of solar air heater. Renew Energy 30:2057–2063
13. Hans VS, Saini RP, Saini JS (2010) Heat transfer and friction factor correlations for a solar air heater duct roughened artificially with multiple V-ribs. Sol Energy 84:898–911
14. Kumar A, Saini RP, Saini JL (2013) Development of correlations for Nusselt number and friction factor for solar air heater with roughened duct having multi v-shaped with gap rib as artificial roughness. Renew Energy 58:151–163
15. Yadav AS, Bhagoria JL (2014) A CFD based thermo-hydraulic performance analysis of an artificially roughened solar air heater having equilateral triangular section rib roughness on the absorber plate. Int J Heat Mass Transfer 70:1016–1039
16. Tanda G (2011) Performance of solar air heater ducts with different types of ribs on the absorber plate. Energy 36(11) 6651–6660, Journal homepage. www.elsevier.com/locate/energy
17. Chaube A, Sahoo PK, Solanki SC (2006) Analysis of heat transfer augmentation and flow characteristics due to rib roughness over absorber plate of a solar air heater. Renew Energy 31:317–331

# Thermodynamic Investigation of Solar Energy-Driven Diffusion Absorption Refrigeration Cycle

**Kishan Pal Singh and Onkar Singh**

**Abstract** The increasing demand of refrigeration and air conditioning with associated consequence of global warming across the world has made it inevitable for scientific community to look for an alternative of conventional energy sources and to minimize effects of CFC's and HCFC's on global warming and ozone layer depletion while facilitating the requirements of refrigeration and air conditioning. It is evident that the geographical locations on the earth having ample sunshine have more refrigeration requirements; however, these locations also offer potential opportunity for utilizing solar radiations for solar energy-driven refrigeration systems. This study focuses on the thermodynamic modelling and analysis of solar energy-driven ammonia–water diffusion absorption refrigeration cycle with helium as pressure equalizing inert gas. It is seen that the loss percentage in the coefficient of performance (WPL and WHPL) is 2.8% higher than cooling capacity percentage loss at low generator temperature while there is no marginal drops at higher temperature. It is also found that the generator temperature in the range of 110–150 °C is best suited to produce maximum refrigerating effect.

**Keywords** Diffusion · Pressure equalizing gas · Aqua ammonia solution · Absorption · Coefficient of performance · Ambient temperature

## Nomenclature

| | |
|---|---|
| $\dot{Q}$ | Heat transfer rate (J/s) or (W) |
| $T$ | Temperature (°C, K) |
| $h$ | Enthalpy (kJ/kg) |
| $P$ | Pressure (kPa, bar) |
| $\xi$ | Mass fraction of ammonia in liquid phase |

K. P. Singh (✉)
Mechanical Engineering, A.K.T.U., Lucknow, Uttar Pradesh, India
e-mail: kishan.amu@gmail.com

O. Singh
Mechanical Engineering, H.B.T.U., Kanpur, Uttar Pradesh, India

| $\zeta$ | Mass fraction of ammonia in vapour phase |
|---|---|
| COP | Coefficient of performance |
| $\dot{m}$ | Mass flow rate (kg/s) |
| $X$ | Quality of vapour |
| $\Pi$ | Mass flow ratio |
| $I$ | Inert Helium gas |
| $\varepsilon$ | Effectiveness of heat exchanger |
| SHX | Solution heat exchanger |
| WPL | With pressure loss |
| WHPL | Without pressure loss |
| GHX | Gas heat Exchanger |

**Subscripts**

| v and $f$ | stands for vapour or gas and liquid |
|---|---|
| g | Generator |
| r | Rectifier |
| a | Absorber |
| c | Condenser |
| e | Evaporator |
| ar | Ammonia gas residuals |
| rh | Recuperative heat exchanger |
| sys | Total system pressure |
| Numeric | 1, 2, 3, … System's states |

## 1  Introduction

The first diffusion absorption system was based on three-fluid system invented by Von Platen and Munters in the year 1928 [1, 2]. In this cycle, aqua ammonia was used as working fluids and hydrogen as pressure equalizing inert gas. Zohar et al. [3] developed a complex thermodynamic model that explored the diffusion absorption refrigeration (DAR) cycle performance. It was found that the maximum COP with a DAR cycle can be obtained when the ammonia concentrations in rich and weak solutions are 0.25–0.30 and 0.10, respectively, for the generator temperature being around 150 °C. It also showed that COP of the system working with helium gas was higher up to 40% as compared to one with hydrogen. Research studies [4, 5] assumed that vapour leaving the rectifier was only pure ammonia with no droplets of water. Numerical analysis carried out by Starace and De Pascalis [6] shows that as the generator temperature increases beyond 150 °C, the rich solution mass flow rate reduces more than that of the refrigerant one and COP decreases. The results found were compared with the predictions of Zohar et al. [5] and showed the difference of

6.1, 8.5, and 2% in rich and poor solution, and COP, respectively. Srikhirin & Aphornratana [7] tested a heat power-driven DAR system with heat input from 1000 to 2500 W using aqua ammonia as working fluid and helium as pressure equalizing gas at vapour pressure 6.1 bar. The system cooling capacities were found to be between 100 and 180 W with a COP between 0.09 and 0.15. The impact of evaporator and absorber mass transfer performance has a strong effect of on the system performance. The cooling capacity does not only depend upon the refrigerant flow but also on the liquid solution circulation rate. Wang et al. [8] worked on a DAR system using binary refrigerant R23/R134a, absorbent DMF, and auxiliary gas helium. It was seen that for the best performance of the DAR system, the generating temperature should be in the range of 110–160 °C and the system total pressure should be in the range of 9–26 bar. Sözen et al. [9] investigated three DAR cycles having different configurations in which first DAR was similar to electrolux refrigerator in which the condensate is subcooled before evaporator entrance and second DAR, the condensate was not subcooled prior to evaporator entrance and the gas heat exchanger was separated to evaporator while in third DAR an ejector was placed at absorber inlet. The study showed a 40% reduction in energy consumption for relatively low temperature ($\sim 6$ °C) by DAR-3 for the same cooling area. Ben Ezzine et al. [10, 11] numerically investigated DAR cycle with working fluid R124/ DMAC and light hydrocarbon mixture as working fluid and helium as pressure equalizing gas. In this paper [10], the cycle was simulated for cooling medium temperature in range of 27–35 °C, and the driving generator temperature range was 90–180 °C. The result obtained shows that the capacity to attain lowest temperature in evaporator and performance of the system are largely dependent upon the absorber efficiency and the generator temperature. The fluid mixture [10] used for refrigeration showed a higher COP at lower generator temperature as compared to aqua ammonia system. This pair of working fluid also works on lower vapour pressure for inert gas and provides to decrease wall thickness of system. Ben Ezzine et al. studied the use of [11] binary hydrocarbon mixture ($C_4H_{10}/C_9H_{20}$) as working fluid with helium as pressure equalizing gas. The results show that for the range (120–150 °C) of generator temperature, at the generator temperature 138 °C, the lowest evaporator temperature attained was −10 °C. Wang [12] studied a DAR system using $LiNo_3$–$NH_3$–He as working fluid and a spray absorber with plate type to enhance the mass and heat transfer. This study shows that evaporator temperature mainly depends upon absorber temperature rather than generator and condenser temperatures. It shows the lowest evaporator temperature is of −13 °C, corresponding refrigerating capacity and COP are 1.9 kW and 0.156 at heat source, generator, absorber, and condenser temperature 92.7, 87, 29.6, and 21.6 °C, respectively. In different studies [1–15], it is assumed that the effects of pressure losses in fluid flow in pipe due to friction and dynamic pressure losses in different components of the diffusion absorption refrigeration system are negligible. Acuña et al. [16] presented in their study that the best option for transfer of heat between the hot fluids circulating in solar compound parabolic collector and the cooling refrigerants pair of DAR is glycerol-water ($C_3H_8O_2$–$H_2O$).

It is evident from the published work that the effects of pressure losses have significant impact and could deviate experimental results from theoretical results. In view of the prevailing gap, the present work is carried out for thermodynamic modelling and computer simulation of ammonia–water diffusion absorption refrigeration cycle considering pressure losses for its thermodynamic analysis. In Indian climatic conditions in summer season, the atmospheric temperature raises up to 44 °C. While in winter season, ambient temperature falls down up to 8–16 °C. So, considering round the year climatic conditions and received solar radiations, the operating ranges of ambient temperature for condenser and absorber are taken between 35 and 45 °C. The operating temperature ranges for the generator/desorber are taking between 110 and 150 °C which can be easily achieved round the year.

## 2   Model Description

Figure 1 shows the schematic of diffusion absorption refrigeration cycle. The DAR model has an evaporator, a condenser, a rectifier, a solution heat exchanger, a gas heat exchanger, an absorber, a receiver tank, and a generator which is basically a combination of a boiler and a bubble pump. The bubble pump is a cylindrical concentric hollow tube used to raise fluid from lower level to higher level due to thermosyphon. The rich solution of aqua ammonia is coming from receiver tank state 14 to the generator though the solution heat exchanger. Where it is heated with transfer of heat from the counter flow hotter solution of lean aqua ammonia is returning from the rectifier and separator through bubble pump state 15. This rich solution is further heated by the driving thermal power $Q_g$ in the generator as per the arrangement shown in diagram. The heated rich solution starts boiling and the bubbles of ammonia vapour rise carrying slugs of lean solution through bubble pump to the separator state 4. Lean aqua ammonia liquids flow down from separator, state 3, through annular outer pipe of bubble pump getting heat from inner tube of pump. For any possibilities of liquid in evaporated refrigerant vapours, evaporated vapour passes through rectifier. In rectifier, lean aqua ammonia solutions droplets filter rejecting heat $Q_r$ to ambient conditions and revert back to state 3 through state 5. Now the pure refrigerant vapours (state 6) at total system pressure enter into the condenser, which is a finned tube with natural convection cooling. In condenser, refrigerants vapour starts de-superheating and condenses into liquid at total system pressure after rejecting heat to the cooling medium of condenser. The uncondensed refrigerant vapour, if any, bypasses state 8 to the receiver tank. The condensed refrigerant liquid at state 7 drifts into evaporator at state 9 passing through gas heat exchanger; transferring heat and sub cooled to vapours of refrigerant and inert gas mixture coming from evaporator. The pressure equalizing gas with some contents of ammonia residual leaving absorber state 10, loose heat and enter into evaporator at state 11 after passing through the gas heat exchanger. The inert gas mixes with liquid refrigerant at state 12. The partial pressure of liquid refrigerant is reduced and allows the refrigerant to evaporate at lower temperature.
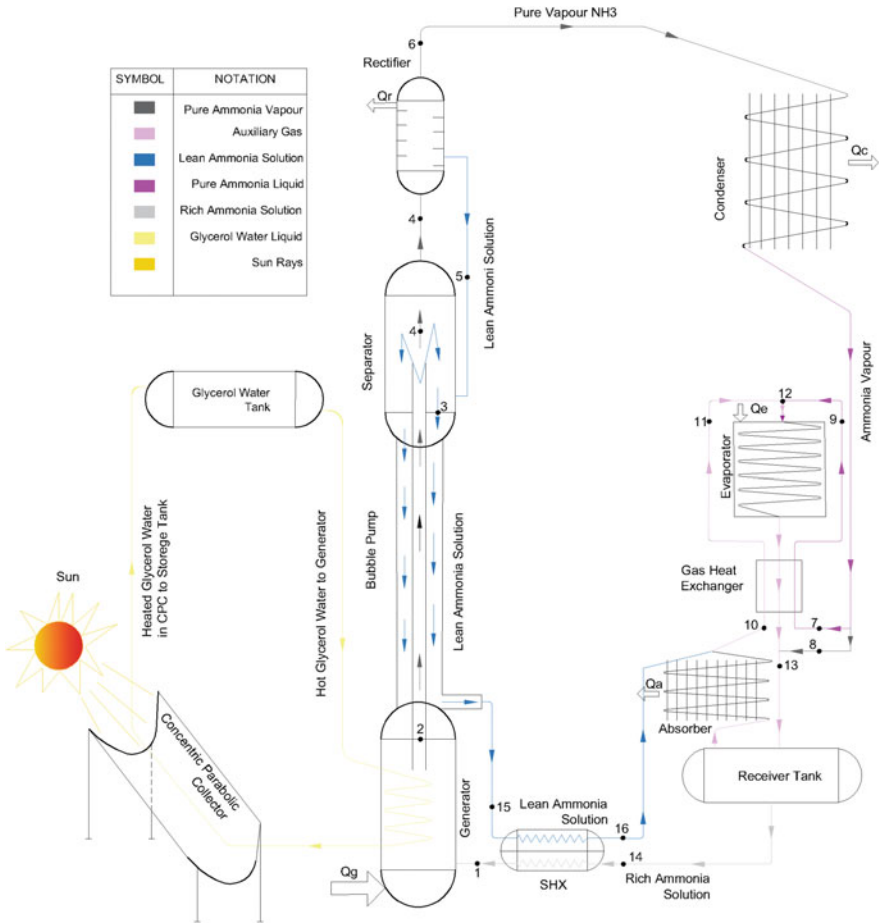
**Fig. 1** Schematic diagram of diffusion absorption refrigeration cycle modelled in this study using solar energy

The evaporation of refrigerant extracts heat $Q_e$ from the evaporator providing refrigeration effect. From the evaporator, mixtures of refrigerant and pressure equalizing gas return to receiver tank at state 13 passing through gas heat exchanger. In the passage of exchanger, the mixture absorbs some amount of heat, separately from the liquid ammonia from condenser and helium gas with some ammonia residuals coming from absorber and moving towards evaporator.

The ammonia and helium gas mixture enters into absorber coil from bottom and drifts upward while lean solution of aqua ammonia enters into absorber coil from the top at state 16 and flows downward in a counter flow arrangement. Ammonia vapours are readily absorbed in the lean solution rejecting heat $Q_a$ to the cooling

medium of the absorber which consequently forms rich solution of aqua ammonia drifting to the receiver tank. Helium gas is not absorbed and continues to flow to the evaporator with ammonia residuals at state 10. Helium leaving absorber is at higher temperature since it absorbs some part of heat liberated during absorption of ammonia in lean solution. The helium and ammonia gas circulation loop is driven by natural convection caused primarily by the larger density difference associated with the ammonia mass fraction in vapour. The rich solution of aqua ammonia leaves the receiver tank at state 14 and flows towards the generator.

The thermodynamic modelling of DAR system has been done to study and evaluate the performance of diffusion absorption refrigeration cycle. The modelling details for various components of DAR System are as under.

## 3   Thermodynamic Modelling

For the ease of thermodynamic modelling, some assumptions and considerations as detailed ahead are used in the present study.

- Solution and gas heat exchanger effectiveness are constant.
- Mixing of refrigerant liquid and inert gas at inlet of evaporator is adiabatic.
- The refrigerant vapours leave the gas heat exchanger at state 13 as saturated vapour.
- The gas mixture behaves like an ideal gas. The properties of mixtures are calculated according to the ideal gas considerations.
- The ambient temperature, generator, and evaporator temperature are specified.
- Pressure loss in pipe flow and dynamic pressure losses in components are considered as specified in input parameters.
- The components and piping of diffusion absorption refrigeration cycle are properly thermally insulated.
- There is no absorption taking place in the receiver tank.
- Ammonia refrigerant after rectification is 99.8% pure.
- The cooling medium for condenser is air. So, the condensation temperature is assumed to be ambient temperature. This assumption will provide a proper temperature gradient for heat transfer between refrigerant and condensing medium. Therefore, $T_7 =$ (ambient temperature) corresponds to saturation pressure (total system pressure). The condensation medium for both condenser and absorber is same ($T_{14} = T_7$).
- The temperature of the refrigerant and of the pressure equalizing inert gas leaving the gas heat exchanger ($T_{13} = T_{13}, I$).
- There is no temperature difference between lean solution and vapour bubbles leaving the generator, i.e., both are at equal temperature ($T_3 = T_4$).
- The heat transfer in gas heat exchanger provides 3 °C subcooling to liquid refrigerant; ($T_9 = T_7 - 3$).

## 3.1 Thermal Modeling and Governing Equations for Diffusion Absorption Refrigeration Cycle

The thermodynamic analysis of vapour absorption cycle is based on the following three governing equations.

i. Mass balance $\sum m = 0$
ii. Material balance (or partial mass balance) $\sum m\xi = 0$
iii. Energy balance $\sum Q + \sum \dot{m}h = 0$

The mass, ammonia mass balance, and energy balance equations for various components of the diffusion absorption refrigeration cycle are presented below.

## 3.2 Generator, Bubble Pump, and Separator as Unit

For simplification of balancing, generator, bubble pump, and separator are combined into a single unit. The generator used to heat the rich solution in ammonia comes from state 1. Vapours of ammonia and water are produced and slug flow induced in bubble pump with liquid portion of solution and rise to rectifier through separator and then rectifier after lean solution removal.

General mass balance equation

$$m_2 = m_3 + m_4 \tag{1}$$

where $m_1 = m_2$.

Ammonia mass balance equation

$$m_2 \xi_2 = m_3 \xi_3 + m_4 \zeta_4 \tag{2}$$

Energy balance equation

$$\dot{Q}_g = \dot{m}_3 h_3 + \dot{m}_4 h_4 - \dot{m}_2 h_2 \tag{3}$$

## 3.3 Rectifier

The rectifier has the gaseous ammonia–water solution at 4 being cooled to produce almost pure ammonia refrigerant at state 6 and condensed solution at state 5 that returns into separator to form weak solution at state 3. Thus, energy balance equation for rectifier gives the heat rejection from the rectifier as:

General mass balance equation

$$\dot{m}_4 = \dot{m}_5 + \dot{m}_6 \tag{4}$$

Ammonia mass balance equation

$$\dot{m}_4 \zeta_4 = \dot{m}_6 \zeta_6 + \dot{m}_5 \xi_5 \tag{5}$$

Or

$$\dot{m}_6 = \frac{\zeta_4 - \xi_5}{\zeta_6 - \zeta_4} \dot{m}_5 \tag{6}$$

Energy balance equation

$$\dot{Q}_r = \dot{m}_5 h_5 + \dot{m}_6 h_6 - \dot{m}_4 h_4 \tag{7}$$

## 3.4 Condenser

Ammonia vapour after leaving the rectifier at state 6 condenses by rejecting heat into the atmosphere. Ammonia is condensed in the condenser at constant pressure in the condenser.

General mass balance equation

$$\dot{m}_7 = \dot{m}_6 \tag{8}$$

Ammonia mass balance equation

$$\zeta_6 = \zeta_7 \tag{9}$$

Thus, heat rejected to cooling medium in the condenser can be written as

$$\dot{Q}_c = \left[ \dot{m}_7 X_7 h_{7f} + \dot{m}_8 X_8 h_{8v} - \dot{m}_6 h_6 \right] \tag{10}$$

where $X_7 = (1 - X_8)$.

The condensed refrigerant liquid at state 7 is coming from the condenser and flows into the evaporator through gas heat exchanger while the non condensed refrigerant vapour, if any, bypasses evaporator and gas heat exchanger and flows into the receiver tank and flows to the receiver tank.

## 3.5  Evaporator and Gas Heat Exchanger

Subcooled liquid ammonia state 9 mixes with inert gas with some ammonia residual gas state 11. This causes pressure both of ammonia liquid and helium gas drop, and mixtures of ammonia and helium gas with their respective partial pressures flow through the evaporator state 12.

For ease of balancing equation, the following mass flow rate are defined as

Mass flow rate of ammonia vapour after expansion

$$\dot{m}_{12v} = [\dot{m}_7 X_7 + \dot{m}_{ar}]X_{12} \tag{11}$$

Mass flow rate of ammonia fluid after expansion

$$\dot{m}_{12f} = [\dot{m}_7 X_7 + \dot{m}_{ar}](1 - X_{12}) \tag{12}$$

General mass balance of ammonia at state 12 considering control volume approach and at gas heat exchanger.

Mass balance equation

$$\dot{m}_9 + \dot{m}_{11} = \dot{m}_{12} \tag{13}$$

$$\dot{m}_7 + \dot{m}_{10} = \dot{m}_{13} \tag{14}$$

Or

$$(\dot{m}_7 X_7 + \dot{m}_{ar} + \dot{m}_{10I}) = \dot{m}_{13v} + \dot{m}_{13f} = \dot{m}_{12v} + \dot{m}_{12f} \tag{15}$$

where $\dot{m}_{13} = \dot{m}_{12} = \dot{m}_{11} + \dot{m}_9$; $\dot{m}_9 = \dot{m}_7$ and $\dot{m}_{11} = \dot{m}_{10}$.

Ammonia mass balance equation

$$\dot{m}_7 \xi_7 + \dot{m}_{10}\zeta_{10} = \dot{m}_{13}\zeta_{13} \tag{16}$$

where $\zeta_{10} = \zeta_{11}$ and $\xi_7 = \xi_9$.

Combined energy balance equation for condensed ammonia refrigerant enters at state 7, residual gas mixture of ammonia and helium enters at state 10 and passes through the tube and meets with subcooled ammonia at state 12; ammonia and helium gas mixture leaves the evaporator as well as gas heat exchanger state 13.

Energy balance equation

$$\dot{Q}_e = (\dot{m}_{13v}h_{13v} + \dot{m}_{13f}h_{13f}) + \dot{m}_I C_{PI}(T_{13} - T_{12}) - (\dot{m}_{12v}h_{12v} + \dot{m}_{12f}h_{12f}) \\ + \dot{m}_7 X_7(h_9 - h_7) + \dot{m}_I C_{PI}(T_{11} - T_{10}) + \dot{m}_{ar}(h_{11} - h_{10}) \tag{17}$$

## 3.6  Absorber and Receiver Tank

In the receiver tank, ammonia and helium gas mixture leaves the evaporator state 13 and uncondensed ammonia gas from the condenser state 8 gets mixed with the lean solution coming from the solution heat exchanger state 16. Ammonia vapour is readily absorbed into the weak ammonia solution to produce strong ammonia solution. During the absorption processes, helium gas is liberated which leaves the receiver tank along with some amount of unabsorbed ammonia gas. Thus, residual gas mixture (helium and unabsorbed ammonia) leaves the receiver tank and moves towards gas heat exchanger.

Ammonia vapour leaves the evaporator and bypasses from condenser at state 13.

$$\dot{m}_{13v} = [\dot{m}_7 X_7 + \dot{m}_{ar}]X_{13} + \dot{m}_8 X_8 \tag{18}$$

Liquid ammonia leaving the evaporator

$$\dot{m}_{13f} = [\dot{m}_7 X_7 + \dot{m}_{ar}](1 - X_{13}) \tag{19}$$

Mass balance equation

$$\dot{m}_{13} + \dot{m}_{16} = \dot{m}_{14} + \dot{m}_{10} \tag{20}$$

where $\dot{m}_{13} = \dot{m}_{13v} + \dot{m}_{13f}$.

Ammonia mass balance equation

$$\dot{m}_{13}\zeta_{13} + \dot{m}_{16}\xi_{16} = \dot{m}_{14}\xi_{14} + \dot{m}_{10}\zeta_{10} \tag{21}$$

where $\zeta_{10} = \zeta_{13} = 1$   ($\because$ pure ammonia).

Heat rejected in the absorber is given by

$$\dot{Q}_a = (\dot{m}_{14}h_{14} + \dot{m}_{10l}h_{10l} + \dot{m}_{10}h_{10}) \\ - (\dot{m}_{13v}h_{13v} + \dot{m}_{13f}h_{13f} + \dot{m}_{13l}h_{13l} + \dot{m}_{16}h_{16}) \tag{22}$$

Heat of absorption is liberated when ammonia is absorbed in weak solution. Due to this, temperature of leaving strong solution and inside gas increases. Also heat is rejected from the absorber into the atmosphere.

## 3.7  Solution Heat Exchanger

In solution heat exchanger, strong solution is heated from state 14 to state 15 by extracting heat from the weak solution which returns from the bubble pump.

Mass balance for lean solution

$$\dot{m}_{15} = \dot{m}_{16} \tag{23}$$

where $\dot{m}_{15} = \dot{m}_3 + \dot{m}_5$.

Mass balance for rich solution

$$\dot{m}_1 = \dot{m}_{14} \tag{24}$$

Ammonia mass balance

$$\xi_{15} = \xi_{16} \tag{25}$$

$$\xi_1 = \xi_{14} \tag{26}$$

Energy balance equation

$$(\dot{m}_1 h_1 + \dot{m}_{16} h_{16}) - (\dot{m}_{15} h_{15} + \dot{m}_{14} h_{14}) = 0 \tag{27}$$

Relation between mole fraction and mass fraction for ammonia is presented below:

$$\xi = \frac{17.03x}{17.03x + (1 - x)18.01} \tag{28}$$

The partial pressure of $NH_3$ in the gas mixture is defined as

$$\frac{P_{\text{partial}}}{P_{\text{total}}} = \frac{N_{NH_3}}{N_{NH_3} + N_{He}} \tag{29}$$

where $N$ shows the number of moles of specific species.

**Mass Flow Ratio** The mass flow ratio ($\Pi$) is described as the ratio of the mass flow rate of the rich solution leaving the receiver tank to the mass flow rate of pure refrigerant.

$$\Pi = \frac{\dot{m}_{14}}{\dot{m}_6} \tag{30}$$

## 3.8 Cycle Performance

The performance of DAR system is given by the amount of cooling by a refrigerant machine per unit heat supplied. However, COP is also defined as refrigerant rate over the rate of heat addition at the generator.

$$\text{COP} = \frac{\dot{Q}_e}{\dot{Q}_g} \qquad (31)$$

For solving the thermodynamic equations, properties of the ammonia–water solutions at different pinch points in the cycle are needed. These properties of the working fluid and gas mixture at different pinch points are calculated with the help of Refprop 7 based on the assumptions of an ideal gas. The results are checked with the calculated values from EES 6.832.

# 4   Result and Discussion

Computer simulation based on the thermodynamic modelling has been used for carrying out parametric analysis for the input parameters as detailed in Table 1. Details of result obtained through parametric variations are graphically presented (Fig. 2).

It is obvious that the rise in temperature occurs due to build-up in solar energy supplied to the generator. An EES software-based study has been carried out to the diffusion absorption refrigeration cycle using ammonia as refrigerant and water as absorbent. The heat input rate to the generator increases with the generator temperature as shown by the gradient of $Q_g$ in Fig. 3.

This rise in energy supplied will energize the rate of distillation. Consequently, more irreversibilities occur and hence downfall the coefficient of performance. It is occurred due to more water vaporized with the refrigerant vapour at a nonlinear rate. This is shown by the trends of curve $Q_r$. This water vapour needs more heat removal in rectifier to rectify and return back to receiver, so that pure ammonia vapour could be supplied to the condenser.

**Table 1** Input parameters range and component characteristics for operating designed diffusion absorption refrigeration cycle

| Component characteristics | Value/range | Unit |
|---|---|---|
| Mass fraction of ammonia in aqua ammonia mixture | 0.35–0.75 | – |
| Generator temperature | 110–150 | °C |
| Acceleration due to gravity—Kanpur | 9.8 | m/s$^2$ |
| Mass flow of strong solution | 1 | kg/s |
| System pressure range | 16–25 | bar |
| Maximum condenser temperature—results in 5-degree subcooling | 35–50 | °C |
| Absorber temperature | 45–60 | °C |
| Minimum evaporator temperature | (−20) to 5 | °C |
| Generator dynamic pressure loss | 0.1 | bar |
| Bubble pump dynamic pressure loss | 0.15 | bar |
| Heat exchanger dynamic pressure loss | 0.15 | bar |
| Pipe loss fraction, in percentage | 1.5% | |
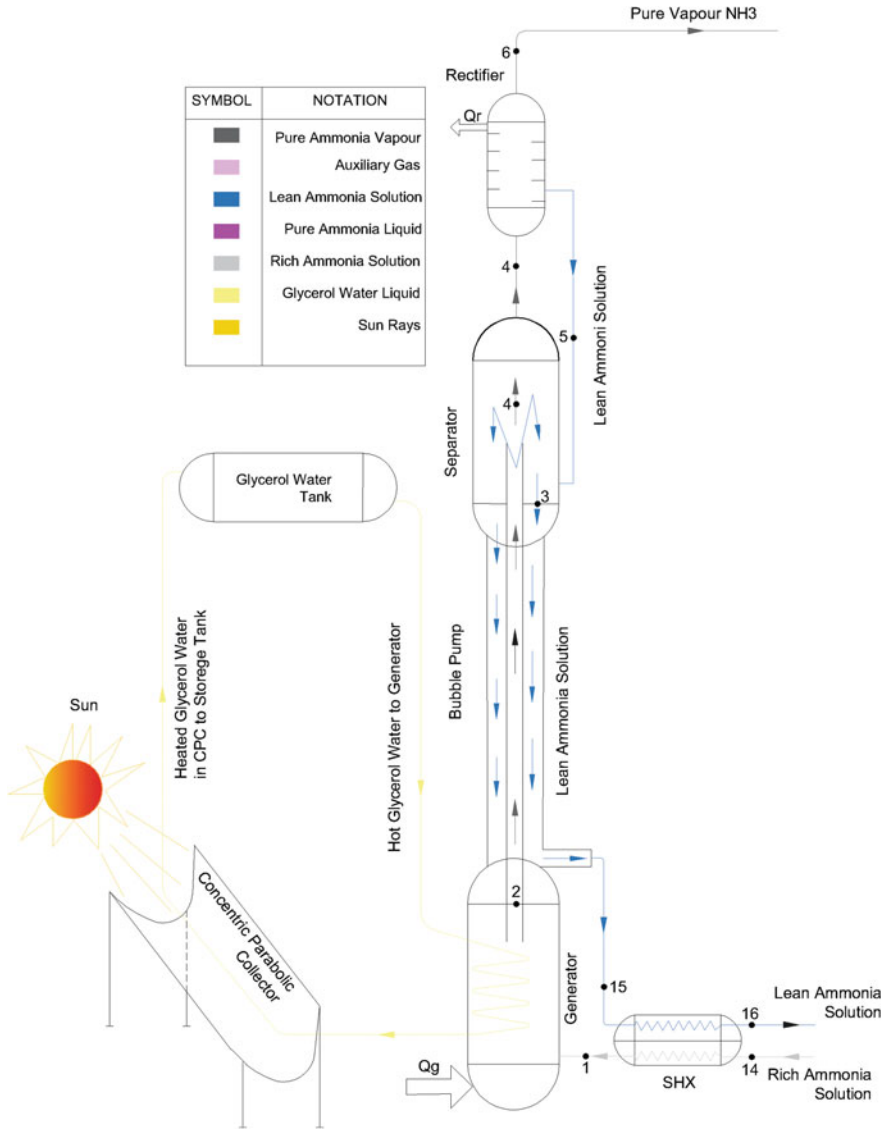
**Fig. 2** Combined schematic diagram of generator, bubble pump, and separator modelled in this study using solar energy

Figure 3 also depicts that for the generator temperature below 390 K, the COP of cycle increases. Now as the generator temperature increases, more heat is supplied to the aqua ammonia solution and more quantity of water is evaporated with refrigerant. This increased amount of water vapour goes to rectifier through separator. The rectifier needs more heat rejection to the ambient state to condense water
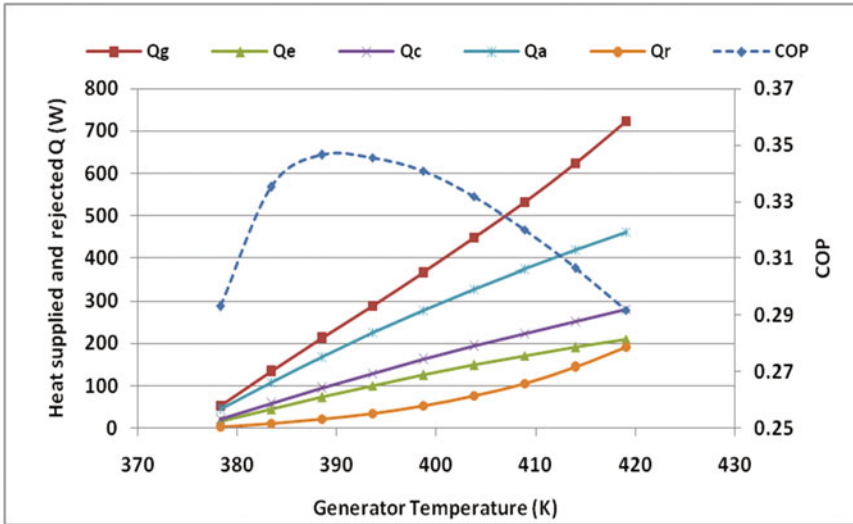
**Fig. 3** Effect of generator temperature of coefficient of performance at fixed concentration in aqua ammonia
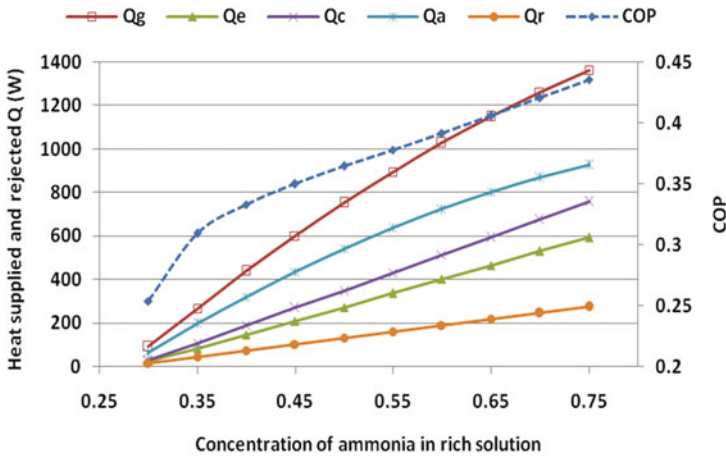


**Fig. 4** Effect of concentration of generator on coefficient of performance at fixed generator temperature (130 °C)

vapours so that only pure refrigerant vapour reaches condenser. The refrigerating effect produced by evaporator does not show any rise and varies statically linear as shown in Fig. 3.

Figure 4 shows the effects of ammonia mass fraction on coefficient of performance. It depicts that coefficient of performance increases almost linearly with an

**Fig. 5** Effect of generator temperature on performance for particular ammonia concentration in aqua ammonia solution
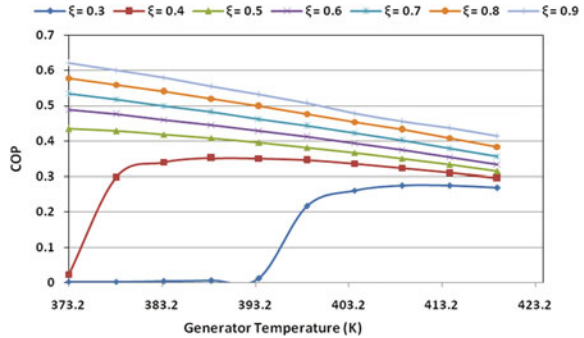


increase in ammonia mass fraction. The increased amount of ammonia concentration will release more amount of refrigerant vapour per unit mass of mixture flow. Moreover, heat added to the low mass fraction of ammonia solution mixture will be removed in rectifier and absorber with little bit contribution to the cooling capacity. This will affect coefficient of performance adversely. So, a minimum amount of ammonia mass fraction in the solution is required to start diffusion absorption refrigeration cycle normally. On contrary for higher concentrations it becomes more difficult for ammonia vapour to be reabsorbed in the absorber for the specified pressure. From the literature study, it was found that a minimum concentration, say 30%, should be needed to run the system without detrimental effects, thus increasing COP and cooling effect.

Figure 5 shows that the performance of the system for mass concentrations below 30% at generator temperature below 393.2 K is too low. The best performance of the considered arrangement is found at 0.9 concentration of ammonia at temperature 373.2 K. It shows that if the mass of ammonia in aqua ammonia solution is high, then the low temperature of the generator gives high performance of the system. High mass fraction of ammonia in solution will easily distillate with low amount of water; hence heat removed from the rectifier will be low and pure ammonia can be obtained in sufficient amount at the inlet of evaporator. The minimized heat rejection by rectifier will increase the coefficient of performance of the diffusion absorption refrigeration system. As the generator temperature increases for particular mass fraction of ammonia, coefficient of performance decreases linearly with the generator temperature due to more heat rejected by rectifier.

Figure 6 shows the variation in heat supplied with ammonia mass fraction in the solution at varying generator temperatures. It is obvious that if the generator temperature increases, heat supplied to the aqua ammonia solution will also be increased. The supply of heat increases linearly with the mass fraction of ammonia. The noticeable impact is a decrease in heat supplied after a concentration of 0.70 for temperature higher than 413.2 K.

Figure 7 shows the effect of ammonia concentrations on refrigerating capacity. It shows that for a particular generator input, refrigerating capacity of DAR increases
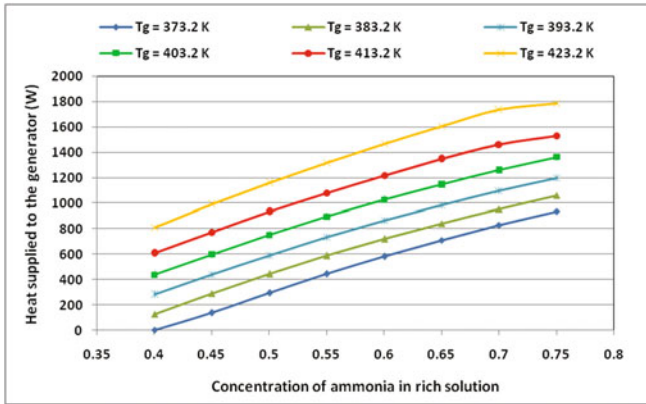
**Fig. 6** Variation in heat supplied to the generator for varying concentrations of ammonia in aqua ammonia solution
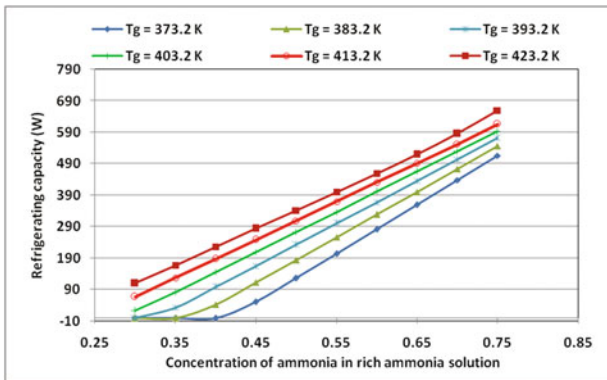


**Fig. 7** Effect of concentration of ammonia in aqua ammonia solution on refrigerating capacity of a DAR system

linearly with an increase in concentrations of ammonia. At higher generator temperature, refrigerating capacity is high for high ammonia concentration in rich solutions. This is caused by higher mass flow rate of refrigerant through the evaporator for given mass flow rate of ammonia water solution through the generator at higher concentrations.

The maximum refrigeration capacity of 0.66 kW is obtained for ammonia concentration of 0.75 at a generator temperature of 423.2 K for varying concentrations of ammonia. It is not necessary that maximum COP obtained at some temperature should be same as the one at which maximum refrigerating capacity is obtained.

Moreover, it also shows that for low concentrations, the refrigerating capacity for the generator temperature below than 393.2 K shows negative values for the reasons as discussed previously. So for actuating the system, a minimum 0.35 mass concentration of ammonia is needed for low heat supplied to the generator or desorber or lower availability of solar radiations.

Figures 8 and 9 show the effect of evaporator temperature and condenser temperature at coefficient of performance of the cycle. Figure 8 depicts effect of evaporator temperature on COP for different generator temperatures of the DAR system.

Figure 8 depicts that the coefficient of performance does not have an accountable value at generator temperature 373.3 K and below. This shows an outrageous cycle operating conditions and it can be avoided. It is evident that the performance of the system increases linearly with an increase in evaporator temperature for a particular
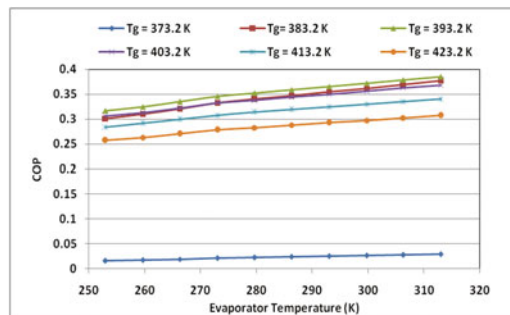


**Fig. 8** Effect of evaporator temperature on coefficient of performance at fixed generator temperature of DAR system
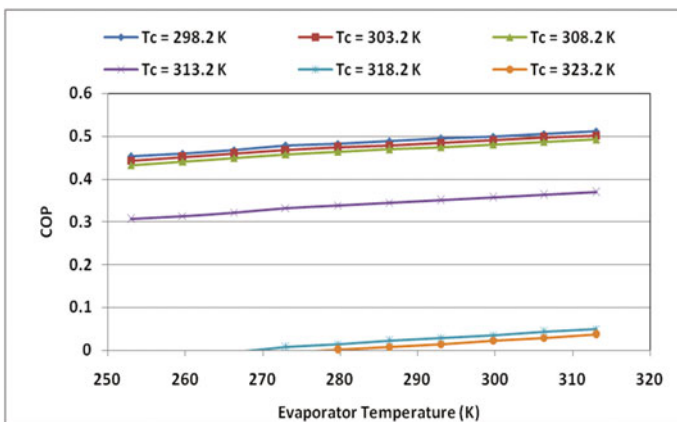


**Fig. 9** Effect of condenser temperature on coefficient of performance at varying evaporator temperatures

generator temperature. Figure 8 also shows that an optimum value for generator temperature 393.2 K gives highest value of COP for varying evaporator temperature values.

When the temperature is above the optimum temperature of 393.2 K, the performance of the system starts decreasing. Further increase in generator temperature shows the same pattern as discussed above.

Figure 9 shows the variation in COP with evaporator temperature at varying condenser temperatures. It shows that COP depends significantly on condenser temperatures, while at higher condenser temperatures; the performance of the system decreases and reached very low value. In fact, performance shows negative value at higher condenser temperature. For working of a DAR at higher ambient temperature, condensing medium needs to change from air cooling to water cooling. At condenser temperature (298.2 K), the performance of the system gets highest value. COP increases linearly with an increase in evaporator temperature. Figure 9 also shows performance of the system at condenser temperature 318.2 K and above, and values of COP for evaporator temperature below than 290 K show negative value and above shows a very little increase in COP. The condenser temperature more than 318.2 K is impracticable for specified condition and should be precluded.

Figure 10 shows variation in coefficient of performance and cooling capacity with and without considering pressure losses to the generator temperature. It is delineated that the loss percentage in coefficient of performance with and without pressure loss at the generator temperature 390 K is 46.7 and 26.8, and 22.7% corresponding to the generator temperature 410 and 430 K, respectively. As the generator temperature increases, the loss percentage in coefficient of performance decreases. Similarly, the loss percentage in cooling capacity with and without pressure loss show the values 43.9, 26.2, and 22.1% corresponding to the generator temperatures 390, 410, and 430 K, respectively. This depicts the decrease in cooling capacity with respect to the coefficients of performance at slower rate. This is due to proper evaporation of the refrigerant in the evaporator to the increase rate of heat supplied with the increasing generator temperature.

To validate the model proposed in the present study, results obtained in this study were compared with previous experimental and numerical studies data

**Fig. 10** Effect of pressure looses on coefficient of performance and refrigerating capacity at varying generator temperatures
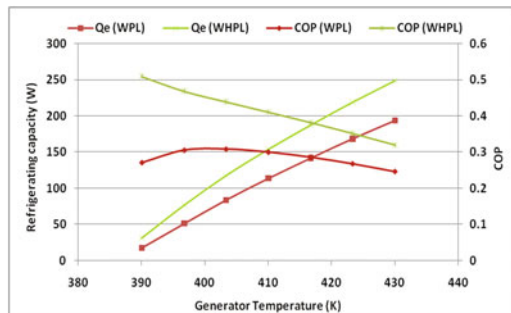
**Table 2** Comparison between our obtained results and previously published data

|  | Chen et al. [15] | Result of present model | Srikhirin et al. [7] | Result of present model | Zohar et al. [4] | Result of present model |
|---|---|---|---|---|---|---|
| COP | 0.1–0.20 | 0.164 | 0.09–0.16 | 0.157 | 0.20–0.21 | 0.207 |

[4, 7, 15]. Since these three have different operating conditions, for comparison, it is necessary that the operating conditions should be almost similar to the compared experimental or numerical data. Therefore, the comparison of COP is made separately for each study under the specific operating conditions and is presented in Table 2. This table 2 shows that the obtained values of our model are almost near or coincide to the data presented in each study.

## 5 Conclusion

A computer simulation based on thermodynamic modelling has been carried out in the present work to predict the performance of the diffusion absorption refrigeration cycle for various generator, evaporator, and condenser temperatures including concentrations of the refrigerant in the rich solution of ammonia–water solution. It is concluded that in general, the performance of diffusion absorption refrigeration cycle is poor due to large amount of heat lost during cooling process in rectifier, condenser, absorber, and gas heat exchanger. The loss percentage in cooling capacity (WPL and WHPL) is low: 22.1% at generator temperature 430 K, 26.1% at 410 K, and 43.9% at 390 K corresponding to percentage loss in coefficient of performance (WPL and WHPL) as 22.7, 26.8, and 46.7%, respectively for same generator temperature due to dynamic and hydrostatic pressure losses in diffusion absorption refrigeration system. It is seen that loss percentage in coefficient of performance (WPL and WHPL) is 2.8% than cooling capacity at low generator temperature 390 K while there is no marginal drops at higher temperature. So, at lower generator temperature, pressure losses have great impact on coefficient of performance and cannot be neglected but at higher generator temperature pressure effects may be neglected. The aqua ammonia diffusion absorption refrigeration cycle can be used for maintaining temperatures below 0 °C. The ammonia water mixture is not being a good impending pair for absorption refrigeration cycles, operating with lower generator temperatures. The performance of aqua ammonia diffusion absorption refrigeration cycle can be increased by changing heat transfer medium for condenser, rectifier, and absorber as ambient air or as water in those countries where the ambient temperature is high as in summer season as in India. The additional advantage of this system is that the system can utilize heat sources like solar, geothermal, and industrial waste or others in place of conventional energy sources.

# References

1. Von Platen BC, Munters CG (1928) US Patent 1, 685–764
2. www.dometic.com (formerly known as Electrolux in Europe), 2004
3. Zohar A, Jelinek M et al (2005) Numerical investigation of a diffusion absorption refrigeration cycle. Int J Refrig 28:515–525
4. Zohar A, Jelinek M et al (2007) The influence of diffusion absorption refrigeration cycle configuration on the performance. Appl Therm Eng 27:2213–2219
5. Zohar A, Jelinek M et al (2008) The Influence of the generator and bubble pump configuration on the performance of diffusion absorption refrigeration system. Int J Refrig 31:962–969
6. Starace G, De Pascalis L (2011) An advanced analytical model of the diffusion absorption refrigerator cycle. Int J Refrig 35:605–612
7. Srikhirin P, Aphornratana S (2002) Investigation of a diffusion absorption refrigerator. Appl Therm Eng 22:1181–1193
8. Wang Q et al (2011) A numerical investigation of a diffusion absorption refrigerator operating with the binary refrigerant for low temperature applications. Appl Therm Eng 31:1763–1769
9. Sözen A, Menlik T, Özbas E (2012) The effect of ejector on the performance of DAR system: an experimental study. Appl Therm Eng 33–34:44–53
10. Ben Ezzine N, Garma R, Bellagi A (2010) A numerical investigation of a diffusion-absorption refrigeration cycle based on R124-DMAC mixture for solar cooling. Energy 35:1874–1883
11. Ben Ezzine N, Garma R, Bourouis M, Bellagi A (2010) Experimental studies on bubble pump operated diffusion absorption machine based on light hydrocarbons for solar cooling. Renew Energy 35:464–470
12. Wang H (2012) A new style solar driven diffusion absorption refrigerator and its operating characteristics. Energy Procedia 18:681–692
13. Jacob U, Eicker U, Schneider D, Taki AH, Cook MJ (2008) Simulation and experimental investigation into diffusion absorption cooling machines for air-conditioning applications. Appl Therm Eng 28(10):1138–1150
14. Koyfman A et al (2003) An experimental investigation of bubble pump performance for diffusion absorption refrigeration system with organic working fluids. Appl Therm Eng 23:1881–1894
15. Chen J, Kin KJ, Herold KE (1996) Performance enhancement of a diffusion-absorption refrigerator. Int J Refrig 19(3):208–218
16. Acuña A, Velázquez N, Sauceda D, Rosales P, Suastegui A, Ortiz A (2016) Influence of a compound parabolic concentrator in the performance of a solar diffusion absorption cooling system. Appl Therm Eng 102(5):1374–1383

# Flow Characteristics of Crude Oil with Additive

**Praveen Kumar and Chetan Badgujar**

**Abstract** In the present work, flow characteristics of high sulfur crude oil (HSCO) with the addition of low sulfur crude oil (LSCO) were studied. LSCO was mixed in high sulfur crude oil in concentration of 10–15% by volume. The rheological characteristics of the heavy crude oil suspension were determined using ISO-certified Rheometer for the range of shear rate varying from 0 to 500 s$^{-1}$, and temperature range varies from 25 to 45 °C. The rheological characteristics of the HSCO include steady-state flow behavior, yield stress, and thixotropic characteristic, etc. Optical microscopy and dynamic light scattering were used to analyze the size of wax crystals and crystal size distribution, respectively. The average size of wax crystals was 2550 nm for 100% HSCO which further reduced to 350 nm after adding 15% LSCO. HSCO shows the non-Newtonian flow characteristics at low temperature and decreases with increase in temperature. Rheological results of HSCO show that there is a reduction in viscosity with the addition of LSCO. The LSCO as an additive in HSCO can be beneficial for design of crude oil transportation pipeline.

**Keywords** Crude oil · Dynamic light scattering (DLS) · Optical microscopy (OM)

## 1 Introduction

The present investigation deals the rheological characteristics of HSCO with LSCO. Largest reserves of HSCO are present inside the earth, but due to complex property of hydrocarbon its production and extraction process in small fraction are difficult. Viscosity is a major problem for crude oil, so various methods are adopted for reduction in viscosity such as thermal enhanced oil recovery (EOR) methods. Production and thermal recovery method are the commonly used to study the behavior of HSCO with and without emulsions in pipeline. Rheological

P. Kumar (✉) · C. Badgujar
Indian Institute of Technology Delhi, New Delhi, India
e-mail: praveen.dimenssion@gmail.com

characteristics such as steady-flow behavior, yield stress behavior, and thixotropic behavior of heavy oil and its emulsion are measured with the help of rheometer. The elastic behavior of non-Newtonian fluid follows the Hooke's law [1]. It indicates that shear stress is directly proportional to shear rate within elastic limit, in contrast to a non-Newtonian fluid under shear stress. HSCO viscosity behavior exhibits frequency or dependence of time which was measured by researchers [2–5]. Temperature also plays an important role in the viscoelasticity of HSCO. The constituent of crude oil has polar fraction (asphaltenes, resins, and wax) behaving as solid, while HSCO with large amount aromatics component behaves like liquids. The flow characteristics of crude oil in pipeline show variations from one crude well to the other [6]. The flow characteristic of crude oil also depends on age and depth of crude oil well [7]. HSCO exhibits the non-Newtonian flow characteristics due to difficulty of its transportation at very long distances [8]. During the transportation from sea to refinery, wax substance deposits on the pipeline wall cause the reduction in flow diameter of pipeline. This leads to blockage of transportation pipeline and failure of valve. The most important data required for designing a transportation system are the rheological characteristics of the suspension at various operating conditions. Rheological characteristics of the HSCO depend on several parameters such as flash point, pour point, specific gravity, operating temperature, yield stress, and thixotropic structure [9, 10]. Investigators [6–8, 11–15] also studied the rheological characteristics of HSCO with the addition of different types of additives. A small proportion of the some drag reducing agents is able to reduce the viscosity of the HSCO which helps in the improvement of pipeline flow characteristics. The viscosity of crude oil reduced in water emulsion [11]. The literature indicates that the addition of different types of additives can be helpful in improving flowability of HSCO. The aim of this investigation is to investigate the rheological behavior and microstructure of HSCO and its emulsions with LSCO.

## 2  Materials and Methods

In the present investigation, HSCO and LSCO were supplied from Indian Oil Corporation Limited (IOCL), Panipat, India, which were mixed with low sulfur crude oil with the help of magnetic stirrer. A magnetic stirrer was operated at 1500 rpm for each emulsion with a time duration of 1 h. The concentration of LSCO in HSCO was taken as 10 and 15% (by volume). The physical parameters, namely density, viscosity, pour point, basic sediment, and water percentage, were tested according to the norms of American Society for Testing and Materials (ASTM) methods. The rheological characteristic of crude oil and its emulsions (with low sulfur crude oil) was evaluated using ISO-certified Rheometer (Rheolab QC, APC Ltd., Germany).

## 3 Experiments

The physical parameters and testing method of HSCO and LSCO are represented in Table 1. In the present study, CR mode of rheometer is used to determine the viscosity ($v$) and a shear rate of HSCO and its emulsions which represent their flow behavior.

## 4 Results and Discussion

### 4.1 Steady-Flow Behavior

Steady-flow behavior of (in terms of viscosity) samples of HSCO at three different concentration levels of LSCO, i.e., 10 and 15% (by volume), was observed at three different temperature levels which are shown in Fig. 1. It was further revealed that HSCO shows non-Newtonian shear thinning behavior while increasing the temperature from 25 to 45 °C. However, the viscosity of crude oil decreases with increase in temperature of crude oil from 25 to 45 °C. It was also revealed that viscosity difference between crude oil and emulsion samples was smaller at a high shear rate and larger at the low shear rate.

This happens due to the fact that the component of high molecular weight like waxes, resins, and asphaltenes, etc. does not form complex bond at high temperature which results in viscosity reduction [15]. For LSCO, the viscosity reduction in HSCO was found from 5.8 to 5.1 mPa.s at 25 °C, as shown in Fig. 1a. While HSCO with 15% LSCO was used, the viscosity drops from 5.8 to 5.3 mPa.s, as shown in Fig. 1b. It can be observed that viscosity reduction also remains significant at lower temperatures. Dynamic viscosity reduction (DVR %) of HSCO was reduced more economically by using light crude oil which can be confirmed from Table 2. Figure 1c represents the flow behavior of HSCO. It was observed that HSCO shows non-Newtonian shear thinning behavior while increasing the temperature from 25 to 45 °C. This happens due to the fact that the component of

**Table 1** Physical properties and test method

| S. No. | Parameter | Units | Method | HSCO | LSCO |
|--------|-----------|-------|--------|------|------|
| 1 | Density | kg/m$^3$ | ASTM D1250 | 874.6 | 837.6 |
| 2 | Basic sediment and water | wt% | ASTM D4007 | 0.125 | 0.10 |
| 3 | Water | wt% | ASTM D4928 | 0.06 | 0.04 |
| 4 | Sulfur | wt% | ASTM D4294 | 2.58 | 0.18 |
| 5 | Viscosity | Pa.s | Rheometer | 0.006 | 0.0054 |
| 6 | Pour point | °C | ASTM D97 | 55 | 53 |
| 7 | Color | – | – | Black | Black |

Weight percentage (wt%)
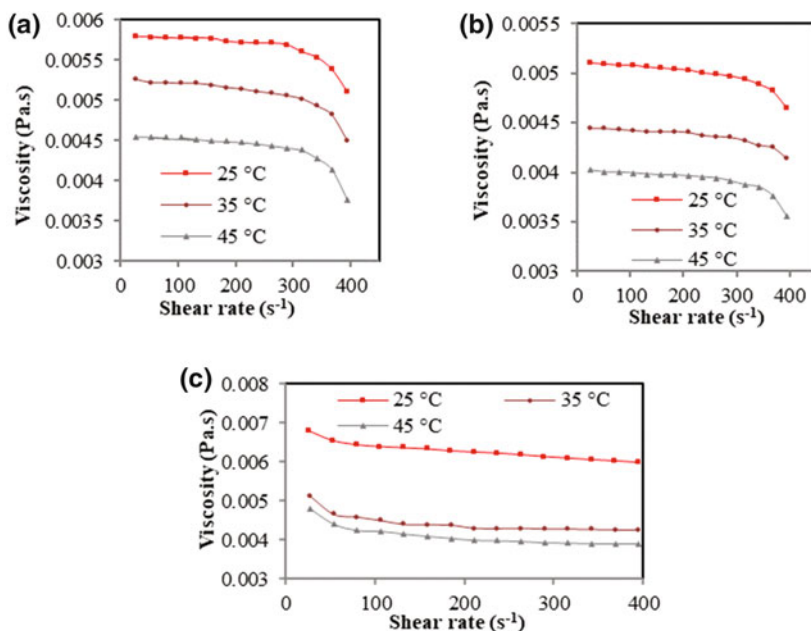
**Fig. 1** Viscosity behavior of **a** 90% HSCO–10% LSCO, **b** 85% HSCO–15% LSCO, and **c** 100% HSCO, at different temperatures

**Table 2** Properties of crude oil at a shear rate of 500 s$^{-1}$

| Sample | 25 °C | | 35 °C | | 45 °C | |
|---|---|---|---|---|---|---|
| | Viscosity (mPa.s) | DVR (%) | Viscosity (mPa.s) | DVR (%) | Viscosity (mPa.s) | DVR (%) |
| S1 | 5.8 | – | 5.6 | 3.4 | 4.3 | 25.8 |
| S2 | 5.4 | 6.9 | 5.2 | 10.3 | 4.1 | 29.3 |
| S3 | 5.3 | 13.8 | 4.2 | 27.5 | 4.0 | 31.0 |

S1 100% HSCO; S2 90% HSCO–10% LSCO; S3 85% HSCO–15% LSCO

high molecular weight like waxes, resins, and asphaltenes, etc. does not form complex bond at high temperature which results in viscosity reduction [11].

## 4.2 Yield Stress Behavior

In the following study, the yield stress of the samples was determined from shear stress to shear rate curve obtained from rheometer. The controlled stress (CS) mode of rheometer is used to measure the yield stress which produces high precision results as compared to controlled rate (CR) mode, as recommended by [16].
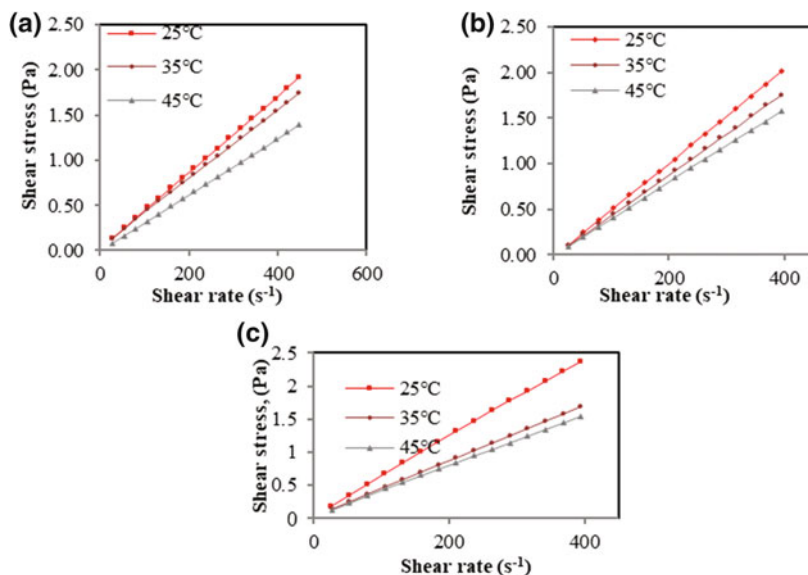
**Fig. 2** Yield stress behavior of **a** 90% HSCO–10% LSCO, **b** 85% HSCO–15% LSCO, and **c** 100% HSCO, at different temperatures

Yield stress of each sample was recognized/identified with the help of Bingham model. As per the observation, yield point decreases with increase in temperature. Figure 2a indicates that apparent yield stress diminishes with the addition of 10% of LSCO in HSCO. This happens due to the elimination of stresses from crude oil with the addition of surfactant which tends toward decrease in viscosity of crude oil; while 15% of LSCO was added more, the stresses in HSCO were eliminated due to change in inner mechanism of crude oil, as shown in Fig. 2b. The small variation in stress level causes a significant change in mechanical properties of structured fluid. However, the material tends to deform elastically below the specified stress level. This happens due to reason that beyond this stress level the applied stress produces continuous deformation in the fluid which results in smooth flow of crude oil emulsion [17]. The shear stress to shear rate response at different temperatures is represented in Fig. 2c. The yield point of HSCO shifts from 1.6 to 1 Pa with increase in temperature from 25 to 45 °C.

## 4.3 Thixotropic Behavior of Crude Oil and Its Emulsions

The thixotropic behavior of HSCO and HSCO–LSCO mixture was investigated in the present study to determine the magnitude of change in microstructure from one state to other and vice versa. Thixotropic experiments were carried out on HSCO

**Table 3** Hysteresis area at different temperatures

| S. No. | Temperature (°C) | Hysteresis area (Pa.s$^{-1}$) | | |
|--------|------------------|------|------|------|
| | | S1 | S2 | S3 |
| 1 | 25 | 226 | 195 | 130 |
| 2 | 35 | 196 | 192 | 126 |
| 3 | 45 | 89 | 0 | 0 |
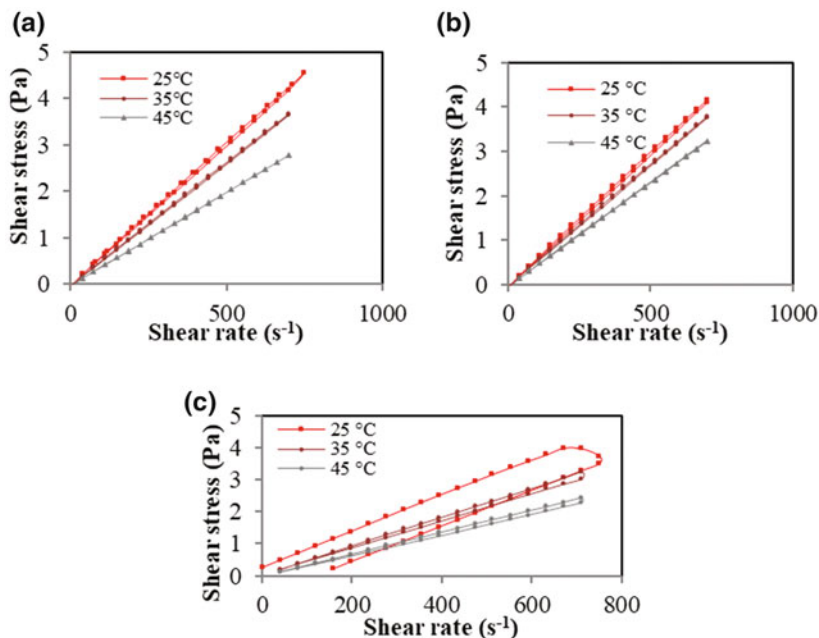


**Fig. 3** Thixotropic behavior of **a** 90% HSCO–10% LSCO, **b** 85% HSCO–15% LSCO, and **c** 100% HSCO, at different temperatures

for the up- and down-cycle of 100 s which was required to break the thixotropic structure of HSCO. The shear rate ramped up 0.8–700 s$^{-1}$ within 100 s and quickly ramped down from 700 to 0.8 s$^{-1}$ in equal time. The value of thixotropy in terms of energy per unit volume was calculated from the hysteresis loop area which enclosed between the up-curve and down-curve rheograms [18–21]. Hysteresis loop area of HSCO and its emulsions is summarized in Table 3. It was found that the mixing of LSCO in HSCO depletes the thixotropic behavior and results in the reversal of processes which makes the up- and down-curve to coincide for the concentration of 10 and 15%, respectively, which is shown in Fig. 3a, b. An identical up- and

down-curve was noticed at temperature of 25 and 35 °C which indicates the unnoticeable thixotropic behavior of HSCO. The thixotropic behavior of HSCO at different temperatures is shown in Fig. 3c.

## 4.4  Dynamic Light Scattering (DLS)

Dynamic light scattering instrument (Model ZEN3600, Malvern Instruments Ltd., Malvern, UK) was used to measure the particle size by diffusing scattered light through the crude oil. Zetasizer system of DLS instrument had analyzed the diameter of particle crystals by calculating Brownian motion and then interpreted their diameter using recognized theories.

Zetasizer module determines the size distribution of wax particles with the help of relation between diffusion speed and size. The size of particles can be found by analyzing their movements. When the position of wax particles from each other appears same and their movements were minimum, then it denotes the existence of larger-sized wax particles. When a movement of particles becomes arbitrary from each other, then it denotes toward their small size. In the present study, DLS instrument was used to perform the quantitative analysis of the micrographs of pure crude oil and its emulsions with LSCO and natural surfactant. Figure 4 represents the DLS graphs of pure crude oil and its emulsions. From Fig. 4a, it is found that the radius of HSCO wax crystals lies in the range of 2000–3100 nm. The average size of wax crystals seems to be larger, i.e., approximately 2550 nm, which would abstract the smooth flow in the pipeline. Figure 4b represents the DLS graph of 85% HSCO and 15% LSCO mixture, and the radius of the wax crystal was found in the range approximately 350 nm.

## 4.5  Optical Microscopy (OM)

Optical microscopy (OM) was used to analyze the change of wax crystal size before and after the addition of LSCO. A simple polarized light-based inverted microscope (Model MA100, Eclipse, Nikon Metrology, Europe) was used to perform the optical microscopy at 25 °C. Microscopic images of HSCO are shown in Fig. 5a which explained that the larger-sized spherical globules appeared in HSCO. Larger-sized globulite structure adheres to the smooth flowability in the pipeline. The effect of the addition of LSCO in HSCO decreases the size of wax particles, as shown in Fig. 5b. The addition of LSCO dispersed the globulite structure of wax particles into the rod-like structure. Therefore, the flowability of HSCO increases with the addition of LSCO. Hence, LSCO acts as a better wax inhibitor.
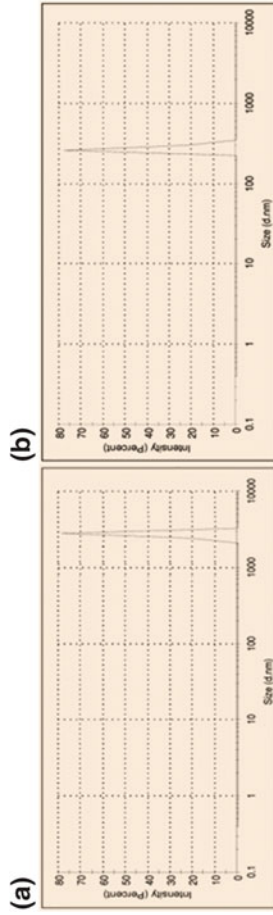
**Fig. 4** Average particle size of **a** 100% HSCO paraffin crystals range from 2000 to 3100 nm and **b** 85% HCSO–15% LSCO crystal ranging from 210 to 350 nm
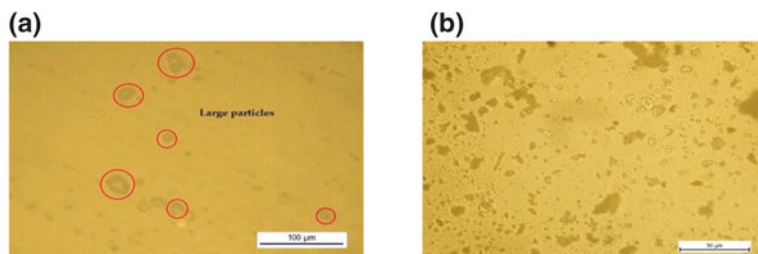
**Fig. 5** Optical microscopic images of **a** 100% HSCO and **b** 85% HSCO + 15% LSCO

## 5 Conclusions

In the present study, the rheological behavior and microstructure of HSCO and its emulsions were investigated. LSCO was used as additives for HSCO at three concentrations. Dynamic light scattering (DLS) and optical microscopy (OS) of crude oil and its emulsions were performed. Rheological results reveal that the presence of LSCO in HSCO approximately eliminates its thixotropic behavior. HSCO shows the non-Newtonian shear thinning characteristics. As the temperature increases, the viscosity of crude oil decreases and shows the Newtonian flow behavior at 45 °C. The addition of LSCO as an additive in HSCO can be useful for the design of crude oil pipeline transportation system. It was found that the HSCO with HSCO–LSCO mixture has a lesser degree of aliphaticity as compared to pure HSCO. Optical microscopy also confirms that the addition of LSCO causes a drastic change in shape of HSCO wax crystals from globules to a rod-like structure which improves its flowability.

## References

1. Lakes RS (2009) Viscoelastic materials. Cambridge University Press, UK
2. Batzle M, Zadler B, Hofman R (2004) Heavy oils—seismic properties. SEG, Denver (Colorado)
3. Han DH, Liu J, Batzle M (2007) Shear velocity as the function of frequency in heavy oils. SEG/San Antonio Annual Meeting, San Antonio (Texas), pp 1716–1719
4. Spencer JW (1979) Bulk and shear attenuation in Berea sandstone: the effects of pure fluids. J Geophys Resour 84(B13):7521–7523
5. Spencer J (2013) Viscoelasticity of Ells River bitumen sand and 4D monitoring of thermal EOR processes. SEG Houston, annual meeting, vol 78, no 6, D419–D428
6. Meriem-Benziane M, Abdul-Wahab SA, Benaicha M, Belhadri M (2012) Investigating the rheological properties of light crude oil and the characteristics of its emulsions in order to improve pipeline flow. Fuel 95:97–107

7. Barry EG (1971) Pumping non-Newtonian waxy crude oils. J Inst Pet 57(554):74–85
8. Chen W, Zhao Z, Yin C (2010) The interaction of waxes with pour point depressants. Fuel 89:1127–1132
9. Randoph AD, Larson MA (1998) Theory of particulate processes: analysis and techniques of continuous crystallization. Academic Press, New York
10. Banerjee S, Kumar R, Mandal A, Naiya TK (2015) Use of a novel natural surfactant for improving flowability of Indian heavy crude oil. Petrol Sci Technol 33(7):819–826
11. Al-Zahrani SM, Al-Fariss TF (1998) A general model for the viscosity of waxy oils. Chem Eng Process: Process Intensif 37(5):433–437
12. Messick MA (1982) Pipeline transportation of heavy crude oil. U.S. Patent No. 4(343), pp 323
13. Tao R, Tang H (2014) Reducing viscosity of paraffin base crude oil with electric field for oil production and transportation. Fuel 118:69–72
14. Farah MA, Oliveira RC, Caldas JN, Rajagopal K (2005) Viscosity of water-in-oil emulsions: variation with temperature and water volume fraction. J Petrol Sci Eng 48(3):169–184
15. Khan MR (1996) Rheological properties of heavy oils and heavy emulsions. Energy Source 18(4):385–391
16. Schramm GA (1994) Practical approach to rheology and rheometry. Gebrueder Haake GmbH, Karlsruhe, Germany
17. Rashed MK, Salleh MAM, Abdulbari HA, Ismail MHS (2016) Enhancing the drag reduction phenomenon within a rotating disk apparatus using polymer-surfactant additives. Appl Sci 6(355):1–11
18. Barnes HA (1979) Thixotropy—a review. J Non-Newton Fluid Mech 70:1–33
19. Mewis J (1979) Thixotropy—a general review. J Non-Newton Fluid Mech 6:1–2
20. Weltmann RN (1960) Rheology theory and applications. In: Eirich FR (ed). Academic Press, New York
21. Wang Z, Yu X, Li J, Wang J, Zhang L (2016) The use of biobased surfactant obtained by enzymatic syntheses for wax deposition inhibition and drag reduction in crude oil pipelines. Catalysts 6(61):1–16

# Refrigerating Effect Produced by Engine Exhaust Heat

**Raman Kumar Sahu , Vinay and Aniket Das**

**Abstract** Many new technologies appear and developing in automobile field helpful for humanity. Vapour compression refrigeration technique is used in automobile vehicle that acquires cooling effect inside the vehicle. Due to riding obtain well comfortable and keep them in an optimal temperature range by refrigerating effect. Currently, the fuel consumption rate increases due to the external load on the engine. The ambition of 'refrigerating effect production' by the engine exhaust heat system is used in the vehicle cabin to reduce the fuel consumption of the casual traveller using air conditioning. The compressor replaces by the heat exchanger and heating coil. Heat exchanger using as energy source of refrigerating effect, and "REPEEH" is few mechanical power being done by engine running of air-condition. After using this technology through obtain refrigeration effect and also increase the engine life due to reducing load on automobile engine. Increases the pollution level of our country due to consumption of more fuel is major parts.

**Keywords** Compressor · Exhaust heat · Vapours compression refrigeration

## 1 Introduction

The vapour absorption refrigeration system is refrigeration system which uses absorption instead of compression unlike most common refrigeration system. The refrigerant is absorbed by water to produce the required refrigerating effect. In the early 1900s, refrigeration with this system using kerosene burner was popular [1, 2]. Then, chlorofluorocarbons were communicated and electricity was cheap to derive compression system and got better COP. But increase some problem with

R. K. Sahu (✉) · Vinay · A. Das
Department of Mechanical Engineering, Manav Rachna International University,
Faridabad, India
e-mail: ramanjeemalin@gmail.com

electricity and Phase out of the CFC's, the drive system is again introducing popular in large capacities. Drive system arrangement has the condenser and the evaporator [2, 3] as the main working part. Then working process of refrigerant place at two different pressure levels in evaporation and condensation takes to drive the systems [4]. They also differ in which the refrigerant is circulated in the system.

Guillen et al. are used monomethylamine-water as a refrigerant to produce cooling effect in refrigeration system at lower temperature like solar energy at −6 ° C to easily vaporize monomethylamine-water refrigerant [5].

Sarbu et al. are explained solar energy driven vapour absorption refrigeration has advantages in energy conservation. The COPs are calculated in refrigerating system by using solar energy value. The COP of refrigerator is 2.36 and there is saving energy consumption of 220 kJ [6]. Meng et al., Sarbu, Dev, Guillen compare to Guillen is more energy save in automobile engine by monomethylamine refrigerant used in refrigeration system [7].

As compared to the vapour compression system, the vapour absorption system uses absorber and generator in place of moving mechanical parts like compressor. A solution of refrigerant and water is called the absorbent [8–10]. The refrigerant is sucked by the absorbent inside the absorber, this vapors comes from the evaporator and hence due to suction and low pressure is maintained inside the evaporator enabling the refrigerant to evaporate. The refrigerant vapour is released as a high pressure vapour due to the heating of strong solution in the generator [11]. There are two controlling pressure gauges on the evaporator and condenser. Higher the pressure to higher the boiling point temperature, lower the pressure to lower the boiling point temperature.

The exhaust from the automobiles acts as a heat source for the vapour absorption refrigeration system which reduces the power requirement as compared to vapour compression system. Therefore, the engine exhaust heat which was initially unutilized is now used as the heat source. This cycle plays a vital role in selection of the appropriate refrigerant-absorbent pair; working fluid used refrigeration as ammonia and absorbent is water [8]. These pair offer good thermodynamic performance and they are environment friendly. It is selected to conduct the strength of this force refrigeration collection or combination of parts forming a complex temperature as used refrigeration-absorption pair of ammonia-water to make a strong solution, where chilled water is required at 7–10 °C [12].

The generator exchanges heat inside heat exchanger in vapour absorption refrigeration systems. The vapour absorption refrigeration system has many fundamental advantages besides being environment friendly. These are low preventive and curative maintenance, simple operation, less pumping power, no rotating component, no vibration, no noise and heat can be input at high temperatures [3, 13]. All the parameters mention above increase the life of system.

The main drawback of currently producing refrigeration in automobile vehicle by using vapour compressor in place of vapour absorption refrigeration system. VCRS required more power to run the compressor and power is obtained from the main shaft of engine. Overall requirement of power in automobile engine to

consume more fuel for maintain running of automobile engine. Also VARS required extra power to driven the generator by engine.

## 2 System Description of Vapour Absorption Refrigeration System

In the generator, the ammonia vapour is formed due to heating of strong ammonia solution. This formed $NH_3$ is passed through separator, analyser and rectifier to remove the water particles and water vapour carried by the ammonia [10, 14].

Now the ammonia vapour is made to pass through the condenser where most of the vapour is condensed and the remaining vapour which remains uncondensed is further made to condense inside the auxiliary condenser.

The mixture of $NH_3$ vapour and water is passed to the generator through the gas heat. The current refrigerating set-up of vapour absorption refrigeration system is used to produce refrigerating effect. The vapour refrigeration system, where the compressor is replaced by the absorber, pump, throttle valve, waste heat pipe passed through the heat exchanger [4, 13].

The vapour refrigerator system in the used refrigerant is ammonia ($NH_3$) and water ($H_2O$) as an absorber [10]. The required power of pumping is absolutely negligible and the refrigerating effect is obtained from vapour refrigerator system without extra mechanical power. And cooling effect produced by vapour compression refrigeration system is comparatively higher cooling effect than that of vapour absorption refrigeration system as its refrigerating cooling effect in the same volume. Main advantage of vapour absorption refrigerator system is to produce refrigerating effect without the use of compressor for the same volume. The advantages of vapour absorption refrigerator system to avoid compression system, there are no moving parts in the system, the operation is actually quiet and typically involves very little damage, so the maintenance cost is very low (Fig. 1).

The power consumed by a motor pump is comparably small to the power consumption required for a compressor system of the same volume. Now in present generally refrigeration effect produce in automobiles is vapour compression



Fig. 1 Working cycle of vapour absorption refrigeration system
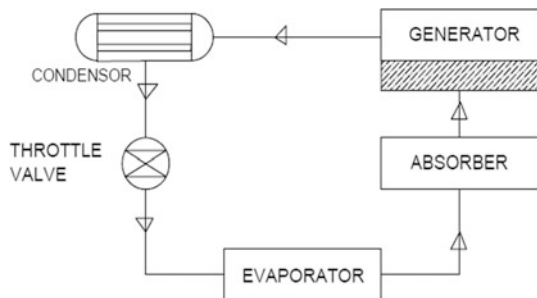
refrigeration method used in an automobile vehicle [1, 15]. The refrigerating effect produced by vapour refrigeration system used in this experimental setup, the absorbents are water and refrigerant are ammonia is used, to the very profitable option of refrigerating effect producing in automobiles availability due to heat in exhaust heat coming from the combustion engine [7].

## 3   Theory of Refrigeration Cycle

### 3.1   *Coefficient of Performance (COP)*

The coefficient of performance of refrigeration cycle is ratio of heat transfer from evaporator and heat absorb to the generator works as input and evaporator is output device [16].

$$
\begin{aligned}
&\mathtt{COP = Refrigeration\,effect/work\,input}\\
&\mathtt{COP = \{TE/(TC-TE)\}/\{(TG-TC)/TG\}}
\end{aligned}
\tag{1}
$$

### 3.2   *Selection of Refrigerant*

The thermodynamic property of refrigerant selected in the refrigeration system, which physical and protect working properties obtain by evaporator before selection purpose of refrigerant for producing refrigeration effect.

The following properties should be obtained in the evaporator before selection of refrigerant, working pressure range, pressure ratio, corrosiveness and flame ability, space limitation, temperature required in the evaporator pass through refrigerant [17]. Ammonia is an inorganic compound, which does not create carbon-hydrogen bond to use an inorganic material. Ammonia is used in refrigeration cycle as a refrigerant, because its boiling point and freezing point are very low [10]. And less amounts of heat provided to ammonia refrigerant for get vaporize into ammonia vapour. Ammonia is a cheap cost, light weight and good performance liquid refrigerant. So that it is used in refrigeration air-conditioning systems.

## 4   Experimental Assumption

Many assumptions avoid that Refrigeration effect produce by waste engine exhaust, all those assumptions are justified by involving scientific tests in waste engine exhaust experimental model.

The temperature effect on condenser, evaporator, absorber and rectifier are homogeneously over all component. Refrigerant vapour in vapour refrigeration cycle is absorbed in absorber with thermodynamics strong solutions. This strong solution is pumped into generator and weak solution is separated due to ammonia vaporization, weak solution is pumped back for absorption into the absorber [12]. The weak solution separates into the heat exchanger at absolute the same play with a different temperature and concentration on the heat exchanger with the thermo-dynamics. Fraction parts of refrigerant disappear into heat exchanger may consider as a vapour because of a measure of the amount of dissolved substance contained per unit of volume. So the refrigerant vapour is passed through the rectifier to obtain the vapour in pure state. The water is separated by the rectifier and sent back into the heat exchanger that converts one form of energy to another form of chemical element formation. External energy causes rise in temperature and the heat is rejected in the condenser due to which the work required by the pump is negligible. Since the same cooling medium is used therefore the temperature change in con-denser and absorber is assumed to be same. The overall heat exchanger efficiency is assumed 70%.

## 4.1  Experimental

Radically condenser is an apparatus which is using condense the particle gas into liquid by decreasing temperature, due to latent heat reject into surrounding. Obtainable liquefy drop will transfer to the condenser, thus a component introduced of vapour refrigerator cycle which uses it as the liquid refrigerant, it is expanded in storage space due to absorb the heat from enclosed area to cooling effect is obtained inside the storage space, thus a Rectifier is a device which used in vapour refrig-erator cycle to circulate the water vapour, which amount of water vapour present in refrigerant vapour. After that absorber is used as a chamber of strong solution, which mixed the absorb refrigerant from evaporator and circulated water to make a strong solution. A pump is connected to absorber and pumped the strong solution into heat exchanger, to complete the refrigeration cycle and obtained the refriger-ation effect. Then observe pressure and temperature controlled by using mechanical equipment to increase or decrease fluid by using suction pressure, pressurize the air to compress the air into objects compressing the air using the pressure pump. An expansion valve is a device used in refrigeration and air-conditioning systems, which controls the amount of cooling effect in evaporation, so that the superheat is controlled on the evaporation outlet. A throttle valve is an apparatus using refrig-eration system that some amount of pressure releasing, and to absorb temperature and weak solution pressure from heat exchanger by the absorber. In this system, the heating coil is used to maintain the temperature in the generator to passed exhaust heat to absorb and utilize as a heat source, and protect the corrosion on heat pipe passed through heat exchanger during the chemical reaction. An apparatus in which vapor is formed by machine, which mechanical energy is changed into electrical

energy by the mathematical entity that when subjected to one or more operations yield another mathematical entity or its elements. Which is introduced through heat exchangers, the Heat exchanger is used to exchange the strong solution of ammonia to superheated vapor, where passed through the waste heat of the engine [7, 18]. The solution is fractions parts of refrigerant are more quantity present in solution and minimum no. of the absorber are present in solution. The weak solution is fractions parts of refrigerant are the minimum quantity and absorber are maximum quantity is present in solution (Fig. 2).

## 5   Working Procedure to Achieve Cooling Effect

The working process follows step of refrigerator cycle, the strong solution of ammonia and water is pumped into the generator by using a small positive displacement pump to increase the pressure of solution in heat exchanger [12, 19, 20]. The heat exchanger is the main component in whole refrigeration system. Then generator works through waste heat from engine are used into the heat pipe passed in generator and heat carry form heat pipe to attach heat coil, without any require external power to vaporised strong solution react with heat coil, and using rectifier to separate water vapour from mixture and circulate the water vapour. And the remaining weak solution comes back from the absorber by throttle valve.

The refrigerant vapour enters the condenser to condense the refrigerant vapour. And carry the liquid refrigerant temperature desired temperature, and then it's passed through the expansion valve to continuo the flow of refrigerant in evaporator. And evaporator absorbed heat from enclosed storage space and evaporates
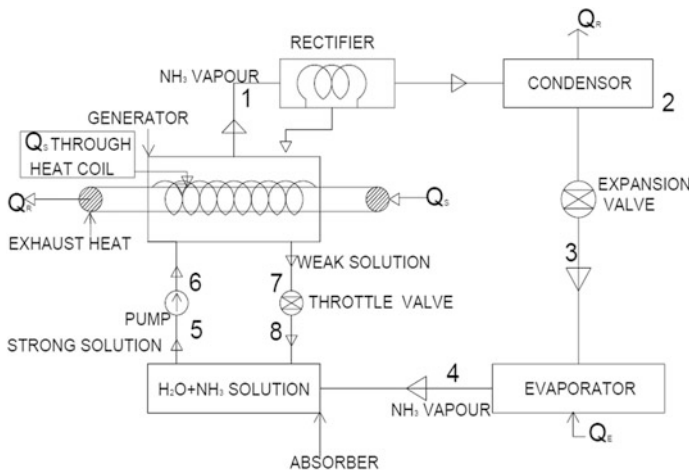


**Fig. 2** Working cycle diagram of refrigerating effect produced by engine exhaust heat

into the absorber. Absorber absorbed the evaporative refrigerant mixed with circulated water to make a strong solution and continue the refrigeration cycle to achieve the desired cooling effect in enclosed storage space [21].

## 6 Observation of Experiment

Mass of ammonia (Mn) = 0.080 kg
Temperature of Generator (Tg) = 85.73 °C
Temperature of Condenser (Tc) = 35.75 °C
Temperature of Evaporator (Te) = 9.525 °C
Temperature of Absorber (Ta) = 30 °C

Pressure and enthalpy of ammonia refrigerant data analysis corresponding to temperature from refrigeration table and psychometric chart.

Pressure at condenser (Pc) = 13.9 bar
Pressure at evaporator (Pe) = 6.15 bar
Enthalpy of generator (hgg) = 1460.51 kJ/kg
Enthalpy of Condenser (hcf) = 369.92 kJ/kg
Enthalpy of Evaporator (hef) = 244.57 kJ/kg
Enthalpy of Absorber (haf) = 341.76 kJ/kg
Enthalpy of Absorber (hag) = 1486.17 kJ/kg
Boiling point of ammonia = −33 °C
Latent heat of ammonia = 1369.5 kJ/kg
Specific heat ammonia (Cp) = 4.968 kJ/kg K

### 6.1 Calculation Design Condition of Air-Conditioning Refrigerant

Design of per ton of refrigerator of ammonia:
For ammonia,

$$Qx = \text{m Cp}\Delta T = 112.475 \text{ kJ} \tag{2}$$

$$Qy = \text{m hfg} = 109.52 \text{ kJ} \tag{3}$$

$$TR = (Qx + Qy)/210 = 1.057.\text{ton of refrigerator.} \tag{4}$$

We take several reading on the basis of experiment performance.
Experimental reading shown in Table 1.

**Table 1** Experimental reading of refrigerating effect produced by engine exhaust heat

| S. No. | Time (min) | TG (K) | TC (K) | TE (K) | COP |
|---|---|---|---|---|---|
| 1 | 5 | 354 (81 °C) | 307 (34 °C) | 283 (10 °C) | 0.241 |
| 2 | 10 | 357.2 (84.2 °C) | 308.6 (35.6 °C) | 282.8 (9.8 °C) | 0.219 |
| 3 | 15 | 360.6(87.6 °C) | 309.4 (36.4 °C) | 282.3 (9.3 °C) | 0.2005 |
| 4 | 20 | 363.1 (90.1 °C) | 310 (37 °C) | 282 (9 °C) | 0.1873 |

## 6.2 Calculation of Actual Cop of Refrigeration System

First value of COP is shown below and similarly as following the values from Table 1

$$\mathtt{COP1} = \{\mathtt{TE}/(\mathtt{TC} - \mathtt{TE})\}/\{(\mathtt{TG} - \mathtt{TC})/\mathtt{TG}\} = 0.241. \tag{5}$$

## 7 Result of Work

Variation of cop with generator temperature.

The optimum increasing value of the generator is various with decreasing COP value of refrigeration system, shown in Fig. 3.

The result of work model of REPEEH is similar to the COP result as compared to refrigerating effect produced by the engine. According to standard COP of a refrigerator is vary 0.5–2.0 and also REPEET model of COP of a refrigerator is 0.24–1.5.
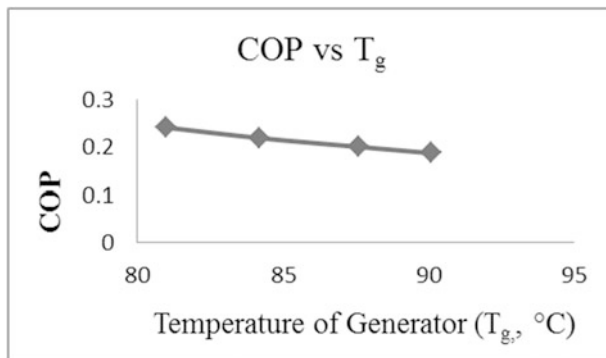


**Fig. 3** Graph of coefficient of performance versus temperature of generator

# 8 Conclusion

The refrigeration system, coefficient of performance of the refrigerating cycle is low, means the system is considered to use a lot of energy with respect to the cooling. There is an advantage of this case of our air-conditioner refrigerators system, because of the energy uses is the engine as form waste heat energy available in automobile vehicles in exhaust waste heat system. In this experiment of new model automobile vehicle used this vapour refrigeration system that would be able to get refrigeration effect without use of electricity also.

The vapour refrigerating air condition system of operational cost is very low, moving parts are also not the noise and vibrations are decreased to the minimum in this system. Ammonia is a very cheap gas. This reduces the cost of the system. Waste heat is needed for the system to operate to cool down the storage space of evaporator are used to inside storage space of car or other vehicle. To use this methodology through producing refrigeration effect by reducing fuel consumption rate during the riding of vehicle.

# References

1. Beggs RE (2001) Renewable oil fuels and diesel engines as components of sustainable system design. R Road Univ
2. Soares C (2011) Microturbines: applications for distributed energy systems. Butterworth-Heinemann
3. Calm JM (2008) The next generation of refrigerants—historical review, considerations, and outlook. Int J Refrig 31:1123–1133
4. Grosso D, Cagnol F, de Soler-Illia GA, Crepaldi EL, Amenitsch H, Brunet-Bruneau A, Bourgeois A, Sanchez C (2004) Fundamentals of mesostructuring through evaporation-induced self-assembly. Adv Funct Mater 14:309–322
5. Romero RJ, Guillen L, Pilatowsky I (2005) Monomethylamine–water vapour absorption refrigeration system. Appl Therm Eng 25:867–876
6. Sarbu I, Sebarchievici C (2013) Review of solar refrigeration and cooling systems. Energy Build 67:286–297
7. Meng X, Zheng D, Wang J, Li X (2013) Energy saving mechanism analysis of the absorption–compression hybrid refrigeration cycle. Renew Energy 57:43–50
8. Florides GA, Kalogirou SA, Tassou SA, Wrobel LC (2003) Design and construction of a LiBr–water absorption machine. Energy Convers Manag 44:2483–2508
9. Wang J, Zheng D, Fan L, Dong L (2010) Vapor pressure measurement for the water + 1, 3-dimethylimidazolium chloride system and 2, 2, 2-trifluoroethanol + 1-ethyl-3-methylimidazolium tetrafluoroborate system. J Chem Eng Data 55:2128–2132
10. Lazzarin RM, Gasparella A, Longo GA (1996) Ammonia-water absorption machines for refrigeration: theoretical and real performances. Int J Refrig 19:239–246
11. Khaliq A (2009) Exergy analysis of gas turbine trigeneration system for combined production of power heat and refrigeration. Int J Refrig 32:534–545
12. Wonchala J, Hazledine M, Boulama KG (2014) Solution procedure and performance evaluation for a water–LiBr absorption refrigeration machine. Energy 65:272–284

13. Santoyo-Gutiérrez S, Siqueiros J, Heard CL, Santoyo E, Holland FA (1999) An experimental integrated absorption heat pump effluent purification system. Part I: operating on water/lithium bromide solutions. Appl Therm Eng 19:461–475
14. Srikhirin P, Aphornratana S, Chungpaibulpatana S (2001) A review of absorption refrigeration technologies. Renew Sustain Energy Rev 5:343–372
15. Akerman JR (1971) Automotive air conditioning systems with absorption refrigeration. SAE Technical Paper
16. Rowe DM (1995) Conversion efficiency and figure-of-merit. In: CRC handbook of thermoelectrics. CRC Press, pp 31–37
17. Sun D-W (1998) Comparison of the performances of $NH_3$-$H_2O$, $NH_3$-$LiNO_3$ and $NH_3$-NaSCN absorption refrigeration systems. Energy Convers Manag 39:357–368
18. Keçeciler A, Acar Hİ, Doğan A (2000) Thermodynamic analysis of the absorption refrigeration system with geothermal energy: an experimental study. Energy Convers Manag 41:37–48
19. Lang Q, Shen J, Zou T (2003) The study review of heat and mass transfer mechanism enhancement by additive in absorption refrigeration absorber. Refrig Air Cond 3:005
20. Imai S, Shimazaki S (1991) Vibration absorbing mounting mechanism for an automotive air conditioning compressor
21. Dev K, Pal KS, Siddiqui SA (2014) An empirical study of helical coil heat exchanger used in liquid evaporization and droplet disengagement for a laminar fluid flow. Int J Eng Sci Res Technol. ISSN 2277–9655

# Thermal Design and Numerical Analysis of Transportable Bitumen Storage Tank for Improved Liquefied Bitumen Supply

**Pankaj V. Sirsikar, Chandrakant R. Sonawane, Ashok Tanna and Manoj Yadav**

**Abstract** Asphalt plant manufactures the hot black mix required for road construction. Bitumen is used as a binding agent that binds the aggregates (stones) together. Liquid bitumen ranging between 150 to 160 °C is sprayed on aggregates in a twin shaft mixer having mixer pads mounted on both shafts rotating in opposite direction with respect to each other (inward direction). Hence, asphalt plant needs the supply of hot and liquid bitumen, which is stored in storage tanks and is used as and when required. In this paper, the thermal design and simulation-based numerical analysis of 42,000 and 50,000 L capacity of transportable bitumen storage tank are presented. Usually, bitumen in the storage tank is heated by a thermal fluid called Therminol, having an inlet temperature of 180 °C, flows through tube bank present inside the storage tank. Therminol is heated by the fire-tube boiler. Thus, an effective heat exchanging system in the bitumen storage tank is crucial. In the existing storage tank, the solid bitumen rocks need 12 h of heating to obtain liquid bitumen ranging between 150 to 160 °C. Here, computational fluid dynamics (CFD)-based simulations are carried out to design the effective heat transferring system. Various flow conditions of Therminol, as well as different tube bank configuration, are been simulated and presented. The CFD analysis shows that with proper and modified distribution of tube bank inside the storage vessel helps to improve the heat transfer by a factor 2–3 and hence is capable to liquefy bitumen within 6 h.

**Keywords** Thermal analysis · Heat exchange · Simulation · Bitumen

P. V. Sirsikar · C. R. Sonawane (✉)
Symbiosis Institute of Technology, Symbiosis International (Deemed University), Pune, Maharashtra, India
e-mail: chandrakant.sonawane@sitpune.edu.in

A. Tanna · M. Yadav
Linnhoff India Pvt. Ltd., Mumbai, India

# 1   Introduction

In asphalts plants, cold aggregate (combination of stones of sizes 7, 10, 12, 20, 40 mm, etc.) is fed in cold feeder, and further, they are carried to drying drum, dried there, and then transferred to the hot mineral bin where the dried aggregate is stored. Further, the aggregate from the hot bins is dropped into the mixer according to the recipe of desired black mix. Further in mixer, 5% of mixer capacity, bitumen is sprayed on the aggregate and mixed for a certain period of time. After mixing, the black mix is discharged into the truck/lorry. Currently, 12 h are required for liquefying bitumen present in the tank. There is much scarcity on the literature available regarding the experimental as well as the numerical study of the design of asphalt plant and necessary bitumen melting/heating system. Very few guidelines were published [1–3] along with some standards like [4–6]

Asphalt plants fall under the category of heavy machinery. This segment of machinery produces the plants that manufacture the hot black mix required in road construction. Aggregate first undergoes the heat treatment and it is dried completely. Complete drying of aggregates is necessary to obtain the best level of bitumen coat over aggregates. A typical plant has minimum one tank of bitumen capacity 42,000 L. The asphalt plant is strictly shut down in rainy season as; the initial temperature of the aggregate is low, i.e., near about 20 °C, and it is wet. This leads to more consumption of coal as the aggregate is to be completely dried; it proves to be more expensive. Now when the plant is shut down, the bitumen changes it phase from liquid to solid. Thus before starting the plant, bitumen has to be heated for 12 h so that it gets back to liquid. The temperature of bitumen is maintained between 150 to 160 °C. The bitumen in the tank is heated by passing the thermal fluid Therminol through heating coil in the tank.

Bituminous materials or asphalts are extensively used for roadway construction, primarily because of their excellent binding characteristics and waterproofing properties and relatively low cost. Bituminous materials consist of bitumen which is a black or dark-colored solid or viscous cementitious substances consist of chiefly high-molecular-weight hydrocarbons derived from the distillation of petroleum or natural asphalt, has adhesive properties, and is soluble in carbon disulfide. Tars are residues from the destructive distillation of organic substances such as coal, wood, or petroleum and are temperature sensitive than bitumen. Bitumen will be dissolved in petroleum oils where unlike tar. Bitumen is the residue or by-product when the crude petroleum is refined and is available in various forms like (i) cutback bitumen, (ii) bitumen emulsion, (iii) bituminous primers, and (iv) modified bitumen form.

Bitumen storage tanks are typically horizontal and designed using API 650 Code which deals with Welded Steel Tanks for Oil Storage where internal pressure is less than 0.17 bar. The API 650 code helps to evaluate the thickness of the storage wall and should the tank be bolted to ground using anchor bolts or not. The API 650 code has two methods for determining the parameters mentioned in the above statement. The methods are (i) calculations of thickness by the 1-foot method and (ii) calculation of thickness by the variable point method.

In this paper, the bitumen storage tanks designed by API 650 code have working temperature under 260 °C are presented. The detailed numerical design of the thermal system, which is basically a heat exchanging system capable of melting bitumen within 6 h, is also discussed. While designing the storage tank, dimensions of it are within the trailer sizes available in India for easy transportation.

## 2 Problem Under Consideration: Designing Bitumen Storage Tank

Figures 1 and 2 show the 3D CAD model generated for bitumen storage tank using solid works. Initially, this CAD model of the storage tank is generated with the help of 2D CAD drawings provided by the company (Linnhoff India Pvt. Ltd).

The primary calculations for the bitumen storage tank are:

Dimensions of tank:

Diameter (inner) of tank = 2438.40 mm = 2.4384 m
Length (inner) of tank = 9000 mm = 9.00 m
The volume of tank = 42028.30 L.

Now when the tank is filled to its fullest capacity, i.e., 42028.30 L of bitumen, the pressure exerted by the bitumen on the wall of the tank will be:

Density of bitumen = 1011 kg/m$^3$
Mass of bitumen in tank = 42490.6113 kg.



**Fig. 1** Bitumen storage tank

| |
|---|
| 1 – Saddle Support (Plate 8t.) |
| 2 – Shell (Plate 6t.) |
| 3 – Shell 2 (Plate 6t.) |
| 4 – Checqured Plate (Plate 5t.) |
| 5 – Stiffener Plate (Plate 6t.) |
| 6 – Lifting Hook (Plate 15t.) |
| 7 – 2inch Butterfly Valve |
| 8 – C Channel (150 x 75 x 5.7 x 9) |
| 9 – End Plate (Plate 6t.) |
| 10 – Heat Exchanging Pipe (2inch SCH 40.) |
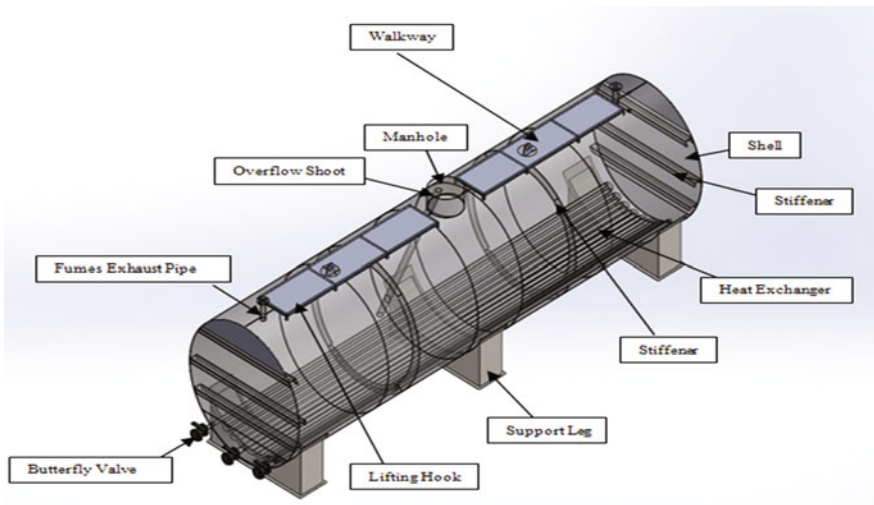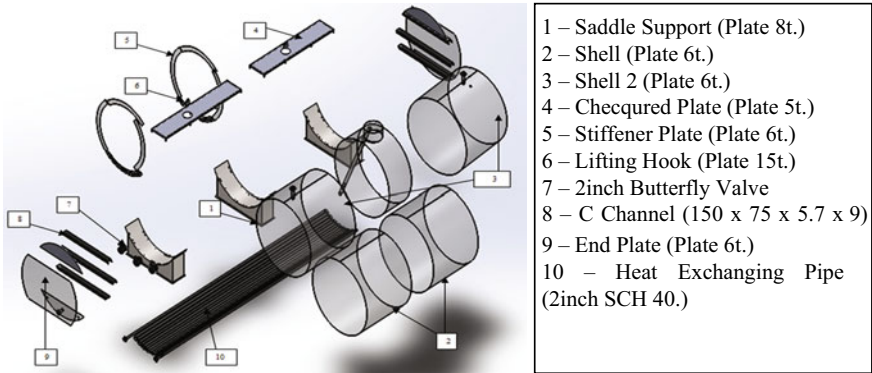
**Fig. 2** Exploded view of bitumen storage tank

Force exerted on the wall by bitumen = 416832.8969 N
The pressure exerted by the bitumen on the wall = 0.05324.6401 Bar.

As the storage tank is used to store bitumen, the standard that is used to design the tank is American Petroleum Institute (API). API 650 code is entitled to Welded Steel Tanks for Oil Storage. The API 650 answers the question of how thick the wall should be.

(i) As per 1-foot method:

$$\text{Thickness Required} = \frac{[2.6D(H-1)G]}{S} + \text{CA} \tag{1}$$

where,

| | |
|---|---|
| $D$ | Diameter of the tank in meters |
| $H$ | Design fluid eight in meters |
| $G$ | Specific gravity of the content |
| $S$ | Allowable tensile stress of the wall |
| CA | Corrosion allowance if any |

Therefore, thickness $(t)$ = 0.006000002174, $m$ = 6 mm.

$$\text{Lift Force} = P_i \times D^2 \times 4.08 - W \tag{2}$$

where

$P_i$  Internal pressure in meters of water
$D$  Diameter of the tank in meters
$W$  Static weight tank in kg.

Lift Force = −5741.23 N. Hence, there is no need of bolting the tank to the ground with anchor bolts as the direction of the force is downwards.

The static analysis for the Old bitumen tank is also been cross-verified using the ANSYS-based FEA analysis. Figure 3 shows the equivalent (von Mises) stress developed on the bitumen tank due to the full loading of bitumen as well as due to the own weight load. The maximum value of equivalent stress is 41.13 MPa which is much less than the elastic yield point of tank material used. Figure 5 shows the factor of safety obtained which has a minimum value of 6.37. The deflection of the storage tank is also within allowable limits, shown in Fig. 4. The existing design is safe but is not supporting with heat exchanger system as well as transportation capability. Hence, there is a need to design a new tank with current demands.



**Fig. 3** Equivalent stress generated on bitumen storage tank
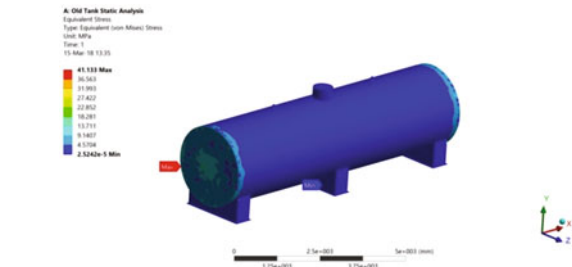


**Fig. 4** Total deformation of bitumen storage tank
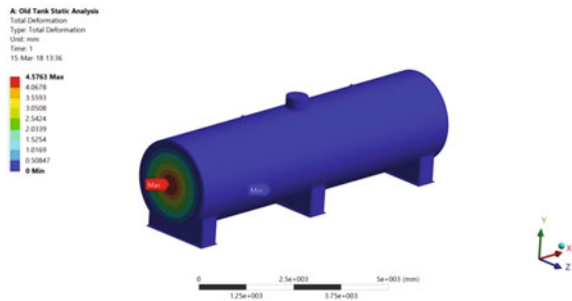


**Fig. 5** Safety factor calculated for bitumen storage tank
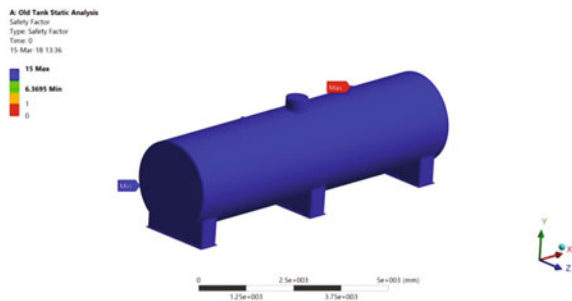
## 3  Proposed Design of Bitumen Storage Tank

In order to incorporate the new thermal—heat exchanger system as well as to have transportation capabilities, the new tank is proposed. The tank diameter is kept almost the same as the older one; however, the length is now increased to around 10 m. The tank has more supporting sniffing. The increased length will help to occupy the thermal system. The bitumen storage now has two manholes. Figure 6 shows 3D CAD model generated in solid works for the proposed bitumen storage tank.

Calculation for proposed bitumen storage tank:

Dimensions of tank:

Diameter (inner) of tank = 2438.40 mm = 2.4384 m
Length (inner) of tank = 10,668 mm = 10.668 m
Volume of tank = 49.8175 m$^3$ = 49,817.5 L
Density of bitumen = 1011 kg/m$^3$
Mass of bitumen in tank = 50365.5920 kg
Force exerted on the wall by bitumen = 494086.4578 N
The pressure exerted by the bitumen on the wall = 0.07 Bar.

According to the American Petroleum Institute (API) 650 code, the thickness of the cylinder wall can be evaluated as:

As per 1-foot method:

Thickness ($t$) = 6 mm
Lift force = −7908.3471 N.

Hence, there is no need of bolting the tank to the ground with anchor bolts as the direction of the force is downward. The FEA analysis for the proposed tank also shows that the tank is safe for the applied load of bitumen weight; refer Figs. 7, 8, and 9.



**Fig. 6** Proposed bitumen storage tank
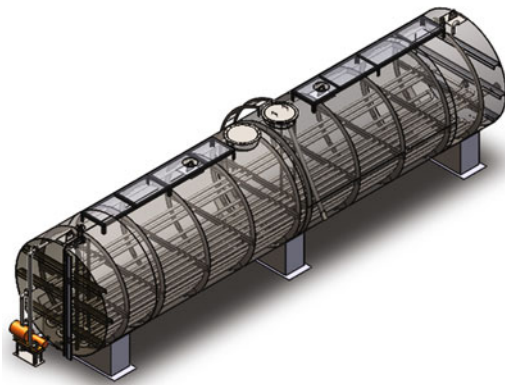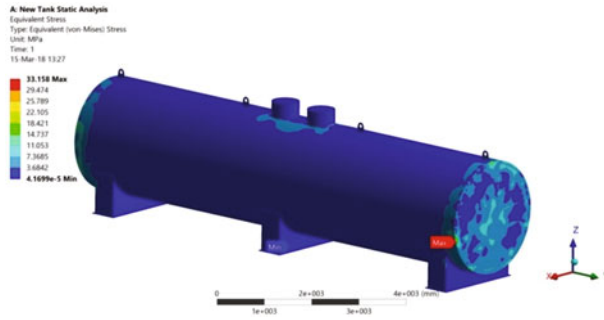
**Fig. 7** Equivalent stress on proposed bitumen storage tank
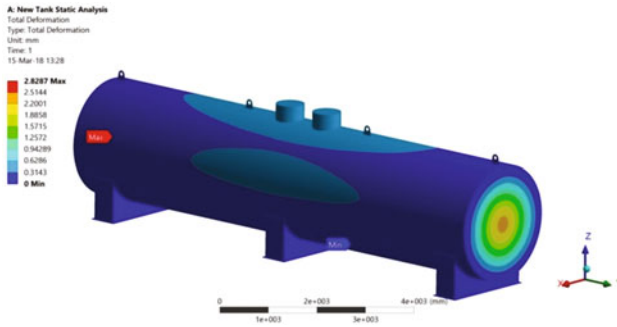


**Fig. 8** Total deformation of proposed bitumen storage tank

**Fig. 9** Safety factor for proposed bitumen storage tank
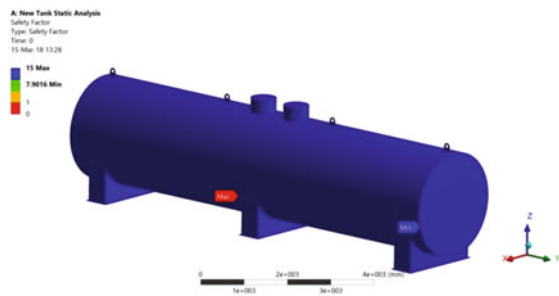
## 4  CFD Analysis of the Thermal System Used Inside the Bitumen Tank

Currently, 12 h are required for melting the bitumen present in the bitumen tank. This time needs to slash down to 6 h by making changes in the heating coil. Hence, the new proposed tank made few changes in the heating coil orientations, dimensions as well as in a number of operating pipes.

The number of pipes has been increased from 16 to 18. Also, the orientation of the coil is different as shown in the CAD model below; refer Figs. 10, 11 and 12 which shows the arrangement of old and proposed thermal system inside the bitumen storage tank. The other difference in the proposed tank is the molten hot bitumen that has liquefied due to heat received by a coil which is passed over or showered on the top layer of solid bitumen by a pump (continuously). This would significantly help to bring down the melting time.

Following are the properties of Therminol used at temp. 180 °C in the CFD analysis

Density = 899.5 kg/m$^3$

Thermal conductivity = 0.107 W/m °K

Heat capacity = 2.122 kJ/kg °K

Kinematic viscosity = $1.17 \times 10^{-6}$ m$^2$/s

Discharge of Therminol by pump = 6000 L/h = $1.66 \times 10^{-3}$ m$^3$/s.

$$Q_{\text{pumpdischrage}} = \text{Area} \times V_{\text{averagevelocity}} \tag{3}$$

Fig. 10  Old heating coil



Fig. 11  Inlet and outlet temperature of the old coil
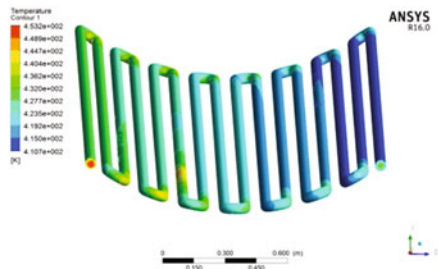
**Fig. 12** New heating coil



Velocity inside the pipe, $v = 0.84694$ m/s.

Hence, Reynolds's number based on pipe diameter, Re of Therminol $= 36194.02$

Following are the properties of bitumen used for CFD analysis

Density $= 1011$ kg/m$^3$, Latent heat $= 450.367$ kJ/kg.

From CFD numerical analysis, it can be observed that for supply inlet temperature of Therminol of 453 K (180 °C), the outlet temperature of 374.20 K is observed. The Therminol is passed through the coil for 8.33 min, i.e., 500 s at $v = 0.84694$ m/s.

Therefore, the temperature difference is 450.8–374.20 = 76.6 °C; refer Fig. 11.

Now,

Mass of Therminol flown through coil for 8.33 min = 746.3259 kg

$$Q = m_{\text{massoftherminolfor 8.33 min}} \times C_p \times (\Delta T) \tag{4}$$

$Q = 121{,}311.6297$ kJ

The Now amount of bitumen changed its phase from solid to liquid

$$L_{\text{latentheatofbitumen}} = \frac{Q_{\text{heatenergy}}}{m_{\text{massofbitumen}}} \tag{5}$$

Mass of bitumen melted $= 269.36$ kg in 8.33 min.

Now, the CFD analysis for the proposed thermal system is shown in Fig. 13. The same properties of Therminol and bitumen are used for numerical simulation at a temperature of 180 °C. For the same discharge, as of old one, of Therminol pump $= 6000$ L/h, the Reynolds number of Therminol flow through the pipe is 36194.02 at $v = 0.84694$ m/s.

Therefore, the temperature difference = 450.6–370.3 = 80.3.

But the mass of the Therminol passed in through the coil for 8.33 min = 1071.66 kg.

Heat received by bitumen = 182,607.2204 kJ.

Mass of bitumen liquified = 405.463 kg in 8.33 min.

For the discharge of Therminol pump = 8000 L/h, $v$ = 1.046 m/s. The following Fig. 14 shows the inlet and outlet temperature.

For the discharge of Therminol pump = 10,000 L/h, $v$ = 1.30 m/s. The following Fig. 15 shows the inlet and outlet temperature (Tables 1 and 2).



**Fig. 13** Inlet and outlet temperature of the new coil
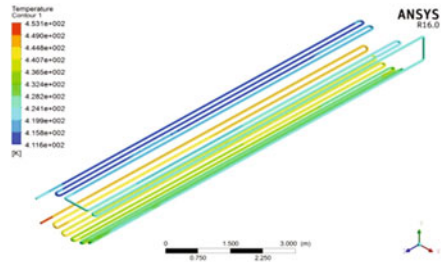


**Fig. 14** Inlet and outlet temperature of the new coil at $v$ = 1.046 m/s



**Fig. 15** Inlet and outlet temperature of the new coil at $v$ = 1.30 m/s
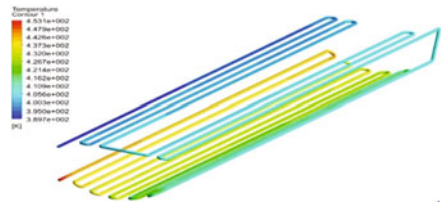
**Table 1** Result of heat generated at different velocities of Therminol passed through the proposed heating coil

| S. No. | Velocity of Therminol (m/s) | Mass of Therminol used (kg) | Heat generated, $Q$ (kJ) | Mass of bitumen melted (kg) | % of increase in bitumen melting w.r.t old coil |
|---|---|---|---|---|---|
| 1 | 0.84694 | 1071.66 | 182607.22 | 406.46 | 33.56 |
| 2 | 1.4046 | 1433.91 | 197653.69 | 438.87 | 38.62–39 |
| 3 | 1.30 | 1796.93 | 241749.61 | 536.78 | 49.81–50 |

**Table 2** Comparison of FEA static analysis of both tanks

| S. No. | Analysis | Old tank | Proposed tank |
|---|---|---|---|
| 1 | Equivalent (von Mises) stress | 41.13 MPa (max) | 33.15 MPa (max) |
| 2 | Total deformation | 4.57 mm (max) | 2.87 mm (max) |
| 3 | Safety factor | 6.36 (min) | 7.91 (min) |

# 5 Conclusion

In this paper, the mechanical as well as thermal designed for the bitumen storage tank if presented. The API 650 code is used for mechanical design, and FEA analysis is also carried out to cross-check the results. During FEA static analysis of both tanks, following main results are obtained.

The thermal analysis of heat exchanger system is also carried out using CFD analysis. Comparison of both old and proposed system is presented, and it is concluded that the melting time of 12 h is slashed down to 6 h by the new proposed system and passing Therminol through the coil at $v = 1.30$ m/s by using pump of discharge capacity of 10,000 L/h.

# References

1. Diamant RME (1986) Thermal insulation for industry (Chap. 7). Thermal Acoustic and Insulation, pp 231–273
2. Li H, Huang X, Yang P, Yang H (2017) A new pressure vessel design by analysis method avoiding stress categorization. Int J Press Vessel Pip 152:38–45
3. Hunter RN, Self A, Read J (2015) The shell bitumen hand book, 6th edn
4. 2015 ASME Boiler and Pressure Vessel Code. Section III, 2015 edition, 1 July 2015
5. API 650 Standard, 12th edn., 2 Jan 2016
6. Pressure rating for pipe (1977) ANSI Standard, Section B31.1
7. Linnhoff India Pvt. Ltd. Catalogues

# Steady-State Modelling and Validation of a Thermal Power Plant

Ravinder Kumar, Ravindra Jilte, B. Mayank
and Manujender Singh

**Abstract** In the present work, steady-state modelling and validation of a 210-MW sub-critical thermal power plant located in North India using mass, energy, and exergy balance equations. The first and second law efficiencies have analysed for each component. MATLAB calculation tool and Engineering Equation Solver (EES) software have used for performing analyses. The results conclude that 277.2 MW (72.50%) of the total energy lost in the condenser as the main equipment wasting energy to the environment followed by boiler with 101.4 MW (26.52%) in the cycle. On the other hand, the maximum exergy destruction is seen to be in the boiler system 274.48 MW (85.64%) followed by the other components. The calculated thermal efficiency and the exergy efficiency of the overall plant are found to be 36.60 and 35%.

**Keywords** Energy analysis · Exergy analysis · Coal-fired power plant · Energy efficiency · Exergy efficiency

## Nomenclature

| | |
|---|---|
| BFP | Boiler feed pump |
| CEP | Condensate extraction pump |
| COND | Condenser |
| ECO | Economizer |
| HPT | High-pressure turbine |
| HPH | High-pressure feedwater heater |

R. Kumar (✉) · R. Jilte · B. Mayank · M. Singh
Lovely Professional University, Phagwara 144411, Punjab, India
e-mail: ravchauhan8@gmail.com

R. Jilte
e-mail: rdjilte@gmail.com

B. Mayank
e-mail: mayankking7@gmail.com

M. Singh
e-mail: manujendersingh@gmail.com

511

| H | Enthalpy (kJ kg$^{-1}$) |
|---|---|
| IPT | Intermediate pressure turbine |
| LPT | Low-pressure turbine |
| LPH | Low-pressure feedwater heater |
| LHV | Lower heating value of coal (kJ/kg) |
| $\dot{m}_f$ | Coal consumption rate (Ton/h) |
| $\dot{m}_{uw}$ | Unit mass flow rate of water (Ton/h) |
| Mwe | Electric power output |
| MW | Plant capacity |
| P | Pressure in bar |
| S | Entropy (kJ/kg K) |
| $\dot{W}_P$ | Work done by pump |
| $\dot{W}_T$ | Power output of turbine |
| $x_i$ | Fraction of mass flow rate of steam at '$i$th' state |
| $\dot{X}$ | Exergy function |
| $Y_i$ | Fractional mass flow rate of bled steam at '$i$th' state |

**Greek Symbols**

| $\eta_{plant}$ | Overall plant efficiency |
|---|---|
| $\eta_{boiler}$ | Boiler efficiency |
| $\eta_P$ | Pump efficiency |
| $\lambda_{ex}$ | Exergy efficiency |

# 1 Introduction

Thermal power plant working is to convert coal-stored energy into usable electricity. In India, the basic fuel coal is available in ample quantity and may be used further for 50 years easily to run coal-fired power plants. In India, about 80% of the coal produced consume by India's electricity sector. Recently, worldwide concern about energy crisis and climate changes has provided continuous opportunities to extend energy-efficient technologies [1]. Thermal power plants' performance can be evaluated through energetic performance criteria. In recent years, a number of researchers have focused their research on thermal power plant of different capacities [2–4]. Some researchers have been contributed review paper on exergy analysis which helps the researchers to get in touch with the previous year's problems [5]. Boiler and furnace performance analysis in a coal-fired power plant were carried out [6]. So, in present work energy, exergy analysis along with validation has been done of a 210 MW thermal power plant using mass, energy, and exergy balance equations.

## 2 Plant Layout

A sub-critical thermal power plant of 210 MW capacity situated in North India with superheating, reheating and regeneration was chosen for present 2E analysis. The detailed schematic view of plant is shown in Fig. 1 and operating conditions along with thermodynamic properties of plant at each point are shown in Tables 1 and 2.

## 3 Thermodynamic Modelling

In the present work, a simulation model having modular structure is prepared using the mass balance, energy balance, and exergy analysis equations. Numerical integration has been done using MATLAB calculation tool. The temperature and pressure values of the reference environment considered in the analysis are $T0 = 30\ °C$ and $P0 = 1.01$ bar.
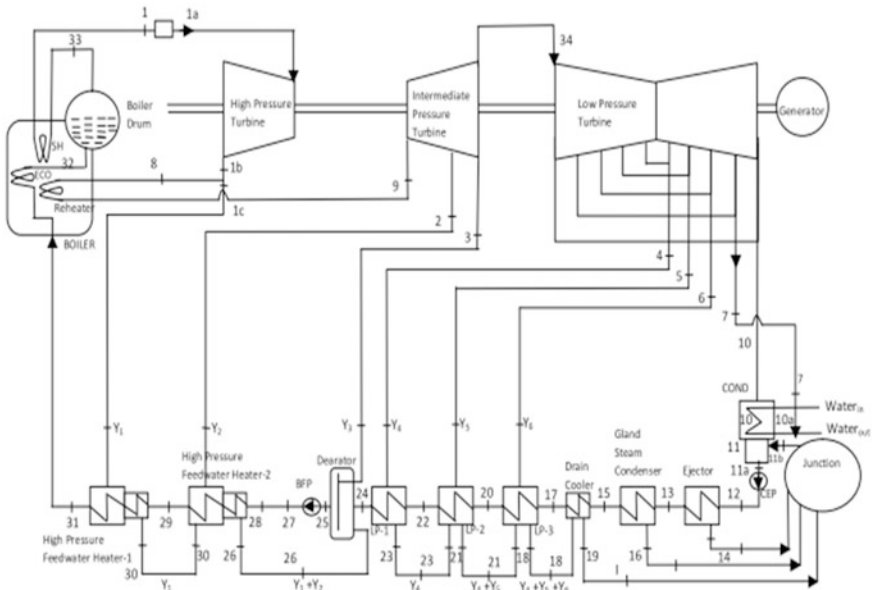


**Fig. 1** Steam turbine cycle-based coal-fired power plant

**Table 1** Operating conditions of the 210-MW coal-fired power plant

| Operating conditions | Value | Unit |
|---|---|---|
| Power produced | 210 | MW |
| Steam boiler rate | 174.40 | kg/s |
| Fresh steam pressure | 160 | bar |
| Fresh steam temperature | 537 | °C |
| Superheated steam pressure | 145 | bar |
| Superheated steam temperature | 537 | °C |
| Stack gas temperature | 148 | °C |
| Combined pump/motor efficiency | 95 | % |
| Fuel mass flow rate | 30.55 | kg/s |
| Lower heating value of coal | 18,910 | kJ/kg |

**Table 2** Thermodynamic properties of points in cycle (refer to Fig. 1)

| Stream | $\dot{m}$ (kg/s) | $t$ (°C) | $p$ (bar) | $h$ (kJ/kg) | $s$ (kJ/kg K) |
|---|---|---|---|---|---|
| 0 | 0 | 30 | 1.01 | 125.7 | 0.43 |
| 1 | 174.40 | 537 | 151.5 | 3412.51 | 6.46 |
| 1a | 174.16 | 537 | 151.5 | 3412.51 | 6.46 |
| 1b | 172.69 | 348.8 | 41.68 | 3087.15 | 6.55 |
| 1c | 16.74 | 348.8 | 41.68 | 3087.15 | 6.55 |
| 2 | 10.04 | 420.6 | 16.41 | 3295.83 | 7.29 |
| 3 | 8.91 | 300.7 | 6.49 | 3059.55 | 7.33 |
| 4 | 7.72 | 193.5 | 2.41 | 2852.12 | 7.38 |
| 5 | 4.01 | 101.1 | 0.86 | 2677.31 | 7.43 |
| 6 | 5.65 | 0.976 | 0.43 | 2582.38 | 0.012 |
| 7 | 0.50 | 61.7 | 0.22 | 257.61 | 0.85 |
| 8 | 155.94 | 348.8 | 41.68 | 3087.15 | 6.55 |
| 9 | 155.94 | 537 | 37.51 | 3528.35 | 7.23 |
| 10 | 119.88 | 45 | 0.05 | 2496.7 | 8 |
| 11a | 138.75 | 45.6 | 0.10 | 190.69 | 0.64 |
| 11b | 18.28 | – | – | – | – |
| 12 | 138.75 | 45.9 | 22.22 | 193.62 | 0.64 |
| 13 | 138.75 | 47.2 | 0.10 | 198.22 | 0.66 |
| 14 | 0.30 | 167 | – | 705.08 | 1.99 |
| 15 | 138.75 | 47.6 | 0.11 | 199.89 | 0.67 |
| 16 | 0.081 | 99.9 | 1.01 | 417.78 | 1.29 |
| 17 | 138.75 | 50.7 | 0.12 | 212.86 | 0.71 |
| 18 | 17.39 | 77.2 | 0.41 | 322.85 | 1.03 |
| 19 | 17.39 | 52.6 | 0.14 | 219.97 | 0.7 |
| 20 | 138.75 | 74.2 | 0.37 | 311.14 | 1.01 |
| 21 | 11.74 | 94.7 | 0.83 | 396.45 | 1.25 |
| 22 | 138.75 | 91.7 | 0.74 | 384.32 | 1.21 |

**Table 2** (continued)

| Stream | $\dot{m}$ (kg/s) | $t$ (°C) | $p$ (bar) | $h$ (kJ/kg) | $s$ (kJ/kg K) |
|---|---|---|---|---|---|
| 23 | 7.72 | 125.4 | 2.40 | 529.6 | 1.59 |
| 24 | 138.75 | 122.4 | 2.11 | 513.54 | 1.55 |
| 25 | 174.46 | 159.9 | 6.34 | 674.13 | 1.94 |
| 26 | 26.79 | 168.1 | 7.55 | 710.52 | 2.01 |
| 27 | 174.46 | 163.1 | 191.9 | 698.81 | 1.95 |
| 28 | 174.40 | 163.1 | 191.9 | 698.81 | 1.95 |
| 29 | 174.40 | 201.2 | 191.9 | 864.00 | 2.37 |
| 30 | 16.74 | 206.2 | – | 880.31 | 2.38 |
| 31 | 174.40 | 245 | 38.77 | 1076.02 | 2.71 |
| 32 | 193.99 | 67 | 340 | 1593.25 | 3.66 |
| 33 | 193.99 | 67 | 340 | 2630.01 | 5.35 |
| 34 | 137.60 | 301.4 | 7.05 | 3059.55 | 7.23 |
| Water$_{in}$ | 6703.61 | 30 | 1.01 | 125.7 | 0.43 |
| Water$_{out}$ | 6703.61 | 40 | 1.01 | 167.5 | 0.57 |

## 4 Energy Analysis of Coal-Fired Power Plant

Mass balance equation:

$$\sum \dot{m}_{in} = \sum \dot{m}_{out} \tag{1}$$

Energy balance equation:

$$\dot{Q} - \dot{W} = \sum \dot{m}_i \left( h_{out,i} - h_{in,i} \right) \tag{2}$$

$$\dot{m}_f = \dot{m}_{uw} \left( \dot{m}_1 (h_1 - h_{31}) + \dot{m}_8 (h_9 - h_8) \right) / (\eta_{boiler} \times LHV) \tag{3}$$

The overall plant efficiency can be calculated as follows:

$$\eta_{plant} = \frac{\dot{W}_{Net}}{\dot{m}_f \cdot LHV} \tag{4}$$

## 5 Exergy Analysis of Coal-Fired Power Plant

Exergy analysis is related to the second law of thermodynamics and helpful in diminishing the irreversibility taking place at various points in the plant.

**Table 3** Exergy function for different energy stream conditions [8]

| Description | Expression | Equation |
|---|---|---|
| For a pure substance | $\dot{X} = \dot{m}\left[(h - h_\mathrm{o}) - T_\mathrm{o}(s - s_\mathrm{o})\right]$ | (6) |
| For a solid fuel (semi-empirical correlation) | $\dot{X} = [(\mathrm{NCV})^o + 2442\,w]\phi_\mathrm{dry} + 9417(s/100)$ where, $\phi_\mathrm{dry} = 1.0437 + 0.1882\dfrac{h}{c} + 0.0610\dfrac{o}{c} + 0.0404\dfrac{n}{c}$ | (7) |
| For a gas phase (flue gas) | $\dot{X} = \dot{m}\left[(h - h_\mathrm{o}) - T_\mathrm{o}(s - s_\mathrm{o}) + \sum x'_\mathrm{k} \cdot e^\mathrm{CH}_\mathrm{k} + \bar{R} \cdot T_\mathrm{o} \cdot \sum x'_\mathrm{k} \cdot \ln x'_\mathrm{k}\right]$ | (8) |

$$\dot{X}_\mathrm{Q} = \left(1 - \frac{\dot{T}_\mathrm{o}}{T_\mathrm{i}}\right)\dot{Q}_\mathrm{i} \tag{5}$$

where $T$ is the absolute temperature (K), whilst subscripts (i) and (o) refer to the surface and environment conditions, respectively. The exergy losses are zero for a single component taken into consideration of a thermal system [7]. Also, 'w' is mass fraction of moisture in the fuel and 'hfgo' is the enthalpy of evaporation of H2O at the standard temperature $T0$ given as 2442 [8]. Some expressions for exergy are also presented (see Tables 3 and 4).

## 6 Results and Discussion

Energy and exergy flow rates have been evaluated using design data of 210 MW plant capacity and are tabulated in Table 5. The results obtained from the energy point of view have been validated by comparing the plant in operating conditions. Moreover, overall plant efficiency, defined as the ratio of net electrical energy output to coal energy input, is found to be 36%. This value also ranges from 35 to 38% in real operating conditions of plant, and thus, it validates the prediction of the model. The energy balance reveals that 72.50% of the energy added in the boiler is lost in the condenser and lost to environment, whilst 26.52% is lost in the boiler for operating regime with 100% of the maximum load. Other component losses as compared are negligibly small. The energy losses which take place in the condenser are of low quality; hence, these cannot be utilized practically for the improvement in plant performance.

Exergy destruction, per cent of exergy destruction, and exergy efficiencies of various plant components have been summarized in Table 6. Exergy analysis reveals that the exergy destruction rate of boiler is 274.48 MW accounts for 85.64% total exergy destruction of the plant for operating regimes with 100% load which is dominant over all other irreversibility in the plant. Combined exergy destruction of steam turbine including HPT, IPT, and LPT was found to be 23 MW which is 7.18% of total cycle exergy destruction. On the other hand, exergy destruction found to be in condenser is 3.42 MW which is only 1.08% of total plant exergy

**Table 4** Exergy destruction rate and exergy efficiency equations for various plant components

| Component | Exergy destruction | Equation | Exergy efficiency | Equation |
|---|---|---|---|---|
| Pump | $\dot{X}_{D,P} = \dot{W}_P + \sum \dot{X}_{in,P} - \sum \dot{X}_{out,P}$ | (9) | $\lambda_{ex,P} = \left(\dot{X}_{out,P} - \dot{X}_{in,P}\right)/\dot{W}_P$ | (15) |
| Condenser | $\dot{X}_{D,C} = \sum \dot{X}_{in,C} - \sum \dot{X}_{out,C}$ | (10) | $\lambda_{ex,C} = \dot{X}_{out,C}/\dot{X}_{in,C}$ | (16) |
| Boiler | $\dot{X}_{D,B} = \dot{X}_F + \sum \dot{X}_{in,B} - \sum \dot{X}_{out,B}$ | (11) | $\lambda_{ex,B} = \left(\dot{X}_{out,B} - \dot{X}_{in,B}\right)/\dot{X}_F$ | (17) |
| Steam turbine | $\dot{X}_{D,T} = \sum \dot{X}_{in,T} - \sum \dot{X}_{out,T} - \dot{W}_T$ | (12) | $\lambda_{ex,T} = \dot{W}_T/\left(\dot{X}_{in,T} - \dot{X}_{out,T}\right)$ | (18) |
| Heater | $\dot{X}_{D,H} = \sum \dot{X}_{in,H} - \sum \dot{X}_{out,H}$ | (13) | $\lambda_{ex,H} = \dot{X}_{out,H}/\dot{X}_{in,H}$ | (19) |
| Cycle | $\dot{X}_{cycle} = \sum \dot{X}_{all_{components}}$ | (14) | $\lambda_{ex,total} = \dot{W}_{netout}/\dot{X}_F$ | (20) |

**Table 5** Energy and exergy analysis of a 210-MW thermal power plant (refer to Fig. 1)

| Stream | Energy (MW) | Exergy (MW) | Stream | Energy (MW) | Exergy (MW) |
|--------|-------------|-------------|--------|-------------|-------------|
| 0 | – | – | 17 | 12.1 | 0.40 |
| 1 | 573.4 | 254.39 | 18 | 3.4 | 0.25 |
| 1a | 572.6 | 254.04 | 19 | 1.6 | 0.25 |
| 1b | 511.6 | 191.18 | 20 | 25.7 | 1.62 |
| 1c | 49.6 | 18.54 | 21 | 3.2 | 0.28 |
| 2 | 31.9 | 10.97 | 22 | 35.9 | 3.37 |
| 3 | 26.2 | 7.50 | 23 | 3.1 | 0.41 |
| 4 | 21.1 | 4.78 | 24 | 53.8 | 6.95 |
| 5 | 10.3 | 1.72 | 25 | 95.7 | 16.19 |
| 6 | 13.9 | 14.62 | 26 | 15.7 | 2.87 |
| 7 | 0.1 | 0.0032 | 27 | 100.0 | 19.96 |
| 8 | 461.9 | 172.64 | 28 | 100.0 | 19.95 |
| 9 | 530.8 | 209.51 | 29 | 128.8 | 26.14 |
| 10 | 284.3 | 9.38 | 30 | 12.6 | 2.73 |
| 11a | 9.0 | 0.101 | 31 | 165.8 | 45.57 |
| 11b | – | – | 32 | 256.3 | 85.64 |
| 12 | 9.4 | 0.57 | 33 | 437.3 | 177.22 |
| 13 | 10.1 | 0.30 | 34 | 403.7 | 120.33 |
| 14 | 0.2 | 0.032 | Water$_{in}$ | 0.003 | 0.0005 |
| 15 | 10.3 | 0.32 | Water$_{out}$ | 280.2 | 5.86 |
| 16 | 0.0 | 0.002 | | | |

**Table 6** Power plant component's exergy destruction and exergy efficiency at 100% load

| Components | Exergy destruction, MW | Percentage exergy destruction, % | Percentage exergy efficiency, % |
|-----------|------------------------|----------------------------------|---------------------------------|
| Boiler | 274.48 | 87.32 | 51.92 |
| HPT | 6.2 | 1.97 | 90.20 |
| IPT | 0.5 | 0.15 | 99.30 |
| LPT | 16.3 | 5.18 | 81.82 |
| COND | 3.42 | 1.08 | 63.55 |
| HPH-1 | 5.56 | 1.76 | 87 |
| HPH-2 | 4.64 | 1.47 | 86.21 |
| Deaerator | 1.15 | 0.36 | 93.36 |
| LP-1 | 0.78 | 0.24 | 90.42 |
| LP-2 | 0.10 | 0.031 | 85.08 |
| LP-3 | 0.03 | 0.009 | 75.04 |
| BFP | 0.76 | 0.24 | 83.09 |
| CEP | 0.41 | 0.13 | 81.23 |
| Power cycle | 314.33 | 100 | 35 |

destruction. The second law efficiency of boiler and turbine has been evaluated to be 51.92 and 78.92%, respectively. Overall plant exergy efficiency has been calculated to be 35%. It is concluded that the boiler requires some necessary modification for the reduction of its exergy destructions for the improvement in plant performance.

# 7 Conclusions

Energy and exergy analysis of a 210 MW thermal power plant situated in North India are presented in this study. On the basis of first law analysis, i.e. energy analysis, this study concludes that condenser having the greatest energy losses in the plant in comparison to other components. Moreover, overall plant efficiency is found to be 36%. However, energy analysis was unable to reveal the information about the quality of energy. So, the second law of analysis serves to identify the irreversibility in the power plant. A large portion of exergy destruction takes place in boiler, so the possibility for efficiency improvement is found to be in boiler. Low quality exergy losses in condenser is found to be thermodynamically insignificant. Overall exergy efficiency of plant has been calculated to be 35%. Overall efficiency and exergy efficiency of plant under study have been validated against other coal-fired power plants of different capacities, and the results obtained are satisfactory.

# References

1. Seyyedvalilu MH, Mohammadkhani F (2015) A parametric study on exergy and exergoeconomic analysis of a diesel engine based combined heat and power system. Int J Eng 28(4):608–617
2. Kumar R (2016) Thermodynamic modeling and validation of a 210-MW capacity coal-fired power plant. Iran J Sci Technol Trans Mech Eng 40(3):233–242
3. Aljundi IH (2009) Energy and exergy analysis of a steam power plant in Jordan. Appl Therm Eng 29:324–328
4. Karmakar S, Kolar AK (2011) Thermodynamic analysis of high-ash coal-fired power plant with carbon dioxide capture. Int J Energy Res 37(6):522–534
5. Sciubba E, Wall G (2007) A brief commented history of exergy from the beginnings to 2004. Int J Thermodyn 10(1):1–26
6. Kumar R (2014) Availability analysis of thermal power plant boiler air circulation system using Markov approach. Decis Sci Lett 3(1):65–72
7. Ameri M, Ahmadi PO, Khanmohammadi SH (2008) Exergy analysis of a 420 MW combined cycle power plant. Int J Energy Res 32(2):175–183
8. Kotas TJ (1985) The exergy method of thermal plant analysis. Butterworths, London

# Cooling of Solar Photovoltaic Cell: Using Novel Technique

**Rajat Satender Rathour, Vishal Chauhan, Kartik Agarwal, Shubham Sharma and Gopal Nandan**

**Abstract** Over the past few decades, the world has started moving towards renewable resources of energy from non-renewable resources for meeting today's energy demand. The solar energy is available abundant in nature and easy to harvest it, and provides a natural solution to move ahead in fulfilling the energy requirement. The solar photovoltaic cells convert solar energy to electrical energy. In general, the regular PV module cell converts nearly about 5–18% of the incidental solar radiation into electricity, and in order to maintain energy balance nearly 60% of incidental radiations are converted in the form of heat energy and with scientific and experimental analysis; it is already pre-determined that with increase in internal PV cell temperature there is an exponential decrease in electrical efficiency of the solar cell gradually with this alternate cooling and superheating process over a time period thermal stresses are formed in solar cell which eventually degrades the cell. A practical way of marginally increasing the output efficiency of solar PV cell is to decrease the operating and surrounding temperature of solar PV, which can be achieved by maintaining a stipulated temperature when solar photovoltaic cell is in operation. Therefore, in the following work, a novel passive technique of cooling has been introduced by basic principles of evaporation using sand dunes concept of cooling and will be investigated experimentally.

**Keywords** Evaporation · Solar photovoltaic module · Passive cooling · Forced cooling · Capillary action · Active cooling · Electrical efficiency · Conversion efficiency

## 1 Introduction

Harnessing solar energy through photovoltaic cells is the future and the most renewable source of energy to be dependent upon which allows one to directly convert the solar radiations into electricity by use of solar photovoltaic cell, i.e. heat

R. S. Rathour (✉) · V. Chauhan · K. Agarwal · S. Sharma · G. Nandan
Amity University Uttar Pradesh, Noida, India
e-mail: Rajatrathour1995@gmail.com

energy into electrical energy. However, while operating the solar photovoltaic cell its output and its efficiency are affected by various factors over the course of operation cycle and certainly it decreases the durable electrical performance of the cell. The major factor to affect the electrical output of the cell significantly is temperature and specially in hot, humid areas and conditions when the solar photovoltaic cell is addressed for the performance and output, the cell inside and on surface temperature crosses 70 °C mark, and as prevailing to such conditions the output of solar photovoltaic cell certainly may decrease by 0.55–0.65%/K and conversion rate of radiations to electricity by 0.08%/K of the solar photovoltaic cell because of operation above the permissible temperature [1–3]. As per the research and development studies till date in field of Thermal & Heat and Mass Transfer Engineering it is acknowledged as a fact that solar photovoltaic cells work on 80–90% efficiency on the rated operation temperature, i.e. 25–28 °C and when the on surface and system temperature increases due to constant solar radiations on a unit area hence reducing the efficiency and conversion rate of solar photovoltaic cell per degree Celsius rise in temperature by 0.5%. And as a matter of fact, approximately more than 80–85% of the incident solar radiations on solar photovoltaic cell are not actually converted to give out the electricity but rather they are absorbed in form of thermal energy or radiated back in atmosphere, henceforth increasing the system temperature [4].

## 2   Peer Research Work

Citing the above problem, various studies and practical research have been carried out in order to cut short the problem stated; for the same to overcome the issue, it is proposed that as similar to heat exchangers a cooling system for solar photovoltaic cell is essential for higher degree of solar radiations and hot system temperature conditions. Majorly, some general techniques like forced air cooling, use of phase-changing materials, using of nanofluids a channel water flow cooling, in order to cool the system and on surface temperature in order to lower the operating and surrounding temperature, to increase efficiency. Generally, on a unit solar cell, channel flow of water cooling method is used for cooling solar photovoltaic cell because as per the research and studies it is cited that water cooling is the most efficient method in the selected case of solar photovoltaic cell.

Krauter in his research studies proposed a method for reducing the incident reflections in order to cool the solar photovoltaic cell by replacing the surface glass with a 1-mm transparent glass over the solar photovoltaic cell surface; as a following result the system temperature of solar photovoltaic cell reduced to 22 °C further resulting to an increase of 10.3% of electrical performance over the day; the major drawback for this study was non-homogenous water film thickness which

was duly necessary in order to actually obtain the optimum thickness of water film which was used to increase the optical performance of the earlier designs and efficiency of solar photo voltaic cell [5].

The detailed study was carried out for hybrid system assembly of solar photovoltaic cell with temperature and for the practical experimentation he used both water channel flow and air to eliminate the extra heat of solar photovoltaic module [6]. In his design he designed a hybrid module with air channel flow duct beneath the solar photovoltaic cell for extraction of majority of heat and another system with a water channel flow assembly through heat exchanger was used in his proposed design the water was segmented and circulated over the solar photovoltaic cell through pipes which were spread across the surface which was made up of copper sheet placed at the rear side of solar photovoltaic module with a thermal contact on it.

Using analytical study, it has been proved the future potential outcomes and benefits of hybrid solar photovoltaic modules as compared to typical photo voltaic cells with justification of energy outcomes with costs analysis of their designed hybrid system; this design can be considered as an alternative to present solar photovoltaic modules practices which are less cost-effective [7]. Intense research and practical studies have been carried out over a course of time for increasing the efficiency of solar photovoltaic cell by using different and variety of methods to lower down the system temperature of cell by extracting majority of excess heat inside the module. Dorobantu and Popescu [8] stated in their design an increase in electrical output by 9.5% by merely cooling the solar photovoltaic module face merely by using a thin film of flowing water over the surface. The major outcome of this design was focused on decreasing the temperature of the module which in turn increased the electrical efficiency of the solar cell as because of minimal rate of reflection losses [8].

Hosseini et al. studied the effectiveness by merely sprinkling the water as coolant over the surface of solar photovoltaic cell rather than directly flowing a laminar vertex flow of coolant over the surface, casually without taking in account the power rating of the pump used for spraying of coolant. This model was able to lower down the overall temperature of the solar photovoltaic cell and in turn increasing the electrical output performance at 18% [9]; further on readjusting the water pump for allowing to flow a channel of water layer over the surface for a due course of time, this model was able to increase the efficiency to 26% in instantaneous peak output of module [9].

Moharram et al. in his study and design were able to calculate and state the maximum permissible temperature of solar photovoltaic is 45 °C, after which just by merely spraying the coolant over the surface would improve the efficiency of solar PV module [10]. In the study, he observed that the designed system assembly for cooling the solar photovoltaic module needs to operate every 5 min after reaching 45 °C on the resistance temperature detector (RTD) to reduce the system temperature by 100 °C [10], casually by just allowing the coolant to flow like a film on the glass surface of the solar photovoltaic cell so as to reduce the reflection which may in

turn increase the potential electrical efficiency of the module. K.A. Moharram et al. framed the idea to decrease the use of electrical energy and water required for cooling to solar panels. Extreme solar radiation and elevated ambient temperatures posed a problem of overheating for photovoltaic panels on operation. This reduced the panel efficiency dramatically. Firstly, to obtain maximum cooling, by natural convection, the construction of the module was modified. It allowed air to flow under the panels. The efficiency of panels under given cases was reported to be:

> Absorbers of the solar collector fully cover panel
>
> Absorber 50% covered by panel
>
> Absorber partially covered by panel, i.e., 30%.

From case A to case C, increase in efficiency observed from 33 to 64% due to increase in glazing area. The usage of water coolant proved better as compared to air. In the modelling, all parameters like solar radiation and ambient temperature were considered. Using it, requirement of cooling can be predicted for its optimal usage. Abdolzadeh and Ameri [12] further worked and improved the operations on module by bringing improvisation in operation of pump over a cycle of period by merely spraying water as coolant of the front surface of solar photovoltaic cell.

The electrical efficiency of panel depends on cooling methods, type and scale/size of the module, geographical location and environmental condition. The overall efficiency of PV cells drops drastically with panel temperature [12]. In active cooling, external fan or pump is used which takes power panel itself. Whereas, the passive cooling does not require power for heat extraction. In active cooling working, fluids are air or water mainly [11]. Researchers tried nanofluid, instead of de-ionized water, which improved the average thermal output by nearly 5% for the PVT system [15]. Five different PCMs having melting point of around 25 °C were incorporated in four individual PV/PCM systems. The temperature drop of panel was 18 °C. For hot and stable climatic conditions, the effectiveness is independent of the type of PCM [12].

Peng et al. prepared an experimental setup using a polycrystalline-Si module using incandescent electric lamps to simulate solar radiation. The average radiation values were maintained from 160 to 400 W/m$^2$. The experimental result showed that as the surface temperature increased the current. The maximum value of current was 0.15 A, after that it becomes constant. The surface temperature at 400 W/m$^2$ radiation flux was 38 °C [13].

Using cotton wick structure with water, the temperature of panel was maintained at 45 °C, while it was 65 °C without cooling arrangement. This resulted increase in efficiency and about 30% decrease in temperature of PV cell. The cotton wick structure with nanofluids decreased the temperature of panel to 59 and 54 °C, which reduces the temperature 11 and 17% of the module compared to module temperature without cooling [14]. Haidar et al. [15] incorporated heat and mass exchange between layers of water and the ambient air, as well as the heat transfer with PV panel. They simulated the temperature distribution of air, water in duct and PV panel bottom surface, under various solar radiation conditions [15].

Under Iraqi weather condition, Hussain et al. [16] designed an active cooling using a small heat exchanger by placing it beneath the PV module. They used water and Zinc-water nanofluids with five concentrations ratios. They presented their comparative analysis. Using nanofluid, the electrical efficiency of PV module is best at 0.3% volume concentration. The variations in solar radiation mainly influence the output current, while the changes in temperature mainly affect the output voltage. Mehrotra et al. [17] conducted experiment by immersion of panel in water. They varied the depth of water on the panel and obtained an optimum depth for maximum increased efficiency. The experiment was carried out in Bhopal and observed the maximum efficiency of 4.26% when water depth was 1 cm with the proposed design and operating conditions. To avoid overheating of panel, Hashim et al. [18] used heat exchanger with water as circulating fluids in the pipes just behind the panel. The best result was at the optimum mass flow rate 0.2 litre per second. Zhu et al. used dish concentrator with two axes tracking to evaluate performance using de-ionized water for immersion cooling [19]. Amonix back point contact silicon cells were used to design and build a liquid immersion-based receiver. In CPV system, solar cells subject to greater illuminations will experience increase in temperature with the attendant cell efficiency drops. The water flow rate is studied in consideration to the effect of temperature rise. It was recorded that the rate of temperature rise diminished with the mass flow rate of water. But constant flow rate, the rate of temperature rise was high with an increase in irradiance [20]. Several researchers have reported the heat transfer enhancement using nanofluids area of solar photovoltaic and power production [21–26].

## 3 Pragmatic Solution

So far, various studies done on the cooling of PV cell to increase the power output and to increase the overall efficiency of the module, one of the proposed which we will be using for cooling the PV cell or to decrease the temperature of the PV module will be by mode of evaporation.

A thermal conductive material will be used at the base of PV module which will extract the heat from the module with the combination of water, and water will act as the coolant for the conductive material which will extract the heat from the solar photovoltaic module. The water will be evaporated by the process of evaporation naturally which will help to decrease the temperature further when the material at the base of module start getting heated. The process will be similar to the earthen pots which use the evaporation of water droplets from the surface of pots and cools the water kept inside it. A designed box made of earthen mud with a line system assembly of air channels and drip irrigation lines have been affixed on the side lines of box as veins to allow coolant transfer across the walls and through natural evaporation technique and passage of air through air columns and channels should

**Fig. 1** Pallet fan assembly
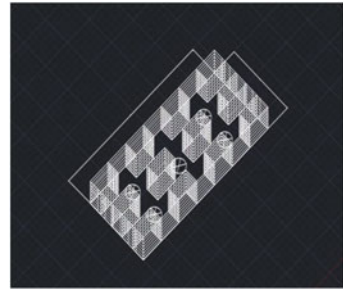


lower down the temperature of the system assembly as the heat will be absorbed from the rear of solar photovoltaic module and transferred to thermal conductive material welded with the solar PV module and then the thermal conductive material will be exposed to the inside of designed box laterally affixed with rear of solar photovoltaic module and with natural process we expect that by no means of passive techniques the temperature of system assembly should lower down to a vast extant and in turn increasing the electrical efficiency of the solar photovoltaic cell (Fig. 1, 2, 3 and 4).

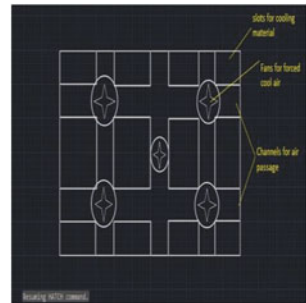**Fig. 2** Air channels with fans base
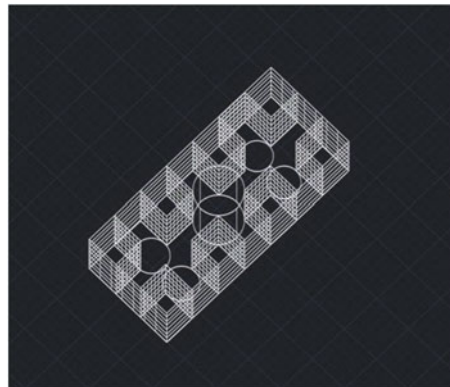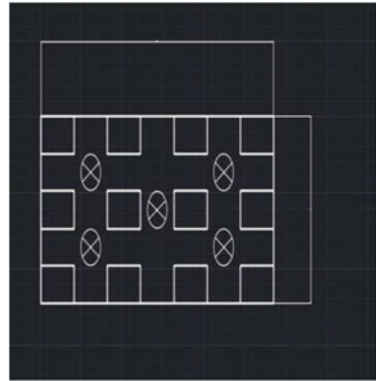


**Fig. 3** Natural draft flow

**Fig. 4** Schematic channels



## 4 Conclusion

A review study has presented the practical implication with electrical output and thermal efficiency of a solar photovoltaic cell with various cooling techniques used and their outcomes on efficiency. A proposed solution has been explained in this paper to tackle the variations in efficiency without much cost and is successfully designed by using an ordinary mixture of clay bricks and normal water used as a coolant on the back side of solar panel allowing the air to pass through the well-designed air channels in order to increase the efficiency of solar photovoltaic cell and also as with the studies over various techniques which were used for cooling solar photovoltaic cell; it is observed that:

- The net efficiency output of solar photovoltaic cell is very sensitive in relation to temperature which exponentially decreases with rise in system temperature of solar photovoltaic cell.
- Usually flowing a thin film of water over the glass of solar photovoltaic cell generally reduces the rate of reflection of solar radiations and also cools the solar panel to a considerable temperature.
- By means of water cooling techniques, a solar photovoltaic panel can be established to a desired temperature.
- Tertially the water which will be drained out after flowing through channel flow assembly can be used as a utility to heat.
- In the thermal photovoltaic cell with tested practical work, it has been observed that by applying a film of water for cooling photovoltaic cell resulted in decreasing the system temperature of solar photovoltaic cell which will initially reduce the reflection rate with cooling down of solar panel and gradually increasing the electrical efficiency of solar panel.
- Also in a case, it was seen that evaporation can constantly cool the solar panel temperature with clay pot effects being triggered constantly, through which it was stated that the temperature inside pot is always 5–8 °C lower than ambient air.

- By cooling solar photovoltaic cell, the total energy output of system increases gradually while the electrical efficiency increases slowly.
- In this literature review, a study has been shown about various types of cooling techniques which are practically researched, and a method is proposed in order to systematically control the variations in efficiency of solar photovoltaic cell.

# References

1. Luque A (2003) Handbook of photovoltaic science and engineering. Wiley
2. Dupeyrat P, Ménézo C, Wirth H, Rommel M (2011) Improvement of PV module optical properties for PV-thermal hybrid collector application. Sol Energy Mater Sol Cells 95 (8):2028–2036. https://doi.org/10.1016/j.solmat.2011.04.036
3. Brinkworth B, Cross B, Marshall R, Yang H (1997) Thermal regulation of photovoltaic cladding. Sol Energy 61(3):169–178. https://doi.org/10.1016/s0038-092x(97)00044-3
4. Chow T (2010) A review on photovoltaic/thermal hybrid solar technology. Appl Energy 87 (2):365–379. https://doi.org/10.1016/j.apenergy.2009.06.037
5. Krauter S (2004) Increased electrical yield via water flow over the front of photovoltaic panels. Sol Energy Mater Sol Cells 82(1–2):131–137. https://doi.org/10.1016/j.solmat.2004.01.011
6. Tripanagnostopoulos Y, Nousia T, Souliotis M, Yianoulis P (2002) Hybrid photovoltaic/thermal solar systems. Sol Energy 72(3):217–234. https://doi.org/10.1016/s0038-092x(01)00096-2
7. Kalogirou S, Tripanagnostopoulos Y (2007) Industrial application of PV/t solar energy systems. Appl Therm Eng 27(8–9):1259–1270. https://doi.org/10.1016/j.applthermaleng.2006.11.003
8. Dorobantu L, Popescu NO (2013) Increasing the efficiency of photovoltaic panels through cooling water film. U.P.B. Sci Bull. Series C 15(4):223–230
9. Hosseini R, Hoesseini N, Khorasanizadeh H (2011) An experimental study of combining a photovoltaic system with a heating system. World Renew Energy Congress 8:2993–3000
10. Moharram K, Abd-Elhady M, Kandil H, El-Sherif H (2013) Enhancing the performance of photovoltaic panels by water cooling. Ain Shams Eng J 4(4):869–877. https://doi.org/10.1016/j.asej.2013.03.005
11. Abdolzadeh M, Ameri M (2009) Improving the effectiveness of a photovoltaic water pumping system by spraying water over the front of photovoltaic cells. Renew Energy 34(1):91–96. https://doi.org/10.1016/j.renene.2008.03.024
12. Sardarabadi M, Passandideh-Fard M, Maghrebi MJ, Ghazikhani M (2017) Experimental study of using both ZnO/ water nanofluid and phase change material (PCM) in photovoltaic thermal systems. Sol Energy Mater Sol Cells 161:62–69. https://doi.org/10.1016/j.solmat.2016.11.032
13. Peng Z, Herfatmanesh MR, Liu Y (2017) Cooled solar PV panels for output energy efficiency optimisation. Energy Convers Manag 150:949–955. https://doi.org/10.1016/j.enconman.2017.07.007
14. Chandrasekar M, Suresh S, Senthilkumar T, karthikeyan MG (2013) Passive cooling of standalone flat PV module with cotton wick structures. Energy Convers Manage 71:43–50. https://doi.org/10.1016/j.enconman.2013.03.012
15. Haidar ZA, Orfi J, Oztop HF, Kaneesamkandi Z (2016) Cooling of solar PV panels using evaporative cooling. J Therm Eng 2(5):928–933

16. Hussein HA, Numan AH, Abdulrahman RA (2017) Improving the hybrid photovoltaic/thermal system performance using water-cooling technique and Zn-$H_2O$ nanofluid. Int J Photoenergy 2017:1–14. https://doi.org/10.1155/2017/6919054
17. Mehrotra Saurabh, Rawat Pratish, Debbarma Mary, Sudhakar K (2014) Performance of a solar panel with water immersion cooling technique. Int J Sci Environ Technol 3(3):1161–1172
18. Hussein A, Numan AH, Abdulmunem AR (2015) Improving of the photovoltaic/thermal system performance using water cooling technique. In: IOP conference on series materials science and engineering
19. Zhu L, Boehm RF, Wang Y, Halford C, Sun Y (2011) Water immersion cooling of PV cells in a high concentration system. Sol Energy Mater Sol Cells 95(2):538–545. https://doi.org/10.1016/j.solmat.2010.08.037
20. Bahaidarah H, Subhan A, Gandhidasan P, Rehman S (2013) Performance evaluation of a PV (photovoltaic) module by back surface water cooling for hot climatic conditions. Energy 59:445–453. https://doi.org/10.1016/j.energy.2013.07.050
21. Sekhar TVR, Prakash R, Nandan G, Muthuraman M (2017) Preparation of $CO_3O_4$-$H_2O$ nanofluid and application to Cr-60 concentrating solar collector. Progress Industrial Ecol Int J 11(3):227. https://doi.org/10.1504/pie.2017.091296
22. Sekhar TVR, Nandan G, Prakash R, Muthuraman M (2018) Investigations on viscosity and thermal conductivity of cobalt oxide-water nano fluid. Mater Today: Proc 5(2):6176–6182. https://doi.org/10.1016/j.matpr.2017.12.224
23. Sekhar TVR, Nandan G, Prakash R, Muthuraman M (2018) Modeling a renewable energy collector and prediction in different flow regimes using CFD. Mater Today Proc 5(2):4563–4574. https://doi.org/10.1016/j.matpr.2017.12.026
24. Sekhar TVR, Prakash R, Nandan G, Muthuraman M (2018) Pressure drop characteristics & efficiency enhancement by using $Tio_2$-$H_2O$ nanofluid in a sustainable solar thermal energy collector. Int J Environ Sustain Dev 17(2/3):273–294. https://doi.org/10.1504/IJESD.2018.094039
25. Sekhar TVR, Prakash R, Nandan G, Muthuraman M (2018) Performance enhancement of a renewable thermal energy collector using metallic oxide nanofluids. Micro Nano Lett 13(2):248–251. https://doi.org/10.1049/mnl.2017.0410
26. Vadhera J, Sura A, Nandan G, Dwivedi G (2018) Study of phase change materials and its domestic application. Mater Today: Proc 5(2):3411–3417. https://doi.org/10.1016/j.matpr.2017.11.586

# Experimental and Numerical Study of Heat Transfer in Double-Pipe Heat Exchanger Using $Al_2O_3$, and $TiO_2$ Water Nanofluid

**Abhishek Mund**[iD]**, Bikash Pattanayak**[iD]**, J. S. Jayakumar**[iD]**,
Kajal Parashar**[iD] **and S. K. S. Parashar**[iD]

**Abstract** Nanofluid is a two-phase fluid of solid-liquid mixture. Nanofluid provides higher effective thermal conductivity when compared with the base fluid. Thermal properties of heat transfer fluid are one of the important topics of concern for research in heat transfer analysis. In recent years, there are stances about the study of agglomeration of two or more nanoparticles in base fluid, i.e., hybrid or composite nanofluid, and they also have good heat transfer characteristics. In this experiment, $Al_2O_3$ and $TiO_2$ and hybridized $Al_2O_3$, $TiO_2$ nanoparticles were prepared by using high-energy ball milling technique. These nanoparticles were characterized by using XRD, SEM, and TEM. It was found that crystalline size is 30 nm. Polyvinyl alcohol of 3% was used in 1:10 ratio of the mass of the nanoparticle for preparing stable nanofluid. The stability was observed for 32 h which was good to conduct an experiment. The densities, viscosity, thermal conductivity, and the specific heat of the nanofluid were calculated. The overall heat transfer coefficient, logarithmic mean temperature difference, friction factor, and effectiveness of the hybrid double-pipe heat exchanger using the nanofluid were calculated by NTU method. The data obtained using ANSYS (FLUENT) 18.2 were compared with the experimental result. An optimized volume concentration of the nanofluid was found out to be used as an effective cooling fluid in the hybrid heat exchanger.

**Keywords** XRD · ANSYS · NTU · Nanofluid

A. Mund · B. Pattanayak · J. S. Jayakumar (✉)
Department of Mechanical Engineering, Amrita Vishwa Vidyapeetham,
Amritapuri, India
e-mail: jsjayan@gmail.com

K. Parashar · S. K. S. Parashar
Nano Sensor Lab, School of Applied Science, Kalinga Institute of Industrial Technology
(KIIT) Deemed to be University, Bhubaneswar 751024, Odisha, India

## Nomenclature

$A$    Surface area (m$^2$)
$C_p$    Specific heat (J/kg K)
$k$    Thermal conductivity (W/mK)
$m$    Mass flow rate (kg/s)
$T$    Temperature (°C)
$U$    Overall heat transfer coefficient (W/m$^2$ K)

## Greek Symbols

$\rho$    Density (kg/m$^3$)
$\mu$    Dynamic viscosity (kg/ms)
$\epsilon$    Effectiveness
$\varphi$    Volume concentration

## Subscripts

$c$    Cold fluid
$ci$    Cold fluid inlet
$co$    Cold fluid outlet
$h$    Hot fluid
$hi$    Hot fluid inlet
$ho$    Hot fluid outlet
$i$    Inner
$nf$    Nanofluid
$p$    Nanoparticle
$1$    Al$_2$O$_3$ nanopowder
$2$    TiO$_2$ nanopowder
$w$    Water

# 1 Introduction

Nanofluid is a two-phase fluid, basically a colloidal suspension of nanoparticles in base fluids like oil and water. Hybrid nanofluids are engineered fluids of two different nanoparticles dispersed into base fluid. A hybrid material combines the properties (physical and chemical) and exhibits them homogeneously [1]. The thermo-physical properties of hybrid nanofluid are comparatively higher than single-particle nanofluid and base fluid [2]. An instrument devised to make the exchange of heat between two fluids at different temperature without mixing them is known as a heat exchanger. In this experiment, a counterflow double-pipe heat

exchanger was used. It is found that the processes of double-pipe heat exchangers are being widely in use for industrial as well as commercial purposes [3]. From the analysis of various research papers, it has been inferred that a material does not inherit all the properties needed for a specific purpose. Hybrid nanofluids have a wide application in the field of electro-mechanical, HVAC, automotive cooling, etc. So in this experiment, hybrid nanofluid has been used in hybrid double-pipe heat exchanger, and it has been compared with a single material nanofluid, and the usage of these fluids to enhance the effectiveness of the heat exchanger has been analyzed. Chopkar et al. analyzed that the thermal conductivity was enhanced by using $Al_2O_3$-Cu/water hybrid nanofluid in electronics cooling through a heat sink by comparing the results obtained with base fluid and single-particle nanofluid [4]. An experiment was conducted using a tubular heat exchanger for $Cu/TiO_2$ hybrid water-based nanofluid, and it was observed that the overall heat transfer has increased to 30.4% at a volume concentration of 0.7% [5]. Suresh et al. conducted an experiment for $Al_2O_3$–Cu/water hybrid nanofluid in a tube and suggests that at Reynolds number of 1730, Nusselt number enhanced by 13.56% [6]. Madhesh et al. conducted an experiment in a tube-type counter flow heat exchanger using $Cu$–$TiO_2$ deionized double-distilled water hybrid nanofluid and observed that thermal conductivity enhanced as compared to base fluid [7]. Basically, nanofluids exhibit higher thermal conductivity and enhance the heat exchanger's effectiveness. The reason behind such enhancement may be the increase in surface area and heat capacity of the fluid by suspending particles [8]. In this experiment, the thermo-physical properties of the nanofluids and their role in enhancing the effectiveness of the heat exchanger have been discussed.

## 2 Experimental Analysis

### 2.1 Synthesis of Nanoparticles

The nanometer-sized powder of titanium dioxide and aluminum oxide was prepared by HEBM technique at 300 rpm with the ball to powder ratio 10:1. The powders of 25 microns and 99.8% purity were mechanically milled in tungsten carbide jars with tungsten carbide balls for 15 h, with 60 min milling time and 30 min gap to avoid overheating. The density, specific heat, and thermal conductivity values of the $TiO_2$ and $Al_2O_3$ powders are 4010 kg/m$^3$, 690 J/kg K, 8.3 W/mK and 3880 kg/m$^3$, 703 J/kg K, 25.6 W/mK, respectively. The $TiO_2$ and $Al_2O_3$ nanopowders are shown in Fig. 1a, b. It was clearly observed from Fig. 1a, b that the color of the $Al_2O_3$ nanoparticle is white and that of the $TiO_2$ nanoparticle is gray.
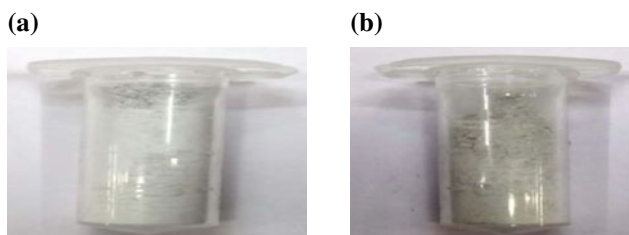
Fig. 1 **a** Al$_2$O$_3$ and **b** TiO$_2$ nanopowders

## 2.2 Characterizations of Nanoparticles

The X-ray diffraction (XRD) patterns were obtained using PANalytical X'Pert PRO machine for TiO$_2$ and Al$_2$O$_3$ nanoparticles analyzed for this work and were plotted in Fig. 2a, b. The peaks were indexed as (012), (104), (110), (006), (113), (024), (116), (018), (214), (300) for TiO$_2$ and (012), (104), (110), (006), (113), (024), (116), (018), (214), (300), for Al$_2$O$_3$. In case of Al$_2$O$_3$, the powder was of rhombohedral crystal system with a lattice constant (A$^0$) $a = 4.751$, $b = 4.751$, $c = 12.97$. These data match well with JCPDS card (Joint committee on Powder Diffraction Standard) reference code 00-003-1033 for TiO$_2$ and 00-003-1033 for Al$_2$O$_3$. The strong intensity and sharp narrow width peaks indicate that the nanopowders were of high crystalline. SEM images were taken using JEOL JSM-6510 machine at $\times$10,000 resolution and 1 $\mu$m reference size. The particles are uniform and spherical in nature shown in Fig. 3a, b. However, TiO$_2$ nanoparticles are smaller than the Al$_2$O$_3$ nanoparticles. The confirmation of nanoparticles was done by FEI, Tecnai TEM. It was found that the synthesized 15-h dry ball-milled powder of TiO$_2$ and Al$_2$O$_3$ was at 30–40 nm shown in Fig. 4a, b. The particles are uniform and spherical in nature.
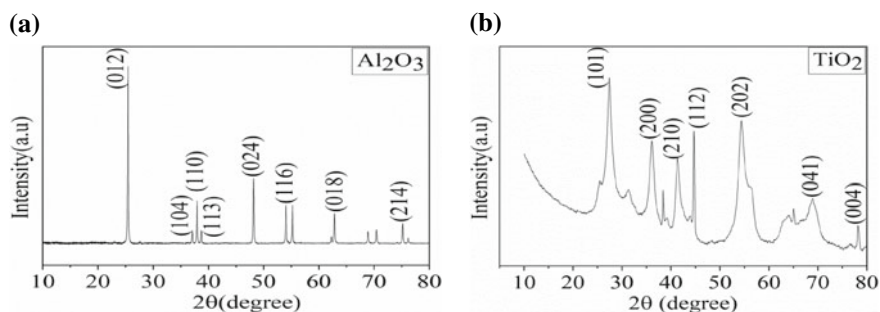


Fig. 2 XRD patterns of **a** Al$_2$O$_3$ and **b** TiO$_2$ nanoparticles

**(a)** **(b)**
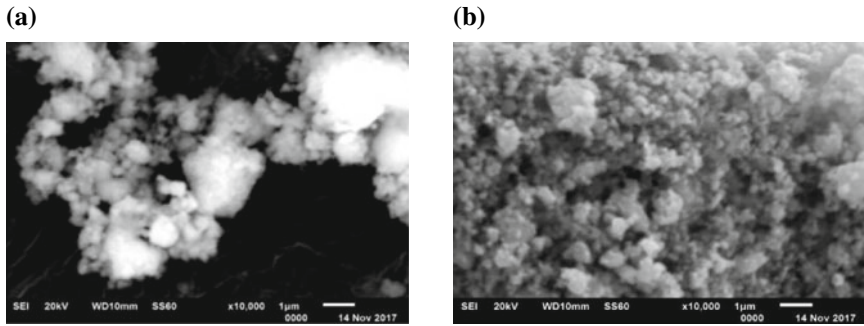


**Fig. 3** SEM micrographs of **a** $Al_2O_3$ and **b** $TiO_2$ nanoparticles

**(a)** **(b)**
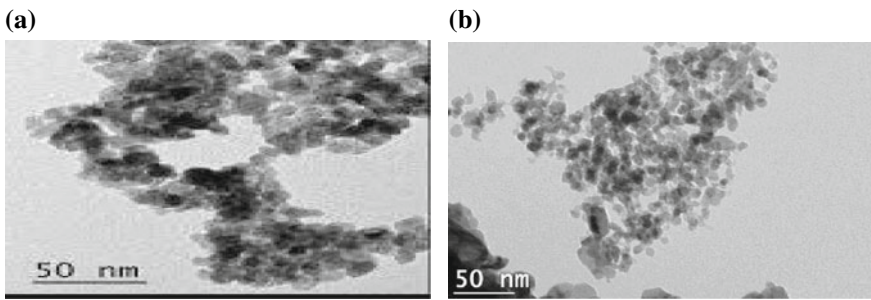


**Fig. 4** TEM images of **a** $Al_2O_3$ and **b** $TiO_2$ nanoparticles

## 2.3 Preparation of Nanofluids

The nanofluids were prepared by using two-step method [9]. The methodologies followed to prepare the nanofluids were same. Different concentrations of nano-fluids were prepared by mixing a quantified volume concentration of nanopowder (0.025, 0.05, 0.075, and 0.1%) in water. The nanopowder-added fluid was then magnetically stirred at 1000 rpm speed for 6 h and then was ultrasonically agitated for 2 h. The stability of the nanofluid was maintained up to 12–18 h by adding 3% PVA in one-tenth ratio to the mass of the nanoparticle. In the experimental practice, some nanofluid without surfactant was taken in a petri dish, and after sometimes, cluster formation occurs, and it settles down. The petri dish was then heated, and the residue was measured. The same methodology was applied with the PVA-added nanofluid, and it was observed that after 12 h, cluster formation started, and after 18 h, it stopped. The residue was heated and measured. The mass was compara-tively low, so it has been concluded that the fluid is stable.

## 2.4  Experimental Setup and Procedures

In this experiment, a hybrid double-pipe heat exchanger was used where the inner tube is of copper and the outer pipe is of unplasticized polyvinyl chloride (UPVC). The $TiO_2$ water nanofluid and $Al_2O_3$ water nanofluid were made to flow into the annulus section with the mass flow rate of 21.95 L/H; hot water is made to flow into the copper pipe with the mass flow rate of 31.57 L/H. The LMTD, U, and effectiveness of all the nanofluids at different volume concentrations keeping same inlet temperature were calculated. Basically, double-pipe heat exchanger consists of two metallic concentric tubes and some insulating materials externally applied on the outer pipe to restrict the heat flow. In this experiment, hybrid heat exchanger consists of a concentric tube of metal and plastic, no insulating material being used because plastic tube itself behaves as an insulator to heat flow shown in Fig. 5. The thermo-physical properties obtained were given as input in the ANSYS 18.2. The k-epsilon and SIMPLE method were followed during the simulation. In this experiment, the models used to measure thermo-physical properties have certain limitations such as they can be used for spherically shaped nanoparticle and the volume concentration is limited to 4%. The temperature of the hot water and nanofluids at the inlet and outlet was measured by using digital temperature display TPM-10 with reference accuracy $\pm 0.1$ °C.
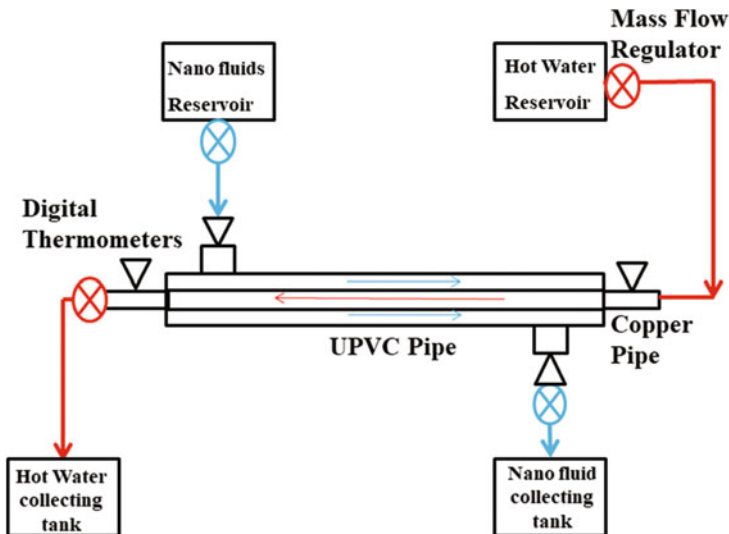


**Fig. 5**  Schematic diagram of double-pipe heat exchanger

# 3 Results and Discussions

## 3.1 Calculation of Various Thermo-physical Properties

The density, thermal conductivity, viscosity, and specific heat of the nanofluids were calculated using various models. It was observed that volume concentration increases, the density, viscosity, thermal conductivity increases, but specific heat decreases. In nanofluids, thermal conductivity can be enhanced by the collision between the solid particles. By increasing the volume concentration, the number of collision between the solid particles increases, and the internal energy of the particle increases resulting in the increase in effective thermal conductivity of the nanofluid [10]. Nanofluids are dual-phase dispersion system having high surface energies; therefore, they are thermodynamically unstable. Due to the strong Brownian motions, agglomeration of nanoparticles increases and dispersion of nanoparticles in the fluids may deteriorate with time because of van der Waals forces [11]. For this reason, with an increase in volume concentration, the viscosity increases. Equations 1, 2, 3, and 4 represent Pak and Choi model, Wasp model, LS Sundar model, and homogeneous mixture specific heat formula used to determine density, thermal conductivity, viscosity, and specific heat, respectively. The data obtained were tabulated in Table 1.

$$\rho_{nf} = \varphi_1 \rho_1 + \varphi_2 \rho_2 + (1 - \varphi_1 - \varphi_2)\rho_w \tag{1}$$

$$k_{nf} = k_w \frac{k_p + 2k_w - 2\varphi(k_w - k_p)}{k_p + 2k_w + \varphi(k_w - k_p)} \tag{2}$$

Table 1 Thermo-physical properties of the nanofluids

| Nanofluid | Volume concentration | Density | Viscosity | Thermal conductivity | Specific heat |
|---|---|---|---|---|---|
| $Al_2O_3$-water | 0.025 | 1074.6 | 0.00088 | 0.673 | 3862.6 |
| | 0.05 | 1149.2 | 0.00093 | 0.721 | 3583.7 |
| | 0.075 | 1223.8 | 0.00096 | 0.771 | 3335.8 |
| | 0.1 | 1298.5 | 0.00099 | 0.823 | 3117.7 |
| $TiO_2$-water | 0.025 | 1075.2 | 0.00088 | 1.041 | 3860.9 |
| | 0.05 | 1150.5 | 0.00093 | 1.094 | 3577.5 |
| | 0.075 | 1225.7 | 0.00098 | 1.145 | 3328.9 |
| | 0.1 | 1301.0 | 0.00107 | 1.196 | 3109.1 |
| $TiO_2$-water $Al_2O_3$-doped | 0.025 | 1147.2 | 0.00191 | 0.671 | 3587.6 |
| | 0.05 | 1294.5 | 0.00356 | 0.717 | 3124.6 |
| | 0.075 | 1441.7 | 0.00575 | 0.765 | 2756.2 |
| | 0.1 | 1589.0 | 0.00850 | 0.816 | 2456.1 |

$$\mu_{\text{nf}} = \mu_{\text{w}}\left(1 + 39.11\varphi + 533.9\varphi^2\right) \tag{3}$$

$$C_{\text{p nf}} = \frac{(\varphi_1 \rho C_{\text{p}})_1 + (\varphi_2 \rho C_{\text{p}})_2 + \left((1 - \varphi_1 - \varphi_2)\rho C_{\text{p}}\right)_{\text{w}}}{\rho_{\text{nf}}} \tag{4}$$

## 3.2 Determination of the Effectiveness of the Counter Flow Heat Exchanger Using NTU Method

The effectiveness of the hybrid double-pipe heat exchanger is calculated using the number of transfer units (NTU) method. Calculation for effectiveness using ANSYS is tabulated in Table 2, and calculation for effectiveness by the experimental method is tabulated in Table 3. LMTD (°C) is logarithmic mean of temperature difference of the fluids flowing in heat exchangers. The temperature difference is the driving force for heat transfer. For the counter flow heat exchanger, LMTD is given by:

$$\text{LMTD} = \frac{(T_{\text{hi}} - T_{\text{co}}) - (T_{\text{ho}} - T_{\text{co}})}{\ln(T_{\text{hi}} - T_{\text{co}})/(T_{\text{ho}} - T_{\text{co}})} \tag{5}$$

The heat lost by the hot fluid, heat gained by the cold fluid (nanofluids), and the net transfer were estimated using the following expressions, respectively

$$Q_{\text{h}} = m_{\text{h}} C p_{\text{h}}(T_{\text{hi}} - T_{\text{ho}}) \tag{6}$$

$$Q_{\text{c}} = m_{\text{c}} C p_{\text{c}}(T_{\text{co}} - T_{\text{ci}}) \tag{7}$$

$$Q = 0.5(Q_{\text{h}} + Q_{\text{c}}) \tag{8}$$

The overall heat transfer coefficient and NTU is given by:

$$U = \frac{Q}{A_{\text{i}} \times \text{LMTD}} \tag{9}$$

$$A_{\text{i}} = \pi d_{\text{i}} L$$

**Table 2** Calculation of effectiveness using ANSYS

| Nanofluids | $T_{\text{hi}}$ | $T_{\text{ci}}$ | $T_{\text{ho}}$ | $T_{\text{co}}$ | LMTD | NTU | C | $\epsilon$ |
|---|---|---|---|---|---|---|---|---|
| $Al_2O_3$ (0.1) | 60 | 26 | 48.03 | 28.94 | 26.28 | 0.5217 | 0.5170 | 0.3723 |
| $TiO_2$ (0.1) | 60 | 26 | 47.49 | 27.24 | 26.73 | 0.4674 | 0.5156 | 0.3440 |
| $Al_2O_3$-doped $TiO_2$ (0.1) | 60 | 26 | 52.96 | 39.26 | 23.71 | 0.6108 | 0.4073 | 0.4239 |

**Table 3** Calculation of effectiveness by the experimental method

| Nanofluids | $T_{hi}$ | $T_{ci}$ | $T_{ho}$ | $T_{co}$ | LMTD | NTU | C | $\epsilon$ |
|---|---|---|---|---|---|---|---|---|
| Al$_2$O$_3$ (0.1) | 60 | 26 | 42.3 | 34.7 | 20.47 | 1.048 | 0.5170 | 0.5770 |
| TiO$_2$ (0.1) | 60 | 26 | 38.4 | 31.9 | 19.19 | 1.245 | 0.5156 | 0.6308 |
| Al$_2$O$_3$-doped TiO$_2$ (0.1) | 60 | 26 | 35.5 | 33.1 | 16.71 | 1.344 | 0.4073 | 0.6726 |

$$\text{NTU} = \frac{(U * A)}{(mC_p)_{\text{small}}} \tag{10}$$

$$\epsilon = \frac{1 - \exp^{-(1-c)\text{NTU}}}{1 - c\exp^{-(1-c)\text{NTU}}} \tag{11}$$

## 3.3 Contours Obtained Using ANSYS 18.2

From the experiment, the obtained input temperatures and thermo-physical properties were given as the input value to obtain the following contours using ANSYS 18.2 workbench. A turbulence effect came into the picture near the nanofluid inlet when vector velocity graph was obtained (Fig. 6).
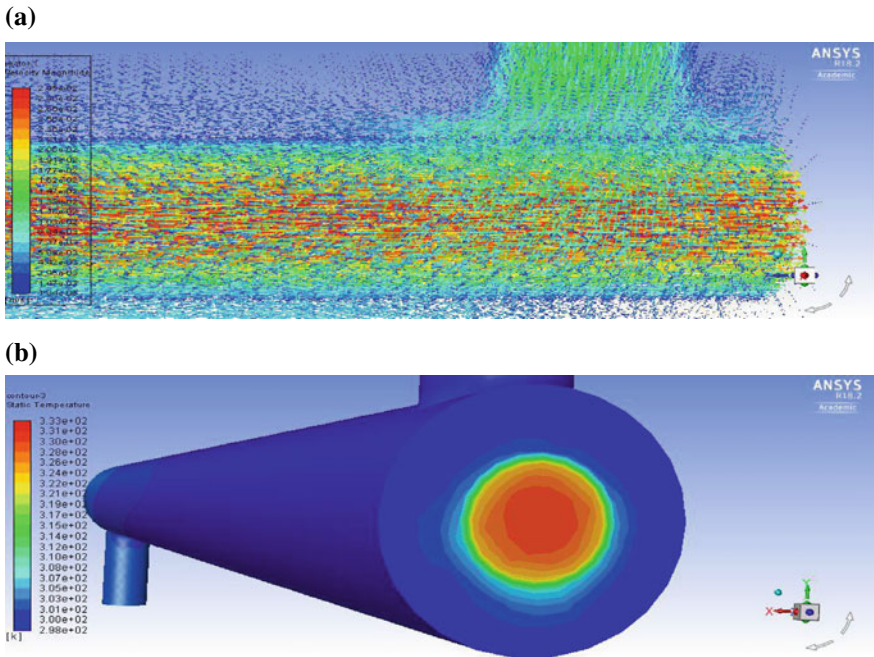
**(a)**



**(b)**



**Fig. 6 a** Velocity vector, **b** static temperature of Al$_2$O$_3$-doped TiO$_2$ nanofluid

# 4    Conclusions

It was inferred from the experiment that for both experimental and numerical analysis, aluminum oxide-doped titanium dioxide nanofluid provides higher effectiveness. So it can be used as a cooling fluid for heat transfer application. It was observed that at the inlet of the nanofluid, vortex formation takes place, and it can be considered as a factor for heat transfer enhancement.

# References

1. Sarkar J, Ghosh P, Adil A (2015) A review on hybrid nanofluids: recent research, development, and applications. Renew Sustain Energy Rev 43:164–177
2. Taylor P, Das SK, Choi SUS, Patel HE (2007) Heat transfer in nanofluids—a review. Heat Transf Nanofluids 37–41
3. Omidi M, Farhadi M, Jafari M (2017) A comprehensive review of double pipe heat exchangers. Appl Therm Eng 110:1075–1090
4. Chopkar M, Kumar S, Bhandari DR, et al (2007) Development and characterization of $Al_2Cu$ and $Ag_2Al$ nanoparticle dispersed water and ethylene glycol based nanofluid 139:141–148
5. Dhinesh Kumar D, Valan Arasu A (2017) A comprehensive review of preparation, characterization, properties, and stability of hybrid nanofluids. Renew Sustain Energy Rev 1–21
6. Suresh S, Venkitaraj KP, Selvakumar P, Chandrasekar M (2012) Effect of $Al_2O_3$–Cu/water hybrid nanofluid in heat transfer 38:54–60
7. Madhesh D, Parameshwaran R, Kalaiselvam S (2014) Experimental investigation on convective heat transfer and rheological characteristics of Cu–$TiO_2$ hybrid nanofluids 52:104–115
8. Lee SW, Park SD, Bang IC (2012) Critical heat flux for CuO nanofluid fabricated by pulsed laser ablation differentiating deposition characteristics. Int J Heat Mass Transfer 55:6908–6915
9. Haddad Z, Abid C, Oztop HF, Mataoui A (2014) A review on how the researchers prepare their nanofluids. Int J Therm Sci 76:168–189
10. Tawfik MM (2017) Experimental studies of nanofluid thermal conductivity enhancement and applications: a review. Renew Sustain Energy Rev 75:1239–1253
11. Philip J (2012) Shima PD thermal properties of nanofluids. Adv Colloid Interface Sci 183–184:30–45

# Improving Thermal Efficiency by Varying Input Parameters of a Four Stroke Single Cylinder S.I Engine

**Rahul Ajitkumar, Sumit Sharma and Vipin Kaushik**

**Abstract** The use of automobiles is growing day by day and so does the need to improve efficiency in all stages. Thermal efficiency is a factor that is measured by work done by the heat supplied to it. For improving the efficiency of an S.I engine, the inlet air conditions were altered to support various parameters. Kirloskar TV1 variable compression engine was used to run the tests. Using a variable compression engine helps us to alter the compression ratio without stopping the engine by using the tilted cylinder arrangement. The engine can be run easily at variable load as well as rpm. The orifice was modified to equip the alterations and to run the tests. Atmospheric air contains moisture, and since this air gets inside the engine, initial test was based on to reduce this moisture content and alter the temperature of the air. Various conditions were taken into consideration on how to vary the inlet air parameters. Various modes were sequenced to test out the efficiency. Test 1 involved humidifying the inlet air. Test 2 involved cooling the inlet air. Test 3 involved dehumidifying the inlet air. Test 4 involved altering oxygen content in an inlet air, and test 5 involved a combination of cooling the inlet air and dehumidifying it. The engine was run at constant load and at variable rpm, and test 5 gave optimum results.

**Keywords** Thermal efficiency · Dehumidification · Variable compression engine

## 1 Introduction

Manufacturers have been going on researching various methods on how to increase efficiency. Spark ignition engine lowers fuel change efficiency contrasted with compressed control units, yet a few upgrades can be gotten by utilizing diverse control systems. Here, altering the inlet air was the main criteria of testing. The reason behind is that since the engine breathes, the air quality alters the actual

R. Ajitkumar (✉) · S. Sharma · V. Kaushik
Amity School of Engineering and Technology, Amity University, Noida Uttar Pradesh, India
e-mail: rahul.ajitkumar89@gmail.com

engine efficiency [1]. When the moisture quantity of the air increases, it gets densified inside the engine and water particles get mixed with fuel leading to a change in proportion of the fuel. This leads to higher carbon content and thus reduces efficiency.

The temperature of air is also another criterion which alters the engine efficiency. When the density becomes very low, availability of oxygen reduces which results in lesser thermal efficiency. There are odds of pre-start and thumping if temperature of the inlet air is higher than ordinary. As the temperature of the air will be higher, the temperature of air–fuel charge will likewise be higher (petrol engine) which implies there are odds of start of air–fuel blend even before the cylinder achieves its exact point during typical burning. It is distinguishable that the air inlet mass stream rate shrivels when the engine power diminishes. At higher temperature, charge thickness can endure and ignition temperatures can turn out to be too high. This can constrain motor yield. In the event that temperatures are too low, beginning the motor at low temperatures can be tricky. Lower admission air temperatures tend to cause poor carburetion, in some cases notwithstanding prompting carburetor icing, particularly under full load activity. Moreover, the admission of extremely chill crude air will likewise defer the warm-up of the engine amid cool begin, along these lines drawing out activity in an inadequately greased upstate. In conclusion, a speedy warm-up is vital on the grounds that the emanation of fumes toxins is significantly higher when the motor runs chilly. In any case, the expansion of charge air temperature in another way could conceivably enhance the fuel vaporization in engine. Difference of ignition and motor execution will be introduced efficiently with changes in channel air temperature. In this research, tests were done to explore the impacts of inlet air temperature and coolant temperature on brake thermal efficiency in a four-stroke S.I engine. Test comes about demonstrated that, inlet air temperature lightly affects brake thermal efficiency during partial load activity. During high load, a diminishing in admission air temperature enhanced brake warm proficiency because of a change in showed warm effectiveness and reduction in debilitating misfortune. It was additionally uncovered that the blend of high-temperature cooling water for the motor square and low-temperature cooling water for the chamber warm is powerful to improve brake thermal efficiency.

## 2   Methodology

The setup comprises of single cylinder, four strokes, variable compression ratio (VCR) petroleum motor associated with eddy current compose dynamometer for stacking. The pressure proportion can be changed without ceasing the motor and without adjusting the ignition chamber geometry by exceptionally composed tilting cylinder square course of action. Setup is furnished with fundamental instruments for burning weight and wrench edge estimations. These signs are interfaced to PC through motor marker for PV graphs. Arrangement is additionally made for interfacing wind current, fuel stream, temperatures, and load estimation. The setup

has remained solitary board box comprising of air box, two fuel tanks for dual fuel test, manometer, fuel estimating unit, transmitters for air and fuel stream estimations, process marker, and motor pointer. Rotameters are accommodated cooling water and calorimeter water stream estimation. The setup empowers investigation of VCR motor execution for brake control, showed control, frictional power, BMEP, IMEP, brake warm productivity, demonstrated warm proficiency, mechanical effectiveness, volumetric proficiency, particular fuel utilization, A/F proportion, and warmth adjust. LabVIEW-based Engine Performance Analysis programming bundle "Motor delicate LV" is accommodated online execution assessment. An electronic diesel infusion weight estimation is alternatively given.

## 2.1 Humidification Test

After the device was set up, the engine was on run on variable speed (rpm) at a fixed load (variable up to 1 kg). The results were drawn using I.C engine soft 2.0. Here, the test results show that brake thermal efficiency was reduced. When the steam was passed through the inlet hose, the quality of air is being decreased as the density of air decreases and the mass of air decreases. This results in choking of the engine as the amount of air decreases. Thus, the brake thermal efficiency is reduced drastically. The emission results show an improvement in nitrogen oxides and particulate emission. Expansion of water into the petrol burning procedure is a known strategy to decrease NOx and, in a few executions, at the same time lessen NOx and PM discharges. The very idea of bringing water into the chamber of the diesel motor may sound dubious. All things considered, engineers have been taking awesome care to achieve the correct inverse and shield the ignition chamber from water pollution, be it from the fuel or from water buildup in consumption air coolers. The debate around water expansion is established on the perception that water beads impinging on the barrel dividers can instantly obliterate the grease oil film. This risk nonetheless, albeit genuine, is postured only by fluid water. When water is dissipated, it can never again influence the lube oil film. Consequently, water expansion techniques which guarantee that water beads cannot contact the chamber liner surface might be viewed as innocuous. Additionally, concerns have been raised that expanded convergences of water vapor in motor chamber may bring about buildup of water or potentially sulfuric corrosive prompting consumption issues. Evidently, these doubts are not supported either, as the dew purpose of sulfuric corrosive at high water: Fuel proportion of 1:1 is expanded by just up to 15 °C. Thinking about the temperatures in petrol ignition, buildup in the burning chamber is not conceivable whenever.

## 2.2 Dehumidification Test

Since moisture gets inside the cylinder and there are chances of improper burning, the idea of dehumidification was developed. The process in which the moisture or water vapor or the humidity is removed from the air keeping its dry bulb (DB) temperature constant is called the dehumidification process. The mode of dehumidification in this test was by using a desiccant inside an air filter. The main idea of using a desiccant was to avoid any chemicals participating in the combustion process. Here, activated alumina was used. Activated alumina is made from aluminum hydroxide by dehydroxylating it in a way that delivers a profoundly permeable material; this material can have a surface region fundamentally more than 200 m$^2$/g. The compound is utilized as a desiccant (to keep things dry by engrossing water from the air) and as a channel of fluoride, arsenic, and selenium in drinking water. It is made of aluminum oxide (alumina; Al$_2$O$_3$), an indistinguishable compound substance from sapphire and ruby (however without the polluting influences that give those diamonds their shading). It has a high surface territory-to-weight proportion, because of many "passage-like" pores that it has. Utilized as a desiccant, it works by a procedure called adsorption. The water noticeable all around really adheres to the alumina itself in the middle of the little entries as the air goes through them. The water particles wind up caught with the goal that the air is dried out as it goes through the channel. This procedure is reversible. On the off chance that the alumina desiccant is warmed to ~200 °C, it will discharge the caught water. Activated alumina was used as the desiccant because of its easy availability, cost, and shelf life. Here, activated alumina balls ranging from 3 to 5 mm were used. The balls were placed inside an air filter, and the porous fiber was soaked in liquid alumina and dried. The air filter was sealed using a bond and was placed inside air filter housing. One end on the filter housing was connected to the orifice, while the other was left open so that air gets in through (Figs. 1 and 2).



**Fig. 1** Activated alumina

**Fig. 2** Dehumidifier
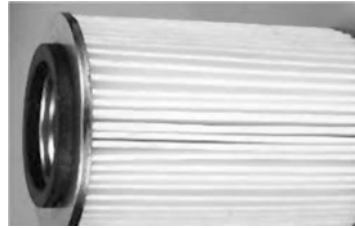


## 2.3 Density Test

Density of air is an important factor in the combustion process. The actual amount of oxygen available for combustion depends on the density of the air. As the density of air increases, the molecules of air are closer and that means there is more amount of oxygen available for burning. When the humidity of the air increases, density falls resulting in improper combustion. Here, density of the air was increased by cooling the inlet air. For this, dry ice was used. Dry ice is the strong type of carbon dioxide. It is utilized principally as a cooling specialist. Its points of interest incorporate lower temperature than that of water ice not leaving any buildup. Dry ice was placed inside an air filter and was closed with a porous fiber. The air filter was placed inside a manifold. One end of the manifold was connected to the orifice, while the other end was left for the engine to breathe.

## 2.4 Dehumidification–Density Test

Here, a combination of both density and dehumidification tests is used. Initially, the density test is set up as in Sect. 2.3 and its outlet is connected to the air filter housing of the dehumidifier. The outlet of the dehumidifier is connected to the orifice. This is done so that temperature of the air is reduced as well as the moisture is trapped.

## 3 Results and Discussion

## 3.1 Humidification Test

The performance test shows us that the brake thermal efficiency is reduced. This is because of the presence of water droplets in the inlet air due to moisture. Water gets mixed in combustion and causes improper combustion resulting in lesser efficiency. Emission results show a better change in hydrocarbon emission and nitrogen oxide. This is because of conversion of molecules into $CO_2$ and $O_2$ (Table 1 and Fig. 3).

**Table 1** Emission levels at variable speed (rpm)

| Speed (rpm) | Normal condition | | Humidified air | |
|---|---|---|---|---|
| 1810 | CO | 0.01% vol | CO | 0.02% vol |
| | HC | 22 ppm | HC | 16 ppm |
| | $CO_2$ | 0.40% vol | $CO_2$ | 0.40% vol |
| | $O_2$ | 21.12% vol | $O_2$ | 20.95% vol |
| | NO | 116 ppm | NO | 50 ppm |
| 1710 | CO | 0.02% vol | CO | 0.02% vol |
| | HC | 14 ppm | HC | 13 ppm |
| | $CO_2$ | 0.60% vol | $CO_2$ | 0.50% vol |
| | $O_2$ | 21.12% vol | $O_2$ | 21.31% vol |
| | NO | 204 ppm | NO | 116 ppm |
| 1610 | CO | 0.02% vol | CO | 0.02% vol |
| | HC | 17 ppm | HC | 21 ppm |
| | $CO_2$ | 1.10% vol | $CO_2$ | 1.10% vol |
| | $O_2$ | 21.5% vol | $O_2$ | 21.72% vol |
| | NO | 370 ppm | NO | 310 ppm |



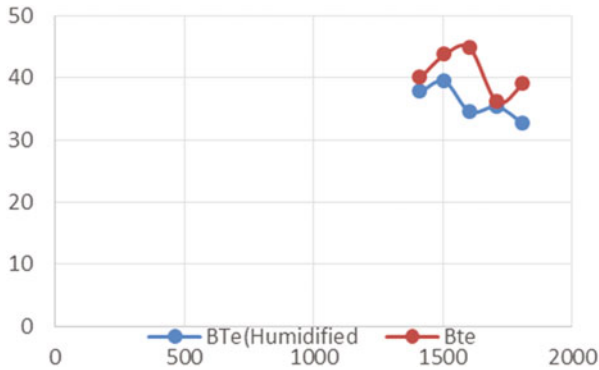**Fig. 3** Speed (rpm) versus brake thermal efficiency

## 3.2 Dehumidification Test

See Fig. 4 and Table 2.

Upon testing, brake thermal efficiency has increased at an average of 6–8% at variable rpms. This is because dry air is being passed in for combustion resulting in better efficiency. Emission stats have also shown better results. Hydrocarbon as well as nitrogen oxide is reduced effectively.
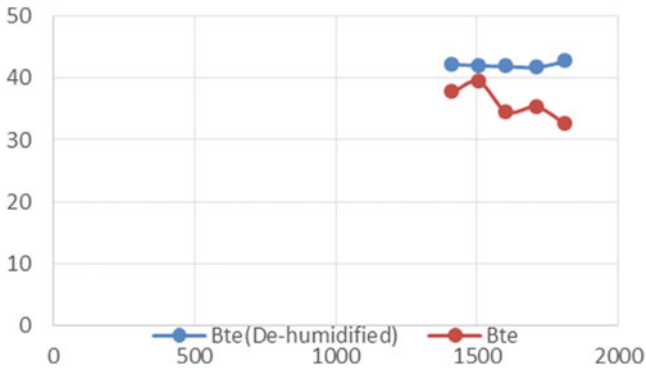
**Fig. 4** Speed (rpm) versus brake thermal efficiency

**Table 2** Emission levels at variable speed (rpm)

| Speed (rpm) | Normal condition | | Dehumidified air | |
|---|---|---|---|---|
| 1810 | CO | 0.01% vol | CO | 0.01% vol |
| | HC | 22 ppm | HC | 8 ppm |
| | $CO_2$ | 0.40% vol | $CO_2$ | 0.30% vol |
| | $O_2$ | 21.12% vol | $O_2$ | 19.83% vol |
| | NO | 116 ppm | NO | 88 ppm |
| 1710 | CO | 0.02% vol | CO | 0.01% vol |
| | HC | 14 ppm | HC | 3 ppm |
| | $CO_2$ | 0.60% vol | $CO_2$ | 0.40% vol |
| | $O_2$ | 21.12% vol | $O_2$ | 21.15% vol |
| | NO | 204 ppm | NO | 151 ppm |
| 1610 | CO | 0.02% vol | CO | 0.02% vol |
| | HC | 17 ppm | HC | 2 ppm |
| | $CO_2$ | 1.10% vol | $CO_2$ | 1.10% vol |
| | $O_2$ | 21.5% vol | $O_2$ | 19.82% vol |
| | NO | 370 ppm | NO | 440 ppm |

## 3.3   Density Test

See Fig. 5.

After carrying out the density test, the engine ran very smooth and the air was densified properly. Densified air had better amount of oxygen, and it helps to give a proper fuel-to-air ratio leading to a better combustion and thus efficiency.
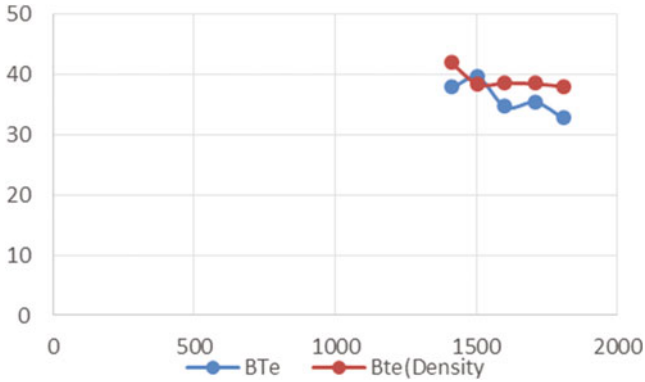
**Fig. 5** Speed (rpm) versus brake thermal efficiency

## 3.4 Dehumidified–Densified Test

See Fig. 6 and Table 3.

The combination of using dehumidified and densified air gave better combustion results leading to better efficiency. Dry ice was used to cool the inlet air, and further the moisture was captured leading to dry cold air resulting in better efficiency. Emission stats also show a good progress in limiting the levels.



**Fig. 6** Speed (rpm) versus brake thermal efficiency

**Table 3** Emission levels at variable speed (rpm)

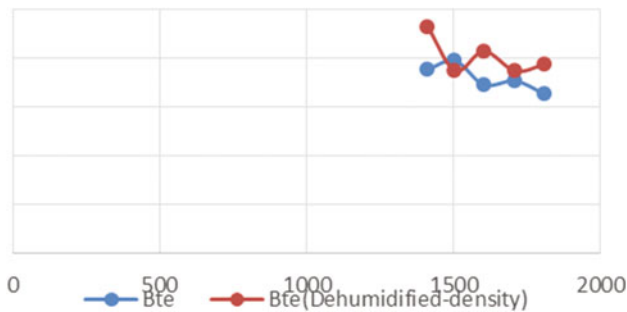| Speed (rpm) | Normal condition | | Dehumidified–densified condition | |
|---|---|---|---|---|
| 1810 | CO | 0.01% vol | CO | 0.01% vol |
| | HC | 22 ppm | HC | 11 ppm |
| | $CO_2$ | 0.40% vol | $CO_2$ | 0.30% vol |
| | $O_2$ | 21.12% vol | $O_2$ | 20.95% vol |
| | NO | 116 ppm | NO | 66 ppm |
| 1710 | CO | 0.02% vol | CO | 0.02% vol |
| | HC | 14 ppm | HC | 12 ppm |
| | $CO_2$ | 0.60% vol | $CO_2$ | 0.40% vol |
| | $O_2$ | 21.12% vol | $O_2$ | 20.84% vol |
| | NO | 204 ppm | NO | 118 ppm |
| 1610 | CO | 0.02% vol | CO | 0.01% vol |
| | HC | 17 ppm | HC | 9 ppm |
| | $CO_2$ | 1.10% vol | $CO_2$ | 0.90% vol |
| | $O_2$ | 21.5% vol | $O_2$ | 20.85% vol |
| | NO | 370 ppm | NO | 280 ppm |

# 4 Conclusion

The air the engine breathes is altered on various bases, and results were plotted out. The combination of using a dehumidifier and a densifier resulted in better efficiency. The basis of such results is because when densified air goes in for combustion, the amount of oxygen molecules available is better and richer. The current fuel-to-air ratio can be delivered easily. Furthermore, dehumidifying the air helps us to trap all the moisture present in the air, and reducing the amount of water particles makes the fuel to burn better leading to hassle-free combustion. Efficiency of an engine is the most sought, and for this many techniques are being developed to improve the combustion characteristics of the engine. Emission characteristics are also tested out in all conditions; a proper work is dined in developing so. This imperative method of using dehumidified–densified air will result in greater mileage as well as lesser pollution levels.

# References

1. Caton JA (2017) Maximum efficiencies for internal combustion engines: thermodynamic limitations. Int J Engine Res 19:1005–1023
2. Abd Alla GH (2002) Computer simulation of a four stroke spark ignition engine. Energy Convers Manage 43:1043–1061 (Al-Ain Technical School, P.O. Box 17835, Al-Ain, United Arab Emirates)
3. Jehad AA, Yamin MH (2004) Performance simulation of a four-stroke engine with variable stroke-length and compression ratio. Appl Energy 77:447–463

4. Al-Baghdadi MARS, Al-Janabi HAKS (2000) Improvement of performance and reduction of pollutant emission of a four stroke spark ignition engine fuelled with hydrogen gasoline fuel mixture. Energy Convers Manage 41:77–91 (Department of Mechanical Engineering, College of Engineering, University of Babylon, Babylon, Iraq)
5. Kutlar OA, Arslan H, Calik AT (2004) (Department of Mechanical Engineering, Faculty of Engineering and Technology, University of Jordan, Amman, 11942 Jordan). Methods to improve efficiency of four stroke, spark ignition engines at part load. Energy Convers Manage 46:3202–3220
6. Butt QR, Bhatti AI (2008) Estimation of gasoline-engine parameters using higher order sliding mode. IEEE Trans Ind Electron 55(11)
7. Shudo T (2007) Improving thermal efficiency by reducing cooling losses in hydrogen combustion engines. Int J Hydrogen Energy 4285–4293 (Applied Energy System Group, Division of Energy and Environmental Systems, Hokkaido University, N13 W8, Kita-Ward, Sapporo, Hokkaido 060-8628, Japan)
8. Hariram V, Shangar RV (Department of Automobile Engineering, Hindustan Institute of Technology & Science, Hindustan University, Padur, Chennai, Tamil Nadu, India). Influence of compression ratio on combustion and performance characteristics of direct injection compression ignition engine. Alexandria Eng J

# Calibrating the Performance of Pelton Turbine by Using Helical Penstock

**Punj Lata Singh, Akash Chaudhary and Devansh Rautela**

**Abstract** This paper presents a study on the comparative analysis of the penstock used in the micro-hydropower plants with the aim of inventing a new design of penstock with the efficiency benefits in the future. The Pelton wheel is designed for 0.000143 m³/s flow rate with a diameter of penstock 0.75 in., and detailed study is done on the benefits of the new penstock which is helical in shape, so the helical penstock can also be considered as a replacement of the old conventional penstock which is straight and its design strategies are discussed. It was found that the helical penstock was approximately 22–23% more efficient in the voltage generation with the additional benefits such as saving in the material cost, less land acquisition, and less wear and tear of the penstock line due to cavitation. This is thus more economical, more viable as it produces more with the same input of water, and thus helps in generating more power.

**Keywords** Hydropower · Helical penstock · Efficiency · Voltage · Pelton turbine

## 1  Introduction

The hydropower is the power derived from the energy of the water falling from a high level with a pressure which is used to rotate the blades of the turbine, thus producing electricity. Water is a renewable source of energy which can be used as a replacement for the conventional methods of fossil used for energy generation protecting both the fossils for future generations and the environment. India is the seventh largest producer of hydropower in the world with the installed capacity of 44,594 MW or 13.5% of the total potential of hydropower, and it also has additional micro-/mini-hydropower plants with installed capacity of 4,380 MW, i.e., 1.3% of its total utility power generation capacity [1]. There are two types of turbine used for the power generation.

P. L. Singh (✉) · A. Chaudhary · D. Rautela
Department of Civil Engineering, Amity University, Noida, Uttar Pradesh, India
e-mail: plsingh@amity.edu

Action turbine, e.g.—Pelton turbine.

Reaction turbine, e.g.—Francis turbine (for radial flow), Kaplan turbine (for axial flow).

As an radial flow turbine, the water which is stored at a higher elevation in a dam is made to flow on the turbine which is located at a lower elevation by the means of penstock with a nozzle installed at the penstock end so as to increase the jet velocity of water to rotate the turbine wheel at a high speed which is further connected to an alternator with a shaft whose consecutive rotation leads to the generation of electricity which is supplied to the main grid or the sub-divisional zone with the help of transmission lines.

The current method of the power generation is a very old conventional method in which there is not much research done in the design of the new penstock and calibrating the turbine wheel in accordance with that. As India has a huge scope of hydropower and day by day increasing demand for the electricity, the need arises for the increment in the power generation [2]. The setting up of the new plant takes out a huge load of the budget of the government and investment of the private sector as India is a developing country so it has to utilize its resources judicially to increase the efficiency of the power generation so that the old plants can be altered and the new one could be set by using new innovation.

This paper consists of the alteration of the old conventional straight penstock with the helical one so as to analyze its impact on the efficiency and increment/decrement in the power generation so as to help this sector produce more with the same input. It also deals with the designing of the wheel of the Pelton wheel turbine according to the discharge and finding out the nozzle diameter in accordance with it. The main criteria for the designing of any hydropower are discharged available from the river stream which helps in the calibration of the working model. The working model aims to find out the impact of the new penstock over the power generation with the same level of inputs, thereby telling us about the efficiency of the new design with proper calculations as well as comparative analysis.

## 2 Benefits of Helical Penstock Over Normal One

### 2.1 The Benefits of the Helical Penstock Over the Normal Penstock Could Be Explained as [2, 3]

- In the normal penstock, the pressure at the inner portion of the curve is less than the outer portion due to which the flow separation occurs and the energy is lost in the form of eddying turbulence; this further results in the cavitation of the penstock line, and to overcome this problem and to make the curves of the bend smoother, we have to place the turbine at a large distance which is usually

required from the Dam thus increases the overall length of the penstock and further causing the frictional losses and reducing the power generation capacity.

- Moreover, in the normal penstock, the velocity profile at the downstream portion of the penstock which is curved becomes peaked or skewed with a lesser velocity of flow at the inner portion of the wall and vice versa. As by nature of the hydroelectric turbines, it is seen that they perform better when the velocity profile is uniform but here we get a non-uniform skewed profile, thus causing the inefficient power generation from the turbine.
- But, to recover from the skewed or non-uniform velocity profile we have to place a penstock at the end of penstock which is horizontal and straight. This is known as spacer penstock whose work is to minimize the non-uniform velocity and does not have any role in the power generation process but just increases the length of the penstock and results in the increment on the length of the penstock, thus causing the frictional losses.
- The benefit of using the penstock in curved format or the 3D concept is that it helps in the development of the swirl flow and because of this the axial velocity profile becomes less non-uniform. This also makes the speed of the flow at the inner portion to be greater than the outer portion resulting in making the velocity profile to be more uniform around the circumference; then it would also be possible when the geometry was plane.
- As the velocity profile is now more uniform, so the tendency for the flow separation to take place will be less at the inner wall of the curve and thus we can say that the loss of the energy due to turbulence or due to eddy currents will be less.
- The loss of the head is less in the tubular penstock in comparison with the straight 2D penstock, and the pressure recovery at the tailrace portion is also more.
- The process of the cavitation is also less in tubular penstock; thus, the damage to the material is also less.
- The tubular portion helps in the development of the flow which could be called as the plunger flow because it tends to remove the deposition of silts and debris or does not allow them to accommodate; thus acting like a plunger during the time when the flow is less. But in the normal penstock during the time of the less flow, the silt and debris tend to settle at the joints and at the penstock base and a regular cleaning is required which only adds to the cost; and moreover, excessive deposition causes hindered flow.
- The abrasion by the silt and debris is also reduced on the penstock surface as the flow speed is less.
- The blunter velocity profile avoids the bending stresses to hoop or ring, thus reducing the wall stresses.
- With the use of the helical penstock, it is also possible to place the turbine near to the water storage area and to use the sharper bends in the shape of S in the penstock and thus the cost of material goes down as it uses a less length of the penstock than the normal penstock. Moreover, the need to acquire a more area as in the normal penstock is sorted out; thus, the cost of the land is saved too.

Also, the quantity of the excavation and the concrete required is also saved. As land is the main cause of the problem in any property, so the amount of dispute is less.

## 2.2 Alignment of the Curved Penstock Is as Follows [4]

- The tubular portion is provided after a little straight portion of the dam gate for a good support.
- The penstock may have a steep or sloppy shaft dropping at a high gradient in the shape of S.
- There is no need to provide the spacer penstock as the velocity profile is already uniform.
- The two ends of the penstock must be axially aligned from both the ends.
- The helical penstock can branch off laterally from the straight part, but the diameter of the straight part is to be kept larger than the tubular one so as to accompany the laminar flow in normal penstock and the turbulent flow in the helical penstock.
- More than one helical penstock may be connected to normal straight penstock; each of one is connected to the respective turbine.
- The inlet to the penstock could be made bell mouth in shape.
- A bent at the upstream end portion is avoided altogether by shaping the dam such that it lies perpendicular to the penstock or alternatively the entire portion could be made helical with no straight portion at all.
- If the angle turned off the tubular portion more than 360°, the phase of the inlet and outlet will thus lie in the different planes, thus disturbing the axial alignment of the penstock as the two phases will lie in the different planes.
- The direction of the curvature of the penstock and the turbine inlet is kept altogether same so as to reduce the losses due to flow.

## 3 Methodology

Then, we started to test the above benefits in the real world, and for that, we made a working model of the hydropower plant. The methodology of analysis includes the following steps [5]:

Set the fixed discharge for the plant as 0.000143 m$^3$/s, and the further designing of the turbine is done by keeping it fixed.

Fix the head of the model on a reduced scale of 1:50 while considering a real project site.

Design the turbine wheel, blades, and nozzle diameter according to the discharge. Fix the diameter of the penstock as 0.75 inches for both the helical and the normal. Align the various components of the model in a proper geometry for working as well as efficiency.
Calculate the results from the model.

## 3.1  Steps Involved in the Designing of Pelton Wheel Turbine

The steps involved in the designing Pelton wheel are required to calculate the following values:

- **Calculation of the Net Head ($Hn$)**

  The net head of the turbine can be calculated with the use of the formula

  $$H(n) = H(g) - H(l)$$

  where

  $H(n)$  is the net head
  $H(g)$  is the gross head
  $H(l)$  is the head loss in the total distance covered by the water which includes penstock, tailrace, joints, and valves. And this is taken as the 5% of the total gross head (as told in the research paper quoted in reference).

- **Calculation for the Velocity of the Jet or Nozzle ($V$jet)**

  The jet of water is created at the bottom of the penstock due to the pressure of the water stored in the dam at a particular elevation; this is called as the $V$jet.

  $$V(\text{jet}) = K(2gH(n))1/2$$

  where

  $K$  is a nozzle velocity coefficient which lies between 0.95 and 0.99
  $H(n)$  is the net head of the nozzle
  $g$  is acceleration due to gravity.

- **Calculation of Jet Diameter ($d_{\text{jet}}$)**

  $$d_{\text{jet}} = 0.54/Hn^{1/4} * ((Q/n_{\text{jet}})^{1/2}))$$

  where $n_{\text{jet}}$ is the no. of jet/nozzle.

- **Calculation of the Pitch Circle Diameter (PCD)**

  The turbine speed can be expressed as

  $$2 * 3.14 * N/60 * D/2 = x * V(\text{jet})$$

  where $D$ is the pitch circle diameter.
  And $x = 0.46$.
  Also,

  $$D = 37.7 * H(n)/N$$

  The value of $N$ is found out with the help of the spreadsheet using the real data of the site, but we have used the data of the test turbine initially set.

- **Turbine Bucket Calculations**

  Depth of bucket: $d = 0.121\ D$
  Length to impact point: $h' = 0.114\ D$
  Width of bucket opening: $a = 0.14\ D$
  Bucket thickness: $t = 0.002\ D$
  Width of bucket: $w = 0.38\ D$

- **Calculations**

  1. **Net Head ($Hn$)**

     $$= Hg - Hl$$
     $$= 1.36 - 0.05(1.36)$$
     $$= 1.292\ \text{m}$$

  2. **Velocity of Jet ($V_{\text{jet}}$)**

     $$= Kn * ((2gHn)^{1/2})$$
     $$= 0.99 * ((2 * 9.81 * 1.292)^{1/2})$$
     $$= 50.34 * 0.99$$
     $$= 4.98\ \text{m/s}$$

  3. **Jet Diameter ($d_{\text{jet}}$)**

     $$= 0.54/(1.292)^{1/4}((0.000143)^{1/2})$$
     $$= 0.54/1.065 * (0.012)$$
     $$= 0.006\ \text{m}$$

4. **Pitch Circle Diameter (*D*)**

$$= 37.7 * ((Hn)^{1/2})/(N) = 37.7 * ((1.292)^{1/2})/(210) = 0.204 \text{ m}$$

5. **Turbine Bucket Calculations**

    a.  Depth of bucket: $d = 0.121\,D = 0.121 \times 0.204 = 0.07$ m
    b.  Length to impact point: $h' = 0.114\,D = 0.114 \times 0.204 = 0.023$ m
    c.  Width of bucket opening: $a = 0.14\,D = 0.14 \times 0.204 = 0.02856$ m
    d.  Bucket thickness: $t = 0.002\,D = 0.002 \times 0.204 = 0.00041$ m
    e.  Width of bucket: $w = 0.38\,D = 0.38 \times 0.204 = 0.0077$ m
    f.  No. of buckets = 15

6. **Power**

$$= pgQHn$$
$$= 1000 \times 9.81 \times 0.000143 \times 1.292$$
$$= 1.81 \text{ Watt}$$

# 4 Components of the Model

- **Reservoir**—the reservoir in the model is designed to store 20 L of water on a wooden stool of height 0.8 m. The gross head of the plant is equal to 1 m.
- **Penstock penstocks**—two types of penstock are considered: One is the normal straight penstock of length 0.2 m (horizontal portion) and 0.81 m (inclined portion), and the other penstock used is of helical shape of the same diameter (Fig. 1).



**Fig. 1** Pelton wheel

**Table 1** Basic design calculation for turbine's geometry and setup values for the model

| Description | Data | Unit |
|---|---|---|
| Net head ($Hn$) | 1.292 | M |
| Speed ($N$) | 210 | RPM |
| Discharge ($Q$) | 0.000143 | m³/sec |
| Jet velocity ($V$jet) | 4.98 | m/s |
| Power ($p$) | 1.81 | Watt |
| Runner diameter ($D$) | 0.204 | M |
| Depth of bucket ($d$) | 0.07 | M |
| No. of buckets ($Z$) | 15 | – |
| Bucket thickness ($t$) | 0.00041 | M |
| Width of bucket ($w$) | 0.0077 | M |
| Length of impact point ($h'$) | 0.023 | m |



**Fig. 2** Setup using helical penstock



**Fig. 3** Setup using normal penstock

**Pelton wheel**—the turbine designed is of 15 blades of Pelton wheel turbine having runner diameter of 0.092 m, bucket width of 0.023 m, bucket depth of 0.015 m (Table 1; Figs. 2 and 3).

# 5   Result and Conclusion

The use of the helical penstock with the Pelton wheel turbine proved out to be much efficient than the normal penstock and suits the current demand of time and needs. The results are given in Table 2 for straight penstock and Table 3 for helical penstock in the form of discharge, voltage, rpm of dynamo, and rpm of turbine wheel.

Now, the tables are plotted in graphs (as shown in Fig. 4) for different valve openings considering both the types of penstocks in terms of voltage against rpm which will help in comparing the results of efficiency.

From the reading taken above, it is seen in Fig. 5 that the helical penstock is efficient in the energy generation with the other constructional benefits as well. It is found to be 23.77% more efficient in the full discharge and 20.58% more efficient when the valve was 3/4th open. Thus, it would benefit to construct the new projects with this penstock and to replace the older ones also so as to attain maximum benefits in terms of electricity generation and cost.

From Fig. 6, we found that the bars for helical penstock for voltage and rpm are more than the normal penstock for full and ¾ of the discharge which obviously explains that the normal penstock can be replaced with a helical penstock so as to increase the efficiency of the turbine. However, it is found that the new penstock was approximately 22–23% more efficient in the voltage generation with the additional benefits such as saving in the material cost, less land acquisition, less wear and tear.

The objective of this study is to improve the electric power generation in India as well as the world with the aim of utilization of the existing working sites of the hydropower. Considering the rapidly increasing demand of the electricity in our country, this research work was important moreover in this sector; i.e., hydropower is one of the most untouched and uses the simple and conventional techniques to produce the electricity. The existing technology on which this industry is dependent

**Table 2**  Output using straight penstock

| S. no. | Voltage (AC) | RPM of dynamo | RPM of turbine wheel |
|--------|--------------|---------------|----------------------|
| *For full valve open, i.e., Q = 0.000143 m³/s* | | | |
| 1. | 4.2 V | 1550 | 472 |
| 2. | 4.1 V | 1498 | 460 |
| 3. | 3.9 V | 1439 | 439 |
| *For 3/4th wall open, i.e., Q = 0.00010725 m³/s* | | | |
| 1. | 3.5 V | 1291 | 393 |
| 2. | 3.3 V | 1217 | 373 |
| 3. | 3.4 V | 1254 | 380 |

**Table 3** Output using helical penstock

| S. no. | Voltage (AC) | RPM of dynamo | RPM of turbine wheel |
|--------|--------------|---------------|----------------------|
| *For full valve open, i.e., Q = 0.000143 m³/s* | | | |
| 1. | 5 V | 1845 | 562 |
| 2. | 5.2 V | 1920 | 590 |
| 3. | 4.9 V | 1799 | 551 |
| *For 3/4th wall open, i.e., Q = 0.00010725 m³/s* | | | |
| 1. | 4.0 V | 1485 | 451 |
| 2. | 4.2 V | 1560 | 478 |
| 3. | 4.1 V | 1516 | 463 |
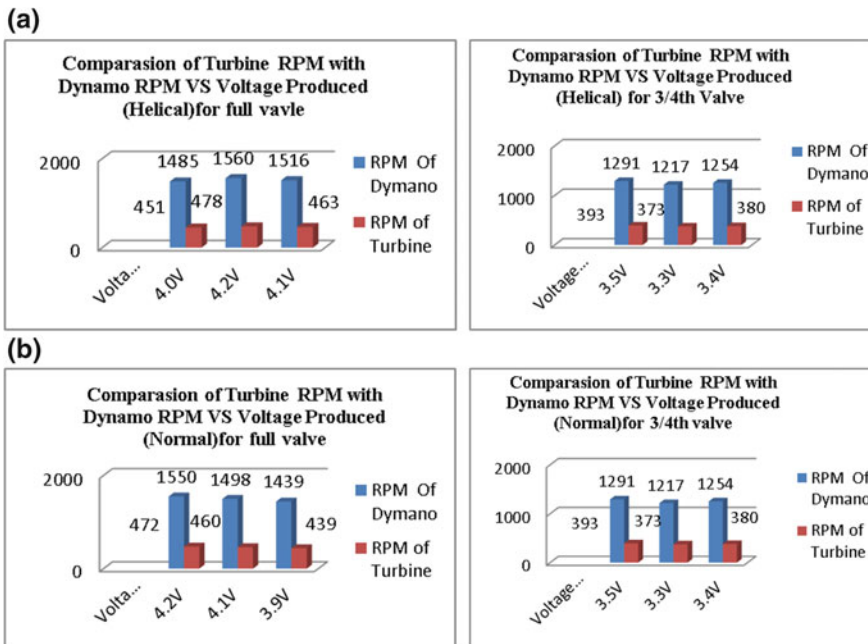


**Fig. 4** Comparison of turbine rpm with dynamo rpm versus voltage produced by helical and normal penstocks for full valve opening and 3/4th valve opening

is very old and uses the conventional straight penstock for the power generation which has many types of minor losses through bends and joints which turns into major losses. With the availability of the modern computer software and the technology available with us, it is now very easy to create such shapes (helical) on a large scale which initially could be costly but when it comes to the revenue, it brings a return considerably much greater than the initial investment.
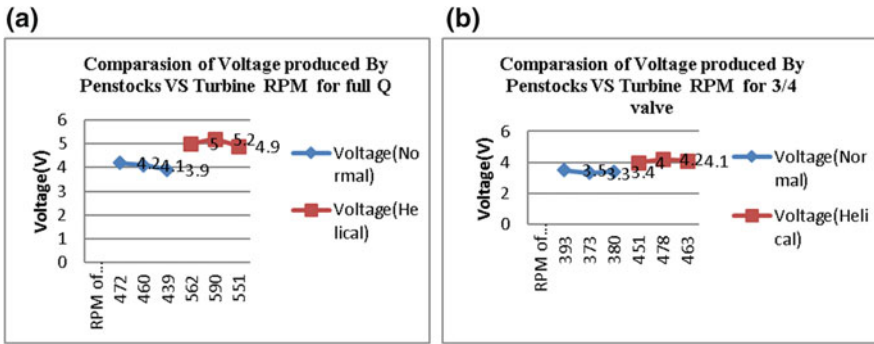
**(a)**



**(b)**



**Fig. 5** Comparison of voltage produced by penstocks versus turbine rpm for full Q and 75% Q
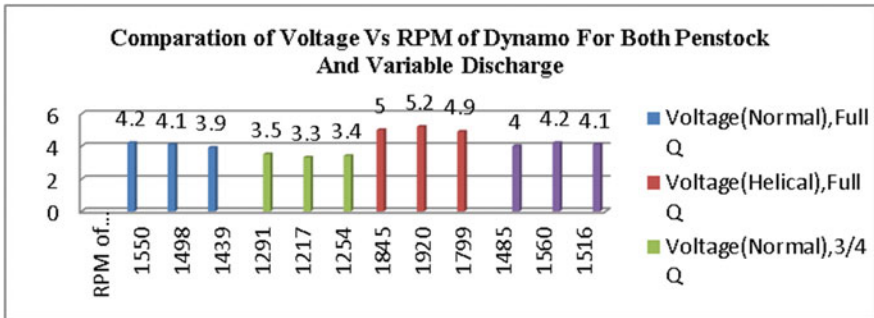


**Fig. 6** Comparison of voltage versus rpm of dynamo for both penstock and variable discharge

## 6   Future Scope

With the invention of the helical penstock in the field of the hydropower, there is a need for its analysis on a more design as well as constructional aspects so as to support the industry. In today's world, it is hard to find even a single example of the site which is working with the use of this technology. There lies a great need for the flow analysis of the helical penstock by using the CFD software so as to compare the two and to understand the flow patterns in more detail. This paper is just a minor work done in this regard, but a big start could be enhanced by this for a more relevant and realistic work to be done actually in the form of a live working micro-hydropower plants.

# References

1. Nigussie T, Engeda A, Dribssa E (2017) Design, modeling, and CFD analysis of a micro hydro Pelton turbine runner: for the case of selected site in Ethiopia. Int J Rotating Mach
2. Kholifah N, Setyawan AC, Wijayanto DS, Widiastuti I, Saputro H (2018) Performance of Pelton turbine for hydroelectric generation in varying design parameters. In: IOP conference series: materials science and engineering, vol 288, no 1, p 012108. IOP Publishing
3. Solemslie BW, Dahlhaug OG (2014) A reference Pelton turbine-design and efficiency measurements. In: IOP conference series: earth and environmental science, vol 22, no 1, p 012004. IOP Publishing
4. Panagiotopoulos A, Židonis A, Aggidis GA, Anagnostopoulos JS, Papantonis DE (2015) Flow modeling in Pelton turbines by an accurate Eulerian and a fast Lagrangian evaluation method. Int J Rotating Mach
5. Kumar DS (2012) Fluid mechanics and fluid power engineering, 9th edn. Katson Publishing House

# To Reduce Pollution Due to Burning of Coal in Thermal Power Plant

**Ankush Agrawal, Harshit Ahuja and R. K. Tyagi**

**Abstract** Over the past decades, many techniques or resources are used in order to generate electricity or to produce power and many more. To generate electricity or power, some substance needs to be burned those sources include fuels and coals. Coals are the major sources which are used in thermal power industries. And due to the burning of such fuel or coal, the production of harmful gases arises. These gases include $CO_2$, sulphur, nitrogen, and soot particles. According to various researches, the production of $CO_2$ is much larger than the production of other elements which mostly affects the global warming. This project has a new concept which aims to reduce most of those gases which comes out of the thermal power plant. An experimental study has been conducted to check the amount of pollutants coming out from our prototype, and on the basis of the results, the amount of pollutants reduction will be calculated. This project mainly focuses to reduce the particulate matter coming out of the power plant. Since by burning of a coal, the production of particulate matter is much higher that's why this paper aims to reduce that $CO_2$ from entering into the atmosphere and hence reducing pollution as well as the ozone layer depletion.

**Keywords** Particulate matter reduction · PM 2.5 · Coal pollution · Experimental study · Thermal power plant

## 1 Introduction

In India, around 70% of the total electricity produced is produced by the thermal power plant, so it is of prime necessity that the side effects from these power plants should be visibly reduced, so that the environment should not have to compromise with the present and future expectations. Coal, which is one of the most abundant fossil fuel resources, currently meets about 70% of India's energy demands and

A. Agrawal · H. Ahuja · R. K. Tyagi (✉)
Department of Mechanical Engineering, Amity University Noida, Noida, Uttar Pradesh, India
e-mail: rktyagi@amity.edu

563

about 40% globally. Though the utility of coal is much of a positive use, it has got many adverse effects too. The major being ecological impact which also effects environment directly. Burning of fossil fuels generates a lot of energy but, it also produces many harmful gases which are directly left into atmosphere though after various treatment processes many are still remaining in the flue gas which is then left to atmosphere majorly constituting of oxides of sulphur, nitrogen, carbon, and mainly the particulate matter, which causes various respiratory diseases.

## 1.1 Classification of Chimneys

Based on number of flues: single flue (each boiler will have an independent chimney), multi-flue (single chimney serves more than one boiler; more flues are housed inside a common concrete windshield).

Based on material of construction: concrete (Chimney), reinforced/pre-stressed, steel (stack).

Based on structural support: guyed stacks (used in steel stacks for deflection control), self-supporting (cantilever structures).

Based on lining: with lining: lined chimneys/stacks, without lining: unlined chimneys/stacks [1] (Fig. 1).

## 2 Literature Review

An analysis has been done with respect to environmental and energy performance parameters of burning high-potential coal water slurries containing petrochemicals instead of using fuels such as coal, etc. The pollutants such as sulphur and nitrogen oxides have been readily emphasized in this research. The research shows that the quantity can be brought down to a great extent if coal processing waste mixed with water is used as a fuel in thermal plants. It concludes that it is worthwhile to use CWSP based on filter cakes to be used as a fuel in thermal power plant [1]. Emphasizes on how carbon storage and capture can play a vital role in bringing

down the air pollution to a very low level. It includes a case study on the prospects of coal thermal power plants operated in UK to find out whether it is implementable or not. Potential design routes have been identified to study CCS in UK thermal power plant and what is cost incurred is also specified. The study shows that CCS is possible and is a good means to reduce the pollution but its implementation in coal fired thermal power plant is still a matter of concern. This is due to the usage of sophisticated instruments and equipment used in this process that can incur higher costs for its effective implementation [2]. It gives information on the pollutants produced in thermal power plants and highlights a greater emphasis on thermal power plants operated in India (Fig. 2).

It analyses on how fuel gas desulphurization and updating and tightening of environmental laws have brought the pollution caused by thermal power plants. Also, it emphasizes various health hazards that are caused due to increase in pollutants in our atmosphere [3]. It describes the use of a novel method to use microalgae as an additive to reduce the pollution. It proposes the use of resistant microalgae for the treatment of fuel gas and using its biomass as a good and a novel additive in coal. A novel additive known as "green coal" was produced in this system whose constituents includes 8.7% lower amount of ash and has about 26.18% higher calorific value. As this technique has lower usage of chemicals and has low energy expenditure, therefore, this technique can replace the conventional use of coal and other fuels in coal-fired thermal power plants [4]. It gives a general description on how a thermal power plant functions. It gives a detailed description on the various thermodynamic cycles operating in a thermal power plant. The details include the functioning of Rankine cycle, diesel cycles, and also about the operation of gas turbine in production of electricity in thermal power plant [5]. Overview about energy and economic performance of integrated gasification cycle in combination with cycle power plant that has the potential to use carbon dioxide storage which is based on oxygen-fuel combustion processes in the thermal power plant. But this process requires great amount of oxygen flow rates. So to facilitate this technology is put forward for production of oxygen by means of oxygen transport membranes. Thus, various main performance characteristic of these



Fig. 2 2D model

membranes has been put forward to analyse the integration of this technology in thermal power plants [6]. It focuses on reducing the content of fly ash because it is the most toxic by-product as it contains the heavy metal particles. The conclusion states that the plasma after reaction with the fly ash detoxifies the fly ash by plasma vitrification and the product formed was glassy and amorphous in nature [7]. Overview about various developments that have been carried out in designing chimney. It covers the structural conception, modelling, method of analysis and describes the construction of the chimney as well as the materials deployed in order to build a chimney [8].

## 3 Methodology

Researches would be held regularly in order to find out the best and feasible solution to reduce the amount of soot particles production from the plant. The idea consists of making an experimental setup, which will have a four-walled chamber, two walls each of acrylic and mild steel. The steel is used for providing strength to the chamber and glass is used for the visibility of the processes taking place inside the container. Industry grade needs not to be exactly similar to the model; it is for experimentation not the actual prototype. A base container is provided which stores water to absorb the particulate matter. The transfer of the flue gases takes place via pipe connection from the top of chimney extended till the bottom of base directly into the water (Fig. 3).

There would be two bed of sponge and a bed of pebbles, inside the chamber. The side walls are attached with supporting structures to hold the layers of such. The base needs to be of more hard material so that the structure doesn't fall off with base and the walls would be designed to hold the pebbles bed and sponge layers firmly, with not much affected by the constant pressure of gas, load due to the pebbles and the water being collected at the base. The pebbles and the sponge would be put in layers with sponge on top followed by pebbles. This is so done to minimize the possibility of the gases trying to escape. The gases being warm in temperature try to move upwards due to convection or pressure difference. Hence, the layers are set up to prevent this.
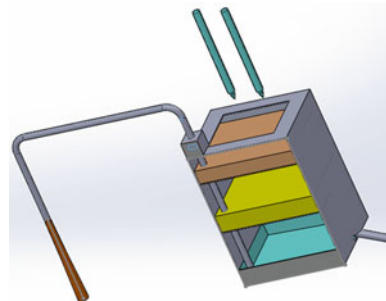
**Fig. 3** CAD model

**Fig. 4** Setup



Particulate particle would be collected via the pipe connecting from the top opening of the chimney and it is put into the tub deep inside all the layers till the base of the tub. It is done so that the gases are directly mixed with the prevailing water. Water injector would be used to sprinkle water on the sponge layer on the top, so that the pores of the sponge don't get blocked by the gases trying to escape upwards and to ensure the maximum dissolution of gas into the water.

Blower is used in the prototype in order to create up the pressure and blow the gases coming from the chimney to the water at the bottom layer, eradicating the problem of back pressure. It is placed just above the filtering chamber (Fig. 4).

## 3.1 Prototype Dimensions

The prototype that had been made to bring down the amount of particulate matter has the following dimensions (Table 1).

## 3.2 PM 2.5 Device

It is a device which is used to measure particulate matters (PM) with diameter of 2.5 μm or less present in the atmosphere (Tables 2 and 3).

**Table 1** Dimensions of the prototype

| | |
|---|---|
| Top diameter of chimney | 6 cm |
| Bottom diameter of chimney | 18 cm |
| Height of the chimney | 50 cm |
| Dimension of the base | 45 × 45 cm |
| Dimension of each wall of container | 45 cm |
| Pipe diameter | 6 cm |
| Height of base | 9 cm |

| Table 2 Conditions of atmosphere | 1. Initial temperature | 32 °C | 2. Mass flow rate | 0.02 kg/s |
|---|---|---|---|---|

| Table 3 Specifications of PM 2.5 device | PM2.5 measuring range | 0–500 μg/m$^3$ |
|---|---|---|
| | Temperature measuring range | −10 to 50 °C |
| | Humidity measuring range | 0–99 %RH |
| | Working temperature | −10 to 50 °C, 0–99 %RH |

## 4 Limitations

The water needs to be continuously circulated because water gets saturated on continuous passing of gas and may not be able to dissolve particulate matter into it furthermore. The prototype must be made with great care, as a little constructional defect may lead to the escape of gases into the atmosphere.

## 5 Future Scope

In this modern era, pollution had become a major problem for the whole world and countries are spending billions of dollars every year to move towards sustainable development by means of sustainable energy. Our prototype has a great scope in future as it can help in solving various problems related to environment and global warming.

This project has a great scope in future specially in the area of sustainable energy.

It can bring down the level of particulate matter produced due to burning of coal in thermal power plant. It can also find application in solving the problem of stubble crop burning in cities like Punjab and Haryana, as stubble crop burning during the harvest season leads to pollution. During drastic pollution in cities like Delhi, it is advised to the people not to go to parks for jogging or cycling. This prototype can be attached to the exercise bikes installed in the parks and it can provide air (having very low level of PM 2.5) to the people.

## 6 Results and Discussion

A test has been conducted in order to check out whether the setup infeasible or not. When the coal was burned and tested with PM 2.5 device it showed better results. And the results are as follows in Table 4 and Graph 1.

**Table 4** Readings of the particulate matter

| S. No. | Time (s) | (µm) | S. No. | Time (s) | (µm) | S. No. | Time (s) | (µm) |
|--------|----------|------|--------|----------|------|--------|----------|------|
| 1 | 5 | 93 | 8 | 40 | 107 | 15 | 75 | 274 |
| 2 | 10 | 95 | 9 | 45 | 123 | 16 | 80 | 284 |
| 3 | 15 | 99 | 10 | 50 | 141 | 17 | 85 | 307 |
| 4 | 20 | 87 | 11 | 55 | 231 | 18 | 90 | 305 |
| 5 | 25 | 90 | 12 | 60 | 189 | 19 | 95 | 296 |
| 6 | 30 | 93 | 13 | 65 | 230 | 20 | 100 | 301 |
| 7 | 35 | 88 | 14 | 70 | 289 | – | – | – |
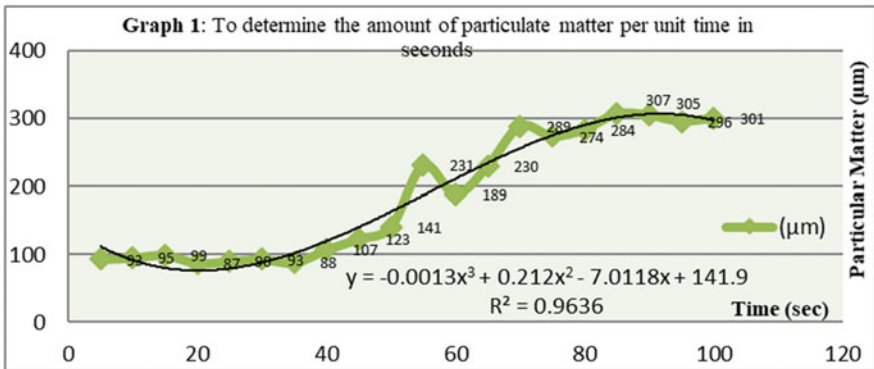


**Graph 1** To determine the amount of particulate matter per unit time in seconds

## 7 Conclusion

When the coal is burned and let the smoke to pass through the setup. It was noted that higher value of $R^2$ indicates that the model fits our data or experimental values very well.

The third-degree polynomial equation formed by the graph is given by the formula:

$$y = -0.0013x^3 + 0.212x^2 - 7.0118x + 141.9$$

where

$y$   Particular Matter content in micron meter
$x$   time in seconds.

The value of the $R^2$ is found to be as: $R^2 = 0.9636$.

# References

1. Dmitrienko MA, Strizhak PA (2018) Coal-water slurries containing petrochemicals to solve problems of air pollution by coal thermal power stations and boiler plants: an introductory review. J Sci Environ 613–614:1117–1129. https://doi.org/10.1016/j.scitotenv.2017.09.189
2. Hammond GP (2014) The prospect for coal fired power plant with carbon capture and storage: A UK perspective. Energy Convers Manag 86:476–489
3. Guttikunda SK (2014) Atmospheric emissions and pollution from the coal-fired thermal power plants in India. Atmos Environ 92:449–460
4. Taştan BE, Tekinay T (2016) A novel coal additive from microalgae produced from thermal power plant flue gas. J Cleaner Prod 133:1086–1094
5. Sagar K, Manthan K, Sandeep T, Mayank C, Aggarwal KM, RK Tyagi RK (2015) Biodiesel production & its performance characteristics measurement: a review and analysis. J Chem Pharmaceut Res 7:1075–1082
6. MarcoGambini M (2015) $CO_2$ capture in advanced power plants fed by coal and equipped with OTM. Int J Greenhouse Gas Control 36:144–152
7. Al-Mayman S, Al-Shunaifi I (2017) Treatment of fly ash from power plants using thermal plasma. Beilstein J Nanotechnol 8:1043–1048
8. Carrion LE, Dunner RA (2000) Seismic analysis and design of industrial chimneys. Int Jo Eng Res Appl 2:154–161

# Experimental Investigation of the Performance of a Double-Pass Unglazed Transpired Solar Air Heater

**D. K. Rabha, D. Pathak, R. Baruah, T. Kalita and A. Sharma**

**Abstract** This study presents an experimental investigation of the performance of a double-pass unglazed transpired solar air heater. The performance of the solar air heater was evaluated from the experimental data by energy and exergy analyses. The average thermal efficiency of the solar air heater was found to be 16.9 and 20.6% at the air flow rate of 0.015 and 0.019 kg/s, respectively. The average exergy efficiency was found to be 0.49 and 0.57% at the air flow rate of 0.015 and 0.019 kg/s, respectively. The thermal effectiveness of the heater was 66.6 and 67.1% at the air flow rate of 0.015 and 0.019 kg/s, respectively. The energy and exergy efficiencies and the thermal effectiveness increased with increase in the mass flow rate of air. The performance of this solar air heater is comparable to the conventional glazed solar air heater although it does not have any cover plate.

**Keywords** Double pass · Unglazed · Solar air heater · Thermal effectiveness · Energy efficiency · Exergy efficiency

## 1 Introduction

Many applications such as drying of fruits and agricultural products, timber seasoning, and space heating require the hot air of the temperature below 100 °C [1]. The hot air for these applications can be easily produced in a device known as the solar air heater. The solar air heater is one kind of heat exchanger which converts solar radiation into thermal energy [2]. A conventional solar air heater consists of a transparent cover or glazed, an absorber plate, a base plate, and a box covered with insulation. The absorber plate is a thin metal sheet which is 1 mm in thickness. It is painted black and placed in a certain space beneath the cover plate. A thin metal sheet is provided as the base plate beneath the absorber plate and

D. K. Rabha (✉) · D. Pathak · R. Baruah · T. Kalita · A. Sharma
Department of Mechanical Engineering, Jorhat Engineering College, Jorhat, Assam 785007, India
e-mail: devaktra@gmail.com

571

above the insulation. The bottom and sides of the box are insulated to reduce heat losses [3].

Solar air heaters are inexpensive and easy for designing and maintenance. However, the poor heat transfer from the surface of the absorber plate to the air is one of the main limitations of the solar air heater. To improve heat transfer, many kinds of solar air heaters such as single-pass heater, double-pass heater, matrix-type heater, finned plate heater, corrugated-plate heater, and glazed and unglazed heater have been designed and developed [4].

The unglazed transpired solar air heater is one of the low-cost solar air heaters. It does not have any transparent cover and is widely used for space heating in cold countries and crop drying. The absorber plate of the unglazed solar heater is generally perforated, and it is directly exposed to the solar radiation. Numerous studies on unglazed solar air heaters are reported in the literature. Burch et al. [5] presented a simulation model of an unglazed solar heater which was used for space heating and domestic hot water production. Golneshan and Nemati [6] reported that the thermal effectiveness of the unglazed solar air heater should be equal to 0.457 for the maximum exergy efficiency. Badache et al. [7] investigated the performance of a perforated unglazed solar air heater both experimentally and numerically and reported that the efficiency of the heater increased with increase in the mass flow rate of air. Vaziri et al. [8] estimated the performance a glazed and an unglazed solar air heater with perforated absorber plates at the air flow rate varying between 0.017 and 0.036 kg/s and reported that the maximum efficiency of the unglazed transpired solar air heater was 50%. Decker et al. [9] developed a mathematical model for predicting the thermal effectiveness of an unglazed solar air heater with circular holes absorber plate, and the model could predict the effectiveness of the unglazed solar air heater suitably. Stojanovic et al. [10] applied the fin theory approach to develop a one-dimensional analytical thermal model of an unglazed solar air heater which can be used for design optimisation of unglazed transpired solar air heaters. It can also be used for calculating energy performance and temperature profile of the heater fluid. Croitoru et al. [11] tested an unglazed solar air heater with a perforated absorber plate used for the building heating application. The investigator reported that the newly developed solar air heater was more efficient (around 40%) than the conventional unglazed transpired solar air heater. Rad and Ameri [12] developed a mathematical model of an unglazed two stage solar air heater and validated the model with experimental results. They also reported that the developed model had 10% error with the experimental data. Gao et al. [13] simulated an unglazed solar air heater numerically applying field energy–synergy principle and reported that the heat transfer rate improved with a good synergy between the temperature and velocity. Collins and Abulkhair [14] developed a model of a perforated unglazed solar air heater with trapezoidal corrugation for investigating the heat losses and the effectiveness of the heater. The authors developed a correlation between the heat loss and the effectiveness. Paya-Marin et al. [15] developed a wall integrated non-perforated back-pass unglazed solar air heater. They reported that the outlet temperature of the heater was affected by the solar radiation intensity, air flow rate, and the height of the heater.

The suitable air temperature for drying fruits and agricultural products varies from 45 to 60 °C [16] The air of this temperature range can be easily generated in glazed solar air heaters. However, the cost of the glazed solar air heater is comparatively higher. In addition, the breakage of the cover plate due to the hailstorm is a major problem associated with glazed solar air heaters, especially in regions where hailstorm occurs frequently during a certain period of the year.

The heat transfer rate in the solar air heater can be improved by circulating air above and below the absorber plate. The solar air of this kind is known as the double-pass solar air heater [17–20]. It is observed that all the studies on the unglazed solar air heater reported in the literature are of the single-pass type with perforated absorber plates. There is no study on the double-pass unglazed solar air heater reported in the literature. Therefore, the objective of this study is to develop and investigate the performance of a double-pass unglazed solar heater. In this study, an unglazed solar air heater has been developed in such a way that the air can be circulated twice (double pass) in the heater. The performance of the air heater has been investigated by the energy and exergy analysis.

## 2 Unglazed Double-Pass Solar Air Heater and Experimental Set-up

The photograph of the developed unglazed double-pass solar air heater is shown in Fig. 1. It consists of a black absorber plate, a base plate, and a wooden box. The size of the absorber plate of the heater is 1 m × 2 m. The absorber plate of the heater is a plane mild steel sheet of 10.2 mm in thickness, and six rectangular channels are welded to the plate in equal space. The size of each rectangular
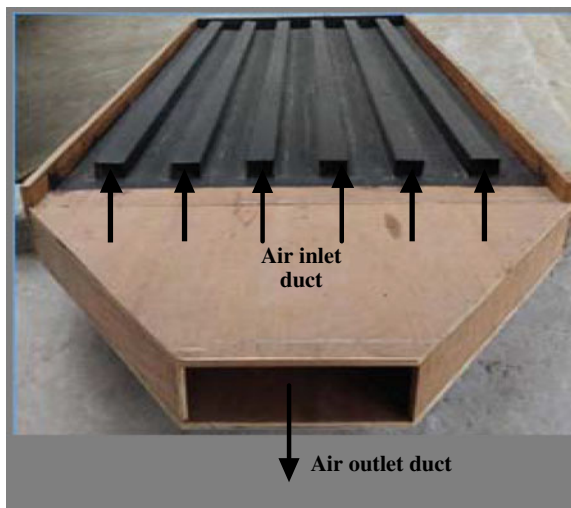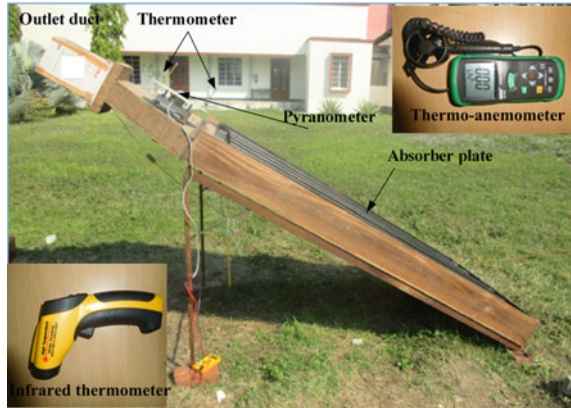
**Fig. 1** A photograph of the air heater

**Fig. 2** Experimental set-up
with measuring instruments



channel is 60 mm in width and 40 mm in height. The channels are also made of the same material as the main plate. The channels are the first path of the air flow. First, the ambient air is passed through the rectangular channels and is heated up due to the convective and radiative heat transfers from the plate to the air. Then, the heated air flows through the rectangular holes provided at the end of each channel and enters the chamber below formed by the absorber plate and the base plate. The air is further heated up as it flows through the chamber. The hot air is continuously sucked by a fan through the outlet duct.

In the experimental set-up (Fig. 2), an exhaust fan of 150 mm in diameter having five blades and consuming a power of 24 W was used to circulate the air through the solar air heater. It sucks the heated air from the solar air heater. The mass flow rate of air was varied with a damper provided with the fan. The solar radiation intensity was measured with a pyranometer (thermoelectric pyranometer, model: M-304, make: National Instrument Laboratory). The inlet and outlet temperatures were measured with glass thermometers (measuring range −10 to 100 °C; accuracy ±1 °C). A non-contact-type infrared thermometer (operating range −50 to 1000 °C; accuracy ±1.5%; make: HTA Instrumentation (p) Ltd; model no. EQ: 8839) was to measure the surface temperature of the absorber plate. The wind velocity and the average velocity of air at the outlet of the fan were measured with a digital thermo-anemometer (accuracy ±0.1%; operating range 0–45 m/s; model: Equinox EQ-618B; make: HTA Instrumentation (p) Ltd).

## 3 Energy and Exergy Analyses

The energy analysis of the solar air heaters was carried out primarily based on the general mass and energy conservation equations. The mass conservation equation is written as:

$$\dot{m}_{ia} = \dot{m}_{oa} = \dot{m}_{a} \tag{1}$$

The energy conservation equation of the solar air heater is written as:

$$\dot{Q}_{in} - \dot{Q}_{ls} = \dot{m}_{a}(h_{oa} - h_{ia}) \tag{2}$$

The heat input to the solar air heater is given by:

$$\dot{Q}_{in} = IA_{SAH} \tag{3}$$

The total heat loss ($\dot{Q}_{ls}$) from the solar air heater is caused by radiation loss, convection loss, and conduction losses through the bottom and sides of the heater. The right-hand part of Eq. (2) is known as the useful heat gained of the SAH, and it can be estimated by Eq. (4) [21].

$$\dot{Q}_{uSAH} = \dot{m}_{a}c_{pa}(T_{o} - T_{i}) \tag{4}$$

The energy efficiency of the solar air heater is calculated by Eq. (5) [22].

$$\eta_{en} = \frac{\dot{m}_{a}c_{pa}(T_{o} - T_{i})}{A_{SAH}I} \tag{5}$$

The performance of the unglazed solar air heater is also usually expressed by thermal effectiveness. It is defined as the ratio of actual temperature rise of air in the air heater to the maximum possible temperature rise and is estimated by Eq. (6) [6].

$$\varepsilon = \frac{T_{o} - T_{amb}}{T_{s} - T_{amb}} \tag{6}$$

The exergy received by the working fluid (air) of the SAH is given by Eq. (7)

$$\dot{Ex}_{re} = \dot{m}_{a}c_{pa}\left[(T_{o} - T_{i}) - T_{r}\ln\left(\frac{T_{o}}{T_{i}}\right)\right] \tag{7}$$

The exergy inflow of the SAH is evaluated by Eq. (8) [23].

$$\dot{Ex}_{in} = \left[1 - \frac{T_{r}}{T_{sun}}\right]\dot{Q}_{in} \tag{8}$$

$T_{sun}$ is the apparent sun temperature and is assumed to be 4500 K [24]. The exergy efficiency of the solar air heater is expressed as follows [25]:

$$\eta_{ex} = 1 - \frac{\dot{Ex}_{dest}}{\dot{Ex}_{in}} \tag{9}$$

**Table 1** Uncertainty in the independent variables and some of the dependent variables

| Parameters | Uncertainty |
|---|---|
| Uncertainty in the air temperature measurement (°C) | ±0.1 |
| Uncertainty in the surface temperature measurement (°C) | ±0.015 |
| Uncertainty in the solar radiation measurement (W) | ±1.3 |
| Uncertainty in the measurement of velocity (m/s) | ±0.001 |
| Uncertainty in the mass flow rate of air (%) | ±0.6 |
| Uncertainty in the energy efficiency (%) | ±6.2 |
| Uncertainty in the exergy efficiency (%) | ±3.4 |
| Uncertainty in the thermal effectiveness (%) | ±1.1 |

$$\text{Or } \eta_{\text{ex}} = \frac{\dot{\text{Ex}}_{\text{re}}}{\dot{\text{Ex}}_{\text{in}}} \tag{10}$$

The exergy destruction in the solar heater is given by Eq. (11) [26].

$$\dot{\text{Ex}}_{\text{dest}} = \left(1 - \frac{T_{\text{r}}}{T_{\text{sun}}}\right)\dot{Q}_{\text{in}} - \dot{m}_{\text{a}}c_{\text{pa}}\left[(T_{\text{o}} - T_{\text{i}}) - T_{\text{r}}\ln\left(\frac{T_{\text{o}}}{T_{\text{i}}}\right)\right] \tag{11}$$

Uncertainty in any measurement occurs due to calibration, observation, wear and tear, sensitivity drift, etc. The various independent operating parameters measured during this experiment were the temperature of the air, the surface temperature of the absorber plate, the mass flow rate of the air, and the solar radiation intensity. The uncertainties in the independent variables are given in Table 1. The uncertainties in the dependent parameters are calculated by employing Eq. (12). If an experimental result $N$ is a given function of independent variables $X_1, X_2, X_3, \ldots, X_n$, and if $\Delta N$ is the uncertainty in the results and $\Delta N_1, \Delta N_2, \Delta N_3, \ldots, \Delta N_n$ are the uncertainties in the independent variables, then the uncertainty in the results is given by the following equation [27]:

$$\Delta N = \left[\left(\frac{\partial N}{\partial X_1}\Delta N_1\right)^2 + \left(\frac{\partial N}{\partial X_2}\Delta N_2\right)^2 + \left(\frac{\partial N}{\partial X_3}\Delta N_3\right)^2 + \cdots + \left(\frac{\partial N}{\partial X_n}\Delta N_n\right)^n\right]^{1/2} \tag{12}$$

The mass flow rate was determined by measuring the average velocity of air at the outlet of the fan. The mass flow rate was calculated by Eq. (13)

$$\dot{m}_{\text{a}} = \rho a v \tag{13}$$

Assuming that the density of air is the function of the air temperature, then the uncertainty in the measurement of the mass flow rate is given by:

$$\Delta \dot{m}_a = \pm \sqrt{\left(\frac{\partial \dot{m}_a}{\partial T} \Delta T\right)^2 + \left(\frac{\partial \dot{m}_a}{\partial v} \Delta v\right)^2 + \left(\frac{\partial \dot{m}_a}{\partial A} \Delta A\right)^2} \tag{14}$$

The uncertainty in the measurement of the efficiency of the solar air heater is given by:

$$\Delta \eta_{en} = \pm \sqrt{\left(\frac{\partial \eta_{en}}{\partial \dot{m}_a} \Delta \dot{m}_a\right)^2 + \left(\frac{\partial \eta_{en}}{\partial T_o} \Delta T_o\right)^2 + \left(\frac{\partial \eta_{en}}{\partial T_i} \Delta T_i\right)^2 + \left(\frac{\partial \eta_{en}}{\partial I} \Delta I\right)^2 + \left(\frac{\partial \eta_{en}}{\partial A_{SAH}} \Delta A_{SAH}\right)^2} \tag{15}$$

The uncertainty in the energy input is calculated by the following equation:

$$\Delta Q_{in} = \sqrt{\left(\frac{\partial Q_{in}}{\partial I} \Delta I\right)^2 + \left(\frac{\partial Q_{in}}{\partial A_{SAH}} \Delta A_{SAH}\right)^2} \tag{16}$$

The uncertainty in the measurement of the exergy efficiency of the solar air heater is estimated by Eq. (17).

$$\Delta \eta_{ex} = \pm \sqrt{\left(\frac{\partial \eta_{ex}}{\partial \dot{m}_a} \Delta \dot{m}_a\right)^2 + 2\left(\frac{\partial \eta_{ex}}{\partial T_o} \Delta T_o\right)^2 + 2\left(\frac{\partial \eta_{ex}}{\partial T_i} \Delta T_i\right)^2 + \left(\frac{\partial \eta_{ex}}{\partial Q_{in}} \Delta Q_{in}\right)^2} \tag{17}$$

The uncertainty in the measurement of the thermal effectiveness is obtained by:

$$\Delta \varepsilon = \pm \sqrt{\left(\frac{\partial \varepsilon}{\partial T_o} \Delta T_o\right)^2 + \left(\frac{\partial \varepsilon}{\partial T_s} \Delta T_s\right)^2 + 2\left(\frac{\partial \varepsilon}{\partial T_{amb}} \Delta T_{amb}\right)^2} \tag{18}$$

## 4  Results and Discussions

The air heater was oriented towards the south at the local latitude of 26°.75, Jorhat, India. The performance of the air heater was investigated at the air flow rates of 0.015 and 0.019 kg/s. The experiment was performed for four days consecutively (two days at the air flow rate of 0.015 kg/s and two days at the air flow rate of 0.019 kg/s) in the direct sun. The variation in the solar radiation intensity and the wind velocity is shown in Figs. 3 and 4. The solar radiation intensity varied between 400 and 926 $W/m^2$ with an average of 756 $W/m^2$. The maximum solar

**Fig. 3** Variation in the solar radiation intensity and the wind velocity ($\dot{m}_a = 0.015$ kg/s)
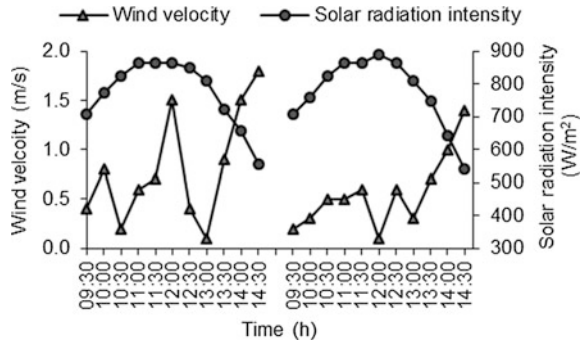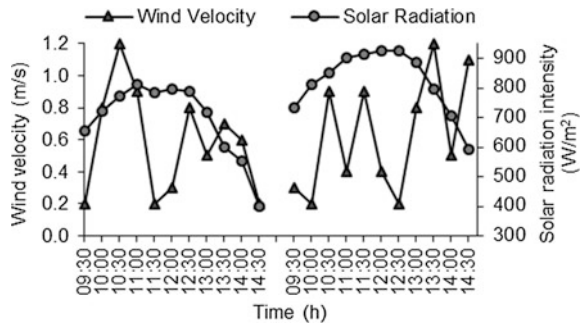


**Fig. 4** Variation in the solar radiation intensity and the wind velocity ($\dot{m}_a = 0.019$ kg/s)



radiation intensity was recorded between 12 and 13 h. The wind velocity varied between 0.2 and 1.2 m/s with an average of 0.6 m/s.

The surface temperature of the absorber plate was measured at three positions (S1, S2, and S3). One position was located in the middle of the plate (S2), and the other two positions were located at the two ends of the plate (S1 and S3). The S1 was located near the inlet and outlet of the air heater (since it is a double-pass air heater, the inlet and outlet are located at the same end of the heater). It was observed that the surface temperature of the absorber plate was different at different mass flow rates of air (Figs. 5 and 6). It was in the range of 44.8–63.3 °C with an average of 53.6 °C at the mass flow rate of 0.015 kg/s and was in the range of 41.1–56.3 °C with an average of 50.6 °C at the mass flow rate of 0.019 kg/s. As expected, the surface temperature of the absorber plate was higher at the lower air flow rate and increased with increase in the solar radiation intensity. The surface temperature at the middle position was higher than the temperature of the other two positions.

The variation in the inlet and outlet temperatures, average surface temperature of the absorber plate and the solar radiation intensity are shown in Figs. 7 and 8 at the air flow rate of 0.015 and 0.019 kg/s, respectively. The outlet temperature of the solar heater increased with increase in the solar radiation intensity. It varied

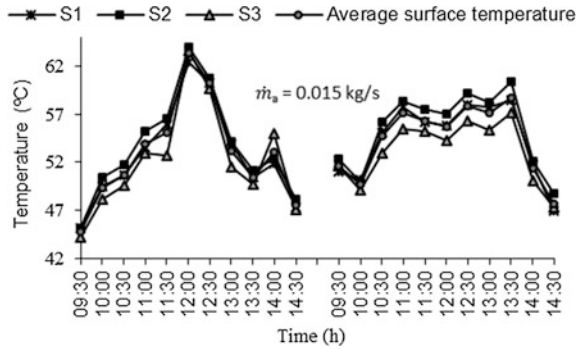**Fig. 5** Variation in the surface temperature of the absorber plate ($\dot{m}_a = 0.015$ kg/s)



**Fig. 6** Variation in the surface temperature of the absorber plate ($\dot{m}_a = 0.019$ kg/s)
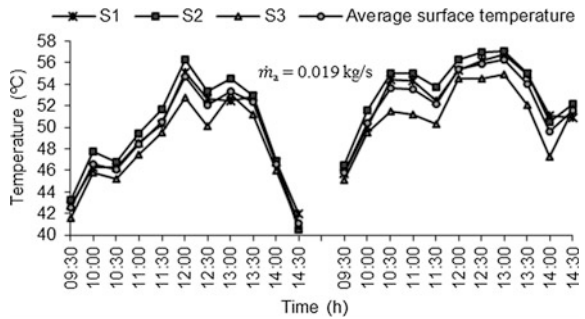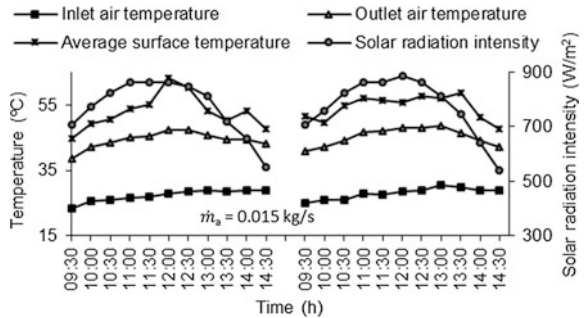


**Fig. 7** Variation in the inlet and outlet temperature, average surface temperature of the absorber plate, and the solar radiation intensity ($\dot{m}_a = 0.015$ kg/s)



between 38.8 and 49.3 °C and 36.0 and 46.8 °C at the air flow rate of 0.015 kg/s and 0.019 kg/s, respectively. A high outlet air temperature was observed at the low mass flow rate of air.

The average thermal effectiveness of the solar air heater was found to be 66.6 and 67.1% at the air flow rate of 0.015 and 0.019 kg/s, respectively. It is observed that the trends in the instantaneous thermal effectiveness curve and the absorber plate surface temperature curve are opposite. The thermal effectiveness decreases with increase in the surface temperature (Figs. 9 and 10). The useful heat gain

**Fig. 8** Variation in the inlet and outlet temperatures, average surface temperature of the absorber plate, and the solar radiation intensity ($\dot{m}_a = 0.019$ kg/s)
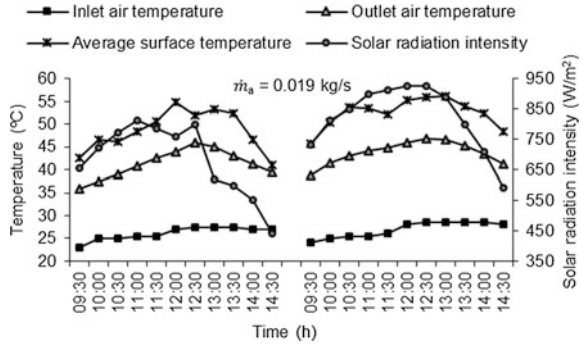


**Fig. 9** Variation in the outlet temperature, absorber plate surface temperature, and the thermal effectiveness ($\dot{m}_a = 0.015$ kg/s)
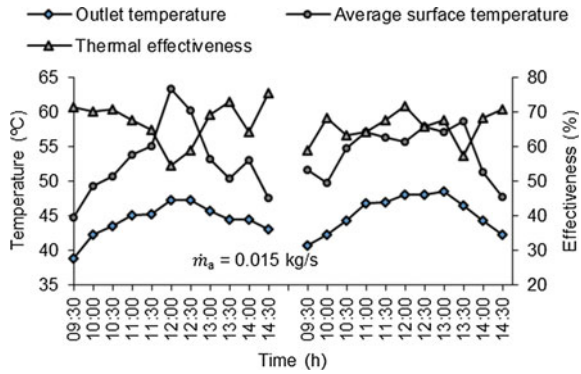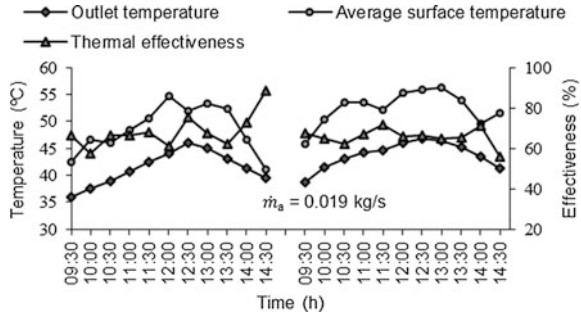


**Fig. 10** Variation in the outlet temperature, absorber plate surface temperature, and the thermal effectiveness ($\dot{m}_a = 0.019$ kg/s)



increases with increase in the surface temperature, while the thermal effectiveness decreases with increase in the surface temperature (Figs. 11 and 12).

The variation in the energy and exergy efficiencies with time is shown in Figs. 13 and 14. The energy efficiency of the heater at the air flow rate of 0.019 kg/s was found to be in the range of 16.6–24.7% with an average of 20.6%, and the exergy efficiency was in the range of 0.36–0.71% with an average of 0.57%. The energy efficiency of the heater at the mass flow rate of 0.015 kg/s was found to be in the

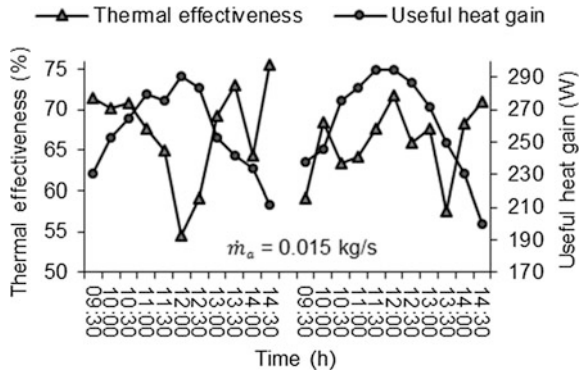**Fig. 11** Variation in the thermal effectiveness and the useful heat gain with time ($\dot{m}_a = 0.015$ kg/s)



**Fig. 12** Variation in the thermal effectiveness and the useful heat gain with time ($\dot{m}_a = 0.019$ kg/s)
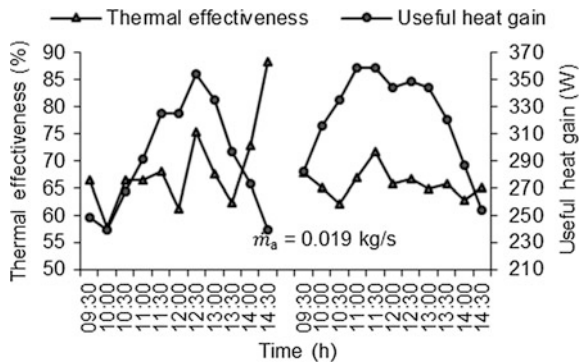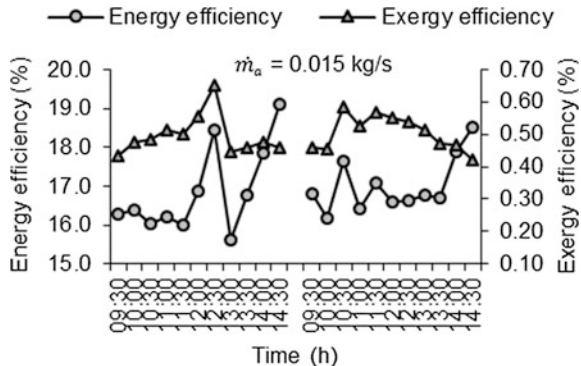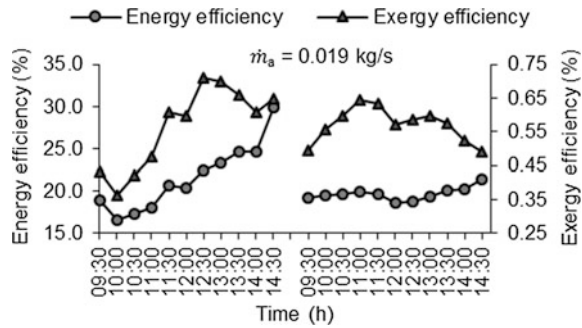


**Fig. 13** Variation in the energy and exergy efficiencies at the mass flow rate of 0.015 kg/s



range of 15.6–19.1% with an average of 16.9%, and the exergy efficiency was in the range of 0.42–0.65% with an average of 0.49%. It was observed that the energy and exergy efficiencies increased with increase in the mass flow rate of air through the air heater. The energy and exergy efficiencies also increased with increase in the solar radiation intensity.

**Fig. 14** Variation in the
energy and exergy efficiencies
at the mass flow rate of
0.019 kg/s



It is found that the energy efficiency of this unglazed solar heater is comparable to a conventional glazed solar air heater although it does not have any cover plate or glaze. The energy and exergy efficiencies are lower than the perforated absorber plate unglazed solar air heater. The low exergy efficiency may be due to the low surface temperature of the absorber plate since the re-radiation and convection losses are high in the case of the unglazed solar air heater. The energy efficiency of this solar air heater was found to be in the range of 15.6–19.1% at a air flow rate of 0.015 kg/s. Kurtbas and Durmus [28] and Sabzpooshani et al. [29] reported a similar range of energy efficiency, i.e. 12.9–19.1% at the air flow rate of 0.017 kg/s and 21.7% at the air flow rate of 0.016 kg/s for a conventional glazed solar air heater. The exergy efficiency of the developed heater was found to be slightly lower than the conventional solar air heater. The exergy efficiency of a conventional solar air heater reported by Sabzpooshani et al. [29] was 0.84% at the air flow rate of 0.016 kg/s. The average exergy efficiency of this unglazed solar air heater was 0.49% at the air flow rate of 0.015 kg/s and 0.57% at the air flow rate of 0.57%.

## 5  Conclusions

A double-pass unglazed transpired solar air heater was developed. The performance of the heater was investigated experimentally. The following observations have been made in this study.

- The energy efficiency of the solar heater increased with increase in the mass flow rate of air. The average energy efficiencies of the solar air heater were found to be 16.9 and 20.6% at the air flow rate of 0.015 and 0.019 kg/s, respectively.
- The average exergy efficiency was 0.49% at the air flow rate of 0.015 kg/s, while it was 0.57% at the air flow rate of 0.019 kg/s.
- The thermal effectiveness of the heater increased with increase in the mass flow rate of air and decreased with increase in the surface temperature of the absorber plate of the heater. The thermal effectiveness of the heater was 66.6 and 67.1% at the air flow rate of 0.015 and 0.019 kg/s, respectively.

# References

1. Aldabbagh LBY, Egelioglu F, Ilkan M (2010) Single and double pass solar air heaters with wire mesh as packing bed. Energy 35(9):3783–3787
2. Saxena A, Varun, El-Sebaii AA (2015) A thermodynamic review of solar air heaters. Renew Sustain Energy Rev 43:863–890
3. Sukhatme SP, Nayak JK (2008) Solar energy, principles of thermal collection and storage, 3rd edn. McGraw Hill Education Pvt. Ltd., New Delhi
4. Garg HP, Prakash J (2001) Solar energy fundamentals and applications, 1st revised edn. McGraw Hill Education Pvt. Ltd., New Delhi
5. Burch J, Christensen C, Salasovich J, Thornton J (2004) Simulation of an unglazed collector system for domestic hot water and space heating and cooling. Sol Energy 77(4):399–406
6. Golneshan AA, Nemati H (2014) Exergy analysis of unglazed transpired solar collectors (UTCs). Sol Energy 107:272–277
7. Badache M, Rousse DR, Halle S, Quesada G (2013) Experimental and numerical simulation of a two-dimensional unglazed transpired solar air collector. Sol Energy 93:209–219
8. Vaziri R, Ilkan M, Egelioglu F (2015) Experimental performance of perforated glazed solar air heaters and unglazed transpired solar air heater. Sol Energy 119:251–260
9. Decker GWEV, Hollands KGT, Brunger AP (2001) Heat-exchange relations for unglazed transpired solar collectors with circular holes on a square or triangular pitch. Sol Energy 71 (1):33–45
10. Stojanovic B, Hallberg D, Akander J (2010) A steady state thermal duct model derived by fin-theory approach and applied on an unglazed solar collector. Sol Energy 84:1838–1851
11. Croitorua C, Nastasea I, Voicub I, Meslemc A, Sandua M (2016) Thermal evaluation of an innovative type of unglazed solar collector for air preheating. Energy Procedia 85:149–155
12. Rad HM, Ameri M (2016) Energy and exergy study of unglazed transpired collector-2stage. Sol Energy 132:570–586
13. Gao L, Bai H, Wu X (2013) Numerical analysis of heat transfer in unglazed transpired collectors based on field synergy principle. Sol Energy 95:336–344
14. Collins MR, Abulkhair H (2014) An evaluation of heat transfer and effectiveness for unglazed transpired solar air heaters. Sol Energy 99:231–245
15. Paya-Marin MA, Lim JBP, Chen J, Lawson RM, Gupta BS (2015) Large scale test of a novel back-pass non-perforated unglazed solar air collector. Renew Energy 83:871–880
16. Agarwal A, Sarviya RM (2014) A review of research and development work on solar dryers with heat storage. Int J Sustain Energ 35:583–605
17. Ravi RK, Saini RP (2016) A review on different techniques used for performance enhancement of double pass solar air heaters. Renew Sustain Energy Rev 56:941–952
18. Ramani BM, Gupta A, Kumar R (2010) Performance of a double pass solar air collector. Sol Energy 84:1929–1937
19. El-khawajah MF, Aldabbagh LBY, Egelioglu F (2011) The effect of using transverse fins on a double pass flow solar air heater using wire mesh as an absorber. Sol Energy 85:1479–1487
20. Ho C, Lin C, Chuang Y, Chao C (2013) Performance improvement of wire mesh packed double-pass solar air heaters with external recycle. Renew Energy 57:479–489
21. Midilli A, Kucuk H (2003) Energy and exergy analyses of solar drying process of pistachio. Energy 28:539–556
22. Benli H (2013) Experimentally derived efficiency and exergy analysis of a new solar air heater having different surface shapes. Renew Energy 50:58–67
23. Yadav S, Kaushal M, Varun S (2014) Exergetic performance evaluation of solar air heater having arc shape oriented protrusions as roughness element. Sol Energy 105:181–189
24. Jafarkazemi F, Ahmadifard E (2013) Energetic and exergetic evaluation of flat plate solar collectors. Renew Energy 56:55–63
25. Akpinar EK, Koçyigit F (2010) Energy and exergy analysis of a new flat-plate solar air heater having different obstacles on absorber plates. Appl Energy 87:3438–3450

26. Esen H (2008) Experimental energy and exergy analysis of a double-flow solar air heater having different obstacles on absorber plates. Build Environ 43:1046–1054
27. Holman JP (1994) Experimental methods for engineers, 6th edn. McGraw Hill Book Co., Singapore
28. Kurtbas I, Durmus A (2004) Efficiency and exergy analysis of a new solar air heater. Renew Energy 29:1489–1501
29. Sabzpooshani M, Mohammadi K, Khorasanizadeh H (2014) Exergetic performance evaluation of a single pass baffled solar air heater. Energy 64:697–706

# Power Management and Energy Optimization in Hybrid Electric Vehicle—A Review

**Ravi Dutt Sharma** , **Dheeraj Sharma** , **Kartik Awasthi** and **Nazish Ahmad Shamsi**

**Abstract** The continuous depleting reserves of fossil fuel triggered the requirement of vehicles equipped or semi-equipped with alternative fuel resources. The dependence on fossil fuels could be reduced using an alternative method. The technology used in the hybrid electric vehicle might play an important role in preserving fossil fuel reserves and the environment simultaneously. A hybrid powertrain transmission utilizes an integrated assembly of renewable and non-renewable energy resources for power generation. It requires an accurate and flexible control system to achieve the required output. Typically, hybrid electric vehicles are furnished with IC engine and electrical storage devices like ultra-capacitors or batteries for power supply. The entire vehicle framework is preoccupied with one comprising of two power sources. This paper gives an overview of hybrid powertrain transmission along with a systematic review of energy optimization (EO) and power management (PM) strategies in terms of fuel consumption and emissions.

**Keywords** Hybrid powertrain control system · Regenerative brakes · IC engine · Power management · Energy optimization · Power-split device

## 1 Introduction

The focus of automakers shifted from traditional vehicles to hybrid electric vehicles (HEV) due to the stringent environmental norms imposed by several countries. Additionally, the fossil fuel reserves are limited and need to utilize elegantly. HEVs have the potential to remarkably improve fuel efficiency and drivability in typical road conditions. The architecture of such type of vehicles primarily based on multiple energy sources. Normally, required power for the vehicle is fetched from

R. D. Sharma · D. Sharma (✉) · K. Awasthi · N. A. Shamsi
Department of Mechanical Engineering, Manav Rachna University,
Faridabad, Haryana, India
e-mail: dheerajjangra68@gmail.com

internal combustion (IC) engine which is closely associated with an electric motor. Therefore, power generation and storage unit contain IC engine, fuel tanks, and a bunch of rechargeable batteries or supercapacitors. Another essential part of the hybrid power unit is energy converters [1]. Several authors presented an overview of HEV technology concerning the factors like the necessity of the development, classifications, types of batteries used, and electronic power converters [1–4]. Raslavičius et al. [5] proposed new algorithms for achieving better economic and ecological properties and their real-time assessment. Many optimization techniques were utilized for the estimation of fuel economy and energy optimization (EO) in different configurations of the HEVs [3, 6, 7]. Liu and Peng [8] proposed a power-split planetary gear model for acquiring the benefits of series and parallel systems combinedly along with high fuel economy in typical driving conditions. An intelligent power switching system is required to assist in changing the power mode as per the requirement. Also, optimum power output could be retrieved if EO and efficient power management (PM) system between two power sources are in place. This problem was addressed worldwide, and a large number of papers explaining different strategies for the same were published in different journals. The objective of the current article is to provide a comprehensive review of PM and EO techniques used in HEVs. A comparison of various PO strategies used recently in the HEVs is also provided in the present review. The usefulness of several algorithms, models, and approaches for the same is also discussed.

## 2   Battery Technologies Used in HEVs

As discussed in introduction section, typically two or more power sources are used in hybrid electric vehicles. The primary power source is IC engine, and its operation is properly synchronized with the power extracted from the batteries. The batteries used in the HEVs are essentially fallen into one of the following categories.

Lead acid batteries have low specific energy ranges in between 20 and 40 Wh/kg. The main disadvantages of lead acid batteries are heavy weight and poor longevity. As the cost is low, the batteries might be used in small-range vehicles [9].

Toyota Motor Corporation used nickel-metal hydride batteries in Toyota Prius model. The specific energy density of such type of batteries is ranging in between 60 and 80 Wh/kg. In terms of economy and technology, these batteries are costlier, and the technology is matured enough for further improvements. These batteries were rarely used in HEVs due to insufficient power output for driving a powertrain [9, 10].

Nowadays, most of the instruments powered by battery technology house Li-ion battery in it. It is compact in size with huge specific energy density (i.e., 100–265 Wh/kg). This is the most promising battery technology for future HEVs. It is relatively new technology, and the energy capacity might increase in future [9]. It has minimal maintenance requirements with a long lifespan [11, 12].

The state-of-the-art Li-ion batteries are suitable alternatives in multiple power source-driven powertrains.

Molten-salt electrolyte battery is one of the safest and low-cost battery technologies. Its specific power is lower than 150 W/kg and not considered for powering electric vehicles. It has a long lifespan with the ability to charge or discharge completely without hampering its life expectancy. In HEVs, it could be used as a power source when supercapacitors are associated with the batteries [9].

## 3 Hybrid Electric Vehicle

A HEV houses an IC engine and an electric propulsion unit. The inclusion of electric powertrain resulted in improved fuel economy and better performance than a conventional gasoline engine vehicle [13]. Most recent HEVs are also equipped with regenerative brakes which are capable of charging the battery from the vehicle's acceleration/deceleration. The emission is reduced by shutting down the IC engine when the vehicle is stuck in traffic. In HEVs, the IC engine would start and stop as per the requirement during driving. Therefore, the HEVs are producing less emission than its gasoline engine counterpart. The architect of HEVs is of three types, and a brief detail of all three is provided here.

### 3.1 Series Hybrid Drivetrain

In a series hybrid platform, the driveline is receiving power from an electric motor. The electric motor is receiving power either from a pack of batteries or from a generator. The generator is powered by a gasoline engine. The power output from generator not only runs electric motor but also recharges the batteries. It has a regenerative brake system which is also capable of recharging the batteries while breaking. The battery pack is more powerful in series hybrids than the parallel hybrid architect. The block diagram of series hybrid power transmission is shown in Fig. 1a [2, 14].

### 3.2 Parallel Hybrid Drivetrain

In parallel hybrid architect, the driveline is directly receiving power from the electric motor and IC engine concurrently. It has a smaller battery pack than the series hybrid architect, and only regenerative brake system is utilized for charging them. Direct attachment of IC engine to the driveline facilitated the conversion process of mechanical energy into electricity resulted in improved vehicle
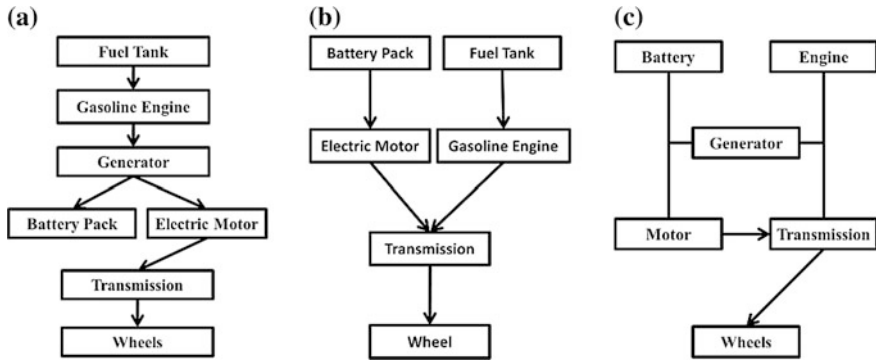
**Fig. 1** Schematic diagrams of **a** series, **b** parallel, and **c** series–parallel hybrid configuration

efficiency. The block diagram of parallel hybrid powertrain transmission is shown in Fig. 1b [2, 13].

### 3.3 Series–Parallel Drivetrain

The benefits of series and parallel powertrains are merged in series–parallel powertrain system. In this architect, the driveline can extract energy from IC engine, electric motor, and a combination of both as per the necessity (shown in Fig. 1c). At slow speeds, it can take advantage of series hybrid, whereas at high speeds, parallel hybrid drivetrain serves the needs. The use of generator, larger battery pack, and complicated PM system make it costlier than other two alternatives [13]. A power-split device is required for smooth functioning of a series–parallel hybrid drivetrain. It helps to effortlessly operate the vehicle in series hybrid mode or parallel hybrid mode or combined mode [15]. Besides, incorporation of some advanced technologies such as electric motor drive, regenerative braking, automatic power on/off, vehicle-to-vehicle communication, and automated manual transmission (AMT) is flourishing the advancement of HEVs in a rapid pace [2].

## 4 Power Management (PM) and Energy Optimization (EO)

As already discussed in the previous section, different configurations of HEVs needed distinctive power control strategies for smooth functioning and regulation of power in various components [2]. The primary objectives of the PM and EO techniques are to achieve highest fuel economy, lower emissions, minimum maintenance cost, improved driving performance, and efficient temperature control.

A dynamic balance between the utilization of engine power and battery power not only reduces the load on the engine but also minimizes the harmful emissions by the lesser burning of fuel. The EO is a mammoth task in HEVs owing to complicated arrangements of two power sources which are all the configurations (shown in Fig. 1). Various algorithms were utilized by several authors for the formulation of proper PM or EO strategies for different drivetrain HEVs. Moura et al. [16] studied the optimization of PM in a plug-in hybrid electric vehicle (PHEV). They did a stochastic dynamic programming (DP) to evaluate the fuel and electricity usage in PHEV when PM was optimized. They achieved higher engine efficiency with slow battery drainage. Brahma et al. [17] studied the optimization and energy management (EM) in series hybrid electric vehicles (SHEV). They used a rule-based approach using DP for optimizing the power splitting among energy sources, electric machines, and battery efficiencies. A proper balance of accuracy and speed could be achieved using precise level of state variable discretization. Perez et al. [18] optimized the power-split arrangement in HEV using DP. The main advantage of this algorithm is the prevention of switching nonlinearities effectively. Musardo et al. [19] described a new adaptive equivalent consumption minimization strategy (ECMS). They found suboptimal EM, and the operations are charge-sustaining. Lin et al. [20] presented a near-optimal PM strategy in HEVs concerning the power split between the engine and motor and gear-shifting sequence using DP. They found that harmful emission is significantly reduced (10.3% lower particulate matter and 17.3% lower $NO_x$ emission) with slightly high fuel consumption. Banvait et al. [21] discussed a rule-based EM strategy for a PHEV. This rule-based EM strategy primarily based on strategies like charge-depletion/sustaining and electric assist. The mileage of the vehicle is increased about 16% by the implementation of this strategy in PHEV. Bashash et al. [22] studied the problem of optimization in the charge pattern of a PHEV. They reiterated already-developed PM strategy and Li-ion batteries' life degradation. They obtained a new Pareto front of optimal charge patterns. This Pareto front indicated that energy cost and battery degradation could minimize if PHEV was adequately charged just before the travel started. Lin et al. [23] discussed a stochastic optimization model for the PM in HEVs. The simulation was conducted for standard and random driving cycles to check the effectiveness of the approach. This approach of control algorithm outperforms a suboptimal rule-based control strategy. Borhan et al. [24] formulated a nonlinear and constrained optimal control for the EM in a power-split HEV. An optimal EM in HEVs is a challenge owing to multiple modes of operation. The implemented nonlinear model predictive control (MPC) strategy exhibited remarkable improvement in fuel economy. Borhan et al. [25] devised a model to solve the optimal EM problem using MPC strategy in power-split HEVs. Their results indicated better fuel economy over multiple driving cycles. Also, they claimed that the proposed algorithm might implement for real-time situations. Rodatz et al. [26] presented PM in a fuel cell supercapacitor powered hybrid vehicle in real-time operation. They proposed an equivalent consumption minimization strategy (ECMS) for PM in hybrid vehicles. Optimum fuel efficiency was achieved using slightly optimized fuel cells in ECMS. Lai and Nelson [27] discussed the

**Table 1** An overview of power management and energy optimization techniques exercised so far

| S. No. | Hybrid vehicle | Optimization | Energy management (EM) strategy | Result obtained | Ref. |
|---|---|---|---|---|---|
| 1 | PHEV | Battery voltage and state of charge | Fuzzy logic EM system | High fuel efficiency Battery over-discharging prevention | [34] |
| 2 | Fuel cell HV | Parameterizable electronic controller | Stochastic dynamic programming (DP) | Excellent fuel economy Fuel cell compressor downsizing Utilization of regenerative braking | [35] |
| 3 | Parallel HEV | Power electronic controller | Fuzzy logic-based EM | Improvement over other strategies that only optimize the IC engine efficiency | [36] |
| 4 | Parallel HEV | Optimization of control parameters | Genetic algorithm-based electric assist control strategy (EACS) | Reduced fuel consumption (27.65%) and emissions (18.35% HC, 25.30% CO, 35.35% NOx) | [37] |
| 5 | Power-split PHEV | Online intelligent EM controller | Genetic algorithm and quadratic programming | High efficiency of engine Reduce fuel consumption | [38] |
| 6 | Feed-forward parallel HEV | Fundamental architecture | Rule-based and DP algorithm | Improved fuel economy in urban driving cycle | [39] |
| 7 | Series PHEV (bus) | Tank to wheel energy conversion efficiency | Convex modeling-based algorithm | Tradeoff between the battery downsizing and energy efficiencies | [40] |
| 8 | Power-split PHEV | EM electronic controller | DP and neural networks | Improved fuel economy | [41] |
| 9 | PHEV | Battery sizing, charging, and on-road PM | Convex programming | On-road PM strategy assisted in reduced emissions (max. 0.84% $CO_2$) | [42] |
| 10 | PHEV | Energy flow management | Genetic algorithm | Lower harmful gas emission (17% lower CO) | [43] |
| 11 | Series HEV | Power distributions | Stochastic model predictive control (SMPC) for PM | The PM is governed in a causal, time-invariant, state-feedback way | [44] |
| 12 | PHEV | Fuel consumption and emissions | Model-based control approach supervisory EM | Fuel consumption and $CO_2$ emissions are affected by the driving cycle characteristics | [45] |

importance of power converters and their circuitry employed for EM in hybrid electric/fuel cell vehicles. Moreno et al. [28] developed a very efficient EM system for HEVs using neural networks (NNs). This system not only reduced the energy requirement but also able to work with alternate power sources. Lin et al. [29] suggested a strategy for the improvement in EM in a PHEV truck using DP optimization. This new EM strategy showed better fuel efficiency via simulations. Gong et al. [30] studied and optimized the PM of PHEVs in the charge-depletion mode. The proposed DP algorithm provided significant improvement and consistency in fuel efficiency in comparison with rule-based and depletion sustenance control. He et al. [31] presented an EO strategy for a power-split drivetrain PHEV. The highest fuel efficiency of 14–31% was reported for urban dynamometer driving schedule (UDDS). Mets et al. [32] investigated the advantages of control mechanisms in the situations where energy consumption is optimized for PHEVs. A quadratic programming-based smart energy control strategies for lower peak loading were put forward by the authors for charging. Moura et al. [33] tried to establish a dynamic balance between the algorithm formulated for PM and energy-holding capacity of commonly used batteries in PHEV. They suggested that a low-power battery could be used if an adequate algorithm for PM catering all the energy needs of vehicle is utilized. Brief reviews of different strategies proposed by other authors are listed in Table 1.

From the discussion, it could be inferred that the outcomes of almost all the PM strategies used in the literature are fuel economy, low greenhouse gas emission, and improved drivability. Also, stochastic-based approaches are better than rule-based approaches with all the algorithms used. It was also noted that the fuel economy or harmful gas emission or both are primarily dependent on driving cycle characteristics of the vehicle. This article is an endeavor to summarize the development of strategies used for PM or EO in complex HEVs structures concerning fuel economy, reduced environmental impact, reduced cost of fabrication, and improved driving comfort.

## 5 Conclusion

In this article, an overview of PM and EO techniques for latest HEVs is discussed. This review exhibited that different PM strategies are required for different configuration of HEVs. However, if the EO strategy is working well in the series hybrid vehicle, it is not necessary that it will work for parallel or combined hybrid configurations. Multiple PM strategies were formulated using a different algorithm for different configurations. Furthermore, the power flow control in different components of various HEVs for EO has also been summarized. Finally, it was found that the stochastic approach of strategy formulation for PM is better than rule-based and depletion sustenance control-based approach in modern HEVs. An efficient engine performance along with low battery drainage was reported for stochastic dynamic programming-based PM. Therefore, the presence of efficient

power management and energy optimization in HEVs can provide fuel economy, low greenhouse gas emission, and improved drivability. The appropriateness of EO and PM strategies under different driving conditions needs to consider as sometimes it may exhibit unpredictable response from the original driving cycle. Battery technology needs to grow further as high-capacity batteries are required to optimize the power and reduce the load on IC engine in HEVs.

# References

1. Kebriaei M, Niasar AH, Asaei B (2015) Hybrid electric vehicles: an overview. In: IEEE international conference on connected vehicles and expo (ICCVE), pp 299–305
2. Chau KT, Wong YS (2002) Overview of power management in hybrid electric vehicles. Energy Convers Manage 43:1953–1968
3. Shen C, Shan P, Gao T (2011) A comprehensive overview of hybrid electric vehicles. Int J Veh Technol 2011:1–7
4. Momoh OD, Omoigui MO (2009) An overview of hybrid electric vehicle technology. In: IEEE vehicle power and propulsion conference (VPPC'09), pp 1286–1292
5. Raslavičius L, Keršys A, Makaras R (2017) Management of hybrid powertrain dynamics and energy consumption for 2WD, 4WD, and HMMWV vehicles. Renew Sustain Energy Rev 68:380–396
6. Kepple BE (2010) The triple hybrid electric vehicle. In: IEEE 20th Australasian universities power engineering conference (AUPEC), pp 1–6
7. Sciarretta A, Guzzella L (2007) Control of hybrid electric vehicles. IEEE Control Syst 27:60–70
8. Liu J, Peng H (2008) Modeling and control of a power-split hybrid vehicle. IEEE Trans Control Syst Technol 16:1242–1251
9. Andwari AM, Pesiridis A, Rajoo S, Martinez-Botas R, Esfahanian V (2017) A review of battery electric vehicle technology and readiness levels. Renew Sustain Energy Rev 78:414–430
10. Offer GJ, Howey D, Contestabile M, Clague R, Brandon NP (2010) Comparative analysis of battery electric, hydrogen fuel cell and hybrid vehicles in a future sustainable road transport system. Energy Policy 38:24–29
11. Liu G, Ouyang M, Lu L, Li J, Hua J (2015) A highly accurate predictive-adaptive method for lithium-ion battery remaining discharge energy prediction in electric vehicle applications. Appl Energy 149:297–314
12. Schuster SF, Brand MJ, Berg P, Gleissenberger M, Jossen A (2015) Lithium-ion cell-to-cell variation during battery electric vehicle operation. J Power Sources 297:242–251
13. Kumar MS, Revankar ST (2017) Development scheme and key technology of an electric vehicle: an overview. Renew Sustain Energy Rev 70:1266–1285
14. Evangelou SA, Shabbir W (2016) Dynamic modeling platform for series hybrid electric vehicles. IFAC-Pap 49:533–540
15. Cao J, Peng J, He H (2016) Modeling and simulation research on power-split hybrid electric vehicle. Energy Procedia 104:354–359
16. Moura SJ, Fathy HK, Callaway DS, Stein JL (2011) A stochastic optimal control approach for power management in plug-in hybrid electric vehicles. IEEE Trans Control Syst Technol 19:545–555

17. Brahma A, Guezennec Y, Rizzoni G (2000) Optimal energy management in series hybrid electric vehicles. In: IEEE American control conference, pp 60–64

18. Pérez LV, Bossio GR, Moitre D, García GO (2006) Optimization of power management in an hybrid electric vehicle using dynamic programming. Math Comput Simul 73:244–254

19. Musardo C, Rizzoni G, Guezennec Y, Staccia B (2005) A-ECMS: an adaptive algorithm for hybrid electric vehicle energy management. Eur J Control 11:509–524

20. Lin C-C, Peng H, Grizzle JW, Kang J-M (2003) Power management strategy for a parallel hybrid electric truck. IEEE Trans Control Syst Technol 11:839–849

21. Banvait H, Anwar S, Chen Y (2009) A rule-based energy management strategy for plug-in hybrid electric vehicle (PHEV). In: IEEE American control conference ACC'09, pp 3938–3943

22. Bashash S, Moura SJ, Forman JC, Fathy HK (2011) Plug-in hybrid electric vehicle charge pattern optimization for energy cost and battery longevity. J Power Sources 196:541–549

23. Lin C-C, Peng H, Grizzle JW (2004) A stochastic control strategy for hybrid electric vehicles. In: IEEE American control conference, pp 4710–4715

24. Borhan H, Vahidi A, Phillips AM, Kuang ML, Kolmanovsky IV, Di Cairano S (2012) MPC-based energy management of a power-split hybrid electric vehicle. IEEE Trans Control Syst Technol 20:593–603

25. Borhan HA, Vahidi A, Phillips AM, Kuang ML, Kolmanovsky IV (2009) Predictive energy management of a power-split hybrid electric vehicle. In: IEEE American control conference (ACC'09), pp 3970–3976

26. Rodatz P, Paganelli G, Sciarretta A, Guzzella L (2005) Optimal power management of an experimental fuel cell/supercapacitor-powered hybrid vehicle. Control Eng Pract 13:41–53

27. Lai J-S, Nelson DJ (2007) Energy management power converters in hybrid electric and fuel cell vehicles. Proc IEEE 95:766–777

28. Moreno J, Ortúzar ME, Dixon JW (2006) Energy-management system for a hybrid electric vehicle, using ultracapacitors and neural networks. IEEE Trans Ind Electron 53:614–623

29. Lin C-C, Kang J-M, Grizzle JW, Peng H (2001) Energy management strategy for a parallel hybrid electric truck. In: IEEE American control conference, pp 2878–2883

30. Gong Q, Li Y, Peng Z-R (2008) Trip-based optimal power management of plug-in hybrid electric vehicles. IEEE Trans Veh Technol 57:3393–3401

31. He Y, Chowdhury M, Pisu P, Ma Y (2012) An energy optimization strategy for power-split drivetrain plug-in hybrid electric vehicles. Transp Res Part C Emerg Technol 22:29–41

32. Mets K, Verschueren T, Haerick W, Develder C, De Turck F (2010) Optimizing smart energy control strategies for plug-in hybrid electric vehicle charging. In: IEEE network operations and management symposium workshops (NOMS), pp 293–299

33. Moura SJ, Callaway DS, Fathy HK, Stein JL (2010) Tradeoffs between battery energy capacity and stochastic optimal power management in plug-in hybrid electric vehicles. J Power Sources 195:2979–2988

34. Li SG, Sharkh SM, Walsh FC, Zhang C-N (2011) Energy and battery management of a plug-in series hybrid electric vehicle using fuzzy logic. IEEE Trans Veh Technol 60:3571–3585

35. Kim M-J, Peng H (2007) Power management and design optimization of fuel cell/battery hybrid vehicles. J Power Sources 165:819–832

36. Schouten NJ, Salman MA, Kheir NA (2003) Energy management strategies for parallel hybrid vehicles using fuzzy logic. Control Eng Pract 11:171–177

37. Montazeri-Gh M, Poursamad A, Ghalichi B (2006) Application of genetic algorithm for optimization of control strategy in parallel hybrid electric vehicles. J Frankl Inst 343:420–435

38. Chen Z, Mi CC, Xiong R, Xu J, You C (2014) Energy management of a power-split plug-in hybrid electric vehicle based on genetic algorithm and quadratic programming. J Power Sources 248:416–426

39. Lin C-C, Filipi Z, Wang Y, Louca L, Peng H, Assanis DN, Stein J (2001) Integrated, feed-forward hybrid electric vehicle simulation in SIMULINK and its use for power management studies. SAE Technical Paper

40. Hu X, Murgovski N, Johannesson L, Egardt B (2013) Energy efficiency analysis of a series plug-in hybrid electric bus with different energy management strategies and battery sizes. Appl Energy 111:1001–1009
41. Chen Z, Mi CC, Xu J, Gong X, You C (2014) Energy management for a power-split plug-in hybrid electric vehicle based on dynamic programming and neural networks. IEEE Trans Veh Technol 63:1567–1580
42. Hu X, Moura SJ, Murgovski N, Egardt B, Cao D (2016) Integrated optimization of battery sizing, charging, and power management in plug-in hybrid electric vehicles. IEEE Trans Control Syst Technol 24:1036–1043
43. Piccolo A, Ippolito L, zo Galdi V, Vaccaro A (2001) Optimisation of energy flow management in hybrid electric vehicles via genetic algorithms. In: IEEE advanced intelligent mechatronics, pp 434–439
44. Ripaccioli G, Bernardini D, Di Cairano S, Bemporad A, Kolmanovsky IV (2010) A stochastic model predictive control approach for series hybrid electric vehicle power management. In: IEEE American control conference (ACC), pp 5844–5849
45. Stockar S, Marano V, Canova M, Rizzoni G, Guzzella L (2011) Energy-optimal control of plug-in hybrid electric vehicles for real-world driving cycles. IEEE Trans Veh Technol 60:2949–2962

# Computational Analysis of Active and Passive Evacuated Tube Solar Collector

**Harender, Dhruv Mittal, Deepank Deo, S. Aditya and Arvind Kumar**

**Abstract** A computational study on active and passive evacuated tube solar collector system is examined in this paper. The paper gives us an understanding of the performance of the ETC system under natural flow as well as forced circulation. Major parameters for useful solar thermal energy gain by evacuated tube solar collector are tilt angle, mass flow rate and specific heat capacity of working fluid. To make sure that the system receives maximum useful heat gain, the optimum mass flow rate has been analyzed using ANSYS Fluent CFD. Thermal efficiency of active evacuated tube solar collector at optimum mass flow rate is compared with thermal efficiency of passive evacuated tube solar collector. It is observed from the numerical modeling of the evacuated tube solar collector that passive system is more efficient than active system.

**Keywords** Solar energy · Solar collector · CFD

## 1 Introduction

The sun emits $3.8 \times 1020$ MW energy in all the directions, and $1.7 \times 1014$ kW solar energy is intercepted by the earth [1]. Solar energy accounts for less than 1% of the total energy produced in India [2]. By using the solar energy for different applications, dependency on foreign country for fossil fuel would be overcome. In India, solar energy is being used for water heating and photovoltaic systems mainly since last decade. Firstly, proposed by Speyer (1965), the development for evacuated tube collectors was initially hampered by the high cost of manufacturing complex metal heat extraction manifolds [3]. A number of heat extraction manifold

Harender (✉) · D. Mittal · D. Deo · S. Aditya · A. Kumar
Mechanical Engineering Department, Shiv Nadar University, Greater Noida 201314, India
e-mail: harender@snu.edu.in

designs for a single-ended evacuated tube were investigated by Window et al. and Yin et al. [4]. The development of low-cost manufacturing processes for evacuated tubular solar collectors has been the main feature about the recent changes in the solar water heater market [5].

To maximize the absorption of solar radiation and on the basis of maximum useful heat gain, there are different types of solar collectors [6]. The stationary designs of solar collectors are classified into two general types of solar collectors, i.e., flat plate solar collector and evacuated tube solar collector. In flat plate collectors, the sun rays fall on a flat surface while the fluid that has to be heated is passed through the pipes connected to the flat surface [7]. In evacuated tube collector, absorber tube is covered by glass cover having vacuum between absorber tube and glass cover [8]. Furthermore, flat plate collectors are only useful for warm and high radiation receiving areas and comparatively less efficient in cold and cloudy atmosphere [9]. The vacuum between two glasses in evacuated tube solar collector minimizes the heat losses due to convection and conduction [10].

ETCs can be divided further into two systems, i.e., active and passive systems [11]. Active system works well in climates where temperature is cold and sunlight is rarely available [12]. Mazarron et al. [13] concluded that investment in a properly sized active solar water heating system generates savings around 15–23% and fuel consumption can be reduced by 70%. Passive system relies on natural convection to circulate the water and is generally less costly than active systems, but usually not as proficient. However, passive frameworks can be more reliable [14].

The principle of the passive system or thermosiphon is that cold water has a higher specific density than warm water, and so being heavier will sink down [15]. Therefore, the collector is always mounted below the water storage tank, so that cold water from the tank reaches the collector via a descending water pipe. If the collector heats up the water, the water rises again and reaches the tank through an ascending water pipe at the upper end of the collector.

In order to maximize the useful heat gain by evacuated tube solar collector, numerical analysis of active and passive evacuated tube solar system has been carried out in this paper using ANSYS Fluent.

## 2 Numerical Modeling

A computational analysis of evacuated tube solar collectors was performed and analyzed for both passive system and active system using ANSYS Fluent 17.2 and compared the average temperature rise of water for one hour of operation. All the losses related to heat transfer in solar collectors are neglected for this analysis.

**Fig. 1** Geometry
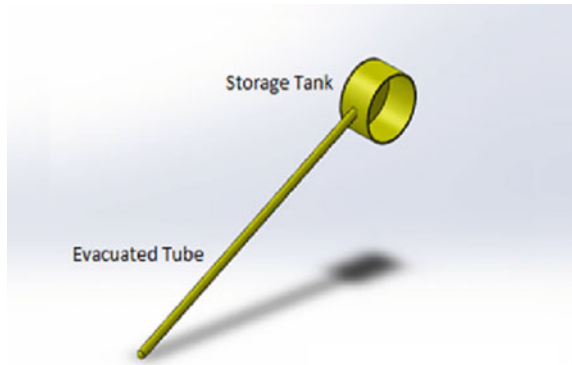


## 2.1 Design

The geometry of evacuated solar tube collector used in our simulations contains mainly two components, which are: (1) storage tank and (2) evacuated tube (Fig. 1).

The first component characteristics are: storage tank width 200 mm and tank diameter 356 mm. The second component characteristics are: evacuated tube having a length of 1800 mm and diameter 47 mm [7]. Analysis is done for the two different geometries inclined at 30° and 45° from the horizontal.

## 2.2 Discretization

The finite volume method is used for discretization of the problem. For assembly meshing, the tetrahedron method is used, which is effective in the case of circular geometries [16]. The figure shows the meshing of complete geometry (Fig. 2).

**Fig. 2** Meshing of fluid domain

## 2.3  Model

For geometry analysis, following governing equations are used and the Boussinesq approximation is taken for the density variation to take care of the effect of natural convection. The energy, continuity and momentum equations can be written as [17]:

**Energy Equation:**

$$\frac{\partial}{\partial t}\left(\rho h_{\text{tot}}\right) + \frac{\partial}{\partial x_j}\left(\rho h_{\text{tot}} u_j\right) = \frac{\partial P}{\partial t} + \frac{\partial}{\partial x_j}\left(u_i \tau_{ij} + \lambda \frac{\partial T}{\partial x_j}\right) \tag{1}$$

**Continuity Equation:**

$$\frac{\partial \rho}{\partial t} + \frac{\partial \rho u}{\partial x} + \frac{\partial \rho v}{\partial y} + \frac{\partial \rho w}{\partial z} = 0 \tag{2}$$

**Momentum Equations:**

$$\text{Momentum, } x: \quad \rho \frac{Du}{Dt} = \rho g_x - \frac{\partial p}{\partial x} + \mu \left(\frac{\partial^2 u}{\partial x^2} + \frac{\partial^2 u}{\partial y^2} + \frac{\partial^2 u}{\partial z^2}\right) \tag{3}$$

$$\text{Momentum, } y: \quad \rho \frac{Dv}{Dt} = \rho g_y - \frac{\partial p}{\partial y} + \mu \left(\frac{\partial^2 v}{\partial x^2} + \frac{\partial^2 v}{\partial y^2} + \frac{\partial^2 v}{\partial z^2}\right) \tag{4}$$

$$\text{Momentum, } z: \quad \rho \frac{Dw}{Dt} = \rho g_z - \frac{\partial p}{\partial z} + \mu \left(\frac{\partial^2 w}{\partial x^2} + \frac{\partial^2 w}{\partial y^2} + \frac{\partial^2 w}{\partial z^2}\right) \tag{5}$$

## 2.4  Boundary Conditions

The boundary conditions of evacuated tube collector are described as follows. Initial temperature of water was set to 300 K. All velocities throughout the geometry were set to zero for passive tube system. For active tube system, inlet velocity was set to 0.005 m/s.

For both the systems, a constant heat flux of 500 W/m$^2$ was given on the surface of evacuated tube. We took the laminar regime, and for water density, the condition was set to Boussinesq approximation.

## 3 Results and Discussion

After one hour of operation for both passive tube system and active tube system, the temperature varies throughout the geometry inclined at 30° and 45° (Figs. 3, 4, 5, and 6).

Further, the analysis is done for the average temperature rise of water for one hour of operation for both systems inclined at 30° and 45°, and the results are compared for passive and active tube systems.

**Fig. 3** Temperature stratification of passive tube at 30°
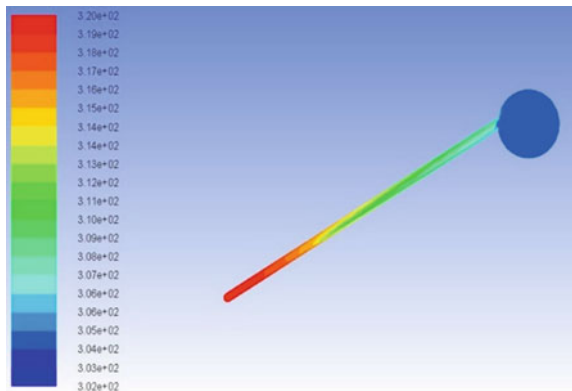
**Fig. 4** Temperature stratification of passive tube at 45°
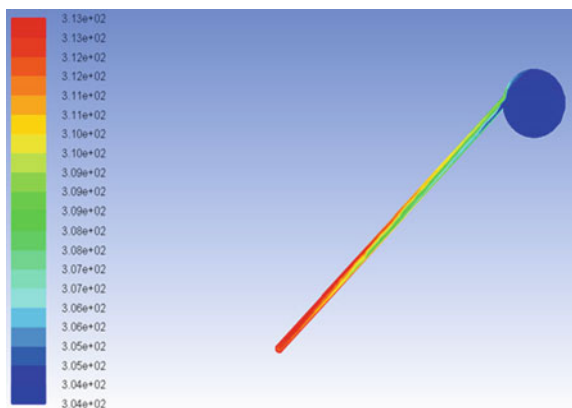
**Fig. 5** Temperature stratification of active tube at 30°
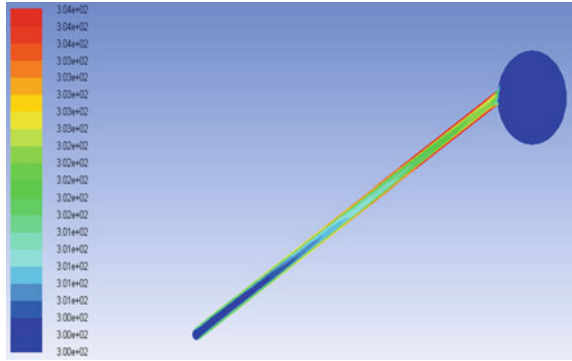


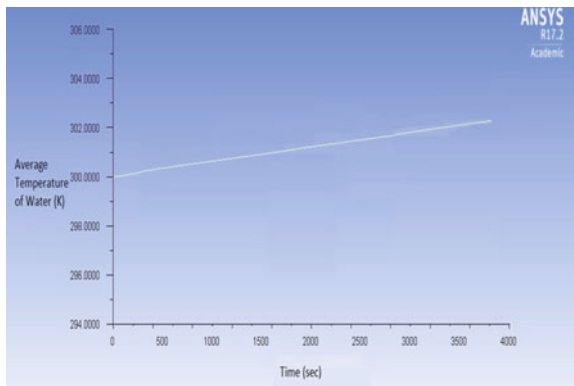**Fig. 6** Temperature stratification of active tube at 45°
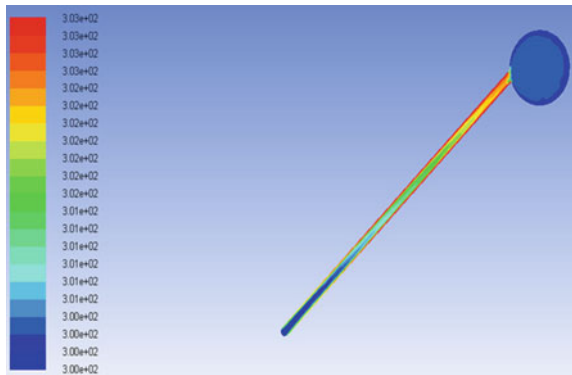


**Fig. 7** Average temperature of water versus time for passive tube inclined at 30°
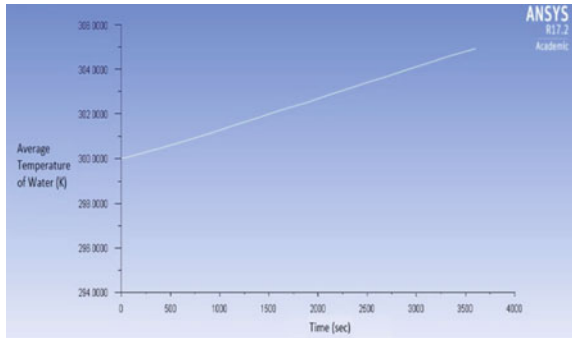


For one hour of operation, from Figs. 7 and 8, it is concluded that for passive tube systems inclined at 30° and 45° the average temperature rise of water is almost similar. For one tube analysis, in passive system, temperature rise is around 5 K temperature in 3600 s.

Fig. 8 Average temperature of water versus time for passive tube inclined at 45°
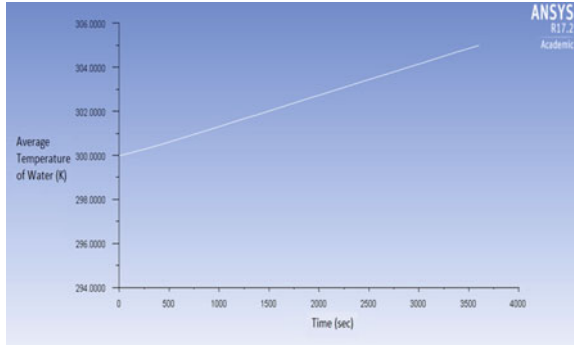


Fig. 9 Average temperature of water versus time for active tube inclined at 30°
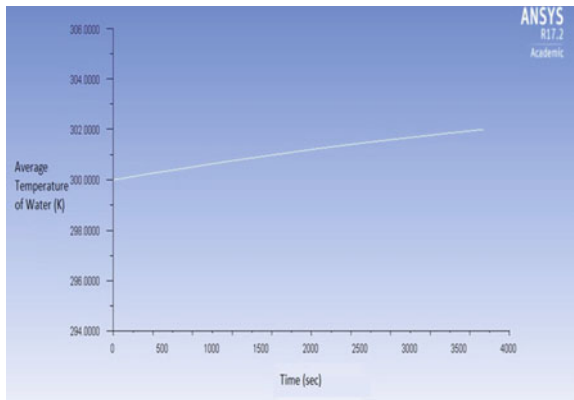


Fig. 10 Average temperature of water versus time for active tube inclined at 45°



Similarly for one hour of operation, from Figs. 9 and 10, for active tube systems it can be analyzed that the average temperature rise of water for the system inclined at 30° is bit higher when compared to the system inclined at 45°. In active systems, temperature rise is around 2 K in 3600 s.

# 4    Conclusion

The results show that in active tube system, the average rise in water temperature over a period of 3600 s is comparatively less than the average rise in passive tube system in the same time. The system when kept under natural flow exhibited a rise of 5 k over a period of 3600 s compared to when the system was kept under forced circulation where the rise noted was 2 K over the same period. After analyzing both the systems, it is concluded that thermal efficiency of passive tube system is higher than the active tube system and useful heat gain is also higher in passive tube system comparatively. Since active tube systems cost more and the thermal efficiency is also low compared to the passive tube systems, it is advised to use passive tube systems.

# References

1. Kreith Frank, Krumdieck Susan (2014) Principle of sustainable energy systems, 2nd edn. CRC Press Taylor & Francis Group, Boca Raton, Florida
2. Pandey S (2013) Success in scaling up solar energy in Rajasthan, India, p 2
3. Speyer E (1965) Solar energy collection with evacuated tubes. J Eng Power 86:270–276
4. Window B (1983) Heat extraction from single ended glass absorber tubes. Sol Energy 31(2): 159–166
5. Yin Z, Harding GL, Window B (1984) Water-in-glass manifolds for heat extraction from evacuated solar collector tubes. Sol Energy 32(2):223–230
6. Kalogirou SA (2004) Solar thermal collectors and applications. Prog Energy Combust Sci 30(3):231–295
7. Morrison GL, Budihardjo I, Behnia M (2005) Measurement and simulation of flow rate in a water-in-glass evacuated tube solar water heater. Sol Energy 78:257–267
8. Sabiha MA, Saidur R, Mekhilef S, Mahian O (2015) Progress and latest developments of evacuated tube solar collectors. Renew Sustain Energy Rev 51
9. Ayompe LM, Duffy A, Mc Keever M, Conlon M, McCormack SJ (2011) Comparative field performance study of flat plate and heat pipe evacuated tube collectors (ETCs) for domestic water heating systems in a temperate climate. Energy 36(5):3370–3378
10. Rabl A (1985) Active solar collectors and their applications. Oxford University Press on Demand
11. Anderson R, Kreith F (1987) Natural convection in active and passive solar thermal systems. Adv Heat Transfer 18:1–86
12. Budihardjo I (2005) Evacuated tubular solar water heaters. Ph.D. Thesis, University of NSW
13. Mazarron FR, Porras-Prieto CJ, Garcia JL, Benavente RM (2016) Feasibility of active solar water heating systems with evacuated tube collector at different operational water temperatures. Energy Convers Manag 113:16–26
14. Peuportier B, Michel J (1995) Comparative analysis of active and passive solar heating systems with transparent insulation. Sol Energy 54(1):13–l8
15. Budihardjo I, Morrison GL, Behnia M (2005) A study of natural circulation flow rate through single-ended evacuated tube solar collectors. In: Proceedings of ISES solar world congress, Orlando, USA, electronic proceedings
16. ANSYS (2015) ANSYS fluent theory guide. ANSYS 16.2 Doc., p 80
17. Duffie JA, Beckman WA (1991) Solar engineering of thermal processes. Wiley, New York

# Thermal and Resistance Analysis of Perforated Fin Using CFD

**Kuldeep Panwar, Etkaf Hasan, Renu Singh, Vijay Chaudhary and Kuldeep Rawat**

**Abstract** The present paper deals with the study of the heat transfer and friction characteristics under turbulent flow within a perforated fin. Standard computational methods using CFD have been used for creating the flow and heat transfer environment similar to that of experiments done by various researchers. To simulate the turbulent flow regime, k–Ɛ turbulence model is selected during the CFD simulation. The results obtained from the simulation for both solid and perforated fin is compared on the basis of fin geometries and effectiveness. The results clearly indicate that the perforation in fin increases heat transfer rate as compared to the solid fin.

**Keywords** Perforation · CFD · Fin performance

## 1 Introduction

Today the greatest challenge before thermal engineers is to provide innovative design concepts so that a large amount of heat could be removed from the microelectronic devices. To overcome this challenge, fins are attached to the base surfaces to the devices so that more heat could be removed. From the concept of heat transfer, we know that the heat transfer from fin to its surrounding include both convection and radiation modes. Due to low emissivity of fin materials, the radiative heat transfer can be neglected. The heat transfer rate from a fin surface can be expressed as function of convective heat transfer coefficient only as shown by the following expression:

K. Panwar (✉) · E. Hasan · R. Singh
Delhi Technical Campus, 201306 Greater Noida, India
e-mail: kuldeeppanwar.kec@gmail.com

V. Chaudhary
Amity School of Engineering & Technology, Amity University, Noida, India

K. Rawat
Shivalik College of Engineering, 218497 Dehradun, India

$$Q_\mathrm{f} = hA_\mathrm{f}(T_\mathrm{b} - T_\infty) \tag{1}$$

The effectiveness of fin is defined as the ratio of heat transfer from fin to heat transfer from fin base without fin and can be expressed as [1]:

$$\varepsilon_\mathrm{f} = \frac{Q_\mathrm{f}}{hA_\mathrm{c,b}\theta_\mathrm{b}} \tag{2}$$

The perforated fin effectiveness [2] is given as the percentage increase of heat transfer due to using perforated fin relative to solid fin and can be expressed as:

$$\varepsilon_\mathrm{pf} = \frac{Q_\mathrm{pf} - Q_\mathrm{sf}}{Q_\mathrm{sf}} \times 100 \tag{3}$$

## 2 Literature Review

Many researchers have focused their research in exploring the heat transfer performance and its effect on fin configurations. To start with Dogruoz et al. [3] presented experimental results of pressure drop for in-line pin square pin fin taking various pitch sizes. In addition to this, the measurement of overall thermal resistance was done as a function of Reynolds number.

The experimental results reviled that there is a good agreement between the temperature predictions based on the mathematical model and the experimental data.

An experimental investigation on enhancement of combined conduction, free convection, and radiation heat transfer using pin fin was carried by Yu and Joshi [4]. The temperature measurement and flow visualization within the pin fin were studied to explore the heat transfer characteristics as heat sinks. A similar theoretical investigation of the effects of fin characteristics such as fin spacing, fin height, fin length on the natural convection heat transfer from horizontal fin arrays was carried out by Baskaya et al. [5]. Panwar et al. [6] carried out the comparative study of CFD and experimental results of a thermal regenerator.

Ledezma et al. [7] conducted experimental studies on heat transfer through a pin fin array heat sink in an impinging air stream. In the experiment, they considered pin fins with square cross section and calculated the optimal fin spacing. A comparative study between experimental and numerical studies pertaining to the influence of the geometry, fin material, and Reynolds number on thermal performance of pin fin was done by Maveety and Jung [8].

An experimental investigation of calculation of local convective heat transfer coefficient was conducted by Meinders et al. [9]. The experiment was carried out in turbulent flow through wall mounted cubes. The results showed substantial variation in heat transfer coefficient along the array of cubes, especially up to first three

cubes. Similar study on heat transfer for three-dimensional developing turbulent flows over an array of cubes in the cross-stream direction was done by Yaghoubi and Velayati [10]. The investigation of Sahin et al. [11] explained the effects of the longitudinal and lateral separations enlarged-contracted arranged fin pairs. The paper investigated the effect of thermal and resistance characteristics using the Taguchi experimental design method. Later on, the examination of heat transfer coefficients and friction factors was done by Xiao and Tao [12] for wavy plate-fin heat exchangers with different fin lengths.

Thermal performances of solid and perforated rectangular blocks attached on a flat surface in a rectangular duct were determined by Sara et al. [13]. In addition, to it, the comparison with heat transfer from the same plate without blocks was also done.

Investigation of heat transfer characteristics of multi-perforated plates was done by Dorignac et al. [14]. The report stated that convective exchange on the upstream side of a multi-perforated plate depends on the pitch between perforations. Chang et al. [15] conducted experimental study to find a design criterion for selecting the optimal length-to-gap ratio of a finned heat sink. A similar study on the design of regenerators was done by Panwar et al. [16].

Shaeri et al. [17] investigated array of solid and perforated fins for studying the fluid flow and convective heat transfer coefficient. It was reported by them that fins with longitudinal pores have remarkable heat transfer enhancement in comparison with solid fins for the same weight ratios.

After thorough review of the literature, it is necessary to examine the heat transfer performance of a fin with perforations of varied geometrical parameters.

## 3 Computational Domain

The computational model for the simulation is made in GAMBIT (CFD). And the parameters for the geometry of computational model are made according to the experimental study of Shaeri et al. [2]. $k$–$\varepsilon$ turbulence model is chosen for the simulation of flow conditions. Figure 1a–d shows the inlet section and Fig. 1i–l shows the outlet section. The details of geometry of fin are given in Table 1.

Perforated fins with rectangular perforations are shown in Fig. 2. The perforations of width ($W_p$) and height ($h_p$) are separated by perforation pitch ($P_f$); height and width of slot are identical with that of perforation. The relative height of perforation ($h_p/h_f$) is defined as the ratio of perforation height to the fin height. The width of perforation is expressed in a dimensionless form as relative perforation width ($W_p/L$) which is the ratio of perforation width to the fin length. The relative perforation pitch ($P_f/W_p$) is given as the ratio of pitch to width of perforation.
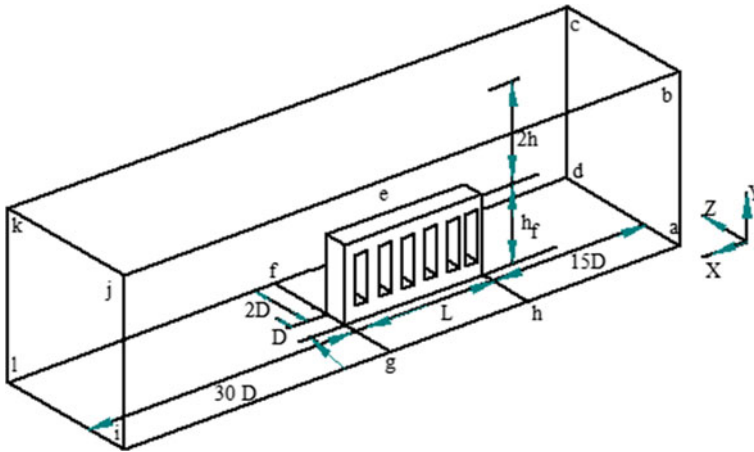
**Fig. 1** Computational domain

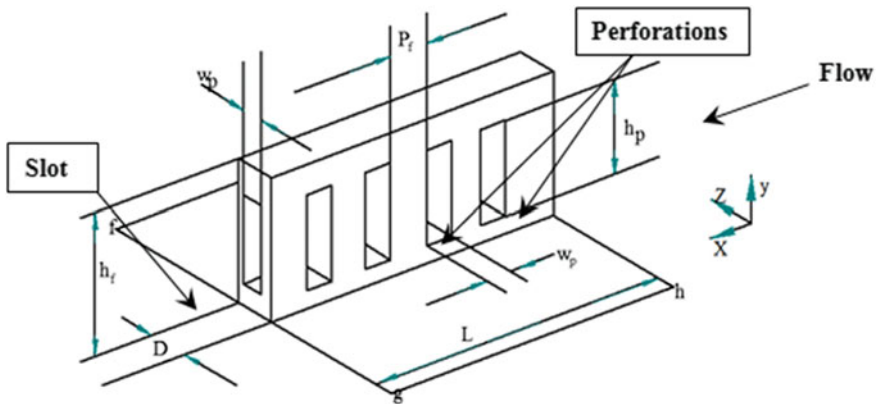| **Table 1** Geometrical details of computational model | Length of fin ($L$) | 50 mm |
|---|---|---|
| | Height of fin ($h_f$) | 25 mm |
| | Thickness ($D$) | 5 mm |
| | Fin material | Aluminum |



**Fig. 2** Perforated fin geometry

## 3.1 Grid Configuration

To capture the flow and temperature grid accurately, grid points are densely located in the vicinity of the fin surfaces and near the perforation sites. Figure 3a, b shows
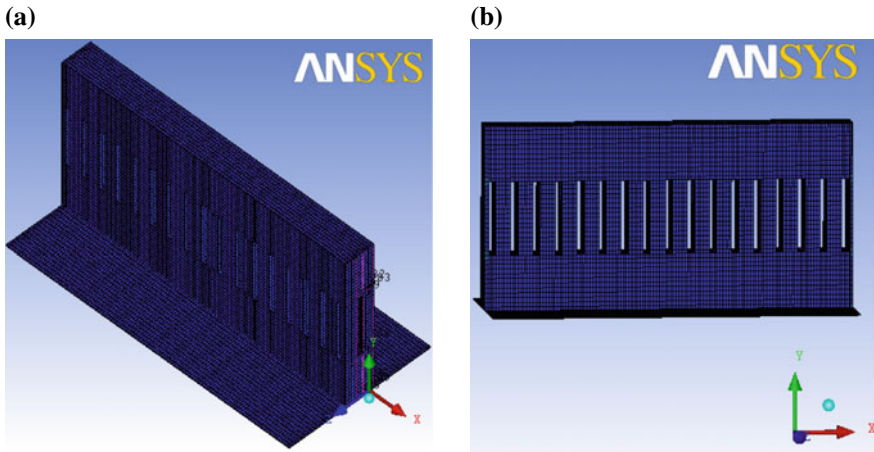
**(a)**                                    **(b)**



**Fig. 3** **a** Grid configuration for slotted fin with 17 perforations. **b** Fin with 17 perforations without slot

the grid configurations for a solid fin, a slotted fin with 17 perforations, and a perforated fin without slot, respectively. Before proceeding further, the grid independency test has been carried out with the different grid sizes.

# 4 Results and Discussion

## 4.1 Heat Transfer Characteristics

It is already found that the rate of heat transfer from material (may be a solid or hollow) subjected to a forced convection is very sensitive to the fluid flow conditions near the fin surfaces. It has been observed that the fin dissipates heat energy at a considerably higher rate, when fluid flow rate is increased. Figure 4 shows the plot of fin rate of heat transfer $v/s$ Reynolds number corresponding to different values of relative perforation pitch ($P_f/W_p$) for relative perforation height ($H_p/H_f$) of 0.4. Figure 4 shows that as we increase the Reynolds number value the rate heat transfer increases of all fins configuration. Plot shows that the rate of heat transfer increase in perforated fin with slot as compared with solid fins and is independent of height of perforation.

The effect of perforation width ($W_p$) on heat transfer rate from fin surface is shown in Fig. 5 for fixed relative perforation pitch ($P_f/W_p$) of 2 and relative perforation height ($H_p/H_f$) of 0.4 and 0.8, respectively.

The maximum rate of heat transfer for perforation with ($W_p/L$) of 0.02 as compare with solid fin; however, fin with perforated and slot has approximately same heat transfer rate with relative width perforation ($W_p/L$) of 0.02, and a little bit
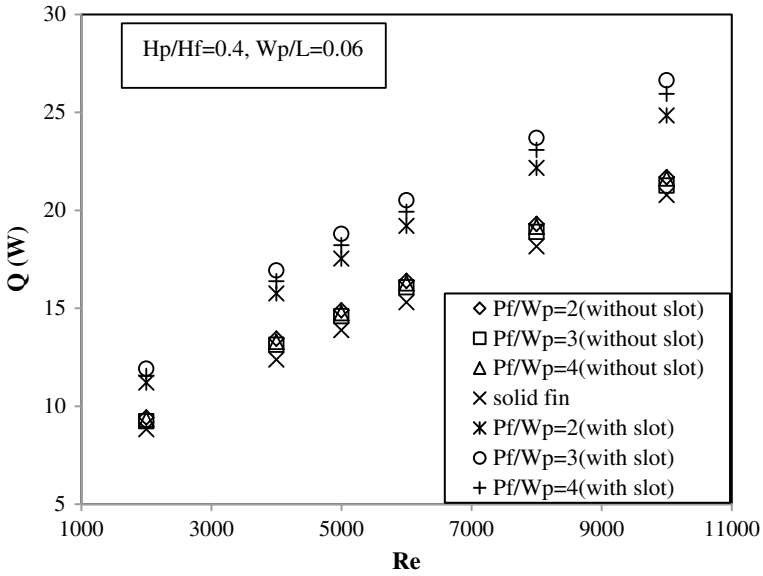
**Fig. 4** Variation of Reynolds number with fin heat transfer rate for different perforation pitch ($P_f/W_p$)
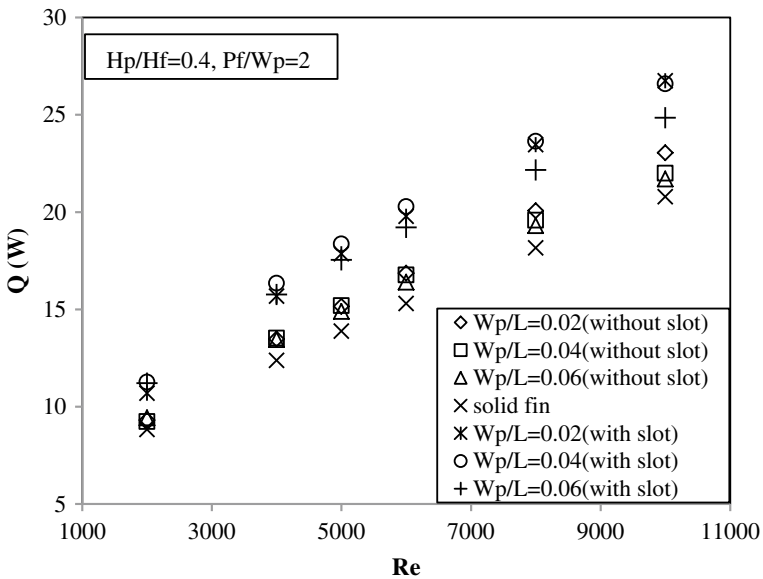


**Fig. 5** Variation of Reynolds number with fin heat transfer rate for different relative perforation width ($W_p/L$)
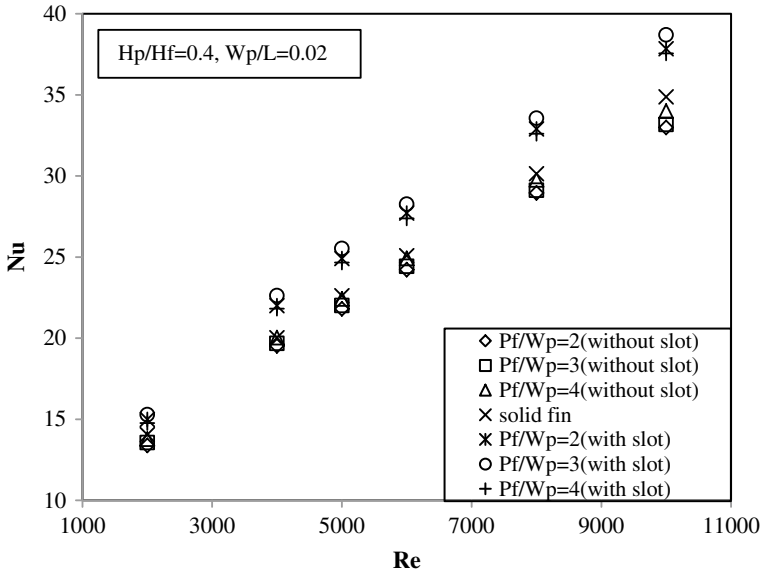
**Fig. 6** Variation of Nusselt number with Reynolds number and relative perforation pitch ($P_f/W_p$)

high heat transfer rate is found in relative perforation width ($W_p/L$) as width for slotted fin is decreases from 0.06 to 0.02 in case of higher perforation height.

To understand the variation of Nusselt number throughout the whole fin surface, the Nusselt number is plotted as function of flow Reynolds number for different fin configurations. Figure 6 shows the variation of Nusselt number with Reynolds number varying between 2000 and 10,000 for different values of relative pitch of perforation ($P_f/W_p$), relative width of perforation ($W_p/L$), and relative perforation height ($H_p/H_f$), respectively. It was observed that for different Reynolds number values the Nusselt number values for perforated fin without slot remain less than that of a solid fin.

It is evident from the results that when the perforation height is more the heat transfer rate from the fin is high which could be due to the availability of larger heat transfer area as a result of higher perforation height.

## 4.2 Effectiveness of Perforated Fin

The variation of effectiveness of perforated fin with respect to Reynolds number for different values of relative perforation pitch ($P_f/W_p$) keeping the relative perforation height ($H_p/H_f$) as 0.4 is shown in Fig. 7. The plot shows that the maximum effectiveness corresponds to relative perforation pitch ($P_f/W_p$) of 3 in case of perforated fin with slot, whereas perforated pitch has negligible effect on fin
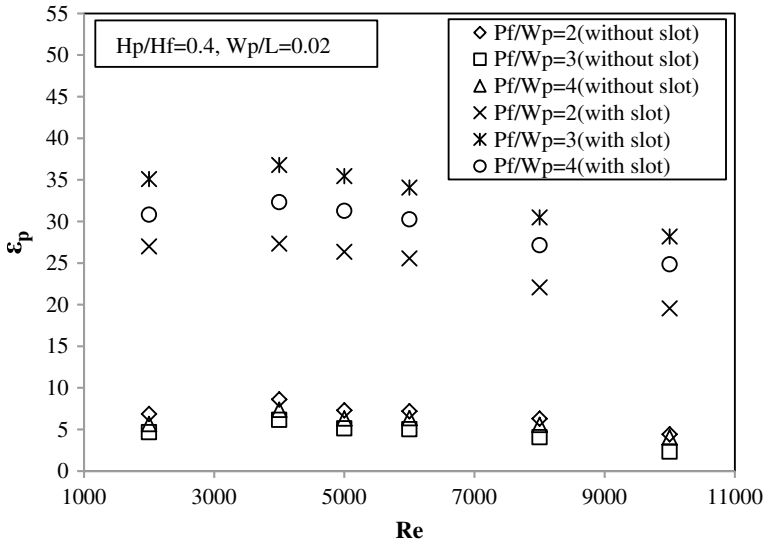
**Fig. 7** Perforated fin effectiveness as function of Reynolds number and relative perforation pitch $(P_f/W_p)$

effectiveness for the perforated fin without slot as Reynolds number approaches to the higher values.

It is fitting to say, based on the above results, that the use of perforated fins with a longitudinal slot brings out huge enhancements in heat transfer with the simultaneous rise in skin friction due to larger wetted area of the fin.

## 5    Conclusions

It can be concluded that a significant increase in heat transfer with the concurrent increase in frictional losses is seen with the perforated fin having slot with respect to a solid fin.

As the Reynolds number for all fin configurations increases, the heat transfer also increases, and friction factor decreases. The effectiveness of a perforated fin increases up to a particular point; otherwise, it decreases throughout the scope of the Reynolds number. Maximum heat transfer is achieved using the perforated fin with slot and maximum friction corresponds to relative perforation pitch $(P_f/W_p)$ of 3 irrespective of height of perforation. The perforated fin with no slot has insignificant effect on heat transfer as well as friction.

# References

1. Incropera FP, DeWitt DP (1996) Fundamental of heat and mass transfer to heat transfer, 3nd edn. Wiley
2. Shaeri MR, Yaghoubi M (2009) Heat transfer analysis of lateral perforated fin heat sinks. Appl Energy 86:2019–2029
3. Dogruoz MB, Urdaneta M, Ortega A (2005) Experiments and modeling of the hydraulic resistance and heat transfer of in-line square pin fin heat sinks with top by-pass flow. Int J Heat Mass Transfer 48:5058–5071
4. Yu E, Joshi Y (2002) Heat transfer enhancement from enclosed discrete components using pin–fin heat sinks. Int J Heat Mass Transfer 45:4957–4966
5. Baskaya S, Sivrioglu M, Ozek M (2000) Parametric study of natural convection heat transfer from horizontal rectangular fin arrays. Int J Therm Sci 39:797–805
6. Panwar K, Murthy DS (2015) Analysis of thermal characteristics of the ball packed thermal regenerator. Procedia Eng 127:118–1125
7. Ledezma G, Morega AM, Bejan A (1996) Optimal spacing between pin fins with impinging flow. ASME J Heat Transfer 7:118–570
8. Maveety JG, Jung HH (2000) Design of an optimal pin–fin heat sink with air impingement cooling. Int Commun Heat Mass Transfer 27(2):229–240
9. Meinders ER, Hanjalic K, Martinuzzi RJ (1999) Experimental study of the local convection heat transfer from a wall-mounted cube in turbulent channel flow. J Heat Transfer 73:121–564
10. Yaghoubi M, Velayati E (2005) Undeveloped convective heat transfer from an array of cubes in cross-stream direction. Int J Therm Sci 44:756–765
11. Sahin B, Yakut K, Kotcioglu I, Celik C (2005) Optimum design parameters of a heat exchanger. Appl Energy 82:90–106
12. Xiao Q, Tao WQ (1990) Effect of fin spacing on heat transfer and pressure drop of two–row corrugated–fin and tube heat exchangers. Int Com Heat Mass Transfer 17:577–586
13. Sara ON, Pekdemir T, Yapici S, Yilmaz M (2001) Heat-transfer enhancement in a channel flow with perforated rectangular blocks. Int J Heat Fluid Flow 22:509–518
14. Dorignac E, Vullierme JJ, Broussely M, Foulon C, Mokkadem M (2005) Experimental heat transfer on the windward surface of a perforated flat plate. Int J Thermal Sci 44:885–893
15. Chang SW, Su LM, Yang TL, Chiou SF (2004) Enhancement heat transfer of forces convective fin flow with transverse ribs. Int J Thermal Sci 43:185–200
16. Panwar K, Murthy DS (2016) Design and evaluation of pebble bed regenerator with small particles. Mater Today 3:3784–3791
17. Shaeri MR, Yaghoubi M (2009) Numerical analysis of turbulent convection heat transfer from an array of perforated fins. Int J Heat Fluid Flow 30:218–228

# Heat Transfer and Friction Characteristics of an Artificially Roughened Solar Air Heater

**Rakesh Prasad, Anil Singh Yadav, Nishant K. Singh and Dilip Johari**

**Abstract** In the present work improvement of warmth conveying rate by creating harshness underside of onlooker surface in sun-powered air warmer has been explored. CFD examine has been done, to appraise warm course through convection and grinding factor in SAH pipe in which symmetrical triangular formed transverse rib unpleasantness is utilized. Computational outcomes are accomplished utilizing CFD apparatus Ansys-Fluent. The computational area has a width five times of stature ($W/H = 5$), relative unpleasantness tallness ($e/D$) of 0.042, and vertical projection ($e$) is 1.4 mm. The separation between two back to back ribs ($P/e$) and Reynolds numbers ($Re$) are in the scope of 7.14–17.86 and 3800–18,000 separately. The powerful scope of working parameters unpleasantness on Nusselt no. ($Nu$) and Friction factor ($f$) is watched and the result is exhibited to make an examination with the smooth pipe of a sun-based air radiator. The most extreme value of $Nu$ and $f$ in this present work are accomplished s 2.94 and 3.27 individually.

**Keywords** Absorber plate · Convective heat transfer · Artificial roughness · Thermal augmentation factor · Pressure drop

## Nomenclature

| | |
|---|---|
| $C_p$ | Sp heat of air, J/kg k |
| $D$ | Duct's hydraulic diameter, m |
| $e$ | Rib's height, m |
| $h$ | Conv. heat transfer coeff., W/m$^2$k |
| $H$ | Duct's depth, m |
| $k$ | Thermal conductivity of air, W/m k |

R. Prasad (✉) · N. K. Singh · D. Johari
Mechanical Engineering Department, Hindustan College of Science and Technology, Mathura, India
e-mail: rprasadrose@gmail.com

A. S. Yadav
Mechanical Engineering Department, Lakshmi Narain College of Technology-Excellence, Bhopal, India

$L$    Duct's length, m
$L_1$   Duct's length at inlet, m
$L_2$   Test length of duct, m
$L_3$   Duct's length at exit, m
$\Delta P$   Pressure drop, Pa
$P$    Rib's pitch, m
$v$    Velocity of air in the duct, m/s
$W$    Duct's width, m

## Dimensionless parameters

$e/D$   Roughness height (relative)
$f$     Friction factor
$f_r$    Friction factor (rough surface)
$f_s$    Friction factor (smooth surface)
$Nu$    Nusselt number
$Nu_r$   Nusselt number (rough duct)
$Nu_s$   Nusselt number (smooth duct)
$Pr$    Prandtl number
$P/e$   Pitch of roughness (relative)
$Re$    Reynolds number
$W/H$   Aspect ratio of duct

## Greek symbols

$\mu$    Dynamic viscosity, Ns/m$^2$
$\mu_t$   Turbulent viscosity, Ns/m$^2$
$\rho$    Density of air, kg/m$^3$
$\alpha$    Angle of attack, degree
$\varepsilon$    Dissipation rate
$\omega$    Specific dissipation rate
$\delta$    Transition sub-layer thickness, m
$\kappa$    Turbulent kinetic energy, m$^2$/s$^2$
$\Gamma$    Molecular thermal diffusivity
$\Gamma_t$   Turbulent thermal diffusivity

## Subscripts

$r$   Roughened
$s$   Smooth
$t$   Turbulent

# 1 Introduction

The sun tracking is the most advantageous approach to bridle the sun-oriented vitality for warming applications, by its change into warm vitality utilizing sun-oriented authorities. Sun powered gatherers get sun-based irradiance and convert them into warmth vitality. Among the assortment of gatherer gadgets, sunlight-based air radiators (SAHs) were utilized at a vast scale on account of its straightforwardness and cost-viability. Convective warmth exchange at the interface of liquid and safeguard plate is altogether low as a result of the presence of laminar sub-layer. The convective warmth exchange with smooth plate safeguard in SAH very less and consequently execution is poor. With the end goal to expand the warmth exchange, there is a requirement for the breaking of laminar sub-layer. Presenting unpleasantness on the safeguard plate drives the stream to be tempestuous and convective coefficient can be expanded in the middle of liquid and surface of safeguard plate. Machining, sand-blasting, welding, sticking of wires and so on are diverse strategies to present harshness on safeguard plate [1]. A few exploratory preliminaries have been done to structure a roughened surface that can increment convective warmth exchange with no misfortunes in pumping [2–4]; however, the numerical examination has been finished by not very many specialists. A nitty gritty writing survey relating to various numerical investigations dependent on surface roughening with different geometries and corresponding sizes and their introductions has been done [5].

The audit of the writing demonstrates that not very many specialists have demonstrated their enthusiasm for the CFD examination of misleadingly roughening of safeguard plate in SAH with a symmetrical triangular molded transverse rib. The present work is planned to ponder the impacts of different parameters on falsely roughening with CFD device. Chaube et al. [6] proposed that 2-D displaying of warmth stream have great concurrence with test esteems and better than 3-D demonstrating. With the end goal to spare registering force and time, 2-D stream show is conveyed for reproduction. The work is centered to account impact around liquid stream and warmth exchange properties of the 2-D pipe have roughened by giving symmetrical triangular rib in a sun-oriented air warmer by CFD system. In this work, Ansys-Fluent v16 is utilized as CFD device, to display warm exchange and liquid stream procedure to research warm exchange attributes and erosion factor for a safeguard plate which is falsely roughened. The present article is composed with this point:

1. To examine the impact of *P/e* proportion with Reynolds number on warmth exchange and liquid stream.
2. To get the appropriate plan of ribs in terms of *P/e*.

## 2  Simulation Technique

The symmetrical triangular rib is utilized to create uneven surface of the sun-oriented radiator, convective warmth exchange process is reproduced in 2-D by business CFD programming Ansys-Fluent (v.16). The fluid is streaming over the uneven anticipated surface of the safeguard plate of the sun-based air radiator, a district for numerical computational in 2-D is appeared in Fig. 1. The computational space is made according to the ASHRAE Standard [7].

The detail of geometry and quantitative parameters used in this CFD simulation is listed in Table 1.

A run of the mill putting of symmetrical triangular formed transverse ribs under the safeguard plate is spoken to by line graph as appeared in Fig. 2.

ANSYS ICEM CFD v16 is utilized for creating a work of non-uniform compose. The created lattices are utilized for all unique CFD reenactments work. The network is characterized by 239,662 quad cells, every cell size of 0.2 mm for characterizing the computational space in (Fig. 3). The network autonomy test is directed for lattices contained distinctive quantities of cells for effective ramifications of control parameters.

The governing equation used in the heat and fluid flow is as follows [25]:

**Continuity equation**:

$$\frac{\partial}{\partial x_i}(\rho u_i) = 0 \tag{1}$$

**Momentum equation**:

$$\frac{\partial}{\partial x_i}(\rho u_i u_j) = -\frac{\partial p}{\partial x_i} + \frac{\partial}{\partial x_j}\left[\mu\left(\frac{\partial u_i}{\partial x_j} + \frac{\partial u_j}{\partial x_i}\right)\right] + \frac{\partial}{\partial x_j}\left(-\rho\overline{u_i'u_j'}\right) \tag{2}$$
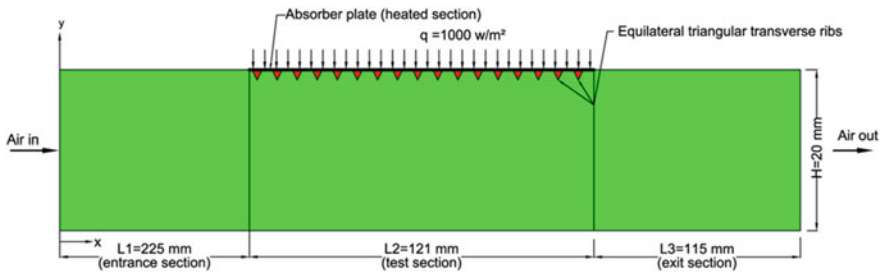


**Fig. 1**  2-D computational zone

**Table 1** Defined domain dimensions and control parameters for CFD analysis [6]

| Geometrical and operating parameters | Range |
|---|---|
| Duct length at entrance, '$L_1$' | 225 mm |
| Test duct length, '$L_2$' | 121 mm [17] |
| Duct length at exit, '$L_3$' | 115 mm [17] |
| Duct width, '$W$' | 100 mm [17] |
| Duct depth, '$H$' | 20 mm [17] |
| Duct hydraulic dia., '$D$' | 33.33 mm [17] |
| Aspect ratio of duct, '$W/H$' | 5 |
| Rib's height, '$e$' | 1.4 mm |
| Rib's pitch, '$P$' | 10–25 mm (4 values) [17] |
| Reynolds number, '$Re$' | 3800–18,000 (6 values) |
| Pitch of roughness (relative), '$P/e$' | 7.14–17.86 (4 values) [25] |
| Height of roughness (relative), '$e/D$' | 0.042 (fixed value) [25] |
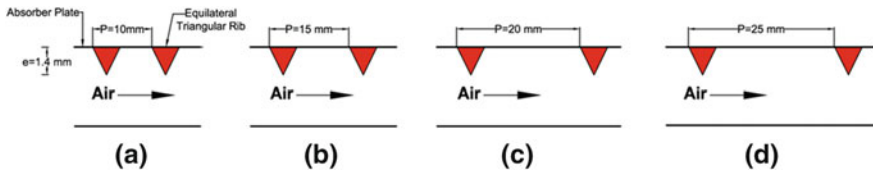


**Fig. 2** Roughened absorber plate
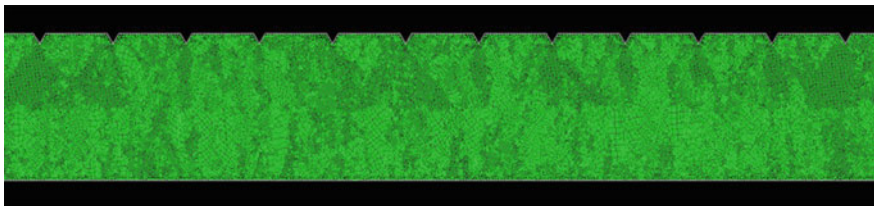


**Fig. 3** 2-D (non-uniform) meshing

**Energy equation**:

$$\frac{\partial}{\partial x_i}(\rho u_i T) = \frac{\partial}{\partial x_j}\left((\Gamma + \Gamma_t)\frac{\partial T}{\partial x_j}\right) \tag{3}$$

The daylight-based air hotter has been reproduced by considering air at the delta with uniform speed and leaving at an outlet with enduring weight $1.013 \times 105$ Pa. Air temperatures at the inlet are 300 K and it is kept up consistent in the midst of stream over the warmed surface. Yadav and Bhagoria considered the properties

**Table 2** Thermo-physical data chosen for air and absorber plate for CFD modeling [8]

| Properties | Air | Absorber plate (aluminum) |
|---|---|---|
| Density, '$\rho$' (kg m$^{-3}$) | 1.225 | 2719 |
| Specific heat, '$C_p$' (Jkg$^{-1}$K$^{-1}$) | 1006.43 | 871 |
| Viscosity, '$\mu$' (Nsm$^{-2}$) | 1.7894e−05 | – |
| Thermal conductivity, '$k$' (Wm$^{-1}$K$^{-1}$) | 0.0242 | 202.4 |

related to working fluid and shield plate are orchestrated in Table 2. The points of confinement with impermeability and no-slip divider condition have been normal over the dividers of the pipe. The got warmth change of 1000 W/m$^2$ at protect plate is settled at the most noteworthy mass of the channel and base most divider considered as an adiabatic divider [8].

In the present numerical recreation Renormalization-gathering (RNG) $k$–$\varepsilon$ show has been chosen. For the determination of best disturbance display for a falsely roughened sun-powered air warmer has been explored by Yadav and Bhagoria [5]. To shows the dependences of different choppiness, a demonstration has been carried by a few agents [9, 10]. Limited volume strategy has been picked as a scientific model to achieve the CFD results. Points of interest of the CFD show are as per the following:

- A weight based and enduring state solver
- $k$–$\varepsilon$ RNG choppiness show
- Discretization (second-arrange upwind plan is chosen)
- Simple calculation.

## 3 Data Reduction

Produced CFD information must be utilized to assess the convective warmth exchange and frictional obstruction of the roughened pipe. For the estimation of Nusselt number, erosion factor and warm improvement factor, following conditions were utilized [11, 12]:

$$Nu_r = h\,D/k \tag{4}$$

$$f_r = \frac{(\Delta P/l)\,D}{2\rho v^2} \tag{5}$$

$$\text{Thermal enhancement factor} = \frac{(Nu_r/Nu_s)}{(f_r/f_s)^{\frac{1}{3}}} \tag{6}$$

The estimation of this record ought to be more than one to make expansion plan to be attainable.

The Nusselt number and grinding element might be ascertained for the smooth surface of the sun-oriented air warmer by utilizing Dittus–Boelter condition [13] and Blasius condition [14] individually and is given by:

$$Nu_s = 0.023 \, Re0.8 \, Pr0.4 \, [13] \tag{7}$$

$$f_s = 0.0791 \, Re - 0.25 \, [14] \tag{8}$$

## 4 Result and Discussion

The estimation of this record ought to be more than one to make increase plan to be feasible. The Nusselt number and grating element might be figured for the smooth surface of the sun-oriented air warmer by utilizing Dittus–Boelter condition and Blasius condition separately and is given by: The two-dimensional numerical reproduction of the roughened sun-powered air radiator has been examined for the normal warmth exchange and liquid stream qualities. The impact of the geometrical and stream parameters related with the ribs has been talked about in this segment.

The impact of $P/e$ on the Nusselt number is exhibited in Fig. 4, which is delineated that the estimation of Nusselt no. runs up as for Reynold no. for all cases as made reference to by Yadav and Bhagoria [8]. It can likewise be seen that for a settled estimation of relative unpleasantness stature ($e/D$) the Nusselt number qualities diminish with the expansion in relative harshness pitch ($P/e$).

The impact of $P/e$ over grating component is shown in Fig. 5. This delineated the contact factor runs down with the expanded estimation of $Re$. It can likewise be seen that for the settled estimation of relative unpleasantness stature ($e/D$) the grinding factor esteems diminish with the expansion in relative harshness pitch ($P/e$) as this had been examined by Yadav [15].

Variety of the violent power forms as a component of Reynolds number is appeared in Fig. 6. The choppiness powers are decreased close to the divider, and high disturbance force is found between the ribs, close to the front of the rib top. The expansion in the choppiness power with increment in Reynolds number can be seen in Fig. 6.

In the Yadav and Bhagoria's examination for choppiness power form for rib of squared shape for separate Reynolds no. 3800, 5000, 8000, 12,000, 15,000 and 18,000 have been selected in the present article additionally [16].

Variety of improvement [proportion of the Nusselt number ($Nu$) to the roughened surface Nusselt number ($Nu_r$)] with Reynolds number appeared in Fig. 7.
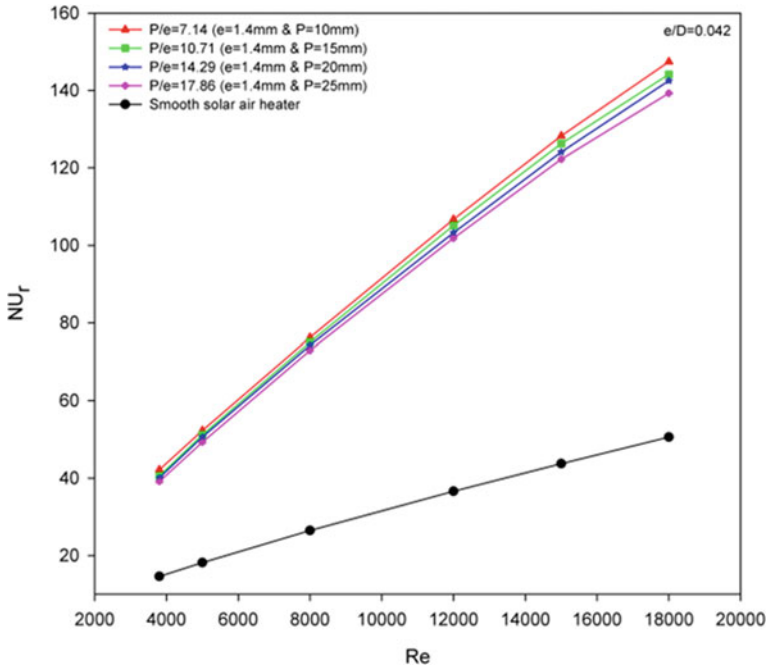
**Fig. 4** $Nu_r$ versus $Re$ for corresponding values of $P/e$
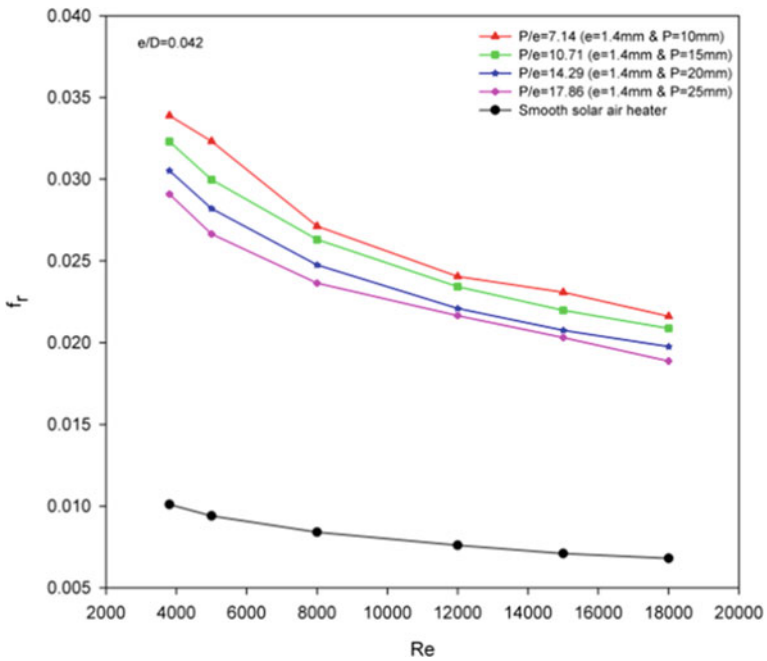


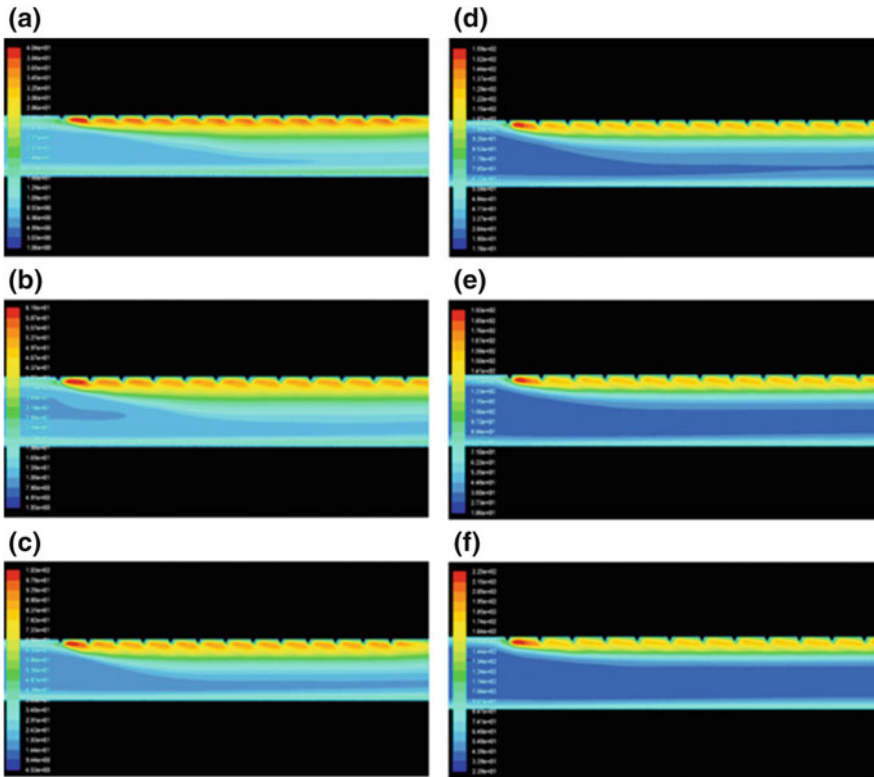**Fig. 5** $f_r$ versus $Re$ for corresponding values of $P/e$

**Fig. 6** The plot of turbulent intensity contour for rib pitch, $P = 10$ mm at a Reynolds number **a** $Re = 3800$, **b** $Re = 5000$, **c** $Re = 8000$, **d** $Re = 12{,}000$ **e** $Re = 15{,}000$ **f** $Re = 18{,}000$

It very well may be seen that the proportion of Nusselt no's abatements with the expanding estimation of $P/e$. It is additionally seen that the upgrade proportion increments with expanding Reynolds number to achieve a specific esteem then it diminishes encourage with the expansion in Reynolds number. Gawande work, for the Nusselt number for smooth conduit comparing to $P/e = 7.14$ and $e/D = 0.042$ at a $Re = 5000$, is assessed [17]. This is discovered that most extreme improvement in Nusselt number 2.94 occasions of smooth conduit as contrast with Gawande work.

Variety of grating element improvement proportion ($Nu/Nu_r$) with Reynolds number can be found in Fig. 8. It very well may be seen that as the $P/e$ builds, the contact factor proportion continues diminishing. It tends to be noticed that as Reynolds number increment, rubbing factor proportion diminishes. The most elevated estimation of contact factor, which is 3.27 occasions the estimation of the grinding factor for a smooth pipe comparing to $P/e = 7.14$ and $e/D = 0.042$ at a $Re = 3800$ [18].

Variety of the warm upgrade factor with Reynolds number can be found in Fig. 9. The warm improvement factor differs between the scopes of 1.89–1.99 for
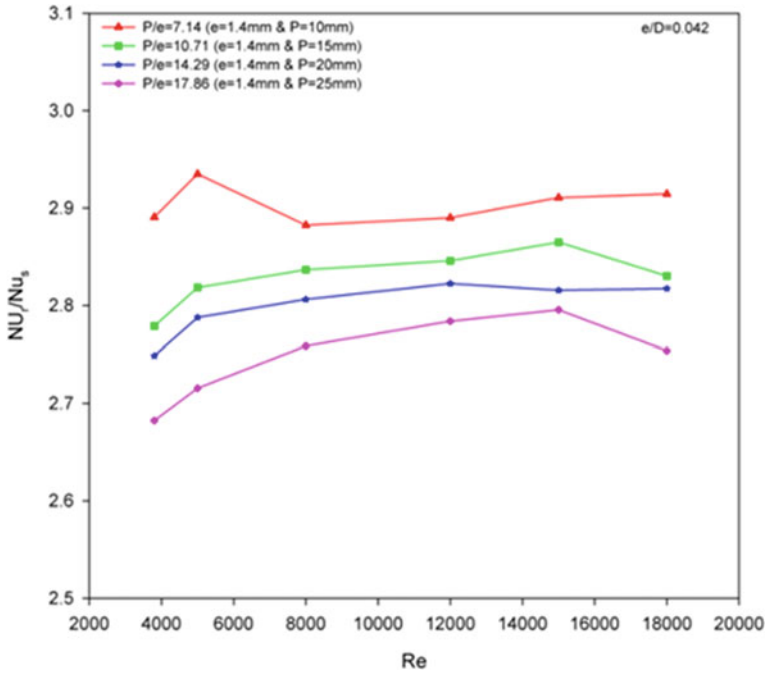
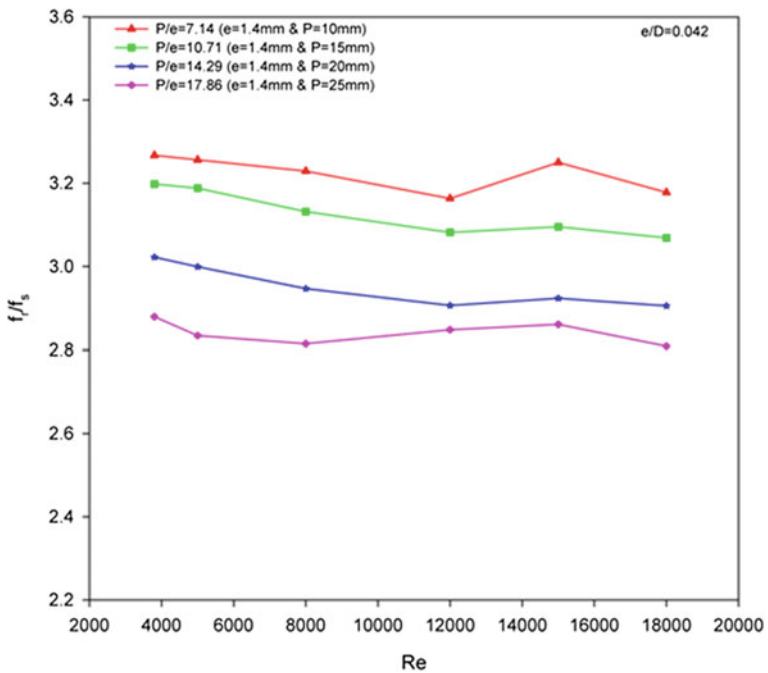**Fig. 7** Friction factor enhancement ratio ($Nu/Nu_r$) versus $Re$ for corresponding values of $P/e$



**Fig. 8** Variation of friction factor ratio ($f_r/f_s$) versus Reynolds number for different values of $P/e$
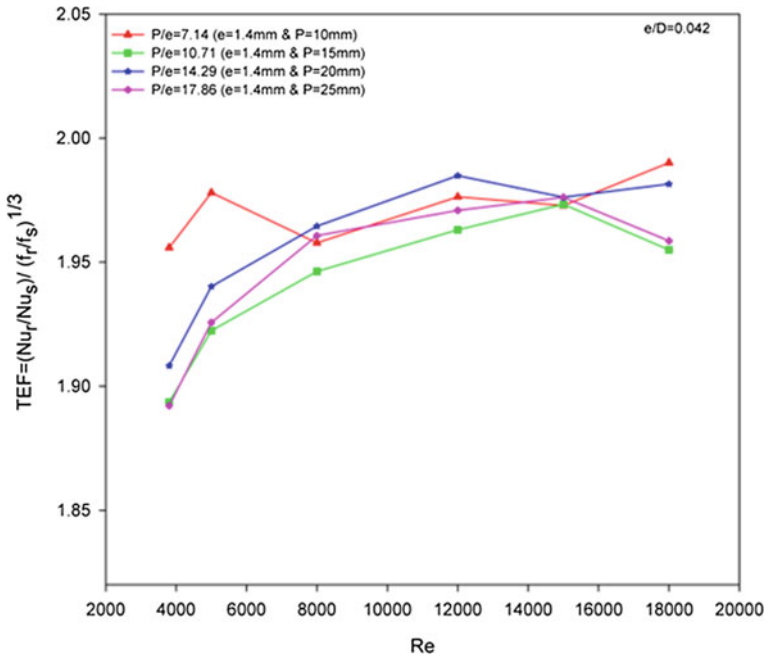
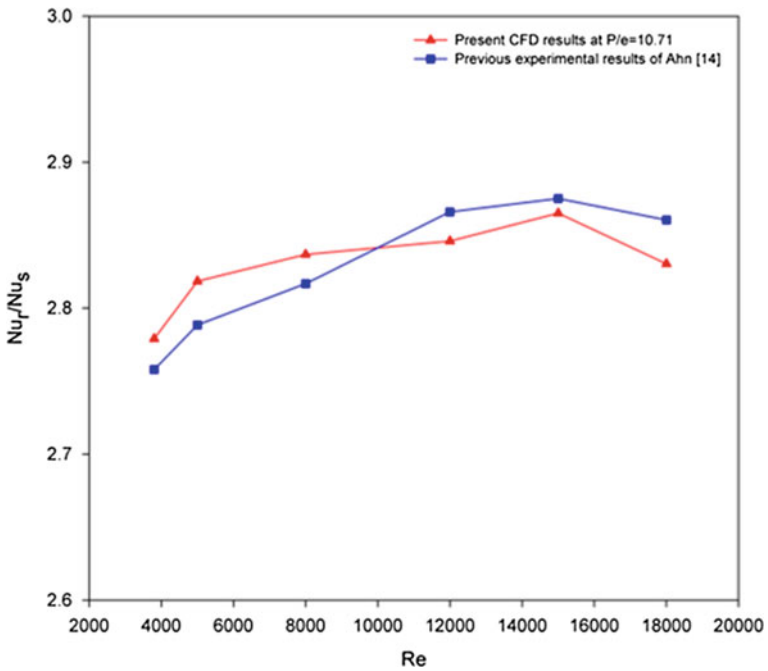**Fig. 9** (TEF) versus Rey. no. for corresponding values of *P/e*



**Fig. 10** Comparison of Nusselt number ratio with previous experimental results of Ahn [19]

all examined cases. The present numerical examination containing the rib blend gives the most astounding warm improvement factor of 1.99 at concerning $P/e$ = 10.71 and $Re$ = 18,000.

For the approval of the produced information, the correlation has been finished with the current trial information of Ahn [19]. Fig. 10 demonstrates the correlation of the present CFD results with existing exploratory consequences of Ahn [19]. It very well may be seen that both the outcomes are considerably nearer to one another. Comparative outcomes are gotten by Hans et al. [20], Ravi and Saini [21], Sharma and Kalamkar [22] and Singh and Singh [23], who completed trial examines on the wonder of convection and stream grating attributes for stream of air over the surface of falsely roughened with various kinds of unpleasantness [24].

## 5    Conclusions

The value of this index should be more than one to make augmentation scheme to be feasible. The Nusselt number and friction factor may be calculated for the smooth surface of the solar air heater by using Dittus–Boelter equation and Blasius equation, respectively, and is given by: The two-dimensional numerical simulation of the roughened solar air heater has been performed.

In this article, a two-dimensional numerical simulation of an equilateral triangular rib roughened solar air heater has been carried out. The numerical simulation predicts the heat transfer and flows friction characteristics. The effect of geometrical alterations, over $P/e$ and flow parameter, with respect to $Re$ has been studied for the range of parameters considered. The major conclusions of this study have been drawn as follows:

1. The utilization of counterfeit harshness as symmetrical triangular segmented transverse rib on a surface is a successful method to upgrade the rate of warmth exchange.
2. The CFD system has been utilized as it is great for managing the extensive variety of parameters and confused examination that include liquid stream. The CFD strategy can likewise be connected effectively by utilizing cross-approval system on an extensive variety of parameters and convoluted examination which is impossible through trial examinations.
3. The Renormalization-gathering (RNG) $k$–$\varepsilon$ disturbance display anticipated close outcomes to the test results, which yields trust in the expectations done by numerical examination in the present investigation.
4. The outcomes anticipated by the present CFD examination are considerably nearer to past trial results. It can, along these lines, be inferred that the present numerical outcomes have approved the proposed framework.
5. The measure of upgrade of $Nu_r$ and fr relies upon the geometry of rib and liquid stream states of the ribbed channel.

6. The extraordinary additions in the esteem Nusselt number are observed to be 2.94 occasions at $P/e$ = 7.14 and $Re$ = 5000.
7. The greatest upgrade in grinding factor is observed to be 3.27 occasions at $P/e$ = 7.14 and $Re$ = 3800.
8. Better warm productivity is observed to be 1.99 at $P/e$ = 7.14 and $Re$ = 18,000 for pipe roughened with symmetrical triangular molded transverse ribs on the safeguard plate and subsequently can be utilized for warmth exchange enlargement examined for the normal warmth exchange and liquid stream attributes. The impact of the geometrical and stream parameters related with the ribs has been examined in this area.

The impact of $P/e$ on the Nusselt number is exhibited in Fig. 4, which is delineated that the estimation of Nusselt no. runs up as for Reynold no. for all cases as specified by Anil and Bhagoria [8]. It can likewise be seen that for a settled estimation of relative harshness stature ($e/D$) the Nusselt number qualities diminish with the expansion in relative unpleasantness pitch ($P/e$).

# References

1. Duffie JA, Beckman WA (1980) Solar engineering of thermal processes. Wiley, New York
2. Singh Bisht V, Kumar Patil A, Gupta A (2018) Review and performance evaluation of roughened solar air heaters. Renew Sustain Energy Rev 81:954–977
3. Kumar K, Prajapati DR, Samir S (2017) Heat transfer and friction factor correlations development for solar air heater duct artificially roughened with 'S' shape ribs. Exp Thermal Fluid Sci 82:249–261
4. Varun, Saini RP, Singal SK (2017) A review on roughness geometry used in solar air heaters. Solar Energy 81(11):1340–1350
5. Yadav AS, Bhagoria JL (2013) Heat transfer and fluid flow analysis of solar air heater: a review of CFD approach. Renew Sustain Energy Rev 23:60–79
6. Chaube A, Sahoo PK, Solanki SC (2006) Analysis of heat transfer augmentation and flow characteristics due to rib roughness over absorber plate of a solar air heater. Renew Energy 31:317–331
7. ASHRAE Standard 93 (2003) Method of testing to determine the thermal performance of solar collectors. American Society of Heating, Refrigeration and Air Conditioning Engineers, Atlanta, GA, 30329
8. Yadav AS, Bhagoria JL (2014) A numerical investigation of turbulent flows through an artificially roughened solar air heater. Numer Heat Transfer Part A, Int J of Comput Methodol 65(7): 679–698
9. ANSYS FLUENT (2003–04) Documentation. ANSYS, Inc
10. Launder BE, Spalding DB (1972) Lectures in mathematical models of turbulence. Academic Press, London, England
11. Patankar SV (1980) Numerical heat transfer and fluid flow. Hemisphere, Washington, DC
12. Webb RL, Eckert ERG (1972) Application of rough surface to heat exchanger design. Int J Heat Mass Transf 15(9):1647–1658
13. McAdams WH (1942) Heat transmission. McGraw-Hill, New York
14. Fox W, Pritchard P, McDonald A (2010) Introduction to fluid mechanics. Wiley, New York, p 754

15. Yadav AS (2015) CFD investigation of effect of relative roughness height on Nusselt number and friction factor in an artificially roughened solar air heater. J Chinese Inst Eng 38(4): 494–502
16. Yadav AS, Bhagoria JL (2014) A numerical investigation of square sectioned transverse rib roughened solar air heater. Int J Therm Sci 79: 111–131
17. Gawande VB, Dhoble AS, Zodpe DB, Chamoli S (2015) Experimental and CFD based thermal performance prediction of solar air heater provided with chamfered square rib as artificial roughness. J Brazilian Soc Mech Sci Eng 38(2): 643–663
18. Gawande VB, Dhoble AS, Zodpe DB, Chamoli S (2016) A review of CFD methodology used in literature for predicting thermo-hydraulic performance of a roughened solar air heater. Renew Sustain Energy Rev 54: 550–605
19. Ahn SW (2001) The effects of roughness types on friction factors and heat transfer in roughened rectangular duct. Int Comm Heat Mass Transfer 28(7):933–942
20. Hans VS, Gill RS, Singh S (2017) Heat transfer and friction factor correlations for a solar air heater duct roughened artificially with broken arc ribs. Exp Thermal Fluid Sci 80:77–89
21. Ravi RK, Saini RP (2018) Nusselt number and friction factor correlations for forced convective type counter flow solar air heater having discrete multi V shaped and staggered rib roughness on both sides of the absorber plate. Appl Therm Eng 129:735–746
22. Sharma SK, Kalamkar VR (2017) Experimental and numerical investigation of forced convective heat transfer in solar air heater with thin ribs. Sol Energy 147:277–291
23. Singh A, Singh S (2017) CFD investigation on roughness pitch variation in non-uniform cross-section transverse rib roughness on Nusselt number and friction factor characteristics of solar air heater duct. Energy 128:109–127
24. Yadav AS, Bhagoria JL (2014) Heat transfer and fluid flow analysis of an artificially roughened solar air heater: a CFD based investigation. Front Energ 8(2): 201–211
25. Jedsadaratanachai W, Jayranaiwachira N (2015) Effect of pitch to height ratio on flow visualization, heat transfer, and thermal performance in a round tube with upstream RWVG. Adv Mech Eng. SAGE Journal 6: 1–13

# Attic Space Convection Analysis with Full-Blown Heat Condition with Different Possible Geometries

**Anuj Gupta and Harishchandra Thakur**

**Abstract** An issue with the design optimization of building attic space has been addressed in this paper in an artistic manner with the consideration of full-blown condition. Different values for the ratio (0–1) of the roof and the floor length in the rectangular cavity has been considered. It includes triangular-, rectangular-, and trapezoidal-shaped enclosure. For finding the optimized shape, the study has included the consideration of different values for the Rayleigh number $10^4$–$10^6$. The assumption of uniform temperature over the wall and no-slip condition is considered. Isotherm and streamlines are computed to observe the temperature distribution and fluidity of laminar air at Prandtl number 0.71. With the use of ANSYS 18.1, the present study finds the ratio of roof and floor of an attic space to be in between 0.8 and 0.9 for best thermal performance.

**Keywords** Attic space · Natural convection · Rectangular enclosure · Triangular enclosure · Trapezoidal enclosure

## 1 Introduction

With an ideation for the development of the Green Buildings, view of the architects and builders is enlightened on human comfort. Attic space inside a building is considered as one of the most complex heat transfer zones inside a building. It plays a very important role because it contributes to 12% of the heat transfer from the room of the building [11].

Natural convection is the most effective mode of heat transfer inside an attic space. It occurs due to the difference in temperature of the walls which influences the motion of the fluid [1]. Various studies have been performed analytically [14]

A. Gupta (✉) · H. Thakur
Gautam Buddha University, Greater Noida 201308, Uttar Pradesh, India
e-mail: gupta1992anuj@yahoo.in

H. Thakur
e-mail: harish@gbu.ac.in

and experimentally [10, 15, 18] to understand the development of flow field and heat transfer inside an enclosure. Various studies have been found in the literature to analyze natural convection in rectangular-/square-, triangular-, and trapezoidal-shaped attic space.

In 1995, a study of natural convection within a triangle has been executed by Salmun [22]. Rayleigh number was considered in the range of $10^2$–$10^5$. With the reference to previously executed research, half of the domain has been considered. This study disagreed with the study of Poulikakos by linear stability analysis of the steady-state asymptotic solution in a triangular enclosure. Asan and Namli [2], in 2001, examined the effect for the change in aspect ratio and rayleigh number for the variation in temperature and flow field. While in 2002, Haese and Teubnner [13] investigated triangular enclosure with the consideration of realistic attic structure with the value of Rayleigh number $10^{10}$–$10^{11}$.

Various research work for the analysis of the natural convection inside a square- or rectangular-shaped enclosure is conducted. Bejan et al. [8] studies the effect of heat on the natural convection inside a square cavity. With the consideration of Prandtl number (0.01–0.7) and Rayleigh number ($10^3$–$10^9$), the study had been concluded. Aydin et al. [3] analyzed the effect of aspect ratio for the rectangular-shaped enclosure. The sidewall was considered at high temperature while ceiling at the lower temperature. Sarris et al. [23] considered sinusoidal temperature profile in the rectangular shaped enclosure for upper wall, while others were considered as the adiabatic wall. He concluded with the observation over aspect ratio that intensity of fluid movement increases with an increase in aspect ratio. Basak et al. [4] stated in the reference of his observation for the square cavity that overall heat transfer rate will be higher in the case of the uniform wall heating case in comparison with the non-uniform heating case. Gupta et al. [12] discussed simulative analysis for the study of natural convection inside the various shapes of the enclosure. The study has been executed for finding the most appropriate shape of the enclosure in natural convection with the maximum rate of heat transfer. Different values for the Grashof number and aspect ratio has been considered which lies in the range of $10^4$–$10^8$ and 0.2–0.5, respectively.

Maukalled et al. [19] executed a numerical analysis over a trapezoidal-shaped enclosure with the mounted baffles on the upper wall. Two conditions were examined as one with the short vertical wall at low temperature and long vertical wall at high temperature while the second condition will be vice-versa. The study has been executed for the four Rayleigh numbers and three Prandtl numbers.

Natural convection inside a partially divided trapezoidal has been examined by Emin et al. [9]. The model has been simulated for the summer and winter conditions separately. The horizontal divider has been placed to oppose the buoyancy which results in weaker flow strength while trapezoidal with two internal baffles and inclined top wall has been simulated by Silva [24]. The thermal model has been formed with the isothermal left heated and isothermal right cooled walls. The study has been executed for various values of Rayleigh number ($10^3$ $Ra$ $10^6$), Baffles height (Hb = $H$/3, 2$H$/3, and $H$), and Prandtl number ($Pr$ = 0.7, 10, and 130).

Basak et al. [5, 6] simulated a trapezoidal cavity for the study of natural convection. The model has been designed with the assumption of uniformly heated over the bottom wall and linearly heated vertical wall in the presence of the insulated top wall. Simulation is conducted for various values of the Rayleigh number ($10^3$–$10^5$) and Prandtl number ($Pr = 0.7$–$1$). He also analyzes the domain for the study of entropy generation inside an enclosure and concluded that an increase in Prandtl number increases the entropy generation. Basak concludes the best design on the basis of low value for the entropy generation instead of Nusselt number.

In 2013, Ramakrishna et al. [21] discussed the entropy generation in the presence of the fluid friction and the heat transfer inside a trapezoidal shaped enclosure. A physical model for the study has been considered same as in Basak et al. [5]. Baytas [7] executed a numerical study for the steady-state condition of natural convection inside an inclined trapezoidal-shaped enclosure. The top surface has been kept at low temperature while bottom at high temperature. With the use of Alternative Direction Implicit finite numerical method, Darcy and energy equations are solved. The study has been concluded with the flow and heat transfer characteristics by using streamlines, isotherm, and Nusselt number for various values of Rayleigh number, aspect ratio, and inclined angle.

Kumar et al. [16] concluded that with an increase in the value of Grashof number and the Rayleigh number, Nusselt number increases. The study also observed that Nusselt number increases with an increase in the angle of inclination of the side wall.

Kuyper et al. [17] investigated the influence of the angle of inclination in natural convection with respect to different values for the Rayleigh numbers. Literature review on the topic brings out the gap to find the optimum shape of a trapezoidal attic corresponding to triangle and rectangle. Current article performs the numerical investigation of natural convection to find attic's specification having minimum heat transfer from roof to the floor under three different heat load conditions.

## 2 Assumption, Geometry, and Governing Equation

Physical model for the numerical simulation is described in Fig. 1. Following assumptions are considered for the simulation:

1. Laminar flow.
2. Two-Dimensional flow.
3. Viscous dissipation is neglected.
4. Internal heat source or sink has not been introduced.
5. The fluid is Newtonian.
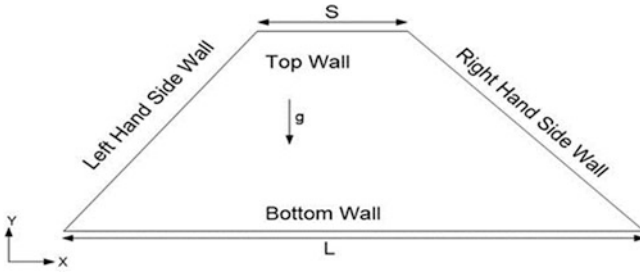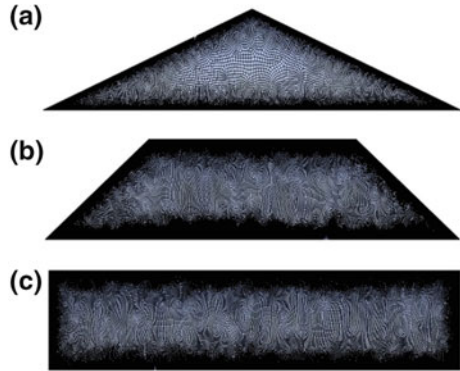6. Compressibility effects are neglected.

**Fig. 1** Physical domain

**Fig. 2** Mesh for the physical domain, **a** S/L = 0; **b** S/L = 0.5; **c** S/L = 1



With an objective to find an attic shape structure with minimum heat transfer, the ratio for the length of the upper wall and lower wall varies between 0 (isosceles triangle) and 1 (rectangle), which is defined as S/L. The heat load condition is considered with the consideration of sun rays normal to the surface of the earth, and upper, left, and right walls of the attic are considered as the hot wall while lower wall as cold. This condition can also be defined as noon of the day. This condition is stated as full-blown heat load condition.

Mesh structure for some of considered attic space is represented in Fig. 2. Dense structure of mesh is considered for the near the area of the wall that helps in the formation of the good-quality boundary layer near the wall of the enclosure.

From Fig. 1 and assumptions, the basic conservation of laws of mass, momentum, and energy can be written in a dimensionless format as:

Continuity equation

$$\frac{\partial U}{\partial X} + \frac{\partial V}{\partial Y} = 0 \tag{1}$$

*X*-momentum equation

$$U\left(\frac{\partial U}{\partial X}\right) + V\left(\frac{\partial U}{\partial Y}\right) = -\frac{\partial P}{\partial X} + \left(\frac{\partial^2 U}{\partial X^2} + \frac{\partial^2 U}{\partial Y^2}\right) \tag{2}$$

*Y*-momentum equation

$$U\frac{\partial V}{\partial X} + V\frac{\partial V}{\partial Y} = -\frac{\partial P}{\partial Y} + \left(\frac{\partial^2 V}{\partial X^2} + \frac{\partial^2 V}{\partial Y^2}\right) + \left(\frac{Ra}{Pr}\right)\theta \tag{3}$$

Energy

$$U\frac{\partial \theta}{\partial X} + V\frac{\partial \theta}{\partial Y} = \frac{1}{Pr}\left(\frac{\partial^2 \theta}{\partial X^2} + \frac{\partial^2 \theta}{\partial Y^2}\right) \tag{4}$$

where

$$X = \frac{x}{H}, \quad Y = \frac{y}{H}, \quad U = \frac{uH}{v}, \quad V = \frac{vH}{v}, \quad \theta = \frac{T - T_c}{T - T_H}, \quad P = \frac{(p + \rho gy)H^2}{\rho y^2}$$

Boundary conditions for the domain introduced as:
Velocity of the wall, $U = V = 0$
Temperature on the adiabatic wall, $\frac{\partial \theta}{\partial X} = 0$
For hot wall, $\theta = 1$
For cold wall, $\theta = 0$
Grashof number is considered as a dimensionless input parameter for the domain, which can be expressed as:

$$G_r = \frac{g\beta H^3 (T_H - T_L)}{v^2} \tag{5}$$

Nusselt number is considered as an output parameter, which is used as a comparing parameter among the different cases:

$$Nu = \frac{h.H}{k} \tag{6}$$

## 3 Validation of the Model

### 3.1 Pure Convection

Vivek et al. [25] investigated tilted enclosure of square-shaped enclosure in the presence of air as a fluid. To validate the model, the square enclosure has been

**Table 1** Validation for the pure convection at $Ra = 10^5$

| Aspect ratio | Vivek et al. [25] | Present |
|---|---|---|
| 1 | 4.56 | 4.55 |
| 2 | 4.15 | 4.27 |
| 3 | 3.85 | 4.10 |
| 5 | 3.50 | 3.81 |

considered for the analysis of pure convection. Model for the Rayleigh number $10^5$ has been simulated for different values of aspect ratio considering no slip on the wall. Table 1 represents a comparison of numerical simulation with the numerical simulation.

## 4 Results and Discussion

Streamlines, isotherm, and value for the Nusselt number are discussed in this section. Simulation is conducted for different values of Grashof number and $S/L$ ratios.

### 4.1 Heat Flow Analysis

For the isotherm contours, the effect of the Rayleigh number ($Ra = 10^4$, $10^5$ and $10^6$) and the inclination angle of an inclined wall ($S/L$ ratio = 0.1–1.0) are examined with the bottom wall at low temperature and all other at high temperature. Uniform temperature is distributed along the walls. In Fig. 3, thermal field inside an enclosure is represented with the use of isotherm lines. At a low value of Rayleigh number. i.e., $10^4$, the pattern of isotherm is observed very similar from the conduction as buoyancy-driven convection is found to be weaker. Isotherm lines are densely packed near to the hot wall. For $Ra = 10^5$ and $10^6$, value of the Nusselt number increases as convection initiates to dominate over the conduction heat transfer, while the nature for the isotherm remains same. For $Ra = 10^6$, generation of the transient condition is observed with the disturbed isotherm lines inside an enclosure.

### 4.2 Flow Field Analysis

The problem has been investigated for the analysis of natural fluid flow inside an enclosure with the effect of buoyancy force. The result of streamlines is illustrated in Fig. 4 for the Rayleigh number $10^4$, $10^5$, and $10^6$. At $Ra = 10^4$, value for the
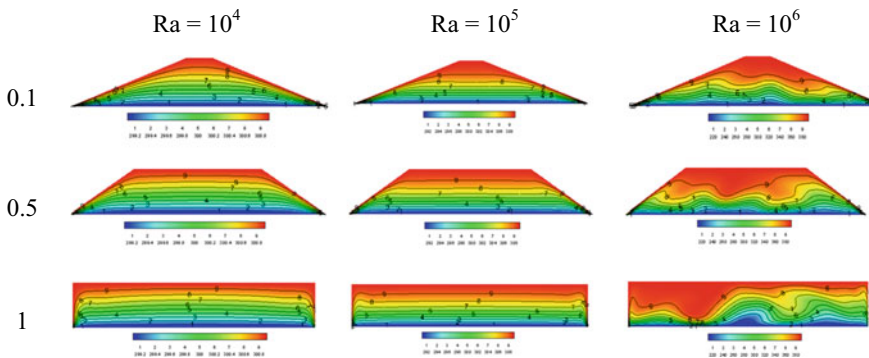
$Ra = 10^4$     $Ra = 10^5$     $Ra = 10^6$



**Fig. 3** Isotherm lines for different values of Rayleigh number at different ratios of *S/L*

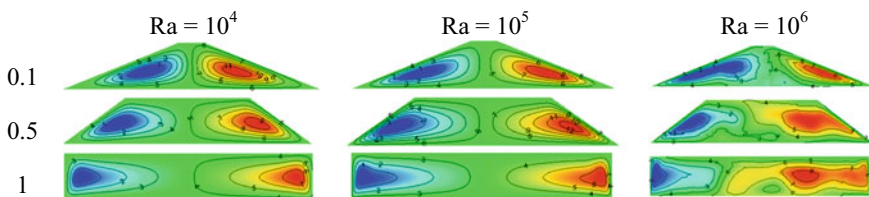$Ra = 10^4$     $Ra = 10^5$     $Ra = 10^6$



**Fig. 4** Streamlines for different values of Rayleigh number at different ratios of *S/L*

stream function is considerably low which supports the transfer of heat by conduction for the low value of Rayleigh number, and two loops of fluidic motion are generated clockwise and anti-clockwise. The flow circulation inside the cavity begins when the hot fluid adjacent to side walls rises above due to buoyancy forces and then circulated downward at the center of the enclosure. Similar to the isotherm lines, $Ra = 10^6$ provides disturbance in the pattern which is approaching towards the generation of turbulence inside the enclosure.

## 4.3   Effect of Rayleigh Number

Figure 5 representing the plot for the change in the average value of Nusselt number with the change in *S/L* ratio. The maximum value of Nusselt number achieved within the triangular-shaped enclosure (*S/L* = 0) while the minimum for the square-shaped enclosure (*S/L* = 1). With an increase in *S/L* ratio, the slope for the change in Nusselt number decreases (from 11 to 6).
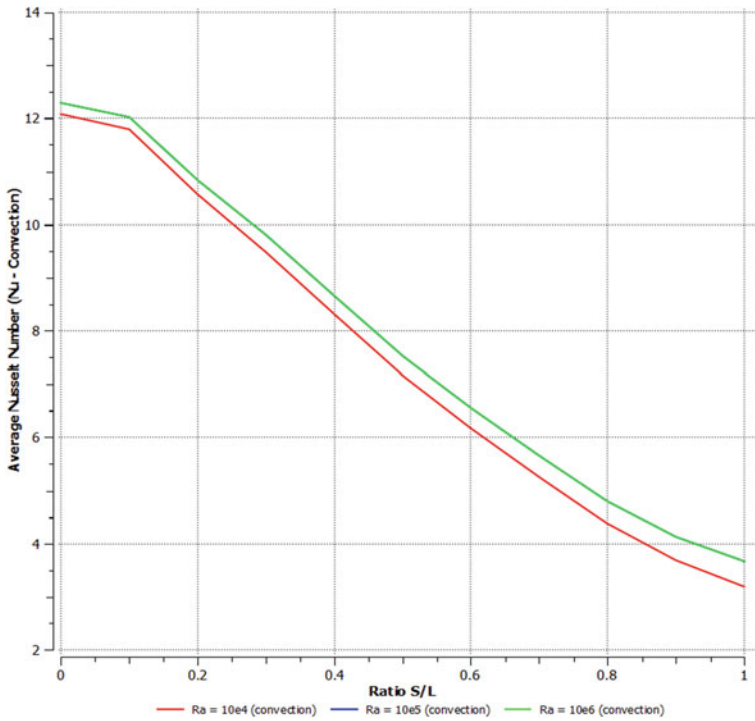
**Fig. 5** Average Nusselt number plot for variation in *S/L* ratio

## 5    Conclusion

With the computational simulation of different cases and different possible shapes of the domain, following conclusions are marked as the outcome of the study:

(a) Turbulence nature is observed for the $Ra = 10^6$ with the disturbance in the pattern of the isotherm and streamlines.
(b) Triangular enclosure has the maximum rate of heat transfer while rectangular enclosure has lowest.
(c) The decrease in value of slope for the value of Nusselt number with the rise in the value of the *S/L* ratio.

With all these studies, we can conclude for the shape of the attic space should be between 0.8 and 0.9 as it is not having much difference from the rectangular enclosure and also having not much difference in the value of the slope for the change in Nusselt number.

# References

1. Akiyama M, Chong Q (1997) Numerical analysis of natural convection with surface radiation in a square enclosure. Numer Heat Transf Part A Appl 32(4):419–433
2. Asan H, Namli L (2001) Numerical simulation of buoyant flow in a roof of triangular cross-section under winter day boundary conditions. Energy Build 33:753–757
3. Aydin O, Ünal A, Ayhan T (1999) Natural convection in rectangular enclosures heated from one side and cooled from the ceiling. Int J Heat Mass Transf 42(13):2345–2355
4. Basak T, Roy S, Balakrishnan A (2006) Effects of thermal boundary conditions on natural convection flows within a square cavity. Int J Heat Mass Transf 49(23):4525–4535
5. Basak T, Roy S, Singh A, Kumar P (2012) Entropy generation vs energy flow due to natural convection in a trapezoidal cavity with isothermal and non-isothermal hot bottom wall. Int J Heat Mass Transf 37(1):514–532
6. Basak T, Roy S, Singh A, Pandey BD (2009) Natural convection flow simulation for various angles in a trapezoidal enclosure with linearly heated side wall(s). Int J Heat Mass Transf 52 (19–20):4413–4425
7. Baytas AC, Pop I (2001) Natural convection in a trapezoidal enclosure filled with a porous medium. Int J Eng Sci 39(2):125–134
8. Bejan A (2004) Convective heat transfer, 3rd edn. Wiley, New York
9. Emin AM, Birol S (2009) Natural convection heat transfer in a partially divided trapezoidal enclosure. Therm Sci 13(4):213–220
10. Flank RD, Turner BL (1980) The experimental measurement of natural convection heat transfer in triangular enclosures heated or cooled from bellow. J Heat Transf 102:770–772
11. Fontanini AD, PrOut KM, Kosny J, Subramanian BG (2016) Exploring future climate trends on the thermal performance of attics: part 1 standard roofs. Energy Build 129:32–45
12. Gupta A, Thakur HC, Vats B (2016) Study of steady natural convection with laminar flow in the enclosures of different shapes. In: ASME international mechanical engineering congress and exposition paper ID—65065, V008T10A027
13. Haese PM, Teubnner MD (2002) Heat exchange in an attic space. Int J Heat Mass Transf 45:4925–4936
14. Iyican L, Bayazitoglu Y, Witte LC (1980) An analytical study of natural convective heat transfer within a trapezoidal enclosure. J Heat Transf 102(4):640–647
15. Iyican L, Witte L, Bayazitoglu Y (1980) An experimental study of natural convection in trapezoidal enclosures. J Heat Transf 102(4):648–653
16. Kumar B, Kumar B (2004) Parallel computation of natural convection in trapezoidal porous enclosures. Math Comput Simul 65(3):221–229
17. Kuyper R, Hoogendoorn C (1995) Laminar natural convection flow in trapezoidal enclosures. Numer Heat Transf Part A: Appl 28(1):55–67
18. Lage J, Bejan A (1993) The resonance of natural convection in an enclosure heated periodically from the side. Int J Heat Mass Transf 36(8):2027–2038
19. Maukalled F, Darwish M (2010) Natural convection in a trapezoidal enclosure heated from the side with a baffle mounted on its upper inclined surface. Heat Transf Eng 28(8):80–93
20. Poulikakos D, Bejan A (1980) Natural convection experiments in a triangular enclosure. J Heat Transf 102:770–772
21. Ramakrishna D, Basak T, Roy S (2013) Analysis of heatlines and entropy generation during free convection within trapezoidal cavities. Int J Heat Mass Transf 45:32–40
22. Salmun H (1995) Convection patterns in a triangular domain. Int J Heat Mass Transf 38:351–365
23. Sarris I, Lekakis I, Vlachos N (2002) Natural convection in a 2d enclosure with sinusoidal upper wall temperature. Numer Heat Transf: Part A: Appl 42(5):513–530

24. Silva AD, Fontana E, Mariani VC, Marcondes F (2012) Numerical investigation of several physical and geometric parameters in the natural convection into trapezoidal cavities. Int J Heat Mass Transf 55(23–24):6808–6818
25. Vivek V, Sharma AK, Balaji C (2012) Interaction effects between laminar natural convection and surface radiation in tilted square and shallow enclosures. Int J Therm Sci 60:70–84

# An Analysis of a Duct with Different Vortex Generators for Performance Enhancement of a Solar Air Heater: Computational Fluid Dynamics (CFD)

**Noel Vinsent Chand, Vineet Kumar and Anuj Kumar Sehgal**

**Abstract** A two-dimensional computational fluid dynamics (CFD) analysis of the artificially roughened solar air heater rectangular duct with three different types of vortex generators (rectangular, triangular, and circular) on the absorber plate is conducted in order to increase the transfer of heat in the flow. ANSYS FLUENT 16.0 is used as a solver to determine the nature of flow in the solar air heater duct having vortex generators using finite element method with the SIMPLE algorithm as a base. The variation of average Nusselt number was investigated with the change in Reynolds number ranging from 3800–18,000 and with the constant heat flux of 1100 W/m$^2$. The research has found that the average Nusselt number was considerably increased with every range of Reynolds number in all the geometries but most significantly increased in triangular vortex generator with negligible pressure drop. The value of average Nusselt number found in triangular vortex generator at Reynolds number 18,000 was 3.848 times to that of average Nusselt number of the smooth duct at same Reynolds number. The thermo-hydraulic performance and enhancement ratio of Nusselt number is also studied and found to be the best for the duct with triangular vortex generator at Reynolds number 3800.

**Keywords** Vortex generator · Solar air heater · CFD · Thermo-hydraulic performance

## 1 Introduction

Solar air heater is a simple device, which absorbs the coming solar radiations from the space and converts them as usable heat energy using absorber plate as a major component. The solar radiation converted into the usable heat can be used in several places with enormous applications. Currently, solar air heaters are used for space

N. V. Chand · V. Kumar (✉) · A. K. Sehgal
Department of Mechanical Engineering, SET, Sharda University,
Greater Noida 201306, Uttar Pradesh, India
e-mail: anujsehgal2000@gmail.com

heating and drying processes effectively with reduced energy consumption. Solar air heaters are efficient and less costly in terms of installation and operations. It is evident that earth is abundant of energy resources but not in usable form and therefore needed to be converted in the form that can be used by human. Many research studies emphasizing improvement in the existing devices are attempted for the better and efficient conversion of such available energy. Thus in present study, the three geometries, i.e., triangular, rectangular, and circular vortex generators are considered for performance enhancement of a solar air heater.

## 2 Literature Review

CFD analyses have been done to see the effect of circular vortex generator in rectangular duct considering different aspect ratio and pitch which proves the thermal enhancement ratio to be 1.06 times than with circular ribs [1]. Similar work was done to analyze the enhancement of transfer of heat using artificial semi-circular roughness which gives the thermo-hydraulic performance parameter of 1.616 with roughness size of 0.06 and 7.5 was the relative-roughness pitch [2]. Also, a same case using circular sectioned transverse ribs at six different Reynolds number ranges found the thermo-hydraulic performance to be best at Reynolds number 15,000 at 10.71 relative pitch roughness [3]. The investigation carried on semi-circular transfer ribs shows that the friction factor and Nusselt are completely dependent on the rib height which provides the best thermo-hydraulic performance parameter when relative-roughness height of 0.042 was considered [4, 5]. Many researches are going on the wedge-shaped transverse rib which also shows very satisfactory results for the enhancement of heat transfer [6]. Experimental investigation shows the effect of W-shaped vortex generator on the heat transfer. The Nusselt number was $0.216 \times 10$ to that of smooth duct and friction factor was found $0.275 \times 10$ to that of smooth pipe when the attack angle was 60° and 0.0338 was roughness height [7]. The research is not limited till semi-circular, W-shaped, or circular. A study in rectangular solar air heater duct having rectangular-roughness portion on the absorber plate shows that highest value of Nusselt number gives 1.4–2.7 times enhancement in Nusselt number as compared to smooth duct [7]. Another simulation at higher Reynolds number was conducted on square-sectioned roughness on the absorber plate. The research considered three different values of pitch (P) and rib height (e) with the different values of Reynolds number ranging from 3800–18,000 and relative-roughness pitch remains constant. The research shows that friction, average heat transfer, and thermo-hydraulic performance were found to be 1.8 for the given range [8]. In many researches, triangular ribs are also seen, which shows triangular rib roughness enhances the Nusselt number from 1.4–2.7 as compared to smooth duct and Nusselt number was found highest at 10 relative-roughness pitch [9]. The development in the solar air

heater is to modify the duct, in which the air heats up and flow by the temperature difference without the use of electric pump. Introduction of the ribs in the duct is the main ingredient for the enhancement of the heat transfer coefficient as it separates the laminar sub-layer in every Reynolds number and formation of vortices mix the flowing air through which heat transfer is enhanced and thermal losses are reduced by transparent plate which is kept on the rectangular absorber plate with ribs. However, the introduction of ribs can certainly create a pressure drop at the outlet of the duct with ribs [10].

# 3 CFD Analysis

## 3.1 Computational Domain

Circular, triangular, and rectangular vortex generators have been used to enhance the heat transfer of the solar air heater duct by increasing the mixing of the fluid inside the duct which is accomplished by increasing the turbulence. A two-dimensional analysis is carried out in order to reduce computational time and power. The study involves Reynolds number ($Re$) ranging from $3800 \leq Re \leq 18{,}000$ under which the solar air heat is operated. The vortex generators in every case are considered under the absorber plate with a uniform flux of 1100 W/m2. Relative pitch ($P/e$) is taken as 14.29, relative height ($e/Dh$) is 0.12, and aspect ratio of duct ($W/H$) is 5. The dimensions of the domain, shown in Fig. 1a–c, consist of three lengths. L1 is the inlet length of the duct, L2 is the test length where vortices are created, and L3 is the outlet of the duct. Rectangular, circular, and triangular vortex generators employed in the downside of the absorber plate have the height (e) of 4 mm and the constant pitch (P) is taken 53.16 mm, and height of the heater duct is 20 mm (Fig. 2; Tables 1 and 2).
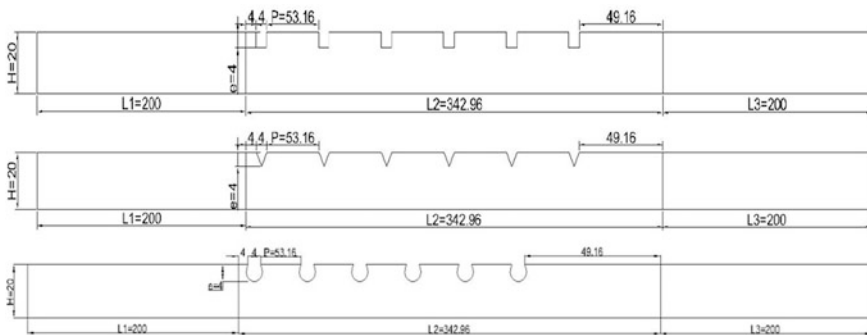


**Fig. 1** Two-dimensional computational domain for **a** rectangular vortex generators, **b** triangular vortex generators, and **c** circular vortex generators

**Fig. 2** Mesh in the duct with circular, triangular, and rectangular vortex geometry

**Table 1** Operating parameters for all three geometries used in the analysis

| Operating parameters | Range |
| --- | --- |
| Reynolds number (Re) | 3800–18,000 (5 values) |
| Uniform heat flux (q) | 1100 (W/m$^2$) |
| Prandlt number (Pr) | 0.7441 |
| Relative pitch (P/e) | 14.29 |
| Relative height (e/D$_h$) | 0.1200 |
| Aspect ratio of duct (W/H) | 5 |

**Table 2** Properties of the working fluid (air) and the duct material (Aluminum)

| Properties | Air | Aluminum |
| --- | --- | --- |
| Density ($\rho$) (Kg/m$^3$) | 1.225 | 2719 |
| Specific heat (C$_p$) (J/Kg.K) | 1006.43 | 871 |
| Dynamic viscosity ($\mu$) (N.s/m$^2$) | $1.7894 \times 10^{-5}$ | – |
| Thermal conductivity (K) (W/m.K) | 0.0242 | 2024 |

## 3.2  Mesh Generation

The mesh in all three geometries are generated by using ANSYS ICEM CFD version 16 software with patch conforming. After grid independence test, duct with triangular vortex generator that contains 162,425 elements, duct with circular vortex generator that contains 125,888 elements and duct with rectangular vortex generator that contains 192,000 elements are selected as there was 1–2% deflection in average Nusselt number and friction factor. RNG (renormalizing group)-k-Epsilon turbulence model is used for the analysis of the flow as it gives close results for a given condition of flow. All governing equation is discretized by SIMPLE (semi-implicit method for pressure-linked equation) algorithm as the flow is completely based on pressure and second-order up-winding scheme is used for the transport equations. The name selection is given inlet as INLET, walls as WALLS, walls of the vortex generators including the underwalls of the of the absorber plate is named as HEATED_WALLS and the cell zone/fluid region is named as FLUID.

## 3.3 Conservation of Mass

The continuity equation is a mathematical expression of the principle of conservation of mass. In case of multiple inlets and outlets for control volume and steady state flow, the continuity equation takes the sum of mass flow rates of all inlets and outlets, the equation becomes;

$$\Sigma\left(A_1 v_1\right) = \Sigma\left(A_2 v_2\right) \tag{1}$$

$\nabla \cdot v = 0$ (for incompressible flow)

## 3.4 Equations Involved in the Current Research

Considering a two-dimensional, steady state and incompressible flow with zero influence of radiation portion

Equation hydraulic diameter:

$$D_h = \frac{2(a \times b)}{a + b} \tag{2}$$

Heat transfer enhanced with the use of certain types of vortex generators in a rectangular duct of solar air heater is determined by calculating the Nusselt number

$$Nu = \frac{h D_h}{K} \tag{3}$$

where $Nu$ = Nusselt number, $h$ = convective heat transfer coefficient, $Dh$ = hydraulic diameter, and $K$ = coefficient of heat transfer.

Due to the friction provided by vortex generator, there is a pressure drop at the outlet of the rectangular duct. The average friction factor is computed by:

$$f_{\text{avg}} = \frac{\left(\Delta P/_l\right) D_h}{2\rho \, v U^2} \tag{4}$$

where $\Delta P$ = pressure drop at the end of the duct and $l$ = test length of the rectangular duct. Reynolds number of the flow is defined by

$$Re = \frac{\rho u D_h}{\mu} \tag{5}$$

where $\mu$ = dynamic viscosity.

The enhancement of the heat transfer and the increase of heat transfer coefficient of a duct with vortex generators as compared to that of smooth duct are calculated by thermal enhancement factor proposed by Webb and Eckert:

$$\text{TEF} = \frac{Nu_v/Nu_s}{\left(f_v/f_s\right)} \tag{6}$$

According to Dittus–Bolter equation, Nusselt number for the smooth duct ($Nu_s$) is defined by:

$$Nu_s = 0.023 \times Re^{0.8} \times Pr^{0.4} \tag{7}$$

Friction factor is defined by Blasius equation for smooth duct:

$$f_s = 0.0791 \times Re^{-0.25} \tag{8}$$

## 4 Results and Discussion

In the CFD analysis, heat transfer is enhanced as the velocity increases, the average Nusselt number is increased as expected in all three cases of solar air heater duct. Figure 4 shows the increment of average Nusselt number with the Reynolds number keeping aspect ratio same. It can be seen that application of vortex generators has increased the transfer of heat as compared to heat transfer in smooth duct. When the flow of certain velocity comes across the vortex generator geometries, the vortex generator projects the flow beyond the viscous sub-layer which gives increment in mixing of the fluid and heat taken from the vortex generator surface is evenly distributed throughout the flow as shown in Fig. 3. The increment in Nusselt number totally depends on the turbulence and turbulent dissipation. Laminar sub-layer starts on decreasing as the Reynolds number increases and vortex generators in between the flow mix the fluid which makes a better contact of heated wall and fluid leading to enhance the transfer of heat.

The friction factor is maximum at lowest Reynolds number of 3800 in triangular vortex generator as the vortices formed by the them are larger which give rise in pressure drop and turbulent kinetic energy is highest in this section ($Re = 18,000$). Pressure drop is noted less in duct with rectangular and circular vortex generators as compared to triangular vortex generator.
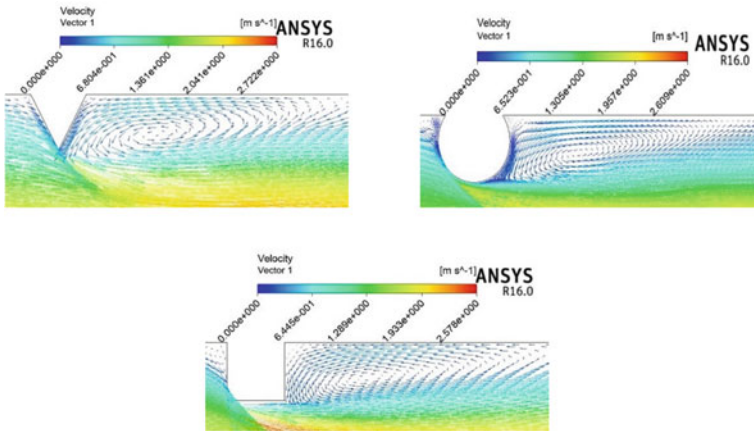
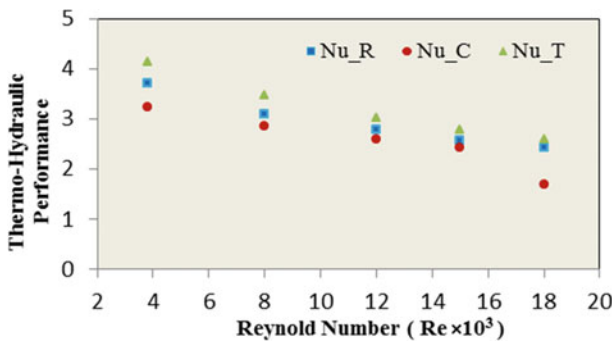**Fig. 3** Contour of velocity vector shows the vortices formed by the different vortex generators



**Fig. 4** Thermo-hydraulic performance versus Reynolds number

## 5 Conclusion

The heat enhancement techniques are applicable if thermo-hydraulic performance parameter is greater than unity. Figure 4 represents the thermo-hydraulic performance for the triangular, rectangular, and circular vortex geometries of duct. The maximum value of thermo-hydraulic performance for the triangular, rectangular, and circular vortex geometries of duct is obtained to be 4.1278, 3.87, and 3.2270, respectively at Reynolds number of 3800 while the minimum value of thermo-hydraulic performance is obtained to be 2.59, 2.41, and 1.42, respectively at Reynolds number of 18,000. Figure 5 represents the variation of average Nusselt number with respect to Reynolds number for different geometries. The average Nusselt number is found to be maximum (199.48265) with triangular vortex generator at $Re = 18,000$, which is about 3.848 times that of smooth duct at same
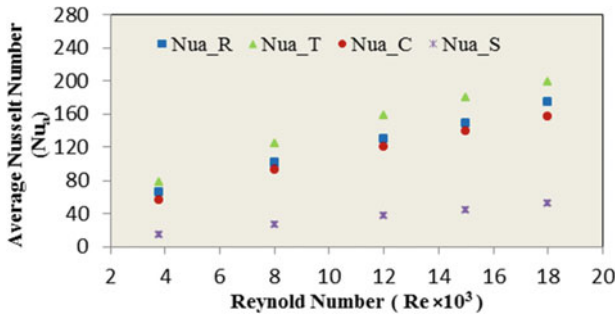
**Fig. 5** Average Nusselt number at given Reynolds number for different geometries
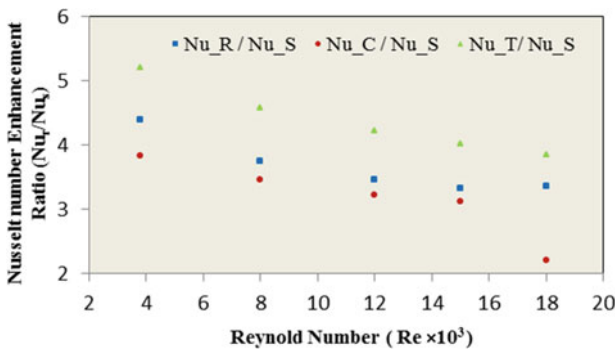


**Fig. 6** Enhancement of Nusselt number at given Reynolds number for different geometries

Reynolds number. Figure 6 represents the enhancement of Nusselt number at given Reynolds number for different geometries. The Nusselt number enhancement ratio is found to be 5.20216 at $Re = 3800$ in triangular vortex generator case, which keeps on decreasing with the increase in Reynolds number due to decrease in friction factor and reach down to 3.2 at $Re = 15,000$ in circular vortex generator case.

## References

1. Gawande VB, Dhoble AS, Zodpe DB (2014) Effect of roughness geometries on heat transfer enhancement in solar thermal systems—a review. Renew Sustain Energy Rev 32:347–378. https://doi.org/10.1016/j.rser.2014.01.024
2. Gawande VB, Dhoble AS, Zodpe DB, Chamoli S (2016) A review of CFD methodology used in literature for predicting thermo-hydraulic performance of a roughened solar air heater. Renew Sustain Energy Rev 54:550–605. https://doi.org/10.1016/j.rser.2015.10.025

3. Yadav AS, Bhagoria JL (2014) A CFD based thermo-hydraulic performance analysis of an artificially roughened solar air heater having equilateral triangular sectioned rib roughness on the absorber plate. Int J Heat Mass Transf 70:1016–1039. https://doi.org/10.1016/j.ijheatmasstransfer.2013.11.074

4. Yadav AS, Bhagoria JL (2014) A numerical investigation of square sectioned transverse rib roughened solar air heater. Int J Therm Sci 79:111–131. https://doi.org/10.1016/j.ijthermalsci.2014.01.008

5. Yadav AS, Bhagoria JL (2014) A numerical investigation of turbulent flows through an artificially roughened solar air heater. Numer. Heat Transf Part A Appl 65:679–698. https://doi.org/10.1080/10407782.2013.846187

6. Aharwal KR, Gandhi BK, Saini JS (2009) Heat transfer and friction characteristics of solar air heater ducts having integral inclined discrete ribs on absorber plate. Int J Heat Mass Transf 52:5970–5977. https://doi.org/10.1016/j.ijheatmasstransfer.2009.05.032

7. Kumar A, Saini RP, Saini JS (2012) Heat transfer and friction factor of solar air heater having duct roughened artificially with discrete multiple v-ribs. J. Renew Sustain Energy **4** (2012). https://doi.org/10.1063/1.4717511

8. Gawande VB, Dhoble AS, Zodpe DB, Chamoli S (2016) Experimental and CFD investigation of convection heat transfer in solar air heater with reverse L-shaped ribs. Sol Energy 131:275–295. https://doi.org/10.1016/j.solener.2016.02.040

9. Singh Yadav A, Kumar Thapak M (2014) Artificially roughened solar air heater: Experimental investigations, Renew. Sustain. Energy Rev 36:370–411. https://doi.org/10.1016/j.rser.2014.04.077

10. Kumar A (2014) Analysis of heat transfer and fluid flow in different shaped roughness elements on the absorber plate solar air heater duct. In: Energy Procedia, pp 2102–2111. https://doi.org/10.1016/j.egypro.2014.10.176

# Experimental Investigation on a Solar Thermal Energy Packed Bed Sensible Heat Storage Combined with Latent Heat Storage

**Vineet Kumar, Anuj Kumar Sehgal and Abhishek Gupta**

**Abstract** The thermal energy storage is required to store the solar energy, which can be stored by using sensible, latent and thermo-chemical heat storage energy systems. The sensible heat storage is more reliable and full-fledged technology, but it is low efficient due to low heat storage density. In the present study, experimental setup is developed by combining the sensible heat storage with a latent heat storage unit in order to store the solar energy. The developed thermal energy storage unit contains an insulated cylindrical tank having hollow spherical capsules of HDPE (filled with fatty acid which has phase-change property). The water and oil liquid transport medium is used as a heat-carrying substance which works as a transporting heat energy from high-temperature container to TES tank and act as SHS materials. The temperature of the transport medium is maintained constant at inlet of the tank during charging and discharging processes. The effect of flow rate and inlet temperature of HTF is analyzed on charging time with the help of charging experiments. The performance parameters viz. cumulative heat stored and efficiency are analyzed during charging and discharging processes. The result shows that efficiency of the system with water as HTF is more than that of oil.

**Keywords** Sensible heat storage · Phase-change material · Encapsulated phase-change material · Thermal energy storage

## 1 Introduction

Sensible heat storage systems are easy in design compared to latent heat or thermo-chemical storage systems. They have disadvantages of non-isothermal behavior during the charging (heat storage) and discharging (heat recovery) processes and low amount of heat storage capacity per unit volume of the storage

V. Kumar · A. K. Sehgal (✉) · A. Gupta
Department of Mechanical Engineering, SET, Sharda University,
Greater Noida 201306, Uttar Pradesh, India
e-mail: anujsehgal2000@gmail.com

medium, i.e., low storage density. On the other hand, there are some features due to which LHS system has received attention such as storing a large amount of heat in a small volume, i.e., high storage density and isothermal behavior during charging and discharging processes. Singh et al. [1] reviewed that the large-sized pebble was used mostly as compared to medium-sized pebble material in packing and therefore recommended more investigations considering medium storage material in packed bed. Saez and McCoy [2] analyzed the effect of Biot number and the mathematical analysis showed that the intra-particle diffusion can only be neglected if Biot number ≪1. Khan et al. [3] reviewed the performance enhancement of phase-change material-based LHS system within the context of materials, thermal stability, and compatibility. Author found that core-to-coating ratio determines the thermal and mechanical stability of encapsulated PCM. If core-to-coating ratio is too high, then it will produce weak shell and if it is too low, then it will decrease the amount of phase-change material in encapsulation. Hence, optimum value of core-to-coating ratio is required. Ghare et al. [4] studied the effect of fins in rectangular container of phase-change material and concluded that increase in heat transfer rate cannot be obtained by increase in number of fin beyond a critical value. Wai et al. [5] investigated that the phase-change spherical-type capsule has better heat release performance as compared to other shapes of capsule. Nallusamy et al. [6] conducted comparative analysis between the combined energy storage system and conventional SHS system. The analysis showed that when heat transfer fluid is mixed directly with hot water, then conventional sensible heat storage system results inferior as compared to the combined storage energy system. Nallusamy et al. [7] concluded a numerical and experimental analysis of a solar water heating system considering combined sensible and latent heat storage. The analysis showed that the heat extraction rate from the collector and charging rate of thermal energy storage tank has been significantly affected by volume flow rate. Pandiyarajan et al. [8] explained that the energy efficiency can be increased by using different phase-change materials in cascaded arrangement. Zanganeh et al. [9] proposed that behavior of combined thermal energy storage is significantly influenced by phase-change material thermal properties, while addition of PCM has substantially less effect on the overall efficiency.

## 2  Development of TES Tank

In thermal energy, storage tank capsules are placed which contains the phase-change material fatty acid and high-density Polyethylene. The thermal and physical properties of PCM materials are given below in Table 1. Figure 1 shows the EPCM (Encapsulated phase-change material) and its arrangement in TES tank. Thermal energy storage tank has various parts such as cylinder with flange, upper and lower plenum, and cover plate at top and bottom ends. Different dimensions of various parts of TES tank are tabulated in Table 2.

**Table 1** Thermal and physical properties of PCM (fatty acids)

| Property | Value | Property | Value |
|---|---|---|---|
| Melting temp (°C) | 57 °C | Solid thermal conductivity (W/mK) | 0.16 |
| Freezing temp (°C) | 55 °C | Base material | Organic |
| Latent heat (kJ/kg) | 210 | Flammability | No |
| Solid density (kg/m$^3$) | 840 | Thermal stability (cycles) | $\sim 2000$ |
| Liquid specific heat (kJ/kgK) | 3.05 | Maximum operating temperature (°C) | 120 |
| Liquid thermal conductivity (W/mK) | 0.1 | Flash point (°C) | 200 |



**Fig. 1** Photograph of EPCM and arrangement in TES tank

**Table 2** Details of dimensions of part of TES tank

| Parameter | Value (in mm) | Parameter | Value (in mm) |
|---|---|---|---|
| *Cover plate* | | *Plenum* | |
| Diameter/thickness | 360/2 | Height/inner/outer diameter | 100/290/294 |
| *Cylinder* | | Thickness/flange thickness | 2/33 |
| Height | 510 | *Fastener* | |
| Inner/outer diameter | 295/300 | Bolt length/diameter | 30/10 |
| Thickness/flange thickness | 2.5/30 | | |

# 3 Experimental Investigations

## 3.1 Experimental Setup

A schematic view of experimental setup is shown in Fig. 2. This consists of a thermal energy storage tank, hot and cold water tank, electric heater, circulating pump, flow meter, pipe line, and valves. Thermal energy storage tank contains spherical capsule of high-density polyethylene (HDPE) with outer diameter of 75 mm. Total number of spherical capsules is 48 and are uniformly packed in four

**Fig. 2** Schematic diagram of experimental setup
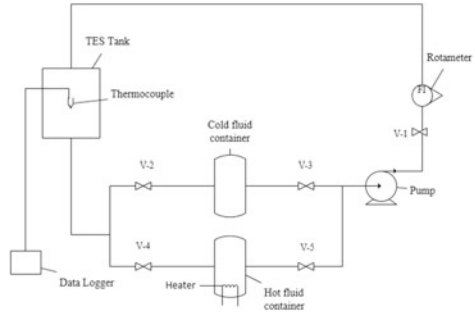
layers and each layer is supported by wire mesh. A tank is provided with number of holes to insert the thermocouple wire to measure the temperature. Thermocouple TP1, TP2, TP3, and TP4 (Temperature of PCM at four segments of TES tank) are inserted into encapsulated PCM and they are used to measure the temperature of PCM at different segments of TES tank. Thermocouple TF1, TF2, TF3, and TF4 (Temperature of HTF at four segments of thermal energy storage (TES) tank) are used to measure the temperature of HTF at different segments. Thermocouple TFI [inlet temperature of heat transfer fluid HTF (°C)] and TFO (outlet temperature of HTF) are used to measure the temperature of HTF at inlet and outlet, respectively. All the thermocouples are connected to data logger, and data logger is connected to computer. Hot and cold HTFs are stored in two different plastic containers. Electrical heater is fitted with hot water tank to heat the water up to required temperature. HTF in pipeline is circulated by pump driven by 0.5 HP, single phase, and 230 V. Valve V1 is used to control the volume flow rate through rotameter and extra amount of HTF goes to tank through bypass line.GI pipeline is used for fluid supply from plastic containers to storage tank. Polyethylene foam is used to insulate the pipeline to minimize the heat loss. All pipe joints are sealed properly to prevent any leakage of fluid. Distributor is provided at inlet of pipeline in upper plenum of storage tank to distribute the HTF in storage tank.

## 3.2 Experimental Trial

Hot and cold HTFs are stored in two different plastic containers. Electrical heater is fitted with hot water tank to heat the water up to required temperature. HTF in pipeline is circulated by pump driven by 0.5 HP, single phase, 230 V. Valve V1 is used to control the volume flow rate through rotameter and extra amount of HTF goes to tank though bypass line. GI pipeline is used for fluid supply from plastic containers to storage tank. Polyethylene foam is used to insulate the pipeline to minimize the heat loss. All pipe joints are sealed properly to prevent any leakage of

fluid. Distributor is provided at inlet of pipeline in upper plenum of storage tank to distribute the HTF in storage tank. The experimentation was done to investigate the effect of inlet temperature and flow rate of heat transfer fluid (water and oil) on charging time and temperature distribution of PCM. Charging process was carried out at inlet temperature of 70 and 75 °C and flow rate of 1, 2, and 3 lpm, respectively. Discharging process was carried out at flow rate of 1 lpm and inlet temperature of 30 and 40 °C for water and oil, respectively.

# 4 Results and Discussions

## 4.1 Charging Process

### 4.1.1 Temperature Variation of HTF and PCM

Figures 3, 4, 5, and 6 show the temperature variation for heat HTF and phase-change materials for water and oil transporting medium. Figures 3 and 4 represent the HTF temperature variation as it flows at constant temperature 70 °C with flow rate 1 lpm from TES reservoir tank. The observation shows that heat transfer fluid temperature falls when it moves in storage tank from top side to bottom side and this fall in temperature takes place because it transfers heat to phase-change material. Figures 5 and 6 show the PCM temperature at four segments that are measured by considering heat transfer fluid mean temperature 70 °C and constant flow rate 1 lpm. The heat transfer fluid is considered water and oil. It is observed that in starting the PCM temperature increases slowly during charging and it is constant during melting and after melting temperature raises suddenly. The temperature difference between PCM and HTF at first layer is more than that of second layer, as heat transfer fluid gets cooled from top side to bottom side of tank.
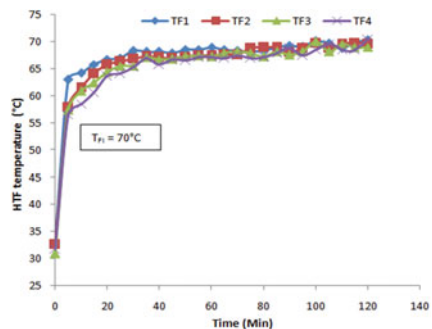
**Fig. 3** Temperature of HTF (water) during charging

**Fig. 4** Temperature of HTF
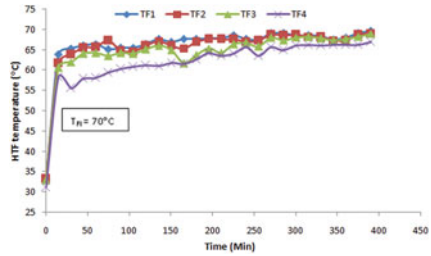(oil) during charging



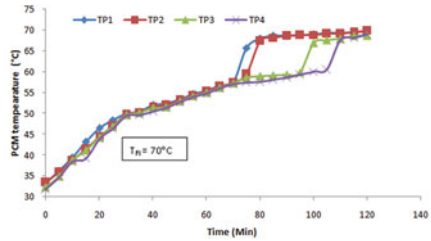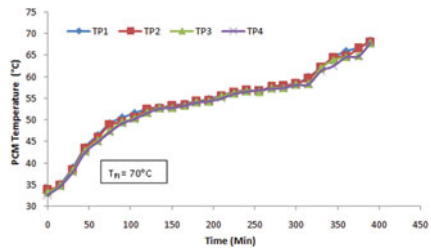**Fig. 5** Temperature of PCM
during charging with water



**Fig. 6** Temperature of PCM
during charging with oil



### 4.1.2 Effect of HTF Inlet Temperature on Charging Time

Figures 7 and 8 show time taken in charging decreases as the temperature of the
inlet increases from 70 to 75 °C. The charging time for water is reduced from 120
to 95 min and for oil, the charging time is reduced from 390 to 345 min.

### 4.1.3 PCM Temperature Effect on Charging Time

Figures 9 and 10 show the effect of flow rate on charging time. The results show the
effect of flow rate on charging time; as the flow rate increased from 1 to 3 lpm,

**Fig. 7** Effect of inlet
temperature of HTF (water)
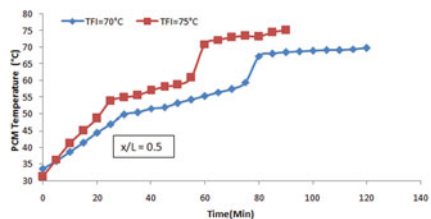
**Fig. 8** Effect of inlet temperature of HTF (oil)
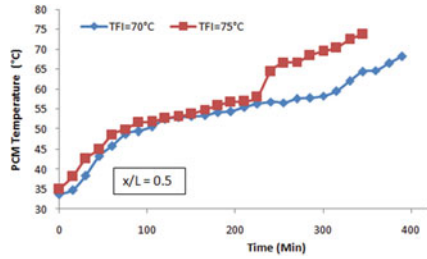


**Fig. 9** Effect of water flow rate on the charging time
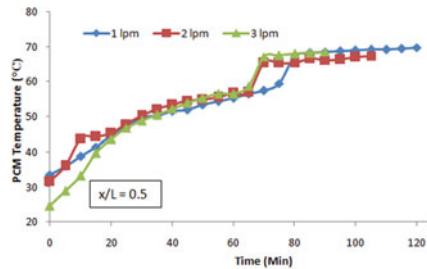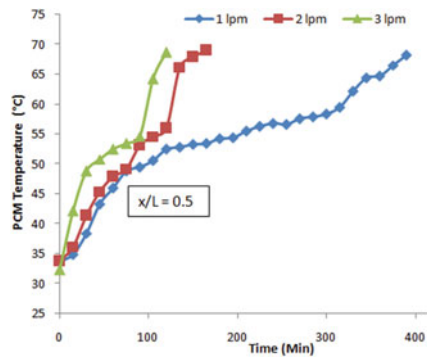


**Fig. 10** Effect of oil flow rate on the charging time



the charging time taken in process is reduced from 120 to 90 min for water, and for oil the time taken in charging process is also reduced from 390 to 120 min.

## 4.2 *Discharging Process*

Figures 11 and 12 show the variations of temperature of PCM at different segments of TES tank for water and oil as HTF, respectively. It is observed that temperature of PCM at first segment is less than that of second segment due to more temperature difference between PCM and HTF at first segment. It is also observed that initially

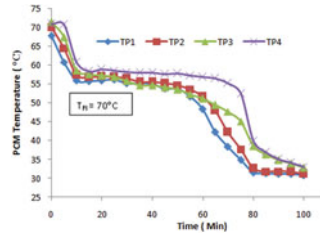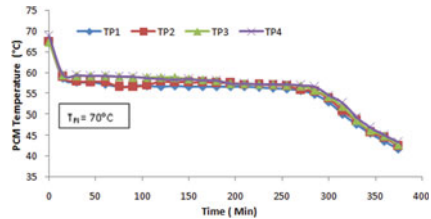**Fig. 11** Temperature during
discharging with water



**Fig. 12** Temperature during
discharging with oil



fall in temperature is significantly more until PCM achieved phase transition
temperature and that fall in temperature is negligible due to latent heat released by
PCM.

## 4.3 Cumulative Heat Stored

Figures 13 and 14 show the amount of cumulative heat stored in the storage tank
for average inlet HTF temperature 70 °C and different flow rate with water and oil
as HTF, respectively. Figures 13 and 14 cumulative heat storage graph trends show
that the flow rate has more effect on cumulative heat stored. Thermal performance
of TES system in terms of efficiency is shown in Table 3.

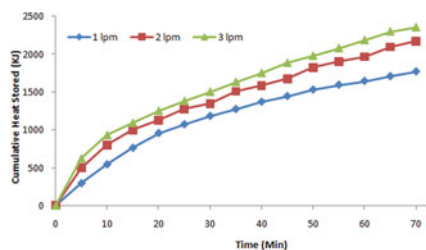**Fig. 13** Cumm. heat stored
during charging water
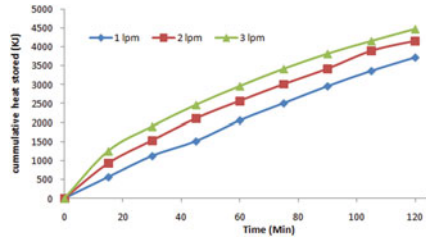
**Fig. 14** Cumm. heat stored
during charging with oil



**Table 3** Thermal performance of TES system

| HTF | Water | Oil |
|---|---|---|
| Inlet HTF temperature during charging process | 70 °C | 70 °C |
| Inlet HTF temperature during discharging process | 30 °C | 40 °C |
| Flow rate during charing process | 1 lpm | 1 lpm |
| Flow rate during discharging process | 1 lpm | 1 lpm |
| Energy released by HTF during charging | 2371.93 kJ | 9301.63 kJ |
| Energy extracted by HTF during discharging | 749.47 kJ | 1742.25 kJ |
| Efficiency | 31.59% | 18.73% |

## 5 Conclusions

A thermal energy storage system is developed to store the energy, in which fatty
acid is used to store the energy. The fatty acid phase-change material stores energy
by changing the phase change from solid to liquid and liquid to solid. In this
system, oil and water is used as a heat transfer fluid. The PCM container taken is
cylindrical type having upper and lower plenum at top and bottom, respectively.
The conclusions drawn from the study are as follows:

Charging process is carried out at inlet HTF temperature 70 °C and flow rate 1,
2, 3 lpm for water and oil. Charging process is carried out at inlet HTF temperature
75 °C, flow rate 1 lpm for water and oil. Discharging process is carried out at inlet
HTF temperature 30 °C, flow rate 1 lpm and inlet HTF temperature 40 °C, and
flow rate 1 lpm for water and oil, respectively.

The result obtained from experiments show that with increasing inlet tempera-
ture and flow rate of HTF, the charging time of storage is decreased due to the
improvement in heat transfer rate. As inlet temperature is increased from 70 to 75 °
C, charging time is decreased from 120 to 95 min and 390 to 345 min in case of
water and oil, respectively. As flow rate is increased from 1 to 3 lpm, charging time
is decreased from 120 to 90 min and 390 to 120 min in case of water and oil,
respectively.

The rise in temperature of storage material has been found faster in case of water
compared to oil. Also efficiency is found to be higher in case of water compared to

oil due to lower convective heat transfer coefficient of oil than water. Efficiency when using water as HTF is 31.59%, whereas for oil it is 18.73%. It is concluded that water is better HTF than oil due to high efficiency.

# References

1. Singh H, Saini RP, Saini JS (2010) A review on packed bed solar energy storage systems. Renew Sustain Energy Rev 14:1059–1069. https://doi.org/10.1016/j.rser.2009.10.022
2. Saez AE, McCoy BJ (1982) Dynamic response of a packed bed thermal storage system—a model for solar air heating. Sol Energy 29:201–206
3. Khan Z, Khan Z, Ghafoor A (2016) A review of performance enhancement of PCM based latent heat storage system within the context of materials, thermal stability and compatibility. Energy Convers Manag 115. https://doi.org/10.1016/j.enconman.2016.02.045
4. Gharebaghi M, Sezai I (2008) Enhancement of heat transfer in latent heat storage modules with internal fins. Numer Heat Transf Part A Appl 53:749–765. https://doi.org/10.1080/10407780701715786
5. Wei J, Kawaguchi Y, Hirano S, Takeuchi H (2005) Study on a PCM heat storage system for rapid heat supply. Appl Therm Eng 25:2903–2920. https://doi.org/10.1016/j.applthermaleng.2005.02.014
6. Nallusamy N, Velraj R (2009) Numerical and experimental investigation on a combined sensible and latent heat storage unit integrated with solar water. J Sol Energy Eng 131:1–8. https://doi.org/10.1115/1.3197600
7. Nallusamy N, Velraj R (2007) Experimental investigation on a combined sensible and latent heat storage system integrated with constant/varying (solar) heat sources renewable. Energy Eng 32, 1206–1227
8. Pandiyarajan V, Chinnappandian M, Raghavan V, Velraj R (2011) Second law analysis of a diesel engine waste heat recovery with a combined sensible and latent heat storage system. Energy Policy 39:6011–6020. https://doi.org/10.1016/j.enpol.2011.06.065
9. Zanganeh G, Commerford M, Haselbacher A, Pedretti A, Steinfeld A (2014) Stabilization of the outflow temperature of a packed-bed thermal energy storage by combining rocks with phase change materials. Appl Therm Eng 70:316–320. https://doi.org/10.1016/j.applthermaleng.2014.05.020

# Numerical Simulation of Cold Flow Analysis of Internal Combustion Engine with Double-Lobed Piston Head

**B. Bibu and Vikas Rajan**

**Abstract** The demand for cost-effective eco-friendly automobiles is increasing day by day because of its impact on reducing air pollution. We cannot compromise with the usage of automobiles and its advancements as it is inevitable for the development. The only way to combat the problem of air pollution is the reduction of the harmful emissions, and it can be achieved by introducing new innovative engine designs which can give a complete combustion. This paper proposes a new double-lobed piston head design which can give better in-cylinder air flow patterns (Tumble and Swirl), turbulence and air–fuel mixing for an IC engine and thereby result in complete combustion. The in-cylinder airflow patterns developed during the intake stroke and the compression stroke of this newly designed IC engine were analyzed and compared with that of conventional flat piston head engine using the numerical simulation of cold flow analysis. No change in tumble was observed which means the piston head configuration has a negligible effect on the tumble. But there is a 66.67% increase in swirl during intake stroke and 91.47% increase during the compression stroke. This increased swirl creates high turbulence and thereby increasing the engine's combustion efficiency. These results proved the efficiency of the double-lobed piston head configuration in providing better engine performance and thereby reducing the air pollution.

**Keywords** Cold flow analysis · Double-lobed piston head · Flat piston head · Swirl motion · Tumble motion

B. Bibu (✉) · V. Rajan
Department of Mechanical Engineering, Amrita Vishwa Vidyapeetham,
Amritapuri, India
e-mail: bibubjohn@gmail.com

V. Rajan
e-mail: vikasrajan@am.amrita.edu

# 1   Introduction

We need constant innovations and new engine designs in order to satisfy today's growing demands for eco-friendly, economically feasible, high-performance automobiles [1]. Recently, a new analysis method called computational fluid dynamics (CFD) has emerged for understanding the complex fluid dynamics and chemical reactions occurring inside an engine. CFD simulation is one of the powerful tools available for solving in-cylinder processes [2]. ANSYS Fluent is one of the computer-aided engineering (CAE) packages used for obtaining accurate results in CFD simulation. It also ensures improved meshing capabilities for complicated problems [3]. Tools like hot-wire anemometry (HWA), laser Doppler anemometry (LDA) were used for experimental purpose, but it measures flow only at few locations. Therefore, it cannot give the full details of the flow pattern. Flow bench test is another method for quantifying the flow performance and to investigate the swirl in the engine at steady state, but it could not provide detailed insight into the phenomenon occurring inside the engine cylinder. Nowadays, optical tools like particle image velocimetry (PIV) are extensively used for the experimental in-cylinder flow measurement.

In-cylinder airflow motions have a significant role on the performance characteristics like combustion and emission. Swirl is the rotational motion of air around the vertical axis of the cylinder, whereas tumble is the secondary rotational motion of air due to the squish by the piston located near top dead center (TDC). During intake stroke, high intensity induced flow increases the turbulence together with tumble. The configuration of combustion chamber is also important as the airflow structures in creating turbulence in engine. In 1988, Heywood reported a significant vortex flow generation inside an internal combustion (IC) engine cylinder during the intake process. High turbulence will be generated during the intake process, and then fast burning occurs during compression stroke [4]. Payri et al. have done CFD simulation during intake and compression stroke of a single-cylinder diesel engine with different chambers and concluded that swirl ratio at all locations is almost same, where exhaust port is not taken into consideration [5]. Complete combustion with less emission and soot can be achieved by mixing air and fuel evenly. The combustion efficiency of an engine depends mainly upon the factors like in-cylinder air flow patterns, fuel mixing, and turbulence occur during different strokes. Combustion efficiency can be increased by reducing incomplete combustion losses like heat loss to the wall and exhaust loss [5]. Mallikarjuna [6] explained that the turbulence can be increased during compression stroke by inducing vortex generation which leads to high thermal efficiency and less burning time. Joshua et al. in [7] proved the increase in turbulence and air–fuel mixing by using swirling grooves on the top of the piston face. So a research study on in-cylinder air flow structures with direct injection system needs to be carried out with double-lobed piston head. A double-lobed piston was designed by modifying a flat piston head while retaining all other engine parts. The effect was studied using cold flow analysis (CFA), and then the results obtained were compared with that of a flat piston head. Here, a

complete engine cycle is simulated without considering the chemical reactions. CFA used here is a transient analysis. The CFA is able to analyze and depict the air flow all through the cycle by monitoring the induction of air and by predicting the development of swirl, tumble, and squish [8].

This paper is structured as follows. In Sect. 2, the numerical method is discussed. The methodology is included in Sect. 3. The results are discussed in Sect. 4. The concluding remarks are in Sect. 5.

## 2 Numerical Method

The simulation was done based on a single-cylinder engine. Numerical method enables us to carry out iterative parametric studies with well-defined boundary conditions [1]. Mass, energy, momentum, and standard k-epsilon turbulence model without the fuel injection and chemical reactions are described using Eqs. (1)–(5), where $\rho$ is the mass density, $u$ is the velocity vector, $P$ is the pressure, $\sigma$ is the turbulent viscous stress tensor, $I$ is the specific internal energy and $J$ is the heat flux factor, Pr is the prandtl Number, $k$ is the turbulent kinetic energy, $\varepsilon$ is the turbulent dissipation rate, $\mu$ is the turbulent viscosity, and $c_{z1}$, $c_{z2}$ are constant coefficients [5, 8, 9]. Finite volume method (FVM) approach can perform the calculations within each computational cell to ensure the conservative properties [10].

$$\frac{\partial \rho}{\partial t} + \nabla(\rho \vec{u}) = 0 \tag{1}$$

$$\frac{\partial}{\partial t}(\rho \vec{u}) + \nabla(\rho \vec{u}\vec{u}) = \nabla P - \nabla\left(\frac{2}{3}\rho k\right) + \nabla \cdot \vec{\vec{\sigma}} + \rho g \tag{2}$$

$$\frac{\partial}{\partial t}(\rho I) + \nabla(\rho I \vec{u}) = -(\nabla \cdot \vec{u}) - \nabla\left(\frac{2}{3}\rho k\right) + \nabla \cdot \vec{\vec{J}} + \rho \varepsilon \tag{3}$$

$$\frac{\partial}{\partial t}(\rho \vec{k}) + \nabla(\rho \vec{u} k) = -\frac{2}{3}\rho k \nabla \vec{u} + \vec{\vec{\sigma}} \cdot \nabla \vec{u} + \nabla\left(\frac{\mu}{\mathrm{Pr}}\nabla k\right) - \rho \varepsilon \tag{4}$$

$$\frac{\partial}{\partial t}(\rho \varepsilon) + \nabla(\rho \vec{u}\varepsilon) = \left(\frac{2}{3}c_{z1} - c_{z2}\right)\rho \varepsilon \nabla \cdot \vec{u} + \nabla\left[\left(\frac{\mu}{\mathrm{Pr}}\right)\nabla \varepsilon\right] + \frac{\varepsilon}{k}\left[c_{z1}\vec{\vec{\sigma}} \cdot \nabla \vec{u} - c_{z2}\rho \varepsilon\right] \tag{5}$$

Pressure Implicit with Split Operator (PISO) algorithm is employed to convert partial differential equation (PDE) to a system of algebraic equations.

**Table 1** Engine
specifications

| Parameters | Values |
|---|---|
| Crank radius | 45 mm |
| Connecting rod length | 144.3 mm |
| Engine speed | 2000 rpm |
| Piston offset | 0 mm |
| Stroke | 88 mm |
| Bore | 84 mm |
| Compression ratio | 5.89 |
| Minimum lift | 0.5 mm |
| Radius of both lobes | 6.5 mm |

## 3  Methodology

The engine considered in this work is a canted valve engine with two intake valves
and two exhaust valves. The specifications of the engine design used in this work
are given in Table 1. The geometry is modeled using ANSYS 18.2. The simulation
design includes intake valves, exhaust valves, cylinder head, and piston bowl. The
piston bowl shape used in the analysis is shown in Fig. 1. The engine model is
symmetrical, so that we took one half for the computational domain to get less
computational time. The valve lift values and piston motion profile are based on the
geometric parameters of the engine. The in-valve and ex-valve get displaced at each
crank angle as shown in Fig. 2.

   The geometry is decomposed into different zones for easy meshing.
Decomposition separates the entire volume into subvolumes and meshed separately.
Each volume will be meshed into hexagonal and tetragonal elements depending
upon the purpose, so that each zone has its own quality and grid cell shape. Finer
grid cells can be observed in the cylinder combustion chamber and valve seat.
Piston bowl will move along the stroke line from TDC to bottom dead center
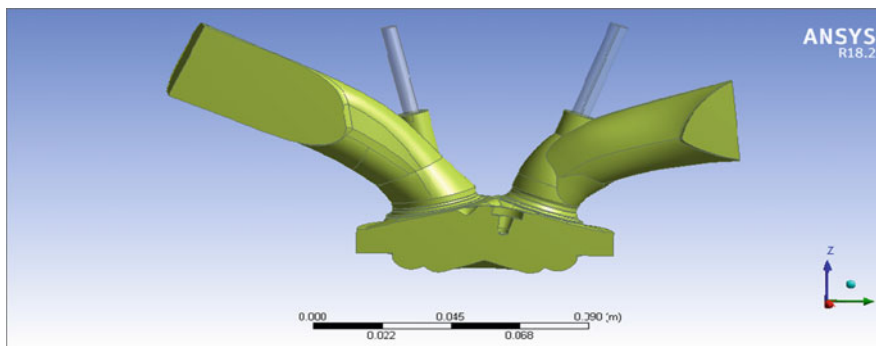


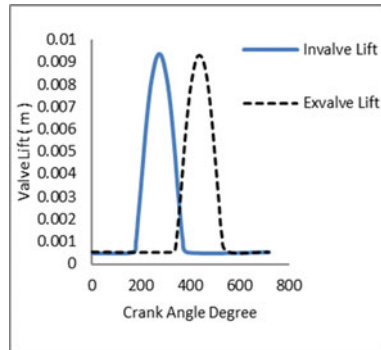**Fig. 1**  Piston bowl shape used in this analysis
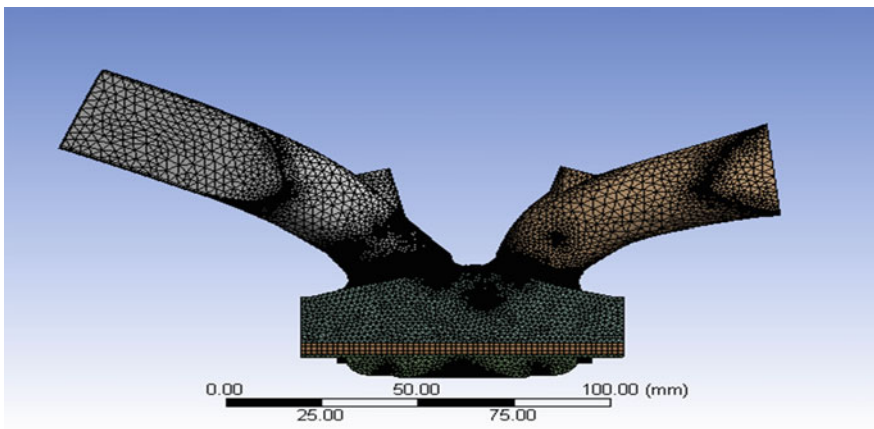
**Fig. 2** Valve lift profile



**Fig. 3** Decomposition and meshing of the model

(BDC) during the intake stroke and compression stroke. Smoothing, layering, and re-meshing are the various stages in dynamic meshing process. It is used for the combustion chamber and the valves with the changes in the crank angle. Hexahedral cells are used in moving zones, and tetrahedral cells are used in static zones to reduce the computational time, and thereby increasing the accuracy of the analysis. The complete meshed geometry contains 1,387,105 elements and 492,863 nodes. The mesh geometry is shown in Fig. 3.

Grid independence test has performed and seems fine. Medium-sized mesh (0.935 mm) in ANSYS meshing shows a deviation of <3% in swirl ratio with fine mesh. So a medium mesh with reference size is used for this analysis in order to reduce the computation time [11]. Standard k-epsilon model engine with enhanced wall treatment is used in this analysis. The enhanced wall treatment is a near-wall modeling approach for combining two-layer model and enhanced wall functions.

PISO scheme is used along with Green-Gauss Node Based for gradient and PRESTO! for pressure. Second-order upwind scheme is used for achieving accuracy in density, momentum, and turbulent kinetic energy [12, 13].

## 3.1 Initial Conditions and Boundary Conditions

The flow domain for simulation is the combustion chamber, and it consists of the inlet valve, exhaust valve, piston, intake port, and exhaust port. Both the inlet and exhaust ports are at constant pressure initially. The inlet boundary is given as "pressure-inlet" with a value of −1325 Pa, and outlet boundary is "pressure-outlet" with a value of −21,325 Pa. The turbulence intensity is taken as 5%. Frictional effects on the walls are not considered in the simulation. Cylinder walls were treated as free-slip. The temperature of the cylinder wall, piston crown, and cylinder head are 348, 318, and 348 K, respectively.

## 4 Results and Discussion

During simulation, the suction stroke, compression stroke, expansion stroke, and exhaust stroke were observed in the range of 360–550, 550–720, 720–890, and 890–1080 CAD, respectively. Here, we are comparing the results obtained while using double-lobed piston head with that of the flat base piston head. The results of the flat base are verified with the results given in [2] and shown in Fig. 4. The trends in the experimental results were validated using the results of [14].
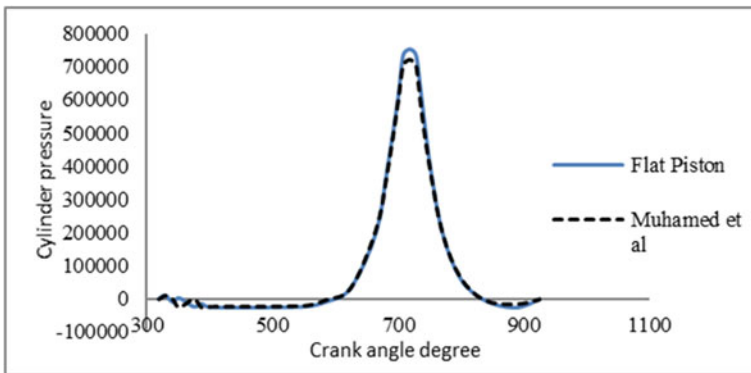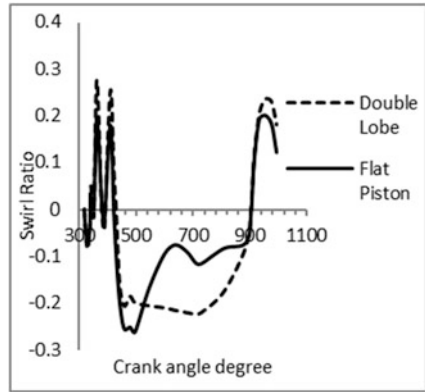


**Fig. 4** Cylinder pressure versus crank angle degree

**Fig. 5** Swirl ratio versus crank angle degree



The air flow in the engine was quantified after analyzing various parameters such as swirl ratio, tumble ratio, turbulent kinetic energy, cylinder pressure, and cylinder temperature.

The swirl ratio computed within the range of 329–980 CAD is given in Fig. 5, and certain fluctuations in the suction stroke were observed. This is due to the air jet revolving around the valve opening. From the graph, it is clear that during the compression stroke the double-lobed piston has a higher swirl ratio than the flat piston. Now, it is obvious that the swirl generated during suction stroke was utilized as turbulence during the compression stroke. Double-lobed piston has an increase of 66.67% in swirl during the suction stroke and an increase of 91.47% during the compression stroke while compared to that of flat piston head geometry.

The results obtained while analyzing tumble ratio is shown in Fig. 6. We cannot see much variation in the tumble during suction and compression strokes. The positive and negative values in the graph indicate the generation of clockwise tumble and counterclockwise tumble inside the cylinder. This can be shown in Fig. 10. This air movement can be seen more on the right side compared with the

**Fig. 6** Tumble ratio versus crank angle degree
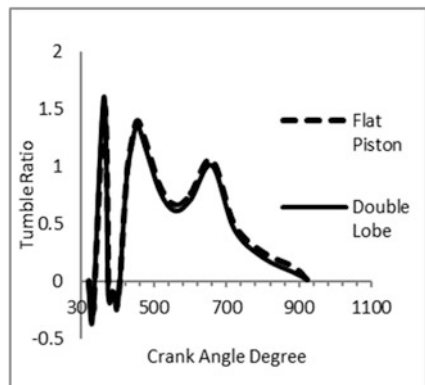
left side. This clockwise vortex movement was mainly guided by cylinder walls and piston top surface. These vortices compress during the compression stroke and transform as the rate of rotation in order to conserve the angular momentum [14, 15]. Thus, tumble increases at the beginning of the suction stroke, and it gradually reduces toward the end. A similar pattern can be seen in the compression stroke also. It means that the piston shape does not influence much on both suction and compression strokes.

Initially, the turbulent kinetic energy increases and then decreases when the piston moves from TDC to BDC during the suction stroke, and it again decreases gradually during the compression stroke, and it is clear from Fig. 7. We can see that flat base shows lesser value than the double-lobed geometry during the compression stroke. This decrease in the value in the flat piston head is due to the settling down of the turbulence during compression stroke.

Another main parameter for the cold flow analysis is cylinder pressure, and it is shown in Fig. 8. Initially, the air rushes into the cylinder and the pressure is slightly oscillating at that time. Then, the pressure settles down due to the movement of the piston and at the end of the compression stroke, it reaches the peak value. Here, it is observed an 8.13% increase in pressure while comparing with that of a flat base. It is evident from Fig. 9 that the cylinder temperature is directly proportional to the pressure. Increase in temperature will help to reduce ignition delay period, thereby reduces the combustion duration.

The velocity contours obtained in the beginning of the iteration 329 CAD is shown in Fig. 10. The air is coming from the inlet at velocity of 55.2 m/s. Exhaust valve is approaching to the valve seat, and suction stroke is going to start at this crank angle. The pressure difference on the outside and inside will guide the airflow toward the cylinder. The velocity contours obtained in the beginning of the iteration 420 CAD is shown in Fig. 11. Here, intake stroke is taking place and we can see air flow around the valves in both direction. There a clockwise rotation of air through the right side and a counterclockwise rotation through the left side. The inflow velocity increases 88.1 m/s. At 567 CAD, refer to Fig. 12, there exist a bigger
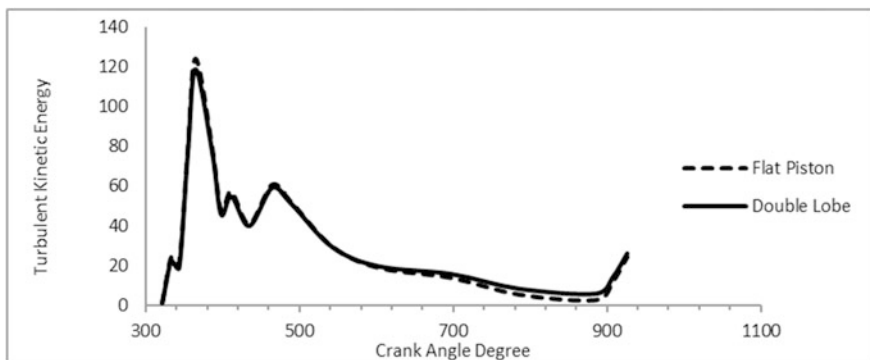


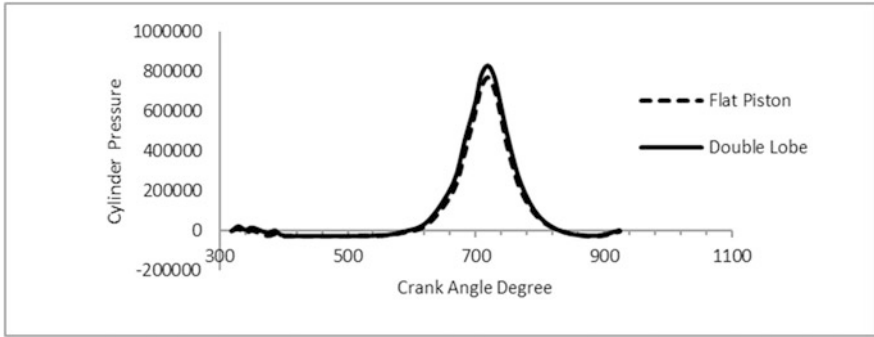Fig. 7 Turbulent kinetic energy versus crank angle degree
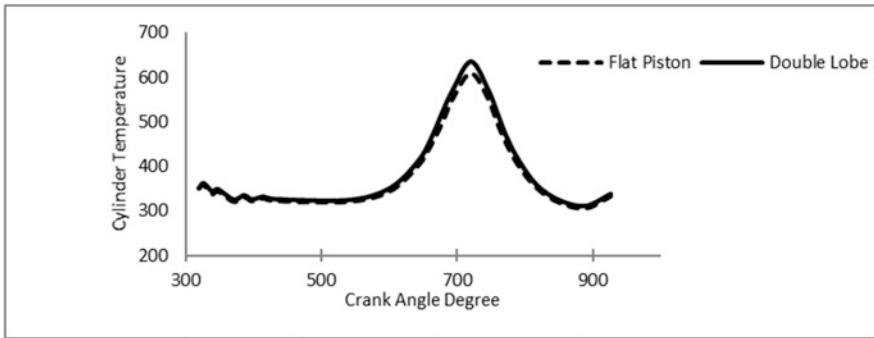
**Fig. 8** Cylinder pressure versus crank angle



**Fig. 9** Cylinder temperature versus crank angle
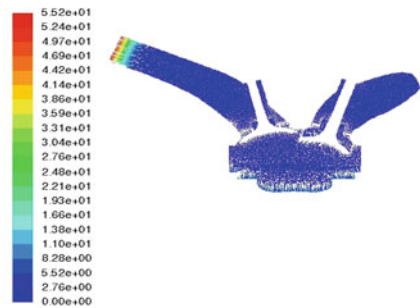
**Fig. 10** Velocity contours obtained at the beginning of the iteration 329 CAD



recirculation zone in the center of the piston. The air around this zone acts as a rotational vortex, and hence it increases the turbulence on the cylinder. Here, we can see two small recirculation zones just above the bigger one while considering the entire space, hence the turbulence increased.

**Fig. 11** Velocity contours obtained in beginning of the iteration 420 CAD
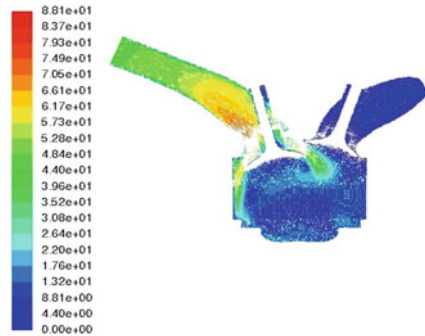


**Fig. 12** Velocity contours obtained in the beginning of the iteration 567 CAD
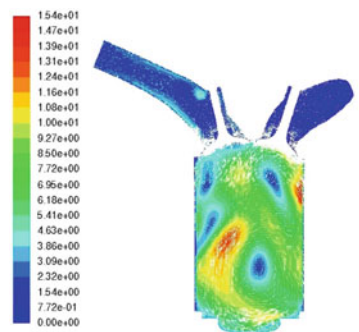


**Fig. 13** Velocity contours obtained in the beginning of the iteration 747 CAD
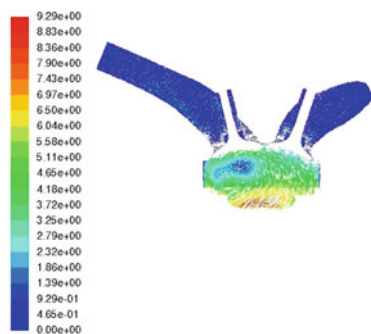


At 747 CAD, refer to Fig. 13, a vortex is seen in the velocity contours after compression stroke. A large vortex can be seen under the intake valve. This vortex is created due to the combined effects of tumble and squish on the cylinder. This tumble tries to push the piston toward the BDC.

At 1030 CAD, refer to Fig. 14, exhaust valve became similar to 329 CAD. Hence, it is the end of the simulation and the air flow velocity through the exhaust is higher.

**Fig. 14** Velocity contours obtained in the beginning of the iteration 1030 CAD

## 5   Conclusion

All the four strokes and their effects on in-cylinder air motion are studied numerically. Cold flow analysis is performed to analyze the in-cylinder flow properties of a double-lobe-canted engine during suction and compression stroke. The obtained results were compared with that of the flat base piston head and found a considerable increase in swirl ratio during suction and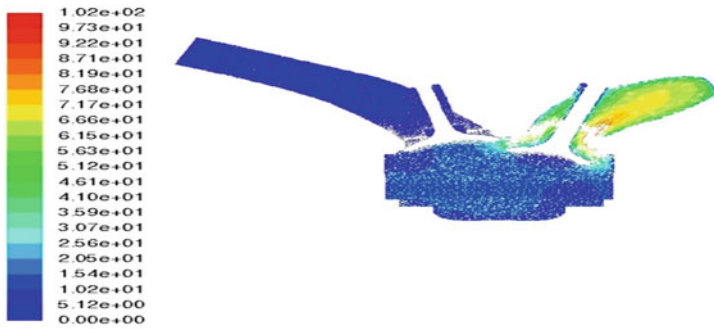 compression stroke and lead to rapid flame propagation and help in better combustion during the power stroke. So, it concluded that double-lobed piston geometry is a better option to have very good swirl ratio and turbulent kinetic energy for the engine under consideration.

## References

1. Zunaid M, Upadhyay L, Gupta N, Kushwala S (2017) Cold flow simulation for an IC engine with different lengths of connecting rod, vol 14, pp 50–54. IOSR-JMCE, e-ISSN:2278-1684
2. Mohammed Shafie NA, Muhammed Said MF (2017) Cold flow analysis on internal combustion engine with different piston bowl configurations. J Sci Eng 12:1048–1066
3. Patil Vijayendra M, Agarwal A (2013) In cylinder cold flow CFD simulation of IC engine using hybrid approach. NCAME 13, ISSN 2231-2587
4. Heywood JB (2017) Internal combustion engine. Mc Graw Hill. ISBN-13 978-1-25-900207-6
5. Payri F, Benajes J, Margot X, Gil A (2004) CFD modelling of the in-cylinder flow in direct-injection diesel engines. Comput Fluids 33(8):995–1021
6. Murali Krishna B, Mallikarjuna JM (2011) Effect of engine speed on in cylinder tumble flows in a motored internal combustion engine—an experimental investigation using particle image velocimetry. J Appl Fluid Mech 4:1–14

7. Joshua A, Ramesh Lalvani J, Parthasarathy M, Dhinesh B, Annamalai K (2009) Experimental investigation of combustion, performance and emission characteristics of a modified piston. J Mech Sci Technol 29(10):4519–4525
8. Kurniawan WH, Abdullah S, Shamsudeen A (2007) A computational fluid dynamics study of cold-flow analysis for mixture preparation in a motored four-stroke direct injection engine. J Appl Sci 7(19):2710–2724
9. Abey K, Colak U, Yuksek L (2018) Computational fluid dynamics of flow and combustion of a diesel engine. J Thermal Eng 4:189–1878
10. Rahiman A, Abdul Razak RK, Mohammad Samee AD, Ramis MK (2014) CFD analysis of flow field development in a direct injection diesel engine with different manifolds. Am J Fluid Dyn 102–113
11. Lakshman A, Karthikeyan CP, Padmanabhan R (2013) 3D In cylinder cold flow simulation studies in an IC engine using CFD. Int J Res Mech Eng 1:64–69, 2347–5188
12. Thirumalini S, Lakshmikanthan C, Dhandapani S (2009) CFD modelling for parametric investigation of flow through the inlet valve of a four—stroke engine. Int J Appl Eng Res 4 (7):1369–1384
13. James Cheeran J, Padmanaban R, Thirumalini S, Bhaskar V (2015) Design and optimization of a diesel engine connection rod. Int J Appl Eng Res 10(32)
14. Murali Krishna B, Mallikarjuna JM (2010) Comparative study of in-cylinder tumble flows in an internal combustion engine using different piston shapes—an insight using particle image velocimetry. Exp Fluids 48:863–874. Springer
15. Raj ARGS, Mallikarjuna JM, Ganesan V (2013) Energy efficient piston configuration for effective air motion—a CFD study. Appl Energy 102:347–354
16. Su L, Li XR, Liu F (2014) Numerical analysis on the combustion and emission characteristics of forced swirl combustion system for DI diesel engines. Energy Convers Manage 86:20–27
17. Jafarmadar S, Taghavifar H, Navid A (2016) Numerical assessment of flow dynamics for various DI diesel engine designs considering swirl number and uniformity index. Energy Convers Manage 86:347–355

# Vortexing Behaviour During Draining of a Liquid Through Two Unequally Eccentric Drain Ports in Cylindrical Tanks

**S. Kiran, Rajeev Warrier, Batchu Sai Naga Vinay Mouli, S. Harisankar and R. Ajith Kumar**

**Abstract** This paper presents the results of an experimental study on the vortexing behaviour during draining of a liquid (water at room temperature) from a cylindrical tank of inner diameter $D = 96$ mm through two circular drain ports ($d1$ and $d2$) placed at unequal eccentricities ($e1$ and $e2$) from the tank center. $e2$ is fixed as 42 mm, whereas $e1$ is varied giving $e1/e2$ ratios of 0, 0.25, 0.5, and 0.75. After imparting an initial rotation ($N$ rpm), the liquid is drained from the cylindrical tank. The critical height of vortex formation '$Hc$' and the corresponding time of draining were recorded. The results of the present study show that vortex formation gets completely suppressed at all diameters $d1$ when $e1/e2 = 0.5$ and 0.75. Furthermore through flow visualization experiments, an upward axial flow (above the drain port) establishment is observed in this study which is thought to influence the dynamics and characteristics of the vortex air-core formation. The phenomenon of vortex intermittency is also observed in the cases where vortex formation occurs. This attempt is the first of its kind in the research history of vortex dynamics.

**Keywords** Vortex air core · Critical height · Vortex intermittency · Drain time

S. Kiran (✉) · R. Warrier · B. S. N. V. Mouli · S. Harisankar · R. Ajith Kumar
Department of Mechanical Engineering, Amrita Vishwa Vidyapeetham, Amritapuri, India
e-mail: kiransanthosh11@gmail.com

R. Warrier
e-mail: rajwar31497@gmail.com

B. S. N. V. Mouli
e-mail: vinaymouli1997@gmail.com

S. Harisankar
e-mail: harisankart3@gmail.com

R. Ajith Kumar
e-mail: amritanjali.ajith@gmail.com

# 1 Introduction

In majority of engineering applications dealing with fluid flow systems, vortex formation of any sort is almost inevitable. Apart from fluid systems like vortex flow meters and vortex tube refrigerators where vortex is favorably utilized, vortex phenomenon is an undesirable consequence due to the ill effects it brings into the system. In units like steel teeming, nuclear reactors, pump intakes, and rocket propellant systems, vortex formation adversely affects the system performance and efficiency. The motivation for this work is the occurrence of vortex during draining of a liquid from a cylindrical tank when the liquid is imparted an initial rotation before draining. The rotation imparted to the liquid simulates 'disturbance' in the real fluid flow systems. When liquid with an initial rotation drains from a tank through a concentric orifice, at first a dip forms on the free surface of the liquid when the liquid surface reaches a certain height. The dip very quickly grows and extends downward toward the drain port to form a vortex with an air core. The height of liquid at which the vortex core touches the drain port is known as 'critical height' ($Hc$). This air-core vortex reduces the effective cross-sectional area of the drain port and thus reduces the flow rate considerably. The consequence of this is longer drain time of liquid in the tank. This vortexing phenomenon during a tank draining is closely similar to the air-core vortex phenomenon occurring in liquid propellant tanks in rocket engines. During flight conditions, liquid propellant tanks rotate about its axes, thus imparting rotational motion to the propellant inside. This in turn can result in an air-core vortex formation which reduces the propellant flow rate. Thus, suppression of such vortex formation is of great practical importance in space applications.

Abramson et al. [1] studied the problems of liquid rotation and vortexing in liquid rocket propellant tanks and suggested that adequate baffling or other suppression devices could ameliorate this vortexing behavior. Gluck et al. [2] studied the dependence of gas ingestion height on various non-dimensional parameters such as Froude number and Reynolds number. Lubin and Springer [3] investigated the formation of vortex core during draining of a liquid column using different fluid combinations and attempted to predict analytically the critical height based on some assumptions. Odgaard [4] derived an analytical expression for critical height in terms of different non-dimensional numbers. Ramamurthi and Tharakan [5] revealed that stepped port is effective in arresting air-core vortex formation compared to bell-mouth and cylindrical ports. The same authors in their later work [6] visualized the internal flow structures in draining vortex using tufts and nets and tried to explain the causes of the air-core generation. Gowda et al. [7] showed that vortex air core during draining can be suppressed by giving suitable inclination to the liquid container base. Sohn et al. [8] suggested that providing an eccentric drain port can weaken or suppress the vortex formation. Mahadev et al. [9] in their study proposed that the intensity of vortex formation can be reduced by providing surface roughness to the cylinder base. Ajith Kumar et al. [10, 11] proved that vortexing gets completely suppressed below a critical value of drain port diameter; also a

suitable combination of port diameter and eccentricity can substantially suppress the vortex formation. Recently, Gopikrishnan et al. [12] studied the vortexing phenomenon during draining from a cylindrical tank through two drain ports with equal eccentricity. The study was first of its kind reported on vortex formation during liquid draining through multiple drain ports. Their results [12] showed a very different trend of air-core formation from that of a single drain port case. Most predominantly, they reported that even at the highest rotation speed of the liquid column, vortexing gets suppressed in twin drain port configuration with equal port size. They further reported that smaller drain port size gives higher critical height. Both these findings are counterintuitive in fact not revealed earlier. Their study has generated two major questions in author's mind: (a) how the vortexing character-istics change if the drain ports carry unequal eccentricities? and (b) can vortexing be better suppressed if port eccentricities are unequal? Present study is an attempt to answer these questions. This paper presents the results of an experimental study on vortex formation during draining of a liquid from a cylindrical tank through two drain ports placed at unequal eccentricity from the tank base center.

## 2  Experimental Setup

The experimental setup used for the study consists of an acrylic cylindrical tank of height 410 mm and inner diameter ($D$) 96 mm. The tank is attached to an acrylic base plate of 12 mm thickness which has the drain ports drilled on it. Clear silicone gel is used for gluing the tank and the base plate. The liquid used for the experiment is water at room temperature. Liquid column in the tank is given initial rotation by the use of a motor stirrer. Initial rotation ranging from speed 40 to 200 rpm with an increment of 20 rpm was given to the liquid column. Draining of water from the tank is made through two drain ports. One of the drain ports (primary drain port) is of diameter ($d_2$) 10 mm and is placed at a maximum eccentric location possible viz. $e_2 = 42$ mm so that $e_2/D = 0.4375$. The other drain port (secondary drain port) has its diameter ($d_1$) varying from 4 to 10 mm and is placed at eccentricity ($e_1$) given by the eccentricity ratios $e_1/e_2 = 0$, 0.25, 0.5, and 0.75. The eccentricity ($e_1$) used as per the ratios mentioned are 0, 10.5, 21, and 31.5 mm. The experiment was done on three initial height of water column such as 400, 350, and 300 mm (Fig. 1).

The experimental procedure is as follows. The cylindrical tank is filled with water up to a required initial height '$H_i$'. The liquid column is given an initial rotation ($N$ rpm) at a desired speed using an electric motor stirrer. Later the liquid is allowed to drain through the drain ports. As the liquid drains observations such as critical height of vortex formation '$H_c$' (height of liquid column at which the air-core vortex touches the drain port for the first time), critical time '$T_c$' (time required to reach the critical height), time for complete draining of liquid with initial rotation given '$T_d$', time for complete draining of liquid without imparting any initial rotation '$T_o$' were noted.
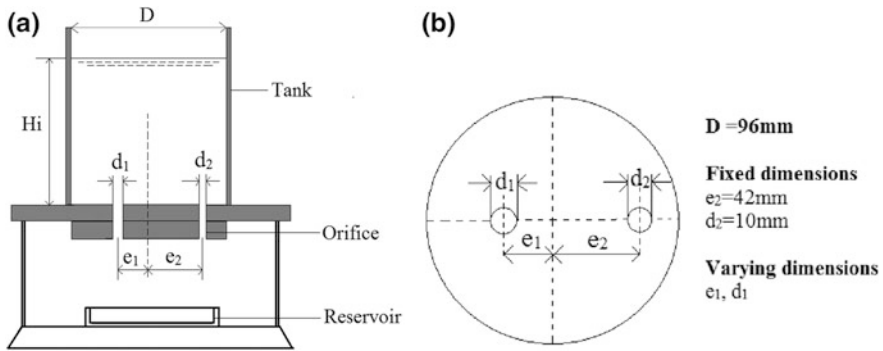
Fig. 1 a Schematic diagram of experimental setup; b cylinder base plate

## 3    Results and Discussion

The results of this study are presented in terms of $H_c/H_i$ (non-dimensional critical height) and $T_d/T_o$ (non-dimensional time of draining). Figure 2 shows the plot of $H_c/H_i$ versus $N$(rpm) for the case $e_1/e_2 = 0$ at different secondary port diameters ($d_1$) when the eccentricity of the port $e_1 = 0$ mm. The vortex air core was found to extend only toward the concentric port at $e_1 = 0$ mm. We can see that vortexing is completely suppressed at all initial rotational speeds and initial heights for $d_1 = 4$ mm. At $d_1 = 5$ and 6 mm, vortexing is suppressed below a particular value of initial rotational speed (100 rpm for $d_1 = 5$ mm and 60 rpm for $d_1 = 6$ mm). The maximum value of critical height is occurring for $d_1 = 10$ mm which has strong vortex formation. In general as Fig. 2 shows, $H_c/H_i$ increases with $N$. The plot is having same trend for all the three initial liquid heights tested. The results show similarity in trend with the single concentric drain port cases reported by [11], but with lower critical height values than that of single port cases. This indicates that the intensity of vortexing at the concentric port is reduced by introducing a second drain port at a maximum eccentricity within the cylinder. Also, the phenomenon of 'vortex intermittency' as mentioned by Ajith Kumar et al. [11] was found in all the cases with vortex formation except $d_1 = 9$ and 10 mm.

The non-dimensional time of draining ($T_d/T_o$) versus $N$ plot for different diameters $d1$ for the case $e1/e2 = 0$ is shown in Fig. 3. It can be observed that the $T_d/T_o$ value increases with an increase in rotational speed $N$ as expected for all cases of $d1 > 6$ mm. At $d1 = 6$ mm, the $T_d/T_o$ value is close to unity. We have $T_d/T_o < 1.0$ for $d1 = 5$ and 4 mm at certain values of $N$, which indicates that a faster drain occurs in those cases compared to the free draining without any initial rotation given. This indicates a possible change in the flow field occurring near the drain ports. Similar characteristics were reported by Gopikrishnan et al. [12]. This further indicates that some complex flow phenomenon is occurring in twin port draining configuration as compared to single port draining.

**Fig. 2** Variation of $H_c/H_i$ w.r.t $N$ for the case ($e_1/e_2 = 0$, $e_1 = 0$ mm, $e_2 = 42$ mm, and $d_2 = 10$ mm) at different initial heights $H_i$. **a** $H_i = 400$ mm, **b** $H_i = 350$ mm, and **c** $H_i = 300$ mm



**Fig. 3** Variation of $T_d/T_o$ w.r.t $N$ for the case ($e_1/e_2 = 0$, $e_1 = 0$ mm, $e_2 = 42$ mm, and $d_2 = 10$ mm) at different water initial heights $H_i$, **a** $H_i = 400$ mm, **b** $H_i = 350$ mm, and **c** $H_i = 300$ mm

For $e_1/e_2 = 0.25$, the results are shown in Fig. 4a, b. It is to be noted that the results are almost identical for all the three initial liquid heights $H_i$ tested, and hence, the results for $H_i = 400$ mm only are shown here. The plot of $H_c/H_i$ versus $N$ corresponding to $H_i = 400$ mm is shown in Fig. 4a. $H_c/H_i$ versus $N$ plot shows that vortexing is most predominant (higher $H_c/H_i$ value) for $d_1 = 9$ and 10 mm. Quite interestingly, at $d_1 = 6$, 7, and 8 mm vortex formation occurs only at

**Fig. 4** Variation of $H_c/H_i$ w.r.t $N$ (**a**) and $T_d/T_o$ w.r.t $N$ (**b**) for the case ($e_1/e_2 = 0.25$, $e_1 = 10.5$ mm, $e_2 = 42$ mm, and $d_2 = 10$ mm) at initial height $H_i = 400$ mm

intermediate initial rotational speeds between 60 and 140 rpm. Vortexing is completely suppressed at all rotational speeds for $d_1 = 5$ and 4 mm.

Corresponding to $H_c/H_i$, the non-dimensional time of draining ($T_d/T_o$) versus $N$ plot for the case $e_1/e_2 = 0.25$ is given in Fig. 4b (at $H_i = 400$ mm). $T_d/T_o$ value shows an increasing trend with '$N$' for $d_1 = 9$ and 10 mm, which is expected as strong critical height formation occurs in both the cases. For $d_1 = 8$ mm, $T_d/T_o$ value at first increases, then drops to a minimum value, and again starts to increase. For $d_1 = 7$ and 6 mm, the drain time with initial rotation is not increasing much from that of quiescent liquid draining time '$T_o$'. The $T_d/T_o$ values are going below 1 at different rotational speeds for $d_1 = 4$ and 5 mm. As mentioned earlier, vortexing is completely suppressed in these cases and it seems that imparting an initial rotation is enabling a faster drain which is an interesting phenomenon. However, the flow physics underlying in this drain characteristics is not yet known.

Results for $e_1/e_2 = 0.50$ at $H_i = 400$ mm are given in Figs. 5($H_c/H_i$ vs. $N$) and 6a ($T_d/T_o$ vs. $N$). As seen in Fig. 5, $H_c/H_i = 0$ at all initial rotational speeds '$N$' for all values of $d_1$ indicating that vortexing is fully suppressed. This has reflected in the values of $T_d/T_o$ which falls in the range $0.98 \leq T_d/T_o \leq 1.06$ thus close to unity (Fig. 6a). For other $H_i$ values, also the parametric trends are the same as those shown in Figs. 5 and 6a and hence not presented here.

For the last eccentricity ratio $e_1/e_2 = 0.75$ also, vortex formation is completely suppressed, and therefore, the results are quite identical to those presented for $e_1/e_2 = 0.5$ (Figs. 5 and 6a). But the $T_d/T_o$ values are much more closer to 1.

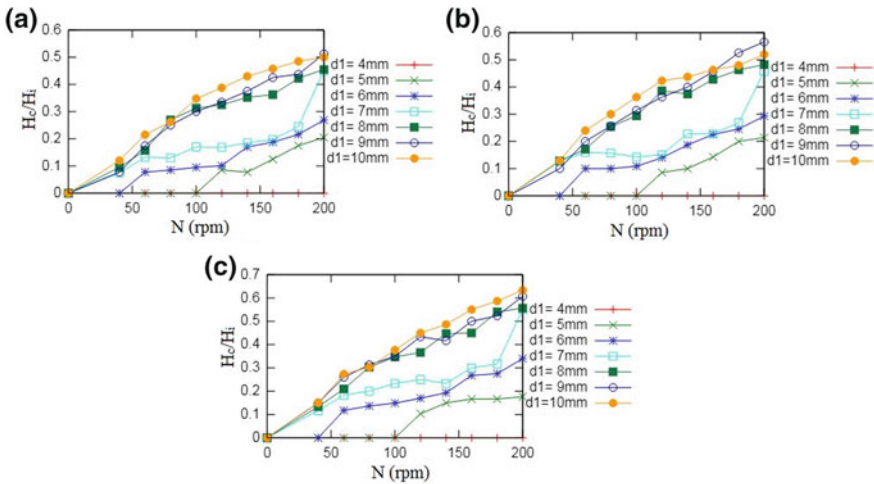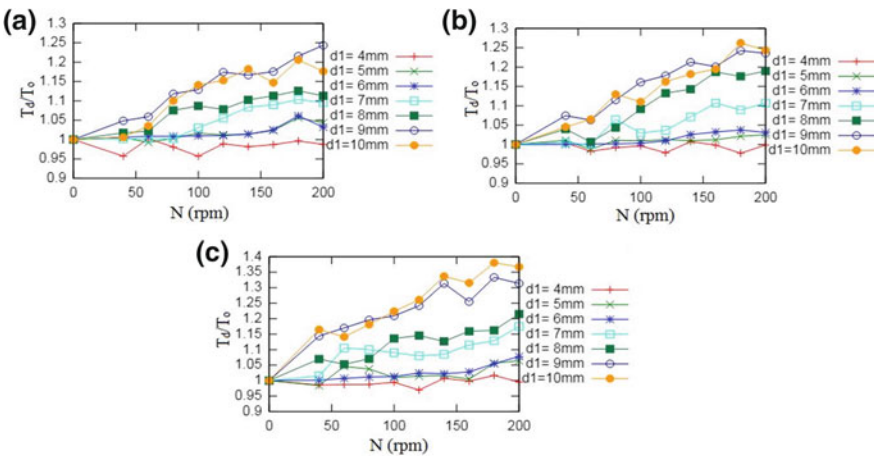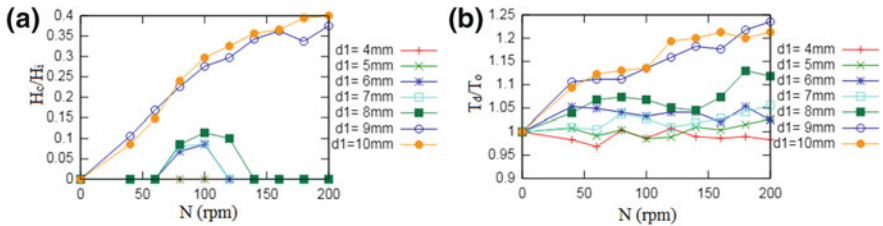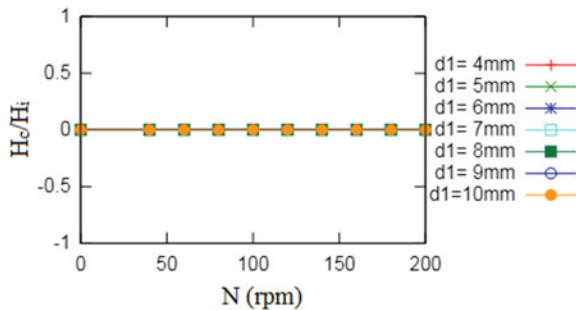**Fig. 5** Variation of $H_c/H_i$ w.r.t $N$ for the case ($e_1/e_2 = 0.5$, $e_1 = 21$ mm, $e_2 = 42$ mm, and $d_2 = 10$ mm) at initial height $H_i = 400$ mm
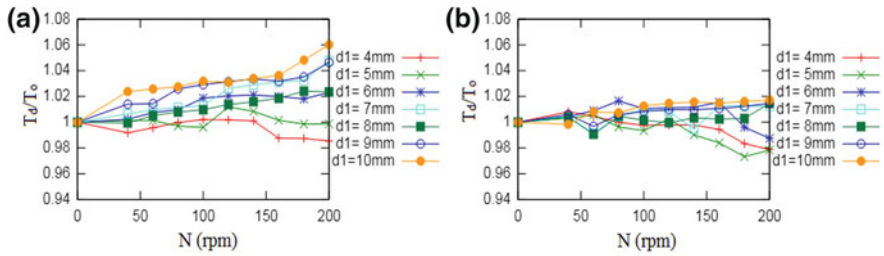
**Fig. 6** Variation of $T_d/T_o$ w.r.t $N$ at initial height $H_i = 400$ mm. **a** Case ($e_1/e_2 = 0.5$), **b** case ($e_1/e_2 = 0.75$)
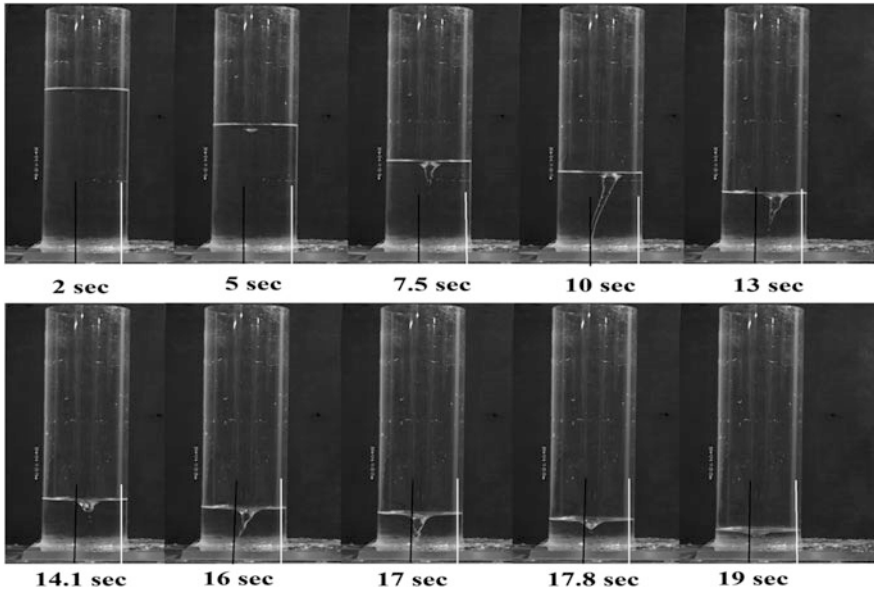


**Fig. 7** Transient evolution and transformation of vortex core for the case $e_1/e_2 = 0.25$, $d_1 = 9$ mm at $N = 160$ (white line indicates primary port at $e_2 = 42$ mm, black line indicates secondary port at $e_1 = 10.5$ mm)

Hence, results for $e_1/e_2 = 0.75$ are not shown here, except the trend of $T_d/T_o$ versus $N$ for $e_1/e_2 = 0.75$ (Fig. 6b) at $H_i = 400$ mm. However, initial dip formation was observed at higher initial rotational speeds ($N > 160$ rpm) in both these cases, but it was not transforming into a fully developed vortex air core.

Figure 7 shows the flow visualization snapshots of the transient evolution and transformation of a vortex air core for the case $e_1/e_2 = 0.25$, with $d_1 = 9$ mm and at $N = 160$ rpm. As seen, the critical height is reached at time $t = 10$ s (10th sec after the start of draining) but the vortex withdraws back to its 'dip' configuration at $t = 14.1$ s. Interestingly, vortex once again appears at $t = 16$ s and then disappears

**Fig. 8** **a** Withdrawal of vortex tip from drain port after the occurrence of upward axial flow and **b** concentration of particles beneath the vortex tip

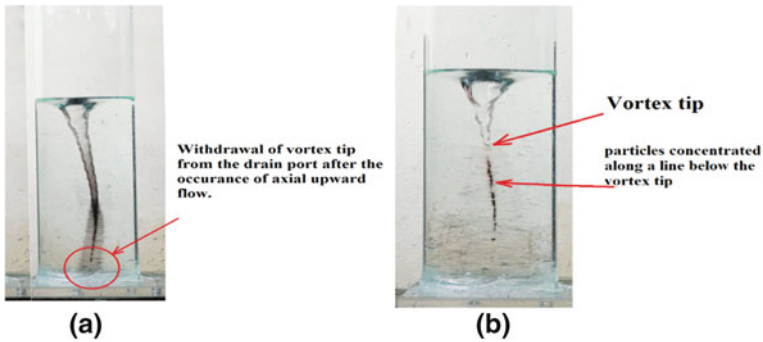at t = 19 s executing 'vortex intermittency.' Similar visualization studies were conducted for $e_1/e_2 = 0$ also. It is to be mentioned that the vortex air core extends down and touches the secondary drain port (at $e_1$) only and never the primary drain port (at $e_2$). The vortex air core is observed to have a 'curvy' profile.

To further investigate the flow physics involved in vortex core formation, visualization study was done using tea powder and the video of the phenomenon was recorded. Tea powder was introduced into the vortex air core from the top free surface just after the formation of initial surface dip. One of the interesting flow features observed in the visualization study was the occurrence of an upward axial flow from the drain port encompassing the tail of the vortex air core. The upward flow was observed right after the vortex core touched the drain port. Just after the occurrence of this upward flow, the vortex tip seemed to be withdrawn from the drain port. Figure 8a shows the video snapshot image of observed upward flow. Another point to be highlighted is that, when the vortex withdraws back to the 'dip' configuration, the said upward flow changes into a swirl flow. This upward axial flow like feature indicates that complex flow structure and pressure variations exist within the rotational flow field. This phenomenon could be one of the reasons for the occurrence of withdrawal of vortex tip from the secondary drain port and subsequent vortex intermittency. Another feature observed was the concentration of introduced tea particles along a line below the vortex tip after the withdrawal of vortex from the drain port as shown in Fig. 8b.

The observed features of critical height formation and drain time in the present study could be attributed to the variations in axial, radial, and tangential components of velocity within the rotational flow field and may possibly be influenced by the establishment of upward axial flow seen during vortex formation. The static pressure variation around the drain ports also could play a vital role in the observed vortex core behavior. However, further studies such as using particle image velocimetry and detailed numerical simulations are to be performed to clearly understand the flow physics involved.

As the results of this study show, for majority of the cases with unequal drain port eccentricities, vortex suppression is achieved, as against fewer cases of suppression in equal eccentricity cases studied by Gopikrishnan et al. [12]. Findings of this study could be favorably utilized in practical applications such as in rocket liquid propellant tanks, hydraulic engineering, and casting process in steel making, where vortex air-core formation brings undesirable consequences and therefore need to be eliminated.

## 4    Conclusions

From the results presented and discussed, the following conclusions could be drawn.

(a) Draining of a liquid from a cylindrical tank through two drain ports at unequal eccentricities (asymmetrical draining positions) is found to be very effective in reducing the intensity of vortex formation.

(b) Vortexing is completely suppressed at all initial rotational speeds '$N$' for all the diameters $d_1$ when the eccentricity ratio ($e_1/e_2$) is 0.5 and 0.75. Whereas, for twin drain ports with equal eccentricities, only at $e/D = 0.32$ and equal drain port diameters, full vortex suppression could be achieved as revealed in the previous study [12].

(c) For the eccentricity ratio $e_1/e_2 = 0.25$, vortexing is suppressed either fully or partially for $d_1 < 9$ mm in the range of rotational speeds $N$ tested. The same happens for $d_1 < 7$ mm at $e_1/e_2 = 0$.

(d) The phenomenon of vortex intermittency is observed in all the cases with vortex core generation except when $d_1 = 10$ and 9 mm for the case $e_1/e_2 = 0$.

(e) Initial height of liquid '$H_i$' is observed to have only a weak influence on the vortexing behavior in the present study.

(f) Flow visualization shows that though draining occurs through two ports, the vortex core extends and touches only the drain port closer to the tank center and the vortex is observed to have a curvy profile.

(g) Occurrence of an upward axial flow is observed right after the vortex core touches the drain port. This upward axial flow feature is expected to be an influential factor for the phenomenon of vortex intermittency.

## References

1. Norman Abramson H, Chu W-H, Garza LR, Ransleben GE Jr (1962) Some studies in liquid rotation and vortexing in rocket propellant tanks. NASA Technical note, D-1212
2. Gluck DF, Gille JP, Zukoski EE, Simkin DJ (1966) Distortion of a free surface during tank discharge. J Spacecraft Rock 3(11):1691–1692

3. Lubin BT, Springer GS (1967) The formation of a dip on the surface of a liquid draining from a tank. J Fluid Mech 29(2):385–390
4. Odgaard AJ (1986) Free-surface air core vortex. J Hydraul Eng 112:610–620
5. Ramamurthi K, Tharakan TJ (1992) Shaped discharge ports for draining liquids. J Spacecraft Rockets 30(6):786–788
6. Ramamurthi K, Tharakan TJ (1996) Flow visualisation experiments on free draining of a rotating column of liquid using nets and tufts. Exp Fluids 21:139–142
7. Gowda BHL, Akhuli S, Anudeep BR, Ipe KR, Kishore K (2013) Influence of base inclination on vortex formation during draining from cylindrical tanks. Indian J Eng Mater Sci 20:361–366
8. Sohn CH, Gowda BHL, Ju MG (2008) Eccentric drain port to prevent vortexing during draining from cylindrical tanks. J Spacecraft Rockets 45:638–640
9. Mahadev JP, Nair RR, Ajith Kumar R (2015) Vortexing during draining from cylindrical tanks: Effect of base roughness. In: Proceedings of the 17th ISME conference, pp 8–10 ISME 17, IIT Delhi
10. Ajith Kumar R, Joykutty J, Shaji R, Srikrishnan AR (2015) Vortex suppression through drain port sizing. J Aerospace Eng 29. https://doi.org/10.1061/(asce)as.1943-5525
11. Ajith Kumar R, Nair RR, Prabhu M, Srikrishnan AR (2016) Vortex formation during draining from cylindrical tanks: effect of drain port eccentricity. J Aerospace Eng 893–1321
12. Gopikrishnan TH, Anandakrishnan U, Kiran AS, Ajith Kumar R, Anith TA (2017) Vortexing during draining through twin drain ports in a cylindrical tank. In: Proceedings of 2nd international conference for convergence in technology. IEEE, Pune

# Effect of Temperature and Pressure on the Leakage Flow Characteristics of the Bent Axis Hydro-Motors—An Experimental Study

**Ajit Kumar Pandey, Alok Vardhan, Yash Kumar and K. Dasgupta**

**Abstract** This article investigates the steady-state leakage flow (hydraulic oil) characteristics of the bent axis hydro-motor fitted in an in-house fabricated hydrostatic transmission (HST) system. In this respect, two different classifications of the bent axis hydro-motors, fixed displacement and variable displacement types, are taken into consideration, which is generally used in heavy earth moving vehicles. The leakage flow paths in these two selected hydro-motors are studied considering their constructional detail. A mathematical model is established to estimate the leakage flow of the said hydro-motors that accounts the change in viscosity with respect to the operating state variable, i.e., absolute temperature and operating pressure, where the coefficient model is obtained from the test data. Using the established model, the leakage flow characteristics of the hydro-motors are obtained at different operating conditions and are verified experimentally. From the study, it is concluded that with the increase in load pressure and temperature of the working system, the leakage flow of the hydro-motors used in the heavy earth moving vehicles also increases.

**Keywords** Hydrostatic transmission (HST) system · Dynamic viscosity · Absolute temperature · Leakage flow · Heavy earth moving vehicles

## 1 Introduction

Hydrostatic transmission (HST) system used in heavy earth moving vehicles catering the fluctuating load demand exhibits many benefits that make them suitable for applications requiring the controlled and efficient transmission of power. During the operation of the HST system, effects of the components' behavior on the system performance are very much crucial and need detailed study. In order to select the

A. K. Pandey (✉) · A. Vardhan · Y. Kumar · K. Dasgupta
Indian Institute of Technology (Indian School of Mines),
Dhanbad 826004, Jharkhand, India
e-mail: ajit.saurabh100@gmail.com

hydraulic components for heavy earth moving vehicles, especially the hydraulic motors, it is important to understand how they affect the overall performances so that the system components and the control algorithms can be chosen to achieve the optimum efficiency zone. In most commercial power supplies, the maximum system pressure is regulated by adjusting the set pressure of the pressure relief valve, whereas the operating pressure varies with respect to the load demand. The temperature of the oil also varies with respect to the load pressure and the operating time, resulting in the variation of its viscosity. This leads to the variation of the volumetric efficiency and thus the overall performance of the hydro-motors [1].

In order to investigate the performance of the hydro-motors with respect to the operating pressure and oil temperature, various mathematical models were proposed. The laminar leakage flow characteristic of the hydrostatic displacement machine, as investigated by Wilson [2], presented a mathematical model, where the coefficients are obtained experimentally. Thoma [3] and Schlösser [4] extended the work of Wilson [2] and studied the effects of the variation of the clearances and the turbulent nature on the leakage flow characteristics. In order to study the performance of the variable displacement hydraulic pumps and the motors, Rydberg [5] derived the basic equations needed to calculate the steady-state performance characteristic of an HST system with respect to the energy losses. The effects of the pressure and temperature on the leakage flow characteristic of the non-piston-type positive displacement pumps have been investigated by Inaguma [6]. In the investigation, they presented a practical approach to predict the influence of the operating pressure and the temperature on the leakage losses and the friction torque losses in different hydrostatic pumps. While establishing the leakage loss model, the variation of clearances with respect to the differential pressure was also taken into consideration. The effects of the operating pressure on the leakage flow characteristic of the piston-type bent axis hydro-motors of different sizes have also been investigated by Kumar et al. [7]. Hall [8] presented a methodology for comparing the performance of multiple steady-state flow loss models of the hydraulic axial piston pumps. However, the study could not incorporate the effect of variation of oil temperature on the leakage flow. The experimental flow loss model and the resultant pressure dynamics of the axial piston pump using analytical approach have been carried out by Bergada et al. [9]. In the investigation, they developed a set of new algebraic leakage model to estimate the flow losses and the pressure ripples. They validated the established model through simulation and experimentation. Further study by Bergada et al. [10] reveals the effect of the operating pressure and the oil temperature on the barrel film thickness and the dynamic responses of the swash plate. However, they could not describe the effect of variation of operating pressure and temperature on the leakage flow of the hydraulic pumps. In order to increase the efficiency of the hydrostatic system, Li et al. [11] presented a thermal–hydraulic model of a piston pump. They developed a mathematical model from the set of lumped parameters based on the energy conservation. In their study,

they analyzed the model through the heat transfer analysis to describe the heat flow inside the piston pump. The impact of operating pressure and the temperature of the oil on its viscosity has been investigated by Knezevic and Savic [12]. They found that the impact of variation of oil temperature on its viscosity is more than that of the operating pressure. However, the study could not correlate the leakage flow of the oil in the hydraulic pumps and the motors with its viscosity as function of state variables.

This article investigates the influence of the operating pressure and the temperature on the viscosity of the mineral oil, considered for the analysis. The effect of the viscosity as function of state variables on the leakage flow of the two different types of bent axis hydro-motors is also highlighted. In this respect, a closed-circuit HST system is designed and fabricated. The article also develops a mathematical model to estimate the leakage flow of the hydro-motors, which may be implemented to obtain the performance parameters of the bent axis hydro-motors as a function of load pressure and oil temperature. The model presented in this article guides the design of the experiments and may assist in the identification of dependence of the performance parameters on the state variable of the components.

## 2 The Physical System

Referring to Fig. 1, a swash-plate-controlled variable displacement axial piston pump (2) driven at a constant speed (Np) supplies pressurized fluid (Qp) to a variable displacement bent axis hydro-motor (4). Depending upon flow (Qp), the load torque (τld) on the motor shaft, the hydro-motor speed (Nm), and the pump input torque (τp) vary. The load on the HST drive is varied by adjusting the displacement of the loading pump (5) and the set pressure of proportional pressure relief valve (7). The charge pump (3 and 6) in the circuit compensates leakage losses; for detailed functioning of the component, the interested readers may refer to the standard textbook [13]. The pressure transducers (8), flow sensors (9), and the torque sensors (10) are used to measure the operating pressure, flow rate, and torque generated by the drive, which are stored in the data acquisition system (DAS). The controller gives command signals to pumps, hydro-motor, and the proportional pressure relief valve to obtain the desired operating condition for performance investigation.

Figures 2 [14] and 3 [15] present the schematic representation of the fixed displacement bent axis hydro-motor and the variable displacement bent axis hydro-motor, respectively. With reference to Figs. 2 and 3, it is obvious that there is an additional fluid flow path in the variable displacement hydro-motor that is provided to lubricate the sliding lens.
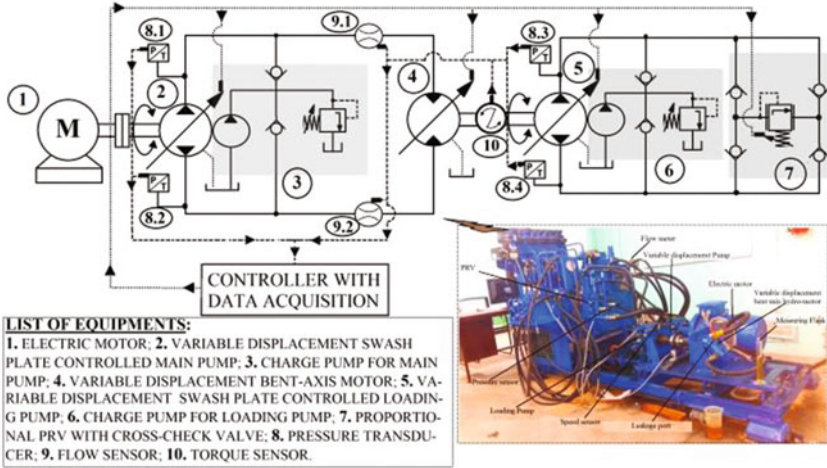
**Fig. 1** Experimental setup
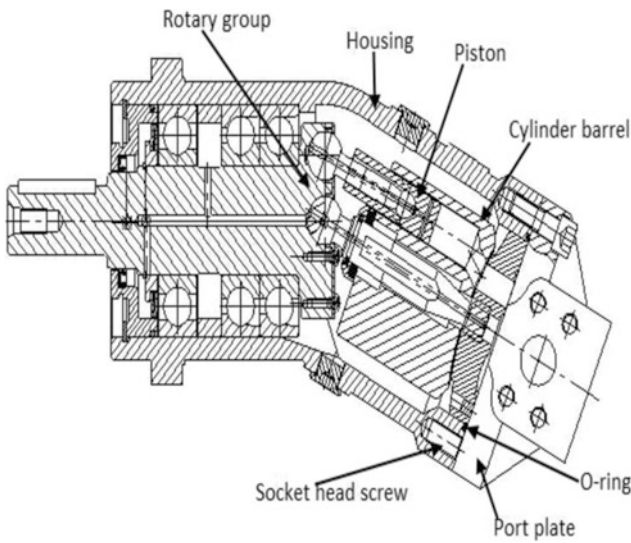


**Fig. 2** Fixed displacement bent axis hydro-motor
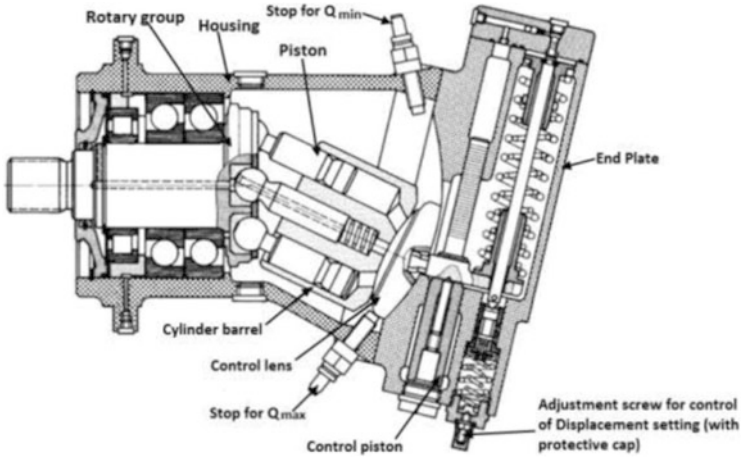
**Fig. 3** Variable displacement bent axis hydro-motor

## 3 Mathematical Modeling

To measure the leakage flow of the hydro-motor, a mathematical relationship between viscosity and temperatures as expressed by Vogel equation was given by Stachhowiak et al. [16]. This model accounts the variation of dynamic viscosity of the oil with respect to its temperature.

Vogel equation may be expressed as:

$$\mu_0 = ae^{\frac{b}{T_A - c}} \tag{1}$$

where $\mu_0$ is the dynamic viscosity (Ns/m) of the mineral oil at atmospheric pressure; $T_A$ is the absolute temperature (K) of the oil; and $a$, $b$, and $c$ are the coefficient models, which are obtained from the viscosity characteristic curve of the test oil as obtained from the Servo Product Data Sheet. The test oil used for the analysis is the servo system hydraulic oil (Viscosity grade 68). Using the logarithmic function, Eq. (1) gets modified to:

$$\log \mu_0 = \log a + 0.4343 \left( \frac{b}{T_A - c} \right) \tag{2}$$

Also, accounting the effects of pressure and temperature, the leakage flow ($Q_l$) of the hydro-motor may be expressed as:

$$Q_l = f(T_A, P) \tag{3}$$

**Table 1** Dynamic viscosity of mineral oil servo system 68 grade at different temperatures

| Sl. no. | Temperature (K) | Dynamic viscosity (Ns/m) |
|---------|-----------------|--------------------------|
| 1 | 373 | 0.007395 |
| 2 | 323 | 0.3635 |
| 3 | 313 | 0.580 |

where $f$ is the leakage function which accounts the dependency of $Q_l$ on the operating pressure ($P$) and the absolute temperature ($T_A$).

Combining Eqs. (2) and (3), the leakage flow of the hydro-motor may be obtained as function of the operating pressure and the viscosity of the oil, where viscosity of the oil depends on its temperature. The dependency of leakage flow of the hydro-motor on its temperature and pressure, as expressed by Eq. (3), is obtained from the test data.

## 4 Estimation of the Coefficient Model

The coefficient model of the Vogel equation, as expressed in Eq. (1), is obtained from the dynamic viscosity of the test oil at three different temperatures. They are obtained from the Servo Product Data Sheet [17] and are shown in Table 1.

where $a = 0.0000294$, $b = 2285.43$, and $c = 80.390$.

## 5 Experimentation, Estimation of Leakage Function, and Verification of the Mathematical Model

The standard procedures were followed while carrying out the experimental investigation of the system. The repeatability of the system was also verified before collecting the data. A stable source of power supply was used to drive the main pump that supplies the flow to either of the hydro-motors. The speed ($\omega_m$) of the hydro-motor was varied by varying the displacement setting of the main pump, while the operating pressure ($P$) of the hydro-motor was controlled by varying the load. The leakage flow rate ($Q_l$) of the hydro-motor was measured by collecting the leakage oil for a time interval of 25 s, at a different operating pressure and temperature. The estimated leakage flow was verified from the inlet shown and flow of outlet of hydro-motor, obtained from the respective sensors (item no. 9.1 and 9.2, as shown in Fig. 1).

The leakage flow characteristics of the two hydro-motors are obtained by using the best fit line through the test data points. They are shown in Figs. 4 and 5. Using them, the leakage function as expressed in Eq. (3) is obtained.
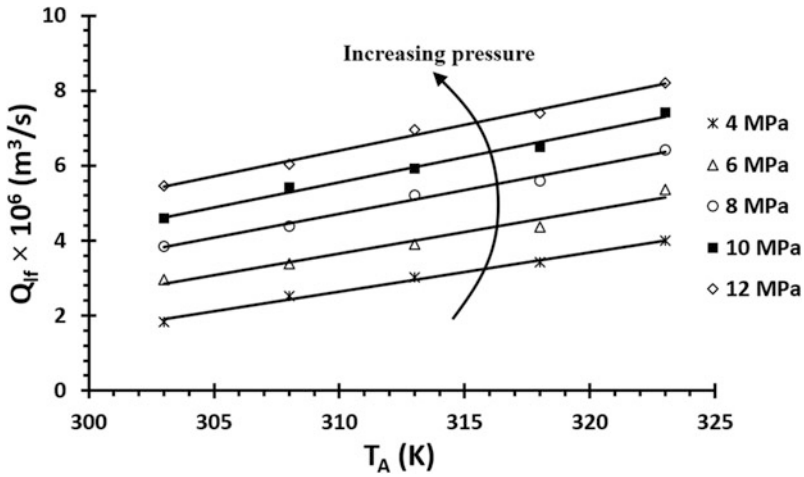
**Fig. 4** Leakage flow characteristic of fixed displacement motor
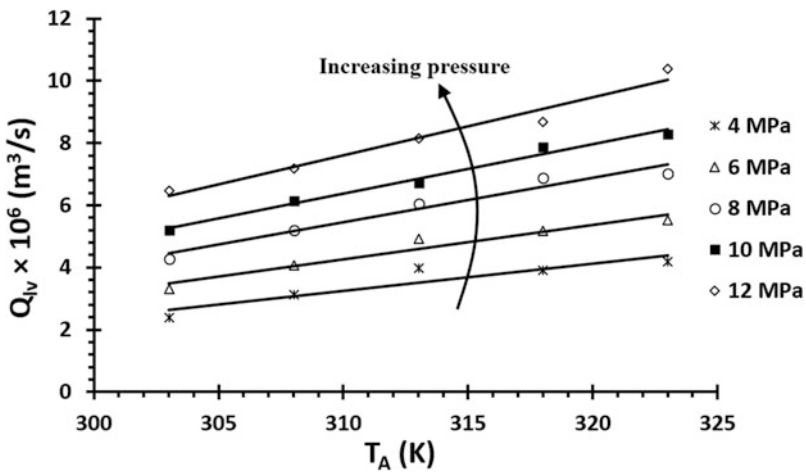


**Fig. 5** Leakage flow characteristic of variable displacement motor

From the characteristic shown in Figs. 4 and 5, it is obvious that within the pressure and the temperature range of 4–12 MPa and 300–325 K, the leakage function is linear with temperature and pressure as well. The generalized empirical relation for the leakage flow as shown in Figs. 4 and 5 may be expressed as:

$$Q_l \times 10^6 = mT_A + k \tag{4}$$

where $m$ and $k$ are constants, which depend on the operating pressure.

For fixed displacement hydro-motor, the coefficients at specific pressure may be expressed as (from Fig. 4):

$$m_f = 0.0042P + 0.0903$$
$$k_f = -0.8254P - 27.167$$

(5)

For variable displacement hydro-motor, the coefficients at specific pressure may be expressed as (from Fig. 5):

$$m_v = 0.0123P + 0.0388$$
$$k_v = -3.2728P - 10.965$$

(6)

Using Eqs. (2) and (4), the expression for the leakage flow of the hydro-motors ($Q_l$) as a function of state variable is expressed as:

$$Q_l \times 10^6 = m\left(\frac{0.4343b}{\log \mu_0 - \log a} + c\right) + k$$

(7)

where $a$, $b$, and $c$ are obtained from Sect. 4, $\mu_o$ is obtained from Eq. (1), and $m$ and $k$ are obtained from Eqs. (5) and (6), respectively.

For fixed displacement hydro-motor, the leakage flow ($Q_{lf}$) as function of pressure and temperature may be expressed as:

$$Q_{lf} \times 10^6 = (0.0042P + 0.0903)\left[\frac{0.4343b}{\log \mu_0 - \log a} + c\right] + (-0.8254P - 27.167)$$

(8)

For variable displacement hydro-motor, the leakage flow ($Q_{lv}$) as function of pressure and temperature may be expressed as:

$$Q_{lv} \times 10^6 = (0.0123P + 0.0388)\left[\frac{0.4343b}{\log \mu_0 - \log a} + c\right] + (-3.2728P - 10.965)$$

(9)

Comparing Figs. 4 and 5, it is obvious that the leakage flow rate of the variable displacement hydro-motor ($Q_{lv}$) at a given pressure and temperature is higher than that of the fixed displacement motor ($Q_{lf}$) at same operating conditions. This is due to the fact that there is an additional leakage flow path provided in the variable displacement hydro-motor as described in Sect. 2. Also, increase in pressure increases the leakage flow in the hydro-motors linearly (Figs. 4 and 5). This is because increase in the pressure increases the fluid flow rate through the clearances provided. The effect of temperature on the leakage flow rate is also found to be linear. This is due to the fact that increase in the temperature of oil decreases its viscosity.

## 6 Conclusions

This article investigates the steady-state leakage flow characteristic of the fixed and variable displacement bent axis hydro-motors. In this respect, a closed-circuit hydrostatic system is fabricated. The constructional details of the said hydro-motors are also studied with respect to their leakage flow paths. A mathematical model is developed to estimate the leakage flow characteristic of the hydro-motors, which accounts for the effect of the state variables like operating pressure and oil temperature. The coefficients of the model are obtained from the test data. The proposed method of the steady-state leakage flow characteristic of the hydro-motors may be useful to the application engineers for the selection of similar motors for HST drives. The model proposed here would have considerable value to study the control aspects of the plants where such motors in the drives are the integral part of the vehicle transmission system. It also may be useful for initial design and selection of similar machine for a particular application, where one can easily obtain more economical solutions using the idea developed here. By measuring leakage flow of the HST drives as shown in Figs. 4 and 5, suitable control schemes may be formulated for hydro-motor of variable displacement to reduce the slip and the torque losses of the hydrostatic drives.

In this respect, effect of the bulk modulus, noise levels, density of oil, and piston dynamics on leakage flow needs to be established. Studies in this regard require the detailed modeling which may be a potential future scope of work.

## References

1. Korn J (1969) Hydrostatic transmission systems. Transatlantic Arts
2. Wilson WE (1949) Performance criteria for positive displacement pumps and fluid motors. Trans. ASME 71(2):115–120
3. Thoma J (1970) Mathematical model and the effective performance of hydrostatic machines and gear. Oil Hydraul Pneumatic 14(2):233–237
4. Schlosser WMJ (1961) A mathematical model for pump and motors. Oil Hydraul Pneumatic 5 (4):122–129
5. Rydberg KE (2009) Efficiencies for variable hydraulics pumps and motors—mathematical models and operation conditions. Thesis, Department of Management and Engineering, Linköpings University, Sweden
6. Inaguma Y (2012) Oil temperature influence on friction torque characteristics in hydraulic pumps. Proc Inst Mech Eng Part C J Mech Eng Sci 226(9):2267–2280
7. Kumar N, Dasgupta K, Ahmad F (2013) Analysis of leakage flow characteristics in bent axis motors. In: Proceedings of the 1st international and 16th national conference on machines and mechanisms (iNaCoMM2013), pp 318–323
8. Hall SJ (2014) Statistical analysis of multiple hydrostatic pump flow loss models. M.Sc. thesis, Iowa State University, US
9. Bergada JM, Kumar S, Davies DL, Watton J (2012) A complete analysis of axial piston pump leakage and output flow ripples. Appl Math Model 36(4):1731–1751

10. Bergada JM, Davies DL, Kumar S, Watton J (2012) The effect of oil pressure and temperature on barrel film thickness and barrel dynamics of an axial piston pump. Meccanica 47(3): 639–654

11. Li CG, Jiao ZX (2006) Thermal-hydraulic modeling and simulation of piston pump. Chin J Aeronaut 19(4):354–358

12. Knežević D, Savić V (2006) Mathematical modeling of changing of dynamic viscosity, as a function of temperature and pressure, of mineral oils for hydraulic systems. Facta Universitatis, Series, Mechanical Engineering, Serbia 4(1):27–34

13. Watton J (2010) Fundamentals of fluid power control. Cambridge University Press, pp 133–163

14. Product catalogue of the fixed displacement bent axis hydro-motor, RE 91000/09.00, Bosch Rexroth group

15. Product catalogue of the variable displacement bent axis hydro-motor, RE 91001/09.00, Bosch Rexroth group

16. Stachowiak G, Batchelor AW (2013) Engineering tribology. Butterworth-Heinemann

17. Product data sheet (servo system 22-150) Technical service department, Indian oil corporation ltd. Mumbai-400051

# Experimental Analysis of Thermal Conductive Properties on Aerogel-Filled Composite Structure

**Bommidi Atcharao, P. Poorna Mohan and P. N. E. Naveen**

**Abstract** Aerogels are well known for its ultimate thermal resistive characteristics and its low density, i.e., several times less than air. Because of these favorable properties, aerogels are mostly used in thermal insulations. The main drawbacks of these insulations are poor strength and limited operating temperatures. In this paper, an attempt has been made to enhance the strength and broaden the range of operating temperature of the insulation made of silicon aerogel. To acquire these properties, a composite structure filled with silicon aerogel has been proposed and experimentally investigated to evaluate its thermal conductivity at different temperatures and heat flow rates. Results have been compared with empty structure and glass wool-filled structure by using plots. From the plots, it was concluded that the structure filled with the aerogel has less thermal conductivity than the other structures and also the percentage change of thermal conductivity was determined at different temperatures with different heat transfer rates.

B. Atcharao (✉)
Godavari Institute of Engineering & Technology (A), Rajahmundry, India
e-mail: atcharaobommidi@gmail.com

P. Poorna Mohan
Faculty of Mechanical Engineering, Godavari Institute of Engineering & Technology (A), Rajahmundry, India

P. N. E. Naveen
GITAM Deemed to be University, Vizag, India
e-mail: pne.naveen@gmail.com

689

# 1 Introduction

Most of the industries or firms are focusing on energy efficiency through sustainable development in which thermal insulation plays a very important role. The following are the major areas where thermal insulation is required:

- For buildings
- For various processes which involve energy loss in the form of heat
- For various machines and devices having energy loss in the form of heat.

Most of the above applications require only high thermal resistive characteristics and low operating temperatures but not strength. But some special applications like aerospace applications, thermal insulation needs to have very high strength to weight ratio along with high thermal resistive characteristics and high operating temperatures. Not only aerospace applications, other applications also require this kind of properties.

Aerogels are best suited for aerospace applications because of its low density and low thermal conductivity. As per the International Union of Pure and Applied Chemistry [1], aerogel is defined as a gel comprised of a microporous solid in which dispersed phase is a gas. Aegerter et al. [2] defined aerogels as gels in which the liquid has been replaced with air, with very moderate shrinkage of a solid network. Aerogel is basically a synthetic porous ultralight material derived from a gel, in which the liquid component of the gel has been replaced with a gas; for example, graphene aerogels are so light that they can rest on top of a grass leaf. The combination of high porosity and extremely small pores provides aerogels with their extreme properties: solid with extremely low density and low thermal conductivity [3].

Aerogels are very weak to withstand the loads, because of this reason aerogels find [4] limited applications. In this paper, a structure filled with aerogel is proposed to increase the strength of the insulation.

# 2 Proposed Structure

The structure has two plates sandwiched together with a square honeycomb structure between those two plates as shown in the Fig. 1. Square honeycomb structure between two plates provides strength. Galvanized iron is used as a structure material and silicon aerogel is filled in square honeycomb structure and it is sandwiched between the two plates by riveting process. Silicon aerogel can withstand high temperatures and it has low thermal conductivity [5]. The developed structure has high strength, high thermal resistivity and can be subjected to high operating temperatures, i.e., less than melting temperature of galvanized iron. For higher temperatures, materials like ceramics [6–8] are to be employed as the structural material instead of galvanized iron.
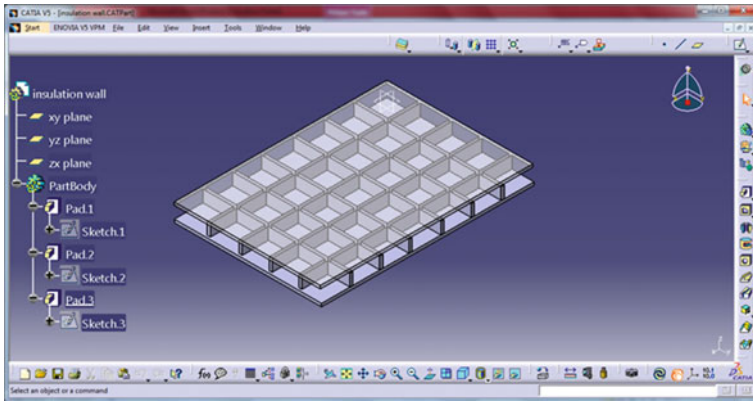
**Fig. 1** Development of the proposed structure by CATIA

## 3　Experimental Setup to Evaluate Thermal Conductivity

A simple thermal conductivity experiment is used to evaluate the thermal conductivity of proposed structure. The setup is equipped with a uniform electrical heater insulated in a sealed compartment and a temperature indicator cum thermocouple selector switch to which thermocouples are connected to measure the temperature at various locations of proposed structure. It is also equipped with an ammeter and voltmeter to measure the electrical power supply for the heater along with power regulator switch to vary the power supply. Schematic diagram of setup is shown in Fig. 2.

T1, T2, T3, and T4 are temperatures of proposed structure at various locations measured by thermocouples. Heater used in the experiment is uniform and due to structural symmetry heat is equally transferred to both top and bottom sides of heater. T1 and T2 are the temperatures at different locations on the heater surface or bottom surface of proposed structure and T3 and T4 are the temperatures at different locations on insulation surface or top surface of the proposed structure.

Thermal conductivity is evaluated by placing the proposed structure in between insulation plate and heater. Thermal conductivity is calculated by Fourier law of heat conduction. Heat flux flowing through the structure from heater can be

**Fig. 2** Schematic diagram of setup
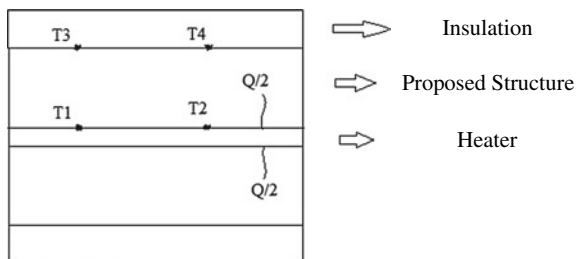
measured by the amount of power supply required to maintain the constant temperatures of heater and insulator.

Thermal behavior of proposed structure was studied with the above setup. Along with the proposed structure filled with aerogel in between the structure top plate and bottom plate, the structure filled with glass wool and empty structure were also experimentally investigated to evaluate the thermal behavior and to compare with the result of proposed structure filled with silicon aerogel.

Thermal conductivity is determined by Fourier's law as:

$$K_s = t_s q / (T_H - T_C)$$

Here, $K_s$ is thermal conductivity of the structure, $t_s$ is the structure thickness (thickness includes the two faces of the structure), $q$ is heat flux though unit normal area of structure, $T_H$ is average temperature of T1 and T2, $T_C$ is the average temperature of T3 and T4. As the thickness of the structure is very small, i.e., 13 mm, it is assumed to be one-dimensional heat conduction problem.

## 4   Results and Discussions

From the above experimentation, thermal conductivity of proposed structure is evaluated at different temperatures for various varieties of structures and the results were plotted as follows:

Variation of thermal conductivity of proposed structure filled with silicon aerogel at various heat transfer rates by taking thermal conductivity (w/m-k) on X-axis and temperature of the hot surface (°C) on Y-axis (Graph 1).
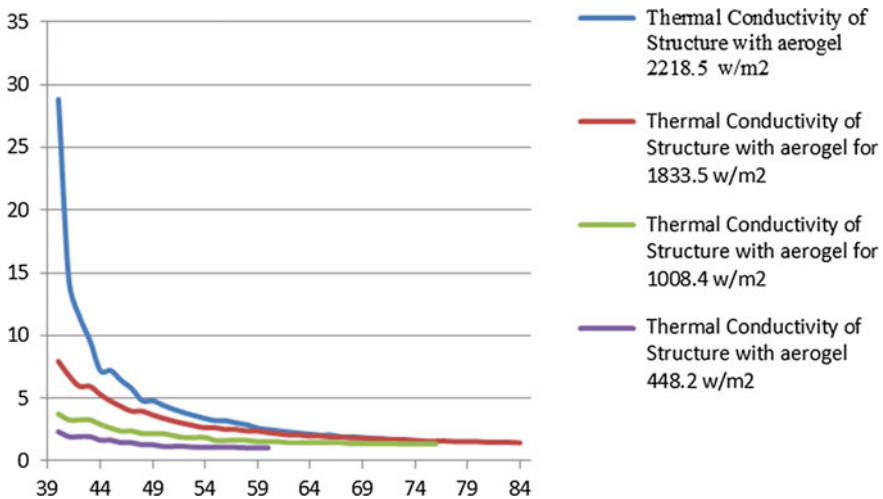


Graph 1  Proposed structure filled with aerogel at various heat transfer rates
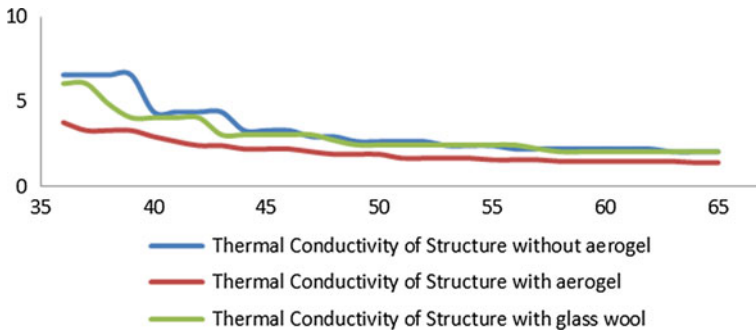
**Graph 2** Variation of thermal conductivity for various varieties of structures at a heat transfer rate of 1008.5 w/m²

Comparison of thermal conductivity variation for various varieties of structures at a uniform heat transfer rate of 1008.5 w/m² through the surface normal to the structure, i.e., along the direction of thickness by taking thermal conductivity (w/m-k) on X-axis and temperature of the hot surface (°C) on Y-axis (Graph 2).

Comparison of thermal conductivity variation for various varieties of structures at a uniform heat transfer rate of 1833.5 w/m² through the surface normal to the structure, i.e., along the direction of thickness by taking thermal conductivity (w/m-k) on X-axis and temperature of the hot surface (°C) on Y-axis (Graph 3).

Comparison of thermal conductivity variation for various varieties of structures at a uniform heat transfer rate of 448.2 w/m² through the surface normal to the structure by taking thermal conductivity (w/m-k) on X-axis and temperature of the hot surface (°C) on Y-axis (Graph 4).



**Graph 3** Variation of thermal conductivity for various varieties of structures at a heat transfer rate of 1833.5 w/m²

**Graph 4** Variation of thermal conductivity for various varieties of structures at a heat transfer rate of 448.2 w/m$^2$

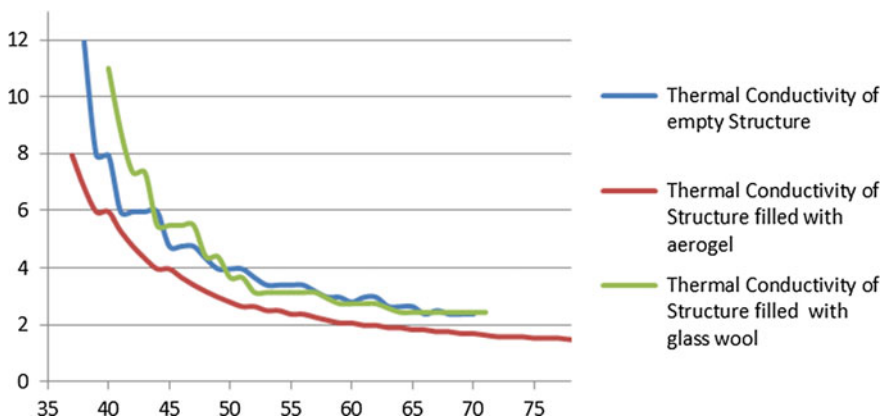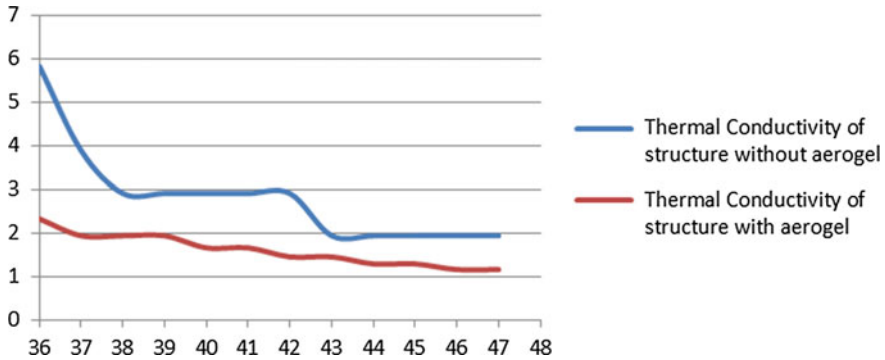From the above results, it is clear that thermal conductivity of the structure filled with aerogel is less than the any other type of structure at different temperatures and also found that, as the temperature of the structure increased then thermal conductivity of proposed structure decreases. Thermal conductivity of silicon aerogel-filled structure is 1.49 w/m-k at a temperature of 80 °C with a heat transfer rate of 1833.5 w/m$^2$ which is less than thermal conductivity of structure filled with glass wool and empty structure. Due to which it enables us to use silicon aerogel-filled structure of same thickness can be operated for higher temperatures than other insulation structures at a fixed heat transfer rate. Proposed structure is sandwiched with the square honeycomb structure made of galvanized iron in the middle layer of the structure as a result the overall thermal conductivity is increasing along with it, strength of the structure is also increased because of increased flexural rigidity. Without the honeycomb structure in between the faceplates, thermal conductivity is decreased and strength is decreased. So, the proposed structure filled with silicon aerogel can be used as an insulation wall with higher operating temperatures and high strength than normal glass wool insulations with same thickness and same cross-sectional area.

## 5　Conclusions

Experimental study was done on the proposed structure to evaluate the thermal conductivity at different temperatures and heat transfer rates. Results have been compared with different varieties of structures and graphs were plotted at different heat transfer rates and limited temperatures. In this study, faceplates and square honeycomb structures used in proposed design were developed with galvanized iron to simplify the design for evaluating the conductive behavior of the structure at minimum temperature ranges. Other than galvanized iron high melting point

temperature materials may also be employed in the same study to evaluate thermal conductive behavior at higher temperatures which enables us to use those insulation walls for very high operating temperature applications.

The following conclusions were drawn from the experimental results:

- The percentage change in thermal conductivity of silicon aerogel-filled structure with respect to empty structure and glass wool-filled structure is 28.5 and 22.6% respectively at the temperature of 50 °C with a uniform heat transfer rate of 1008.4 w/m$^2$.
- The percentage change in thermal conductivity of silicon aerogel-filled structure with respect to empty structure and glass wool-filled structure is 29.4 and 36.2% respectively at the temperature of 50 °C with a uniform heat transfer rate of 1833.46 w/m$^2$.
- The percentage change in thermal conductivity of silicon aerogel-filled structure with respect to empty structure and glass wool-filled structure is 28.5 and 30.3% respectively at the temperature of 70 °C with a uniform heat transfer rate of 1833.46 w/m$^2$.

# References

1. McNaught AD, Wilkinson A (2007) Compendium of Chemical Terminology, IUPAC Goldbook, PAC, 791801, Blackwell Science, 2nd edn. Oxford, Cambridge, UK
2. Aegerter MA, Leventis N, Koebel MM (2011) Aerogels handbook. Springer, New York, NY, USA
3. Guinness Records Names JPL's Aerogel World's Lightest Solid (2002) NASA Jet Propulsion Laboratory
4. Bao Y, Zhao X (2018) Research article: the research applications of new heat insulation composite material in automobiles. Heat Transf Asian Res 103–110
5. Mulder CAM, Van Lierop JG (1986) Preparation, densification and characterization of autoclave dried $SiO_2$ gels. In: Fricke J (ed) Aerogels. Springer, Berlin, Germany, pp 68–75
6. Li K, Li JH, Chan HLW (2004) Fabrication of Sm- and Mn-doped lead titanate ceramic powder and ceramics by sol-gel methods. Mater Chem Phys 86(1), 83–87. View at Publisher—View at Google Scholar—View at Scopus
7. Jain R, Gupta V, Mansingh A, Sreenivas K (2004) Ferroelectric and piezoelectric properties of non-stoichiometric $Sr_1 − xBi_2 + 2x/3Ta_2O_9$ ceramics prepared from sol-gel derived powders. Mater Sci Eng B 112(1):54–58
8. Xu Y, Huang G, He Y (2005) Sol-gel preparation of $Ba_6 − 3xSm_8 + 2xTi_{18}O_{54}$ microwave dielectric ceramics. Ceram Int 31(1):21–25

# Effect of Selectively Applied Surface Roughness and Wake Splitter Plate on the Aerodynamic Characteristics of a Circular Cylinder

**Shruthi Sivadas, K. Arun Kumar and R. Ajith Kumar**

**Abstract** This paper investigates flow over a stationary circular cylinder (diameter, $D$) with locally applied roughness height, '$k$' applied at certain circumferential locations of the cylinder in the presence of a detached wake splitter plate with varying length, $L$. The numerical simulations are done by using commercial software ANSYS Fluent. This numerical study is conducted at a Reynolds number value of 25,000, $k/\delta = 1.1$ ($\delta$ is the boundary layer thickness at a given circumferential location) and $L/D = 0.5, 1, 1.5, 2.0$ at different roughness locations $\alpha = 0°$, $9°$, $31°$, $65°$, and $75°$. The results indicate that lift coefficient, drag coefficient, and Strouhal number are significantly affected as the $L/D$ ratio increases, whereas with the change in the roughness location, the aerodynamic/hydrodynamic characteristics are not notably affected. Longer splitter plate along with roughness application is found to cause two effects: (a) considerable reduction in drag coefficient and Strouhal number and (b) considerable increase in the lift coefficient.

**Keywords** Drag coefficient · Lift coefficient · Strouhal number

## Nomenclature

| | |
|---|---|
| $G$ | Gap between the cylinder and splitter plate |
| $D$ | Diameter of cylinder |
| Cl* | Non-dimensional lift coefficient |
| Cpb | Base pressure coefficient |
| $\theta$ | Circumferential range of the roughness strip |
| $G/D$ | Gap-to-diameter ratio |
| $\alpha$ | Circumferential location of the roughness strip |
| $\delta$ | Boundary layer thickness |
| $L/D$ | Length of splitter plate to cylinder diameter ratio |

S. Sivadas (✉) · K. A. Kumar · R. Ajith Kumar
Department of Mechanical Engineering, Amrita Vishwa Vidyapeetham, Amritapuri, India
e-mail: shruthisivadas92@gmail.com

| $U$ | Freestream velocity |
| Cd* | Non-dimensional drag coefficient |
| $k$ | Roughness height |
| St* | Non-dimensional Strouhal number |
| $L$ | Length of the splitter plate |

# 1 Introduction

Flow over a bluff body is a very common phenomenon that can be seen over various engineering structures like cooling towers, stacks, bridges, high-rise buildings, and aircrafts. Right from 1960s, various researchers report measurements on the lift and drag forces on a circular cylinder at various Reynolds numbers. Gerrard [1] explained the mechanics of the formation region of vortices behind the circular cylinder. Further, Achenbach [2] investigated the effect of surface roughness on the cross flow around a circular cylinder by representing a curve of the drag coefficient as a function of Reynolds number. As the roughness parameter $k/D$ increases ('$k$' is the surface roughness height), the flow will be modified by increasing the minimum drag coefficient and shifting the critical Reynolds number to lower values. Niemann [3] discussed the sudden drop of the drag and the Strouhal number in the critical regime.

Catalano [4] found that at high Reynolds numbers, the lift (rms) increases rapidly. Bernitsas [5] has proved that the application of roughness at a certain circumferential position of a circular cylinder has shown to bring significant effect on the flow-induced vibration (FIV) of a circular cylinder. But, all the works of Bernitsas's group was on a flexibly mounted cylinder exposed to water flow, wherein the fundamental aspects of lift and drag forces were not dealt with. The present study is aimed at filling this gap.

Apart from the roughness, effect of the splitter plate which is one of the devices (also known as wake stabilizer) attached/detached to the circular cylinder has been studied extensively in the past due to its significant effect on the parameters such as lift and drag forces, and Strouhal number around a circular cylinder. It was reported by Roshko [6] that the vortex shedding was completely eliminated at $L/D \geq 5$ which was supported by Gerrard [1] that as the splitter plate length increases, Strouhal number decreases. Apelt and Isaacs [7] conducted a wind tunnel test which measured a drag reduction of 17 and 32% for different ratios of $L/D$ which was verified by Apelt and Szewczyk [8] by numerical simulation. It has been found that a detached plate behind the cylinder may also change the pattern of vortex shedding and reduce the shedding frequency.

Park et al. [5, 9] reported the effect of roughness, its location and orientation on a circular cylinder, wherein it was noted that the roughness strip location in the range 60°–80° exhibits significant variation in the amplitude trend, whereas 90°–106°
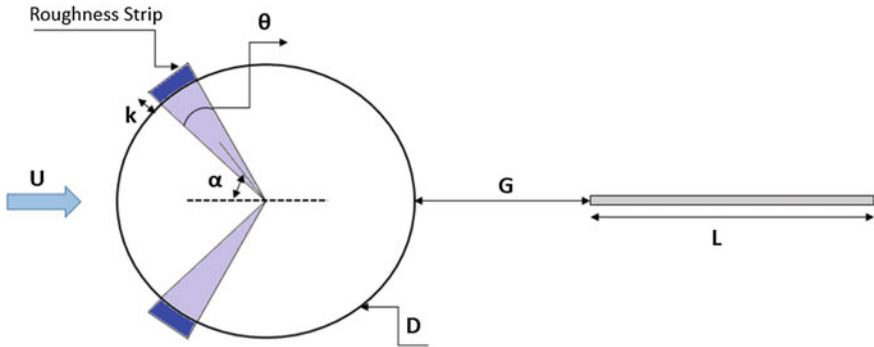
**Fig. 1** Model geometry and test configuration

range shows a similar trend to that of smooth circular cylinder. On a further study, Park [10] identified one strong-suppression zone and two weak-suppression zones based on passive turbulence control location (local surface roughness application).

All the previous studies show that both local surface application and splitter plate have the individual impact on the aerodynamics/hydrodynamics of a circular cylinder. This has generated a curiosity in the authors as to how the aerodynamics of a cylinder would change if both are simultaneously applied on a cylinder. Being motivated thus, this paper is basically intended to investigate the combined effect of both splitter plate and roughness applied selectively on a circular cylinder in water flow, having a roughness strip with width '$b$' (circumferential coverage = 10°) and roughness height ($k$) applied selectively (locally) at five different angles and a detached splitter plate of different length introduced into the body wake at a Reynolds number value of 25,000. The study configuration is shown in Fig. 1.

## 2 Computational Model and Validation

This investigation is studied using numerical simulation tool ANSYS Fluent, in order to clarify the flow physics related to the gradual reduction of the flow-induced forces on a circular cylinder, wherein finite volume method is used to solve the Navier–Stokes equations, and the coupling of pressure and velocity field is done, and therefore, coupled scheme is used. The SST $k - \omega$ turbulence model is used due to its efficiency in predicting the flow separation under adverse pressure gradient and recirculation which was stated by Vu [11] and Pang [12]. The incompressible continuity and momentum equations are used as the governing equations,

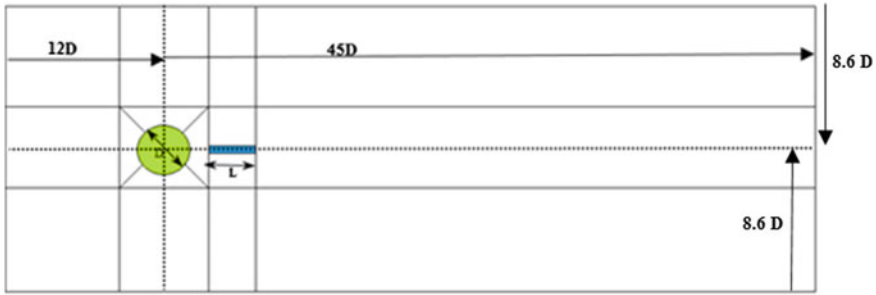$$\text{Continuity equation: } \partial \rho / \partial t + \nabla \cdot (\rho V) = 0 \tag{1}$$

**Fig. 2** Domain

**Table 1** Validation result of simulation data with experimental results for a smooth cylinder, the cylinder with roughness and cylinder with splitter plate

| Reynolds number | k/D | Achenbach [2] | | Present study | | Ozono [13] | |
|---|---|---|---|---|---|---|---|
| | | Cd | St | Cd | St | | |
| $2.5 \times 10^4$ | Smooth cylinder | 1.48 | 0.22 | 1.45 | 0.223 | | |
| 17,000 | $75 \times 10^{-5}$ | 1.48 | 0.23 | 1.45 | 0.228 | | |
| 17,000 | $3000 \times 10^{-5}$ | 1.48 | 0.157 | 1.479 | 0.15 | | |
| $2.5 \times 10^4$ | $75 \times 10^{-5}$ | 1.385 | 0.155 | 1.4 | 0.1558 | | |
| $3 \times 10^5$ | $75 \times 10^{-5}$ | 0.63 | 0.22 | 0.625 | 0.226 | | |
| $2.5 \times 10^4$ | Only splitter plate | | | Cpb = 0.77 | 0.15 | Cpb = 0.8 | 0.148 |

$$\text{Momentum equation: } \rho(\partial V/\partial t) + \rho V \nabla \cdot V = -\nabla P + \mu \nabla^2 V + \rho g \qquad (2)$$

The computational domain is selected, where the inlet and outlet boundaries are located at 12D and 48D from the center of the cylinder. In Fig. 2, the length of splitter plate varies from 0.029 to 0.058 m. No-slip boundary condition is used for the cylinder wall and the splitter plate. The fluid medium considered is water. The freestream turbulence intensity is 1%. Second-order upwind scheme is used for pressure, momentum, turbulent kinetic energy, and dissipation. Velocity is 0.8662 m/s which is calculated for the given Reynolds number (based on *D*). A mesh size of 700,000 cells is found to be sufficient for a grid-independent solution with mesh quality of 0.989. In order to check the domain and mesh size of the circular cylinder at the selected diameter, the coefficient of drag at the same Reynolds number is validated with Achenbach [2] with roughness applied over the cylinder. Similarly, the coefficient of base pressure and Strouhal number for the case with splitter plate is validated with Ozono [13] (Table 1).

| α | δ (m) |
|---|---|
| 0° | 0.000299215 |
| 9° | 0.000300321 |
| 31° | 0.000313966 |
| 65° | 0.000370096 |
| 75° | 0.000401496 |

**Table 2** Boundary layer thickness at various locations

Different geometries are made with roughness strip located at $\alpha = 0°$, $9°$, $31°$, $65°$, and $75°$ from which boundary layer thickness $\delta$ is calculated which is referred from Khan et al. [14] by using modified Pohlhausen method. For the given $\alpha$, the boundary layer thickness ($\delta$) is calculated and substituted to calculate the roughness height, $k$, for $k/\delta = 1.1$ which is fixed at all strip locations tested in this study. From the table, it can be noted that the boundary layer thickness value is maximum at $75°$. Hence, the roughness height, $k = 1.1 * \delta$ (m) (at $75°$), is used as constant throughout all the circumferential locations coverage of the roughness strip $10°$. The simulation is conducted for various cases over a circular cylinder with roughness strip located at selected test angles and a detached splitter plate at $L/D = 0.5$, 1, 1.5, and 2 for constant ratio of $G/D = 1$ (Table 2).

## 3  Results and Discussion

In this section, results are presented with non-dimensionalized values of Strouhal number, coefficients of drag and lift with respect to the circumferential location of the roughness strip. The aerodynamic/hydrodynamic parameters are non-dimensionalized using the respective values for a smooth cylinder at the same
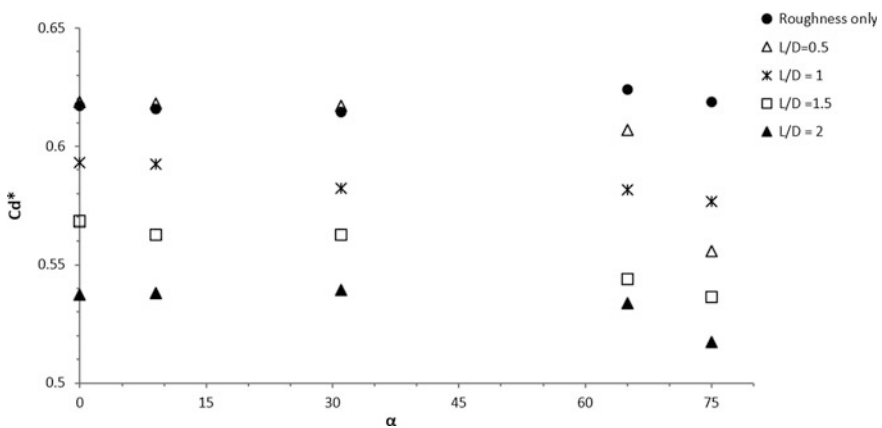


**Fig. 3** Variation of non-dimensional drag coefficient with roughness location

Reynolds number. Figure 3 shows the variation of dimensionless drag coefficient for roughness alone cases and cases with roughness and splitter plate simultaneously applied.

It is noted that at $L/D = 2$ and roughness location $\alpha = 75°$, there is 48.2% drag reduction when compared with smooth cylinder. As the splitter plate length to cylinder diameter ratio varies from 0.5 to 2, it is observed that there is a significant reduction in drag coefficient from which complies with the results of Kawai [15] for $G/D = 1.0$ which is a critical gap as the rolling-up vortices is prevented until this gap ratio. It could also be noted that, till $\alpha = 65°$, drag remains nearly invariant further to which it notably drops (Fig. 3).

Variation of non-dimensional lift coefficient with roughness location is shown in Fig. 4. For cases such as roughness only, splitter plate only and with $L/D = 0.5$, 1, and 1.5, there is 50–80% reduction in rms lift coefficient as compared to smooth cylinder. But again, the interesting fact observed is that when the splitter plate length to cylinder diameter ratio is 2.0, the lift coefficient is higher as compared to the other ratios. It is interesting to note that the selective application of roughness tends to subdue drag similar to a splitter tends at $G/D = 1.0$. It is to be noted that, due to roughness alone, drag coefficient is the higher than other cases of combined roughness and splitter plate, whereas a roughness alone configuration brings down the lift coefficient to significantly lower values compared to the lift values of smooth cylinder and also compared to configurations with combined roughness and splitter plate. Further, it could be seen that, at a particular roughness location, lift variation is not following a trend w.r.t $L/D$. Drop in lift at $\alpha = 65$ could also be seen in Fig. 4 similar to that of drag. Therefore, it could be inferred that by applying both roughness and splitter together at certain locations of the cylinder, both the aerodynamic characteristics can be significantly controlled. More specifically, the
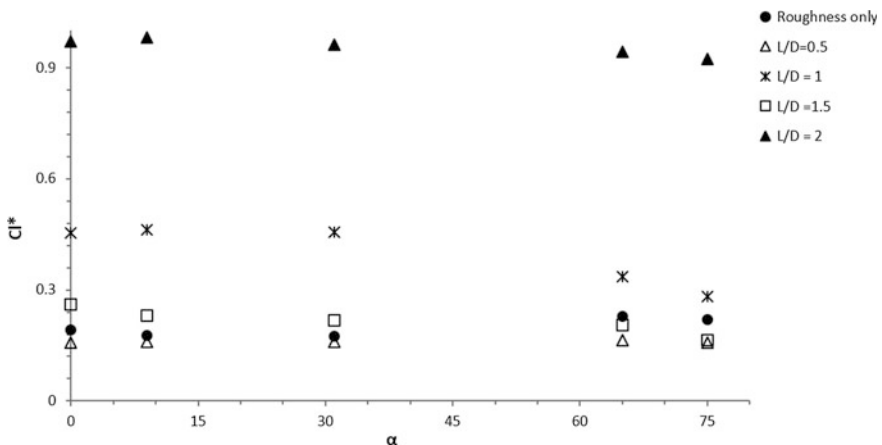


Fig. 4 Variation of non-dimensional lift coefficient with roughness location
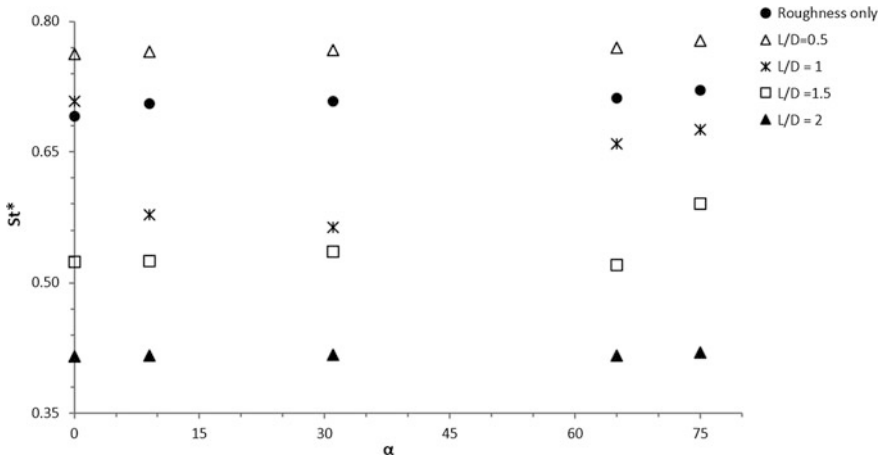
**Fig. 5** Variation of Strouhal number with roughness location

present results clearly demonstrate that both local roughness and splitter plate are very good wake flow stabilizers.

Figure 5 shows that non-dimensional Strouhal number variation with respect to local roughness application alone and also with respect to roughness with splitter plate combined configurations. Strouhal number appears to be nearly invariant with respect to the roughness location till $\alpha = 65°$ further to which it slightly increases. With roughness alone, non-dimensional Strouhal number reduces to about 30% as seen in Fig. 5. But, with splitter plate addition, this shedding frequency parameter greatly modifies too much lower values (as low as 0.38) and much higher values (as high as 0.75) depending on $L/D$ ratio. The highest Strouhal number value is for $L/D = 0.5$ (short splitter plate) case. This could be attributed to the amplification of flapping of free shear layers at this configuration as revealed by Kawai [15] and Vu [11]. It could also be seen that, as $L/D$ increases, Strouhal number decreases for a given particular roughness location, whereas this parameter does not seem to vary significantly with respect to change in roughness location as evident from Fig. 5. The observed trends of the aerodynamic characteristics depicted in Figs. 3, 4, and 5 could be attributed to the changes in the flow field particularly the modifications in the characteristics of the shear layers, their subsequent roll-up the process, and the vortex formation region downstream. All these could very much affect the surface pressure distribution of the cylinder, thereby influencing the lift and drag forces as well as the vortex shedding frequency.

# 4   Conclusions

The flow around a circular cylinder is numerically simulated using ANSYS Fluent with a detached splitter plate and varying roughness at a subcritical Reynolds number value of 25,000. The aerodynamic characteristics such as the Strouhal number, and drag and lift force coefficients are investigated with respect to the splitter plate length and roughness location, and the following conclusions are obtained:

1. When both splitter plate and roughness are applied together, the aerodynamic characteristics such as the drag coefficient have shown the maximum reduction of about 48.2% compared to smooth cylinder.
2. For all the L/D ratios, Strouhal number remains nearly constant till $\alpha = 65°$ further to which it registers a slight increase.
3. The present study has given more clarity to the fact that even if the critical gap is set constant, the effect of splitter plate length and roughness location is very much critical to control the aerodynamic characteristics as both these passive flow controllers are found to bring in more stability to the cylinder.

# References

1. Gerrard JH (1966) The mechanics of the formation region of vortices behind bluff bodies. J Fluid Mech 25:401–413
2. Achenbach E (1971) Influence of surface roughness on the cross-flow around a circular cylinder. J Fluid Mech 46:321–335
3. Niemann HJ, Holscher N (1990) A review of recent experiments on the flow past circular cylinders. J Wind Eng Ind Aerodyn 33:197–209
4. Catalano P, Wang M, Iaccarino G, Moin P (2003) Numerical simulation of the flow around a circular cylinder at high Reynolds numbers. Int J Heat Fluid Flow 24:463–469
5. Park H, Bernitsas MM, Kumar AR (2012) Selective roughness in the boundary layer to suppress flow-induce motions of circular cylinder at 30,000 < Re < 120,000. J Offshore Mech Arct Eng 134
6. Roshko A (1954) On the drag and shedding frequency of two-dimensional bluff bodies. N.A. C.A. Technical note, no. 3169
7. Apelt CJ, Isaacs LT (1970) Effects of splitter plates placed in the wake of bluff cylinders. In: C.A.A.R.C. Symposium on separated flows and wakes, University of Melbourne
8. Apelt CJ, West GS, Szewczyk AA (1973) The effects of wake splitter plates on the flow past a circular cylinder in the range $10^4 < R < 5 \times 10^4$. J Fluid Mech 61, part 1:187–198
9. Park H, Kumar AR, Bernitsas MM (2013) Enhancement of flow-induced motion of rigid circular cylinder on springs by localized surface roughness at $3 \times 104 \leq Re \leq 1.2 \times 105$. Ocean Eng 72:403–415
10. Park H, Ajith Kumar R, Bernitsas MM (2016) Suppression of vortex-induced vibrations of a rigid circular cylinder on springs by localized surface roughness at $3 \times 10^4 \leq Re \leq 1.2 \times 10^5$. Ocean Eng 111:218–233
11. Vu HC, Ahn J, Hwang JH (2015) Numerical investigation of flow around circular cylinder with splitter plate. KSCE J Civ Eng. https://doi.org/10.1007/s12205-015-0209-3

12. Pang LJ, Skote M, Lim SY (2016) Modeling high Re flow around a 2D cylindrical bluff body using the k-ω (SST) turbulence. Prog Comput Fluid Dyn 16
13. Ozono S (1999) Flow control of vortex shedding by a short splitter plate asymmetrically arranged downstream of a cylinder. Phys Fluids 11(10)
14. Khan WA, Culham JR, Yovanovich MM (2003) Fluid flow and heat transfer from a pin fin: analytical approach. In: 41st Aerospace sciences meeting and exhibit, 6–9 January, Reno, Nevada
15. Kawai H (1990) Discrete vortex simulation for flow around a circular cylinder with a splitter plate. J Wind Eng Ind Aerodyn, 21 November 2016

# Mixing Studies in Turbulent Oxy-Methane Jets with and Without Reaction

**Jana Tamal, A. R. Srikrishnan, B. Deependran and R. Ajith Kumar**

**Abstract** Interactions of multiple jets have several industrial applications like jet mixing in rocket engine and in combustion chambers. Non-premixed (diffusion) flame is used in many applications owing to its stability. The present study considers three-dimensional simulation of three separated oxy-methane jets which shows that combustion has a prominent impact on their velocity distribution. The radial distributions of longitudinal velocity at different axial locations have been examined. Comparison has been done on reactive and non-reactive jets. Velocity decay for reactive jets is found to be slower relative to non-reactive jets. Turbulent intensity is higher in non-reactive jets which causes faster spreading. The temperature profile shows that the peak temperature does not exist on the centerline plane but at some offset height from the oxy-fuel centerline plane. The study has been carried out for different jet inlet temperatures. Increase in inlet temperature of reactant leads to a faster velocity decay.

**Keywords** Coherent vortical structure · Non-reactive jets · Reactive jets · Turbulent intensity

J. Tamal (✉) · R. Ajith Kumar
Department of Mechanical Engineering, Amrita Vishwa Vidyapeetham,
Amritapuri, India
e-mail: tfortamal@gmail.com

R. Ajith Kumar
e-mail: amritanjali.ajith@gmail.com

A. R. Srikrishnan
Department of Aerospace Engineering, Amrita Vishwa Vidyapeetham,
Coimbatore, India
e-mail: arsrikrishnan@gmail.com

B. Deependran
Vikram Sarabhai Space Centre, Thiruvananthapuram, India
e-mail: b_deependran@vssc.gov.in

# 1   Introduction

Jets are pressure-driven flow of fluid which can be classified mainly as reactive jets and non-reactive jets based on their chemical reactivity. Reactive jets can be classified as premixed (fuel and oxidizer mixing takes place before combustion) and non-premixed (reactants are diluted with the combustion products and combustion takes place at the interface between fuel and oxidizer). Several studies concentrate on non-premixed flames experimentally and numerically since no fundamental characteristic like flame velocity can readily be measured in non-premixed flame jets. Since flame stabilization is one of the most important factors, studies have addressed parameters like flame length, lift-off height, blow-out limit, etc. An experimental study done by Leite et al. [1] shows that increasing the separation distance between acetylene flames decreases the flame length. Another work done by Menon and Gollahalli [2] found out the blow-out limit for interacting jets in cross-flow. A comparative study on dimethyl ether, methane, and LPG diffusion flames was reported by Yin et al. [3] which analyzes diffusion flame temperature and flame length for laminar to fully turbulent regime. Study of separated parallel natural gas and oxygen jets has been carried out by Sautet et al. [4] which showed that lift-off height increases with increasing separation distance between fuel and oxidizer as well as decreasing jet diameter. Numerical work done on three oxy-methane jets by Mergheni et al. [5] shows that decreasing the equivalence ratio within flammability limit increases the interaction between oxygen and fuel which promotes mixing. The numerical work done by Brahim et al. [6] on enrichment effect of hydrogen on oxy-fuel flame shows that the temperature reaches the maximum quickly since hydrogen enhances mixing between oxygen and fuel and accelerates the combustion reaction. Studies of Boushaki et al. [7] show that inclination of two lateral oxygen jets toward central fuel jet stabilizes the flame at more upstream distance. Though some numerical work has been done for three parallel oxy-fuel reactive jets in two-dimensional domain, since mixing is a three-dimensional phenomenon, it requires a three-dimensional analysis for a comprehensive assessment. In the present study, focus is on three-dimensional jet interaction with emphasis on velocity and temperature distributions. The simulation study is carried out on three parallel oxy-methane jets to analyze the three-dimensional interaction as well as the velocity and thermal fields.

# 2   Flow and Numerical Domains

The flow domain of three oxy-methane jets is shown in Fig. 1, where central jet corresponds to methane and lateral two jets correspond to oxygen. Numerical domain is taken as one-fourth of the flow domain to reduce computation time. Diameter of oxygen and the fuel jet is 0.006 m.
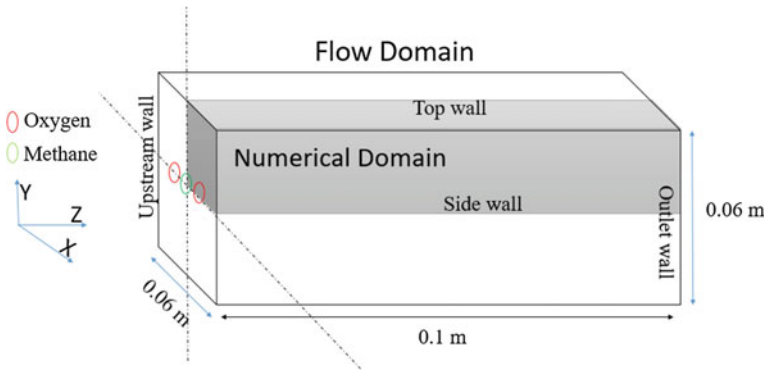
**Fig. 1** Flow and numerical domains

## 2.1 Mesh Modeling

Meshing for that numerical simulation was done using the preprocessor tool Gambit. Hexahedral unstructured mesh is used inside the curved wall for oxygen and fuel jets. Hexahedral structured mesh is used for all other parts. 385,000 nodes are used after grid independence study. The mesh configuration is shown in Fig. 2.

## 2.2 Boundary Conditions

The stoichiometric ratio (volume-based) of oxygen–methane mixture is 2. Since the calorific value of methane is 45 MJ/kg, for getting 25 KW power the flow velocities of oxygen and methane jets are 27.13 m/s each. The density of methane is
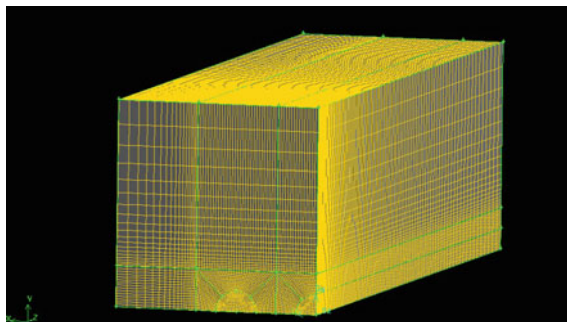


**Fig. 2** Generated grid in numerical domain

$0.724 \ kg/m^3$, and the density of oxygen is taken as $1.331 \ kg/m^3$. The mass fractions of oxygen and methane at inlet are taken as 0.995 and 1, respectively. The outlet is specified as pressure outlet with zero gauge pressure. The non-symmetry walls of the domain are specified with zero heat flux and no slip condition. Turbulent intensity is taken as 10%. Reynolds number of methane and oxygen jet is 12,272 (both).

| | |
|---|---|
| Designed power for oxy-methane flame | 25 KW |
| Stoichiometric oxy-fuel ratio (volume-based) | 2 |
| Density of methane | $0.724 \ kg/m^3$ |
| Density of oxygen | $1.331 \ kg/m^3$ |
| Mass fraction of methane at the fuel exit | 0.995 |
| Mass fraction of oxygen at oxidizer exit | 1 |
| Velocity of oxygen and methane jets at inlet | 27.13 m/s |
| Pressure outlet | Zero gauge pressure |
| Walls | No slip condition with zero heat flux |
| Turbulent intensity | 10% |
| Reynolds number for methane jet | 12,272 |
| Reynolds number for oxygen jet | 12,272 |

## 2.3 Numerical Modeling and Methods

The numerical methods solve steady equations for conservation of mass, momentum, energy, and species for separated jet burner. ANSYS Fluent 18.2 is used as the solver.

In simulations, k-epsilon standard model is used since this model gives fairly accurate results for circular flame jets. For species transport, eddy dissipation model is used since turbulent mixing dominates the reaction mechanism. Steady-pressure-based simple solver is used. Momentum and pressure discretization is taken as first order. Residual convergence criteria for energy equation are taken as $10e^{-6}$ and for continuity equation is taken as $10e^{-3}$. For non-reactive jets, velocity profile has been validated for same numerical domain. K-epsilon realizable model is used as a viscous model and volume of fluid method is chosen as multiphase model in case of non-reactive jets. K-epsilon realizable model has been used for both species transport and multiphase model as it gives better result for round jets.

Overall combustion reaction equation is:

$$CH_4 + 2O_2 \rightarrow CO_2 + 2H_2O$$
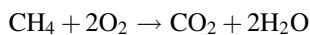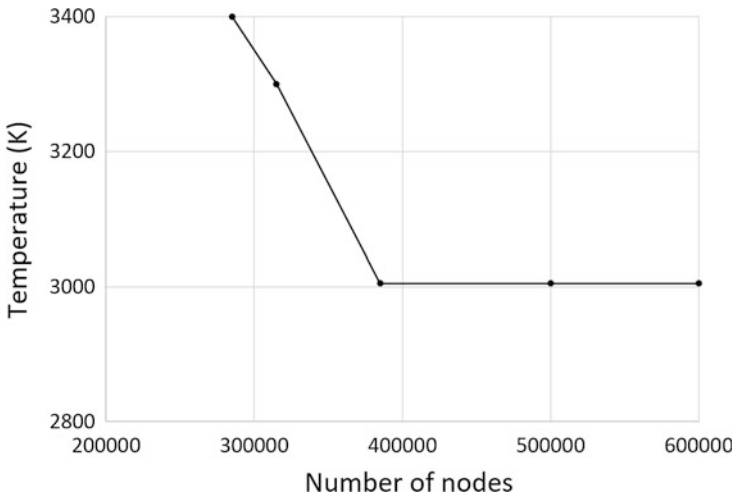
**Fig. 3** Grid independence test

## 2.4 Grid Independence Study

A grid independence study has been done for different number of grids to find out the optimum number of grids for desired accuracy. Around 385,000 nodes have been used after grid independence study (Fig. 3) where maximum temperature for oxy-methane stoichiometric flame has been found out as 3005 K. This maximum obtained temperature for stoichiometric oxy-methane mixture at one atmosphere has been validated with NASA CEARUN online code where maximum temperature has been observed as 3050 K. Percentage of error for measuring the maximum temperature is 1.5%.

## 3 Validation with Previous Numerical Work

The predicted velocity profile at an axial downstream distance for three parallel oxy-methane reactive jets was validated (Fig. 4) with the numerical work of Merghani et al. [5]. The velocity profile is plotted radially where non-dimensional radial distance has taken along $x$-axis. $r$ is the radial distance along $X$-axis, and $D$ is the diameter of the oxygen and methane jets. The axial length along the flame has taken as $Z$-axis (Fig. 1). The non-dimensional axial length along the flame is taken as $Z/D$.

For non-reactive oxy-methane jets, velocity profile validation (Fig. 5) has been done with the numerical work of Brahim et al. [6] for the same numerical domain and for flow velocity of 24 m/s for both oxygen and methane non-reactive jets.

Validation of radial distribution of axial velocity profile
at Z/D 8.33
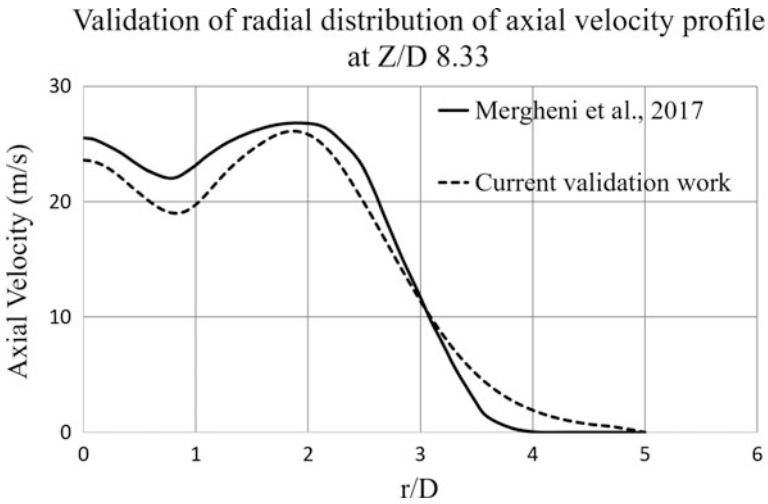


Fig. 4 Numerical validation of radial profile of axial velocity at *Z/D* 8.33

Axial Velocity profile validation at the centerline
plane at Z=3mm
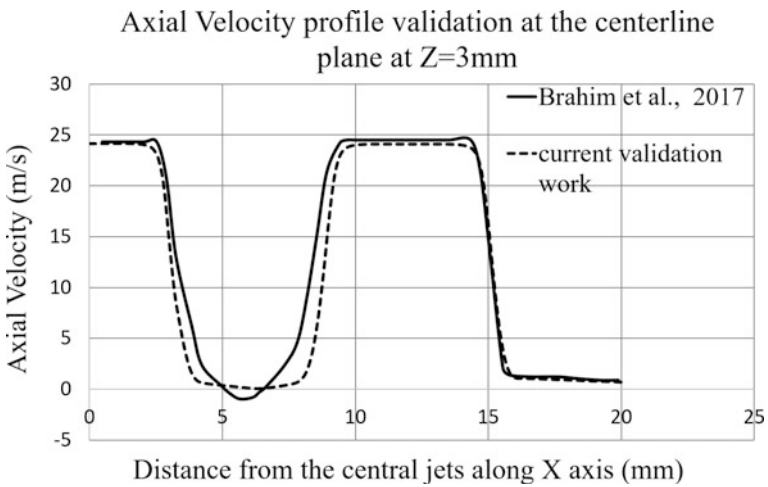


Fig. 5 Numerical validation of non-reactive oxy-methane jets

In both the cases, small deviation arises due to the fact that the jet interaction phenomenon is extended in three-dimensional numerical domain, so the three-dimensional effect of velocity comes into account.

# 4    Results and Discussions

Mixing characteristics of the jets in the three-dimensional domain are examined by way of analyzing the radial distributions of velocity and temperature in the near field.

## 4.1    Velocity Profile Variation

The radial distribution of longitudinal centerline velocity profile at various axial locations is shown in Fig. 6. It can be noted that at the near field of the nozzle exit the radial fluctuation of longitudinal velocity between methane and oxygen is higher. But at further downstream, mixing between jets takes place resulting in a more uniform radial velocity distribution.

Figure 7 shows the comparison of velocity distribution between reactive and non-reactive jets. It can be seen that for non-reactive jets velocity decays faster than that of reactive jets due to their higher mixing rate. But reactive jets spread further than that of non-reactive jets due to heat release from oxy-fuel flame.

## 4.2    Turbulent Intensity

Turbulent intensity is plotted in Fig. 8. Turbulent intensity is higher at the interface between fuel and oxygen as well as oxygen and surrounding static air. This is due to the formation of coherent vertical structure at the interface.
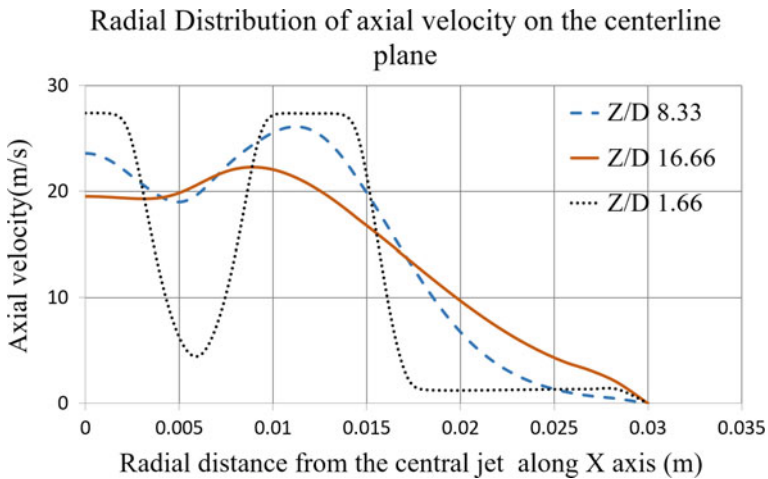


**Fig. 6**   Axial velocity distribution along *X*-axis
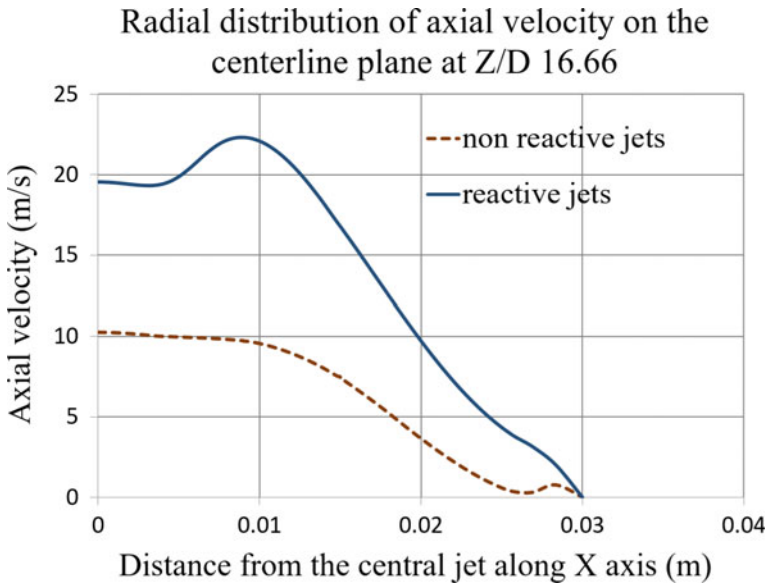
**Fig. 7** Comparison of reactive and non-reactive jets' velocity profile

The comparison of turbulent intensity (Fig. 8) between the reactive and non-reactive oxy-methane jets shows that for non-reactive jets turbulent fluctuations are very high at the near field of jet exit from the nozzle. The high turbulent intensity causes velocity to decay faster, and velocity distributions are more uniform at further downstream distance relative to reactive jets.

## 4.3 Temperature Distribution

The centerline plane containing the three jets has temperature distribution as shown in Fig. 9 for different axial downstream distances. Flame starts after a certain downstream distance at the interface of oxygen and methane. This is because at the near-field region oxygen and methane jets cannot mix with each other due to their potential core characteristics. After the potential core region jets start spreading and mix with each other and the diffusion flame forms at the interface between fuel and oxygen where mixture is stoichiometric or within flammability limit.
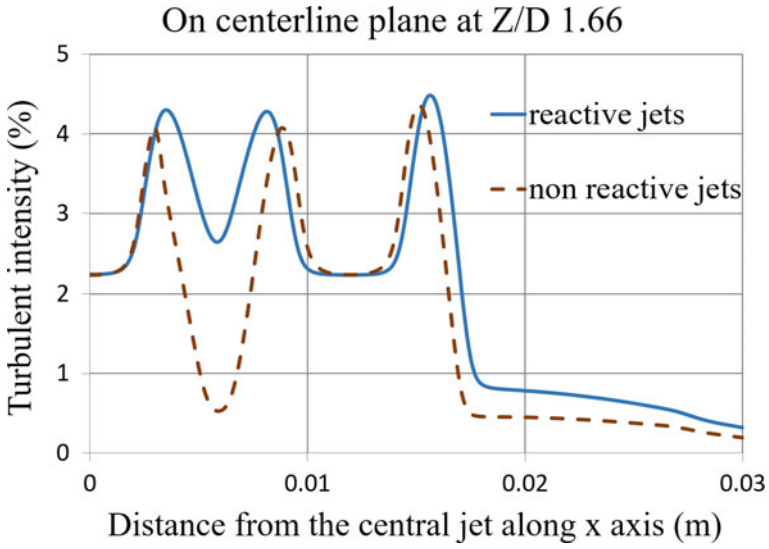
**Fig. 8** Turbulent intensity comparison for reactive and non-reactive jets at *Z/D* 8.33
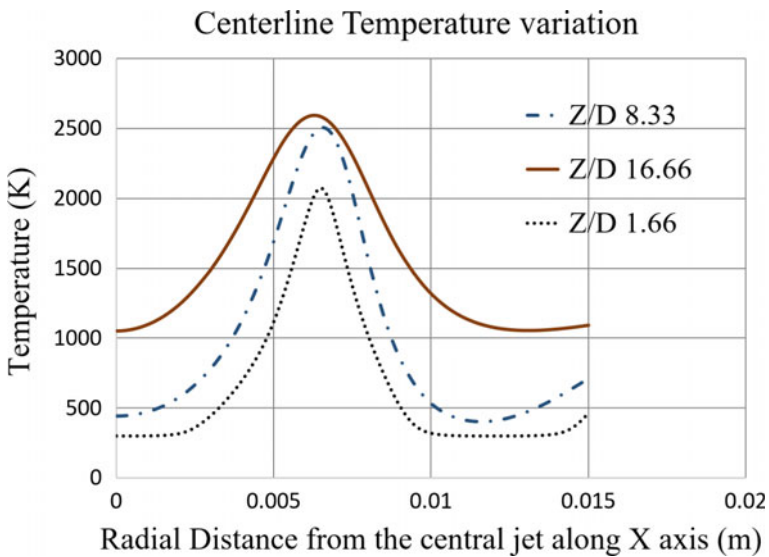


**Fig. 9** Centerline plane temperature profile distribution at different downstream distances

## Temperature distribution on Maximum temperature plane
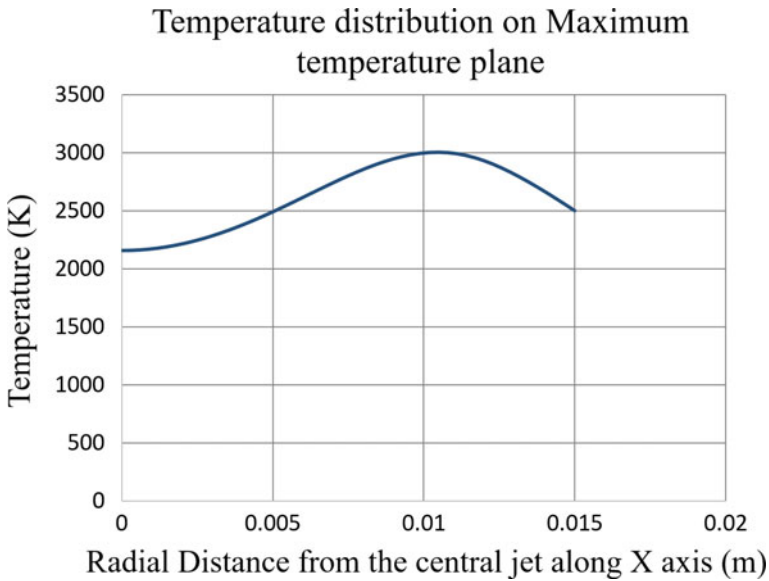


**Fig. 10** Maximum temperature profile at a plane above the centerline plane at $Y = 15$ mm

The maximum temperature value is obtained as 3005 K for oxy-methane jets (Fig. 10) which is at some offset height from the centerline plane. Since at the centerline plane oxygen and methane jets have high velocity, methane jets cannot diffuse properly inside oxygen stream to get exact stoichiometric condition.

## 4.4 Effect of Inlet Temperature on Velocity Distribution of Reactive Jets

The comparison of velocity distribution at different inlet temperatures is shown in Figs. 11 and 12.

The velocity is seen to decay at a faster rate with increase in inlet temperature. This can probably be attributed to the drop in density (with increase in temperature) which in turn leads to a lower axial momentum.

Particularly, for plotting Figs. 11 and 12, computations were carried out by realizable k-epsilon model to show that the deviation of velocity profile in realizable k-epsilon model is not significant from standard k-epsilon model in case of reactive jets.
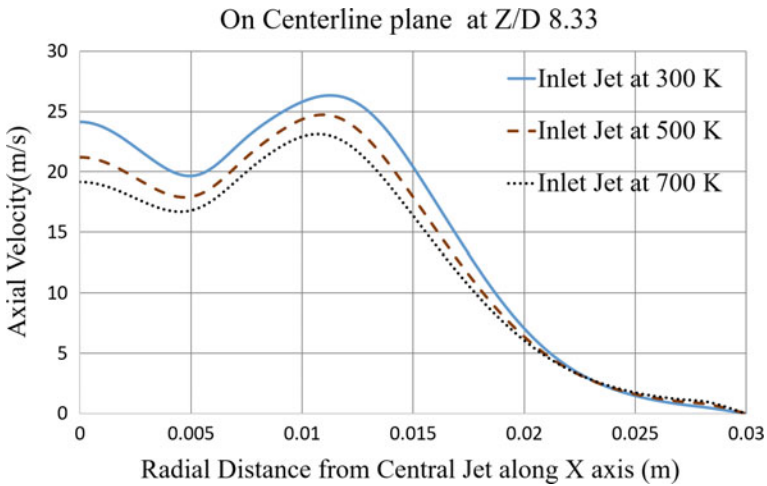
Fig. 11 Centerline plane temperature profile for different inlet temperatures at *Z/D* 8.33
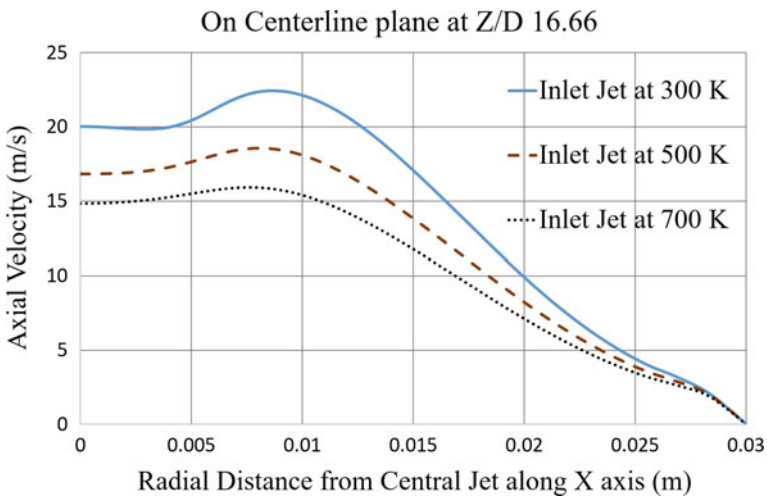


Fig. 12 Centerline plane temperature profile at different inlet temperatures at *Z/D* 16.66

## 5 Conclusion

Distributions of velocity and temperature in oxy-methane jets are analyzed to characterize the near-field mixing. A comparison of velocity profile between reactive and non-reactive jets shows that in non-reactive jets velocity decays quickly due to high turbulent fluctuations within the shear layer relative to reactive jets. The diffusive flame burns at the interface between oxygen and fuel jets where it

gets stoichiometric ratio. Maximum temperature does not exist at centerline plane but at some offset height from that plane. Increase in inlet jet temperature is found to cause a faster velocity decay of the jets.

# References

1. Leite AOP, Ferreira MA, Carvalho JA (1996) An investigation of multiple jet acetylene flames. Int Commun Heat Mass Transf 23:959–970
2. Menon R, Gollahalli SR (1988) Combustion characteristics of interacting multiple jets in cross flow. Combust Sci Technol 60:4–6
3. Kang Y-H, Wang Q-H, Lu X-F, Ji X-Y, Miao S-S, Wang H, Guo Q, He H-H, Xu J (2015) Experimental and theoretical study on the flow, mixing, and combustion characteristics of dimethyl ether, methane, and LPG jet diffusion flames. Fuel Process Technol 129:98–112
4. Sautet JC, Baushaki T, Salentey L, Labegorre B (2006) Oxy-Combustion properties of interacting separated jets. Combust Sci Technol 178:2075–2096
5. Mergheni M, Boushaki T, Sautet JC, Ben Nasrallah S (2017) Numerical study of oxy-flame characteristics in a burner with three separated jets. Appl Therm Eng 111:1–7
6. Brahim MMB, Mergheni MA, Khedher NB, Nasrallah SB, Sautet JC (2017) Numerical study of hydrogen enrichment effects in oxy-flame turbulent of three separated jets. Appl Therm Eng 113:490–498
7. Boushaki T, Mergheni MA, Sautet JC, Labegorre B (2008) Effects of inclined jets on turbulent oxy-flame characteristics in a triple jet burner. Exp Therm Fluid Sci 32:1363–1370

# Combustion Simulation of a Four Stroke Single Cylinder S.I Engine for Reducing Emissions

**Akshay Kumar Vijayendernath and Sumit Sharma**

**Abstract** The requirement to reduce the pollutants from the atmosphere is currently needed and the major part of it is caused by IC engine, so as to reduce such emissions, an analysis is being carried out in Ansys IC engine Fluent model. A design of basic combustion engine with a bowl type piston is modeled and a simulation is carried out in Ansys 17.1 Workbench. Simulation of combustion cycle from IVC to EVO is being simulated and the pollutants evolved during this process is being calculated and tabulated by varying the pressure and temperature accordingly and obtaining the best outcome possible from it. The design of valves, inlet, and outlet manifolds and a piston is created which would be further decomposed in the simulation software and chamber is created inside which the pollutants data are collected from. By providing the fuel composition that needs to be injected at 4.5° CA bTDC up to 35.5° CA aBDC as it is a gasoline direct injection engine. Spark at 11° CA bTDC is introduced to make sure whole of the fuel is burnt without any unburnt fuel which may produce soot in the system. The results show a variation when the pressure and the temperature of the intake is varied when compared to that of the intake parameter which has high pressure and temperature. The experimental value of pressure 101,325 Pa (1 atm) and temperature 300 K is taken as the initial condition values and is being used as ideal value for comparison and determining the best among the results obtained.

**Keywords** Pollutants reduction · ANSYS · IC engine Fluent · EGR · Combustion simulation

A. K. Vijayendernath (✉) · S. Sharma
Amity School of Engineering and Technology, Amity University, Noida Uttar Pradesh, India
e-mail: akshayk1504@gmail.com

# 1   Introduction

We know that nowadays transportation has become a daily need for everyone to travel which is possible by means of an IC engine. To improve the performance of the engine, various research is being carried on and mainly the research to reduce the pollution or the emissions obtained by the burning of the fuel inside the engine. So, this paper is also related to the methods on how emissions can be reduced [1].

We know that about 75% of the pollution is caused due to vehicles. So that to reduce emissions, combustion simulation of a SI engine is carried out. The model is designed as per the specification given in the manual of Kirloskar TV1 engine is being simulated in this research. Ansys 17.1 Workbench [2–6] is used for carrying out the simulation of the IC engine according to the model described and according to input parameters the output varies [3]. A solid body is decomposed in the software and required crank angle is specified for which the simulation [4–6] needs to be carried out, then decomposition process [5] is carried out to decompose the combustion chamber, spark timings are varied to obtain variable output with reduced emissions. Here, octane number [5–8] of fuel ranges from 92 to 95 [5]. The input molecular content of fuel is also altered so that emissions may reduce. Input parameters are being varied for obtaining the better output which would result in reduction of the pollutants produced due to burning of fuel and producing harmful gases, which are harmful for both living beings and engine, as this would reduce the efficiency of the engine [6] by causing various problems in the engine.

There are different methods of simulations in an IC engine Fluent model. Here, we are dealing with the combustion simulation of the engine from IVC to EVO [6]. We require the dimensions of the engine we are working on so that the piston profile and valve profile [7–9] are created and all these data are being entered into the simulation workbench. Ansys Workbench provides a high endurance in performance and simulation compared to the simulation softwares available in the market. The design of valves and manifolds (ports) provides a variety of decomposition of model for air flow and fuel that is injected [7, 9] into the system as it is a gasoline direct injection model. Computational fluid dynamics (CFD) [1–14] has emerged as the most high-rated software in the field of conducting fluid flow and create turbulence for various models by improving the mixing property of contents like gas, fuel, biogas, and many more.

# 2   Methodology

See Table 1.

**Table 1** Specifications of Kirloskar TV1 single cylinder engine

| Description | Specifications |
|---|---|
| Make and model | Kirloskar TV1 make |
| General details | Four stroke, spark ignition, constant speed vertical, water cooled, and direct injection |
| No. of cylinders | One |
| Bore * Stoke | 87.5 mm × 110 mm |
| Rated output | 5.2 kW |
| Compression ratio | 10.5:1 (standard engine) and 8:1–12:1 (VCR) |
| Swept volume | 661 cc |
| Clearance volume | 38.35 cc |
| Rated speed | 1500 RPM |
| Connecting rod length | 238 mm |
| Valve diameter | 34.2 mm |
| Maximum valve lift | 10.1 mm |

## 2.1 Specifications Considered for Design

Cylinder and piston dimensions

(a) Diameter of Cylinder = 87.5 mm
(b) Thickness of upper chamber (cylinder liner) = 5 mm
(c) Thickness of lower chamber (cylinder liner) = 2 mm
(d) Piston bowl diameter = 52 mm

Inlet and exhaust manifold dimensions

(a) Inlet port diameter = 34.2 mm
(b) Exhaust port diameter = 34.2 mm

Valve dimensions

(a) Inlet valve diameter = 34.2 mm
(b) Exhaust valve diameter = 34.2 mm
(c) Valve seat angle = 300
(d) Valve stem length = 60 mm
(e) Valve stem diameter = 5 mm (Fig. 1)

By using SolidWorks 2015, the above model is designed and exported into PARASOLID (.X_T) [8] file format so that it can be imported into the design modeler [5, 6] of Ansys Workbench IC engine Fluent model for further editing and decomposition of the design. We have also described the position of spark plug by providing the slot designed in the above model. For further simulation of the combustion chamber, this model is imported into the Ansys Workbench and is decomposed by providing the input parameters of design required as per the method to solve in IC engine Fluent (Fig. 2).
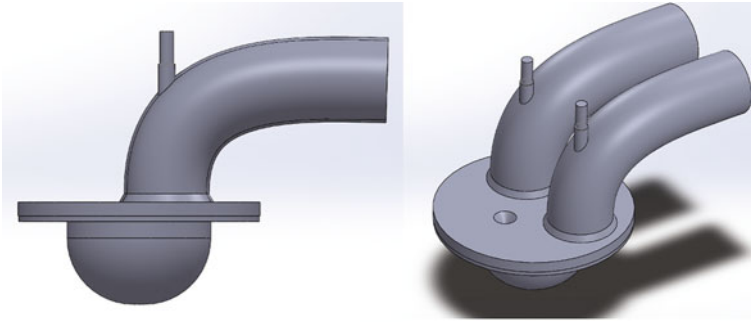
**Fig. 1** Solid port body with inlet and exhaust valves designed in SolidWorks 2015 describes the cylinder head, piston, valves (inlet and exhaust), spark plug, and inlet and exhaust manifolds

## 2.2 Meshing Operation

Various types of meshing methods are used for accuracy for the model designed. Various elements metrics like tetrahedral, hexahedral, quadrilateral, and triangle are used for meshing of the model [8, 9] described in the graph (Fig. 3). After the mesh is generated in the mechanical modeler, the errors are rectified as this may cause the simulation of the model to fail. So, once this meshing is done successfully, it is then updated into the fluent modeler where all the domains are set to fluid [11–14].

Various types of mesh methods were used for different faces and edges of the decomposed model. Mesh like body mesh, face sizing mesh, sizing mesh, inflation mesh, sweep method, and edge sizing were used to define the mesh for this decomposed model. As fine the mesh is, the accurate the result obtained in Fluent simulation.
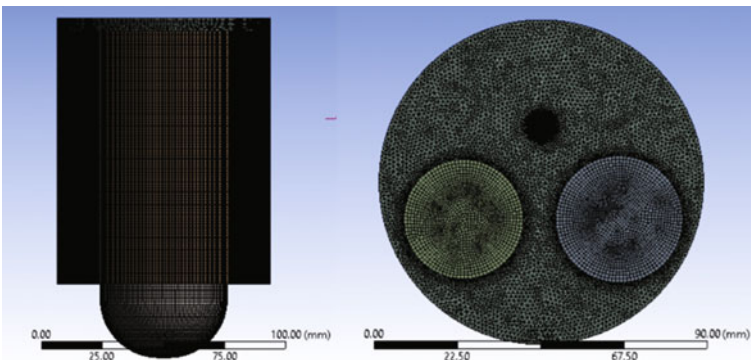


**Fig. 2** Mesh model of the decomposed chamber model
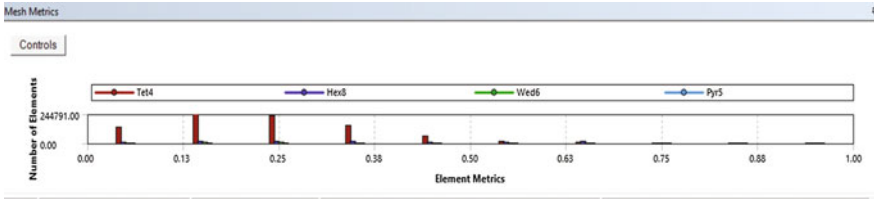
**Fig. 3** Showing the number of elements generated under particular type of mesh matrix

## 2.3 Simulation Parameters

ICE solver [1–14] is set up with the required boundary conditions and by providing crank angles for which data needs to be calculated, monitors are defined for the required values of the simulation which will be generated as a report after the final analysis. Profile of valve is adjusted according to the required lift for the valves. Lift 0.2 is provided in this case and variations are observed. The profiles of valve, piston, and timestep are given in Fig. 4. Solution summary chart describes all the profile angles and the lift provided to that particular profile.

In the boundary conditions, the inlet pressure and temperature are set to 1 atm, 300 K for initial case and later on this parameter is varied upon by keeping one parameter constant and other rising. Monitors are set to obtain temperature, pressure, and mass fraction of, $O_2$, $CO_2$, and pollutant NO.

Spark timing according to crank angle is defined as at 11° CA bTDC. Injection period is also defined according to crank angle as 4.5° CA bTDC up to 35.5° CA aBDC. We need to define the spark point and fuel point in the input manager of the solver so that the geometry will be further decomposed and simulation on which is carried on.
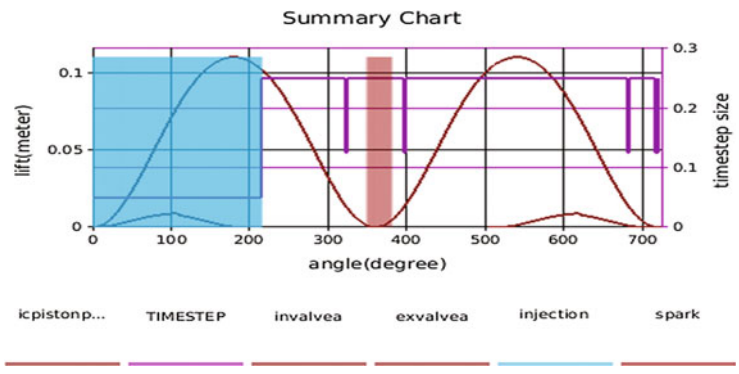


**Fig. 4** Profile chart of combustion cycle and allowable lift

# 3   Result and Discussion

The initial condition is as follows.

a. Valve lift—0.2 mm
b. Engine Speed—1500 RPM
c. Inlet pressure—101,325 Pa
d. Temperature—300 K

Fuel input parameters

a. Octane fuel rating—92–97
b. Mass fraction of $O_2$—0.232
c. Mass fraction of $H_2O$—5E−7
d. Mass fraction of $CO_2$—0.00046

So, for further variation or reduction in emissions of the pollutants, the input parameters are changed and the conditions are varied to obtain various results. This result shows that the best model to reduce the emission in these four Cases will be considered as the output of this research work. This analysis is presently carried out in Ansys 17.1 Workbench in ICE Fluent model. These values show that due to variable input values, provides appropriate solution which would help in determining the various possibilities to reduce or control the emissions.

The initial conditions were calculated using gas analyzer for practical condition and this result was compared with the simulation values so as to validate the result for actual condition or for practical condition when the engine testing is carried out. Now after the emissions are calibrated, the values are written in parts-per-million and simulation values are obtained in mass fraction of the pollutant.

The formula to convert PPM in mass fraction is:

$$\text{Mass Fraction} = \frac{\text{PPM}}{1,000,000} \times \frac{\text{molecular weight of element}}{\text{total molecular weight}} \tag{1}$$

The Pollutants NO, $CO_2$, and $O_2$ are compared with the simulation values (Fig. 5).

The following figures show the amount of $CO_2$ and Pollutant NO emission in the combustion process.

Figures 6 and 7 show the mass fraction of NO and $CO_2$ which are for initial or actual condition taken in case 1, to which the remaining values are being compared and valuated accordingly to determine the better case compared to case 1.

Figures 8 and 9 show the mass fraction of NO and $CO_2$ of case 3 which is comparatively better than that of initial or actual case and remaining cases, as this reduces the NO pollutant and $CO_2$ further more. This improves the exhaust gases and reduces pollution.

**Fig. 5** Calibrated values in gas analyzer



**Fig. 6** Mass fraction of pollutant NO for case 1
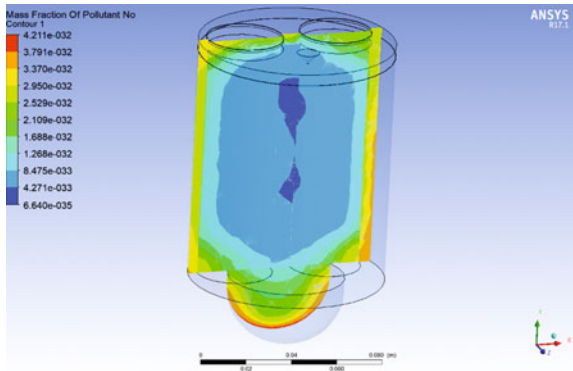


**Fig. 7** Mass fraction of $CO_2$ for case 1
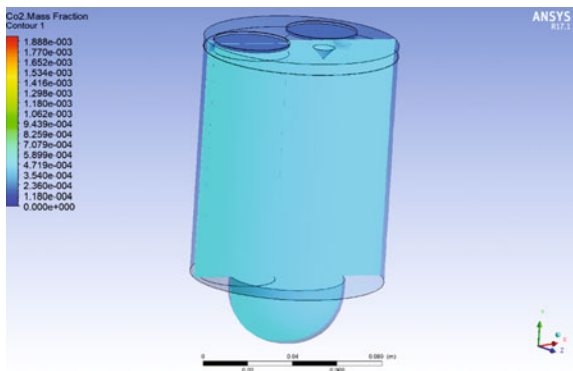


Now, this result shows an improvement in how the pollutants are being reduced with the variation in the input temperature and pressure. This change causes the fuel to burn with maximum particle dispersion which would split the molecules of the fuel further more and due to change in temperature the burning of fuel is appropriate, so as a result of this change in the parameters improves the burning capacity which would result in reduction of the pollutant NO and $CO_2$.

**Fig. 8** Mass fraction of
pollutant NO for case 3
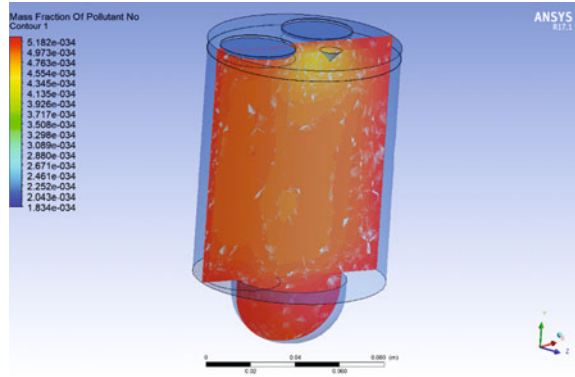


**Fig. 9** Mass fraction of $CO_2$
for case 3
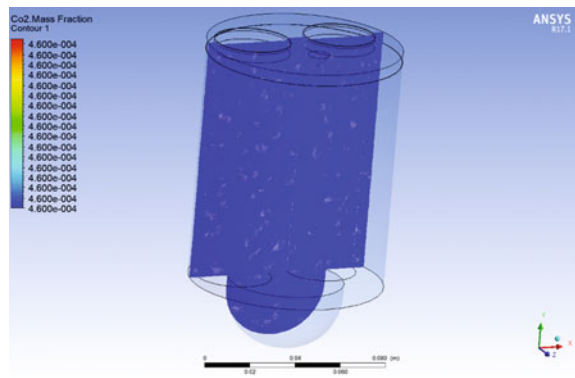


## 4    Conclusion

An approach toward analysis was carried out for simulating the combustion process
of an IC Engine to vary input parameters and obtain a result which would reduce
the pollutants releasing from the exhaust manifold. So, accordingly simulation is
carried out in Ansys Workbench under IC Engine Fluent technique and practical
emissions for initial condition were conducted using gas analyzer.

By observing the table (Tables 2 and 3) from the result section it describes the
results for different cases where the parameters are varied by keeping one parameter
constant. The comparison of actual emissions in an engine and simulation provided
little difference. We got to know that the emission of pollutants NO and $CO_2$ is less
in case 3 compared to the other cases. We observe that the mass fraction of pol-
lutants NO and $CO_2$ 5.182e−32 and 4.605e−04 are comparatively less than that of
the actual/initial condition of the parameters, i.e., in case 1.

**Table 2** Gas analyzer values converted into mass fraction

| Exhaust gases | CO | HC | $CO_2$ | $O_2$ | NO |
|---|---|---|---|---|---|
| Mass fraction | 5.7151e−05 | 1.3351e−05 | 2.312e−03 | 0.219601 | 3.432e−32 |

**Table 3** CFD results for various cases

| Parameter | Case 1 (initial/actual) | Case 2 | Case 3 | Case 4 |
|---|---|---|---|---|
| Temperature (K) | 300 | 300 | 350 | 350 |
| Pressure (Pa) | 101,325 | 121,325 | 101,325 | 121,325 |
| Mass fraction of pollutant NO | 4.211e−32 | 2.133e−34 | 5.182e−34 | 4.263e−33 |
| Mass fraction of $CO_2$ | 1.88e−03 | 1.755e−03 | 4.605e-04 | 4.718e−04 |
| Mass fraction of $O_2$ | 0.232644 | 0.23418 | 0.76854 | 0.68754 |

The results of case 3 prove that when the temperature is around 350 K and pressure around 101,325 Pa (1 atm) then the pollution can be reduced for up to 1.2% as compared to the actual condition of the combustion process. This combustion simulation if implemented in the actual condition of the functioning of the engine could help in reducing the exhaust parameter, i.e., pollutants NO and $CO_2$ from the exhaust gases which would help in enhancing the properties of engine for better performance and efficiency and mainly help in reducing the pollution.

# References

1. Abdalla MO, Nagarajan T (2015) A computational study of the actuation speed of the hydraulic cylinder under different ports' sizes and configurations. J Eng Sci Technol (JESTEC) 10(2):160–173
2. Aroussi A, Lad NM, Said MF, Adebayo D, Al-Atabi M (2010) The interaction of a cold atomised spray with a circular cylinder. J Eng Sci Technol (JESTEC) 5(3):361–372
3. Bakar RA, Ismail AR (2008) Computational visualization and simulation of diesel engines valve lift performance using CFD semin. Automot Focus Group Malays Am J Appl Sci 5 (5):532–539
4. Bhagat AR, Jibhakate YM (2012) Thermal analysis and optimization of I.C. Engine Pist Using Finite Element Method Int J Mod Eng Res 2(4):2919–2921
5. ANSYS 15.0 Help Library
6. Alkidas AC (1989) Performance and emissions achievements with an uncooled heavy duty, single cylinder diesel engine SAE 890141
7. Alkidas AC (1987) Experiments with an uncooled single cylinder open chamber diesel SAE Paper 870020
8. Mohamad Shafie NA, Muhamad Said MF (2017) Cold flow analysis on internal combustion engine with different piston bowl configurations. J Eng Sci Technol 12(4):1048–1066

 9. Payri F, Benajes J, Margot X, Gil A (2004) CFD modelling of the in-cylinder flow in direct-injection diesel engines. Comput Fluids 33(8):995–1021
10. Aita S, Tabbal A, Munck G, Montmayeur N, Takenaka Y, Aoyagi Y, Obana S (1991) Numerical simulation of swirling port-valve-cylinder flow in diesel engine, SAE Paper No 910263
11. Bianchi GM, Cantore G, Fontanesi S (2002) Turbulence modeling in CFD simulation of ICE intake flows. In: The discharge coefficient prediction, SAE Paper No 2002-01-1118
12. Priscilla, Meena P (2013) A comprehensive study on in-cylinder IC engine due to swirl flow. Int J Eng Res Technol 2(7):1156–1161
13. Barbouchi Z, Bessrour J (2009) Turbulence study in the internal combustion engine. J Eng Technol Res 1(9):194–202
14. Zhao F, Lai MC, Harrington DL (2000) Automotive spark-ignited direct-injection gasoline engines. Elsevier, Pergamon

# Applying ECFM Combustion Model to Spark Ignition Engine, Comparison with Experimental Data

A. Jeevan Sai, R. Balamurugan, Cedric Servant, Frederic Ravet and S. Ajith Kumar

**Abstract** In order to increase the efficiency of the engine and reduce emissions, right sizing plays a predominant role. Validation of turbulent combustion in engine environment using numerical tools is even more challenging. For better understanding of the thermodynamic and chemical behaviour of gas, a proper CFD models set-up should be used to represent turbulence, heat model, ignition, flame propagation and knock. This paper presents an application of ECFM (Extended Coherent Flame Model) as a combustion model coupled with ISSIM (Imposed Stretch Spark Ignition Model) to create the flame kernel due to spark. Two mechanisms named stretching and wrinkling affect the development of the flame front. Stretching is a result from turbulent velocity, and wrinkling is a result from turbulent length scale. The effect of the ECFM model constant addressing stretching and wrinkling, and the process to fix those parameters are briefed in this paper. The simulation results have showed a very good agreement with the combustion test results of RENAULT Engine in terms of pressure, heat release rate and combustion duration.

**Keywords** ECFM model · Premixed combustion · Stretching · Wrinkling factor

A. Jeevan Sai (✉) · S. A. Kumar
Department of Mechanical Engineering, Amrita Vishwa Vidyapeetham, Amritapuri,
Coimbatore, India
e-mail: jeevan2.aero@gmail.com

R. Balamurugan
Renault Nissan Technology and Business Centre India Pvt. Ltd., Chennai, India

C. Servant · F. Ravet
Renault S.A.S, Paris, France

729

# 1   Introduction

For the past one decade, one of the major problems being faced by the automobile industries in development of engines is the "Engine knock". With the advent of right-sized (downsized) engines, this problem is taking a serious toll on design time of engines. Hence, for engine designers to keep up with the demands in the automobile industry, whilst working on many prototypes, a cost-effective approach to rule out engine knock is to apply CFD approach with a proper combustion model for helping to determine a reliable design. By reducing assumptions in the estimation of combustion behaviour and thermal loads acting on the engine components, CFD tools may replace experimental investigations.

The flow in IC engines is highly turbulent and subjected to stagnation, separation, recirculation and density variation. The classical turbulence model applied for IC engine flows is $k_\varepsilon$ RNG [1]. This is a two-equation eddy viscosity model and was derived from the fundamentals governing equations for fluid flows using the Renormalization Group theory (RNG). Like all other two equations turbulent models, the model is based on homogeneous and isotropic assumptions of the turbulence structures to normalize Reynolds tensor to only one proper value.

In IC engines, during compression phase and combustion phase, the gas temperatures are comparatively higher than wall temperatures, so these flows cannot be considered isothermal at all. Then the models able to account for variations of gas properties with temperature were proposed, Angelberger [2] and Hans and Reitz [3]. Both models have been validated for a range of Reynolds and Nusselt numbers. The range of validated numbers matches with current applications in compression and combustion phases. But the Reynolds number is lower during the expansion phase and unfortunately the accuracy of models is down that affects the global accuracy of the combustion simulation.

In order to consider the initial flame kernel development due to spark, Colin [4] had developed ISSIM model with LES turbulence model. The model was turned later for RANS application. To account the stretch due to the intermittent turbulence, Meneveau and Poinsot [5] developed ITNFS model in 1991. Here in this, it considers the production of flame surface due to stretch and wrinkle and destruction by mutual annihilation of vortices. So, this term goes as the source term for the flame surface density with a constant multiplied to it. This constant is varied based on the engine speed mainly [6].

For combustion, CFM (Coherent Flame Model) model was developed by Marble [7] in 1977. Basically, this model divides the combustion chamber into two zones, fresh gas and burnt gas, separated by flame surface, and this flame surface was modelled for combustion. This model was developed for premixed combustion. CFM model is based on one flamelets combustion regime that means the flame front is a coherent structure characterized by a thickness lower than the Kolmogorov scale of the turbulence [8]. Later ECFM was developed by Colin et al. [9] in 2003.

This paper focuses on the effect of initial flame wrinkling factor and turbulent stretch on combustion at higher engine speed and the behaviour of flame when interacted by turbulent eddies.

## 2 Governing Equations

The governing equations involved in simulation are mass, momentum, energy and species transport equations [10] listed below.

$$\frac{\partial \rho}{\partial t} + \frac{\partial \rho u_i}{\partial x_i} = S \tag{1}$$

$$\frac{\partial \rho u_i}{\partial t} + \frac{\partial \rho u_i u_j}{\partial x_j} = -\frac{\partial P}{\partial x_i} + \frac{\partial \sigma_{ij}}{\partial x_j} + S_i \tag{2}$$

$$\frac{\partial \rho e}{\partial t} + \frac{\partial u_j \rho e}{\partial x_j} = -P\frac{\partial u_j}{\partial x_j} + \sigma_{ij}\frac{\partial u_i}{\partial x_j} + \frac{\partial}{\partial x_j}\left(K\frac{\partial T}{\partial x_j}\right) + \frac{\partial}{\partial x_j}\left(\rho D \sum_m h_m \frac{\partial Y_m}{\partial x_j}\right) + S \tag{3}$$

$$\frac{\partial \rho_m}{\partial t} + \frac{\partial \rho_m u_j}{\partial x_j} = \frac{\partial}{\partial x_j}\left(\rho D \frac{\partial Y_m}{\partial x_j}\right) + S_m \tag{4}$$

## 3 Combustion Model Theory

Apart from the governing equations, the equations and models used for combustion are discussed in this section. Figure 1 shows how combustion model works with sources as ISSIM (Imposed Stretch Spark Ignition Model) and ITNFS (Intermittent Turbulent Net Flame Stretch) to model the flame surface density. Then flame surface density combined with laminar flame speed is used to calculate rate of fuel consumed.

### 3.1 ECFM Model [9]

This model is an extension of Coherent Flame Model (CFM) which calculates the flame surface density, i.e., flame surface per unit volume. This model divides the combustion chamber into burnt and unburnt zones by a thin flame surface.

The flame surface density equation [10] is given by

**Fig. 1** Working principle of combustion model
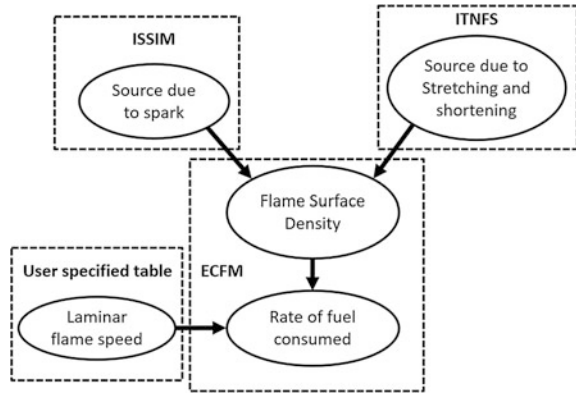


$$\frac{\partial \Sigma}{\partial t} + \frac{\partial u_i \Sigma}{\partial x_i} = \frac{\partial}{\partial x_i}\left(\left(\frac{\mu}{Sc} + \frac{\mu_t}{Sc_t}\right)\frac{\partial \Sigma/\bar{\rho}}{\partial x_i}\right) + (P_1 + P_2 + P_3)\Sigma - D + P_k \quad (5)$$

where $\mu$ and $\mu_t$ are the laminar and the turbulent viscosities, respectively, and $Sc$ and $Sc_t$ are the laminar and the turbulent Schmidt's numbers.

$P_1 = \alpha K_t \rightarrow$ flame surface production by turbulent stretch,
where $K_t \rightarrow$ ITNFS stretch and $\alpha = 1.6$(default)
$P_2 = \frac{2}{3}\frac{\partial u_i}{\partial x_i} \rightarrow$ production by the mean flow dilatation;
$P_3 = \frac{2}{3}S_l\frac{1-c}{c}\Sigma \rightarrow$ flame thermal expansion and curvature;
$D = \beta\bar{S}_l\frac{\sum^2}{1-\bar{c}} \rightarrow$ destruction term, where $\beta = 1$
$P_k \rightarrow$ source term due to ignition by spark plug.

Then the rate of fuel consumption $\left(\bar{\omega}_F^u\right)$ is given by the product of flame surface density $(\Sigma)$ and the local speed at which it consumes the mixture $\left(\bar{S}_l\right)$ [7].

$$\bar{\omega}_F^u = \bar{\rho}^u|_u * Y_F^u\big|_u * \bar{S}_l * \Sigma \quad (6)$$

### 3.2 ISSIM Model [4]

Basically, there are two circuits for ignition system. Primary circuit which is connected to the battery and the secondary circuit connected to spark plug. In ISSIM model, it considers only the secondary circuit and the energy induced in this is given as input. There are three stages during ignition, i.e. breakdown, arc phase and glow phase. The total energy required for spark plug (in three phases) to initiate combustion is given by

$$E_{ign} = 0.6E_{bd} + \int\limits_{tspk}^{t} V_{gc} i_s \, dt \tag{7}$$

where $E_{bd}$ is breakdown energy, $V_{gc}$ is the gas column voltage and $i_s$ is current in secondary circuit.

After the three stages of ignition, a fully developed flame kernel is produced. The radius of the flame kernel is given by

$$r_b^{ign} = \left( \frac{3}{4\pi} \int \bar{c}_{ign} \, dV \right) \tag{8}$$

where $\bar{c}_{ign}$ is the target volume fraction of gas burned. So, the flame surface density due to ignition is given by

$$\sum_{ign} = C_{surf} \frac{3\bar{c}}{r_b^{ign}} \tag{9}$$

where $C_{surf}$ is an initial flame wrinkling factor. As it is well known that the flame kernel produced at the spark timing is assumed spherical, but in actual condition the flame kernel surface is wrinkled due to turbulence. And it requires a costlier equipment to measure the wrinkling of flame kernel during the spark experimentally. So, in order to produce the actual wrinkling same as that of experimental this $C_{surf}$ should be tuned.

The source term due to the spark is given by

$$\bar{\omega}_{\sum}^{ign} = \max \left( \left( \sum_{ign} - \sum_{\bar{c}} \right) / dt, 0 \right) \tag{10}$$

## 3.3　ITNFS Model [5]

Basically, this model is applied to the flow containing flamelet reactions where main parameters for combustion due to turbulence is flame stretch and flame wrinkle. This mainly depends on the turbulent eddy scales and vortices through which the flame front is interacting. So, the variation of surface due to turbulence is given by this model.

This model accounts the production of flame surface due to interaction of flame front with intermittent turbulent eddies and destruction due to high eddy velocity which leads to mutual annihilation of flame surface. And the eddies length scale smaller than laminar flame thickness will have negligible effect on stretching even at higher strain rate. The strain created due to turbulence not only affects the increase in the flame surface area but also determines the reactant consumption per unit of flame surface.

There are three phases of vortex interacting with flame surface. The first one is an induction phase in which the vortex pair enters into influence zone. The second phase is the vortex pair starts stretching the flame which increases the total reaction rate with time. The third phase is the flame fronts interact and merge, leading to flame surface consumption by mutual annihilation.

A curve fitting method is used to calculate source term due to flame stretch which is given by the equation [10]

$$\frac{K_t}{\varepsilon/k} = \text{ITNFS}_{\text{factor}} * f\left(\frac{u'}{S_L}, \frac{L}{l_F}\right) \tag{11}$$

The function $f\left(\frac{u'}{S_L}, \frac{L}{l_F}\right)$ has been validated by DNS in flamelet combustion regime [5].

## 4 Experimental Data

The experiment was carried out in a three-cylinder engine with pent-roof cylinder head and bowl piston. Table 1 lists the engine specifications and operating point.

## 5 Numerical Methodology

See Table 2.

**Table 1** Engine specifications and operating point

| Engine specifications | | Operating point | |
|---|---|---|---|
| Cylinders | 3 | Engine speed | 5000 rpm |
| Bore | 72.2 mm | Equivalence ratio | 1.1 |
| Stroke | 81.3 mm | Fuel | Surrogate fuel |
| Connecting rod | 128.4 mm | Spark timing | $4^0$ bTDC |
| Displacement | 1000 m$^3$ | Compression ratio | 9.5 |

**Table 2** Tools used

| | |
|---|---|
| 1D Simulation(TPA) | GT Suite |
| 3D Simulation | Converge |

### 5.1  1D Simulation

The objective of the 1D simulation is to extract boundary conditions. A 1D TPA (Three Pressure Analysis) provided by GT Suite software is used. The inputs provided to this software are measured intake, exhaust and in-cylinder pressure based on which it calculates fuel burn rate. This approach requires minimum modelling of engine components with valves and ports and removes uncertainties in intake and exhaust system geometry and combustion modelling, allowing more accurate estimation of cylinder conditions.

The intake and exhaust boundaries are specified with experimental pressure, temperature and air–fuel mixture composition are imposed. The apparent burn rate is calculated before cycle starts using the trapped conditions at IVC and the heat transfer of the previous cycle and imposed to the current cycle for combustion prediction. The cycles repeat until steady state convergence is reached. The engine compression ratio is an important input to the TPA model in order to simulate cylinder pressure traces that match well with the measured cylinder pressure data.

### 5.2  Internal Aerodynamics

The objective of internal aerodynamics is to match the in-cylinder pressure and mass after IVC with the experimental data. Figure 2 represents the flow domain for internal aerodynamics.

Here this engine uses the turbocharger, so the inflow and exhaust temperature and pressure and the valve lift profiles are taken from experimental. Rest all the boundary conditions are taken from 1D. As it is well known that in transient case, the solution depends on the initial conditions. So, the initial conditions are taken from 1D.

When it comes to solver, the software uses the AMR (Adaptive mesh refinement) for refinement of mesh, so a base mesh of 4 mm is given and a maximum refinement of 0.125 mm is maintained during the spark timing. Here variable time step is used, which calculates based on the CFL number provided. The algorithm used pressure-velocity coupling is PISO. The SOR method is used to solve the



**Fig. 2** 2D view of CFD domain for internal aerodynamics
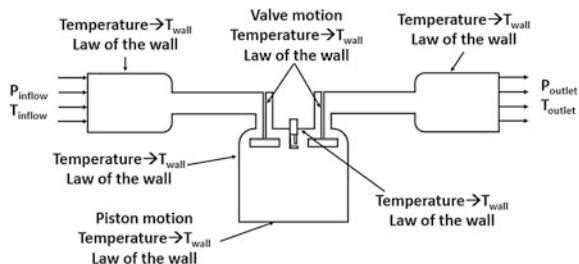
**Fig. 3** 2D view of CFD domain for combustion
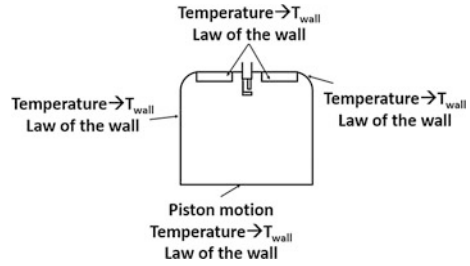


equations. The convective schemes used are first-order and second-order upwind scheme. Here the software provides an advantage of providing the tolerance and based on the tolerance the shifting of schemes takes place. And a $y+$ value of 30–100 is maintained because the RNG k-epsilon turbulence model considers only the log layer which starts from $y+$ value 30. Finally, Angelberger model is chosen as a heat model.

After applying all the boundary conditions, one cycle simulation is carried from 300 CA (before IVO) to 650 CA (few degrees after IVC). And a map file is extracted at the end of the simulation, which is used as an input for combustion.

## 5.3 Combustion

The objective of combustion simulation separately is to tune the parameters with lesser computational time and effort. The CFD domain for combustion simulation is shown in Fig. 3.

Here the simulation involves compression and combustion phase only. So, the valves are always closed. Rest all the other boundary conditions are specified the same as internal aerodynamics. Additionally, modelling of combustion is involved (ECFM-ISSIM), and a user-specified table is given as input to calculate laminar flame speed.

At the end of the aerodynamic simulation, the map file is extracted which contains the conditions of all the variables ($P$, $T$, velocity, species, turbulence variables like $k$, epsilon, and ECFM tracers) inside the combustion chamber and is given as an initial condition for in-cylinder combustion. Then the combustion simulation starts from 650 to 800 CA, i.e., till the end of the combustion.

## 6 Results and Discussion

The simulation has done from 300 to 650 CA to have a developed in-cylinder turbulence, tumble and other flow variables for combustion. At the end of simulation, the in-cylinder pressure, temperature and trapped mass are compared with

the experimental data. And it was found that in-cylinder mass is matching with 0.4% difference, in-cylinder temperature with 8 K difference and pressure with 0.6% difference.

To control the behaviour of combustion numerically, two constants are calibrated, both these constants show the effect due to turbulence. First, effect of two parameters on combustion behaviour is explained and then calibration of these parameters to validate the combustion is shown.

## 6.1　Effect of Initial Flame Wrinkling Factor ($C_{surf}$)

When the spark is ignited, the flame kernel produced will have wrinkling on the surface due to induced turbulence in the cylinder. $C_{surf}$ has dominating effect on kernel growth up to CA5–CA10 depending on the fuel used. The continuous line in Fig. 4 shows effect of $C_{surf}$ on initial flame kernel surface. $C_{surf} = 1$ shows the laminar flame and $C_{surf} > 1$ shows the turbulent flame. It is evident from Eq. (9) that as $C_{surf}$ increases, the flame surface area also increases, as the flame surface area increases the rate of combustion also increases (from Eq. 6).

The scale of the wrinkles is typically about 2 mm at engine speed 1000–2000 rev/min [11]. Therefore, it is evident that for 5000 rpm, value of $C_{surf}$ has to be more than 2 in order to achieve a turbulent flame brush for flame propagation. Initial Flame wrinkling is responsible for transition of a self-sustained flame kernel (where $Q_{generated} > Q_{loss}$) into a stable laminar flame. Due to the effective thickness of this high $C_{surf}$ flame kernel, the average distance between the region ahead of the kernel where only unburned mixture exists and the region behind the flame, where only burned mixture exists is higher as compared to lower $C_{surf}$ flame kernel. This thick flame kernel entraps higher temperature from phase 3 of flame kernel formation, due to higher diffusion rate and lower radiation losses. This high-temperature flame kernel, when diffuses with unburnt mixture, diffusion rate increases drastically. This increased diffusion rate aggravates the reaction rate. Therefore, it is evident that, at higher engine speed, the dominant flame speed for combustion is turbulent. Therefore, in order to achieve extended turbulent flame duration, $C_{surf}$ has been increased.
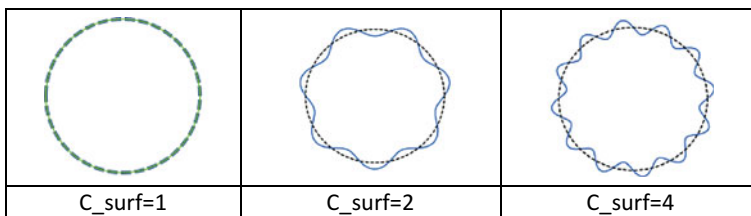


| C_surf=1 | C_surf=2 | C_surf=4 |

**Fig. 4**　Variation of initial flame kernel surface with $C_{surf}$

## 6.2   Effect of Stretching Factor Constant (α)

Stretching factor constant (α) is the constant which is multiplied to $K_t$ which is modelled from ITNFS. Altering flame wrinkling ($C_{surf}$) will alter the flame stretch and curvature, therefore, in order to neutralize the over and under compensation of flame stretch on combustion, alpha has been modified. The equation given below shows the relation of flame wrinkling with turbulent stretch [12].

$$\frac{1}{\Sigma}\frac{d\Sigma}{dt} = \Gamma\left(\frac{u'}{S_L^0}, \frac{L_T}{\delta_L}\right)\frac{u'}{L_T}\left(\frac{\Sigma_{equ} - \Sigma}{\Sigma_{equ} - 1}\right) - \frac{2}{R_f}\frac{\rho_u}{\rho_b}(\Sigma - 1)S_L^0 \qquad (12)$$

It can be observed from Eq. (12) that wrinkling (Left-hand side) is directly proportional to turbulent stretch (first term on right-hand side). Due to high surface averaged tangential strain rate, reaction rate will be high. Due to increased strain, decomposition of fuel into its simpler compound is faster; these smaller $C_xH_y$ need less energy to burn resulting in faster combustion in thick flame brush. As the concave stretch increases, the density at the flame surface decreases which creates a density gradient, then the diffusion of mass takes place towards the flame surface.

Due to high stretching high turbulence at 5000 rpm in the engine, highly stretched flame might be transformed into small pockets of flame with different densities and temperature. Since quenching of some of the flame pockets is not taken into account, alpha needs to be calibrated to compensate over temperature, HRR and pressure.

For higher engine speed, due to increased $C_{surf}$ resulting in increased flame surface density and flame structure, alpha should be decreased. Over prediction of these parameters due to flame structure alteration needs to be studied further.

## 6.3   Validation

The above two parameters are varied to validate combustion. $C_{surf}$ is varied to match CA10 and the deviation of 1.1 is achieved (see Table 3). Simultaneously varying alpha which has the impact on CA50 and CA90 and the deviation of 0.8 and 3.5, respectively, are achieved. The final results of the calibration are shown in Table 3. The final values after the calibration of $C_{surf}$ and α are 5 and 0.67, respectively.

Table 3 shows the deviation of Simulation HRR, Pressure and Temperature and combustion progress from experimental.

As the $C_{surf}$ has been increased to 5 to match the ignition delay and to compensate this effect on later combustion stage, alpha is reduced to 0.67, so the HRR max. CA is shifted by 1.3 CA (see Fig. 5a) and the Pmax CA is shifted by 0.5 CA (see Fig. 5b). As it is apparent heat release rate, due to the effect of heat model (over prediction of heat transfer) in the expansion phase, the deviation from the

**Table 3** Simulation results of $C_{surf} = 5$ and $\alpha = 0.67$

|  | Exp | Sim |  | Exp | Sim |
|---|---|---|---|---|---|
| HRR max CA | 743.5 | 742 | CA10 | 17.4 | 18.5 |
| HRR max(J/°) | 84.82 | 84.82 | CA50 | 27.4 | 28.2 |
| Pmax CA | 749.5 | 749 | CA90 | 42.1 | 38.6 |
| Pmax (MPa) | 7.12 | 7.08 | CA10-75 | 16.8 | 15.0 |
| Tmax (K) | 2468 | 2478 | CA10-90 | 24.8 | 20.1 |

experimental data is observed and the temperature is slightly under predicted (see Fig. 5c).

As the fuel is premixed (homogenous), the mass fraction of iso-octane is same everywhere before the spark (see Fig. 6) and after the spark as the fuel reacts with oxidizer, the fuel mass fraction reduces and the $CO_2$ mass fraction increases as the combustion propagates. As the time step is very small, the diffusion of temperature is clearly observed. As the flame propagates the temperature of unburnt gases near to flame also increases, due to which the breakdown of fuel into its sub-components takes place. This breakdown leads to reduction of mass fraction in front of the flame surface.
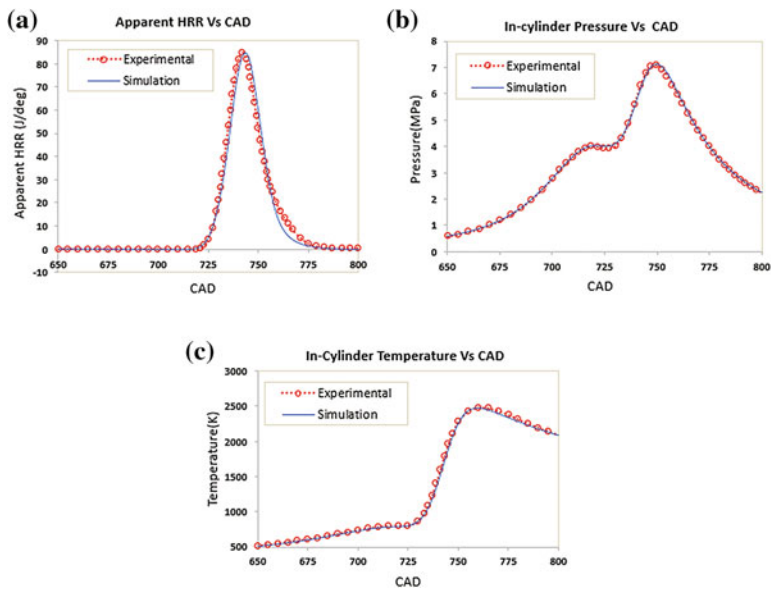


**Fig. 5** Comparison of simulation **a** Apparent HRR, **b** pressure, **c** temperature with experimental data
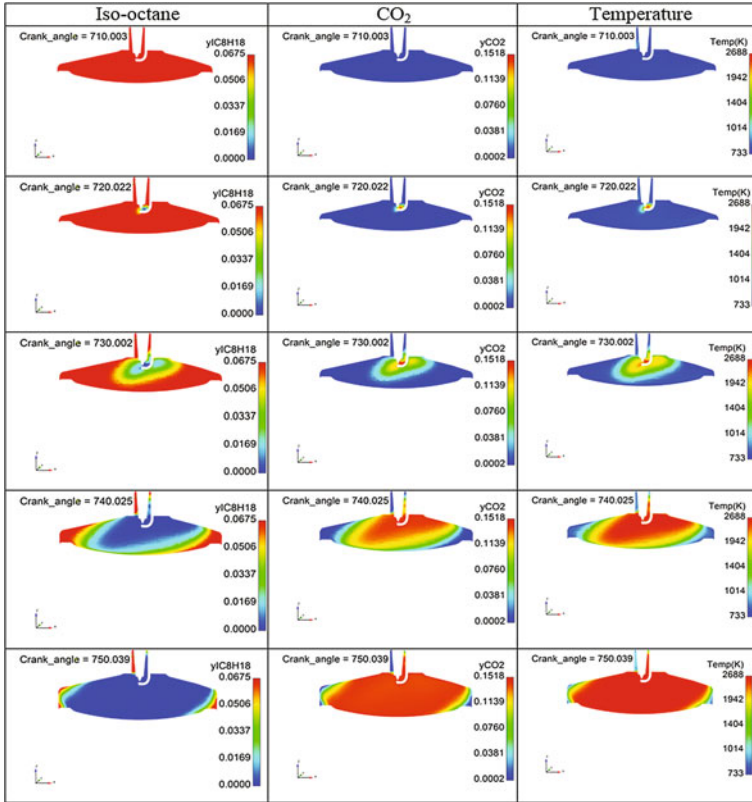
**Fig. 6** Variation of fuel mass fraction, $CO_2$ mass fraction and temperature with CAD on a sectional view of combustion chamber

## 7 Conclusion

From the simulations, it has been observed that

- The actual ignition delay can be achieved by adjusting $C_{surf}$ and increasing $C_{surf}$ actually increases the flame kernel surface area due to wrinkling. So, this shows an effect on the later stages of combustion.
- To control later stages of combustion mostly after CA10, the alpha (flame stretch factor) should be decreased/increased which corrects the decrease/ increase in flame surface due to stretch.
- It should be understood that these constants vary based on the engine geometry, rpm, fuel used, equivalence ratio, compression ratio because these parameters mainly depend on turbulence and fuel behaviour inside the combustion chamber.

Finally, the ECFM combustion results by tuning of $C_{surf}$ and alpha shows good agreement with the experimental data in terms of pressure, temperature and heat release rate and the prediction of emissions is open to the future work.

# References

1. Han Z, Reitz RD (1995) Turbulence modeling of internal combustion engines using RNG κ-ε models. Combust Sci Technol 106(4):267–295
2. Angelberger C, Poinsot T, Delhay B (1997) Improving near-wall combustion and wall heat transfer modeling in SI engine computations. SAE Technical Paper 972881
3. Han Z, Reitz RD (1997) A temperature wall function formulation for variable density turbulent flows with application to engine convective heat transfer modeling. Int J Heat Mass Transf 40(3):613–625
4. Colin O, Truffin K (2011) A spark ignition model for large eddy simulation based on an FSD transport equation (ISSIM-LES). Combust Inst 33:3097–3104
5. Meneveau C, Poinsot T (1991) Stretching and quenching of flamelets in premixed turbulent combustion. Combust Flame 86:311–332
6. Chevillard S, Colin O, Bohbot J, Wang M (2017) Advanced methodology to investigate knock for downsized gasoline direct injection engine using 3D RANS simulations. SAE Technical Paper 2017-01-0579
7. Marble FE, Broadwell JE (1977) The coherent flame model for turbulent chemical reactions. Purdue University Technical Report TRW
8. Peters N (1992) A spectral closure for premixed turbulent combustion in flamelet regimes. J Fluids Mech 242:611–629
9. Colin O, Benkenida A, Angelberger C (2003) 3D modeling of mixing, ignition and combustion phenomena in highly stratified gasoline engines. Oil Gas Sci Technol Rev IFP 58 (1):47–62
10. Converge Manual V2.4 (2017) Convergent Science Published
11. Heywood JB (2017) Internal combustion engine fundamentals, 16th Reprint. McGraw Hill Publication, India
12. Demesoukas S, Brequigny P, Caillol C, Halter F, Mounaïm-Rousselle C (2016) 0D modeling aspects of flame stretch in spark ignition engines and comparison with experimental results. Appl Energy 179:401–412

# Numerical Investigation of Scheffler Concentrator Receiver for Steam Generation Using Phase Change Material

**Shubham**, **Rahul Kumar** and **Soumen Mandal**

**Abstract** This study is about the numerical modelling of concentrated solar power (CSP) system using a Scheffler dish solar concentrator which can be used for steam generation and its applications. Water is used for direct steam generation from the receiver. In the proposed model, phase change material (PCM) is present in between the inner and the outer cylinder of the copper receiver. A binary mixture commonly known as solar salt (60% $NaNO_3$-40% $KNO_3$) is used as PCM for analysis. It helps to get rid of fluctuations due to sudden weather changes. Scheffler solar concentrator of 16 $m^2$ area with fixed focus is used to concentrate the solar radiations to the receiver. The purpose of this study is to see the effects of temperature distribution with and without the PCM and also the rate of steam generation for the system numerically using Finite Element Method. Numerical analysis was performed using Transient thermal analysis module in ANSYS Workbench. Results showed that the proposed design of the cylindrical receiver containing the solar salt enhances the performance of the system.

**Keywords** Concentrated solar power · Scheffler solar concentrator · Direct steam generation · Phase change material

## 1 Introduction

The world in the twenty-first century is trying to develop technology which can satisfy their growing energy needs through clean energy. This is mainly done to reduce the massive dependence on the conventional energy resources which is a major source of pollution in the whole world. This inspires for new innovations as there is dearth of better technologies with higher efficiencies. Solar energy can serve a broad range of our energy need and can be easily implemented for different applications including electricity production [1–3]. Thermal energy storage system

Shubham (✉) · R. Kumar · S. Mandal
Birla Institute of Technology, Mesra (Patna Campus), Patna 800014, Bihar, India
e-mail: adshubh51@gmail.com

743

is an important feature to make an efficient use of solar energy due to the inherent intermittency of this energy source. The thermal energy storage systems allow making use of thermal energy accumulated in hours of high solar radiation, reducing the unbalance between supply and demand of energy [4, 5].

Scheffler concentrator or collector is used to concentrate solar rays to the cylindrical receiver positioned at the focus. Cylindrical receiver contains the fluid as well as solar salt which is heated due to incident concentrated solar flux. Reflector of solar concentrator has efficiency in range of 85–90% while overall efficiency in range of 30–45%. The coefficient of absorption of the receiver decides the amount of heat absorbed. The losses due to radiation and conduction start to rise with temperature of receiver; however, the convective losses are dependent on many variables including wind flow of surface of the receiver. Many efforts are being made to study losses in order to improve efficiency of receiver and thereby total system [6–10].

To serve the purpose of thermal storage, nitrate salts are selected because of their favorable properties as compared with other options. These nitrate salts have low corrosion rates with common piping materials and are thermally stable in the upper-temperature range as required by steam rankine cycle. They also have low vapor pressure and are widely available as well as relatively inexpensive as shown in Table 1 [11].

Solar salt was selected among the nitrate salts for the experiment purpose as the upper operating temperature of it is higher (600 °C) as compared to others. Solar salt is one of the lowest cost nitrate salt. The only disadvantage is the high freezing point of 220 °C. Hitec Salt offers a lower freezing point of about 140 °C but at a higher cost [12–14].

**Table 1** Characteristics of the nitrate salts and Therminol VP-1

| Property | Solar salt | Hitec | Hitec XL (Calcium nitrate salt) | LiNO$_3$ mixture | Therminol VP-1 |
|---|---|---|---|---|---|
| Composition (%) | | | | | Biphenyl/diphenyl oxide |
| NaNO$_3$ | 60 | 7 | 7 | | |
| KNO$_3$ | 40 | 53 | 45 | | |
| NaNO$_2$ | | 40 | | | |
| Ca(NO$_3$)$_2$ | | | 48 | | |
| Freezing point (°C) | 220 | 142 | 120 | 120 | 13 |
| Upper temperature (°C) | 600 | 535 | 500 | 550 | 400 |
| Density @ 300 °C (kg/m$^3$) | 1899 | 1640 | 1992 | | 815 |
| Viscosity @ 300 °C (cp) | 3.26 | 3.16 | 6.37 | | 0.2 |
| Heat capacity @ 300 °C (J/kg-k) | 1495 | 1560 | 1447 | | 2319 |

## 2   Modeling and Transient Thermal Analysis

A geometrical model is proposed of a cylindrical receiver for Scheffler solar collector. The solar radiation falling on the Scheffler concentrator is focused on to the cylindrical receiver. The concentrated solar radiation is then transmitted to the working fluid as well as the solar salt which acts as the phase change material and stores the thermal energy as the latent heat. The receiver is made of copper and painted by black color to reduce the heat losses to the surroundings. The cylindrical receiver is divided into sections as shown in Fig. 1. The inner cylinder will contain the working fluid water and the outer cylinder will contain the solar salt.

The analysis was carried out on two cases. The first case in which the simulation was carried out on a receiver that does not contain solar salt. In the second case, the simulation was carried out with receiver containing the solar salt.

### 2.1   Pre-processing: Creating Mathematical Model and Domain

There are three basic modes of heat transfer used in the numerical analysis:

**Conduction**—Internal energy exchange between one body in perfect contact with another or from one part of a body to another part due to temperature gradient. Conduction heat transfer defined by Fourier's Law of conduction:

$$q = -K_{nn} \frac{\partial T}{\partial n} = \text{heat flow rate per unit area in direction } n \tag{1}$$

where $K_{nn}$ = thermal conductivity in direction $n$, $T$ = Temperature, $\frac{\partial T}{\partial n}$ = thermal gradient in direction $n$, Negative sign indicates that heat flows in the opposite direction of the gradient.



**Fig. 1** **a** Front view of the cylindrical receiver. **b** Side view of the cylindrical receiver
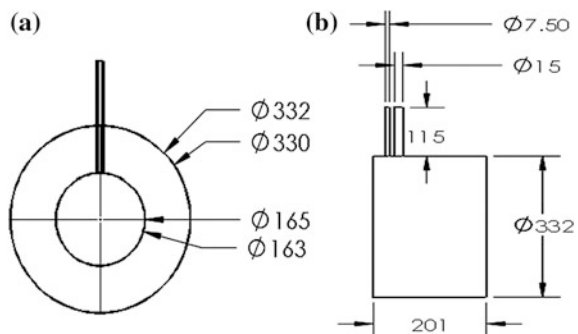
**Convection**—Heat transfer is defined by Newton's Law of Cooling:

$$q = h(T_\text{s} - T_\text{B}) = \text{heat flow rate per unit area between surface and fluid} \qquad (2)$$

where $h$ = convective film coefficient, $T_\text{s}$ = surface temperature, $T_\text{B}$ = bulk fluid temperature.

**Radiation**—Radiation heat transfer derived from the Stefan-Boltzmann Law:

$$Q = \sigma \varepsilon A_i F_{ij}\left(T_i^4 - T_j^4\right) = \text{heat flow rate from surface } i \text{ to surface } j \qquad (3)$$

where $\sigma$ = Stefan-Boltzmann constant, $\varepsilon$ = emissivity, $A_i$ = Area of surface $i$, $T_i$ = absolute temperature of surface $i$, $T_j$ = absolute temperature of surface $j$.

**First Law of Thermodynamics**: Conservation of energy requires that the net change of the energy of a system is always equal to the net transfer of energy across the system boundary as heat and work. Conservation of energy, for a small time increment, can be expressed in equation form as:

$$E_\text{stored} + E_\text{in} + E_\text{out} + E_\text{generated} = 0 \qquad (4)$$

When one applies this to a differential volume, the governing differential equation for heat conduction is obtained. The differential equation expressing the above mentioned thermal equilibrium is

$$\frac{\partial}{\partial x}\left(K_{xx}\frac{\partial T}{\partial x}\right) + \frac{\partial}{\partial y}\left(K_{yy}\frac{\partial T}{\partial y}\right) + \frac{\partial}{\partial z}\left(K_{zz}\frac{\partial T}{\partial z}\right) + \dddot{q} = 0 \qquad (5)$$

where $\dddot{q}$ is internal heat generation/volume, $K$ is the thermal conductivity, $T$ is temperature.

**Transient Thermal Analysis Governing Equation**: A non-linear transient thermal analysis is done for the proposed model. The cause of analysis to be non-linear is temperature dependent material properties. It is transient analysis as the load may vary with time. Equation used for transient analysis is expressed as

$$[C]\{\dot{T}\} + [K]\{T\} = \{Q\} \qquad (6)$$

where $[C]\{\dot{T}\}$ is the heat storage term added to the equation expressing thermal equilibrium.

Heat Storage Term = (Specific Heat Matrix) × (Time Derivative of Temperature)

and,

$$[K]\{T\} = \{Q\} \tag{7}$$

is the finite element equation expressing thermal equilibrium from the First law of thermodynamics.

Equation used for transient analysis is expressed as

$$[C]\{\dot{T}\} + [K]\{T\} = \{Q(t)\} \tag{8}$$

where $\{Q(t)\}$ is the load varying with time.

And in case of non-linear transient analysis,

$$[C(T)]\{\dot{T}\} + [K(T)]\{T\} = \{Q(T,t)\} \tag{9}$$

Here, all the properties become temperature dependent.

A 3D mesh model was prepared in software and the materials were assigned to the corresponding geometrical parts as shown in Fig. 2a, b and Table 2.
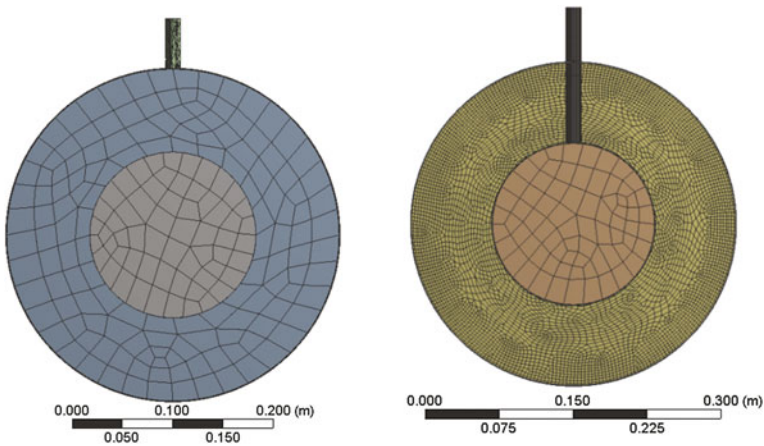


**Fig. 2 a** Meshing models for cylindrical receiver with solar salt. **b**. Meshing models for cylindrical receiver without solar salt

**Table 2** Meshing properties

| Receiver type | Meshing properties | |
| --- | --- | --- |
| | Number of meshing elements | Number of meshing nodes |
| Receiver with PCM | 32,338 | 170,210 |
| Receiver without PCM | 110,635 | 772,755 |

## 2.2  Solver

Analysis involving phase change which can be approached using ANSYS Mechanical products are:

(a)  The freezing of a liquid determined by solidus temperature of material.
(b)  The melting of a solid determined by the liquidus temperature of material.

A phase change analysis must be solved as a thermal transient analysis. Phase change analysis was done considering the following points:

– A small initial and minimum time step size was used.
– The "Line Search" solution option is used in the phase change analysis.
– The material property of solar salt was not available in Workbench Mechanical Engineering Data. The property was added to the Engineering Data sources.

Figure 3 shows the enthalpy of the solar salt which was used as the input data in the software for the transient thermal analysis. It can be clearly seen that at 220 °C there is a sudden growth in enthalpy which is because of the latent heat.

Table 3 contains the list of properties of the receiver material and the solar salt which was given as input in the software.
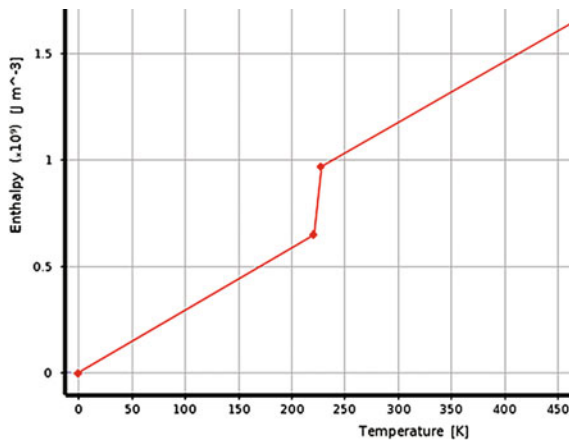


**Fig. 3**  Enthalpy input for the solar salt

**Table 3**  Properties of receiver and PCM

| Properties | Receiver | PCM |
|---|---|---|
| Material | Copper | NaNo$_3$:KNo$_3$ (60:40 by weight) |
| Melting point (°C) | 1084.62 | 220 |
| Specific heat (kJ/kg-k) | 0.385 | 1.6 |
| Thermal conductivity @ 20 °C (W/(m k)) | 401 | 30.51 |
| Mass (kg) | 4.42 | 28.22 |

## 2.3 Post-processing

In post-processing, the output of simulations from solver was converted to graphics form. In both cases of simulation, namely receiver with PCM and receiver without PCM, results are in form of graphics for the temperature distribution on the surface of receiver. The volume fraction of water gave the value of mass flow rate which is calculated by mass of water evaporated divided by time taken by it.

## 3 Result and Discussions

The initial quantity of water is 4000 mL which is nearly about that of the volume of the cylinder of the receiver containing water. Figures 4 and 5 show the distribution of temperature on the outer surface of cylindrical receiver with and without PCM.

From Figs. 4 and 5, we can clearly see that the receiver containing the solar salt temperature reaches a higher maximum temperature as compared to that of the receiver not containing the solar salt.

Figure 6a shows the difference in temperature that occurs on the surface of receiver when the solar salt is used and when it is without the solar salt when the concentrator is focused on the receiver. Hence, we can see the clear difference in the growth of temperature in both conditions that the receiver without the solar salt achieves a temperature lower than that of receiver with a solar salt.

Also, Fig. 6b shows the difference in temperature that occurs on the surface of receiver when the solar salt is used and when it is without the solar salt when the concentrator is defocused on the receiver. This shows the difference in cooling rate of receiver in both conditions of the receiver.



**Fig. 4** **a** Side view of the receiver without PCM. **b** Front view of the receiver without PCM

**Fig. 5** **a** Side view of the receiver with PCM. **b** Front view of the receiver with PCM
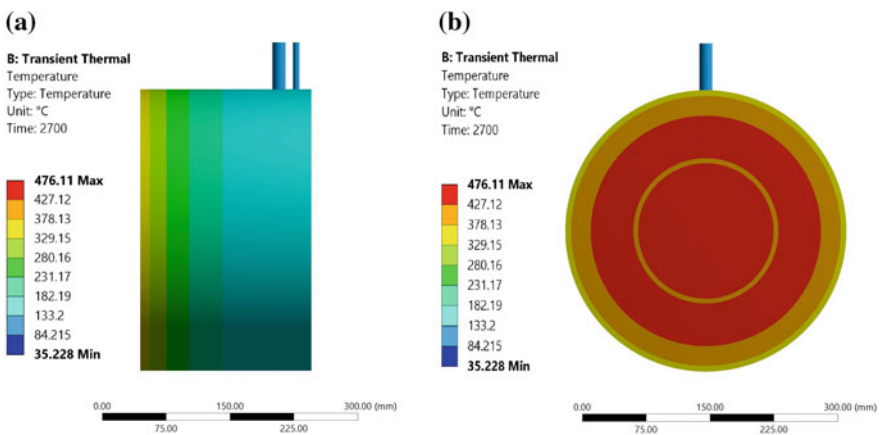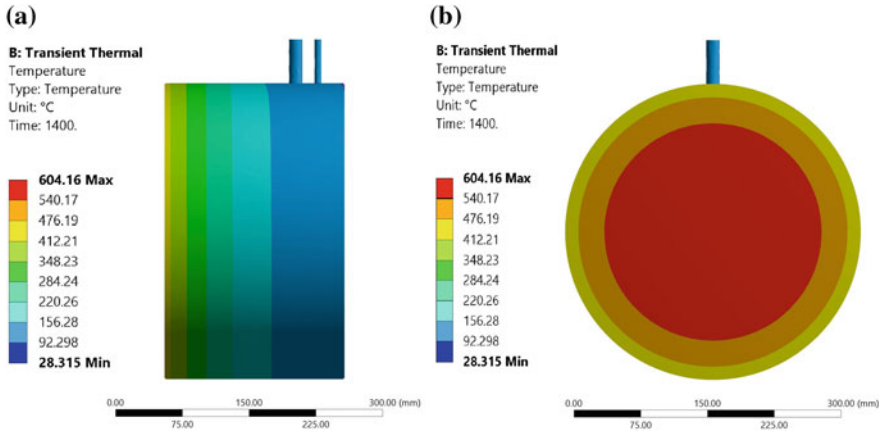


**Fig. 6** **a** Maximum outer receiver temperatures of the two receivers while the dish is focused. **b** Maximum outer receiver temperatures of the two receivers while the dish is defocused
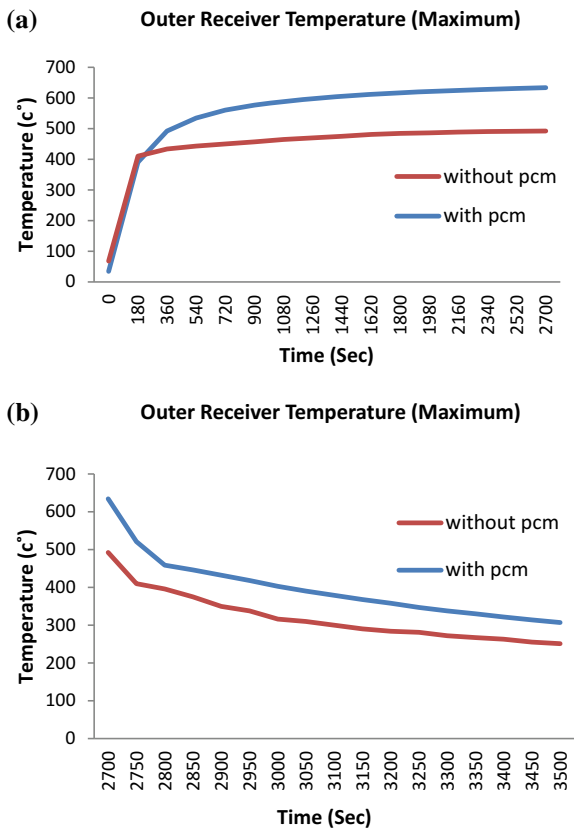
**Table 4** Numerical mass flow rate without and with PCM

| Parameters | Mass flow rate of steam (Kg/h) |
|---|---|
| Without PCM | 0.72 |
| With PCM | 0.87 |

The numerical results show that higher quantity of steam is converted when the phase change material is used in the receiver with an inlet temperature of water of 30 °C. The temperature distribution model using transient thermal analysis in each case makes it clear and easy to visualize the results. From Table 4, it is clear that the receiver with PCM shows better steam generation rate as compared to that without PCM.

## 4   Conclusion

Numerical analysis was carried out for two cylindrical receivers in which one contains the solar salt and other does not under same ambient condition with inlet water temperature 30 °C. The emphasis was on investigation of temperature distribution and mass flow rate of steam as it is an essential parameter to design any application of solar concentrator and use solar power. The analysis showed that the cylindrical receiver containing the solar salt gives better steam generation rate than the same receiver not containing the solar salt since solar salt stores the thermal energy and acts as a thermal battery reducing the fluctuations in heat and rising the overall temperature of the receiver. The numerical analysis was performed using Transient Thermal Analysis module. The graphical representation of temperature distribution helps to understand the change with respect to time in both receivers. It can now be expected that the receiver model developed can be used for further study to optimize its performance for better.

## References

1. Crabtree GW, Lewis NS (2007) Solar energy conversion. Phys Today Online 60:37–42
2. Malayeri MR, Zunft S, Eck M (2004) Compact field separators for the direct steam generation in parabolic trough collectors: an investigation of models. Energy 29(5):653–663
3. Kabir E et al (2018) Solar energy: potential and future prospects. Renew Sustain Energy Rev 82:894–900
4. Galione PA, Perez-Segarra CD, Rodriguez I, Lehmkuhl O, Rigola J (2013) A new thermocline-PCM thermal storage concept for CSP plants. Numer Anal Perspect, Energy Proc 49:790–799
5. Prieto C, Rodríguez A, Patiño D, Cabeza LF (2018) Thermal energy storage evaluation in direct steam generation solar plants. Sol Energy 159:501–509
6. Nene AA, Ramachandran S (2017) Numerical and experimental investigation of Scheffler concentrator receivers for steam generation rate under different operating conditions. IJRER 7(4)

7. Xiao L, Wu SY, Li YR (2011) Effect of cavity wall temperature and opening ratio on the natural convection Heat loss characteristics of a solar cavity receiver. In: Computer distributed control and intelligent environmental monitoring (CDCIEM), Changsha, china, pp 1112–1115

8. Fang J, Wei J, Dong X (2009) A calculation method for evaluating thermal loss for cavity receiver. In: Power and Energy Engineering conference, Wuhan, China

9. Zakaria S, Khaled A, Mustapha H (2017) Experimental study of a flat plate solar collector equipped with concentrators. Int J Renew Energy Res 7(3):1028–1031

10. Mosbah CA, Tad Jine M, Chakir M, Boucherit MS (2016) On the control of parabolic solar concentrator: the zipper approach. Int J Renew Energy Res 6(3):1101–1108

11. Kearney D, Herrmann U, Nava P, Kelly B, Mahoney R, Pacheco J, Cable R, Potrovitza N, Price H (2003) Assessment of a molten salt heat transfer fluid in a parabolic trough solar field. J Solar Energy Eng 121:170–176

12. Zhang P, Cheng J, Jin Y, An X (2018) Evaluation of thermal physical properties of molten nitrate salts with low melting temperature. Solar Energy Mater Solar Cells 176:36–41

13. Nexant Inc. (2001) USA trough initiative: nitrate salt HTF rankine cycle, steam generator, and thermal storage analyses, prepared for NREL

14. Pacheco JE, Showalter S, Kolb W (2001) Development of a molten salt thermocline thermal storage system for parabolic trough plants. Solar Forum 2001, Washington, DC

# Parametric Investigations and Thermodynamic Optimization of Regenerative Brayton Heat Engine

**Rajesh Arora and Ranjana Arora**

**Abstract** The modified configuration of regenerated Brayton heat engine along with pressure drop losses in its irreversible mode is thermodynamically investigated and optimized. The temperature difference between the system and the reservoirs is considered as the source of external irreversibility. On the other hand, frictional losses in compressor/turbine, regenerative heat and pressure losses induce internal irreversibilities in the system. The output power of the cycle is thermodynamically optimized in context with cycle temperature. It is found that regenerative effectiveness plays a vital role in obtaining maximum possible output power, and first law efficiency predominantly depends on the cold-side effectiveness in the system. It is also observed that the thermodynamic performance of the proposed system/ device prominently depends on the efficiency of the turbine and consequently is less dependent on compressor efficiency. Moreover, the model investigated in this study yields lesser output power/first law efficiency and exactly follows the results/ outcomes presented in the available literature at $\alpha_1 = \alpha_2 = 1$, which are the pressure recovery coefficients at two ends.

**Keywords** Regenerative Brayton cycle · Thermodynamic optimization · Regenerators · Output power and first law efficiency

## 1 Introduction

The designing of gas power station carries equal importance for output power and thermal efficiency. Many researchers have proposed the ways to improve these parameters globally. Leff [1] investigated the gas power station on the basis of

R. Arora (✉)
Department of Mechanical Engineering, Amity University Haryana, Gurgaon, India
e-mail: rajesharora1219@rediffmail.com

R. Arora
Renewable Energy Department, ASAS, Amity University Haryana, Gurgaon, India

research findings of Curzon and Ahlborn [2]. He analyzed that highest possible work can be achieved by altering the temperature of the cycle. Wu and Kiang [3] applied finite-time thermodynamics (FTT) principles to optimize work output, whereas Wu [4] maximized the output power of an endoreverse operated Brayton cycle. Wu and Kiang [5] combined real expansion/compression operations and observed the dependence of output power and first law efficiency on turbine/compressor outputs. Additionally, the output power maximization for ideal Brayton is performed by Ibrahim et al. [6]. Afterward, Cheng and Chen [7] extended the analysis for endoreversible mode and found the fall in output power/efficiency while employing regenerator in the cycle. On the similar path, the output/performance of regenerated Brayton cycle is investigated with the application of thermodynamic principles [8, 9]. The finite-time thermodynamic principles are applied to by Kaushik and Tyagi [10] to study the output of a regenerated closed Brayton engine in irreversible mode. In addition to it, the irreversible closed mode of the system is analyzed by Wang et al. [11]. Afterward, the system with isothermal heat addition is investigated by Kaushik et al. [12] in order to optimize the output power implied with temperature of operating media. Tyagi et al. [13] considered a complex-mode system for maximizing ecological parameters and observed their optimal values with respect to different performance parameters, viz. ecological function, output power/efficiency of the cycle. Chen et al. [14] investigated the output power and system efficiency of intercooled closed Brayton cycle in endoreversible mode. Subsequently, Wang et al. [15, 16] carried out the power maximization of the system by changing effectiveness parameter of different heat exchangers, while Tyagi and Kaushik [17] ecologically improved upon intercooled Brayton cycle in irreversible mode, with/without heat addition at constant temperature. In due time, various ecological function optimizations are found in the current literature for the proposed system in endo- and irreversible mode [18–32]. Based on the present literature, thermodynamic model of regenerated Brayton cycle in irreversible mode is developed and investigated along with pressure drop as additional irreversibility in view of maximizing output power and first law efficiency. The thermodynamic impacts of different heat exchanger effectiveness, turbine/compressor efficiency, rate of heat capacitances, reservoir temperature ratios, and pressure recovery coefficients are investigated and formulated.

## 2 Thermodynamic Analysis

Figure 1 shows the regenerative Brayton heat engine in irreversible mode equipped with heat source/sink of definite thermal dimensions. In this system, states 1 and 2 show the entry nodes and compressed zone of the working media, which afterward get into a regenerator. It is then heated up to point 2R, with the help of a turbine exhaust. After this, the fluid gets along a heat exchanger with a certain pressure fall as indicated by pressure recovery coefficient, $\theta_1 = p_2/p_3$, and heated up to a point state 3. Thereafter, the fluids get into the turbine to produce output power and then

**Fig. 1** Temperature–entropy diagram for regenerated Brayton system
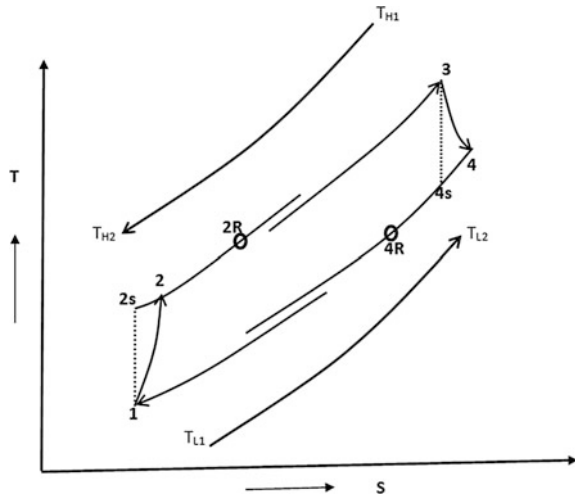


to cold-/sink-side heat exchanger along a slight pressure drop shown by another pressure recovery coefficient, $\theta_2 = p_4/p_1$. The working media encounters a drop-in temperature till it reaches state 1, on the other hand, the temperature of the sink rises from $T_{L1}$ to $T_{L2}$. The subsequent processes (1–2s) and (4–5s) are constant entropy in behavior as illustrated by spotted outlines in Fig. 1.

The different heat transfers are evaluated as:

$$Q_H = U_H A_H \chi_H = (T_3 - T_{2R})C_W = (T_{H1} - T_{H2})C_H = \varepsilon_H(T_{H1} - T_{2R})C_{H,min} \quad (1)$$

$$Q_L = U_L A_L \chi_L = (T_{4R} - T_1)C_W = (T_{L2} - T_{L1})C_L = \varepsilon_L(T_{4R} - T_{L1})C_{L,min} \quad (2)$$

$$Q_R = U_R A_R \chi_R = (T_{2R} - T_2)C_W = (T_4 - T_{4R})C_W = \varepsilon_R(T_4 - T_2)C_W \quad (3)$$

Here, $\chi_H$, $\chi_L$, and $\chi_R$ are the log mean temperature differences of hot, cold, and regenerative sides, whereas $\varepsilon_H$, $\varepsilon_L/\varepsilon_R$ are the effectiveness of the heat source zone, sink/regenerated heat exchanger, respectively.

Further, the component efficiencies of turbine/compressor are written as:

$$\eta_c = \frac{T_{2s} - T_1}{T_2 - T_1} \text{ and } \eta_t = \frac{T_3 - T_4}{T_3 - T_{4s}} \quad (4)$$

Applying second law of thermodynamics for an irreversible regenerative Brayton model,

$$T_1 T_3 = \theta T_{4s} T_{2s} \quad (5)$$

where $\theta = (\theta_1 \theta_2)^{\frac{k-1}{k}}$; $\theta_1$ and $\theta_2$ are pressure recovery coefficients.

Replacing the values of different temperatures into Eq. (5), quadratic equation in $T_2$ is obtained as:

$$X_1 T_2^2 + Y_1 T_2 + Z_1 = 0 \tag{6}$$

Solution of Eq. (6) gives

$$T_2 = \frac{-Y_1 + \sqrt{Y_1^2 - 4X_1 Z_1}}{2X_1} \tag{7}$$

Using thermodynamics' first law

$$P = Q_H - Q_L = \varepsilon_L C_{L,\min}(T_{L1} - T_{4R}) - \varepsilon_H C_{H,\min}(T_{2R} - T_{H1}) \tag{8}$$

Differentiating Eq. (8) with respect to $T_4$ and equating it to zero, i.e., $\frac{\partial P}{\partial T_4} = 0$ gives

$$X_2 T_4^2 + Y_2 T_4 + Z_2 = 0 \tag{9}$$

Solution of Eq. (9) is obtained as:

$$T_{4,\text{opt}} = \frac{-Y_2 - \sqrt{Y_2^2 - 4X_2 Z_2}}{2X_2} \tag{10}$$

## 3  Results and Discussion

The influence of different factors is analyzed while considering the remaining parameters as the constant valued as given $\varepsilon_H$, $\varepsilon_{H1}$, $\varepsilon_L$, and $\varepsilon_R$ are taken as 0.75, $T_{H3} = 1250$ K, $T_{H1} = 1000$, $T_{L1} = 300$ K, $T_0 = 295$ K, $\eta_{\text{turb}} = \eta_{\text{comp}} = 0.81$, $C_W = 1.06$ kW/K, $C_H = C_{H1} = C_L = 1$ kW/K, $U_H = U_{H1} = U_L = U_R = 2.0$ kWK$^{-1}$m$^{-2}$, $\theta_1 = \theta_2 = 0.96$ [12, 13]. The detailed discussion of the obtained outcomes is discussed in the subsequent sections.

### 3.1  Impacts of $\varepsilon_H$, $\varepsilon_R$, and $\varepsilon_L$

The thermodynamic influence of different effectiveness is presented in Fig. 2a, b on the output power and first law efficiency. It is well notified from the obtained results that the highest attainable values of output power and first law efficiency rise as the heat sink-/source-side effectiveness and regenerated heat exchanger effectiveness are raised. It is also observed that the influence of ($\varepsilon_L$) is much more dominant on
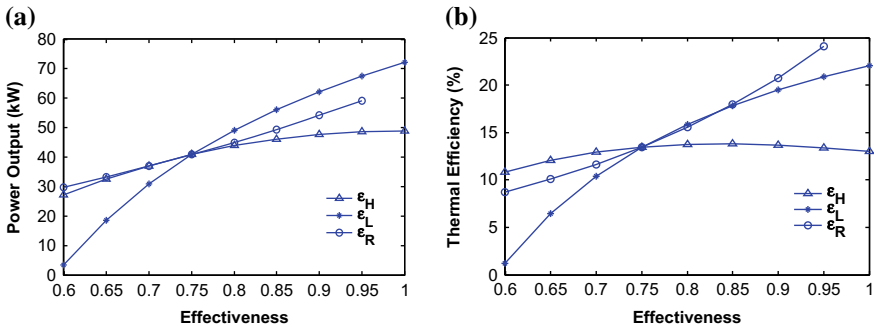
**Fig. 2** Impacts of **a** output power and **b** first law efficiency with a different effectiveness of heat exchanger

output power, whereas first law efficiency primarily depends on ($\varepsilon_R$). The obtained outcomes may show their relations with heat exchanger area of the engine, which needs to be as maximum as possible for obtaining maximum effectiveness. Eventually, the cost of the system goes up with the heat transfer area. Therefore, one has to be vigilant while choosing the effectiveness factor for different heat exchanger designs. Generally, the influences of several performance variables in context with this factor are not its linear function, and $\varepsilon_L > \varepsilon_R > \varepsilon_H$ is the best and optimized relation for realizing the practical systems.

## 3.2 Impacts of $C_H$, $C_L$, and $C_W$

Figure 3a, b shows the influence of different thermal capacitance rates on highest possible values of output power and corresponding first law efficiency. It is very much clear that output power and first law efficiency rises with the rise in rate of heat capacitances for source-/sink-side reservoir, whereas all the performance parameters reveal sharp dip along the rise in rate of heat capacitances of the cycle working medium. It is also observed, the rate of heat capacitances along sink side is more prominent on the performance factors compared to fixed temperature source zone of the system model. Generally, the change in different performance factors for the rate of heat capacitance does not result in linear relationship, and the mutual relation $C_L > C_H > C_W$ is found to be best suited for system execution in most optimized manner.

**(a)**



**(b)**
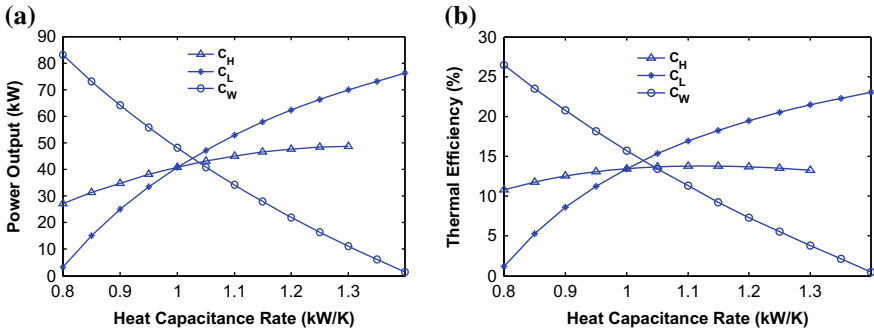


**Fig. 3** Impacts of **a** output power and **b** first law efficiency with different heat capacitance rates

## 3.3  Impacts of Compressor/Turbine Efficiency

The change of compressor/turbine efficiency on output power and first law efficiency of regenerative Brayton cycle in irreversible mode along definite capacity thermal reservoir is illustrated in Fig. 4a, b. It is found here that the highest possible power/first law efficiency rises with the rise in component efficiencies which shows that the higher the values of component efficiencies are, better the system performance is achieved. It is also observed that the impact of turbine efficiency is dominant on the thermodynamic system outcome compared with the compressor efficiency. Consequently, for the designing of real Brayton systems, exhaustive literature research and analysis are essential on the efficiency of compressor.

**(a)**



**(b)**
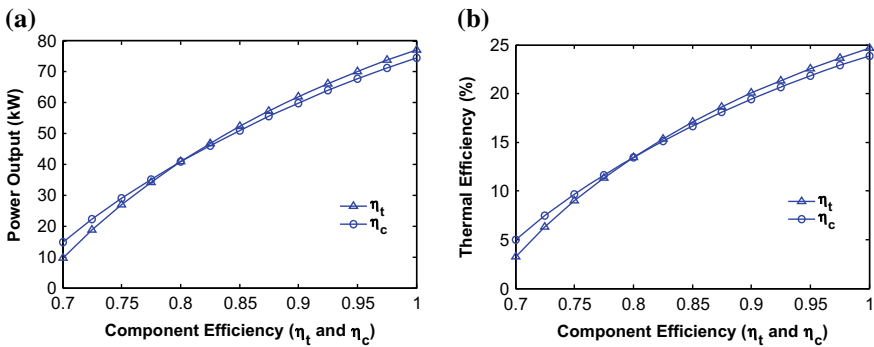


**Fig. 4** Effects of **a** output power and **b** first law efficiency with turbine/compressor efficiencies
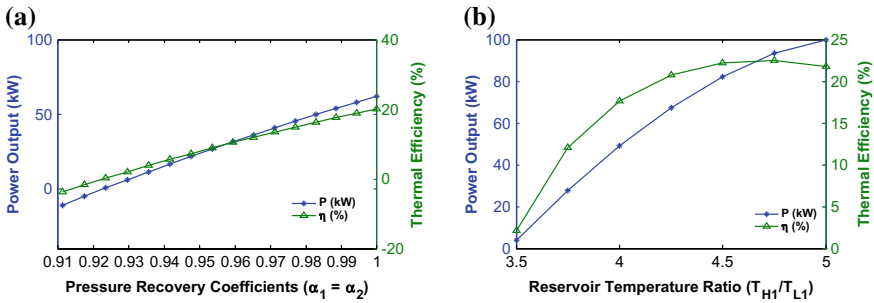
**Fig. 5** Impacts of output power and first law efficiency with **a** pressure recovery factors and **b** reservoir temperature ratios

## 3.4 Impacts of Pressure Recovery Factors

Figure 5a illustrates the influence of recovery factors on different outcome factors of Brayton cycle in irreversible mode. It is observed that highest output power and first law efficiency go up as the pressure drop falls. It is also observed that the different performance factors achieve their highest values at zero magnitude of pressure drop which is nearly impossible to attain in practical Brayton system. Furthermore, output power and first law efficiency possess linear variations with respect to pressure recovery coefficients.

## 3.5 Impacts of Temperature Ratio ($T_{H1}/T_{L1}$)

Figure 5b reveals the influence of temperature ratio ($T_{H1}/T_{L1}$) of the heat source/sink on different output factors of Brayton system in irreversible mode. It can be reported here that the highest output power and corresponding first law efficiency show a significant increase between $T_{H1}/T_{L1}$ ratio of 3.5 and 4.75, and thereafter, power output increase, while corresponding efficiency starts decreasing at higher $T_{H1}/T_{L1}$ ratio. Further, $T_{H1}/T_{L1}$ ratio is improved either by reducing sink temperature or by growing the temperature of the source. Again, it is not practical to cut lower-side temperature as to increase the temperature of the source. Therefore, for efficient operation of real gas power plant, high heat source inlet temperature should be achieved.

# 4   Conclusions

The Brayton heat engine possessing design/performance parameters near to the real one is investigated. The output power is thermodynamically optimized for different cycle temperatures, and the respective first law efficiency is computed typically for varying operating factors. The major outcomes of the present work are summarized as follows:

- The output power and first law efficiency rise with $\varepsilon_H$, $\varepsilon_L$, $\varepsilon_R$, component efficiencies, $C_H$, $C_L$, reservoir temperature ratio, and coefficients of pressure recovery, whereas their value falls down for the fall in $C_W$.
- It is also observed that the impact of turbine efficiency is higher on the peak value of output power, and the respective first law efficiency is also compared to the efficiency of compressor.
- It is seen that the highest output power and first law efficiency show significant increase between $T_{H1}/T_{L1}$ ratio of 3.5 and 4.75, and thereafter, power output increases, while corresponding efficiency starts decreasing at higher $T_{H1}/T_{L1}$ ratio.
- It is also noticed that the exhaustive investigations and analysis are still required for the efficiency of compressor while designing realistic gas power plants.
- The formulated results of the system possess a decreasing pattern of $\varepsilon_L$, $\varepsilon_R$, $\varepsilon_H$ and heat capacitances as $C_W$, $C_H$, and $C_L$ for the executed results near to practical power plant.

# References

1. Leff HS (1987) Thermal efficiency at maximum power output: New results for old engine. Am J Phys 55(7):602–610
2. Curzon FL, Ahlborn B (1975) Efficiency of Carnot heat engine at maximum power output. Am J Phys 43(3):22–24
3. Wu C, Kiang RL (1990) Work and power optimization of a finite time Brayton cycle. Int J Ambient Energy 11(3):129–136
4. Wu C (1991) Power optimization of an endoreversible Brayton gas heat engine. Energy Convers Mgmt 31(6):561–565
5. Wu C, Kiang RL (1991) Power performance of a nonisentropic Brayton cycle. J Eng Gas Turbines Power 113:501–504
6. Ibrahim OM, Klein SA, Mitchell JW (1991) Optimum heat power cycles for specified boundary conditions. J Eng Gas Turbine Power 113(4):514–521
7. Cheng C-Y, Chen C-K (1996) Power optimization of an endoreversible regenerative Brayton cycle. Energy 21(4):241–247
8. Wu C, Chen L, Sun F (1996) Performance of a regenerative Brayton heat engine. Energy 21(2):71–76
9. Chen L, Sun F, Wu C, Kiang RL (1997) Theoretical analysis of the performance of a regenerative closed Brayton cycle with internal irrreversibilities. Energy Convers Manag 38(9):871–877

10. Kaushik SC, Tyagi SK (2002) finite time thermodynamic analysis of an irreversible regenerative closed cycle Brayton heat engine. Int J Solar Energy 22(3–4):141–151
11. Wang W, Chen L, Sun F, Wu C (2003) Performance analysis for an irreversible variable temperature heat reservoir closed intercooled regenerated Brayton cycle. Energy Convers Manag 44:2713–2732
12. Kaushik SC, Tyagi SK, Singhal MK (2003) Parametric study of an irreversible regenerative Brayton cycle with isothermal heat addition. Energy Convers Manag 44:2013–2025
13. Tyagi SK, Kaushik SC, Tiwari V (2003) Ecological optimization and parametric study of an irreversible regenerative modified Brayton cycle with isothermal heat addition. Entropy 5:377–390
14. Chen L, Wang W, Sun F, Wu C (2004) Power and efficiency analysis of an endoreversible closed intercooled regenerated Brayton cycle. Int J Energy 1(4):475–494
15. Wang W, Chen L, Sun F, Wu C (2005) Power optimization of an endoreversible closed intercooled regenerated Brayton cycle. Int J Thermal Sci 44(1):89–94
16. Wang W, Chen L, Sun F, Wu C (2005) Power optimization of an irreversible closed intercooled regenerated Brayton cycle coupled to variable temperature heat reservoirs. Appl Therm Eng 25(8–9):1097–1113
17. Tyagi SK, Kaushik SC (2005) Ecological optimization of an irreversible regenerative intercooled Brayton heat engine with direct heat loss. Int J Ambient Energy 26(2):81–92
18. Kumar R, Kaushik SC, Kumar R (2013) Efficient power of Brayton heat engine with friction. Int J Eng Res Technol 6(5):643–650
19. Kumar R, Kaushik SC, Kumar R (2015) Power optimization of an irreversible regenerative Brayton cycle using isothermal heat addition. J Therm Eng 1(4):279–286
20. Arora R, Kaushik SC, Kumar R (2015) Performance optimization of Brayton heat engine at maximum efficient power using temp. dependent specific heat of working fluid. J Therm Eng 1(2):345–354
21. Arora R, Kaushik SC, Kumar R (2015) Multi-objective optimization of an irreversible regenerative Brayton cycle using genetic algorithm. In: 2015 international conference on futuristic trends on computational analysis and knowledge management (ABLAZE), IEEE, pp 340–346. https://doi.org/10.1109/ablaze.2015.7155017
22. Kumar R, Kaushik SC, Kumar R (2015) Performance analysis of an irreversible regenerative Brayton cycle based on ecological optimization criterion. Int J Therm Environ Eng 9(1): 25–32
23. Kaushik SC, Kumar R, Arora R (2016) Thermo-economic optimization and parametric study of an irreversible Brayton heat engine cycle. J Therm Eng 2(4):861–870
24. Arora R, Kaushik SC, Kumar R, Arora R (2016) Soft computing based multi-objective optimization of Brayton cycle power plant with isothermal heat addition using evolutionary algorithm and decision making. Appl Soft Comput 46:267–283
25. Kumar R, Kaushik SC, Kumar R, Hans R (2016) Multi-objective thermodynamic optimization of irreversible regenerative Brayton cycle using evolutionary algorithm and decision making. Ain Shams Eng J 7(2):741–753
26. Arora R, Kaushik SC, Kumar R (2016) Multi-objective thermodynamic optimization of solar parabolic dish Stirling heat engine with regenerative losses using NSGA-II and decision making. Appl Solar Energy 52(4):295–304
27. Arora R, Kaushik SC, Kumar R, Arora R (2016) Multi-objective thermo-economic optimization of solar parabolic dish Stirling heat engine with regenerative losses using NSGA-II and decision making. Int J Electr Power Energy Syst 74:25–35
28. Arora R, Kaushik SC, Kumar R (2015) Multi-objective optimization of solar powered Ericsson cycle using genetic algorithm and fuzzy decision making. In: 2015 international conference on advances in computer engineering and applications (ICACEA), IEEE, pp 553–558. https://doi.org/10.1109/icacea.2015.7164754
29. Arora R, Kaushik SC, Kumar R (2017) Multi-objective thermodynamic optimization of solar parabolic dish Stirling heat engine using NSGA-II and decision making. Int J Renew Energy Technol 8(1):64–92

30. Arora R, Kaushik SC, Arora R (2015) Multi-objective and multi-parameter optimization of two-stage thermoelectric generator in electrically series and parallel configurations through NSGA-II. Energy 91:242–254
31. Arora R, Kaushik SC, Arora R (2016) Thermodynamic modeling and multi-objective optimization of two-stage thermoelectric generator in electrically series and parallel configurations. Appl Therm Eng 25(103):1312–1323
32. Arora R, Arora R (2018) Multiobjective optimization and analytical comparison of single- and 2-stage (series/parallel) thermoelectric heat pumps. Int J Energy Res 1–19. https://doi.org/10.1002/er.3988

# Recent Developments in Finding Laminar Burning Velocity by Heat Flux Method: A Review

**Ashok Patil Abhishek and G. N. Kumar**

**Abstract** This paper reviews the recent developments in heat flux method to determine the laminar burning velocity of a liquid or a gaseous fuel. Laminar burning velocity is an elementary property in designing the combustion chamber and turbulent combustion model and to validate kinetic simulation. There are numerous methods to find the laminar burning velocity such as Bunsen burner method, flat flame burner method, counterflow method, soap bubble technique, tube propagating technique, and heat flux method. In this paper, some of these methods are discussed in brief and recent developments of heat flux method have been elaborated, as this method is simple and accurate. To find out laminar adiabatic burning velocity, there are two requirements to be satisfied. First is the flame should be one-dimensional, thus flat and stretchless; second is adiabatic which means net heat exchange with the burner is zero. But, satisfying both these conditions at the same time is very difficult. The other methods have failed in satisfying both the conditions. However, heat flux method proved to satisfy these conditions. Results of laminar burning velocity using heat flux technique for methane–air have been compared with other methods of finding laminar burning velocity.

**Keywords** Laminar adiabatic burning velocity · Heat flux method

## 1 Introduction

### 1.1 Laminar Adiabatic Burning Velocity

Laminar adiabatic burning velocity is velocity of unburnt gas through the flame front in the direction normal to flame surface, and complete heat must be transferred to the gas mixture which is generated due to chemical reaction [1]. It mainly dependent on pressure, temperature, and equivalence ratio of the fuel–oxidizer

A. P. Abhishek (✉) · G. N. Kumar
National Institute of Technology, Surathkal, Karnataka, India
e-mail: abhi.ap4@gmail.com

mixture. It is a critical parameter which affects many combustion characteristics of a fuel. It is used as input for turbulent modeling, flashback, minimum ignition energy, to test the thermo-kinetic combustion models which can predict characteristics of combustion for various fuels. For analysis and performance predictions of burner and combustion engine, laminar burning velocity is the essential property. Because of these reasons, accurate experimental values of laminar adiabatic burning velocity of the fuel are required [2].

## 1.2 Methods of Determining Laminar Burning Velocity

There are numerous methods of finding laminar burning velocity such as Bunsen burner method, counterflow burner method, spherical bomb method, flat flame burner method, soap bubble technique, slot burner technique, and heat flux method. The problem with determining laminar adiabatic burning velocity is the flame shape which influences the burning velocity [1, 3]. Because of this reason, a lot of early experiments showed complete scattered experimental values when plotted in a single graph. The flame must be flat to the maximum extent to determine laminar adiabatic burning velocity; in other words, flame should be one-dimensional. To stabilize the flame, the flame loses some heat to the burner which implies non-adiabatic state [1, 4]. To obtain accurate value of laminar adiabatic burning velocity, it should satisfy two conditions:

- One-dimensional and thus flat and stretchless.
- Adiabatic and hence net heat interaction with the burner.

Following are some of the general methods of determining laminar burning velocity.

**Bunsen Burner Method** In finding laminar burning velocity, this is the oldest method. Premixed mixture of fuel and oxidizer is fed into the tube, and flame stabilizes on the rim of the burner tube. Net mass flow coming out of the tube is equal to net mass flow crossing through the flame surface. Now, the fraction of laminar burning velocity and unburnt gas velocity is equal to fraction of area of cross section of exit of the tube and the surface area of the flame. As burner exit area is smaller than conical surface area of the flame, burning velocity will be smaller than the velocity of mixture of unburnt gases as shown in Fig. 1a. Though this method is straightforward and time-saving, the uncertainties in determining the surface area of the flame are high, which can vary up to 10% [4].

**Counterflow Method** It works on stabilization of flames between counterflow jets. Both the jets deliver premixed mixture of fuel and oxidizer. Since the flame stabilizes in the flow, not on the burner, and does not have heat transfer to the burner, adiabatic state is accomplished. However, the streamlines of the flow of gases are not normal to the flame outer surface which is the reason for strain in the flow as explained in Fig. 1b because of which flame gets stretched. By altering the gap of
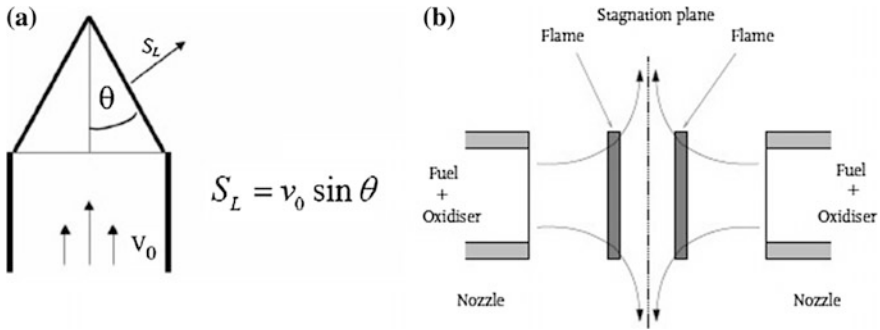
Fig. 1　**a** Bunsen burner flame [15]. **b** Counterflow burner setup
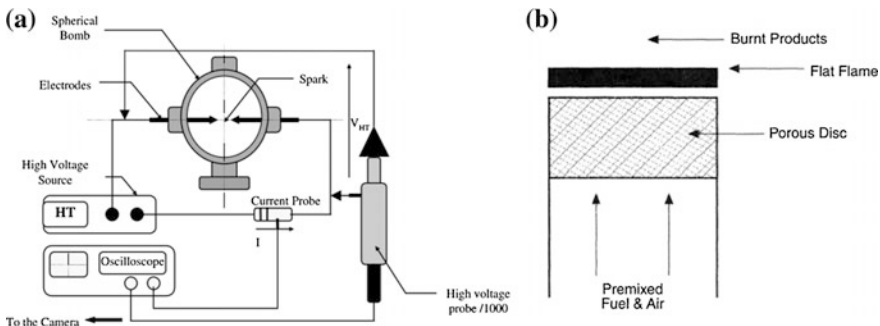


Fig. 2　**a** Spherical bomb setup [16]. **b** Flat flame burner setup [8]

separation of the nozzles, the stretch rate can be controlled [5]. A relation is found between strain rate and burning velocity. When it is extrapolated to zero strain rate, laminar burning velocity can be found out.

**Spherical Bomb Method** In this method, the combustion chamber is filled with the fuel and oxidizer mixture. It is ignited by igniter placed at the center of spherical bomb combustion chamber as shown in Fig. 2a. When the mixture is ignited, the flame expands spherically from the center to the wall. A correlation can be found between the radius of flame and time. Also, the increase in pressure because of temperature rise can be determined from which laminar burning velocity is found out [6, 7].

**Flat Flame Burner Method** First time, the flat flame was used to determine the laminar burning velocity using this particular method. Flame was stabilized on the porous metal plate which is placed at the end of tube which is water-cooled as shown in Fig. 2b. In further improvement of this method, the metal disk is cooled so that flame comes close to the porous disk. The temperature difference of inlet and outlet of water is measured. The temperature differences are measured at different

cooling rates, and respective gas velocities are also measured. To determine the exact laminar adiabatic burning velocity, the graph is extrapolated to zero cooling [8]. Experimentally achieving zero cooling is difficult because the flame will become instable and blow off. However, the temperature difference between inlet and outlet of water is small and tedious to measure.

**Heat Flux Method** The extension of flat flame burner method is heat flux technique. It was proposed by de Goey et al. The changes made to flat flame burner are: instead of cooling water supply to porous metal disk, hot water is supplied. Heat loss is measured by knowing the temperature difference of cooling water in flat burner method, whereas in heat flux method net heat transfer is reflected by measuring temperature at different radii of the burner plate [9].

The theory behind this technique is by heating the burner head it will compensate the heat which is lost from the flame to the burner. Heat which is gained by unburnt gases is only when unburnt gas temperature is less than the burner plate. This is facilitated by providing hot water jacket around the burner plate. By doing so, heat is transferred from burner head to porous plate and from burner plate to unburnt gas. The profile of temperature is generally parabolic in nature. Laminar adiabatic burning velocity is calculated when the parabolic coefficient is zero [10, 11]. Heat flux technique is more accurate as there is no requirement of extrapolation to find out laminar burning velocity.

## 2 Experimental Setup

The experimental heat flux method setup is shown in Fig. 3. The mass flow of unburnt gases is monitored by mass flow controllers (MFCs). The provision of buffering vessel is to reduce the pressure fluctuations within piping. Premixed fuel–oxidizer mixture is fed into the burner. MFCs and thermocouples are monitored by using an interface to PC. Each part of the burner is explained in the next section.

### 2.1 Plenum Chamber

The plenum chamber is used to supply gas mixture at constant velocity without fluctuation. At the lower end, distributor plate is placed, which has solid part at the center and periphery is filled with holes of 3-mm diameter. The CFD package CFX is used by de Goey et al. to design this [4]. Unburnt gas before entering chamber is premixed; this is ensured by several meters long piping arrangement. This chamber is cooled by a cooling water jacket provided. Because when gas is burnt, heat is transferred to chamber. As laminar burning velocity is depending on temperature, pressure, and equivalence ratio, it will vary with temperature. This water jacket is also useful to determine laminar burning velocity at elevated temperature.
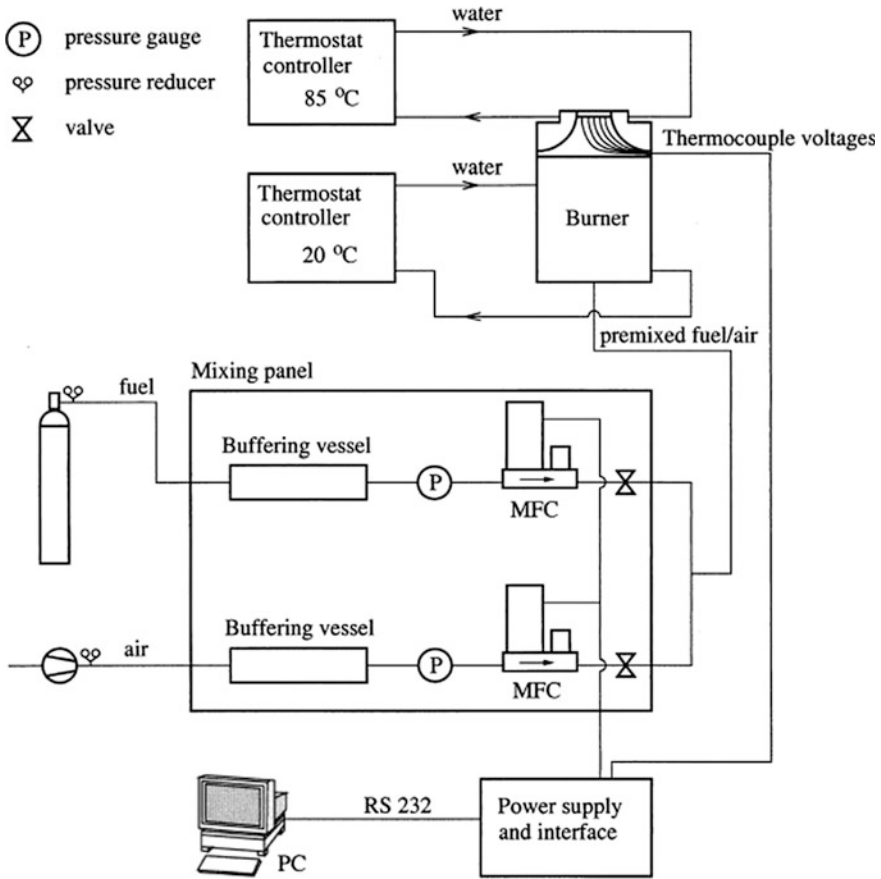
**Fig. 3** Skeleton representation of heat flux method setup [4]

## 2.2 Burner Head

Burner head is designed in such a manner that the outflow of mixture of gases is nearly uniform. The average gas velocity is computed from volumetric mass flow passing through outlet orifice cross section. At the edges of the burner, care should be taken in order to avoid the deviations occurring because of boundary layer formation near the edges of orifice [1].

In this method, the upper head is heated above the room temperature. To facilitate this, separate hot water jacket is provided to the burner head. Figure 4 explains the setup of the burner. To avoid the heat transfer from burner head to chamber, a layer of ceramic insulation is provided [12].
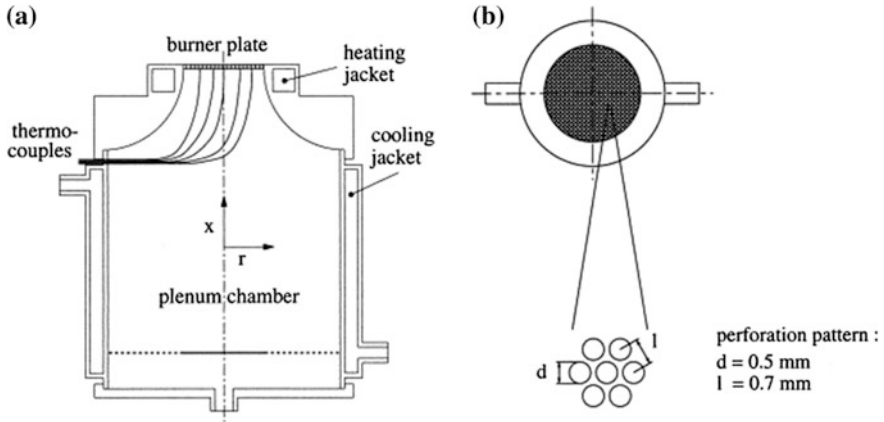
**Fig. 4 a** Heat flux plenum chamber. **b** The burner plate with perforation pattern (top view) [1, 4, 10]

## 2.3 Burner Plate

Brass is used for manufacturing the perforated heat flux burner plate. Thickness of the plate is 2 mm, and it is perforated with 0.5-mm hole diameter and 0.7-mm pitch in hexagonal pattern as shown in Fig. 4. The diameter of hole is calculated by velocity of mass flow through the burner. Numerical simulation was conducted out by de Goey to find out the dimensions of hole. Previously, the porous plate was fixed inside the head of the burner through tight fit. As an improvement, to increase the thermal contact burner plate is fixed using a press ring [4].

## 3 Temperature Measurement

The distribution of temperature in the porous plate is measured using K-type thermocouples at different radii. At first, the thermocouples were attached barely to the bottom of the burner plate. It caused systematic deviation. To reduce that, a small cylinder of length 2 mm and diameter of 0.5 mm is drilled a hole of 0.1-mm diameter to a depth of 1.5 mm. The wire of thermocouple is inserted within this hole and glued [1, 10].

## 3.1 Vertical Temperature Measurement

The energy conservation is applied to the burner plate under the assumption of heat transfer to the perforated uniform plate. The expression shows that the temperature is a function of radius only and it is parabolic in nature

$$T_P(r) = T_e\left(1 - \frac{1}{4}a^2 r^2\right) \text{ with } C = -\frac{1}{4}a^2 \tag{1}$$

where $T_e$ is the temperature of the plate at $r = 0$ (center). $T_p(r)$ indicates the temperature of the plate at any radius $r$. $\alpha$ is a constant.

For stoichiometric $CH_4$–air gas mixture, distinct temperature profiles are plotted at different inlet unburnt gas velocities. The inlet gas velocity of this mixture is altered about the laminar burning velocity value. For $CH_4$–air mixture, the temperature profiles are given in Fig. 5a. The measured temperatures are plotted against the different radii where the thermocouples are mounted on the burner plate. The parabolic coefficient $C$ determines whether a flame is sub-adiabatic or super-adiabatic [13]. Negative $C$ value indicates gas temperature is more than burner temperature and hence burner plate gains the heat. A positive $C$ value signifies that gas temperature is lower than burner plate and hence heat is transferred to the gases [11, 14]. The parabolic coefficient $C$ of different gas velocities is plotted against gas velocity. The gas velocity corresponding to this flat temperature profile is the laminar adiabatic burning velocity which is calculated by interpolation which is given in Fig. 5b.
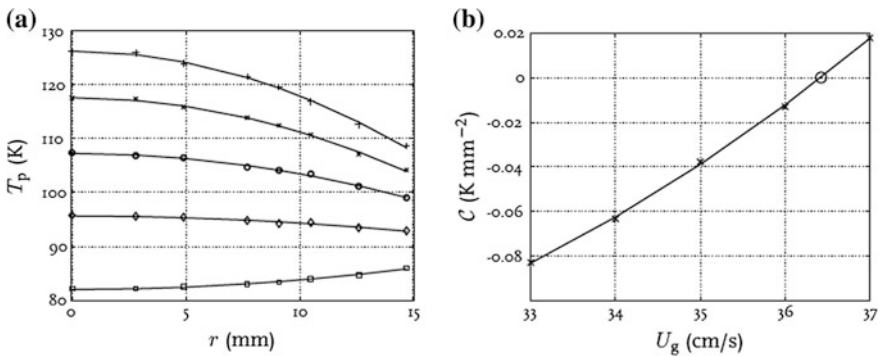


Fig. 5 a Plate temperature at different radii versus radius. b Parabolic coefficient versus gas velocity

**Table 1** Results of burning velocities of $CH_4$–air mixture ($S_L$ in cm/s) for the three equivalence ratios from different authors

| Author | Correlation | $\Phi = 0.8$ | $\Phi = 1.0$ | $\Phi = 1.2$ | Method |
|---|---|---|---|---|---|
| Hermanns [17] | $S_L (\phi)$ | 25.6 | 36.3 | 33.2 | Heat flux |
| Coppens et al. [18] | $S_L (\phi)$ | 25.0 | 36.7 | 34.0 | Heat flux |
| Huang et al. [6] | $S_L (\phi)$ | 31.1 | 41.7 | 39.2 | Spherical bomb |
| Rahim [19] | $S_L (\phi, T_u, P_u)$ | 25.8 | 38.2 | 28.3 | Spherical bomb |
| Gu et al. [20] | $S_L (\phi, T_u, P_u)$ | 25.9 | 36.0 | 31.4 | Spherical bomb |
| El-Sherif [21] | $S_L (\phi)$ | 25.0 | 36.0 | 33.7 | Counterflow |
| Stone et al. [22] | $S_L (\phi, T_u, P_u)$ | 26.5 | 37.5 | 30.9 | Spherical bomb |
| Haniff et al. [23] | $S_L (\phi)$ | 32.4 | 41.1 | 38.5 | Flat flame |
| Iijima et al. [24] | $S_L (\phi, T_u, P_u)$ | 26.4 | 34.5 | 35.4 | Spherical bomb |
| Gulder [25] | $S_L (\phi)$ | 27.6 | 41.0 | 40.0 | Spherical bomb |
| Kurata et al. [26] | $S_L (\phi, T_u, P_u)$ | 26.4 | 34.5 | 35.4 | Bunsen burner |

## 4 Comparison of Results

In this sub-unit, results of laminar burning velocity of $CH_4$–air mixture calculated using different methods are discussed. For this mixture, the results of Huang et al. and Gulder and Haniff et al. at stoichiometric condition show a lot of deviation from the exact laminar adiabatic burning velocity values of $CH_4$–air mixture. Recent experimental results of laminar adiabatic burning velocities draw good agreement that stoichiometric $CH_4$–air mixture is $36 \pm 1$ cm/s. According to the results shown in Table 1, heat flux method and counterflow method gave reasonably good results compared to other methods.

## 5 Conclusion

Overview of heat flux method and comparison of other methods are given in this paper. The setup of this method and experimental procedure are explained as well. This method serves a measurement technique which is advantageous in addition to other techniques, as the results are extrapolated. The methods used for evaluating and rectifying the present setup are quite easy and not complicated physical mechanisms, as stretch models are required. The only technique in which both 1D flame condition and adiabatic state are satisfied is by heat flux technique, and in addition to it, this method facilitates the great way of yielding a specific reference flame.

# References

1. Hermanns RTE (2007) Laminar burning velocities of methane–hydrogen–air mixtures. Ph.D. thesis, Technische Universiteit Eindhoven
2. Alekseev VA, Naucler JD, Christensen M, Nilsson EJK, Volkov EN, de Goey LPH, Konnov AA (2016) Experimental uncertainties of the heat flux method for measuring burning velocities. Combust Sci Technol 188(6):853–894
3. Khudhair O, Shahad HAK (2017) A review of laminar burning velocity and flame speed of gases and liquid fuels. Int J Curr Eng Technol 7(1):183–197
4. Bosschaart KJ, de Goey LPH (2003) Detailed analysis of the heat flux method for measuring burning velocities. Combust Flame 132:170–180
5. Van Maaren A, de Goey LPH (2007) Stretch and the adiabatic burning velocity of methane and propane-air flames. Combust Sci Technol 102(1–6):309–314
6. Huang Z, Zhang Y, Zeng A, Wang Q, Jiang D (2006) Measurements of laminar burning velocities for natural gas–hydrogen–air mixtures. Combust Flame 146:302–311
7. Halter F, Chauveau C, Djebaıli-Chaumeix N, Gokalp I (2005) Characterization of the effects of pressure and hydrogen concentration on laminar burning velocities of methane–hydrogen–air mixtures. Proc Combust Inst 30:201–208
8. Botha JP, Spalding DB (1954) The laminar flame speed of propane/air mixtures with heat extraction from the flame. Proc R Soc Lond Ser A, Math Phys Sci 225(1160):71–96
9. Christensen M (2016) Laminar burning velocity and development of a chemical kinetic model for small oxygenated fuels, Ph.D. thesis, Lund University, Sweden
10. Bosschaart KJ (2002) Analysis of the heat flux method for measuring burning velocities. Ph.D. thesis, Technische Universiteit Eindhoven
11. de Goey LPH, ven Maaren A, Quax RM (2007) Stabilization of adiabatic premixed laminar flames on a flat flame burner. Combust Sci Technol 92(1–3):201–207
12. Rau F, Hartl S, Voss S, Still M, Hasse C, Trimis D (2015) Laminar burning velocity measurements using the Heat Flux method and numerical predictions of iso-octane/ethanol blends for different preheat temperatures. Fuel 140:10–16
13. Ebaid MSY, Al-Khishali KJM (2016) Measurements of the laminar burning velocity for propane: air mixtures. Adv Mech Eng 8(6):1–17
14. Goswami M, Derks S, Coumans K, de Andrade Oliveira MH, Konnov AA, Bastiaans RJM, Luijten CCM, de Goey LPH (2011) Effect of elevated pressures on laminar burning velocity of methane + air mixtures. In: 23rd international colloquium on the dynamics of explosion and reactive systems, paper 127, Irvine, USA
15. Thermopedia (2011) Flames. http://www.thermopedia.com/content/766/. Last modified 2011/2/14
16. Lamoureux N, Djebaili-Chaumeix N, Paillard C-E (2003) Laminar flame velocity determination for $H_2$–air–He–$CO_2$ mixtures using the spherical bomb method. Exp Thermal Fluid Sci 27:385–393
17. Hermanns RTE, Konnov AA, Bastiaans RJM, de Goey LPH, Lucka K, Köhne H (2010) Effects of temperature and composition on the laminar burning velocity of $CH_4$ + $H_2$ + $O_2$ + $N_2$ flames. Fuel 89:114–121
18. Coppens FHV, de Ruyck J, Konnov AA (2007) Effects of hydrogen enrichment on a diabatic burning velocity and NO formation in methane + air flames. Exp Therm Fluid Sci 31(5):437–444
19. Rahim F (2002) Determination of burning speed for methane/oxidizer/diluent mixtures. Ph.D. thesis, Northeastern University Boston
20. Gu XJ, Haq MZ, Lawes M, Woolley R (2000) Laminar burning velocity and Markstein lengths of methane–air mixtures. Combust Flame 21(1–2):41–58
21. El-Sherif SA (2000) Control of emissions by gaseous additives in methane–air and carbon monoxide–air flames. Fuel 79(5):567–575

22. Stone R, Clarke A, Beckwith P (1998) Correlations for the laminar burning velocity of methane/diluent/air mixtures obtained in free fall experiments. Combust Flame 114:546–555
23. Haniff MS, Melvin A, Smith DB, Willians A (1989) The burning velocities of methane and SNG mixtures with air. J I Energy 62:229–236
24. Iijima T, Takeno T (1986) Effects of temperature and pressure on burning velocity. Combust Flame 65(1):35–43
25. Gülder ÖL (1984) Correlations of laminar combustion data for alternative S.I. engine fuels. SAE Technical Paper Series SAE 841000
26. Kurata O, Takahashi S, Uchiyama Y (1994) Influence of preheat temperature on the laminar burning velocity of methane–air mixtures. SAE Trans 1057:119–125

# Dynamics and Control of Thermally Heat-Integrated Systems

**Asma Iqbal** and **Syed Akhlaq Ahmad**

**Abstract** The most crucial objective in a chemical process is to synthesize/design a robust control structure, which can ensure a safe, smooth, and profitable operation within the process, even in case of disturbances. In this work, a plantwide control structure has been synthesized for an example process where tetrahydrofuran (THF)–water mixture is separated using an extractive distillation technique. The process design flow sheet consists of two distillation columns from where THF and water are being recovered at high purities while the entrainer is recovered and recycled as a material recycle stream within the process. Further, two feed-effluent heat exchangers (FEHEs) are used to exchange the heats between the hot and the cold streams within the process to provide the heat integration, thus making the process more energy efficient. An improvement of 20.79% in the overall energy requirements has been observed upon applying the heat integration circuit. A plantwide control structure is later synthesized on the base case design, and its performance is evaluated for $\pm10\%$ change in throughput change and $\pm5\%$ change in composition change. The significant feature of this work is the synthesis of control strategy when the control degree of freedom is lost during the implementation of heat integration circuits. To counter this issue, Hi-Select control loop is used along with supervisory composition controllers.

**Keywords** Control structure · Heat integration · Industrial effluents · FEHE

## 1 Introduction

Chemical processes are dynamic in nature and are subject to certain periodic disturbances which induce nonlinearity in the system. In order to ensure optimal economic operation in a plant, certain variables (e.g., temperature, pressure, composition) need to be controlled. An efficient control structure does not allow the

A. Iqbal (✉) · S. A. Ahmad
Department of Chemical Engineering, Aligarh Muslim University, Aligarh, India
e-mail: asma.rs@amu.ac.in

773

plant to drift too much from its desired steady-state operation points. The main idea behind control structure is to maintain certain variables at their desired values against any disturbances and to reduce nonlinearity in the system.

Distillation, being an efficient and interesting separation process, is perhaps the most studied unit operation in control studies. Besides several known advantages of the distillation process, it is recognized to constitute 40–50% operational cost of the entire plant [1, 2]. Keeping these higher costs in consideration, nowadays researchers are focusing on making distillation an environmentally friendly and cost-effective process through various energy intensification techniques [3]. Heat integration is one of the competent techniques which reduce both energy and operational costs [4]. The process of heat integration in distillation columns is based on the best utilization of process cold stream in the reboiler and process hot stream in condenser [5]. Fundamentally, there are different ways of achieving heat integration in distillation columns, viz., internal heat integration between whole rectifying and stripping sections, stage-wise heat transfer between two columns, vapor recompression column, concentric heat-integrated distillation column, and use of FEHEs [6–10]. Feed-effluent heat exchangers (FEHEs) are considered to be the key components in the design of heat-integrated processes. The working principle behind FEHEs is to transfer the heat of hot outlet stream to the cold inlet stream leading to the reduction in overall energy cost by giving a positive feedback to the energy of the system. Due to this positive feedback of energy, there are complexities in the dynamics of the system which needs an appropriate control structure to be implemented. Most of the reported work in the literature is based on the implementation of FEHEs in reactors [11–13]. Only few case studies reported in the literature have discussed control studies of FEHEs in distillation columns. Hence, this area has become a sought attribute for researchers.

In this work, an analysis of the control structure of thermally heat-integrated system which is inherently energy efficient in nature is presented. An example separating tetrahydrofuran–water mixture (which is primarily an industrial effluent from pharmaceuticals and semiconductors industries), using entrainer solvent, has been studied. Because of the hazardous nature of tetrahydrofuran (THF), its presence in the environment needs to be strictly regulated. A plantwide control structure for the thermally heat-integrated extractive distillation scheme is developed which provides stable base-level regulatory control for large disturbances. Furthermore, the importance of Hi-Select control logic has been highlighted. Dynamic performances based on the disturbances induced in feed flow rate and feed composition have been evaluated.

## 2  Process Flow Sheet Schematic

The present case study deals with the separation of an interesting azeotropic mixture which is discharged as an industrial effluent from industries Fig. 1 represents the process flow sheet schematic which consists of two distillation columns and two
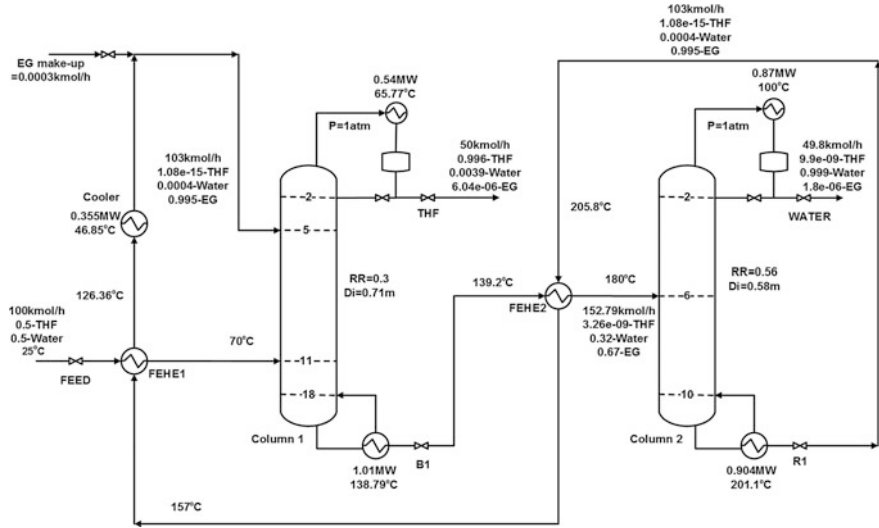
**Fig. 1** Design flow sheet for extractive distillation using FEHEs

FEHEs. A high boiling entrainer, ethylene glycol, is used to break the azeotrope between THF and water. An equimolar mixture (0.5, 0.5) of THF–water is fed to distillation column 1 at 25 °C, 1 atm pressure. The two products (THF and water) are obtained from the distillate of two columns, respectively. The high boiling entrainer recovered from the bottom of column 2 at high temperature (205.8 °C) is recycled to column 1. The heat of hot stream coming out from the bottom of column 2 is used to preheat the feed of both columns, thus utilizing the internal heat produced within the system and reducing overall energy costs. The feed of column 1 at 25 °C is preheated to 70 °C and is fed at stage 11. Similarly, the feed to column 2 fed at stage 6 is heated from 139.2 to 180 °C. This preheating of feed helps in reducing the load on the two reboilers of two columns, thereby reducing the energy consumption of the process.

## 2.1 Economic Benefits of FEHEs

FEHEs have been found to save energy costs in comparison with the conventional extractive distillation process, highlighting the economic benefits over other schemes. This has been justified by comparing the total annual cost (TAC) of the present work and the extractive distillation scheme [14]. TAC has been calculated using the correlations adopted in [15]. The results obtained are summarized in Table 1.

From Table 1, one can observe that there is a saving of approximately 20.79% in heat duties and 1.98% in terms of TAC for extractive distillation with thermal heat

**Table 1** Comparison of optimized parameters and TAC values of extractive distillation process with and without heat integration

| Parameters | Extractive distillation [14] | Heat-integrated extractive distillation (present work) |
|---|---|---|
| NT1 | 18 | 18 |
| NT2 | 10 | 10 |
| QR1 (MW) | 1.14 | 1 |
| QR2 (MW) | 1.16 | 0.904 |
| TAC ($\times 10^5$ \$/year) | 1.54 | 1.51 |

integration, ascertaining that indeed the use of FEHEs has been proven to be very beneficial for cost savings of the process.

## 3 Control Structure of the Process

Figure 2 describes the detailed control structure of the thermally heat-integrated extractive distillation process. It consists of 13 controllers which include two flow controllers, four level controllers, two pressure controllers, three temperature controllers, and two composition controllers, with direct/reverse action depending upon the manipulating variables of the process. The key feature of this control structure is the use of Hi-Select control logic which has played a vital role in maintaining the recycle flow rate at the desired value. A Hi-Select control is incorporated which measures and compares two input signals and selects the value of a signal having higher magnitude, and then sends it forward to make necessary manipulations. The details of all controllers used are given in Table 2.

### 3.1 Dynamic Responses of Process

The dynamic performance of the proposed control structure has been analyzed by inducing a step change in the feed flow rate ($\pm 10\%$) and feed composition ($\pm 5\%$) at 5 h. The response of the disturbances has been shown in Figs. 3 and 4. From these responses, it has been observed that the plant has attained a steady-state condition immediately after the disturbance is induced, showing the robustness of control structure.
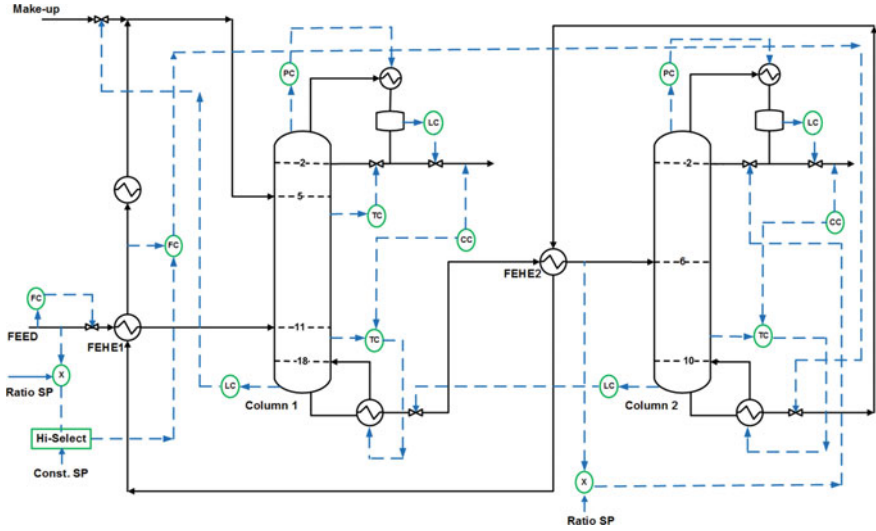
**Fig. 2** Proposed control structure of the process

**Table 2** Controlled variable (CV) and manipulation variable (MV) pairing details

| S. no. | Controlled variable (CV) | Manipulated variable (MV) |
|---|---|---|
| 1 | Flow controller (FC1) | % opening of valve (V1) |
| 2 | Flow controller (FC2) | % opening of valve attached to the bottom of column 2 (V2) |
| 3 | Level controller (LC11) | Distillate rate (D1) |
| 4 | Level controller (LC12) | Makeup flow rate |
| 5 | Level controller (LC2) | Distillate rate (D2) |
| 6 | Level controller (LC22) | Bottom rate of column 1 (B1) |
| 7 | Pressure controller (P1) | Condenser duty (Qcond1) |
| 8 | Pressure controller (P2) | Condenser duty (Qcond2) |
| 9 | Temperature controller (TC1) | Reflux rate (Fm.R) |
| 10 | Temperature controller (TC12) | Reboiler duty (Qreb1) |
| 11 | Temperature controller (TC2) | Reboiler duty (Qreb2) |
| 12 | Composition controller (CC1) | Cascade with TC1 |
| 13 | Composition controller (CC2) | Cascade with TC2 |
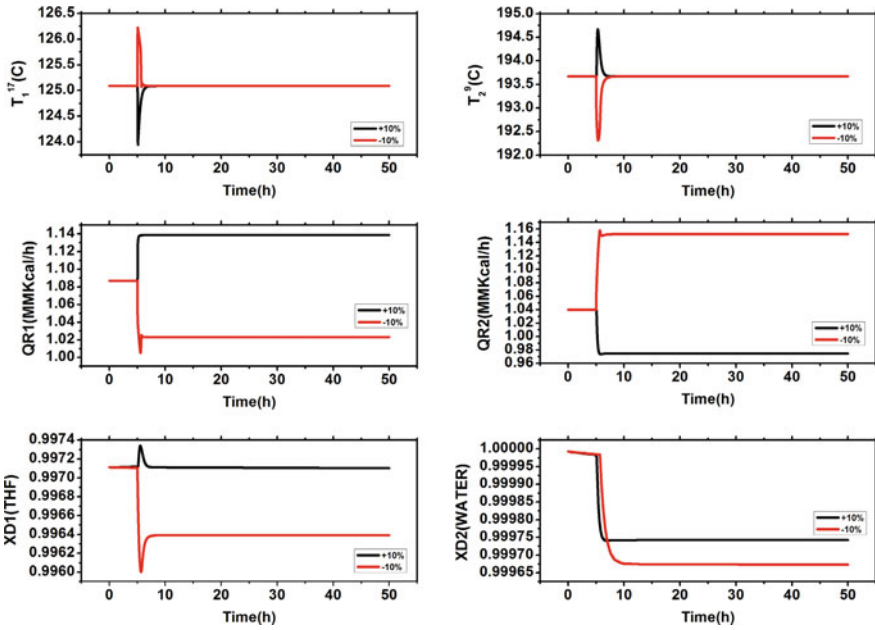
**Fig. 3** Dynamic responses for control structure: ±10% feed flow rate disturbances



**Fig. 4** Dynamic responses for control structure: ±5% composition change disturbances

# 4 Conclusion

Based on the proposed steady-state design, the use of FEHEs has been appreciated in saving energy of the process to a huge extent (20.79% saving in heat duties and 1.98% in terms of TAC). The prominent feature of this work is to maintain a desired entrainer flow rate to achieve high product purities by means of an appropriate control structure. This desired flow rate of recycle stream (that is exclusively an entrainer) has been achieved by the use of Hi-Select control logic. Since the bulk p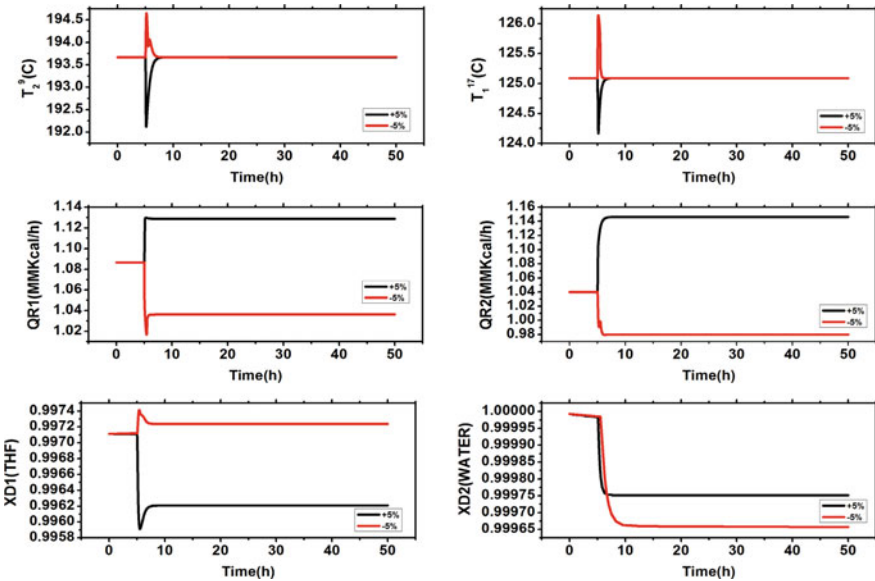ricing of entrainers has a significant effect on the economy of the process, hence an appropriate control structure leads to a decrease in overall costs of the process. This unique feature of Hi-Select control has made the process very interesting and also helps in realizing the implementation of appropriate control structure to achieve process objectives.

# References

1. Jing F, Yuqi H, Chunli L (2013) Energy-saving mechanism in heat transfer optimization of dividing wall column. Ind Eng Chem Res 52(51):18345–18355
2. Kiss AA, Flores Landaeta SJ, Infante Ferreira CA (2012) Towards energy efficient distillation technologies—making the right choice. Energy 47(1):531–542
3. Kiss AA (2014) Distillation technology—still young and full of breakthrough opportunities. J Chem Technol Biotechnol 89(4):479–498
4. Jana AK (2010) Heat integrated distillation operation. Appl Energy 87(5):1477–1494
5. Smith R, Linnhoff B (1988) The design of separators in the context of the overall processes. Chem Eng Res Des 66:195–228
6. Meili A (1990) Heat pumps for distillation columns. Chem Eng Progress 60–65
7. Agrawal R (2001) Multicomponent distillation columns with partitions and multiple reboilers and condensers. Ind Eng Chem Res 40:4258–4266
8. Dunnebier G, Pantelides CC (1999) Optimal design of thermally coupled distillation columns. Ind Eng Chem Res 38:162–176
9. De Rijke A (2007) Development of a concentric internally heat integrated distillation column. Ph.D. thesis, Technische Universiteit Delft, Delft, The Netherlands
10. Douglas JM (1988) Conceptual design of chemical processes. McGraw Hill
11. Chen YH, Yu CC (2003) Design and control of heat integrated reactors. Ind Eng Chem Res 42:2791–2808
12. Luyben WL (2001) Effect of design and kinetic parameters on the control of cooled tubular reactor systems. Ind Eng Chem Res 40:3623–3633
13. Chen YH, Yu CC (2000) Interaction between thermal efficiency and dynamic controllability for heat integrated reactors. Comput Chem Eng 24:1077–1082
14. Iqbal A, Ahmad SA, Ojasvi (2017) Entrainer based economical design and plantwide control study for Tetrahydrofuran/Water separation process. Chem Eng Res Des 130:274–283
15. Turton R, Bailie RC, Whiting WB, Shaeiwitz JA, Bhattacharyya D (2001) Analysis, synthesis, and design of chemical processes, 3rd edn. Prentice Hall

# Thermodynamic Analysis of an Integrated Gasification Fuel Cell-Combined Cycle Power Plant Using Indian Coal

A. Pruthvi Deep, Ashutosh Jena and Sujit Karmakar

**Abstract**  In the present study, a detailed thermodynamic analysis of an integrated gasification fuel cell-combined cycle (IGFC-CC) power plant is carried out wherein gasification technology is coupled with solid oxide fuel cell (SOFC) with Brayton and Rankine cycles as bottoming cycles. The proposed power plant is modelled and simulated using a computer flowsheet program called 'Cycle-Tempo'. The thermodynamic analysis of the cycle with Indian coal as fuel suggests that the steam at higher temperature coming out from the exit of an anode of the SOFC can be used as a potential source for the endothermic gasification reactions in the gasifier. Steam with a flow rate of about 5.43 kg/s extracted from the anode exhaust of SOFC is supplied to the gasifier. The variations of syngas compositions, $H_2/CO$ ratios and heating values of syngas with different steam–fuel ratios (SFR) at different gasifier reaction temperatures among three different commercially available gasifiers, viz. fixed bed, fluidized bed and entrained flow gasifiers have been presented in the results. With an increase in SFR, it has been observed that the $H_2$ composition in the syngas increases, whereas the heating value of the syngas decreases. With an increase in SFR from 0.1 to 0.7 at gasifier reaction temperature of 800 °C, $H_2/CO$ ratio has increased from 0.613 to 1.707, whereas at 1300 °C, this ratio has increased from 0.46 to 0.95 since lower temperatures favour steam reforming reaction. The net overall plant energy and exergy efficiencies are observed to be maximum in case of entrained flow gasifier with SFR of 0.7 and the values are 46.55% (HHV basis) and 42.65%, respectively. The exergy analysis of the plant indicates that the maximum exergy destruction takes place in the gasifier component with a value of 24.85% suggesting a detailed study for its design optimization.

**Keywords**  Gasification · Solid oxide fuel cell · Combined cycle · Carbon conversion efficiency · Heating value · Water gas shift reactor · Exergy

A. P. Deep · A. Jena · S. Karmakar (✉)
Department of Mechanical Engineering, National Institute of Technology Durgapur, Durgapur, India
e-mail: sujitkarmakar@yahoo.com

# 1   Introduction

Indian power sector is heavily reliant on coal. As per Central Electricity Authority (CEA), coal-based power plants account for 57.31% of the total installed power capacity in India [1], and these are the major sources for emission of greenhouse gases especially carbon dioxide ($CO_2$). Hence, it is high time for planning ways to boost clean energy methods like increasing the overall plant efficiencies, utilizing renewable sources for energy production, employing clean technologies like gasification, fuel cell, $CO_2$ capture, etc.

Gasification is a process of converting carbonaceous feedstock (like coal, biomass) into synthetic gas (syngas) using a gasifying medium (steam with air/oxygen) and heat. It has a great advantage of producing low emissions because fuel gas (syngas) cleanup is more effective and economical when compared to large-volume flue gas clean up after combustion in conventional power plants. The three majorly used commercial gasifiers are fixed bed, fluidized bed, and entrained flow gasifiers. The typical operating temperatures are 800–1200 °C for fixed bed, around 1000 °C for fluidized bed and 1300–1800 °C for entrained flow gasifiers [2]. The hydrogen produced during gasification is considered as the best alternative to fossil fuels in the near future. It is also worth mentioning the importance of biomass in the renewable energy sector which is widely spread throughout the world. When biomass is produced at the same rate equivalent to its consumption, the $CO_2$ emissions produced when biomass is used as fuel can be considered to be almost zero since the amount of $CO_2$ emitted during its energy conversion process is almost same as that of its absorption during photosynthesis of plant life. Therefore, biomass is a promising energy source to bring down the harmful emissions into the environment [3].
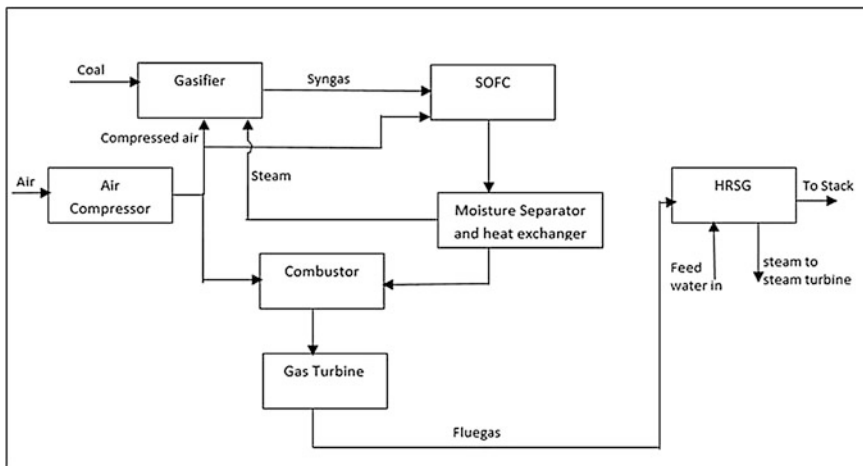


**Fig. 1**  Block diagram of IGFC-CC plant

Fuel cells are devices that can directly convert the chemical energy of fuel into electrical energy. Most often, hydrogen is used as the fuel in fuel cells. Practically, it produces no harmful emissions since the reaction product is water/water vapour depending upon low-temperature or high-temperature fuel cells. In addition, many literatures have suggested that direct conversion of chemical energy into electrical energy reduces energy as well as exergy losses when compared to that of conventional power plants operating on Brayton or Rankine cycles. Hence, these fuel cells are considered to be the pioneers in the clean energy generation [4].

Integration of the above said technologies to the conventional power plants appears to be promising with respect to improving efficiencies of the plants, reducing harmful emissions into the environment (Fig. 1). The exergy analysis of power plants with SOFC indicates high-efficiency improvements due to electrochemical conversion of fuel at solid oxide fuel cell (SOFC) rather than combustion [5–8]. Existing integrated gasification combined cycle (IGCC) power plants (coal/biomass based) are suggested that they can be operated without major plant modifications and relatively high efficiencies of more than 40% (LHV basis) by retrofitting with SOFC. Samiran et al. [9] suggest that the production of syngas in a gasifier depends on various parameters like steam to biomass ratio (S/B), temperature and biomass feed rate. Increasing the values of these parameters will increase syngas yield and reduce formation of tar as well. Moreover, the high operating temperatures of SOFC can be used as a potential source for the endothermic reactions occurring in the gasifier, instead of partial burning of the coal during the initial stages of gasification. Hence, the ways of transferring heat from SOFC to gasifier with minimum energy losses are being studied. Athanasiou et al. [10] suggest that the main concern with the integration of fuel cell technology in thermochemical processes conversion is the sufficient heat energy production in the cell in order to cover the thermal requirements of the thermochemical conversion in gasifier. From the thermodynamic analysis of the integrated process of gasification coupled with the SOFC, it has been observed that the overall heat generated can accommodate the heat demands of the reforming procedure and furthermore, the cathode outlet of the cell can be directly fed to the gasifier. The study of Grol [11] demonstrates that IGFC-CC plant has water consumption benefits as compared to that of an IGCC as power obtained from steam cycle in IGCC plant is more to that of an IGFC-CC plant.

## 2 Plant Description

Figure 2 shows the schematic diagram of IGFC-CC plant consisting of a gasifier with Indian coal as a feed stock. The different commercially available gasifiers, viz. fixed bed, fluidized bed, entrained flow gasifiers are modelled separately. The syngas from the gasifier which mainly comprises of carbon monoxide (CO) and Hydrogen ($H_2$) then undergoes high-temperature gas cleaning process to remove impurities like sulphides and fly ash before reaching the SOFC. Even though low-temperature gas cleaning process is widely used, it results in large exergy
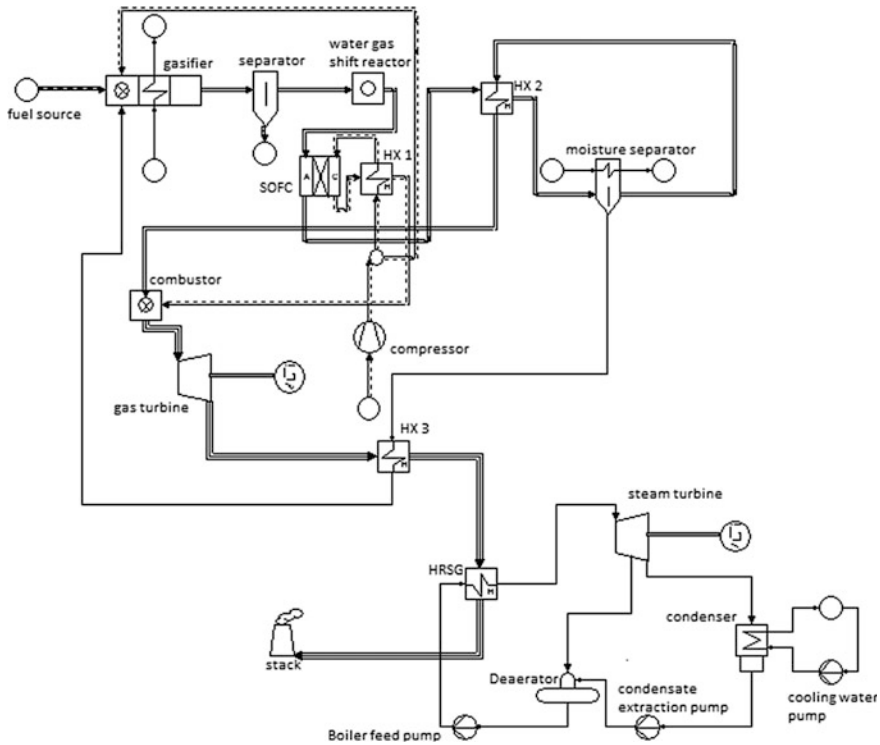
**Fig. 2** Schematic diagram of IGFC-CC plant

losses since the hot syngas from the gasifier is cooled to temperatures around 120 °
C [5]; hence, it is preferable to go for high-temperature gas cleaning which requires
proper study to develop materials to withstand high temperatures like ceramic
filters. The syngas after passing through the separator undergoes water–gas shift
reaction in the reactor. During this reaction, CO in the syngas reacts with steam to
form $CO_2$ and $H_2$; thereby increasing the concentration of $H_2$ in the syngas, which
eventually is helpful in increasing the power generation from SOFC. Also the
capturing of high concentration of $CO_2$ from this small volume of syngas under
pressure of 6 bar is relatively easy and economical compared to the $CO_2$ capturing
from large volume of flue gas after combustion. The syngas then reaches the anode
side of SOFC while air is being supplied at its cathode side. The $H_2$ in the syngas is
oxidized and the liberated electrons then are passed through some external load to
deliver power. At the cathode side, oxygen is reduced, the oxygen ions thus formed
pass through the electrolyte and reach the anode side where they combine with
hydrogen ions to form water. Since SOFC operates at very high temperature
(850 °C), the water vapour formed at the anode side can be used as a gasifying
agent instead of using separate water source at the gasifier. For this purpose, the
anode exhaust is passed through a moisture separator where the syngas is cooled to

a temperature below to that of the saturation temperature of the water vapour at that condition. Prior to this, the hot syngas coming out from the anode side is passed through a heat exchanger (HX 2) wherein, the heat extracted from it is utilized to again raise the temperature of the gas coming out from the moisture separator. In this way, the heat released during cooling down of the syngas to remove moisture is utilized to increase the enthalpy of the syngas before reaching the combustor of the gas turbine cycle. On the other hand, the cathode exhaust from SOFC is passed through a heat exchanger (HX 1) in order to heat the air reaching the cathode inlet side and eventually reaches the combustor of the gas turbine cycle. After the combustion, the hot flue gases from the combustor gets expanded in the gas turbine thus producing mechanical work. The hot flue gas from the gas turbine is passed through a heat exchanger (HX 3) to raise the temperature of the condensate from the moisture separator. This increase in temperature of the steam does have an effect on the gasification process since the important reactions like water–gas reaction is endothermic in nature. The hot flue gas then passes through the heat recovery steam generator (HRSG) in which the water from the feed pump is converted into steam at higher enthalpy, which then expands in the steam turbine to generate mechanical work output. The thermodynamic analysis of this entire proposed IGFC-CC plant is done using a flow sheet computer program called Cycle-Tempo [12]. The plant description is represented using a block diagram as shown in Fig. 1.

# 3   Assumptions

The thermodynamic analysis of the proposed IGFC-CC plant is done considering the following assumptions:

(a) **Operating temperatures of the gasifier for**:

   (i)   Fixed bed: 800 °C
   (ii)  Fluidized bed: 1000 °C
   (iii) Entrained flow gasifier: 1300 °C

(b) **SOFC**:

   (i)   The temperature at which electrochemical reaction occurs is 850 °C
   (ii)  Cell voltage of 0.8 V
   (iii) Fuel utilization factor of 0.85

(c) **Gas turbine cycle**:

   (i)   Pressure ratio: 6 bar
   (ii)  The combustion chamber reaction temperature: 1000 °C
   (iii) Pressure at the exhaust of the turbine: 1.01 bar

**Table 1** Composition of Indian coal

|  | As received basis (wt%) | As dry basis (wt%) |
|---|---|---|
| *Proximate Analysis* |  |  |
| Fixed carbon | 24.00 | 27.27 |
| Volatile Matter | 21.00 | 23.86 |
| Ash | 43.00 | 48.87 |
| Moisture | 12.00 | – |
| *Ultimate Analysis* |  |  |
| Carbon | 34.46 | 39.16 |
| Hydrogen | 2.43 | 2.76 |
| Oxygen (by difference) | 6.97 | 7.92 |
| Nitrogen | 0.69 | 0.78 |
| Sulphur | 0.45 | 0.51 |
| Ash | 43.00 | 48.87 |
| LHV (MJ/kg) | 13.14 | 15.23 |
| HHV (MJ/kg) | 13.96 | 15.83 |

(d) **Steam turbine cycle**:

    (i)   Inlet pressure and temperature at the turbine: 25 bar and 275 °C,
    (ii)  Bled steam pressure: 3 bar
    (iii) Condenser pressure: 10 kPa

(e) The composition of Indian coal considered and its heating values are shown in Table 1 [13].

## 4 Results and Discussion

The SFR values are varied for different gasifiers and their influence on the syngas compositions, $H_2$/CO ratios, net overall plant energy and exergy efficiencies are discussed in the present study. SFR is varied from 0.1 to 0.7 at the operating temperatures of 800, 1000 and 1300 °C for fixed bed, fluidized bed and entrained flow gasifiers, respectively. The syngas composition with main constituents at the outlet of each gasifier is shown in Table 2.

The graph plotted for $H_2$ (in mole fraction) versus SFR for three different gasifiers in Fig. 3 illustrates an increase in the production of $H_2$ with increase in SFR. The slope of the curves tends to decrease with increase in SFR, which suggests that the raise in $H_2$ production is more during increments of SFR from 0.1 to 0.3. However, with SFR being varied from 0.5 to 0.7, there is a little increment in $H_2$ synthesis. On the other hand, CO production decreases with increase in SFR.

**Table 2** Syngas composition at the outlet of gasifiers

| Component (mole fraction) | IGFC-CC type with varying SFR | | | | | | | | | | | |
| | IGFC-CC with fixed bed gasifier | | | | IGFC-CC with fluidized bed gasifier | | | | IGFC-CC with entrained flow gasifier | | | |
| | 0.1 | 0.3 | 0.5 | 0.7 | 0.1 | 0.3 | 0.5 | 0.7 | 0.1 | 0.3 | 0.5 | 0.7 |
|---|---|---|---|---|---|---|---|---|---|---|---|---|
| $H_2$ | 0.1169 | 0.1405 | 0.1513 | 0.1552 | 0.1095 | 0.1268 | 0.1348 | 0.1379 | 0.0989 | 0.1121 | 0.1183 | 0.1208 |
| $N_2$ | 0.6215 | 0.6196 | 0.627 | 0.6388 | 0.6299 | 0.6338 | 0.6438 | 0.6562 | 0.6405 | 0.6486 | 0.6604 | 0.6733 |
| $CO_2$ | 0.0693 | 0.0951 | 0.1083 | 0.1147 | 0.0564 | 0.0781 | 0.0898 | 0.0960 | 0.0458 | 0.0633 | 0.0732 | 0.0789 |
| $CH_4$ | 0.0019 | 0.0011 | 0.0007 | 0.0004 | 0.0000 | 0.0000 | 0.0000 | 0.0000 | 0.0000 | 0.0000 | 0.0000 | 0.0000 |
| CO | 0.1904 | 0.1437 | 0.1127 | 0.0909 | 0.2042 | 0.1613 | 0.1316 | 0.1099 | 0.2148 | 0.1760 | 0.1481 | 0.1270 |
| Higher Heating Value (HHV) in $MJ/m^3$ | 4.80 | 4.56 | 4.36 | 4.20 | 4.86 | 4.62 | 4.42 | 4.25 | 4.88 | 4.65 | 4.46 | 4.29 |

**Fig. 3** Variation of $H_2$
synthesis versus SFR for
different gasifiers
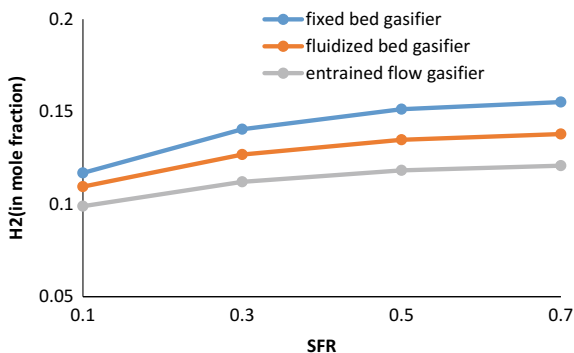


This can be attributed to the steam reforming reaction wherein CO reacts with $H_2O$ to form $CO_2$ and $H_2$. This conversion ratio for gasification temperatures of 800, 1000 and 1300 °C is expressed in the form of $H_2/CO$, which is shown in Fig. 4. It is observed that at gasification temperature of 800 °C, $H_2/CO$ ratios are more when compared to that of 1300 °C since steam reforming reaction favours the products at lower temperatures as it is exothermic in nature.

Since the syngas produced from the gasifier is sent to SOFC for power generation, it is preferable to choose parameters such that the amount of $H_2$ constitutes more in syngas since it is this hydrogen that gets oxidized resulting in liberation of more numbers of electrons thus resulting in the production of more power at SOFC. The heating value of syngas is observed to be decreasing with increase in SFR, and this may be attributed to the fact that the temperature of the gasifying agent is lower when compared to that of core reacting temperature of the gasifier. Hence, when more steam is sent to the gasifier (i.e. increase in SFR), the core reaction temperature of the gasifier starts decreasing which results in lower heating value gases being produced.

The net overall plant energy efficiency (HHV basis) and exergy efficiency of the proposed IGFC-CC with three different gasifiers having SFR = 0.7, gasifying agent temperature of 180 °C are shown in Figs. 5 and 6.

**Fig. 4** Variation of $H_2/CO$
ratio versus SFR for different
gasifiers
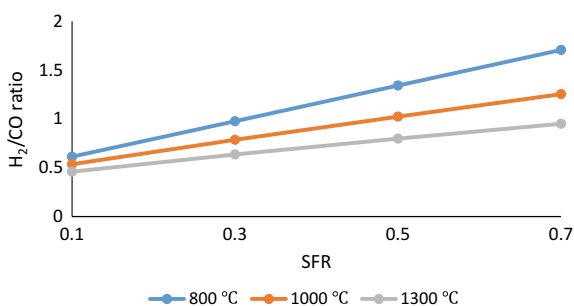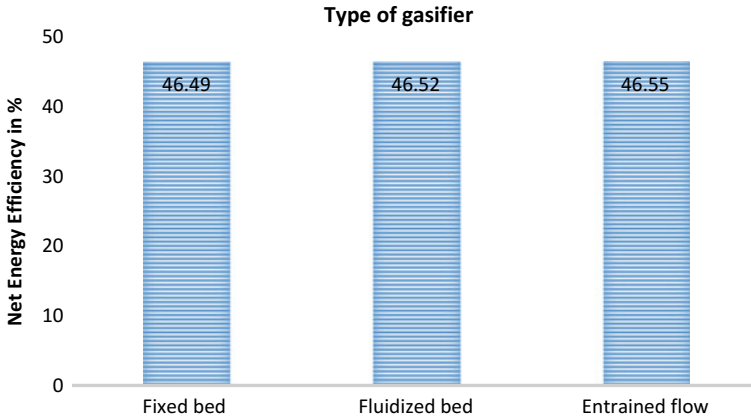
**Fig. 5** Comparison of net plant energy efficiency with different gasifiers
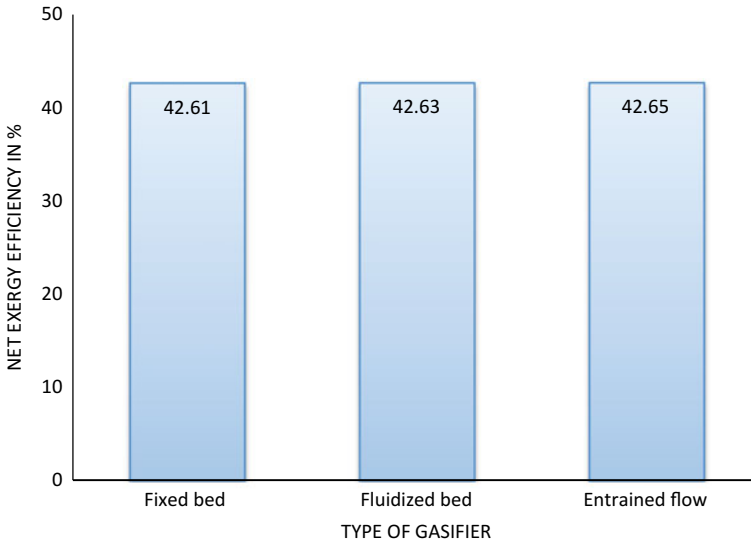


**Fig. 6** Comparison of net plant exergy efficiency with different gasifiers

It is observed from Figs. 5 and 6 that net overall plant energy, as well as exergy efficiencies are higher in case of IGFC-CC with gasifier reaction temperature of 1300 °C (i.e. entrained flow gasifier) when compared to that of IGFC-CC with gasifier reaction temperatures of 800 and 1000 °C (i.e. fixed and fluidized bed gasifiers).

Considering IGFC-CC with entrained flow gasifier, the delivered power contributed by SOFC is 40 MW, the gas turbine is 30.8 MW and by the steam turbine

**Table 3** Energy balance of IGFC-CC with entrained flow gasifier having SFR = 0.7

| Components | Energy balance (%) |
|---|---|
| Power obtained from the plant (efficiency of the plant) | 46.55 |
| Heat rejected through cooling water at condenser and moisture separator | 31.8 |
| Heat rejected through the stack | 11.9 |
| Heat rejected through separated components at the separator | 4.25 |
| Other losses (by difference) | 5.5 |

**Table 4** Exergy balance of IGFC-CC with entrained flow gasifier having SFR = 0.7

| Components | Exergy balance (%) |
|---|---|
| Power (exergy efficiency of the system) | 42.65 |
| Loss in gasifier | 24.85 |
| Loss in heat exchanger (HX) 3 | 4.14 |
| Loss in HX 1 | 3.98 |
| Loss through cooling water at condenser and moisture separator | 3.73 |
| Loss through combustor | 3.18 |
| Loss through stack | 3.18 |
| Loss through separator | 2.50 |
| Loss through gas turbine | 2.41 |
| Loss through HX 2 | 2.08 |
| Loss through Fuel cell | 1.57 |
| Other losses (by difference) | 5.73 |

is 5 MW with auxiliary power consumption of 18.58 MW. Thus, the net power obtained is 57.21 MW. The majority of power is obtained from SOFC followed by the gas turbine and then the steam turbine. One of the major advantages of this combined cycle power plant being a reduction of the huge quantity of water consumption by the Rankine cycle since the power delivered from steam turbine accounts to only 8.7% of the net power delivered.

Tables 3 and 4 show the energy balance and exergy balance of the plant, respectively, wherein the energy losses are calculated as the ratio of energy rejected at a component to the energy input through fuel source for the plant and exergy losses are calculated as the ratio of irreversibility to the exergy input through fuel [13].

It is observed from Table 3 that majority of the energy loss occurs at condenser and moisture separator through cooling water. But from exergy analysis shown in Table 4, it can be seen that the loss of energy through cooling water is of low grade when compared to that of major exergy destruction occurring at the gasifier (i.e. 24.85%) which suggests for its design optimization. Results of the similar trend are also obtained for the fixed bed and fluidized bed gasifiers.

# 5    Conclusions

The present study of thermodynamic analysis of an integrated gasification fuel cell-combined cycle power plant (IGFC-CC) using Indian coal shows the influence of SFR, gasifier reaction temperature on the syngas composition, $H_2/CO$ ratio, heating value of the syngas. As the majority of the delivered power of the overall plant is contributed by the SOFC, it is essential to choose the operating parameters of the gasifier in such a way that $H_2$ composition is more in syngas which implies more power from SOFC. The net overall plant energy efficiency for the IGFC-CC power plant with entrained flow gasifier having SFR = 0.7 is found to be about 46.55% (HHV basis) which is superior to the same capacity conventional coal-fired power plants. The moisture present in the hot exhaust of the SOFC anode is separated and supplied as a gasifying agent with a flow rate of 5.43 kg/s. The exergy analysis suggests that a detailed investigation on reaction kinetics is necessary for finding ways to reduce exergy losses contributed by different reactions during gasification apart from physical exergy losses which account for major exergy loss in the plant.

# References

1. Central Electricity Authority (CEA), Ministry of Power, Government of India. http://www.cea.nic.in/reports/monthly/installedcapacity/2018/installed_capacity-03.pdf. Last accessed 2018/06/12
2. Khartchenko NV, Kharchenko VM (2013) Advanced energy systems, 2nd edn. CRC Press
3. Din ZU, Zainal ZA (2016) Biomass integrated gasification-SOFC systems: technology overview. Renew Sustain Energy Rev 53:1356–1376
4. Stambouli AB (2011) Fuel cells: the expectations for an environmental-friendly and sustainable source of energy. Renew Sustain Energy Rev 15(9):4507–4520
5. Thattai AT, Oldenbroek V, Schoenmakers L, Woudstra T, Aravind PV (2017) Towards retrofitting integrated gasification combined cycle (IGCC) power plants with solid oxide fuel cells (SOFC) and $CO_2$ capture—a thermodynamic case study. Appl Therm Eng 114:170–185
6. Welaya YMA, Mosleh M, Ammar NR (2013) Thermodynamic analysis of a combined gas turbine power plant with a solid oxide fuel cell for marine applications. Int J Naval Architect Ocean Eng 5(4):529–545
7. Ali OH, Hossein G, Hooman F (2013) Energy efficiency improvement analysis considering environmental aspects in regard to biomass gasification PSOFC/GT Power Generation System. Procedia Environ Sci 17:831–841
8. Sakai N, Yamaji K, Horita T, Xiong YP, Kishimoto H, Yokokawa H (2003) Effect of water on oxygen transport properties on electrolyte surface in SOFCs I. Surface reaction mechanism of oxygen isotope exchange on solid oxide electrolytes. J Electro Chem Soc 150(6):689–694
9. Samiran NA, Jaafar MNBM, Tung CC, Jo-Han N (2014) A review of biomass gasification technology to produce syngas. Am Eurasian J Sustain Agric 8(7):69–74
10. Athanasiou C, Couteliers F, Vakouftsi E, Skoulou V, Antonakou E, Marnellos G, Zabaniotou A (2007) From biomass to electricity through integrated gasification/SOFC system-optimization and energy balance. Int J Hydrogen Energy 32(3):337–342

11. Grol E (2009) Technical assessment of an integrated gasification fuel cell combined cycle with carbon capture. Energy Procedia 1:4307–4313
12. Cycle-Tempo release 5.0, Delft University of Technology (2008)
13. Kalimuthu S, Karmakar S, Kolar AK (2017) 3-E Analysis of a pressurized pulverized combined cycle (PPCC) power plant using high ash Indian coal. Energy 128:634–648

# Numerical Study of TiO$_2$ Nanofluid in Multistage-Bifurcated Microchannel Subjected to Hotspots

**Amit Kumar, G. Narendran and D. Arumuga Perumal**

**Abstract** The present study discusses implementation of multiple passive structures along the flow length using TiO$_2$ nanofluid with 0.1% volume fraction to analyze a multistage-bifurcated microchannel. Fully developed laminar flow for different multistage plate configurations is used for the computational study, and additional investigations were done to evaluate pressure drop for Reynolds Number ranging from 250 to 500. Two different heat fluxes have been used: 4000 W/cm$^2$ given for hotspot area and 1000 W/cm$^2$ for the entire heat sink. Furthermore, the influence of flow rate on bifurcation stages combined with hotspot is highly investigated. Also, the pressure drop, temperature distribution, and flow streamlines are studied to evaluate cooling performance.

**Keywords** MEMS · Nanofluid · Microchannel · Bifurcation · Hotspot

## 1 Introduction

The rapid advances and miniaturization in electronic devices have motivated electronic industries to make very compact devices of microscale to get the desired performance with enhanced efficiency. As an outcome, electronic chips are dissipating excess amount of heat from surfaces in the range of 10$^2$–10$^6$ W/cm$^2$ [1]. In the compact designing of these electronic components, proper cooling techniques are required to ensure reliability and avoid any failures. Since, more fresh gases are required to cool these microprocessor chips which in turn take a large pumping power and large space making system oversized. So, to overcome all these problems, Tuckerman and Pease [2] first initiated microchannels heat sink using water as a base fluid for efficient cooling and to give thermal balance to the system. He used rectangular microchannels heat sinks made of silicon material having high

A. Kumar · G. Narendran · D. A. Perumal (✉)
Department of Mechanical Engineering, NITK Surathkal, Mangalore 575025, Karnataka, India
e-mail: Perumal.iit@gmail.com

thermal conductivity. Maximum substrate temperature reached up to 71 °C with high penalty in pressure drop of 214 kPa corresponding to a heat flux of 790 W/ cm$^2$. The cooling took place mainly by forced convection. In the course of recent decades, numerous investigations have focused on the conduct of heat exchange and liquid flow in microchannel heat sinks with various cross-sections [3, 4].

In addition, for efficient heat removal, different flow streams were fabricated in a different configuration, and thus improved thermal performance was achieved for microchannels heat sinks. A numerical investigation on wavy microchannels of a rectangular cross-section in three-dimensional shapes was performed by Sui et al. [5]. He concluded that heat transfer performance was higher and uniform temperature of walls was obtained with smaller penalty in pressure drop. Furthermore, longitudinal and transversal wavy microchannels were designed by Xie et al. [6, 7] for laminar flow and enhancement of heat transfer under hotspots. They observed superior thermal performance for higher amplitude wavy microchannel.

Also, Khoshvaght-Aliabadi [8] investigated the effect of different volume concentrations of $Al_2O_3$ nanoparticles in $Al_2O_3$–water nanofluid in wavy microchannel of varying amplitudes. Han et al. [9] experimentally investigated hotspots cooling using microchannel heat sinks made of gallium nitride (GaN) and accompanied with diamond heat spreader. They used 8 microheaters to develop hotspots in the range of 10–50 W. Maximum temperature was reduced by 22.9% using diamond heat spreader. Similar experimentation using copper heat spreader was investigated by Narendran et al. [10]. They reported that by implementing a thin heat spreader with microchannel considerably reduced flow-induced hotspots.

It has been perceived that heat transfer may be augmented by bifurcation flow (where multiple downstream flow parts are achieved due to splitting of flow) due to redevelopment boundary layers. In this case, transport of fluid looks like "Y" diagram [11]. Various constructal designs are established for microchannels to augment the heat transfer by introducing multi-scale pins or structures [12], multi-scale plate length, and "Y" or "T" structures [13] along the flow by making boundary layers thinner and thinner. Wang et al. [14] designed leaf-like branching and tree-like branching for electronic cooling application in order to overcome high pressure drop. Results showed better stability along with more uniform temperature distribution which is lower than the traditional one. Liu et al. [15] experimentally and numerically investigated "T-Y" joint bifurcation using gallium lanthanide tin coolant for heat transfer enhancement for a heat flux in the range of $10^6$ W/cm$^2$ only 27 K temperature difference was observed.

Despite the fact that there are a few papers about bifurcated channels are accessible, only a few pieces of research have been focused on cooling fluid such as nanofluid through the bifurcated channels and using hotspots at some specific locations. For this present study, the first five cases are taken with bifurcation mostly occurring near the outlet region and temperature contours are validated through the results obtained from Xie et al. [16] work. Out of the five cases, best one is taken, i.e., Case 2B, and the extended investigation is performed by adding hotspots of $0.125 \times 0.125$ mm$^2$ area which is located at three different positions

along the channel length which was not investigated in the previous study. The plate's arrangement resembles "Y" structures, and hotspots are located at three different positions with two types of fluids flowing through multistage plates: One is pure water and other is 0.10 vol. % TiO$_2$ nanofluids.

Computational fluid dynamics (CFD) is used for numerical investigation of laminar fluid flow and thermal performance of three-dimensional-bifurcated microchannel with multistage structures induced with hotspots. This study mainly focuses on the effects of hotspots and multistage bifurcated structures on the thermal execution of microchannel heat sinks.

## 2 Representation of the Different Heat Sinks with Hotspots

### 2.1 Microchannel Heat Sinks Without Structures

For the practical application use, 100 microchannels are designed in a silicon substrate of bottom area $35 \times 35$ mm$^2$ ($L \times W$). However, a single microchannel is taken for computational domain to reduce the computational time and grid size, due to their symmetric structures as shown in Fig. 1a. The geometric dimensions of single rectangular channel are as follows: $W_c$ is 315 µm; $H_c$ is 400 µm; $T_w$ is 35 µm; and measurement of $T_s$ and $T_{cp}$ is 50 µm, where $W_c$ is width of the channel, $H_c$ is height of the channel, $T_w$ is wall thickness, $T_s$ is substrate thickness, and $T_{cp}$ is the cover plate thickness. Total height of heat sinks is 500 µm. Figure 1b manifest cross-sectional view of heat sinks without bifurcation which is used for computational domain and in both left and right walls, and $T_w/2 = 17.5$ µm is taken. The
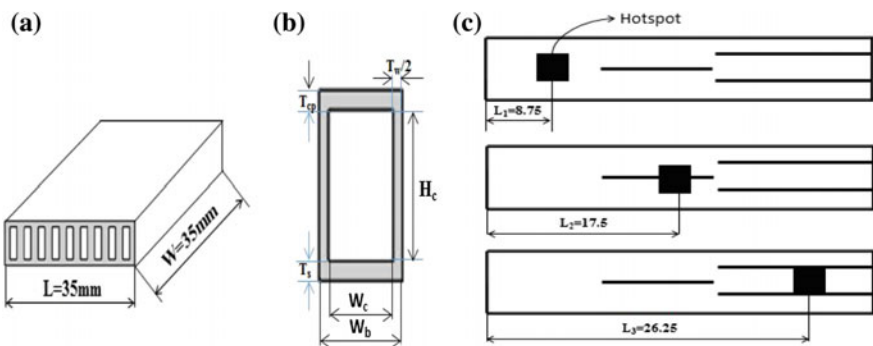


**Fig. 1** **a** 3D simplified diagram of rectangular microchannel heat sinks; **b** the cross-sectional view of single microchannel used for computational domain; **c** microchannel heat sink of case 2B subjected to hotspot at three different locations along the length of the channel

performance evaluation of microchannels for cases 1–3 are added with plates of variable lengths and compared with the heat sinks without bifurcation mentioned as case 0.

## 2.2 Microchannel Heat Sinks with Multistage Structures

Based on the previous investigation, many researchers suggest that if bifurcation stages are designed properly, then desired thermal performances may be achieved. Keeping this in mind the multistage bifurcated microchannel is designed by placing multiple plates along the channel by Xie et al. [16]. They investigated to enhance thermal performance by varying number of bifurcation stage and plate length. Five cases with bifurcation plates used are shown in Fig. 2 with different lengths.

## 2.3 Microchannel Heat Sinks Subjected to Hotspots

For this study, best case according to thermal performance and lower pressure drop after optimization is Case 2B. The investigation is performed in case 2B which is second stage bifurcation. The hotspots were introduced along the flow length at three different locations with a footprint area of $0.125 \times 0.125$ mm$^2$ at bottom surface of the sink. The first location is set at 8.75 mm along the flow length, second at a distance of 17.5 mm, and the third hotspot is positioned at 26.25 mm. Three locations of hotspots are shown in Fig. 1c.
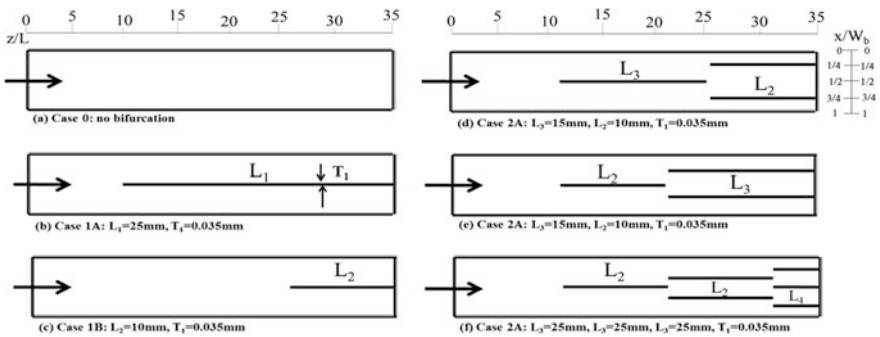


**Fig. 2** Cross-sectional view of a single microchannel with or without various stages of bifurcation. Width, length, and thickness are in mm

## 3 Governing Equations and Boundary Conditions

Silicon is used as a material for the fabrication of integrated circuit chips because it reduces the thermal stresses developed due to high temperature.
Continuity equation:

$$\nabla.(\rho u) = 0 \tag{1}$$

Momentum equation:

$$(u.\nabla)\rho u = -\nabla p + \mu \nabla^2 u \tag{2}$$

Energy equation:

$$u.\nabla T = \frac{k}{\rho C_p} \nabla^2 T \tag{3}$$

Energy equation in solid domain is given by:

$$\nabla^2 T = 0 \tag{4}$$

For this validation study, a uniform heat flux is given to the bottom of the wall. The top and outer surfaces of side walls are assumed to be insulated and no slip cond. is given to all the walls.

## 4 Computational Study

### 4.1 Grid Independence Study

The grid framework utilized in the numerical analysis has 795,682 elements in the x-, y-, and z-directions. The affectability of the numerical outcomes is checked with four different grids 580,299, 695,688, 795,682, and 835,692 elements, respectively. The outcomes from the last two grids are near to each other as indicated in Fig. 3a. Considering less computational time and assets that are needed for performing the simulation, the second grid system is utilized in the present work. For grid independence study, temperature and length of the channel are taken.

### 4.2 Validation Study

The created single computational model is validated with Xie et al. [16] work by taking temperature distribution on the bottom surface where uniform heat flux of
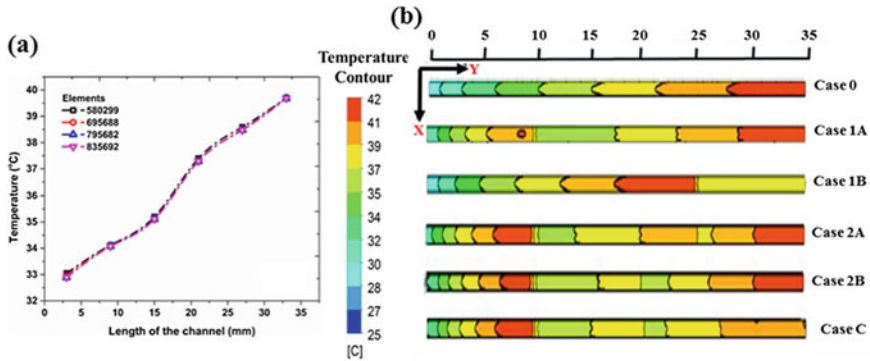
**Fig. 3** **a** Temperature along the length of the channel; **b** contours of temperature distribution from present work on the bottom surface for all the cases

24.50 W/cm$^2$ is given in all the six cases for inlet velocity of 0.8 m/s, i.e., inlet Reynolds number of 280 by taking water as the cooling fluid. Later, comparison analysis is done for temperature distribution on the bottom surface along with results provided by Xie et al. [16], and considerable agreement with the present work with 4% error is presented in Fig. 3b. It shows the temperature distribution on the bottom surface along the channel length of the microchannel heat sink for the simulated condition.

Figure 3b shows the temperature distributions of the bottom wall which is uniformly heated. Maximum temperature observed is 311 K in the case of the no bifurcation and thus resulting in increased thermal stresses. Maximum temperature in the case of multistage bifurcation is observed lesser than that of without bifurcation Case 0. In cases 1A to 3, low-temperature region is observed after the bifurcation stages and high temperature is observed before the bifurcation stage. Uniform temperature distribution and temperature field are observed for the cases with bifurcation stages and thus resulting in decreased thermal stresses.

## 5 Results and Discussions

### 5.1 Effect of Reynolds Number on Pressure Drop and Streamline Contours Without Hotspot

Figure 4a depicts the variation of pressure drop with inlet Reynolds number for all the six cases. In general, heat transfer enhancement occurs at high flow rates and so wall temperature decreases although a decrease in pressure drop is seen at the same time. This figure shows a linear increase in pressure drop at with inlet Reynolds number. Pressure drop is found highest for Case 3 compared to all other cases and
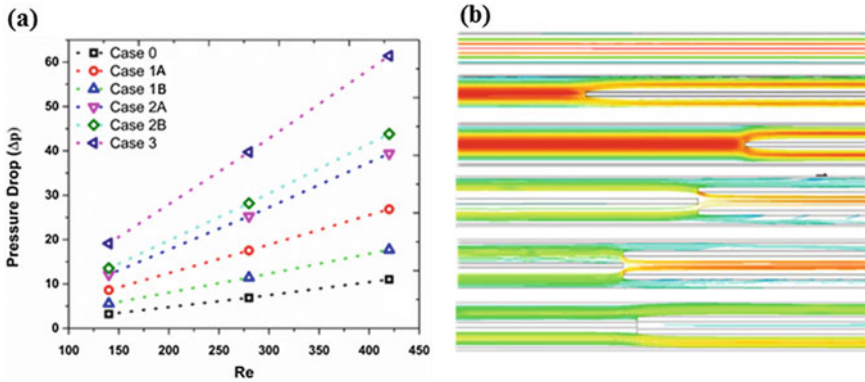
**Fig. 4** **a** Pressure drop as a function of Reynolds number; **b** streamline contours for all the six cases for inlet Reynolds number of 280

found lowest for Case 0. Largest pressure drop may happen due to decreased aspect ratio near the outlet, i.e., larger blockage. Pressure drop for single stage bifurcation near the outlet is higher for larger bifurcation length, i.e., Case 1A develops higher pressure drop than Case 1B. However, for second bifurcation stages, Case 2B, which is having smaller first-stage plate length and bigger second-stage plate length producer larger pressure drop than that of Case 2A. Case 3 has essentially biggest pressure loss due to three-stage bifurcation resulting in more blockages. Thus, further stages are not recommended to design because of larger pressure drop.

Figure 4b depicts streamline contours for all the cases for Reynolds number of 280 and a section from the middle of the microchannel. It is contemplated that disregarding the number of stages, flow is smoothly redirected along the length and is independent of maximum velocity. As bifurcation stages are increasing, the maximum velocity is also increasing because of larger flow area compared to smooth microchannel. As the flow cross-section is decreasing, local velocity is increasing in the case of multistage bifurcation. Since there is no separate flow occurring along the length, it is evident that laminar flow consideration is valid.

## 5.2 Effect of Reynolds Number and Different Heat Fluxes on Hotspot

Figure 5a depicts the effect of coolant when hotspot position is changed along the length. When the hotspot is placed near exit, for the same Reynolds number and heat flux, temperature distribution will be uniform in the case of the nanofluid because of increased thermal conductivity and enhanced heat transfer as shown in Fig. 5b. Also, with hotspot streamline velocity will be more near bifurcated plate because of density difference causing more pressure difference and hence increased
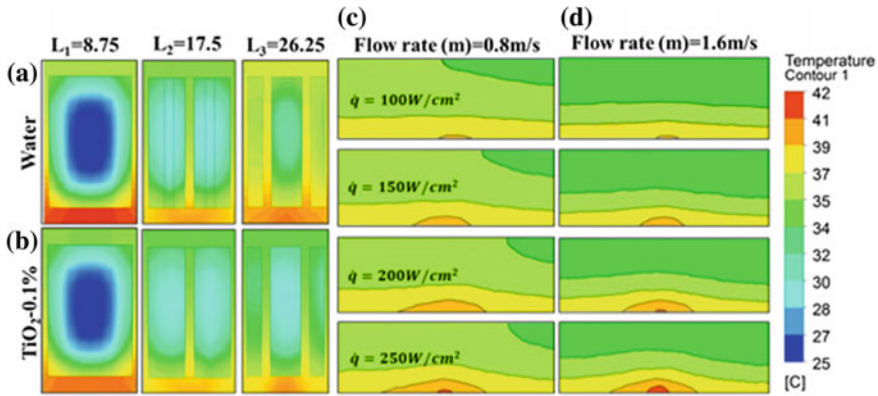
Fig. 5 **a**, **b** Temperature distribution for water and nanofluid on different locations (*L*) at same Reynolds number. **c** and **d** Effect of Reynolds number and heat flux influencing temperature distribution when the hotspot is placed at center

velocity in the vicinity of the plate. Also, Fig. 5c and d depicts about the influence of Reynolds number and different heat fluxes on the influence on walls of channel. In Fig. 5c as heat flux increases from 100 to 250 kW/cm$^2$, extent of temperature can be seen in both horizontal and vertical directions. In Fig. 5d as heat flux increases, then for fixed Reynolds number, extent of temperature is increasing only in horizontal direction and decreasing from vertical direction. Streamline contours and flow vectors in all the cases depict that the maximum velocity is found just at the outlet of the multistage channel. No flow separation and recirculation is observed in any of the cases.

## 6 Conclusions

To improve the cooling potential of bifurcated microchannel heat sinks subjected to the hotspot, numerical studies were conducted to place the hotspot of size $0.125 \times 0.125$ mm$^2$ for Case 1B along the length of the channel. The heat enhancement and fluid flow characteristics were investigated for all the three cases of bifurcated microchannel heat sinks with TiO$_2$ nanofluid and water as cooling fluid. Based on this study, the following main fundamental conclusions are drawn as:

1. The size and location of hotspot play a significant role in the thermo-hydraulic potential of microchannel heat sinks.
2. When hotspots are placed in single- and double-stage bifurcation cases it enhances the thermal performance with increased Nusselt number by 25% in the case of TiO$_2$ nanofluid which is 15% more than by using only water.

3. It is observed that for the cases of hotspot near the outlet, increased bifurcation increases the performance of the heatsink.
4. More uniform temperature distribution is obtained at the outlet wall temperature in Case 2B (b) when nanofluid is used which indirectly signifies decreased thermal stresses and increased performances.

# References

1. Mahajan R, Chiu CP, Chrysler G (2006) Cooling a microprocessor chip. Proc IEEE 94 (8):1476–1485
2. Tuckerman DB, Pease RFW (1981) High-performance heat sinking for VLSI. IEEE Electron Device Lett 2(5):126–129
3. Qu W, Mudawar I (2002) Experimental and numerical study of pressure drop and heat transfer in a single-phase micro-channel heat sink. Int J Heat Mass Transf 45(12):2549–2565
4. Hedge SS, Narendran G, Gnanasekaran N (2016) Conjugate heat transfer in hexagonal microchannels using hybrid nanofluid. In: Conference 2016, ICNMM, vol 7961. ASME, USA
5. Sui Y, Teo CJ, Lee PS, Chew YT, Shu C (2010) Fluid flow and heat transfer in wavy microchannels. Int J Heat Mass Transf 53(14):2760–2772
6. Xie G, Liu J, Zhang W, Sunden B (2012) Analysis of flow and thermal performance of a water-cooled transversal wavy microchannel heat sink for chip cooling. J Electron Packag 134 (4):41010
7. Xie G, Liu J, Liu Y, Sunden B, Zhang W (2013) Comparative study of thermal performance of longitudinal and transversal-wavy microchannel heat sinks for electronic cooling. J Electron Packag 135(2):21008
8. Khoshvaght-Aliabadi M (2017) Thermal-hydraulic characteristics of novel configurations of wavy channel: nanofluid as working fluid. Heat Transf Eng 38(16):1382–1395
9. Han Y, Lau BL, Tang G, Zhang X, Rhee DMW (2017) Si-based hybrid microcooler with multiple drainage microtrenches for high heat flux cooling. IEEE Trans Compon Packag Manuf Technol 7(2):50–57
10. Narendran G, Gnanasekaran N, Perumal DA (2018) Flow induced hotspot migration studies with heat spreader integrated microchannels using reduced graphene oxide nanofluids. In: Conference 2018, EuroSimE. IEEE, France
11. Wechsatol W, Bejan A, Lorente S (2005) Tree-shaped flow architectures: strategies for increasing optimization speed and accuracy. Numer Heat Transf Part A Appl 48(8):731–744
12. Bello-Ochende T, Meyer JP, Bejan A (2010) Constructal multi-scale pin-fins. Int J Heat Mass Transf 53(14):2773–2779
13. Lorenzini G, Rocha LAO (2009) Constructal design of T-Y assembly of fins for an optimized heat removal. Int J Heat Mass Transf 52(6):1458–1463
14. Wang XQ, Mujumdar AS, Yap C (2006) Thermal characteristics of tree-shaped microchannel nets for cooling of a rectangular heat sink. Int J Therm Sci 45(11):1103–1112
15. Liu HL, An XK, Wang CS (2017) Heat transfer performance of T-Y type micro-channel heat sink with liquid GaInSn coolant. Int J Therm Sci 120:203–219
16. Xie G, Zhang F, Sundén B, Zhang W (2014) Constructal design and thermal analysis of microchannel heat sinks with multistage bifurcations in single-phase liquid flow. Appl Therm Eng 62(2):791–802

# Flow of Ferro-Fluid in a Circular Tube Under the Influence of Magnetic Forces

**Achhaibar Singh and P. K. Rohatgi**

**Abstract** This study deals with the flow of ferro-fluid in a circular tube under the influence of a magnetic field. Ferro-fluid comprises ferromagnetic particles of small size suspended in a liquid. Magnetic force sets a motion of ferro particles that causes fluid to move due to drag between fluid and the particles. Magnetic pumping will be useful in enhancing cooling of electronic devices at the expense of small amount of energy leading to the increased life of such devices. An expression is derived for velocity profile in a circular duct. Magnetic field and magnetic force distributions are presented for a colloidal solution of 50μ iron particles suspended in water. The magnetic pressure induced is found to be significant which causes the drift of the solution.

**Keywords** Ferro-fluid · Drag · Magnetic pumping · Micro-channel

## 1 Introduction

The motion of magnetic particles suspended in a fluid has many applications such as medicines, environmental science, separation of metals, and microchannels. The present investigation focuses on the flow of a suspension of ferro-magnetic particles in fluid in a circular microchannel under the influence of a magnetic field due to current in concentric windings. The particles magnetize owing to a magnetic field and are attracted to the source of the magnetic field. This force is called magnetic force and sets the magnetized particles in motion. The moving particles drag the fluid molecules along. As a result, the fluid also starts flowing. The flowing fluid carries heat from hotter to colder sections. The ferro-fluid can be prepared as a colloidal solution of ferro particles in a solvent.

The flow of aqueous suspension of superparamagnetic beads in a microchannel driven by magnetic forces was investigated by Shevkoplyas et al. [1]. They created

A. Singh (✉) · P. K. Rohatgi
Amity University Uttar Pradesh, Noida, India
e-mail: drasingh@hotmail.com

a magnetic field with the help of an electricity-carrying metal wire. They carried out measurements of electric field and flow parameters. Their mathematical model included the effect of initial magnetization to predict the magnetic forces accurately. McKnight et al. [2] created pressure gradient in the magnetic fluid with the help of thermal and magnetic fields. Thus, a ferro-fluid pump without moving mechanical parts was developed. They synthesized magnetite nanoparticles and coupled magnetic, thermal, and fluid dynamics to predict design parameters of a ferro-fluid pump. Good agreement between finite element, experimental and theoretical results was found.

The influence of magnetic forces on micromagnetic particles suspension in a fluid has been studied by Tokura et al. [3]. Their work was focused on cell/DNA manipulation and drug delivery applications. They used flow visualization, experiment and theoretical model to investigate this problem. An appreciable higher magnetic force is required to observe the effect on microparticles. Several authors reviewed the work done in this area. Gijs et al. [4] studied the role of magnetic particles for biological applications. Pamme et al. [5] compiled research work of many researchers on magnetic detection and particles manipulation. Use of various nature of magnetic forces for the flow of fluid was discussed by Weston et al. [6]. Fisher and Ghosh [7] discussed the application of magnetism for the motion of suspended particles. They explained how micro- and nanostructures of magnetic particles of non-conventional shapes can be controlled using an external magnetic force. Weddemann et al. [8] discussed the manipulation and detection of magnetic beads for biomedical applications. Ganguly and Puri [9] studied the flow of magnetic particles and ferro-fluid in biomedical devices. Friedman and Yellen [10] presented a simple method for analysis of magnetic force for magnetic separation, manipulation, and assembly. The eutrophication control of waters with the help of magnetic forces has been studied by Martos et al. [11]. They removed phosphorus molecules from water by using magnetic material as seeding adsorbent of phosphorus molecules. The magnetic particles along with the phosphorous molecules are removed from water by high gradient magnetic separation. The majority of researchers have focused their investigation on the flow of ferro-fluid under the influence of transverse magnetic field. The present study is aimed at the prediction of the velocity of colloidal suspension due to a magnetic field in the direction of flow.

## 2 Theoretical Models

### 2.1 Magnetic Field and Magnetic Force

Figure 1 shows the flow of a colloidal suspension of iron particles in water flowing in a tube. The electromagnetic field is applied by passing an electric current in the coils wounded on a small length of the tube. When current flows in the coil,
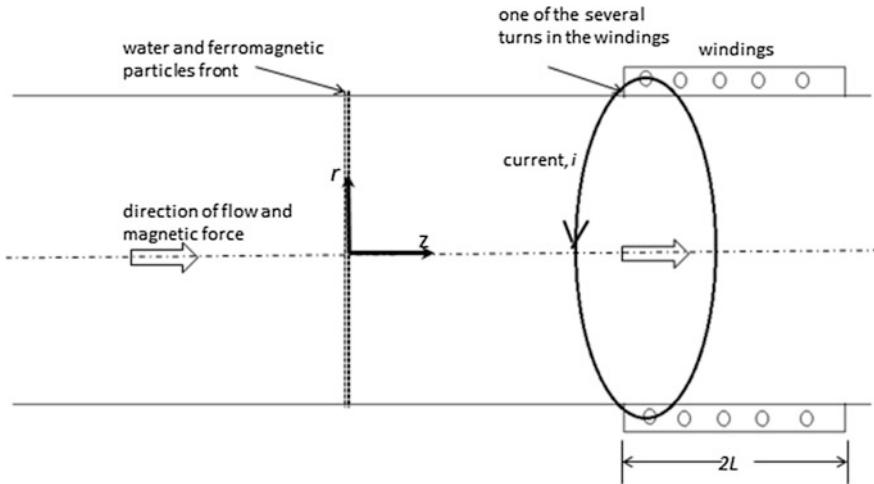
**Fig. 1** Geometry and coordinate system

a magnetic field develops that magnetizes solid particles. The magnetized particles are pulled toward the coil and move toward the windings. The moving particles drag the fluid molecules along and the whole suspension starts moving.

The magnetic field due to a current in a coil at the axis of the tube will have two components—one in radial direction and other in axial direction. It is assumed that the diameter of the pipe is small as compared to the length of the coil. The magnetic field is assumed to be the same at all points in a cross section of the tube. The radial component of the magnetic field vanishes due to rotational symmetry. However, there is a net axial magnetic field at the axis of the pipe. The axial magnetic field, for $n$ number of turns of a winding length of $L$, can be expressed [12]

$$B_z = \frac{\mu n i R^2}{2\left((z+L)^2 + R^2\right)^{3/2}} \tag{1}$$

where $\mu$ is permeability of the medium, $z$ denotes the distance of a particle from the center of the coil, $L$ is the length of the coil, $R$ is the radius of the coil, $n$ is the number of turn in the coil, and $i$ is current in the coil. The tube is filled with the colloidal solution. Therefore, the permeability of medium can be taken as an average of the permeability of magnetic particles and solvent as given below.

$$\mu = \varphi \mu_p + (1 - \varphi)\mu_s \tag{2}$$

Suffixes $p$ and $s$ stand for particle and solvent, and $\varphi$ is volume fraction of the ferromagnetic particles in the solution.

Due to the above magnetic field, magnetic particles are magnetized. The magnetization of a particle can be expressed as

$$M_p = \chi B_z \tag{3}$$

The magnetized particles experience a magnetic force due to the magnetic field as given below

$$F_p = \mu \chi B_z \nabla B_z \tag{4}$$

It is assumed that there is no significant relative motion between ferromagnetic particles and fluid. The colloidal solution considered being homogeneous and the magnetization can be averaged for the concentration of ferromagnetic particles in the solution. Force per unit volume of the solution can be written as

$$F_z = -3\mu\chi\varphi B_z B_z \frac{z+L}{(z+L)^2 + R^2} \tag{5}$$

## 2.2 Governing Equations for Flow

The flow through a circular tube is governed by momentum and continuity equations in cylindrical polar coordinate. Since the flow is rotationally symmetric, axisymmetric approximation is used.

Continuity equation

$$\frac{\partial(ru)}{r\partial r} + \frac{\partial w}{\partial z} = 0 \tag{6}$$

Momentum equation

$$u\frac{\partial u}{\partial r} + w\frac{\partial u}{\partial z} = -\frac{1}{\rho}\frac{\partial p}{\partial r} + \frac{\eta}{\rho}\left[\frac{\partial^2 u}{\partial r^2} + \frac{1}{r}\frac{\partial u}{\partial r} - \frac{u}{r^2} + \frac{\partial^2 u}{\partial z^2}\right] \tag{7}$$

$$u\frac{\partial w}{\partial r} + w\frac{\partial w}{\partial z} = -\frac{1}{\rho}\frac{\partial p}{\partial z} + \frac{\eta}{\rho}\left[\frac{\partial^2 w}{\partial r^2} + \frac{1}{r}\frac{\partial w}{\partial r} + \frac{\partial^2 w}{\partial z^2}\right] \tag{8}$$

where $u$ and $w$ are the radial and axial velocities. $\eta$ and $\rho$ are average viscosity and density, respectively. Radial and axial coordinates are denoted as $r$ and $z$. The boundary conditions are as follows: $u = w = 0$ *at* $r = R$ and $u = \frac{\partial w}{\partial z} = 0$ *at* $r = 0$.

As the flow velocity under the influence of magnetic forces is small, the flow is assumed laminar. Equations (6–8) can be reduced to Hagen Poiseuille flow for steady state as follows:

$$\frac{1}{r}\frac{d}{dr}\left(r\frac{dw}{dr}\right) = \frac{1}{\eta}\frac{\partial p}{\partial z} \tag{9}$$

The magnetic force (Eq. 5) provides the necessarily favorable pressure gradient for the flow of the colloidal solution as given below

$$\frac{dp}{dz} = -F_z = 3\mu\chi\varphi B_z B_z \frac{z+L}{(z+L)^2 + R^2} \tag{10}$$

Now Eq. 9 can be written as

$$\frac{1}{r}\frac{d}{dr}\left(r\frac{dw}{dr}\right) = \frac{3\mu\chi\varphi}{\eta} B_z B_z \frac{z+L}{(z+L)^2 + R^2} \tag{11}$$

Under the given boundary conditions, Eq. (11) can be integrated to obtain an expression for axial velocity.

$$w = \frac{3\mu\chi\varphi}{4\eta} B_z B_z \frac{z+L}{(z+L)^2 + R^2} \left(R^2 - r^2\right) \tag{12}$$

The viscosity of the colloidal solution [13] can be expressed as

$$\eta = \eta_s \left(1 + 5.2\varphi + 5.00\varphi^2\right) \tag{13}$$

## 3 Results and Discussion

Equation (12) is an expression for velocity distribution in the tube. It is obvious that the flow velocity can be increased by the geometrical parameters as well as by the material properties. In order to get a high flow rate, the magnetic field should be high. The windings should be designed based on the limiting conditions of an application such as the availability of electrical power, space, magnetic particles, and solvent and tube diameter. The result has been obtained for the following values of involved parameters (Table 1).

The magnetic field is shown in Fig. 2. It can be seen from the figure that the magnetic field is maximum at the edge of the windings and rapidly decreases away

**Table 1** Calculation parameters of a typical case of iron-water colloidal solution

| Parameter | Symbol | Value |
|---|---|---|
| Current | $i$ | 2–22 mA |
| Length of windings | $L$ | 0.08 m |
| Number of turns in the windings | $n$ | 100 |
| Radius of the tube | $R$ | 0.01 m |
| Magnetic permeability of iron | $\mu_p$ | $12.57 \times 10^{-6}$ m$^{-1}$ |
| Magnetic permeability of water | $\mu_s$ | $12.57 \times 10^{-7}$ m$^{-1}$ |
| Dynamic viscosity of water | $\eta_s$ | $1 \times 10^{-6}$ (N s)/ m$^2$ |
| Volumetric concentration of iron particles | $\varphi$ | 0.2–0.5 |
| Density of iron | $\rho_p$ | 7800 kg/m$^3$ |
| Density of water | $\rho_s$ | 1000 kg/m$^3$ |
| Magnetic susceptibility of iron for 50-µm particle size [13] | $\chi$ | 25 |

from the windings. The magnetic field increases with the product of current and number of coils in the windings (Fig. 2a). It is interesting to know that the magnetic field is dependent on concentration. High magnetic field can be achieved by increasing concentration. High concentration increases the viscosity and viscous losses. The volumetric concentration is calculated by simple averaging the volume of particles and solvent. Characterization of material properties of a specific colloidal solution should be done for accurate prediction of flow velocity.

Force per unit volume is plotted in Fig. 3. The force decreases more rapidly with axial distance than the magnetic field. The force is a function of magnetic field (Eq. 5). Therefore, it increases with an increase in current and concentration similar to the magnetic field.
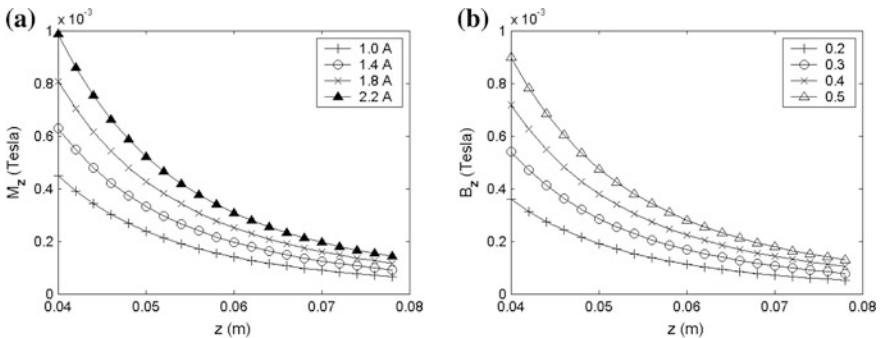


**Fig. 2** Magnetic field at the center of tube versus axial distance from edge of the windings for $\eta_s = 10^{-6}$ (N s)/m$^2$; $\chi = 25$: **a** at different $ni$ for $\varphi = 0.5$, **b** at different $\varphi$ for $ni = 2$ A
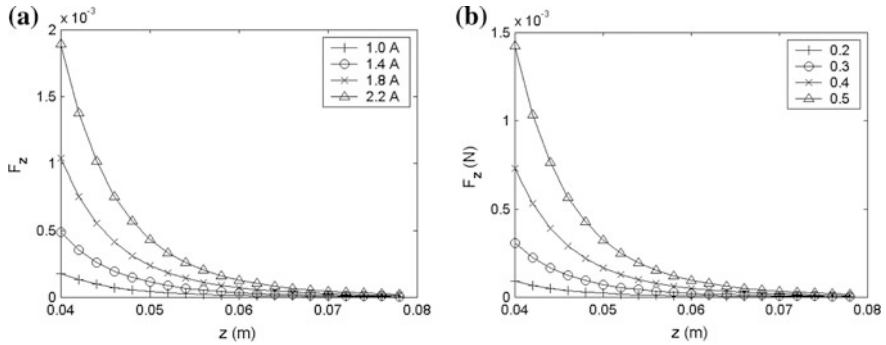
**Fig. 3** Force per unit volume at the center of tube versus axial distance from edge of the windings for $\eta_s = 10^{-6}$ (N s)/m$^2$; $\chi = 25$: **a** at different $ni$ for $\varphi = 0.5$, **b** at different $\varphi$ for $ni = 2$ A

The objective of the present study was to investigate the flow of a colloidal solution of a ferromagnetic material. It is encouraging that a significant flow velocity can be achieved by energizing a colloidal solution and may serve the purpose of enhancing flow in microchannels. This can be used as a replacement of capillary draft and to enhance the surface-tension-driven flow. However, there are several challenges in pumping fluid using magnetic force. The fluid flows from edges of the windings toward the center of the windings, and as a result there will be no net flow in the tube. Further investigation is required on shielding the magnetic field and diversion of the flow so that there is net flow in the tube. As expected the velocity distribution in the tube is parabolic. The magnitude of velocity increases with an increase in current and concentration of iron particles (Fig. 4).
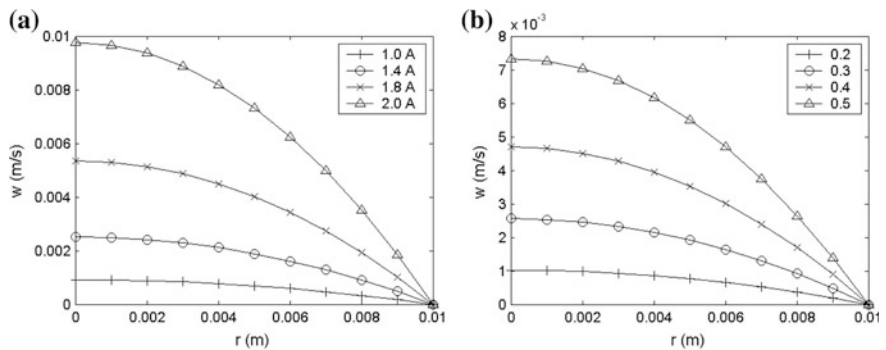


**Fig. 4** Axial velocity versus radial distance at edge of the windings for $\eta_s = 10^{-6}$ (N s)/m$^2$; $\chi = 25$: **a** at different $ni$ for $\varphi = 0.5$, **b** at different $\varphi$ for $ni = 2$ A

# 4 Conclusions

Appreciable flow velocity was obtained in the colloidal solution of iron-water using magnetic field. The combination of material properties, operating parameters, and geometrical parameters affect the flow. Several aspects of the flow need to be investigated for the successful utilization of magnetic pumping. Getting net flow rate, sedimentation of solid particles, interaction between solid and liquid particles, and behavior of colloidal solution in vapor phase are some of the challenges for future research.

# References

1. Shevkoplyas SS, Siegel AC, Westervelt RM, Prentissc MG, Whitesides GM (2007) The force acting on a super paramagnetic bead due to an applied magnetic field. R Soc Chem 7:1294–1302
2. McKnight TE, Roh Y, Phelps TJ, Yeary LW, Cunningham GT (2005) Ferro fluid field induced flow for microfluidic applications. IEEE/ASME Trans Mechatron 10(1):68–76
3. Tokura S, Hara M, Kawaguchi N, Amemiya N (2014) The behavior of nano- and micro-magnetic particles under a high magnetic field using a superconducting magnet. IEEE Trans Appl Supercond 24(3):2–5
4. Gijs MAM, Lacharme F, Lehmann U (2010) Microfluidic applications of magnetic particles for biological analysis and catalysis. Chem Rev 110(3):1518–1563
5. Pamme N, Eijkel JCT, Manz A (2006) On-chip free-flow magnetophoresis: separation and detection of mixtures of magnetic particles in continuous flow. J Magn Magn Mater 307 (2):237–244
6. Weston MC, Gerner MD, Fritsch I (2010) Magnetic fields for fluid motion. Anal Chem 82 (9):3411–3418
7. Fischer P, Ghosh A (2011) Magnetically actuated propulsion at low reynolds numbers: towards nanoscale control. Nanoscale 3(2):557–563
8. Weddemann A, Albon C, Auge A, Wittbracht F, Hedwig P, Akemeier D, Rott K, Meiner D, Jutzi P, Htten A (2010) How to design magneto-based total analysis systems for biomedical applications. Biosens Bioelectron 26(4):1152–1163
9. Ganguly R, Puri IK (2010) Microfluidic transport in magnetic MEMS and bioMEMS. Wiley Interdiscip Rev Nanomed Nanobiotechnol 2(4):382–399
10. Friedman G, Yellen B (2005) Magnetic separation, manipulation and assembly of solid phase in fluids. Curr Opin Colloid Interface Sci 10(3–4):158–166
11. De Merino-Martosa A, Vicenteb J, Cruz-Pizarroa L, de Vicentea I (2011) Setting up high gradient magnetic separation for combating eutrophication of inland waters. J Hazard Mater 186:2068–2074
12. Resnick R, Author S, Author T (2017) Physics, vol 2, 5th edn. Wiley, India
13. Verberg R, De Schepper IM, Cohen EGD (1997) Viscosity of colloidal suspensions. Phys Rev E 55(3):3143–3194

# Flow Around Curved Plates at Low Subcritical Reynolds Number: Investigation of Wake Characteristics

**Amala Anil, K. ArunKumar, R. Ajith Kumar, C. M. Hariprasad
and Thamil Mani**

**Abstract** In this paper, numerical simulation results of flow over flat plate and curved plates at a Reynolds number of 8000 are presented. Drag coefficient and Strouhal number trends are reported at different chord length (CL)-to-diameter ($D$) ratios of 0, 6/13, 3/4, and 1 with varying angle of incidence (ranging from $\alpha = 0°$ to 30° in steps 10°). The curvature of the plate was adjusted by varying the radius of curvature keeping the chord length fixed at 40 mm. The results of this study show that the aerodynamic characteristics, viz., drag force and Strouhal number, are significantly affected by the introduction of curvature and flow angle of incidence (plate orientation). The maximum reduction of drag coefficient obtained is 58% by the introduction of both plate curvature and plate orientation. Further, it is noted that base pressure coefficient complies with the trend of the drag and the maximum flow field vorticity shows an abrupt increase in CL/$D$ beyond 6/13.

**Keywords** Plate curvature · Flow incidence angle · Aerodynamic characteristics · Coefficient of drag · Strouhal number · Base pressure coefficient · Vorticity magnitude

A. Anil (✉) · K. ArunKumar · R. Ajith Kumar · C. M. Hariprasad · T. Mani
Department of Mechanical Engineering, Amrita Vishwa Vidyapeetham, Amritapuri, India
e-mail: amalaanili47@gmail.com

K. ArunKumar
e-mail: akmallasseril@gmail.com

R. Ajith Kumar
e-mail: amritanjali.ajith@gmail.com

C. M. Hariprasad
e-mail: hariology@yahoo.co.in

T. Mani
e-mail: thamilthedal@gmail.com

**Nomenclature**

| | |
|---|---|
| CL | Chord length of the plate |
| $U$ | Uniform flow velocity |
| $C_{pb}$ (base pressure coefficient) | $\frac{P_b - P_\infty}{\frac{1}{2}\rho U^2}$ |
| $C_l$ (lift coefficient) | $\frac{2F_l}{\rho A U^2}$ |
| $P_b$ | Base pressure |
| $F_l$ | Lift force |
| $\zeta_{max}$ | Maximum value of vorticity |
| $g$ | Acceleration due to gravity |
| $f_s$ | Vortex shedding frequency |
| $D$ | Diameter of plate |
| CL/$D$ | Chord length-to-diameter ratio |
| $C_d$ (drag coefficient) | $\frac{2F_d}{\rho A U^2}$ |
| $F_d$ | Drag force |
| $P_\infty$ | Pressure at uniform flow field |
| $\mu$ | Dynamic viscosity |
| $St$ (Strouhal number) | $\frac{f_s D}{U}$ |
| $A$ | Cross-sectional area |

# 1   Introduction

Flow characteristics of a bluff body have been extensively investigated in the past few years due to its wide variety of engineering applications. Among the bluff bodies, a flat plate is one with possibly the simplest configuration. Few works were reported on flow over flat plates.

Modi et al. [1] investigated the effect of blockage ratio on the aerodynamic characteristics of a flat plate in a subcritical Reynolds number range. Authors reported that increase in the blockage ratio will result in an enhancement of drag and lift. Lisoski [2] discussed the effect of flat plate thickness by representing a curve of the drag coefficient as a function of plate thickness, wherein an increment of drag coefficient with plate thickness was noted. Xu et al. [3] experimentally investigated the flow over corner modified flat plate and concluded that front-edge modification of flat plate will lead to a reduction of wake width and coefficient of drag. Further, Chen and Fang [4] conducted wind tunnel tests on the flat plate with beveled sharp edges to discuss the relation between Strouhal number and angle of attack. Through flow visualization, Radhakrishnan [5] explained the mechanism behind the origin and size manipulation of twin vortices that shed from a flat plate and the relation of reverse flow location with the Reynolds number.
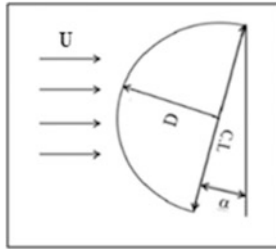
**Fig. 1** Model geometry and test configuration

Sharma et al. [6] reported that it is possible to control the size of the vortex shed from flat and also curved plates changing its orientation to the flow. Balu et al. [7] experimentally analyzed vortex length, vortex size, and Strouhal number in flow over curved plates at a subcritical Reynolds number of 5878. They found that by the introduction of curvature and angle of incidence, the wake vortex characteristics can be considerably manipulated. Damu et al. [8] numerically investigated flow over flat plate and curved plates with varying diameter and orientation. They found that an increase in the angle of incidence leads to a reduction of the coefficient of drag. However, their results are expected to be notably influenced by the higher blockage ratio ($\sim 17\%$) set in their simulations.

The objective of the present study is to numerically investigate the effect of curvature (convex) and orientation in the aerodynamic characteristics of a plate placed in water flow at a Reynolds number of 8000 (based on CL). The chord length-to-diameter ratios (CL/$D$) selected for the study are 0 (flat plate), 6/13, 3/4, and 1. For all the plates, constant chord length (CL) of 40 mm was maintained and angle of incidence ($\alpha$) was varied from $0°$ to $30°$ in steps of $10°$. The test configuration for the simulation is shown in Fig. 1. Care is taken to keep the model blockage as low as 3.8% so as to avoid its influence.

## 2 Computational Model and Validation

ANSYS Fluent 14.0 was used for the computational analysis. Turbulent flow is analyzed by SST $k–\omega$ model for better vortex capture. First-order upwind scheme was used for convective and diffusive terms. The fluid medium considered is water, and free stream turbulence intensity was taken as 1%. The blockage ratio had set to be 3.8%. Figure 2 shows the details of the computational domain considered in the present study.

The governing equations for a 2D incompressible flow are as follows

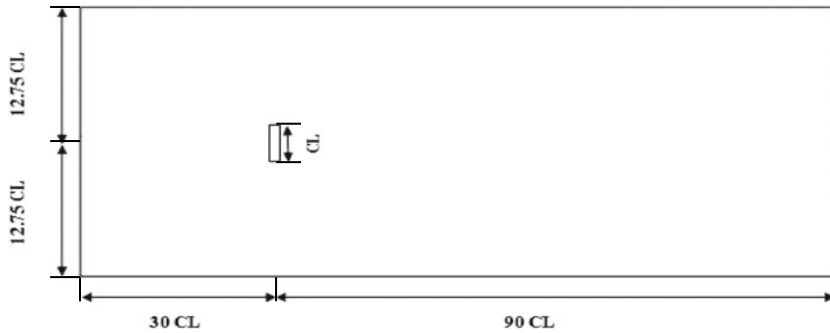$$\text{Continuity equation } \partial\rho/\partial t + \nabla \cdot (\rho U) = 0 \tag{1}$$
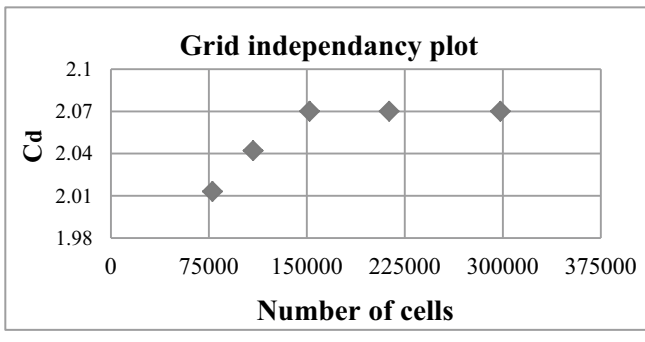
**Fig. 2** Computational domain



**Fig. 3** Grid independency plot

$$\text{Momentum equation } \rho(\partial U/\partial t) + \rho U \nabla.U \ = \ -\nabla P + \mu \nabla^2 U + \rho g \qquad (2)$$

Grid independency test is carried out for five different sizes of the grid in the same computational domain of flat plate. From Fig. 3, it was seen that the mean drag coefficient becomes a constant value of 2.07 beyond 150,000 cells. Hence, the number of cells is chosen as 150,000 for saving memory and computational time.

The numerical simulation requires validation to be carried out. In this study, flat plate kept normal to the flow, the numerically obtained values of $C_d$ and $St$ complies with those reported in the literature at Reynolds number = 8000. Till now, no literature results are available for validating curved plate at this Reynolds number range. So, results for curved plate ($CL/D = 1$) were validated using the experimental results obtained employing a three-component force-balancing mechanism in a subsonic wind tunnel in the Aerodynamics Laboratory of Amrita School of Engineering at Amritapuri Campus. Figure 4 shows the curved plate mounted in the wind tunnel. Validation results are shown in Table 1.
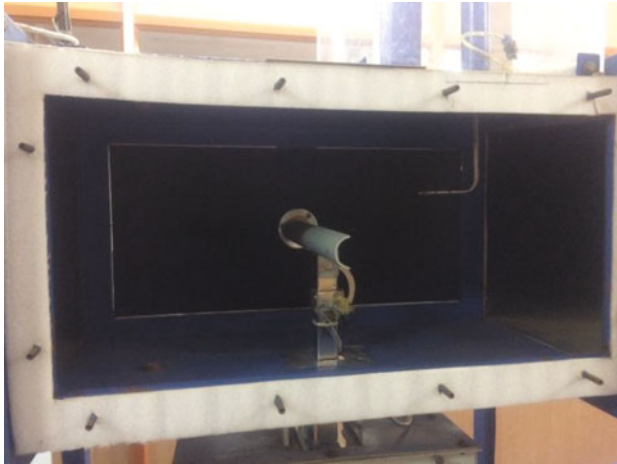
**Fig. 4** Curved plate mounted in the test section of wind tunnel

**Table 1** Comparison of values obtained in the present study with experimental values for flat plate and curved plate (CL/D = 1)

| Geometry | Aerodynamic characteristics | Experimental values | Present study |
|---|---|---|---|
| Flat plate (CL/D = 0) | $C_d$ | 2.07 [1] | 2.07 |
| | St | 0.149 [1] | 0.15 |
| Curved plate (CL/D = 1) | $C_d$ | 1.13 [Wind tunnel result] | 1.07 |

# 3  Results and Discussion

The aerodynamic drag coefficient, Strouhal number, base pressure coefficient, and magnitude of maximum flow field vorticity were numerically obtained for all the models having 40-mm chord length kept normal to the flow. The simulations were carried out for all the CL/D ratios by varying the angles of incidence in steps of 10° up to 30°.

## 3.1  Coefficient of Drag ($C_d$)

Figure 5a shows the typical time series of drag coefficient for CL/D = 1.0 at α = 0° from which the mean drag coefficient value is estimated. Similarly, mean $C_d$ values for other models were taken from their respective time series at all flow angles of
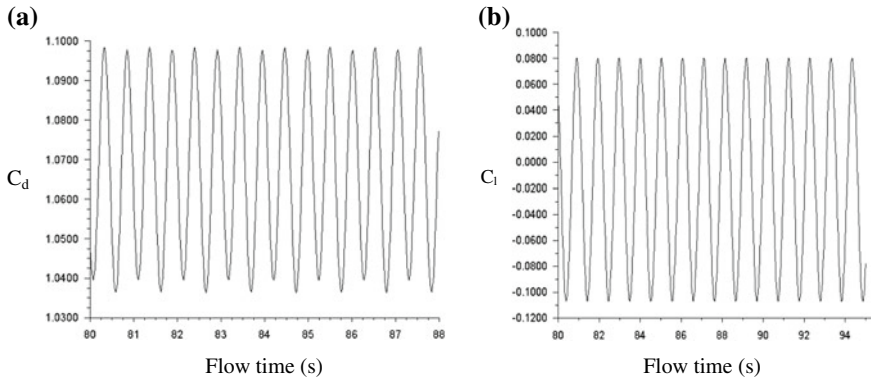
**(a)**



$C_d$

Flow time (s)

**(b)**



$C_l$

Flow time (s)

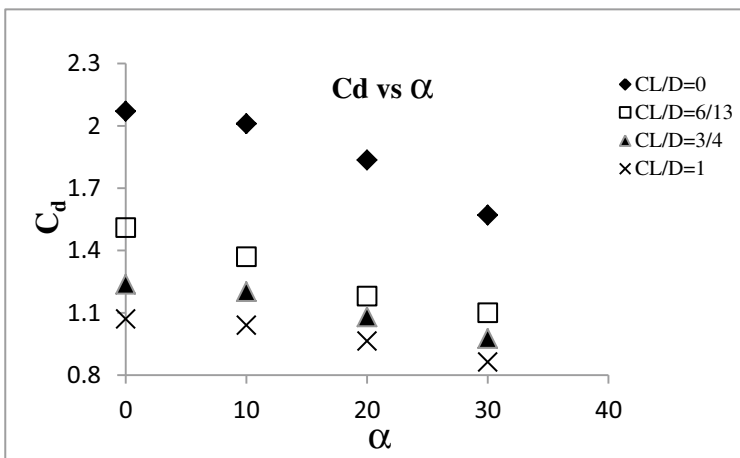**Fig. 5** Time series of $C_d$ and $C_l$ for the curved plate with CL/$D$ = 1 at $\alpha$ = 0°



**Fig. 6** Variation of drag coefficient versus angle of incidence

incidence. Figure 6 shows the variation of mean drag coefficient of all the CL/$D$ models at different angles of attack. For all the models, coefficient of drag shows a decreasing trend when the angle of incidence increases. It could also be seen that, for a given value of $\alpha$, Cd decreases with increase in CL/$D$ ratio. The same declining trend is obtained for lift (rms) coefficient w.r.t. CL/$D$ (but not presented here due to space constraints). Compared to all other CL/$D$ ratios, the curved plate of CL/$D$ = 6/13 shows a maximum reduction of 27% at 30° incident angle. Also from Fig. 6, it is clear that the effect of plate curvature is comparatively less at 30° incident angle. The maximum value of $C_d$ was obtained on flat plate at 0° incidence, viz., 2.07 which is close to that of a square cylinder [9]. Considering both the plate curvature and the plate orientation, a total reduction of drag of about 58% is achieved as revealed in Fig. 6.
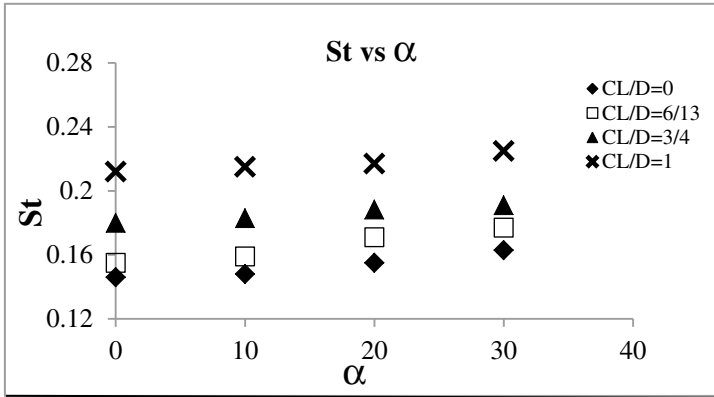
**Fig. 7** Strouhal number variation for different models at different incidence angles

## 3.2 Strouhal Number (St)

Figure 7 shows the Strouhal number variation for all CL/*D* models at different angles of incidence. The inverse of the time between two adjacent troughs from the lift time series (see Fig. 5b) is used to calculate the vortex shedding frequency which in turn gives the Strouhal number for each case. It can be seen that St registers a very gradual increase with an increase in angle of incidence for all the models. Comparing with Fig. 6, the trends of *St* and $C_d$ show that there exists a near-inverse relationship between them as revealed for bluff bodies in the literature [10]. Strouhal number value is the maximum for the model with CL/*D* = 1 at 30° incidence and is minimum for the flat plate at 0°. This is due to the fact that, when CL/*D* ratio increases, the body will become more streamlined wherein the upper and lower shear layers become close to each other facilitating closer interaction between the shear layers thereby speeding up the shedding process.

## 3.3 Coefficient of Base Pressure ($C_{pb}$)

In Fig. 8, $C_{pb}$ values for all models are reported at the angle of incidence 0°. From the figure, it can be observed that $-C_{pb}$ is having a decreasing trend with the introduction of curvature. Base pressure coefficient has got the maximum negative value (or minimum positive value) for flat plate at 0°, so the value of drag coefficient is the highest for the same. This could be attributed to the larger wake width for the flat plate (CL/*D* = 0) for which the separation points are fixed. The maximum increase of base pressure coefficient (decrease of negative $C_{pb}$) w.r.t the CL/D ratio is found to be around 24%.
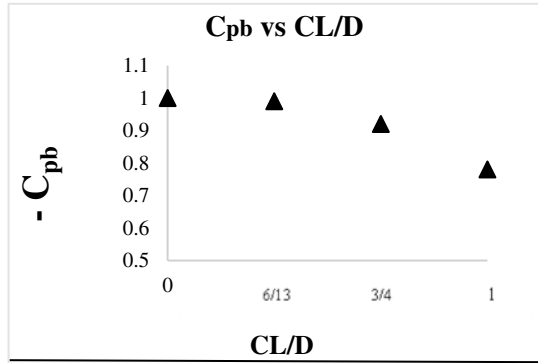
**Fig. 8** Variation of $C_{pb}$ with different CL/$D$ ratios at $\alpha = 0°$

## 3.4 Vorticity Magnitude ($\zeta$)

Vorticity is twice the angular velocity vector for the rotating fluid. The maximum value of vorticity magnitude occurs at $x/D = 2.25$ and $y/D = 0.32$ in the flow domain for all models kept normal to the flow ($\alpha = 0°$); '$x$' and '$y$' are measured from the body center along the wake centerline. From Fig. 9, it can be observed that $\zeta_{max}$ shows an increasing trend with the introduction of curvature. $\zeta_{max}$ abruptly increases for CL/$D$ beyond 6/13, and the maximum value was observed for the curved plate with CL/$D = 1$. Maximum vorticity increases by about 6%.

In general, the observed aerodynamic features described in Figs. 3, 5, 6, 7, and 8 could be attributed to the change in the shear layer configuration and corresponding changes in the wake vortex structures around the body when the plate curvature and flow incidence angle are changed.
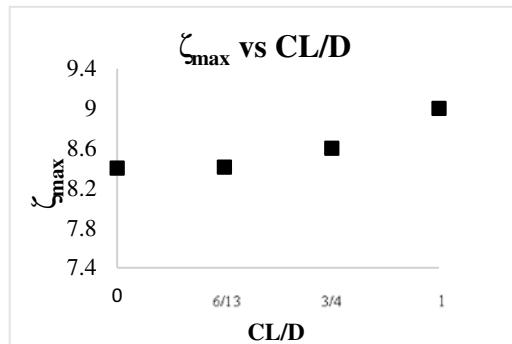


**Fig. 9** Variation of $C_{pb}$ with different CL/$D$ ratios at $\alpha = 0°$

# 4 Conclusions

From the numerical simulation and analysis performed in this study, the following conclusions were drawn.

1. It is observed that there is a significant drag variation for a plate by varying its curvature and orientation to the flow. The coefficient of drag decreases with respect to an increase in both flow incidence angle and CL/D ratio. The drag value is found to be minimum for the model with CL/$D$ ratio = 1.0 at an angle of 30° with a corresponding drag reduction of about 20%. Considering both plate curvature and its orientation, a total reduction of 58% could be achieved in the drag value which is a notable highlight in the present results.
2. For all the models, Strouhal number is found to exhibit a gradual increase with an increase in the incidence angle and exhibits a near-inverse relationship with the drag coefficient.
3. The maximum flow field vorticity is found to increase w.r.t the CL/$D$ ratio beyond CL/$D$ = 6/13.

# References

1. Modi VJ, EL-Sherbiny SE (1977) A free-streamline model for bluff bodies in confined flow. J Fluids Eng 99(3):585–592
2. Lisoski DLA (1993) Nominally 2-dimensional flow about a normal flat plate. Dissertation (Ph.D.), California Institute of Technology
3. Xu Y-Z, Feng L-H, Wang J-J (2015) Experimental Investigation on the flow over normal flat plates with various corner shapes. J Turbul 16(7):607–616
4. Chen JM, Fang Y-C (1996) Strouhal number of inclined flat plate. J Wind Eng Ind Eng 61 (3):99–112
5. Rathakrishnan E (2012) Visualization of the flow field around a flat plate. IEEE Instrum Measur Magaz 15
6. Sharma H, Vashishtha A, Rathakrishnan E (2008) Twin-vortex flow physics. J Aerosp Eng 222:783–788
7. Balu Haridas, Ajith kumar R, Arunkumar K (2016) Vortex manipulation in flow over curved plates. In: Proceedings of the 43th national conference on fluid mechanics and fluid power
8. Damu Murali, Arunkumar K, Ajith Kumar R, Srikrishnan AR (2017) Flow past a curved plate: analysis of drag coefficient and Strouhal number. In: Proceedings of the 44th national conference on fluid mechanics and fluid power
9. Yen SC, Yang CW (2011) Flow patterns and vortex shedding behavior behind a square cylinder. J Wind Eng Ind Aerodyn 99(8):868–878
10. Ahlborn B, Seto ML, Noack BR (2002) On drag, Strouhal number and vortex-street structure. J Fluid Dyn Res 30(6):379–399

# Study on Performance Analysis of Earth-Air-Pipe Heat Exchanger as Passive Cooling and Heating System

**Mahendra Kumar Verma, Vikas Bansal and Kunj Bihari Rana**

**Abstract** The energy demand for the private and business building increases quickly with the population. In the last two decade indicated extreme energy emergency found in creating nations particularly amid summer season. For hot atmosphere nations like India, the use of cooling framework assumes essential part. The Mechanical Vapor Compression (MVC) frameworks toward this path are demonstrating effective however in the present situation when the demand of energy is expanding, and the supply isn't adequate one should center around the passive cooling techniques or other substitute which can meet necessity at least cost and energy utilization. As the passive cooling not just gives the course of the outside air to keep up the freshness yet in addition keep up the solace at low energy necessity, such a significant number of analysts have been working over these frameworks to discover it as a substitute of MVC units. Earth-air-pipe heat exchanger (EAPHE) can be utilized as a passive cooling and heating framework by using geothermal energy. This paper intends to display the audit on execution ponder and mechanical advancement of EAPHE at various atmosphere conditions. Exploratory outcomes demonstrate that normal temperature drops to 12–20 °C which can be accomplished that relies upon atmosphere conditions. Normal pipe length, measurement, and air speed inside pipe were discovered 10–100 m, 0.05–0.5 m, and air speed 2–5 m/s separately. These papers additionally recognize the purpose behind non-successful working of the EAPHE and proposed strategies to enhance the effectiveness of the framework to improve cooling of heating impact.

**Keywords** EAPHE · Energy · Effectiveness

M. K. Verma (✉) · V. Bansal · K. B. Rana
Rajasthan Technical University, Kota, Rajasthan, India
e-mail: vermamv81@gmail.com

# 1 Introduction

Passive cooling and active cooling are the two main types of cooling system. Active cooling requires power source to provide the desired effect whereas passive cooling includes the application of natural process along with passive technology without the use of power source. Passive cooling is used as low energy-driven technique to remove undesired heat from the building to bring the comfort condition of occupant. There are numerous methods of passive cooling system, but the present study discusses earth-air-pipe heat exchanger (EAPHE). Increasing energy demand of the sustainable energy sources and energy conservation methods in recent year because of fast economic growth and increasing population. Shortage of conventional energy sources and high energy cost have raised the demand of alternate methods for cooling and heating purpose of buildings.

Power usage in buildings accounts 30–40% of global energy consumption. Passive cooling method is one of the many alternative methods of energy sources. The present study discusses the performance of EAPHE and solar chimney as passive ventilation and cooling systems as well as performance of some integrated passive cooling systems [1] (Fig. 1).

The earth-air-pipe heat exchanger usage geothermal energy for the cooling effect inside the building. Mechanism of heat exchangers basically controls the temperature of the system by adding or extracting heat. Thermal energy can be exchanged from one medium to another medium only by means of temperature difference without using any power source. EAPHE works on the principle that the average
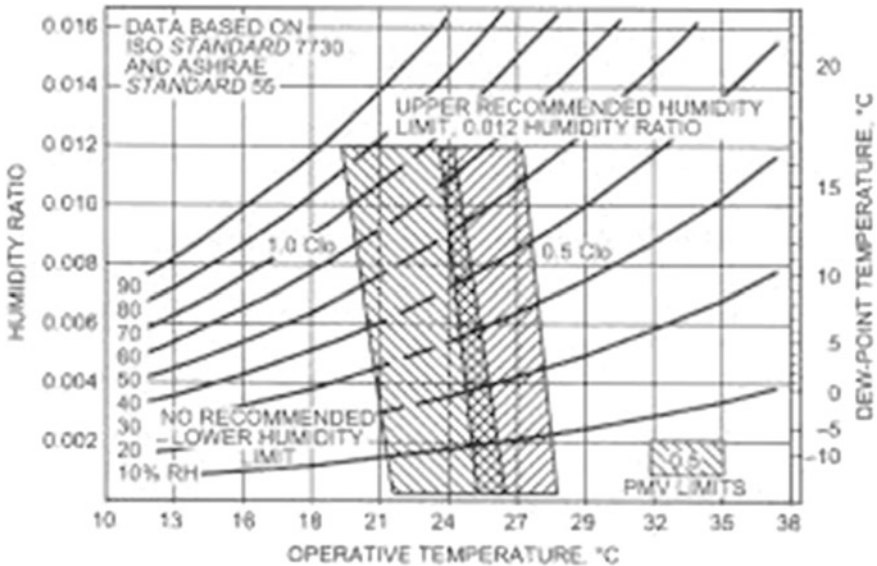


**Fig. 1** Human comfort range (ASHRAE) [1]

underground temperature at certain depth, i.e., 2–4 m, remains constant and it remains lower than the atmospheric temperature in summer and higher than the atmospheric temperature in winter. When atmospheric air is drawn through underground long pipes, then outlet temperature of air reduces in summer and gets heated in winters. It uses underground soil as heat source.

## 2 Motivation of the Research

- Prolonged summer period in the northern region of India.
- High temperature (40–45 °C).
- High energy demand for heating and cooling purpose.
- Inadequate electric energy for all.
- Go green concept.
- Increasing demand for alternate energy sources.

## 3 Literature Review

Earth-air-pipe heat exchangers are simple in operation; it has high cooling and heating capacity, low maintenance, and operation cost. Figure 2 shows the different arrangement of EAPHE system. EAPHE systems are the alternate solution of active mechanical cooling in building. Previous literature survey shows the performance of earth-air-pipe heat exchanger (EAPHE) at different climate conditions, and also study shows the different parameter which affects the performance of EAPHE [2]. Figure 2 shows the different arrangement of EAPHE used for the cooling and heating purpose.

**Fig. 2** Different EAPHE system



Connection in series

Connection in parallel
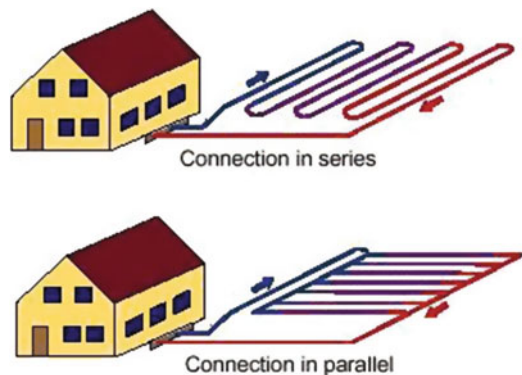
Sardana et al. [3] shows by experimental study optimum air velocity 2 m/s for the tube length 10–70 m and also found that there is no significant effect of pipe material on the performance of EAPHE. Performance of an integrated system with earth-air-pipe heat exchanger and solar chimney also shows the improved performance and ventilation effect. Researcher shows by mathematical model that indoor temperature maintains at 21.3–25.1 °C and humidity ratio maintains at an acceptable range of 50–78% [4]. Various literatures found show different parameters which affect performance of EAPHE. As per previous literature [5–10], it was found that optimum pipe length has been studied 10–100 m, tube or pipe diameter 0.1–0.5 m gives optimum result, air flow velocity 2–5 m/s gives better result, and it has been observed that beyond 3 m depth of buried pipe, temperature remains constant.

There are various studies found where researcher assumed steady-state condition but Bansal et al. [11] found by experimental and CFD simulation that performance of earth-air-pipe heat exchanger under unsteady-state or transient condition depends on thermal conductivity of soil and duration working operation. It reduces temperature from 18.7 °C at steady state to 16.6 °C at transient condition. Researcher [11] established a new concept of 'derating factor' to monitor performance of EAPHE under transient or unsteady-state condition that is the ratio of the difference between temperature drop of exit air by EAPHE in steady state and unsteady state to the air temperature drop obtained by EAPHE in steady state. Higher derating factor means lower thermal performance of EAPHE. It shows that derating factor is an important factor to consider for designing of EAPHE. EAPHE can be used for heating purpose of building in winter with great effect. Bansal et al. [12] set up experimental model and shows by CFD analysis that EAPHE is not affected by pipe material; hence, cheap material can be used for cost-effective. Researchers [12] also found temperature rise of 4.1–4.8 °C for the air velocity 2 m/s in winter. Temperature distribution along the pipe length at different flow velocities as shown by Fig. 3 shows that higher temperature differences at flow velocity of 2 m/s for the two different pipes [12].

Experimental study shows the use of photovoltaic (PV) to run the earth-air-pipe heat exchanger in energy park, New Delhi. The PV systems are used to handle the daily electrical load of 10 kWh/day which runs the air blower used for heating or cooling of adobe house [13].

Researchers also evaluated the performance of underground air pipes with the help of exergy analysis to measure efficiency of process and its losses. Expression for energy and exergy analysis was derived using energy, mass, and exergy balance equations which shows the range of exergy efficiency among 57.8–63.2% for the optimum pipe radius 0.28 m [14]. Researcher also uses methods of energy and exergy analysis to enhance the performance of earth-air heat exchangers. Efficiencies' values of the system studied were found to be 72.10 and 19.18% at a reference state temperature of 0 °C. Efficiency of exergy analysis decreased from 19.18–0.77% when reference temperature increased from 0 to 18 °C [15].

EAPHE can be integrated with solar chimney to enhance the air flow velocity and performance of EAPHE. Haghigh and Maerefat [10] establish a mathematical model for integrated solar chimney and EAPHE and found optimum performance at
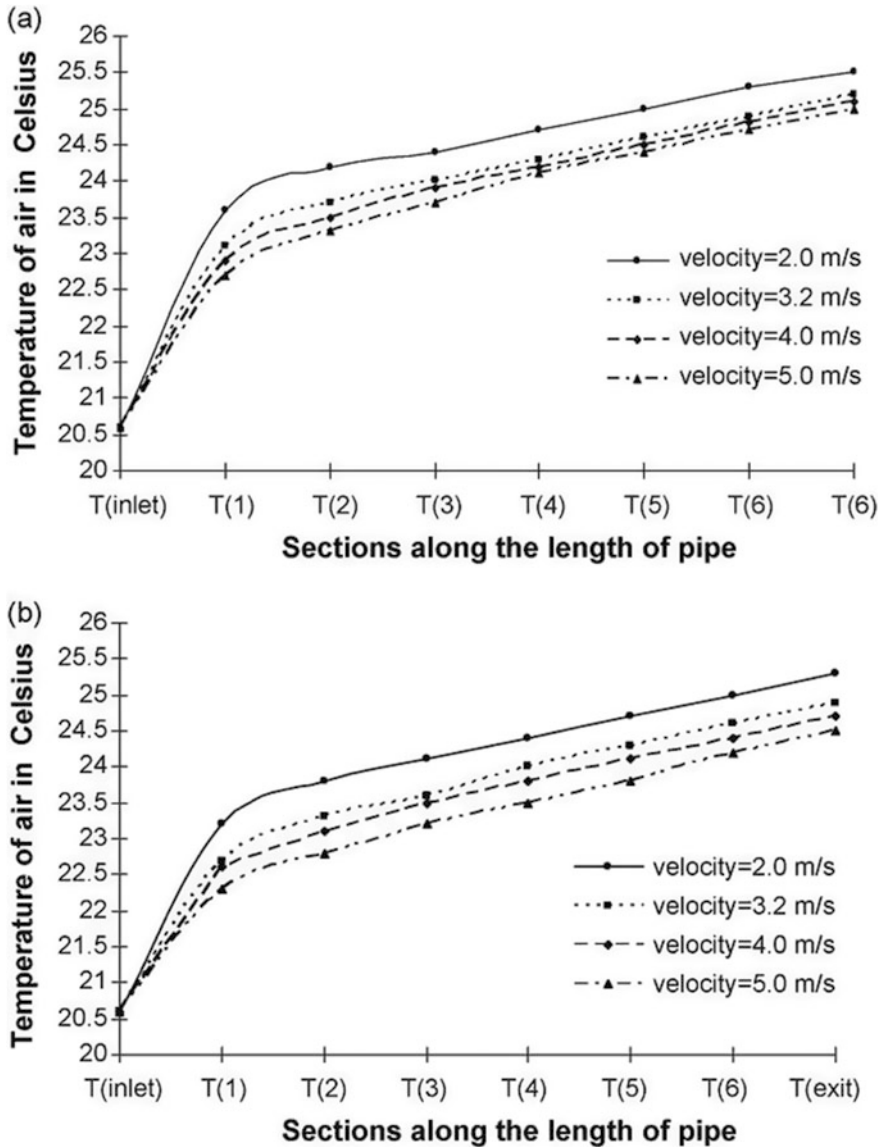
**Fig. 3** Temperature distribution along the pipe length [12]

air gap of 0.2 m, diameter of pipe 0.5 m and pipe length 35 m. Figure shows the integrated solar chimney and EAPHE [10]. Figures 4 and 5 show the integrated EAPHE and SC system and acceptable limit of comfort condition, respectively [16–18]. Figure 3 represents the inlet and outlet of the buried pipe, and it shows the validation of simulated temperatures with experimental result.
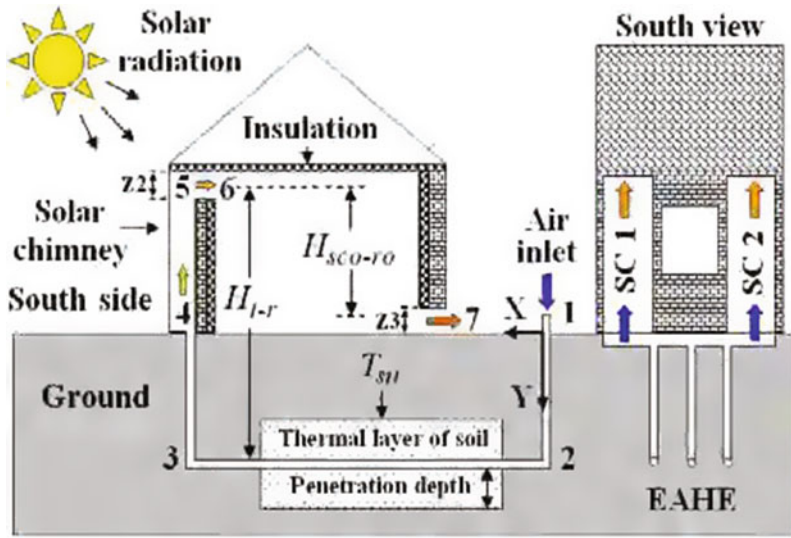
**Fig. 4** Schematic diagram of integrated EAPHE and SC [16]
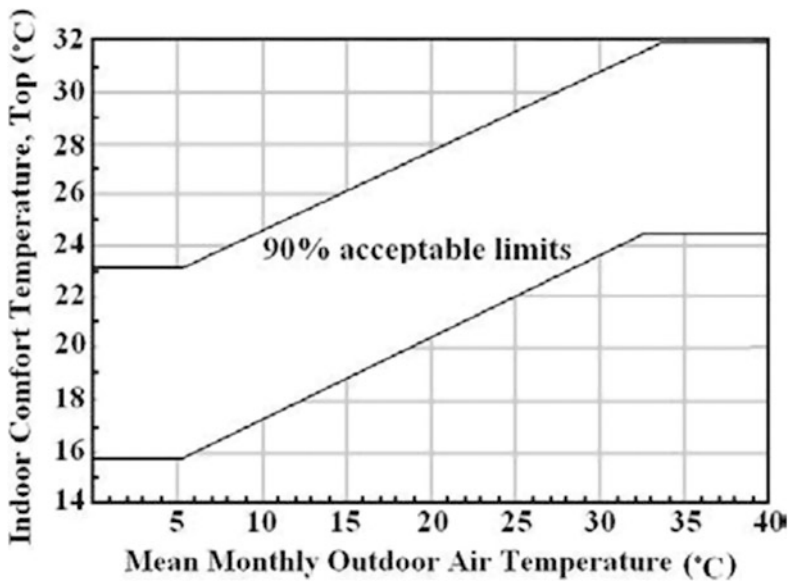


**Fig. 5** Adaptive comfort standard [16]

Maerefat et al. [16] also developed mathematical model for integrated EAPHE and SC and found that increased surface area increases ventilation rate and temperature reduction up to 18–20 °C for optimum diameter 0.5 m. EAPHE can be

directly coupled with active room air conditioner (AC) to reduce the energy consumption by AC. Bansal et al. [19] coupled the earth-air-pipe heat exchanger with air cooled condenser of 1.5TR window AC and shows experimentally that electrical consumption reduced by 18% when 100% air from EAPHE is used to cool the condenser tube.

Alexandre et al. studied by experimental and mathematical model and showed that use of underground multiple layer heat exchanger configurations reduces the large horizontal installation area compare to using single layer of pipe. Parametric analysis was also performed to understand the input parameter which affects the performance of earth-air-pipe heat exchanger. Analyzed parameter showed that the heat exchanger duty increases with the floor depth until 3 m and the optimum space between layers is 1.5 m, but distance up to 2 m is also efficient and the limit of maximum air velocity 5 m/s [29].

Researcher also shows by experimentally that soil temperature depends on depth and time. It is very difficult to simulate the thermal behavior of earth since there are numbers of parameters such as changing weathers, variations in moisture content of soil, and thermal conductivity and diffusivity affecting on the temperature of ground. Mathematical model was established using sinusoidal function of depth and time. Principle of transient heat flow was used with assumption of one dimensional heat flow, constant thermal diffusivity, and homogeneous soil. Soil temperature was predicted at depth of 5, 10, 20, and 300 cm and compared with experimental field result and found percentage error 10.78, 10, 10.26, 14.95%, respectively [30]. Mathematical model has been developed by the researcher for the deeply buried air rock tunnel heat exchanger. The maximum error of the air temperature found to be 1.4 0C, and the maximum error of relative humidity found to be 10% [31]. Experimental study by Joaquim et al. shows the effect of transient behavior of temperature field for the external air, soil, and buried pipe and the best periods of time for employment of device. The ducts are installed at depth of 1.6 and 0.6 m apart and result showed that the months of May and February were the best for heating and cooling, respectively [32].

Table 1 shows the review of literature of the performance of EAPHE at different climate conditions. It also shows the different parameters studied for optimum performance of EAPHE (Fig. 6).

## 4  Result and Discussion

The continuing increase of energy consumption of air conditioning and energy efficient cooling systems are needed to replace the current electrical air conditioners used in most commercial and residential buildings. An energy crisis in developing country like India raises the demand of passive cooling systems which runs without using power source. This paper also reviews the use of geothermal energy as earth-air-pipe heat exchanger (EAPHE) for the cooling or heating purpose. SC and EAPHE are the most commonly used as a passive cooling system. Integrated SC

**Table 1** Summary of literature review

| Name of the author/title | Methodology | Parameters studied | Finding/remark |
|---|---|---|---|
| Sookchaiya et al. [1] | Review of different techniques | Combination of active and passive cooling system | Integrated system of active and passive system source significant result in saving energy |
| Chaturvedi et al. [2] | Experimental study | Material of pipe, tube length | 1. Length of pipe is small then temperature difference is very less 2. Material of pipe is not affected in the output result 3. Length of pipe should be at least 100 m for optimum result |
| Sardana et al. [3] | Experimental studies | 1. Effect of material 2. Velocity of air inside pipe 3. Tube length 4. Tube depth | 1. Cheap PVC material gives better result 2. Optimum air velocity found 2 m/s 3. After 1.5 m tube depth temperature found constant |
| Li et al. Performance of a coupled cooling system with earth to air heat exchanger and solar chimney [4] | Mathematical model | Combined cooling effect and relative humidity | 1. Integrated coupled system maintain an indoor air temperature 21.3–25.1 °C 2. Humidity ratio was maintained at a range of 50–78% |
| Bisoniya et al. [5] | Experimental and analytical studies | Various aspects of EAHE were studied | Optimum pipe length has been studied 10–100 m, tube or pipe diameter 0.1–0.5 m gives optimum result, air flow velocity 2–5 m/s gives better result |
| Chaturvedi et al. [6] | Experimental setup | Various parameters studied | Temperature drop of 3.93–12.6 °C observed for optimum pipe length of 9 m and diameter 0.05 m. |
| Joen et al. [7] | Mathematical model | 1. Air inlet temperature 2. Tube length and diameter | 1. EAPHE can give better performance using shorter pipe length and larger diameter 2. EAHE system uses small diameter tubes which can be installed easily |

**Table 1** (continued)

| Name of the author/title | Methodology | Parameters studied | Finding/remark |
|---|---|---|---|
| Dokkar et al. [8] | CFD Analysis | 1. Outlet temperature of EAHE 2. Flow rate and velocity | Temperature in the middle of the shelter does not exceed 29 °C |
| Woodson et al. [9] | Experimental study | 1. Outlet temperature 2. Tube depth and length | Tube length 25 m long and 1.5 m underground used, it was able to cool by 7.6° from outside |
| Haghigh and Maerefat [10] | Experimental and mathematical modeling | Effect of no. of buried pipe and solar chimney | Numbers of solar chimney and pipe channels are dependent by outdoor condition and heating load of building |
| Mishra et al. [11] | Experimental and CFD simulation | Thermal conductivity of earth soil and continuous operating time | Performance of EAPHE under transient condition depends upon thermal conductivity of earth soil and continuous operating time. It reduces temperature drop 18.7 °C at steady state to 16.6 °C at transient condition |
| Bansal. et al. [12] | Experimental setup and CFD | Pipe material and air velocity | 1. EAPHE system is not affected by the pipe material 2. 4.1–4.8 °C temperature rise found for the air velocity 2–5 m/s |
| Tiwari et al. [13] | Experimental | Performance of EAHE | PV cells were used to run the fan of EAHE to improve the performance of EAHE |
| Ozgener et el. [14] | Experimental | Exergy efficiency of underground air tunnel system | The exergy efficiency values for the underground air tunnel obtained to be in a range of 57.8–63.2% and maximum cooling capacity system occurred at approximately 3:00 PM. Optimum buried pipe radius of 0.28 m |

**Table 1** (continued)

| Name of the author/title | Methodology | Parameters studied | Finding/remark |
|---|---|---|---|
| Hepbasli [15] | Experimental | Energy and exergy efficiency of EAHE | Energy and exergy efficiency values for the EAHE system studied were determined to be 72.10 and 19.18% at a reference state temperature of 0 °C |
| Maerefat et al. [16] | Mathematical model and numerical calculation | Outlet temperature | Solar chimney used with cooled inlet air cooled by geothermal temperature. Temperature reduction up to 18–20 °C |
| Poshtiri et al. [17] | Experimental and mathematical | 1. Air gap depth of SC 2. Diameter of heating pipe 3. Length of pipe | Results show that optimum size of air gap 0.2 m, diameter of pipe 0.5 m and length 35 m provide thermal comfort condition |
| Poshtiri et al. [18] | Experimental and mathematical modeling | Cooling effects | Result shows SC-EAPHE system is best choice for the building with poor insulation |
| Mishra et al. [19] | Experimental | Power consumption of 1.5TR window AC | EAPHE is coupled with air cooled condenser, and it was found that electrical consumption reduced by 18% when 100% air from EAPHE is used to cool the condenser tube |
| Kumar et al. [20] | Experimental study | 1. Effect of air velocity on cooling effect 2. Effects of different cooling pads | 1. Saturation efficiency increases by 47% at 0.10 m/s 2. Cellulose cooling pad gives higher efficiency compared to straw and coir 3. SC-ECC is better for well insulated building |
| Bisoniya et al. [21] | CFD modeling | 1. Pipe length 2. Pipe radius 3. Air flow velocity 4. Depth of pipe buried | 1. Optimum pipe length found 20–30 m to decrease air temp. 15 °C 2. Pipe diameter 0.101–0.152 m at air velocity 5 m/s 3. Depth of pipe buried 2–3 m |

**Table 1** (continued)

| Name of the author/title | Methodology | Parameters studied | Finding/remark |
|---|---|---|---|
| Tiwari et al. Design of an earth-air-pipe heat exchanger for climate condition of Chennai [22] | Mathematical model | Various parameter studied | Satisfactory result found |
| Dubey et al. [23] | Experimental study | Outlet temperature and COP | At 1.5 m depth maximum temperature difference varies from 8.4 to 4.18 °C. COP varies from 5.7 to 2.6 |
| Miyazaki et al. [24] | Simulation | Cooling load | System can reduce up to 10% of cooling load |
| Zukowski et al. [25] | Computer simulation and experimental investigation | Cooling load | Experimental data shows that EAPHE reduces cooling energy load by 595 KWH |
| Maerefat et al. [26] | Mathematical model | 1. System performance 2. SC dimension 3. ECC dimension 4. Wettability factor | 1. Maintains air temperature of 27.31–31.1 °C 2. Air change number is found around 3 for the minimum radiation 200 W/m 3. Optimum air gap is 0.2 m 4. Optimum ECC length found 2 m for the present study 5. Evaporation can be enhanced when wetted surface area increases |
| Bansal et al. [27] | Thermal model | 1. Buried pipe length 2. Pipe diameter 3. $S/V$ ratio | 1. As no. of pipe increases, the length of pipe reduces for same cooling effect 2. Length of pipe reduces when BPF reduces 0.5–0.2 3. As $S/V$ ratio increases length of buried pipe decreases for same cooling effect |
| Pfafferott et al. [28] | Mathematical analysis | Length of tube and diameter | Pipe length up to 100 m and diameter around 250 mm are advisable |

**Table 1** (continued)

| Name of the author/title | Methodology | Parameters studied | Finding/remark |
|---|---|---|---|
| Alexandre et al. [29] | Mathematical and experimental study | Multiple layer heat exchanger configurations, depth | Multiple layer heat exchanger configurations reduces the large horizontal installation area compared to using single layer of pipe, floor depth 3 m, and the optimum space between layers is 1.5 m |
| Ozgener et al. [30] | Mathematical and experimental study | Depth of underground pipe | Predicted soil temperature at depth 5, 10, 20, and 300 cm was compared with experimental field result and percentage of error was 10.78, 10, 10.26, 14.95%, respectively |
| Su et al. [31] | Mathematical study | Air temperature and humidity | The maximum error of the air temperature is 1.4 °C and the maximum error of relative humidity is 10% |
| Vaz et al. [32] | Experimental | Transient behavior of temperature | The ducts are installed at depth of 1.6 and 0.6 m apart and result showed that the months of May and February were the best for heating and cooling, respectively |

and EAPHE system can replace the conventional AC system. It reduces the building energy load. A combination of passive and active cooling system has shown significant result in saving of energy and provides good thermal comfort without causing much pollution to the surroundings. The range of parameters studied as per researchers has been shown in Table 2.

As per previous literature survey shows that performance of earth-air-pipe heat exchanger reduces after some time of continuous operation because the heat rejected from the air reduces the moisture content of the soil surrounded by pipe hence reduces the heat transfer rate, and for effective performance of earth-air-pipe heat exchanger the heat transfer rate should be constant throughout its operation. Our objective of the research is to design the soil and pipe in such a way that the performance of EAPHE should not reduce after long run of operation.
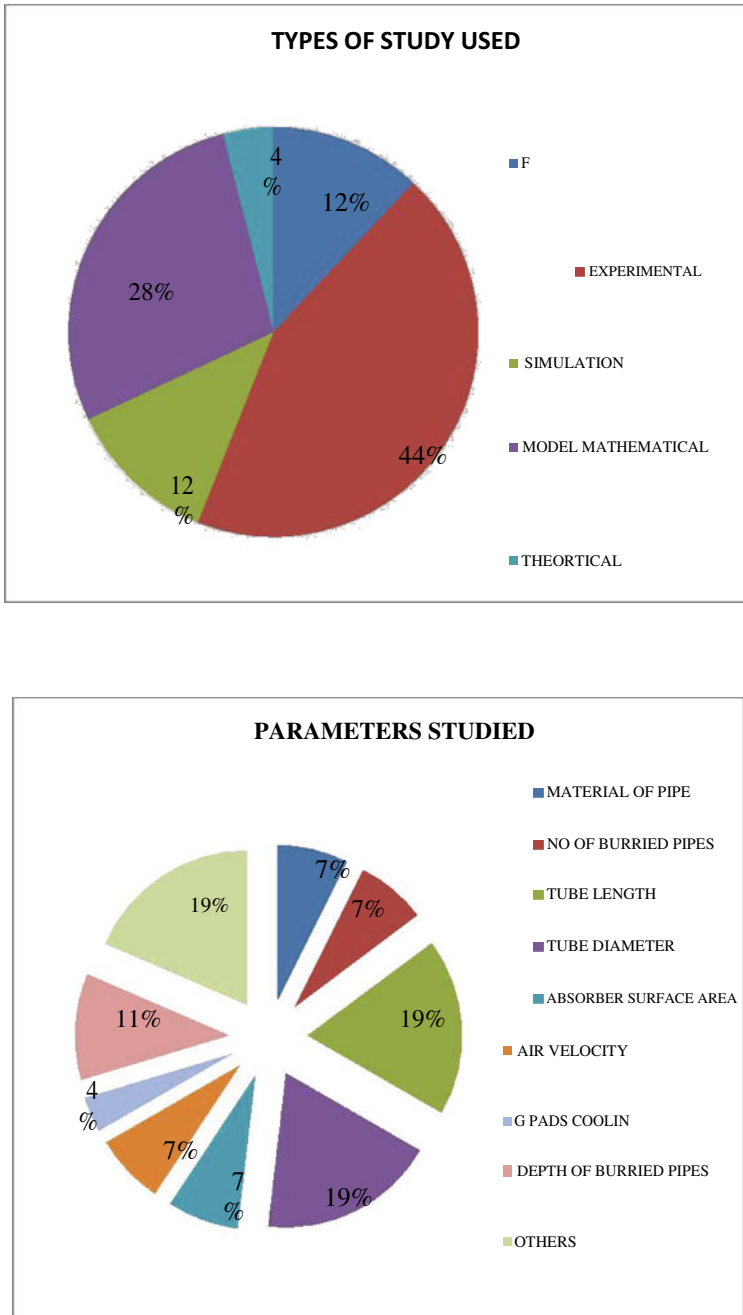
Fig. 6 Pie diagram shows types of study used and parameter studied for EAPHE

**Table 2** Range of parameter studies

| S. No. | Parameters | Range of data studied |
|--------|------------|----------------------|
| 1 | Material of pipe | PVC or steel |
| 2 | Tube length | 10–100 m |
| 3 | Tube diameter | 0.05–0.5 m |
| 4 | Air velocity inside pipe | 2–5 m/s |
| 5 | Depth of buried pipe | 1.5–3 m |

## 5 Conclusion

Because of growing demand of energy and increasing cost of electrical energy, it is required to reduce peak load as well save energy. Solar chimney and earth-air-pipe heat exchanger are the new approach to reduce the cooling load by means of passive ventilation and cooling which requires low energy to run the system. It was found that integrated system along with EAPHE gives more satisfactory results. If solar chimney can be used for optimum result, it reduces the electrical consumption by 10–20%. Solar chimney can be used at night by installing rotary turbine at the outlet of solar chimney to charge the battery. Performance of integrated SC-ECC system can be enhanced by increasing the evaporation rate of water and that can be achieved by adding some additives. It was found that EAPHE is the commonly used methods for cooling of heating purposes. The literature review shows that temperature drops to 12.6 °C which can be achieved and energy consumption gets reduced by 18% when coupled with air cooled condenser of 1.5TR window AC. EAPHE outlet can be directly connected to the AC suction to reduce the cooling load.

Future study can be done to study the effects of thermal properties of soil on the performance of EAPHE, and theoretical model should be developed to measure the effectiveness of EAPHE. Research can be carried out to increase the heat transfer rate of buried pipe to increase the cooling and ventilation effects.

## References

1. Sookchaiya T, Monyakul V, Thepa S (2010) Assessment of the thermal environment effects on human comfort and health for the development of novel air conditioning system in tropical regions. Energ Buildings 42(10):1692–1702
2. Chaturvedi AK, Bartaria VN (2015) Performance of earth tube heat exchanger cooling of air—a review. Int J Mech Eng Robotics Res 4(1):378–382
3. Sardana D, Kumar R, Patel S, Saini G (2015) Effect of parameters on performance of earth heat exchanger system(EAHE): a review. Int J Adv Technol Eng Sci 03(02):657–661
4. Li H, Yu Y, Niu F, Shafik M, Chen B (2014) Performance of a coupled cooling system with earth to air heat exchanger and solar chimney. Renew Energy 62:468–477
5. Bisoniya TS, Kumar A, Baredar P (2013) Experimental and analytical studies of earth air heat exchanger (EAHE) systems in India: a review. Renew Sustain Energy Rev 19:238–246

6. Chaturvedi AK, Bartaria VN (2014) Performance of earth tube heat exchanger cooling of air. Int J Sci Prog Res 06(02):103–111
7. Joen CT, Liu L, Paepe MD (2012) Comparison of earth-air and earth-ground tube heat exchanger for residential air conditioning purpose. In: International refrigeration and air conditioning conference at Purdue, pp 1–10, 16–19 July 2012
8. Dokkar B, Negrou B, Chenouff N, Settou N, Benmhid A (2012) Passive cooling telecom shelter using solar chimney with earth air heat exchanger. Recent Adv Energy Environ Biol Ecol 134–138
9. Woodson T, Coulibaly Y, Traore ES (2012) Earth air heat exchangers for passive air conditioning, case study. J Constr Developing Countries 17(1):21–32
10. Haghighi AP, Maerefat M (2014) Design guideline for application of earth to air heat exchanger coupled with solar chimney as natural heating system. Int J Low Carbon Technol Adv Access 1–11
11. Mishra R, Bansal V, Agrawal GD, Mathur J, Aseri T (2013) Transient analysis based determination of derating factor for earth air tunnel heat exchanger in summer. Energy Build 58:103–110
12. Bansal V, Mishra R, Agrawal GD, Mathur J (2009) Performance analysis of earth pipe air heat exchanger for winter heating. Energy Build 41:1151–1154
13. Chel A, Tiwari GN (2010) Stand-alone photovoltaic (PV) integrated with earth to air heat exchanger (EAHE) for space heating/cooling of adobe house New Delhi (India). Energy Conserv Manag 51:393–409
14. Ozgener L, Ozgener O (2010) An experimental study of the exergetic performance of an underground air tunnel system for greenhouse cooling. Renew Energy 35:2804–2811
15. Hepbasli A (2013) Low exergy modeling and performance analysis of greenhouse coupled to closed earth to air heat exchanger (EAHE). Energy Build 64:224–230
16. Maerefat M, Haghighi AP (2010) Passive cooling of building by using integrated earth to air heat exchanger and solar chimney. Renew Energy 35:2316–2324
17. Poshtiri AH, Gilani N, Zamiri F (2011) Feasibility study on using solar chimney and earth to air heat exchanger for natural heating of buildings. In: World renewable energy congress, 8–13 May 2011
18. Poshtiri AH, GIlani N, Zamiri F (2011) Comparative survey on using two passive cooling systems, solar chimney-earth air heat exchanger and solar chimney-evaporative cooling cavity. In: World renewable energy congress, 8–13 May 2011
19. Mishra R, Bansal V, Agarwal GD, Mathur J, Aseri T (2012) Thermal performance investigation of hybrid earth air tunnel heat exchanger. Energy Build 49:531–535
20. Kumar MA, Krishnaveni U (2015) Analysis of solar chimney with evaporative cooling cavity to improve indoor air quality. J Chem Pharm Sci 249–253
21. Bisoniya TS, Kumar A, Baredar P (2014) Parametric analysis of earth air heat exchanger system based on CFD modeling. Int J Power Renew Energy Syst 1:36–46
22. Tiwari GN, Singh V, Joshi P, Shyam D, Deo A, Prabhakant D, Gupta A (2014) Design of an earth air heat exchanger(EAHE) for climate condition of Chennai, India. Open Environ Sci 8:24–34
23. Dubey MK, Bhagoria JL, Atullanjewar A (2013) Earth air heat exchanger in parallel connection. Int J Eng Trend Technology 4(6):2463–2467
24. Miyazaki T, Akisawa A, Nikai I (2011) The cooling performance of a building integrated evaporative cooling system driven by solar energy. Energy Build 43:2211–2218
25. Zukowski M, Sadowska B, Sarosiek W (2011) Assessment of the cooling potential of an earth tube heat exchanger in residential buildings. In: Environmental engineering, 8th international conference, 19–20 May 2011
26. Maerefat M, Haghighi AP (2010) Natural cooling of stand-alone houses using solar chimney and evaporative cooling cavity. Renew Energy 35:2040–2052
27. Bansal V, Mathur J (2009) Performance enhancement of earth air tunnel heat exchanger using evaporative cooling. Int J Low Carbon Technol Adv Access 1–9

28. Pfafferott J (2003) Evaluation of earth to air heat exchanger with a standardized method to calculate energy efficiency. Energy Build 35:971–983
29. Jesus A, Alexandre JLC, Silva VB, Couto ND, Rouboa A (2013) Compact buried pipes system analysis for indoor air conditioning. Applied Therm Energy 51:1124–1132
30. Ozgener O, Ozgener L, Tester JW (2013) A practical approach to predict soil temperature variation for geothermal (ground) heat exchangers application. Int J Heat Mass Transf, 62:473–480
31. Su H, Liu XB, Ji L, Mu JY (2012) A numerical model of a deeply buried air earth tunnel heat exchanger. Energy Build 48:233–239
32. Vaz J, Sattler MA, Brum RS, Santos ED, Isoldi LA (2014) An experimental study on the use of earth air heat exchangers. Energy Build 72:122–131

# Review of Flows Past Arrays of Elliptic and Square Cylinders

Rajesh Kumar and N. K. Singh

**Abstract** The bodies which create the separation of flow for a certain area of their surface are known as bluff bodies. The bluff bodies can have sharp edges or these can also have a continuous surface. Vortex shedding is important phenomena related to bluff bodies which are present in both laminar and turbulent flows. When more than one cylinder or array of cylinders of the various cross sections is taken, then the results are highly different from the case of flow over one cylinder. Flows past arrays of cylinders of different cross-sectional areas are experienced in numerous engineering relevant. The several cylinders of cross-sectional areas such as of circular, square, ellipse, rectangular, and semi-circular can be organized in side-by-side, tandem or staggered layout. This paper evaluates the prevailing appreciation of the flows past arrays of cylinders with emphasis on the near-wake flow patterns, the transitional wake formation and conduct, Reynolds number influences and aerodynamic force coefficients. A principal attention is on the major numerical and experimental discourse that has noticeably since the last significant review of this issue. In this paper, a vigorous has been made to review the study of the work of various researchers for flows past arrays of elliptic and square cylinders, which will be helpful to perceive the various gaps in the research for conducting further new research work in this field.

**Keywords** Large eddy simulation · Vortex shedding · Reynolds number

## 1 Introduction

When the fluid flow is having a very low velocity, then the flow over the body is called an attached flow. If the velocity increases, the flow separates from the body, and shear layers or vortex sheets starts forming. A low-pressure region known as wake is also formed near the cylinder. When the Reynolds number increases

R. Kumar (✉) · N. K. Singh
National Institute of Technology, Kurukshetra, India
e-mail: rajesh29.er@gmail.com

beyond a certain limit, then these vortex sheets start to oscillate and collapse into small vortices. This phenomenon is given by Theodore von Karman, who discovered this pattern. Flow over arrays of cylinders has many applications in industries that include nuclear rods, offshore structures, heat exchangers, boilers, condensers, construction of bridges, etc. To achieve the analysis of the above-mentioned, one of the foremost processes is the simulation of flow over arrays of cylinders not only for the purpose of heat transfer but also for wake interaction and vortex shedding behind the cylinders. Flows over circular and elliptical cylinders are an important topic of research in marine engineering. Many offshore structures in marine engineering have a cylindrical cross section, such as risers and pipelines. The uses of these pipelines and other structures have increased and will increase further due to demand for oil. It is important to understand the flow around elliptical and circular cylinders to calculate the forces acting on them. Separation occurs over a large part of the surface of a bluff body, which creates a high-pressure drag and a large wake region behind the bluff body. Bluff body wakes involve complex phenomenon, in which three shear layers interact with each other in the same problem: a boundary layer, a free shear layer, and a wake. The wake of a bluff body is quite complex and few patterns can be characterized as periodic, vortex shedding, and a von Karman vortex street. The relationship between the drag coefficient, pressure, and vortex shedding frequency, and the size of the wake region is complex and requires improved insight, for 3-D bluff bodies. This increased physical understanding will help engineers in the prevention of flow-induced vibrations. Despite the fact that two-dimensional and three-dimensional instabilities in wakes have been a subject of interest to engineers and scientists for many years, an understanding of the flow behind a bluff body is a great challenge.

## 1.1 Cylinders Arrangements

When flow passes over the array of cylinders, then flows interference occurs which is the result of various parameters such as the distance between the adjacent cylinders and the angle of the flow. In the practical observance, staggered arrangement of the cylinders is most common because mostly the flow over the cylinders is not accurately perpendicular to them. In this arrangement, a certain angle is used to create a position of the geometry. The various arrangements of the different cross-sectional cylinders can also be made in alternate rows and columns to find out the various flow characteristic changes occurring due to flow interferences between the cylinders. These arrays of cylinders of various cross sections are used in practical life, such as in the construction of buildings, bridges, and pillars. When a fluid flows across these

**Fig. 1** Two square cylinders in cross-flow: **a** tandem configuration; **b** side-by- side configuration; and **c** staggered configuration
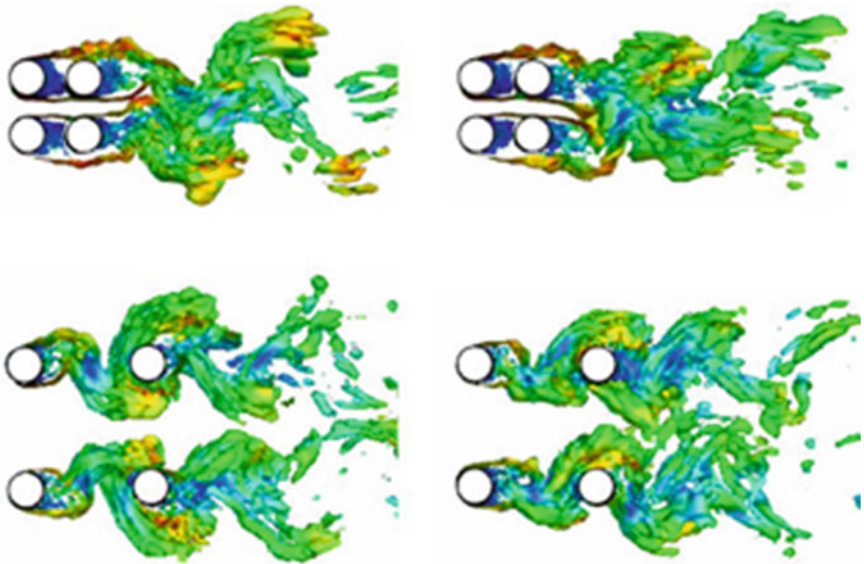


**Fig. 2** Vortex formations for four circular cylinders **a** upward deflected $L/D = 1.5$, **b** downward deflected $L/D = 1.5$, **c** anti-phase $L/D = 3.5$, and **d** in-phase $L/D = 3.5$ ($L/D$ is spacing ratio) [1]

cylinders, various characteristics of flowing fluid come into picture which affects these constructions. So, these are necessary to be studied to have better and safer designs for various engineering applications. There are various arrangements of the cylinders, whether they are of circular, elliptical, or square cross sections. These can be arranged in various forms such as in tandem placement, side-by-side placement and staggered placement of cylinders (Figs. 1 and 2).

## 2 Literature Review

### 2.1 *Review of Flow Past Array of Elliptic Cylinders*

Elliptic cylinders are considered as a basic form since it can be altered into a circular and a flat plate by varying the axis ratio. Also, an elliptic cylinder is sometimes preferred over circular cylinders due to its small wake region and drag coefficient values than that of the circular one. There had been a few numerical simulations of flow past elliptic cylinders. Flow over arrays of cylinders is a complicated phenomenon and had been a research topic for many studies of elliptical as well as of circular cylinders. Ota et al. [2] conducted the research on two elliptical cylinders which were tandemly arranged and investigated the heat transfer study. The axis ratio taken was 1:2, the fluid selected for the study was air and the Reynolds number taken was ranging from 15,000 to 80,000 which were based on the major axis length. Castiglia et al. [3] investigated the flow over an array of elliptic cylinders. The modeling of the flow was done by large eddy simulation (LES). The study of the flow over tandem cylinder arrangement of an elliptic cross section was done by using fluid which was non-Newtonian. They used the Smagorinsky model for the 3-D simulation. It was found out that vortex shedding does not start from the first cylinder, free shear layer separates from the surface and attaches to the downstream cylinder and again it gets separated and does not roll up into vortices, but attaches to the surface of the third cylinder. After the third cylinder vortex shedding starts, formed vortices impinge on the next downstream cylinder. As we move downstream, the vortex shedding increases and by the power spectral study it was shown that the peak of vortex shedding increases. They had also shown that in the direction of flow, the turbulence intensity increases because of the presence of the cylinder and due to vorticity transport from the surface of the cylinders.

Ibrahim and Gomaa [4] investigated experimentally and numerically the heat transfer characteristics of flow over arrays of the elliptical cylinder in cross-flow in the turbulent regime. The range of the Reynolds number which was used for the study was ranging from 5600 to 40,000, minor to major axis ratio used for the study were 0.25, 0.33, 0.5, and 1, and angle of attack used for the study was 0 to 150°. In their study, it was found that average Nusselt number for the angle of attack of 90° was higher than the angle of attack of 0° and 30°, also for the angle of attack of 0° and 30° the value of friction was lower than the values of friction at other angles. Lam and Zou [1] had experimentally and numerically studied the flow over circular cylinder arrays at the spacing ratio of 1.5, 2.5, 3.5, and 5.0 in subcritical flow regime from 11,000 to 20,000. The LES was used for the simulation at Reynolds number of 15,000. The bistable flow was found in the study at a spacing ratio of 1.5 and it was confirmed experimentally. At a spacing ratio of 3.5, the flow pattern was different and two phases was found out that was anti-phase vortex shedding and in-phase vortex shedding. The spacing ratio and the Reynolds number affect the vortex formation length. Lin et al. [5] numerically investigated the laminar flow

characteristic of flow over the diamond arrangement of cylinder arrays. The simulation was carried out in three dimensions, the Reynolds number used for the study was 200, and the spacing ratio used was ranging from 1.2 to 5. The flow pattern varied from a single bluff body flow behavior to vortex impingement on the cylinder. The transition of the flow occurs at the critical spacing ratio of 3.0 which causes the lift force to increase drastically.

Yu et al. [6] conducted the numerical simulation to find the effect on the drag force of flow over circular arrays of cylinders. A 2-D simulation was carried using (RANS/LES) model. Nejat et al. [7] studied the effect of various numbers, ratios, and the distance between the cylinders on the fluid coefficients. Chatjigeorgion and Mavrakos [8] gave a result of the scattering of waves by the arrangement of the array of elliptic cross-sectional cylinders. Alawadhi [9] conducted the study on the laminar forced convection flow around an elliptic cylinder array in an in-line configuration with some angle of inclination. The angles of inclination used were 0°, 22.5°, 45°, 67.5°, and 90°. The finite element method was used for the solution of the governing equations. The Reynolds number used for the study was ranging from 125 to 1000. Nair and Sengupta [10] numerically investigated the flow past elliptic cylinder using DNS and compared the results for Reynolds number of 3000. In their study, they found that the vortices which were released from the surface were strong and in alignment and depends on the angle of attack taken for the study. Kim et al. [11] corrected Darcy's law non-linearly for the flow over array of elliptic cylinders and found coefficients which are dependent on the outer structure of the body and concluded that little change in the geometry does not affect the flow coefficients. Woods et al. [12] showed the results for the flow over arrays of elliptic cylinders by using the different aspect ratios in the form of a summary. Berbish [13] investigated the change in the flow and heat transfer characteristics over four elliptic cylinders in a staggered configuration in cross-flow. Peng et al. [14] studied the flow behavior for two elliptic cylinders placed in side-by-side configuration and analyzed the effect of various flow parameters on the cylinders. Mittal and Balachander [15] did the direct numerical simulation of the flow over elliptic cylinders and compared the results with the values from the experiments and found satisfactory matched parameter (Fig. 3).

## 2.2 Review of Flow Past Array of Square Cylinders

Square geometries are observed in various engineering applications and can create complex flow patterns around them. Rodi [16] had made a comparison of large eddy simulation (LES) and Reynolds-averaged Navier–Stokes equation (RANS) for the flow over bluff bodies. The vortex shedding over square cross-sectional cylinders was observed. Agrawal et al. [17] investigated the flow over the side-by-side square cylinders and found the effect of the gap ratio on the incident flow. Burattini and Agrawal [18] showed that a continuous and repeated pattern of the amplitudes occurs when the flow over a set of square cylinders in side-by-side
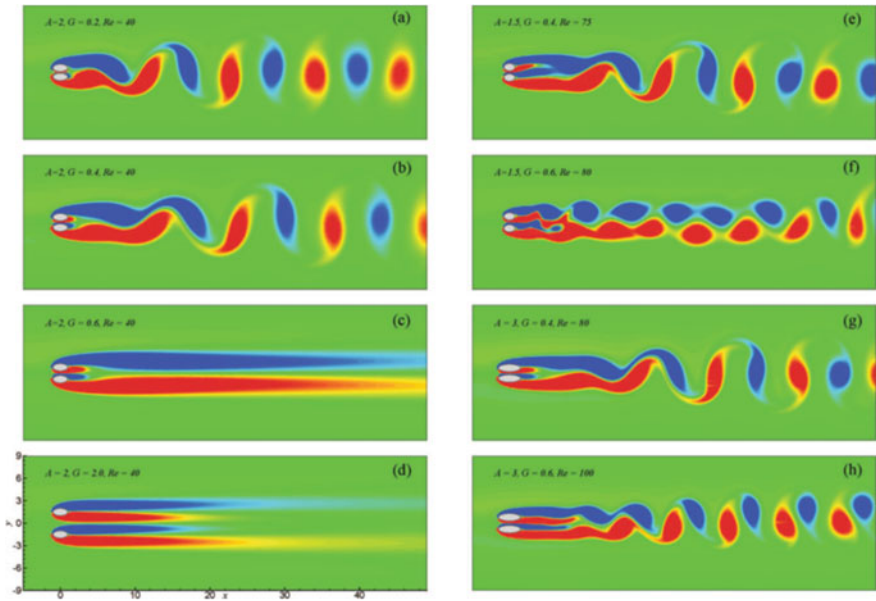
**Fig. 3** Illustrating dependence of vorticity contours on the gap ratio ($G$) for two side-by-side placed elliptic cylinders [14]

configuration was made on the surface of the cylinders. A numerical simulation of the 3-D flow over two similar square cylinders arranged in staggered configuration was done.

Niu and Zhu [19] observed the difference in the correlation coefficients for the above-placed and bottom-placed cylinders in the flow stream. Bao et al. [20] did the computations on the six square cylinders placed in the inline arrangement with the help of the finite element technique. Kumar and Vengadesan [21] used the LES technique for the study of flow over long square cylinders of infinite length having side-by-side configuration. The study of various flow characteristics was conducted. Abbasi et al. [22] investigated numerically flow around three inline square cylinders with the help of Lattice Boltzmann method and found that the flow forces can be decreased with the help of different combinations of gap spacing (Fig. 4).

Islam et al. [23] investigated the flow over four square cylinders arranged in a rectangular manner with the help of Lattice Boltzmann Method (LBM) and established that the results are satisfactory with the experimental values. Kim et al. [24] did the study of the flow over two square cylinders arranged in a tandem configuration. Sewatkar et al. [25] investigated both numerical and experimental methods flow over six cylinders of square cross section arranged with in-line configuration and gave the results for lift and drag coefficients. Liu et al. [26] investigated various characteristics of flow by using the subcritical value of Reynolds number for flow over the array of four square cylinders. Various values of
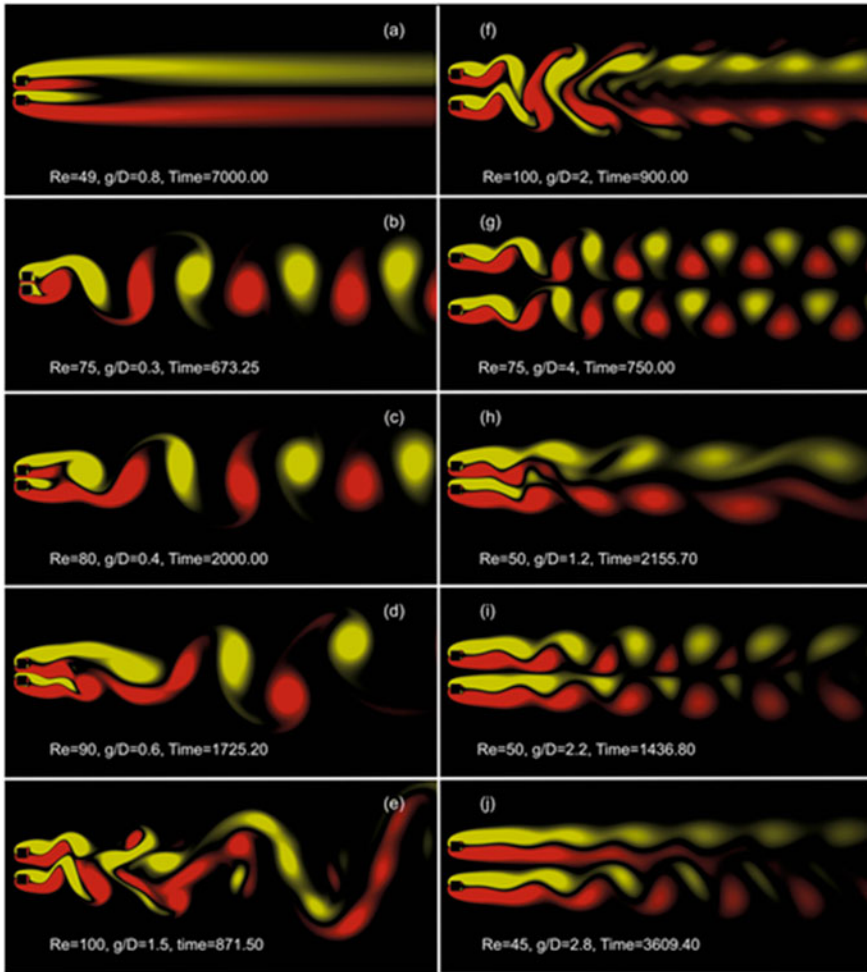
**Fig. 4** Formation of different wake patterns for two side-by-side placed square cylinders [18]

gap ratios and the angle of incidence were taken to search for the effect of these different values on flow parameters. Liu and Chen [27] observed the hysteresis in the flow over two square cross-sectional cylinders arranged in tandem configuration and found the effect of hysteresis on the various flow parameters. Chatterjee et al. [28] studied the numerical simulation of flow over a row of square cross-sectional cylinders arranged at various separation ratios. The difference in the frequency at higher and lower ratios of separation was observed. Ehsan et al. [29] did the investigation of the fluid flow over two square cylinders arranged in tandem. It was found that there is a distinction in the separation of leading edge when thin and thick fluids passed over the cylinders. Ma et al. [30] explored wake interactions
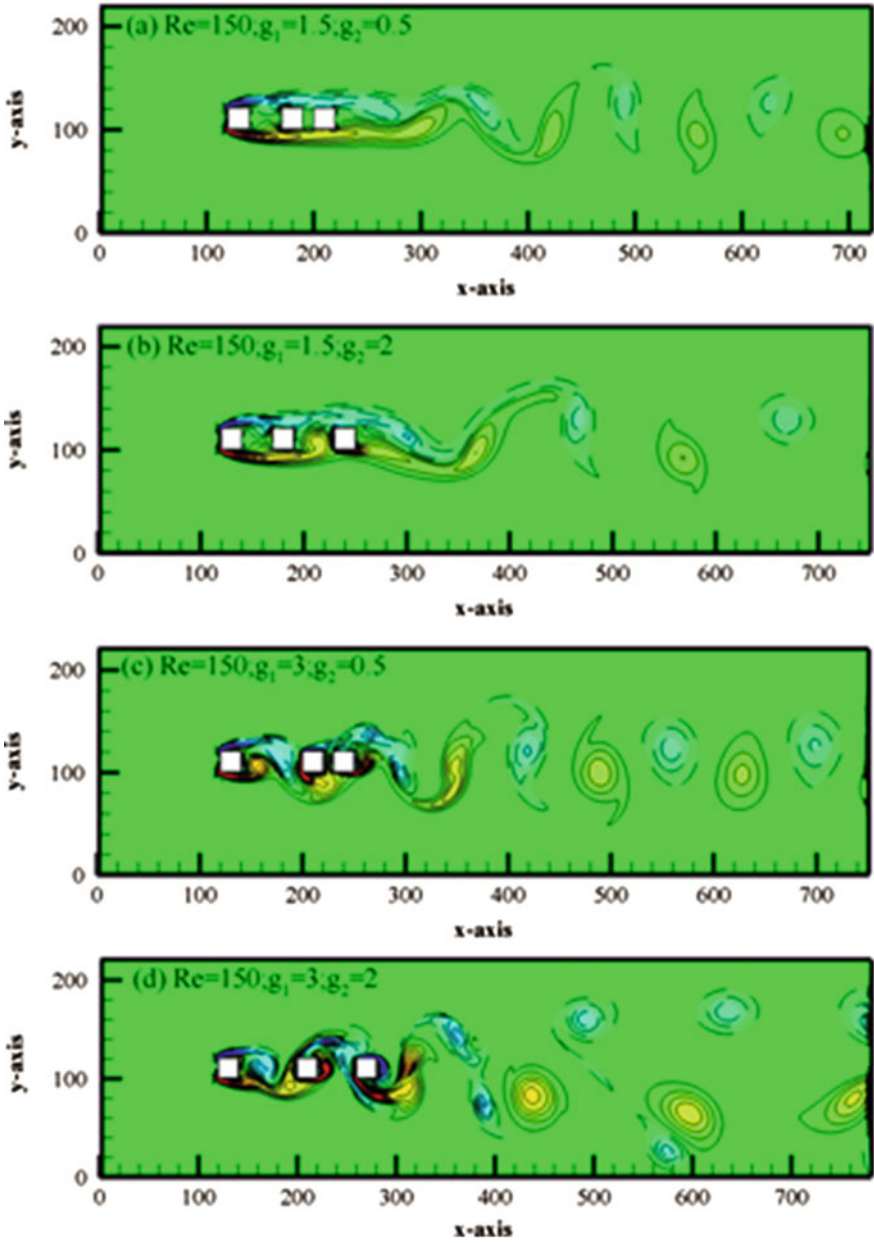
**Fig. 5** Vortex formations in three inline square cylinders with different gap spacing [22]

between two square cylinders by using direct numerical simulation (DNS) at small values of the Reynolds number. A certain range of the distance between the cylinders was taken and various sequences of wakes were observed. Islam et al. [31] analyzed 17 square cylinder array with the help of the lattice Boltzmann method (LBM) for 2-D. The changes caused by the different values of the distance between the cylinders and various values of the Reynolds number were noticed. Various graphs using different parameters were also obtained. It was observed that the primary important parameter was Reynolds number and the distance between the cylinders is secondary. Rahman et al. [32] analyzed three square cylinders placed in a side-by-side configuration at various values of the Reynolds number and the disparate distance between the cylinders. They showed that the patterns of wake were different for the disparate distance between the cylinders. Zdravkovich [33] simulated for the steady flow over different arrangements of cylinders. It was found that the vortices produced for an array of cylinders were different from that produced by one cylinder at a particular Reynolds number. Chatterjee and Gupta [34] simulated for the flow past over square cylinders in a staggered configuration. It was observed that when the distance between the cylinders was minor, then the vortex shedding is small and for high values of the distance between the cylinders, vortex shedding is significant (Fig. 5).

# 3 Conclusion

Research work for flow past array of cylinders had taken place on a large scale, but due to the reason of complex flow situations which occur in practical life, it will be always a motivating field of research for the coming generations. A large number of observations can be made in this area of research. The values of different Reynolds number can be used for the study of various flow parameters. The various arrangements of the array of cylinders can be formed to study the difference in the flow characteristics when the flow passes over the various cross-sectional cylinders. The study of important phenomena such as vortex shedding and wake formation is very beneficial in the design of various useful and desired structures for having a better future of the coming generations. Various researchers investigated array of cylinders with different configuration and of various cross-sectional cylinders. They found different observation by simulation technique using various different methods such as LES, LBM, and RANS and made many conclusions from the results which they got which are very helpful in the technology development and in design industries of the aerodynamic field and ocean engineering. The various fluid flow parameters were studied by the researchers on the arrays of cylinders which are supportive in the design of heat exchangers, which can be designed by the help of study of simulation of fluid passing over the tube bundles of various cross sections. The research in this field is very significant for the future designs of various technical aspects.

# Refrences

1. Lam K, Zou L (2009) Experimental study and large eddy simulation for the turbulent flow around four cylinders in an in-line square configuration. Int J Heat Fluid Flow 30(2):276–285
2. Ota T, Nishiyama H, Kominami J, Sato K (1986) Heat transfer from two elliptic cylinders in tandem arrangement. J Heat Transfer 108(3):525–531
3. Castiglia D, Balabani S, Papadakis G, Yianneskis M (2001) An experimental and numerical study of the flow past elliptic cylinder arrays. Proc Inst Mech Eng 215(Part C):1287–1301
4. Ibrahim TA, Gomaa A (2009) Thermal performance criterion of elliptic tube bundles in cross flow. Int J Therm Sci 48(11):2148–2158
5. Zou L, Lin YF, Lu H (2011) Flow patterns and force characteristics of laminar flow past four cylinders in diamond arrangement. J Hydrodyn 23(1):55–64
6. Yu LH, Zhan JM, Li YS (2013) Numerical investigation of drag force on flow through circular array of cylinders. J Hydrodyn 25(3):330–338
7. Nejat A, Mirzakhalili E, Aliakbari A, Niasar MSF, Vahidkhah K (2012) Non-Newtonian power-law fluid flow and heat transfer computation across a pair of confined elliptical cylinders in the line array. J Non-Newton Fluid Mech 171:67–82
8. Chatjigeorgiou IK, Mavrakos SA (2010) An analytical approach for the solution of the hydrodynamic diffraction by arrays of elliptical cylinders. Appl Ocean Res 32(2):242–251
9. Alawadhi EM (2010) Laminar forced convection flow past an in-line elliptical cylinder array with inclination. J Heat Transf 132(7):071701–0171702
10. Nair MT, Sengupta TK (1997) Unsteady flow past elliptic cylinders. J Fluid Struct 11(6): 555–595
11. Kim J, Lee J, Lee KC (2001) Nonlinear correction to Darcy's law for a flow through periodic arrays of elliptic cylinders. Phys A Stat Mech Appl 293(1–2):13–20
12. Woods JK, Spelt PDM, Lee PD, Selerland T, Lawrence CJ (2003) Creeping flows of power-law fluids through periodic arrays of elliptical cylinders. J Non-Newton Fluid Mech 111:211–228
13. Berbish NS (2011) Heat transfer and flow behavior around four staggered elliptic cylinders in cross flow. Heat Mass Transf 47:287–300
14. Peng YF, Sau A, Hwang RR, Yang WC, Hsieh C-M (2012) Criticality of flow transition behind two side-by-side elliptic cylinders. Phys Fluids 24:034102
15. Mittal R, Balachandar S (1996) Direct numerical simulation of flow past elliptic cylinders. J Comput Phys 124:351–367
16. Rodi W (1997) Comparison of LES and RANS calculations of the flow around bluff bodies. J Wind Eng 69–71:55–75
17. Agrawal A, Djenidi L, Antonia RA (2006) Investigation of flow around a pair of side-by-side square cylinders using the lattice Boltzmann method. Comput Fluids 35:1093–1107
18. Burattini P, Agrawal A (2013) Wake interaction between two side-by-side square cylinders in channel flow. Comput Fluids 77:134–142
19. Niu J, Zhu Z (2006) Numerical study of three-dimensional flows around two identical square cylinders in staggered arrangements. Phys Fluids 18:044106
20. Bao Y, Wua Q, Zhou D (2012) Numerical investigation of flow around an inline square cylinder array with different spacing ratios. Comput Fluids 55:118–131
21. Shyam Kumar MB, Vengadesan S A study of the influence of gap ratio on turbulent flow past two equal sized square cylinders placed side by side. In: Proceedings of the 37th national & 4th international conference on fluid mechanics and fluid power, 16–18 Dec 2010, IIT Madras, Chennai, India
22. Abbasi WS, Islam SU, Rahman H, Manzoor R (2018) Numerical investigation of fluid-solid interaction for flow around three square cylinders. AIP Adv 8:025221
23. Islam SU, Zhou CY, Ahmad F (2009) Numerical simulations of cross-flow around four square cylinders in an in-line rectangular configuration. Int J Mech Mech Eng 3(9):1138–1147

24. Kim MK, Kim DK, Yoon SH, Lee DH (2008) Measurements of the flow fields around two square cylinders in a tandem arrangement. J Mech Sci Technol 22:397–407
25. Sewatkar CM, Patel R, Sharma A, Agrawal A (2012) Flow around six in-line square cylinders. J. Fluid Mech 710:195–233
26. Liu M, Xiao L, Yang L (2015) Experimental investigation of flow characteristics around four square cylinder arrays at subcritical Reynolds numbers. Int J Naval Architect Ocean Eng 7:906–919
27. Liu C-H, Chen JM (2002) Observations of hysteresis in flow around two square cylinders in a tandem arrangement. J Wind Eng Ind Aerodyn 90:1019–1050
28. Chatterjee D, Biswas G, Amiroudine S (2010) Numerical simulation of flow past row of square cylinders for various separation ratios. Comput Fluids 39:49–59
29. Ehsan I, Mohammad S, Mohammad Reza N, Ali J, Sharifi Tashnizi E (2013) Power law fluid flow passing two square cylinders in tandem arrangement. J Fluids Eng 135:061101
30. Ma S, Kang C-W, Arthur Lim T-B, Wu C-H, Tutty O (2017) Wake of two side-by-side square cylinders at low Reynolds numbers. Phys Fluids 29:033604
31. Islam SU, Nazeer G, Ying ZC (2018) Numerical investigation of flow past 17-cylinder array of square cylinders. AIP Adv 8:065004
32. Rahman H, Sham UI, Zhou CY, Kiyani T, Saha CS (2015) On the effect of Reynolds number for flow past three side-by-side square cylinders for unequal gap spacing's. KSCE J Civil Eng 19:233–247
33. Zdravkovich M (1977) Review of flow interference between two circular cylinders in various arrangements. J Fluid Eng 99:618–633
34. Chatterjee D, Gupta SK (2015) Convective transport around rows of square cylinders arranged in a staggered fashion at moderate Reynolds number. Num Heat Transf Part A Appl 68:388–410